XXIII Russian Particle Accelerator Conference

RuPAC'2012

September, 24 - 28, 2012

Saint-Petersburg, Russia

XXIII Russian Particle Accelerator Conference

RuPAC'2012

September, 24 - 28, 2012
Saint-Petersburg, Russia

PREFACE

The XXIII Russian Particle Accelerator Conference (RuPAC 2012) was held in Petergof, Saint-Petersburg, September 24 –28, 2012. It was organized by Saint-Petersburg State University (SPbSU), Efremov Scientific Research Institute of Electrophysical Apparatus (NIIEFA), Joint Institute for Nuclear Research (JINR), Budker Institute of Nuclear Physics SB RAS (BINP), Scientific Council for Accelerators of Russian Academy of Sciences, State Atomic Energy Corporation ROSATOM, MONOMAX PCO and was hosted at faculty of Applied Mathematics and Control Processes of Saint-Petersburg State University. The Conference was supported in part by the Russian Foundation for Basic Research. The RuPAC scope provided a forum for exchange of new information and discussion in the field of acceleration science and engineering: particle beam physics, new projects of particle colliders, new accelerator designs and modernization of existing accelerator facilities for basic researches and applications (having an emphasize on medical applications). The scientific program covered the following topics:

- Modern trends in accelerators
- Colliders
- Particle dynamics in accelerators and storage rings, cooling methods, new methods of acceleration
- High intensity cyclic and linear accelerators
- Heavy ions accelerators
- Synchrotron radiation sources and free electron lasers
- Magnetic and vacuum systems, power supplies
- Superconducting accelerators and cryogenics
- RF power structures and systems
- Control and diagnostic systems
- Ion sources and electron guns
- Medical and industrial applications
- Radiation problems in accelerators

More than 260 participants took part at the RuPAC 2012 from 19 countries and 71 organizations. At the conference was organized an Industrial Exhibition, in which 5 companies took part. The Accelerator Prizes for young physicists and engineers for the best work presented at the Conference were nominated. The First Prize was awarded to Yaroslav Getmanov (BINP) who presented the paper “Longitudinal Stability of ERL with Two Accelerating RF Structures” and The Second Prize – to Nickolay Azaryan (JINR) presented the paper “Dubna-Minsk Activity on the Development of 1.3 GHz Superconducting Single-Cell RF-cavity” and to Konstantin Nikiforov (SPbSU) with the paper “Non-gated Field Emission Array as Low-Energy Electron Source: Experiment and Simulation”. The Prizes were awarded by the decision of the Selection Committee formed at the Conference and chaired by academician Sergey Ivanov (IHEP, Protvino).

Processing of the electronic files of the contributions, during and after the Conference was fulfilled by Maxim Kuzin (BINP). The final version was published at the JACoW site.

The success of the RuPAC 2012 is thanks to the efforts of the Program and Organizing Committees, the local staff of the host University-SPbSU, and, of course, to all of the participants.

Dmitri Ovsyannikov, Chair of Organizing Committee of the RuPAC-2012
Igor Meshkov, Co-Chair of Program Committee

Contents

Program Committee

Chairman: A. Skrinsky (BINP SB RAS)

Co-Chairman: I. Meshkov (JINR)

Secretary: E. Akhmanova (JINR)

- N. Alexeev (ITEP)
- S. Ivanov (IHEP)
- E. Kotina (SPbSU)
- L. Kravchuk (INR RAS)
- E. Levichev (BINP SB RAS)
- D. Ovsyannikov (SPbSU)
- V. Parkhomchuk (BINP SB RAS)
- V. Romanov (IPPE)
- B. Sharkov (ITEP/FAIR)
- G. Shirkov (JINR)
- M. Vorogushin (NIIEFA)

Organizing Committee

Chairman: D. Ovsyannikov (SPbSU)

Co-Chairman: O. Filatov (NIIEFA)

Co-Chairman: G. Shirkov (JINR)

Scientific Secretary: E. Kotina (SPbSU)

- N. Alexeev (ITEP)
- S. Andrianov (SPbSU)
- N. Egorov (SPbSU)
- A. Feschenko (INR RAS)
- Yu. Gavrish (NIIEFA)
- V. Glukhikh (NIIEFA)
- L. Kravchuk (INR RAS)
- M. Kuzin (BINP SB RAS)
- O. Lebedev (IHEP)
- E. Levichev (BINP SB RAS)
- V. Matveev (INR RAS)
- I. Meshkov (JINR)
- O. Patarakin (ROSATOM)
- B. Sharkov (ITEP/FAIR)
- Yu. Shatunov (BINP SB RAS)
- A. Strokach (NIIEFA)
- G. Trubnikov (JINR)
- M. Vorogushin (NIIEFA)








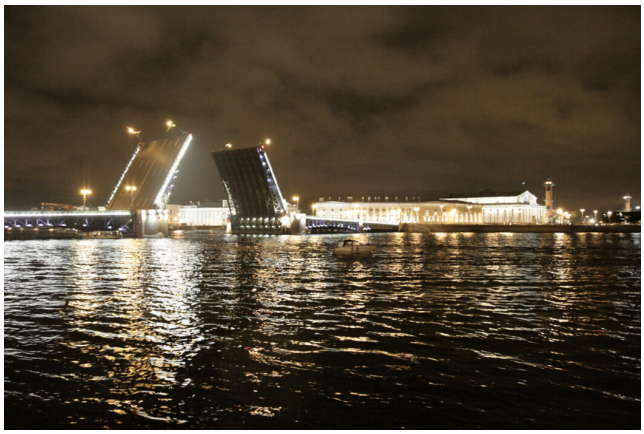


ООО "Марафон"
Управляемые источники тока
National Instruments


SAMSUNG






The Winner!




Photos by A.Sharley and M.Kuzin

ACCELERATORS: ENGINES FOR TRAVERSING A LARGE AND OFTEN DIFFICULT LANDSCAPE*

Andrew M. Sessler
Lawrence Berkeley National Laboratory, Berkeley, CA 94720, USA
Dedicated, with fond memories, to Dieter Moehl and Andre Lebedev

Abstract

The many applications of accelerators are presented, with pictures and comments, upon the machines and the results obtained with them. Attention is then given to possible future applications, and some remarks are made on the future development of accelerators. In short, the presentation should serve as an introduction to the Conference itself where there shall be many – wonderfully detailed – contributions to all of this.

INTRODUCTION

In this paper I will try to show – all in only five pages – the breadth of accelerator types and, more importantly, the many uses (applications) of particle accelerators. For a number of decades, starting in about 1930, accelerators were used primarily for nuclear and then high-energy physics. This wasn't exclusively true, for even in the 1930's Lawrence was employing his cyclotrons for medical purposes, but it was almost exclusively true.

However, now-a-days accelerators are widely used for many different purposes. Essentially all these accelerators are of a type particularly chosen for the application and specially designed to the particular use. This short report can't possibly go into the details --- which is the heart of the subject (and the topic of many contributions at this Conference) – but can only show the general sweep and extent of these applications. Nevertheless, it should prove interesting, especially to the many deep into the details of some particular application, to look broadly and see how extensive is the range of application of particle accelerators.

TYPES OF ACCELERATORS

There are some 30,000 accelerators in the world and these are of the six major types, or small modifications of these types. That is there are electrostatic machines, cyclotrons, linacs, betatrons, synchrotrons or colliders. We are all rather familiar with modern versions of these machines, but perhaps not many of us have looked back at their humble beginnings. In Fig. 1 is shown the very beginning; namely the first electrostatic machine that was able to fulfill Rutherford's dream, which was to achieve artificial radioactivity.

Looking to the future – and surely – the future will contain ever-more of the types mentioned; there may well be two very different accelerators. The first is an accelerator of muons. True, this may be a linac or a synchrotron at its heart, and culminate in a collider, but the handling of the short lifetime muon would seem to justify considering this a new type of accelerator. Muons are diffusely produced in hadron collisions, so they must be captured and "cooled" into a beam; a non-trivial task. A section of the proposed 2D cooling channel is incorporated in the experimental demonstration of cooling: Muon Ionization Cooling Experiment (MICE). This is an international collaboration and is underway at the Rutherford-Appleton Laboratories.

The second is the use of lasers and plasmas as accelerators. Effort is this direction has gone on for decades, and 1 GeV of acceleration has been achieved, but much still remains to be accomplished before the method produces a practical accelerator. Two methods are under particular study; a wakefield accelerator at SLAC and a laser/plasma accelerator at LBNL. Of course there is activity in many other places.

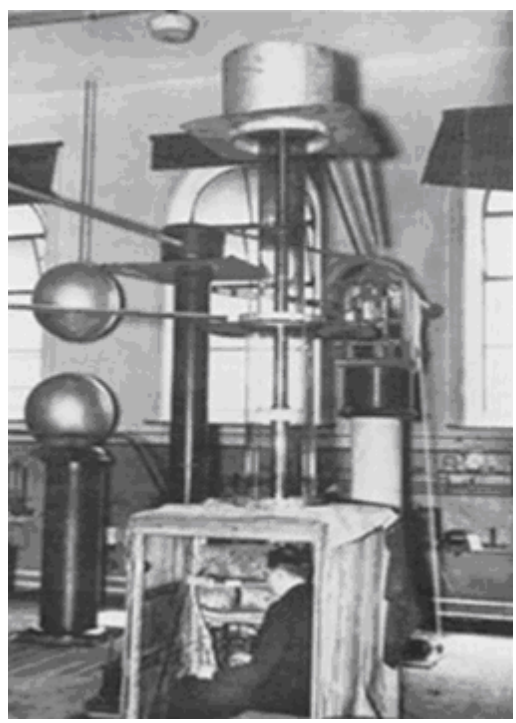

Figure 1: The first electrostatic accelerator. The original Cockcroft-Walton installation at Cavendish Laboratory in Cambridge. Walton is sitting in the observation cubicle (experimental area) immediately below the acceleration tube.

* This work was supported by the Director, Office of Science, and Program Office of High Energy Physics, of the U.S. Department of Energy under Contract No. DE-AC02-05-H11231.

APPLICATIONS OF ACCELERATORS

In the remainder of this paper – the largest part of the paper – I will describe the various applications; i.e., uses of accelerators. The first to consider, are the uses in basic science that was, of course, the original driving force that led to the development and ever-improvement of accelerators. However, as we shall note, there are really a great many diverse uses for the very many accelerators in the world.

High-Energy and Nuclear Physics

In high-energy physics the leading machine is shown in Fig. 2, which is a view of the LHC at CERN, where the Higgs was discovered just this year. Fig. 3 is an overview of RHIC at Brookhaven, the largest machine for nuclear physics, where many interesting things are being seen in relativistic heavy ion collisions.

Of course these needs are not ending, and effort is already going into improving the luminosity – and even thinking of increasing the energy – of the LHC, and also the development of electron collisions with ions at RHIC. I don't have space to describe the many neutrino experiments that are searching for effects beyond the Standard Model. Nor can I describe the work on anti-hydrogen and on many other aspects of pure science.

Figure 2: The Large Hadron Collider (LHC), where the Higg's was just discovered.

Figure 3: The Relatively Heavy Ion Collider (RHIC).

Synchrotron Radiation Source

Sources of synchrotron radiation, electron storage rings and free electron lasers (FEL), have become vital research tools in surface science, chemistry, biology and drug design for medicine. There are more than 100 dedicated facilities, serving about 100,000 scientists in more than 20 different countries. In Fig. 4 is shown the large European Synchrotron Radiation Facility. Even larger facilities exist in the US and in Japan, while ever-better ones are under construction. The present generation (4^{th}) of sources includes FELs such as the SLAC Facility shown in Fig. 5. This facility produces coherent radiation at 1.5 Angstroms (0.15 nm). FELs are now under construction, or already operating, in a range of wavelengths and in a number of different countries.

Figure 4: The European Synchrotron Radiation Facility (ESRF). The doors were open for users in 1994.

Figure 5: The SLAC site showing the LCLS, a 1.5 Angstrom Free Electron Laser (FEL).

Spallation Neutron Sources

Spallation sources are a complement to synchrotron sources. A number of smaller machines have been in existence for some time. The first of the large new machines, linac based, is the Spallation Neutron Source at Oak Ridge, which is shown in Fig. 6. A similar facility is at JPARK in Japan, and ones are under construction in China and in Sweden (a European Project), while the cyclotron based Swiss facility (SINQ) is quite competitive. Typically, 1 GeV protons are used to spall a nucleus and produce 30 neutrons. The neutrons are used to study magnetism, high-temperature superconductors, biological structures, etc.

Fig. 6: A view of The Spallation Neutron Source (SNS).

Isotope Production and Cancer Therapy

Although reactors are the primary source of isotopes for short-lived isotopes medical imaging, near-by accelerators play an important role in production of isotopes (that are not the daughters of a longer lived mother).

A very important role is in the X-Ray treatment and the external particle beam treatment of cancer. Almost every major hospital has an accelerator produced – rotating on a gantry – source of X-Rays. In fact there are more than 15,000 of these devices installed. A typical treatment facility is shown in Fig. 7. Because there are distinct medical advantages to treatment with heavy particles an ever-increasing number of facilities have been constructed and are, already, treating patients. Ion beams, up to carbon, are even more effective (i.e., less peripheral damage associated with killing a tumor) and facilities with ions are operating in Japan since 1994 and more recently in Europe.

Figure 7: The Varian Medical System for treating a patient with x-ray produced by a high-energy electron beam.

National Security

As far as I know the first use of accelerators in National Defense was during WWII. The Americans had a betatron at Los Alamos to help in designing the first atomic bomb and the British used a betatron to X-Ray Nazi un-exploded bombs dropped on England. (It is interesting that the betatron, just after the war was converted into the very first demonstration of a synchrotron.) Also, of course, it was on the Berkeley 184 inch cyclotron that electromagnetic separation of uranium was developed. This then led to more than 1,000 Calutrons through which passed all the material used in the Hiroshima bomb.

In recent years, accelerators are still used to study nuclear bomb implosions as shown in Fig. 8. Of more pressing concern, is securing borders against terrorist actions. This has become a very large industry, with many companies producing scanners of many different types. See Fig 9.

Figure 8: The Dual Axis Radiological Hydrodynamics Test Facility (DARHT).

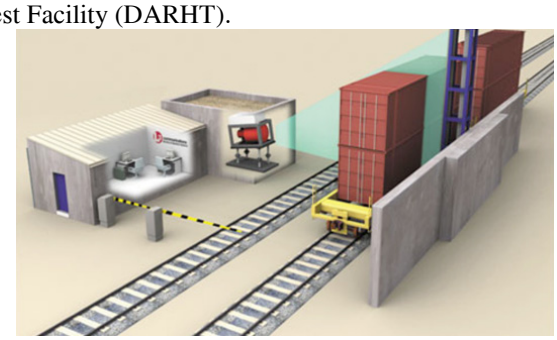

Figure 9: A rail cargo scanner.

Energy and Environment

Accelerators are used just a bit in conventional energy production from fossil fuels; namely accelerated neutrons are employed in down-hole well logging. However the primary use of accelerators is in the nuclear production of energy.

The use in fission is still in the future. Nevertheless there has been considerable work, in many different countries, on accelerator driven reactors. Besides being safer, but still having many possible fault paths, the degree of burn up (percentage of uranium) can be larger, thorium can be used as a fuel (with many advantages) and, perhaps most importantly, waste isolation from the environment can be reduced from a few hundred thousand years to only a few hundred years. Nevertheless the idea is still at the concept stage.

In fusion the use of accelerators is very real. For many decades tokomak reactors have had neutral beam drivers. These injectors supply fuel and current for the fusion reactors. Neutral beam injectors are planned for ITER. The other approach to fusion is inertial fusion that requires a driver. A major effort involves the development and use of glass lasers, but there are other approaches such as krypton-fluoride lasers, or pulsed

power or heavy ions. It is the later that is of particular interest to our community. One approach is the use of induction acceleration and an artist's view of how such a power plant would look is shown in Fig. 10.

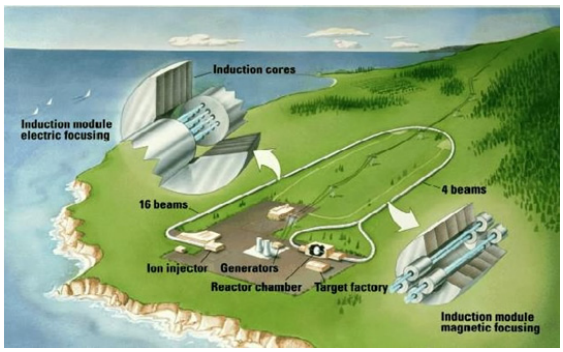

Figure 10: A conceptual view of a heavy ion inertial fusion power plant.

Industrial Uses

The industrial production of accelerators is a large business (in the range of many B$/year), but here I want to focus attention upon the use, in industry, of accelerators in the process of producing a commercial product rather than producing an accelerator. To be particular, accelerators are widely used for ion implantation, for electron cutting and welding, for sterilization, for isotope production, for non-destructive testing, and for treating material surfaces. In many of these applications a high current, low voltage (a few MeV) machines are employed.

Fig. 11 shows a facility employed for the coating of cables. Another need for accelerators is for the treating of shrink-wrap. Without accelerator treating we wouldn't have, the ubiquitous, shrink-wrap. Other uses in industry include the hardening of auto tires, making of biologically compatible components for implantation in humans, and the treatment of material surfaces on furniture. The list goes on and on and one can expect ever-more industrial uses of accelerators.

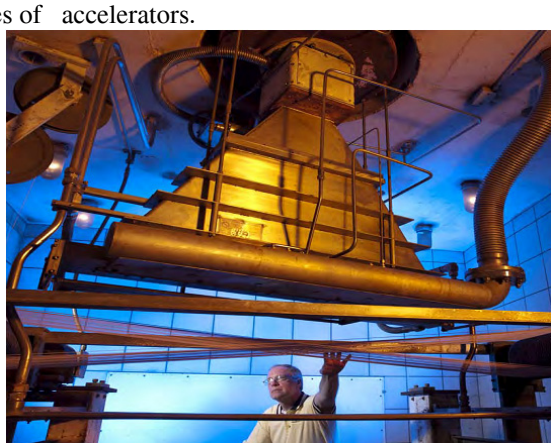

Figure 11: Electron beam cross-linking of polymers improves heat resistance of coatings for wires and cables.

Finally, in Fig. 12 is shown a very non-industrial use of accelerators. This application surely is surprising to some. I believe we can look forward to many other "surprising applications" in the future.

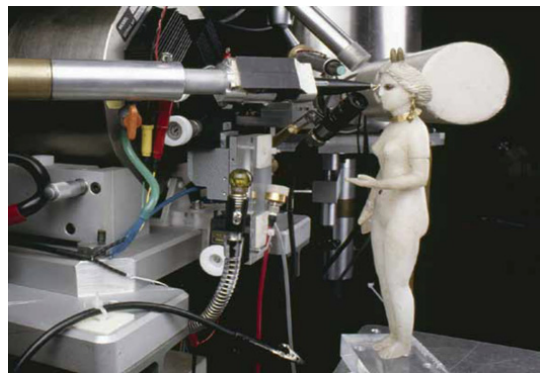

Figure 12: AGLAE, Accélérateur Grand Louvre d'Analyse Élémentaire in Paris, is an accelerator facility devoted to the study and investigation of works of art and archeological artifacts. The proton beam (4 MeV) probes: jewels, ceramics, glass, alloys, coins, statues, paintings and drawings.

CONCLUSIONS

The variety and capability of accelerators has made them instrumental in a surprisingly large number of endeavors. Their use can be expected to ever-increase.

It is necessary, and possible, to ever-improve accelerators. Since the use of accelerators is broad, in contrast with what it once was (namely almost exclusively for nuclear and high-energy physics), the necessary R&D on accelerators must be supported either from a variety of sources (appropriate to their particular interest) or by one sponsor (but with an understanding of the broad applications of accelerators). In most countries this will require a change in administrative practices.

In the very-long-term accelerators will probably look very different than now they do. (They may, for example, be laser/plasma accelerators or collective accelerators.) It is important that support be given to these activities with the understanding that some will not work ("If we knew what we are doing, it wouldn't be research."), but some will revolutionize the field and open up possibilities we can't even dream about.

ACKNOWLEDGMENTS

To the tens of thousands of scientists, engineers, and technicians who, working over the last century, in a hundred different places and in about twenty-five different countries, who have made accelerators powerful, diverse, and so capable. Pictures, and the concepts and words that go with them, are from: "Engines of Discovery: Particle Accelerators at Work" by Andrew Sessler and Edmund Wilson, World Scientific, 2012.

NICA PROJECT AT JINR

N. Agapov, V. Kekelidze, R. Lednicky, V. Matveev, I. Meshkov*,
A. Sorin, G. Trubnikov, JINR, Russia

Abstract

The project of Nuclotron-based Ion Collider fAcility NICA/MPD (MultiPurpose Detector) under development at JINR (Dubna) is presented. The general goals of the project are providing of colliding beams for experimental studies of both hot and dense strongly interacting baryonic matter and spin physics (in collisions of polarized protons and deuterons). The first program requires providing of heavy ion collisions in the energy range of $\sqrt{s_{NN}} = 4 \div 11$ GeV at average luminosity of $L = 1 \cdot 10^{27}$ cm^{-2}·s^{-1} for $^{197}Au^{79+}$ nuclei. The polarized beams mode is proposed to be used in energy range of $\sqrt{s_{NN}} = 12 \div 27$ GeV (protons) at luminosity of $L \geq 1 \cdot 10^{30}$ cm^{-2}·s^{-1}. The key issue of the Project is application of cooling methods – stochastic and electron ones. The report contains description of the facility scheme and characteristics in heavy ion operation mode, status and plans of the project development.

NUCLOTRON-M & NICA PROJECT

The **N**uclotron-based **I**on **C**ollider f**A**cility (NICA) [1] is a new accelerator complex (Fig. 1) being constructed at JINR. It is aimed to provide collider experiments with[*)]

- heavy ions $^{197}Au^{79+}$ at $\sqrt{s_{NN}} = 4 \div 11$ GeV (1÷4.5 GeV/u ion kinetic energy) at average luminosity of $1 \cdot 10^{27}$ cm^{-2}·s^{-1} (at $\sqrt{s_{NN}} = 9$ GeV);
- light-heavy ions colliding beams of the same energy range and luminosity;
- polarized beams of protons $\sqrt{s} = 12 \div 27$ GeV (5÷12.6 GeV kinetic energy) and deuterons $\sqrt{s_{NN}} = 4 \div 13.8$ GeV (2÷5.9 GeV/u ion kinetic energy) at average luminosity $\geq (1 \div 10) \cdot 10^{30}$ cm^{-2}·s^{-1}.

The proposed facility consists of the following elements (Fig. 1):

– "*Old*" *injector* (pos. 1): set of light ion sources including source of polarized protons and deuterons and Alvarez-type linac LU-20[*)];

– "*New*" *injector* (pos. 2, under construction): ESIS-type ion source that provides $^{197}Au^{31+}$ ions of the intensity of $2 \cdot 10^9$ ions per pulse of about 7 μs duration at repetition rate up to 50 Hz and linear accelerator consisting of RFQ and RFQ Drift Tube Linac (RFQ DTL) sections. The linac accelerates the ions at $A/q \leq 8$ up to the energy of 6 MeV/u at efficiency not less than 80 %.

– *Booster-synchrotron* housed inside Synchrophasotron yoke (pos. 3). The Booster (pos. 4) has superconducting (SC) magnetic system that provides maximum magnetic rigidity of 25 T·m at the ring circumference of 215 m. It is equipped with electron cooling system that allows to provide cooling of the ion beam in the energy range from injection energy up to 100 MeV/u. The maximum energy of $^{197}Au^{31+}$ ions accelerated in the Booster is of 600 MeV/u. Stripping foil placed in the transfer line from the Booster to the Nuclotron allows to provide the stripping efficiency at the maximum Booster energy not less than 80 %.

– *Nuclotron* – SC proton synchrotron (pos. 5) has maximum magnetic rigidity of 45 T·m and the circumference of 251.52 m provides the acceleration of completely stripped $^{197}Au^{79+}$ ions up to the experiment energy in energy range of 1÷4.5 GeV/u and protons up to maximum energy of 12.6 GeV.

– *Transfer line* (pos. 6) transports the particles from Nuclotron to Collider rings.

– *Two SC collider rings* (pos. 8) of racetrack shape have maximum magnetic rigidity of 45 T·m and the circumference of about 400 m. The maximum field of SC dipole magnets is 1.8 T. For luminosity preservation an electron and stochastic cooling systems will be constructed.

– *Two detectors* – MultiPurpose Detector (*MPD*, pos. 9) and Spin Physics Detector (*SPD*, pos. 10) are located in opposite straight sections of the racetrack rings.

– *Two transfer lines* transport particle beams extracted from Booster (pos. 11) and Nuclotron (pos. 12) to the new research area, where fixed target experiments both basic and applied character will be placed.

The NICA parameters (Table below) allow us to reach the goals of the project formulated above.

One of NICA accelerators – Nuclotron is used presently for fixed target experiments on extracted beams (Fig. 1, pos. 7).

This program is planned to be developed further and will be complementary to that one to be performed at Collider in heavy ions beam mode operation. The program includes experimental studies on relativistic nuclear physics, spin physics in few body nuclear systems (with polarized deuterons) and physics of flavours. At the same time, the Nuclotron beams are used for research in radiobiology and applied research.

*Corresponding author: meshkov@jinr.ru

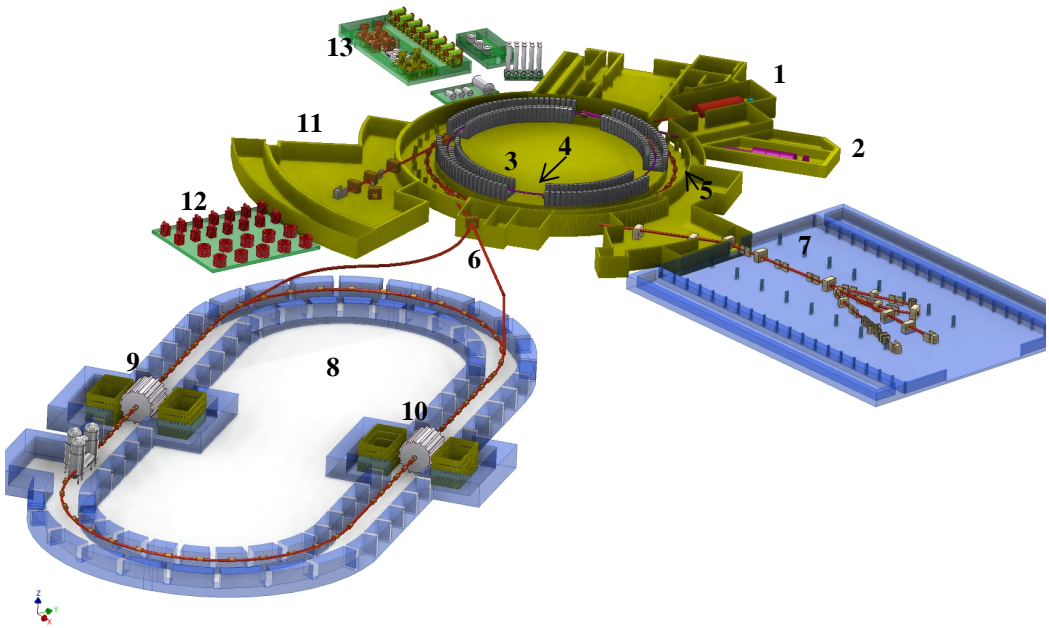

Figure 1: Scheme of NICA facility: 1 – light and polarized ion sources and "old" Alvarez-type linac; 2 – ESIS source and new RFQ linac; 3 – Synchrophasotron yoke; 4 – Booster; 5 – Nuclotron; 6 – beam transfer lines; 7 – Nuclotron beam lines and fixed target experiments; 8 – Collider; 9 – MPD; 10 – SPD; 11 – new research area, 12 – cryogenic plant, 13 – auxiliary equipment

Table 1. Parameters of NICA accelerators

Acceleration	**Booster project**	**Nuclotron**		**Collider project**
		Project	**Status (April 2011)**	
1. Circumference, m	212.2	251.5		503.0
2. Max. magn. field, T	2.0	2.0	2.0	1.8
3. Magn. rigidity, T·m	25.0	45	39.5	45
4. Cycle duration, s	4.0	4.02	5.0	≥ 2000
5. B-field ramp, T/s	1.0	1.0	1.0	< 0.1
6. Accelerated/stored particles	p-$^{197}Au^{79+}$, p↑, d↑		p-Xe, d↑	p ÷ $^{197}Au^{79+}$, p↑, d↑
Maximum energy, GeV/u				
Protons	–	12.6	–	12.6
Deuterons	–	5.87	5.1	5.87
Ions, GeV/u	$^{197}Au^{31+}$ 0.4	$^{197}Au^{79+}$ 4.5	$^{54}Xe^{24+}$ 1.0	$^{197}Au^{79+}$ 4.5
Intensity, ion number per cycle (bunch)				
protons	$1{\cdot}10^{11}$	$1{\cdot}10^{11}$	$1{\cdot}10^{11}$	$1{\cdot}10^{11}$
deuterons	$1{\cdot}10^{10}$	$1{\cdot}10^{10}$	$1{\cdot}10^{10}$	$1{\cdot}10^{10}$
$^{197}Au^{79+}$	$2{\cdot}10^{9}$	$2{\cdot}10^{9}$	$1{\cdot}10^{6}$ ($^{54}Xe^{24+}$)	$1{\cdot}10^{9}$

COLLIDER LUMINOSITY

The collider design has to provide the project luminosity and its maintenance during a long time necessary for an experiment performance. That requires, correspondingly:

1) formation of ion beams of high intensity and sufficiently low emittance,
2) ion beam life time.

Beam intensity is limited, in principle, by beam space charge effects, which can be estimated by so called "tune shift criteria". *The first one*, and most strong of them usually, is so called betatron oscillation tune shift (or *"The Laslett tune shift"*):

$$\Delta Q = \frac{Z^2}{A}\cdot\frac{r_p N_i}{\beta^2\gamma^3 4\pi\varepsilon_{geom}}\cdot k_{bunch},\ \ k_{bunch} = \frac{C_{Ring}}{\sqrt{2\pi}\cdot\sigma_s}. \quad (1)$$

Here Ze and A are ion charge and mass number, r_p is proton classic radius, N_i is ion number per bunch in the bunched ion beam, β, γ are the ion Lorentz factors, k_{bunch} is bunch factor, C_{Ring} is the Collider ring circumference, σ_s is bunch length (σ-value for Gaussian beam), ε_{geom} is the ion bunch "geometrical" transverse emittance (do distinguish with "normalized" one ε_{norm} used below). *The second criterion* is so called *beam-beam parameter* that describes ion betatron tune shift related to scattering of ion on he electromagnetic field of encountering ion bunch:

$$\xi = \frac{Z^2}{A}\cdot\frac{r_p N_i\left(1+\beta^2\right)}{4\pi\beta^2\gamma\varepsilon_{geom}} \quad (2)$$

For practical estimates one can use the numerical criterion for beam stability as follows:

$$\Delta Q_{total} \equiv \Delta Q + n_\xi\xi \le 0.05. \quad (3)$$

n_ξ is number of interaction points.

One of instabilities and major problems of the NICA collider is suppression of intrabeam scattering (IBS) in intense ion bunches. The last one defines mainly the beam life time. For this purpose we have proposed to use both electron cooling [2] and stochastic cooling [3] methods. In the first case we assume achievement of an equilibrium between cooling and space charge forces when space charge tune shift ΔQ_{total} reaches a resonant value (e. g., 0.05). We call it *space charge dominated regime* (SCD regime). Then using Formulae (1), (2) and well known expression for luminosity of round colliding beams one can derive simple relations between parameters:

$$L \propto \Delta Q_{total}^2\cdot\varepsilon_{geom}\cdot f_L(E_{ion})\cdot f_{HG},$$
$$N_i \propto \Delta Q_{total}\cdot\varepsilon_{geom}\cdot f_N(E_{ion}), \quad (4)$$

where E_i is ion energy, f_L, f_n are the functions describing energy dependence of parameters, f_{HG} is hour-glass effect function. We see that maximum luminosity is achieved if beam emittance ε_{geom} has maximum, i. e. coincides with the ring acceptance. At some circumstances the luminosity can be limited by "not the beam reasons (e. q., detector performance). Then one can optimise the SCD regime decreasing equilibrium emittance and N_i (Fig. 2). Such an optimisation can be done with variation of N_i number. In the case of limited luminosity one can also avoid SCD regime decreasing ion number and allowing, by weakening cooling force, the beam emittance keeping ΔQ_{total} below resonant value. We call it *IBS Dominated regime* (IBS DR) when equilibrium state is provided with equality IBS and cooling rates:

$$R_{IBS} = R_{cool}. \quad (5)$$

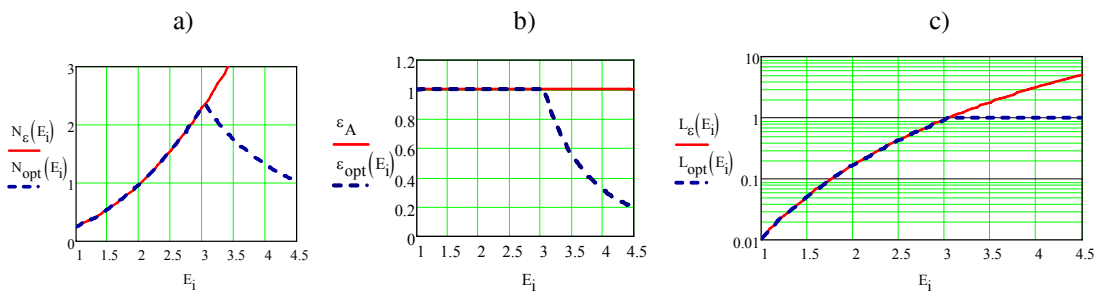

Figure 2: Space charge dominated regime; ion number per bunch (a), beam emittance (b) and luminosity (c) versus ion energy in two cases: full acceptance if filled with ions (red solid curves) and luminosity is limited (blue dash curve); the ring acceptance = 40 π·mm·mrad, parameter units: $[N_i] = 10^9$, $[\varepsilon]$ = π·mm·mrad, $[L] = 10^{27}$ cm^{-2}·s^{-1}.

Then, at fixed luminosity, similar by to Formulae (4) one can write

$$L = \text{const}, \quad N_i \propto \sqrt{L \cdot \varepsilon_{geom}} \cdot \varphi_L(E_i),$$
$$\Delta Q_{total} \propto \sqrt{\frac{L}{\varepsilon_{geom}}} \cdot \psi_L(E_i) < \Delta Q_{\max}. \quad (6)$$

As we see, minimum ΔQ_{total} corresponds to maximum emittance, i. e. full acceptance filling with ions. Simultaneously, it gives us maximum τ_{IBS} at relatively increased ion number (Fig. 3). One should mention that at IBS DR ion number dependence of energy is rather weak – proportional to $(N_{ion}/C)^{-1/2}$.

For NICA parameters, as it follows from Fig. 3, IBS DR regime can be used at $E_i > 3$ GeV/u where $\Delta Q < 0.05$. At the same energy range we plan to use stochastic cooling. At lower energy electron cooling application is preferable (if not to say more realizable) [3, 2]. However, then another problem appears: ion recombination with cooling electrons. This effect can be significantly diminished by increase of cooling electrons temperature [4].

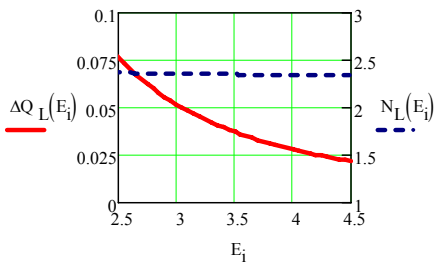

Figure 3: IBS dominated regime; beam tune shift ΔQ_{total} (red solid curve) and ion number per bunch N_i (blue dash curve) at constant luminosity $L = 1 \cdot 10^{27}$ cm^{-2}·s^{-1} and beam emittance of 1.0 π·mm·mrad; $[N_i] = 10^9$.

The described approach (SC and IBS dominated regimes) can be developed even further. One can, for instance, increase luminosity in low energy range (below 3 GeV/u) by enlarging minimum beta-functions in IP area. That will be followed by decrease of beta-functions in the lenses of final focus and lead correspondingly to increase of the ring acceptance. Those steps are planned for future development.

NICA CRYOGENIC SYSTEM

The NICA cryogenics (Fig. 4) will be based on the modernized liquid helium plant that was built in the early 90's for the Nuclotron. The main goals of the modernization consist of increasing of the total refrigerator capacity from 4000 W to 8000 W at 4.5 K and construction a new distribution system of liquid helium. These goals will be achieved by construction of a new 1000 l/hour helium liquefier, "satellite" refrigerators located near the accelerator rings, and a liquid nitrogen system that will be used for shield refrigerating at 77 K and at the first stage of cooling down of three accelerator rings with the total length of about 1.5 km and "cold" mass of 220 tons.

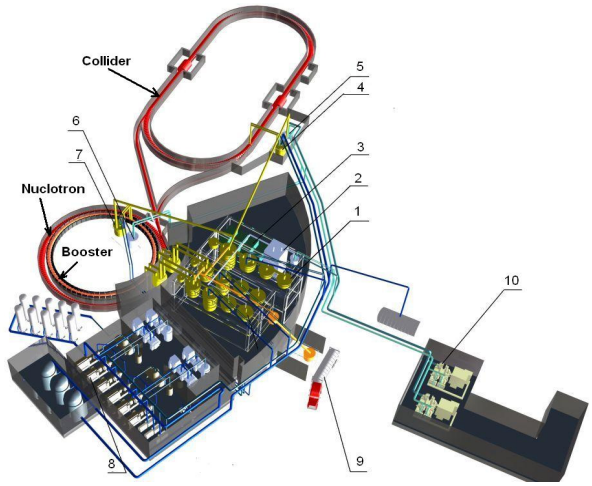

Figure 4. The general view of the NICA cryogenic system. New units for the NICA accelerators: 1 – 1000 l/h Helium liquefier OG-1000; 2 – 1300 kg/h Nitrogen liquefier OA-1,3; 3 – draining and oil-purification units; 4 – satellite refrigerator of the collider; 5 – 500 kg/h Nitrogen re-condenser RA-0,5 of the collider; 6 – 500 kg/h Nitrogen re-condenser RA-0,5 of the Booster; 7 – satellite refrigerator of the Booster; 8 – 6600 N·m^3/h screw compressors Kaskad-110/30; 9 – liquid Helium tank; 10 – Nitrogen turbo compressors.

CONCLUSION

The status main characteristics of NICA project and principle problems related to the NICA collider creation are considered in this report. The NICA project as a whole has passed the phase of concept formulation and is presently under development of the working project, manufacturing and construction of the prototypes.

The project realization plan foresees a staged construction and commissioning of the accelerators that form the facility. The main goal is beginning of the facility commissioning in 2017.

REFERENCES

[1] Search for a QCD Mixed Phase at the Nuclotron-based Ion Collider fAcility (NICA White Paper), http://theor.jinr.ru/twiki/pub/NICA/WebHome/WhitePaper_5.03.pdf.

[2] S. Yakovenko, E. Ahmanova, A. Kobets et al., Cooler for Collider NICA, Proc. of COOL'2011, TUPS13.

[3] G. Trubnikov, Application of Cooling Methods in the NICA Project, Proc. of COOL'2011, MOIO07.

[4] A. Philippov, A. Kuznetsov, I. Meshkov, Radioactive Recombination of Bare Nuclei and Ions in Electron Cooling System, Proc. of COOL'2011, THCOB01.

LASER-PLASMA ACCELERATION – TOWARDS A COMPACT X-RAY LIGHT SOURCE AND FEL

Andrei Seryi, John Adams Institute for Accelerator Science, UK

Abstract

Advances in many scientific and technical fields depend on availability of instruments, which can probe the structure of materials or molecules on unprecedented levels of spatial or temporal resolution. Many of such instruments are based on accelerators of charged particles, with particular examples of synchrotron radiation light sources and coherent X-ray Free Electron Lasers. The high cost of such facilities, however, preclude wide spread of such instruments. Modern accelerator science witnesses emergence of a new direction – compact x-ray sources are coming to the scene, enabled by the synergy of accelerators and lasers, where high gradient laser-plasma acceleration can significantly reduce the size and cost of the facilities. Compact x-ray sources will be developed in the nearest future and will share their scientific and market niche with large national scale x-ray facilities. The compact sources will in particular be suitable for placement in universities and medical or technological centres. The compact x-ray light sources are being developed by many centres in UK. Development of compact x-ray FEL is a promising topic for scientific and technological collaboration between UK and Russia, where expertise of partners will cross-fertilize their ability to solve scientific and technological challenges.

ACCELERATOR SCIENCE AND TECHNOLOGICAL PROGRESS

Science is a driver for the economy. This is a commonly accepted statement —however, the mechanisms of the impact are complicated and their analysis is necessary not only from a philosophical point of view, but also in order to optimize research priorities and define the strategy for technological innovation.

Particle accelerators have already impacted many areas of our lives via their medical and industrial use, and in research instruments. Tens of millions of patients receive accelerator-based diagnoses and treatment each year around the world, and the total annual market value for all products that are treated or inspected by accelerators is more than US$500B [1]. Approximately 30% of the Nobel Prizes in physics, as well as many in other areas, are directly connected to the use of accelerators [2].

The ideas that enabled use of accelerators in everyday life and industry were developed decades ago; therefore, new ideas will be essential for ensuring the future impact of this field. Analysis of the mechanisms how accelerator science affects the economy and technological progress is needed in order to make predictions and optimise the future directions of research. In the text presented below in this section, we follow the approach and views expressed by the author earlier in [3], [4] and [5].

One of the attempts to analyze the model for research and technology transfer was done by the famous Vannevar Bush, who, during the WWII, was instrumental in reorganizing the research and science community according to the needs of that difficult time. Vannevar Bush's post-war report, "Science, the Endless Frontier", prepared for the USA President, has defined the post-war scientific policy in the USA and in many other countries for decades to come.

In this report, Bush describes what will later be called a one-dimensional or linear model for research and technology transfer. In this report, Bush, in particular, claims that research that is more basic is less applied and vice versa. According to Bush, applied research invariably drives out pure if the two are mixed, and therefore basic research must be completely isolated from considerations of use.

Correspondingly, the dynamic linear model of technology transfer looks like a pipeline wherein government funding stimulates basic research, which then in turn feeds to applied research, which then results in technology and product development, with eventual benefits for the society.

These views of the relationship between basic science and technological innovation have since then been analyzed, criticized, and a new model has been developed.

The contradiction between these linear models and practice can be illustrated via the example of accelerator science and technology. The invention of the so-called "strong focusing" in the fifties was a revolutionary change in accelerator technology. It enabled numerous applications. This invention may have come about as a result of pure fundamental interest— however it was developed as a result of the pursuit of a certain concrete goal, and was made possible due to certain technologies available at that time.

A new model of research and technology transfer was suggested by Donald Stokes, who worked on the Advisory Committee on Research for the USA National Science Foundation. In his report to NSF, and in the book he subsequently published [6], Donald Stokes argued against Bush's linear model and introduced the notion of use-inspired research, of "research with consideration to use", which redefined the paradigm of the relationship between basic science and technological innovation.

To illustrate his views, Donald Stokes suggested considering research on a two-dimensional plane, where the axis are fundamental knowledge impact and consideration of use.

A characteristic example of a purely fundamental scientific pursuit is the research works of Niels Bohr on the structure of nuclei, while the other examples are

Thomas Edison's development works. The quantitative assessments of these examples — or other research placed on this two dimensional diagram — can be done by the number of either academic papers or patents, resulting from a particular research.

Donald Stokes suggested, however, that an optimized approach should balance the fundamental pursuit of knowledge with consideration of use, which is illustrated by the works of Louis Pasteur.

In the field of modern accelerator science and technology, characteristic examples can be colliders aimed at exploration of fundamental properties of elementary particles on one axis, and accelerator-based devices for homeland security and medical applications on the other axis.

The criteria suggested by Donald Stokes are universal and applicable to any scientific and technological area. Applying these criteria to accelerator science and technology, we can conclude that the preferred direction — which balances best the fundamental pursuit of knowledge with consideration to use — will be the direction of novel light sources or neutron sources. These could potentially produce scientific instruments applicable to the investigation of protein structures or materials, which may be almost directly applicable to the creation of new medicines or metals with controllable properties.

This analysis also shows that, as many other disciplines, accelerator science and technology can truly span the entire range of directions from pure fundamental science to pure applied development.

The research and technology innovation model is indeed not just linear, but at least two-dimensional, as Donald Stokes outlined in his revised dynamic model.

In the 21st century, the driving forces of technological innovation — as well as the global compact between science and society — are different now than they were in the middle of the last century. The revised criteria — as illustrated in this article via the example of accelerator science — are universal, and can be applied to any discipline, which can help us to optimize the impact of our research investments on our economy and society.

COMPACT LIGHT SOURCES AS TECHNOLOGY DRIVERS

Armed with the general understanding expressed in the above section, we can now consider a particular area of accelerator science – the compact light sources, and discuss how their development can help the technological progress of our society.

Conventional accelerators, no matter how advanced, are primarily based on the acceleration of particles in cavities – metal vessels shaped to resonate and create accelerating fields. The ability of metals to tolerate high electromagnetic fields is intrinsically limited. However, an accelerating wave can be created when gas is ionised and exited by an intense beam of particles or by a laser pulse, becoming plasma – an indestructible medium able to withstand a thousand-times higher accelerating gradient.

The promise of plasma acceleration, indicated by theory and the first pilot experiments, is actively being explored. Many laser and accelerator laboratories around the world have launched plasma acceleration research. In California, the FACET and BELLA projects were begun in SLAC and LBNL to study beam-driven or laser-driven plasma acceleration.

Advanced studies for laser, beam and plasma interaction are being pursued in many countries of Europe and Asia. Many universities and research teams in particular in the UK have made pioneering contributions to this field and continue to be at the forefront of the developments.

Accelerator science and technology is on the edge of a breakthrough enabled by synergy with laser and plasma physics. The most immediate outcome that this synergy will enable is the creation of novel, compact X-ray lasers and light sources. The direct collision of beam and laser light also opens another opportunity for the creation of X-ray sources via use of the Compton effect (when visible light photons are reflected from a relativistic electron beam and thereby decrease their wavelength down to Angstrom level).

Science is indeed the driver of our civilisation's progress. However, the path from ideas and experimental demonstrations to widespread commercial applications is difficult. Various studies performed in different countries have all found a gap, a so-called 'valley of death' in technology transfer. It is difficult to bridge the middle range of the technological readiness of ideas. On one side, the research institutions are usually not positioned to develop ideas into commercial applications, while on the other side, the risk is often too high for industry to pick up ideas that are too fresh and undeveloped.

The challenge originates from different motivations, methods and timescales of three key players: academic institutions, industry and investors. Their corresponding aims and motivations – the front end fundamental scientific results, development of commercial devices in foreseeable future, and optimisation of investments versus risk/return factors – are often incompatible.

Crossing the 'valley of death' of technology transfer is a challenge that often requires a nationwide, coherent initiative to create both the necessary infrastructure and a system that stimulates research organisations, industry and investors while also managing risk.

Accelerators in synergy with lasers and plasma may in fact offer a solution for the academia-industry-investor puzzle via simultaneous, parallel work on a portfolio of three different types of compact X-ray light sources.

The first type, Compton X-ray sources, is now actively being developed and is a lower-risk investment for industrial use. Yet a more challenging, but promising, Compton source requires superconducting acceleration to allow for a much higher electron beam current and X-ray brightness. This second option is placed in the middle of the range for both the projected availability and

risk/return. The most challenging, but also the most promising one, is an X-ray source based on laser-plasma acceleration – a free electron laser (FEL) that nevertheless may be less than a decade from realisation.

Properly scheduling the relative progression of the different stages of research and development of these three types of X-ray sources, one can balance the typical risks associated with development of innovative products, and the opportunities they offer.

UK research institutions have the necessary expertise and the aspiration to lead – in collaboration with each other, with industrial partners and with world leading centres – the work on this portfolio of compact X-ray sources. This cooperation and technology transfer will enable widespread use of compact X-ray lasers. Every university lab will aspire to have and will eventually be able to obtain an X-ray laser, which will revolutionise future science and technology yet again – not unlike how the spread of near-visible light lasers impacted science and industry in the 20th Century.

COLLABORATION ON LASER-PLASMA BASED COMPACT LIGHTS SOURCES

The Advances in many scientific and technical fields depend on availability of instruments, which can probe the structure of materials or molecules on unprecedented levels of spatial or temporal resolution.

Many of such instruments are based on accelerators of charged particles, with particular examples of synchrotron radiation light sources and coherent X-ray Free Electron Lasers. The high cost of such facilities, however, preclude wide spread of such instruments.

Following trends in accelerator science shows that a new direction is emerging – compact x-ray sources are coming to the scene, enabled by the synergy of accelerators and lasers, where high gradient laser-plasma acceleration can significantly reduce the size and cost of the facilities.

Compact x-ray sources will be developed in the nearest future and will share their scientific and market niche with large national scale x-ray facilities. The compact sources will in particular be suitable for placement in universities and medical or technological centres.

The compact x-ray light sources are being developed by many centres in UK. Some of the major milestones in laser-plasma acceleration have been achieved by UK scientists.

Many scientific centres in Russia have capabilities to contribute significantly to the development of laser-plasma based compact x-ray sources.

Development of compact x-ray FEL is a promising topic for scientific and technological collaboration between UK and Russia, where expertise of partners will cross-fertilize their ability to solve scientific and technological challenges.

Joint UK-Russia activity has recently been initiated for development of compact x-ray light sources, to be performed by coordinated efforts of several centres in the two countries.

The aim of the project under planning is to create new knowledge and new infrastructure, aiming to make several working compact x-ray light sources, in the UK and in Russia, and to develop a design that can be reproduced for installation in many locations.

The project will be carried out by a collaboration of UK and Russia science centres, where the partners are: the John Adams Institute for Accelerator Science, an Institute of the University of Oxford, Royal Holloway University of London and Imperial College London (UK), the Institute of Applied Physics (Nizhny Novgorod, Russia), the Joint Institute of Nuclear Research and the JINR University Centre (Dubna, Russia), Budker Institute of Nuclear Physics (Novosibirsk, Russia), Joint Institute for High Temperatures RAS (Moscow, Russia) and Skolkovo Nuclear Cluster (Russia).

The collaborative project will engage PhD students, postdocs and researchers from the participating institutions, working on experimental facilities enhanced and enabled by this activity.

The proposed project is aimed at solution of scientific and technological challenges that haven't been solved to this moment. Search for solutions requires investigations on many fronts, and also requires development of a new paradigm in research and training – when knowledge of three disciplines, lasers, plasma, and accelerators, will be combined. To this moment, experts were trained in each of these fields separately.

Realisation of the collaborative project will result in creation of the new scientific experimental infrastructure in the participating institutions, in creation of new knowledge, training of young researchers, development of the exchange programme for young researchers, and development of designs of X-ray source suitable for reproduction and commercialisation.

ACKNOWLEDGMENT

The author would like to acknowledge contribution of his colleagues in the JAI, collaborators, and the UK STFC Council for support of this work.

REFERENCES

[1] Accelerators for America's Future, DOE, 2009.
[2] A. Chao et al, Physics in Perspective, 2010.
[3] A. Seryi, "Accelerating Progress" Public Service Review: UK Science & Technology: issue 6, 2012.
[4] A. Seryi "An X-ray Vision" Public Service Review: UK Science & Technology: issue 4, 2011, p.18-19.
[5] A. Seryi, G. Blair, Z. Najmudin, P. Burrows, "Accelerators Everywhere" Public Service Review: UK Science & Technology: issue 4, 2011, p.20-21.
[6] Donald E. Stokes, "Pasteur's Quadrant - Basic Science and Technological Innovation", Brookings Institution Press 1997.

DESIGN AND SIMULATION OF PRACTICAL ALTERNATING-PHASE-FOCUSED (APF) LINACS – SYNTHESIS AND EXTENSION IN TRIBUTE TO PIONEERING RUSSIAN APF RESEARCH

R. A. Jameson, Inst. Angewandte Physik, Goethe Uni Frankfurt, Max-von-Laue Str. 1, Frankfurt-am-Main, Germany

Abstract

A high fraction of the cost and complexity of conventional linacs lies in the use of magnetic transverse focusing. The strong-focusing effect of alternating patterns (sequences) of gap phases and amplitudes – known as Alternating-Phase-Focusing (APF) – can produce both transverse and longitudinal focusing from the rf field. APF has undeservedly been deemed largely impractical because simple schemes have low acceptances, but sophisticated schemes have produced short sequence APFs with good acceptances and acceleration rates that are now used in a number of practical applications. Suitable sequence design has been difficult, without direct theoretical support, inhibiting APF adoption. By synthesizing reported details and adding new physics and optimization technique, a new, general method for designing practical APF linacs is demonstrated, using simple dynamics and no space charge – incorporation of space-charge and more accurate elements is straight-forward. APF linacs can now be another practical approach in the linac designer's repertoire. APF can be used in addition to conventional magnetic focusing, and could be useful in minimizing the amount of additional magnetic focusing needed to handle a desired amount of beam current.

ALTERNATING PHASE FOCUSING

Particles exposed to an rf field in a gap may receive focusing or defocusing forces in the transverse and longitudinal directions, according to the phase and amplitude of the gap field. Arranging a sequence of gaps in some particular manner, termed here an "APF sequence", can provide large simultaneous transverse and longitudinal acceptances with high acceleration rates and good emittance preservation.

Typical transverse focusing and energy gain per unit length (dW/dz) forces over the full 360° range of rf phase (phi) are shown in Fig. 1.

There is no adequate theory for determining an APF sequence with acceleration. There are some APF linacs in operation, but their designs were laboriously produced by hand, and the sequences are short. Further APF development has also been hindered by a misconception that APF acceptances are necessarily small.

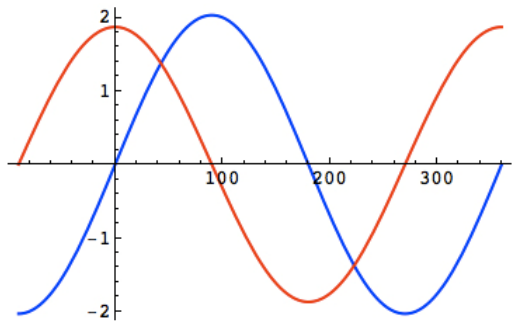

Fig. 1. Typical longitudinal acceleration (red) and transverse focusing forces (blue) over the full 360° range of phi.

THE APF SEQUENCE, AND SYNTHESIS OF A GENERAL METHOD

The most sophisticated work was realized in the USSR during the 1960's-1980's [1,2, and culminated in the "Garaschenko Sequence" [3], a 51-cell synchronous phase sequence for a 0.0147-1.0 MeV/u (factor 68), $_{238}U^{7+}$(qom=1/24), 6.8m, 25 MHz uranium-ion linac shown in Fig. 2, resulting from a complicated nonlinear optimization procedure to find the maximum longitudinal and transverse acceptances. The longitudinal acceptance was larger than for a typical RFQ.

A nonlinear optimization program must be given good enough starting points that it can converge to the correct optimum. Here the preliminary sequence was based on the extant schemes and a successfully operating APF linac at Dubna, which set out the general properties of the sequence in six separate focusing periods of 6-13 gaps and different spacings in each.

The great value of this paper is not that it helps find a good initial sequence, but that *it shows the form of an optimized sequence.* From this, we can draw very useful general conclusions. In particular, the full ±90° range can be used for high acceleration rate, and the period is extended as acceleration occurs to maintain the focusing strength, as with magnetic focusing.

During the next decades, work continued, especially in Russia by V.V. Kushin, V.K. Baev, and S. Minaev, who was a leading practitioner of actual APF designs until his death in 2010 and who influenced many extent APF designs. However, Minaev noted in [4] that "there is no theory for optimization of drift tube array so far" (i.e., for determining the underlying sequence); this is still the situation at this date. Summarizing details from the literature leads to a practical design method [5].

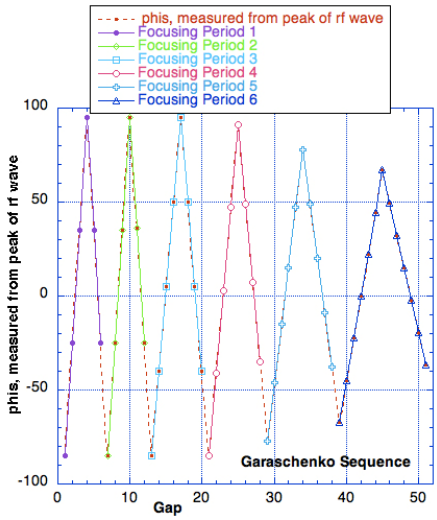

Fig. 2. Garaschenko APF sequence. Phis is measured from the peak of the wave. Overall the sequence is quasi-sinusoidal.

The IH linacs now in operation at NIRS, U. Gunma, and similar therapy machines under construction in Japan [6], have an underlying 72-cell quasi-sinusoidal APF synchronous phase pattern very similar to that of Garaschenko, expressed by a general 5-parameter sequence function written as:

$f_s(n) = f_0\, exp(-an)\sin((n-n_0)/(b\, exp(cn))$, where n is the cell number. The five parameters were searched, and the sequence then optimized for small output energy spread and output matching to the following section.

The well-known smooth approximation method was used to characterize the stability region, acceptances, and other features of the sequence [7], allowing sequence trajectories can be investigated on a transverse stability chart. The method is not well suited to determining an actual sequence with acceleration. However, it has an important utility in the synthesis of the new method.

Alternating both the field phase and amplitude allows small transverse emittance growth by aligning the sequence more along a line of constant phase advance on the stability chart [8].

There should be an offset of 5°-10° in the initial average value of the synchronous phase [3,8], and it is helpful to also have a tilt [3] so that the average synchronous phase tends from ~+5° to ~-5°. A tilt also helps avoid the danger of emittance equipartitioning via a synchrobetatron coupling resonance [9].

The first main result of the new method [5] is to extend the formulation of a general underlying gap synchronous phase phis sequence to a 7-parameter function:

```
phisapf =  phioffset*radian -
phitilt*radian*ncell +
phiampl*radian*Exp(phiatten*ncell)*Sin[2.*P
i*ncell/
(phiperiod*(1.d0-peratten*ncell)) +
phistart*radian]
```

A similar function could be applied to the gap amplitudes. The APF linac is then designed by simulation. A simple chain matrix representing each cell as a drift and an rf gap can be used. The linac is designed cell by cell, and thus acceleration is taken into account in fitting the phase sequence. The cell lengths are irregular, as determined by the local phase difference across the cell from the APF phase sequence, and the local velocity beta. A 7-dimensional grid search over the seven parameters can be performed quickly for zero beam current with a fast simulation code, with finer and finer grids. When parameters are found which give an initial adequate transmission, the sequence is optimized, using a new strategy, for the desired beam properties using nonlinear optimization techniques. The modeling can then be refined, with more accurate modeling, with space-charge, etc., and the process repeated.

It is useful for preliminary design work not to insist on completely realistic conditions. The gap voltage should be realistic, as determined from the Kilpatrick Criterion and structure peak field characteristics. However, at first the aperture should not be a restriction. Zero beam current and small input beam emittances are useful when searching for workable sequences.

Initial design of an ~60x energy gain linac by searching on Eq.(1) resulted in 23 cells, one sequence giving 99.97% best transmission, and another giving 99.47% best accelerated fraction, Fig. 3.

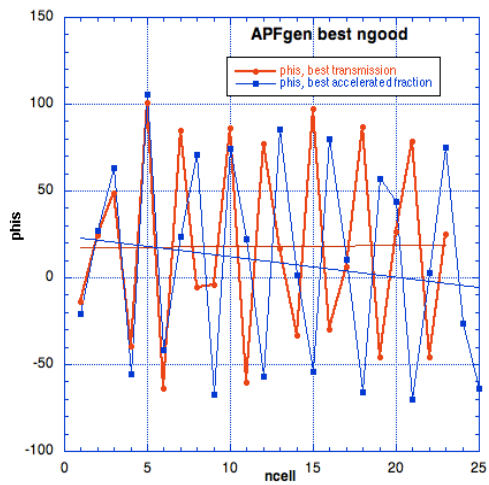

Fig. 3. The APF gap phase sequences for the best transmission (red) and best accelerated fraction (blue) cases. The linear fits show the effect of the tilt parameter.

Nonlinear constrained optimization directly on the 23 phis's for minimum emittance growth or output energy spread was straightforward. However, when a longer 164-cell sequence was explored, this direct method and others became difficult. The solution is the second main result of the new method [5]. The local sequence period at each cell is obtained by applying the sequence formula (1) at that cell, and computing the ncell ahead for which the period accumulates by 1. (phase advance of 2π). The new optimization strategy is then, at each cell sequentially, to optimize over the local period length,

with the objective function computed for the whole linac. This optimization strategy produced large improvements over the underlying Eq.(1) initial strategy; typical changes are indicated in Fig. 4.

APF linacs can now be another practical approach in the linac designer's repertoire, and can be considered as a candidate for any application, either alone or in conjunction with magnetic focusing.

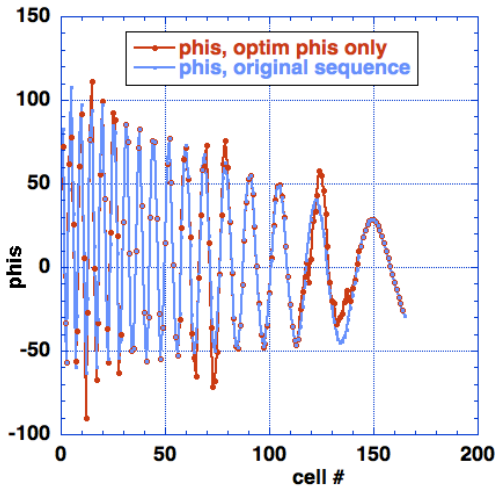

Fig. 4. Changes to original sequence by optimization on phis only, ±5° bounds.

ACKNOWLEDGEMENTS

This synthesis and extension of much foregoing detailed research in APF accelerator physics and modern control theory optimization techniques is based in particular on those authors cited in the references, particularly in Russia and Japan, and on pioneering work in optimal control of particle accelerator dynamics and Beam Dynamics and Optimization (BDO) Workshops at the Institute of Prof. D. Ovsyannikov, St.Petersburg State University. The support for part of this work from KEK, Japan, during visits as KEK Short-Term Invited Fellow is gratefully acknowledged.

REFERENCES

[1] "Efficiency of ion focusing by the field of a traveling wave in a linear accelerator", V.K. Baev & S. A. Mineav, Sov. Phys. Tech. Phys, 26(11), November 1981, p 1360.

[2] "Linear resonance ion accelerators with a focusing axisymmetric accelerating field", V.K. Baev, N.M. Gavrilov, S.A. Minaev & A.V. Shal'nov, Sov. Phys. Tech. Phys. 28(7), July 1983, p.788.

[3] F.G. Garaschenko, V.V. Kushin, et. al., "Optimal regines of heavy-ion acceleration in a linear accelerator with asymmetric variable-phase focusing", Zh. Tekh. Fiz. 52, 460-464 (March 1982)

[4] "APF or KONUS Drift tube Structures for Medical Synchrotron Injectors – A comparison", S.Minaev, 1999 PAC, p. 3555-3557.

[5] "Practical design of alternating-phase-focused linacs", R. A. Jameson, submitted to PRSTAB, June 2012.

[6] Y. Iwata, et. al., Proc. EPAC 2004, p.2631-2633; Y. Iwata, et.al., NIM A 567 (2006) p.685-696

[7] "Beam dynamics of Alternating Phase Focused Linacs", H. Okamoto, NIM A284 (1989) 233-247, North-Holland, Amsterdam

[8] Alternating Phase Focusing (APF) Linacs Developments and their Possible Applications", V.V. Kushin and S.V. Plotnikov, EPAC 1994, pp2661-2663.

[9] W.H. Cheng, H. Okamoto, et. al., "Synchrobetatron-coupling effects in alternating-phase-focusing linacs", Phys. Rev. E, Vol. 48, No. 6, December 1993, p. 4689-4698.

STATUS OF ELECTRON-POSITRON COLLIDER VEPP-2000*

D. Berkaev, A. Borisov, Yu. Garinov, A. Kirpotin, I. Koop,
A. Lysenko, I. Nesterenko, A. Otboyev, E. Perevedentsev, Yu. Rogovsky, A. Romanov,
P. Shatunov, D. Shwartz, A. Skrinsky, Yu. Shatunov#
Budker INP SB RAS, Novosibirsk, Russia

Abstract

The main goal of VEPP-2000 construction is to measure the cross sections of hadron production in e^+e^- annihilations and to collect an integral luminosity about few inverse femtobarns in the energy range 0.4 – 2 GeV. To reach these goals, the Round Beam Concept (RBC) was realized at VEPP-2000 collider. RBC requires equal emittances, equal small fractional tunes, equal beta functions at the IP, no betatron coupling in the arcs [1]. Such an approach results in conservation of the longitudinal component of particle's angular momentum. As a consequence, it yields an enhancement of dynamical stability, even with nonlinear effects from the beam-beam force taken into account.

The first beam was injected in VEPP-2000 machine 5 years ago and RBC was successfully tested at VEPP-2000 in 2008 [2]. Two experimental seasons in 2010-2012 were performed with two detectors SND and CMD3 in the energy range between 500 and 1000 MeV. Now, the total luminosity accumulated at VEPP-2000 is near to the final result of the VEPP-2M collider. The single bunch luminosity of 3×10^{31} $cm^{-2}s^{-1}$ was achieved together with a maximum beam-beam tuneshift as high as 0.15. At present, the work is in progress to increase the rate of positron delivery and upgrade the booster ring BEP for the beam transfer up to the top collider energy of 1 GeV.

COLLIDER OVERVIEW

The VEPP-2000 electron-positron collider has to operate in the beam energy range 0.2 – 1 GeV. It was constructed at the place of its predecessor VEPP-2M, using the existing beam production chain of accelerators: ILU – a pulsed RF cavity with a voltage of 2.5 MeV, a 250 MeV synchrotron B-3M and a booster storage ring BEP with the maximum beam energy of 800 MeV (see Fig. 1). The lattice of VEPP-2000 has a two-fold symmetry with two experimental straight sections of 3m length, where Cryogenic Magnetic Detector and Spherical Neutral Detector are located. Two other long straights (2.5m) are designed for injection of beams and RF cavity, and 4 short technical straight sections accommodate triplets of quadrupole magnets (max. gradient 50 T/m). To avoid dispersion in the detectors, RF cavity and injection straights, a pair of dipoles together with the triplet in between constitute 4 achromats. Chromaticity corrections are performed by two families of sextupole magnets located in the technical straight section, where the dispersion is high.

Design parameters of the collider are given in Table 1.

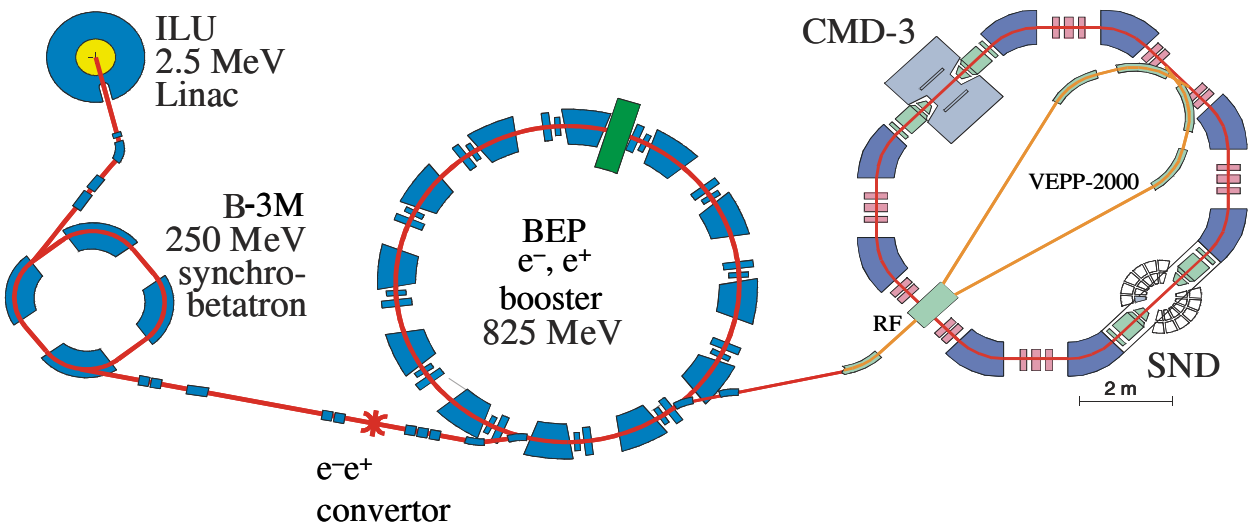

Figure 1: VEPP-2000 complex layout

* Work supported by Russian Ministry of Education and Science, basic project of BINP SB RAS 13.3.1, Physics branch of RAS project OFN.1.1.2, Scientific school NS-5207.2912.2 and Grant of the Novosibirsk region Government 2012
# Yu.M.Shatunov@inp.nsk.su

Table 1: VEPP-2000 Main Parameters (at $E = 1$ GeV)

Parameter	Value
Circumference, Π	24.39 m
Betatron functions at IP, $\beta^*_{x,z}$	10 cm
Betatron tunes, $\nu_{x,z}$	4.1, 2.1
Beam emittance, ε	1.4×10^{-7} m rad
Momentum compaction, α	0.036
Synchrotron tune, ν_s	0.0035
Energy spread, $\sigma_{\Delta E/E}$	6.4×10^{-4}
Beam-beam parameters, ξ	0.075
Luminosity, L	10^{32} cm^{-2}s^{-1}

The closed orbit steering and gradient corrections are done with 1-2% coils placed in the dipole and quadrupole magnets.

The accelerating HOM-damping RF cavity operates at the 14-th harmonic of the revolution frequency (172.0 MHz)[6]. It provides for a bunch length of about 3 cm at the top energy and stability of design bunch current of 200 mA.

Beam diagnostics is based on 16 optical CCD cameras that register the synchrotron light from either end of the bending magnets and give the full information about beam positions, intensities and profiles (see Fig. 2). In addition to optical BPMs, there are also 4 pick-up stations in the technical straight sections and one current transformer as an absolute current monitor.

The density of magnet system components and detectors environment is so tight that it is impossible to arrange the beam separation in the arcs. As a result, only one-by-one bunch collision mode is allowed at VEPP-2000.

The magnetic field of 2.4 T in the bends is required to reach the design energy of 1 GeV in the constrained area of the experimental hall.

LATTICE CORRECTIONS

RBC at VEPP-2000 was implemented by placing two pairs of superconducting focusing solenoids (max. field 13 T) in the two Interaction Regions symmetrically with respect to the collision points. This provides equal beta-functions of the horizontal and vertical betatron oscillations. There are several combinations of solenoid polarities that satisfy the round beams requirements. The simplest combinations ($+-\ +-$ or $+-\ -+$) have been chosen which satisfied the RBC constrains with the betatron tunes lying on the coupling resonance $\nu_1 - \nu_2 = 2$. The Dynamic Aperture (DA) in this case achieves about $15\text{-}20\,\sigma_{x,z}$ apart strong resonances. This value is two times less than the simulated one. Probably, it can be explained by the influence of lattice-asymmetry resonances: $\nu = 1/k$, where $k = 3,4,5,6$.

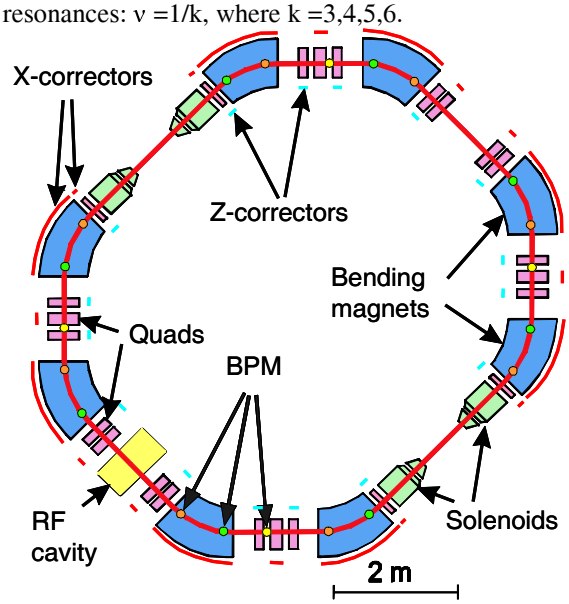

Figure 2: VEPP-2000 ring

To adjust the Closed Orbit (CO) and machine lattice to the design regime, an Orbit Response Matrix (ORM) method is applied. ORM measured from BPM response to small offsets given to the focusing elements (quads and solenoids) provides for control and corrections of the CO. Routinely, a sufficient accuracy (± 0.2 mm) is obtained after 2-3 iterations with a Single Value Decomposition analysis of the taken ORM. In addition, steering coil currents are minimized. This is important for a DA optimization, because many dipole correctors, being embedded in quadrupoles, give rise to strong nonlinear field components.

The lattice corrections at VEPP-2000 appear a more complicated task, especially for high energies, taking into account different saturation of magnetic elements. All the BPMs are used to measure ORM by the orbit steering deviations. As a rule, this procedure is done in a few steps in semi-automatic regime. The resulting setting of the lattice has to approach designed tunes, dispersion and beta functions. It is necessary to make 3-4 iterations to achieve a desirable symmetry of the machine optics including perfect tuning of the 4 achromats.

The lattice symmetry and zero dispersion in the Interaction Points are crucially important for the round beam collision. The residual coupling has not to exceed $2\text{-}3\times10^{-3}$. The main source of coupling and symmetry violations is the CMD detector solenoid (1.5 Tm). To compensate for its influence on the optics, special coils in two nearest solenoids are used. Finally, the coupling is suppressed by a set of skew quadrupole coils which are embedded in each sextupole magnet of all the 3 families.

BEAM-BEAM STUDY

The result of machine tuning is demonstrated in Fig. 3 showing the design X-Z beam envelopes (curves) and the measured X-Z beam sizes (points). The beam sizes for this plot have been measured with e^+ and e^- beam currents below 1 mA. At these currents, a mutual influence of the colliding beams is negligible. But, already at a few mA the beam-beam focusing causes a visible perturbation of the beam sizes. This effect ("dynamical beta-function") at VEPP-2000 leads to squeeze of $\beta^*_{x,z}$ and at the same time to an increase in the equilibrium beam emittances [3]. However, the resulting beam size at the IP is left practically unchanged. The simulation shows such a behaviour for both colliding round beams [4] up to the same critical currents I_{CR}.

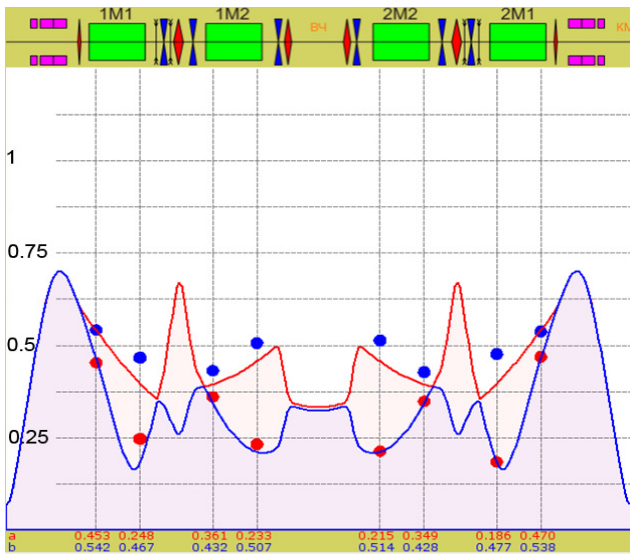

Figure 3. Beam sizes (mm) around the lattice.

Experimentally, a study of the beam-beam threshold currents was at first done in the "week-strong" mode for different tunes along the coupling resonance. A result of such a scan is presented in Fig. 4 at the beam energy of 510 MeV. We can see a resonance dependence of the I_{CR} on the tunes which is much stronger than mentioned above machine imperfection resonances $\nu = 1/k$, For a few intervals of the tune, the threshold current I_{CR} exceeds a level of $I^- = 48$ mA, that corresponds to a value of the beam-beam parameter $\xi = \frac{N r_e}{4\pi\gamma\varepsilon} = 0.1$.

It is necessary to remark that apparent strengths of the resonances in the beam-beam interaction differ day by day and, of course, vary at different energies. As a rule, the best working point found in the "week-strong" study, proves good for the "strong-strong" operation. Only a local tune scan is needed before starting the data-taking run with the detectors. A good parameter for quantitative assessment of the ring performance at collision is the specific luminosity $L_s = L / I^+ \times I^-$. For the round beams we have found that this parameter is constant with equal beam currents as long as the beam-beam parameter does not exceed 0.05 (see Fig. 8). There is a reduction of the specific luminosity for higher currents, but it is not so dramatic as for the flat beams. [2]

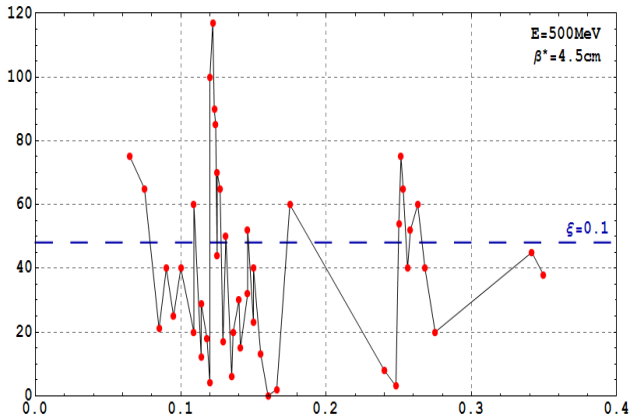

Figure 4: "Week-strong" threshold current vs. tune.

LUMINOSITY MEASUREMENTS

At VEPP-2000, the luminosity monitoring is available from both detectors. Electrons and positrons from elastic scattering are easily detected in coincidence by detector's calorimeters with an efficiency near 100% and counting rates about 1 kHz at $L=1\times 10^{31}cm^{-2}s^{-1}$.

For a "technical" usage, a method for the luminosity measurement was developed based on the beam size data from the optical diagnostics. To calculate the luminosity one should know only the beam currents and sizes at the IP. As we discussed above, due to the beam-beam effects the lattice functions and beam emittances show a significant current-dependent difference from their design values. Assuming no other focusing perturbations in the lattice other than those caused by the collision and thus located at the IP, one can use unperturbed transport matrices to evaluate beam sizes at the IP from the beam size measurements by CCD cameras placed around the ring. 8 measurements for each betatron mode of the both beams are more than enough to determine dynamic beta-function and dynamic emittance of the modes The accuracy of the method degrades at high beam intensities close to beam-beam threshold, where the beam distribution deviates from the Gaussian. Data from this lumi-meter, routinely taken during 1.25 hour at the energy E=888.25 MeV, are presented in Fig.5. Beta-function in this run was 8.5 cm at the IP, and the luminosity reached $2.4\times 10^{31}cm^{-2}s^{-1}$.

The advantages of this instrument over the SND and CMD luminosity monitors are the higher measurement speed and lower statistical jitter. Nominally, the accuracy of the new method is about 3-4% and it does not depend on the luminosity level in contrast to the detectors' data.

On the other hand, the new technique is not sensitive to possible focusing difference in two IPs. Generally, all the three luminosity monitors give results coinciding within a 10% accuracy.

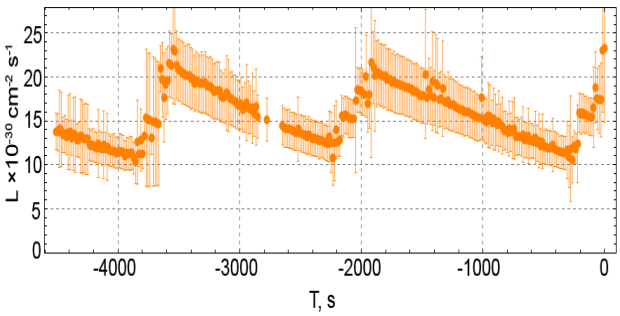

Figure 5: Luminosity log at the energy E=888.25 MeV.

EXPERIMENTAL RUNS 2010-2012

First of all, it is necessary to say that the existing beams production system is not able to provide enough positrons at the energies above 500 MeV. Besides that, a limitation of the booster ring BEP energy was found. It comes from insufficient chromaticity correction strength at the energies above 800 MeV. The strong head-tail instability arises and limits the positron beam intensity (50 mA). Another trouble appeared in ramping the VEPP-2000 ring up and down, between the injection and experiment energies, with non-separated colliding beams. A strict requirement to keep the betatron tunes equal to each other while ramping, and to stay within a narrow interval far enough from the resonances (see Fig. 7), leads to slowing the ramp speed down and thus to reduction of the average luminosity.

These problems have been (partly) resolved in operation. An appropriate matching of saturated magnets and solenoids was found, allowing a reasonably fast energy ramp with $\xi \leq 0.06$. It succeeds in a few-minutes ramping, 10 times shorter than the time between refills (see Fig. 5). By the way, the luminosity lifetime in Fig. 5 is determined by the luminosity effect: a cross-section of the single bremsstrahlung for VEPP-2000 conditions is equal to $2 \times 10^{-25} cm^2$. So, particle losses in two interaction points approach to the positron production rate.

It is clear that the most interest of both detector teams was attracted to the beam energy above that of VEPP-2M. A few scans in the energy range 0.7- 1.0 GeV with a step 12.5 MeV were carried out during years 2010-2012. A summary of the whole run is presented in Fig.6, where all the luminosity measurements by CMD detector are given. The luminosity accumulated by two detectors at VEPP-2000 has already approached the VEPP-2M total obtained during 25 years of its operation.

It is necessary to say that VEPP-2000 experiments were twice interrupted for half a year shutdowns due to financial problems caused by a very low state funding.

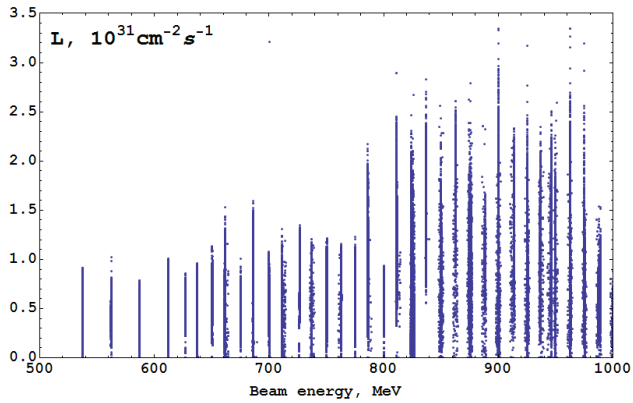

Figure 6: Luminosity measurements in the 2010-2012 runs.

Processing of the taken data is in progress at both detectors. A number of interesting events with multi π-meson productions are observed. But a more exiting result is measurement of the cross-section of p-p_{bar} and n-n_{bar} pairs production.

Simultaneously with data taking, a part of the machine time was spent for the beam-beam study. To demonstrate the luminosity dependence on the parameter ξ, an analysis of the SND luminosity data at the energy E=537.5 MeV has been done. One can see in Fig.7 that parameter ξ achieves a record value ξ=0.15 in the real "strong-strong" situation. This result coincides with our expectations based on the computer simulations for round beams [4].

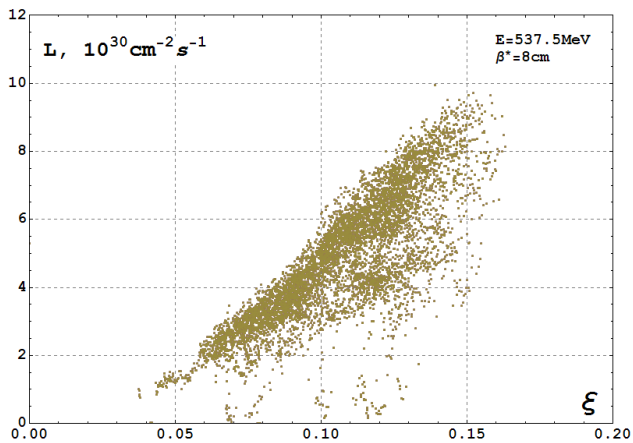

Figure 7. Luminosity vs the beam-beam parameter ξ.

BEAM ENERGY MEASUREMENTS

One goal of VEPP-2000 is an accurate measurement of hadron production cross sections in the whole energy range of 0.4 -2 GeV. This requires a knowledge of the beam energy with an accuracy of about 10^{-4}.

In addition to conventional magnetic field measurements by NMR probes in each bending magnet, two methods of the absolute energy calibration are under development at VEPP-2000.

The first method is the resonance depolarization technique which originates from VEPP-2M [5]. At VEPP-

2000, the strong solenoids complicate obtaining a polarised beam. But the present solenoid option allows to get a polarization degree of about 60% with a polarization time about 10 minutes at the top energy [6]. This is enough for observation of a jump in the counting rate of the intra-beam scattered positrons, when a frequency of the RF depolarizer coincides with the spin precession frequency. Figure 8 summarizes data of three depolarization runs. All together it gives the energy calibration: E = 750.67 ± 0.03 MeV.

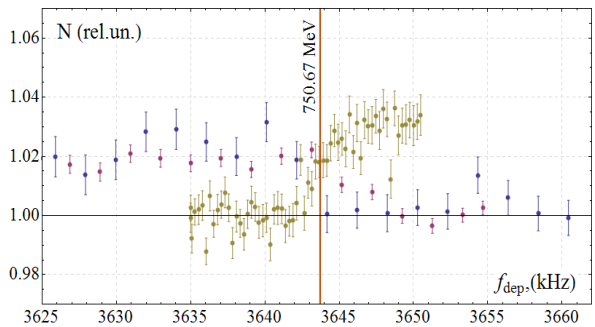

Figure 8. Resonant beam depolarization at VEPP-2000.

The second method which is in progress at VEPP-2000, is the Compton back-scattering of laser photons with the energy of $\hbar\omega_0$ on the counter electron beam. The energy of secondary γ-quanta $\hbar\omega_1=4\gamma^2\hbar\omega_0/(1+\gamma^2\theta^2)$ has a maximum at zero scattering angle (θ=0). The γ-quanta are detected by a Ge crystal, which is energy-calibrated against reference isotope γ-sources [7]. It was only possible to arrange the electron-photon collision point inside the bending magnet.

The first test of this system was carried out last April. Figure 9 shows the recorded spectrum at the beam energy of E=990 MeV.

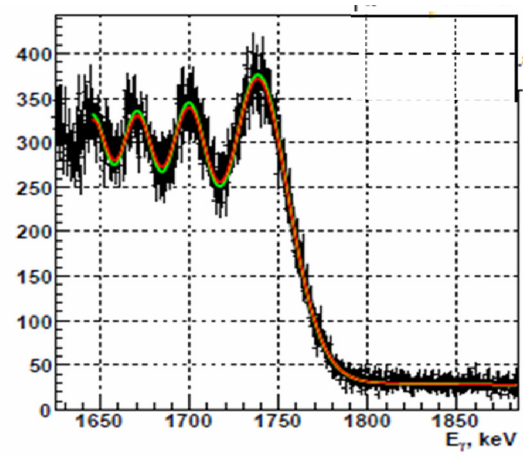

Figure 9. Compton back-scattering spectrum at VEPP-2000 at the energy of 990 MeV, $\hbar\omega_0$=0.117 eV.

Since the collision point in our case is in the magnetic field, the γ-quanta spectrum in addition to a sharp edge at $\omega_1=4\gamma^2\omega_0$ clearly indicates an interference of scattered radiation caused by the bend of electron trajectory [8].

Till now both methods of the energy calibration were tested separately in different conditions. Our nearest goal is to match all three methods and get the beam energy calibration accuracy of 10^{-4} in the whole energy span.

UPGRADE PLANS

The mentioned-above problems of the chronic positron deficit together with the collider ramping necessity will be solved soon after completion of the new positron injector at BINP. A transfer line (200 m long) is also under construction. It will deliver positron and electron beams from the damping ring of the positron source to the booster ring BEP at the energy of 500 MeV.

The booster and beam transfer lines BEP-VEPP will be upgraded to provide the beam injection into VEPP-2000 at any experiment energy. To do that, the bending fields of 2.6 T is required in the booster and transport line magnets.

CONCLUSION

VEPP-2000 is successfully running for data tacking with 2 detectors. A number of interesting results are observed. Round beams give the luminosity enhancement. The space charge parameter achieves value ξ = 0.15.

Beam energy calibration is in progress to achieve the accuracy of 10^{-4}.

To reach the target luminosity, more positrons and the upgrade of booster BEP are needed.

REFERENCES

[1] .V.Danilov et al., EPAC'96, Barcelona, p.1149, 1996
[2] D.E.Berkaev, et. al., in Proc. EPAC 2008, Genoa, p.956.
[3] A.V.Otboyev, E.A.Perevedentsev, Phys.Rev. ST Acc. Beams **2**, 104401, (1999).
[4] A.A.Valishev et al., PAC 2003, Oregon, p.3398
[5] Yu.M.Shatunov, A.N.Skrinsky, Phys.Lett. **B198**, p.302, (1987).
[6] Yu.M.Shatunov, in Proc. SPIN-2010 Symposium, Julich, published in J. Phys. Conf. Ser. **295**: 012016, (2011).
[7] Ian C. Hsu et. al., Phys. Rev. E 54, 5657, 1996.
[8] V.Ch. Zhukovsky, I. Herrmann, Yad. Fiz. **14**, 150 (1971).

e^+e^- COLLIDER VEPP-4M: STATUS AND PROSPECTS

E.Levichev for the VEPP-4 team [1]
BINP, Novosibirsk 630090, Russia

Abstract

VEPP-4M is an electron-positron collider operating in the wide beam energy range from 0.9 GeV to 5.5 GeV. Since 2002 experiments on HEP are conducted at the collider with detector KEDR. Besides HEP, there are other scientific programs at the VEPP-4 accelerator complex including SR experiments, nuclear physics studies with internal gas target, CPT-theorem verification, accelerator physics experiments, etc. The paper discusses the recent results, present status and prospective plans of the facility.

INTRODUCTION

Starting from 2002 experiments are carried out with the universal magnetic detector KEDR [2] at the electron-positron collider VEPP-4M [3]. The VEPP-4M collider consists of the booster ring VEPP-3 with energy from 350 MeV to 2000 MeV and the main ring operating in the beam energy range from 0.9 GeV to 5.5 GeV. The physics program of the detector is focused on the study of ψ-, Υ-mesons and $\gamma\gamma$-physics. Precise mass measurements of J/ψ, $\psi(2s)$, $\psi(3770)$, D mesons and τ lepton were the goal of the first series of the experiments. Also electron partial width for J/ψ and ψ'-mesons were measured.

Table 1: Main Parameters of VEPP-4M.

Parameters	Values	Units
Circumference	366	m
Bending radius	34.5	m
Tunes Q_H/Q_V	8.54/7.58	
Mom. compaction	0.017	
Max. energy	5.5	GeV
Nat. chromaticity C_H/C_V	-13/-20	
RF-frequency	181.8	MHz
Harmonic number	222	
RF power	0.3	MW
RF voltage	5	MV
No.of bunches per beam	2	

The resonant depolarization (RD) technique [4] was used for precise instantaneous energy calibration. Continuous energy measurements were performed by determination of the utmost energy of the γ-quanta obtained from the Compton backscattering of laser photons against the electron beam [5, 6]. Main parameters of VEPP-4M are given in Table 1. The layout of the complex is shown in Fig.1.

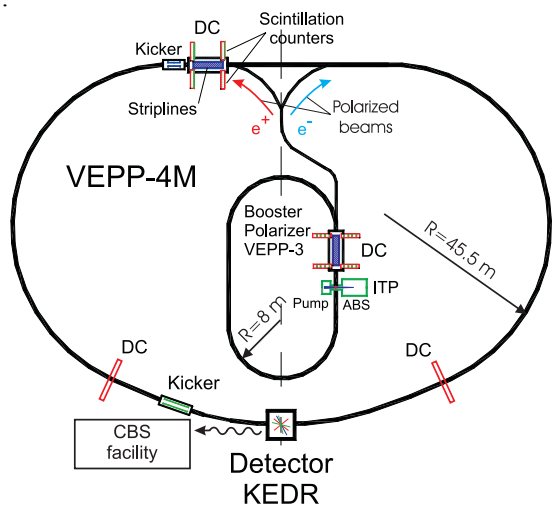

Fig.1: The VEPP-4 layout with main HEP experimental set-up: detector KEDR, Compton backscattering (CBS) system, gas internal target (ITP), counters (DC) and kickers for precise polarization experiments.

Besides the particles physics, there are other various experimental programs at VEPP-4 including studies with the synchrotron light, nuclear physics with polarized/unpolarized internal gas target, extracted test beam of e^- or γ for methodical goals, etc.

As the scientific program initially planned at 2000 for the decade is close to completion, it is good time for discussion of the results obtained and future plans.

HEP PROGRAM

In spite of rather moderate luminosity of the collider we were able to conduct experiments providing interesting and actual results due to the following factors:

- Wide beam energy span available for experiments that extends from 0.9 GeV to 5.5 GeV;
- The record-breaking accuracy (~10^{-6}) beam energy calibration that was developed at VEPP-4M with the help of the RD technique invented at BINP in the past;
- On-line monitoring of the beam energy during the luminosity run by Compton backscattering of the laser photons (accuracy is ~$3\cdot10^{-5}$);
- Universal magnetic detector KEDR with *LKr* calorimeter and Cherenkov aerogel counters with characteristics comparable with the best detectors in the world.

Fig.2 depicts a long time stability run when the energy was measured directly by RD, CBS and determined with the NMR probe inserted in the main dipole field.

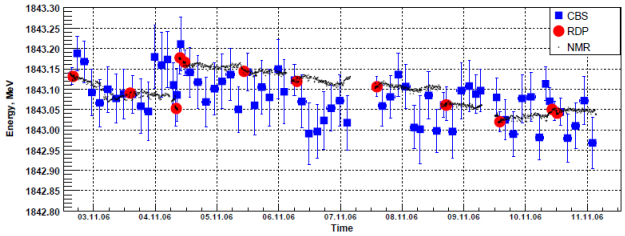

Fig.2: RD, CBS and NMR calibration of the VEPP-4M beam energy.

Table 2 lists the particles from the Particle Data Group booklet with the most precisely measured masses and two of them (J/ψ and ψ') were defined at VEPP-4M.

Table 2: Accuracy of the particle mass measurement

Particle	$\Delta M/M$ (PDG)
p	$0.1 \cdot 10^{-6}$
n	$0.1 \cdot 10^{-6}$
e	$0.1 \cdot 10^{-6}$
m	$0.1 \cdot 10^{-6}$
$\pi^{\pm}$	$2.5 \cdot 10^{-6}$
ψ'	$3.0 \cdot 10^{-6}$
J/ψ	$3.5 \cdot 10^{-6}$
π^0	$4.5 \cdot 10^{-6}$

Besides the ψ-mesons, the mass of the τ lepton was determined at VEPP-4M with the world record precision:

$$M_\tau = 1776.81^{+0.25}_{-0.23} \pm 0.15 \text{ MeV}$$

Other recent HEP results from VEPP-4M/KEDR include D^0- and $D^{\pm}$- mesons mass measurement, search for narrow resonances in e^+e^- annihilation in the beam energy interval 0.92 GeV-1.55 GeV, study of $\psi(3770)$, $\psi(2s)$, η_c and many more experiments presented in detail in [7-12].

The next experimental run will relate to the VEPP-4M operation with the energy increase, measurement of the hadron cross-section and $\gamma\gamma$-physics. In order to prepare for the run, in 2011 we tested the collider operation with energy ramp up to 4 GeV. The main goal was to check performance of all the accelerator systems (PS, SR absorbers, magnet cooling, etc.) with higher electrical/radiation power and tune the beam parameters for optimal luminosity, beam lifetime, etc. Fig.3 shows the testing run log and the luminosity obtained.

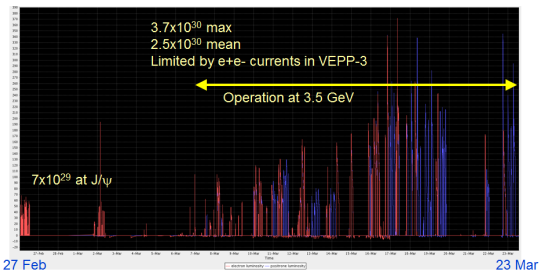

Fig.3: VEPP-4M test run at 3.5 GeV. On the left side of the plot (end of February 2011) the low energy luminosity is shown.

The collider performance increase at high energy is provided by development of the transverse and longitudinal feedback systems installed at VEPP-4M and suppressing the collective instabilities. Fig.4 depicts the e^- beam current during the test run.

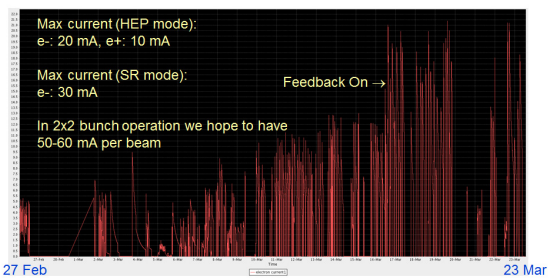

Fig.4: Electron current in VEPP-4M; a feedback system ON increases the maximum achievable current.

NUCLEAR PHYSICS

For many years nuclear physics experiments at VEPP-3 with internal gas target (proton or deuteron, polarized or unpolarized) have been carried out [13]. Advantages of our installation include easy change of the beam energy, relatively high current (up to 150 mA of e^-), precise beam energy calibration (CBS technique is applied also at VEPP-3), using of e^+e^- beams in the same geometry (both rotate anti-clockwise).

The recent experiments were dedicated to the proton form factor study. In the late ninetieth it was found that measurement result of the proton electric and magnetic form factor by elastic e^- scattering depends on whether the electron beam is polarized or not. It is explained now by contribution of the two-photon processes in the scattering. As this contribution depends on the electron charge, there is a possibility to estimate the two-photon contribution experimentally by comparison of e^+p and e^-p scattering. At VEPP-3 such experiment was performed initially in 2009 and continued in 2011 according to a modified kinematic scheme. During the run either e^+ or e^- beam is injected and accelerated in VEPP-3, and its elastic scattering at the hydrogen target is registered by a detector. After 15-20 min of the data collection, the beam

charge is changed. Fig.5 shows the beam charge integral collection.

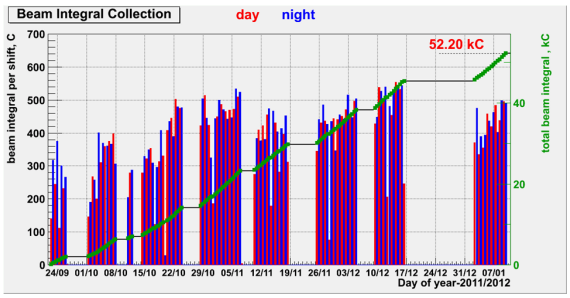

Fig.5: The beam integral collection in (e^+p/e^-p) scattering at VEPP-3.

The experimental data processing is presently under way; Fig.6 shows the time-of-flight analysis of the detected particles.

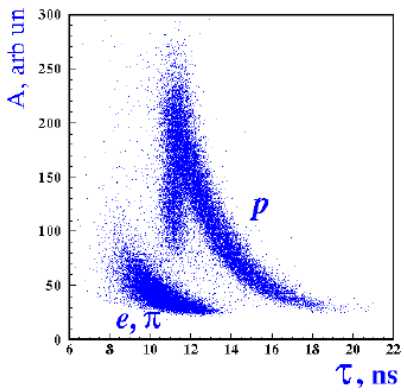

Fig.6: Escaped protons resolution by the time-of-flight measurement.

EXTRACTED TEST BEAM

To calibrate HEP detectors components, electron or γ beams with well-defined properties are used. In 2010 new experimental facility aimed for this purpose was developed at VEPP-4M. High energy electrons circulating in the accelerator collide either with residual gas atoms or with a specially inserted tungsten target and produce a flux of hard γ rays, which can be used directly or be converted to the electron/positron beams [14].

The experimental hall equipped with collimators, magnet spectrometer and detectors is shown in Fig.7. Parameters of the test γ or e^- beams are given in Table 3.

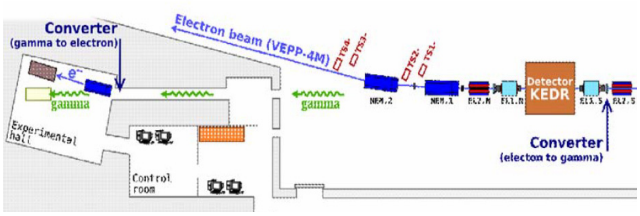

Fig.7: Test beam facility at VEPP-4M.

The realized experimental set-up allowed us to observe and measure, for the first time in Russia, focusing of the Cherenkov radiation from a four-layer aerogel with refraction index changing from layer to layer (Fig.8).

Table 3: Test beams parameters

	e^-	γ
E, GeV	0.1 ÷3.0	0.1 ÷3.0
σ_E/E, %	0.5 ÷5.0	~ 1
Intensity, Hz	10 ÷1000	1000
Resolution, mm	0.5	-

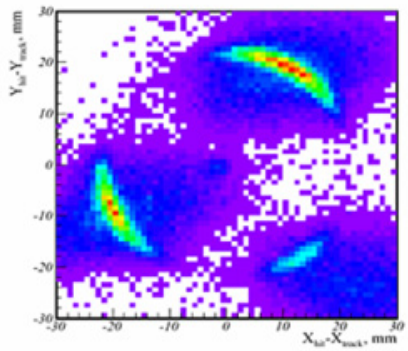

Fig.8: A Cherenkov-light ring observed at the VEPP-4M test beam facility

Width of the focused Cherenkov-light ring (~1 mm) corresponds well to that theoretically predicted.

Besides, scintillating crystals for detector for the COMET experiment (JPark, Japan) were calibrated at the test beam bench in 2011.

SR EXPERIMENTS

Experiments with synchrotron light have been carried out at VEPP-3 for more than 30 years. Twelve stations are installed in the experimental hall providing study on X-ray lithography, high pressure and time resolving diffractometry, EXAFS, X-ray fluorescence analysis, X-ray microscopy, small-angle scattering and others. One beam line is intended for stabilizing of the SR ray through a feedback between light monitors and VEPP-3 steering magnets. For details of numerous results we refer to [15].

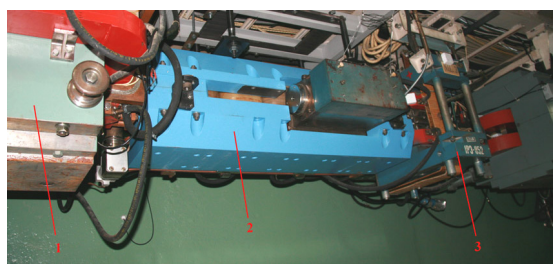

Fig.9: New wiggler installed at VEPP-4M.

Few years ago experiments in a new hall of VEPP-4M were started. In 2011 a 7-pole electromagnetic wiggler was installed at VEPP-4M (Fig.9) to enhance the radiation flux almost by one order of magnitude as compared to the bending magnet radiation used before. As the wiggler magnetic field exceeds the field in the bend, the radiation wavelength decreases. These facts allow starting a new program on extremely fast time resolution experiments with different explosive materials.

ACCELERATOR PHYSICS

Advanced beam diagnostics and other unique equipment (single-turn kickers/pick ups, Touschek polarimeter, nonlinear magnets, etc.) allow us to perform different studies in the area of accelerator science and technique. Due to the lack of space I can mention here only few of them.

Precise Polarization Experiments

A new system for extremely precise measurement of the beam polarization degree based on a Touschek electron pairs registration was recently applied at VEPP-4M. Number of counters installed in the ring vacuum chamber increases the registration efficiency by factor 10 as compared to the previous set-up. The count rate for the scattered electrons is now 1.5 – 2.0 MHz for 2 mA beam current. An absolute record accuracy ($1.5 \cdot 10^{-9}$) of the measurement of depolarization frequency is achieved. We hope that this feature will open new horizons for the energy calibration experiments. Another interesting application is a *CPT* theorem proving by comparison of the e^+/e^- spin precession frequency. Earlier such experiments were carried-out in BINP at VEPP-4M collider and now we hope to improve the spin frequency resolution up to 10^{-8}.

Fig.10 shows the process of a slow depolarization of electrons due to the extremely precise scanning of a depolarizer frequency with the rate corresponding to the energy shift of 2.5 eV/s.

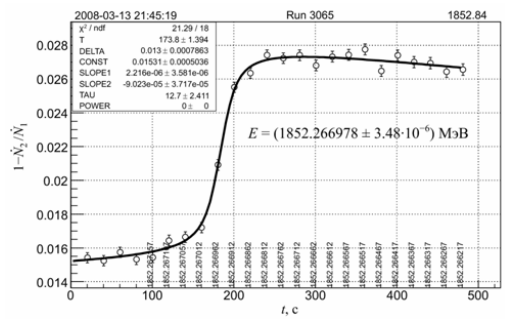

Fig.10: Nano-scale resolution of the energy measurement

Bunch Rotation in Longitudinal Phase Space

Generation of the ultra-short electron bunches in storage rings (for *ps*-time-resolving SR spectroscopy, laser-plasma acceleration experiments, etc.) is discussed extensively. Our experiment was based on the method described in [16], when the beam rotates vertically due to the coupling of the vertical/synchrotron motion under the short coherent kick. A large enough positive chromaticity (in our case – vertical) should be applied to the beam. The experimental study relates to the question: if natural decoherence allows us to see the beam tilt at all? Fig.11 (left) shows the BPM signal as a function of the turn number while the right plot corresponds to the beam tilt in the $y - s$ plane. The vertical chromaticity was set as +5 in this measurement.

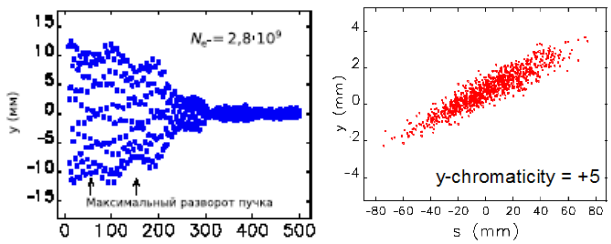

Fig.11: The bunch tilt and decoherence after the vertical kick. Arrows in the left plot show the moment of maximum beam tilt (~ half of synchrotron oscillation).

Experiment has shown [17] that at VEPP-4 this method works for $I_{bunch} < 1$ mA ($N < 10^{10}$ particles). For more intense beams decoherence of betatron oscillations due to head-tail interaction becomes important.

Resonance Crossing Observation

Turn-by-turn BPMs measuring the beam centre-of-charge evolution became a routine diagnostic instrument at circular accelerators many years ago. At VEPP-4M we have recently developed a unique synchrotron light monitor allowing observation of the transverse beam profile turn-by-turn during 2^{17} revolutions. The Fast Profile Meter is based on a Hamamatsu R5900U-00-L16 Multi-Anode Photomultiplier Tube with single anode size of 0.8 mm [18]. As an example of the new device potential the results of the nonlinear resonance crossing as a function of time are shown in Fig.12.

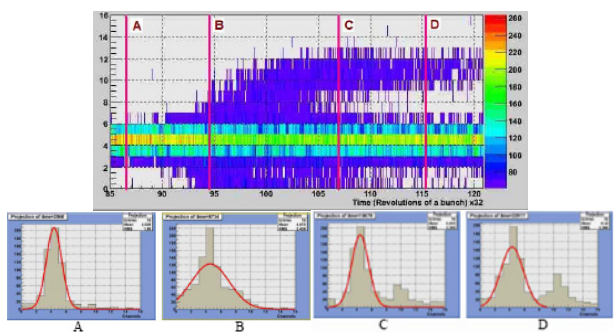

Fig.12: The resonance crossing experiment. Upper plot shows creation of a stable resonance island and particles trapping. Lower plot shows the beam profile evolution; a moment of the particle trapping in the island is clearly seen.

FUTURE PLANS AND PROSPECTS

The HEP program at the collider VEPP-4M formulated for a decade in 2000 by the BINP scientific community is almost over. The last remaining item from that list is experiment with energy increase up to 4.5 GeV – 5 GeV, which relate to measurement of the hadron cross-section R in the wide energy range and $\gamma\gamma$-physics. We are expecting that this experiment will be completed in 2-3 years. The question arises: what kind of future studies can be carried out at our facility afterwards? The answer is not simple but one point is clear for us: experimental programs planning at VEPP-4M must be challenging, interesting and satisfy prospective demands of relevant scientific communities. Among such plans I will mention here very briefly the following ones:

- Longitudinally polarized e^+e^- beams and HEP experiments with them. Future super-factories (SuperB in Italy, SuperCτ in Novosibirsk, etc.) will essentially apply longitudinally polarized e^+e^- beams. But the world experience on operation with such beams is very poor so production and study of longitudinally polarized electrons and positrons in circular colliders look rather attractive and actual. A strong point of the VEPP-4 complex is a possibility to polarize the beams in VEPP-3 in a reasonable time (~30 min).
- Converting of VEPP-4M in SR source. Several scenarios are now under consideration starting from moderate modernization of the storage ring (say, just insertion of modern wigglers and undulators) to the deep reconstruction when all magnets and vacuum components are replaced by new ones. In the last case a preliminary study [19] has shown that one may have 1 nm horizontal emittance at 3 GeV beam energy and 250 mA current.
- A new e^+e^- collider in the VEPP-4M tunnel is now under exploration. The project (with preliminary name Super K-meson Factory) is based on the Crab Waist collision scheme [20] and is considered as a prototype of the Super Cτ Factory. The double-ring collider allows us to have the peak luminosity from 10^{34} $cm^{-2}s^{-1}$ at the ϕ-meson energy (0.5 GeV per beam) to 5×10^{34} $cm^{-2}s^{-1}$ at the ψ-meson energy (1.55 GeV per beam).

ACKNOWLEDGEMENTS

The work is supported by the Ministry of Education and Science of the Russian Federation, RFBR (grants 10-02-00645, 11-02-01064, 11-02-01422, 10-02-00904), SB RAS, Joint Grant 103. The project of the Super K-meson Factory is supported by the Ministry of Education and Science of the Russian Federation through the Novosibirsk State Technical University, grant 2012-1.1-12-000-1011-1812.

REFERENCES

[1] A.Aleshaev, V.Anashin, O.Anchugov, V.Blinov, A. Bogomyagkov, D. Burenkov, S. Vasichev, S. Gluhkhov*, Yu. Glukhovchenko, O. Gordeev, V. Erokhov, K. Zolotarev, V. Zhilich, A. Zhmaka, A. Zhuravlev*, V. Kaminsky, S. Karnaev, G. Karpov, V. Kiselev, E. Kravchenko, G. Kulipanov, E. Kuper, G. Kurkin, A. Medvedko, O. Meshkov, L. Mironenko, S. Mishnev, I. Morozov, N. Muchnoi, V. Neifeld, I. Nikolaev, D. Nikolenko, I. Okunev*, A. Onuchin, V.Petrov, P. Piminov*, O. Plotnikova, A. Polyansky, Yu. Pupkov, E. Rotov, V. Sandyrev, V .Svistchev, I. Sedliarov, E. Simonov, S. Sinyatkin*, A. Skrinsky, V. Smaluk, E. Starostina, D. Sukhanov, S. Tararyshkin, Yu. Tikhonov, D. Toporkov, G. Tumaikin, I. Utyupin, A. Khilchenko, V. Tsukanov, V. Cherepanov, A. Shamov, D. Shatilov, D. Shvedov, S. Shiyankov, E. Shubin, I,Churkin
* Novosibirsk State Technical University
[2] V.V. Anashin et al., NIM A 478 (2002) 420.
[3] V.V. Anashin et al., EPAC 1998, v. 1, p. 400, BINP Preprint 2011-20, 136 pages.
[4] V.E. Blinov et al., NIM A 494 (2002) 81.
[5] N.Yu. Muchnoi, et al., EPAC 06, Edinburgh, Scotland, 26-30 Jun 2006, 1181-1183.
[6] V.E.Blinov et al. NIM, A598(2009)23.
[7] V.E.Blinov et al.Yader.Fizika 72, N 3, p. 1-6 (2009)
[8] V.V. Anashin et al. JETP, 2009, V.109, N4, pp. 590–601
[9] V.E.Blinov et al. Nuclear Physics B (Proc. Suppl.) 189(2009)21-23
[10] V.E.Blinov et al. Phys.Letters B 686 (2010) 84-90
[11] V.E.Blinov et al. Phys.Letters B 685 (2010) 134-140
[12] V.E.Blinov et al. Phys.Letters B703 (2011)543-546
[13] L.Barkov et al. 19th Int.Spin.Phys.Symp. (SPIN 2010), Julich, Germany, Sep.27-Oct.2, 2010, p.152.
[14] A.Yu.Barnyakov et al., NIM A 639 (2011) 290.
[15] BINP Annual Report, 2011, Novosibirsk, Rissia.
[16] W.Guo et al., Phys. Rev. ST Accel. Beams 10, 020701 (2007).
[17] A.Petrenko, PhD Thesis Work, BINP, Novosibirsk, 2012.
[18] V.Gurko et al., ICFA Beam Dynamics Newsletter, No.48, April 2009, 195-207.
[19] K.Zolotarev, private communication.
[20] P.Raimondi, 2nd Workshop on SuperB Factory, LNF-INFN, Frascati, March 2006.

TECHNOLOGY DEVELOPMENTS FOR CLIC

H. Schmickler, CERN, Geneva, Switzerland

Abstract

Just after the publication of its Conceptual Design Report (CDR) the CLIC study has made detailed plans for necessary technology developments in the coming years. This program includes the development of fully working prototypes of several technical subsystems as well as first pre-series or industrialization concepts of components needed in large identical quantities. The presentation will explain the development program and show in particular fields for potential collaboration.

INTRODUCTION

CERN's latest and foremost accelerator, the LHC, will probe the "terascale" energy region and provide a rich program of physics at a new high-energy frontier over the coming years. In this energy domain, it will study the validity of the standard model and explore the possibilities for physics beyond the Standard Model, such as super-symmetry, extra dimensions and new gauge bosons. The discovery potential is huge and will set the direction for future high-energy colliders. Particle physicists worldwide supported by ICFA [1] have reached a consensus that the results of the LHC will need to be complemented by experiments at a lepton collider in the Tera-Electron-Volt (TeV) energy range. The required beam collision energy range will be better defined following Physics requirements based on LHC results when substantial integrated luminosity will have been accumulated, tentatively by 2013-15.

The highest energy of lepton collisions so far, 209 GeV, was reached with electron–positron colliding in LEP at CERN. In spite of the 27 km diameter of LEP, beam energy was limited by synchrotron radiation losses just compensated by the most powerful super-conducting RF system built so far and providing up to 3640 MV per revolution. Since synchrotron radiation is inversely proportional to the bending radius and proportional to the fourth power of the particle mass, two alternatives are being explored to overcome this limitation and build a terascale lepton collider:

- use muons with a mass 207 times larger than electrons. The feasibility of Muon Colliders is being studied [2] addressing critical challenges specially the limited muon lifetime and their production in large emittances requiring developments of novel cooling methods,
- mitigate bends of particle trajectories in e+/- linear colliders where two opposing linear accelerators accelerate the particles to their final energy in one pass before focusing and collision in a central interaction point inside a detector.

Following preliminary Physics studies based on an electron-positron collider in the multi-TeV energy range [2,3], the CLIC study is focused on the design of a linear collider with a colliding beam energy of 3 TeV and a luminosity of 2.10^{34} cm-2 s-1 at the extreme of the considered parameter space. A scaled-down design is deduced at a lower energy, arbitrarily set at 500 GeV with the same luminosity for comparison with the alternative ILC technology.

The layouts of a 3 TeV linear collider using the CLIC technology is displayed in Fig 1.

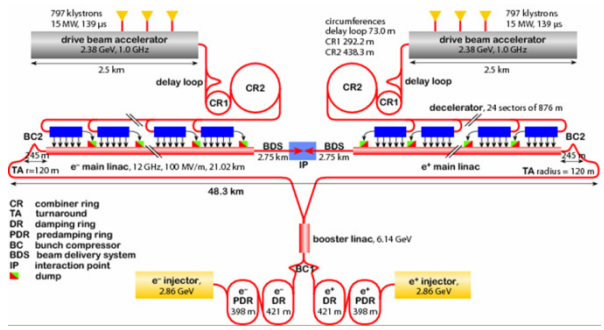

Figure 1: Layout of a 3 TeV cms energy linear collider based on the CLIC specific two-beam acceleration scheme.

WHY TWO-BEAM ACCELERATION?

In order not to confuse the arguments, no explicit references are given in this section. All important
Details including further references can be found in the CLIC Conceptual Design Report [4].

– The main objective is to build at reasonable cost and at a reasonable size a linear collider for the Multi-TeV range. This requires a very high acceleration gradient (100 MV/m), which cannot be achieved with super-conducting technology.

– For a given breakdown rate there is a very steep scaling between gradient and RF pulse length, hence the beam pulse has to be limited to about 150 ns. This short beam pulse is the fundamental design parameter, which has major consequences for the physics analysis of the events, for beam parameters to achieve the required luminosity, and for the RF power generation.

– In a circular accelerator the counter-rotating beams collide with a high repetition frequency, typically in the tens of kHz range. The repetition frequency of a linear collider by contrast is typically only 5–100 Hz. The luminosity necessary for the particle physics experiments has then to be reached with challenging parameters for bunch charge, beam emittance, and strength of the final focusing magnets. In the case of CLIC about 300 bunches

at high bunch charge spaced by only 0.5 ns have to be accelerated.

- For the generation of very high RF power only klystrons are currently available as power sources. There are, however, no klystrons on the market which can generate the required power for the short RF pulses (some 200 ns, which accounts for the 150 ns beam pulse plus some filling time of the accelerating cavities). The available klystrons can only deliver power into pulses which are about one order of magnitude longer. Hence klystrons with subsequent pulse compression networks would have to be used. A klystron powered linear collider with 100MV/m accelerating cavities would need about 35 000 high power klystrons (about 50MW each) with each klystron having a factor of five pulse compression.

– The numbers presented for klystron powering are not feasible in terms of cost and maintenance; they might be reconsidered as an option in case of a collider with a very low center-of-mass energy.

– The so-called CLIC scheme foresees the generation of the necessary RF power through the production of a second low-energy Drive Beam over a very long pulse (high-power klystrons are readily available) followed by a sophisticated compression scheme, in which the RF pulse is not time compressed, but the generated electron 'Drive Beam' itself is. The time-compressed Drive Beam then travels along with the Main Beam and generates the necessary RF power for acceleration by losing its energy in the 'decelerator' in special RF structures (PETS).

TECHNOLOGY DEVELOPMENTS

After publication of the CDR the mandate of the CLIC study for the next five years will be the development of all technologies needed for the construction of the accelerator. The present publication is restricted to a selected number of technology items, for which the CLIC study is actively looking for collaboration partners.

These developments cover the following domains:

- Industrial production of x-band (12 GHz) RF structures for beam acceleration, power extraction or interconnectivity.
- Test stands for long term high power testing of these x-band structures. This will need the procurement of the corresponding power source.
- Development of high efficiency 1 GHZ high power klystrons. Most likely this will be done in collaboration with industry.
- Continuation of the present CTF3 experimental program at CERN.
- Complete engineering integration of all components for the main beam acceleration and drive beam power extraction into so called "Two beam acceleration" modules. (TBM modules)

These (2m long) TBM modules integrate also a number of other technology development items, such as:

- active quadrupole stabilization against mechanical vibrations
- precision alignment system with remote controlled actuators
- vacuum manifolds
- the x-band RF system

In the following text more details are given.

TWO-BEAM ACCELERATION MODULES

Overview

The CLIC two-beam acceleration configuration consists of repeated 'modules' [5]. Each main linac contains more than 10000 "repeated "modules. The drive-beam, running parallel to the main linac, regularly powers two Accelerating Structures (AS) from one Power Extraction and Transfer Structures (PETS). Each module contains up to four PETS (see Figure 2), feeding two AS each, and two drive-beam quadrupoles, as a very dense lattice is required for the low-energy drive beam. Space for quadrupoles in the main linac is made by leaving out two, four six or eight accelerating structures and suppressing the corresponding PETS.

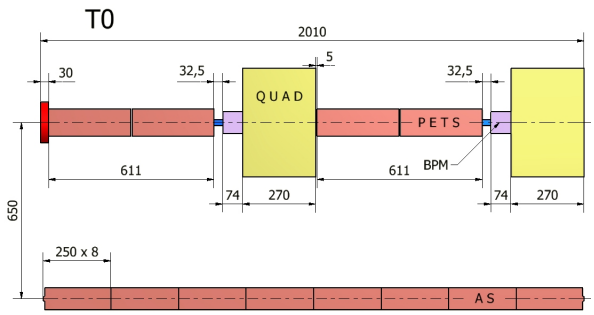

Figure 2: Schematic layout of CLIC type 0 module.

The module components are mounted on alignment girder. The stagger between the two linacs is made to give the correct relative RF to beam timing. The module length (2010 mm) is determined mainly by the length of accelerating structures (230 mm) and the fact that a PETS feeds two structures (a number which depends on the high-power capability of the PETS). Drive linac beam dynamics simulations show that the drive beam quadrupole spacing must be about 1 m with a quadrupole length of about 270 mm for sufficient strength. The remaining space is then available for two PETS and the BPM which is just sufficient. A 30 mm length has been reserved for inter-girder connections. A few modules with main beam and drive beam quadrupoles only are required in the end sector regions (about 10 m) where each drive beam is fed into and out of a drive beam linac sector. The two-beam module design has to take into consideration the requirements for the different technical systems. The main components are designed and integrated to optimize the filling factor and gain in compactness. Figure 3, shows the 3-D view of a typical two-beam module, with the main components, such as AS, PETS and quadrupoles. In this chapter the

main technical systems are reviewed and the main technical requirements recalled.

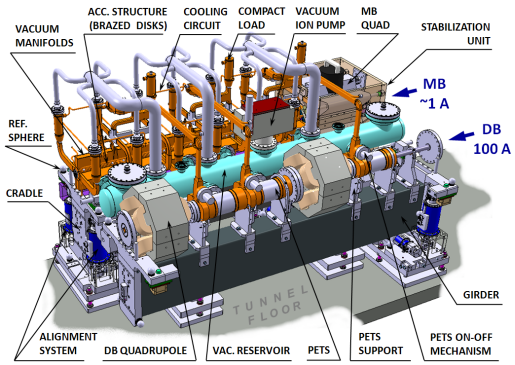

Figure 3: 3-D view of the CLIC two-beam module.

Quadrupole Stabilization System

One of the required actions to preserve the ultra-low transverse emittances during the beam transport is the mechanical stabilization of all 3992 main beam quadrupoles (MBQ) The integrated Root Mean Square (RMS) [17] of the vertical absolute displacements of the magnetic field centre of each quadrupole shall stay below 1.5 nm above 1 Hz. Similarly, it shall stay below 5 nm in the lateral direction.

To reach such a mechanical stability for the CLIC MBQ, ground vibration measurements in operating particle accelerators [6] have shown that a mechanical stabilization system is needed under each quadrupole. At each MBQ, the interconnected girders and supports with accelerating structures will be interrupted by the independent MBQ support. The MBQ will be supported by the stabilization system that is supported inside a magnet girder placed on the eccentric cams of the alignment system. The MBQ stabilization strategy is based on a stiff actuating support with stiff piezoelectric actuators, the measurement of the relative displacement between the quadrupole and an inertial reference mass (seismometer) and an active reduction of the transmissibility of the magnet support at low frequencies [7]. The main reason for the choice of this strategy is the robustness against external disturbance forces. The actuators are mounted in pairs in a parallel structure with flexural hinges, inclined and in the same plane. Each actuator pair is mounted inside an x-y guidance that will allow vertical and lateral motion but will block motion along and around (roll) the longitudinal axis of the magnet. A conceptual drawing of the quadrupole stabilization system is shown in Figure 4.

The displacement range and the stiffness of the actuators also allows to reposition the quadrupole in vertical and lateral direction between beam pulses with steps up to 50 nm in a range of ± 5 µm.

Beam Instrumentation

The linac module beam instrumentation mainly consists of Beam Position Monitors (BPM) and Beam Loss Monitors (BLM).

The present design of the BLM system is not advanced enough to be integrated in the mechanical layout of the module at this stage.

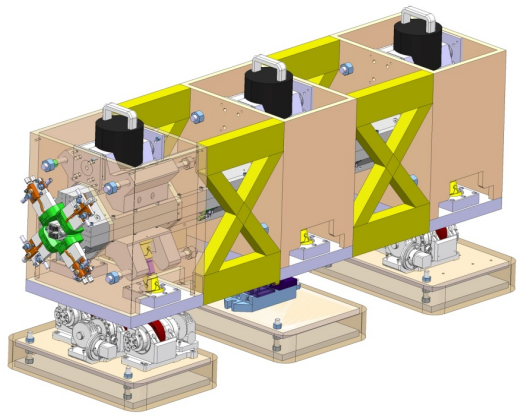

Figure 4: Conceptual drawing of the quadrupole stabilization system for MBQ type 4 placed on the alignment stage.

CLIC modules will be produced in large quantities and the BPM system is extensive. The main beam contains about 7500 BPMs while the drive beams require about 42000. There will be two drive beam BPMs per module. In the main beam, there will be a BPM for each quadrupole.

The main beam BPM consists of two cavities, a position cavity measuring both X and Y directions, and a reference cavity measuring beam charge and phase. Both cavities are resonant at 14 GHz. The reference cavity has two monopole mode coupling ports which allows for redundancy of the readout electronic in order to ensure optimal reliability, as required for the orbit feedback controller. The main BPM will be connected rigidly to the quadrupole with no possibility to adjust its position. Alignment targets are mounted on the top, in order to measure its relative position with respect to the quadrupole. The BPM is not connected to the Wire position system, (WPS). A 3D image of the main beam BPM is depicted in Figure 5.

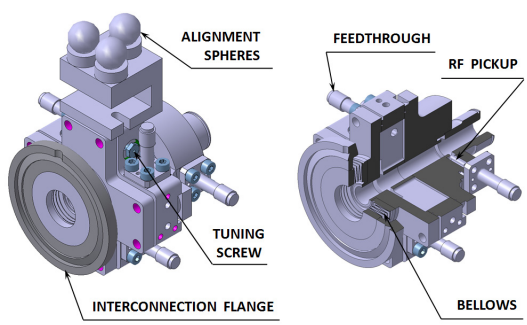

Figure 5: Main beam cavity BPM.

For the drive beam BPM, the current plan is to use short stripline BPMs, only 25mm long, with position signals processed at baseband in a bandwidth of 4-40

MHz. The strip lines are built into the quadrupole vacuum chamber, as shown in Figure 6.

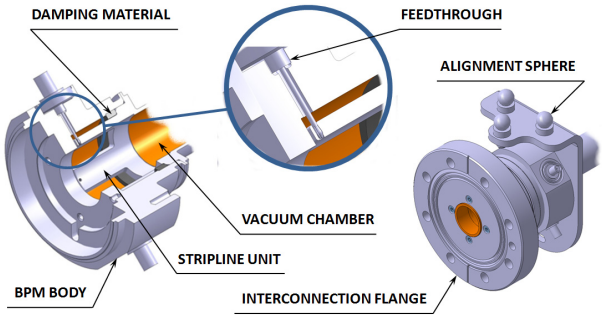

Figure 6: Drive Beam BPM.

Alignment System

Pre-alignment of two beam module will take place when beam is off. It will consist of two steps: a mechanical pre-alignment, which will pre-align all the components within +/- 0.1 mm with respect to the Metrological Reference Network (MRN), and an active pre-alignment fulfilling the requirements here after. For a sliding window of 200 m, the standard deviations of the transverse position of each component with respect to the straight fitting line must be inferior to a few microns. The total error budget in the determination of the position of components has been calculated. It corresponds to 14 µm for the RF accelerating structures and 17 µm for the main beam quadrupoles [8].

The determination of the position of the components will be performed thanks to a combination of two measurement networks:

1) A Metrological Reference Network (MRN) providing an accuracy and precision of a few microns over at least 200 m, and consisting of overlapping stretched wires

2) A Support Pre-alignment Network (SPN), associating to each support proximity sensors (capacitive based Wire Positioning Sensors (cWPS)) measuring with respect to a stretched wire, providing a precision and accuracy of a few microns over 10-15 m. Both networks will perform measurements with respect to the same stretched wire alignment reference. Overlapping stretched wires will be located between the two beams, as illustrated in Figure 7.

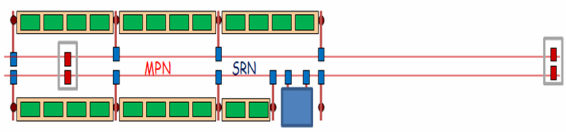

Figure 7: Module and measurements networks.

Several issues must be taken into account concerning the pre-alignment solution. First, the integration of the alignment systems must be considered. As a matter of fact, hydraulic network linking HLS sensors follows the equipotential surface of the Earth's gravity field; this will not be the case of the tunnel which will be straight. So every few hundred meters along the tunnel, superposed sensors will compensate the slope (see Figure 8).

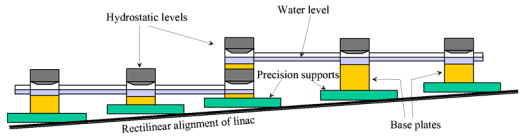

Figure 8: Configuration of HLS network in a laser straight tunnel.

A second issue is the constraints on the re-adjustment system from the other systems, which will apply additional transversal loads on the actuators and on the associated mechanics. Some simulations concerning their impact is under way; these constraints will be studied on the two beam module prototypes.

Third issue is the difference of temperature foreseen concerning the components between installation and operation. Fiducialisation and pre-alignment of the components on their supports will be performed at a standard temperature of 20°C, which will be modified during operation, generating dilatation of the components on the girders (mainly in the longitudinal direction) and misalignments. Simulations concerning misalignments are under way and will be validated on the two beam module prototypes. Temperature variation in the tunnel will also imply dilatation of the supports on which the position of the sensors have been determined. Temperature probes will be added on each support to correct dilatation effects. This means that the distance between sensors on their support and the stretched wire should be minimized. The sag of the wire could be limited (shorter length of wires, develop wires with small linear mass and high resistance to traction). Then, materials with low expansion coefficient should be used for the sensors supports.

SUMMARY

Using the example of the two beam acceleration module the complexity of the technologies needed for the future 3 TeV CLIC linear collider has been demonstrated. Starting from the published CDR in the year 2012 a technology development phase of about 5 years has been launched in order to define all components ready for construction. This large task is well suited to integrate international collaboration with institutes and industrial partners, which are cordially invited to contact the CLIC study team in order to establish such collaborations.

REFERENCES

[1] "ICFA Statement on Linear Colliders", http://www.fnal.gov/directorate/icfa/icfa_r&d.html (1993) and http://www.fnal.gov/directorate/icfa/icfa_LCstatement.html (1999)

[2] LCD: http://lcd.web.cern.ch/LCD/

[3] J. Ellis et al., Nature (London) 409, 431 (2001).

[4] M.Aicheler et al., A Multi-TeV Linear Collider based on CLIC Technology, CLIC Conceptual Design Report, CERN-2012-007

[5] G. Riddone, A. Samoshkin, et al., "Technical Specification for the CLIC Two-Beam Module", EPAC08, Genova, Italy
[6] C. Collette, K. Artoos, M. Guinchard, and C. Hauviller. "Seismic response of linear accelerators". Physical reviews special topics - accelerators and beams, 13:072801, 2010.
[7] C. Collette, K. Artoos, A. Kuzmin, S. Janssens, M. Sylte, M. Guinchard and C. Hauviller. "Active quadrupole stabilization for future linear particle colliders". Nuclear Instruments and Methods in Physics Research A, 621 (1-3):71-78, 2010
[8] D. Schulte, "Beam based alignment in the new CLIC main linac", PAC09, Vancouver, Canada, 2009

STORAGE, ACCELERATION AND SHORT BUNCHED BEAM FORMATION OF $^{197}AU^{+79}$ IONS IN THE NICA COLLIDER

A.V. Eliseev, O.S. Kozlov, I.N. Meshkov, A.V. Sidorin, A.V.Smirnov, G.V. Trubnikov,
JINR, Dubna, Moscow Region, Russia
T. Katayama, GSI, Darmstadt, Germany
V.N. Volkov, E.K.Kenzhebulatov, G.Y. Kurkin, V.M. Petrov, BINP SB RAS, Novosibirsk, Russia

Abstract

The regimes of high intensity beam of $^{197}Au^{+79}$ ions in NICA Collider are considered. The first stage – ion storage is proposed to be performed with Barrier Bucket technique at ion energy of 1 – 4.5 GeV/u. Ion accumulation at optimum for cooling energy level accompanied by slow acceleration with the same BB method to the energy of experiment also considered. Formation of bunched beam is fulfilled in two steps – first, at 24th harmonics and then, final formation, at 72th harmonics of the revolution frequency. The possibility of achievement of designed bunch parameters is shown.

INTRODUCTION

The goal of the NICA facility in the heavy ion collision mode is to reach the luminosity level of the order of 10^{27} $cm^{-2}s^{-1}$ in the energy range from 1Gev/u to 4.5 Gev/u. Collider circumference is 503 m and beta-function in IP is supposed to be 0.35m. The beam parameters required to achieve the design luminosity are listed in the Table 1 [1]:

Table 1: $^{197}Au^{+79}$ beam parameters

Number of bunches	24		
Rms bunch length	0.6m		
Ion energy, GeV/u	1	3.0	4.5
Ion number per bunch	$2.75\cdot10^8$	$2.4\cdot10^9$	$2.2\cdot10^9$
Rms dp/p, 10^{-3}	0.62	1.25	1.65
Rms beam emittance, h/v, (unnormalized), π·mm·mrad	1.1/ 1.01	1.1/ 0.89	1.1/ 0.76

Collider RF systems have to provide:

- Accumulation of required numbers of Ions in the energy range 1÷4.5 Gev/u.
- Accumulation at some optimum energy and acceleration up to the energy of experiment
- Formation of necessary number of bunches (24)
- Achievement of designed bunch parameters

This can be done with the help of three RF systems: one broad band type and two narrow-bands. The first one accumulates particles in longitudinal phase space with application of RF barrier bucket (BB) technique. By applying additional voltage meander between barriers it can be used also for acceleration (inductive acceleration). Second RF system works on 24-th harmonics of revolution frequency and is used for formation of proper number of bunches. The third RF system is used for the final bunch formation and maintenance bunch parameters during collision mode.

All stages of bunch formation as well as collision mode are accompanied by cooling process either stochastic or electron. General scheme of beam preparation is represented in the Fig. 1.

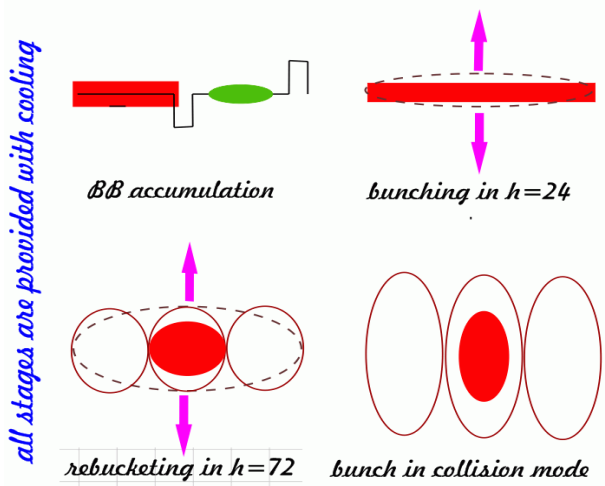

Figure 1: Scheme of RF cycle in Collider.

SHORT BUNCHED BEAM FORMATION

Accumulation of Ions $^{197}Au^{+79}$

Application of RF barrier bucket (BB) technique provides independent optimization of the bunch intensity, bunch number as well as controlling of the beam emittance and momentum spread during the bunch formation. In presence of cooling the number of the injection pulses can be large enough with suitable stacking efficiency. Intensity of the injected portion influences on the stacking process duration only and can vary widely.

Collider rings receive bunch every 4-5 seconds from Nuclotron. Bunch contains $1\div2\cdot10^9$ particles. Its total length and momentum spread are about 10 m and 10^{-3} accordingly. The BB pulses divide the ring circumference by two zones of equal length: the injection zone (where the synchrotron motion is unstable) and that one for the stack (with stable synchrotron motion). Barrier pulse phase width – π/6 rad and voltage amplitude – 2kV.

Numerical simulations of ion stacking with barrier bucket method have been performed independently by T.

Katayama [2] and A. Smirnov [3]. Both simulations have shown a sufficiently high efficiency of the stacking procedure (Fig. 2).

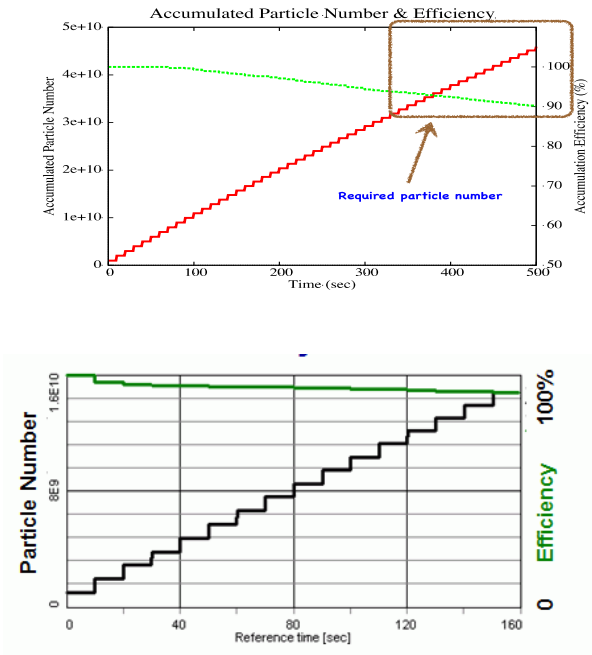

Figure 2: Increase of accumulated particle number as a function of time: up) - T. Katayama (3.5 GeV/u), down) - A. Smirnov (1.5 GeV/u); step curves: accumulated particle number vs. time, green lines: accumulation efficiency vs. time.

It was shown that time duration of approximately 200 seconds is enough for accumulation of required number of ions in energy range 1÷2.5 Gev/u notwithstanding the substantial dropping of its efficiency with the energy increase: At 1.5 GeV/u – 92% and at 2.5 GeV/u – 67%. The equilibrium between cooling and IBS processes corresponds to the momentum spread of ~$2 \cdot 10^{-4}$. This number is used for longitudinal emittance evaluation of coasting beam after barriers are off. Similar results were obtained for accumulation process accompanied by stochastic cooling for the energy 4.5 Gev/u [3].

Acceleration in Collider

There are two main reasons for acceleration in the Collider:

- Significant dependence of the accumulation efficiency on the ion energy
- Saturation flux density of Nuclotron's magnets is about 1.8T while 4.5 GeV/u corresponds to 2.2 T.

The possibility of ion accumulation at "optimal" energy level and further acceleration up to the energy of experiment with the help of BB RF system (induction acceleration) was considered. Design of BB resonator permits to create an accelerating "meander-type" voltage up to 300V amplitude. This implies acceleration rate at 0.024 T/s and acceleration time from 1 GeV/u to 4.5 GeV/u – 51 sec.

Beam Preparation for Collision Regime

At collisions the bunch has to have proper longitudinal emittance (see Table 1.). At 1 Gev/u rms emittance is equal to 1.25 eV·s while after accumulation its equivalent portion is about 5 eV·s. Final emittance is lesser then starting one over the whole energy range thus further beam manipulations have to be accompanied by cooling.

Preparation of beam for collision occurs in two stages. Firstly 24 bunches are produced using adiabatic capture technique: slow increase of RF voltage starting from "zero" level (ideally). Under cooling the bunch shrinks not only in its length but in emittance as well. Then the bunch length becomes short enough it is intercepted into third collider RF system working on 72th harmonics. Here it is possible to make a lower estimation of RF2 voltage needed in collider: emittance at interception must be equal to the final emittance and its length (±3σ) just fitted into bucket of RF3 (Fig. 3).

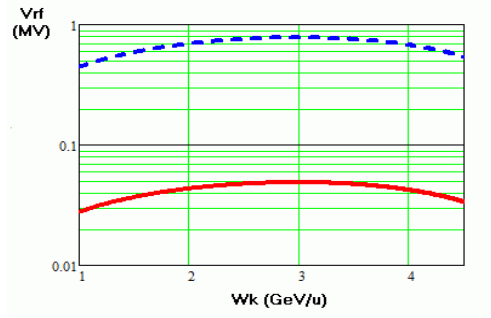

Figure 3: RF voltage amplitudes. RF2 – red. RF3 – blue vs. energy.

Although wide variety of scenarios is possible it is preferable to finish longitudinal emittance formation before RF3 starts working. In this case total voltage of RF2 can be limited by 50 kV. Bunch formation continues until its parameters meet conditions shown in Table 1. ESME code [4] was used for simulation of bunch transformation in longitudinal phase space after the rebucketing. Digest of simulation is represented on Fig. 4.

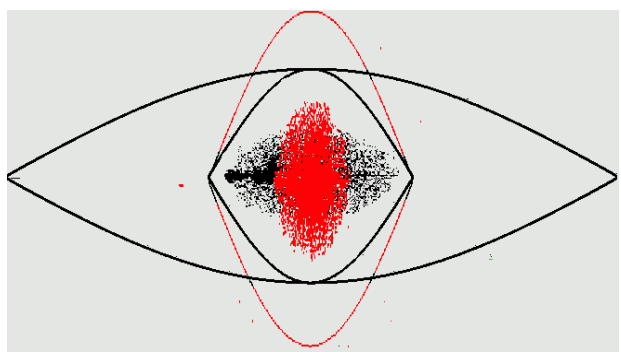

Figure 4: Bunch transformation after rebucketing

Total time of cooling needed for beam preparation after its accumulation in BB RF in both harmonic RF systems was estimated for the stochastic cooling with Palmer

method at 4.5 GeV/u [3]. The result is about 250 c. Time needed for e-cooling is of the order of 10 seconds.

RF STATIONS

Preliminary design of all RF stations has been done in BINP Novosibirsk.

BB Station

Induction accelerator of BB station has 14 sections 12 of which are used for BB accumulation and 2 sections for acceleration. The total amplitude of pulses gathered on BB sections is equal to ± 5 V. Two acceleration sections create meander shaped pulse of amplitude ± 300 V. Other parameters are: magnetic permeability of amorphous iron - ~60000, saturation flux density – 1.3 T, maximum dissipated power of the station – 22 kW.

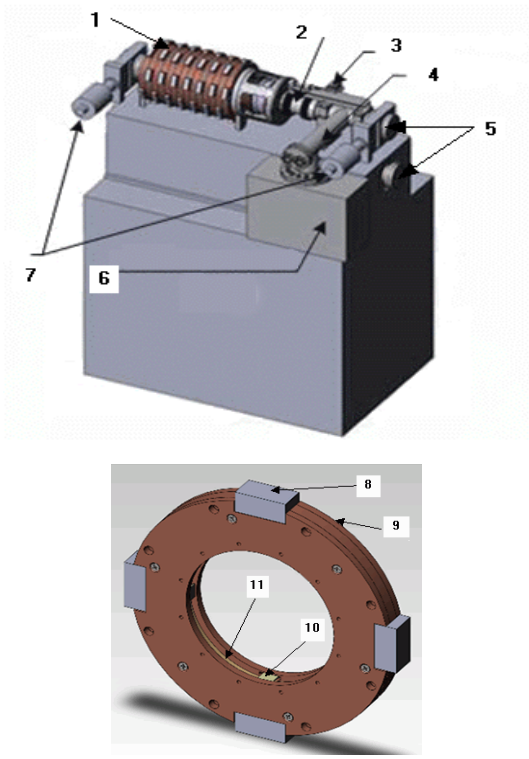

Figure 5: General view of BB station (up) and design of a section of the inductive accelerator (down). 1. Induction accelerator. 2. Contactor within vacuum chamber. 3. Drive for contactor. 4. Manometric tube. 5. Vacuum chambers. 6. Vacuum pump. 7. Gates. 8. Box of electronic keys. 9. Cover. 10. Excitation coil. 11. Amorphous iron coil

RF2 and RF3 Stations

Accelerating stations of 2^{-nd} and 3^{-d} RF systems (Table 2) have similar design and its general view is represented on the Fig. 6.

Table 2: Parameters of RF2 and RF3 resonators

parameter	RF2	RF3
Frequency range, MHz	12.528÷ 14.088	37.584÷ 42.264
Characteristic impedance, Ohm	15.4÷17.3	36.9÷42.5
Quality	3570÷3750	5490÷ 5820
Shunt impedance, kOhm	54.8÷60.0	252÷304
Accelerating voltage, kV	25	125
Dissipated power, kW	4.8÷5.7	32.1÷ 38.6
Number of resonators per ring	4	8

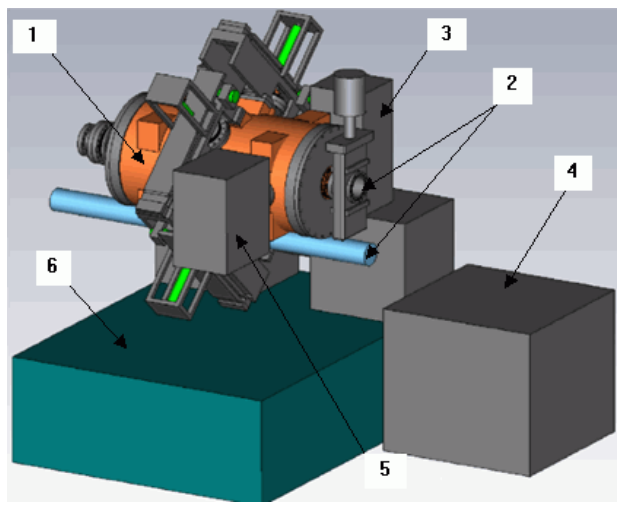

Figure 6: General view of the accelerating resonators of RF2 and RF3 for the upper collider ring. 1. Resonator. 2. Vacuum chambers. 3. Generator. 4. Air cooling for generator. 5. Vacuum pump. 6. Stand

CONCLUSIONS

1. The presented scheme of the bunch formation based on three RF systems seems to be optimal.
2. The parameters of all RF systems are achievable with present-day technologies.

REFERENCES

[1] I. Meshkov, NICA Project at JINR, Proc. Of COOL2011, Alushita, 2011.
[2] T. Katayama et. al., BEAM cooling at NICA collider, these proceedings.
[3] A. Smirnov, A.Sidorin, Long Term Beam Dynamics Simulation with the BETACOOL CODE, these proceedings.
[4] http://www-ap.fnal.gov/ESME

BEAM INSTABILITY PHENOMENA OBSERVED AT HIRFL-CSR IN THE PRESENCE OF ELECTRON COOLER*

Xiaodong Yang#, Jie Li, Lijun Mao, Guohong Li, Xiaoming Ma, Tailai Yan, Ruishi Mao, Tiecheng Zhao, Junxia Wu, Youjin Yuan, Jiancheng Yang, Peng Li
Institute of Modern Physics, CAS, Lanzhou, 730000, P. R. China

Abstract

Some signal samples acquired from Schottky probes and beam position monitor during operation were presented in this paper, and they were observed in the different operation stages such as during injection, after cooling and cooling force measurement. These signals were considered related with the ion beam instability. The central frequency of ion beam varied with the time. Some were caused by the ripple of hardware, the other were created by ion beam itself. The reasons which caused these phenomena were analyzed. The possible solutions were suggested, and some necessary upgrade and improvements were expected. These results were helpful to attempt the Schottky Mass Spectrometry measurement in the CSR.

INTRODUCTION

The Cooler Storage Ring of Heavy Ion Research Facility at Lanzhou (HIRFL-CSR) has been operating since 2007. The heavy ion beams in the energy range of few MeV/u to few GeV/u can be produced and delivered for the mass spectrometry experiments, the cancer therapy and atomic experiments and so on [1]. The latest results were reported in many papers and conferences [2-5].

In several machine runs the beam instability phenomena has been observed in the different operation stages such as during injection, after cooling and cooling force measurement. Besides this, the beam loss was also happened and investigated for electron cooling force measurements.

The instability resulted in beam loss and emittance growth, thus the achievable beam intensity and experimental precision is however limited. The instability of electron cooled beam has been studied in the different accelerators and reported by several laboratories in the world [6-9]. In this paper, the instability phenomena of electron cooled beam observed at HIRFL-CSR was described, and the Schottky spectra were analyzed.

The Schottky Mass Spectrometry (SMS) [10-12]is one of the high precision mass spectrometers based on storage ring with 10^{-6} or higher precision [13,14]. At HIRFL-CSR, the ultimate relative frequency spread $\Delta f/f$ of about 5×10^{-7} and about 1000s long-term beam stability are necessary for high precision mass measurements.

In order to improve the stable increasing beam intensity at HIRFL-CSR, and prepare the condition for SMS experiments, the mechanisms of instability have to be investigated and different cures methods should be tested.

BEAM ACCUMULATION IN CSRM

The main goal of the electron cooler application at HIRFL-CSR main ring is to increase the beam intensity with the help of stacking-electron cooling procedure at the injection energy [15,16]. A typical longitudinal Schottky signal during stacking-cooling procedure was shown in Fig. 1.

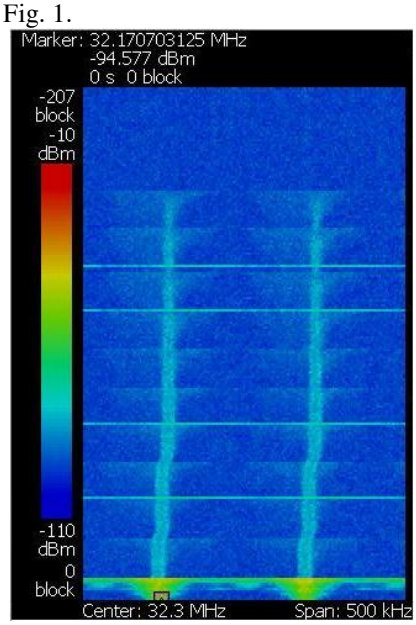

Figure 1: A typical Schottky spectrum of ion beam accumulation in CSRm under electron cooling.

For an effective electron cooling, the ion beam and electron beam have to overlap coaxially, and in principle the relative velocity of the ion beam and electron beam should be zero in the particle reference frame. It's obviously in Fig. 1 that the ion beam was symmetrically cooled down to the central frequency, which means that the injected ion energy, the electron beam energy, the magnetic field of dipole and the RF frequency were matched well. In addition, the deep colour of Schottky signal means the beam intensity increased step by step.

The cooling time obtained from Fig. 1 is corresponding to the simulation result, and there is no obvious sideband signal between the neighbour harmonic. It demonstrated that the HIRFL-CSRm was operated at reasonable work-point settings. The average velocities of electron and ion were almost equal. Further more, the central frequency shifted to left at the end of stacking procedure because of the changing of beam orbit at injection point.

*Work supported by The National Natural Science Foundation of China, NSFC(Grant No. 10975166, 10905083)
#yangxd@impcas.ac.cn

INSTABILITY OF ACCUMULATED HIGH INTENSITY BEAM

The betatron oscillation of high intensity cooled beam was observed in several cooling storage rings [17-19]. Fig. 2a was shown the analog signal from one of the BPM electrodes. After few seconds, the signal suddenly becomes very strong. It's clearly demonstrating the transverse oscillations of the high intensity cooled beam. Exactly at the same time the fast beam losses were observed in the DC current transformer. This was the factor which limited the attainable beam intensity. The corresponding beam current signal was shown in Fig. 2b.

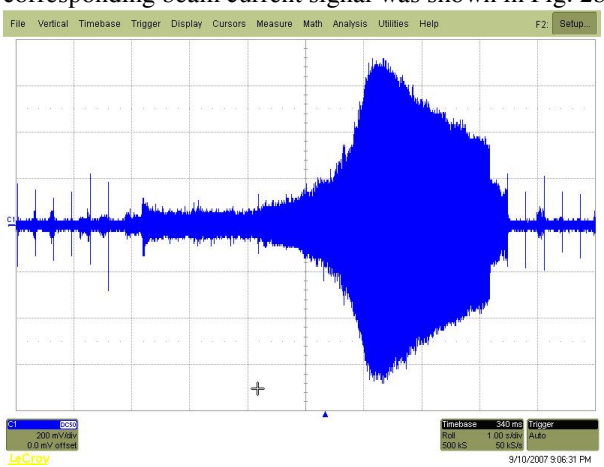

Figure 2a: The signal from one electrode of beam position monitor(BPM) during beam instability.

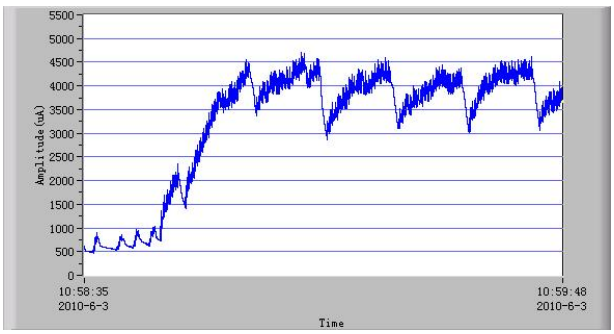

Figure 2b: The corresponding beam intensity signal from DC current transformer during beam instability.

The ion beam intensity during accumulation was not always increased linearly with the continuous injection. The stored beam seriously lost suddenly at some certain beam intensity, but not lost completely. A part of stored beam was remained in the ring. The intensity increased again with coming injections, and the beam loss happened again when the accumulated intensity achieved that certain value. The loss-increase-loss indicated some iterative character.

The space charge fields created by the stored ions in the beam influence its motion and changed the betatron tune value. For designed betatron tune value of CSRm (Qx/Qy=3.63/2.61), the difference resonance would appears and produce the serious beam loss during stacking procedure. The further work should be focused on the investigation with the tune value measurement and some simulation work.

INSTABILITY DURING INJECTION AND ACCUMULATION

In order to increase the intensity of the stored ion beams, a betatron stacking method in the horizontal phase plane is used at CSRm [20]. The closed orbit at injection point is distorted by means of four bump magnets. From the very beginning the bump is as large as pass close to the septum and then it is gradually reduced to zero within few milliseconds. The electron cooling device was turned on in the whole stacking procedure. The behavior of longitudinal Schottky signal during stacking was shown in Fig. 3. It's clearly that the frequency shift was happened at the beginning of injection.

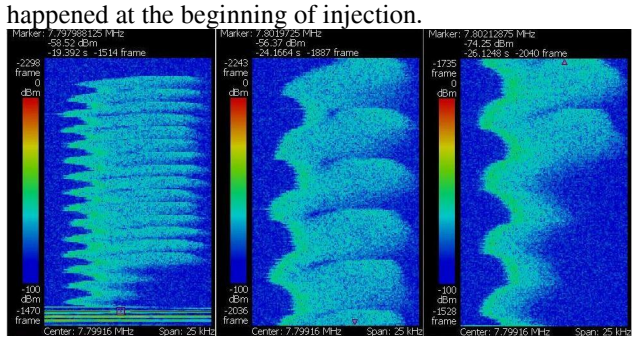

Figure 3: The Schottky spectra of a complete accumulation and injection under electron cooling. Left - whole, Middle - beginning of injection, Right - end of injection.

SIDEBAND DURING ACCUMULATION

Generally in the synchrotron, the frequency of transverse oscillation of the beam for each signal turn (usually called betatron tune or just "tune") is one of fundamental controllable knobs to avoid the instability phenomena. One of the most popular methods to measure the tune is using the sideband of the transverse Schottky signal with help of the beam exciter [21]. Fig. 4 shows the sidebands around the revolution frequency without any external exciting source. It seems that the transverse oscillation of cooled beam is large enough to make obvious sideband.

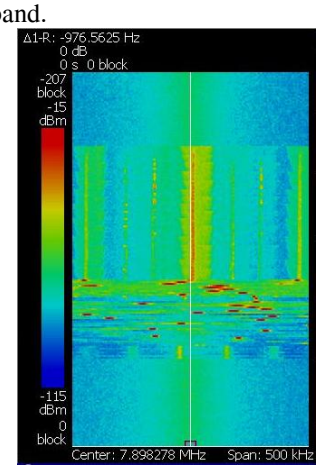

Figure 4: The Schottky spectrum with obvious sideband.

BEAM INSTABILITY AFTER ELECTRON COOLING IN CSRE

The ion beam with higher energy was injected into CSR experimental ring after accumulation and acceleration in CSR main ring, it was cooled again by electron at higher energy level in CSR experimental ring. The related physics experiments such as internal target one and ion-electron recombination etc. was carried out in the experimental ring. In the case of lower stored particle number, some investigation on the beam crystallization will be performed [22]. The high precision Schottky mass spectroscope will be carried out in the CSR experimental ring with the help of new developed resonance Schottky probe [23], the high beam instability was necessary to get so high required precision. The Schottky spectrum of 200MeV/u $^{86}Kr^{36+}$ ion beam after cooling equilibrium in CSR experimental ring were demonstrated in Fig. 5a, obvious instability was observed from these spectra. The frequency shift range was about ±25kHz/243MHz=±1×10^{-4}.

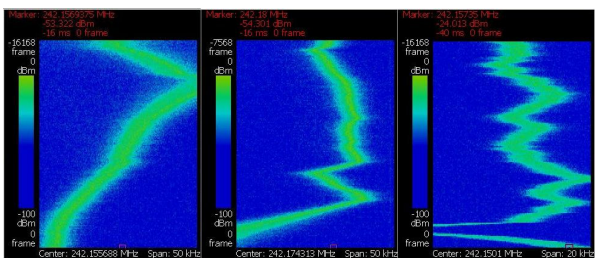

Figure 5a: The Schottky spectra of ion beam after cooling equilibrium in CSR experimental ring.

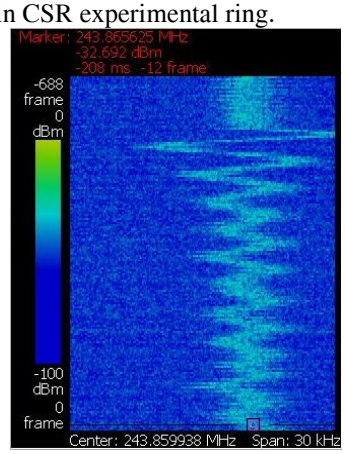

Figure 5b: The Schottky spectrum of ion beam in the absent of electron cooling at the isochronous operation mode in CSR experimental ring.

The possible reason caused the beam instability were the stabilities of dipole field, quadrupole field, correction dipole field, and the electron energy. Due to lack of the corresponding synchronous beam and field monitoring system, the instability relationship between ion beam and the fields was not correlated with each other, and the source of instability identification was difficult. A special data acquisition system was expected to establish in order to synchronously monitor the ion beam intensity, magnetic fields and the high voltage of electron cooler, obtain the relation between the changes of these parameters, built the contact each other, This system will be helpful to search the reason of ion beam instability.

The Schottky spectrum of 434.8MeV/u $^{86}Kr^{36+}$ ion beam in the absent of electron cooling at the isochronous operation mode in CSR experimental ring was shown in Fig. 5b. From the picture the ion beam instability was observed without electron cooler, but the amplitude was smaller than the above description. The reason maybe came from the operation mode of storage ring, magnetic field level of dipole and the time of data acquisition. Due to the magnets and their power supplies of CSR were not placed the constant temperature circumstance, the temperatures of storage ring channel and power supplies space varied with natural entironment in the different seasons, and also varied with day and night. The stability was higher in the early morning and winter than in the later morning and summer. By the way, the external disturbance of electrical power network had also the influence on the ion beam.

PHENONEMA DURING COOLING FORCE MEASUREMENT

In order to study the difference of electron cooling force between hollow profile electron beam and solid, several experiments was carried on the two cooler storage rings at HIRFL [24]. A typical Schottky spectrum of cooling force measurement process is shown by the left figure in Fig. 6a in measuring the cooling force of 400MeV/u $^{12}C^{6+}$ at the experimental ring CSRe. It can be noticed that when cooling action and heating by various factors attains balance, the spectrum peak width and area of cooled ion beam will keep nearly unchanged, i.e. the momentum spread and stored ion number will keep almost invariable. When the electron beam jump to other new energy, the ion beam will be slowly pull away and follow the electron beam for new equilibrium. With a vertical angle existing between ion beam and electron beam in the cooling section in cooling force measurement, Fig. 6a shows the process of electron beam energy jumps from 221.3keV down to 220.9keV by the middle spectrum and from 220.9keV up to 221.3keV by the right one.

It can be seen from the two spectra that: when an angle between the two beam exists, only a certain amount of ion beam was pulled away normally for new equilibrium point while the other part appears unusually slowly shift and tails. The possible causes is that: (1) beams uncoaxiality cause ion beam was only partly pulled away; (2) the distribution of ion beam may be layered or cylindrical, not normal Gaussian, which makes a certain amount of ions subject to a small cooling force; (3) higher transverse temperature of electron beam exists, which makes electron cooling less effective.

Another phenomenon is shown by Fig. 6b in the cooling force measurements of 200MeV/u $^{129}Xe^{54+}$ at CSRe. The left one shows a normal cooling force measurement process with an optimized toroid field,

while the middle and the right spectra correspond to the measurement with a smaller toroid field than the optimized one and with the electron energy jump from 108.96keV to 109.16keV and from 108.96keV to 109.16keV respectively. It is shown by the middle and right spectra that only a small part of ion beam was pulled away with the conventional manner and cooled down for the new equilibrium while the other part moves exceptional slowly and contribute to the broadening of attainable momentum spread at new equilibrium. This phenomenon can be explained by the increased transverse electron temperature which was caused by the change of toroid magnetic field from optimized one. The temperature affects the attainable momentum spread at the new equilibrium.

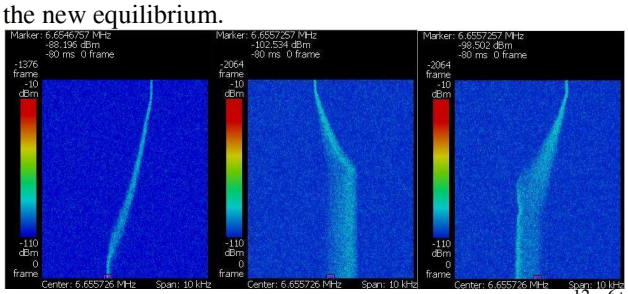

Figure 6a: The Schottky spectra of 400MeV/u $^{12}C^{6+}$ during cooling force measurement in CSR experimental ring. Left---zero angle between ion and electron beams, I_{CX6}=1.0A, I_{CY6}=3.0A. Middle---with an angle in vertical direction, I_{CX6}=1.0A, I_{CY6}=3.4A. Right---with an angle in vertical direction, opposite electron energy change, I_{CX6}=1.0A, I_{CY6}=3.4A.

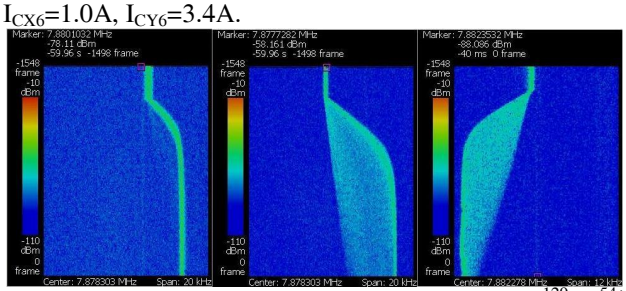

Figure 6b: The Schottky spectra of 200MeV/u $^{129}Xe^{54+}$ during cooling force measurement in CSR experimental ring. Left---optimal toroid current, I_{toroid}=602.3A, 108.96---109.16keV. Middle--- I_{toroid}=584.24A, 108.96---109.16keV. Right--- I_{toroid}=590.27A, 108.96---108.76keV.

THE ACTION OF RF MODULATION ON THE ION BEAM

A trapezoidal frequency modulation was applied to 200 MeV/u $^{12}C^{6+}$ ion beam at the experimental ring CSRe by RF station during its performance test [25]. The modulation wave is shown in Fig. 7, of which the voltage is 1 kV, both the rising and falling time are 5s, the plateau time is 50 s, and the center frequency is 6.60895 MHz with a frequency modulation relative width of $\Delta f/f=\pm 3\times 10^{-4}$. The Schottky spectra at the left in Fig.8 indicated that the whole ion beam changes its revolution frequency by closely following RF modulation waveform. But the enlarged momentum spread of ion beam shown by broaden spectrum peak indicates that ion beam is not well cooled down longitudinally. This can be ascribed to regular velocity mismatch between ion beam and electron beam. The 60 seconds periodically RF modulation brings ion beam a regular velocity change in longitudinal and can be used as a reference of slowly change, analyzing the change in other experiments. This experiment also shows that ion beam can be changed just following the action character of external force.

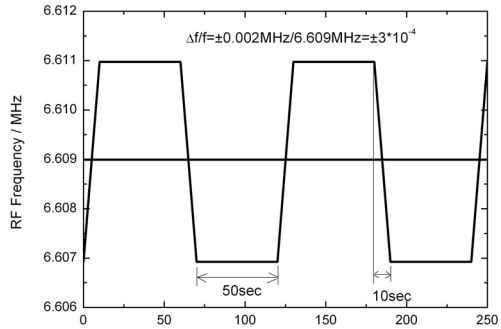

Figure 7: Waveform of RF frequency modulation.

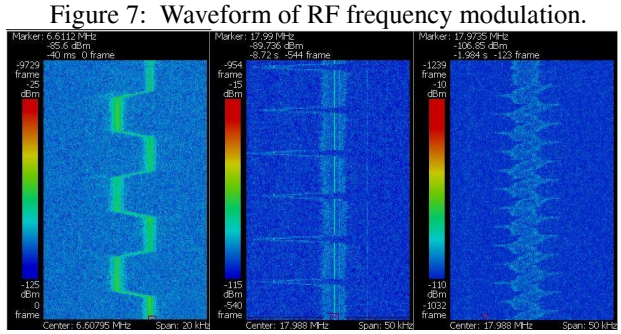

Figure 8: The Schottky spectra of ion beam under the action of external factor. Left---the action of the change of RF frequency. Middle--- the unilateral change of electron energy. Right--- the bilateral change of electron energy

THE ACTION OF ELECTRON ENERGY MODULATION ON THE ION BEAM

In order to carry out experimental research on electron-ion recombination at CSR, electron beam energy modulation module was added to CSRm electron cooler [26]. Fig. 9 shows the modulation process of electron beam acceleration voltage under optimal cooling and accumulation at CSRm with a rise-time of 20μs, plateau time of 100-1000ms, time interval of 1-2s, and amplitude of 5-1500V. As a typical Schottky spectra of unilateral modulation of electron beam energy, the middle figure in Fig. 8 shows that ion beam shifted its energy quickly corresponding to the change of electron beam energy, however such a plateau like the RF action in previous section was not observed. The right one in Fig. 8, as typical Schottky spectra of bilateral electron beam energy modulation, shows that only small part ions followed closely up to the change of electron beam energy while the majority was still far from new equilibrium location even at the next beginning of reverse direction modulation. The lag of majority ions leads to a momentum spread expansion of ion beam after several modulation cycles. This modulation is always taken as a fast change example.

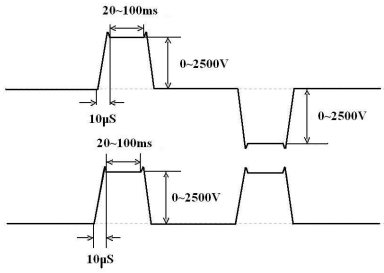

Figure 9: Waveform of electron beam energy modulation.

SUMMARY AND PROSPECTS

The beam instability phenomena related with electron cooler in HIRFL-CSR were briefly described and roughly analyzed in this paper. The described phenomena should be carefully investigated seriatim both theoretically and experimentally in order to understand their mechanism and causes. The monitor system will be established for measuring these instabilities in the near future. From the measurement results, the reason and characters will be revealed. The solution for alleviation and suppression should be considered from the technical point of view. The proper and effective methods of instability suppression should be proposed and developed hereafter. The useful and constructive information should be provided for machine improvement and upgrade in the interest of providing the high quality heavy ion beam satisfied the various requirements for high precision physics experiments.

REFERENCES

[1] Yuan Youjin, Xia Jiawen, Present status of storage rings at HIRFL, 8th International Conference on Nuclear Physics at Storage Rings (Stori11) Laboratori Nazionali di Frascati dell'INFN , Italy October 9-14, 2011.

[2] Wu Qingfeng, Li Qiang, Jin Xiaodong, et al. Bystander effect in human hepatoma HepG2 cells caused by medium transfers at different times after high-LET carbon ion irradiation, Nuclear Instruments and Methods in Physics Research B 269 (2011) 153–158.

[3] Yu Deyang, Xue Yingli, Shao Caojie et al. Observation of K- and L-REC in 200 MeV/u Xe^{54+}-N_2 collisions at HIRFL-CSR, Nuclear Instruments and Methods in Physics Research B 269 (2011) 692–694.

[4] Mei Bo, Tu Xiaolin, Wang Meng et al. A high performance Time-of-Flight detector applied to isochronous mass measurement at CSRe Nuclear Instruments and Methods in Physics Research A 624 (2010) 109–113.

[5] Tu X L, Xu H S, Wang M et al. Direct Mass Measurements of Short-Lived A=2Z-1 Nuclides ^{63}Ge, ^{65}As, ^{67}Se, and ^{71}Kr and Their Impact on Nucleosynthesis in the rp Process PHYSICAL REVIEW LETTERS 18 MARCH 2011 PRL 106, 112501 (2011).

[6] Liu Y D, Guo Z Y, Qin Q et al. Simulation of the electron cloud instability for BEPCII Proceedings of APAC 2004, Gyeongju, Korea 97-99.

[7] Wang J Q, Guo Z Y, Liu Y D et al. Beam instability studies of BEPC and BEPCII, Proceedings of EPAC 2004, Lucerne, Switzerland 2131-2133.

[8] Jiang B C, Chen G L, Chen J H et al. Observation of beam instability in the SSRF storage ring, Chinese Physics C CPC(HEP & NP), 2009, 33(Suppl.2): 75-77.

[9] Hofmann I, Beckert K, Cocher S et al. Diagnostics and instability studies of cooled ion beam, Proceedings of EPAC1990, 229-233.

[10] Dai G X, Schottky mass spectroscope, Nuclear Physics Review, Vol. 14, No. 4, Dec. 1997

[11] Tu X L, Xu H S, Xia J W et al. A pilot experiment for mass measurement at CSRe, CPC(HEP & NP), 2009, 33(7): 516-520.

[12] Tu X L, Wang M, Hu Z G, et al. Secondary electron time detector for mass measurements at CSRe, CPC(HEP & NP), 2010, 34(3): 363-367.

[13] Franzke B, Beckert K, Eickhoff H, et al. Schottky Mass Spectrometry at the Experimental Storage Ring ESR Physica Scripta. Vol. T59, 176-178, 1995.

[14] Geissel H, Litvinov Y A, Beckert K, et al. Present and future experiments with stored exotic nuclei at the FRS-ESR facility Eur. Phys. J. Special Topics 150, 109−115 (2007).

[15] Yang X D, Li G H, Li J, et al. Electron cooling experiments in CSR Science China Physics, Mechanics & Astronomy, 2011, Vol.54 Suppl.2,s274-s278.

[16] Yang X D, Li J, Mao L J, et al. Electron cooling performance at IMP facility, Proceedings of COOL'11, Alushta, Ukraine 1-5.

[17] Bosser J, Carli C, Chanel M, et al. Stability of cooled beams, Nuclear Instruments and Methods in Physics Research A 441 (2000) 1–8.

[18] Uesugi T, Fujisawa T, Noda K, et al. Observation of beam-size blowup due to half-integer resonance in a synchrotron Physical Review Special Topics - Accelerators and Beams Volume 7, 064203(2004).

[19] Uesugi T, Noda K, Syresin E, et al. Cooled-stacking injection and damping of a a transverse ion-beam instability at the HIMAC synchrotron, Nuclear Instruments and Methods in Physics Research A 545 (2005) 45–56.

[20] Tang J Y, Injection and Extraction Techniques in Circular Accelerators, Chinese Physics C (HEP & NP) Vol. 32, (S1) , 2008 256-258.

[21] Zhao T C, Mao R S, Zheng J H, et al. Tune measurement system for HIRFL-CSR, Atomic energy Science and Technology, Vol. 43 No. 3 Mar. 2009 263-265.

[22] Wei J and Yu P C, Status and challenges in beam crystallization http://accelconf.web.cern.ch/AccelConf/COOL2009/papers/tua2mcio01.pdf

[23] Zang Y D, Mao R S, Wu J X, et al. Schottky beam diagnostic system at CSRe[J]. High Power Laser and Particle Beams, 2011, 23(07):1899-1903.

[24] Mao L J, Li G H, Li J, et al. Cooling force measurements with variable profile electron beam at HIRFL-CSR Proceedings of COOL09, Lanzhou, China THM1MCCO03 107-110.

[25] Xu Z, Zhao H W, Wang C X et al. RF system design and measurement of HIRF-CSRe Chinese Physics C CPC(HEP & NP), 2009, 33(5): 387-392.

[26] Meng L J, Ma X, Liu H P et al. The first test experiment performed at the electron cooler of storage rings in Lanzhou, (HCI 2008), IOP Publishing, Journal of Physics: Conference Series 163 (2009), doi:10.1088/1742-6596/163/1/012031.

HIGH VOLTAGE ELECTRON COOLER*

M. Bryzgunov, A. Bubley, A. Goncharov, V. Panasyuk, V. Parkhomchuk, V. Reva,
D. Skorobogatov, BINP SB RAS, Novosibirsk, Russia
J. Dietrich, TU Dortmund and Helmholtz Instituit Mainz, Germany
V. Kamerdzhiev, FZJ, Jülich, Germany

Abstract

Discussions on physical requirements and technical design of the 2 MeV electron cooler for the synchrotron COSY began in 2002.

In 2009 contract for cooler production was signed. In this report results of cooler commissioning with electron beam at BINP are discussed.

INTRODUCTION

The new generation of particle accelerators operating in the energy range of 1-8 GeV/u for nuclear physics experiments requires very powerful beam cooling to obtain high luminosity. For example the investigation of meson resonances with PANDA detector requires momentum spread in antiproton beam, which must be better than 10^{-4}. To obtain such a momentum spread cooling time in the range of 0.1- 10 s is needed. The 4 MeV electron cooler at the RECYCLER ring (FNAL) [1] achieves cooling time about 30 min. The new cooler for COSY should provide a few orders of magnitude more powerful longitudinal and transverse cooling that requires new technical solutions. [2] The basic idea of this cooler is to use high magnetic field along the orbit of the electron beam from the electron gun to the electron collector. In this case high enough electron beam density at low effective temperature can be achieved in the cooling section [3].

The basic parameters of the COSY cooler are listed in Table 1. The length of the cooling section is given by the space available in the COSY ring.

Table 1: Basic Parameters of the 2 MeV electron cooler.

Energy Range	0.025 ... 2 MeV
High Voltage Stability	$< 10^{-4}$
Electron Current	0.1 ... 3 A
Electron Beam Diameter	10 ... 30 mm
Length of Cooling Section	2.69 m
Toroid Radius	1.00 m
Magnetic Field (cooling section)	0.5 ... 2 kG
Vacuum at Cooler	10^{-9} ... 10^{-10} mbar

The calculation of cooling of a 2GeV proton beam with high density electron beam is shown in fig.1 The beam on each turn passes hydrogen target with density 10^{15} 1/cm^2. Magnetic field in the cooling section was taken as B=2 kGs.

*Work supported by the Ministry of Education and Science of the Russian Federation

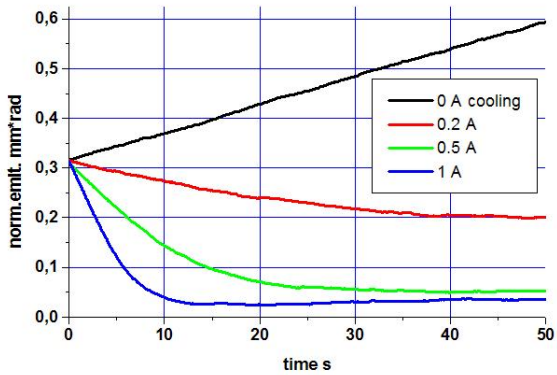

Figure 1: Cooling of 2 GeV proton beam .

From fig.1 one can clearly see that cooling shrinks the proton beam to small emitance and just 0.2 A suppressed the scattering on target. The equilibrium emittance decreases with increasing electron current by the more powerful cooling.

MAIN COMPONENTS OF COOLER

. The main features of the cooler are [2]:

1. The design of the cooling section solenoid is similar to the ones of CSR (IMP) and LEIR (CERN) coolers designed by BINP [3]. However, for the 2 MeV cooler the requirement on straightness of magnetic field lines is so high ($\triangle\theta < 10^{-5}$) that a system for control of magnetic field lines in vacuum becomes necessary.
2. For suppression of high energy electron beam losses at IMP and LEIR coolers electrostatic bending was used [4]. The shape of the 2 MeV transport lines, however, dictates a different approach. The collector (inside the HV terminal) is complemented by a Wien filter to suppress return electron flux.
3. Both acceleration and deceleration tubes are placed in the common high voltage tank.
4. The high power cascade transformer is installed around high voltage column for powering solenoids for generation of magnetic field along electron beam trajectory(Fig.2).

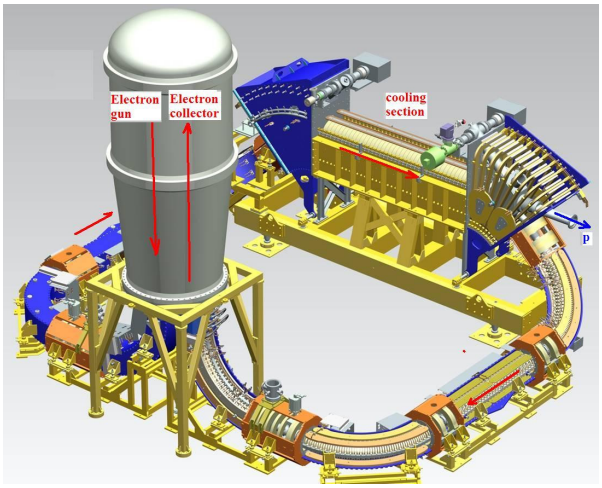

Figure 2:Sketch of 2 MV cooer for COSY.

The high voltage tank is shown in fig 3.

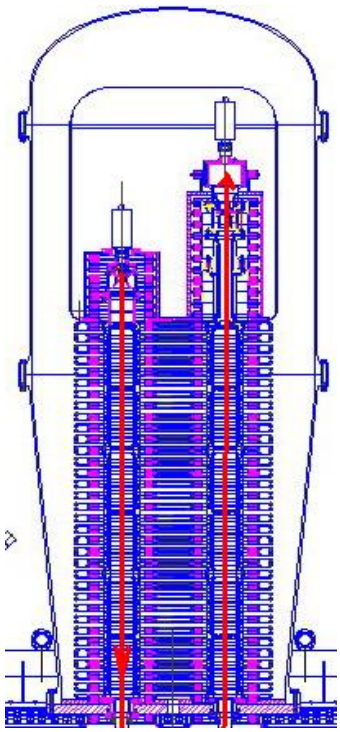

Figure 3:The high voltage tank of the cooler.

High Voltage Experiments

The high voltage tank was filled with SF_6 gas. Fig.3 shows the corona current versus high voltage for different pressures. Most of the time the cooler was operated at 6 bar (+5 atm). This pressure allows for electron beam with energy up to 1.5 MeV. The corona current decreased with time but once happened jump with increasing corona from nominal value 15 mkA on 1 MV to 100 mkA by destroy the aluminium scotch used for smoothing inner rough surface of tank. Small pane of aluminium rise perpendicular of surface. For stable operation cooler (without sparking) the pressure 7-8 bar (6-7 atm) can be used.

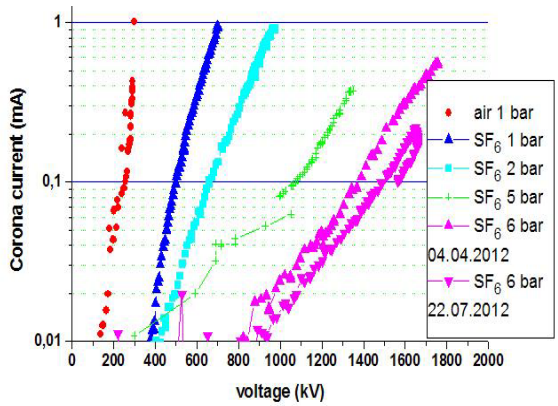

Figure 4: Corona current versus voltage for different SF_6 pressures.

Electron Gun

The electron gun design is based on the concept of the "hollow" electron gun [4]. It uses a ring-shaped near-cathode electrode (grid electrode) for changing the profile of the electron beam. The new feature is splitting the ring in 4 sectors. This allows generating four AC beams with different position relative to the centre.

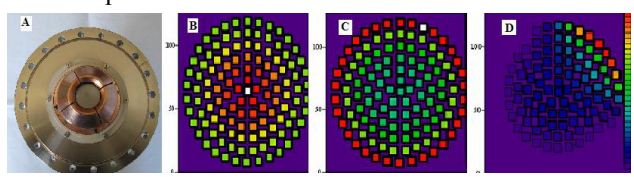

Figure 5: A is a photo of the cathode with four sector gridelectrodes, B is parabolic shape beam with maximum at centre C is "hollow" beam with minimum at the centre, D is AC component of beam with RF voltage applied to a single sector.

This design can be used as diagnostic tool for space charge of electron beam along the cooler. The pick-up monitors can detect position of this AC fractions(components?) (4 sectors and centre when the same AC voltage is applied to all 4 sectors) of the electron beam. The space charge (including ions accumulated in the electron beam) generate rotation of AC fractions around the beam axis. The experiments with clearing ions from the main electron beam demonstrated changing of this rotation.

Electron Collector with Wien Filter

The high voltage cooler produces high level of radiation in case of high electron current to ground. In order to avoid this, efficiency of recuperation (which is equal to the efficiency of collector) should be as high as possible.

Efficiency of the collector in the cooler is improved by suppression of the secondary electron flux by crossed transverse electric and magnetic fields (Wien filter). For primary beam influence of electric field is compensated by magnetic field, but for secondary beam, which moves

in opposite direction, electrostatic and Lorenz forces act in one direction and the beam is shifted (deflected away ..?) from primary beam and absorbed by special electrode (secondary collector).

On fig. 6 scheme of the collector with filter and part of magnetic screen with permanent magnets are shown. Electron beam comes from the acceleration tube (1) to the vacuum chamber of Wien filter (2), which contains electrostatic plates (3) for production of transverse field in the filter. After the filter the beam goes to the collector (4), which is cooled by oil. Combination of magnetic screen shape (5) and current in coils of solenoid (6) distributes electrons across the internal surface of the collector. Solenoid is also cooled by oil through the holes in one plate of the solenoid screen (8). Transverse magnetic field in the filter is produced by a set of permanent magnets (9). Diaphragm (10) provides sharper edge of transverse magnetic field distribution.

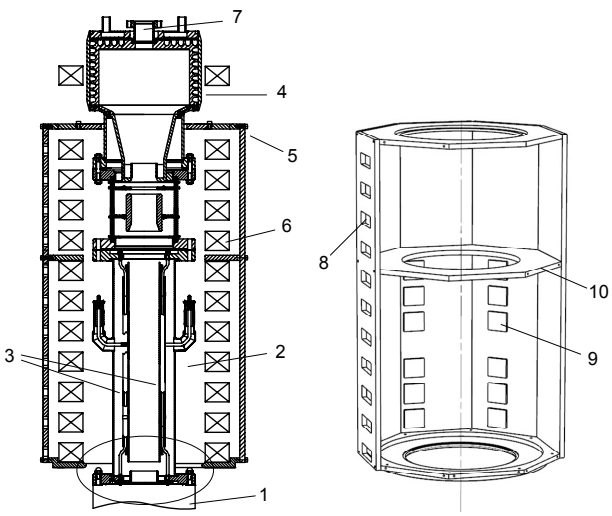

Figure 6: Collector with Wien filter inside solenoid magnet(s) (left) and magnetic screen of the solenoid with permanent magnets (right)

Clearing Electron Beam System

The BINP low voltage coolers used electrostatic bending electrodes that simultaneously remove secondary ions generated by ionization of residual gas from the electron beam . It is a good solution for low energy cooler. However for 2 MV the electric field for compact bending with 1 m radius requires electric field of 24 kV/cm resulting in +-100 kV on the bending plates . These values were considered impractical.

For COSY cooler clearing electrodes installed in toroid magnet are used. At strong magnetic field B the low energy electrons and ions move across magnetic and electric fields. Radius of drift oscillation in electric field E equal to: $R = \frac{E}{B^2}\frac{mc^2}{e}$ is very small.

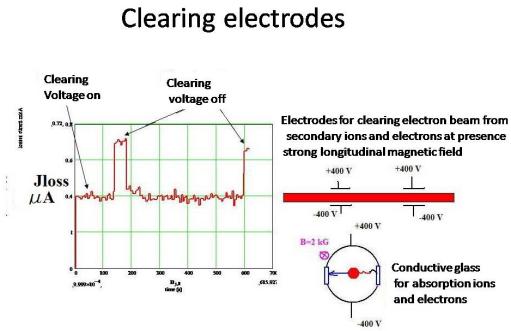

Figure 7: The principle of system for clearing the electrons and ions from main beam.

For electric field of 60 V/cm (+-300 V on electrodes) electron Larmor radius is only $8*10^{-5}$cm and proton Larmor radius is 0.15 cm. For easier clearing conductive glass is installed between electrodes so that equipotential lines cross the glass where electrons and ions are catches. Fig 7. shows that using clearing electrodes decreased losses of electron current by almost factor of 2 from 0.7 μA to 0.4 μA.

Magnetic System

The main component of the magnetic system is the cooling solenoid where electron and proton beams move at (on?) the same orbit. To satisfy the requirements on straightness of the magnetic field, the cooling solenoid is assembled from numerous short coils. The required field quality is achieved by mechanically adjusting the angles of individual coils. Dipole magnets are installed along the proton orbit for compensation of the vertical field action on protons by the toroids. For better compensation of transverse components of magnetic field generated by current leads, two types of coils with opposite direction of winding are used. Magnetic field measurement along the electron beam orbit from gun to collector was performed by a set of calibrated Hall probes, which were located on a carriage. Representative parts of the magnetic system were selected for measurements. The carriage passed step by step through selected part on rails. Longitudinal, normal and binormal magnetic field components were measured. Each component is measured at four different points that gives information about dipole and gradients of these field components???.

Discontinuities of field arise at joints of different parts of magnetic system (solenoid – toroid, bend – solenoid etc). Profiles of curvature of longitudinal field $B_{long}(s)$ of bends and toroids and profiles of their bending fields $B_{bend}(s)$ do not coincide and centrifugal drift counteracts only on average. From here resonant dependence arises between electron energy and values of magnetic fields for passing of electron through magnetic system without heating. Fig.8 shows longitudinal and bend component of magnetic fields along the beam orbit for 1.5MeV electrons. Joints are marked by ×.

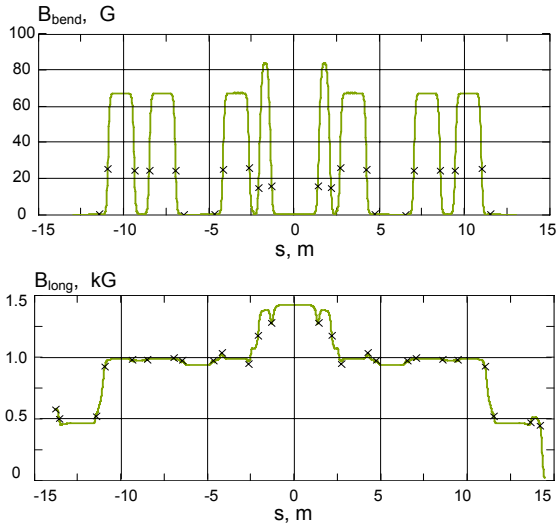

Figure 8: Bending and longitudinal components of magnetic field on path from cathode to collector

Beam orbit optimizations for different electron energies were made by computations of corresponding values B_{long} and B_{bend}.

Dynamics of Electron Motion in the Magnet System

High energy electrons can reach high amplitudes of oscillations while moving along magnetic field with small variations. This can occur at edges of solenoids with different diameter of coils. The criterion of low energy is small length of spiral in comparison with length of perturbation (lb) in magnetic field B according to equation $\lambda = \frac{mc^2 \beta\gamma}{qB} << lb$. Fig. 9 shows that high energy electron (1MeV) is excited to high amplitude oscillation.

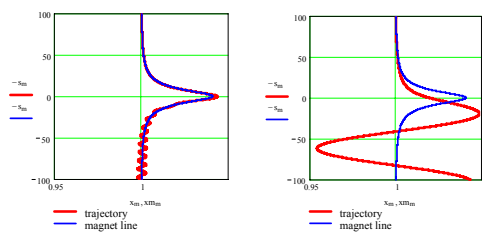

Figure 9: Passing of 10% variation of magnetic field by 0.2 MeV and 1MeV electron.

To obtain low amplitude of this oscillation in the cooling section a short dipole magnet is used to compensate the rest amplitude. Figure 10 shows the rotation amplitude in the cooling section for different amplitudes of vertical and horizontal dipole kick.

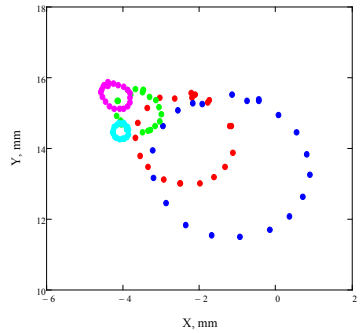

Figure 10: Larmor rotation of electron beam for different horizontal and vertical kick generated by the short dipole corrector. Energy of electron is 1MeV.

We see that radius of Larmor circle changes from 2 mm to 0.1 mm.

ELECTRON BEAM EXPERIMENTS

First experiments with electron beam were started November 23, 2011. A 30 keV electron beam was transferred along the magnet system and captured in the collector.

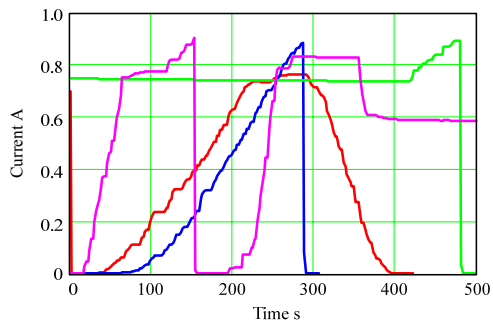

Figure 11: Experiment with 30 keV electron beam.

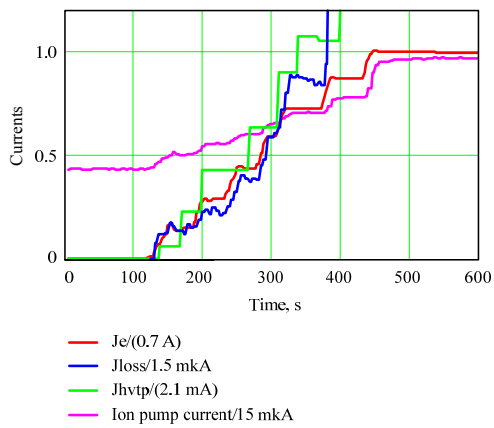

Figure 12: Measuring efficiency of collector capture at 30 keV.

The collector efficiency was about J_{hvtp}/J_e= 3.0E-3 and Wien filter suppressed reflection current to J_{loss}/J_e=2E-6 as shown in fig12. The main source of losses are the

secondary ions generated by ionisation of residual gas. An increase of electron current causes a rise of residual gas pressure. For this condition exists a maximal steady current.

$$J_{loss} = (\alpha + a * p) * J_e$$

$$p = p_0 + b * J_{loss}$$

Where *a* describes losses generated by ionization of residual gas and *b* describes the increase of residual gas pressure due to bombardment the vacuum chamber by lost particles. At a*b*Je>1 stable recuperation is not possible. Extended conditioning of vacuum surfaces with electron beam helps increasing electron current. This behaviour is explained by lower desorption efficiency (coefficient b).

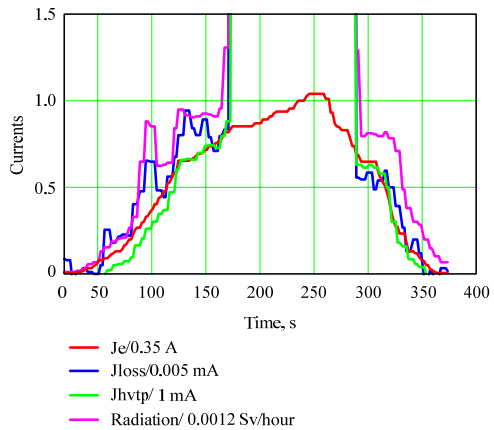

Figure 13: Experiment with 1000 keV electrons.

The experiments at high energy (fig.13) show very similar behaviour. At current values close to maximum, losses were a few times higher.

Table 2: Parameters measured during beam experiments

Energy keV	Current A	Losses mA	Rad Sv/hour
30	0.9	0.0015	0
150	0.6	0.0075	0
1000	0.5	0.002	0.001
1250	0.35	0.004	0.002
1500	0.2	0.01	0.01

The main limitation was lack of time for cooler conditioning in radiation regime. The hall where the cooler was commissioned was also used by many other teams. While personel were working in the experimental hall the cooler could not operate at high voltage.

CONCLUSION

Successful commissioning of the electron cooler demonstrated that scientific and engineering solutions were well chosen for the task. Some parameters were limited by using temporary equipment that did not fully fulfil the requirements. For example, for the high voltage tank an old vessel from industrial accelerator was used. The final vessel with smoother inner surface had to be manufactured in Germany due to limitation imposed by the pressure vessel code. Older ion pumps were used. Those will be replaced by the modern ones in Jülich. At time of commissioning it was found that level of pollution of cooler with small pieces of wire was too high causing a few short-circuits. However using cascade transformer along acceleration column showed high efficiency and opened the path for the next magnetized cooler operating at higher energy.

ACKNOWLEDGMENT

The authors would like to thanks designer team, especially V. A. Poluhin, A.M. Kruchkov,A.A. Putmakov, V.K. Gosteev, workshop team that produced elements of cooler V.V. Anashin, B.F. Chirkov, E.S. Ruvinsky, the electronic department team A.S.Medvedko, E.A. Kuper, V.V. Kolmogorov. This interesting job was not possible without support of BINP administration A.N.Skrinsky, E.B. Levichev, I.N. Churkin.

REFERENCES

[1] A. V. Shemyakin, L. R. Prost, Ultimate Performance of Relativistic Electron Cooling at Fermilab, Proceedings of COOL'11, Alushta, Ukraine, http://accelconf.web.cern.ch/AccelConf/COOL2011/papers/thioa01.pdf

[2] J. Dietrich, V. Parkhomchuk, V. Reva, M. Vedenev The proposed 2 MeV electron cooler for COSY, AIP Conference Proceedings 821, pp.299-307 (2006) http://conferences.fnal.gov/cool05/Presentations/Thursday/R10_Dietrich.pdf

[3] V.B. Reva, N. Alinovsky at all. The first commissioning results of the high voltage magnetized cooler for COSY, Proceedings of COOL'11, Alushta, Ukraine http://accelconf.web.cern.ch/AccelConf/COOL2011/papers/thioa02.pdf.

[4] V.V. Parkhomchuk, Development electron coolers at Novosibirsk, Proceedings of IPAC2012, New Orleans, Louisiana, USA, http://accelconf.web.cern.ch/AccelConf/IPAC2012/papers/wexa02.pdf

NEW DEVELOPMENTS IN HIGH ENERGY ELECTRON COOLING

J. Dietrich#, TU Dortmund and Helmholtz Institut Mainz, Germany

Abstract

Electron cooling of hadron beams is a powerful technique by which accelerator facilities achieve the necessary beam brightness for their physics research. An overview on the latest developments in high energy electron cooling (electron beam energy higher than 500 keV) is given. Technical feasibility for electron beam energy up to 8 MeV is discussed.

INTRODUCTION

The use of electron coolers in the range of electron beam energy lower 400 keV is well established and state of the art. For higher electron energies there exists up to now only one machine – the Recycler Electron Cooler (REC) of Fermilab with a terminal voltage of 4.4. MV [1]. The cooler was successful installed into the Recycler during the summer of 2005 and was operating until end of 2011 when the Tevatron was shut off. The cooling opened the possibility for several times higher, record luminosities. The REC overcame not only the great challenge of operating 4.4 MV pelletron accelerator in the recirculation mode with up to 1A beams, but also resolved the hard issue of high quality magnetised beam transport through non-continuous magnetic focusing beamline [2]. The next unique high energy electron cooler -the 2 MV COSY electron cooler- is now under commissioning in the Budker Institut in Novosibirsk and will be installed in the Cooler Synchrotron COSY in spring of next year [3]. Development of high energy electron coolers is a technical challenge due to the engineering problems like high voltage generation, power transmission to the gun and collector in the accelerator "head" and the power transmission to the magnetic coils at the accel/decel tubes for magnetised electron beam transport. Today there is a need for further development. In the high energy storage ring HESR for antiprotons in the FAIR facility in Darmstadt a 4.5 MV electron cooler is planed [4]. The proposed concept of a polarized Electron-Nucleon Collider (ENC) integrates the 15 GeV/c HESR of the FAIR project for protons/deuterons and an additional 3.3 GeV electron ring [5]. A new 8.2 MV electron cooler is an essential part in this concept. In the NICA collider project of the JINR Dubna a 2.5 MV electron cooler is foreseen with one electron beam per each ring of the collider [6]. There are some special features of high energy cooling. The cooling rate decreases with γ^{-2}. To obtain a maximum friction force the "waveiness" of the magnetic force line should be as small as possible to get a smaller contribution to the effective electron velocity [7]. To get a high cooling rate magnetised electron cooling is necessary. All low-energy (3-400 keV) electron coolers are based on magnetised cooling. The electron beam transport and alignment of electron and ion beam is done with continuous magnetic field. Strong magnetic field completely suppresses transverse temperature of electron beam, so that effectiveness of cooling is determined by a very low longitudinal temperature of electrons. Non-magnetised cooling relies on the fact that rms velocity spread of electrons is comparable or smaller than the one of ions which need to be cooled. For the REC (non-magnetised case) cooling times of about one hour was sufficient. The new coolers for COSY and the new future projects should provide a few orders of magnitude more powerful longitudinal and transverse cooling. This requires new technical solutions. The basic idea of the new COSY cooler and for the future HESR and NICA collider coolers is to use a high magnetic field along the orbit of the electron beam from the electron gun to the collector. Faster cooling times are essential for the future projects. The technical problems for electrostatic accelerator at 8-10 MV and needed electron beam currents up to 3 A look too hard. An alternative can be a low frequency linac with bunched electron beam. Today this system achieved electron peak currents of about 10 A [8].

juergen.dietrich@tu-dortmund.de

ENGINEERING PROBLEMS OF HIGH ENERGY ELECTRON COOLERS

The engineering problems are listed in the following:

- High voltage generators (< 10 MV).
- High voltage performance.
- Limiting performance of accelerator tubes.
- Power transmission to the accelerator "head" (gun, collector).
- Power transmission to the magnetic coils (at accel/decel tubes).
- Electron current and high voltage stability (1-3 A, 10^{-5}).
- Electron beam formation, transportation and recovering.
- Magnetic field measurement system in the cooling section.
- Magnetic field straightness in the cooling section (< 10^{-5}).
- Electron beam diagnostics.

Power transmission in commercial available pelletrons is realised by isolated rotating shafts combined with generators located on high voltage level. In case of magnetised coolers, where additional power is needed for the magnetic coils around the accel/decel tubes this method seems to be too complicated. Another solution is cascaded resonant transformers and proposed turbines on high voltage level or combinations of both. The technical solution is strongly influenced by the location of the magnetic coils at the accelerator/ decelerator tubes. Due to the difficulties the magnetic coils (superconducting) in

the NICA collider electron cooler project are arranged out side of the high voltage vessel.

HIGH VOLTAGE SYSTEMS

Overview

There exist different high voltage generators, which are possible candidates for the high voltage system of a high energy electron cooler. The REC of Fermilab is based on a 4.4 MV electrostatic accelerator (pelletron [9]) which works in the energy recovery mode (i.e. electrons are decelerated and captured in the collector after they interact with the antiprotons in the cooling section). The pelletron is a well-tested electrostatic accelerator, which has been built for voltages as high as 25 MV. The pelletron is commercial available. In the Upsalla design for the 4.5 MV electron cooler for the HESR a commercial pelletron is foreseen [10]. The accelerator can be adapted to the inclusion of a longitudinal magnetic field, but the problem of the thermal cooling of the solenoids needs a solution. The pelletron is constructed in a modular way. A future increase of the high voltage to at least 8 MV seems possible. The Cockcroft–Walton (CW) generator (or Greinacher multiplier) is an electric circuit which generates a high DC voltage from a low voltage AC or pulsing DC input. This is proposed for the 2.5 MV electron cooler in the NICA project in Dubna. A compact cyclotron to accelerate negative hydrogen ions up to 8 MeV is proposed as optimal solution to the problem of charging the high voltage terminal of the 8 MV electron cooling system for the High Energy Storage Ring at FAIR [11]. A Dynamitron uses capacitive coupling to the individual stages of the accelerating/decelerating columns for the generation of the high voltage. This technique is difficult to adapt to the requirement of a longitudinal magnetic field in the accelerating/decelerating columns and is not modular. However, Dynamitron accelerators for Accelerator Mass Spectroscopy have demonstrated a high voltage stability of $\leq 10^{-5}$, which meets the requirements for the HESR electron cooler. The industrial electron accelerators of ELV type are constructed on the base of the cascade generator with a parallel feed of cascades. These accelerators are manufactured in the Budker Institute of Nuclear Physics (BINP) in Novosibirsk[12]. The electron beam power for ELV-type accelerators is up to 400 kW. Beam energy range is 0.3 MeV to 2.5 MeV. The distinguishing feature of cascaded rectifier circuits is the method of coupling ac power to all of the rectifier stages. These methods may be classified as inductive or capacitive with series or parallel coupling. With series-coupled systems, the rectifier stages nearer to the input ac power supply must transmit ac power to the farther stages. This increases the internal impedance of the system and the voltage droop under load. With parallel-coupled systems, all of the rectifier stages receive the same input ac power, which reduces the internal impedance and reduces the voltage droop under load. For the COSY high energy electron cooler the high voltage (up to 2 MV) and power for the magnetic coils (of about 300 W per coil pair) at the accel/decel tubes are generated by a cascaded resonant transformer.

A novel idea from Budker institute is to use small turbines. They are used for high voltage generation, power for the magnetic coils in side the high voltage tank and for power of gun and collector in the terminal.

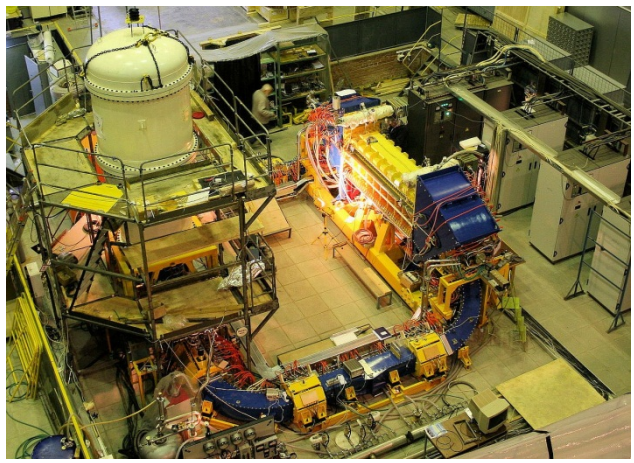

Figure 1: Commissioning of the 2 MV electron cooler at BINP, Novosibirsk [3].

High Voltage System of the 2 MV COSY Electron Cooler

The high voltage terminal is supported by a column consisting of 33 identical high voltage sections (HV sections) [3]. The whole assembly is placed inside a vessel filled with SF_6 under pressure up to 10 bar. Each HV section contains two coils providing guiding magnetic field for acceleration and deceleration tubes and the high voltage power supply generating up to 60 kV. Total power consumption of one section is about 300 W. The key problem of the accelerating/decelerating column is the transfer of the energy to 33 sections and to gun and collector, which are located at high voltage potential. The concept of the power supply is based on idea of a high frequency cascaded resonant transformer (20 kHz, 40 kW). The system consists of 33 transformers with cascaded connection. The electrical energy is transmitted from section to section from the ground to high-voltage terminal. Along this way the energy is consumed by the regular high-voltage section. The main problem of such decision is leakage inductance of the transformers. They are connected in series and the voltage from power supply is divided between inductance leakage and a useful load. In order to solve this problem the special compensative capacitance is used. The impedance of leakage inductance is decreased significantly on the resonance frequency.

Gas Turbines

In the last years the COSY Juelich-BINP Novosibirsk collaboration was studying prototype elements for a magnetised cooler [13]. The turbine electro generator driven by compressed gas was tested. This gas is used to produce power for individual high voltage sections and, at the same time, to cool the 500 Gauss coils (Fig. 2). For

experiments with HV sections in pressurized SF_6 gas the vessel of a 1-1.5 MV industrial accelerator of ELV type was used (Fig. 3). The height of a single HV section equals 4 cm while the gap between them is 2 cm. The voltage between sections at SF_6 pressure of 1.6 bar is shown in Fig. 4. The HV stability was measured using an ADC installed in the HV terminal. The relative HV stability is about 10^{-5}. The concept of turbines looks very promising. But now there needs further development to increase efficiency and reliability of the turbines. One idea is to use more powerful turbines (5kW, commercial available) and combine it with small cascaded resonant transformers [14].

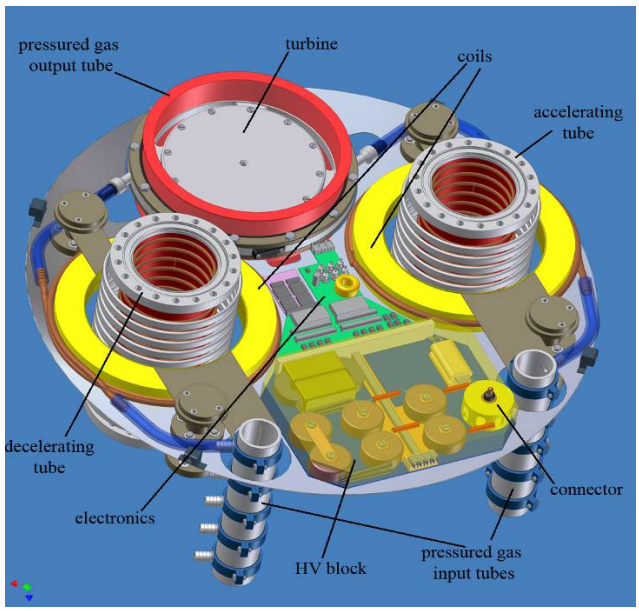

Figure 2: High voltage section with turbine and magnet coils around the acceleration and deceleration tubes [13].

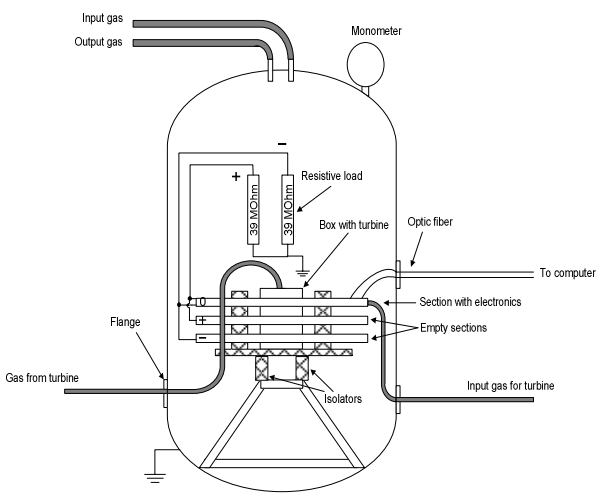

Figure 3: HV sections scheme of experiments.

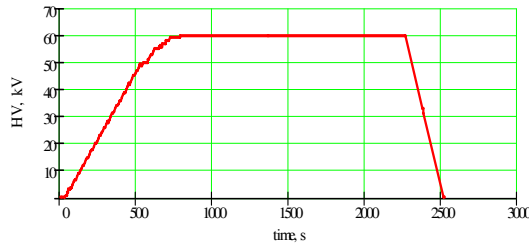

Figure 4: Voltage between sections (SF_6 1.6 bar).

The prototype of a turbine operates at BINP at the accelerator mass spectrometer (AMS) few years at the high voltage terminal (1 MV) to produce power for magnet and stripper target [15].

BEAM DIAGNOSTICS

The new proposed relativistic electron cooling devices have special needs and demands on the beam diagnostics. The cooling beam and the cooled beam have to overlap and propagate with the same velocity to ensure a small cooling time. This matching is done e.g. for cooling of a proton beam by optimising the H^0 signal. In this case the protons of the cooled beam are recombining with the electrons of the cooling beam. The resulting Hydrogen atoms are neutral. They are not deflected by magnetic fields and can be detected after the next bending magnet. For the cooling of antiprotons in the HESR there is no H^0 signal which could indicate a good cooling rate. Due to this fact special beam diagnostics in the cooling section is necessary. One challenge for the electron cooler design is beam alignment between electrons and antiprotons along the long interaction cooling section (e.g. of about 24 m length for HESR cooler). The deviation of the electron beam relative to the antiproton beam should be smaller than 10^{-5} radians rms to fulfil the beam quality and lifetime demands of the antiprotons [10]. To minimise deviations of the electrons relative to the antiprotons, beam-based alignment would be preferable. Then the offset of the electron beam relative to the antiproton beam is measured and corrected using additional corrector windings. This requires beam position monitors in the cooling section with a resolution of 1×10^{-5} m. The diagnostic has to be non destructive because of the high beam power. It should also not affect the magnetic field flatness of the solenoids inside the cooling section. There are already several non destructive beam diagnostic methods established. They are used in different accelerators like a scintillation profile monitor [16], [17] or the Laser wire scanner at the synchrotron source PETRA III [18]. These methods can be adapted for the use in relativistic electron cooling devices.

Beam Profile Monitors

Beam profile measurements are vital for the machine operation, in particular for setting up beam cooling. Profiles have to be measured without affecting the circulating beam. A joint effort by the beam instrumentation groups at GSI Darmstadt and COSY,

Juelich resulted in an ionization profile monitor (IPM) being operational at ESR [19] and COSY [20]. The IPM was designed to become a standard profile monitor for the future FAIR [21] machines. The IPMs real time performance together with high sensitivity and resolution make it a very valuable instrument. However, high cost and presence of components prone to aging in vacuum triggered the search for alternative methods. A profile monitor utilizing scintillation of residual gas offers a viable alternative to an IPM for certain beam conditions [22, 23]. The gas atoms and molecules are excited by the beam particles and emit visible light shortly after the excitation [24]. After passing a vacuum window the light is focused by an optical system and is detected by a multi-channel photomultiplier or an image intensified camera. Measuring the photon distribution allows reconstructing the initial beam profile. The method is also applicable for the electron beam. To increase scintillation light intensity for the scintillation profile monitor (SPM) a local pressure bump is introduced for the duration of profile measurement. Nitrogen injection is done by means of a commercially available piezo-electric valve. At 4×10^{-8} mbar and beam intensities of the order of 5×10^{9} protons in the ring reasonable S/N ratio is achieved. The temporary pressure bumps did not have any impact on machine operation. Fig. 5 shows the measured beam profiles (top plot) as the proton beam was being cooled. The lower plot shows the beam current. The injection occurred at t = 5s and was followed by 10s of electron cooling (accompanied by beam losses). The beam was then accelerated and slowly extracted from the ring to an external experiment. Profile data was recorded during electron cooling at injection energy only (5.9s – 15.3s). Beam shrinking due to cooling is clearly seen. SPM performance was verified by comparing measured profiles with the IPM results. This measurement shows good agreement between SPM and IPM data.

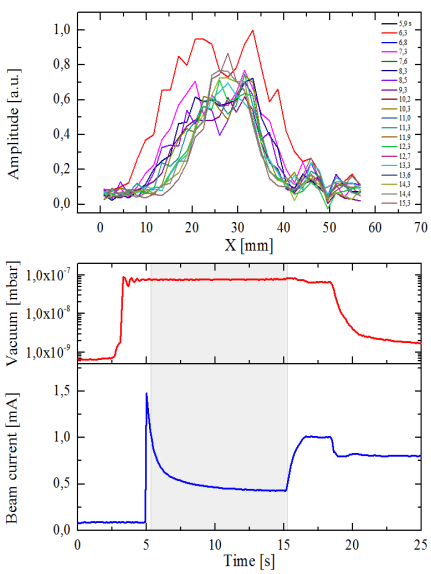

Figure 5: Horizontal beam profiles measured with the SPM (top plot), vacuum reading (centre plot) and beam current (lower plot) [25].

Electron Gun with Variable Beam Profile

The electron gun design is based on the slightly changed gun previously used for electron coolers in Lanzhou CSRe, CSRm and LEIR [26]. The only difference is the four-sector control electrode with separate feeding of all sectors via additional feed throughs (Fig. 6). This small change opens a new possibility for non-axially modulation of the electron beam profile, which could be used in some applications. Combined with beam position monitors this feature of the gun provides beam shape monitoring when it passes the transport channels.

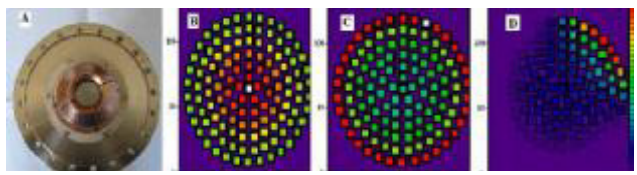

Figure 6: A -photo cathode with grid electrodes, B - parabolic shaped beam with maximum at centre, C - "hollow" beam with minimum at centre, D - AC component of beam with RF voltage on single sector [27].

Thomson Scattering

Thomson scattering describes elastic scattering of a photon on a free electron. It is the low energy limit of the Compton scattering process. In 1987/1988 a pioneer experiment demonstrated the feasibility of Thomson scattering for electron beam diagnostics [28], [29]. At that time, however, the signal to noise ratio suffered from the low power and repetition rate of the Laser system. A revision of this approach make sense due to the enormous developments in Laser technology since that time. The proposed setup (Fig. 7) uses 90 and 180 degrees angles between laser and electron beam like a Laser wire scanner [30]. In this case the rate of the scattered photons only depends on the electron density in the electron beam. By moving the Laser beam through the electron beam a profile measurement can be done. Due to the low cross section, mostly dominated by the classical electron radius squared, the necessary Laser power is very high and it is only reasonable for high electron densities. Another advantage of the Thomson scattering method is the possibility to measure the electron energy. This can be realised with the same setup which is used for the beam profile measurement. In this case a frequency analysis of the scattered photons is needed instead of the scattering rate (e.g. realised with a Fabry-Perot interferometer). This can be very interesting for the cooling of antiprotons. With a good energy measurement the adjustment of the electron beam can be done faster and in a more efficient way.

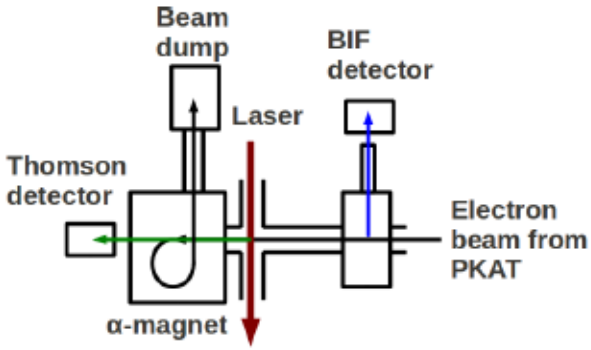

Figure 7: Schematic view of the setup at Mainz [30].

CONCLUSION

The gained experience of the 4.4 MV REC at Fermilab and the 2 MV COSY electron cooler at FZ Juelich will push the development of future relativistic electron coolers for HESR at FAIR Darmstadt and NICA at Dubna. The idea of using turbines for the high voltage system of electron coolers looks very promising and should be developed further. A combination of turbines and small cascade transformers could be a technical solution for the next high voltage magnetised electron coolers. An improved beam diagnostics for the hadron and electron beam will help to optimise the cooling process.

ACKNOWLEDGEMENTS

The author would like to thank V.V. Parkhomchuk, I.N. Meshkov, S. Nagaitsev, L. Conradie, K. Aulenbacher and V. Kamerdzhiev for their valuable contributions and support.

REFERENCES

[1] S. Nagaitsev et al., Phys. Rev. Lett. **96**, 044801 (2006).
[2] A. Burov et al., Phys. Rev. ST-AB **3**, 094002 (2000).
[3] V.N. Bocharov et al., Commissioning of the 2MeV Electron Cooler for COSY / HESR, IPAC2012, New Orleans, p. 379 (2012).
[4] R. Maier, The High Energy Storage Ring (HESR), PAC 2011, New York, p. 2104 (2011).
[5] Andreas Lehrach, Polarized Electron-Nucleon Collider ENC at FAIR, Beam Dynamics Newsletter, No. 58, p.29 (2012).
[6] E.V. Ahmanova et al., Electron Cooler for NICA collider, COOL'11, Alushta, p. 125 (2011).
[7] V.V. Parkhomchuk, New insights in the theory of electron cooling, Nuclear Instruments and Methods in Physics Research A 441 (2000) 9-17.
[8] V.V. Parkhomchuk et al.,Electron Cooling for RHIC, C-A/AP/47, BNL, Upton (2001).
[9] Pelletrons are manufactured by the National Electrostatics Corporation, www.pelletron.com.[10] HESR Electron Cooler Design Study, The Svedberg Laboratory, Uppsala University, Uppsala, 2009.
[11] V.Papash et al., An 8 MeV H^- Cyclotron to Charge the Electron Cooling System for HESR, RuPAC 2006, Novosibirsk, p. 67 (2006).
[12] P.I. Nemytov et al., High Power Transistor Frequency Converter for Supply up to 500 KW DC Electron Accelerators, RuPAC XIX, Dubna , p. 123 (2004).
[13] J. Dietrich et al., Status of the 2 MeV Electron Cooler for COSY Juelich, COOL09, Lanzhou, p.178 (2009).
[14] K. Aulenbacher, private communication.
[15] M. Petrichenkov et al., RuPAC XIX, Dubna , p. 263 (2004).
[16] C. Boehme et al., Gas Scintillation Beam Profile Monitor at COSY Juelich, TUPSM005, BIW2010, Santa Fe, New Mexico, p. 98 (2010).
[17] F. Becker et al., Beam Induced Fluorescence Monitor-Spectroscopy in Nitrogen, Helium, Argon, Krypton, and Xenon Gas, TUPSM020, BIW 2010, Santa Fe, New Mexico, p. 156 (2010).
[18] M.T. Price et al., Beam Profile Measurements with the 2-D Laser-Wire Scanner at PETRA, FRPMN094, PAC 2007, Albuquerque, New Mexico, p. 4303 (2007).
[19] P. Forck, Minimal Invasive Beam Profile Monitors for High Intense Hadron Beams, IPAC 2010, Kyoto, p. 1261(2010).
[20] C. Böhme et al., Nondestructive Beam Instrumentation and Electron Cooling Beam Studies at COSY, IPAC 2010, Kyoto, p. 921(2010).
[21] M. Schwickert et al., Beam Diagnostic Developments for FAIR, DIPAC 2009, Basel, p. 424 (2009).
[22] R. Haseitl et al., ProfileView - A Data Acquisition System for Beam Induced Fluorescence Monitors, DIPAC 2009, Basel, p. 134 (2009).
[23] J. Dietrich et al., Non-destructive Beam Position and Profile Measurements Using Light Emitted by Residual Gas in a Cyclotron Beam Line, EPAC 2008, Genoa, p. 1095 (2008).
[24] M. A. Plum et al., N2 and Xe gas scintillation cross-section, spectrum and lifetime measurements from 50 MeV to 25 GeV at the CERN PS and Booster, Nucl. Instrum. Meth. A 492, p. 74-90 (2002).
[25] V. Kamerdzhiev et al., Towards Routine Operation of the Scintillation Profile Monitor at COSY, IPAC2012, New Orleans, p.382 (2012).
[26] A. Bubley et al., The Electron Gun with Variable Beam Profile for Optimisation of Electron Cooling, EPAC 2002, Paris, p. 1356 (2002).
[27] M. Bryzgunov et al., High Voltage Electron Cooler, these proceedings.
[28] C. Habfast et al., Measurement of Laser Light Thomson-Scattered from a Cooling Electron Beam, Appl. Phys. B 44, 87-92 (1987).
[29] J. Berger et al., Thomson Scattering of Laser Light from a Relativistic Electron Beam, Physic Scripta, Vol. T22, 296-299 (1988).
[30] T. Weilbach et al., Optical Electron Beam Diagnostics for Relativistic Electron Coolin Devices, COOL'11, Alushta, p.121 (2011).

APPROACH TO THE LOW TEMPERATURE STATE ORIENTED FOR CRYSTALLINE BEAM*

Akira Noda#, , Masao Nakao, Hikaru Souda, Hiromu Tongu, ICR, Kyoto University, Uji-city, Japan
Kouichi Jimbo, IAE, Kyoto University, Uji-city, Japan
Hiromi Okamoto, Kazuya Osaki, AdSM, Hiroshima University, Higashi Hiroshima-city, Japan
Yosuke Yuri, Takasaki Advanced Radiation Research Institute, JAEA, Takasaki-city, Japan
Igor Nikolai Meshkov, Alexander V. Smirnov, JINR, Dubna, Moscow Region, Russia
Manfred Grieser, MPIK, 69029 Heidelberg, Postfach 103980, Germany,
Koji Noda, Toshiyuki Shirai, National Institute of Radiological Sciences, Chiba-city, Japan
Zhengqi He, Tsinghua University, 1 Qinqhuayuan, Beijing, China.

Abstract

With the use of S-LSR, an ion storage and cooler ring at ICR, the approach to attain a low temperature beam has been continued. With electron cooling one dimensional ordered state has been realized for 7 MeV proton beam, resulting in an abrupt longitudinal temperature jump from 2K to 0.3 K at a particle number ≈2000. A transverse temperature at a particle number of 4000 at the observation point with a beta-function of ≈1.7 m is estimated to be 12 K. Laser cooling has also been applied to $^{24}Mg^{+}$ ion beam with a kinetic energy of 40 keV. The lowest longitudinal temperature of a coasting beam was limited at 3.6 K for a beam intensity of 4 x 10^4 due to intra-beam scattering (IBS) and residual gas scattering, while a transverse temperature is reduced to ≈500 K by IBS for a beam intensity of 2 x10^7, which is accompanied by the increase of the longitudinal temperature to 11K. In order to actively cool down the transverse temperature, synchro-betatron resonance coupling (SBRC) has been applied to a bunched beam. By reduction of the beam intensity with scraping, the average transverse beam temperature has been cooled down to <15-50 K and 7-15 K for the horizontal and vertical directions, respectively, by SBRC for the beam intensity of 1 x 10^4.

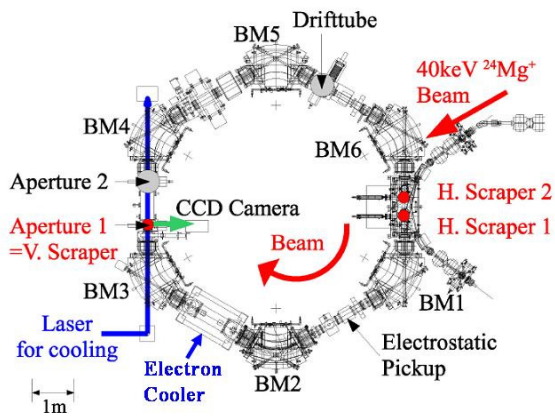

Fig.1 Layout of S-LSR and its beam monitoring and scraping apparatuses.

*Work supported by Advanced Compact Accelerator Development project by MEXT of Japanese government. It is al so supported by GCOE project at Kyoto University, "The next generation of Physics-Spun from Universality and Emergency.
#noda@kyticr.kuicr.kyoto-u.ac.jp

Table 1 Main Parameters of S-LSR

Ion species (energy)	H^{+} (7 MeV), $^{24}Mg^{+}$ (40 keV)
Cooling Methods	Electron beam cooling, Laser cooling
Circumference	22.557 m
Average radius	3.59 m
Length of straight section	2.66 m (including Q mag. parts)
Number of superperiods	6
Betatron tune (ν_x, ν_y)	
Electron cooling	(1.64,1.21)
Laser cooling	(2.07,1.12)
Bending magnet	H-type
Maximum field	0.95 T
Curvature radius	1.05 m
Gap height	70 mm
Pole end cut	Rogowskii cut + field clamp
Deflection angle	60°
Weight	4.5tons
Quadrupole magnet	
Core length	0.20 m
Bore radius	70 mm

INTRODUCTION

A lot of efforts to approach to the low temperature states of a beam have been continued in these two decades so as to improve the beam characteristics which is usually in a gaseous state. At ICR, Kyoto University, an ion accumulation and cooler ring, S-LSR had been constructed and it became in operation in 2005. In Fig.1 and table 1, its layout and main parameters are shown. Originally it was oriented for the realization of compact ion accelerator for cancer therapy by combination of RF accelerator technology and laser plasma interaction [1]. After the successful demonstration of effective electron cooling of a hot ion beam with a relative velocity sweep between the ion and electron beams [2] utilizing TSR at MPIK [3] and S-LSR, the main experimental researches are oriented for the realization of lower beam temperature by application of beam cooling utilizing such a special characteristics of S-LSR lattice satisfying the so-called maintenance condition given by the following relations [4,5],

$$\gamma < \gamma_T \quad (\gamma_T : \text{the transition gamma}) \qquad (1)$$

$$\max(\nu_H, \nu_V) < \frac{N_{sp}}{2\sqrt{2}}\ , \qquad (2)$$

where N_{sp}, ν_H and ν_V are the super-periodicity of the lattice, betatron tunes in the horizontal and vertical directions, respectively.

In the present paper, approaches to low temperature states of the circulating beam at S-LSR with the use of electron cooling and laser cooling are described.

ONE DIMENSIONAL ORDERING OF PROTON BEAM BY ELECTRON COOLING

Stimulated by the report from NAP-M at BIMP [6], particle number dependence of momentum spread of the circulating beam has been studied vigorously in the world and one dimensional ordering has been realized for multi-charge ion beams such as U^{92+}, Au^{79+}, Xe^{54+}, Kr^{36+}, Ni^{28+}, Ar^{18+}, Ne^{10+}, C^{6+} at ESR of GSI [7] and for Xe^{36+} at CRYRING of MSL [8]. Because of a smaller cooling force due to the single charge, the phase transition to the ordered state of a proton beam, had not been observed until its realization at S-LSR with a rather large super-periodicity of 6.

In Fig. 2, the dependence of momentum spread on the particle numbers obtained at S-LSR for 7 MeV protons is given, which shows a sharp jump at the particle number around 2000 [9]. The momentum spread below the transition is estimated to be 1.4 x 10^{-6}, which is close to the minimum longitudinal electron temperature of 1.2 x 10^{-6}. The beam radius at the transition is 17 μm [9] indicating magnetization of the electron beam first pointed out by Derbenev and Skrinsky [10] and experimentally observed at ESR [11].

The longitudinal, $T_{//}$ and transverse, T_u, temperatures can be estimated utilizing the following relations [7, 12].

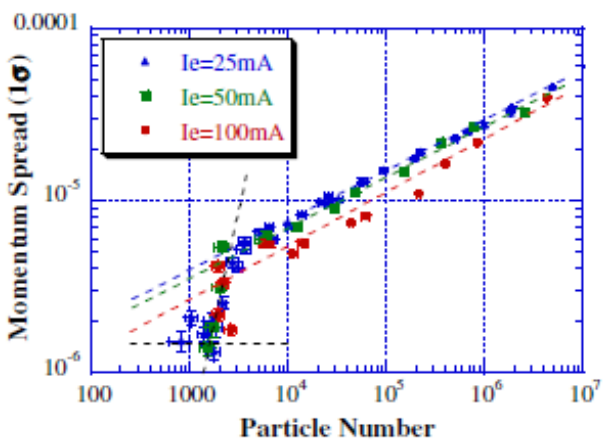

Fig.2 Particle number dependence of the momentum spread (1σ) of 7 MeV proton beam, electron cooled at S-LSR with three different electron currents [9].

$$k_B T_{//} = m_0 c^2 \beta^2 \left(\frac{\delta p}{p}\right)^2 , \qquad (3)$$

$$k_B T_u \cong m_0 c^2 \beta^2 \frac{\varepsilon_u}{C} 2\pi\nu_u\ , \qquad (4)$$

where m_0, c, β, ε_u (u represents either h : horizontal or v: vertical direction) C and ν_u are mass of the ion, velocity of light, the ratio of the ion velocity to the light velocity, the circulating beam emittance in u direction, the circumference of the ring and transverse betatron tune (u =H,V), respectively. The longitudinal temperature was abruptly changed from 2K to 0.3 K at a particle number ≈2000, which is considered to be the evidence of ordering. Transverse temperature with the particle number of 4000 at the observation point with beta -function of ≈1.7 m is estimated to be 12K.

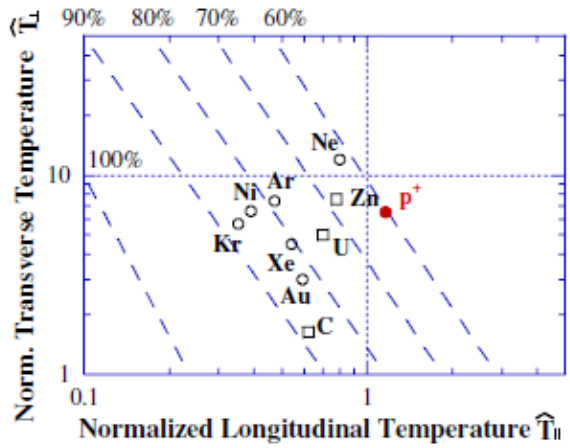

Fig. 3 Reflection probabilities observed for the 1-dimensional phase transition (borrowed from ref.[9])

With the use of the definitions, given by [13]

$$\begin{pmatrix} \hat{T}_{\parallel} \\ \hat{T}_{\perp} \end{pmatrix} = \frac{2}{m_i c^2}\left(2 r_i \beta\gamma \frac{\nu}{R}\right)^{-2/3} \begin{pmatrix} k_B T_{\parallel} \\ k_B T_{\perp} \end{pmatrix}, \qquad (5)$$

$$(T_{\perp} = T_H + T_V)$$

the dimensionless parameters, the normalized temperatures, $\hat{T}_{//}$ and $\hat{T}_{\perp}$ are obtained as shown in Fig. 3 together with the data of other heavier ions measured at ESR [11]. Our data for a 7 MeV proton beam shows that the transition had occurred at a lower reflection probability around 60 %.

The above results are obtained for coasting beams. The importance of such a study to check the capability of similar transition for bunched beam was pointed out [14], which is one item to be studied at S-LSR in the near future.

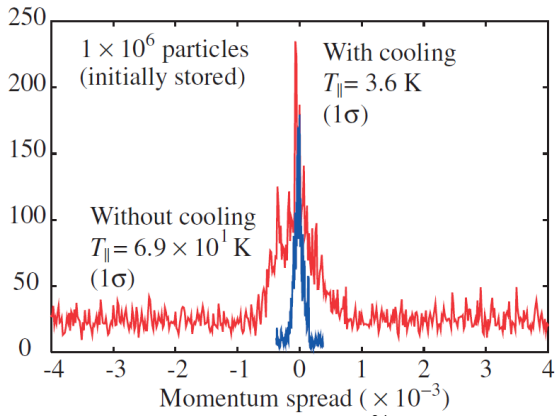

Fig.4 Momentum distribution of the $^{24}Mg^{+}$ ion beam with and without laser cooling.

LASER COOLING

Longitudinal Cooling of Coasting Beam

The laser light co-propagating or counter-propagating with the ion beam can only accelerate or decelerate the ion in the longitudinal direction and can cool down the temperature of the longitudinal direction. Utilizing the heat transfer due to IBS, it was demonstrated that the transverse temperature is also cooled down by performing longitudinal laser cooling. [15, 16] Transverse laser cooling, solely based on single-particle interaction of the ion beam with a laser beam, was also demonstrated. The scheme utilizes the dependence of the horizontal position of the ion on the longitudinal momentum, in combination with a transverse gradient of the light force ("dispersive cooling") [17].

Laser cooling with the use of a ultra-violet laser light (280 nm) co-propagating with the ion beam has been applied to the $^{24}Mg^{+}$ beam with an energy of 40 keV at S-LSR in ICR, Kyoto University. For the counteracting force with the laser cooling force, an induction accelerator was utilized which can generate a decelerating field of 6 mV. In Fig. 4, the momentum distribution of the coasting Mg ion beam with and without the application of laser cooling at an initial beam intensity of 1 x 10^6 is shown. The cooled longitudinal temperature was 3.6 K with a reduced beam intensity of 3 x 10^4 due to IBS and residual gas scattering. IBS effect reduced the transverse temperature to ≈500 K resulting in a higher longitudinal temperature of 11 K at a beam intensity of 2 x 10^7[18].

Indirect Transverse Laser Cooling with SBRC

The degrees of freedom between the longitudinal and horizontal directions can be coupled by accelerating the ion beam at the position with finite dispersion function by the operation point satisfying the following relation (SBRC) [19]:

$$\nu_H - \nu_s = m \text{ (integer).} \qquad (6)$$

Further the horizontal and vertical coupling can be realized with the condition:

$$\nu_H - \nu_V = n \text{ (integer)}, \qquad (7)$$

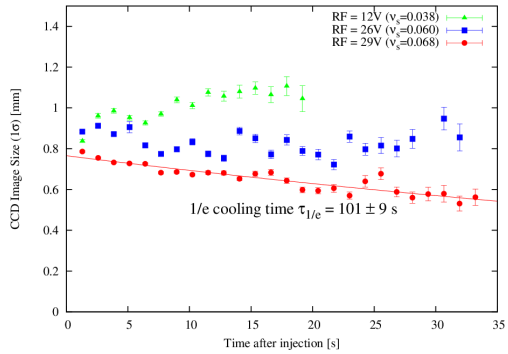

Fig. 5 Time variation of the horizontal beam size for various synchrotron tunes observed by a CCD camera.

satisfying the difference resonance utilizing a solenoidal or a skew magnetic field. Thus the laser cooling force is well expected to be extended to 3 dimensions.

At the first step, the indirect transverse laser cooling with the use of SBRC is experimentally demonstrated as shown in Fig. 5 [20], which gave a rather long cooling time as 101 sec. for a beam intensity of 1x 10^7 due to IBS heating. In Fig. 6, synchrotron tune dependences of cooled momentum spread (red) and the horizontal beam size (blue) are shown. Clear local minimum and maximum appear in these graphs at the SBRC condition.

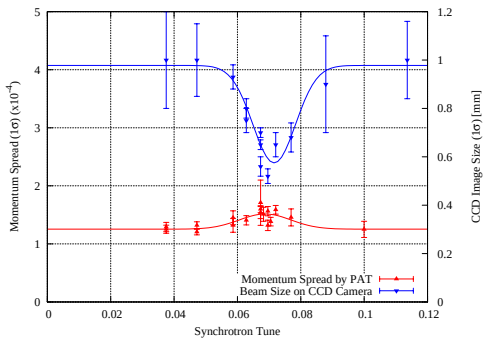

Fig.6. Synchrotron tune dependence of the momentum spread (red) and observed horizontal beam size (blue) after laser cooling.

Controlled Beam Scraping to Suppress IBS

In order to reduce the heating effect by IBS and to increase the efficiency of the indirect transverse laser cooling by SBRC, reduction of the beam intensity with the use of scraping has been proposed [21]. The initial horizontal beam size of 3.9 mm corresponding to the averaged temperature of 8400 K, was cooled down to 1.3 mm and 1.8 mm for SBRC on and off conditions, respectively for a beam intensity of 9 x 10^5 ions. By reducing the beam intensity, the IBS heating is expected to be reduced, however, the signal to noise ratio has also been reduced, which disabled us to perform beam size observation with the use of a standard fluorescence based techniques by a CCD camera described in Ref. [22]. So we utilized another scraper (Horizontal Scraper 2 or Vertical Scraper) to measure the beam profile in addition to the one (Horizontal Scraper 1) to control the beam intensity [23]. By detecting the beam survival ratio at various scraper positions, we could observe the beam

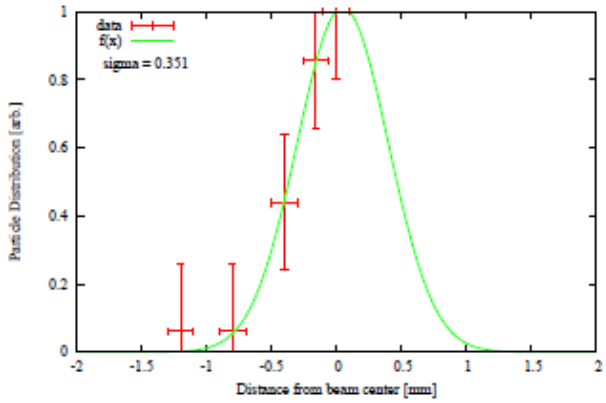

Fig.7 Measured horizontal beam profile with Horisontal Scraper 2.

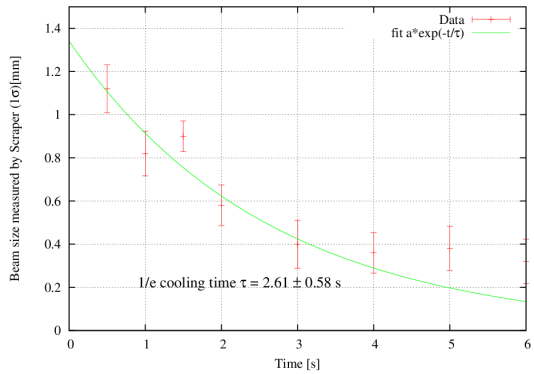

Fig. 9 Time variation of the horizontal beam size after the start of the laser cooling observed with a scraper for the beam intensity of 9 x 10^4 [23].

profile as shown in Fig. 7. We measured the beam sizes for various beam intensities from 1x 10^6 to 1 x 10^4 by changing the insertion position of the first scraper (H Scraper 1 in Fig. 1) which moves in the horizontal direction and after arriving a certain pre-determined position, returns back to its original position, which is 15 mm inner side from the beam center.

In Fig. 8, the beam intensity dependence of the horizontal beam size measured by H scraper 2 (Fig.1), is shown for a laser irradiation power of 8±1mW. By scraping to the intensity of 1 x 10^4, the cooled horizontal beam size was reduced to 0.17-0.30 mm and 0.55-0.61 mm for SBRC on and off, respectively. Taking into account the fractional momentum spread (Δp/p) measurable by a Post Acceleration Tube (PAT) [24], somewhat smaller horizontal beam size is expected, which, however, is not yet obtained experimentally for such a low intensity at the moment. Horizontal beam size uncorrected for this effect is utilized below, standing at the safety side. Thus the horizontal emittance is estimated to be 3.0-9.3 x 10^{-8} π m·rad for SBRC condition which corresponds to the average temperature of 16-50 K through Eq. (4). It is shown that the horizontal beam size reached by indirect transverse laser cooling is reduced by reduction of the beam intensity due to suppression of IBS, resulting in an increase of the indirect laser cooling efficiency. In Fig. 9, the time variation of the horizontal beam size indirectly laser cooled with the scraped beam intensity of 9 x 10^4 is shown, which gives us a cooling time of 2.6 sec, more than one order of magnitude shorter compared with the beam of the intensity of 1 x 10^7. It, however, seems to be still not so good enough to be able to realize the transition to a beam string. Further reduction of the beam intensity attaining enough S/N ratio might be needed for phase transition to a string state.

In Fig. 10, similar beam intensity dependence of the vertical beam size is shown. In the present case, the operation point of (2.07, 1.12) does not satisfy the difference resonance condition given by Eq. (7) and neither a solenoidal nor skew field was applied. So no coupling between the horizontal and vertical motions other than IBS is expected. The vertical heat is considered to be transferred mainly to longitudinal direction through IBS. As is known from Fig.10, the initial vertical beam size of 3.9 mm corresponding to the emittannce of 4.1 π mm·mrad is reduced to 1.9 mm and 3.3 mm by application of indirect transverse laser cooling for 3 sec. for beam intensity of 9 x 10^5 with and without SBRC condition, respectively. With SBRC condition on,

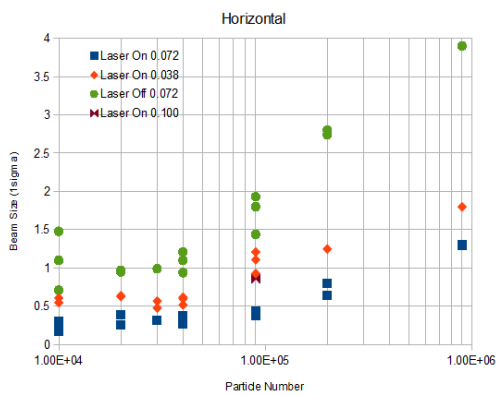

Fig.8 Ion number dependence of the horizontal beam size measured 3 sec. after the start of the indirect transverse laser cooling with the irradiated laser power of 8±1mW.

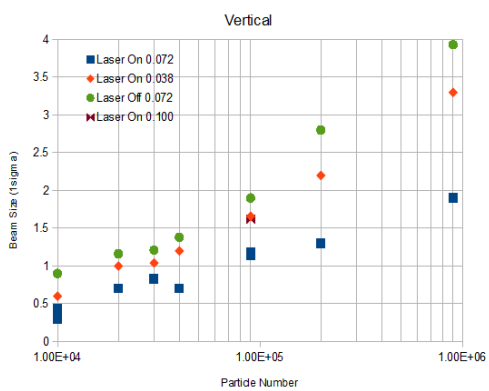

Fig.10 Ion number dependence of the vertical beam size measured 3 sec. after the start of the indirect transverse laser cooling with the irradiated laser power of 8±1mW.

Table 2 List of transverse temperatures attained by the indirect transverse laser cooling

Year	Method	Ion	Kinetic Energy	Intensity	$T_{//}$	T_H	T_V	Ref
1996	IBS	$^{9}Be^{+}$	7.3 MeV	2.0×10^{7}	15	4000	500	[15]
1998	Dispersive cooling	$^{9}Be^{+}$	7.3 MeV	1.0×10^{7}	few tens	≈500#	≈150#	[17]
2001	RFQ	$^{24}Mg^{+}$	1 eV	1.8×10^{4}	<3 m	$T_{\perp}$<0.4		[25]
2008	IBS	$^{24}Mg^{+}$	40 keV	1.0×10^{7}	11	-	500	[18]
2009	W SBRC	$^{24}Mg^{+}$	40 keV	1.0×10^{7}	27	220$		[20]
2009	WO SBRC	$^{24}Mg^{+}$	40 keV	1.0×10^{7}	16	-%		[20]
2012	W SBRC	$^{24}Mg^{+}$	40 keV	1×10^{4}	-	<16-50	7-15	[23]
2012	WO SBRC	$^{24}Mg^{+}$	40 keV	1×10^{4}	-	<150-190	30	[23]

(unit of the temperature is K, #,$estimated from the data in the figures of the reference [17] and [20], respectively. % laser size is too small to give the correct beam size.)

the horizontal beam size is cooled down rapidly compared with the off case and the line density of the ion becomes larger, which results in more efficient cooling of the vertical beam temperature by increase of IBS. For scraped beam intensity of 1×10^{4} ions, cooled vertical beam size becomes 0.30-0.44 mm and 0.6 mm for SBRC on and off, respectively. These values correspond to the vertical emittances of 2.4-5.2 x 10^{-8} π m·rad and 9.6 x 10^{-8} π m·rad, respectively. Thus the average vertical temperature has come down to 7-15 K with SBRC on for the beam intensity of 1 x10^{4}.

As shown in table 2, among the data ever obtained through transverse laser cooling, the above transverse temperatures attained at S-LSR by indirect transverse laser cooling are lower than the others except for PALLAS at Munich which realized crystallization for very slow (1eV) ions [25].

SUMMARY AND DISCUSSION

We have tried to attain the lowest possible temperature of a $^{24}Mg^{+}$ ion beam with the kinetic energy of 40 keV with the use of laser cooling technique to extend a strong laser cooling power for 3 dimensions. Experimental demonstration of SBRC has been performed at S-LSR and an intensity reduction with the use of controlled scraping results in the reduction of the transverse temperature down to 16-50 K for the horizontal direction and 7-15 K for vertical direction, which is the lowest temperature ever realized through laser cooling at storage rings with rather high energy. The longitudinal temperature at our experiment, however, remains at rather high level higher than a few tens K for the intensity of 1 x 10^{7} as shown in Table 2, obstructed by the limitation of the available laser power.

Computer simulation assuming S-LSR lattice predicts a formation of a string for the 35 keV $^{24}Mg^{+}$ ion beam at a intensity of 10^{3} (10 ions per bunch for harmonic number of 100) [26], which, we hope will be demonstrated in a near future experimentally at S-LSR by improvement of the laser power and sensitivity of the beam observation system.

REFERENCES

[1] A. Noda et al., Proc. of EPAC2002, Paris, France, (2002), 2748-2750.
[2] Originally proposed by Y.A.S. Derbenev, A.N. Skrinsky, Sov. Phys. Rev. **1** (1979), 165.
[3] H. Fadil et al., Nucl. Instr. Meth. in Phys. Res. **A517** (2004), 1.
[4] J. Wei, X.-P. Li and A M Sessler *Phys. Rev. Lett.* **73**, (1994), 3089.
[5] X.-P Li, H. Enokizono, H. Okamoto, Y. Yuri, A.M. Sessler and J. Wei Phys. Rev. ST Accel. Beams **9**, (2006), 034201.
[6] V. Parkhomchuk, Proc. Workshop on Electron Cooling and Related Applications (ECOOL84) (KfK Report No3846) ed H. Poth (Karlsruhe) pp71–83.
[7] M. Steck et al., Phys. Rev. Lett. **77**, (1996), 3803.
[8] H. Danared et al., J. Phys. Bat. Mol. Opt. Phys. **36**, (2003), 1003-1010.
[9] T. Shirai et al., Phys. Rev. Lett. **98**, (2007), 204801.
[10]Ya. S. Derbenev and A.N. Skrinsky, Sov. Sci. Rev., Sect. **A3**, (1981), 165.
[11]M. Steck et al., Nucl. Instrum. Methods Phys. Res., Sect. **A532**, (2004), 357.
[12] U. Schramm and D. Habs, Progress in Particle and Nuclear Physics, **53**, (2004), 583-677.
[13] H. Okamoto et al., Phys. Rev. **E69**, (2004), 066504.
[14] H. Danared, private communication at IPAC11.
[15] H.J. Miesner et al., Phy. Rev. Lett., **77**, (1996), 623.
[16] H.J. Miesner et al., Nucl. Instr. Meth. **A393**, (1996), 634.
[17] I. Lauer et al., Phys. Rev. Lett. **81**, (1998), 2052.
[18] M. Tanabe et al., Appl. Phys. Express , **1**, (2004), 028001.
[19] H. Okamoto, A. Sessler and D. Möhl, Phys. Rev. Lett. **72**, (1994), 3977.
[20] M. Nakao et al., submitted to Phys. Rev. ST-AB.
[21] A. Noda et al., Proc. of IPAC12, New Orleans, Louisiana, USA, (2012), MOPPD012.
[22] M. Nakao et al., Proc. of IPAC10, Kyoto, Japan, (2010), MOPD072.
[23] H. Souda et al., submitted to Appl. Phys. Express.
[24] J.S. Hangst et al., Phys. Rev. Lett. **74**, 86 (1995).
[25] T. Schätz, U. Schramm and D. Habs, Nature, **412**, (2001), 717-720.
[26] Y. Yuri and H. Okamoto, Phys. Rev. ST-AB **8** (2005) 114201.

BEAM COOLING AT NICA COLLIDER

T. Katayama, GSI, Darmstadt, Germany
I. Meshkov, A. Sidorin and G. Trubnikov, JINR, Dubna, Russia.

Abstract

At the heavy ion collider NICA presently promoted at the JINR, the beam cooling will play the crucial roles to attain the designed performance. The primary goal of the collider is to achieve the high luminosity ~1e27 /cm^2/sec, preventing the IBS diffusion effects by beam cooling to keep the luminosity during the experimental period. The other purpose of the cooling is to accumulate the required beam intensity up to several times 1e10 from the injector Nuclotron with use of the barrier bucket method. After the BB accumulation the coasting beam is adiabatically bunched with the help of RF field and the beam cooling. In the present paper the detailed simulation results are presented for the above process mainly in the longitudinal freedom.

INTRODUCTION

The heavy ion collider proposed at the JINR aims to achieve the head-on collision of 1-4.5 GeV/u, $^{197}Au^{79+}$ ion beam with the luminosity of ~1e27/cm^2/sec. [1] The number of bunches in the collider is 24 and each bunch contains the ion number of ~1e9, depending upon the operation energy. Thus totally around ~2.4e10 ions should be accumulated in the collider ring. The injector for the collider is the existing superconducting synchrotron, Nuclotron, which could provide the beam of 1-4.5 GeV/u with the intensity of 1e8-1e9/cycle of the cycle time 5 sec. The bunch length of the beam from the Nuclotron is around 1/3 of the circumference, 300 nsec. [2, 3]

In the present scenario, the bunch is transferred to the collider without any manipulation for the short bunch formation in the Nuclotron which allows us much easier operation of the Nuclotron. The long bunch is transferred in the longitudinal injection area which is provided by the barrier voltages, and is accumulated with the assistance of stochastic cooling for the high energy and the electron cooling for the low energy, say below 2 GeV/u.

Thus accumulated heavy ion beam is the coasting beam condition, and then the large RF voltage is applied adiabatically as well as the beam cooling. The beam is gradually bunched to the required rms bunch length for the collision experiment ~2ns (rms). The bunch length is the equilibrium state of RF field, beam cooling, Intra Beam Scattering (IBS) and space charge repulsion. Especialy at low energy, the IBS diffusion and space charge force could affect the beam motion at the short bunch condition.

The detailed analysis of the beam dynamics for the stochastic cooling application was reported elsewhere [4] and here the main emsphasis is given on the electron cooling and space charge problem.

STOCHASTIC COOLING

The operation energy of the collider is from 1 GeV/u to 4.5 GeV/u where the ring slipping factor is drastically changed. In Table 1 the ring slipping factor, transition gamma being fixed as 7.09 and the local slipping factor from the stochastic cooling PU to Kicker are tabulated. The distance from PU to kicker is assumed as 170 m. The coasting equivalent particle number is given as the product of bunch number/ring, number of ions /bunch and the bunching factor. Thus obtained coasting equivalent particle number is corresponding to the condition that the peak intensity of the bunched beam are populated as the coasting beam in the ring.

Table 1. Beam parameters for various energies

Energy (GeV/u)	1.5	2.5	3.0	4.5
Ring slipping factor	0.1268	0.0537	0.0350	0.00949
Local slipping factor	0.1173	0.0442	0.02546	-5.4e-5
Particle number/bunch	3.0e8	1.50e9	2.50e9	6.0e9
Coasting equivalent particle number	7.26e10	3.63e11	6.05e11	1.45e12

The bandwidth of the stochastic cooling system is preferably as wide as possible because the cooling time is inversely proportional to the bandwidth. On the other hand the momentum acceptance of the cooling system is, in general, becomes narrower for the wider bandwidth. Also the momentum acceptance is closely related with the ring slipping factor as well as the local slipping factor. In the present scenario the Palmer cooling method is envisaged where only the local slipping factor limits the momentum acceptance. Presently two bandwidth, 2-4 GHz and 3-6GHz are candidates.

Barrier Bucket Accumulation with Stochastic Cooling

The beam accumulation is designed to use the fixed barrier bucket method whose concept was experimentally verified at the POP (Proof Of Principle) experiment at the ESR GSI.[5] It should be noted that the POP experimental results are in well agreement with the simulation results. [6] The parameters of the barrier voltage as well as the stochastic cooling in the collider are tabulated in Table 2.

In the present simulation, the PU and kicker structure is assumed as the classical $\lambda/4$ electrode structure. In the meanwhile the new structure is being developed [7] which has the larger sensitivity and then the small number of electrode could be enough. Then the parameters of stochastic cooling system could be slightly changed in the construction phase.

The particles are injected in the unstable area between two barrier voltages and they are flowed into the lower potential region, stable area within the cycle time of 10 sec. The particle distribution after 30 pulse stacking is represented in Fig. 1 for 3.5 GeV/u ions. Details of beam simulation code are given in the reference paper [8].

Table 2. Parameters of Stochastic Cooling & Barrier Voltage

Particle	$^{197}Au^{79+}$
Ring circumference	503.04 m
Number of injected particle	1e9/cycle
Injected momentum spread	3e-4 (rms)
Injected bunch length	300 nsec
Ring slipping factor	0.00845
Dispersion at PU & Kicker	5.0 m & 0.0 m
Band width	2 - 4 GHz or 3-6 GHz
Number of PU & Kicker	128 or 64
PU Impedance	50 Ohm
Gain	120 dB
Atmospheric temperature	300 K
Noise temperature	40 K
Barrier voltage	2 kV
Barrier frequency	2.5 MHz (T=400 nsec)
Injection kicker pulse width	500 nsec
Transverse emittance	0.3 π mm.mrad

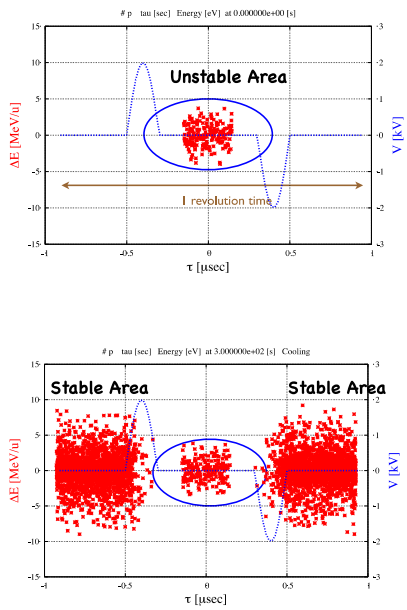

Fig. 1. Phase space mapping of the particles at the 1st injection (top) and after 30 stacking (bottom). The particles are represented with red dots and the barrier voltages are blue line. The injected beam is located in the central unstable area. Ion energy is 3.5 GeV/u.

The increase of the accumulated particle number is given as a function of time in Fig. 2 where also the accumulation efficiency is given. The accumulation efficiency is defined as the ratio of accumulated particle number to the total injected particle number. It is gradually decreased to 90 % after 50 pulse injection. The cooling system gain should be reduced against the increase of particle number so as to suppress the Schottky noise. The required microwave power is 800 Watt at the beginning of gain 115 dB.

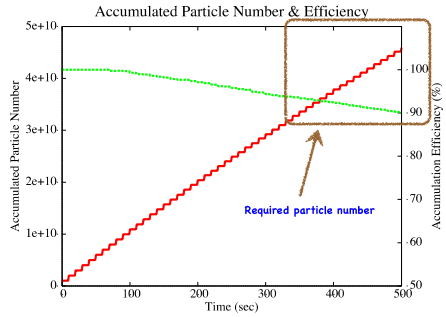

Fig. 2. Increase of accumulated particle number as a function of time. Red line: accumulated particle number. Green line: accumulation efficiency. Energy is 3.5 GeV/u.

Short Bunch Formation with Stochastic Cooling

The process of short bunch formation can be separated in two steps. At the first step the 200 kV RF voltage of harmonic number equal to the required bunch number (h=24), is adiabatically applied to the coasting beam. In parallel the stochastic cooling system is applied of which the gain is gradually decreased. Thus pre-bunched beam has the bunch length of 3 ns (rms) and $\Delta p/p$ of 6e-4 (rms). In the 2nd step, this bunch is re-captured by the 500 kV RF field of harmonic 96 or 120. The gain of stochastic cooling system is kept constant as 80 dB in the 2nd step during further bunching.

The evolution of bunch length and the relative momentum spread during the 2nd bunching process are given in Fig. 3. When the stochastic cooling is applied, the equilibrium values of bunch length is attained at 1.2 nsec and $\Delta p/p$ (rms) is 8e-4 while they are increased gradually due to the IBS heating effects without cooling.

The RF hardware for these beam manipulation is now being designed [9].

ELECTRON COOLING

For the lower energy less than 2.5 GeV/u the stochastic cooling could not work well as the slipping factor becomes so large (see Table 2). For such low energy operation, obviously the electron cooling is effective. The designed electron cooler parameters are given in Table 3.

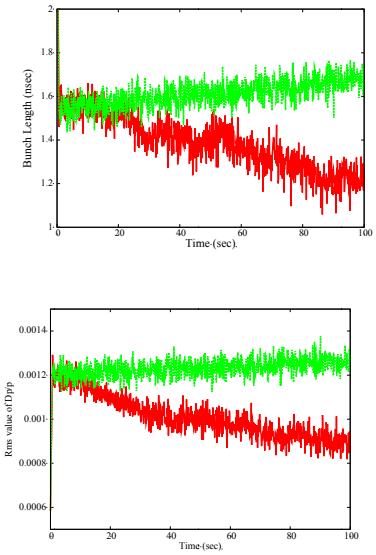

Fig. 3. The evolution of rms bunch length (top) and the $\Delta p/p$ (bottom) are illustrated as a function of time. Red: with stochastic cooling, Green: without stochastic cooling.

Table 3. Parameters of electron cooler for NICA collider

Cooler length	6 m
Electron current	1 A
Electron diameter	2 cm
Effective electron temperature	1 meV
Transverse electron temperature	1 eV
Longitudinal magnetic field	0.1 T
Beta function at cooler section	16 m

Typical cooling process is illustrated in Fig. 4 where the beam energy is 2 GeV/u and the particle number is 3e11 as a coasting beam equivalent. The equilibrium values are attained after 25 sec cooling as the transverse emittance of 0.12/0.09 (H/V) π mm.mrad and $\Delta p/p$=3.7e-4, respectively where the IBS effects are included. In the present analysis, the electron cooling force is derived from the Parkhomchuk empirical formula.

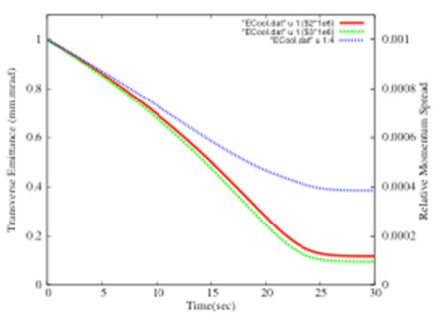

Fig. 4. Evolution of emittance (red: horizontal, green: vertical) and $\Delta p/p$ (blue) of 2.0 GeV/u ions with electron cooling. The IBS effects limit the equilibrium values.

In order to estimate the cooling time for several energies, the cooling process are calculated without IBS effects as in Fig. 5. The rough estimation of full cooling times are 3 sec (1 GeV/u), 20 sec (2 GeV/u), 70 sec (3 GeV/u), 200 sec (4 GeV/u) and 300 sec (4.5 GeV/u), respectively. Thus it could be concluded that the electron cooling would not help enough beyond the energy 2.0 GeV the cooling mechanism of the barrier bucket accumulation method with cycle time 10 sec as the cooling time is much longer than the cycle time.

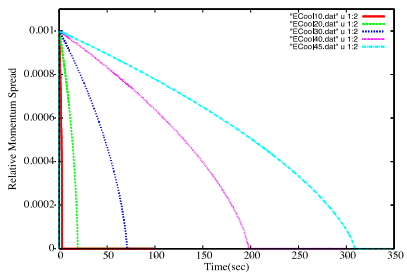

Fig. 5. Evolution of momentum spread for 1.0 (red), 2.0 (green), 3.0 (blue), 4.0 (pink) and 4.5 GeV/u (light blue). The IBS effects are not included. Initial values are, 1.0 π mm.mrad (transverse) and 1.0e-3 ($\Delta p/p$).

Barrier Bucket Accumulation with Electron Cooling

The energy of ion is 1.5 and 3.5 GeV/u, and the initial $\Delta p/p$ is assumed as 5e-4 (rms). Injected particle number is 1e9/shot with cycle time 10 sec. The calculated increase of accumulated particle number and the accumulation efficiency is given in Fig. 6.

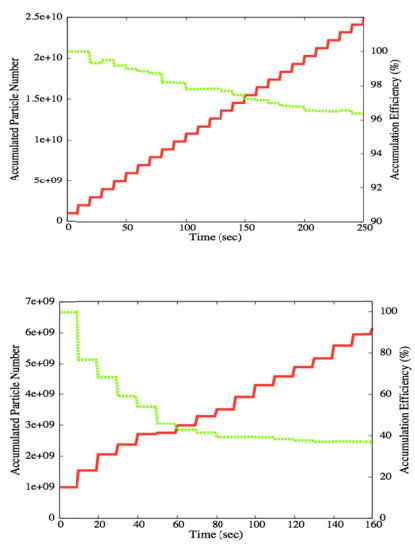

Fig. 6. The increase of accumulated particle number (red) and accumulation efficiency (green) during 25 times injection. Top: 1.5 GeV/u and bottom: 3.5 GeV/u

The accumulation efficiency is around 90 % after 25 times injection at 1.5 GeV/u while it becomes as low as 40 % at 15 times injection at the energy of 3.5 GeV/u. The summary of simulation results of barrier bucket accumulation are tabulated in Table 4.

Table 4/ Summary of barrier bucket accumulation with electron cooling

Energy (GeV/u)	Rms $\Delta p/p$ (1e-4)	Efficiency (%) & Particle Number at 150 sec	Rms Beam Size at 150 sec (mm)	Rms $\Delta p/p$ at 150 sec (1e-4)
1.5	5	98/1.5e10	0.3~1.0	1.0
1.5	10	87/1.4e10	0.4~1.2	2.5
2.5	5	68/1.1e10	0.8~1.2	2.0
2.5	10	54/8e9	1.0=1.5	5.0
3.5	5	28/5e9	1.5~2.2	4.5

SPACE CHARGE EFFECTS

In the previous chapters, results of longitudinal beam dynamics are given without taking account the space charge effects. In the present chapter, the space charge fields are included in the simulation of beam accumulation and short bunch formation. In order to save the computing time the IBS effects are not included in the present study. The energy of ion is selected as 1.5 GeV/u because the space charge effect is proportional to γ^{-2} and the lowest energy is most sensitive to the space charge effects.

The particle tracking including the space charge field is performed with use of the scheme of Particle In Cell (or Cloud In Cell) method. [10]

The longitudinal electric field due to the space charge is given by

$$E_z(z) = -\frac{g}{4\pi\varepsilon_0\gamma^2}\frac{\partial\rho(z)}{\partial z} \qquad (1)$$

where g is the geometric factor, $\rho(\square)$ is the line charge density, z is the longitudinal position. From this electric field the energy variation of ions per unit time is derived and the synchrotron motion is represented by following equation.

$$\frac{d\Delta E}{dt} = \frac{Z}{A}\frac{V_{rf}}{T_0} - E_{cool} - \frac{Z}{A}\frac{g}{4\pi\varepsilon_0\gamma^2}\frac{d\rho}{d\tau} \qquad (2)$$

Here the V_{rf} means the external RF field, E_{cool} the cooling effects and the 3rd term in the right hand side shows the space charge effects. Z is the charge state of ion and A the mass number. The accompanying phase equation is given as usual as

$$\frac{d\tau}{dt} = \frac{\eta}{\beta^2}\frac{\Delta E}{E_0} \qquad (3)$$

The geometric factor is simply given by

$$g = 1 + 2.0\ln(b/a) \qquad (4)$$

where a is the bunch radius and b is the radius of beam pipe.

The beam accumulation process can be performed using the equations (2) and (3). The parameters are as follows; ion energy 1.5 GeV/u, injected ion number 1e9/shot, cycle time 10 sec, ring slipping factor 0.1268, initial momentum spread 5e-4(rms). Barrier voltage=2 kV, barrier frequency=2.5 MHz, injection kicker firing time=0.6e-6 sec.

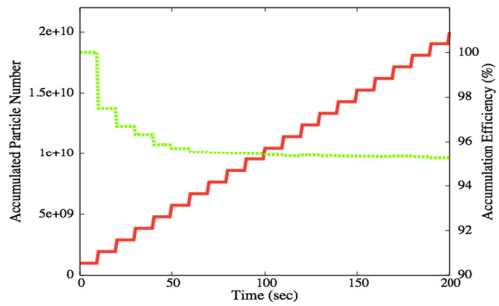

Fig. 7. The accumulated particle number (red) and the accumulation efficiency (green) up to 20 times injection including the space charge effects. Energy is 1.5 GeV/u

Comparing with the result without space charge effects (in Fig. 6), the accumulation efficiency is slightly decreased.

The space charge potential after the accumulation of ions are illustrated in Fig. 8 where the particle density is given in red colour and the space charge potential with green colour. In the central area the injected particle density is shown while two flat areas at left and right sides show the accumulated particle density. The space charge potential arises at the central part due to the derivative of the injected particle density and two sharp peaks are observed at the edge of accumulated area. The space charge potential after 20 times accumulation reaches to +/- 150 Volt while the space charge potential due to the injected particle (1e9 ions) is +/- 10 Volt.

It is clear from these results that the space charge effects do not affect the beam accumulation process as the barrier voltage is large enough 2 kV comparing with the space charge potential.

The next step is the short bunch formation with application of 200 kV RF voltage of harmonic number 24 and electron cooling force.

The comparison of space charge potential and the external RF voltage at the short bunch formation are illustrated in Fig. 9. Just at the starting of bunch formation the space charge potential is less than +/- 1 kV while it reaches to +/- 20 kV at the equilibrium state of bunch length +/- 3 nsec after 100 sec cooling.

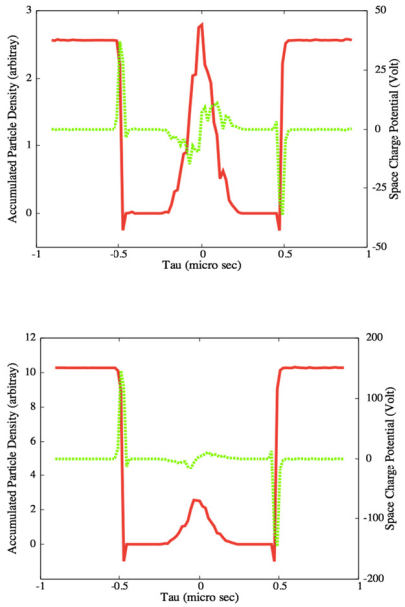

Fig. 8. Accumulated particle density (red) and space charge potential (green). From the top to the bottom, time is 50 (5 times injection) and 200 (20 times injection) sec, respectively.

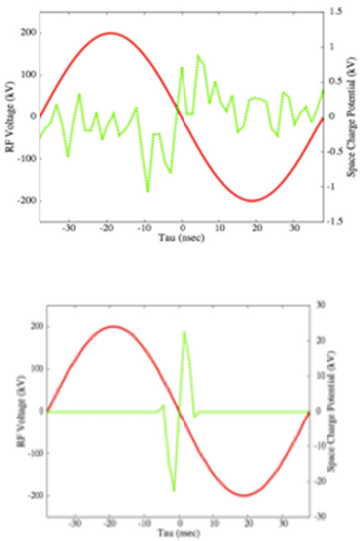

Fig. .9 Comparison of external 200 kV RF (red) & space charge potential (green). From the top to the bottom, time is 1 and 100 sec, respectively. The ion number is 1e9/bunch.

CONCLUSIVE REMARKS

We have performed the simulation work on the barrier bucket accumulation and short bunch formation with stochastic cooling and electron cooling at the operation energy from 1.5 GeV/u to 4.5 GeV/u. It is found that the stochastic cooling well works at the energy beyond 2.5 GeV/u while at the less energy the momentum acceptance of stochastic cooling system becomes too narrow due to the large slipping factor. On the other hand below 2.5 GeV/u the electron cooling could work to accumulate the beam as well as the short bunch formation. In this sense, both cooling method are perfectly complimentary each other.

The space charge potential becomes around +/- 20 kV at 1.5 GeV/u at the bunch length of +/- 3 nsec while at the higher energy the potential becomes small value. Considering the external RF voltage, 200 kV-500 kV, this space charge problem could be minor effects to the short bunch formation.

ACKNOWLEDGEMENT

Authors are indebted to the discussion with A. Smirnov for simulation of the accumulation with the electron cooling. L. Thorndahl confirmed the short bunch formation by the stochastic cooling with use of another algorithm. One of authors (T. K) appreciates the collaboration of space charge code development to T. Kikuchi.

REFERENCES

[1] I. Meshkov, "NICA Project at JINR", Proc. of COOL11, Alushita, 2011
[2] G. Trubnikov et al., "Application of Cooling Method at NICA Project", ibid.
[3] A. Sidorin et al., "Status of the Nuclotron", in this Proceedings.
[4] T. Katayama et al., "Numerical Investigation of Stochastic Cooling at NICA Collider", ibid in Ref. 1.
[5] M. Steck et al., "Demonstration of Longitudinal Stacking in the ESR with Barrier Bucket and Stochastic Cooling", ibid in Ref. 1.
[6] T. Katayama et al., "Simulation Study of Barrier Bucket Accumulation with Stochastic Cooling at GSI ESR", ibid in Ref. 1.
[7] R. Stassen et al., "The stochastic cooling system of HESR", ibid in Ref. 1.
[8] A. Eliseev et al., "Storage, Acceleration and Short Bunched Beam Formation of $^{197}Au^{79+}$ ions in the NICA collider", In this proceedings.
[9] T. Katayama et al., Proc. of IPAC10, Kyoto, May, 2010
[10] T. Kikuchi, T. Kawada and T. Katayama, "Influences of Space Charge Effect during Ion Accumulation Using Moving Barrier Bucket Cooperated with Beam Cooling", Proc. of COOL2007, Bad Kreuznach, Germany 2007.

STATUS OF THE HIGH VOLTAGE ELECTRON COOLER PROJECT FOR NICA COLLIDER

E.V.Ahmanova, I.N.Meshkov, R.V.Pivin, A.U.Rudakov, A.V.Shabunov, A.V. Smirnov, N.D.Topilin, Yu.A.Tumanova, S.L.Yakovenko#, JINR, Dubna
A.G.Kobets, Institute of Electrophysics and Radiation Technologies, NAS of Ukraine
A.V.Ivanov, Budker Institute of Nuclear Physics SB RAS, Novosibirsk
A.A.Filippov, M.P.Kokurkin, N.Yu.Lysov, M.M.Pashin, AREI, Moscow

Abstract

The 2.5 MeV electron cooler for the NICA collider is being designed at JINR [1]. The conceptual design of the electron cooling system has been developed and working design has been started. The 250 kV prototypes of the high voltage (HV) generator of the cooler has assembled and being tested.

DESIGN OF THE COOLER

The electron cooler (Fig. 1) consists of three tanks filled with SF6 gas under pressure of 8 at. The tanks 1 and 3 contain acceleration tube and electron gun for one of the electron beam and deceleration tube and electron collector for opposite direction electron beam. HV generator is placed in the tank 2.

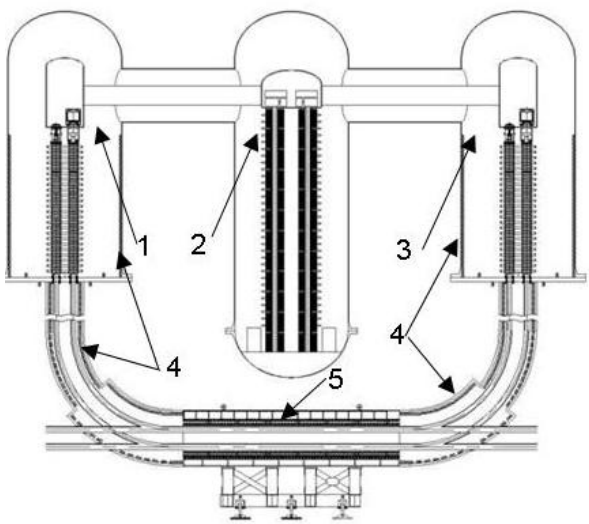

Fig.1. General view of the electron cooler (working design). 1, 3 – tanks with electron gun and acceleration tube and deceleration tube + collector for electron beam of opposite direction, 2 – tank with HV generator, 4 – beam transportation solenoids, 5 - electron cooling section.

MAGNETIC SYSTEM

The magnetic field is formed by a set of straight and toroidal solenoids (Fig.1). The solenoids forming the magnetic field in the region of acceleration/deceleration tubes are placed outside the tanks that resolve the problem of the high voltage insulation (Fig.2).

yakoven@jinr.ru

Table 1. Cooler parameters

Electron energy, MeV	0.5 ÷ 2.5
Electron beam current , A	0.1 ÷ 1,0
Beam diameter, cm	1,0
solenoid magnetic field, T	0.1 ÷ 0.2
HV PS current, mA	1
Collector PS, kW	2×2
HV PS stability, ΔU/U	1×10^{-4}
SF_6 gas pressure, at	5 ÷ 8

To form 2 kG magnetic field the solenoids have to have the next parameters: linear current density of 1.6 kA/cm; height of 2500 mm; diameter of 2100 mm. Comparing warm and superconducting solenoid parameters (cost, weight, power consumption, a.e.t), we have chosen the last one for tanks region (Table 2).

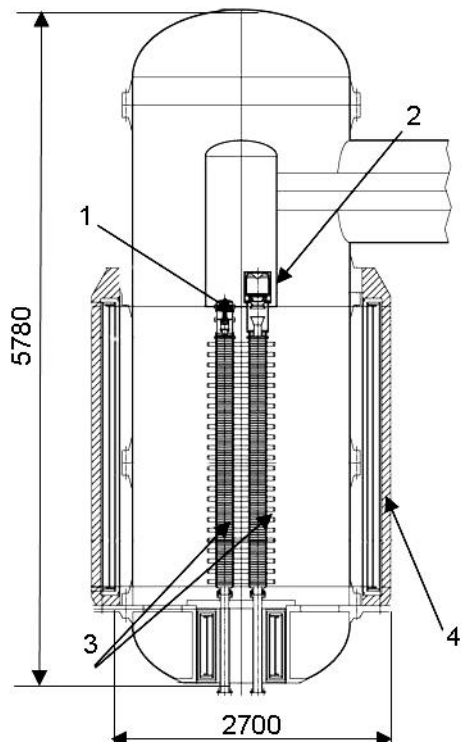

Fig.2. 1 - electron gun, 2 - electron collector, 3- acceleration/deceleration tubes, 4 - the SC solenoid in cryostats with iron shields.

HIGH VOLTAGE GENERATOR

High voltage (HV) generator placed in one of the tank of the cooler (Fig.3) is based on the principle of the cascade scheme [1]. The power transmition to the high potential will be done with rotating rods (shafts).

The 250 kv prototypes of the high voltage generator of the cooler (fig.4) has assembled and being tested.

Table 2. Superconducting solenoids parameters

Magnetic field, T	0.2
Operating current, A	200
Solenoid height, mm	2500
Solenoid inner diameter, mm	2300
Number of winding layers	2
Number of turns	2000
Inductance, H	8.35
Mass of superconductor, kg	50
Superconductor cost, M$	0.07
Cryostat, mandrel, current leads etc, M$	0.47
Power consumption, MW	0.03
Electricity cost per 5000 hours, $M	0.017

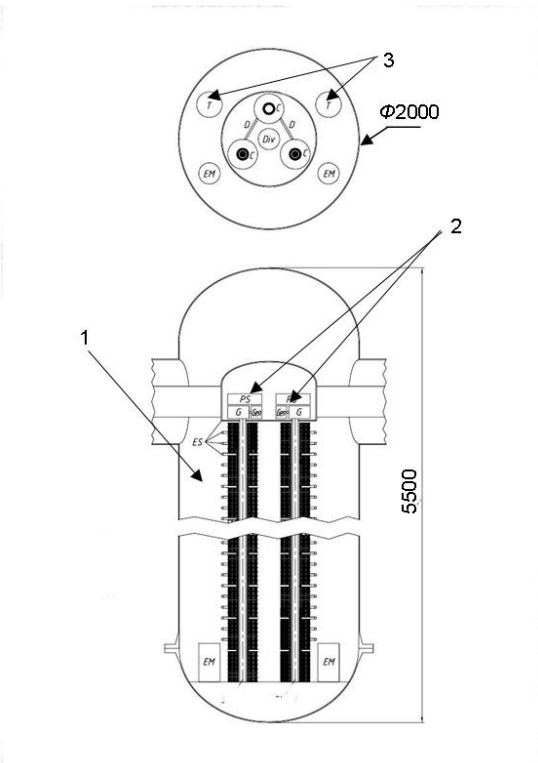

Fig. 3. Design of power supply of 2.5 MV.
1- cascade generator, 2 - gun and collector power supply,
3 - power transmitters to high potential (“shafts”)

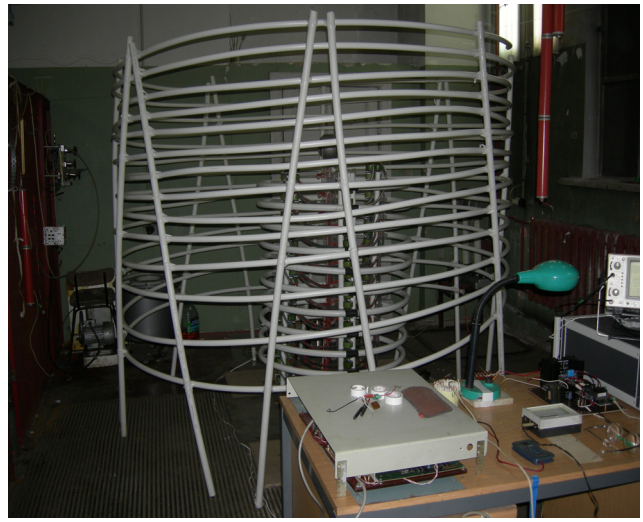

Fig.4. HV generator prototype U = 250 kV, Ii = 1 mA.

CONCLUDING REMARKS

The testing of the 250 kV prototype of HV cooler is in progress. The design and fabrication of HV generator and the design of the superconducting solenoids have been started.

REFERENCES

[1] E.V. Ahmanova, et. al./ “Electron cooler for NICA collider”, http://accelconf.web.cern.ch/accelconf/ COOL”11 , TUPS13, p.125-128.

LONG TERM BEAM DYNAMICS SIMULATION WITH THE BETACOOL CODE

A.O.Siodrin, A.V.Smirnov#, JINR, Dubna, 141980, Russia

Abstract

General goal of the BETACOOL program is to simulate long term processes (in comparison with the ion revolution period) in the ion storage ring leading to variation of the ion distribution function in 6 dimensional phase space. The ion beam motion inside a storage ring is supposed to be stable and it is treated in linear approximation. Results of the numerical simulation of the beam dynamics for new project NICA (JINR, Russia) are presented.

APPLICATIONS OF BETACOOL CODE OVER THE WORLD

The idea of the BETACOOL code was appeared about 18 years ago for the simulation of the beam dynamics under action of the electron cooling. BETACOOL means that simulations take into account the beta function in the cooling section.

In the present time the BETACOOL code includes different models of a few physical process which are usually exist in the storage rings [1]: electron, stochastic and laser cooling, intrabeam scattering, scattering on atoms of the residual gas and different types of internal target, colliding regime and particle losses, etc.

The BETACOOL code was elaborated in the collaboration with different scientific centres in the world where was benchmarked on the existing experiments and used for the simulation of new accelerator projects:

- Benchmarking of IBS and electron cooling models: CELSIUS (TSL) [2], ESR (GSI), TechX (Colorado), RHIC (BNL) [3], Recycler (FNAL), COSY (FZJ) [4], S-LSR (Kyoto Univ.) [5];
- Luminosity preservation in colliders: MUSES (RIKEN) [6], RHIC-II (BNL) [7], PAX (FAIR) [8], NICA (JINR) [9];
- Simulations of experiments with internal target: PANDA@HESR (FAIR) [10], WASA@COSY (FZJ) [11], ESR (GSI) [12];
- Beam ordering (crystalline beams): S-LSR (Kyoto University) [13], NAP-M (BINP), COSY (FZJ) [14], ESR (GSI) [15];
- Simulations of cooling-stacking process: LEIR (CERN), HIRFL-CSR (Lanzhou), NICA Booster (JINR) [16];
- Low energy electron cooling: TSR [17] and USR (MPI) [18], ELENA (CERN);
- RF burrier bucket system: Recycler (FNAL) [19], ESR (GSI), NESR and HESR (FAIR) [20], NICA Collider (JINR).

#smirnov@jinr.ru

Basic algorithms and software structure are described in details in BETACOOL guide [21]. The possibilities of the BETACOOL application for optimization of a storage ring operational regimes are illustrated in this report on example of the heavy ion mode of the NICA collider operation mainly. The beam cooling (both – electron and stochastic) at the NICA collider has two relatively independent goals: beam stacking using barrier bucket technique and luminosity preservation during collisions.

PARTICLE ACCUMULATION WITH RF BARRIER BUCKET SYSTEM

RF barrier bucket system was proposed for the particle accumulation in the NICA collider in order to provide required beam intensity independently on intensity of the bunch at single injection [22]. In the ion energy range from 1 to about 3 GeV/u the beam stacking is planned to be realized using stationary burrier pulses with the electron cooling of the injected beam.

RF barriers divide a ring circumference on two parts: one of them corresponds to unstable synchrotron motion, in the second one the motion is stable. After injection into the unstable region the particles are cooled down with the electron cooling and accumulated between barriers in the part opposite to the injection region. At the next injection all the particles located in the injection region are killed by the injection kicker pulse. The NICA collider RF barrier bucket system is designed to provide the barriers of rectangular shape. Example of the stacking process simulation with BETACOOL is presented in the Fig.1.

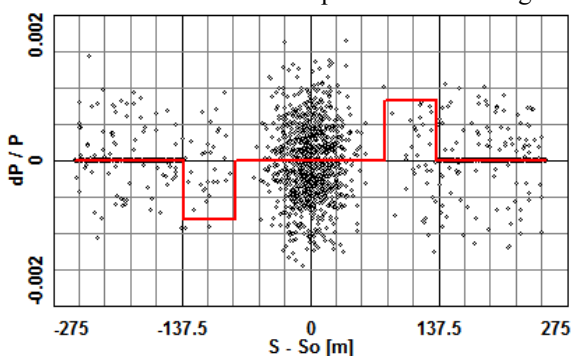

Figure 1: Longitudinal phase space after second injection for the ion energy 1.5 GeV/u: dots – model particles, red line – barrier bucket potential distribution in the momentum deviation units.

The stacking efficiency is determined by the ratio between the injection repetition period and the cooling time. The working cycle of the NICA injection chain is equal to about 5 seconds and it provides single bunch of about 10^9 Gold nuclei. Even accelerated bunch is injected into the first collider ring the odd – into the second ring. It

means that for each collider ring the injection repletion period is about 10 seconds. Dynamics of the stacking process simulated with the BETACOOL is shown in the Fig. 2.

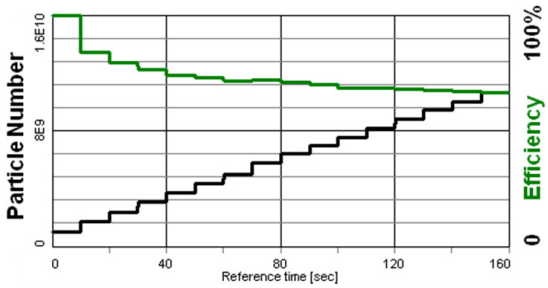

Figure 2: Particle accumulation with barrier bucket and electron cooling: black line – particle number, green – accumulation efficiency. Ion energy 2.5 GeV/u.

The accumulation efficiency decreases with increase of the the ion energy. It is equal to 92% for ion energy 1.5 GeV/u and 66% for 2.5 GeV/u. For the ion energy more than 2.5 GeV/u the electron cooling times are much longer than the injection repetition period (Table 1) and the stacking efficiency decreases very fast.

Table 1: Beam stacking in the NICA collider

Ion ring			
Ion energy, GeV/u	1.5	2.5	4.5
Particle number per injection cycle		10^9	
Initial emittance (h/v), π mm mrad		1.1/0.9	
Initial momentum spread		5×10^{-4}	
Barrier bucket voltage, kV		2	
Electron cooling			
Cooler length, m		6	
Electron current, A		1	
Electron beam radius, cm		1	
Magnetic field, kG		1	
Beta function at cooling section, m		16	
Longitudinal cooling time, sec	3	12	80
Accumulation efficiency, %	**92**	**66**	**34**

These results are in good agreement with independent simulations presented in [23].

The BETACOOL provides tools for optimization of the RF and electron cooler parameters in order to improve the situation. The beam losses during injection are related with the already circulating particles having very small momentum deviation in the unstable region. Such "frozen" particles are not affected practically by the cooling and they can move through the unstable region during a few hundreds of seconds. To push out them from the injection region one can slightly modify the barrier voltage shape introducing small accelerating (or decelerating) voltage in the unstable region keeping the integral over circumference equal to zero. The cooling efficiency can be also increased with the deviation of the electron energy.

For instance, the particle accumulation with electron energy shift ($\Delta P/P=10^{-4}$) and nonzero voltage at the injection region (+10 V) increases the stacking efficiency by about 10% at the ion energy 2.5 GeV/u (Fig.3).

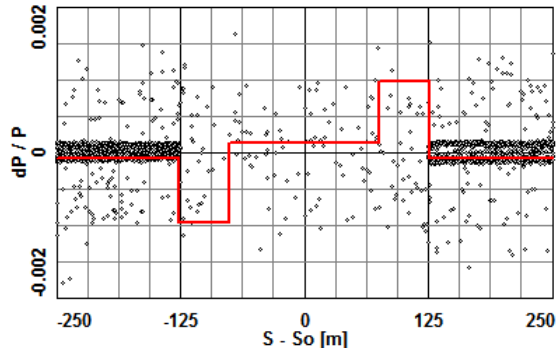

Figure 3: Longitudinal phase space after 160 sec with electron energy shift ($\Delta P/P=10^{-4}$) and nonzero voltage at the injection point (+10 V). Ion energy 2.5 GeV/u.

LUMINOSITY PRESERVATION WITH ELECTRON COOLING

The bunch parameters in the NICA collider are chosen near thermo dynamical equilibrium between all three degrees of freedom in the total energy range. At this condition the intrabeam scattering (IBS) heating times are equal to each other for transverse and longitudinal planes (Table 2). Role of the cooling during the collisions is to compensate the IBS heating and to stabilize the bunch parameters during long period of time. General problems at electron cooling application are the ion recombination with the cooling electrons and formation of specific shape of the ion distribution function. Electron cooling leads to formation of small dense core of the beam and long tails which are not cooled practically. One of the way to avoid both problems is to use so called "hollow" electron beam: the beam with very small electron density in the central part.

Table 2: Colliding regime

Bunch number		24	
Bunch length, m		0.6	
Beta function at colliding point, m		0.35	
Ion energy, GeV	1	3	4.5
Particle number per bunch, 10^8	2.7	24	22
Momentum spread, 10^{-3}	0.62	1.25	1.65
Emittances (hor/ver), π mm mrad	1.1/1	1.1/0.9	1.1/0.8
Luminosity, 10^{27} cm^{-2} sec^{-1}	0.01	1	1
Inrabeam scattering time, sec	**186**	**702**	**2540**

The BETACOOL provides a possibility to simulate the cooling process at arbitrary shape of the electron distribution over the radial coordinate. In the simplest case the hole has to be chosen equal to the ion beam radius in the cooling section corresponding to required emittance. The electron density inside the hole is chosen to stabilize the ion momentum spread (Fig. 4).

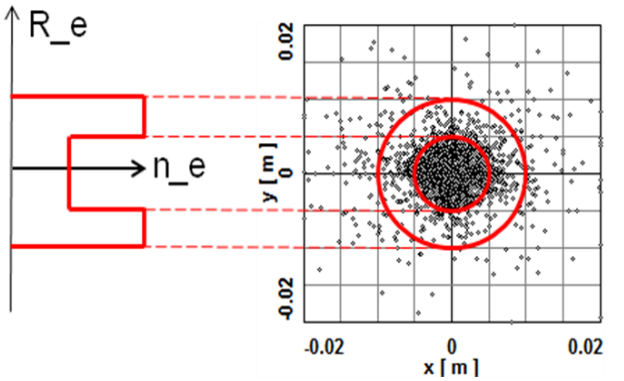

Figure 4: Hollow electron beam with the hole radius of 0.5 cm: black dot – particle distribution in real space, red lines – distribution of the electron beam density.

At optimum choice of the electron beam parameters the ion momentum spread and transverse emittances are practically stable during long period of time (Fig.5a). The slight increase of the luminosity (Fig.5b) is explained by the deviation of the transverse beam profiles from Gaussian shape. However the sharp central peak typical for electron cooling is not formed. The recombination rate is determined by the electron density inside the hole which is about in one order less than in the outer layer.

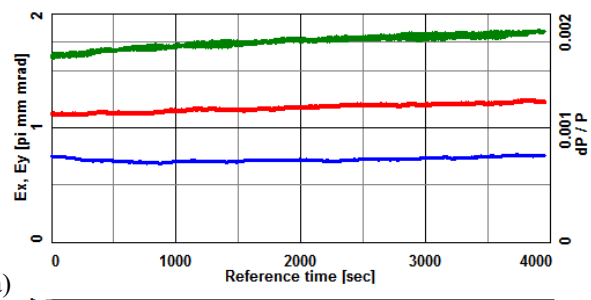

Figure 5: Evolution of beam parameters for ion energy 4.5 GeV/u and electron current 0.33 A: a) green line – momentum spread, blue and red – horizontal and vertical emittances, b) luminosity.

REFERENCES

[1] I.N.Meshkov, A.O.Sidorin, I.A.Seleznev, A.V.Smirnov, et.al. BETACOOL program for simulation of beam dynamics in storage rings. NIM A, 558, 325-328 (2006).
[2] A. V. Fedotov, B. Gålnander, V. N. Litvinenko, et.al. Experimental studies of the magnetized friction force. Phys.Rev.E, 73, 066503 (2006).
[3] A.V. Fedotov, A. O. Sidorin, A. V. Smirnov. IBS for Non-Gaussian Distributions. Proceeding of Hadron Beams'10, Morschach, Switzerland, 62-66 (2010).
[4] J. Dietrich, I. Meshkov, A.Sidorin, A. Smirnov, and J. Stein. Studies of Beam Dynamics in Cooler Rings. COOL'05, FNAL,Galena,USA., 154-158, AIP, 821 (2005).
[5] A. Noda, T. Shirai, H. Souda, et.al. Experimental Approach to Ultra-Cold Ion Beam at S-LSR. PAC'07, FNAL, Albuquerque, USA, p.2035-2037 (2007).
[6] I.Meshkov, A.Sidorin, E.Syresin, et.al. Computer simulation of ECOOL and IBS process in ACR and DSR using BETACOOL program. RIKEN-AF-AC-21, Japan (2000).
[7] A.Fedotov, I.Ben-Zvi, A.Sidorin, et.al. Cooling Dynamics Studies and Scenarios for the RHIC Cooler. PAC'05, Oak Ridge National Laboratory, Knoxville, USA, 4236 (2005).
[8] A.Smirnov. Luminosity for PAX project. Proceeding of Spin in Hadron Physics, Tbilisi Univ. Georgia (2006).
[9] G. Trubnikov, A. Sissakian, A.Smirnov et al. Project of the Nuclotron-based Ion Collider Facility (NICA) at JINR. RuPAC'08, Zvenigorod, Russia (2008).
[10] A.V. Smirnov, A.O. Sidorin, D.A. Krestnikov. Effective Luminosity Simulation for PANDA Experiment at FAIR. COOL'09, IMP, Lanzhou, China., p.127-129 (2009).
[11] A.Smirnov, A.Sidorin, D.Krestnikov, et.al.. Simulation of Pellet Target Experiments with BETACOOL Code. RuPAC'08, Zvenigorod, Russia, p.9-11 (2008).
[12] V.Gostishchev, C.Dimopoulou, A.Dolinskii, et.al. Comparison of measurements and simulations of internal target effects in the ESR storage ring. NIM A 641 (2011) 12–18.
[13] T.Shirai, M.Ikegami, A.Noda, I.Meshkov, A.Smirnov, et.al. One-Dimensional Beam Ordering of Protons in a Storage Ring. Phys. Rev. Lett. 98, 204801 (2007).
[14] I.Meshkov, Yu. Korotaev, A. Smirnov, et.al. Electron Cooling of Proton Beam at COSY and S-LSR. RuPAC'06, ИЯФ им.Будкера, Новосибирск, Россия (2006).
[15] A.Smirnov, I.Meshkov, A.Sidorin, et.al. Necessary Condition for Beam Ordering. COOL'07. Bad Kreuznach, Germany (2007).
[16] S.Kostromin, I.Meshkov, A.Sidorin, et.al. Application of Cooling Methods to NICA projects. COOL'11, Alushta, Ukraine, p.25-30 (2011).
[17] A.Papash, A.Smirnov, M.Siggel-King, C.Welsch. Long Term Beam Dynamics in Ultra-Low Energy Storage Rings. IPAC'11, San Sebastián, Spain (2011) p.2166.
[18] A.V. Smirnov, A.I. Papash, C.P. Welsch. Ion Kinetics in the Ultra-Low Energy Electrostatic Storage Ring (USR). COOL'11, Alushta, Ukraine (2011) p.89.
[19] A.Smirnov, A.Sidorin, D.Krestnikov, et.al. Implementation of Longitudinal Dynamics with Barrier RF in Betacool and Comparison to ESME. COOL'09, Lanzhou, China (2009).
[20] A.V.Smirnov, D.A.Krestnikov, I.N.Meshkov, et.al. Particle Accumulation with a Barrier Bucket RF System. COOL'09, IMP, Lanzhou, China, 67-70, 2009.
[21] http://betacool.jinr.ru
[22] G.Trubnikov, I.Meshkov, et.al.. Application of the Beam Cooling Methods at the NICA Project. This Proceeding.
[23] T.Katayama, I.Meshkov, G.Trubnikov. Beam Cooling at NICA Collider Project. This proceeding.

CURRENT PLANS FOR BEAM COOLING AT FAIR

M. Steck, C. Dimopoulou, A. Dolinskii, O. Gorda, T. Katayama, S.A. Litvinov, Yu.A. Litvinov, F. Nolden, C. Peschke, Th. Stöhlker, GSI Darmstadt, Germany,
J. Dietrich, R. Maier, D. Prasuhn, R. Stassen, H. Stockhorst, FZ Jülich, Germany

Abstract

The improvement of the quality of secondary beams by beam cooling is an essential component in the scenario of the Facility for Antiproton and Ion Research (FAIR). Beam Cooling is applied to match the secondary beams, antiprotons and rare isotopes, which are produced in thick solid targets, to the needs of experiments. Pre-cooling in the Collector Ring, accumulation and preparation for experiments in the High Energy Storage Ring are the main tasks of the Cooling Systems. Many of the beam cooling concepts for FAIR are studied experimentally in the existing Experimental Storage Ring ESR which has been operated at GSI over more than two decades and which will also be available for beam physics experiments in the coming years.

INTRODUCTION

The construction of the international Facility for Antiproton and Ion Research (FAIR) [1] is presently focussed on the Modularized Start Version (MSV). The funding of this first stage of the project is secured and the goal is to provide beams for all major experimental programs. The scientific programs cover research with high energy antiprotons in the PANDA experiment, Compressed Baryonic Matter (CBM), nuclear structure and related astrophysics, and atomic and plasma physics and applications. Already in the MSV, all the various types of experiments expect unprecedented possibilities for their research field. The programs with secondary beams are largely based on beam cooling which will be used for phase space reduction of antiprotons, rare isotope beams and highly charged ions.

The MSV of the FAIR project comprises various existing, but even more new accelerator systems. The program with heavy ion beams requires the existing UNILAC linear accelerator and the heavy ion synchrotron SIS18 as injector chain. By the addition of the synchrotron SIS100 [2] the heavy ion beam energy can be increased according to the higher rigidity of 100 Tm, alternatively lower charge states can be accelerated gaining in beam intensity by abandoning intermediate stripping with associated intensity reduction. With a new 70 MeV proton linac a source of intense proton beams is under construction which serves as injector into the chain with SIS18 and SIS100 which will result in 29 GeV protons for the production of antiprotons.

The high energy, high intensity beams after SIS100 will produce either highly charged ions, rare isotope beams by projectile fragmentation, or antiprotons from a primary proton beam. The antiprotons exit from a nickel production target where antiprotons at 3 GeV are selected in a magnetic separator for injection into the new Collector Ring (CR) [3]. For Rare Isotope Beams (RIBs) the new large acceptance superconducting fragment separator SuperFRS [4] will conduce to the production of high intensity secondary beams which can be used for fixed target experiments or for injection into the CR in order to apply phase space compression.

With respect to beam cooling the CR will be the key accelerator to improve the quality of secondary beams, both antiprotons and RIBs. For both species the primary beams in SIS100 will be compressed into a short single bunch with a length of 50 ns. The secondary particles after production in the target basically retain this time structure, however, with an increased momentum spread. Immediately after injection of the short bunch a bunch rotation system reduces the momentum spread and subsequent stochastic cooling will allow a fast reduction of the momentum spread providing a high quality secondary beam for transport to a subsequent storage ring where it is stored and prepared for the experiment. In the MSV the High Energy Storage Ring (HESR) [5] will be the exclusive user of pre-cooled CR beams. It is mainly designed for the storage of antiprotons and experiments using the PANDA set-up. Recently plans for the operation of the HESR with ion and rare isotope beams were discussed and are being worked out in detail.

As a continuation of ongoing GSI activities and in view of the delay of the RESR and NESR storage rings which are postponed within the FAIR project, the operation of the existing ESR storage ring [6] will be continued. Since it is equipped with a stochastic and an electron cooling system, it can be used as a test bed for FAIR developments. The option to decelerate heavy ions to 4 MeV/u opens already now the field of low energy beams foreseen in the FAIR project. Further deceleration with the HITRAP [7] decelerator and the plan to install the CRYRING [8], which is a contribution to the FAIR program with low energy antiprotons and ions, will allow accelerator and experimental developments for a low energy physics program at FAIR.

PRE-COOLING IN THE COLLECTOR RING CR

The Collector Ring CR is a large acceptance storage ring for the storage of secondary particles. The production of the secondary beams in a thick solid target results in a large emittance increase, both transversely and longitudinally. The large transverse acceptance of the CR allows efficient use in the capturing of secondary beams emerging from the target. Different optical modes will be used for antiprotons and ions. This is a consequence of the requirements of stochastic cooling for proper mixing

conditions of the particles. The increase of the longitudinal momentum spread in the target is minimized by forming a short bunch of the primary beam which is directed to the production target. The bunch length is virtually unchanged in the target and mainly the momentum spread is increased. To be matched with the incoming bunch the CR has large momentum acceptance. However, the cooling time of the beam with the stochastic cooling system in the CR can be reduced by reducing the momentum spread. A dedicated rf system is designed to provide a reduction of the momentum spread by bunch rotation and adiabatic debunching of the incoming bunch. This results in a nearly coasting beam with reduced momentum spread for the subsequent application of stochastic cooling. The main goal is the production of good beam quality in shortest time. For antiprotons the cooling time limits the average production rate, whereas for RIBs the access to short-lived isotopes is determined by the time needed to prepare the beam parameters to values which are useful for the experiment.

The cooling time depends on the ring parameters and the choice of the cooling system. For longitudinal cooling the momentum slip factor of the CR has been optimized. The different velocities of antiprotons and ions (ß = 0.97 and 0.83, respectively) are matched by the optical setting of the ring magnets with optimized momentum slip factor, both locally and averaged over the ring. In addition, the ring lattice has to be designed for proper phase advance between the pick-ups and kickers of the two transverse cooling systems and for their installation in dispersion-free sections. All these aspects, which are relevant for stochastic cooling, were considered in the ring lattice and combined with the requirements for large acceptance which is further optimized by a dedicated sextupole correction scheme [9]. Another more recent consideration came from the necessity to transfer beam directly from the CR to the HESR resulting in a new extraction point.

The actual stochastic cooling system for the coasting beam after bunch rotation was designed on the basis of analytical estimates and numerical simulations. Design issues were the choice of the system bandwidth 1-2 GHz, both for the longitudinal and the transverse cooling systems and the decision for notch filter cooling [10]. For RIBs the notch filter cooling needs additional pre-cooling with a Palmer cooling system which has to be added due to band overlap in the injected hot secondary beam and the relatively large momentum slip factor of the lattice for RIB operation.

The ring installations of the stochastic cooling system consists of horizontal and vertical pick-up and kicker tanks, all four located in the dispersion-free straight sections with proper phase advance between respective pick-ups and kickers. The signals of both transverse systems are also used in a sum mode for the longitudinal notch filter cooling and the correction signals are sent to the kicker electrodes. Each tank accommodates two times eight electrode arrays of the slot line type on both sides of the beam. The slot line electrodes are well suited for operation in the velocity range which is defined by the velocity of ions (ß = 0.83) and antiprotons (ß = 0.97). The low signal to noise ratio for antiprotons and the necessity of fast cooling have resulted in two additional features. The pick-up electrodes can be cooled during operation to 20 K in order to reduce thermal noise and can be moved synchronously with the reduction of the beam size in order to provide optimum pick-up signals.

The electric parameters of the electrodes have been measured on the test bench and their design has been optimized [11]. The measurements also provide the input for the design of the electric circuit and for computer simulations of the cooling process. A new optical notch filter was developed for application in the cooling circuit. After extensive measurements in the laboratory, the expected performance was demonstrated with beam in the ESR. The present funding of the stochastic cooling system foresees installation of a total rf power of 8 kW, an upgrade to higher power with corresponding increase of the cooling rate is an option, if additional funding is available.

Table 1: Main Parameters for the stochastic cooling of antiprotons in the CR.

ring circumference C	221.45 m
revolution frequency	1.315 MHz
slip factor ring total η/ pickup-kicker η_{pk}	-0.011/ -0.033
distance pickup-kicker / C	0.378
antiproton number	1×10^8
initial rms emittance	45 mm mrad
initial rms momentum spread	3.5×10^{-3}
system bandwidth	1 – 2 GHz
pick-up/kicker impedance	11.25 / 45 Ω
number of longitudinal pick-ups/kickers	128 / 128
number of transverse pick-ups/kickers	64 / 64
total installed power at kickers	8 kW

The feasibility of the required fast cooling was studied in computer simulations. The most important parameter is the momentum spread after cooling. It determines the requirements for the efficiency of the transfer to the HESR, due to the limited momentum acceptance of the HESR. The simulations were performed with an existing CERN code which was adopted and optimized for the CR calculations. It calculates the rms momentum spread as the second moment of the distribution function applying the Fokker-Planck equation to the longitudinal degree of freedom and solving it numerically. In the first calculations the cooling of antiprotons was studied. Many parameters of the storage ring and cooling system were taken into account in great detail as listed in Table 1. The simulations were performed not only for notch filter cooling, but also for Time-Of–Flight (TOF) cooling [12]. TOF cooling offers larger momentum acceptance, but no noise suppression [13]. Notch filter cooling is more powerful with a reduced momentum acceptance which is determined by the shape of the notches. According to the

simulations, notch filter cooling is able to reduce the initial momentum spread of 3.5×10^{-3} (rms) with the planned rf power in less than 10 s to a momentum spread below 5×10^{-4} (Fig. 1). This complies with the requirements of efficient antiproton production and transfer to the HESR. A further increase of the cooling rate can be expected by an increase of the installed rf power, which would allow an increase of the antiproton production rate.

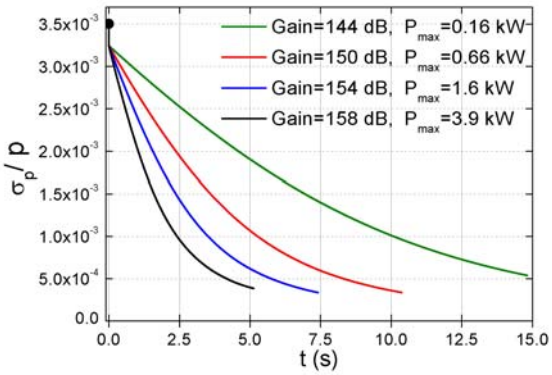

Figure 1: Simulation of the reduction of the momentum spread of a beam of 10^8 antiprotons after bunch rotation in the CR for different gains of the stochastic cooling system.

Similar simulations are needed for the cooling of RIBs from the SuperFRS, where much shorter total cooling times (below 1.5 s) are expected due to the higher charge of the ions. The simulations are crucial for the design of the various subsystems which will be installed in the frame of the MSV and are presently prepared.

HIGH ENERGY STORAGE RING HESR

Storage of antiprotons for experiments with an internal hydrogen target as part of the PANDA physics program was the main motivation for the construction of the high energy storage ring HESR. A magnetic bending power of 50 Tm allows a maximum antiproton energy of 14.1 GeV. Two 132 m long straight sections in the circumference of 575 m provide comfortable space for experimental installations and beam cooling systems. The injection system is designed for antiprotons of 3 GeV energy as provided from the CR, or in a later stage after accumulation in the RESR. After injection the antiprotons can be either accelerated to any energy between 3 and 14.1 GeV or decelerated to a minimum energy of 0.8 GeV. The ramping rate is limited to 0.025 T/s due to available rf voltage and the ramp rate of the main power converters of the ring magnets.

In the MSV the accumulator ring for antiprotons RESR is missing. Therefore an alternative scheme for the accumulation of antiprotons in the HESR by a combination of barrier buckets and cooling was proposed. For antiprotons the stochastic cooling system appears more promising than the planned electron cooling system.

The lack of stored ions and RIBs in the new storage rings constructed within the MSV of the FAIR project triggered a feasibility study of ion beam storage in the HESR [14]. The injection scheme can follow the concept of the injection of antiprotons from the CR. The magnetic rigidity should be 13 Tm as for antiprotons using the same magnetic components with reversed polarity. Changing the polarity is not a severe issue, as the time scale for switching between antiproton and ion operation will be weeks to months. As for antiprotons, accumulation of ions with barrier buckets and cooling is an option, if beam intensities higher than available in a single transfer from the CR will be requested. The available intensities will vary over a large range depending on the ion species. Energies in the range 0.2 to 5 GeV/u, depending on the ion species, can be achieved by acceleration or deceleration in the HESR.

The main cooling system of the HESR considered from the very beginning is stochastic cooling [15]. The cooling system operates in the frequency band 2 – 4 GHz. Special slot coupler rings were designed as electrodes which provide signals for all three phase space planes. The pick-up tanks are designed for cryogenic cooling to 20 K by cold heads. The expected performance of the slot coupler structure could be demonstrated with beam in COSY [16]. Similar to the CR, also in the HESR longitudinal cooling by the TOF-method and by notch filter cooling will be available. The low level rf system components including optical delay lines as well as the power amplifiers are studied and designed for integration into the cooling system. Originally designed for antiprotons above 3 GeV, studies have shown that stochastic cooling can also be used at energies below 3 GeV, which is particularly valuable for the plans to operate the HESR with ions [17]. The system will be able to compensate the heating by the internal hydrogen target, but depending on the target thickness an additional rf system will be needed to compensate the energy loss in the target.

A proposed high energy electron cooling system for the HESR which could cool antiprotons up to 8 GeV, and after an optional upgrade up to the full antiproton energy of 14.1 GeV, was shifted to a later stage of the project. Nevertheless, a detailed design study was preformed for this high energy electron cooler [18]. As a less expensive alternative an electron cooling system is now under construction at the Budker Institute, Novosibirsk, which, for antiprotons, can cover the energy range below the injection energy of 3 GeV [19]. In this energy regime electron cooling is still powerful and can provide high quality beams and can efficiently compensate the heating by the internal target. The electron cooling system presently passes the final commissioning with electron beam at the Budker Institute, where it also was designed and manufactured.

After successful commissioning at the Budker Institute, the electron cooling system will be shipped to Jülich for installation in the COSY storage ring. In the

COSY the performance can be studied with a proton beam and optimized over the full energy range which will be relevant for cooling in the HESR, both at the antiproton injection energy and nearly the full range of ion energies. Thus this electron cooling system will be of high importance in the operation of the HESR with stored ions. It can be used for accumulation but more importantly for the preservation of good beam quality during operation of an internal target. This situation was studied in simulations with the BETACOOL code [20]. Assuming realistic parameters of the electron cooling system even with a hydrogen target in the range 10^{14}-10^{16} hydrogen atoms/cm^2 electron cooling provides emittances below 1 mm mrad and a momentum spread in the low 10^{-4} range (Fig. 2).

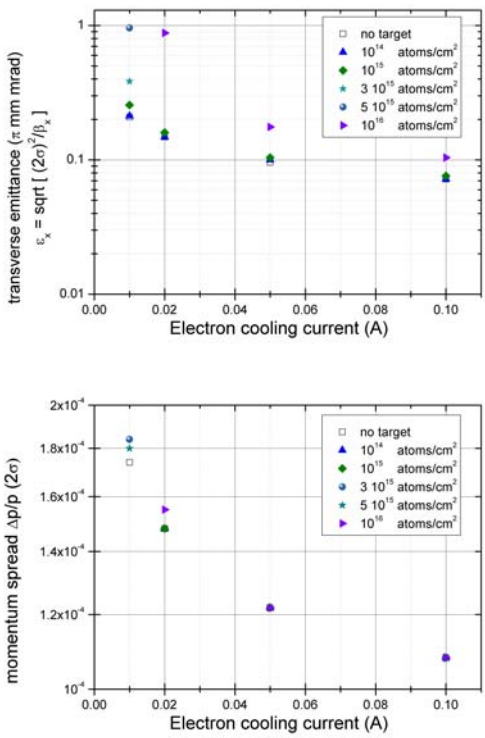

Figure 2: Transverse emittance and longitudinal momentum spread of a cooled beam of 1×10^8 stored U^{92+} ions at 740 MeV/u for various densities of the internal hydrogen target as a function of the electron current.

The ion beams for the HESR will be provided along the same line as the antiprotons. They will be injected from the CR with a magnetic rigidity around 13 Tm. The primary ion beams will be accelerated in the synchrotron SIS18 and, if necessary, in the synchrotron SIS100. They can be stripped to a high charge state or sent to the target of the SuperFRS for the production of rare isotopes. Similar to the production scenario for antiprotons, a short bunch from SIS100 is needed, The CR bunch rotation and debunching rf system is also applicable to ions reducing the momentum spread of the short bunch for subsequent stochastic cooling.

Stable beams of primary highly charged ions can be transported without stochastic cooling in the CR. In case that cooling is required, it has been checked that for up to 1×10^8 ions the cooling time does not exceed 1.5 s, for larger particle numbers the cooling time increases with the particle number. The emittance and momentum spread after cooling should be sufficiently small for injection into the HESR.

The experiments with ions in the HESR will focus on an internal target. Simulations have confirmed that the lifetime even in the unbaked HESR vacuum system with an average pressure in the low 10^{-9} range will be much longer than the lifetime due to the dense internal target which is expected to be in the order of minutes [14]. The ion optical properties are well suited for the detection of projectile-like particles which are used as signature of the interaction of circulating ions with target atoms. The high beam energy could even allow the interaction with a very thin fibre target with efficient use of the stored beam. Another option is the use of lasers for experiments with the stored beam, the long straight sections of the HESR provide long overlap regions between ion and laser beam.

ESR OPERATION FOR ACCELERATOR DEVELOPMENT

The existing ESR storage ring [6] was operated at GSI over more than two decades allowing both accelerator development and physics experiments. In the full version of the FAIR project it was planned to stop ESR operation and use various ESR components in the Recuperated Experimental Storage Ring (RESR). In the full version of the FAIR project the main ring for physics experiments with stored ions was the New Experimental Storage Ring (NESR). Both new rings, RESR and NESR, are not included in the MSV. Therefore it was decided to continue ESR operation. With the large experience in ESR operation, the various operation modes and the advanced diagnostics techniques, the ESR is an ideal test bed for beam physics experiments and the exploration of new concepts and techniques required in the FAIR project.

One of the important concepts in the FAIR project is beam accumulation supported by beam cooling. Originally proposed for the accumulation of RIBs in the NESR, the combination of barrier buckets and cooling is now the proposed method for antiproton accumulation in the HESR. In the NESR electron cooling was proposed, for the HESR stochastic cooling is preferred. The accumulation by barrier buckets and cooling first was studied in the ESR with electron cooling [21], as required for the NESR, and later also with stochastic cooling [22] as needed with antiprotons in the HESR. The successful experiments confirmed the predicted benefits of the accumulation methods and allowed benchmarking of the simulation tools which are applied to predict the performance in the new FAIR storage rings [23][24].

Very recently the stochastic cooling system of the ESR was modified to test the optical notch filter which is under development for the CR. The signals of the Palmer cooling pick-ups are used in sum mode, sent through the notch filter and after amplification applied to the beam. The cooling by the notch filter method was studied with a 400 MeV/u Ar^{18+} ion beam. The performance of the standard Palmer cooling was compared to filter cooling and TOF cooling which was realized by opening the delay line of the notch filter. The comparison proved that notch filter cooling is more powerful resulting in shorter cooling time, but TOF cooling can capture particles with a larger momentum spread at the cost of longer cooling time (Fig. 3). A combination of pre-cooling by the TOF-method and notch filter cooling might offer optimized cooling of hot secondary beams with large momentum spread.

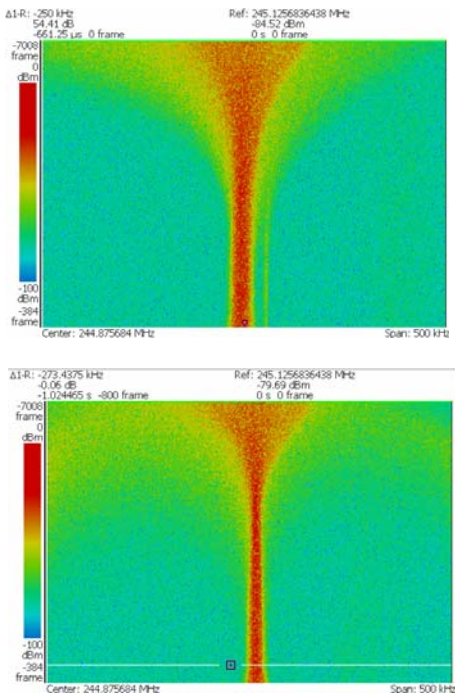

Figure 3: Longitudinal Schottky signal measured during stochastic cooling of a 400 MeV/u Ar^{18+} beam. TOF cooling (upper picture) evidences a larger capture range in longitudinal momentum, whereas notch filter cooling (lower picture) cools the beam in shorter time with a reduced capture range and smaller final momentum spread.

Another important feature of the ESR is the deceleration of highly charged ions. In the FAIR project deceleration of antiprotons in the NESR was proposed. The original CRYRING [8], formerly operated at the University of Stockholm, was proposed as a second stage for the deceleration of antiprotons. As the CRYRING is available already now, but the NESR will not be constructed in the MSV, a scenario was worked out to install the CRYRING behind the ESR and use it with decelerated highly charged ions and RIBs from the existing GSI facility. Electron cooling will be applied both in the ESR and in CRYRING to prepare beams of small phase space volume and to improve the efficiency of deceleration and will again be crucial for optimum performance of the deceleration cycle. The combination of the two rings allows the study of some aspects of the decelerator chain in preparation of future FAIR operation.

The CRYRING with a dedicated injector chain, similar to the one used in Stockholm, will be operated as a small scale test facility for the FAIR accelerators and various aspects of new diagnostics and the new control system can be developed. This will bridge a gap in the operation of the GSI accelerators caused by the inevitable modification of the existing accelerators for FAIR.

REFERENCES

[1] FAIR Baseline Technical Report. GSI, Darmstadt, 2006, http://www.gsi.de/fair/reports/btr.html.

[2] P. Spiller et al., EPAC'08, Genoa, Italy, June 2008, MOPC100, p. 298, http://www.jacow.org.

[3] A. Dolinskii et al., COOL'07, Bad Kreuznach, Germany, September 2007, TUA2C08, http://www.jacow.org.

[4] H. Geissel et al., Nucl. Instr. Meth. B204 (2003) 71.

[5] R. Maier et al., PAC'11, New York, March 2011, THOCN2, p. 2104 (2011), http://www.jacow.org.

[6] B. Franzke, Nucl. Instr. Meth B24/25, p.18 (1987).

[7] F. Herfurth et al. LINAC 2010, Tsukuba, Japan, September 2010, MOP043, p.151, http://www.jacow.org.

[8] K. Abrahamssson et al., Nucl. Instr. Meth. B79 (1993) 269.

[9] A. Dolinskii et al., IPAC'11, San Sebastian, Spain, September 2011, WEPC054, p. 2136, http://www.jacow.org.

[10] G. Carron, L. Thorndahl, CERN-ISR-RF/78-12 (1978).

[11] C. Peschke et al., COOL'09, Lanzhou, China, September 2009, THPMCP003, http://www.jacow.org.

[12] W. Kells, Proc. of 11th Int. Conf on High Energy Accelerators, Geneva, p. 777 (1980).

[13] C. Dimopoulou et al., IPAC'12, New Orleans, Louisiana, USA, May 2012, MOPPD005, p. 376, http://www.jacow.org.

[14] M. Steck et al., IPAC'12, New Orleans, Louisiana, USA, May 2012, THPPP002, p. 3722, http://www.jacow.org.

[15] R. Stassen et al., IPAC'12, New Orleans, May 2012, MOPPD009, p. 385, http://www.jacow.org.

[16] R. Stassen et al., PAC'09, Vancouver, Canada, May 2009, TU5PFP022, p. 861, http://www.jacow.org.

[17] H, Stockhorst et al., IPAC'12, New Orleans, Louisiana, USA, May 2012, MOPPD009, p. 388, http://www.JACoW.org.

[18] B. Gålnander et al. COOL'07, Bad Kreuznach, Germany, September 2007, THAP10, http://www.jacow.org.

[19] J. Dietrich et al., RUPAC 2012, St. Petersburg, Russia, September 2012, http://www.jacow.org.

[20] A.O. Sidorin et al., Nucl. Instr, Meth. A558 (2006) 325.

[21] C. Dimopoulou et al., COOL'07, Bad Kreuznach, Germany, September 2007, MOM2C05, p. 21, http://www.jacow.org.

[22] M. Steck et al., COOL'11, Alushta, Ukraine, September 2011, TUPS20, p. 140, http://www.jacow.org.

[23] T. Katayama et al., COOL'07, Bad Kreuznach, Germany, September 2007, MOM2C05, p. 21, http://www.jacow.org.

[24] T. Katayama et al., COOL'11, Alushta, Ukraine, September 2011, TUPS19, p. 136, http://www.jacow.org.

MA THEMATICAL MODELING AND OPTIMIZATION OF BEAM DYNAMICS IN ACCELERATORS

D. A. Ovsyannikov, SPbSU, Saint-Petersburg, Russia

Abstract

In this paper we treat the problem of beam dynamics optimization as a control theory problem. We consider different mathematical models of optimization. The approach to solving optimization problem for charged particle dynamics in accelerators includes: construction of mathematical model of controlled dynamical process; choice of control functions or parameters of optimization; construction of quality functionals, which allow efficient evaluation of various characteristics of examined controlled motion; analytical representation of the functional variations, which allow to construct various methods of optimization for quality functionals; construction of methods and algorithms of optimization. Problem of statement is considered on the pattern of RFQ channel.

INTRODUCTION

Mathematical methods of modeling and optimization are extensively used in many fields of science and technology. Development of specialized software for various applications is of more and more importance. A special class of tasks attracting attention of numerous researches includes the problems associated with the beam dynamics optimization in accelerator [1–13]. There are not the general methods of accelerating and focusing structures optimization. However as the demand to output beam parameters are progressively increasing it is needed to develop a new approaches and methods to solve these problems. In the paper the different mathematical control models describing beam dynamics are presented. Especially we consider the problems related to charged particles interaction. In this case we investigate the controlled dynamic process described by a system of integro-differential equations. The optimization methods are developed for the different functionals concerned with the quality of beam [3–12]. They are used for solution of various beam dynamics problems in. In particular, we investigate the optimization problem of a radial matching section in RFQ channel. We consider the problem of construction self-consistent distribution for charged particle beam in magnetic field too [14–19].

MATHEMATICAL OPTIMIZATION MODELS

The problem of beam control of interacting particles, which dynamics is described by integro-differential equations, is considered. Let us assume that evolution of particle beam is described by equations

$$dx/dt = f(t,x,u) \tag{1}$$

$$f(t,x,u) = f_1(t,x,u) + \int_{M_{t,u}} f_2(t,x,y_t)\rho(t,y_t)dy_t, \tag{2}$$

$$\frac{\partial\rho}{\partial t} + \frac{\partial\rho}{\partial x}f(t,x,u) + \rho\,\mathrm{div}_x f(t,x,u) = 0, \tag{3}$$

$$x(0) = x_0 \in M_0, \quad \rho(0,x) = \rho_0(x). \tag{4}$$

Here t is is the time; x is n-vector of phase coordinates; $u = u(t) \in D$ is r-dimensional control vector-function; D is the set of admissible control functions; $\rho = \rho(t,x)$ is the particle distribution density in the phase space; f_1 is n-dimensional vector-function determined by external electromagnetic fields; f_2 is n-dimensional vector-function associated with the particle interactions; the set $M_{t,u}$ is the cross-section of the trajectory set. It is obtained by time shift of the initial set M_0 through solutions of equation (1) with given control $u = u(t)$. The set M_0 is a given set in the phase space, which describes the set of initial states for a charged particle beam at the initial time moment. The function $\rho_0(x)$ is a given function describing the particle distribution density at the moment $t = 0$. The equations (1)-(2) can be considered as Vlasov equations. We meet with these equations if interaction between particles, for example the Coulomb repulsion, is taken into account. Let us introduce a functional

$$I(u) = \int_0^T \int_{M_{t,u}} \varphi(t,x_t,\rho(t,x_t),u)dx_t dt + \int_{M_{T,u}} g(x_T,\rho_T(T,x_T))dx_T \to \min_{u\in D}, \tag{5}$$

characterizing the dynamics of the process. Here φ and g are given non-negative functions, T is fixed. Consider the minimization problem of functional (5). Analizing various systems which are designed for acceleration, focusing and transporting of charged particle beams, it should be noticed that electrical and magnetic fields can be treated in a certain structural and parametric form. Thus certain components and parameters of electromagnetic fields and geometric systems of accelerating or focusing can be taken as control variables. The developed approach can be applied to another kind of functionals:

$$I(u) = \Phi(\mu_{ks}^{(1,1)},\ldots,\mu_{ks}^{(i,j)},\ldots,\mu_{ks}^{(n,n)}), \tag{6}$$

where

$$\mu_{ks}^{(i,j)} = \int_{M_{t,u}} (x_i - \overline{x}_i)^k (x_j - \overline{x}_j)^s \rho(t, x_t) dx_t, \quad (7)$$

$$\overline{x}_i = \int_{M_{t,u}} x_i \rho(t, x_t) dx_t, \quad i, j = 1, \ldots n, \quad j \geq i, \quad (8)$$

or

$$I(u) = \max_{t \in TN \in [0T]} \max_{x \in M_{t,u}} \varphi(t, x, \rho(t, x)) \to \min_{u \in D}. \quad (9)$$

OPTIMIZATION OF RADIAL MATCHING SECTION FOR RFQ CHANNEL

Consider the radial matching problem in RFQ accelerator. Let ellipse matrices $G_x(t, \varphi_0)$ and $G_y(t, \varphi_0)$, depending on time t and phase φ_0 , describe beam dynamics in radial matching section. Suppose, that $t = 0$ corresponds to the entrance into the radial matching section, and $t = T$ corresponds to the entrance into the regular part of accelerator. Suppose also, that acceptances of the regular part of the accelerator are known, i.e. the following matrices are given:

$$G_x(T, \varphi_0) = G_{x,T}(\varphi_0), \; G_y(T, \varphi_0) = G_{y,T}(\varphi_0). \quad (10)$$

The optimization problem for the radial matching section is to find a function $a(\tau)$, i.e. law of the radius change along the matching sections, providing under the conditions (10) the maximum possible overlapping of families of ellipses at the entrance of the radial matching section [3, 6, 7].

METHOD OF SOLUTION

Let's consider the following functional which characterizes the quality of the matching section by mismatch of ellipses $G_x(0, \varphi_0)$ and $G_y(0, \varphi_0)$ with given ellipses B_x and B_y:

$$J(a) = \max_{\varphi_0} \lambda_x^{-1}(\varphi_0) + \max_{\varphi_0} \lambda_y^{-1}(\varphi_0), \quad (11)$$

where

$$\lambda_x^{-1}(\varphi_0) = \lambda^{-1}(G_x(0, \varphi_0), B_x), \quad (12)$$

$$\lambda_y^{-1}(\varphi_0) = \lambda^{-1}(G_y(0, \varphi_0), B_y). \quad (13)$$

Here $\lambda = \min(\lambda_1, \lambda_2)$ is a minimum eigenvalue of a cluster of quadratic forms generated by a pair of ellipses with the matrices G and B:

$$\chi(\lambda) = \det(G - \lambda B) = 0, \quad \chi(\lambda_1) = \chi(\lambda_2) = 0. \quad (14)$$

The value of the inverse minimum eigenvalue characterizes the degree of mismatch pairs of ellipses. In the case of fully identical ellipses, this value is equal to unity. So always $\lambda^{-1} \geq 1$.

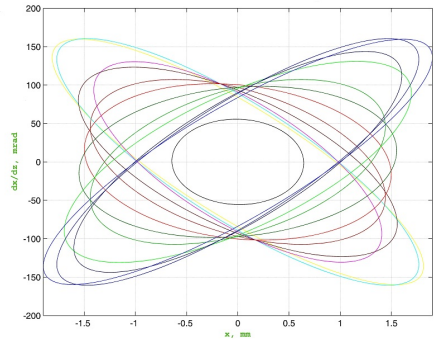

Figure 1: Acceptance without radial matching section, $(x, dx/dz, E_x = 0.050892\ \pi \cdot cm \cdot mrad)$

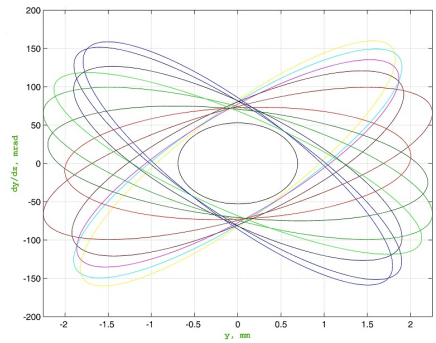

Figure 2: Acceptance without radial matching section $(y, dy/dz, E_y = 0.052122\ \pi \cdot cm \cdot mrad)$

Matrices B_x and B_y describing the desired phase portrait of the beam at the beginning of the matching section.

The problem of minimizing the functional (11) is the minimax optimization problem.

The analytical representation [6, 7] of the variation of the functional (11) were used to find geometric parameters of radial matching section of the RFQ accelerator of protons (initial energy 95keV, output energy 5 MeV, intervane voltage 100kV, RF field frequency 352 MHz, initial cell length 6.06 mm). Several of the possible choices of the law of variation of the channel radius along the radial matching section are presented in Fig. 5, 8, 11. In Fig. 1, 2 the RFQ acceptances without radial matching section are shown. The illustrations of effect of the radial matching sections (with channel radii presented at Fig. 5, 8, 11) are shown in Fig. 3-4, Fig. 6-7, Fig. 9-10 (correspondingly). The first variant (Fig. 3-5) is rather usual and requires converging ellipses at the entrance of the radial matching section. But the two others give us unusual results with neutral and divergent input ellipses: Fig. 6-8 and Fig. 9-11.

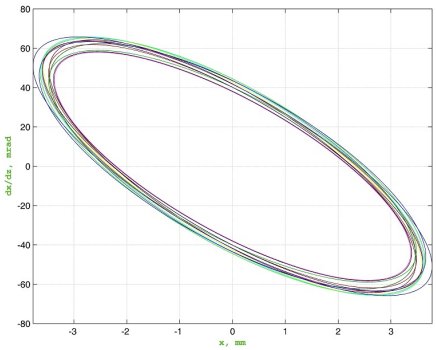

Figure 3: Acceptance with radial matching section $(x, dx/dz, E_x = 0.18393\ \pi\cdot cm\cdot mrad)$

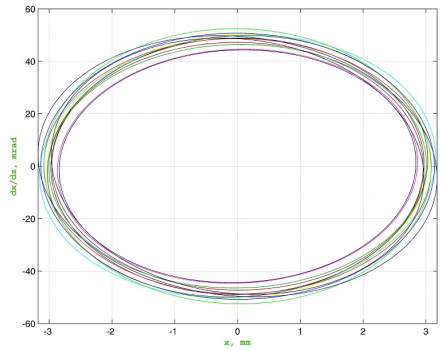

Figure 6: Acceptance with radial matching section $(x, dx/dz, E_x = 0.17945\ \pi\cdot cm\cdot mrad)$

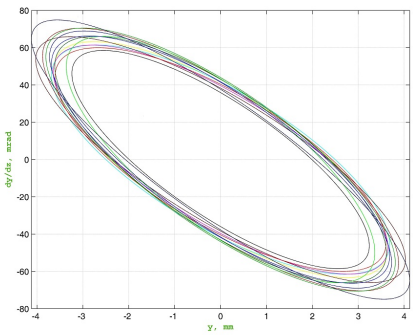

Figure 4: Acceptance with radial matching section $(y, dy/dz, E_y = 0.16571\ \pi\cdot cm\cdot mrad)$

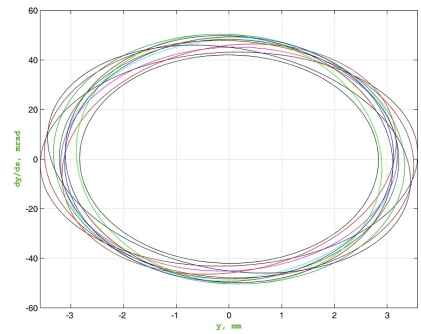

Figure 7: Acceptance with radial matching section $(y, dy/dz, E_y = 0.16955\ \pi\cdot cm\cdot mrad)$

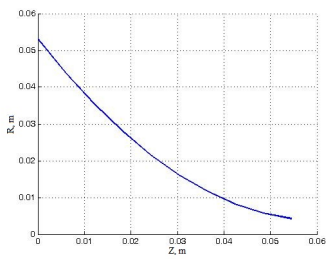

Figure 5: Radius of channel in radial matching section

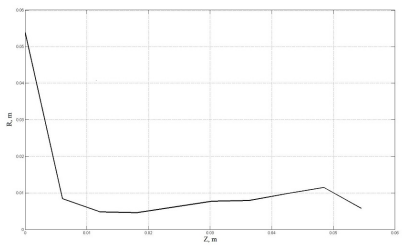

Figure 8: Radius of channel in radial matching section

SELF-CONSISTENT DISTRIBUTIONS

Consider nonrelativistic cylindrical beam in uniform longitudinal magnetic field. Assume that particles are distributed uniformly on the longitudinal coordinate z, and have the same longitudinal velocity. Such beam can be described by four-dimensional particle distribution in the phase space of the transverse motion. The well-known example is the Kapchinsky-Vladimirsky distribution [20].

Additionally assume that particles are evenly distributed on azimuthal angle φ and on phases of their trajectories θ. Then instead of four-dimensional distribution in the phase space, we can consider two-dimensional distribution in some two-dimensional cross-section of the phase space corresponding to the fixed values of φ and θ.

Let us take integrals of the transverse motion

$$M = r^2(\omega_0 + \dot{\varphi}), \quad H = \dot{r}^2 + \omega^2 r^2 + \frac{M^2}{r^2},$$

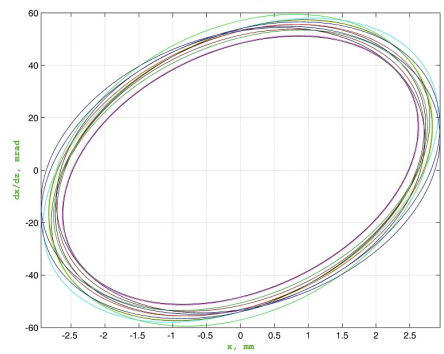

Figure 9: Acceptance with radial matching section $(x, dx/dz, E_x = 0.18023\ \pi \cdot cm \cdot mrad)$

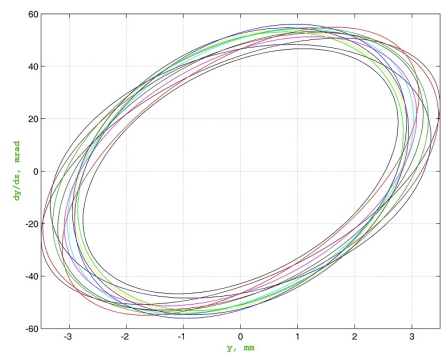

Figure 10: Acceptance with radial matching section $(y, dy/dz, E_y = 0.16834\ \pi \cdot cm \cdot mrad)$

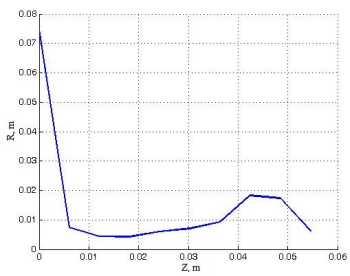

Figure 11: Radius of channel in radial matching section

as coordinates in this cross-section. By this reason, we will regard this cross-section as the space of the integrals of motion. Here $\omega^2 = \omega_0^2 - e\varrho_0/(m\varepsilon_0)$, $\omega_0 = eB_z/(2m)$, e and m are charge and mass of the particles, ϱ_0 is spatial density of the particles inside the beam cross-section, ε_0 is electric constant, B_z is longitudinal component of the magnetic flux density.

If beam is radially constrained, $r < R$, where R is beam radius, the possible values of M and H are bounded. For uniformly charged beam, the set Ω of permissible values M and H is described by inequalities [14–19]

$$2\omega|M| < H \le M^2/R^2 + \omega^2 R^2, \qquad (15)$$

The set Ω is shown on Fig. 12.

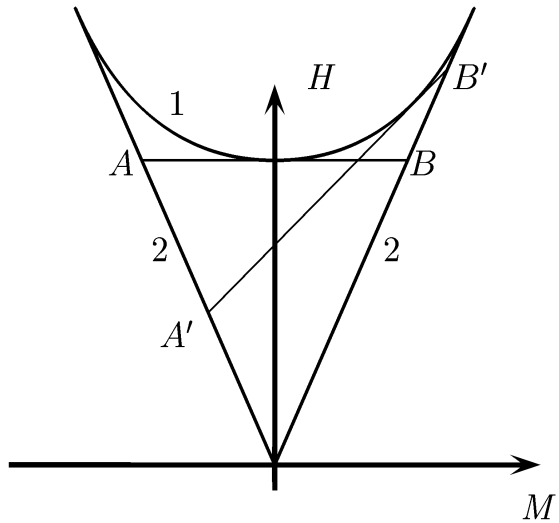

Figure 12: The set Ω for the uniform beam. The curve 1 represents the upper boundary of the set $\Omega : H = M^2/R^2 + \omega^2 R^2$. The segments 2 represent the lower boundary of the set $\Omega : H = 2\omega|M|$.

The simplest known distribution is the Brillouin flow [21]. For this distribution, all particles have the same values of integrals M and $H : M = 0$, $H = 0$.

If we specify particle density $f(M, H)$ in Ω, we get some self-consistent distribution.

When particles are uniformly distributed on segment AB, we get well-known Kapchinsky-Vladimirsky distribution. For this case, distribution density in the space of motion integrals is the simple layer which supporter is segment AB.

Another example is so called "rigid rotator distribution" [22]. In this case, particles are uniformly distributed on some segment $A'B'$ which is tangent to the upper boundary (15). KV distribution is a particular case corresponding to zero slope of segment $A'B'$. The mean angular momentum of the "rigid rotator distributions" is not equal to zero, except for the KV distribution. This can be seen from Fig. 12 where the parts of the segment $A'B'$ lying on the left and on the right of the axis H are not equal.

The beam is uniformly charged for all these distributions. By this reason, if we take any linear combination of these distributions, we get uniformly charged beam. It is easy to take such combination, that the mean angular momentum of particles will be equal to zero. Therefore such distribution can be taken as a

model of a real beam, which is launched with the zero mean angular momentum.

Beam with slowly varied radius can be described analogously [17–19]. In this case, we take another integral of motion I instead of H. Integral I can be expressed through dynamical variables of a particle and the beam envelope. For this case, the set of permissible values of M and I looks like the set Ω on Fig. 12.

CONCLUSION

Mathematical models for beam dynamics optimization were presented. They may be applied to different dynamical systems.The optimization approach to finding geometric parameters of radial matching section is considered. It should be noted, that the proposed approach can be applied to optimize the transverse dynamics in accelerators if the dynamics is described by linear or nonlinear equations. In the case of nonlinear equations it is needed to consider RMS characteristics of the beam. In particular, this method can be used to minimize the growth of the effective emittance in the accelerators.

REFERENCES

[1] A.I.Balabin, V.S.Kabanov, I.M.Kapchinsky, V.V.Kushin, I.M.Lipkin "On beam matching with RFQ channel," Journal of Technical Physics, Vol. 55(3), pp. 586-590, (1985).

[2] K.R.Crandall, R.H.Stokes, T.P.Wangler, "RF Quadrupole Beam Dynamics Design Studies," Proceedings of 1979 Linear Accelerator Conference, Montauk, p. 205.

[3] A.D. Ovsyannikov, "Transverse motion parameters optimization in accelerators," Problems of Atomic Science and Technology, Number 4(80), pp. 74-77. (2012).

[4] A.D. Ovsyannikov, D.A. Ovsyannikov, M.Yu. Balabanov, S.-L. Chung, "On the beam dynamics optimization problem," 2009 International Journal of Modern Physics A 24 (5), pp. 941-951.

[5] A.D.Ovsyannikov, B. I. Bondarev, A. P. Durkin, "New Mathematical Optimization Models for RFQ Structures," Proceedings of the 18th Particle Accelerator Conference, New York, USA, pp. 2808-2810, (1999).

[6] A.D. Ovsyannikov, D. A. Ovsyannikov, A. P. Durkin, Sheng-Luen Chang, "Optimization of matching section of an accelerator with a spatially uniform quadrupole focusing," Technical Physics, Volume 54, Number 11, pp. 1663-1666, (2009).

[7] A.D.Ovsyannikov, D.A.Ovsyannikov, Sheng-Luen Chung, "Optimization of a Radial Matching Section," 2009 International Journal of Modern Physics A, Vol.24, Number 5, pp. 952-958.

[8] D.A.Ovsyannikov, *Modeling and Optimization of Charged Particles Beam Dynamics*, (Lenigrad, 1990, p. 312).

[9] D.A. Ovsyannikov, A.D. Ovsyannikov, Yu.A. Svistunov, A.P. Durkin, M.F.Vorogushin, "Beam dynamics optimization: models, methods and applications," Nucl. Instr. Meth. Phys. Res., A 558, pp. 11-19, (2006).

[10] A.A. Poklonskiy, D. Neuffer, C.J. Johnstone, M. Berz, K. Makino, D.A. Ovsyannikov, A.D. Ovsyannikov, "Optimizing the adiabatic buncher and phase-energy rotator for neutrino factories," Nucl. Instr. Meth. Phys. Res., A 558, pp. 135-141, (2006).

[11] P. Snopok, C. Johnstone, M. Berz, D.A. Ovsyannikov, A.D. Ovsyannikov, "Study and optimal correction of a systematic skew quadrupole field in the Tevatron," Nucl. Instr. Meth. Phys. Res., A 558, pp. 142-146, (2006).

[12] Y.A. Svistunov, A.D. Ovsyannikov, "Designing of compact accelerating structures for applied complexes with accelerators," Problems of Atomic Science and Technology (2), pp. 48-51, (2010).

[13] N.Tokuda, S.Yamada, "New Formulation of the RFQ Radial Matching Section," Proceedings of the 1981 Linear Accelerator Conference, Santa Fe, p. 313.

[14] O.I.Drivotin, D.A.Ovsyannikov, "Determination of the stationary solutions of the Vlasov equation for an axially-symmetric beam of charged-particles in a longitudinal magnetic field," 1987 USSR Computational Mathematics and Mathematical Physics 27 (2), pp. 62-70.

[15] O.I.Drivotin, D.A.Ovsyannikov, "New classes of stationary solutions of the Vlasov equation an axially symmetrical beam of charged-particles of constant density," 1989 USSR Computational Mathematics and Mathematical Physics 29 (4), pp. 195-199.

[16] O.I.Drivotin, D.A.Ovsyannikov, "On self-consistent distributions for charged particles in longitudinal magnecit field," Dokl. Russ. Acad. Nauk, 334, pp. 284-287, (1994).

[17] O.I.Drivotin, D.A.Ovsyannikov, "New classes of uniform distributions for charged particles in longitudinal magnecit field," 1998 Proceedings of the IEEE Particle Accelerator Conference 2, pp. 1944-1946.

[18] O.I.Drivotin, D.A.Ovsyannikov, "Modeling of self-consistent distributions for longitudinally uniform beam," Nucl. Instr. Meth. Phys. Res., A 558, pp. 112-118, (2006).

[19] O.I.Drivotin, D.A.Ovsyannikov, "Self-consistent distributions for charged particles beam in magnetic field," 2009 International Journal of Modern Physics, A 24 (5), pp. 816-842.

[20] I.M.Kapchinsky, *Theory of linear resonance accelerator*, (Moscow, Energoizdat, 1982), pp. 130-165.

[21] L. Brillouin, "A Theorem of Larmor and Its Importance for Electrons in Magnetic Fields," Phys.Rev, 67, pp. 260-266, (1945).

[22] R.C.Davidson, *Physics of Nonneutral Plasmas* (Addison-Wesley Publishing Co., Reading, MA, 1990).

TRANSIENT BEAM RESPONSE IN SYNCHROTRONS WITH A DIGITAL TRANSVERSE FEEDBACK SYSTEM

V. M. Zhabitsky, JINR, Dubna, Russia

Abstract

The transient beam response to an externally applied impulse force in synchrotrons with a digital transverse feedback system is studied. Experimental data from the LHC on damping of coherent transverse oscillations excited by the discrete-time unit impulse are analysed. Good agreement on the measured and theoretically predicted decrements has been obtained. A method of feedback fine tuning, based on measurements of the bunch response to the harmonic excitation impulse, is discussed.

INTRODUCTION

Transverse feedback systems (TFS) in synchrotrons (see Fig. 1) are used for damping coherent transverse oscillations caused by injection errors and for suppression of coherent transverse instabilities [1]. The transverse momentum of a bunch is corrected by the damper kicker (DK) in proportion to the bunch displacement from the reference orbit at the location of the beam position monitor (BPM). The digital signal processor (DSP) module allows to obtain optimum damping by adjustment of the TFS parameters in agreement with the beam time of flight from BPM to DK and the corresponding betatron phase advance.

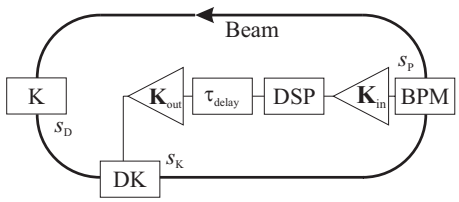

Figure 1: TFS Layout

Coherent oscillations can be originated by DK or a specialised driving kicker K (see Fig. 1). For example, the kicker can be fed with the discrete-time unit impulse or the harmonic excitation impulse. The beam response observed by BPM in this case can be used for tuning the TFS.

The transient beam response to a driving force is analyzed below in framework of the discrete transformation approach developed in [2, 3] for describing transverse beam dynamics in synchrotrons with a digital TFS.

BASIC NOTIONS

Let the column matrix $\widehat{X}[n,s]$ describe the bunch state at the n–th turn and in point s on the reference orbit (see Fig. 1). Its first element $x[n,s]$ is the bunch deviation from the orbit and the second one $x'[n,s]$ is the angle of the bunch trajectory. Let the driving kicker K located in point $s_{\rm D}$ change the angle of the bunch trajectory on $\Delta x'_{\rm D}[n]$. For the bunch states at two consecutive turns after passing the damper kicker DK located in point $s_{\rm K}$ one can write [2, 3]:

$$\widehat{X}[n+1,s] \equiv \widehat{X}[n,s+C] = \widehat{M}(s)\widehat{X}[n,s] + \Delta x'[n,s_{\rm K}]\,\widehat{M}_{\rm K}\widehat{E} + \Delta x'_{\rm D}[n]\,\widehat{M}_{\rm D}\widehat{E}\,, \quad (1)$$

where C is the circumference of the reference orbit; elements $E_1 = 0$ and $E_2 = 1$ in the column matrix $\widehat{E}$. Here 2×2 matrix $\widehat{M}(s_2|s_1)$ for passage from s_1 to s_2 is used [4] so that: $\widehat{M}(s) \equiv \widehat{M}(s+C|s)$, $\widehat{M}_{\rm K} \equiv \widehat{M}(s+C|s_{\rm K})$, $\widehat{M}_{\rm D} \equiv \widehat{M}(s+C|s_{\rm D})$.

$\Delta x'[n,s_{\rm K}]$ is proportional to output voltage $V_{\rm out}$ on the amplifier in a feedback chain and linearly depends on input voltage $V_{\rm in}$:

$$\Delta x'[n,s_{\rm K}] = S_{\rm K}\,V_{\rm out}[n] = S_{\rm K}\,{\rm K}_{\rm out}\,{\rm K}_{\rm in}\times \times \sum_{m=0}^{N_{\rm F}} h[m]\,V_{\rm in}[n-\hat{q}-m]\,u[n-\hat{q}-m]\,, \quad (2)$$

where $S_{\rm K}$ is the DK transfer characteristic; ${\rm K}_{\rm in}$ and ${\rm K}_{\rm out}$ are voltage gains of the output and input amplifiers (see Fig. 1); $u[n]$ is the Heaviside step function; $h[m]$ are coefficients of a finite impulse response (FIR) digital filter in DSP; $N_{\rm F}$ is the FIR filter order. The total delay $\tau_{\rm delay}$ in the signal processing of the feedback path from BPM to DK adjusts the timing of the signal to match the bunch arrival time. If $\tau_{\rm PK}$ is the time of flight of the particle from BPM to DK and $T_{\rm rev} = 1/f_{\rm rev}$ is the particle revolution period, then $\tau_{\rm delay} = \tau_{\rm PK} + \hat{q}\,T_{\rm rev}$.

$V_{\rm in}$ voltage linearly depends on $x[n,s_{\rm P}]$ displacement:

$$V_{\rm in}[n] = (x[n,s_{\rm P}] + \delta x_{\rm P})\,S_{\rm P}\,u[n]\,, \quad (3)$$

where $\delta x_{\rm P}$ is a deviation of the BPM electrical centre from the reference orbit, $S_{\rm P}$ is the BPM transfer characteristic.

Let the driving force be the discrete-time unit impulse with amplitude $a_{\rm D}$ at the $n_{\rm D}$ turn so that

$$\Delta x'_{\rm D}[n]\sqrt{\hat{\beta}_{\rm D}\hat{\beta}_{\rm P}} \equiv V_{\rm D} = a_{\rm D}\,\delta[n-n_{\rm D}]\,, \quad (4)$$

where $\hat{\beta}_i \equiv \hat{\beta}(s_i)$ is the Twiss beta function [4]. In the case of harmonic excitation impulse of $Q_{\rm D}f_{\rm rev}$ frequency, $N_{\rm D}T_{\rm rev}$ duration and $\phi_{\rm D}$ phase one can write: $V_{\rm D} = a_{\rm D}\sin\big(2\pi(n-n_{\rm D})Q_{\rm D}+\phi_{\rm D}\big)\big(u[n-n_{\rm D}]-u[n-n_{\rm D}-N_{\rm D}]\big)$.

The system of linear difference equations (1), (2), (3) and (4) can be solved using unilateral $\mathcal{Z}$–transform [6]:

$$\mathbf{y}(z,s) = \mathcal{Z}\{y[n,s]\} \equiv \sum_{n=0}^{\infty} y[n,s]\,z^{-n}\,, \quad (5)$$

$$y[n,s] = \mathcal{Z}^{-1}\{\mathbf{y}(z,s)\} = \sum_k {\rm Res}\left[\mathbf{y}(z,s)\,z^{n-1};\,z_k\right].$$

For $\widehat{\mathbf{X}}(z,s) = \mathcal{Z}\{\widehat{X}[n,s]\}$ one can obtain the following:

$$\widehat{\mathbf{X}}(z,s) = \frac{z\widehat{I} - \widehat{\mathbf{M}}^{-1}\det\widehat{\mathbf{M}}}{\det\left(z\widehat{I} - \widehat{\mathbf{M}}\right)}\left(\mathcal{Z}\{\Delta x'_{\rm D}[n]\}\,\widehat{M}_{\rm D}\widehat{E} + \right.$$
$$\left. + z\widehat{X}[0,s] + \frac{g\,z^{-\hat{q}}\,\mathbf{K}(z)\,\delta x_{\rm P}}{(1-z^{-1})(\hat{\beta}_{\rm K}\hat{\beta}_{\rm P})^{1/2}{\rm K}_0}\,\widehat{M}_{\rm K}\widehat{E}\right), \quad (6)$$

where $\widehat{I}$ is the identity matrix; $\mathbf{K}(z) = \mathbf{K}_{\rm out}H(z)\mathbf{K}_{\rm in}$ is the transfer function of the feedback circuit; $H(z) = \mathcal{Z}\{h[n]\}$; $g = (\hat{\beta}_{\rm K}\hat{\beta}_{\rm P})^{1/2}\,{\rm K}_0 S_{\rm K} S_{\rm P}$ is the feedback gain where ${\rm K}_0$ is determined in such a way (see further) that $g > 0$ corresponds to damped oscillations. Matrix $\widehat{\mathbf{M}}$ is

$$\widehat{\mathbf{M}} \equiv \widehat{\mathbf{M}}(z,s) = \widehat{M}(s) + \frac{g\,z^{-\hat{q}}\,\mathbf{K}(z)}{(\hat{\beta}_{\rm K}\hat{\beta}_{\rm P})^{1/2}\,{\rm K}_0}\,\widehat{M}_{\rm K}\,\widehat{T}\,\widehat{M}(s_{\rm P}|s),$$

where $\widehat{T}$ is 2×2 matrix in which $T_{21} = 1$ and other elements are equal to zero. Eigenvalues z_k at $a_{\rm D} = 0$ are solutions of equation $\det\left(z\widehat{I} - \widehat{\mathbf{M}}(z,s)\right) = 0$, that is:

$$z_k^2 - \left(2\cos(2\pi Q) + \frac{g\,z_k^{-\hat{q}}\,\mathbf{K}(z_k)}{{\rm K}_0}\,\sin(2\pi Q - \psi_{\rm PK})\right) z_k$$
$$+ 1 - \frac{g\,z_k^{-\hat{q}}\,\mathbf{K}(z_k)}{{\rm K}_0}\,\sin\psi_{\rm PK} = 0, \quad (7)$$

where Q is the betatron number of oscillations per turn and $\psi_{\rm PK}$ is the betatron phase advance from BPM to DK. If $g = 0$ then $z_{1,2} = \exp(\pm{\rm j}\,2\pi Q)$, that is a well known result for free betatron oscillations. If $g \neq 0$ then the number $k > 2$ of eigenvalues z_k depends on $N_{\rm F}$ and $\hat{q}$. The bunch state $\widehat{X}[n,s] = \widehat{M}(s|s_{\rm K})\widehat{X}[n,s_{\rm K}]$ can be calculated from components $\widehat{X}[n,s_{\rm K}]$ after passing DK in accordance with (5) as the sum of harmonics with $A_k\hat{\beta}^{1/2}$ amplitudes, Φ_k phases, $\alpha_k \equiv -\ln|z_k|$ logarithmic decrements and $2\pi\{Q_k\} \equiv \arg z_k$ phase shifts per turn so that

$$x[n,s_{\rm K}] = \sum_k A_k\sqrt{\hat{\beta}_{\rm K}}\,{\rm e}^{-n\alpha_k + {\rm j}\,(2\pi n\{Q_k\} + \Phi_k)}.$$

It can be done if $|z_k| < 1$ and

$$\lim_{n\to\infty}\widehat{X}[n,s] = \lim_{z\to 1}(z-1)\,\widehat{\mathbf{X}}(z,s) = 0.$$

Consequently $\mathbf{K}(z=1) = 0$. Thus, all poles z_k of function $\widehat{\mathbf{X}}(z,s)$ should lie inside the unit circle, and influence of $\delta x_{\rm P}$ in $\widehat{\mathbf{X}}(z,s)$ function should be excluded. The later condition is reached by using the feedback circuit with the notch filter whose transfer function is $H_{\rm NF}(z) = (1-z^{-1})$.

If $g \ll 1$ and $\mathbf{K}_{\rm in}(\omega)\mathbf{K}_{\rm out}(\omega)$ depends weakly on frequency then from (7) one can obtain the following:

$$\alpha_m = \frac{g\,|\mathbf{K}(\omega_m)|}{2{\rm K}_0}\,\sin\Psi_{\rm PK}\,, \quad (8)$$
$$\{Q_m\} = \{Q\} - \frac{g\,|\mathbf{K}(\omega_m)|}{4\pi{\rm K}_0}\,\cos\Psi_{\rm PK}\,,$$
$$\Psi_{\rm PK} = \psi_{\rm PK} + 2\pi\hat{q}\,Q - \arg\mathbf{K}(\omega_m)\,,$$
$$\mathbf{K}(\omega_m) = \mathbf{K}_{\rm in}(\omega_m)\,\mathbf{K}_{\rm out}(\omega_m)\,H\left(z = {\rm e}^{{\rm j}\,2\pi Q}\right),$$
$$|{\rm K}_0| = |\mathbf{K}(\omega_{\rm min})|, \qquad {\rm K}_0\sin\Psi_{\rm PK}(\omega_{\rm min}) > 0,$$

where $\omega_m = 2\pi(Q+m)f_{\rm rev}$ and m is a positive or negative integer. For the fractional tune $\{Q\}$ the following definition is used: $-0.5 < \{Q\} \leqslant 0.5$. The $|{\rm K}_0|$ value is equal to the gain transfer characteristic of the feedback circuit at the minimal frequency of ω_m. The sign of ${\rm K}_0$ is chosen in such a way that $g > 0$ corresponds to the damped oscillations.

The optimum damping corresponds to phase balance $\Psi_{\rm PK}$ of $|\sin\Psi_{\rm PK}| = 1$, so that $\{Q_m\} = \{Q\}$.

Hence, it is necessary to tune the TFS in such a way to provide two conditions: the BPM signal should correspond to the decay amplitude mode and zero frequency shift $(\{Q_m\} - \{Q\})f_{\rm rev}$ should be tuned for optimum damping.

BEAM RESPONSE TO DRIVING FORCE

From Eq. (6) for $\widehat{\mathbf{X}}(z,s)$ it is clear that the bunch state $\widehat{X}[n,s]$ in accordance with Eqs. (5) depends on initial conditions $\widehat{X}[0,s]$, the deviation $\delta x_{\rm P}$ of the BPM electrical centre from the reference orbit and the driving force. In the case of damped oscillations after some time the bunch state is determined by the driving force only.

If the driving force is the $\delta[n-n_{\rm D}]$ function then $\widehat{\mathbf{X}}(z,s)$ includes the term $\mathcal{Z}\{\Delta x'_{\rm D}[n]\} = a_{\rm D}\,z^{-n_{\rm D}}/(\hat{\beta}_{\rm P}\hat{\beta}_{\rm K})^{1/2}$ that leads to damped oscillations starting at the moment $n_{\rm D}T_{\rm rev}$ with decrements and frequencies in accordance with z_k from the characteristic equation (7). Fig. 2 (left) shows an example of the beam response signal at BPM in the case of two δ-kicks at different gains g. Calculations were

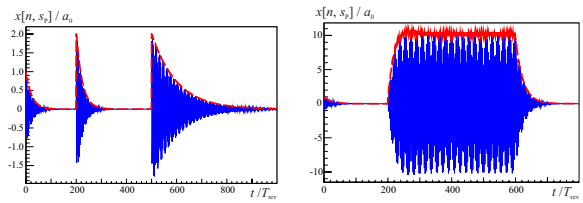

Figure 2: Beam response signal (solid blue lines) and its envelope (dashed red lines) on two δ-kicks (left), harmonic impulse (right) and damped injection oscillations at $t = 0$

done according to (1), (2), (3) and (4) at optimum damping, $x[0,s_{\rm P}] = a_0$, $x'[0,s_{\rm P}] = 0$, $\delta x_{\rm P} = a_0$, $Q = 59.31$, $\psi_{\rm PK} = 2\pi\times 59.25$, $\psi_{\rm PD} = 2\pi\times 58.30$, $a_{\rm D} = 2a_0$, $\hat{q} = 0$, ${\rm K}_0 = 1.576$, $H(z) = (1-z^{-1})(1+0.576z^{-1})$; the Twiss functions in $\widehat{M}(s_2|s_1)$ are $\hat{\beta}_{\rm P} = \hat{\beta}_{\rm K} = \hat{\beta}_{\rm D} = 71.538$ m, $\hat{\alpha}_{\rm P} = \hat{\alpha}_{\rm K} = \hat{\alpha}_{\rm D} = 0$. The corresponding dependences of

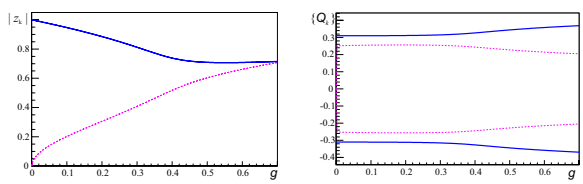

Figure 3: Dependences of $|z_k|$ and $\{Q_k\}$ on gain g

$|z_k|$ and $\{Q_k\}$ on gain g are shown in Fig. 3. There are four

solutions of the characteristic equation (7) because of $H(z)$ chosen. Two solutions (solid lines) correspond to eigenvalues $z_{1,2}$ with frequencies $|\{Q_{1,2}\}|f_{\rm rev}$ close to $|\{Q\}|f_{\rm rev}$ at $g < 0.3$. Eigenvalues $z_{3,4}$ (dotted lines) correspond to fast damped modes at $g < 0.3$.

The rf-signal at $n_{\rm D} = 200$ in Fig. 2 (left) corresponds to $g = 0.08$. In this case the decrement value from (7) is $\alpha_{\min} = -\ln|z_k^{(\max)}| = T_{\rm rev}/\tau = 0.0429$. Consequently the amplitude decay is faster in comparison with the linear approximation $g/2$ in (8). The rf-signal at $n_{\rm D} = 500$ corresponds to $g = 0.02$. The decrement $\alpha_{\min} = 0.01$ from (7) is in a good agreement with the linear approximation (8).

The BPM signal in the case of the harmonic impulse in TFS with gain $g = 0.08$ is shown in Fig. 2 (right) at $Q_{\rm D} = 0.315$, $a_{\rm D} = a_0$, $n_{\rm D} = 200$ and $N_{\rm D} = 300$. It is visible that in 100 turns after the excitation start the vibration amplitude approximately by 12 times more than $a_{\rm D}$ is achieved. The amplitude of the forced oscillation also increases at $Q_{\rm D} \to \{Q\}$, but it is not converted in infinity as it occurs at a resonance without damping.

Function $a(n, Q_{\rm D})$ of two variables n and $Q_{\rm D}$ can be presented on a plane in the form of a graph of isoamplitudes. Each line is characterized by constant amplitude in any point. For example, for isoamplitudes one can choose:

$$a(n, Q_{\rm D}) = a_i, \qquad -0.01 < \{Q_{\rm D}\} - \{Q\} < 0.01, \quad (9)$$
$$a_i = a_{\max}\sqrt{i/10}, \quad i \in [0, 10),$$

where $a_{\max}(Q_{\rm D}^{(\max)})$ is the peak amplitude of steady state oscillations in the specified frequency range (Fig. 4, left).

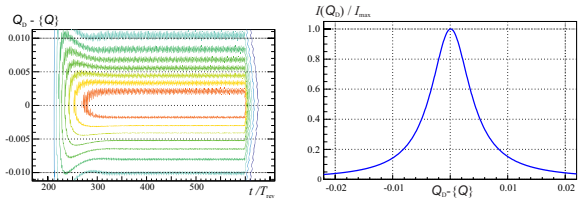

Figure 4: Graph of isoamplitudes (left) and resonance curve (right)

When the bunch makes forced oscillations, its transverse energy $I(Q_{\rm D})$ on the average remains invariable in the field of steady state oscillations: on each turn after the driving kicker the bunch gains an additional transverse impulse which is compensated by the damper kicker. Quantity $I(Q_{\rm D})$ is proportional to a quadrate of the amplitude of steady state oscillations. Consequently for a resonance curve (see Fig. 4, right) one can write in accordance with (6) and (5):

$$\frac{I(Q_{\rm D})}{I_{\max}} = \frac{1}{I_{\max}} \left|\det\left(z_{\rm D}\widehat{I} - \widehat{\mathbf{M}}(z_{\rm D})\right)\right|^{-2}, \qquad (10)$$
$$z_{\rm D} = \exp(\mathrm{j}\,2\pi\{Q_{\rm D}\}), \quad I_{\max} = I\left(Q_{\rm D}^{(\max)}\right).$$

In $g \ll 1$ then $I(Q_{\rm D})/I_{\max}$ in accordance with Eqs. (8) is

$$\frac{I(Q_{\rm D})}{I_{\max}} = \frac{\alpha_m^2}{4\pi^2(\{Q_{\rm D}\} - \{Q_m\})^2 + \alpha_m^2}.$$

This function coincides with a resonance curve which is used for the analysis of forced oscillations in the presence of friction. The function $I(Q_{\rm D})/I_{\max}$ has a maximum at

$$\{Q_{\rm D}^{(\max)}\} = \{Q_m\} = \{Q\} - \frac{g\,|\mathbf{K}(\omega_m)|}{4\pi \mathrm{K}_0}\cos\Psi_{\rm PK}.$$

Thus, the resonance curve maximum is shifted relatively the betatron frequency under violation of the phase balance condition $|\sin\Psi_{\rm PK}| = 1$.

CONCLUSION

The beam tests based on measurements of a bunch response to the δ-impulse were used at the LHC for tuning the LHC Damper [1] at injection and collision [7]. Good

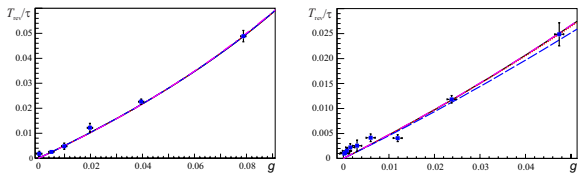

Figure 5: Calculated decrements (curves) and results of measurements for vertical (left) and horizontal (right) feedback chains of the LHC Damper at the energy of 3.5 TeV

agreement on the measured and calculated decrements has been obtained (see, for example, Fig. 5).

Analytical expressions have been obtained for the bunch response to the harmonic excitation impulse taking into account real performances of a TFS. The dependences based on the resonance curve can be used for thin adjustment of the TFS and selective measurements of circulated bunches.

ACKNOWLEDGMENTS

The author thanks M. Gasior, W. Höfle, R. Louwerse and D. Valuch (CERN) for the data sets from the LHC transverse feedback system and fruitful discussions.

REFERENCES

[1] V. M. Zhabitsky et al. Beam Tests of the LHC Transverse Feedback System. Proc. of XXII Russian Particle Accelerators Conference RuPAC-2010, 27 September–1 October 2010, Protvino, Russia. IHEP, Protvino, 2010. Pp. 275–279.

[2] V. M. Zhabitsky. The Z-Transfom Application for Solving the Problem of Free Beam Oscillation Damping in the Accelerator. JINR Communications. P9-91-91. Dubna. 1991.

[3] V. M. Zhabitsky. Stability of an Ion Beam in Synchrotrons with Digital Filters in the Feedback Loop of a Transverse Damper. Physics of Particles and Nuclei Letters. 2010. Vol. 7, No.7(163). Pp. 742–747.

[4] E. D. Courant, H. S. Snyder. Theory of the Alternating-Gradient Synchrotron. Annals of Physics. 2000. Vol. 281. P. 360.

[6] W. McC. Siebert. Circuits, Signals, and Systems. The MIT Press, 1986. 651 p.

[7] U. Wienands, W. Höfle, D. Valuch. Gain measurements of the LHC transverse feedback system at 3.5 TeV beam energy. CERN–ATS–Note–2011–131. Geneva. 12 December 2011.

SIMULATION OF BEAM DYNAMICS IN THE EXTRACTION SYSTEM OF THE JINR PHASOTRON

S. Kostromin, L. Onischenko, A. Chesnov, S. Shirkov, JINR, Dubna, Russia

Abstract

Beam dynamics is studied in the extraction by the regenerative method from the JINR Phasotron (657 MeV, 3μA protons) using special complex of computer programs. Parameters of the beam at the deflector entrance are calculated. The beam extraction efficiency is found to be ~40%. The mean movement in the extraction channel is investigated. Calculated beam transverse parameters agree with the experimental ones to accuracy of~20%.

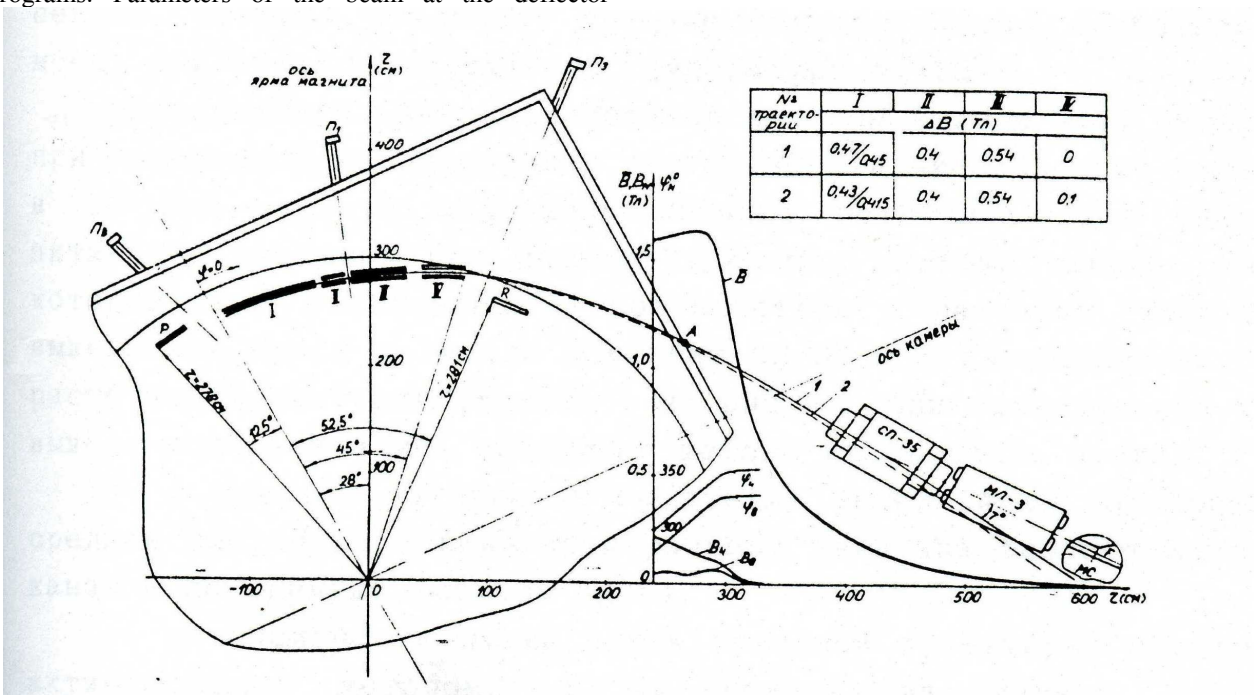

Figure 1: Layout of the Phasotron extraction system P is the peeler, R-regenerator, I, II, III, IV are the sections of the extraction channel.

EXTRACTION SYSTEM OF THE JINR PHASOTRON

The calculation of the beam acceleration in the JINR Phasotron ("F") and its throe to the extraction channel entrance is performed [1] with e special computer code for the beam dynamics simulation in the cyclotron-type accelerators. The regenerative method [2] is used for the beam extraction from "F". The extraction efficiency is ~40% and mainly depends on the beam losses at the entrance to the extraction system.

The position of the beam extraction system inside "F" vacuum chamber is shown in Fig. 1. System consists of peeler, regenerator and four channels. Each element has adjustable radial position. First of four channels is a current supplied channel with the thickness of the septum of 4mm. Other three sections are passive magnetic channels.

Figures 2-5 show portraits end energy distribution of the accelerated beam (2000-proton bunch) at the entrance to the extraction channel.

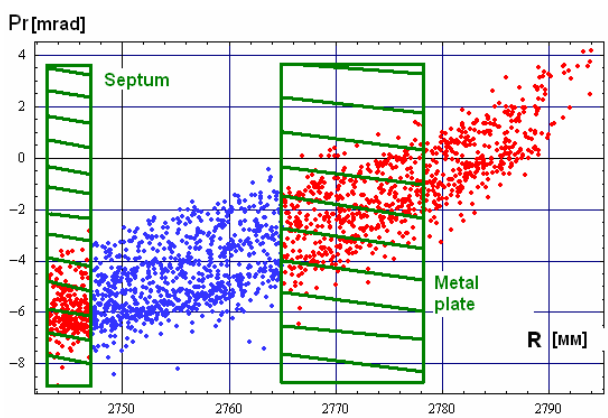

Fig 2: Position of the beam particles on the radial phase plane at the extraction channel entrance

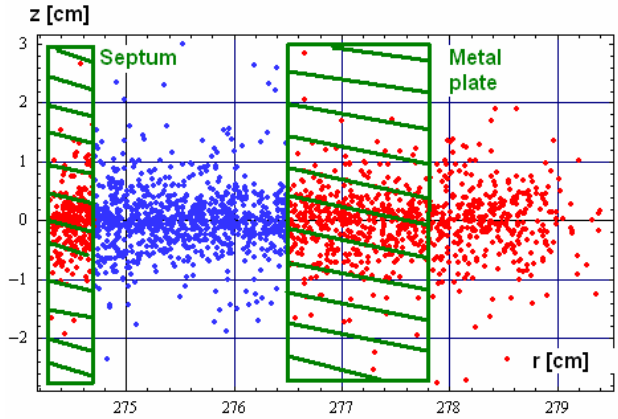

Fig 3: Position of the particles on *R-Z* plane at the extraction channel entrance

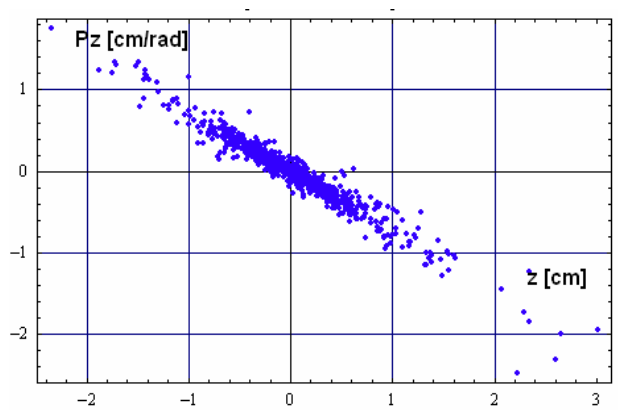

Fig 4: Position of the particles on the axial phase plane at the extraction channel entrance

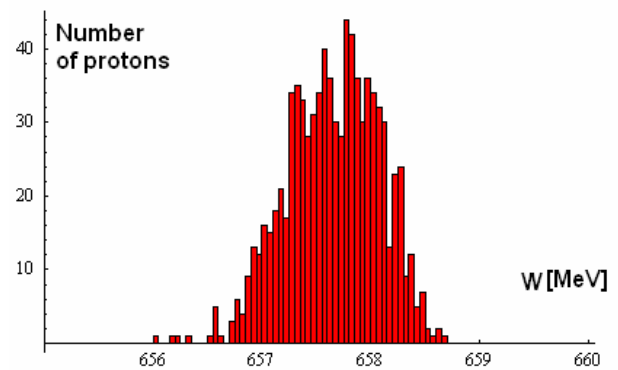

Fig 5: Energy distribution of the particles at the extraction channel entrance

Out of 2000 protons (which were injected from the ion source and came after 3000 turns to the radius of 80cm) 1951 (**98%**) protons were accelerated (37000 turns) to the extraction channel entrance. 49(**2%**) protons were lost due to large radial oscillation amplitudes. Out of 1951 particles which came to the extraction channel entrance (see Fig. 2) 857 (**43%** of 2000) particles were pushed inside the channel aperture, 241(**13%**) hit the septum tip, and 814(**42%**) were lost on the back wall of the current section. Transversal emitances of the beam that entered the channel aperture are ε_r= 25π mm•mrad, ε_z=8π mm•mrad.

After the channel beam is extracted from the vacuum chamber and transported to the SP-35 magnet. The parameters of the extraction system elements are given in the Table 1.

Table 1: Parameters of the extraction system elements

Parameter	current supplied channel		passive magnetic channels			peeler	regenerator
	1	2	3	4	5	6	7
φ_1, °	1.0	9.8	20.0	25.2	36.5	348.0	50.7
φ_2, °	9.8	18.7	24.7	35.8	44.7	353.7	56.4
ΔB, kG	-4.7	-4.5	-4.0	-5.4	0.0	-2.48	2.16
dB/dX kG/cm	0.15	0.03	-0.1	-0.1	1.0	-0.31	0.27
Radial aperture, cm	1.8	1.8	2.2	2.6	5.0	11.0	13.0
R_1, cm	275.6	276.2	279.5	282.3	291.0	272.5	274.5
R_2, cm	276.2	279.0	282.0	290.5	299.0	272.5	274.5

In Table 1 R_1 and R_2 are axis entrance and exit radii of each element. ΔB is the magnetic fields drop at the central line of each element. dB/dX – additional gradient from the element.

2σ beam rms-envelopes inside the extraction system are shown in Figure 6.

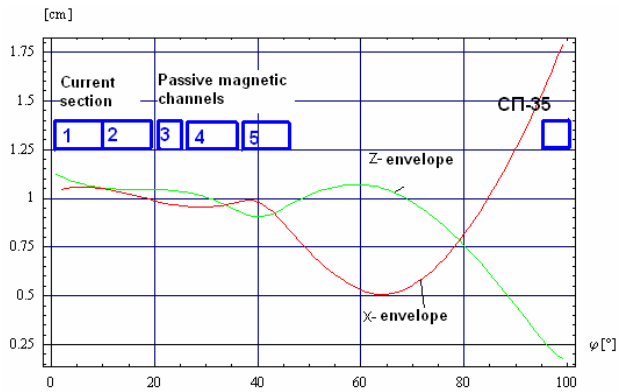

Fig 6: 2σ beam rms-envelopes inside the extraction system

The extracted beam profiles are shown in Figure 7 (calculated) and Figure 8 (experimental). One can see that both results agree with the accuracy of ~20%.

It is supposed that the developed code used in the calculations for the study of the beam dynamics can be helping for more careful investigation of the possibility of increasing the beam extraction efficiency at JINR Phasotron.

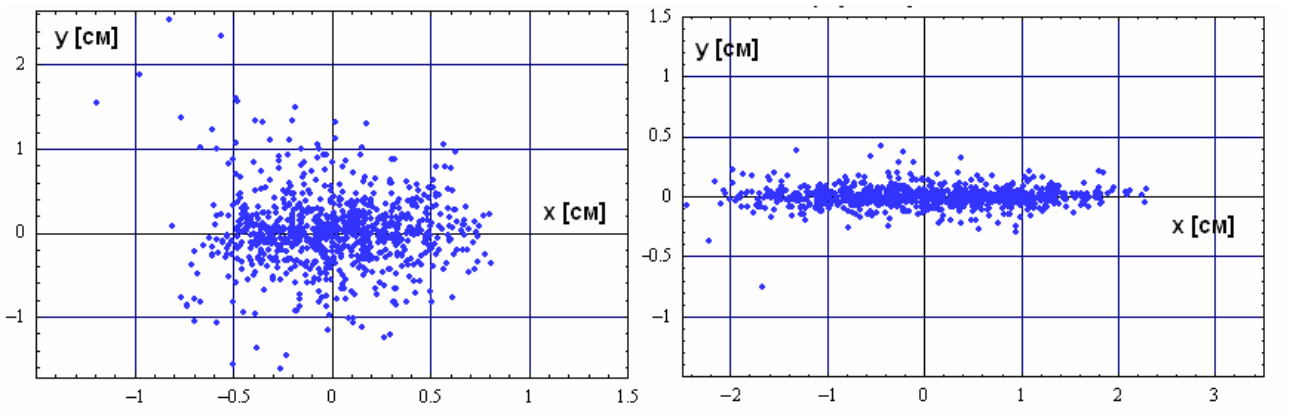

Fig 7: Beam profiles (calculated) at point A (see Figure 1) and at the entrance to the SP-35 magnet

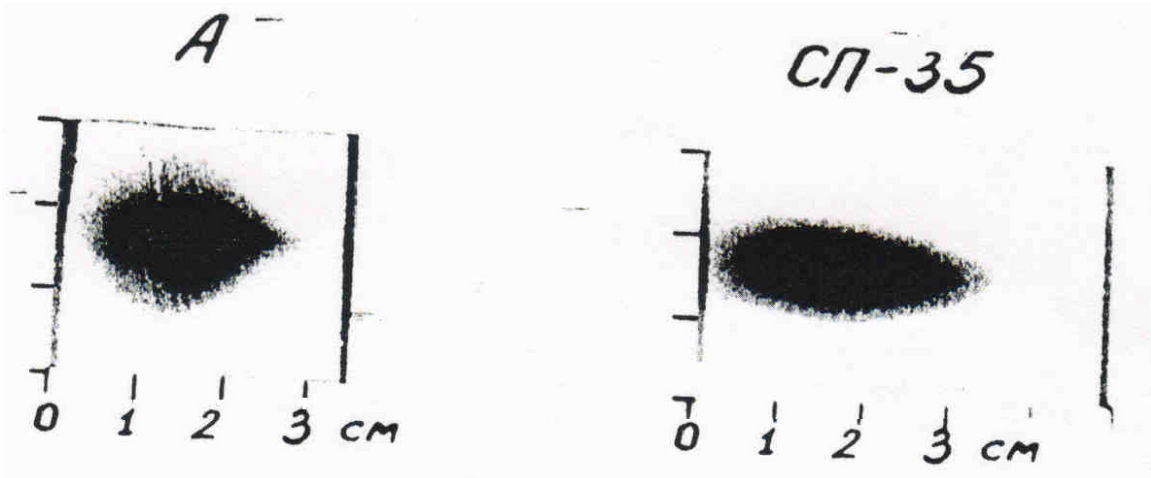

Fig 8: Beam signatures (experimental) at point A (see Figure 1) and at the entrance to the SP-35 magnet

CONCLUSIONS

Beam dynamics is studied in the extraction by the regenerative method from the JINR Phasotron using special complex of computer programs. Parameters of the beam at the deflector entrance are calculated. The beam extraction efficiency is found to be ~40%. The mean movement in the extraction channel is investigated. Calculated beam transverse parameters agree with the experimental ones to accuracy of 20%.

The developed code can be used for more careful investigation of the possibility of increasing the beam extraction efficiency.

REFERENCES

[1] S. Kostromin, L. Onischenko, Computer Simulation of the Beam Acceleration and Extraction from the JINR Phasotron, Particles and Nuclei, Letters [ISSN 1814-5957], 2012, V. 9, № 4-5, p.388-393

[2] V. P. Dmitrievsky et al. PTE 1, 11(1957)

[3] A. F. Chesnov, Extraction System of the JINR Phasotron, 1987, PhD thesis.

NEW IDEAS FOR CRYSTAL COLLIMATION*

V.V. Tikhomirov, A.I. Sytov, INP, BSU, Minsk, Belarus

Abstract

Both channeling and volume reflection (VR) effects are used for proton beam deflection by bent crystal. We propose the modifications of both these two effects to drastically improve the deflection efficiency. For the channeling it is a narrow plane cut [1] increasing the fraction of channeled particles up to 98-99%. In order to simplify the fabrication technology we suggest to use a buried amorphous layer instead of a crystal cut [2]. We also suggest to use the multiple volume reflection in one crystal (MVROC) [3], instead of single one because the MVROC increases the deflection angle in 5 times in comparison with VR.

The cut method can be applied with high efficiency for the extraction of high intensity proton beam from the Recycler Ring (FNAL) [5] as well as the MVROC will provide very good deflection parameters for the future LHC crystal-based collimation system. We also argue that the channeling effect is not efficient in the LHC case because of large angular divergence of halo beam particles caused by the elastic nuclear scattering on residual gas.

INTRODUCTION

Bent crystals possess wide capabilities for accelerator physics. Very strong intracrystal electric fields applied with accuracy of Angstrom provide high deflection efficiency. The main advantages of crystals are very compact size, low price of production and simplicity of installation and exploitation. Additionally, they can efficiently deflect the beams of different types of charged particles, of very different energies (from hundreds MeV up to tens TeV and higher) and of different beam angular divergence. The latter parameter is critical for the proper effect choice.

For small beam angular divergence the channeling effect provides rather high performance. For the best case the deflection efficiency exceeds 80%. For multiturn case it can exceed 95%. If the angular divergence is large, the volume reflection will be efficient. It provides less deflection efficiency than the channeling but the angular acceptance of it is much higher.

The efficiency of the channeling can also decrease because of the miscut angle characterizing nonparallelity of the channeling planes and crystal surface. It is shown in [4] that for UA9 experiment [6] the nuclear reactions rate in crystal increases by a factor of 4.5. So, we should consider both the beam impact parameter and angular divergence for effect choice. If the beam impact parameter is rather large for most of particles not to enter in the miscut influence zone and the beam angular divergence is less than the critical angle for the channeling, the latter will provide good deflection efficiency. Otherwise the VR must be chosen.

In this paper we will consider bent crystal application for two opposite cases relevant to two different machines: the future LHC crystal-based collimation system and the 8GeV proton beam extraction from the Recycler Ring at Fermi National Accelerator Laboratory (FNAL) [5]. As we will show below the volume reflection should be chosen in the LHC case while the channeling in the case of the Recycler Ring. Also we suggest for both cases some modifications: a narrow plane cut increasing the channeling efficiency up to 98-99% [1] for channeling and multiple volume reflection in one crystal (MVROC) instead of "single" one.

MVROC FOR LHC COLLIMATION

In order to solve the future LHC collimation problem it is very important to understand the main source of halo formation. Knowing the latter we can calculate the beam profile as well as both the impact parameter and angular divergence distributions in the beam collimation zone (6σ). Then we can exactly choose the proper deflection effect. The main mechanisms of beam loss are inelastic, diffractive and elastic scattering in interaction points (IP) and on residual gas. We can exclude as halo particle production reasons the inelastic and diffractive scattering on gas and in IP because of large scattering angles and energy losses. So, only elastic scattering on residual gas and in interaction points should be considered.

It is known that β-function of interaction points is 2-3 orders less than the average value. That's why the scattering at the same angle increases the amplitude of betatron oscillations for gas 10 times more than for IP:

$$X = \sqrt{\beta_{avr}\epsilon} = \sqrt{\beta_{avr}\beta\theta^2}, \quad (1)$$

where X is an amplitude of betatron oscillations, β_{avr} is average beta function, ϵ is emittance after scattering, β is β-function in a scattering point, θ is a scattering angle. According to (1) the multiple Coulomb scattering on residual gas gives emittance increase of less than initial LHC beam emittance. So, we can exclude the multiple coulomb scattering. The single coulomb scattering at large angles can be excluded because of very small probability and scattering angle of such events insufficient to achieve 6σ. Thus, only elastic nuclear scattering stands for examination.

One obtains that for sufficient scattering angle (at IP) the probability is 5 orders less than for the distribution maximum. More accurate estimates give that about 10^4 particles enter the collimation zone per second. It is at least two or-

* Work supported by Belarusian State Program of Scientific Research "Convergence".

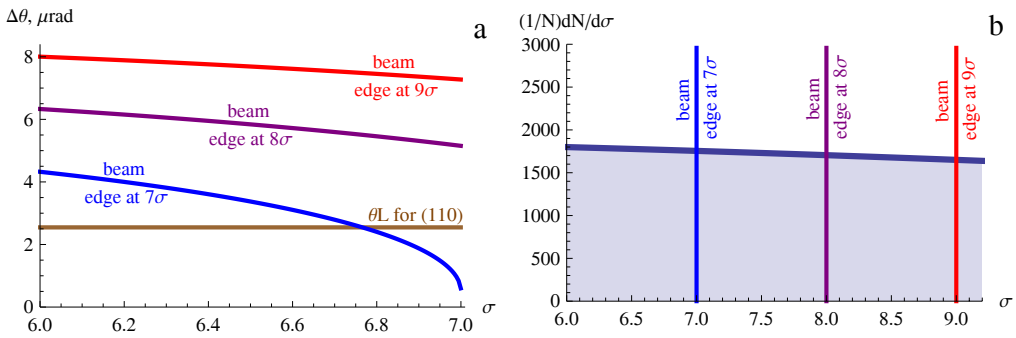

Figure 1: Elastic nuclear scattering on residual gas (LHC): beam profile (a) and angular divergence distribution (b).

ders less than the LHC quench limit. So, the elastic nuclear scattering in IP can be excluded.

Thus, we consider only elastic nuclear scattering on residual gas. In this case even small scattering angle (several μrad) is sufficient for particle to enter the collimation zone because of high β-function (about 10^2m). The R.M.S. scattering angle is about 40 μrad that is more than enough to achieve 6σ. The distribution of differential cross section at small angles is exponential, so we can simply obtain the beam profile shown in Fig. 1a. Here the beam intensity at 6, 7, 8σ remains almost the same. So, for channeling we can neglect the miscut angle influence.

The angular divergence distribution (see Fig. 1b) obtained from the beam profile shows that the crystal incident angle for the LHC is much higher than the channeling critical angle. That's why the channeling is not applicable in this case. Only volume reflection can be applied at the LHC. But the deflection angle of VR is very low - 7 times less than we can expect from the channeling. The solution of this problem can be obtained by MVROC [3] with deflection from several bent *skew* crystal planes (not from a single one as at VR). When these reflections almost compensate each other in the vertical direction, in the horizontal one they will sum.

The deflection angle for it can be 5 times larger than for VR and the angular acceptance and deflection efficiency will also increase [3]. Here we notice that the deflection efficiency of the MVROC is a bit less than of the channeling but large enough for the LHC collimation purposes.

The MVROC was observed for proton beam at U-70 accelerator in Protvino (Russia) and at SPS (CERN) for both protons and negative charged pions. In all cases high deflection efficiency was obtained. So, we suggest the MVROC as the main candidate for the application at the future LHC crystal-based collimation system.

CRYSTAL CUT FOR THE RECYCLER RING

There is an opposite situation for the project of high intensity 8GeV proton beam extraction from the Recycler Ring [5]. This beam is planned to be extracted in the Main Injector for application for neutrino and muon experiments.

According to our simulations, the angular divergence of the beam is small enough for capture of most particles in the channeling regime and the beam impact parameter is large enough to neglect the miscut angle influence (Fig. 3a). That's why the channeling effect choice is evident.

Additionally, because of low beam energy the angle of amorphous scattering on crystal exceeds the volume reflection angle. Moreover for farther use of the beam in another machine the particle deflection must be of similar angles. So, we can say that the volume reflection is not applicable for the Recycler Ring (like the channeling for the LHC).

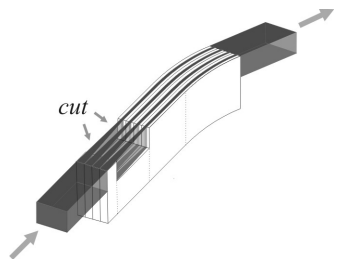

Figure 2: Narrow plane cut.

The main problem is very high intensity of the beam. So, a reasonable question of the crystal radiation damage can be asked. Thereby, one should minimize the number of particle passages of crystal. Additionally, the beam losses during the extraction must be minimized in order to achieve the high final beam intensities in the future neutrino and muon experiments. All these problems can be solved by application of the narrow plane cut (Fig. 2) [1]. When particle enters the cut it loses the potential energy because it simply becomes far away from crystal plane electric fields. For the optimal cut parameters [1] the particle escaping the cut will obtain the potential energy less than the loss, so, the final transverse energy will decrease.

Thus, most of particles will be captured in the regime of stable channeling motion. Because of low transverse energy they will oscillate far away from zone of nuclear scattering. So, most of them will achieve the end of the crystal in the channeling regime with high probability.

The width of the cut must be very small. It is proportional to the root square of the beam energy and achieves

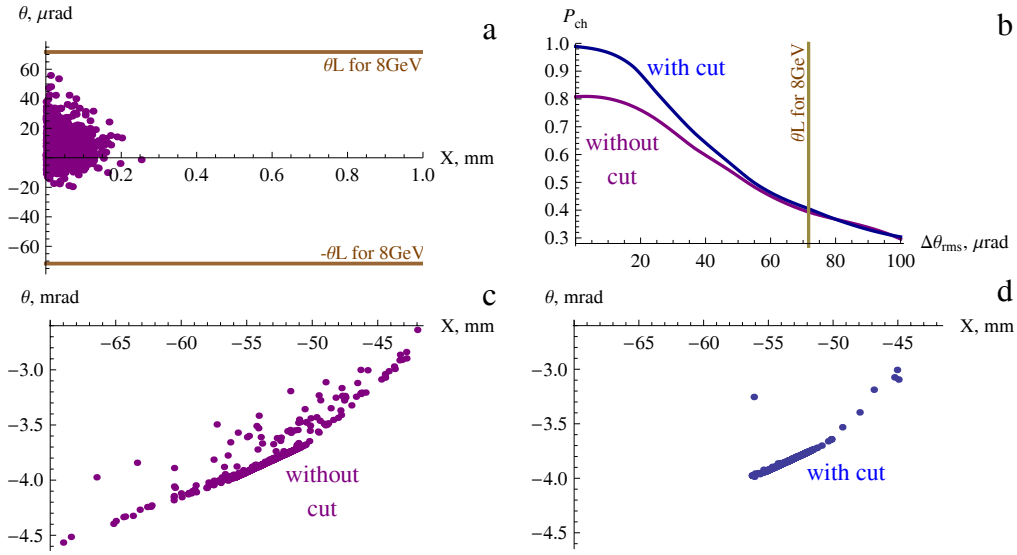

Figure 3: Beam extraction from the Recycler Ring: phase space at the 1^{st} crystal entrance (a), the channeling efficiency *vs* R.M.S. incident angle (b), phase spaces of the extracted beam without cut (c) and with cut (d). Crystal parameters: (110) silicon crystal of 1mm length and thickness, deflection angle 0,5mrad.

about 1μm at 8GeV. It is very difficult technologically to make such crystal. Much simpler is to make the amorphous layer [2] instead of the cut. The R.M.S. scattering angle is negligible at such narrow layer. So, the crystal lattice disturbance is equivalent to the cut.

Now let us consider the cut effect performance for 8GeV beam of the Recycler Ring. In Fig. 3b the dependence of the channeling efficiency on the R.M.S. incident angle obtained by our simulations is shown. The efficiency in the case with cut is more than without it. This difference decreases with the incident angle rise. But in Fig. 3a the incident angular divergence is small enough for high performance of the cut method. So, we can conclude that there are good conditions for the first experiment with crystal cut.

The phase spaces of the extracted beam from the Recycler Ring are shown in Fig. 3c-d. This result (and Fig. 3a) was obtained with our simulation code of particle motion in crystal combined with the program for the simulation of beam dynamics in accelerator - "STRUCT" [7], developed in FNAL. One can see here that the phase space is much narrower for the cut case. Thus, the latter will considerably improve the quality of obtained proton beam. In addition, the fraction of particles extracted after the first crystal passage exceeded 95% (compare a bit more than 80% without cut). So, the limiting intensity of the extracted beam increases considerably.

Finally, the beam losses decreased in 4 times due to the cut method. It allowed to increase the extraction efficiency from 94-95% up to 98-99%.

CONCLUSION

The application of bent crystals for two different machines was considered. The main deflection effect was chosen: volume reflection for the LHC and channeling for the Recycler Ring. The new methods considerably increasing the deflection efficiency were proposed. In the first case it is the MVROC increasing 5 times the deflection angle being almost independent from the incident angle. In the second one it is the cut method decreasing the beam losses up to 4 times, increasing the extraction efficiency from 94-95% up to 98-99% and providing much higher intensity of the beam. All these improvements provide the high performance of future high energy accelerators.

ACKNOWLEDGMENT

The authors are obliged to Fermilab group and especially to Dr. N. Mokhov, Dr. A. Drozhdin, Dr. V. Shiltsev and Dr. D. Still for the collaboration during the participation of one of the authors (A. S.) in the Summer Intern Program "Physics of Accelerators and Related Technology for International Students" (PARTI).

REFERENCES

[1] V.V. Tikhomirov, JINST 2 (2009) P08006.

[2] V. Guidi, A. Mazzolari and V.V. Tikhomirov, J. Phys. D: Appl. Phys. 42 (2009) 165301.

[3] V.V. Tikhomirov, Phys. Lett. B 655 (2007) 217-222.

[4] V.V. Tikhomirov and A.I.Sytov, VANT 57 N1 (2012) 88-92.

[5] V. Shiltsev, Work supported by the U.S. Department of Energy under contract No. DE-AC02-07CH11359.

[6] W.Scandale et al., Phys. Let. B 692 (2010) 78-82.

[7] I.S. Baishev, A.I. Drozhdin, N.V. Mokhov, X. Yang, http://www-ap.fnal.gov/users/drozhdin/.

BEAM DYNAMICS INVESTIGATIONS FOR 433 MHZ RFQ ACCELERATOR

Yuri Svistunov, NIIEFA, St. Petersburg, Russia
Alexander Durkin, MRTI RAS, Moscow, Russia
Alexander D. Ovsyannikov#, St. Petersburg State University, St. Petersburg, Russia

Abstract

Modeling results for deuteron dynamics in RFQ structure with operational frequency 433 MHz and 1 MeV output energy are presented. The results are compared with experimental data. The purpose of investigation is to find optimal input RFQ emittance parameters for off-nominal values of input current and vane voltage.

INTRODUCTION

There are presented theoretical and experimental results of researches short length 1 MeV, 433 MHz RFQ which is part of RF neutron generator (NG). Description of this RFQ was given in article [1] where were discussed problems design and tolerances under manufacturing of such resonator. In [1] installation was considered with ECR deuteron (D^+) source and forming beam system including electrostatic preacceleration, focusing solenoid, electromagnetic correctors and electrostatic focusing lens before RFQ entrance. Later injection system was changed because D^+ source don't permit to obtain required beam emittance on RFQ input. The new injection system have multicusp D^- ion source and it is shown on fig.2 together with RFQ and foil monitor which was used for energy measuring during NG testing.

RFQ DESIGN

RFQ design was based on following main parameters presented in table 1.

Table 1: Initial parameters for RFQ design

Frequency	433 MHz
Ions	$D^{\pm}$
Output beam energy	1 MeV
Output pulsed current	10 mA
Output average current	10 mkA
Input beam energy	25-30 keV
Input beam current	≥10 mA
Maximal surface gradient	≤2xKP

Items 2-5 are determined by use of NG for its proper purposes; item 6 is determined by requirement of small gabarits of feed system; item 7 take into account possible loss of beam; item 8 is determined by requirement of absence of electrical break-down. Calculated RFQ parameters are given in table 2.

Table 2: Calculated RFQ parameters

Beam injection energy	25 keV
Beam output energy	1 MeV
Input pulsed current	13 mA
Output pulsed current	10 mA
Input phase length of bunches	360°
Output phase length of bunches	36°
Input beam synchronous phase	-90°
Output beam synchronous phase	-23.4°
Average channel radius	1.8 mm
Minimal radius	1.18 mm
Intervane voltage	50 kV
Vane length	1090 mm

Data of tables 1, 2 may be added experimental results, obtained during tests and working of NG.

Assembling of four-vanes RFQ was made with high accuracy. Difference of distances between adjacent vanes not more 10 mkm (see fig. 1). Vane modulation was roduced with an accuracy of 2…5 mkm Measured quality factor is 6800. It value was provided by good uality of machining of four-cavity RFQ surfaces. Maximal measured vane voltage without breakdown under testing is 70 kV. Deviation of electrical field tensity from average value along RFQ length is ±5%.

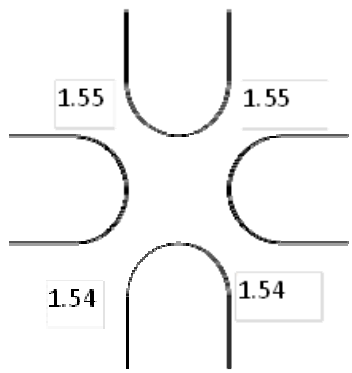

Figure 1: Distances are given in mm between vanes.

#ovs74@mail.ru

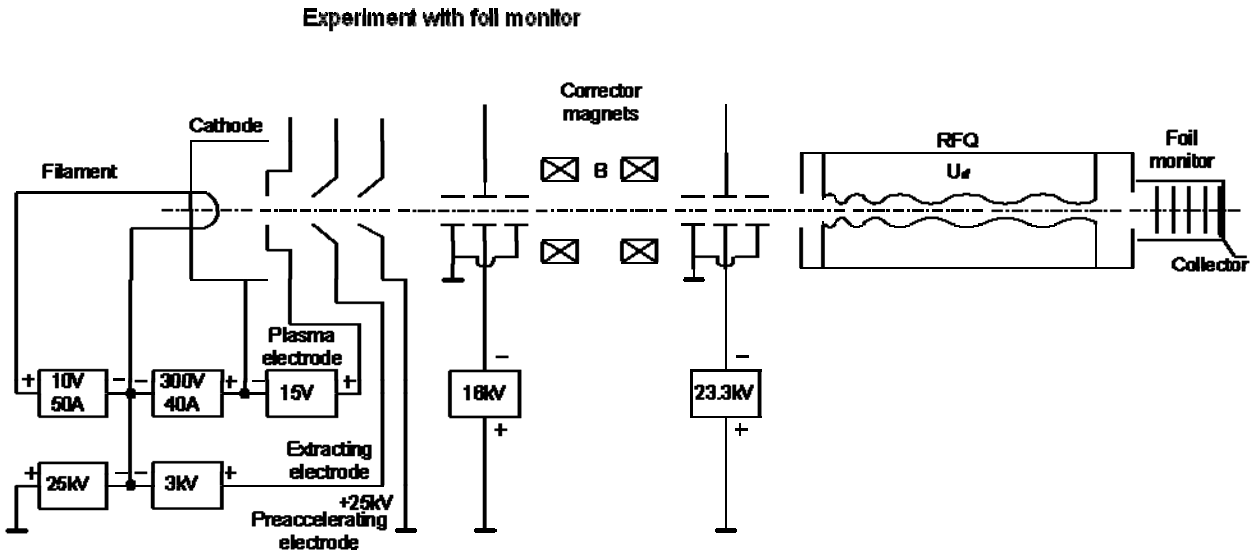

Figure 2: The new injection system together with RFQ and foil monitor.

DYNAMICS PROBLEM

Initial design of RFQ usually supposes dynamics calculation with vane geometry what is known as "ideal" or hyperbolic modulation. "Real" vane's modulation is produced by machine tool and can differ from "ideal" one. Output beam characteristics depend on voltage vane, value and orientation of beam phase volume in phase space. In our calculations three of types of vane's modulation take place. "Ideal" vanes with special match section had places where intensity of electrical field was more than 2KP. Smoothed out "ideal" vanes which satisfy conditions of table 1. Third type is "real" vane modulation which formed by manufacturing process. Below one may see calculation results for different vane types and orientation of beam phase volume in phase space (convergent and divergent beam). Now NG is working with cyclotron multicusp D- ion source which have small enough output current 2..2.5 mA so one consider two possibilities of calculation: nominal output RFQ current 10 mA and variant with input RFQ current 2 mA.

In tables below:

Tr_acc - capture of particles into the acceleration (the number of accelerated particles that have reached the end of the channel to the initial total number of particles)

Ex,y - transverse rms-emittance of the output beam, cm • mrad

P – average total power of lost part of the beam, W

Data of table 5 in principle consistent with the experimental results obtained under NG tests.

Table 3: Calculation results (initial data from table 1, current on RFQ input – 14 mA, beam emittance 0.052π•cm•mrad)

U/U0	Tacc	Ex,y	P
	ideal smooth real	ideal smooth real	ideal smooth real
1	0.906	0.08	0.2
	0.900	0.08	0.17
	0.599	0.09	0.24
1.1	0.932	0.08	0.2
	0.923	0.08	0.20
	0.787	0.09	0.21
1.2	0.2	0.09	0.15
	0.20	0.09	0.19
	0.21	0.09	0.19
1.3	0.937	0.10	0.15
	0.929	0.09	0.19
	0.859	0.10	0.23
1.4	0.927	0.11	0.24
	0.924	0.11	0.22
	0.863	0.11	0.31

Table 4: Calculation results (initial data: current on RFQ input – 2 mA, emittance 0.03π•cm•mrad; "ideal" vanes; initial beam x,y=1.002 mm; dx/dz, dy/dz=-27.4 mrad; "real" vanes; initial beam x,y=1.386 mm; dx/dz, dy/dz=-49.6 mrad)

U/U0	Tacc	Ex,y	P
	ideal real	ideal real	ideal real
1	0.997 0.940	0.06 0.06	0. 0.
1.1	0.999 0.991	0.06 0.06	0. 0.
1.2	0.999 0.996	0.06 0.06	0. 0.
1.3	0.999 0.998	0.07 0.07	0. 0.
1.4	0.999 0.998	0.08 0.08	0. 0.

Table 5: Calculation results (initial data: current on RFQ input – 2 mA, emittance 0.03π•cm•mrad, "real" vanes, initial beam x,y=1.386 mm; dx/dz, dy/dz=+30 mrad)

U/U0	Tacc	Ex,y	P
1	0.580	0.13	0.14
1.1	0.698	0.14	0.16
1.2	0.764	0.15	0.16
1.3	0.791	0.16	0.16
1.4	0.791	0.17	0.18

CONCLUSION

- Results presented in table 3 for "ideal" and "smooth" vanes have small difference.
- On the contrary in our case difference between "ideal" and "real" vanes gives negative effect: transmission efficiency for "real" vanes is less than for "ideal" ones, because beam channel was calculated for "ideal" vanes.
- Increasing of vane voltage proves increasing of transverse RFQ acceptance, but beam turn out uncoordinated with channel. Transmission efficiency is increasing but less than in case of coordinate beam.
- According to table 5 in our case we have divergent beam in RFQ output. One may hope do better transmission efficiency of divergent beam with help of optimal match section as is shown in paper [2] and optimal tuning of focusing elements of beam forming system.

REFERENCES

[1] Yu.A.Svisunov, Yu.V. Zuev, D.A. Ovsyannikov, A.D. Ovsyannikov, "Development of 1 MeV compact deuteron accelerator for neutron generator," Bulletin of St.Petersburg University, series 10, 2011, pp.49-59 (in russian).

[2] D.A. Ovsyannikov, "Mathematical Modeling and Optimization of Beam Dynamics in Accelerators," TUZCH02, these proceedings.

ACCELERATOR COMPLEX U70 OF IHEP: STATUS AND UPGRADES

S. Ivanov, on behalf of the U70 staff#
Institute for High Energy Physics (IHEP), Protvino, Moscow Region, 142281, Russia

Abstract

The report overviews present status of the Accelerator Complex U70 of IHEP-Protvino comprising four machines (2 linear accelerators and 2 synchrotrons). Particular emphasis is put on the recent upgrades implemented since the previous conference RuPAC-2010.

GENERALITIES

Layout and technical specification of the entire Accelerator Complex U70 of IHEP-Protvino were specified in the status report of 2008, Ref. [1]. Since October 2007, the complex comprises four facilities — 2 linear (I100, URAL30) and 2 circular (U1.5, U70), Fig. 1.

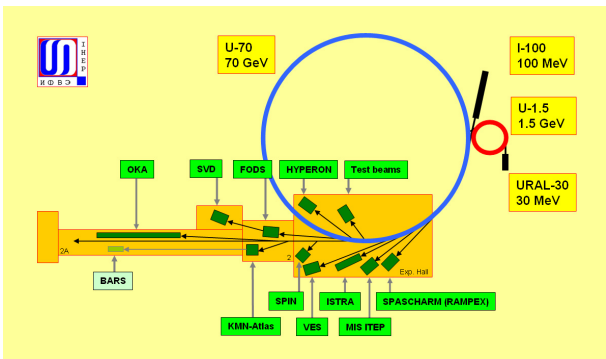

Figure 1: Accelerator Complex U70, beam transfer line network and fixed-target experimental facilities included. Proton mode (default) — cascade of URAL30–U1.5–U70, light-ion mode — I100–U1.5–U70.

Due to recent advances of the light-ion acceleration program, refer to Table 1, former proton synchrotrons U1.5 and U70 can be attributed to the (light-) ion synchrotron category as well.

Table 1: Light-ion program milestones

	Deuterons $^{2}H^{1+}$	Carbon $^{12}C^{6+}$
U1.5	16.7–448.6 MeV/u March 30, 2008	16.7–455.4 MeV/u December 08, 2010
U70	23.6 GeV/u April 27, 2010	34.1 GeV/u April 24, 2011

In the mid-April 2012, IHEP was reorganised into Federal State Budgetary Enterprise and moved under the auspices of the National Research Centre (NRC) “Kurchatov Institute”, which implies a revision of funding schemes to perform R&D and maintain special and general-purpose engineering infrastructure of the IHEP facilities.

N. Tyurin, Yu. Fedotov, O. Zyatkov, A. Minchenko, A. Afonin, E. Ludmirsky, O. Lebedev, D. Demihovskiy, V. Lapygin, A. Ermolaev, Yu. Milichenko, I. Tsygankov, I. Sulygin, N. Ignashin, S. Sytov, V. Zenin, Yu. Antipov, D. Khmaruk, and G. Kuznetsov.

ROUTINE OPERATION

Since RuPAC-2010, the U70 complex operated for four runs in total. Table 2 lists their calendar data. The first run of a year is shorter and solves, mainly, R&D and methodological tasks.

Figure 2 shows beam availability data during machine development (MD) and fixed-target experimental physics program (XPh) with averages over 2002–12. The extracted beam is delivered to experimental facilities with 82.8% availability, on average.

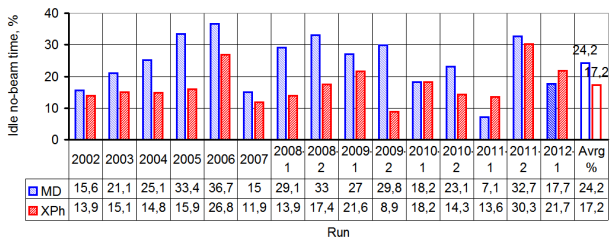

	2002	2003	2004	2005	2006	2007	2008-1	2008-2	2009-1	2009-2	2010-1	2010-2	2011-1	2011-2	2012-1	Avrg %
MD	15,6	21,1	25,1	33,4	36,7	15	29,1	33	27	29,8	18,2	23,1	7,1	32,7	17,7	24,2
XPh	13,9	15,1	14,8	15,9	26,8	11,9	13,9	17,4	21,6	8,9	18,2	14,3	13,6	30,3	21,7	17,2

Figure 2: Beam availability statistics.

Figure 3 is a screenshot of the on-line statistics monitor that is an example (December 2011) of a long-term sustained operation of the complex. The large ring (i.e., the U70 PS itself) delivers $0.98 \cdot 10^{13}$ ppp. Beam losses through a cycle amount to 4%. Slow stochastic extraction spills some $6.7 \cdot 10^{12}$ ppp, while internal targets and Si-crystal deflectors consume the allowed $2.5 \cdot 10^{12}$ ppp.

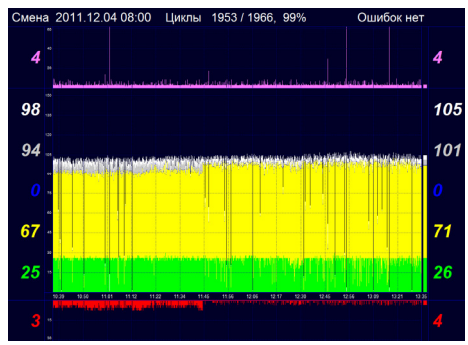

Figure 3: Screenshot of the on-line monitoring over the U70 operation. Time interval (abscissa) extends over 3 hr, or 1000 ramping cycles. Yellow trace slows intensity of slow stochastic extraction, green trace — operation of internal targets and crystal deflectors. Red (inverted) trace indicates spent beam remains dumped onto internal absorber.

Fixed-target experimental setups (from 6 to 10 per a run) acquire the beam via sequential and parallel sharing of the U70 magnetic field flattop (about 3.2 s at 50 GeV).

Table 2: Four runs of the U70 in between RuPAC-2010 and -2012

Run	2010-2	2011-1	2011-2	2012-1
Launching linac URAL30, booster U1.5 and U70 sequentially	October, 04	March, 14	October, 10	March, 12
Proton beam in the U70 ring since	October, 27	April, 06	November, 02	April, 04
Fixed-target physics program with extracted beams	November, 03 – December, 06, 31 days	April 11–21, 10 days	November, 09 –December, 13, 32 ½ days	April, 09–21, 12 days
No. of multiple beam users (of which the 1st priority ones)	11 (8)	9 (7)	9 (6)	9 (6)
MD sessions and R&D on beam and accelerator physics, days	7	5	9 ½	5
Light-ion acceleration MD program	December, 06–10, 4 days	April, 21–27, 6 ½ days	December, 14–18, 4 ½ days	April , 21–27, 6 ½ days

Typically, internal targets (IT) and crystal deflectors (CD) are engaged during the 2nd half of the flattop at 8590 Gs (50 GeV). Fig. 4 shows oscillograms of beam splitting between users. The traces are specified from top to bottom. The first (olive) trace shows beam extraction with CD#19 and IT#24. The next, purple (blue) traces show extraction with IT#27 (IT#35), respectively. The fourth (green) trace is intensity of waiting beam monitored with a DCCT ($2.8\cdot10^{12}$ ppp extracted).

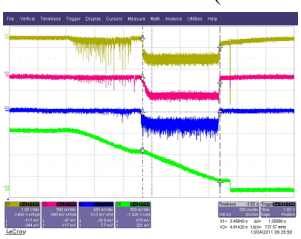

Figure 4: Beam splitting at the 2nd half of the flattop.

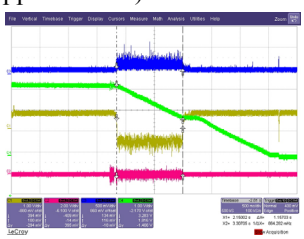

Figure 5: Slow stochastic extraction at the 1st half of the flattop.

Slow stochastic extraction (SSE) operates at the 1st half of the flattop. Fig. 5 shows the SSE technological signals. Again, the traces are specified from top to bottom. The first (blue) trace shows signal from beam loss monitor BLM#106 fed to spill-rate feedback. The second (green) trace is intensity of waiting beam monitored with a DCCT ($1.1\cdot10^{13}$ ppp max of which up to $8.4\cdot10^{12}$ ppp may be slowly extracted, cruise rates being $3–7.4\cdot10^{12}$ ppp). The third (olive) trace is feedback signal that AM modulates the phase noise of the 200 MHz carrier (the fourth (purple) trace). A short pre-pulse of noise has another power spectrum. It is used to cure beam self-bunching by means of controlled reshaping beam distribution over momentu.

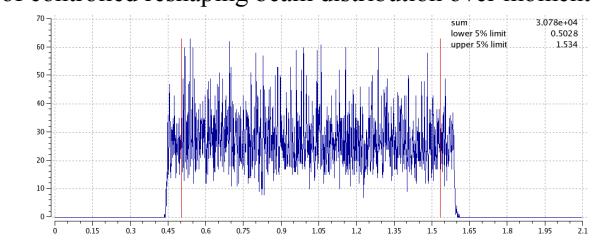

Figure 6: A slow spill delivered to the OKA facility.

Quality of the slow spills (up to 1.6–1.8 s long) seen with headcounters of the OKA experimental facility (rare kaon decays) is shown in Fig. 6. The spill Φ exhibits low ripples, no mains harmonics, no cut-offs and a flat DC spill rate $\langle\Phi\rangle$. Occasionally, spill duty factor $\langle\Phi\rangle^2/\langle\Phi^2\rangle$ rises to comfortable values near 0.95.

Figure 7 presents attainable spill-to-spill sustainability of the SSE. The upper trace is an in-out transfer efficiency ratio for the extracted beam fraction (90%). Slowly extracted beam current is shown by the lower trace ($3\cdot10^{12}$ ppp). Still, given higher beam intensities, the top attainable in-out extraction ratio has a tendency to drop to about 85% causing over-irradiation of the septum magnet SM#24. The nature of this deterioration effect is not yet fully understood and cured.

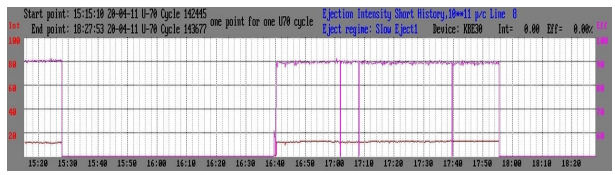

Figure 7: Spill-to-spill sustainability of the SSE.

Occasionally, for applied research, the fast single-turn extraction is employed. Its operation is shown in Fig. 8. At the 50 GeV flattop, the proton bunch extracted has a length of 15 ns at 0.5-level and population of $4\cdot10^{11}$ ppb.

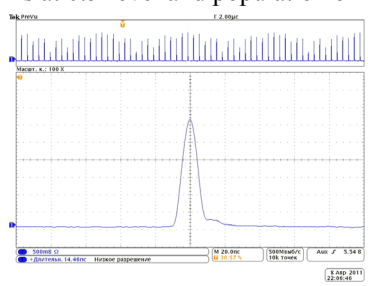

Figure 8: Fast single-turn extraction.

Proton Radiography

Until the run 2011-2, the fast single-turn multi-bunch extraction has fed 50 GeV Proton-Radiographic Facility mounted around two 90°FODO cells in a spare BTL channel, Ref. [2]. This facility with a 60 mm field-of-view and 0.25 mm resolution for > 300 g/cm^2 optical density objects is a successful joint venture of IHEP and RFNC–VNIIEF (Sarov, N. Novgorod Region).

MACHINE DEVELOPMENT

Digital Master Oscillator

Both the synchrotrons, U1.5 and U70, now employ unified DDS master oscillators based on COTS digital processing boards XDSP-3PCM equipped with the Xilinx FPGA and plugged into an industrial PC iROBO.

For the time being, the U1.5 (booster) utilizes only part of the new functionality now available — extended flexibility in generating "B-field–radiofrequency" law allowing acceleration of protons and light ions with charge-to-mass ratio about ½. Other options available are still waiting (and planned) to be implemented.

On the contrary, in the main ring U70, the DDS master oscillator now:

1. routinely introduces embedded bunch-rotation RF gymnastics prior to de-bunching at flattop for prompt control over momentum spread in a circulating beam;
2. provides coordinated variation through a ramping cycle, transition crossing included, of gains in phase-frequency and radial feedback loops around the maser oscillator.

The latter option called for a dedicated study Ref. [3] of the closed-loop configuration (Fig. 9) and locus of complex roots of the characteristic equation (Fig. 10) to attain optimal and balanced tune-up. Experiments with 1.3–50 GeV proton beam have shown promising results.

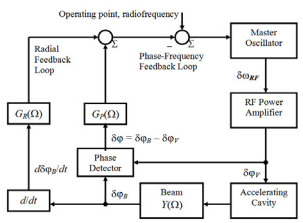

Figure 9: Block diagram of RF control in the U70.

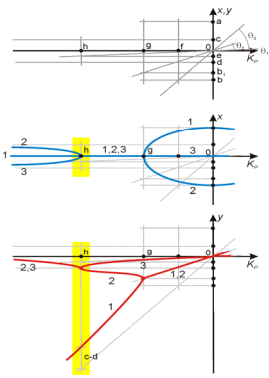

Figure 10: Characteristic equation root map.

Wide-Band Transverse Feedback

The former topology of this network is discussed in the status report of 2010 Ref. [1]. Since then, a novel architecture of the digital feedback circuit, see Fig. 11, was successfully beam-tested in the U70.

It employs a finite-time impulse response (FIR) non-recursive filter layout based on 3 variable (–10%) digital delay lines. Apart of using these natural-to-DSP components, the configuration involved has three operational advantages:

1. A single beam pickup layout (saves room on the orbit and ensures acceptability of an arbitrary betatron phase advance between pickup and kicker).
2. Accessibility of the purely imaginary coherent tune shift.
3. A built-in rejection of DC and higher rotation frequency harmonic signals persisting in raw beam-position readouts.

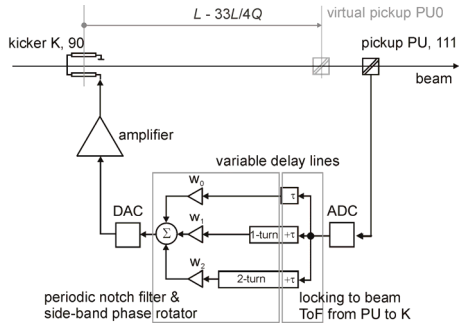

Figure 11: Updated layout of the wide-band feedback.

The latter occurs due to a periodic notch nature inherent in the amplitude-frequency in-out open-loop feedback transfer function.

Beam observations with the updated feedback are presented in Fig. 12. Zoom scan width is 4 ms

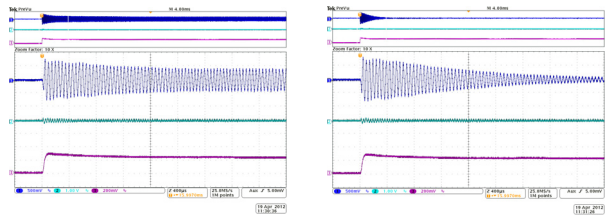

Feedback OFF Feedback ON

Figure 12: Damping of radial oscillations at injection (upper traces). Lower trace is beam intensity (DCCT).

Technically, the circuit implements the similar XDSP board as the RF master oscillators in the U1.5 and U70. Detailed report on the subject can be found in Ref. [4].

Slow Extraction at Flat-Bottom

At its 352–353 Gs flat-bottom, the U70 ring serves in a storage-stretcher mode. To this end, the entire 1.5 km lattice is fed by a stand-alone DC PSU (130 A, 20 kW).

The regime accommodates either a test proton beam (1.32 GeV kinetic), or a carbon $^{12}C^{6+}$ ion beam (453–455 MeV/u).

The challenge of squeezing a new slow extraction system into the densely packed U70 lattice was met with a classic 180° Piccioni-Wright scheme Ref. [5] (Fig. 13).

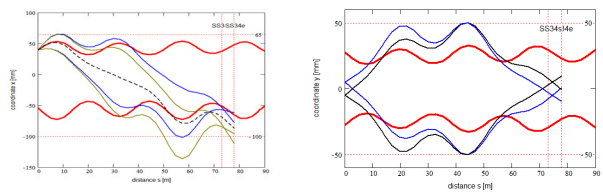

Horizontal Vertical

Figure 13: Waiting beam envelope ($\delta p/p_0 = \pm 3 \cdot 10^{-3}$) and representative traces for extracted fraction (ionization loss $\Delta p/p_0 = -0.69\%$ and $\pm 2\sigma'_{MCS}$ in slope over IT#28).

The scheme uses a thin energy-degrader internal target IT#28 (Fig. 14) followed by a newly-build deflecting septum magnet SM#34 (Fig. 15). The extracted (perturbed) beam fraction travels between IT#28 and SM#34, i.e. via 6 CF magnets of 120 available (1/20 of orbit length only).

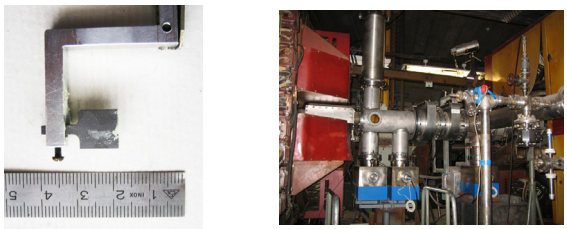

Figure 14: Energy-degrader inner target IT#28 (beryllium, thickness 4.0 mm, height 10 mm) for carbon beam and the IT outer assembly at SS#28.

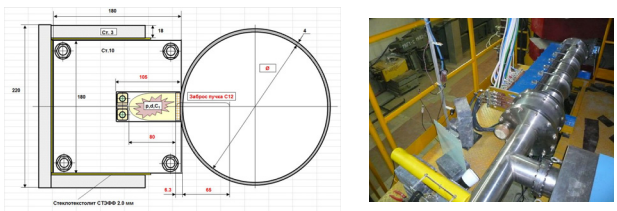

Figure 15: Deflecting septum magnet SM#34 (80 mrad, 0.42 T, 1.3 m, 80×40 mm^2 (h×v)).

In the runs 2011-1,-2, the system was beam-tested and attained the design performance (see Figs. 16, 17) with beam extracted towards the new BTL#25 being mounted.

Figure 16: Finite range (30 cm ca) and stopping point of carbon beam in a plastic scintillator at 455 MeV/u.

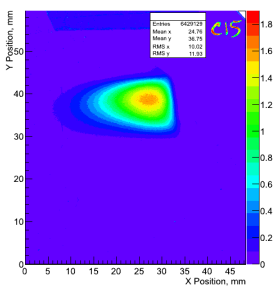

Figure 17: Carbon beam spot at exit from SM#34. Convolution over 3 cycles 8 s long each.

A dedicated scheme to point the beam outskirts to IT#28 for subsequent extraction with a random deflecting force was proposed and tested; see Fig. 18 and Ref. [6].

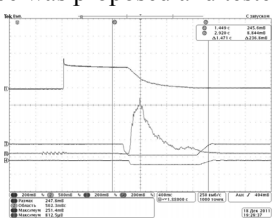

Traces from top to bottom: (1) circulating C beam intensity; (2) slow spill; (3, 4) coil currents for steady closed-orbit bumps near IT#28 and SM#34, resp.

Figure 18: Slow spill under a stochastic horizontal betatron excitation with a fixed noise power.

Intensity-Related Effects

The major goal pursued during MDs for the proton mode of the U70 is to operate with higher intensities > $1{\cdot}10^{13}$ ppp in 29 bunches (of 30 RF buckets) and small phase-space volumes. The consumer of the high intensity is slow extraction (SSE) for the OKA experiment.

For the time being, the challenging effect is spurious self-bunching of beam seeing longitudinal coupling impedance of 40 idle RF cavities at their fundamental mode.

The situation has been aggravated recently with the advance of the light-ion program, which has necessitated the comeback to the extended (factory default) bandwidth 2.7–6.1 MHz of the RF cavities.

Due to the well-known E. Keil–W. Schnell criterion, to ensure the coasting beam stability, one has to obey

$$\left|\frac{Z(k\omega_0)}{k}\right| < \frac{1}{\Lambda}\frac{\beta^2|\eta|E}{eJ_0}\left(\frac{\delta p}{p_0}\right)^2 \qquad (1)$$

where $2\delta p/p_0$ is full fractional momentum spread at base; Λ is form-factor depending on beam distribution function $F_0(\delta p)$; other notations are conventional.

To increase the r. h. s. of Eq. 1, two cures are now optionally applied to in the U70:

1. Blow-up of $\delta p/p_0$ from $\pm 4{\cdot}10^{-4}$ to $\pm 1{\cdot}10^{-3}$ by means of bunch rotation (8 ms long coherent 6 MHz RF gymnastics) prior to de-bunching at flattop using the extended functionality of the new DDS RF master oscillator. Factor Λ is kept unvaried meanwhile.
2. Smooth blow-up of $\delta p/p_0$ accompanied by re-shaping (flattening) $F_0(\delta p)$ and, thus, affecting factor Λ, with a 100 ms long low-pass (2.3–4.2 kHz) phase noise carried by 300 kV voltage driven by the auxiliary 200 MHz RF system.

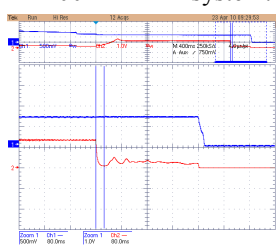

Self-bunching seen as oscillation and slow decay of peak curve (bottom).

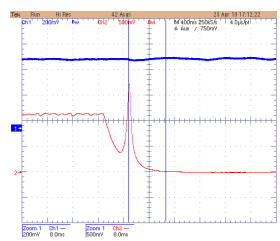

Damping out with bunch compression (surge) accompanied by momentum spread blow-up.

Figure 19: Suppression of self-bunching at 50 GeV flattop and $7{\cdot}10^{11}$ ppp with RF gymnastics. Upper (blue) trace is beam intensity (DCCT). Lower (red) trace is beam peak current signal.

Beam observations over self-bunching and effect of the two cures against are shown in Figs. 19 and 20.

A supplementary measure against self-bunching, when applicable, is injection of even bunch patterns that reduce beam de-bunching time.

Another cure possible is to close dedicated longitudinal beam feedback (digital) whose actuator might be a spare 6 MHz RF cavity. This option is under study now.

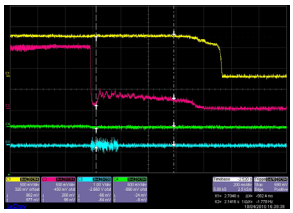

Self-bunching seen as oscillation and slow decay of peak curve (2nd from top).

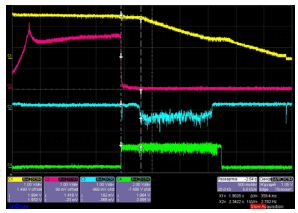

Suppression of self-bunching with noise pre-pulse followed by a transition to the SSE.

Figure 20: Suppression of self-bunching at 50 GeV flattop with 200 MHz phase noise. Upper (yellow) trace is beam intensity (DCCT). Next (red) trace is beam peak current monitor signal. Lower (green) trace is phase noise injected (1st quarter is band-pass 2.3–4.2 kHz, while remainder is low-pass 0–4.2 kHz random signal).

Still, other intensity-related effects in the U70 are waiting to be understood and cured.

The shortest bunches available in the machine cannot cross transition loss-free when injected in a dense one-by-one train of > 6–10 bunches. One has to resort to preliminary longitudinal blow-up with the 200 MHz (spill) RF system. Effect of some short-range wakes is suspected.

Transverse coherent motion of proton beam is well cured with the narrow-band low-pass (analog) and wide-band band-pass (digital) beam feedback circuits installed. Still, in the open-loop configuration, one cannot identify the source of an apparent asymmetry between thresholds of vertical and horizontal instabilities. Threshold of vertical instability is by a factor-of-2 higher than that for horizontal motion, while the opposite ratio is expected for the elliptic resistive steel vacuum chamber with 10×5 mm^2 aperture (inner half-axes, horizontal × vertical).

These and other effects are scheduled for future studies.

Crystal Deflectors

These types of beam transverse deflectors are extensively employed for routine technological purposes and in a dedicated R&D program accomplished with the beams of the U70. Ref. [9] reports on details of this activity.

Light-Ion Program

This program advances incrementally, each recent machine run constituting a noticeable step in accomplishing the task.

Acceleration in the U70 of deuterons to a specific kinetic energy 23.6 GeV/u (flattop 8441 Gs) with $5{\cdot}10^{10}$ dpp was reported in Ref. [8] of RuPAC-2010. Since then, the cascade of I100, U1.5, and U70 involved was switched to the carbon-beam mode.

During the run 2010-2, fully stripped ions (nuclei) $^{12}C^{6+}$ were first accelerated to 455.4 MeV/u in the small ring U1.5. Beam intensity varied between $5.3–3.5{\cdot}10^9$ ipp through 26 ms ramp (once in 8 s). The first turns of the C beam around the U70 ring at flat-bottom were committed.

During the run 2011-1, carbon beam (a single bunch) was accelerated in the U70 to the ultimate available energy of 34.1 GeV/u (flattop 12 kGs) with max $5{\cdot}10^9$ ipp (8 s).

During the runs 2011-1, -2, the U70 also operated in a storage-stretcher mode for a 453–455 MeV/u carbon beam at 352–353 Gs flat-bottom. Top beam intensity observed was $5–10{\cdot}10^9$ ipp, which exceeds the design figure of $3{\cdot}10^9$ ipp. New direction for the slow extraction of the intermediate-energy carbon beam via IT#28 and SM#34 inwards the U70 ring was safely beam-tested. In the aftermath, a new BTL#25 is assembled in the Experimental Hall to transfer the carbon beam for applied research.

During the latest run 2011-2, carbon beam was accelerated to 24.1 GeV/u (flattop 8590 Gs) with $5{\cdot}10^9$ ipp (8 s). All the high-energy beam extraction systems available — fast single-turn, slow resonant (including stochastic), slow with a bent Si-crystal deflector — were readily tested with a carbon beam. The carbon beam extracted was transferred through the existing 190 m long BTL#22 to the FODS (a FOcussing Double-arm Spectrometer) experimental facility and detected there. Operational retuning of optics (momentum acceptance) of the BTL#22 allowed to use this beam-line as an 'ad hoc' Fragment Separator yielding the first ever experimental observations of high-energy nuclear-physics events with a 300 GeV (full energy) carbon beam delivered by the U70.

Further physical and technical details of the light-ion acceleration program progress are reported in Ref. [9].

CONCLUSION

Accelerator Complex U70 of IHEP-Protvino is the sole national proton facility running for the fixed-target research in high-energy physics. It is a subject of an ongoing upgrade program affecting the key technological systems and promising still better beam quality. Functionality of the machine for fundamental and applied research is being enhanced with the advent and adoption of its light-ion beam mode.

REFERENCES

[1] S. Ivanov and the U70 staff, Proc. of RUPAC-2008, Zvenigorod, 2008, p. 130–133; Proc. of RUPAC-2010, Protvino, 2010, p. 27–31.
[2] Yu. Antipov et al., Instruments and Experimental Technique, № 3, p. 5–12, 2010.
[3] S. Ivanov et al., Preprint IHEP 2012–11, Protvino, 2012.
[4] O. Lebedev et al, these Proceedings.
[5] O. Piccioni et al., Rev. Sci. Instrum., 26, p. 232–3, 1955; B. Wright et al., Rev. Sci. Instrum., 25, p. 429–31, 1954.
[6] S. Ivanov, O. Lebedev, Preprint IHEP 2012–10, Protvino, 2012.
[7] A, Afonin et al., these Proceedings.
[8] S. Ivanov and the U70 light-ion task team, Proc. of RUPAC-2010, Protvino, 2010, p. 130–132.
[9] S. Ivanov and the U70 staff, these Proceedings.

MULTIPURPOSE RESEARCH COMPLEX BASED ON THE INR HIGH INTENSITY PROTON LINAC

A.Feschenko, M.Grachev, L.V. Kravchuk, V.L.Serov,
Institute For Nuclear Research, Moscow 117312, Russia

Abstract

Scientific Complex based on 600 MeV Proton Linac is in operation at the Institute for Nuclear Research, Troitsk, Moscow and provides the beam for both basic and applied research. At present proton beam with the energy up to 209 MeV and with the average current up to 130 μA is used for three Neutron Sources and Beam Therapy Complex, located in the Experimental Area, as well as for Isotope Production Facility. The status of the Linac and the Experimental Area is presented. Accelerator tuning procedures providing minimization of beam loss are described as well.

INTRODUCTION

INR Accelerator Complex is located in science city Troitsk (Moscow) 20 kilometers to the south-west from Moscow circular road. It includes the high-intensity proton Linac, Experimental Area with three neutron sources and Beam Therapy Complex as well as Isotope Production Facility (IPF). Though the initial name of the Complex was Moscow Meson Factory in the recent years the main activity has been shifted towards neutron studies, isotope production and other researches connected with the above mentioned experimental facilities.

In nineties INR accelerator was the second large high intensity and medium energy linac after LANSCE (former LAMPF) at LANL, Los Alamos, USA. In the last decade two new linacs of this type with improved parameters have been put in operation (SNS and J-PARC) and several more ones are being constructed or designed now. This activity shows the urgency of the researches made at the accelerators of this type and confirms extreme topicality of the INR multi-purposes complex.

LINEAR ACCELERATOR

General Description and Parameters

The detail description of the INR proton Linac is given in [1, 2]. The simplified diagram of the accelerator is shown in Fig. 1. The accelerator consists of proton and H-minus injectors, low energy beam transport lines, 750 keV booster RFQ, 100 MeV drift tube linac (DTL) and 600 MeV coupled cavity linac (CCL, Disk and Washer accelerating structure). There are seven 198.2 MHz RF channels for five DTL tanks and RFQ (including one spare channel) as well as thirty two 991 MHz RF channels for 27 CCL accelerating cavities and one matching cavity (including three spare channels and one channel for equipment tests). Design, obtained and currently available operational Linac parameters are summarized in Table 1.

Table 1: Main accelerator parameters.

Parameter	Design	Obtained	September 2012
Particles	p, H-minus	p, H-minus	p
Energy, MeV	600	502	209
Pulse current, mA	50	16	15
Repetition rate, Hz	100	50	50
Pulse duration, μs	100	200	0.3÷200
Average current, μA	500	150	130

The accelerator is in regular operation since 1993. 102 accelerator runs with total duration of more than 38000 hours have been carried out so far including 63 runs of total duration of 18000 hours within the last decade. The availability of the beam for the users is 80÷90 % of the total beam time.

Main Current Goals

The main goal for the nearest future is improvement of accelerator efficiency. To attain this goal two problems have to be solved. The first one is increasing the beam pulse repetition rate from the current 50 Hz to 100 Hz. The second one is distribution of the beam between IPF and Experimental Facility. To double the beam pulse repetition rate the repetition rate of RF system pulses as well as that of proton injector must be doubled.

The activity on increasing RF pulses repetition rate is in progress for several years, but has been intensified recently [3]. The studies with the aim of increasing proton injector repetition rate are also being conducted. Completion of building of H-minus injector enabled a task to be formulated on simultaneous acceleration of proton and H-minus beams. It is supposed that two beams will be accelerated pulse by pulse each with the rate of 50 Hz.

With the aim of distributing the beam between IPF and Experimental Facility the intermediate beam extraction area (160 MeV) has been upgraded [4]. Instead of the first DC bending magnet (Fig.1) the pulse magnet along with the power supply developed and fabricated in D.V.Efremov Institute (St. Petersburg) [5] has been installed. The tests of the system including the tests with the beam have been done [4]. The maximum frequency of the magnet pulses is 50 Hz so the possibility to direct up to half of the beam pulses to IPF will be implemented.

The pulses directed to the Experimental Area are positioned between the magnet pulses. The DC supply of the magnet is also foreseen thus enabling a full beam to be extracted to IPF.

To improve an ultimate beam current at IPF target the fast beam circular scan installation has been developed and is being fabricated. Scanning frequency equals to 5 kHz which corresponds to one full circle within the 200 μs beam pulse.

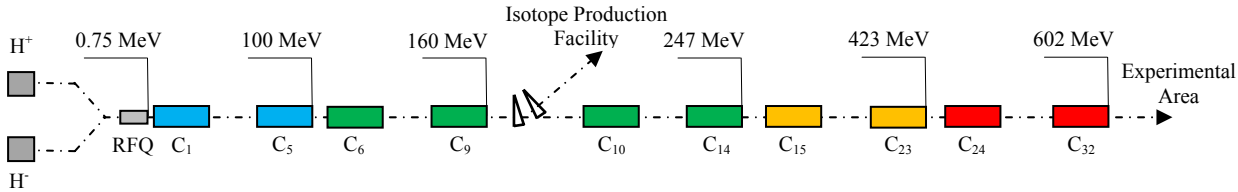

Figure 1: Simplified diagram of the accelerator (C_1÷C_{32} – accelerating cavities). The sectors of the accelerator are marked with different colors (five sectors totally).

One of the problem systems of the accelerator is RF system of DTL linac. The main problems are due to stopping production of grid tubes GI-51A and GI-54A for power amplifier as well as the modulator tube GMI-44A. The activity on replacement the tubes GI-51A and GI-54A by GI-57A and GI-71A correspondingly is in progress for several years. There were doubts if the tandem of two new tubes can provide sufficient RF power for the most powerful RF channel #2. However the doubts disappeared after the tests of the tandem in this channel during several runs of the accelerator [6]. Moreover the manufacturer of the tube GI-71A "S.E.D.-SPb" started its modernization with the aim to increase the gain. We hope that with the modernized tube the difficulties of obtaining higher RF power will become less severe. As for the modulator tube GMI-44A the manufacturer "S.E.D.-SPb" has started to develop a restoration technology. In case of positive result a possibility of restoration of big amount of used tubes in hand will arise.

Available amount of klystrons limited the maximum energy to 502 MeV within the course of accelerator commissioning (Table 1). Now the capabilities of industry to produce the klystrons enable to balance at the level of 209 MeV.

EXPERIMENTAL AREA

Experimental Area is shown in Fig. 2. All the equipment of experimental area is foreseen to work with the beam of 600 MeV but now the power supply system is restricted and enables to work with the energies up to 300 MeV. At present the following facilities are in operation: Spallation neutron source IN-06 with a number of multipurpose instruments, 100-ton spectrometer LNS-100 on slowing down in lead, RADEX facility (a modified beam stop) with neutron guides and stations for time-of-flight spectrometry, Beam Therapy Complex.

Simultaneously with building of H-minus injector the beam separation system was created in Experimental Area. The system is intended for separation of proton and H-minus beams and is based on Lambertson Septum Magnet [7]. When two beams are accelerated simultaneously the system enables to pass the proton beam directly to RADEX facility and to deflect H-minus beam towards Beam Therapy Complex. Formation of beam size is foreseen by inserting a strip foil with a proper central hole in front of the septum magnet. The recharged protons are directed to the beam stop. Recently the line to the Beam Therapy Complex has been equipped with a wedge-shape degrader. The particles lose the energy depending on wedge thickness thus providing fine energy adjustment within the range of 209÷70 MeV.

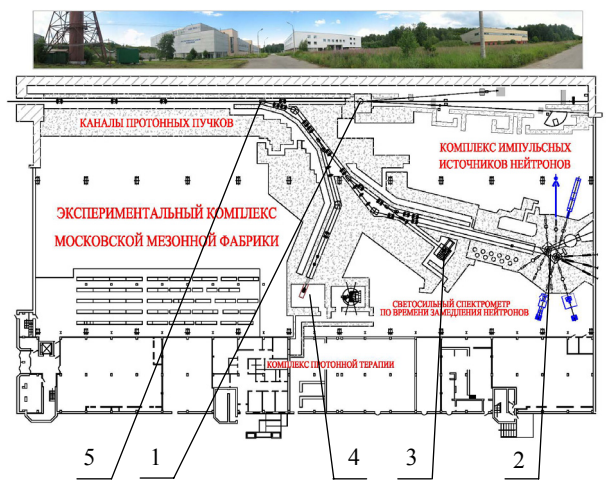

Figure 2: Experimental Area (1 - RADEX facility, 2 - Spallation neutron source IN-06, 3 - LNS-100 spectrometer, 4 – Beam Therapy Complex, 5 – beam separation area).

PECULIARITIES OF ACCELERATOR TUNING

The experience of accelerator operation showed that to implement a high beam intensity and low beam loss mode of operation definite tuning procedure have to be fulfilled. The procedures are related to longitudinal and transverse tuning. Normally the longitudinal tuning is done first.

Longitudinal Tuning

The base of longitudinal tuning is setting the design parameters of amplitudes and phases of RF fields in

accelerating cavities. In DTL linac a phase scan procedure applied for the cavities in series is the main one. The RF phase of the cavity under the test is adjusted within a wide range and the current of the accelerated beam is measured downstream of the cavity. To separate the accelerated particles from non accelerated the degraders of proper thickness are used. In our linac we have one degrader installed at the exit of DTL linac with four plates in series. The thickness of the plates is selected in such a way that the signals from different plates correspond to the intensities of the beam accelerated in different cavities. As an example Fig.3 demonstrates a phase scan curve for the third DTL cavity. The width of the curve depends on the size of the bucket and hence on the amplitude of the accelerating RF field. It is implied that the amplitude is set to the nominal value when the width of the curve equals to the nominal one calculated preliminary. The phase is set to the nominal one by shifting from one of the curve edges by the preliminary calculated value.

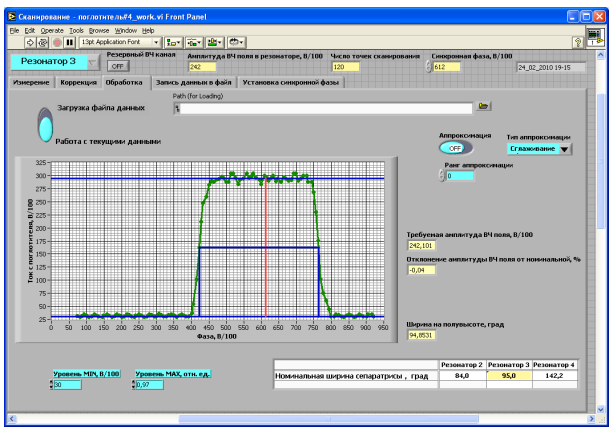

Figure 3: Phase scan results for DTL cavity #3.

To set the phase and the amplitude in the last DTL cavity #5 a dependence of phase difference of the signals induced by the beam in two beam current harmonic monitors installed at the entrance and at the exit of the cavity versus phase is measured (Fig. 4).

Vertical spread of the measured function univocally corresponds to the amplitude of RF field. The phase is set by shifting the phase by the calculated value with respect to the phase position of the vertical middle of the curve.

To check the overall stability of DTL linac the energy at the exit is measured with a time of flight method. Normally the errors can be effectively corrected by fine-tuning the phase of DTL cavity #5 thus compensating the energy errors.

To set the amplitudes and the phases in the cavities of CCL linac (above 100 MeV) the ΔT procedure is used [8,9]. In this procedure the changes of the time of flight through the tuned cavity (Δt_1) and through this cavity plus the subsequent switched off one (Δt_2) are measured when the tuned cavity is turned on and off. The measurements are done for different phases in the tuned cavity in the vicinity of the nominal one. Then the function Δt_1 is plotted versus Δt_2. Figure 5 demonstrated the results of the procedure for CCL cavity #1.

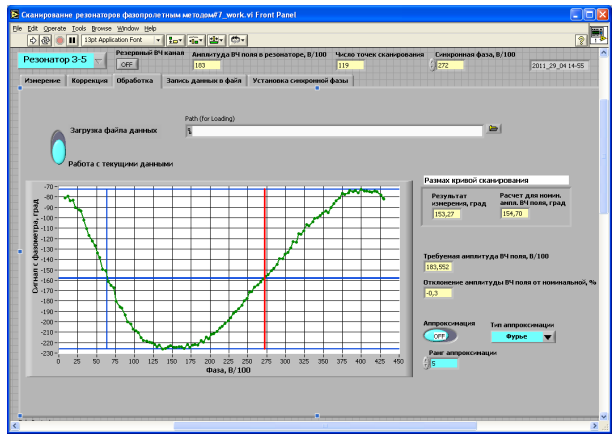

Figure 4: Phase scan results for DTL cavity #5.

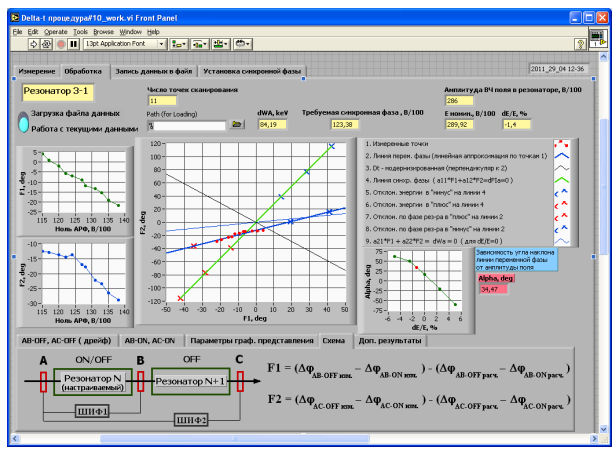

Figure 5: Results of ΔT procedure for CCL cavity #1.

The tilt of the plotted experimental function depends on the amplitude of the accelerating field. Measuring the tilt one can find the amplitude. The position of the function relatively to the plot centre depends on the cavity input energy and input phase shifts with respect to nominal ones. ΔT procedure is a linear one and is valid for small shifts in energy and phase. Preliminary setting of phase is made by observing beam loading versus phase. Normally the centre of the phase area with beam acceleration is a good phase point for starting ΔT procedure. The procedure is used for all the accelerating cavities up to 209 MeV. Setting the phase and the amplitude in the matching cavity located in the intermediate extraction area (160 MeV) is done similarly to DTL cavity #5.

As for RFQ and two buncher cavities their amplitudes and phases are normally fine tuned to obtain a maximum beam current.

Transverse Tuning

Transverse tuning includes beam matching and beam center correction at certain accelerator areas. The first matching and correction is done at the transition area form DTL to CCL. For matching purpose the beam profiles are measured with several wire scanners and

phase ellipses are restored. The profiles are also measured with increased gains of electronics to get information on beam halo. The behavior of beam profiles in time within the beam pulses is also observed. The result of profile measurement is demonstrated in Fig.6.

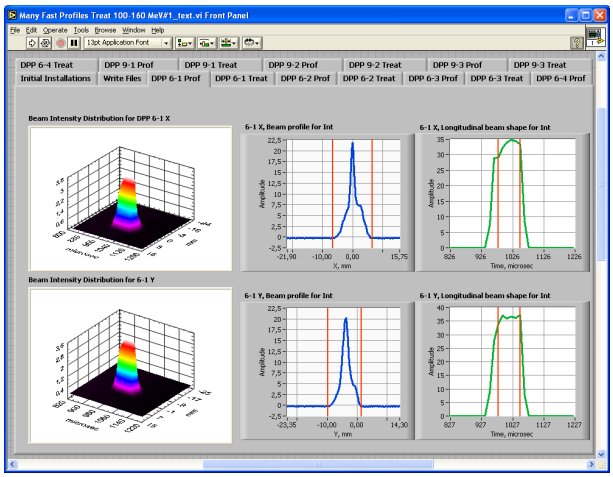

Figure 6: Example of beam profiles at DTL to CCL transition area.

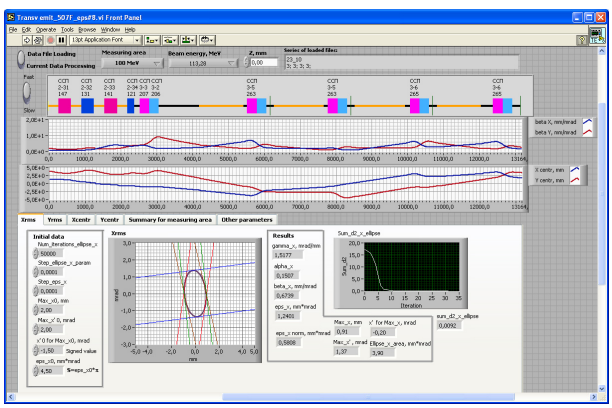

Figure 7: Results of beam profile data treatment.

The parameters of the restored emittance ellipses are used to calculate quadrupole settings in order to match the beam with the subsequent lattice. The variety of settings can be found but the one providing minimum beam size at the matching area is selected. After setting the selected quadrupole parameters one more cycle of measurements is done in order to check the matching results. Figure 7 demonstrates the results of profile data treatment. The lattice, the beam envelopes, the behavior of beam center and the restored emittance ellipse are presented.

Beam centre position correction is done with corrector windings of the quadrupole doublets. Two corrector windings are used for each plane. The first step of the correcting procedure is the measurement of the beam centre positions with several wire scanners. The measured coordinates are transformed to the selected longitudinal position (usually the entrance of the first corrector) and the corresponding point in phase plane is found. Then the correcting currents are calculated to shift the found point to zero after the second corrector. To check the results of correction beam positions are measured one more time. Figure 8 demonstrates the results of correction at the intermediate extraction area. The lattice and the beam centre positions before and after correction are shown.

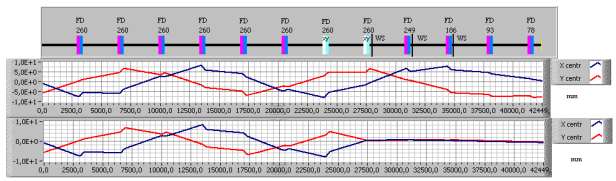

Figure 8: Results of beam correction.

Five areas for matching and correction along the accelerator are foreseen.

There are special procedures for tuning injection lines as well. However their description is outside this report. In majority cases optimization of injection line elements to maximum accelerated current is sufficient.

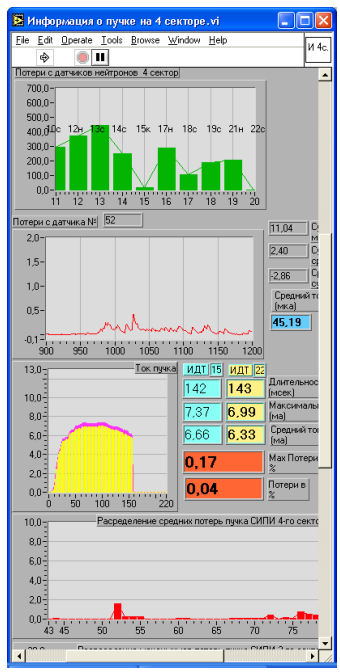

Figure 9: Information on beam losses in accelerator sector #4.

Beam Loss Minimizing

Final tuning of the accelerator is made by the operator, minimum beam loss being a criterion. There are 120 beam loss monitors based on photo-electron multipliers as well as 30 neutron detectors along the accelerator. The information on beam loss available to operator (Fig. 9) includes beam current pulses at the entrance and at the exit of the accelerator sector (Fig. 1), distribution and amount of beam loss along the sector obtained with beam loss monitors and neutron detectors as well as the signals from the loss monitors.

Final stage of accelerator tuning is more art than science and it is impossible to formalize and describe it. It depends on operator experience and preferences.

It should be noted that the minimum beam loss can be obtained without fulfilment of the tuning procedures above described, several sets of accelerator parameters being possible. However the condition thus found appears to be unstable and difficult to maintain for a long period. The experience shows that the stable conditions can be obtained only in case the procedures above described are carried out and the subsequent adjustments are done within the restricted margins.

CONCLUSION

Multi-purpose Scientific Complex based on 600 MeV Proton Linac is in operation at the Institute for Nuclear Research. Permanent modernization of the accelerator and the Experimental Area enables not to only maintain the complex in operational state but also to improve beam parameters and complex capabilities. The existing experimental facilities are the basis for variety of both basic and applied researches.

ACKNOWLEDGMENT

The authors acknowledge the personnel of accelerator division and experimental area division for their contribution to the work.

REFERENCES

[1] L.V.Kravchuk. INR proton Linac operation and applications. Nucl. Instr. and Meth. A 562, (2006), 932-934.
[2] L.V.Kravchuk. Operation and Research Activities at the INR accelerator complex. Proc. of RUPAC2008, pp.137-140.
[3] A.N.Drugakov et al. Investigation of INR Linac DTL RF System Operation at 100 Hz Repetition Rate, MOPPA023, these proceedings.
[4] N.I.Brusova et al. Beam Pulse Separation System of INR Linac, WEPPC003, these proceedings.
[5] B.O. Bolshakov et al. Power Supply System of the Pulse Bending Magnet for the Linear Accelerator Operated at the Moscow Meson Factory, WEPPC034, these proceedings.
[6] A.V. Feschenko et al. Status of INR DTL RF System, MOPPA022, these proceedings.
[7] M.I.Grachev et al. Proton Channel that Provides Simultaneous Independent Operation of a Treatment Room of Proton Therapy and Neutron Sources of the Experimental Complex INR RAS, WEPPC051, these proceedings.
[8] K.R.Crandall and D.A.Swenson. Side Coupled Linac Turn-on Problem. LANL Report MP-3-98, February, 1970.
[9] A.Feschenko et al. Development and Implementation of ΔT procedure for the SNS Linac. Proc. of PAC2005, Knoxville, Tennessee, pp. 3064-3066.

USE OF BENT-CRYSTAL DEFLECTORS TO STEER BEAM IN U-70 ACCELERATOR OF IHEP- STATUS AND PROSPECTS

A.G.Afonin, V.T.Baranov, Yu.A.Chesnokov, V.A. Maisheev,
V.I.Terekhov, I.A.Yazynin, IHEP Protvino, Russia

Abstract

The report presents an overview the results of IHEP activity in the field of study and using bent crystals to steer high-energy proton and ion beam obtained during 2010-2012. The hardware installed to study crystal collimation and extraction is described. A new dedicated beam transfer line was arranged to study the performance of crystals. It has been shown that the crystal deflections developed are capable of sustaining long-term operation to deliver high-energy extracted beams for fixed-target physics. Experience with practical applications of bent crystals are outlined. First results on the extraction

24.1 GeV nucleon carbon ions are also presented.

BEAM EXTRACTION FROM U-70

The method to use bent crystals to extract protons has found the widest practical application on U-70 accelerator of IHEP during more than 20 years.

Different types of extraction schemes with bent crystals and technical equipment are realized now as for extraction so as for experiments to test new crystal devices and to study beam collimation processes.

The location of the stations with bent crystals in U-70 is presented on Table 1.

Table1:Crystal location in U-70.

Crystal station	Si-19 Si-22 Si-106	Si-24	Si - 27	Si-30	Si-84 Si-86
Beam line	8,22,23	2,14	4	8,22.23	absorber

The subscript means the straight section index or the index of a magnet in which the crystal or internal target is installed..

On U-70 three different possibilities to use bent crystals for physics are realized.

1. One way to use bent crystals is to extract proton by crystal directly. In this case we use long crystals which gives the possibility to receive big angles of deflection. We have two station of this type Si-24 and Si-27.

They extract the beams of protons to experimental facilities, which usually work with secondary particle from internal targets. The angles of bending for such deflectors (80-90) mrad and efficiency ~ 10^{-5}.

2. Second way is to use short crystals with small deflection angle.

The small deflection angle (in our case 0.5-2 mrad, it depends on scheme) is sufficient to put the beam into aperture of septum-magnet, which then provide the larger deflection angle need for the extraction

For this purposes we have crystal stations Si-106, Si-19, Si-22 . The length of deflectors 2-5 mm and the efficiency in this case was achieved 85% [1,2].

3. Third way is to split extracted beam by crystal for two directions. For this regime we use Si-30, which is intended to remove a small fraction of a beam (it can be ~ 10^7 protons per cycle) to beam line 8 or 22.

Beam extraction using bent crystals allows simultaneous operation with internal targets. The diagrams of the beam extractions using bent crystals is shown on Fig 1.

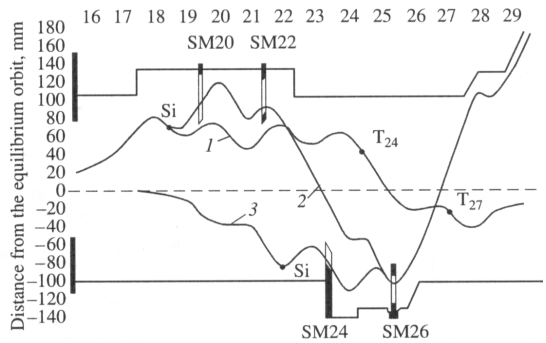

Figure 1. Schematic diagrams of proton beam extraction using bent crystals: (1) the trajectory of circulating beam during its simultaneous guidance onto the crystal in straight section no.19 (Si) and internal target T24 and T27, (2) the trajectory of beam extraction from crystal SS-19 (Si), and (3) the trajectory of beam extraction from crystal Unit 22 (Si).

Since RuPAC-2010, the U-70 complex has been working for four runs in total. Table 2 presents the results of bent crystal extraction during this period.

Table2: The use of slow extraction by bent crystals on U-70 in 2010-2012.

Run of U-70	2-2010	1-2011	2-2011	1-2012
Duration of a run (hours)	744	240	744	288
Crystal extraction (hours)	846	636	672	240

A crystal can extract from 10^6 up to (5-6)* 10^{11} ppp without special cooling technique during hundreds hours without degradation seen. This extraction is a good addition to the slow extraction existing at the U-70 IHEP accelerator, which provided proton beam with intensities of $5*10^{11}$ – 10^{13} particle per pulse. It shows reliable, reproducible and predictable work.

During the runs, all the beam extraction system available in the U-70 were engaged- fast single- turn, slow resonant

(stochastic and classic), internal targets and slow extraction by bent crystal.

Typical picture of cycle flattop utilization presented on Fig.2

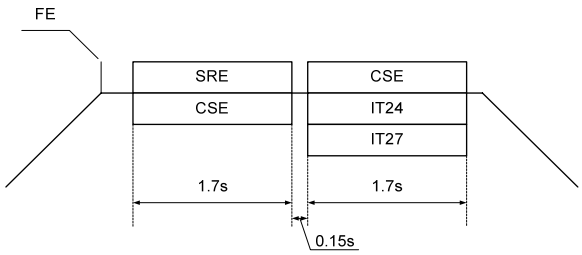

Figure 2. The utilization of the U-70 magnetic cycle flattop.FE- fast extraction, SRE- slow resonant extraction, CSE- slow extraction by crystal, IT- internal target.

EXTRACTION OF CARBON IONS

During last years the program of accelerating light ions in the accelerator complex U-70 is successfully developed..

In spring run of this year the beam of carbon ions was accelerated to kinetic energy 24,1 GeV per nucleon with intensity up to $5*10^9$ nucleon per cycle and then the carbon ions beam was extracted from accelerator in one of external beam line. It was done by all system of extraction- fast, slow resonant and by bent crystal.

In order to extract carbon beam by crystal we have used crystal station Si-22 (Fig.1) and scheme Si 22-24-26-30. It was silicon deflector S-type with dimensions (2*40*0.5) mm^3 (length along the beam, height, thickness) and bending angle ~ 0.9 mrad.

The modeling of carbon ions extraction was performed before of experiment. The results presented on Fig.3

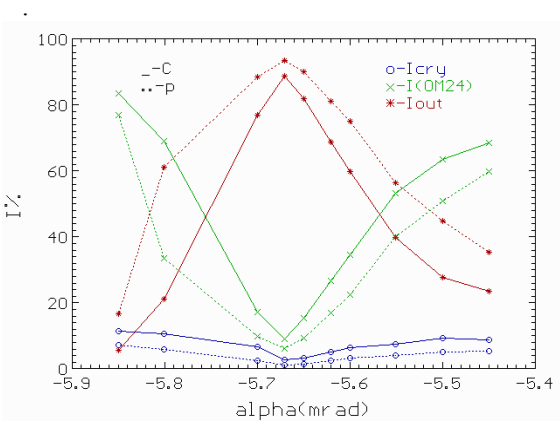

Figure 3. Extracted beam intensity (*) and beam losses (o,x) as a function of the crystal orientation.

The beam of carbon ions was successfully extracted to the beam line №22 and was registered on physical setup FODS.

On Fig.4 one can see the profile of beam in beam transfer line and signal from photomultiplier during extraction process. The efficiency of extraction was defined as 60%.

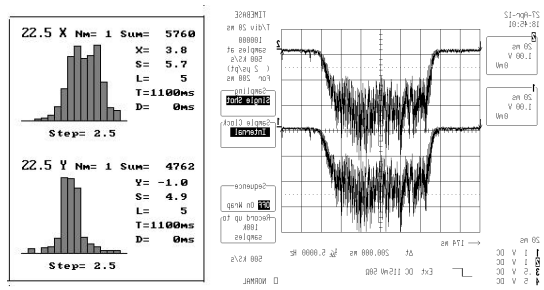

Figure 4. Profile of carbon ions beam (left) and beam spill.

The first results of this experiment should be and will be refined in future sessions of the U-70 operation.

NEW EXPERIMENTS

The novel crystal device for beam focusing was constructed in IHEP. It presents the silicon plate which has been cut out along plane (111). The sizes of a plate are equal x*y*z=1*70*20 mm^3. It was bent in a longitudinal direction by metal holder

Due to anisotropic properties of material of a plate there is a transversal bend which is used for bending and focusing of a beam [3]. Experiment on focusing beam with such device was carried out with 50 GeV proton beam of U-70 IHEP accelerator [4]. The effect of focusing has been registered with the help of nuclear photoemulsions.

The result of calculation and experiment is shown on Fig.5.

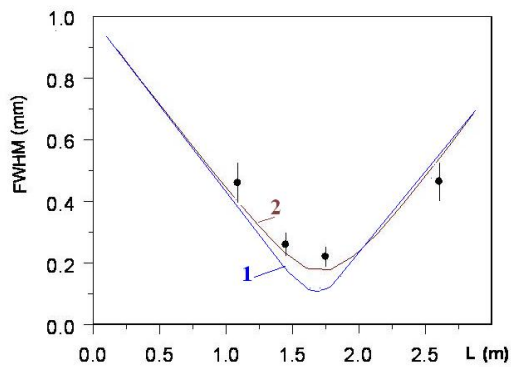

Figure 5: The size of a beam depending on distance from a crystal. Points - experiment. The curve 1 - calculation for transportation of particles in vacuum, the curve 2-calculation for scattering on air and emulsion layers.

Thus, it was evidently presented, as the beam equal on the size to thickness of a crystal (1 mm) was compressed in a line in with width 0.22mm.

The focusing property of the developed device can be applied on the accelerator of high energy to research of low-angular processes. The crystal can be align on a fix target by focusing end face, as shown in Fig.6. Rotating the crystal

around of an axis O, one can deflect the particles from the target and create clean conditions for registration of the necessary particles. Other motive of application of such scheme is reception of a secondary particle beam of high energy by rather simple way.

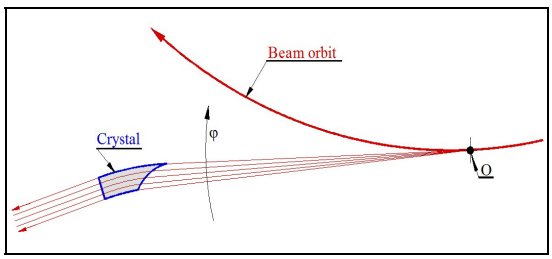

Figure 6: An example of application of a focusing crystal for research of low-angular processes. The same scheme can be a source of a parallel beam of secondary particles.

Recently IHEP group together with employees of several Russian and foreign centers have opened the new physical phenomenon - reflection of high energy protons from the bent atomic planes of silicon crystal [5]. The phenomenon of reflection occurs in wide area of angles and is more effective**,** than usual channeling.

But for real application the increase in angle of reflection in few times is required. Two ways were proposed for this purpose:

- Reflection on a chain of crystals (multiple volume reflection - MVR in sequence of crystals [6].
- Reflection near to an axis in total potential of several skew planes (MVR in one crystal [7]).

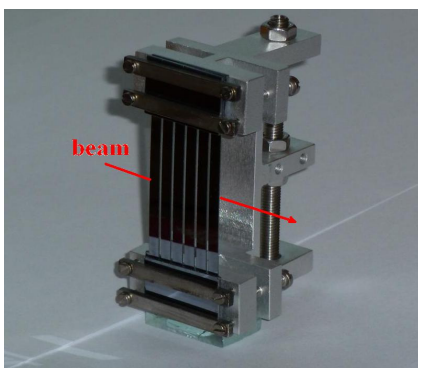

Figure 7: Crystal multistrip structure.

During two last runs we tested amplification of reflection angle due to both effects (multi-crystals and axial enhancement) for improvement of beam collimation scheme in U-70 synchrotron [8]. Multicrystal structure, 6 silicon bent strips (Fig.7), was installed in biaxial goniometer in U-70 circulating beam like a first stage of collimation system.

In experiment reduction of particle losses registered by ionization chambers downstream of collimator was observed during planar crystal rotation and this reduction was increased by vertical rotation (Fig. 8).

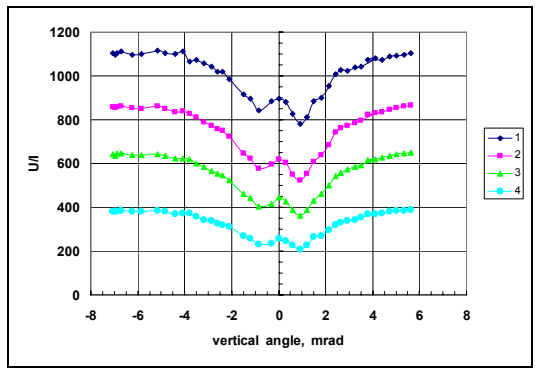

Figure 8: Reduction of particle losses of circulating beam downstream collimator versus vertical crystal rotation.

This effect is confirmed Monte Carlo simulations.

Thus the new method of beam steering was demonstrated, based on reflections of particles in multi-crystal enhanced by axial effect.

CONCLUSION

In this article we briefly describe the IHEP activity, which aims to use the crystals in the practice of extraction system, as well as to explore new aspects of the use of crystals for extraction and collimation. As a part of this topic we work closely with the international collaboration of UA9 at CERN [9] as well as with colleagues in the Ukraine [10]. Our activities are supported by the Directorate of High Energy Physics, the Russian Foundation for Basic Research (grant № 4.45.90.11, 1080 (Russia) and by SFFR grant № F40.2/092 (Ukraine).

REFERENCES

[1] A.G. Afonin et al, Phys. Rev. Lett. 87, 094802 (2001).
[2] A.G. Afonin et al, Physics of Particles and Nuclei, v36, №1, 2005,21-50.
[3] A.G. Afonin, V.T. Baranov, M.K. Bulgakov et al, http://arxiv.org/pdf/1203.5586.pdf.
[4] A.G.Afonin et al, IHEP preprint 2012-15.
[5] W. Scandale et al, PRL98, 154801 (2007).
[6] W. Scandale et al, PRL102, 084801 (2009).
[7] V.V. Tikhomirov Phys. Lett B655 (2007) 217
[8] A.G. Afonin et al, JETP Lett, 2011, v93, p.187
[9] W. Scandale, UA9 Status Report EuCARD-REP-2012-002.
[10] A.G. Afonin, V.T. Baranov, M.K. Bulgakov et al,Phys Rev STAB, 15, 081001, (2012).

NEW DEVELOPMENTS AND A REVIEW OF THE ACCELERATOR FACILITIES AT ITHEMBA LABS

J.L. Conradie, R. Bark, A.H. Botha, J.C. Cornell, M.A. Crombie, J.G. De Villiers, J.L.G. Delsink, H. Du Plessis, J.S. Du Toit, W.D. Duckitt, D.T. Fourie, M.E. Hogan, I.H. Kohler, R.H. McAlister, H.W. Mostert, J.V. Pilcher, P.F. Rohwer, M. Sakildien, R.W. Thomae, M.J. Van Niekerk, P. Van Schalkwyk, J.P. Slabbert, N.P. Stodart, iThemba LABS, Somerset West 7130, South Africa
J. Dietrich, Technische Universitaet Dortmund, Germany
M. Poggi, INFN Laboratori Nazionali di Legnaro, Viale dell'Universita' 2, 35020, Legnaro, Padova, Italy

Abstract

iThemba LABS is a multi-disciplinary research facility that provides accelerator-based facilities for physical, biomedical and material sciences, treatment of cancer patients with neutrons and protons and the production of radioisotopes and radiopharmaceuticals. The successful utilization of beam diagnostic equipment is critical and essential for the effective running of such a facility and will be discussed in more detail. The current status of the facility and future projects, which entail a radioactive-ion beam project as well as a dedicated facility for proton therapy, will also be discussed.

INTRODUCTION

At iThemba LABS proton beams are accelerated with a K=8 injector cyclotron (SPC1) for injection into a K=200 separated sector cyclotron (SSC) [1]. Production of radioisotopes and neutron therapy is done at 66 MeV and a 200-MeV beam is used for proton therapy. For radioisotope production a beam current varying from 80 to 300 μA is used depending on the target material. Low intensity beams of light and heavy ions and polarized protons, pre-accelerated in a second injector cyclotron (SPC2) with K=11, are available for nuclear physics research.

During the past several years extensive development work has been done on the accelerators to increase the beam intensity for radioisotope production. Flat-top acceleration systems were installed in both the injector SPC1 and the SSC which led to a threefold increase in beam intensity for radioisotope production [2]. The increase in beam intensity also necessitated the development of beam diagnostics that can handle the high beam intensity.

OPERATING STATISTICS

The performance of the iThemba LABS facility was outstanding during the 2011 calendar year. The unscheduled interruptions to operations amounted to a meagre 4.8% of the scheduled beam time, down from 7.3% the year before.

Fig. 1 shows the beam outages per failure category for the calendar year 2011. The bulk of the beam outages in 2011 were caused by RF interruptions, amounting to 25%. Despite this, the beam time loss to the user communities as a result of RF interruptions shows a very encouraging decline. In 2010, the beam outages as a result of the RF systems amounted to 224 hours and in 2011 this figure decreased to only 98 hours. This significant drop in interruptions can largely be ascribed to a pro-active approach to maintenance. As part of this approach, a number of water-cooled components in both the 150-kW amplifiers were replaced and ICs on various PCB boards in the amplifiers were resoldered to remove dry joints after 28 years of operation. These steps greatly contributed to the reduced beam time loss as a result of RF interruptions.

Another major interruption that plagued the operations at the facility in 2011 was power failures. In 2011, power failures resulted in a beam time loss of 40 hours, which was significantly lower than the 60 hours of beam time loss it caused the previous year. This beam time loss is mostly caused by power dips, which are brief interruptions of power to the facility. To lessen the impact of such power dips, iThemba LABS has invested in a 4-MW Uninterrupted Power Supply (UPS). The UPS sustains power when the externally supplied power falls away. However for certain beam energies, power cannot be delivered to all equipment by the UPS. Developments are underway to improve this situation.

Other contributions to operational interruptions were caused by water leaks interrupting the vacuum, servicing and tuning of the ion sources, and problems with cooling water and power supplies.

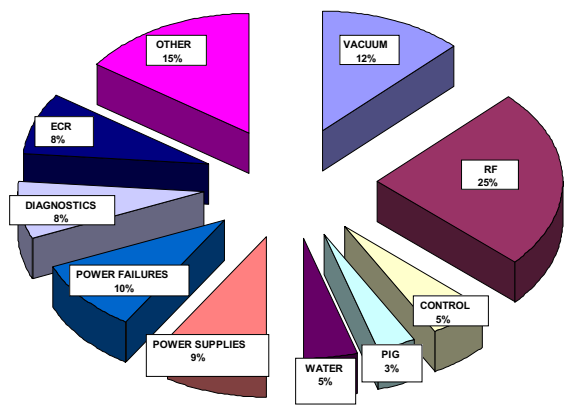

Figure 1: Beam outages per failure category in 2011.

SSC NON-DESTRUCTIVE BEAM PHASE PROBE MEASUREMENT SYSTEM

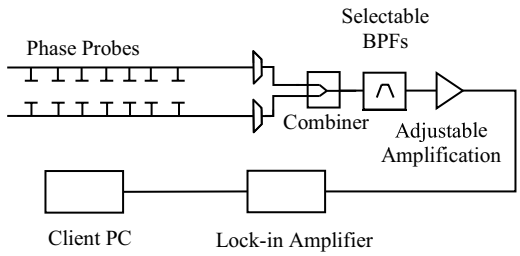

Figure 2: A block diagram of the SSC non-destructive beam phase probe measurement system.

A non-destructive beam phase probe consisting of 21 probes, which spans from the injection radius to the extraction radius, has been installed into the SSC. Each probe consists of two double-shielded electrodes, symmetrically arranged with respect to the median plane. The hardware and software control of the system has been completed. A high level block diagram is shown in Fig. 2.

Each of the upper and lower plates of the phase probes can be selectively multiplexed to a single output port. The signals are then combined. This reduces the unwanted RF pickup in the system. The second harmonic of the beam packet was chosen (for spectral purity reasons) to extract amplitude and phase measurements. The second harmonic is filtered using selectable band-pass filters. The bank of 7^{th}-order band-pass filters comprises thirteen 4-MHz band-pass filters, each with a 1-MHz overlap. The centre frequencies of the filters are evenly spaced from 16 MHz to 52 MHz. Each of the filters is designed to reject the fundamental and higher order harmonics by 60 dB. The signal is then passed through an adjustable amplification unit, with 0–60dB amplification in steps of 20 dB.

Amplitude and phase information of the signal is extracted using a Stanford Research Systems SR844 lock-in amplifier. A LabVIEW interface to the lock-in amplifier, as well as the control hardware for the system has been developed. The LabVIEW client scans through the 21 probes and plots the amplitude and phase of the second harmonic.

The phase information of the beam from the 21 probes is used to isochronize the magnetic field of the SSC.

DIAGNOSTICS

High Intensity Beamstop (Faraday Cup)

A pneumatically operated remote-controlled beamstop, Fig. 3, is used to accurately measure beam current of the extracted beam when optimising the beam transmission through the SSC at high beam intensities. The beamstop has a length of 660 mm and a 120 mm square aperture. It was designed for a 50-kW beam of 66 MeV protons, provided that the beam diameter is not less than 35 mm. For a beam diameter of 10 mm the maximum allowable beam power is 32 kW. The main parts of the beamstop are two 600 mm long water-cooled copper blocks mounted at an angle with respect to each other. Insulated electrodes around the entrance of the beamstop provide current measurements that are used for interlocking in case of beam mis-alignment. The metre-long vacuum chamber of the beamstop is surrounded with a 50 mm thick lead shield to reduce radiation exposure to staff.

Beam Position and Beam Intensity Monitoring

Significant efforts have been made to develop non-destructive beam diagnostic equipment. A beam position monitoring (BPM) system, making use of four-segment capacitive pickup probes, was developed and put into operation to provide beam position data along the injection and the high-energy beam lines and has become an indispensable diagnostic tool for medium- and high-intensity operation [3]. Ionisation chambers mounted around the beam pipes are used as stray-beam detectors.

It is essential that the beam current is monitored continuously during target bombardment at high intensities. Capacitive probes and digital signal processing provide the cheapest and most accurate solution to non-destructive current measurement [4].

High Intensity Beam Scanner

The first element used for splitting the high intensity 66-MeV proton beam for isotope production on two

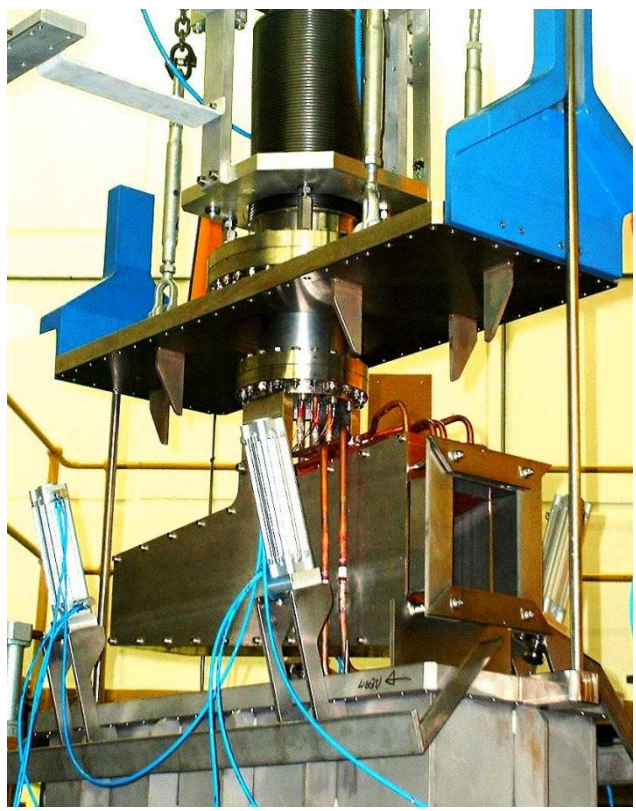

Figure 3: The 50-kW beamstop lifted out of its vacuum chamber; the positioning cylinder is mounted on the lid of the vacuum chamber.

targets simultaneously is an electrostatic channel [5]. In order to position this element in such a way that the beam is split in the right proportions and to minimise beam loss on the septum, two scanners were installed in front of and behind the channel, respectively. On command, a single sweep of the beam is executed, and the profiles of the beam at these positions are displayed. The single sweep prevents the tantalum scanner finger from being exposed to the beam for an extended time, which would result in destruction by melting.

Non-destructive Beam Profile Monitors

Beam diagnostic devices that measure the beam profile and position by registering electrons or ions produced by the interaction between the beam particles and the residual-gas atoms are already in practical use. Non-destructive, two-dimensional beam profile measurements are achieved by measuring these secondary particles, which are accelerated in an electrostatic field towards micro-channel plates (MCP) for signal amplification and processing. One-dimensional residual-gas beam profile monitors are already used successfully but space limitations and the need to measure both dimensions of the beam at the same location, initiated an investigation of two-dimensional systems. Prototypes of these diagnostic devices have been produced and successfully tested; they still need to be developed further before being implemented [6].

Other devices use the light emitted by beam excited residual-gas atoms for these measurements. The light can be focused with a lens onto a photomultiplier (PMT) array. From the signals the beam position and profile can be reconstructed. A prototype device has been installed in the beam lines of iThemba LABS to illustrate the principle and feasibility [7]. The system is in use and we plan to produce a few more of these monitors.

PROGRESS IN THE CONVERSION OF THE IN-HOUSE DEVELOPED CONTROL SYSTEM TO EPICS AND RELATED TECHNOLOGIES

The current iThemba LABS control system is based on a LAN of PCs running OS/2, using C-code and hardware interfacing developed in-house consisting of elderly CAMAC and locally manufactured SABUS modules.

It was decided not to re-invent another in-house system and rather to adopt the now widely used EPICS tool-kit for the many reasons that others have considered previously.

The control system consists of about 4000 devices resulting in approximately 40000 process variables. To date we have moved about 40% of these variables onto EPICS IOCs running the UBUNTU Linux distribution (1004 and 1204 LTS) on low-cost PCs. We are keeping the existing SABUS crates of the previous system and are busy replacing the CAMAC crates with new SABUS cards and crates designed in-house. The in-house card design is challenging at times but does buy us independence from manufacturer changes and their lack of longevity. We have found that the EPICS platform and Channel Access network protocol has proven to be stable and programming at the record layer very useful. By joining with the EPICS community we have saved considerable time in not having to develop everything ourselves. We are also extending Linux and EPICS into the embedded on-circuit-board environment.

ION SOURCE DEVELOPMENT

iThemba LABS operates two Electron Cyclotron Resonance Ion Sources (ECRISs). ECRIS4, which was originally built by GANIL for the Hahn Meitner Institute [8, 9], delivers beams from gases and fluids. Typical intensities and charge states for argon are: 25, 6 and 3 eμA for Ar^{11+}, Ar^{13+} and Ar^{14+}, respectively. Since 2011 a second ECRIS, the GTS2, which is based on the design of the Grenoble Test Source [10] has been installed. The source is connected to the injection beam line via a 104° bending-magnet. This set-up of the beam lines in the ECRIS vault with the new diagnostic beam line for the GTS2 source allows simultaneous operation of both sources, i.e. the required beam for cyclotron acceleration will be delivered from one source, while the second source can be used for beam development. Recently, in the framework of our collaboration with the ion source group at CERN, experiments with the GTS2 source have been performed for the production and optimization of Ar^{11+}. In CW operation a stable current of 90 eμA of Ar^{11+} ions was measured which was increased, for pulsed operation of the source with a duty cycle of 50%, to 110 eμA. In the afterglow mode, Ar^{11+} ion currents of 240 eμA with a pulse width of approximately 2.5 ms were obtained. The layout of the two sources and the beam lines is shown in Fig. 4.

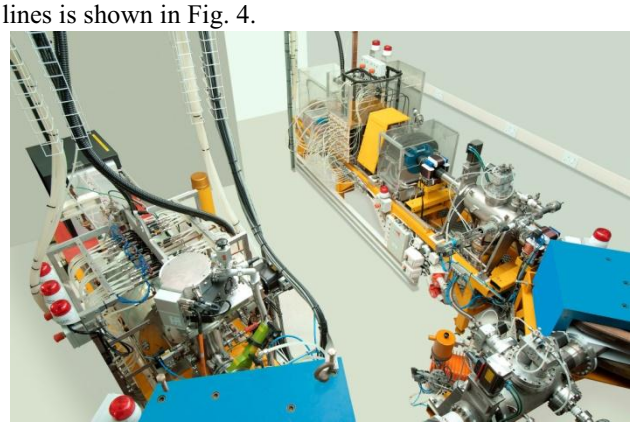

Figure 4: The GTS2 (left) and the ECRIS4 (right) ion sources and sections of the beam line.

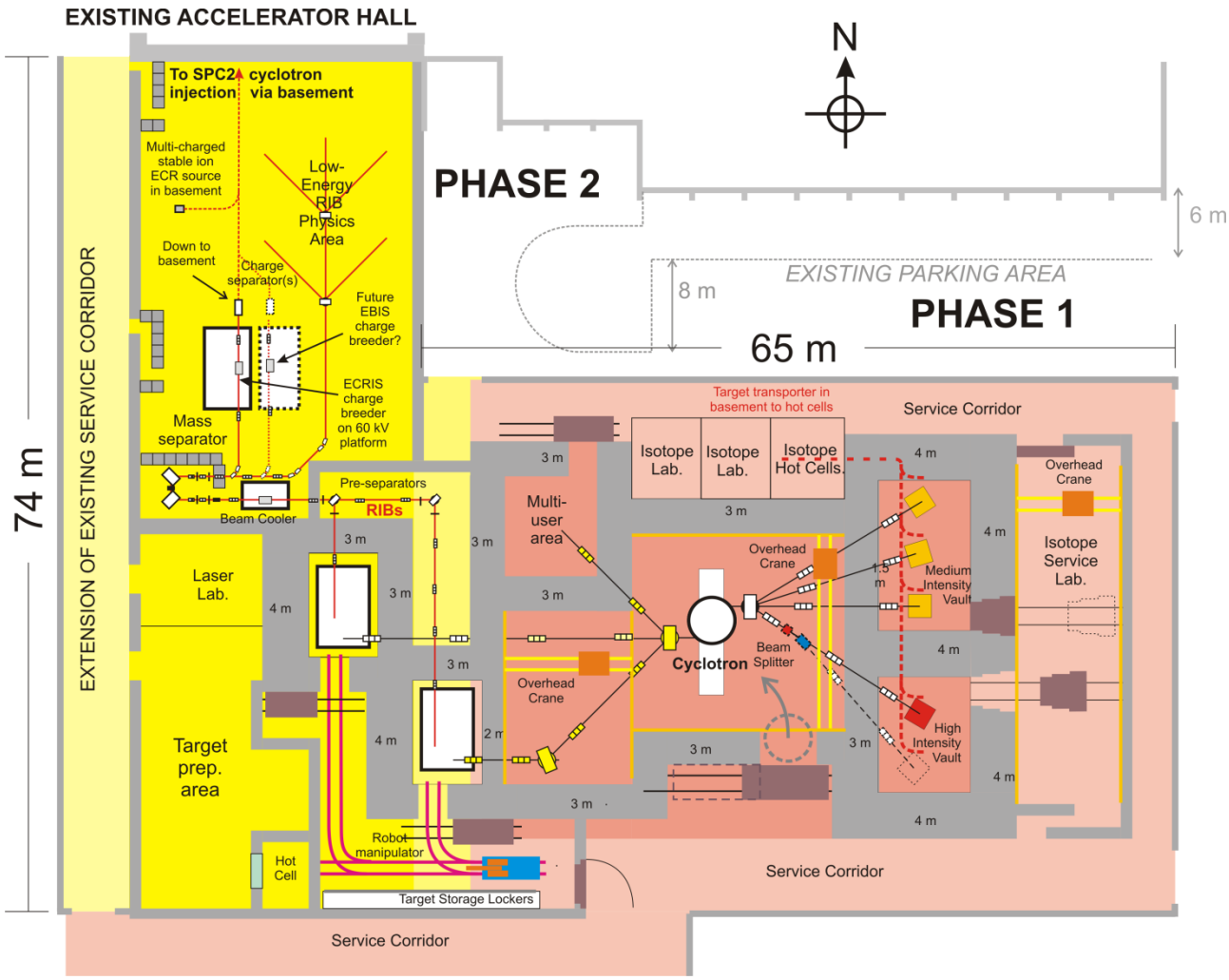

Figure 5: Schematic diagram of the proposed new RIB facility, showing Phase 1 (pink) and Phase 2 (yellow). Darker shades indicate basement areas. Radioactive-ion beams will also be post-accelerated via the SPC2 injector and the SSC (not shown) in the existing Accelerator Hall, indicated at the top left of the diagram.

Since 1992 iThemba LABS has operated an atomic beam source for the production of nuclear spin-polarized protons. We plan to exchange the existing electron ionizer with an ECR ionizer which will result in a reduction of the emittance of the extracted beam and will therefore allow higher beam transmission through the injector cyclotron.

RADIOACTIVE-ION BEAM FACILITY

A new proposal has recently been compiled for a radioactive-ion beam (RIB) facility at iThemba LABS. This project is based on a new, commercially-available, 70-MeV H^- cyclotron, with two beams of protons extracted, one for RIB production and another for the production of medical radioisotopes for local hospitals and for export. The proposal has still to be submitted for consideration by the relevant Government Department. It would involve considerable new construction of buildings, as indicated in Fig. 5. A new experimental area for both nuclear physics (with a large-acceptance spectrometer) and for materials science will be built as an extension to the north end of the existing Accelerator Hall.

Phase 1: Radioisotope Production

The first phase would see the construction of the cyclotron vault and two heavily-shielded concrete vaults with several stations for production of radioisotopes.

Phase 2: RIB Production

The second phase would include construction of the shielded vaults for RIB production, as well as an extension to the existing Accelerator Hall, in which low-energy physics will be possible with un-accelerated RIBs. This hall will also house an RFQ beam cooler, high-resolution mass-spectrometer, with a charge-breeder in the basement close to the existing SPC2 injector cyclotron.

Finally, the high charge-state RIBs will be injected into SPC2, and subsequently into the SSC for acceleration to higher energies. Provision will also be made for

additional experimental areas at the north end of the existing Accelerator Hall, in which devices such as a large-acceptance spectrometer can be installed. The RIBs will be used for experiments in both nuclear physics and materials science.

This project is estimated to cost almost 1 billion rand (about 118 million US dollars, or 94 million euros) and construction will extend over an 8-year period, depending on the rate of financing.

DEDICATED PROTON THERAPY CENTRE

The current utilization of the iThemba LABS cyclotrons permits proton therapy only on Mondays and Fridays and treating with a fixed horizontal beam. These limiting factors prevent the implementation of fully fractionated treatments to a wide variety of cancers. Consequently, iThemba LABS cannot accommodate all the patients that could potentially benefit from such treatment. The proton therapy facility at iThemba LABS was designed mainly for treatment above the clavicle, including lesions in the brain, inter-cranial and base-of-skull lesions [11].

Some 12 years ago a centre for dedicated proton therapy, with fully fractionated treatments using multiple treatment rooms was proposed, but further progress was extremely slow, mainly due to the cost implications of such a facility. The proton therapy centre will be based on an accelerator with a maximum energy of about 250 MeV. The beam from the accelerator will be delivered to treatment vaults with isocentric gantries and fixed horizontal and near vertical beam lines. In this proposal the therapy centre would have been situated at iThemba LABS at Faure near Cape Town.

During the past year there was renewed interaction regarding this proposal between the Department of Health, Department of Education and the Department of Science and Technology, with iThemba LABS part of the latter. From one such strategic discussion it emanated that the proposed proton therapy centre should rather be an integral part of the Department of Health, with iThemba LABS providing the technical support for the project. Such an allocation to the Department of Health will allow the freedom to have the facility at any hospital that already has an infrastructure for oncology, medical imaging and supporting services for radiotherapy patients.

At present there are high-level discussions between the different Government Departments to ensure rapid progress with this project.

GREEN INITIATIVES AND ALTERNATIVE ENERGY

Proposal for a Thermal Storage System for iThemba LABS

The rising electricity demand at the facility and the recent announced tariff increases, forced iThemba LABS to consider a fresh approach in handling these realities.

The cooling facility is the single item with the highest demand (1.5 MW). The solution is to use a Thermal Storage System (TSS). One hundred thousand kg of ice is to be produced during the cooler night temperatures when the cost of electricity is low. The ice is to be melted in the cooling process during hotter day-time when tariffs are high. The more even demand over 24 hours plus the lower power usage will contribute substantially to a lower carbon footprint.

Solar Voltaic Panels - Integration with the Un-interruptible Power Supply

At iThemba LABS the supply from the UPS is isolated from the national electricity supplier. The UPS is fortunately an ideal interface for feeding solar energy into the local grid. This eliminates the need for a solar grid inverter and makes it 25% more economical. The change to solar support can be made modular, as strings of 34 PV panels (80W each) are connected in series to deliver the appropriate voltage. Additional strings can be added in parallel to increase capacity. A pilot installation will be installed soon at a cost of about R100 000.

REFERENCES

[1] A.H. Botha et al., “Commissioning of the NAC Separated-Sector Cyclotron”, Cyclotrons’86, Tokyo, October 1986, p. 9.

[2] JL Conradie et al., “Current Status and Future Projects of the iThemba LABS Cyclotron Facilities” Proceedings of cyclotrons 2010, Lanzhou, China, p.43

[3] J. Dietrich et al., “Beam Position Monitor Development for iThemba LABS Cyclotron Beam Lines”, EPAC’2004, Lucerne, July 2004, p. 2589.

[4] Z. Kormány et al., “Development of Non-Destructive Beam Current Measurement for the iThemba LABS Cyclotrons”, EPAC’2008, Genoa, June 2008

[5] J.L. Conradie et al., “Improvements to the iThemba LABS Cyclotron Facilities”, Proceedings Conference of Cyclotrons and Their Applications 2007, Giardini Naseas, Italy, 2007, p. 140.

[6] M. Poggi et al., “Two-dimensional Ionization Beam Profile Measurement”, DIPAC 2009, Basel, Switzerland, May 2009, p.384.

[7] J. Dietrich et al, “Non-Destructive Beam Position and Profile Measurements Using Light Emitted by Residual Gas in a Cyclotron Beam Line”, EPAC’2008, Genoa, June 2008

[8] P. Sortais, Nucl. Instr. and Meth. B98, 1995, p. 508.

[9] H. Waldmann and B. Martin, Nucl. Instr. and Meth. B98, 1995, p. 532.

[10] D. Hitz, D. Cormier, J.M. Mathonnet, Proceedings of the EPAC’02, Paris, June 2002, p. 1718.

[11] D.T.L. Jones, “Nuclear Particle Therapy at the South African National Accelerator Centre”, Proc. Int. Symp. on Utilizaton of Accelerators, São Paulo, Brazil, 2001, IAEA-CSP-16/CD, IAEA, Vienna, p. 2003.

THE STATUS OF THE SARAF PHASE-I LINAC

L. Weissman*, D. Berkovits, A. Arenshtam, Y. Ben-Aliz, Y. Buzaglo, O. Dudovitch, Y. Eisen, I. Eliahu, G. Feinberg, I. Fishman, I. Gavish, I. Gertz, A. Grin, S. Halfon, D. Har-Even, Y. F. Haruvy, D. Hirschmann, T. Hirsh, Z. Horovitz, B. Keizer, D. Kijel, A. Kreisel, G. Lempert, Y. Luner, I. Mardor, A. Perry, E. Reinfeld, J. Rodnizki, G. Shimel, A. Shor, I. Silverman, E. Zemach, Soreq NRC, Yavne 81800 Israel

Abstract

Phase I of the Soreq Applied Research Accelerator Facility - SARAF is under operation at the Soreq Nuclear Research Center. The status of Phase I main components is reported as well as the beam operation experience accumulated in the recent months. The latter include acceleration of a 1 mA CW protons beam up to 3.9 MeV and 1 mA pulsed, duty cycle of few %, deuterons beam up to 4.7 MeV. Recent and future improvements in the current facility are discussed.

INTRODUCTION

Phase I of SARAF [1] consists of a 20 keV/u ECR Ion Source (EIS), a Low Energy Beam Transport (LEBT) section, a 4-rod Radio Frequency Quadrupole (RFQ) injector, a Medium Energy (1.5 MeV/u) Beam Transport (MEBT) section, a Prototype Superconducting Module (PSM), a Diagnostic plate (D-plate), beam dumps (BD) and temporary beam line (Fig. 1).

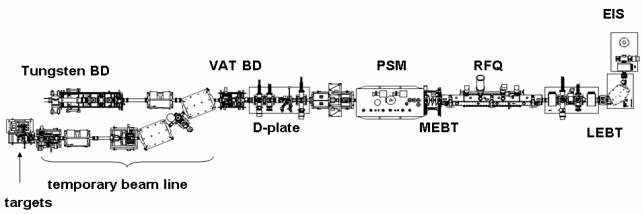

Figure 1. Layout of SARAF Phase I and the temporary beam line.

According to Phase I design specifications; SARAF superconducting linear RF accelerator should yield 2 mA CW beams of protons and deuterons, at energies up to 4 and 5 MeV, respectively. These specifications have not been achieved yet. Nonetheless, during the last two years, alongside with continuous development of the facility, the accelerator has been operated extensively at each opportunity and significant new experience in beam operations has been accumulated.

In the current proceeding we report the accelerator status, improvements of the accelerator subsystems, as well as experience in beam operations that has been accumulated since the last reports [1,2].

* Corresponding author: weissman@soreq.gov.il

STATUS OF MAIN COMPONENTS

EIS/LEBT

The SARAF ECR ion source has been in operation during six years effectively without any maintenance. We experienced two failures connected to the magnetron supply which were promptly resolved. The source could provide up to 6 mA beams of proton or deuteron, in DC or pulsed mode, at the RFQ entrance. The latter mode is used for tuning the accelerator and for beam line optics. The performance of the EIS/LEBT system has been previously reported in detail ([2] and references therein).

First experience with the slow LEBT chopper and plans regarding the fast LEBT chopper are discussed in [3]. Introduction of the chopper would allow for more flexible working range of the beam duty cycle and also allow abandoning pulsed operation of the ion source magnetron.

Reduction of the beam transmission through RFQ at higher LEBT current [2] is still one of the important unresolved issues. It is difficult to explain this reduction without an assumption that the emittance at the RFQ entrance is significantly larger than the value measured upstream the RFQ. . Alternatively, it might be possible that emittance measurements performed with a slit/wire apparatus are dominated by systematic errors which are not yet fully understood. We have performed several measurements aiming at understanding the correlation between the beam emittance in the LEBT and the transmission through the RFQ, as well as attempts to understand the degree of beam neutralization in the LEBT region [4,5]. Further studies are currently in progress.

An additional new water cooled beam-blocker/ collimator has been installed recently in the LEBT, just in front of the RFQ entrance. Installation of this element allows for separate operation of the EIS/LEBT system regardless of the status of the downstream elements.

Increase of hydrogen partial pressure in the RFQ and MEBT was observed when the ion source was operated. To resolve the problem of hydrogen diffusion along the accelerator, hydrogen pumping in the EIS and LEBT sections will be upgraded in the near future.

RFQ/MEBT

The SARAF RFQ is a 176 MHz ~3.8 meter four-rod CW RFQ. The details on the RFQ can be found in [6].

The RFQ can be readily operated at the voltage and power required for a CW proton beams (~60 kW/32 kV). However, the main challenge in this RFQ is to condition it for the range of 250-260 kW (65 kV voltage), required for CW deuteron operation. Several RF conditioning campaigns have been carried out during 2007-2010. However, despite these extensive experimental campaigns, we have not succeeded to bring the device to the level needed for CW deuteron operation.

Since that time we have focused on proton beam operation and limited deuteron beam operation (a few per cent duty cycle). No RFQ conditioning campaign was performed since summer 2010.

During the previous conditioning campaigns, several technical drawbacks in the RFQ design were encountered, that hinder the high power operation. Some of these problems and the corresponding technical modifications were described in [2,7].

A few hundred Viton O-rings are utilized for vacuum sealing between the RFQ body and tubes delivering cooling water for the electrodes. Some of these O-rings were found to be damaged or even destroyed during the RFQ conditioning, as a result of RF field penetration into these regions and, hence, one may expect poor vacuum in these regions. Early in 2012, new flanges were installed in the RFQ. In these new flanges, the RF connection between the water tubes and the RFQ body has been improved at the vicinity of the Viton seals.

This improvement as well as other modifications [2,7] give rise to some optimism on improving RFQ status. However, if the future conditioning campaign will not meet our expectations, options for major modification of the rods structure or even replacement of the entire RFQ should be considered.

Five x-ray detectors were installed in 2011 at viewports positions along the RFQ barrel. The initial objective of installing these detectors was monitoring x-ray flux at various positions of the RFQ during the conditioning. During operation of intense beams it has been noticed that the x-ray detector placed approximately 70 cm downstream the RFQ entrance is sensitive to the beam loss. According to the simulations, beam losses take place primarily in that area. Minimization of the radiation dose rate measured in this detector allows for moderate improving of the RFQ transmission.

New water cooled collimator and beam blocker were installed in the MEBT chamber just in front of the PSM. The collimator works as a beam scrapper and is used for minimizing the interactions of beam tails with cryogenic surfaces. The beam blocker allows for an independent operation of the accelerator's injector, regardless of the status of the cryogenic linac. The partial hydrogen pressure rises significantly in the MEBT region when an intense beam is introduced therein. In the near future the hydrogen pumping in the MEBT section will be significantly upgraded to overcome this hurdle.

PSM

The PSM module includes six $\beta = 0.09$ Half Wave Resonators (HWR) made of bulk Nb and three superconductive solenoids [8]. The SARAF HWRs were found to be sensitive to fluctuations in the Liquid He (LiHe) pressure (60 Hz/mbar compared to designed value 15 Hz/mbar). The ±1.5 mbar pressure variation at the SARAF cryogenic system is manifested by frequency detuning that easily exceeds the cavities loaded bandwidth of 130 Hz. This detuning brings forth challenging demands on the cavities' tuners. These tuners include a stepper motor for coarse tuning and a piezo electric actuator (Pst150 [9]) for fine tuning. In 2009, a dramatic reduction of the piezo range was observed; leading to the replacement of the piezo devices by modified ones [10]. In 2011 the piezo tuners suffered once again from significant reduction of the tuning ranges. During the winter maintenance period, the tuners were replaced by another type of piezo activators (Pst1000 [10]), which operates at higher voltage and have superior mechanical strength. So far, no deterioration of the tuning range has been observed with the new activators.

In 2011, the 2kW RF solid state amplifiers [11] were replaced by 4 kW ones. The latter were designed and built in-house [12]. The operation of cavities with new power suppliers has proven to be more stable, since the higher available power provides a better compensation capability against detuning.

After improving the tuners and RF amplifiers, the remaining warming of the RF coupler has become the main limiting factor in operating the accelerator at high fields. The phenomena of the warming couplers has been recognized earlier [2] but not yet resolved. Thus, we are compelled to reduce the field in the 2nd, 3^{d} and 6th cavities in order to keep the external coupler's temperature below 120 K during long operation. An example of the tuning used for 3.9 MeV is shown in Table I. It is noteworthy that no significant warming is observed at the 5th cavity coupler. This cavity could be operated at a nominal voltage value, just before onset of x-ray emission. Solving the problem of couplers warming will allow one to comfortably operate the PSM at beam energies of 4.5 and 5.5 MeV, for protons and deuterons, respectively.

Table 1. The resonators parameters used for CW proton beam operation. Nominal HWR voltage value is 840 kV.

HWR #	Voltage (kV)	Eacc (MV/m)	Phase (deg)	limiting factor
1	230	1.5	-90	Used for bunching
2	460	3.1	+30	Warming coupler
3	460	3.1	-30	Warming coupler
4	720	4.8	-30	Warming coupler
5	830	5.5	-20	x-ray emission
6	425	2.8	0	Warming coupler

BEAM OPERATION

Several experiments, including beam-on-target ones, have been performed at SARAF with proton and deuteron beams of various beam energy and intensities.

Proton beams at the highest available energy of ~3.5-3.9 MeV were mainly used for the tests of thin (20-30 μm) foil targets cooled by liquid metal [13]. Targets of such types will be used in the future for producing of radiopharmaceuticals isotopes, which will eventually be a major activity at the facility. The maximum current that was delivered to these targets was about 0.3 mA. The thin foil targets were delicate and there were several incidents of target-foils being damaged. Following the insight gained from the first experiments, numerous improvements of the target arrangement and beam diagnostics quality were implemented. We expect a significant progress at this arena in the near future.

Another important direction for the extended future will be production of strong neutron sources by impinging an intense proton beam on the Liquid Lithium Target (LiLiT [14]). Choosing beam energy just above of the ^{7}Li(p,n) reaction threshold (1.880 MeV) allows for producing neutrons with an energy spectrum similar to that of the neutron spectrum in the stellar environment (kT~25 keV). As a first step in that direction, several tests were performed with evaporated LiF targets. The objectives for these tests were accurate measurements of the beam properties (energy and spread), study of the obtained neutron spectra and gaining experience with neutron activation methods. Accurately determining the beam properties is critical for producing a valid astrophysical neutron source. Monitoring of radiation yields from resonance or threshold nuclear reactions while scanning the beam energy have proven to be a valuable method for determining or calibrating the beam energy and spread.

The production of intense high-energy neutrons sources with deuteron beams is another important objective of the SARAF project. Such intense sources will be utilized to produce radioactive beams for multi-disciplinary fundamental research and applications. The first step in this direction was testing a production of high energy neutrons via the LiF(d,n) reactions at 4.75 MeV beam energy. The experiment was performed by bombarding a LiF crystal target with a pulsed deuteron beam. The spectrum of the produced neutrons was measured on-line, employing a liquid scintillator, as well as, off-line, employing a stack of foils in which neutron activated species were counted [15].

CONCLUSION

A significant progress was achieved during 2011-2012, while overcoming numerous hurdles while bridging gaps of knowledge. Improvements and modifications were introduced in practically all the components of SARAF. A temporary beam line was constructed and commissioned, and first scientific experiments were performed. The accumulated experience showed that even at the present stage the SARAF project, it has the challenging potential of becoming a user facility with an intense beam viable schedule and high beam availability. More details on the present status of SARAF can be found in [16,17] and in [18] one can find a report on the design progress of SARAF phase II.

REFERENCES

[1] I. Mardor et al., "The Status of the SARAF CW 40 MeV Proton/Deuteron Accelerator", PAC'09, Vancouver (2009) FR05rep87.

[2] L. Weissman et al., "The Status of the SARAF Linac Project", LINAC'10, Tsukuba (2010) WE102 .

[3] A. Shor et al., "Fast Beam Chopper at SARAF Accelerator via Electrostatic Deflector before RFQ", JINST 7 C06003 (2012).

[4] L. Weissman, D. Berkovits, Y. Yanay, "LEBT Beam Tuning Using Neutralized Ions in the SARAF Front End", LINAC'10, Tsukuba (2010) TUP074 .

[5] B. Vainas et al., "Use of a Wire Scanner for Monitoring Residual Gas Ionization in LEBT Beam Line", Rev. Sci. Instr. 83 02B712 (2012).

[6] P. Fischer et al., "Tuning a CW 4-Rod RFQ", LINAC'06, Knoxville, (2006) THP024.

[7] R. Rodnizki and Z. Horovits, "RF and Heat Flow Simulations of the SARAF RFQ ", LINAC'10, Tsukuba (2010) TP045.

[8] M. Pekeler et al., "Development of Superconducting RF Module for Acceleration of Protons and Deuterons at Very Low Energy", LINAC'06, Knoxville (2006) TUP034.

[9] http://www.piezomechanik.com

[10] A. Perry et al., "SARAF Superconducting Module Commissioning Status", SRF'09 Berlin, (2009) TUPPO029.

[11] B.A. Aminov et al., "Development of Low Level RF Control Systems " PAC'05, Knoxville (2005) WPAT068.

[12] I. Fishman, I. Gertz, B. Kaizer, D. Har-Even, "High power amplifiers system for SARAF Phase II", LINAC'12, Tel-Aviv (2012) TUP092.

[13] I. Silverman et al ,"Production of ^{103}Pd from a thin rhodium foil target ", Nucl. Instr. Meth. B 261 (2007) 747.

[14] G. Feinberg et al., "LiLiT - a Liquid-Lithium Target as an Intense Neutron Source for Nuclear Astrophysics ", Nucl. Phys. A827 (2009) 590c

[15] T. Hirsh, PhD thesis, The Weizmann Institute of Science (2012), submitted for publication.

[16] D. Berkovits et al., "Operational Experience and Future Goals of the SARAF Linac at SOREQ", LINAC'12, Tel-Aviv (2012) MO1A01.

[17] L. Weissman et al., "Operations of the SARAF Accelerator in 2011", Soreq report #4341 (2012).

[18] J. Rodnizki et al., "SARAF Phase 2 Linac Physical Design Study", LINAC'12, Tel-Aviv (2012) FR1A05.

THE C-80 CYCLOTRON SYSTEM. TECHNICAL CHARACTERISTICS, CURRENT STATUS, PROGRESS AND PROSPECTS.

Yu.N. Gavrish#, P.V. Bogdanov, I.N. Vasilchenko, A.V. Galchuck, S.V. Grigorenko, V.I. Grigoriev, L.E. Korolev, A.N. Kuzhlev, Yu.D. Menshov, V.G. Mudrolyubov, V.I. Ponomarenko, Yu.I. Stogov A.P.Strokach S.S.Tsygankov,
D.V. Efremov Scientific Research Institute of Electrophysical Apparatus, Saint Petersburg, Russia,
S.A. Artamonov, G.I. Gorkin, V.P. Gres, E.M. Ivanov, Yu.T. Mironov, G.F. Mikheev, I.A. Petrov, G.A. Ryabov, B.B. Tokarev,
The B.P. Konstantinov Petersburg Nuclear Physics Institute, Gatchina, Leningrad district, Russia

Abstract

A C-80 cyclotron system is intended to produce proton beams with an energy ranging from 40 up to 80 MeV and current up to 200 μA.

Over a number of years, works on the designing a cyclotron for the acceleration of H^- ions up to 80 MeV were carried out in the PNPI in cooperation with NIIEFA specialists [1-4]. Since September 2010, NIIEFA and PNPI have been carrying out works on building the C-80 cyclotron system intended for production of isotopes, proton therapy of eye diseases and superficial oncologic diseases as well as for fundamental and applied research. In addition, the cyclotron is supposed to be used as an injector of the C-230 synchrotron to ensure an additional acceleration of the extracted proton beam up to approximately 230 MeV. This will allow the Bragg's peak-based procedures to be applied in the proton therapy of oncologic patients.

Rapid advancement of modern methods of the nuclear medicine resulted in higher demand for the radioisotopic products used both in diagnostics and therapy. A rapid upgrowth of the PET diagnostics is observed, which uses radiopharmaceuticals based on radioisotopes with a half-life from several seconds up to several minutes. It is clearly enough that PET diagnostics can be done only in the direct vicinity of functioning cyclotron systems, that is, in large regional centers. The situation can be changed by using Sr-Rb generators, which can be produced on 70-90 MeV cyclotrons under irradiation of a Rb-85 target with protons. The parent isotope, Sr-82 with a half-life of 25.3 days decays and produces a daughter positron emitter Rb-82 used in the production of radiopharmaceuticals for PET. Thus, if Sr-82 is available, a PET center can function in hospitals located sufficiently far from the cyclotron system.

In view of the above, the most evident and cost-effective is the use of the C-80 cyclotron for commercial production of Sr-82. At the 200 μA design current of the extracted proton beam, 40-50 mCi of Sr-82 will be produced for one hour; the price of 1 mCi is not less than 250$. However, this fact does not exclude the possibility to produce commercially the whole assortment of isotopes for medicine as well.

#gavrish@luts.niiefa.spb.su

Parameters of the C-80 cyclotron (Table 1) make possible the realization of the proton radiation therapy of eye diseases and superficial oncologic diseases as well as the implementation of a research program aimed at the development of innovative methods of the proton therapy and promising radionuclides for diagnostics and therapy. Long-term fruitful cooperation of specialists from the PNPI and medical specialists from the Research center for Radiology and Surgical Technology, St.Petersburg in the treatment of patients using the TS-1000 accelerator is of great importance in this matter.

Table 1: Major characteristics of the C-80 cyclotron

Systems/Parameters	Characteristics
Accelerated particles	H^-
Extracted particles	H^+
Beam energy, variable, MeV	40...80
Beam current, μA	2000
Electromagnet - type - pole diameter, cm - mass, t	 E-shaped 2050 245
Resonance system - operating frequency, MHz - RF voltage amplitude, kV	 41.2 60
RF-generator power, kW	80
Ion source	external
Operating mode	continuous/pulse
Total power consumption, no more, kW - with the beam on - in the stand-by mode	 500 200

The major unit of the cyclotron, the electromagnet, has been designed using the magnet of the synchrocyclotron functioning in the PNPI. The main electromagnet has a traditional design with an E-shaped magnet yoke. The system to move upward the magnet upper part (the half-yoke) is worn-out and outdated. It was decided to replace it for 4 pairs of ball bearings and screws equipped with servomechanisms and position sensors The height of the half-yoke lifting is not less than 600 mm, the setting accuracy is not worse than 50 μm. Figure 1 shows the

magnet with the half-yoke lifting system. Based on the magnetic measurements, new magnet sectors have been designed and manufactured. To form a magnetic field, 17 packs of metal plates have been assembled on each sector.

Figure 1: Electromagnet.

The resonance accelerating system (Fig. 2) is located completely inside the vacuum chamber. The system consists of two symmetrical quarter-wave resonators. An inner conductor of each resonator consists of a 60º dee and a stem. The dees in the vicinity of the magnet center are galvanically coupled. The accelerating system is equipped with two capacitors for frequency tuning, an AFT trimmer and RF-probe. The operating frequency of the accelerating system RF oscillations is 41.2 MHz. The range for the frequency tuning with the AFT trimmer is 220 kHz. The active loss power is about 29 kW in each resonator at an RF-voltage amplitude of 60 kV.

Figure 2: Resonance System.

The RF power supply system consists of a stabilization and control module (designed in NIIEFA) and an RF-power amplifier (the «Coaxial Power System» firm, Great Britain).

The stabilization and control module of the RF-power supply system is intended for: generation of the main frequency of 41.2 MHz; measuring and stabilization of the dee acceleration voltage amplitude; manipulation of the acceleration voltage and its synchronization with the operation of the rest systems of the cyclotron; tuning and stabilization of the resonance system natural frequency; automatic tuning of the resonance system frequency to the supply voltage frequency.

Structurally the module consists of mother and daughter cards built into an industrial computer housed in the RF-power amplifier cabinet.

The RF-power amplifier shall ensure an output power of 80 kW at a frequency of 41.2 MHz. The amplifier with power supply units is located in a cabinet installed in the experimental hall basement. The RF-power is transmitted to the resonance system via a flexible coaxial feeder.

The external injection system serves for generation, shaping and transport of the H^- ion beam from an external source into the cyclotron through an axial opening in the pole. The system is located under the magnet. It consists of: a plasma ion source with electrostatic optics, beamline with two focusing lenses and two correcting electromagnets, inflector and diagnostics.

The cyclotron is equipped with a stripping device, 2 standard and 3 diagnostic probes.

The stripping device is equipped with a mechanism to adjust radial and angular position of the carbon foil to provide a required range of final ion energies. The head of the stripping device is made as a “three-fingered fan”, onto which three thin carbon foils are fixed. Remote rotation of the head is provided, which allows any of these 3 foils to be placed under the beam

The power supply system of the cyclotron includes the main switchboard and systems for consumers’ secondary power supply.

The electric power to the external injection system is supplied from power supplies produced by the Lambda and Spellman firms. The power supplies are housed in 2 cabinets. The power supply system of the BRUKER firm serves to power the main electromagnet and magnets and lenses of the 1st section of the beam transport system.

To produce high vacuum in the cyclotron chamber, two Velco 322 cryopumps of the HSR firm, Liechtenstein, are used. Turbo-molecular pumps (Edwards, Great Britain) are used in the external injection and beam transport systems.

The water cooling system is intended to remove the heat, totally of about 500 kW, from the heat-loaded components and units of the cyclotron and stabilize the working coolant temperature at the input to these components accurate within 1-2°. A double-circuit system is used. Distilled water (the heat carrier) circulates in the inner circuit, and process water (the coolant) is used in the outer circuit. The heat removed by the heat carrier from heat-loaded components is transferred to the coolant in a plate-type heat-exchanger. To extract the heat released in the process of the cyclotron operation into the atmosphere, the outer circuit is connected to the circulating water cooling system of the building. At the atmospheric air temperature of 25º C, the heat is removed through a water-water chiller.

A distributed automatic control system is used. It consists of Mitsubishi and Fastwel IO controllers and computers, each being responsible for the control of one

or several sub-systems of the cyclotron. The main unit of the control system is an industrial (host) computer, which inquires slave controllers and transmits the information acquired to computers of the operator's workstation; receives commands from the operator's workstation and performs their arbitration and distribution. Data exchange is realized via network interfaces of three types: the Ethernet, an upper level network, the ProfiBus DP and RS-485, low-level networks. The Ethernet networks the host Mitsubishi controller, host computer, computers of the operator's workstation, computer of the beam current measuring system and an industrial computer, which controls the RF system. The ProfiBus DP links the host controller, controllers of devices of the cyclotron, and beam-forming system, vacuum system, power switchboard, power supply cabinets of the external injection system, water cooling system as well as control units of the power supply system for magnets and lenses. The RS-485 networks the host computer, vacuum measuring units and controllers of turbomolecular pumps as well as the computer of the beam current measuring system and drivers of step motors of the devices for measuring the beam current density. In addition, the RS-485 links the controller of the cyclotron and beam-forming system devices with drivers of the step motors of probes and stripping device.

The experimental system of the cyclotron consists of a system for production of radioactive isotopes located in the basement, unit for the radiation ophthalmology installed in the experimental hall and unit for the radiation tests of electronic components and devices. Figure 3 shows the layout of the cyclotron and experimental system in the experimental hall.

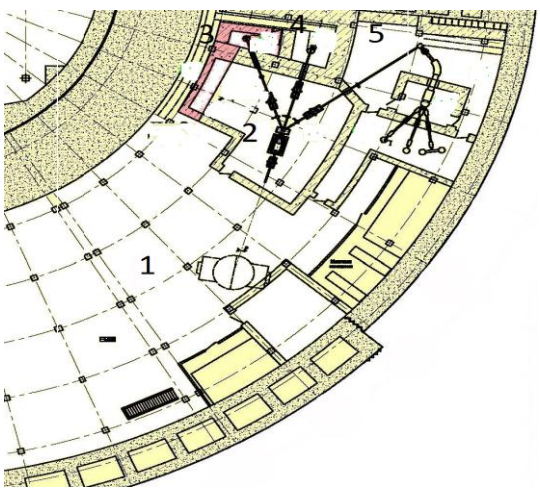

Figure 3: Cyclotron layout: 1-cyclotron; 2-switching magnet; 3, 4 – targets for production of isotopes; 5- target for electromagnetic separation of isotopes.

The beam transport system of the C-80 is intended for transport of the extracted proton beam to interaction chambers and radio-therapeutic units for proton therapy. To date, the equipment for the 1st section of the system (Fig. 4) has been designed and manufactured: matching magnet, correcting electromagnet, quadrupole lens doublet and diagnostics comprising Faraday cup and beam profile monitors. The equipment for the 2nd section of the system, which serves to transport the proton beam to target devices for production of radionuclides, has been designed and is under manufacturing. In this section, a switching magnet is installed, which directs the beam to several beamlines. When the switching magnet power is off, the beam is directed to a system of two bending magnets, which transport the beam to the second switching magnet installed in the basement (Fig. 3, № 2) and further to one of three target devices (Fig. 3, № 3, 4 and 5). For the beam focusing and control of its parameters, 5 quadrupole lens doublets, 4 correcting magnets and 2 diagnostic devices are installed in the 2nd section of the beam transport system.

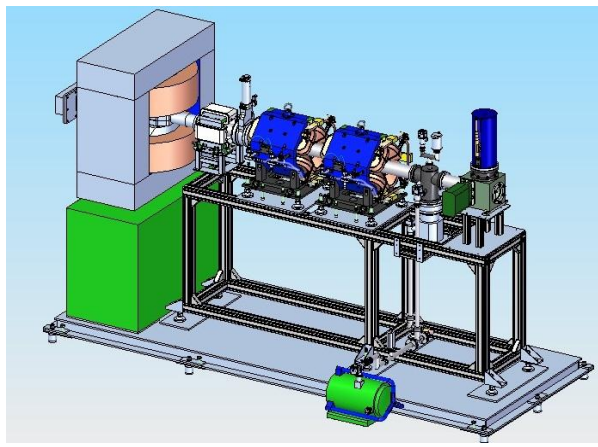

Figure 4: First section of the beam transport system.

If power is on, the magnet will direct the proton beam of ultra-low intensity and high stability to the beamlines for the proton therapy of eye diseases and superficial oncologic diseases. When the polarity of the magnet is changed, the beam is directed to the beamline intended for studying the radiation resistance of radioelectronic devices. These beamlines will be designed in 2013.

To date, reconstruction of the hall and rooms housing the cyclotron equipment has been finished. New sectors, shimms and sector metal plates have been manufactured, and the magnetic field has been formed. The equipment of the cyclotron and the 1st section of the beam transport system has been manufactured and installed in the experimental hall, basement and corresponfing rooms. In compliance with schedule, physical start-up is planned for the end of 2012.

REFERENCES

[1] N.K. Abrosimov, S.A. Artamonov, P.V. Bogdanov et al., Proc. of XIII Intern. Cyclotron conference, Vancouver, Canada, July 1992, p. 58.
[2] N.K. Abrosimov et al. Proc. of XIII Conference on Accelerators, Dubna, 1993, V. 2, p. 205.
[3] N.K. Abrosimov et al., Proc. of XIV Conference on Accelerators, Protvino, 1994, V. 4, p. 5.
[4] N.K. Abrosimov et al. Proc. of V Intern. Cyclotron conference, Caen, France, June 1998, p. 58.

SOME DESIGN FEATURES OF THE 80 MEV H⁻ ISOCHRONOUS CYCLOTRON IN GATCHINA

G.Riabov, S.Artamonov, E.Ivanov, G.Mikheev, B.Tokarev, Yu.Mironov, Petersburburg Nuclear Physics Institute, S-Petersburg, Russia
P.Bogdanov, V.Mudrolubov, NIIEFA, S-Petersburg, Russia

Abstract

The history of the design and costruction of the 80 MeV H⁻ isochronous cyclotron as well as some design features are discribed.

INTRODUCTION

The cyclotron complex is designed for fundamental and applied researches – production of medical isotopes, beam therapy of eye melanoma and surface types of cancer. Besides the cyclotron is to be used as injector for C-230 synchrotron which is planed to be built for proton therapy of cancer diseases of human internal organs utilizing the Bragg peak.

To minimize the expenditures while designing the cyclotron an attempt was made to use at most the existing synchrocyclotron infrastructure, i.e. building, the bridge crane for 30 ton, electric power, water cooling, ventilation system etc. The iron yoke of the existing synchrocyclotron magnet model is used for the magnet system.

Acceleration of H⁻ ions has obvious advantages: possibility for 100% extraction of the beam with high intensity and variable energy. On the other hand it requires special source of H⁻ ions, high vacuum and what is most important magnetic field strength in the magnet sector should not exceed in our case 17 kGs to prevent H⁻ electromagnetic dissociation.

Design and construction of H⁻ isochronous cyclotron have been in progress for many years and by the year 2010 design and drawings for the main accelerator subsystems had been completed [1,2,3]. The cyclotron magnet was designed, produced, commissioned and put into operation, full scale magnetic measurements were begun. The main problem by that time became purchase of industrially and commercially produced equipment that was realized in the frame of the nuclear medicine program of National Research Centre Kurchatov Institute. Starting from September of 2010 the cyclotron and beam transport line equipment is mounted in experimental hall.

GENERAL DESCRIBTION

Main parameters of the cyclotron are presented in Table 1. The detailed information about cyclotron equipment is presented in the report on this conference.

FEATURES OF THE MAGNETIC SYSTEM

In addition to the standard cyclotron for H⁻ machine there is an additional and essential requirement - to keep H⁻ losses on dissociation below than 5%.

H⁻ Losses and the Magnetic Structure

Two alternative versions of the magnetic structures have been examined. The first one (1) have flutter F = 0.04, spiral angle γ =55°, harmonic amplitude A4 = 4.15 kGs and the second one (2) have F = 0.025, γ = 65°, A4 = 3.28 kGs on the final radius. Here γ is an angle between the radius vector at radius r and tangent to the median line of sectors at the same radius. Both modifications provide about the same net axial focusing and differ by the field in the hill region. Fig. l. presents the beam losses due to electromagnetic dissociation for two versions of the magnetic structures. The second version - with low flutter and high spiral angle was selected for Gatchina cyclotron since it provides beam losses below than 5%.

Table 1: Main parameters of the cyclotron

MAGNET	
Pole diameter	2.05 m
Valley gap	386 mm
Hill gap (min)	164 mm
Number of sectors	4
Spiral angle (max)	65 degrees
Isochronous filed in the center	1.352 T
Flatter (max)	0.025
Ampere- turns	3.4×10^5
Power	120 kW
Weight	250 t
HF. SYSTEM	
Frequency	41.2 MHz
Potential	60 kV
Harmonics	2
HF power	2×40 kW
VACUUM	
Pressure	10^{-7} tor
2 cryogenic pumps	2×3500 l/s
1 turmomolecular	(H_2)
H⁻ source	
Multipole	1.5 mA
Injection energy	26 kV
AXIAL INJECTION	
Transport system: solenoid lens, solenoid, inflector	
EXTRACTION SYSTEM	
Stripping method	
Energy range	40-80 MeV

Magnetic Structure with High Spiral Angle

Parameters of the C-80 magnetic structure are presented in table 1. Fig.2 presents top view of the pole tips of the magnetic system

With use of the Novosibirsk MERMAID code which accounts for iron saturation and permit to use up to 20×10^6 nodes the profile of the iron shims was determined. Details are discussed in special poster report at this conference.

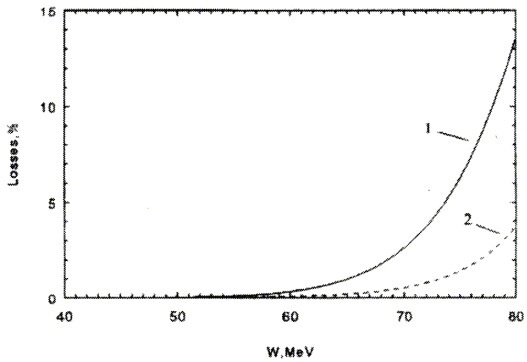

Figure 1: H^- losses due to electromagnetic dissociation for two magnetic structures.

Distribution of the magnetic field in the full scale magnet was measured using the measuring system based on twenty NMR calibrated Hall probes and automated coordinate system which can position probes in cylindrical coordinate system with accuracy of 0.1 mm along the radius and azimuth at the radius of 100 cm. Achieved precision was equal to 2×10^{-4} with total time of measurements of 6-8 hours. Disagreement between experimental measurements and calculations did not exceed 20 Gs. Final distribution of the magnetic field was measured experimentally with 2-5 Gs precision.

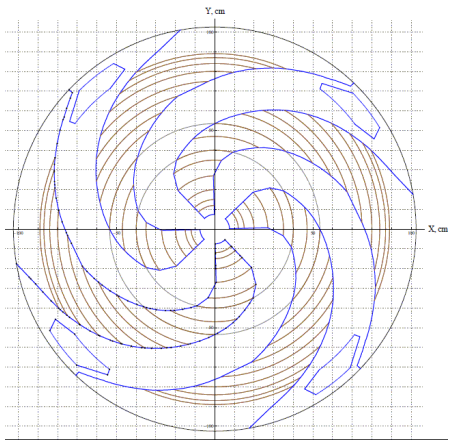

Figure 2: Top view of the pole tip.

Flutter versus Radius for Straight Sectors

The valley and hill gaps have been estimated by using the calculation of the flatter in straight sector structure. Flatter versus radius is presented in Figure 3 for two variants of magnetic structures. The comparison of the different magnetic structures is performed by using a non-dimensional parameter $x = r/N{\cdot}g_h$, where g_h and g_v denote half of hill and valley gaps, N=4 is number of sectors, azimuthally lengths of valley and hill are equal.

Flutter increases when the hill gap is decreased and decreases with growth of sector number. For the case of $x < 0.5$ that corresponds to the range of radii $r < 0.5\cdot Ng_h$ the value of flutter rapidly decreases. In our case at radii smaller than two gaps in the hill the edge focusing became ineffective.

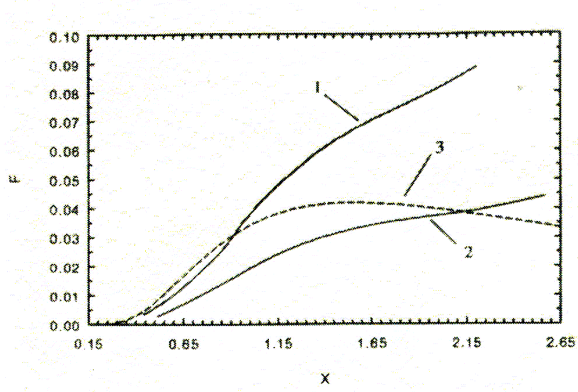

Figure3: Flutter as a function of the non-dimensional parameter:

1. $2g_v = 386$ mm, $2g_h = 170$ mm, $h_1 = 108$ mm;
2. $2g_v = 284$ mm, $2g_h = 145$ mm, $h_2 = 69$ mm;
3. Approximation of the sector uniform magnetization for the case 1.

Effect of Spiral Pole Tips

Spiral angle provides extra focusing due to angular focusing. Effectively flutter is increased by the following factor:

$$S(r, \gamma) = 1 + 2\tan^2\gamma(r),$$

where $\gamma(r)$ is a spiral angle at given radius. However in real life benefit in focusing is smaller than it could be expected from this expression. It is explained by the drop of flutter at small radii and difference between spiral angle for pole tips and magnetic field. Drop of flutter due to introduction of spiral angle can be understood based on simple geometrical considerations [4]. Influence of spiral angle on flutter value can be estimated from calculation of flutter for a straight sector (see Fig.4) if one makes the following replacement: $x_{eff} = x\cos\gamma$.

The total effect from spiral angle can be characterized with parameter which is a product of flutter F and *S(r,γ)*. Since value of flutter rapidly decreases at $x_{eff} < 0.5$ than introduction of spiral angle can result in decreased focusing. For each value of radius and parameter x there is a critical spiral angle that results in increase of focusing from introduction of spiral angle. The value of critical angle for each value of x can be found as a square root of:

$$U(x,\gamma) = (F(x\cos\gamma)/F(x))\cdot(1+2\tan^2\gamma) - 1 = 0,$$

where *F(x)* is a function similar to one shown in Fig. 3. For the spiral angles more than critical one for the given

radius the introducing of the spirally decreases the vertical focusing.

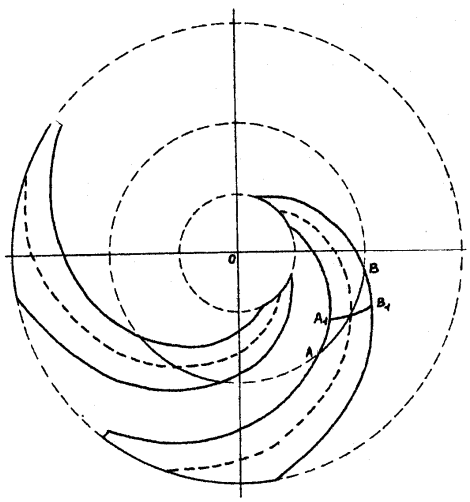

Figure 4: Difference between the sector length along azimuth and "effective" length at large spiral angle. AB-length of sector along azimuth. $A_1B_1 \approx AB \cdot \cos\gamma$ – effective width of sector along perpendicular to the middle line.

Fig.5 shows critical spiral angle in dependence on radius for our accelerator. According to the plot spiral angle becomes ineffective at radii r < 15 cm and structure with high spiral angle is advantages at r > 35cm. In the central region is necessary to use the straight sector structure.

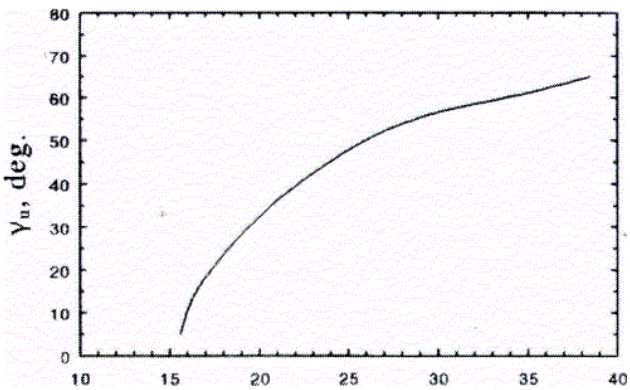

Figure 5: The ultimate spiral angle in dependence on radius for $2g_v$ = 386mm, $2g_h$ = 170mm, r = N·g_h ·x_{eff},, N=4.

VACUUM CHAMBER, INJECTION, EXTRACTION AND EXPERIMENTAL AREA

The external ion source and axial injection are used to obtain high vacuum for the acceleration H^- ions. Moreover in the adopted design magnetic system is placed outside of the chamber of the accelerator. The upper and lower lids of the chamber are attached to the poles of a magnet. Thus, to improve the vacuum conditions, two walls of the chamber (2 × 16 mm) occupy about 10% of the magnet gap, which required an increase in ampere-turns and the power of the magnet.

The extraction with 100% efficiency of high intensity beam and energy variation from 40 up to 80 MeV is realized by H- stripping methods. The schematic view of the extraction system is presented in Figure 6.

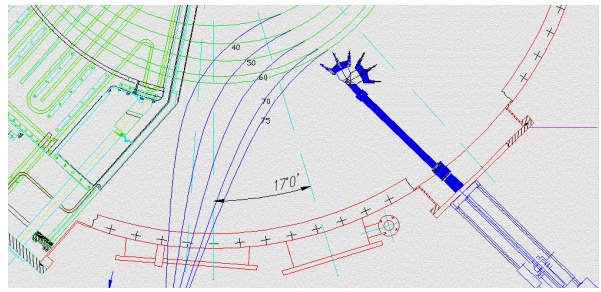

Figure 6: Schematic view of the extraction system.

For more details about extraction system of the cyclotron please refer to the poster presentation at this conference.

The multy-purpose experimental complex consists of the targets of different specialization and the beam transport lines. A beam of high intensity is transported to the basement, where three stationary targets are installed for production of medical radioisotopes and pharmaceutical medications as it shown in Figure 7.

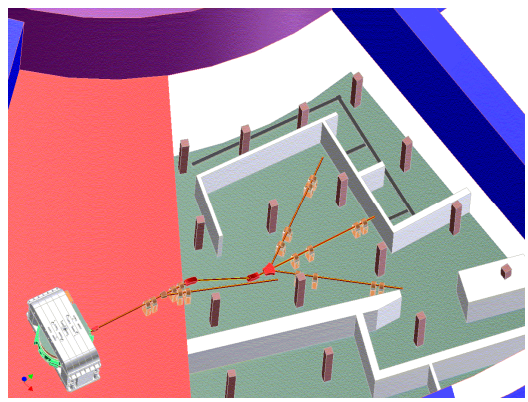

Figure 7: Transport lines to the targets for production of medical radioisotopes.

On the ground floor are disposed the ophthalmology facility with low intensity beam line, centre for radiation testing of electronics components and transport line for the injection in the new medical synchrotron.

REFERENCES

[1] N.K. Abrossimov et al. Proc. XIII Intern. Conf. on Cycl. and their Applic., Vancouver, Canada 1992, p.. 54-62
[2] N.K. Abrossimov et al. RUPAC-XIII , Russia, Dubna, 1993, v.2, p. 205-209
[3] N.K. Abrossimov et al. RUPAC-XIV , Russia, Protvino, 1994, v.4, p. 5-10
[4] N.K. Abrossimov et al. . Proc. XV Intern. Conf. on Cycl. and their Applic., Caen, France 1997, p.. 58-62

ITEP-TWAC RENEWAL AND UPGRADING PROGRAM

N.N.Alexeev, P.N.Alekseev,V.A.Andreev, A.N.Balabaev, A.I.Balabin, V.N.Balanutsa, A.A.Golubev, M.M.Kats, V.I.Nikolaev, A.S.Ryabtsev, Yu.A.Satov, V.S.Stolbunov,V.A.Schegolev, B.Yu.Sharkov, A.V.Shumshurov, V.P.Zavodov, ITEP, Moscow, Russia

Abstract

The ITEP-TWAC facility has been put out of operation this year as a result of some equipment damage by the fire, so the program of machine renewal and its equipment upgrading for accelerated beams parameters improvement and experimental area expansion is now under processing and development. Main items of this program and status of machine restoration activity are presented.

INTRODUCTION

ITEP Ring Accelerator Facility has celebrated last year 50-th anniversary of first 7 GeV accelerated proton beam, so substantial part of the ITEP-TWAC components has been in keeping with its age requiring some additional efforts for rejuvenation of obsolete equipment, communications and structural components and the problem of machine upgrade has been discussed last few years [1]. The main directions of the ITEP-TWAC upgrade were considered for realisation in parallel with machine operation with proton and heavy ion beams in different applications on a base of new accelerator technologies development. The laser ion source technology development was oriented to getting of high current and high charge state ion beam of Z/A up to 0.4 for elements with A ~ 60 to be effectively stacked in the accumulator ring with multiple charge exchange injection technique at the beam energy of up to 700 MeV/u. The new high current heavy ion linac was under construction. Design of proton injection and beam slow extraction for UK ring was performed for its utilizing as self-depending synchrotron in medical application and for imitation of cosmic radiation.

Decommissioning of accelerator facility in this year and destruction of some part of its equipment forced to reconsider the program of machine upgrade on the basis of achieved results in development of ITEP-TWAC project and substantial refinery of the ultimate aim, purpose and main tasks of the proposed reconstruction.

STATUS OF ITEP-TWAC IN 2011

The ITEP-TWAC facility (Fig.1) consisting of main synchrotron-accumulator U-10 with 25 MeV proton injector I-2 and linked to U-10 Ring booster synchrotron UK with 4 MV ion injector I-3 has been in several operation modes accelerating protons in the energy range of 0.1-9.3 GeV, accelerating ions in the energy range of 0.1-4 GeV/u and accumulating nuclei up to Cu at the energy of 200-300 MeV/u. Accelerated beams were used in following modes: secondary beams generated in internal targets of U-10 Ring transferred for experiments to Big experimental hall (BEH); beams extracted from U10 Ring in one turn transferred to Target hall (TH); and proton beam bunch extracted from U-10 ring was transferred to Biological research hall (BRH). Some of secondary beam lines were used for transferring of slow extracted beams from U-10 Ring.

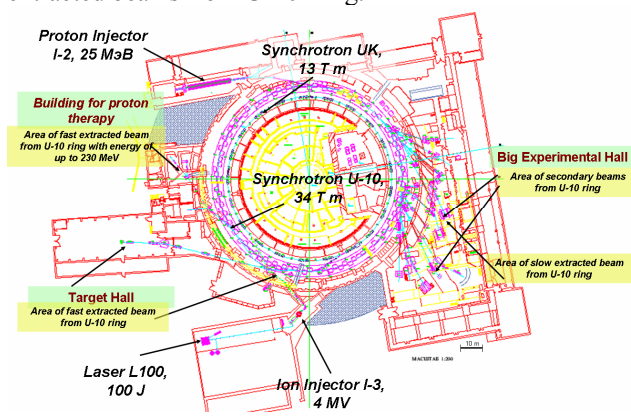

Figure 1: Layout of ITEP-TWAC Facility.

Statistic of machine operation time is shown on Fig.2. The total beam time of near 4000 hours per year was divided between three operation modes: acceleration of protons (~50%), acceleration of ions to intermediate and relativistic energy (~30%) and nuclei stacking (~20%).

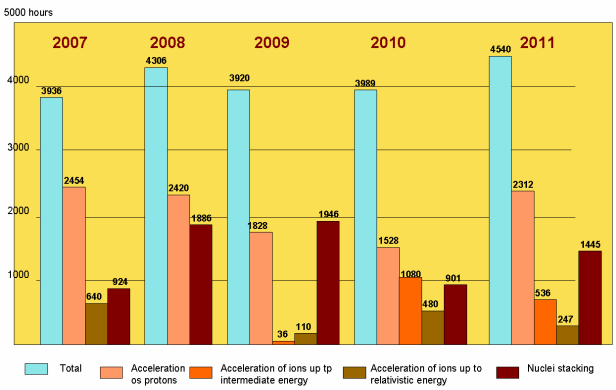

Figure 2: Statistic of ITEP-TWAC operation time.

Statistic of machine using for different research fields (Fig.3) shown the tendency of beam time increase for applications such as biology, medicine, protonography and testing of heavy ion radiation steadiness of electronics destined for cosmic apparatus. The demand for beam time exceeded the offering one by factor of two. This discrepancy was supposed to be cardinally reduced in a result of machine infrastructure improvement.

One of a challenge technologies implemented in ITEP-TWAC is laser ion source (LIS) with high power CO_2-laser. Charge states of ions generated in the LIS are shown in Fig.4.

Research fields with proton and ion beams	Beams	Accelerator operation time, hours		
		2009	2010	2011
Adron physics and relativistic nuclear physics	p (2-9 GeV, $10^{11}s^{-1}$) C (4 GeV/u, $10^{8}s^{-1}$)	1100	850	702
Methodical research	p (1-9 GeV, $10^{11}s^{-1}$) C, Fe(0,2-4 GeV/u, $10^{8}s^{-1}$)	2100	2045	2450
Physics of high density energy in matter	C, Al, Si, Fe (300 MeV/u, $4x10^{10}s^{-1}$)	350	330	288
Radiobiology and medical physics	p (250 MeV, $10^{11}s^{-1}$) C (200-400 MeV/u, 10^{8} s^{-1})	2150	2040	2320
Proton therapy	p (250 MeV, $10^{11}s^{-1}$)			
Radiation treatment of materials	p (20-800 MeV, $10^{11}s^{-1}$) Fe, Ag (40-200 MeV/u, 10^{8} s^{-1})	1100	550	779
Total		6800	5815	6539

Figure 3: ITEP-TWAC usage for different research fields.

Generation of Fe-ions shows pick current for charge state specie Fe^{16+} with IP= 506 V. The higher level of charge state specie Fe^{17+} with IP=1168 V has been also observed but in very few quantity. Generation of Ag-ions shows maximal charge state specie Ag^{20+} with IP= 816 V and very few specie Ag^{21+} with IP= 895 V has been also observed in some measurements.

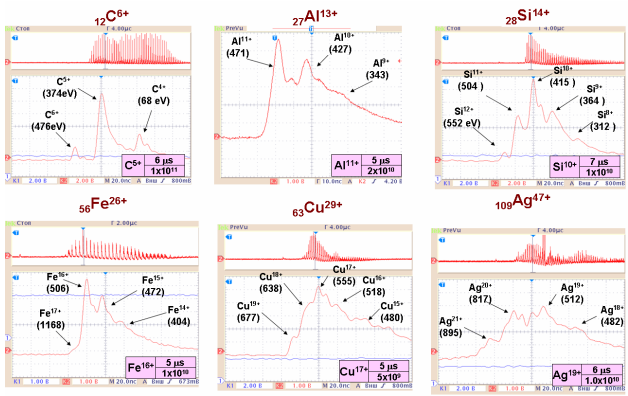

Figure 4: Ions generation in LIS with laser L100.

Acceleration of different ions in synchrotron UK is illustrated by typical oscillograms on Fig. 5. It's seen that the beam loss on the ramp is large enough due to very low injection energy (4 MV) and vacuum as $1x10^{-9}$ Torr.

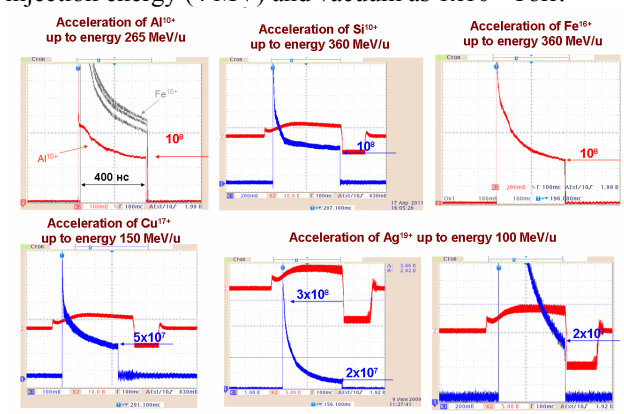

Figure 5: Acceleration of different ions in UK Ring.

Technology of Fe-nuclei acceleration up to relativistic energy of 3.6 GeV/u using three step scheme I-3/UK/U10 is illustrated by sequence of oscillograms on Fig.6.

The charge exchange injection technique has been used for accumulation of C-, Al-, Si - nuclei at the beam energy of ≤300 MeV/u with stacking factor up to several tens. The maximal stacking factor been achieved at optimization of carbon nuclei stacking (Fig.7). The optimal conditions for Al- and Si- nuclei stacking (Fig.8) were not yet obtained to be subject of forthcoming experiments.

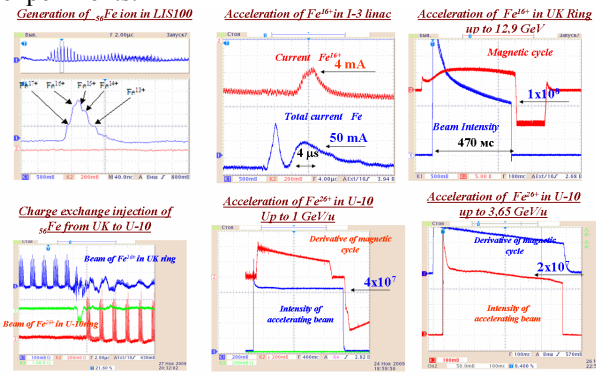

Figure 6: Fe-nuclei acceleration up to relativistic energy.

Energy	300 MeV/u
Intensity of injecting beam	$6x10^{9}$
Repetition rate, s	3
Acceptance, A_x, π mm mrad	10
Vacuum, Torr	$\sim1x10^{-8}$
Stacking factor	~70
Intensity of stacked beam	$4x10^{10}$

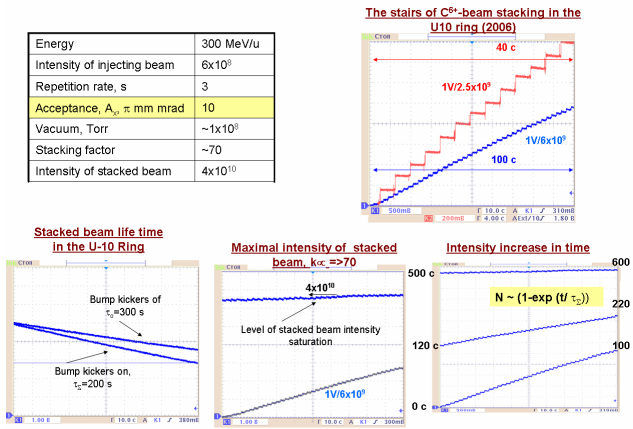

Figure 7: Optimization of carbon nuclei stacking in U-10 Ring by scheme of C^{4+}=>C^{6+}.

	Al	Si	Fe
Energy, MeV/u	265	240	230
Intensity of injecting beam	$\sim1x10^{9}$	$\sim5x10^{7}$	$\sim1x10^{8}$
Repetition rate, s	4		
Acceptance, A_x, π mm mrad	10		
Vacuum, Torr		$\sim1x10^{-8}$	
Stacking factor	~30	~ 20	~10
Intensity of stacked beam	$\sim3x10^{9}$	$\sim1x10^{9}$	$\sim 1x10^{9}$

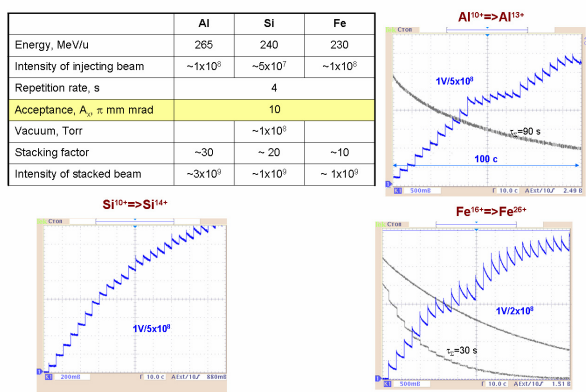

Figure 8: Stacking of nuclei: Al, Si, Fe.

The efficiency of Fe- and Cu- nuclei stacking at the energy of ~200 MeV/u was limited on the level of stacking factor ten due to disturbing effects of beam interaction with stripping foil [2]. Efficiency of beam stacking for nuclei of mass number A~60 has to be essentially increased with progress in LIS technology and at increasing the energy of injected beam up to 600-700 MeV/u. For nuclei with A<30, disturbing effects of beam interaction with stripping foil of optimal thickness are small enough and efficiency of beam stacking was a

function of injection scheme parameters and of storage Ring dynamic aperture.

CONCEPTION OF ITEP-TWAC FACILITY RENEWAL AND UPGRADING

Proton and ion beams generated in ITEP-PWAC in a wide range of parameters have been demanded for different research fields having the tendency of beam time increase for applications as it's shown above. Renewal of multipurpose proton-ion accelerator and nuclei accumulator ITEP-TWAC will allow to resume suspended at the present time:

- fundamental and applied research with relativistic proton and ion beams in the energy range from 1 GeV/u up to 10 GeV for protons and 4 GeV/u for ions;
- applied research with proton and ion beams in the energy range from 10 MeV/u up to 1000 MeV/u in industry, biology and medicine;
- fundamental and technological research with high power stacked nuclei beams of particles with atomic number up to ~60 in the energy range of ~1 GeV/u;
- technological research for high charge state and high intensity heavy ion beams generation, acceleration, stacking, compression, extraction and focusing;
- expansion of scientific and educational activity on the subject of nuclear technologies.

Qualitatively new level of accelerator facility will be achieved as a result of upgrading relevant ITEP-TWAC systems for:

- extending of accelerated ions set up to A ~ 200;
- cardinal increasing of intensity for accelerated ion beams on a base of ion injector upgrading and accelerator technology improvement;
- cardinal increase of intensity and power for stacked nuclei beams on a base of charge exchange technology development;
- mastering of multimode machine operation with maximal efficiency for experiments and applications with proton and ion beams in parallel.

DEVELOPMENT OF LIS TECHNOLOGY

Configuration of LIS includes now CO_2- lasers L5 and L100 with the energy of radiation, respectively, 5 and 100 J per pulse. Laser L5 is used for generation of C-ions only, LIS with laser L100 is in operation from 2008 and it has been used with target materials of C, Al, Si, Fe, Cu and Ag operating ~1000 hours per year.

The first configuration of laser L100 was assembled as auto-generator [2], then it was modified for operation as amplifier and this mode of operation brings increasing three times the pulse amplitude of radiation power as can be seen on Fig.9. Out-of-axis scheme of laser ray focusing on the target don't allow to get the size of radiation spot less then 0.5 mm, so the maximum power density on the target surface is limited now by 1.5×10^{12} W/sm^2.

Experiments on the ion beam generation in LIS give evidence of optic imperfection reducing considerably the laser radiation power density on the target surface.

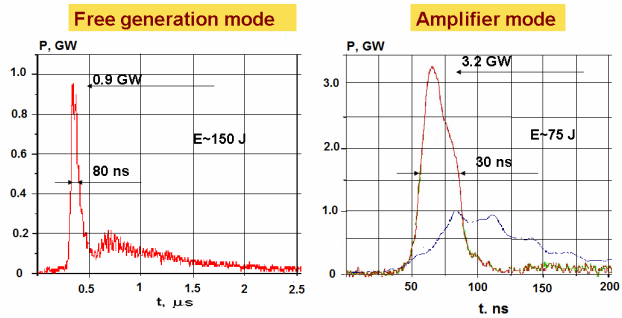

Figure 9: Pulses of L100 radiation for auto-generator and amplifier modes of laser operation.

New focusing scheme for target station is elaborated on a base of new target station construction for axis-symmetrical scheme of laser ray focusing which is free of aberration. Substantial factor of power density increase will be achieved replacing KCl-windows by them of better quality. The elimination of the optical channel defects will allow to increase the radiation power density on the target to the value of more $>10^{13}$ W/sm^2

UPGRADE OF INJECTION COMPLEX

Injection complex with operated in parallel proton and ion injectors I-2 and I-3 is adequate to multipurpose designation and multimode operation of ITEP-TWAC accelerators. However, low energy (4 MV) and low accelerating frequency (2.5 MHz) of ion injector I-3 significantly limit parameters of accelerated and stacked ion beams. Upgrade of ion part of injection complex has to solve the problem of UK Ring intensity increase on the level of no less than 10^{11} nucleons in the pulse for any type of ions from C to U..

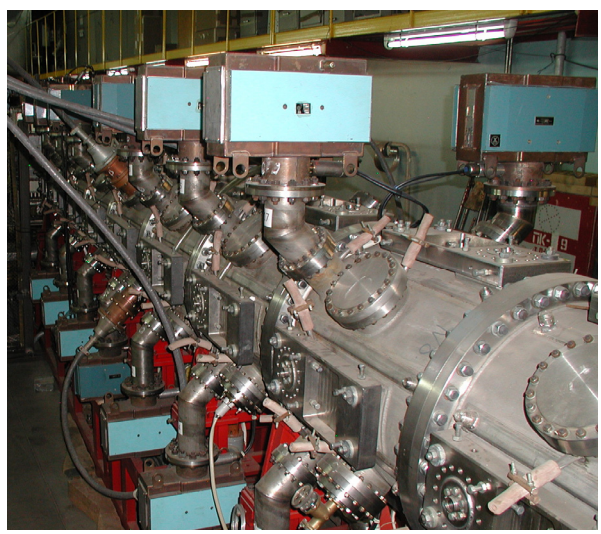

Figure 10: RFQ section of linac I-4.

Proceeding from ion parameters of LIS, optimal on the necessary resources scheme of upgraded injection complex includes two ion injectors: linac I-4 accelerating light ions with A/Z≤3 to the energy of 7 MeV/u [3] and modified linac I-3 for acceleration of heavy ions with A/Z≥3 to the energy of ~12Z/A MeV/u.

RFQ section of I-4 (Fig.10) on the energy 1.6 MeV/u is now constructed and first beam test has been successfully carried out with proton and $H2^+$ beams [4]. Two options of following resonator sections for I-4 is now considered. The first one is three DTL sections based on H Cavity with magnetic quadruples between them for beam focusing [5]. The second one is DTL section based on H Cavity with RFQ insertions for beam focusing [6]. The final version of section will be selected in the near future

Proposed scheme of injector I-3 modification for improvement of accelerated beam parameters (Fig.11) is based on the use of existing two gap resonator which has to be retuned on 5 MHz. Accelerating structure of I-3M will be composed of two resonators with drift tubes optimized for acceleration of ions with A/Z ~ 6. The width of accelerating gaps has to be adjusted for accelerating voltage of 3 MV per gap. The edge focusing of the beam in the first accelerating gap with specially optimized electrodes profile provides transverse stability of accelerating beam along the line channel. Main parameters of this structure is given in Table on Fig .9.

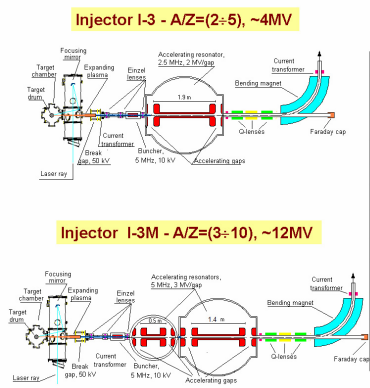

Comparison parameters of I-3 and I-3M

Injector	I-3	I-3M
Accelerating frequency, MHz	2.504	5.0
Number of resonators	1	2
Accelerating gaps	2	4
Accelerating voltage, MV	4	12
Bunching voltage, kV	10	
Accelerating ions, A/Z	2-5	3-10
Injection energy, kV	50	
Trans. acceptance, π· mm mrad	~1000	
Output momentum spread, Δp/p, %	±1	
Transmission factor, %	~50	

Figure 11: Scheme of ion injector I-3 upgrading.

UPGRADE OF UK RING

Increasing of beam energy at the output of ion injector simplifies but doesn't eliminate the problem of heavy ion acceleration in synchrotron. The existing quality of UK Ring vacuum system provides the vacuum of $1x10^{-9}$ Torr which allows to accelerate ions with A no more than ~100. The quality of UK Ring vacuum system has to be cardinally improved on a base of developed technologies [7] and successfully implemented at GSI [8].

Combination of UHV sputter ion pump (IP) and Titanium sublimation pump (TSP) having a pumping speed of S_{IP} = 100ℓ/s, and S_{TSP} = 900 ℓ/s for hydrogen will be used as basic element of distributed pumping system. The outgassing rate of chamber surface for hydrogen has to be reduced to ~ $4x10^{-13}$ Torr×ℓ/s×cm^2. Technology of Non evaporable getter (NEG) has to be mastered for uniform pumping of the whole chamber. Comparison of vacuum system parameters for UK (2011), SIS18 (GSI) and UK (project) is given in Table 1. Calculated distribution of static pressure along the UK chamber with and without NEG pumping is shown on Fig. 12.

Table 1. Comparison of UK and SiS18 Vacuum systems

Parameter	UK (2011)	SIS18 (GSI)	UK (project
q_{H2}, Torr·ℓ/s	~$2x10^{-12}$	$4x10^{-13}$	$4x10^{-13}$
T_{bake}, C^o	150	200	200
S_{IP}, ℓ/s m	7	6	9
S_{TSP}, ℓ/s m	-	50	60
S_{NEG}, ℓ/s cm^2		0.2	0.2
P, Torr	$1x10^{-9}$	$1x10^{-12}$	$1x10^{-11}$(10^{-12})

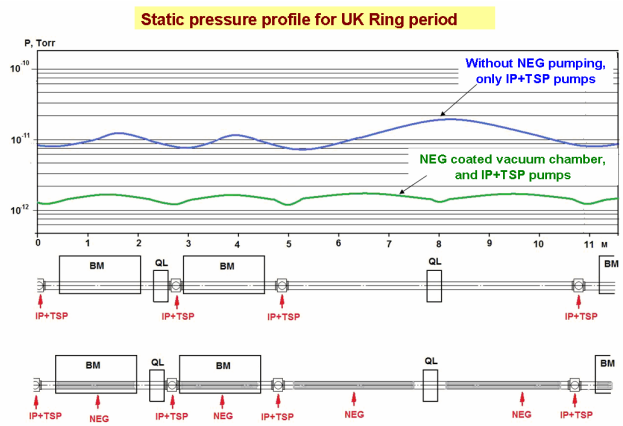

Figure 12: Scheme of UK Ring vacuum pumping.

Upgrade of UK accelerating system is aimed to increase main magnet ramping rate by factor of 3÷4 for reducing the time of ion acceleration up to the maximal energy to ~150 ms. Tuning range of accelerating frequency (0.7÷10) MHz is overlapped by two cavities using procedure of beam recapture from one accelerating cavity to another.

Table 2. Upgrade of UK accelerating system

Parameter	UK(2011)	UK(project)
Magnet ramping rate, T/s	1÷2	4÷6
Number of cavities	2	42
Accelerating peak voltage, MV	10	20
Accelerating frequency, MHz	0.7÷2.5 /2.2÷10	

Parameters of accelerated ion beam in upgraded UK synchrotron with injectors I-4 and with I3M are listed in Tables 3. Maximum intensity of accelerated beams is calculated on incoherent Coulomb limit. Real intensity will be limited by beam current at the outlet of LIS.

Table 3. Ion acceleration in upgraded UK Ring

Accelerated beam parameters with injector I-4

A/Z≤3, U_{inj}=7MV/u, β_{inj}=0.122, f_{acc}=(0.7-6) MHz, T_{UK}=6.1μs

A/Z	3.0	2.8	2.45	2.4	2.33	2.0
Ion	C^{4+}	Si^{10+}	Al^{11+}	C^{5+}	Si^{12+}	C^{6+}
E_m,MeV/u	668	774	910	940	980	1230
N_m	$8x10^{11}$	$3x10^{11}$	$2x10^{11}$	$5x10^{11}$	$2x10^{11}$	$3x10^{11}$

Accelerated beam parameters with injector I-3M

A/Z≥3, U_{inj}=(1-3)MV/u, β_{inj}=(0.05-0.1), f_{acc}=0.7-8MHz, T_{UK}=(9-16)μs

A/Z	10	9	8	6	4	3
Ion	U^{24+}	U^{28+}	Au^{25+}	Ag^{16+}	Fe^{16+}	Ni^{18+}
E_m,MeV/u	80	100	120	200	400	670
N_m	$2x10^{10}$	$1.7x10^{10}$	$2x10^{10}$	$3x10^{10}$	$4x10^{10}$	$5x10^{10}$

UPGRADE OF U-10 RING

The program of U-10 Ring upgrade has been composed last year to be realised during next two-three year and includes the following:

- replacement of vacuum chamber for the expansion of hor. acceptance to 200 π·mm·mrad and improvement vacuum to $<10^{-9}$ Torr;
- expansion of aperture in septum magnet outlet of charge exchange injection channel and improvement of beam bump kickers waveform;
- installation of additional magnet inflector for injection of ions from UK Ring without stripping.

The scheme of U-10 Ring upgraded vacuum pumping is similar to existing one. The improvement will be obtained mainly due replacement of vacuum chamber and reducing of outgassing.

Modification of charge exchange injection system will allow to expand hor. acceptance of the Ring for stacking beam and to increase efficiency of beam stacking by elimination of stripping foil re-crossing by circulated beam at injection of another potion of ions.

Installation of additional magnet inflector in the strait section 505-506 will allow injecting to U-10 Ring the beam of any accelerated in UK synchrotron ions but not only stripped to the nucleus state.

DEVELOPMENT OF ITEP-TWAC INFRASTRUCTURE

Elaborated strategy of ITEP-TWAC infrastructure development is aimed to redouble beam time for physical experiments and applications extending functional capabilities of UK synchrotron for protons acceleration and for generation of slow extracted beams to the area of beam using for applications.

Expanded Injection Complex of ITEP-TWAC with additional beam lines from injectors both I-2 and I-4 to UK Ring was presented in [1].

New projected beam line for slow extracted beam from UK Ring for applications [2] is directed to free space of Target Hall (where setup will be installed for biological research) and linked with beam line from U-10 Ring to Medical Building used now for proton therapy.

We consider also possibility of construction the combined (fast end slow) extraction system for U-10 Ring to BEH (Fig.13) for the beam of maximal momentum 10Z GeV/c. The slow extracted proton or ion beam will be used for research on nuclear and particle physics. The fast extracted proton beam with regulated time intervals between bunches will be used for protonography of fast processes. Area of this beam using in the corner of BEH has to be separated for radiation shielding by additional concrete walls from surrounding environment.

Three modes of machine operation with proton and ion beams in parallel or in time-sharing mode can be realized: 1) acceleration of protons in U-10 Ring and protons or ions in UK Ring; 2) acceleration of ions in U-10 Ring and protons or ions in UK Ring; 3) stacking of nuclei in U-10 Ring with acceleration of protons or ions in UK Ring.

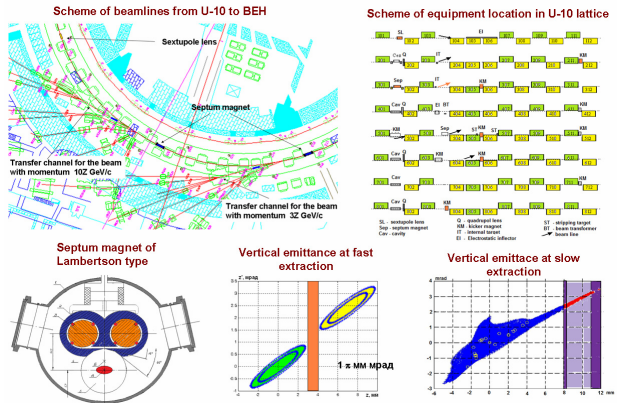

Figure 13: Combined extraction of beam from U-10 Ring.

CONCLUSION

1) Conception of ITEP-TWAC renewal and upgrading is based on demanding of fundamental, applied and technological research with proton and ion beams in the wide range of intermediate energies for nuclear science, industry, biology, medicine and education on the subject of nuclear technologies.

2) The progress in technology of Laser Ion Source with 100J CO_2 laser L100 gives possibility of high charge state ion beam generation with Z/A≥0.4 for ions up to A~60 and with Z/A≥0.1 for ions up to A~200.

3) Upgrading of the heavy ion injector I-3 and commissioning of new light ion injector I-4 will be the base for cardinal increasing of intensity for accelerated in UK Ring ion beams in wide range of mass number values.

4) Acceleration of heavy ions with mass number up to A~200 in synchrotron UK will be achieved first of all as a result of ring vacuum system upgrade on the base of modern vacuum technology implementing for the vacuum less than $1x10^{-11}$ Torr.

5) Upgrading of U-10 Ring Accelerator systems will be directed on cardinal increasing of intensity for accelerated proton and any kind of ion beams and further development of multiple charge exchange injection technology for getting of super high density heavy ion beams.

6) Development of ITEP-TWAC facility Infrastructure is aimed mastering of multimode machine operation making generation proton and ion beams of both U-10 and UK synchrotrons in parallel.

REFERENCES

[1] N.Alexeev, et al. IPAC'11, 2193-2195 (2011)
[2] N.Alexeev, et al. RuPAC'10, 32-34 (2010)
[3] V. Andreev, at al. IPAC'10, 801-803 (2010)
[4] V.Andreev, et al. IPAC'11, 2622-2624(2011)
[5] S. Minaev, et al. EPAC'06, 1615-1617 (2006).
[6] P.Ostroumov, et al. Nucl. Instr. and Meth. in Phys. Res. A 547 (2005) 259–269
[7] V. Nemanič, T. Bogataj, Vacuum 50(3) (1998), 431
[8] St. Wilfert, et al. GSI Scientific report 2008, 120

STATUS OF THE NUCLOTRON

A. Sidorin, N. Agapov, A. Alfeev, V. Andreev, V. Batin, O. Brovko, A. Butenko, D. E. Donets, E. D. Donets, E.E. Donets, A. Eliseev, V.Fimushkin, A. Galimov, E. Gorbachev, A. Govorov, E. Ivanov, V.Karpinsky, V.Kekelidze, H. Khodzhibagiyan, A. Kirichenko, A. Kobets, A. Kovalenko, O. Kozlov, N.Lebedev, I.Meshkov, V. Mikhailov, V. Monchinsky, A. Philippov, S. Romanov, T. Rukoyatkina, N. Shurkhno, I. Slepnev, V.Slepnev, A. Smirnov, A.Sorin, G. Trubnikov, A. Tuzikov, B. Vasilishin, V. Volkov,
JINR, Dubna, Moscow Region

Abstract

The Nuclotron upgrade – the Nuclotron-M project, was successfully completed in 2010. Following the project goals, Xe ions were accelerated to about 1.5 GeV/u in March 2010. In December 2010, the stable and safe operation of the power supply and energy evacuation system was achieved with a field in the lattice magnets of 2 T. In 2011 - 2012 three runs of the Nuclotron operation were carried out. The facility development is aimed to the performance increase for current physical program realization and to test equipment and operational modes of the NICA collider.

INTRODUCTION

The "Nuclotron-M" project, started in 2007 was considered as a key part of the first stage of the JINR general project NICA/MPD [1]. The extension of JINR basic facility capabilities for generation of intense heavy ion and high intensity light polarized nuclear beams, including design and construction of heavy ion collider aimed at reaching the collision energy of $\sqrt{s_{NN}}$ = 4÷11 GeV and averaged luminosity of $1 \cdot 10^{27}$ $cm^{-2}s^{-1}$ is necessary for realization of the NICA/MPD.

During the Nuclotron-M project realization course almost all the Nuclotron systems were modernized and six runs at total duration of about 3200 hours were carried out. To the end of 2010 all general goals of the project were reached : the Xenon ($^{42+}Xe^{124}$) beam was accelerated up to 1.5 GeV/u and reliable work of the Nuclotron magnetic system at 2 T was provided [2].

Presently the creation of the NICA general elements is realizing in the frame of three officially approved JINR projects: "Nuclotron-NICA" (accelerator part), MPD (the project oriented to creation of one of the collider detectors) and BM@N (Baryonic Matter at Nuclotron – the new fixed target experiment with heavy ions, the detector is under construction in the existing experimental building). The Nuclotron is the key element of all three projects: as the ion source for MPD element testing and for experimental program BM@N realization, as the main synchrotron in the injection chain of the future collider and as the basic facility for testing of new equipment of the booster and collider rings.

The results of the Nuclotron upgrade and development of the accelerator complex during last two years are briefly described in this report.

RESULTS OF THE NUCLOTRON UPGRADE PROGRAM

The "Nuclotron-M" program was oriented to the development of the existing Nuclotron accelerator complex to the facility for generation of relativistic ion beams over atomic mass range from protons to gold ions at the energies corresponding to the maximum design magnetic field (2 T) in the lattice dipole magnets. Another important goal of the project was to reach new level of the beam parameters and to improve substantially reliability and efficiency of the accelerator operation, renovate or replace some part of the equipment that have been under operation since 1992-93.

As an element of the NICA collider injection chain, the Nuclotron has to accelerate single bunch of fully stripped heavy ions (as a reference Au^{79+} is considered) from 0.6 to about 4.5 GeV/u. The required bunch intensity is about $1 \div 1.5 \cdot 10^{9}$ ions. The particle losses during acceleration have to be minimized and do not exceed 10%. The magnetic field ramp rate has to be 1 T/s and more. To demonstrate the ability of the Nuclotron complex to satisfy these requirements, the general milestones of the Nuclotron-M project were specified as an acceleration of heavy ions (at atomic number larger than 100) and stable and safety operation at 2 T of the dipole magnet field.

In the frames of the "Nuclotron-M" project the following works on the LHEP accelerator complex development were performed.

1. Full scale modernization of the cryogenic system was carried out. As result the cooling power at 4,5 K was increased up to 4 kW, the reliable work at maximum magnetic field and at prolonged magnetic cycle duration was provided. The operation term was sufficiently increased; today the new equipment can be used for the NICA/MPD purposes already.

2. The vacuum system modernization permitted to decrease the residual gas pressure in the Nuclotron beam pipe by two orders of magnitude and to provide a possibility of heavy ion acceleration. The obtained result allows solving general task of the Nuclotron as a part of

the heavy ion collider injection chain – to provide acceleration of heavy nuclei from 0,6 GeV/u (injection energy from the booster) up to 4.5 GeV/u without losses.

3. Modernization of control system, diagnostic and radio frequency accelerating systems was performed. As result new cycle control equipment, digital generator providing relation between accelerating voltage frequency and magnetic field value, new power supply system for corrector magnets, digital orbit measurement system and others were put into exploitation.

4. New power supply and quench protection system based on consequent connection of the Nuclotron structural magnets, all supply units and energy evacuation switches was created. Practical realization of this scheme required modernization of existing supply units, development and construction of two new units for current variation in focusing and defocusing lenses, disassembly of old cable lines and assembly of a few kilometers of new ones. The new system was put into operation during the last run performed in the frame of the Nuclotron-M project when the stable and reliable operation of the magnetic system at 2 T of dipole field is demonstrated (Fig. 1).

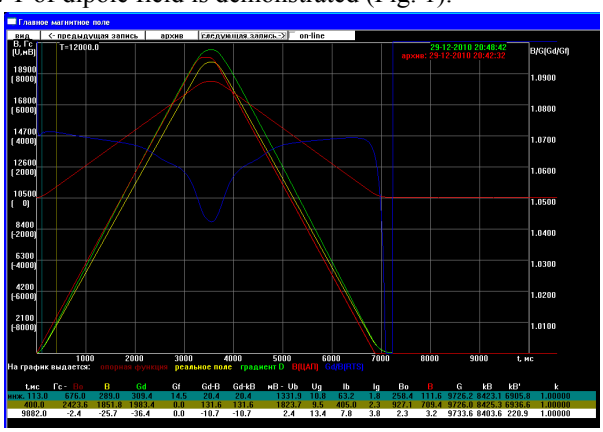

Figure 1: Cycle diagram at dipole magnetic field of 2 T. Red curve – basic function, yellow and green – field of the magnets and gradient of the lenses correspondingly. December 2010.

After completion of the Nuclotron upgrade tree runs (#43 - #45) at total duration of about 2900 hours were performed. About 1400 hours were spent for physical experiments including the shifts dedicated to machine development.

MACHINE DEVELOPMENT

The machine development aimed to increase the Nuclotron ability for the current physical program realization is provided in the following main directions:

- Step by step increase of the beam energy up to maximum design value (6 GeV/u for deuterons);
- Optimization of the beam dynamics in order to minimize the particle losses during acceleration;
- Further development of power supply system in order to provide required quality of slow extraction;
- Development of the diagnostics;
- Development of ion sources and fore-injector modernization.

Before the modernization the Nuclotron provided the beam energy up to 3 GeV/u maximum (for the ions with A/Z = 2). During the run #44 (December 2012) carbon beam was accelerated up to about 3.5 GeV/u and after slow extraction transported along the transport line to the point of the future location of the BM@N detector. During the same run the slow extraction of deuteron beam was realized at 4 GeV/u. In the run #45 (March 2012) the slow extracted 4 GeV/u deuteron beam was routinely used for physical experiments. At the end of the run #45 the possibility of the slow extraction was demonstrated at the deuteron beam energy of 4.5 GeV/u. Further increase of the extracted beam energy is related to development of the slow extraction system (increase of the electrostatic septum Voltage and current of the slow extraction quadrupoles) and optimization of operational conditions of the power supply system.

Decrease of the ion losses during acceleration is related with further development of the accelerating RF system, optimization of the closed orbit (including the orbit bump in the slow extraction region), development of the beam diagnostics. Sufficient part of these works was performed during runs #43 – #45.

Fast current transformer (FCT) installed at the Nuclotron before the run #44 was optimized for work in required dynamic range. Now the analogous device is installed in the beam injection line. In future one plans to use such FCTs at the Booster and collider.

New ionization beam profile monitor based on MCP was installed in the warm section of the Nuclotron. During run#45 it was optimized for work with heavy ion beams at relatively low intensity.

During the runs #44 and #45 experimental fragment (two octants of the ring) of new system of superconducting element thermometry were tested. Full scale implementation of the new system is scheduled to the end of this year.

In the frame of the Nuclotron upgrade program a new quench detection system was designed. Prototypes of the quench detector were consequently tested and serial production of the detectors was started in 2010. During the runs #44 and #45 the fragment of the new quench detection system including 20 quench detectors was operated during more than 1500 hours. Stable and reliable work of all elements was demonstrated [3].

The works oriented to creation of new sources of high intensive heavy ions and light polarized nuclei are in the final stage. In 2011 the 6 T solenoid for the heavy ion source (of electron string type – ESIS) was constructed, assembly of the source was completed this year. Experimental investigations of the source parameters have been started. The atomic beam source for the source of polarized particles was assembled and tested at INR (Troitsk), the plasma ionizer and test bench for the final assembly and test of the source is under construction at JINR. Completion of these works is scheduled for 2012. Reconstruction of LU-20 fore-injector, required for effective operation of the new sources, is in progress.

NUCLOTRON AS A TEST FACILITY FOR NICA

The Nuclotron having the same magnetic rigidity as the future NICA collider and based on the same type of the magnetic system is the best facility for testing of the collider equipment and operational regimes. Simulation of the collider magnetic system operational conditions was performed at the Nuclotron during runs #44 and #45. This presumed test of the Nuclotron magnetic system, power supply and quench protection systems, cycle control and diagnostic equipment in the operational mode with long plateau of the magnetic field. In the run #44 the magnetic field cycle duration was prolonged up to 500 s without beam acceleration, in the run #45 the circulation of accelerated deuteron beam during 1000 s was demonstrated (Fig. 2).

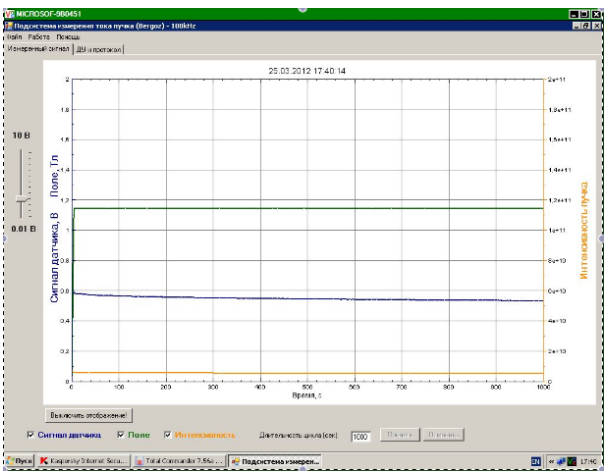

Figure 2: Circulation of the deuteron beam at the field plateau during 1000 s. Dipole field is 1.2 T (upper curve), the beam intensity is $5 \cdot 10^9$ particles (lower curve). Blue curve – BCT signal in Volts. March 2012.

Application of beam cooling methods (electron and stochastic) in the collider ring has the purposes of beam accumulation using cooling-stacking procedure and luminosity preservation during experiments. Experimental test of the stochastic cooling at the Nuclotron is considered as important phase of the collider cooling system design. During 2010-2011 the elements of the stochastic cooling chain for test at the Nuclotron were designed, constructed and after vacuum and cryogenic tests installed at the ring (Fig. 3). Experiments started in December 2011 were prolonged in 2012. We plan step by step investigate longitudinal and transverse cooling of coasting and bunched beams [4].

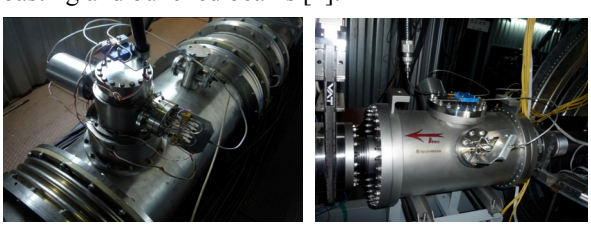

Figure 3: Pick-up (left) and kicker (right) of the Nuclotron stochastic cooling chain.

CONCLUSIONS AND OUTLOOK

In 2010 the Nuclotron-M project was successfully completed. The last three Nuclotron runs (#43 - #45) were performed in the frame of new JINR project, so called “Nuclotron-NICA”, dedicated to construction of the NICA facility main elements. During this project the Nuclotron will be used for prolongation and development of its current experimental program, test of the MPD elements, test of new equipment of the booster and collider rings.

In parallel with the existing accelerator complex development the technical design of the NICA collider injection chain elements (new heavy ion linear accelerator, small booster synchrotron) was prepared. Technical design of the collider is at the final stage.

The full-scale Nuclotron–type superconducting model dipole and quadrupole magnets for the NICA booster and collider were manufactured during 2010 - 2012. First dipole and quadrupole magnets for the NICA booster have successfully passed the cryogenic test on the bench. To construct the Booster and collider rings, it is necessary to fabricate more than two and half hundreds of the dipole magnets and lenses during a short period of time. Special area for the magnet assembly and full-scaled tests required for the magnet commissioning are currently being prepared [5].

ACKNOWLEDGEMENT

Authors are much indebted to the discussion with R.Stassen, L. Thorndah, V.Lebedev, T.Katayma during the Nuclotron stochastic cooling design. We have to express our gratitude to our colleagues from JINR member states participating in the development of the Nuclotron facility.

REFERENCES

[1] G. Trubnikov, N. Agapov, V. Alexandrov, et. al., Project of the Nuclotron-based ion collider facility (NICA) at JINR, Proceedings of RuPAC-2010, Protvino, Russia

[2] A. Eliseev, N. Agapov, A. Alfeev, et.al., Results of the Nuclotron upgrade program, Proceedings of IPAC2011, San Sebastian, Spain.

[3] E. Ivanov, A. Sidorin, G. Trubnikov, The quench detection system for superconducting elements of Nuclotron acceleration complex, these proceedings.

[4] N. Shurkhno, et. al., Development of Stochastic Cooling Technique for NICA Project: Experimental Measurements and Simulations, these proceedings.

[5] H. Khodzhibagiyan, et. al., Status of the design and test of superconducting magnets for the NICA project, these proceedings.

ADVANCES OF LIGHT-ION ACCELERATION PROGRAM IN THE U70

S. Ivanov, on behalf of the U70 light-ion task team#
Institute for High Energy Physics (IHEP), Protvino, Moscow Region, 142281, Russia

Abstract

The paper reports on the recent progress in implementing the program of accelerating light ions in the Accelerator Complex U70 of IHEP-Protvino. The list of milestones achieved since RuPAC-2010 includes: (1) Proof-of-principle acceleration of carbon-12 to the top available 34.1 GeV/u (specific kinetic energy). (2) Circulation and slow extraction from the U70 of the carbon beam at flat-bottom 453–455 MeV/u. (3) The first ever successful extraction of carbon nuclei at 24.1 GeV/u to the existing beam transfer line #22 followed by feeding the FODS experimental facility with carbon beam for fixed-target high-energy nuclear physics start-up.

INTRODUCTION

The program to accelerate light ions (deuterons, carbon nuclei) with a charge-to-mass ratio q/A = 0.4–0.5 in the Accelerator Complex U70 of IHEP-Protvino aims at diversification and development of the accelerator facilities. The ion mode of operation involves a sequence of Alvarez DTL I100 (2 tanks of 3, 4π mode), rapid cycled synchrotron U1.5, and the main synchrotron U70 itself.

This program is fulfilled incrementally, each recent machine run constituting a noticeable step in accomplishing the task.

This report overviews chronologically the progress achieved since the previous conference RuPAC-2010.

The starting point is acceleration in the U70 of deuterons to the specific kinetic energy 23.6 GeV/u (flattop 8441 Gs) with $5{\cdot}10^{10}$ dpp, see Ref. [1], RuPAC-2010.

Since then, the cascade of I100, U1.5, and U70 involved was switched to the **carbon-beam mode.** The procedure implies re-assembly of the solid-state laser (CO_2, 5 J) ion source, acceleration of ions $^{12}C^{5+}$ in the I100, thin-foil (Mylar, 4 μm) stripping to bare ions (nuclei) $^{12}C^{6+}$, and their subsequent acceleration in the synchrotrons U1.5 (6.9 T·m) and U70 (233 T·m).

RUN 2010-2

During this run, on Dec 8, 2010, the fully stripped carbon ions $^{12}C^{6+}$ were **first accelerated** to 455.4 MeV/u (kinetic**) in the U1.5**. Beam intensity varied between 5.3–$3.5{\cdot}10^{9}$ ipp through 26 ms ramp (once in 8 s), Fig. 1.

There were, at least, two prerequisites for this success:

1. Operational experience gained earlier with the more intensive deuteron beam.
2. Abundance of ions delivered by the I100, Fig. 2.

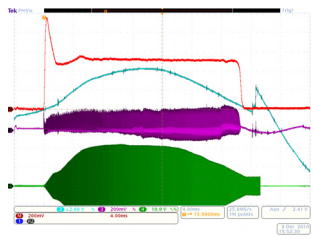

Figure 1: Carbon ($^{12}C^{6+}$) beam intensity monitored with a DCCT (upper (red) trace) and ramping rate of the U1.5 guide field (lower (blue) trace). In-out transfer is 65%.

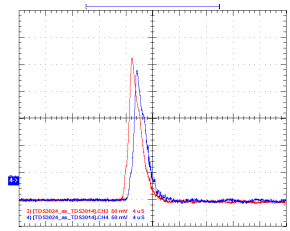

Figure 2: Beam at exits from the I100 (red) and BTL I100–U1.5 (blue). Pulsed current 21 mA, max. Pulse length 5 μs. In-out transfer through the BTL is 90%.

The first turns of carbon beam **in the U70** at flat-bottom 353.1 Gs were committed on Dec 10, 2010, Fig. 3. Bunch length is 80 ns FW at base. The lattice behaves as a magnetic ion separator, and 149.70 kHz beam rotation frequency is a signature of the particular $^{12}C^{6+}$ ion species due to mass defect in a bound system of nucleons (Table 1).

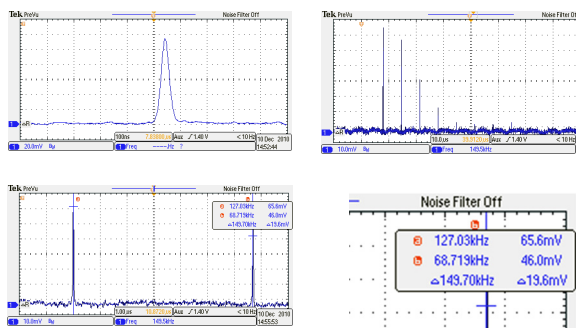

Figure 3: The first turns of carbon beam in the U70.

Table 1: Rotation frequency at 353.1 Gs flattop in the U70

Ion species	Rotation frequency, kHz
Carbon $^{12}C^{6+}$	149.70
Deuterons $^{2}H^{1+}$	149.24
Protons $^{1}H^{1+}$ (*p*)	183.80

RUN 2011-1

During this run, on Apr 24, 2011, carbon beam (single bunch) was **first accelerated in the U70 to the ultimate** available **energy** of 34.1 GeV/u (flattop 12 kGs) with max $5{\cdot}10^{9}$ ipp (8 s), design figure being $3{\cdot}10^{9}$ ipp.

Organizationally, the ion-mode MD was very challenging with the use of a low-intensity pilot proton beam and

N. Tyurin, A. Zaitsev, A. Soldatov, A. Afonin, Yu. Antipov, G. Britvich, A. Bulychev, A. Ermolaev, V. Garkusha, G. Hitev, N. Ignashin, D. Khmaruk, V. Kryshkin, V. Lapygin, O. Lebedev, V. Ledenev, E. Ludmirsky, A. Maximov, Yu. Milichenko, A. Minchenko, V. Seleznev, V. Stolpovsky, I. Sulygin, S. Sytov, and G. Kuznetsov.

multiple switching lattice power supply from rotor machine generators (RMG) to a stand-alone DC PSU (130 A, 20 kW) and back, refer to Table 2.

Table 2: Flow chart of regimes in Apr 21–27, 2011

Field, Gs	8590	352	12000	352
PSU	RMG	DC PSU	RMG	DC PSU
p-beam				
C-beam				

The I100 linac yielded some 12–14 mA (occasionally, up to 17 mA) of pulsed current.

A remotely controlled tool to shift out spent emitting spot on the graphite cylinder surface inside the laser ion source was set in operation to ease in-run maintenance. That time, spot sustainability was some 800 cycles, or just >1½ hr, a new spot requiring about 2 min of pre-training.

The U1.5 machine run smoothly and effectively.

A single bunch of ions was accelerated once per 8 s. Its parameters complied with the best performance data for a proton mode: injected bunch length at base ±60 ns, fractional momentum spread $\pm 2 \cdot 10^{-3}$. Lifetime at flat-bottom is about 40 s. Evolution of bunch length through cycle ±60 ns (flat-bottom), ±10 ns (transition crossing at 7.9 GeV/u kinetic), and ±25 ns (flattop).

Figure 4 shows transition crossing as a "mountain range" display.

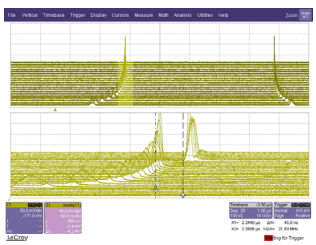

Scan period is 5000 turns. Scans are locked to the RF phase, and apparent jump of the bunch is, thus, virtual.

Figure 4: Transition crossing with C beam in the U70.

During end of the run 2011-1, the U70 operated in a storage-stretcher mode for a 453 MeV/u beam of $^{12}C^{6+}$ at 352 Gs flat-bottom.

On Apr 25, 2011 this intermediate-energy beam was for the **first time slowly extracted** from the U70 (0.6 s long spills of $1.5 \cdot 10^9$ ipp). Both bunched (single bunch) and un-bunched circulating beam options were tried.

Thus, the new slow extraction system was successfully beam-tested. This system is based on a compact cascade scheme "internal energy-degrader target IT#28 — deflecting septum magnet SM#34".

The beam is extracted inwards the U70 lattice from SS#34 pointing to the existing BTL#6. This beam-line and its shielding are now dismounted. Instead, the new BTL#25 is assembled there to deliver carbon beam for applied research (radiobiology, medicine, etc).

Physically, the extraction system at issue employs the well-known scheme by Piccioni-Wright, Ref. [2], adapted for the strong-focusing synchrotron U70. In the latter case, a localized & compact (1/20 of orbit length) layout with 180° betatron phase advances (horizontal and vertical) between IT and SM is feasible and suits the case.

It is the advantageous trade-off between ionisation losses and hampering multiple Coulomb scattering (MCS) across IT that opens a 'feasibility slot' for an effective (tens % of in-out ratio) extraction of multi-charged $^{12}C^{6+}$ at flat-bottom of the U70, see Table 3. A test proton beam was also extracted with the scheme.

Table 3: Internal energy-degrader targets

Ion species	Carbon $^{12}C^{6+}$	Protons *p*
Kinetic energy, MeV/u	353–355	1320
Target material	Beryllium	Graphite
Target thickness, mm	4.0	30
Target height, mm	10	10
Ionisation loss, $\Delta p/p_0$	–0.0069	–0.0069
R.m.s. MCS scattering, mrad	0.96	2.93

The new flat-bottom extraction system was proposed, manufactured, installed and beam-tested (proton and carbon ions) within a tight schedule starting in Jan 2010. Beam spot size observed at exit flange of SM#34 well fits to the design figures — around 20×10 mm^2 (h × v) for azimuthally uniform and 10×10 mm^2 for bunched beams.

In course of beam tests, two ways of pushing the waiting beam onto the IT#28 for slow extraction were tested.

The first one applies varying (dynamical) closed-orbit bumps near IT#28 and SM#34, Fig. 5.

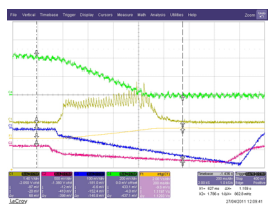

Traces from top to bottom: (1) circulating C beam intensity; (2) slow spill (a saturated signal); (3, 4) coil currents for closed-orbit bumps near IT#28 and SM#34, resp.

Figure 5: Slow spill under bumps of closed orbit.

The second way is to apply horizontal betatron noise causing controlled beam diffusion towards IT#28. To this end, the existing electrostatic deflector ESD#2, otherwise servicing the transverse feedback, is driven by a noise with flat (within 1.5–70 kHz) power spectrum, Fig. 6 and Ref. [3]. This option looks more promising for future routine operation due to inherent stationarity of beam traces.

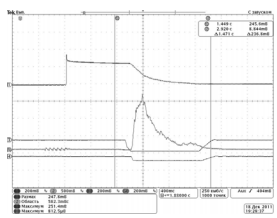

Traces from top to bottom: (1) circulating C beam intensity; (2) slow spill (a proportional signal); (3, 4) coil currents for steady closed-orbit bumps near IT#28 and SM#34, resp.

Figure 6: Stochastic slow spill.

RUN 2011-2

During this ion-beam run, the U70 operated in a storage-stretcher mode for a 455 MeV/u C beam at 353 Gs flat-bottom. Top beam intensity gained was $10 \cdot 10^9$ ipp, design figure being $3 \cdot 10^9$ ipp. Efforts were spent to get more experience with the new slow extraction, the **first observations of Bragg's range** being recorded.

Two experimental shots are shown in Figs. 7, 8. Fig. 9 confirms the expected performance of the slow extraction.

Figure 7: Finite range (30 cm ca) of extracted carbon beam through a plastic scintillator at 455 MeV/u.

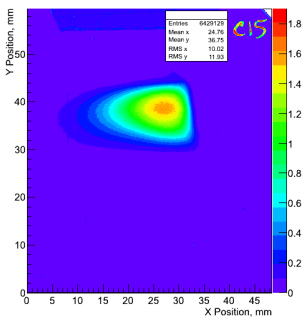

Figure 8: Bunched C beam spot at exit from SM#34 under stochastic slow extraction. Convolution over 3 cycles 8 s long each.

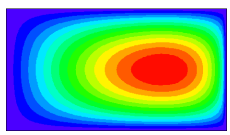

Surface contour plot of

$$F(x,y) = C \cdot x \cdot \sqrt{1-x^2} \times \times \left(1-y^2\right), \quad |x,y| \le 1$$

Figure 9: Calculated beam spot profile for a parabolic bunched beam under stochastic slow extraction.

RUN 2012-1

During the latest run 2011-2, carbon beam was accelerated to 24.1 GeV/u (flattop 8590 Gs) with $5 \cdot 10^9$ ipp (8 s).

The I100 team has managed to improve drastically the performance of the laser ion source. Thorough choice of gas mixture composition and laser pulse energy now allows to operate with 10–12 mA of pulsed current for 4000 cycles (instead of the former 800), i.e. for >8 hr.

All the high-energy beam extraction systems available in the U70 — fast single-turn, slow resonant (both, via lens Q38 and stochastic), slow with a bent Si-crystal deflector — were readily tested with a carbon beam.

The beam thus extracted was transferred through the existing 190 m long BTL#22 to the FODS experimental facility (the FOcussing Double-arm Spectrometer). The primary beam and its fragments were detected with the FODS scintillator counters, calorimeter, monitor and data acquisition systems. The counters and calorimeter were pre-calibrated with a 49.1 GeV (kinetic) pilot proton beam.

To start with, the BTL#22 was tuned to 50 GeV/c central momentum (protons). In this case, it accepts 25 GeV/c/u beam of ion species with charge-to-mass ratio q/A = ½ as well ($^2H^{1+}$, $^4He^{2+}$, $^6Li^{3+}$, $^{10}B^{5+}$). Indeed, the hadron calorimeter saw peaks in energy spectrum at 300 GeV (12 nucleons × 25 GeV/u (full energy) in ^{12}C), 100 GeV (^4He) and 50 GeV (^2H), refer to Fig. 10 (left).

Then, to detect fragments with q/A < ½, the BTL#22 was re-tuned to a higher momentum 60 GeV/c (protons) and fractional momentum acceptance ±1%. In this case, of all ^{12}C fragments, it can accommodate and transfer ^7Li nuclei only. Those indeed show themselves up as 175 GeV peak in the calorimeter readouts, Fig. 10 (right).

Fragmentation of ^{12}C occurs, presumably, due to an unattended presence of substances across the beam path (foils, air gaps, beam monitors, septa, etc).

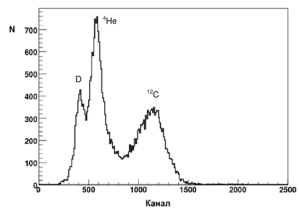

BTL#22 @ 50 GeV/c (p)

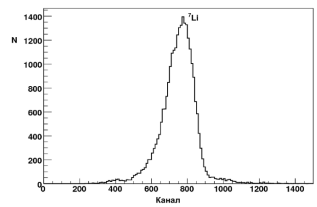

BTL#22 @ 60 GeV/c (p)

Figure 10: Amplitude spectra from the FODS hadron calorimeter. Abscissa division value is 3.2 bins per a GeV.

Thus, operational retuning of optics (central momentum and acceptance) of the BTL#22 allowed to use this beamline as an 'ad hoc' Fragment Separator yielding the **first ever experimental observations of high-energy nuclear-physics events** obtained with a 300 GeV (full energy) carbon beam delivered by the U70 (Apr 27, 2012).

CONCLUSION

In course of the four recent machine runs (2010–12) reported, important milestones of the program to accelerate beams of bare carbon ions in the Accelerator Complex U70 of IHEP-Protvino were achieved. Every run had its specific **highlight** boldfaced in the text above.

The light-ion (carbon) program pursues two goals:

1. To accelerate, extract and deliver high-energy (24.1–34.1 GeV/u, kinetic) carbon beam for fixed-target experiments in relativistic nuclear physics.
2. To accelerate, extract and deliver intermediate-energy (453–455 MeV/u and less) carbon beam for experimental applied research, including radiobiology and radiation medicine.

Steps are taken in either direction. Still, some advances have a flavor of a feasibility 'proof-of-principle' experiment yet. More efforts are planned to elaborate the techniques and attain a reliable routine operation with the better light-ion beam performance data.

REFERENCES

[1] S. Ivanov and the U70 light-ion task team, Proc. of RUPAC-2010, Protvino, 2010, p. 130–2.

[2] O. Piccioni et al., Rev. Sci. Instrum., 26, p. 232–3, 1955; B. Wright et al., Rev. Sci. Instrum., 25, p. 429–31, 1954.

[3] S. Ivanov, O. Lebedev, Preprint IHEP 2012–10, Protvino, 2012.

MARS: FOURTH GENERATION X-RAY LIGHT SOURCE BASED ON MULTITURN ENERGY-RECOVERY LINAC

G. N. Kulipanov, Ya. V. Getmanov, O. A. Shevchenko, A. N. Skrinsky, Budker INP SB RAS, Novosibirsk, Russia
N. A. Vinokurov*, Budker INP SB RAS, Novosibirsk, Russia and KAERI, Daejeon, S. Korea
M. V. Kovalchuk and V. N. Korchuganov, NRC "Kurchatov Institute", Moscow, Russia

Abstract

In the recent years, Russian government and scientific society have been coming gradually to an understanding the way of development science in Russia. Government have accepted a program of building six mega-science projects, and one of them can be a new fourth generation x-ray light source based on accelerator-recuperator. Multiturn energy recovery linacs (ERL) looks very promising for making modern synchrotron radiation sources, being less expensive and more flexible. At this time only one multiturn ERL exists. This Novosibirsk ERL operates with two orbits and two free electron lasers based on one linac now. The conception of Multiturn Accelerator-recuperator Radiation Source (MARS) was proposed in 1997 by G.N. Kulipanov, A.N. Skrinsky and N.A. Vinokurov. The use of the ERL with two separated accelerating structures allows to exclude main disadvantages of scheme with one linac, such as the pass of electron bunches with different energies through the same magnetic arcs. The feasibility study for such ERL-based high brightness x-ray source is presented.

INTRODUCTION

In the recent years, Russian government and scientific society have been coming gradually to an understanding the way of development science in Russia. Government has accepted a program of building one of the six mega-science projects, and one of them can be a new fourth generation x-ray light source. At the last 30 years the development of the synchrotron radiation (SR) sources has been aiming to different purposes. The main ones are the increase of spectral brightness and energy of generated quanta, using specific properties of SR radiation (coherence, polarization, time structure, etc.). Also, it is very important that each SR source is used by a large number of research groups (up to 60) from different areas of science and is worked for 7000 hours a year. Today, the SR sources of the third generation became the efficient factories for generating new knowledge, new technologies and new materials.

REQUIREMENTS TO FOURTH GENERATION SYNCHROTRON RADIATION SOURCES

For the last two decades, the development of SR sources of the fourth generation has been actively discussed. The world's physical community has worked out the following requirements to these sources. Full spatial coherence; the highest temporal coherence ($\Delta\lambda/\lambda<10^{-4}$) without additional monochromatization; the averaged brightness of the sources has to exceed 10^{23}-10^{24} photon$\cdot$ s^{-1}mm^{-2}mrad^{-2}(0.1% bandwidth)$^{-1}$; the full photon flux for the fourth generation sources must be at the level of the third generation SR sources; high peak brightness of the order of 10^{33} photon$\cdot$s^{-1}mm^{-2}mrad^{-2}(0.1% bandwidth)$^{-1}$ is important for some experiments; electron bunch length shorter, than 1 ps; high long-term stability; generation of linear and circular polarized radiation with fast switching of the polarization type and sign; constant heat load on chambers and optics, etc.; servicing the multi-user community [1].

During the last 30 years, the brightness of the x-ray SR sources based on storage rings has been increased by a factor of 10^9. Nevertheless, on the modern sources, the flux of coherent quanta is only 10^{-3} of the total flux. Therefore, in spite of successful demonstrating x-ray holography, it has not become an efficient technique for structural studies of real objects of mostly non-crystalline structure. Even for crystalline structures it is very important to use the speckle spectroscopy, which is accessible only in coherent light. Accordingly, the most important from all the requirements are: - the obtaining a fully spatially coherent flux of quanta with full photon flux at the level of the third generation SR sources, - a possibility of obtaining undulator radiation with a monochromaticity of 10^{-3} - 10^{-4} without using monochromators, which as a rule spoil the beam spatial coherence.

It is impossible to satisfy all requirements for the fourth generation SR sources using only one type of sources. High peak brightness and femtosecond length of light pulses can be achieved by using x-ray free electron lasers based on linacs with high (more than 1 kA) peak current.

Other requirements can be implemented easier and cheaper by using radiation from long undulators installed on the accelerator-recuperator.

ACCELERATOR SCHEME

A concept of accelerators-recuperators with one accelerating structure was proposed for realization a fully spatially coherent x-ray source in 1997 [2, 3]. Today, there is only one multiturn ERL in the world. It is

*vinokurov@inp.nsk.su

Novosibirsk ERL [4], which operates routinely with two orbits and two free electron lasers now. And, at this spring, four pass ERL was commissioned. But, the scheme of acceleration has serious intrinsic problems. The main disadvantage is that two electron beams (accelerating and decelerating) pass simultaneously through every magnetic arc, except the last one. It means, in particular, that variation of any element of this arc (steering coil or quadrupole gradient) changes the motion of accelerating particles, but after that, changes their motion again, when they pass this element during deceleration. Moreover, accelerating and decelerating beams have, in general, different initial conditions (average angles and transverse coordinates, and envelopes). It causes many constrains during the optimization of focusing and orbit correction, and therefore complicates the control of electron beams. Due to this, it is useless to install undulators into the lower-energy arcs. Indeed, since two beams in such undulator have different angles and coordinates, and it is impossible to correct them for both beams, the radiation quality will be poor. Therefore, it has been proposed to use scheme with two accelerating sections (see Fig. 1) and separated magnetic arcs for accelerating and decelerating beams [4, 5].

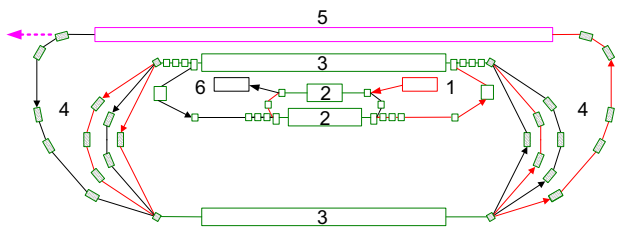

Figure 1: ERL with two separated linacs.

Principle of operation is the following: electrons with energy 8 MeV from injector 1 pass two preliminary accelerating RF sections 2 (42 MeV and 350 MeV) and come to first main accelerating structure 3 (0.7 GeV). Then, magnetic structure 4 bends electrons to the second main RF structure 3 (1.9 GeV). After 2 passes through each accelerating structure 3, electrons gain the final energy 5.6 GeV and pass to the undulator 5. Used electrons are decelerated at the same RF structures. In this case, accelerating and decelerating bunches pass through different magnetic arcs. Decelerated particles drop to the dump 6.

To generate fully spatially coherent undulator radiation with wavelength 0.1 nm it is necessary to decrease emittance of electron beam at the final energy to diffraction limit $\varepsilon_{x,z} < \lambda/4\pi \approx 10^{-11}$m. It corresponds to the normalized emittance 10^{-7} m. Such slice emittance was already demonstrated for single bunches with the 0.1 nC charge. Therefore we suppose that it is also possible for 10 pC in CW mode. For the RF frequency 1.3 GHz that corresponds to the average current about 10 mA. The version suggested for some single-turn ERL projects - using current up to 100 mA for keeping the photon flux - seems to be far from optimum, since with such an increase in current the brightness does not increase and even decreases sometimes. To compensate the decrease in the current value compared with that of the third generation SR sources, we shall use radiation from long undulators. For the planar undulator with $N = 10^4$ periods the diffraction-limited average brightness is about 10^{24} photon $s^{-1}mm^{-2}mrad^{-2}$ (0.1% bandwidth)$^{-1}$. This way we solve the problem of full spatial coherence and at the same time keep the photon flux at the level of the 3rd generation sources. It worth noting, that, since electron energy deviation ΔE leads to the shift of the undulator radiation spectrum by $\Delta\lambda/\lambda = -2\Delta E/E$, and the "natural" undulator radiation spectral width is $1/N$, the spectral brightness is not reduced for low enough energy spread [$\sigma_E/E < 1/(4N)$] only. Another advantage of split accelerating structure is a possibility to provide radiation with different wavelength ranges at different beamlinrs. A scheme with one undulator (Fig.1) can be extended by installations of long undulators into bending arcs 4 (see Fig. 2).

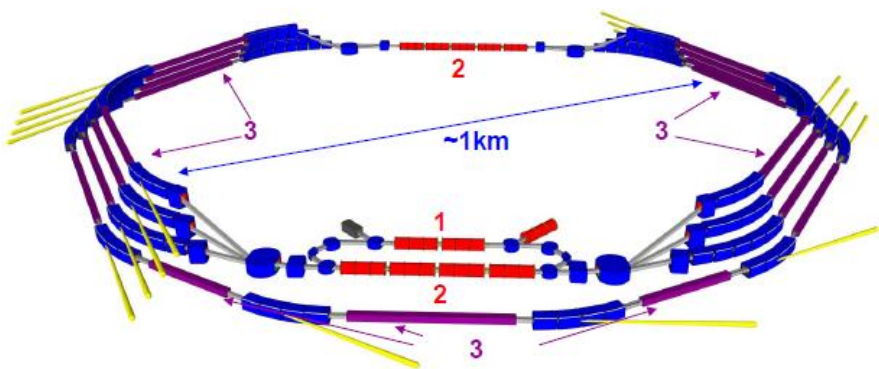

Figure 2: MARS scheme: 1 –cascade injection, 2 – linacs, 3 – long undulators.

There are 7 undulators for 5.6 GeV, and 4 undulators for 3.7 GeV, 3 GeV and 1.1 GeV in this scheme. To simplify the radiation output the magnetic arcs are separated both horizontally and vertically. The radiation parameters comparison of MARS (with average current I = 10 mA) and one of the best of existing third generation SR sources SPring-8 (with the average current I = 100 mA) is presented in the table 1.

Table 1: Comparison of MARS (I=10 mA) and SPring-8 (I=100 mA)

Facility	Number of undulator periods	Number of beamlines	Brightness, photon·s^{-1}mm^{-2}mrad^{-2} (0.1% bandwidth)$^{-1}$	Flux, photon·s^{-1}(0.1% bandwidth)$^{-1}$
MARS	10^3	3	10^{23}	10^{15}
	10^4	16	10^{24}	10^{16}
SPring-8	Bending magnets	23	10^{16}	10^{13}
	130	34	$3\cdot10^{20}$	$2\cdot10^{15}$
	780	4	10^{21}	$1.2\cdot10^{16}$

CONCLUSION

The main ideas of MARS design allow to reduce significantly the cost of the facility and energy consumption, providing the servicing of many users simultaneously. These ideas are simple and clear:

1). Using energy-recovery scheme.

2) Emittance of the electron beam is less than 10^{-11} m, which corresponding to the normalized emittance 10^{-7}m·rad.

3) Bunch charge should not exceed 10 pC. That corresponds to a 10 mA beam current.

4) Photon flux is proportional to the average current I and number of undulator periods N. To compensate the 10-50 times current decrease, it is necessary to use the radiation from undulators and wigglers with large (N > 1000) number of periods.

5) To provide a low level of radiation hazard and eliminate induced radioactivity, electron energy at the beam dump should not exceed 10 MeV.

6) To provide proper focusing for electrons with different energies in accelerating (decelerating) RF structures, it is necessary to use cascade scheme of injection.

7) For simultaneous multi-users servicing a scheme with two separated accelerating structures can be used. This eliminates the main disadvantage of the scheme with single linac, where accelerating and decelerating bunches create two radiation sources in each undulator, and simplifies the control of the beam.

8) Magnetic structure should contain long interspaces (L~200 m) for mounting a large number of undulators with $N \sim 10^2$ - 10^4 periods.

9). Energy spread of electrons at low energy should not exceed $1/N \sim 10^{-4}$.

10). A bending radius in magnetic arcs should exceed 60 m to decrease energy spread and emittance growth due to quantum fluctuations of the synchrotron radiation.

The use of long undulators with the high-quality electron beam of ERL is the solution for the fourth-generation x-ray sources. There are no any essential physical problems in the development of the fourth generation x-ray sources on the base of accelerators-recuperators with the average current about 10 mA. The main problem is the cost of such source and its further maintenance.

After successful commissioning of the third stage of the NovoFEL ERL (four-pass), the next step of MARS development should be a building of its lower energy prototype – ERL for extreme ultraviolet lithography (wavelength 13.5 nm) free electron laser [6].

ACKNOWLEDGMENTS

This work was carried out with the involvement of equipment belonging to the shared research center "SSTRC" and supported by the Ministry of Education and Science of the Russian Federation, Russian Foundation for Basic Research (RFBR Grant Numbers 11-02-12252-ofi_m and 11-02-91320-SIG_a), and the World Class Institute Program of the National Research Foundation of Korea funded by the Ministry of Education, Science and Technology of Korea (NRF Grant Number: WCI 2011-001).

REFERENCES

[1] *Scientific Needs for Future X-Ray Sources in the U.S. A White Paper*, SLAC-R-910, LBNL-1090-E (2008).

[2] Kulipanov G.N., Skrinsky A.N., Vinokurov N.A., J. of Synchrotron Radiation 5 (1998) 176.

[3] Kulipanov G.N., Skrinsky A.N., Vinokurov N.A., Nucl. Instr. and Meth. A 467-468 (2001) 16 – 20.

[4] Vinokurov N.A. et al., "Novosibirsk free electron laser facility: two orbit ERL with two FELs" IPAC'2010, Kyoto, May 2010, p. 2427-2429 (2010); http://www.JACoW.org.

[5] Douglas D., A "Generic Energy-Recovering Bisected Asymmetric Linac (GERBAL)", ICFA BD-Nl 26 (2001) 40.

[6] Socol Y., Kulipanov G.N., Matveenko A.N., Shevchenko O.A., Vinokurov N.A., PRST AB 14 (2011) 040702-1 – 040702-7.

THE DEVELOPMENT OF SYNCHROTRON RADIATION SOURCE OF NRC "KURCHATOV INSTITUTE"

V. Korchuganov, A.Belkov, Y.Fomin, E.Kaportsev, G.Kovachev, M.Kovalchuk, Yu.Krylov, K.Kuznetsov, V.Kvardakov, V.Leonov, V.Moiseev, V.Moryakov, K.Moseev, N.Moseiko, D.Odintsov, S. Pesterev, Yu.Tarasov, S.Tomin, V.Ushkov, A.Valentinov, A.Vernov, Yu.Yupinov, A.Zabelin, NRC Kurchatov Institute, pl. Akademika Kurchatova 1, Moscow,123182 Russia

Abstract

Russia`s first dedicated SR source based on electron storage ring Siberia-2 entered service in late 1999, Kurchatov Institute, Moscow. The report focuses on the consumer parameters of an electron beam and the further development of actual SR source, SR beam lines and experimental stations in 2012.

INTRODUCTION

The accelerating complex of the Kurchatov SR source includes: a for-injector - the linear accelerator of electrons on energy of 80 MeV, the small electron storage ring SIBERIA-1 with energy of electrons of 450 MeV, the big electron storage ring SIBERIA-2 with energy of electrons of 2.5 GeV and two electron-optical channels – EOC-1 and EOC-2 [1]. The accelerator complex parameters are specified in Table 1. Official opening of the Kurchatov SR source took place 1.09.1999.

Table 1: Parameters of KSRS facilities

Linac	**SIBERIA-1**	**SIBERIA-2**
E = 80 MeV	E = 80÷450 MeV	E = 0.45÷2.5 GeV
I = 0.2 A	I = 0.2÷0.3 A (singlebunch)	I = 0.1÷0.3 A (multibunch)
L = 6 m	C = 8.68 m	C = 124.13 m
DE/E = 0.005	B = 1.5 T	B = 1.7 T
ε_0 300 nm·rad	ε_{x0} 800 nm·rad	ε_{x0} 78÷100 nm·rad
τ_{pulse} = 18 ns	T_0 = 29 ns	T_0 = 414 ns
f_{rep} = 1 Hz	T_{rep} = 25 s	τ =10÷25 hrs
	λ_c=61 Å , BMs	λ_c=1.75 Å, BMs λ_c=0.40 Å, SCW
For-injector	Booster, VUV and soft X-ray source	Dedicated SR source 0.1-2000Å [1]

KSRS FACILITIES WORK

Before 2012 the work of SIBERIA-2 on experiments is carried out with use of SR from bending magnets in energy range фотонов 4-40 keV и спектральных потоках (10^{13}-10^{11}) ph/s/mrad/0.1%BW of photons 4-40 keV and spectral flux (10^{13}-10^{11}) ph/s/mrad/0.1%BW during week runs in a round-the-clock mode. Within one week 9 working 12-hour shifts are presented.

But, a regular work of X-Ray structure analysis station (RSA) with SR of 7.5T wiggler`s is planned (beamline 1.4-3, 17 mrad) starting from October 2012.

Diagram in Fig.1 shows the integral time devoted for SR experimental work at Siberia-2 in 2000 – 2011 years. Table 2 presents statistic of SR source Siberia-2 work at experiment in the first half of 2012. Note that in 2012 the SR source spent relatively much time in standby and adjustment mode due to stops for the firms which work according contracts (opening shielding walls, new beam lines installation, etc).

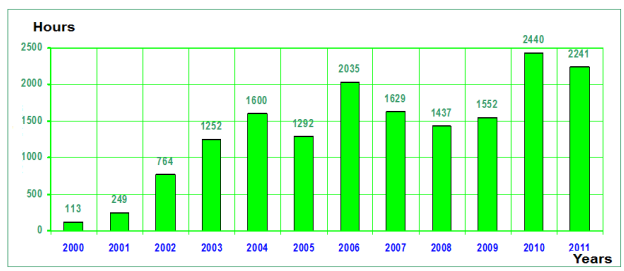

Figure 1: Experimental time at Siberia-2 in 2000-2011.

Table 2. Statistics of Siberia-2 on July 2012.

Parameter	**SIBERIA-1**	**SIBERIA-2**
Total working time, hrs : min	2371:18	2371:24
Experiment mode		
Duration, hrs	43	1074
% of total working time	2%	45%
Maximum current, mA	300	130
Average current, mA	116.6	46.0
Full integral, A-hrs	348.3	1046
One half of year 2012, A-hrs	5.0	49.3
Lifetime, hrs (100 mA)	1:56	38.5
Lifetime, hrs (50 mA)	1:11	51
Injection	10%	5%
Adjustment	34%	24%
Mode on duty	54%	25%

DEVELOPMENT OF KSRS ON 2010-2012

The works on modernization of systems of actually accelerating complex during 2008-2010 were in detail reported at conference RUPAC 2010 [2].

The purpose of works on 2010-2012 is both modernization of the existing equipment of a SR complex, and introduction in a system of new development.

Nanosecond Pulse Generator

During 2011-2012 the pilot copy of the nanosecond pulse generator on pseudo-spark switches (thyrotron TPI1-10k/50) for Siberia-2 injection system is developed and made in KCSR. The first tests with an electron beam were carried out when giving on short-circuited plates of an inflector of impulses of a current (≤3kA) with a semi-sinusoidal form of adjustable duration (100-200 nanoseconds) and a jitter <1ns. Such generators will allow refusing from the use of the high-voltage gas-filled electric discharge devices and from the forming lines. They promise stabilizing the homogeneity of the filling both in multibunch and in single bunch modes of operation during injection to Siberia-2. Work proceeds in a background mode.

Shortening of an Electron Bunch in SIBERIA-1

In 2008 on the SIBERIA-1 a new pulse output septum – magnet with more homogeneous distribution of a magnetic field was established. The increase in ejection factor of an electron current from SIBERIA-1 in EOC-2 to 70 % was received as a result. The following step on increase in ejection efficiency of electrons to SIBERIA-2 was made in 2011 when the RF generator of Siberia-1 was powered for the purpose of increase in accelerating tension at RF resonator of 34.5 MHz. from 15 kV to 30 kV. Now less than in 0.1 second before release of electrons with energy of 450 MeV the RF generator current is charply increased and, at the RF cavity invariable tune, the electric voltage on the cavity jumps from 15 kV to nearly 30 kV, leading to bunch shortening to $6\sigma \approx 130\text{cm} < \lambda_{181\text{MGz}} = 165.6$ cm. This action stabilizes a capture percentage in Siberia-2.

SYBERIA-2 RF System

At the end of 2009 on a ring of SIBERIA-2 three bimetallic resonators (the walls:7 mm of stainless steel and 8 mm of copper, diffusive welding) were installed on purpose to keep possibility of work with 7.5T wiggler causing increase of energy spread in a bunch for 30 percent. Now RF system consists of two RF lines, everyone includes RF generator on 200 kW on two tetrodes of the GU-101A type, a wave guide and 1 or 2 RF 181 MHz cavities with the feeders. The new set of parameters of SIBERIA-2 and RF system is listed in Table 3 [3].

Table 3. SIBERIA-2 and its RF parameters

Electron energy	E_{MAX}	GeV	2.5
Beam current	$I_{B\,MAX}$	A	0.29
SR losses from: bending magnets; bending magnets and SCWs	ΔE_{BMs} ΔE_{BM+WIG}	keV/ turn	681 1021
Accelerating voltage	$2U_1+U_2$	kV	1500

Further increase of the SR source work reliability connected with a transfer of Siberia-2 RF generators output cascades to new type of generating lamps of the TH781 type (powerful tetrodes), let out by THALES firm (France), is planned for 2012-2013. Thanks to pirographite grids they have higher reliability and a warranty period of service (3500 hours) in comparison with tetrodes GU-101A. The maker of the lamps assumes that on frequency 181 MHz , at RF capacity of 150 kW, the lamps will work not less than 7000 hours.

Delivery of TH781 lamps in KCSR will be executed on October, 2012. To minimize costs of their installation, the cases of the powerful output cascades of the RF generators, designed under lamps ГУ101А, will be modified with keeping the former principles of the capacities addition, modules of control and communication with loading (under the contract with BINP, Novosibirsk). Respectively, we are expected by the researches connected with setup of the new RF generators cascades and paths for steady work with a electron beam.

Increase of Electrons Lifetime in SIBERIA-2

On injection to SIBERIA-2 in a multibunch mode with a typical current in one bunch 3-4 мА the lifetime doesn't exceed 30 minutes. Mainly it is defined by Tuschek's effect. The most acceptable method to increase the lifetime at low energy is control of betatron oscillations by means of two skew-quadrupoles [4]. As a result, on injection energy the lifetime grew by (30-40) % depending on a current in one bunch. A speed of accumulation of electrons increased also. The fast and reliable algorithm of reorganization of magnetic structure was developed for ramping the energy in SIBERIA-2 [5] and the lifetime in the course of energy ramping to 2.5 GeV was increased. All process of acceleration borrows 2min.40s, at the losses in a beam current, generally on the energy below 1 GeV, which are not exceeding 2-3 %. During energy ramping the changes of betatron tunes from a working point of Qx = 7.773, Qz = 6.701 don't exceed the value ΔQ=0.015. The most dangerous resonances leading to losses of a beam are the resonances of the 4th order 2Qx + 2Qz = 29 and 4Qx =31. The greatest changes of betatron tunes occur at approach to 2.5 GeV and a stop of energy ramping.

New System "Orbit" at SYBERIA-2

In 2012-2013 24 pickups which are available on a ring of Siberia-2 will be supplied with the new high-precision electronic equipment and software product for measurement of cross-section coordinates of an equilibrium orbit (KCSR and LIBERA, Slovenia). Spatial resolution at measurement time more than 5 milliseconds for an average current of a beam 5-300 мА makes 1 micron.

Feed-back Systems at SYBERIA-2

Now on the SIBERIA-2 we observe mutual influence of control systems of two RF generators at each other through an electron beam. It leads to unstable work of RF

generators and to the electron current losses. The losses depend on a number of bunches. The quantity of particles in separate bunches is modulated according to the excitation mode number of synchrotron oscillation, see Fig. 4.

In 2012-2013 on SIBERIA-2 the Bunch-by-Bunch feedback system for suppression the instabilities in transverse and longitudinal directions (KCSR and LIBERA, Slovenia) will be established.

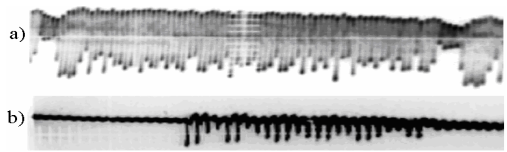

Figure 4: Modulation of particles in bunches at different fillings because of losses at an excitement of a collective mode of instability.

In the Fig. 5 the scheme of feedback for SIBERIA-2 is presented. As a kicker for suppression of coherent sinchrotron fluctuations small special RF cavity with own frequency of 950 MHz and a quality factor of 10 will be introduce at the straight section of ring. The existing strip lines will be used as kickers for suppression of coherent betatrone oscillations in X- and Y- plane. Also digital electronics, broadband amplifiers (25 W and 100 W) and a pickup - electrodes, phase detectors, the modulator, RF control are here entered.

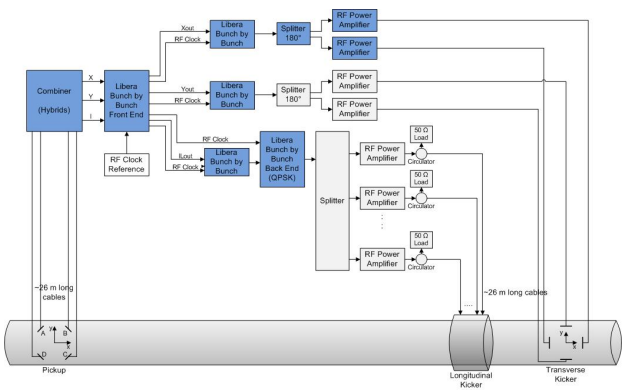

Figure 5: The scheme of BbB transverse and longitudinal feedback for SIBERIA-2.

New Station of Optical Observation [6]

By April, 2013 on Siberia-2 the special vacuum SR beam line will be mounted to release a visible range of SR out of limits of shielding wall of Siberia-2 storage ring where an optical bench with electronics of optical supervision (a CCD - matrix, φ - dissector, the 2-slit interferometer, the photomultiplier, TV) with high spatial and temporary resolution will be installed .

In the Fig. 6 the scheme of optical station is shown. The station of optical supervision includes automatic system for turn-by turn registration of a cross-section profile of a bunch. It is intended for measurement X - and Y - particles density distributions in chosen bunch, frequencies of synchrotron and betatron oscillations, and also for research of dynamics of a bunch form in chosen separatrix on one (from 3) chosen coordinate.

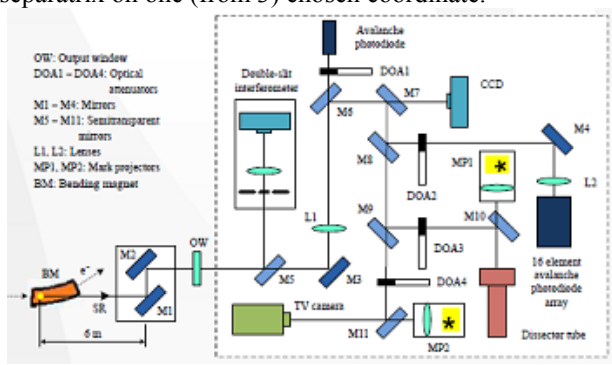

Figure 6: The scheme of optical station

The system turn-by-turn registration includes a lens and a linear detector based on 16 avalanche photo diodes. The signal of each photo diode is integrated and transferred on 12-digit ADC, having frequency of digitization of 50 MHz. The internal buffer memory accumulates results of measurements of ADC and allows to investigate turn-by-turn profiles of a bunch for long time (hundreds thousands of turns).

The station of optical supervision will be located outside of biological protection of storage ring. The work is conducted by KCSR and BINP.

New Power Supplies for Magnetic Correctors

In 2012 KCSR began a replacement of power supplies of the correcting magnetic elements at accelerator complex by the new more exact sources developed by "Marafon" firm (Moscow). At the first half-year of 2013 the all set of the 269 bipolar and unipolar sources (current stability 5E-4) will operate with a new control system and computer programs. Now the tests of pilot samples of sources on 6 A and 20 A are carried out. An installation of new sources at Euro-racks is in progress.

New Control System (KCSR, RT-Soft)

Upgrade of CS consists in changeover of the old equipment of CAMAC on trunk - modular hardware in the VME standard and the organization of new architecture.

In 2010 purchases of the modern electronic equipment are realized, the specialized laboratory of automation of a complex which task includes, in particular, application software development, start into maintenance and maintenance of the difficult equipment in working condition [7] is created.

CS is conditional subdivided into the upper and lower levels, server level and the periphery.

The lower level of CS realizes collection of diagnostic information and execution of control algorithms by executive systems of accelerator complex. It includes trunk-modular equipment in the VME standard and controlling equipment with the built-in processors

working under control of OS of the Lynx OS type. This equipment is connected to server level Ethernet or CAN communication lines.

Server level of CS includes application servers and the server of management system of a database (DBMS). At this level it is implemented: general control algorithm and UNK monitoring; a data interchange with processor modules of the VME standard, with CAN controlers and with an automated workplace of operators; recording of sessions of operators; information storage in DBMS; information representation on requests of users; self-diagnostics of operation of CS.

The top level of CS includes an automated workplaces of operators and other users. The full-function monitoring system and controls - CitectSCADA will work at the top level. The software of CitectSCADA allows to provide: visualization of processes, automated workplace control, tracing of systems in real time in a graphic look and access to contemporary records, preparation of the detailed reports, execution of the sub-programmes developed on CitectVBA and CiCode.

Geodesy (KCSR, "Neva Technology")

In 2011-2012 operations on creation of a high-precision geodesic network on the basis of the acquired exact equipment of type the laser tracker and specially set geodesic markers in the experimental hall of Siberia-2 are carried out for the purpose of an exact exhibition of elements and axes of being created new SR beamlines outside of bioprotection walls. Now the geodesic network in the experimental hall is integrated with a geodesic network of Siberia-2 storage ring tunnel so that they have a single system of coordinates.

NEW STATION AND INSERTION DEVICES

Bending Magnet SR Stations

Now installation ("NT-MDT", Zelenograd) of three experimental stations (hutches and optical components) and the three SR beamlines from 1.7 T bending magnets of SIBERIA-2 comes to an end: "PES" – Photoelectronic spectroscopy - K6.5, "PHASE" - X-ray precision optics-2 - K2.3, "NANOFAB-2" – research of micro and nano-electro-mechanical systems (MEMS and NEMS) - K2.6... Qualitative difference of these beamlines and stations from the already existing is that actually disappears concepts of separate station and the separate beamlines. Components of optics are distributed on all length of SR beamline. For example, the mirrors of complete external reflection are inside bioprotection space, at distance of 5-6 m from a radiation point, the blocks of monochromators at distance of 24-25 m whereas samples are at distance to 40 m from SR source.

Work with 7.5T SC Wiggler [2]

The SR from 7.5T (19+2) poles SCW was deduced for the first time on three SR beamlines in the experimental hall of SIBERIA-2 in November, 2009. In the Fig. 7 TV-images of SR from SCW on the luminescent screens set at end faces of the three SR beamlines are shown.

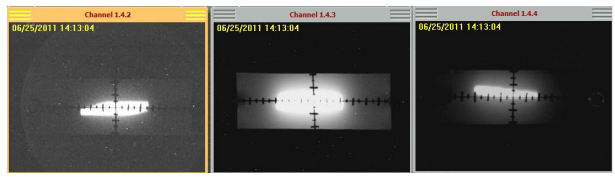

Figure 7: SR of 7.5 T SCW on an output of three beamlines (-13 mrad, 0 mrad, 17 мрад) in the experimental hall of SIBERIA-2.

Then, as a result of superconductivity loss in SCW, there was a collapse of the thin-walled copper liner (the vacuum chamber inside a cryostat) to loss of a vertical aperture. In June, 2011, in case of next superconductivity loss, there was a collapse of already next new and harder liner No. 2.

Figure 8 shows a wavy deformation of the liner No. 2 surfaces in the liner central part especially, repeating the period of a magnetic field of SCW with a longitudinal shift relatively to pole centers with maximum fields on a quarter of period.

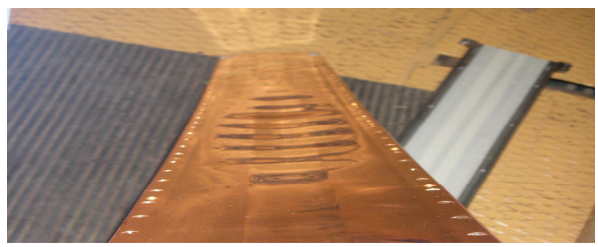

Figure 8: Deformation of walls of the liner No. 2.

After manufacture of the liner No. 3 and two new power supplies (the third pair), in December of 2011 their joint tests were carried out with SCW out of a Sybiria-2 ring, but with failure of superconductivity in the field of 7.5 T.

It was clarified that the current instability of power supplies led to overvoltage on the high-inductive windings and to inadmissible throws of a current. The current proceeding through one of sources, reached 350A instead of 240A, necessary for field 7.5T creation, as provoked failures.

Direct measurements of a vertical aperture of the liner No. 3 showed that deformations after failure remained within 0.1 mm. The decision about SCW installation with the liner No. 3 on a ring of Siberia-2 was made. By May of 2012 two new power supplies were made once more, the beamline K.1.4-3 (17 мрад) was joined with RSA station and continued to the double - crystal monochromator.

Input of SR in optical hutch of RSA stations was made on July 5, 2012. The image of SR at RSA station was observed by means of TV-cameras and the luminescent sensors located after the first optical mirror before and

after the double-crystal monochromator, adjusted for the SR wavelength of 1 Å, see Fig. 9.

Figure 9: A SR from SCW at RSA station. At the left - before, on the right – after the monochromator (1 Å).

Within the program of tests the failure of a superconducting condition of a wiggler in the field of 7.5 T was carried artificially out. The test of the wiggler windings by means of switching on of low currents in the wiggler just after failure showed that windings are serviceable and returned to a superconductivity condition.

The vertical aperture measurement of a liner by means of distortion of an electron beam equilibrium orbit («bump») showed that residual deformation of the liner did not lead to reduction of a vertical aperture. After summer vacations, 13.09.2012, regular operation on the filling of a liquid helium in the wiggler was executed. The sc wiggler magnetic field was increased up to 4.5T to reduce a magnetization of wiggler poles which was happened after last failure. Next work with the wiggler will be devoted to the degassing of the first SR absorber (about 36 kW of X-Ray power at electron current of 100 mA) and the increase of the operating electron current with sc wiggler switched on.

Creation of 4 SR Stations in 2013-2015

According to the Experimental Program in the direction 2 in KCSR the installation in an experimental hall of head samples of new generation experimental stations for complex researches in the field of convergent nano- bio- info- cognitive sciences and technologies is considered. Among them: station of low-angular diffraction (LAD), station of X-Ray absorbtion spectroscopy (EXAFS), station of a protein crystallography (Protein-2), station for substance research in extreme conditions (SEXC).

The Planned SC Wigglers on SIBERIA-2

The KCSR starts a creation of two new superconducting wigglers with a field of 3T at equilibrium orbit with critical wavelength of 1Å (additional to available 7.5 T sc wiggler) and their installation on the Siberia-2 storage ring in 2014. Key parameters of the new SC wigglers are given in Table 4 with a field 3T at energy of electrons E=2.5 GeV and a current of electrons of I=0.1 A.

High-intensity radiation of these wigglers will be used in «Experimental station for substance research in extreme conditions» - К2.4 and at station «A protein crystallography-2» - К3.4.

In comparison with intensity from a wiggler with a field of 7.5 T, the wiggler with a field of 3T has an advantage in a spectral interval of 5-30 keV photon energy.

Table 4. Project parameters of 3 T SCW.

Beamline	К2.4, К3.4
Electron energy, GeV	2.5
Pick magnetic field at axe, T	3.0
Photon critical energy, keV	12.48
Photon energy spectrum, keV	5-40
Magnetic period, mm	44
Angular divergence o SR, mrad	±2.77
Number of poles: main/lateral	69/4
Intensity of SR at ε_c=12.48 keV, ph/s/mrad/0.1%BW (I = 0.1 A).	$3*10^{14}$

CONCLUSION

We are sure that continuous efforts in the solution of the scientific and technical problems rising before employees of KCSR, will lead to high-quality improvement of the Kurchatov Center of Synchrotron Radiation.

REFERENCES

[1] V. Anashin et al., Nucl. Instr. Meth., A282 (1989), p. 369-374.

[2]M.Blokhov, V.Leonov, E.Fomin at al., " Kurchatov synchrotron radiation facility modernization", RUPAC2010.

[3]Proc. of the 8th EPAC, 3-7 June, 2002, Paris, p.2169-2171.

[4] V.Korchuganov, Yu.Krylov, A.Valentinov, Yu. Yupinov, "An increasing of electron beam lifetime at injection energy in SIBERIA-2 storage ring by regulating betatron coupling", RUPAC2010

[5] A.Valentinov, V.Korchuganov et al., "Energy ramping at Siberia-2", RUPAC2012.

[6] E. Fomin, G Kovachev, V. Korchuganov at al., RRC KI and A. Khilchenko, O. Meshkov, L. Schegole at al., BINP, "New station for optical observation of electron beam parameters at electron storage ring Siberia-2".

[7] E. Kaportsev, A.Valentinov…Yu.Efimov et al., « Modernization of the Automated Control System in the Kurchatov Synchrotron Radiation Source», RUPAC2012.

CURRENT FEL PHYSICS RESEARCH AT SLAC*

G. Stupakov, SLAC National Accelerator Laboratory, Menlo Park, CA, USA

Abstract

In this paper we review several techniques being pursued at SLAC National Accelerator Laboratory with the goal of improving the longitudinal coherence and increasing the output power of x-ray FELs. They include echo enabled harmonic generation (EEHG), hard x-ray self-seeding, using undulator tapering to increase the FEL power, and noise suppression in the electron beam.

INTRODUCTION

Free electron lasers (FELs) can provide tunable high-power coherent radiation which is enabling forefront science in various areas. At x-ray wavelengths, most of the FELs operate in the self-amplified spontaneous emission (SASE) mode [1, 2]. The Linac Coherent Light Source (LCLS) at SLAC working in the SASE mode at hard x-ray wavelengths [3] marked the beginning of a new era of x-ray science [4–6]. However, since SASE FEL radiation starts from beam shot noise, the FEL output has limited temporal coherence (i.e. noisy in both temporal profile and spectrum). FELs with improved temporal coherence (i.e. a well-controlled pulse shape and a bandwidth close to transform limit) should benefit many applications and enable new capabilities in many disciplines.

Various techniques [7–13] have been proposed to improve the FEL temporal coherence. In the self-seeding scheme, a monochromator is used to purify the spectrum of a SASE FEL and an additional undulator is employed to amplify the quasi-monochromatic radiation to GW level. Alternatively, seeding with an external source generated from an external laser may provide a fully coherent output having well-defined timing with respect to the laser. One way to directly seed an FEL is to use the high harmonic generation (HHG) source generated when a high power laser is injected to a noble gas.

EEHG SEEDING

To circumvent the need for a high power laser at short wavelength, frequency up-conversion techniques [10–14] have been envisioned to convert the external seed to shorter wavelengths. In the classic high-gain harmonic generation (HGHG), a single modulator-chicane system is used to bunch the beam at a harmonic frequency of the seed laser [10].

* Work supported by the U.S. Department of Energy under contract DE-AC02-76SF00515.

The frequency multiplication efficiency can be greatly improved with the recently proposed echo-enabled harmonic generation (EEHG) technique [12, 13]. In this scheme, an electron beam is first energy modulated by a laser with wave number k_1 and then sent through a chicane with strong momentum compaction after which the modulation is macroscopically smeared. Simultaneously, separated energy bands with a spread much smaller than the initial energy spread are introduced into the beam phase space. It turns out that if a second laser with wave number k_2 (k_2 can equal k_1) is further used to modulate the beam, after passing through a second chicane, density modulation at the wave number

$$k_E = nk_1 + mk_2 \tag{1}$$

can be generated (n and m are integers). The key advantage of EEHG is that by trading the large energy modulation from a laser with a large momentum compaction from a chicane, high harmonics can be generated from those separated energy bands with a relatively small energy modulation. Thus it promises both bunching and gain at very high harmonics, allowing the generation of coherent soft x-rays directly from a UV seed laser in a single stage.

The advanced frequency up-conversion efficiency has stimulated a broad interest in using the EEHG scheme to seed x-ray FELs [15–18]. In recent proof-of-principle experiments performed at SLAC's Next Linear Collider Test Accelerator (NLCTA) [14] and the SDUV-FEL at SINAP [19], the 4th and 3rd harmonics from EEHG have been observed. They demonstrated that a long-term memory of the beam phase space correlations could be properly controlled and preserved in the experiment. The latest results from the NLCTA presented the first evidence of 7th harmonics from the EEHG technique [20].

The novelty of the experiment [20] is that an rf transverse cavity (TCAV) was used to increase the slice energy spread by one order of magnitude such that the ratio of energy modulation to energy spread is similar to that in real seeded x-ray FELs. In this experiment, the 7th harmonic of the second laser at 227 nm was generated when the energy modulation is approximately $2 \sim 3$ times the slice energy spread.

The parameters of the experiment [20] are listed in Table 1.

Representative spectra of beam radiation after the seeding for various TCAV voltage are shown in Fig. 1. Fig. 1(a) through Fig. 1(d) show the HGHG spectra obtained with only the 1590 nm laser on, and Fig. 1(e) was obtained with

Table 1: Parameters of the ECHO-7 NLCTA experiment.

Electron beam energy	120 MeV
Bunch length	0.5-2.5 ps
Bunch charge	20-40 pC
Normalized emittance	$\sim 8\,\mu$m
Slice energy spread	~ 1 keV
First laser wavelength	795 nm
Second laser wavelength	1590 nm

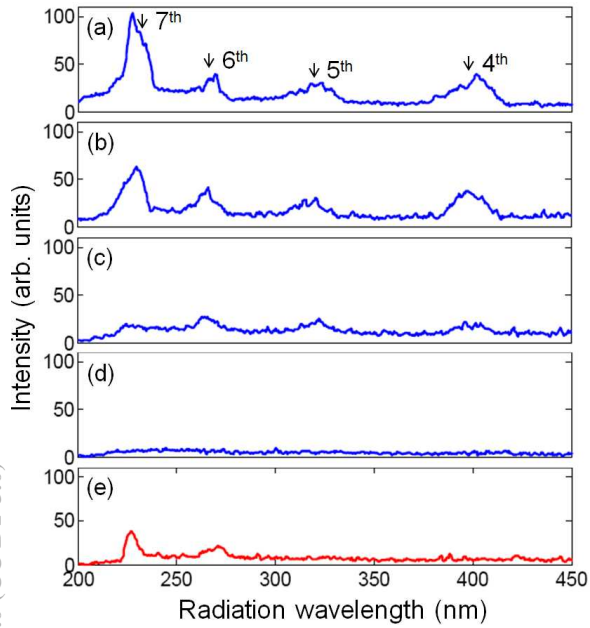

Figure 1: Spectrum of the radiation for various TCAV1 voltage:(a) V=0; (b) V=85 kV; (c) V=170 kV; (d) V=255 kV. The beam slice energy spread increases as we increase TCAV1 voltage. (a)-(d) are the HGHG signals when only the 1590 nm laser is on and (e) is EEHG signal at V=255 kV with both lasers on.

both lasers on. The spectrum of the coherent radiation is broadened due to the relatively large residual energy curvature from the varying rf phase along the bunch. As can be seen from Fig. 1, the harmonic radiation intensity decreases as TCAV voltage is increased. When the TCAV voltage was increased to 255 kV, the 4th to 7th harmonics were all suppressed and only the incoherent radiation was observed (Fig. 1(d)). When the first seed laser at 795 nm was turned on, the 7th harmonic was brought back.

The experiment [20] has presented the first evidence of high harmonics from the EEHG technique which overcomes the limit arising from the beam slice energy spread. It showed a clear signature that by splitting the phase space with a large momentum compaction chicane, high harmonics can be generated with relatively small energy modulation.

HARD X-RAY SELF SEEDING EXPERIMENT AT LCLS

While external laser-based seeding looks promising in the UV range and for soft x-rays, its usage for hard x-ray FELs creates extraordinary challenges and is not envisioned in the nearest future. Because of the difficulties of the direct seeding, the idea of self-seeding was proposed at DESY [7, 21]. It uses the SASE radiation generated in the first half of the undulator operating in a linear regime. An x-ray monochromator is installed between the first and the second halves of the undulators with a bypass for the electron beam. At the exit of the monochromator a narrow-band x-ray beam is combined with the electron beam and serves as a seed for the second half of the undulator.

The problem with this setup is that a typical monochromator delays the x-rays by several picoseconds. The electron beam has to be similarly delayed, requiring strong dipole magnets in the chicane of the bypass line. Incoherent synchrotron radiation and associated with it energy diffusion generate large energy spread in the beam which can suppress the FEL gain in the second half of the undulator. One of the approaches to overcome this difficulty was proposed in Refs. [22, 23]: it uses two bunches with the seed generated by the first one synchronized with the second bunch.

In another paper [24], the authors proposed to use a single diamond crystal in forward Bragg diffraction (FBD) geometry. They observed that due to the reflection of a narrow-band spectral line by the crystal, the transmitted x-ray pulses have a monochromatic tail (wake). While duration of the wake is relatively short (typically in the range of tens of femtoseconds) operation in a low-charge mode with extremely short bunches allows for the overlapping of the delayed bunch with the wake, which serves as a seed in the second part of the undulator. A detailed theory of the monochromatic wake formation is developed in [25].

Experimental demonstration of the crystal-based self seeding has been recently demonstrated at LCLS [26].

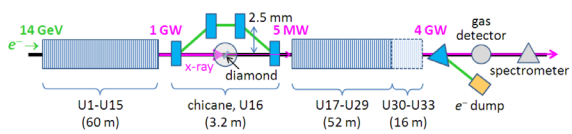

Figure 2: Layout of the LCLS undulator with a self-seeding chicane, diamond monochromator, gas detector and hard-X-ray spectrometer (from [26]).

In the experiment, a 110-μm thick diamond crystal, with a (004) lattice orientation, provided by the Technological Institute for Superhard and Novel Carbon Materials (Troitsk, Russia), was installed in place of one of the undulators. A new 3.2-m long magnetic chicane was added to the system to displace electrons transversely in order to bypass the diamond. The experiment demonstrated a dramatic narrowing of the spectrum from 20-eV FWHM

bandwidth to about 0.4-0.5 eV. The detailed account of the experiment can be found in Ref. [26].

TOWARD TERAWATT FEL

Using a crystal monochromator in the self-seeding scheme in combination with undulator tapering allows one to considerably increase the FEL output power. The underlying method is due to Kroll, Rosenbluth, and Morton (KLM) [27]. It relies on the increase of the energy transfer from the electrons to radiation by adjusting the undulator magnetic field to compensate for the electron energy losses, a tapered undulator. Note that LCLS routinely uses the tapered undulators not only to compensate for the energy loss of electrons due to the incoherent radiation in the undulator, but to double its output power to about 70 GW using its available tapering range of order of 0.8%.

Application of the KLM method for the upgrade LCLS-II was recently studied in [28]. The LCLS-II undulators will have variable gaps and in principle are tunable in a wide range of values of the undulator parameter K. It is important that quasi-monochromatic radiation produced with self-seeding allows a much better control of the trapping and deceleration of the electrons in the electromagnetic field of the radiation. The simulation studies suggest that it is feasible, with LCLS-like electron beam parameters, to generate coherent, TW-level, hard x-ray pulses within a $\sim$ 200m long, tapered undulator system. Together with output at the fundamental resonant wavelength, there will also be strong 3rd harmonic emission ($P_3 \geq 100$ GW) for planar-polarized undulators. To further improve the performance and shorten the undulator length, one can adopt a helical undulator for the FEL.

NOISE SUPPRESSION IN SEEDING

In free electron lasers, shot noise provides the startup radiation for Self-Amplified Spontaneous Emission (SASE), but also drives hazardous instabilities that might impede coherent processes. For example, the microbunching instability incapacitates diagnostics of the beam and can lead to degradation of the FEL performance [29–34]. In seeded FELs shot noise competes with external modulations of the beam being amplified in the process of the seeding [29, 35, 36]. Suppressing shot noise could have numerous accelerator applications, including controlling instabilities, reducing laser power requirements for seeding FELs, and increasing efficiency in cooling relativistic beams [37, 38].

Suppression of long wavelength shot noise was observed in microwave tubes as early as the 1950s, [39], and more recently similar effects (though from different physics) have emerged in semiconductor devices [40]. In the last few years, several groups have independently proposed suppressing shot noise at short wavelengths in relativistic electron beams [38, 41–43].

The quantify that defines the density fluctuations at a wave vector k is

$$F(k) \equiv \frac{1}{N} \sum_{j,l} e^{ik(z_j - z_l)} , \qquad (2)$$

where the sum is over all N electrons in the beam and z_j is the longitudinal position along the bunch of the jth electron. If the positions of electrons in the bunch are uncorrelated (shot noise), the $N(N-1)$ random phases in (2) corresponding to $j \neq l$ cancel each other, and we find the expected noise factor is $F(k) = 1$. If instead the electrons are grouped into microbunches spaced by λ (e.g. in an FEL at saturation), then all $N(N-1)$ terms add in phase and the noise factor reaches a maximum value of $F(k) \approx N$. One can also arrange correlations between the particles in such a way that $F(k) < 1$. We refer to the last case as the *noise suppression*.

Correlations between the particle positions in the beam that can lead to the noise suppression arise from the particle interactions followed by their longitudinal motion along z. Due to the relativistic nature of the beam, the longitudinal velocity is very close to the speed of light, and the relative displacements of the particles in free motion is typically too small. A setup in which the noise suppression can occur was considered in [43]: it consists of an interaction region of length L_a, where space charge forces change particle energies, followed by a magnetic chicane characterized by the dispersive strength R_{56} which shifts the longitudinal particle positions. In a simplified model of [43] it was assumed that the particles are longitudinally frozen in the

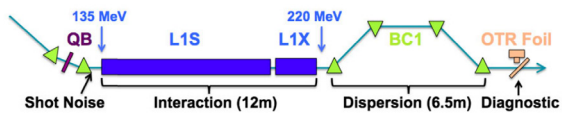

Figure 3: Schematic of the LCLS beam line used in the experiment for shot noise suppression, including the QB quadrupole, L1S and L1X accelerator sections, and bunch compressor chicane BC1. Radiation from the OTR foil served as the diagnostic.

interaction region, and there is negligible energy change through the dispersive region (i.e. the velocity bunching is small compared to the effect of the chicane strength). It was shown that in this case, for a beam with uniform density in the transverse cross section, the noise factor at the exit from the chicane can be written as

$$F(k) \approx (1 - \Upsilon)^2 , \qquad (3)$$

where

$$\Upsilon \equiv n_0 R_{56} A \text{ and } A \equiv \frac{4\pi r_e L_a}{S\gamma} , \qquad (4)$$

with n_0 the longitudinal particles density (number of particle per unit length), r_e the classical electron radius, γ the relativistic factor, and S the transverse beam area. By

choosing R_{56} to set $\Upsilon_{1D} = 1$, we find that the minimal value of $F_{1D}(k)$ is zero. For a transverse Gaussian distribution of rms size σ, the transversely integrated noise factor has the form $F(k) = 1 - 2\Upsilon + \frac{4}{3}\Upsilon_G^2$, where in Eq. 4 one has to replace a by 2σ. For the Gaussian case, optimal shot noise suppression occurs at $\Upsilon = 3/4$, giving $F(k) = 1/4$.

Paper [44] presented the first experimental evidence of shot noise suppression in relativistic electrons. Using the scheme of Ref. [43] it was demonstrated that matching the beam's collective space charge forces to dispersion experienced by the particles in a subsequent magnetic system reduces broad-bandwidth shot noise current fluctuations as observed through a reduction in Optical Transition Radiation (OTR) of the beam.

For an experimental demonstration of shot noise suppression the first linac and bunch compressor sections of the Linac Coherent Light Source (LCLS) was used. The experiment included four components shown in Fig. 3: an initial shot noise distribution system consysting of two dipole magnets and the "QB" quadrupole which reset the beam to an initial shot noise distribution, an interaction region which includes the S-band (L1S) and X-band (L1X) accelerator sections, a dispersive region (magnetic chicane BC1), and a diagnostic station. Table 2 gives main beam and accelerator parameters.

Table 2: Parameter list for experimental conditions.

Beam energy	135-220 MeV
Beam charge	5-20 pC
Norm. Emittance (x,y)	0.2 μm
BC1 Dispersion (R_{56})	0.1-2.5 mm
QB strength	10.3 kG
Interact. Beam Size ($\sigma_{\rm Int}$)	30-200 μm
OTR Beam Size ($\sigma_{\rm OTR}$)	25 μm
Camera Bandwidth (λ)	400-750 nm
Camera Aperture ($\theta_{\rm cam}$)	75 mrad

OTR emitted by the beam from a 1 μm thick aluminum foil inserted into the beam following BC1 was measured and compared with simulations and the analytical model. Fig. 4 shows that both simulations and the analytical model agree reasonably well with experimental results. The OTR intensity was suppressed by as much as 35% of the shot noise level.

SUMMARY

In this paper we reviewed several approaches, currently pursued at SLAC, to one of the main challenges for modern x-ray free electron lasers—an essential improvement of the temporal coherence of their output radiation. For soft x-ray FELs, seeding with an external laser, via harmonic multiplication, looks as a promising candidate. During the last 3 years extensive research work at SLAC, both theoretical and experimental, has been carried out to demonstrate the capabilities of the EEHG method.

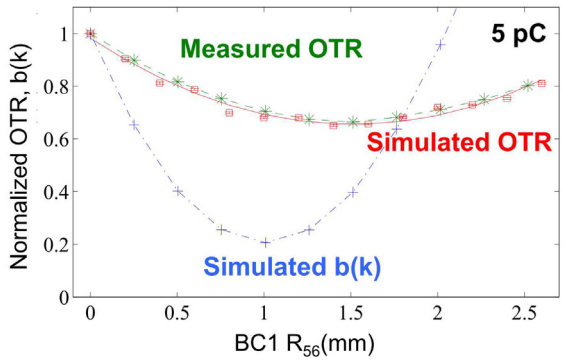

Figure 4: Simulation results compared to the experimental data for the bunch charge of 5 pC. The simulation predicts slightly stronger OTR suppression, perhaps due to the absence of transverse damping in the code. The shift in R_{56} in the OTR minimum is likely due to higher electron density in the experiment.

Hard x-ray self-seeding based on usage of Bragg forward reflection, was recently successfully demonstrated at LCLS. It opens a new road toward FELs with the output power on the terawatt scale.

The noise suppression technique, previously known for RF frequencies, has been experimentally achieved in the optical frequency range using a relativistic beam with typical for the FEL parameters.

ACKNOWLEDGEMENTS

This work was supported by the U.S. Department of Energy contract DE–AC02–76SF00515.

REFERENCES

[1] A. Kondratenko and E. Saldin, Particle Accelerators **10**, 207 (1980).

[2] R. Bonifacio, C. Pellegrini, and L. M. Narducci, Optics Communications **50**, 373 (1984).

[3] P. Emma, A. Akre, J. Arthur, R. Bionta, C. Bostedt, J. Bozek, A. Brachmann, P. Bucksbaum, R. Coffee, F.-J. Decker, *et al.*, Nat. Photonics **4**, 641 (2010).

[4] L. Young, E. P. Kanter, B. Krössig, Y. Li, A. M. March, S. T. Pratt, R. Santra, S. H. Southworth, N. Rohringer, L. F. DiMauro, *et al.*, Nature **466**, 56 (2010).

[5] H. N. Chapman, P. Fromme, A. Barty, T. A. White, R. A. Kirian, A. Aquila, M. S. Hunter, J. Schulz, D. P. DePonte, U. Weierstall, *et al.*, Nature **470**, 73 (2011).

[6] M. M. Seibert, T. Ekeberg, F. R. N. C. Maia, M. Svenda, J. Andreasson, O. Jonsson, D. Odic, B. Iwan, A. Rocker, D. Westphal, *et al.*, Nature **470**, 78 (2011).

[7] J. Feldhaus, E. Saldin, E. Schneidmiller, and M. Yurkov, Opt. Commun. **140**, 341 (1997).

[8] G. Lambert, T. Hara, D. Garzella, T. Tanikawa, M. Labat, B. Carre, H. Kitamura, T. Shintake, M. Bougeard, S. Inoue, *et al.*, Nature Physics **4**, 296 (2008).

[9] T. Togashi, E. J. Takahashi, K. Midorikawa, M. Aoyama, K. Yamakawa, T. Sato, A. Iwasaki, S. Owada, T. Okino, K. Yamanouchi, *et al.*, Opt. Express **19**(1), 317 (Jan 2011).

[10] L. Yu, Phys. Rev. A **44**, 5178 (1991).

[11] L.-H. Yu, M. Babzien, I. Ben-Zvi, L. F. DiMauro, A. Doyuran, W. Graves, E. Johnson, S. Krinsky, R. Malone, I. Pogorelsky, *et al.*, Science **289**(5481), 932 (2000).

[12] G. Stupakov, Phys. Rev. Lett. **102**, 074801 (2009).

[13] D. Xiang and G. Stupakov, Phys. Rev. ST Accel. Beams **12**, 030702 (2009).

[14] D. Xiang, E. Colby, M. Dunning, S. Gilevich, C. Hast, K. Jobe, D. McCormick, J. Nelson, T. O. Raubenheimer, K. Soong, *et al.*, Phys. Rev. Lett. **105**(11), 114801 (Sep 2010).

[15] D. Xiang and G. Stupakov, in *Proceedings of the 2009 Particle Accelerator Conference*, Vancouver, Canada (2009), p. 2327.

[16] E. Allaria, D. Xiang, and G. D. Ninno, in *Proceedings of the 2009 FEL Conference*, Liverpool, UK (2009), p. 39.

[17] S. Reiche, R. Abela, H.-H. Braun, B. Patterson, and M. Pedrozzi, in *Proceedings of the 2009 FEL Conference*, Liverpool, UK (2009), p. 51.

[18] K. Hacker, S. Khanv, G. A. Hamberg, V. Ziemann, A. Azima, P. Salen, and P. van der Meulen, in *Proceedings of the 2011 FEL Conference*, Shanghai, China (2011), p. 279.

[19] Z. T. Zhao, D. Wang, J. H. Chen, Z. H. Chen, H. X. Deng, J. G. Ding, C. Feng, Q. Gu, M. M. Huang, T. H. Lan, *et al.*, Nature Photonics **6**, 360 (2012).

[20] D. Xiang, E. Colby, M. Dunning, S. Gilevich, C. Hast, K. Jobe, D. McCormick, J. Nelson, T. O. Raubenheimer, K. Soong, *et al.*, Phys. Rev. Lett. **108**(2), 024802 (2012).

[21] E. Saldin, E. Schneidmiller, and M. Yurkov, Nucl. Instrum. Methods Phys. Res., Sect. A **475**, 86 (2001).

[22] Y. Ding, Z. Huang, and R. D. Ruth, Phys. Rev. ST Accel. Beams **13**, 060703 (2010).

[23] G. Geloni, V. Kochryan, and E. Saldin, Report 10-033, DESY (2010).

[24] G. Geloni, V. Kochryan, and E. Saldin, *Cost-effective way to enhance the capabilities of the LCLS beamline*, Report 10-133, DESY (2010).

[25] R. R. Lindberg and Y. V. Shvyd'ko, Phys. Rev. ST Accel. Beams **15**, 050706 (May 2012).

[26] J. Amann, W. Berg, V. Blank, F.-J. Decker, Y. Ding, P. Emma, Y. Feng, J. Frisch, D. Fritz, J. Hastings, *et al.*, Nature Photonics (2012), http://dx.doi.org/10.1038/nphoton.2012.180.

[27] N. Kroll, P. Morton, and M. Rosenbluth, IEEE J. Quantum Electron. **QE-17**, 1436 (1981).

[28] W. Fawley, J. Frisch, Z. Huang, Y. Jiao, H.-D. Nuhn, C. Pellegrini, S. Reiche, and J. Wu, in *Proceedings of the 2011 FEL Conference*, Shanghai, China (2011), p. 160.

[29] E. L. Saldin, E. A. Schneidmiller, and M. V. Yurkov, Optics Communications **202**, 169 (2002).

[30] Z. Huang and K.-J. Kim, Phys. Rev. ST Accel. Beams **5**, 074401 (2002).

[31] R. Akre, D. Dowell, P. Emma, J. Frisch, S. Gilevich, G. Hays, P. Hering, R. Iverson, C. Limborg-Deprey, H. Loos, *et al.*, Phys. Rev. ST Accel. Beams **11**, 030703 (2008).

[32] M. Borland, Y. Chae, P. Emma, J. Lewellen, V. Bharadwaj, W. Fawley, P. Krejcik, C. Limborg, S. Milton, H.-D. Nuhn, *et al.*, Nuclear Instruments and Methods in Physics Research Section A: Accelerators, Spectrometers, Detectors and Associated Equipment **483**, 268 (2002).

[33] S. Heifets, G. Stupakov, and S. Krinsky, Phys. Rev. ST Accel. Beams **5**, 064401 (2002).

[34] A. Marinelli and J. B. Rosenzweig, Phys. Rev. ST Accel. Beams **13**, 110703 (2010).

[35] G. Stupakov, in *Proceedings of the 2010 FEL Conference*, Malmö City, Sweden (2010), p. 274.

[36] G. Stupakov, Z. Huang, and D. Ratner, in *Proceedings of the 2010 FEL Conference*, Malmö City, Sweden (2010), p. 278.

[37] A. A. Mikhailichenko and M. S. Zolotorev, Phys. Rev. Lett. **71**, 4146 (1993).

[38] V. N. Litvinenko, in *Proceedings of the 2009 FEL Conference*, Liverpool, UK (2009), p. 229.

[39] C. C. Cutler and C. F. Quate, Phys. Rev. **80**, 875 (1950).

[40] C. W. J. Beenakker and M. Büttiker, Phys. Rev. B **46**, 1889 (1992).

[41] A. Gover and E. Dyunin, Phys. Rev. Lett. **102**, 154801 (2009).

[42] A. Nause, E. Dyunin, and A. Gover, Journal of Applied Physics **107**(10), 103101 (2010).

[43] D. Ratner, Z. Huang, and G. Stupakov, Phys. Rev. ST Accel. Beams **14**, 060710 (2011).

[44] D. Ratner and G. Stupakov, Phys. Rev. Lett. **109**, 034801 (Jul 2012).

BUDKER INP FREE ELECTRON LASER FACILITY – CURRENT STATUS AND FUTURE PROSPECTS *

O.A.Shevchenko#, V.S.Arbuzov, K.N.Chernov, E.N.Dementyev, B.A.Dovzhenko, Ya.V.Getmanov, E.I.Gorniker, B.A.Knyazev, E.I.Kolobanov, A.A.Kondakov, V.R.Kozak, E.V.Kozyrev, V.V.Kubarev, G.N.Kulipanov, E.A.Kuper, I.V.Kuptsov, G.Ya.Kurkin, L.E.Medvedev, L.A.Mironenko, V.K.Ovchar, B.Z.Persov, A.M.Pilan, V.M.Popik, V.V.Repkov, T.V.Salikova, M.A.Scheglov, I.K.Sedlyarov, G.V.Serdobintsev, S.S.Serednyakov, A.N.Skrinsky, S.V.Tararyshkin, V.G.Tcheskidov, N.A.Vinokurov, M.G.Vlasenko, P.D.Vobly, V.N.Volkov, BINP, Novosibirsk, Russia

Abstract

The free electron laser (FEL) facility at Budker INP is being developed for more than 15 years. It is based on the normal conducting CW energy recovery linac (ERL) with rather complicated magnetic system lattice. Up to now it is the only one in the world multiorbit ERL. It can operate in three different regimes providing electron beam for three different FELs. Its commissioning was naturally divided in three stages.

The first stage ERL includes only one orbit placed in vertical plane. It serves as electron beam source for terahertz FEL which started working for users in 2003. Radiation of this FEL is used by several groups of scientists including biologists, chemists and physicists. Its high peak and average powers are utilized in experiments on material ablation and biological objects modification. The second stage ERL is composed of two orbits located in horizontal plane. The second stage FEL is installed on the bypass of the second orbit. The first lasing of this FEL was achieved in 2009. The last stage ERL will include four orbits. Its commissioning is in progress now.

In this paper we report the latest results obtained from the operating FELs as well as our progress with the commissioning of the two remaining ERL beamlines. We also discuss possible options for the future upgrade.

ACCELERATOR DESIGN

The Novosibirsk FEL facility is based on the multiturn energy recovery linac (ERL) which scheme is shown in Fig. 1. In this scheme the beam goes through the linac several times before it enters undulator. As the result one can increase the final electron energy.

Multiturn ERLs look very promising for making ERLs less expensive and more flexible, but they have some serious intrinsic problems. Particularly in the simplest scheme shown in Fig.1 one has to use the same tracks for accelerating and decelerating beams which essentially complicates adjustment of the magnetic system. This problem can be solved by using more sophisticated scheme based on two linacs [1].

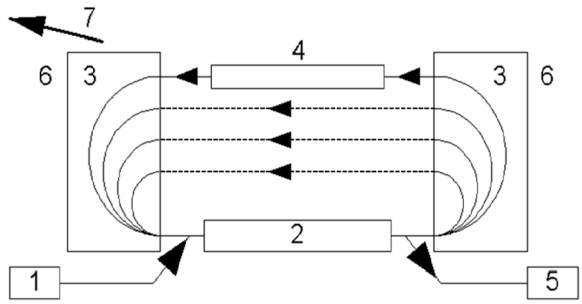

Figure 1: Simplest multiturn ERL scheme: 1 – injector, 2 – linac, 3 – bending magnets, 4 – undulator, 5 – dump.

At present the Novosibirsk ERL is the only one multiturn ERL in the world. It has rather complicated lattice as it can be seen from Fig. 2. The ERL can operate in three modes providing electron beam for three different FELs. The whole facility can be treated as three different ERLs (one-turn, two-turn and four-turn) which use the same injector and the same linac. The one-turn ERL is placed in vertical plane. It works for the THz FEL which undulators are installed at the floor. This part of the facility is called the first stage. It was commissioned in 2003 [2].

The other two ERL orbits are placed in horizontal plane at the ceiling. At the common track there are two round magnets. By switching these magnets on and off one can direct the beam either to horizontal or to vertical beamlines. The 180-degree bending arcs also include small bending magnets with parallel edges and quadrupoles. To reduce sensitivity to the power supply ripples, all magnets on each side are connected in series. The quadrupole gradients are chosen so that all bends are achromatic. The vacuum chambers are made from aluminium. They have water-cooling channels inside.

The second horizontal track has bypass with the second FEL undulator. The bypass provides about 0.7 m lengthening of the second orbit. Therefore when the beam goes through the bypass it returns back to the linac in decelerating phase and after two decelerations it finaly comes to the dump. This part (the second stage) was commissioned in 2009. The final third stage will include full-scale four-turn ERL and FEL installed on the last track.

The basic beam and linac parameters common for all three ERLs are listed in Table 1.

*Work supported by the Ministry of Education and Science of the Russian Federation; RFBR grant 11-02-91320
#O.A.Shevchenko@inp.nsk.su

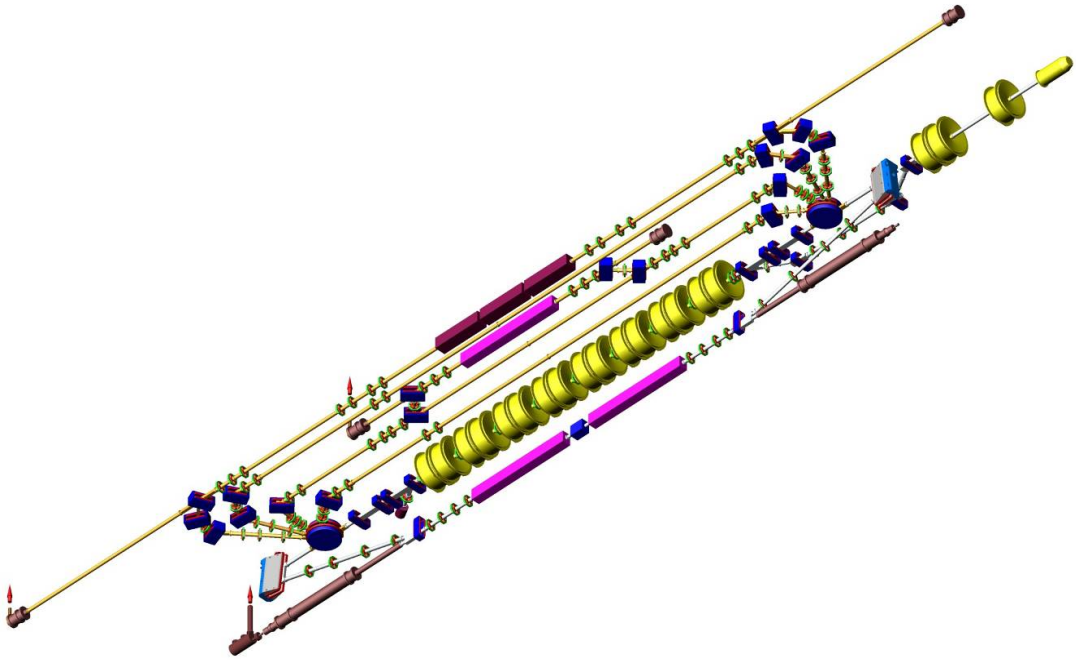

Figure 2: The Novosibirsk ERL with three FELs (bottom view).

Table 1: Basic ERL parameters

Injection energy, MeV	2
Main linac energy gain, MeV	10
Charge per bunch, nC	1.5
Normalized emittance, mm·mrad	30
RF frequency, MHz	180.4
Maximum repetition rate, MHz	90.2

Depending on the number of turns the maximum final electron energy can be 12, 22 or 42 MeV. The bunch length in one-turn ERL is about 100 ps. In two and four-turn ERLs the beam is compressed longitudinally up to 10-20 ps. The maximum average current achieved at one-turn ERL is 30 mA which is still the world record.

One essential difference of the Novosibirsk ERL compared to other facilities [3,4] is using of the low frequency non-superconducting RF cavities. On one hand it leads to increasing of the linac size but on the other hand it also allows to increase transversal and longitudinal acceptances which allows to tolerate longer electron bunches with large transversal and longitudinal emittances.

The location of different parts of the facility in the accelerator hall is shown in Fig. 3.

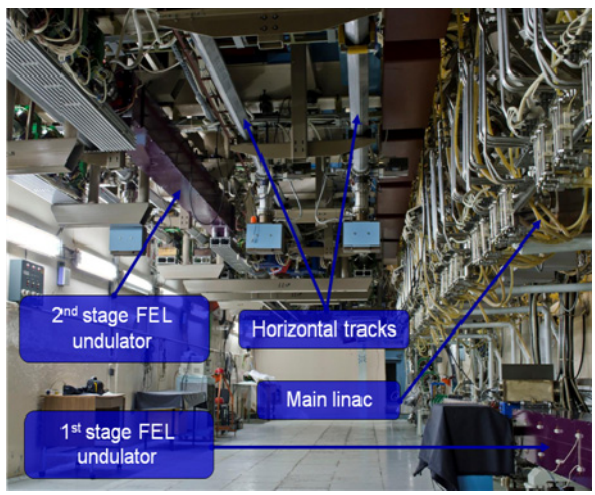

Figure 3: Accelerator hall (bottom view).

THE FIRST STAGE FEL

Design and Basic Parameters

The first stage FEL includes two electromagnetic undulators with period 12 cm, phase shifter and optical cavity. Undulator pole shape is chosen to provide equal electron beam focusing in vertical and horizontal directions. The matched beta-function is about 1 m. The phase shifter is installed between undulators and it is used to adjust the slippage. The optical cavity is composed of two copper mirrors covered by gold. The distance between mirrors is 26.6 m which corresponds to the round-trip frequency (and the resonance electron repetition rate) 5.64 MHz. Radiation is outcoupled

through the hole made in the mirror center. The optical beamline is separated from the vacuum chamber by diamond window. The beamline pipe is filled with dry nitrogen.

The FEL generates coherent radiation tunable in the range 120-240 micron as a continuous train of 40-100 ps pulses at the repetition rate of 5.6 - 22.4 MHz. Maximum average output power is 500 W, the peak power is more than 1 MW [5,6]. The minimum measured linewidth is 0.3%, which is close to the Fourier-transform limit.

Operation experience

For the last two years about 30 experiments were carried out at the Novosibirsk THz FEL. They include: pioneering works on THz ablation; study of micro- and nanoparticles, vaccines, polymers, metamaterials; production of nanotubes and nanostructures; composite diagnostics; terahertz radioscopy, imaging, detection of concealed objects; interferometry, holography & tomography; speckle and Talbot metrology; ellipsometry; fast water vapor detection; flame and gas detonation study; impact of THz radiation on genetic materials; impact of THz radiation on cells; study of integrated proteomic response; coherent effects in gases; ultrafast time-domain spectroscopy; interaction of atoms with strong THz EM-field.

Five user stations are in operation now. Two other are in progress. The new spectrometer has been installed recently. It allows to measure continuously radiation spectrum not interrupting user experiments (Fig. 4). Other radiation diagnostics include Fourier spectrometer, thermograph, microbolometer matrix, Shottky diode together with wideband oscilloscope. The last one is used for time-resolved measurements. It allows to detect longitudinal power distribution of radiation pulses.

Figure 4: Spectrum measurement diagnostic control (white line - the measured FEL radiation spectrum, blue line - water absorption spectrum).

Recently the third harmonics lasing was obtained. It was achieved by suppression of the first harmonics lasing using aperture-decreasing scrapers installed inside the optical cavity and proper adjustment of the phase shifter. The measured detuning curves for the first and third harmonics lasing are shown in Fig. 5.

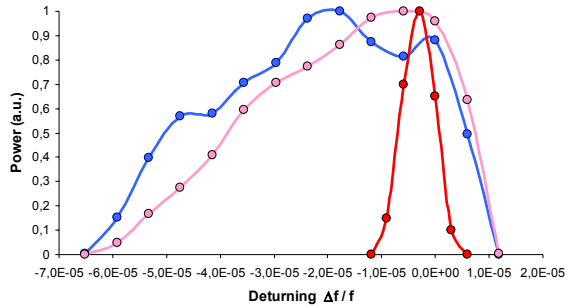

Figure 5. Normalized detuning curves for the lasing at the first (blue) and third (red) harmonics and the detuning curve for the amplified spontaneous emission at the third harmonic (pink).

THE SECOND STAGE FEL

The second stage FEL includes one electromagnetic undulator with period 12 cm and optical cavity. The undulator is installed on the bypass where the electron energy is about 22 MeV. Therefore the FEL radiation wavelength range is 40 - 80 micron. The undulator design is identical to the first stage one but it has smaller aperture and higher maximum magnetic field amplitude. The optical cavity length is 20 m (12 RF wavelengths). Therefore the bunch repetition rate for initial operation is 7.5 MHz.

The first lasing of this FEL was achieved in 2009. The maximum gain was about 40% which allowed to get lasing at 1/8 of the fundamental frequency (at bunch repetition rate ~1 MHz).

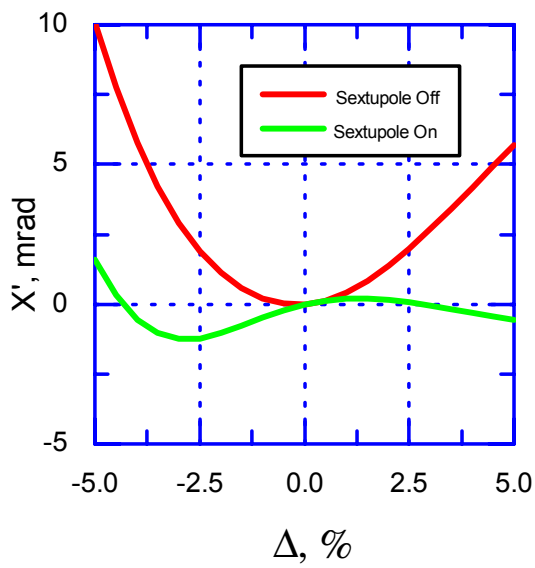

Figure 6: Compensation of quadratic dependence of the bending angle on energy by sextupoles in the first orbit bending arcs.

The significant (percents) increase of beam losses took place during first lasing runs. Therefore sextupole corrections were installed into some of quadrupoles to make the 180-degree bends second-order achromatic. It increased the energy acceptance for used electron beam (Fig. 6).

The optical beamline (Fig. 7) which delivers radiation from new FEL to existing user stations is assembled and commissioned. The output power is about 0.5 kW at the 9 mA ERL average current. Thus, the first in the world multiturn ERL operates for the far infrared FEL.

Figure 7: Optical beamlines for the first and the second stage FELs. Radiation of both FELs is delivered to the same user stations. Switching between FELs is done by retractable mirror.

THIRD STAGE ERL AND FEL

Electron beam in the third stage ERL is accelerated four times. The third FEL undulators will be installed on the last track where the beam energy is 42 MeV. In this FEL three permanent magnet undulators with period 6 cm and variable gap will be used. The wavelength range will be 5-30 microns. The scheme of the third stage ERL with FEL undulators is shown in Fig. 8. The electron outcoupling is planned to be used here [7].

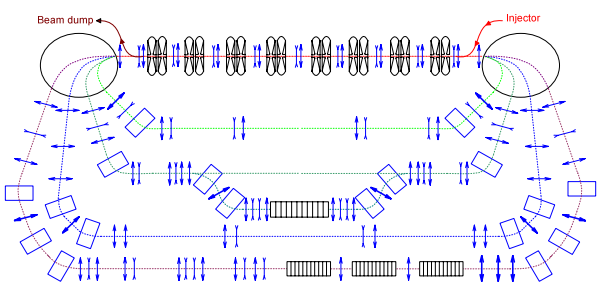

Figure 8: The third stage ERL with FEL undulators.

All magnetic system elements and vacuum chambers of the third stage ERL are assembled and installed. The first shifts for lattice adjustment took place and 80% of recuperation efficiency is already achieved. The signal from the BPM installed in the accelerating structure near the dump is shown in Fig. 9. All eight peaks here correspond to the same beam at different stages – the first four are in accelerating phase and the last four - in decelerating phase. One can see that the first and the last peak amplitudes do not differ significantly. It means that the beam losses mostly take place near the dump.

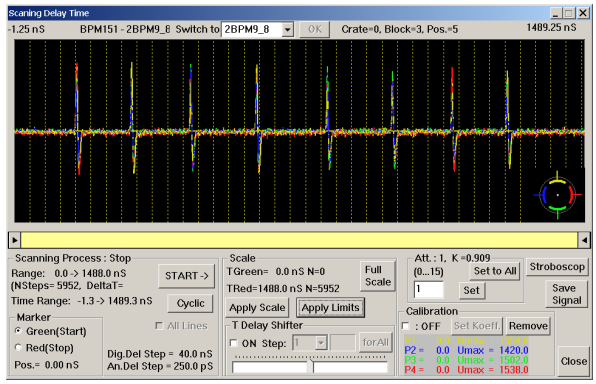

Figure 9: Signal from the BPM installed in the accelerating structure.

FUTURE PROSPECTS

In the nearest future we plan to continue the third stage ERL commissioning. The third FEL undulators will be installed shortly. The optical cavity design and production is in progress now.

The other important issue which we are working on now is the operation stability and improvement of the existing FEL parameters. We plan to make some improvements of the RF system. The new power supply for the exiting gun and new RF gun are being developed now. The lattice optimization is in progress. More serious modernization e.g. using the new type of undulators with variable period [8] is also considered.

REFERENCES

[1] D. Douglas, A Generic Energy-Recovering Bisected Asymmetric Linac (GERBAL), ICFA BD-Nl 26, 2001, P. 40-45.
[2] A E. A. Antokhin et al. NIM A528 (2004) p.15.
[3] G.R. Neil et al. Phys. Rev. Lett. 84 (2000), p. 662.
[4] E.J. Minehara. NIM A483 (2002) p. 8.
[5] V.P. Bolotin et al. NIM A 557 (2006) p.23.
[6] E.A.Antokhin et al., Problems of Atomic Science and Technology, p.3, №1, 2004.
[7] A.N. Matveenko et al., Proc. of FEL2007, p. 204.
[8] N.A. Vinokurov et al., Proc. of FEL2010, p. 696.

INDIRECT COOLED SUPERCONDUCTIVE WIGGLER MAGNET

A.V. Bragin, S.V. Khruschev, N.A. Mezentsev, E.G. Miginskya, I.V. Poletaev, V.A. Shkaruba, V.M. Syrovatin, V.M. Tsukanov, A.A. Volkov, K.V. Zolotarev*,
Budker Institute of Nuclear Physics, Lavrentiev ave. 11, 630090 Novosibirsk, Russia

Abstract

Superconducting wigglers are very popular devices for generation of the synchrotron radiation in the hard X-ray spectral range. The one direction of the future progress in wigglers development is reducing of the technical complexity wigglers design as well as technical service for cryogenic system. The BINP wigglers without liquid helium consumption were a noticeable milestone of these efforts. The next significant step toward additional simplification wiggler design and service is indirect cooling of the wiggler magnet. In this case the wiggler magnet not immersed into the liquid helium, but cooled by thermal connection link with the head of cryogenic cooler.

This approach is used for design of the indirect cooled wiggler for IMAGE beamline on the ANKA light source (KIT, Germany). This wiggler also will be tested as a prototype for damping wiggler for the damping rings in the project of the Compact Linear Collider (CLIC) for CERN.

This report summarizes some details of the wiggler design as well as a result of the short prototype testing.

INTRODUCTION

Budker Institute of Nuclear Physics produced more than twenty superconductive insertion devices which are working now in many SR centres over whole world [1-5].

During thirty years history the number of goals for design has been established and fulfilled. Among different goals, the simplicity of the regular service and cryogenic requirement is a very important.

From this point of view the wigglers development history can be divided by few period. The fist devises used a external storage for liquid helium, and operation procedure included regular refilling, Later the using of the commercial available Gifford-McMahon cryocoolers permits reduced difficulties of regular cryogenic operations, essentially reduce LHe consumptions and increase the refilling time.

Cryocoolers and common progress in the cryostat design permits achieve the real zero consumption of the liquid helium, and since 2005 all manufactured devises have this feature.

A currently developed wiggler can be the next step in the cryogenic design. Here magnetic coils connected with LHe volume by the number of cupper links and thermosiphons. This approach permits to have relatively simple access to the magnet and to the beam vacuum chamber. Principally it's possible to change whole magnetic system inside cryostat during relatively short time period (about two weeks) without complicated operation (machining, welding).

This approach had been selected for prototype of the damping wiggler for CLIC damping ring [6]. The huge number of wiggler on the damping ring requires extremely high reliability for every wiggler, so traditional approach for magnet isolation in the LHe tank is not suitable for this task. Moreover final selection of the CLIC damping wiggler design requires testing different technologies for coils wiring and the beam vacuum chamber coatings. It is possible test different options inside single cryostat.

The currently developed wiggler is dedicated for such research work as well as for regular work for SR user on the IMAGE beam line at ANKA storage ring. In according to agreement between CERN, KIT and Budker INP this wiggler should be installed on the ring in the middle of the 2013.

PARAMETERS OF THE WIGGLER

The main parameters of the wiggler are presented in the Table 1. These parameters are the subject of the compromise between CERN and KIT requirement.

Table 1: Main parameters of the wiggler with indirect cooling

Parameter	Value
Period	51 mm
Peak fiels	3 T
Magnet structure	1/4,-3/4,1,-1,…,-1,3/4,-1/4
Number of the full field poles	68×2
Full number of the poles	72×2
Magnetic gap	18 mm
Vacuum chamber vertical aperture	13 mm
Beam heat load	50 W
Maximum ramping time	< 5 min
Period for LHe refill with beam	> 6 months
LHe boil off @ quench	< 15
Field stability for two weeks	$\pm 10^{-4}$

*Zolotarev@inp.nsk.su

WIGGLER DESIGN

Magnetic Poles

Magnetic pole is a basic element of the wiggler magnetic system. The design of the pole should satisfy the magnetic field requirements, in other hand should provide the reliable cooling of the superconductive coils.

In current project the ARMCO iron pole kernel has a special shape with big parallelepiped in rear side (Figure 1). This part work like a yoke for closing magnetic flux between neighbour poles, and permits make reliable big cross-section connection with cooling links.

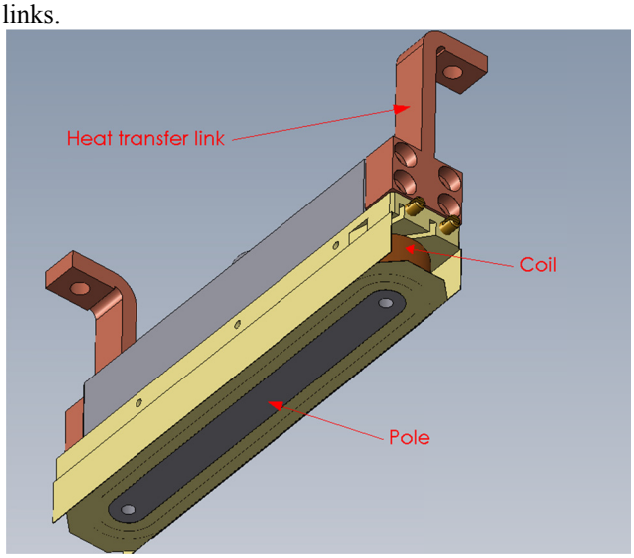

Figure 1. The general view of the wiggler pole

This design of the pole provides effective cooling of the most critical internal layer of the superconductive coil. As in most BINP wigglers each main pole has a two nested coils. This solution more effective satisfies for critical conditions for high currents and magnetic fields values. Coils are wound by 500 A NiTi superconductive wire with 0.9 mm diameter.

Magnetic System

Figure 2 shows the general layout of the magnetic assembling. Assembling consist from two independent halves for providing easy access to vacuum chamber.. Poles are fixed in the yoke frame. On the rear pat of yoke the special cupper plate with LHe channel is located. The cooling links of all poles thermally connected with this plate. Vacuum chamber is connected with 20 K stages of cryocoolers. These links cross-section is selected to evacuate 50 W SR load from internal surface of vacuum chamber. This load is possible in the case of multiply wiggler section of the CLIC damping ring by radiation of the upper flow wigglers.

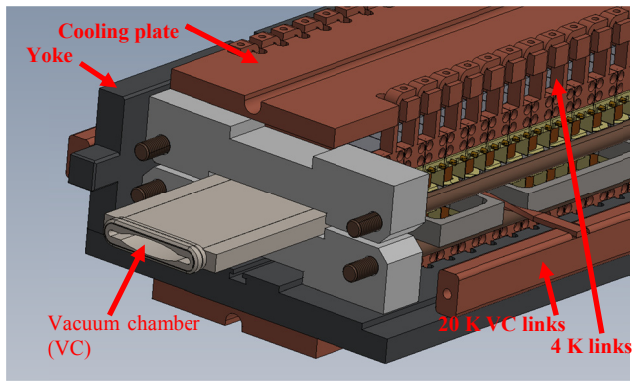

Figure 2. Magnetic system assembling.

Cooling Conception

Figure 3 presents the cooling scheme of the wiggler magnet. Wiggler cold mass includes LHe volume (about 90 l) which connected with magnet by two thermo-siphon pipes.

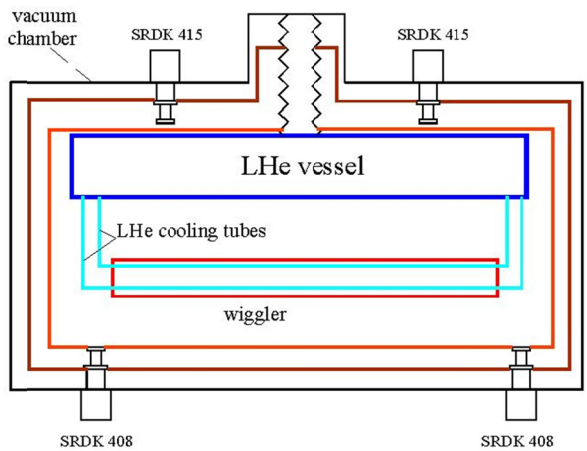

Figure 3. The scheme of the wiggler cooling conceptions

Cold mass is suspended in an isolation vacuum and surrounded two thermal shields with temperatures 20 K and 70 K. Cold mass is connected with 4 K stages of the two SHI SRDK 415 cryocoolers which permit evacuate about 2 W power.

Another two SRDK 408 cryocoolers are connected with thermal shield and vacuum chamber.

Figure 4 show the cross-section of the wiggler in detail.

Other Components

Principally with exception of the cold mass, the designs of other wiggler components are similar to convential BINP wigglers. This set includes current lead system, thermal shields, superisolation mates, Kevlar ropes suspension system, RF shield and temperature transition for vacuum chamber. The designs of these components were optimize during long history of the BINP activity in the developing and fabrication of the superconductive wigglers [1-5].

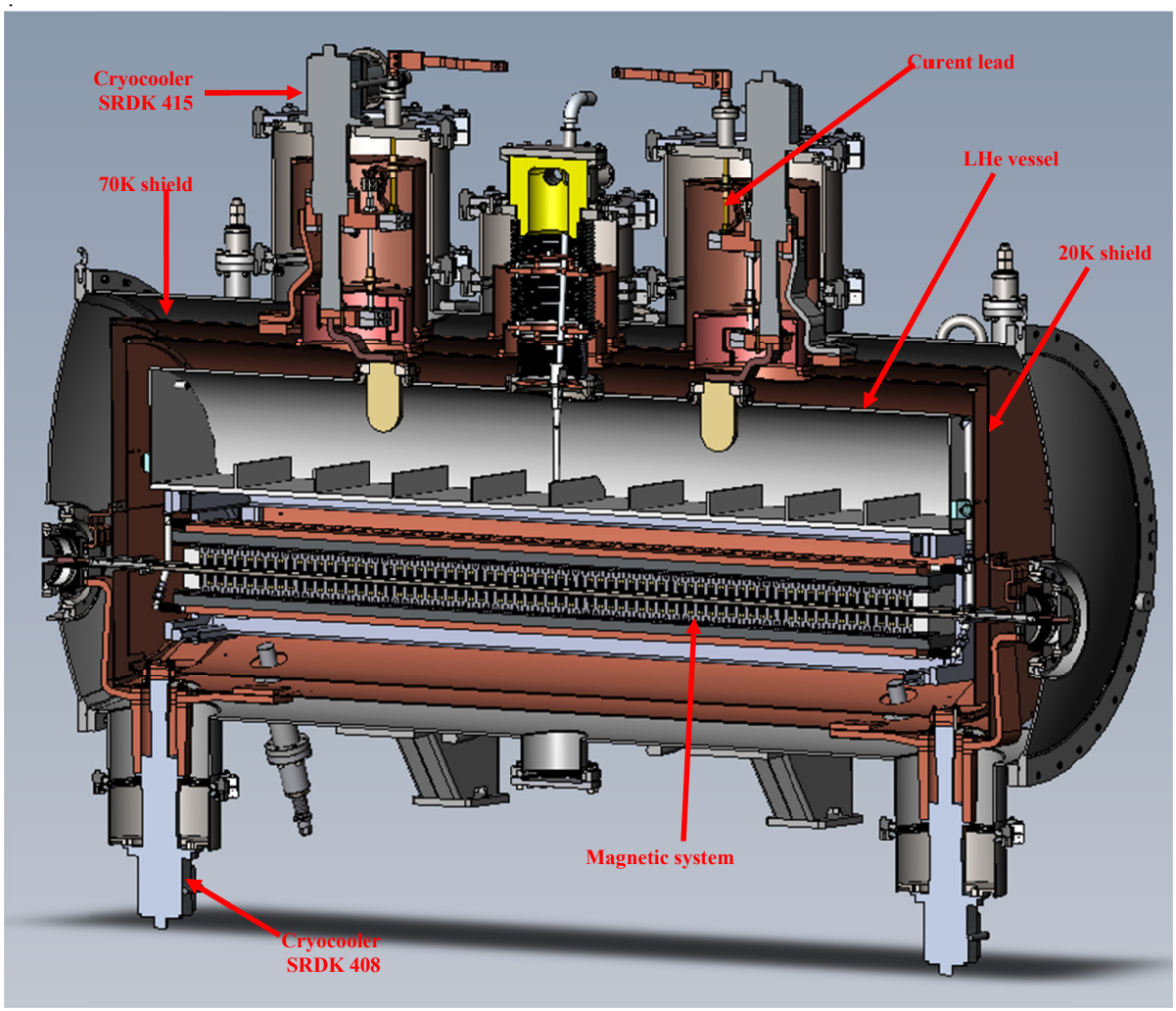

Figure 4: The cross-section of the assembled wiggler..

PROJECT SCHEDULE

In according with current contract between KIT, CERN and Budker INP the next schedule for main milestones had been established:

- Conceptual design report May, 2012
- Short prototype testing Oct., 2012
- Full design report Oct., 2012
- Fabricating June, 2013
- Factory acceptance tests Aug., 2013
- Site acceptance test, commissioning Sept., 2013

REFERENCES

[1] Kulipanov G.N., Mezentsev et al., Development of superconducting compact storage ring for technical purposes in the USSR. Rev. Sci. Instrum. 63(1), 1992, p.731-736.

[2] Mezentsev N.A, Shkaruba V.A., et al., Superconducting 7.5 Tesla wiggler for PLS. NIM, Vol. A359, No.1-2 (1995),p.101-106.

[3] Kulipanov G., Li O., Mezentsev N., et al., Superconducting 7 Tesla wiggler for LSU CAMD. Journal of Synchrotron Radiation (1998), Vol.5, Part 3, p.440-442.

[4] A. Batrakov, V. et al., Magnetic measurements of the 10T Superconducting Wiggler for the SPring-8 storage ring. Proc.of 7th International conference of Synchrotron Radiation Instrumentation, Berlin, 2000.

[5] S.V. Khrushchev, V.K. Lev, N.A. Mezentsev, E.G. Miginsky, V.A. Shkaruba, V.M. Syrovatin, V.M. Tsukanov, A.A. Volkov, J. Campmany, D. Einfeld Superconducting 119-pole wiggler for ALBA light source. Proc. of IPAC-2011, San Sebastian, Spain.

[6] H. Schmickler et al., "Technology Developments for CLIC", MOYCH03, these proceedings.

SUPERCONDUCTING QUADRUPOLE MODULE SYSTEM FOR THE SIS100 SYNCHROTRON

E. Fischer*, P. Schnizer, K. Sugita, J. Meier, A. Mierau,
P. Spiller, O. Kester, GSI, Darmstadt, Germany
H. Khodzhibagiyan, G. Trubnikov, JINR, Dubna, Russia

Abstract

The SIS100 heavy ion synchrotron, the core machine of the FAIR complex, uses fast ramped superconducting magnets. As for its ancestor, the Nuclotron operational at JINR Dubna since 1993, its superconducting magnets are based on iron dominated design and coils made of Nuclotron type cables. The SIS100 magnets differ from the Nuclotron magnets in the following points: they are longer, the beam aperture was enlarged and the field quality improved, its AC losses reduced. The coils have a lower hydraulic resistance and the operation current is doubled. These achievements were obtained in a R&D collaboration between JINR and GSI. Now in the realisation phase GSI will procure and test the SIS100 dipole magnets, while JINR together with GSI will finalise the design of the quadrupoles units (consisting of one quadrupole and one corrector), procure, test and assemble them into doublets. We report on the status of the project, the scheme of the JINR-GSI collaboration for developing and manufacturing the SIS100 quadrupole modules and the steps required to achieve the start of the series production.

INTRODUCTION

SIS100 is following the design of the Nuclotron, but its circumference was increased by a factor of about 4 that had several implications: the dipole magnet length was increased by a factor of about 2, the aperture was increased and a continuous triangular cycle demanded. Even though the AC losses occurring in the magnet were reduced by making a smaller end coil loop, replacing the ferritic brackets with a stainless steel version, which acted as a flux short path and thus created large losses, while the former two parts reduced the eddy currents and thus the AC losses due to the longitudinal B_z field component matching the original set target of 30% total loss reduction, the cable had to be redesigned to adjust the hydraulic resistance for the larger magnet, which now will provide ample cooling margin for the SIS100 magnets [1, 2]. This approach was then picked up for the NICA Booster and collider magnets [3] based on the common R&D conducted from 2002 until now. Further the field quality of the magnets was improved [4, 5, 6].

All that common interactions just naturally lead that GSI is now producing the SIS100 dipoles and JINR the quadrupole units of the SIS100 machine.

* e.fischer@gsi.de

THE SIS100 MAIN MAGNETS

The redesigned Nuclotron cable, necessitated by the cryogenic losses of the SIS100 dipole, is now also used for the quadrupole (see Fig. 1), which allows introducing the

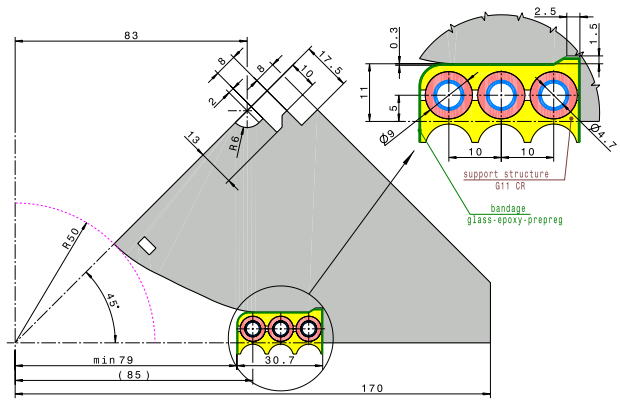

Figure 1: The 3-turn quadrupole magnet lamination design.

reinforcement coil support structure similar to the dipole and reusing the same components for the cable itself, the bus bars, the voltage breakers, soldering joints and current leads. Further low current quadrupoles are required for the extraction and injection section, which now can be produced using the same magnet yoke but using an adjusted low current Nuclotron type cable; the same as foreseen for the correctors. The 3 turn quadrupole design reduces further the types of various utilities as only one type of HTS current leads is required and only one type of bus bars and voltage breakers in the dipoles, quadrupole doublets, bypass lines, feed in lines, superconducting links, current lead boxes. Quench measurements of the dipole can be directly used for the quadrupole and only one single type of high current superconducting joints is needed.

QUADRUPOLE UNITS

The quadrupole units consist of a quadrupole on which one or two corrector magnets or a beam position monitor are mounted.

The corrector magnets are requested to be operated with ¡ow current ($<$ 300 A) in order to reduce the heat leak from the copper current lead pair as each magnet is powered ¡ndividually. Taking into account the advantage of Nuclotron type cables for fast ramped magnets, this design was adopted with individually insulated superconducting

strands, as shown in Fig. 2. After the coil winding the stands are connected in series and the first and last of these strands are connected to the current lead pair.

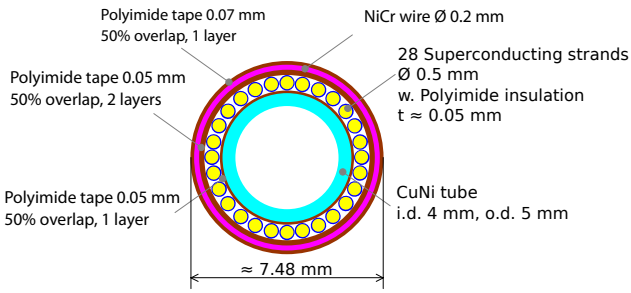

Figure 2: The cable of the corrector magnets.

The steering magnet (Fig. 3(a)), which contains a vertical and a horizontal dipole coil, and the multipole corrector magnet (Fig. 3(b)), which contains a quadrupole, a sextupole and a octupole coil, are designed as $\cos\theta$ type magnet. The chromaticity sextupole magnet (Fig. 3(c)) is a superferric type. As first pre-series corrector the chromaticity sextupole magnet is being built in collaboration between GSI and JINR. GSI has made the conceptual detailed magnet design and JINR finalised the iron lamination shape and manufactured the yoke (Fig. 4). The final design of the coil was made by GSI and the manufacturing will be completed, tested and assembled by JINR. This magnet will be integrated into the first quadrupole unit and then assembled into the first quadrupole doublet.

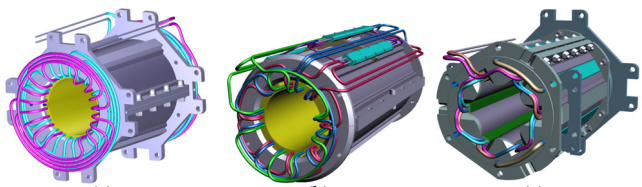

Figure 3: Sketch of the different corrector magnets: a. . . steerer, b. . . multipole corrector, c. . . chromaticity sextupole.

In parallel the design of the cable for the correctors is further improved. A substitute of the CrNi wire is investigated (e.g. Kevlar or carbon tape), which is considered to be less likely to break the insulation of the strands than the hard metal CrNi wire.

The quadrupole magnets and corrector magnets are mounted as one common magnetic and hydraulic unit. The different unit types are listed in Table 1. One of the units is displayed in Fig. 5.

Table 1: The different quadrupole units. QD. . . defocusing quadrupole; QF1. . . focusing quadrupole, family 1; QF2. . . focusing quadrupole, family 2; CH. . . horizontal chromaticity sextupole; CV. . . vertical chromaticity sextupole; ST. . . steering dipole; BPM. . . beam position monitor. ←. . . upstream →. . . downstream

type	quantity	contents	position
1	12	QD	←
2	23	QD + BPM	←
3	24	BPM + QD	←
4	24	CV + QD	←
5	6	ST + QF1	→
6	17	ST + QF2	→
7	18	ST + QF1 + BPM	→
8	18	ST + QF2 + BPM	→
9	12	ST + QF1 + CH	→
10	12	ST + QF1 + CH	→

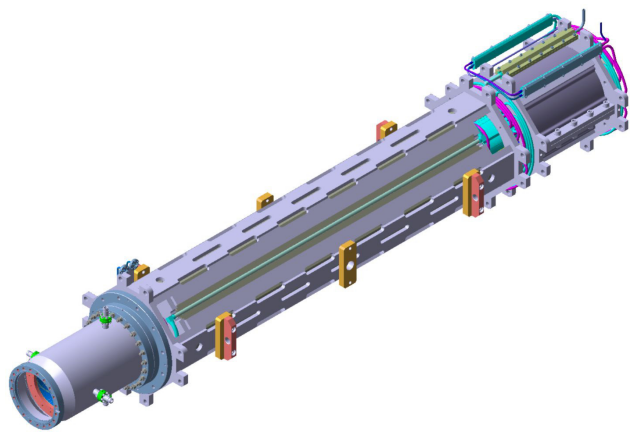

Figure 5: One of the quadrupole units consisting of a BPM (on the left), a quadrupole (in the middle) and a steerer.

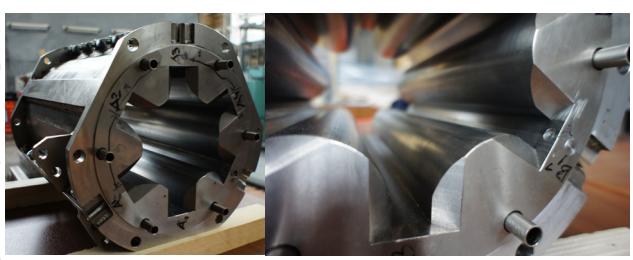

Figure 4: The sextupole yoke.

QUADRUPOLE CRYOMODULES

The SIS100 machine is based on a doublet lattice using the main bending dipoles as spectrometers to deflect any wrong ions on a cryo collimator positioned between the two quadrupoles. Thus two quadrupole units (see also Table 1), which consist of one focusing and one defocusing quadrupole with a corrector, steerer, or beam position monitor mounted on them, and a cryocollimator are assembled to one doublet (see Figure 6). Further at the beginning and the end of the arc a multipole corrector magnet is mounted in the (nearly) dispersion free area. This assembled com-

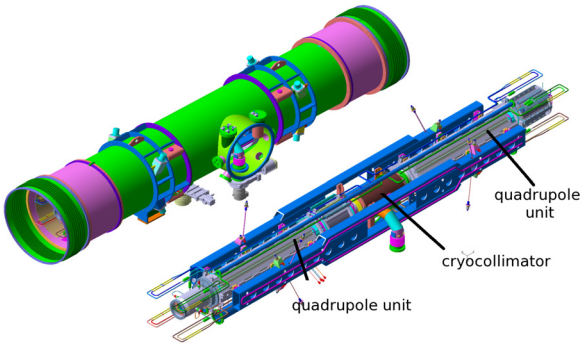

Figure 6: The doublet cryostat (above) and all the components mounted on the common girder.

plex is then inserted in the cryostat. This doublet design has been developed by GSI. Breakage of the cryostat vacuum is an incident which needs to be foreseen in the design of cryo components; thus such a test will be performed with the prototype doublet in Dubna. A failure of this test can be remedied reverting to single units as already used at the Nuclotron.

PROCUREMENT AND TESTING

The doublet is manufactured in the following way:

- the quadrupoles with their corrector magnets are manufactured and these units are tested at cold including the measurement of the magnetic field, its axis and homogeneity. These work packages are executed at JINR. This cold test at this stage is mandatory as the full aperture of the magnets is not accesible after the vacuum chamber has been installed.
- After warm up the vacuum chambers are installed into the unit and the end flange welded on them. If required a BPM is installed on the quadrupole magnet.
- All components are mounted on a common girder and their mutual alignment checked.
- Finally the girder and the thermal shield are mounted inside the cryostat and aligned in the module.

At last this module is made ready for shipping.

Collaboration GSI–JINR for FAIR

The fabrication and testing of these modules will be a collaboration effort (see Table 2). Components manufactured by GSI and its subcontractors and components manufactured by JINR and its subcontractors will finally be integrated at JINR and shipped to GSI as a major contribution of the biggest German partner in the FAIR project. This collaboration also shares the manufacturing responsibility: JINR for the units and the components of the module, GSI for the vacuum chambers, cryo-collimators and beam position monitors; GSI for the doublet functionality, module safety and integration concept. JINR has started with the preparation of a hall.

Table 2: The quadrupole module components and their delivery.

GSI	JINR
doublet design	cables
wires	quadrupoles
vacuum chambers	chromaticity sextupoles
cryo-collimators	steerers
beam position monitors	multipoles
voltage breakers	girders
doublet warm test	unit testing
magnetic measurement consulting	integration and assembly of the doublet

In this hall the test benches capable of testing SIS100 and NICA magnets will be installed. Given the similarity of the magnets the infrastructure of the hall will be shared between the two projects.

CONCLUSION

The SIS100 is now in the procurement phase with the start of the dipole series production. The integration of the already designed modules is now detailed. The quadrupole and corrector magnets will follow swiftly in a joint GSI-JINR collaboration starting 2013. The design of the doublets is being made by GSI. The units (quadrupole plus associated correctors) will be manufactured and tested by JINR. Finally the doublets will be assembled at JINR and shipped to GSI ready for installation following the joint proposal which was accepted by the FAIR council.

REFERENCES

[1] Egbert Fischer, Hamlet Khodzhibagiyan, and Alexander Kovalenko. “Full size model magnets for the FAIR SIS100 synchrotron” IEEE Trans. Appl. Supercon. 18 (2008) p. 260–263.

[2] E. Fischer, H. Khodzhibagiyan, A. Kovalenko, and P. Schnizer. “Fast ramped superferric prototypes and conclusions for the final design of the SIS100 main magnets” IEEE Trans. Appl. Supercon. 19 (2009) p. 1087–1091.

[3] H. G. Khodzhibagiyan et al. “Superconducting magnets for the NICA accelerator complex in Dubna” IEEE T. Appl. Supercon, 21 (2011) p. 1795–1798.

[4] P. Schnizer, B. Schnizer, P. Akishin, A. Mierau, and E. Fischer. “SIS100 dipole magnet optimisation and local toroidal multipoles” IEEE T. Appl. Supercon, 21 (2012) p. 4001505

[5] E. Fischer, P. Schnizer, A. Mierau, S. Wilfert, A. Bleile, P. Shcherbakov, and C. Schroeder. “Design and test status of the fast ramped superconducting SIS100 dipole magnet for FAIR” IEEE T. Appl. Supercon, 21 (2011) p. 1844

[6] E. Fischer, P. Schnizer, A. Mierau, E. Floch, J. Macavei, and P Akishin. “Design and operation parameters of the superconducting main magnets for the SIS100 accelerator of FAIR” IPAC’11, San Sebastián, September 2011, WEPO024, p. 2451

PRODUCTION OF SUPERCONDUCTING MAGNETS AND CRYOGENIC SYSTEMS AT IHEP*

S. Kozub, A. Ageyev, A. Bakay, I. Bogdanov, E. Kashtanov, A. Orlov, V. Pokrovsky, P. Slabodchikov, P. Shcherbakov, L. Shirshov, M. Stolyarov, V. Sytnik, L. Tkachenko, S. Zinchenko, IHEP, Protvino, Russia

Abstract

Results of the development of fast-cycling superconducting magnets for the FAIR project (European Research Centre of Ions and Antiprotons, Germany) are presented. Largest in Russia cryogenic system of 280 W refrigeration capacity at 1.8 K temperature for cooling with superfluid helium of superconducting RF separator for the OKA experimental complex to produce a separated Kaon beam from U-70 proton accelerator was developed and commissioned at Institute for High Energy Physics (IHEP). Experience of the cryogenic system operation is discussed.

RESULTS OF ACTIVITY

New generation of high energy proton accelerators is based on fast cycling superconducting (SC) magnets [1]. From 2002 IHEP collaborated with GSI, Darmstadt, Germany. SC high field fast cycling dipole model was developed and produced for SIS300 accelerator of FAIR project (European Research Centre of Ions and Antiprotons). The dipole is shown in Fig. 1 and its parameters are presented in Table 1 [2].

Figure 1: SIS300 SC high field fast cycling dipole model.

Figure 2 presents the magnet training curve. The dipole reached its operating current at third quench. The quench current continued to increase and finally reached 7738 A (about 6.8 T magnetic field). The ratio between maximum current on the load line and nominal current is 7738/6720 = 1.15. During the training, quenches occurred alternately in the upper and lower poles. This shows that the two poles have the same quality as well as the same level of stress.

*Work supported by ROSATOM

Table 1: Parameters of the SIS300 SC dipole

Magnetic field, T	6
Operating current, kA	6.72
Field ramp rate, T/s	1
Number of layers	2
Strand number in cable	36
Stored energy, kJ	260
Inductance, mH	11.7
Coil inner diameter, mm	100
Length of SC coil, m	1
Mass of magnet, ton	1.8

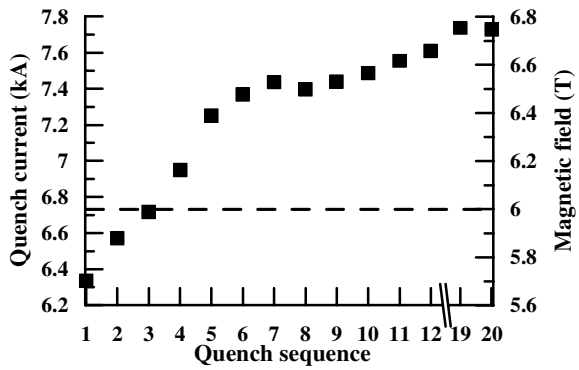

Figure 2: Training curve of the SIS300 dipole model.

Figure 3 presents quench currents for different ramp rates. One can see that the quench current did not decrease up to 1300 A/s (1.2 T/s).

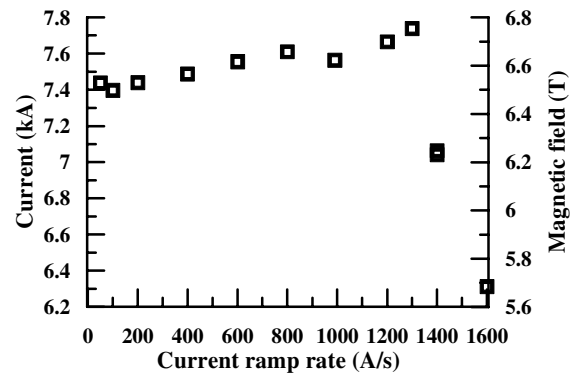

Figure 3: Ramp rate dependence of the SIS300 dipole model.

Special design of SC wire and cable with stainless steel core was developed for this dipole to decrease AC losses. Measured AC losses exceeds computed values at currents more than 3 kA because of eddy current losses in the iron

yoke [2]. 6.8 T magnetic field in dipole aperture was reached and it retains up to 1.2 T/s ramp rate.

Prototype of SIS300 fast cycling quadrupole was produced and tested in 2011 [3, 4]. The dipole is shown in Fig.4 and its parameters are presented in Table 2.

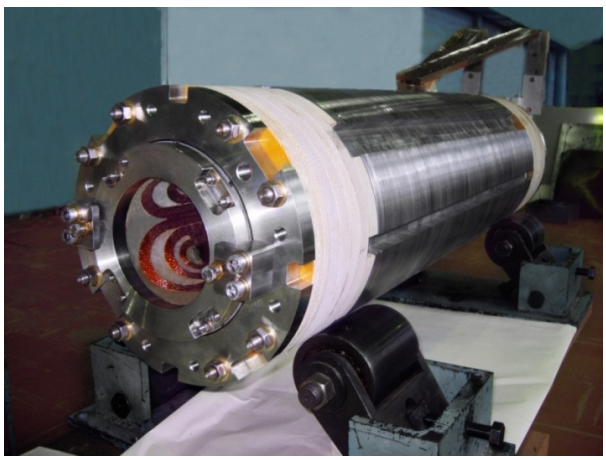

Figure 4: General view of SIS300 fast cycling quadrupole prototype.

Table 2: Parameters of the SIS300 SC quad prototype

Central gradient, T/m	45
Operating current, kA	6.26
Rate of central gradient, T/m/s	10
Stored energy, kJ	38
Inductance, mH	2
Coil inner diameter, mm	125
Effective length, m	1
Number of layers	1
Number of turn in coil	80
Strand number in cable	19
Thickness of collars, mm	22
Thickness of iron yoke, mm	52
Magnet outer diameter, mm	324

Figure 5 presents training of the SIS300 quadrupole prototype. The quench current of the magnet reached 8199 A in the first quench and 8734 A in fifth quench that corresponds to 39% current margin. Measurements of the quench current at various ramp rates showed that the quench current was higher than 8.5 kA up to 5 kA/s (36 T/m/s, 2.8 T/s) ramp rate.

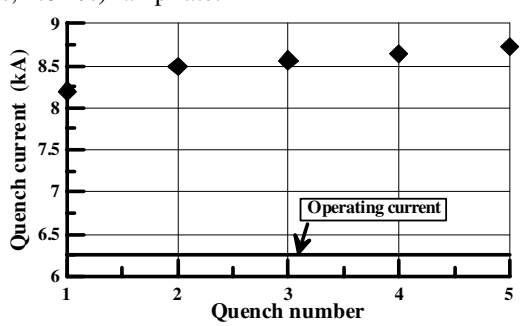

Figure 5: Quadrupole quench current vs. quench number.

Magnetic measurement results showed that measured and calculated quadrupole gradient values practically coincide. Figure 6 shows modules of the central and integral lower harmonics at 3 kA current. Injection current of SIS300 quadrupoles is 1.4 kA. One can see that values of the harmonics are less than 2×10^{-4} (the acceptable level) at current higher than 1.4 kA.

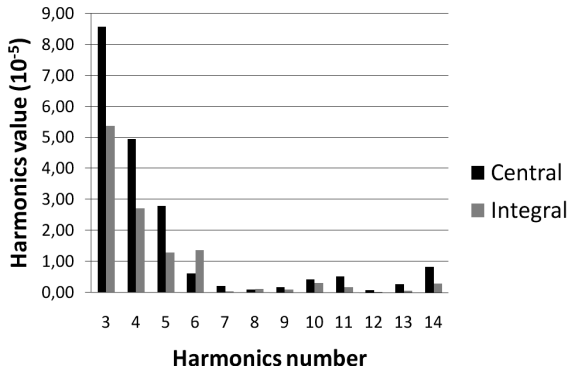

Figure 6: Modulus of lower central and integral harmonics of quadrupole magnetic field at 3 kA current.

At present prototypes of SIS300 fast cycling corrector magnets are developed [5]. Main requirements to these magnets are presented in Table 3, where L is magnet length, t – time of powering to nominal magnetic force. Inner diameter of the magnets is 250 mm, operating current up to 250 A. In 2012 production and test of SIS300 steering magnet prototype is planned.

Table 3: Requirements to SIS300 corrector magnets

Type of corrector	Force	L, m	t, s
Chromaticity sextupole	130 T/m^2	0.78	0.21
Resonance sextupole	325 T/m^2	1	0.5
Steering magnet:			
Vertical dipole	0.5 T	0.65	2.27
Horizontal dipole	0.5 T	0.65	2.27
Multipole:			
Quadrupole	1.8 T/m	0.65	2.25
Sextupole	60 T/m^2	0.65	2.18
Octupole	767 T/m^3	0.65	2.24

IHEP takes part in development of cryogenic system of SIS300. SC fast cycling magnets of SIS300 have increased AC losses as magnetic field ramp rate of the magnets is higher by order of magnitude than the ramp rate of TEVATRON, HERA, LHC magnets. According to calculation heat load for 4.5 K temperature level in SIS300 equals 4.3 kW. SIS300 magnetic ring of 1.1 km length will be halved for cryogenic strings cooled by supercritical helium [6]. UNK cryogenic scheme was took for basis but increased heat load in magnets required using of four additional helium heat exchangers in SIS300 cryogenic system in order to decrease maximal temperature of single-phase helium in cryogenic strings to 4.7 K that it necessary for stable SC magnets operation (Fig. 7).

Proposed scheme solution allows to realize cooling of SIS300 magnets down to 4.5 K during 60 hours, that is acceptable time. At present configuration and technical requirements for cryogenic system equipment are defined.

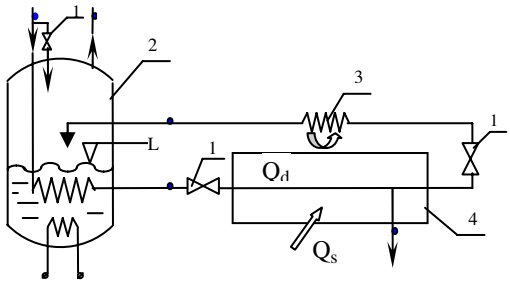

Figure 7: Flow scheme proposed for cryostating the string of SIS300 superconducting magnets. 1 - valves, 2 - subcooler, 3 – heat exchanger, 4 – SC magnets string.

In 2007 the largest in Russia cryogenic system for cooling SC devices by superfluid helium was put in operation at IHEP for separated kaon beam. The system cools two SC RF cavities by superfluid helium at 1.8 K temperature [7]. Design refrigeration capacity of the cryogenic system is 280 W at 1.8 K and it should deliver 5 g/s of liquid helium per the each cavity. Main parts of the system are satellite refrigerator and KGU-500 cryogenic plant (Fig. 8), cryogenic transfer line with distribution box, pumping group. Liquid helium plant of the KGU-500 type to feed the satellite refrigerator is commercially produced by GELIYMASH Company, Moscow, and it has liquefaction rate of 150 l/hr. Satellite refrigerator consists of cryogenic helium vacuum heat exchanger, intercooling helium bath and two small helium heat exchangers placed near each SC RF cavity. These equipments were developed and produced by IHEP.

Figure 8: Cryogenic plant and large helium heat exchanger of superfluid refrigerator system of kaon channel.

To reach 1.8 K the pumping group is to pump helium tanks down to 1.64 kPa. Pumping group is arranged in 3 stages: 8 Roots blowers of the 2DVN-1500 type of the first stage compress helium from 1.5 kPa to 2.5÷3.0 kPa, 8 Roots blowers of the 2DVN-500 type of the second stage compress helium to 4.0÷5.0 kPa, and the third stage of 8 slide-valve pumps of the AVZ-180 type finally compress helium up to 103 kPa.

Control system of the cryogenic system includes 240 channels of data collection and remote control, 72 electronic modules, 5 computers for inputting and outputting information in two control rooms.

Successful operation of the cryogenic system allowed to supply necessary parameters of SC RF cavities and record more than one million of kaon decay events.

CONCLUSION

IHEP successfully develops superconducting fast cycling magnets and cryogenic system for SIS300 accelerator of FAIR project. 6.8 T magnetic field in aperture of the dipole model was reached and the magnetic field value did not reduced up to 1.2 T/s ramp rate. Combination of these dipole parameters is unique in world practice.

The critical current of SIS300 quadrupole prototype is 8734 A that corresponds to 39% current margin. The critical current was higher than 8.5 kA up to 5 kA/s (36 T/m/s, 2.8 T/s) ramp rate.

SIS300 cryogenic system supplies maximal temperature of single-phase helium in cryogenic strings to 4.7 K that it necessary for stable SC magnets operation.

Successful operation of the cryogenic system for separated kaon beam at IHEP allowed to supply necessary parameters of SC RF cavities and record more than one million of kaon decay events.

REFERENCES

[1] GSI. (2006). Baseline technical report. [Online] Available:http://www.gsi.de/fair/reports/btr.html.
[2] S. Kozub et al. SIS 300 Dipole Model, IEEE Trans. on Appl. Supercond. V20, N3, June 2010, p. 200.
[3] E L. Tkachenko et al. Development of Quadrupole, Steering and Corrector Magnets for the SIS 300, IEEE Trans. on Appl. Supercond., V20, N3, June 2010, p. 159.
[4] S. Kozub et al. SIS 300 Fast-Cycling Superconducting Quadrupole Prototype, IEEE Trans. on Appl. Supercond., V22, N3, June 2012, p. 4001104.
[5] L. Tkachenko et al. Development of Corrector Magnet Designs for the SIS 300, IEEE Trans. on Appl. Supercond., V22, N3, June 2012, p. 4002804.
[6] S. Zinchenko, Cooling System of the SIS300 Accelerator, Proc. of RUPAC-2010, p. 303.
[7] A. Ageyev et al. Starting -up and Adjustment Works on Cryogenic and Vacuum System of the Superconducting Radio-Frequency Separator, Proc. of RUPAC-2008, 2008, p. 282.

STATUS OF THE DESIGN AND TEST OF SUPERCONDUCTING MAGNETS FOR THE NICA PROJECT

H. Khodzhibagiyan, P. Akishin, A. Bychkov, A. Donyagin, A. Galimov, O. Kozlov, G. Kuznetsov, I. Meshkov, V. Mikhaylov, E. Muravieva, P. Nikitaev, A. Shabunov, A. Smirnov, A. Starikov, and G. Trubnikov, JINR, Dubna, Russia

Abstract

NICA is a new accelerator complex being under design and construction at the Joint Institute for Nuclear Research in Dubna. The actual design and the main characteristics of superconducting magnets for the NICA booster and collider are given. The magnets are based on a cold window frame iron yoke and a single-layered superconducting winding made from a hollow NbTi composite superconductor cable cooled with the forced two-phase helium flow. The first results of cryogenic tests of the magnets for the NICA project are presented.

INTRODUCTION

The NICA/MPD project [1] started at the Joint Institute for Nuclear Research (JINR) in Dubna in 2007. The goal of the project is to carry out experimental studies of the hot and dense strongly interacting quantum chromodynamics matter and light polarized ions. The NICA accelerator complex will consist of two injector chains, a new 600 MeV/u superconducting booster synchrotron, the existing superconducting synchrotron – Nuclotron [2], and the new superconducting collider having two rings each of about 503 m in circumference.

DESIGN AND MANUFACTURING OF THE PROTOTYPE MAGNETS

The Nuclotron-type design [3-5] based on a cold iron yoke and a saddle-shaped superconducting (SC) winding has been chosen for the booster and the collider magnet. The magnet includes a cold (4.5K) window frame iron yoke and a SC winding made of a hollow NbTi composite SC cable cooled with a two-phase helium flow. Lorentz forces in the winding are supported by the yoke. The main characteristics of the cable for the NICA magnets are given in Table 1. A cross-section view of the booster dipole and quadrupole magnets is shown in Figures 1 and 2, correspondingly. The main characteristics of the NICA booster and collider magnets are summarized in Tables 2 and 3, respectively. A full-scale curved model dipole magnet for the NICA booster was manufactured at the Laboratory of High Energy Physics (LHEP) JINR in April 2011. The magnet is 2.2 m long and has a radius of the curvature of 14 m.

The full-scale model quadrupole magnet for the NICA booster was manufactured by LHEP at the end of 2011.

Table 1: Main characteristics of the cable for the NICA booster and collider magnets

Characteristic	Booster	Collider
Channel diameter	3 mm	3 mm
Number of strands	18	16
SC strand diameter	0.78 mm	0.9 mm
Superconductor	50% Nb – 50% Ti	
Diameter of filaments	7 μm	8 μm
Cable outer diameter	6.6 mm	7.0 mm
Operating current (1.8T, 4.65K)	9.68 kA	10.4 kA
Critical current (2.5T, 4.7K)	14.2 kA	16.8 kA

The Nuclotron-type design was chosen for the NICA collider. Two identical single-layer windings are located in the common straight iron yoke one over the other (see Fig. 3). Lorentz forces in the windings are supported by the yoke. The yoke consists of three parts made of laminated electrical steel. They are held together by longitudinal steel plates welded with laminations and frontal sheets. The magnets are cooled with the two-phase helium flow which in series passes from the supply header through the cooling channels of the bus bars, lower and upper windings, iron yoke and then - enters the return header. Each twin bore dipole or quadrupole magnet is connected in parallel to the supply and return helium headers.

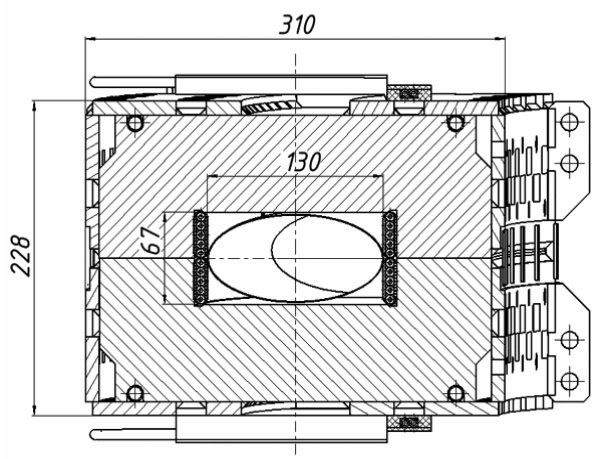

Figure 1: Cross-section view of the bent dipole magnet for the NICA booster.

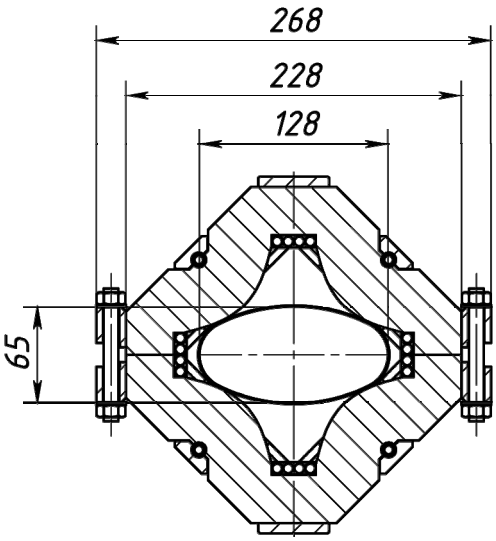

Figure 2: Cross-section view of the quadrupole magnet for the NICA booster.

Table 2: Main parameters of the NICA booster magnets

Parameter	Dipole	Lens
Number of magnets	40	48
Maximum magnetic field (field gradient)	1.8 T	20.2 T/m
Effective magnetic length	2.2 m	0.55 m
Ramp rate	1.2 T/s	13.5 T/(m·s)
Field error at R= 30 mm	$\leq 6 \cdot 10^{-4}$	
Beam pipe aperture (h/v)	128 mm/65 mm	
Radius of curvature	14.01m	-
Overall weight	1020 kg	110 kg
Operating current	9.68 kA	

Table 3: Main parameters of the NICA collider magnets

Parameter	Dipole	Lens
Number of magnets	80	86 (+12*)
Maximum magnetic field (field gradient)	1.8 T	23 T/m
Effective magnetic length	1.94 m	0.46 m
Ramp rate	≤ 0.5 T/s	-
Field error at R= 30 mm	$\leq 2 \cdot 10^{-4}$	
Beam pipe aperture (h/v)	120 mm/70 mm (Ø 180*mm)	
Distance between the beams	0.32 m	
Overall weight	1680 kg	300 kg
Operating current	10.4 kA	

* - the final focus lens

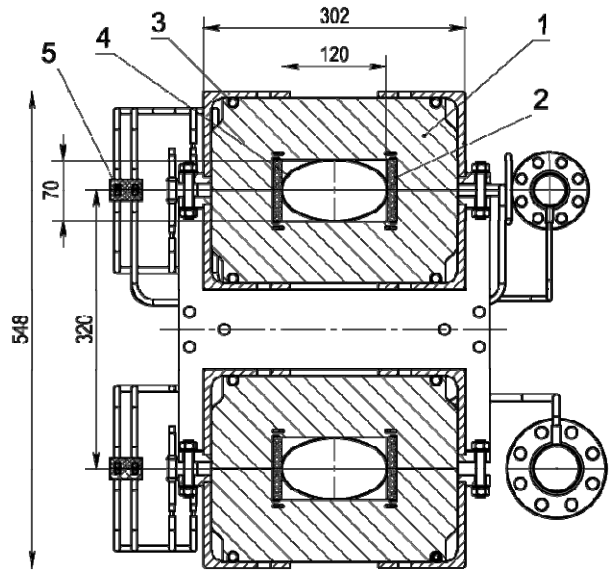

Figure 3: Cross-section view of the twin aperture dipole magnet for the NICA collider: 1 – iron yoke, 2 - SC coil, 3 – tube for cooling the yoke, 4 – beam pipe, 5 - bus - bars.

A twin aperture model dipole magnet for the NICA collider was manufactured at LHEP JINR in August 2011. Production of the model collider twin-bore quadrupole lens with hyperbolic poles (see Fig. 4) has been completed in September this year.

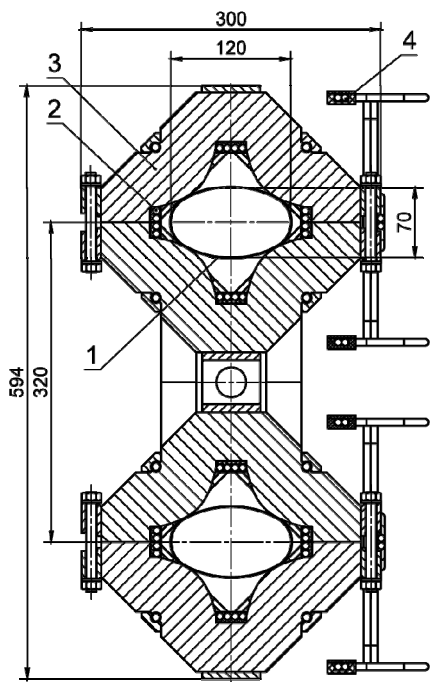

Figure 4: Cross-section view of the quadrupole magnet for the NICA collider: 1 – beam pipe, 2 - SC coil, 3 – iron yoke, 4 – bus - bars.

FIRST NICA MAGNETS TEST RESULTS

A cryogenic test of the first dipole magnet for the NICA booster synchrotron was carried out in May 2011. The first quench occurred at 7705 A. After the 13th quench the current reaches the nominal value of 9690A that corresponds to the magnetic field induction in the gap of 1.8 T. Further training was stopped because of the power supply and current leads limitation.

The measured static (at zero current) heat flow to the magnet was 5.8 W. AC losses of 12 W were measured by means of the calorimetric method while the magnet was operating in the triangular cycle with the magnetic field ramp rate of 1.2 T/s without a pause. This value agrees well with the calculation and confirms the correct choice of steel for the magnet yoke. The pressure drop of the helium flow in the cooling channel of the magnet was 47 kPa during the operation in the indicated mode. Hydraulic resistance of the cooling channel was 2 times higher than the calculated value due to the fact that the cooling channel of the cable has a diameter of 2.6 mm instead of the designed one equal to 3 mm. The new winding of the cable with a cooling channel of 3 mm in diameter was fabricated and installed in the yoke of the magnet in spring 2012. Cryogenic tests of the magnet with the new winding were performed in May 2012. Training for new winding consisted of a single quench at 9475 A. The maximum current in the magnet of 11299 A was determined by quench in the current lead. Measurements of the harmonics of the magnetic field in the aperture of dipole magnet have been done by means of the equipment used for the Nuclotron magnets. Sextupole harmonic of the field in the Booster magnet was about 10 times less than in the Nuclotron magnet. The higher harmonics of the field with the specified equipment was not observed. We are currently developing methods and manufacturing of new equipment for magnetic measurements in the NICA magnets with much higher requirements for the quality of the field in comparison with the Nuclotron magnets. The first phase of the new equipment is scheduled to start operation in mid-2013.

Experimental studies of the booster quadrupole magnet were carried out in spring 2012 after upgrading the power supply on the test bench. The current reached the nominal value of 9690 A after the 4th quench. The measured static heat flow to the quadrupole magnet was 3.3 W. AC losses of 4.4 W were measured by using the calorimetric method while the magnet was operating in the triangular cycle with the following parameters: amplitude of the magnetic field gradient of 20.3 T/m, and ramp rate of 20.3 T/(m·s) without a pause. AC losses as a function of the magnetic field gradient ramp rate are shown in Fig. 5. The pressure drop of the two-phase helium flow in the cooling channel of the lense was 7 kPa during the operation in the indicated mode.

At the moment the construction of the new test facility for cryogenic testing of superconducting magnets is performed at LHEP. Premises with an area of 2,600 m^2 were prepared to install the equipment. The manufacturing of a power supply on 15 kA and HTSC current leads are in the final stage. Contracts for the cryogenic and vacuum equipment for the new test facility for parallel testing of the SC magnets on 6 benches are in preparation. Commissioning of the first stage of the new test facility is scheduled for 2013.

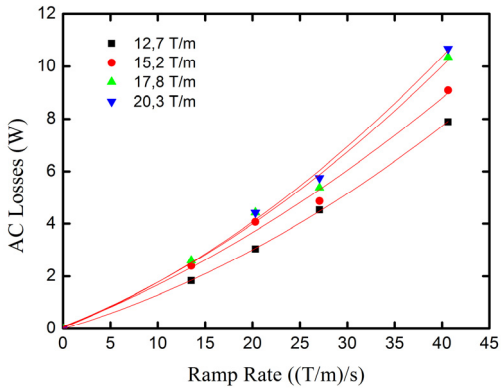

Figure 5: AC losses as a function of the magnetic field gradient ramp rate in the aperture during the operation in the triangular cycle for the NICA booster quadrupole magnet.

CONCLUSIONS

The full-scale Nuclotron–type superconducting model dipole and quadrupole magnets for the NICA booster and collider were manufactured at LHEP JINR. First dipole and quadrupole magnets for the NICA booster have successfully passed the cryogenic test on the bench . The nominal current of 9.7 kA was reached after short training. The magnets were successfully tested in the pulsed mode with a magnetic field ramp rate of up to 4 T/s. The stimated value of the sextupole harmonic of the field in the Booster dipole magnet is about 10 times less than in the Nuclotron magnet. Tests of the model magnet and lense for the collider are scheduled for the autumn of this year. The construction of the new test facility for cryogenic testing of superconducting magnets is in progress.

REFERENCES

[1] Nuclotron - based ion collider facility. Available:http://nica.jinr.ru/
[2] A. Baldin et al., “Nuclotron status report”, IEEE Trans. Nucl. Sci.,4 (1983), pp. 3247-3249.
[3] H. Khodzhibagiyan, and A. Smirnov, “The concept of a superconducting magnet system for the Nuclotron”, Proc. of the Twelfth Int. Cryogen. Eng. Conf., ICIC12, Southampton, (1988), pp. 841-844.
[4] H. Khodzhibagiyan et al., “Superconducting Magnets for the NICA Accelerator Complex in Dubna”, IEEE Trans. Appl. Supercond., 3 (2011), pp. 1795-1798.
[5] H. Khodzhibagiyan et al., “Development of fast-cycling superconducting magnets at JINR”, Proc. of 21 Int. Cryogen. Eng. Conf., ICIC21, CRYOPrague, 1 (2006), pp. 113-116.

UPDATE ON SCRF DEVELOPMENT AT TRIUMF

V. Zvyagintsev, R.E. Laxdal, B. Amini, K. Fong, P. Harmer, D. Kishi, P. Kolb, A. Koveshnikov, D. Lang, A.K. Mitra, N. Muller, C. Schaub, R.W. Shanks, B. Waraich, Q. Zheng,
TRIUMF, Vancouver, Canada
M. Gusarova, I. Petrushina, N. Sobenin, D. Tikhonov, MEPhI, Moscow, Russia
R. Edinger, PAVAC, Richmond, B.C., Canada
A. Vrielink, UBC, Vancouver, B.C., Canada
S.H. Abidi, R.S. Orr,University of Toronto, Toronto, Ontario, Canada

Abstract

Since 2007 TRIUMF started development of e-LINAC which is a 50 MeV 10 mA CW electron superconducting linear accelerator to be used as a driver to produce radioactive ion beams through photofission. The accelerator is based on five 1.3 GHz TTF/ILC elliptical bulk Nb cavities technology to be mounted in three cryomodules; an injector cryomodule with one cavity and two accelerating modules with two cavities each. The ISAC-II project superconducting heavy ion linear accelerator was successfully completed in 2010 and we now have in operation 40 superconducting bulk Nb QWR cavities assembled in eight cryomodules. Results and plans of the SCRF program and experience of ISAC-II operation at TRIUMF will be discussed.

INTRODUCTION

SCRF development at TRIUMF started with the ISAC-II project in 2000 [1]. In 2010 this project was completed with commissioning of a 40 MV superconducting linac for heavy ions. SCRF technology is now being used in a second `in house' linear accelerator, the e-LINAC, to produce 50 MeV electrons with intensities to 10 mA, which will be used as a photo-fission driver for the ARIEL rare isotope program at TRIUMF.

SCRF DEVELOPMENT FOR E-LINAC

E-LINAC [2] will consist of a 300 keV thermionic DC electron gun with RF modulated cathode grid and five elliptical 9-cell cavities, operating at 2^0K, in three cryomodules [3]. The layout and staging of the project are presented in Fig.1.

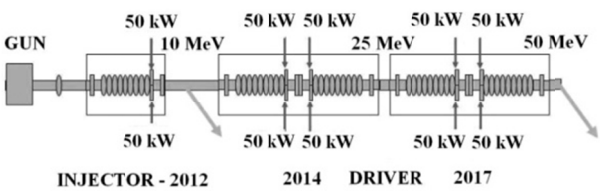

Figure 1: E-LINAC layout

Cavity Design

The e-LINAC cavity design draws from the 1.3 GHz elliptical TESLA-type cavity. Each cavity operates at an effective acceleration voltage of 10 MV with a design goal of Qo=1e10. Operating at 2^0K, the cavity dissipates 10 W in the liquid He system. Operation with 10 mA beam current requires 100 kW CW RF power into the cavity. To deliver RF power into the cavity two symmetrically opposed 65 kW CPI couplers are employed, providing the appropriate beam-loaded power while avoiding asymmetric coupler kicks. In result the e-LINAC 9-cell cavity differs from the TESLA cavity in the end cells, which are customized to adapt to the power couplers on the one end and also to mitigate HOMs and to flatten the field profile for the accelerating mode [4]. The main RF parameters of the cavity are very close to TESLA (Table 1). Simulations [5] show that multipacting occurs in the equatorial region of the cavity. Stable multipacting trajectories (over 40 RF periods) of order 2-4 were obtained in the range of 1.32 … 3.08 MV/m of the accelerating gradient and 1-2 order trajectories are obtained in a range of 3.08…17.16 MV/m.

Table 1: RF parameters of TRIUMF cavity in comparison with TESLA (DESY) cavity

	TRIUMF	DESY	TRIUMF/DESY
Frequency [MHz]	1300	1300	-
R_{sh}/Q [Ohm]	1000	1030	3% less
Geometric factor G [Ohm]	290	270	7% more
E_p/E_a	2.1	2.0	5% more
B_p/E_a [mT/(MV/m)]	4.4	4.2	5% more
Cell coupling [%]	2.0	1.9	-

HOM Dampers

HOM damper design concept is described in [4, 6]. A stainless steel damper ring is used for the coupler end while a CESIC ring is used for the opposite end. The rings are connected to a liquid Nitrogen heat sink. The conductivity of CESIC is measured by using the Q perturbation method in the elliptical cavity at 100^0K [7]. The result lies in the range 600…6200 S/m measured at 1.3 GHz and 660…3400 S/m at 2.4 GHz. The conductivity value is significantly below the rated value for CESIC, which is 15000 S/m.

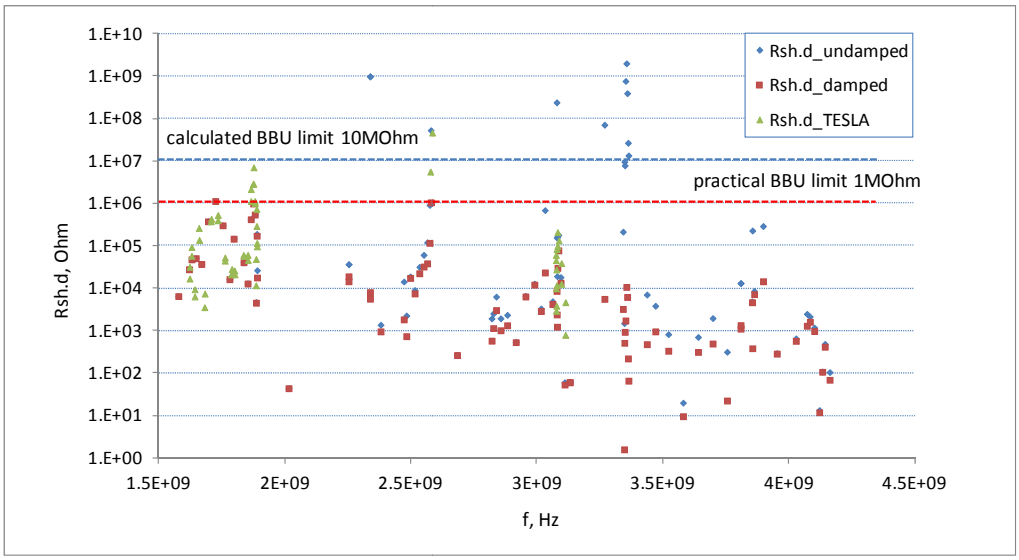

Figure 2: Spectrum of dipole HOM shunt impedances for TRIUMF cavity in comparison with TESLA nine-cell cavity

in the worst case the beam could be deflected by a dipole HOM with accompanying beam loss. This effect is called beam break up (BBU). It is dependent on the beam current as well as the shunt impedance, quality factor and resonant frequency of the dipole mode. The cavity has to be designed so that the shunt impedances and quality factors of the dipole modes do not restrict operation at 10 mA. Beam dynamic simulations result in a BBU criteria of Rsh.d < 10 MΩ. Expected fabrication tolerances result in a spread in $R_{sh.d}$ by a factor of ~2 [6]. Further contingency is gained by adopting a more restrictive criteria of $R_{sh,d}$ < 1 MΩ. Spectrums of $R_{sh.d}$ for HOM dipole modes for the e-LINAC nine-cell cavity with and without dampers together with the spectrum for TESLA cavity are presented on Fig. 2. Note that 1.72, 1.87 and 2.56 GHz modes (TE11) have marginal values of $R_{sh,d}$ compared to the practical BBU limit. The calculations assume the higher quoted value of CESIC conductivity while the measured data are below this value. In this way we could expect better damping at least for the 2.56 GHz mode.

Cavity Fabrication

Fabrication of the nine-cell TRIUMF cavity is on-going in collaboration with PAVAC Industries. A copper seven-cell mock-up of the cavity is completed (Fig.3). This cavity is now used for training on `field flattening' and for HOM studies.

The nine-cell niobium cavity design is shown in Fig.4 and utilizes a unique `smart bell' fabrication sequence with equator welds forming whole cells followed by iris welds to form multi-cells. A J-Lab style scissor tuner is employed and to avoid backlash the cavity is to be stretched by ~1 mm during operation. The nine-cell cavity fabrication now is underway with six `smart bells' fabricated meeting the correct frequency. Work is now starting on the end cells.

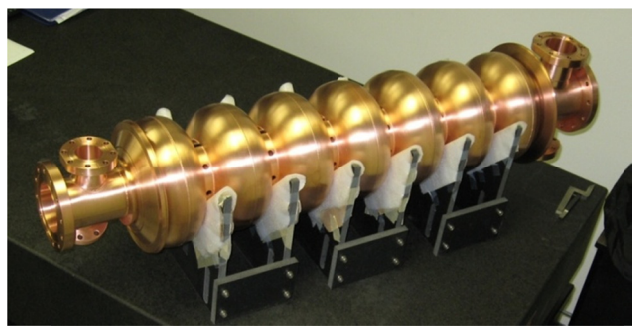

Figure 3: Seven-cell copper mock-up of the TRIUMF e-LINAC cavity

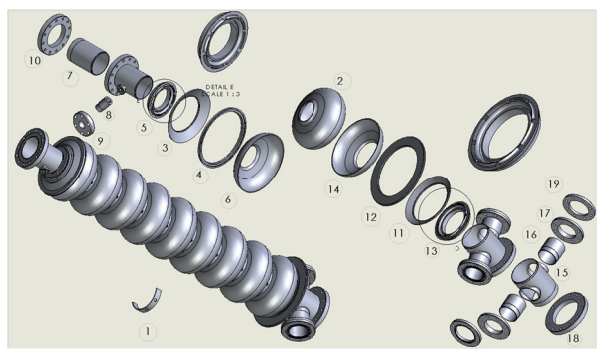

Figure 4: Mechanical design of e-LINAC nine-cell cavity

SCRF Cavity Testing

Single cell cavity tests are important to qualify cavity fabrication and Nb surface preparation processes. A series of preparation process improvements have been done:

- Degassing of PAVAC single cell cavity in a vacuum furnace at 800^{0}C (FNAL) to remove Hydrogen from the cavity surface.
- Completion of automatic HPWR unit to provide extended automatic rinsing.

- Cleaning pumping line to reduce contamination from active pumping during the cavity test.
- Improvement of clean assembly procedure protocol.
- Upgrade RF variable coupler and RF feedthroughs to allow RF multipacting and field emission conditioning without overheating the RF line.

Single cell cavity test results are presented in Fig. 5 with red dots after upgrades and brown squares before upgrades. Currently the cavity quality factor is Q_0~10^{10} up to Ea=20 MV/m with a maximum gradient of 26 MV/m limited by local radiation levels. Green triangles on Fig.5 show the cavity Q-curve after improvements but employing a fast cavity cooldown. We believe that the cavity trapped magnetic flux due to thermal gradients (Seebeck effect) [8]. The `slow cooldown' result (red dots) is obtained after warming the cavity above 10K and re-cooling to reduce thermal gradients.

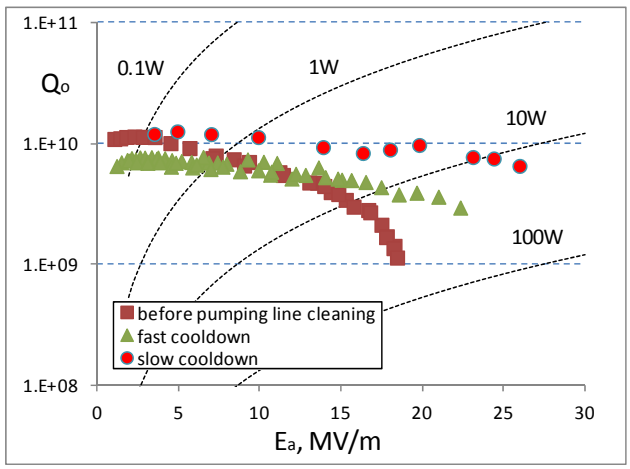

Figure 5: 1-cell cavity test results.

Plans for SCRF Development

For the nine-cell cavity test a vertical test cryostat is in fabrication. A variable transverse coupler is complete and second sound monitors to define quench location by sound wave triangulation are in development. A vacuum RF induction furnace is being developed to provide SC cavities degassing at 600…800^{0}C temperatures.

In addition further fundamental SRF material studies with the μ–SR and β–NMR TRIUMF facilities are in preparation [9].

ISAC-II SCRF DEVELOPMENT

Since the results for ISAC-II reported in [2] we have two years of successful operation. One identified problem is in the coupler line cables inside of the cryomodules with several failures due to RF breakdown in the cable isolation from RF glow discharge. Due to the flexibility of the accelerator structure consisting from many cavities with independent RF systems a failure can be easily compensated by means of increasing gradients and retuning other cavities. During planned shutdowns the damaged cables are replaced. To prevent this particular cable problem we restricted forward power levels in the RF amplifiers and initiated a cable test stand to develop a more robust cable.

Phase I of ISAC-II is using 1 kW tube-type RF power amplifiers, with a tube lifetime of ~12,000 hours. Two prototype solid state amplifiers at 600 W are now developed. Currently they are under test to take a decision about a replacement program.

CONCLUSIONS

In the end of 2012 we expect delivery from PAVAC of the e-LINAC nine-cell cavity and start SRF tests for cavity commissioning. Main resources are concentrated in this direction. Another important task for SRF development is to support the ISAC-II linac for reliable operation for users. TRIUMF is leveraging the installed infrastructure to support fundamental studies in SRF for student education and for implementation in current and future projects.

REFERENCES

[1] V. Zvyagintsev et al., "SCRF Development at TRIUMF," RUPAC2010 Conference, Protvino, Russia, September, 2010, THCHB02.

[2] S. Koscielniak et al., "Electron LINAC Photo-Fission Driver for the Rare Isotope Program at TRIUMF," LINAC'04, Tel-Aviv, Israel, September, 2012, MOOBB01

[3] R.E. Laxdal et al., "The Injector Cryomodule for E-LINAC at TRIUMF," PAC2011, New York, NY, USA, April, 2011, WEOCS6.

[4] V. Zvyagintsev et al., "Nine-Cell Elliptical Cavity Development at TRIUMF," SRF2011, Chicago, USA, July, 2011, MOPO020

[5] M.A. Gusarova et al., "Multipactor Discharge in the ELINAC Accelerator," RUPAC2012, Peterhof, Russia, September, 2012.

[6] P. Kolb et al., "HOM Cavity Design for the TRIUMF eLINAC," SRF2011, Chicago, USA, July, 2011, MOPO047.

[7] P. Kolb et al., "Cold Tests of HOM Absorber Material for the ARIEL eLINAC at TRIUMF," workshop on Higher Order Mode Diagnostics & Suppression in SC Cavities, Daresbury, UK, June, 2012.

[8] S. Aull, et al., "Trapped magnetic flux in superconducting niobium samples," Phys. Rev. ST Accel. Beams 15, 062001 (2012)

[9] A. Grassellino et al., "Application of Muon Spin Rotation to studies of cavity performance limitations," Thin Film Workshop, Padova, Italy, October, 2010

A POSSIBILITY OF HIGH-ENERGY BREMSSTRAHLUNG DOSIMETRY BY INDIUM ACTIVATION

A.N. Dovbnya, V.V. Mytrochenko, V.I. Nikiforov, S.A. Perezhogin, Yu.V. Rogov, V.A. Shevchenko, I.N. Shlyakhov, B.I. Shramenko, A.Eh. Tenishev, V.L. Uvarov#, NSC KIPT, Kharkov, 61108, Ukraine

Abstract

Development of a number of promising photonuclear technologies is connected with the use bremsstrahlung (X-ray) sources having end-point energy up to 100 MeV and average power of tens kW. Commonly, such radiation sources are created on the basis of electron linacs. A possibility of dosimetry of high-energy bremsstrahlung by means of activation of a target from indium of natural composition and establishment of absorbed dose on the specific activity of the ^{115m}In isomer is reported. Preliminary study of isomer activation as well as yield of reference reactions from natural molybdenum in the energy range 8…70 MeV was conducted by simulation technique. Joint measurement of ^{115m}In, ^{90}Mo, ^{99m}Mo activity as well as absorbed dose in the PMMA standard dosimeters were carried out at LU-10 and LU-40 electron linacs of NSC KIPT.

INTRODUCTION

It is known that photoactivation of isomeric states in some nuclei is characterized by low energy threshold values. For example, the threshold of the ^{115}In(γ,γ′)^{115m}In reaction equals 1078 keV [1]. The ^{115m}In isomer goes into the ground state with the half-life $T_{1/2}$=4.48 h, emitting in the process the gamma-quantum of energy 336.2 keV, which is convenient for detection. Owing to a low reaction threshold, the natural indium (the ^{115}In abundance makes 95.8%) can be activated by practically all photons of the bremsstrahlung spectrum. This circumstance allows suggest the presence of a relationship between the specific activity of ^{115m}In and the bremsstrahlung absorbed dose.

In a number of studies, the ^{115}In(γ,γ′)^{115m}In reaction has been used for dosimetry in γ-facilities having ^{60}Co sources [2, 3]. In that case the activation of indium was realized with the photons of energy near the reaction threshold. The present communication deals with the conditions of the method applicability for high-energy bremsstrahlung.

MATERIALS AND TECHNIQUES

Experimental studies on indium activation processes were performed at NSC KIPT linear accelerators LU-10 (electron energy E_0=8…12 MeV) and LU-40 (E_0=35…95 MeV). For absorbed dose measurements, Harwell Red 4034 (HR) detectors were used. They represent 30x11x3 mm plates made from dyed PMMA, commonly used as a standard dosimetry material [4].

To investigate the relationship between the specific activity of ^{115m}In and the dose absorbed in the PMMA, it was suggested that the natural indium detectors together with the HRs should be exposed to X-ray under conditions of electron equilibrium. Besides, each target incorporates a natural molybdenum foil to check the activation conditions against the yields of the reference reactions ^{92}Mo(14.84%)(γ,2n)^{90}Mo and ^{100}Mo(9.63%)(γ,n)^{99}Mo.

The bremsstrahlung-induced γ-spectra of indium and molybdenum were measured with the HPGe detector, which provided FWHM of 1.3 keV at 1332 keV.

For independent analysis of the photoactivation processes and absorption of radiation energy in the detectors, we have used the simulation method based on a modified transport code PENELOPE-2008 [5]. The cross sections for the reference reactions on the ^{92}Mo and ^{100}Mo isotopes (see Figs. 1 and 2) were taken from the database [6]. In the case of the ^{115}In(γ,γ′)^{115m}In reaction the situation has turned out to be more complicated. Namely, the data on its cross section, reported in different works, have shown considerable variations (see Fig. 3).

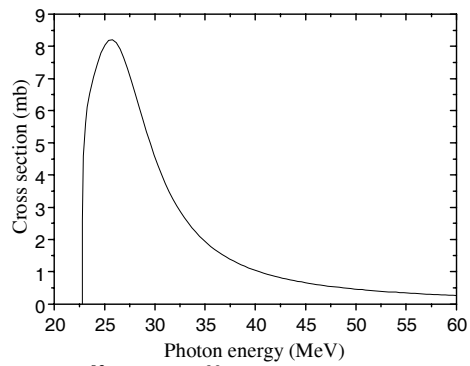

Figure 1: ^{92}Mo(γ,2n)^{90}Mo reaction cross section.

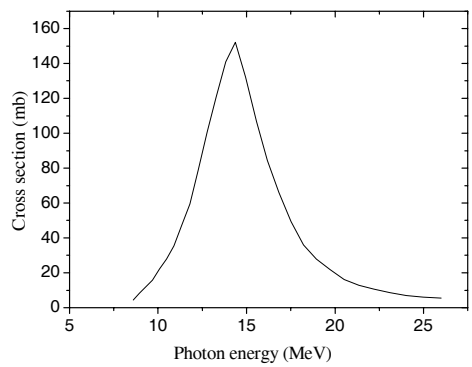

Figure 2: ^{100}Mo(γ,n)^{99}Mo reaction cross section.

uvarov@kipt.kharkov.ua

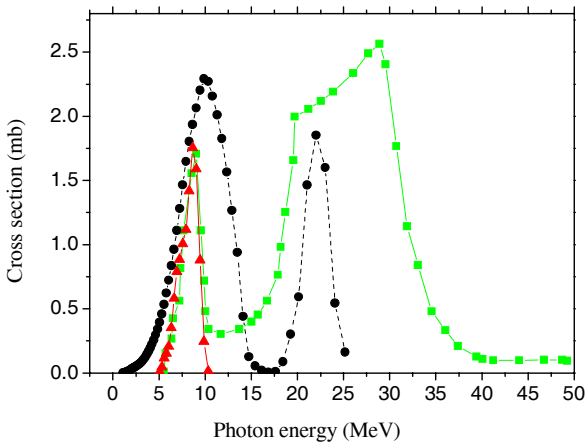

Figure 3: ^{115}In(γ,γ') ^{115m}In reaction cross section: ● - [7]; ▲- [8];■ - [9].

Therefore, we calculated the ^{115m}In yield for different variants of cross section description. Then, the data obtained were compared with the experimental results.

EXPERIMENTAL CONDITIONS

For experimental studies, we have used the output device, which schematic is shown in Fig. 4.

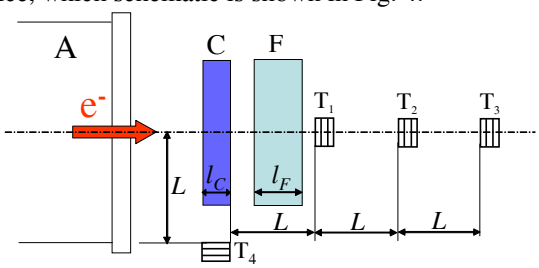

Figure 4: Schematic of the output device.

Behind the exit window of the accelerator A, downstream of the electron beam there follow in succession the converter C as a set of tantalum plates of total thickness l_C, the aluminum electron filter of thickness l_F, and the set of three targets T_1…T_3. The targets were placed at regular intervals L=10 cm one after another. The target T_4 was arranged at the same distance normally to the beam axis in the converter plane. Each target was composed of an indium plate, 2x1x0.1 cm in size, contacting with the HR detector and the molybdenum foil measuring 2x1x0.01cm. The given geometry of the output device permitted the radiation field of various intensity and composition to act upon the targets in one run. In this case, the targets T_1 and T_4 were used for evaluating the contribution of photoneutrons via the (n,n') channel to the ^{115m}In yield. Table 1 lists the parameters of the radiation formation path and target exposure.

Table 1: Characteristics of target irradiation conditions

Accel.	E_0,MeV	l_C,cm	l_F,cm	I_e,μA	Exp.,h
LU-10	9	0.24	1.4	20.0	0.2
LU-40	35	0.4	5	3.7	1.0
	52.5	0.4	7	4.9	0.2
	71	0.4	9	4.0	0.5

RESULTS AND DISCUSSION

Experimental and simulation methods were used to determine the ratio S of the specific activity of the ^{115m}In isomer in indium plates to the absorbed dose in the HR detectors being in contact with the plates. Figure 5 shows the function $S(E_0)$ in the low-energy part of the electron energy range studied. In simulation, the data on the ^{115m}In photoactivation cross section, taken from ref. [8], were used. It can be seen that the calculated results are in good agreement with the experimental data. It should be noted, that in the energy range up to 9 MeV the reported data on the ^{115}In(γ,γ')^{115m}In reaction cross section are also sufficiently close (see Fig. 3).

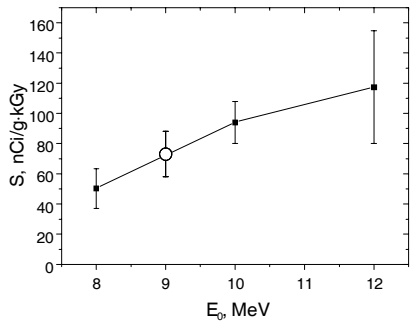

Figure 5: Ratio of specific ^{115m}In activity in indium plate to X-ray absorbed dose in PMMA (○- experiment, ■– calculation).

Figures 6 and 7 show, respectively, the data on the absorbed dose rate and, also, on ^{90}Mo and ^{99}Mo yields in the targets T_2 and T_3 in the electron energy range 26 to 71 MeV. The observed compliance of the computed data with the experimental results bears witness to both the adequacy of the method of radiation process simulation and the accuracy of description of reaction cross sections for molybdenum isotopes. At the same time, the ^{115m}In yield data obtained by the two techniques are essentially different (see Fig. 8).

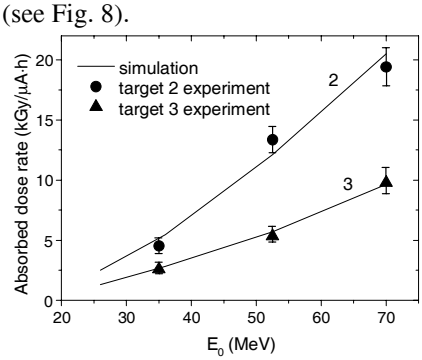

Figure 6: X-ray dose rate in PMMA as function of electron energy.

The comparison between the T_1 and T_4 target activities has shown that even at the photoneutron flux values being the highest for all irradiation regimes (at E_0=71 MeV), the contribution of the (n,n') channel to the ^{115m}In yield is no more than 1%.

Figure 9 shows the function $S(E_0)$. It was obtained by averaging of measuring results on the targets T_2 and T_3. It can be seen that in the E_0 range between 35 MeV and

71 MeV the S value decreases by ~ 10%.

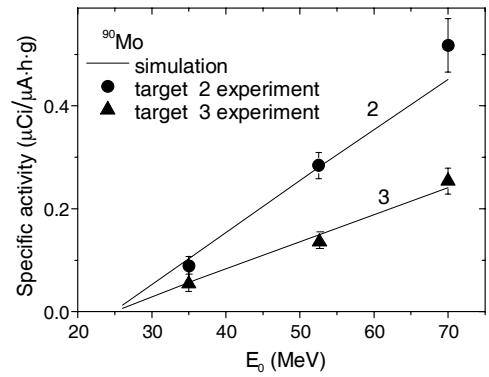

a

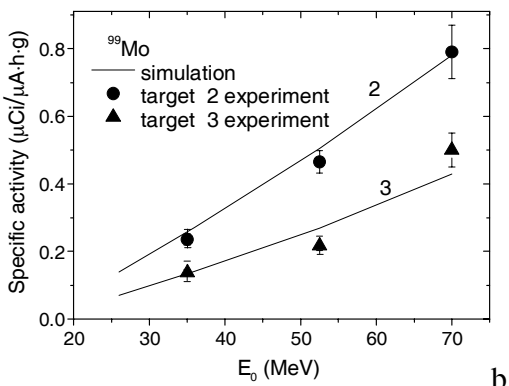

b

Figure 7: Yield of ^{90}Mo (a) and ^{99}Mo (b) versus electron energy.

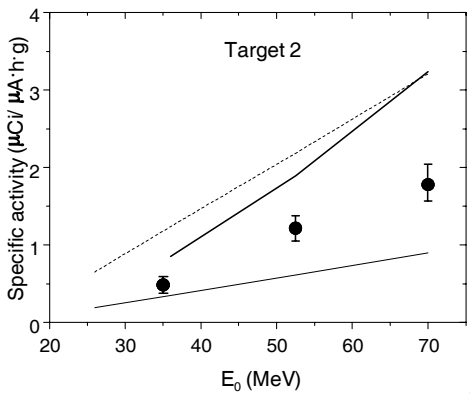

a

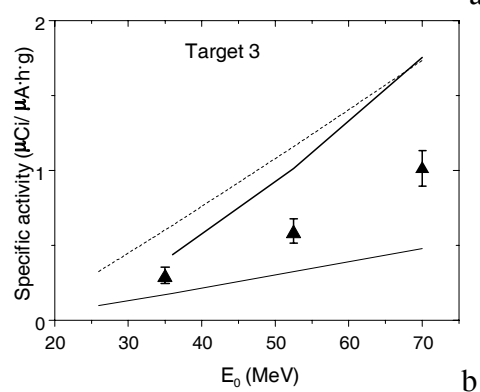

b

Figure 8: ^{115m}In yield versus electron energy:
a) target T_2, b) target T_3 (•,▲- experiment; ----, —, — calculations with cross section data according to [7], [8] and [9], respectively).

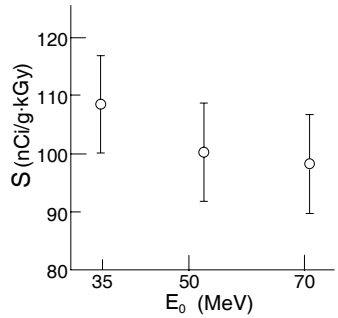

Figure 9: Ratio of specific ^{115m}In activity to absorbed dose in PMMA.

CONCLUSION

The undertaken studies have demonstrated that the ^{115}In(γ,γ′)^{115m}In reaction can be used for dosimetry of bremsstrahlung with the spectrum end-point energy up to 70 MeV and higher.

The highest measured X-ray absorbed dose is determined by the boiling temperature of indium and makes no less than 2 MGy (at adiabatic conditions). The safe level of the In activity can be readily provided by the appropriate choice of the detector mass.

REFERENCES

[1] M. Korsunsky, F. Lange and V. Shpigel, Rep. USSR Acad. Sci. 26(1940) 145.
[2] J.-H. Chao, P.-Ch. Hsu and H.-M. Liu, Appl.Rad.Isot. 55(2001) 549.
[3] A. Murataka, S. Endo, Y. Kojima and K. Shizuma, J.Radiat.Res. 51(2010) 197.
[4] ISO/ASTM 51276:2002. Standard Practice for Use of a Polymethylthacrylate Dosimetry System.
[5] F. Salvat, J.M. Fernandez-Varea and J. Sempau, "PENELOPE-2008 A Code System for Monte Carlo Simulation of Electron and Positron Transport" (OECD Nuclear Energy Agency, Issy-les-Moulineous, France, 2008).
[6] Handbook of photonuclear data for applications: Cross sections and spectra, IAEA-TECDOC-1178, IAEA, 2000.
[7] V. Bokhinyuk et al. Ukr.J.Phys. 51(2006) 657.
[8] Ju. Gangrsky and V. Mazur, Phys. Elem. Part. Atom. Nucl. 32(2002) 158.
[9] K. Kosako et al. J.Nucl.Sci. and Technol. 47(2010) 286.

HIGH PRECISION POWER SUPPLY FOR ACCELERATOR MAGNETS

Ajoy Sankar Banerjee, Variable Energy Cyclotron Centre, Kolkata 700064, India

Abstract

High precision power supplies used in accelerator systems have stability of the order of 5ppm to 100ppm depending on the functional requirement of the magnet to be excited. The paper highlights the various design considerations, aspects and important features for obtaining high current stability of such high precision power supplies.

INTRODUCTION

The stability of the high precision power supplies used in an accelerator system is an important factor for obtaining highly stable beam output required for various experimental studies. Line, load and temperature variations are the three important factors against which these power supplies have to combat to maintain high stability.

MAIN FEATURE OF THE POWER SUPPLY

Stability is the main important feature of these power supplies which lies between ±5ppm to ±100ppm i.e. the output current will have to remain in the error band of ±5ppm to ±100 ppm under various environmental perturbations such as

1. The input AC lines may ramp or step by ±10%
2. The magnet resistance may vary by 20%.
3. The ambient temperature could change from 15°C to 45°C.
4. There are AC line harmonics and notches generated by other power supplies.
5. The power supplies themselves generate a fundamental 600Hz rectifier ripple and some harmonics of 50Hz due to line imbalances.
6. There are R.F. interferences.

The table 1 shows stability requirement of high precision power supplies used for VECC room temperature accelerator system.

Table 1. Stability Table

High precision Power Supply	*Stability*
Main Magnet P.S. 3000A/150V Analyzing Magnet P.S. 500A/150V	5 ppm.
Trim coil P.S. 2500A/30V, 300A/25V Switching magnet P.S. 300A/150V	10 ppm.
Quadrupole magnet P.S. 300A/30V Steering magnet P.S. 10A/100V Valley coil P.S. 300A/30V	100 ppm.

ACTION TO ACHIEVE HIGH STABILITY

- Proper selection of rectifier circuit configuration for high ripple frequency to reduce ripple voltage
- Using both passive and active filter circuit for fine reduction of ripple voltage
- Adoption of proper regulating loops for good voltage and load regulation
- Using DCCT, working on zero flux principle, for sensing load current with 0.001% accuracy for high current regulation and stability
- Proper thermal management to control temperature of the heat dissipating devices and critical components of the power supply to minimize drift in characteristics
- Attenuation of R.F. pick-up and noise
- Taking proper action to reduce line disturbances

BLOCK DIAGRAM OF A HIGH PRECISION POWER SUPPLY

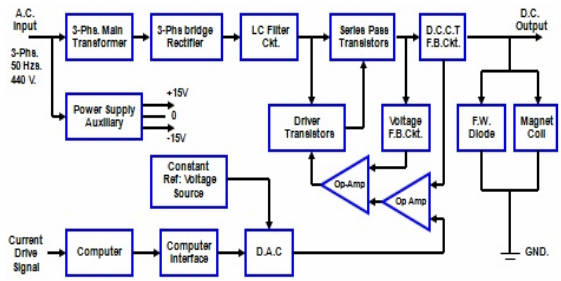

Figure 1: Block diagram of power supply

Series pass transistor controlled linear mode circuit configuration is generally adopted for simplicity in design and control.

Rectifier Circuit

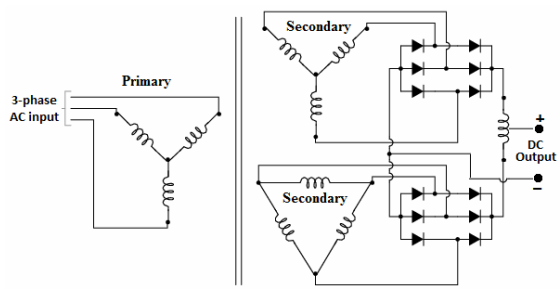

Figure 2: Rectifier circuit

Considering the optimum rectification condition twelve pulse bridge rectifier circuit as shown in the Fig.2 is adopted. This connection provides a low ripple voltage of 1.02%

LC Filter Circuit

The LC filter has almost constant ripple characteristics at all load currents above I_b where the diode conduction angle reaches 180° and the current becomes continuous.

ajoy_banerjee2000@yahoo.com

Because of the good voltage regulation at current above I_b, a bleeder resistor across the output is used.

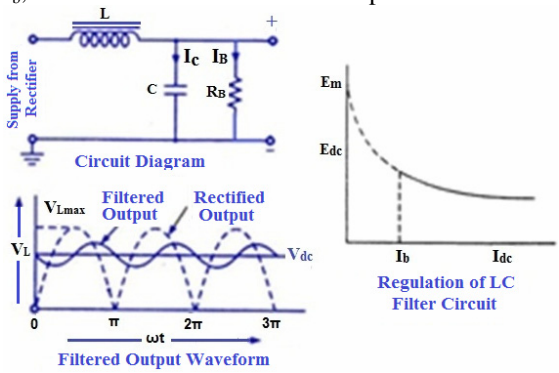

Figure 3: LC filter circuit.

Regulating Loops

3 nos. of regulating loops are used for high stability of the power supply.

1) Inner Fast Voltage Loops: This attenuate the output voltage ripple and hum and the output voltage fluctuation due to main supply fluctuation.

2) Middle Slew Rate Loop: It ensures an excellent slew rate linearity independent of the load and the set value.

3) Outer Slow Current Loop: It ensures the overall stability of the power supply.

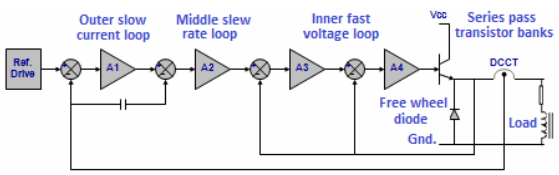

Figure 4: Regulating Loops

For successful operation of the regulating loops

- All the components used in the circuit are required to be of high precision in nature. All the operational amplifiers used should have low noise and low drift, like OP-27 family.
- Current Transducer working on zero flux principal is used for sensing DC current with 0.001% accuracy.
- Digital-to-Analog converter with true 16 bit resolution, 1 ppm/°C temperature drift and 2ppm noise is used in the reference drive circuit.
- Precision low noise & low temperature drift voltage reference source like REF101 is used in the reference drive circuit.
- All the critical components like DAC, Reference voltage source, burden resistance of the zero flux type current sensor and the error amplifier are enclosed in a Peltier cooler for low temperature drift of those components.

High Precision Current Sensor DCCT

DCCT works on zero flux principal is used for sensing DC current with 0.001% accuracy. The electronic control circuitry is completely isolated from the main power circuit of the power supply and earth for reason of safety and stray current path which produces measurement error. The measuring head, consisting of three identical toroids, senses the residual field and controls the amplifier in such a way as to keep the net field zero.

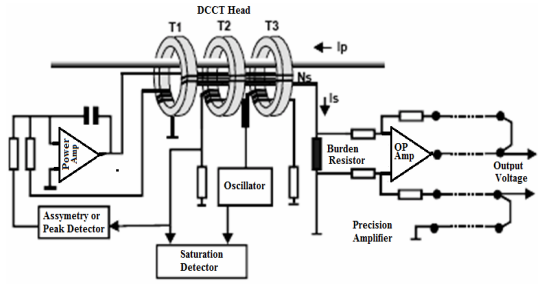

Figure 5: DCCT

A residual flux will cause asymmetry in the magnetizing current resulting in an output voltage fed to the power amplifier in the secondary circuit so that its output current restores perfect flux balance and hence zero residual field.

The secondary current is passed through the burden resistor and the drop across it is calibrated to denote the DC current.

THERMAL MANAGEMENT FOR POWER SUPPLY STABILITY

- Peltier cooler and controller are used to keep the operating temperature of the critical components, mainly error amplifier, DAC and burden resistance of DCCT in the regulating circuit, constant around 35ºC slightly above room temperature with 0.2ºC accuracy in order to avoid characteristic drift due to temperature variation.

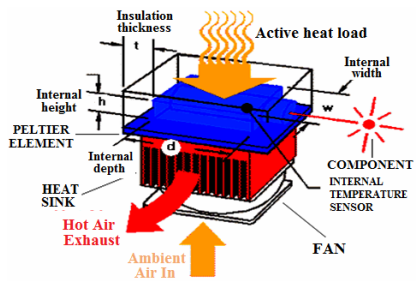

Figure 6: Peltier Cooler

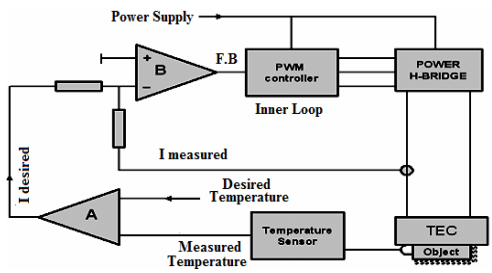

Figure 7: Peltier Controller.

- Low conductivity water cooled heat sinks are used for cooling of power transistors and diodes, small resistor is added to the emitter of each of the transistors in parallel for balance current sharing required for high stability of the power supply.

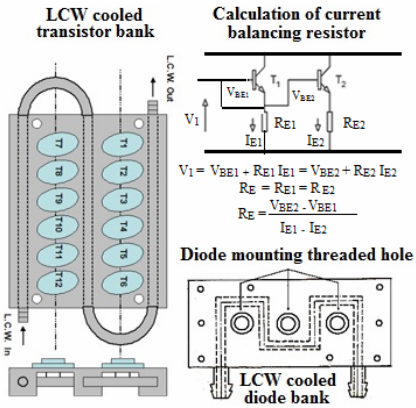

Figure 8: LCW cooled heat sinks

• Pre-regulator System is used to reduce power dissipation in the series pass transistor to improve efficiency and stability of the power supply.

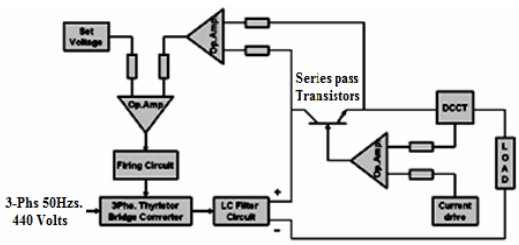

Figure 9: Pre-regulator system

• All the power supplies are placed in an air conditioned environment with temperature around 25°C to 30°C.

R.F. PICK-UP ATTENUATION AND SHIELDING OF POWER SUPPLY

The conducted R.F. pick-up transmitted to P.S. through power cables form magnets in the R.F. field is attenuated with R.F. filter and the radiated R.F. pick-up radiated from the cyclotron chamber is minimized by properly grounding and shielding of the power supply electronics modules and cabinets to improve power supply stability.

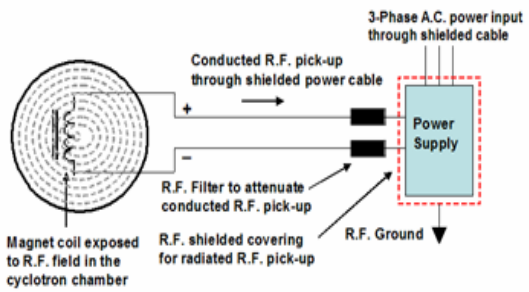

Figure 10: R.F Pick-up Attenuation & Shielding

LINE-INTERACTIVE UPS SYSTEM

This is used to overcome line disturbances. The induction coupling acts as a store of kinetic energy. It handles the line voltage dips, and keeps the generator running before the diesel engine comes into action to run the generator when main power fails. The choke and the synchronous 3-ph. a.c. machine together act as a stabilizing filter and provide clean regulated power from the mains during normal operation.The 3-ph.a.c. machine acts as a synchronous motor when normal power exits. The diesel engine operates when normal power fails. Then the a.c machine acts as a generator.

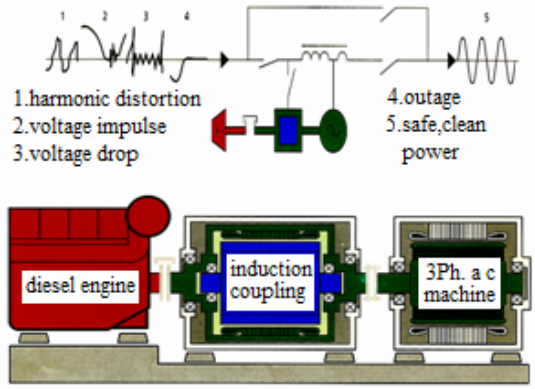

Figure 11: Line Interactive UPS System

PERFORMANCE DATA OF A 5 PPM HIGH PRECISION POWER SUPPLY

Table 2. Performance table

Parameter	*ppm*
Short term stability: (30min)	3ppm
Long term stability: (8hrs)	5ppm
Line regulation: Ramp or step within ±10% of supply line	0.5ppm
Load regulation: Magnet coil resistance change within ±10%	0.5ppm
Temperature coefficient: (per ^{0}C) •Ambient temperature variation at P.S. location in the range of 20°C to 30ºC •Cooling water temperature variation in the range of 20°C to 35ºC	 0.2ppm 0.05ppm
Ripple: Current ripple in magnet	0.15ppm

Stability of a magnet power supply is the net deviation of the load current value from the set value under the condition of +/- 10% variation of input line voltage, load resistance and temperature.

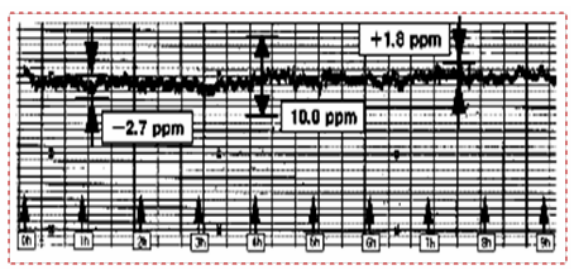

Figure 12: Stability of a main magnet power supply

For the main magnet P.S. (3000Amps.150Volts.) the stability has been calculated to be

+ 1.8 ppm - (- 2.7 ppm) = 4.5

BEAM EXTRACTION SYSTEM FOR INDUSTRIAL ELECTRON ACCELERATOR ILU-14

V. Bezuglov, A. Bryazgin, B. Faktorovich, E. Kokin, V. Radchenko, E. Shtarklev, A. Vlasov,
BINP SB RAS, Novosibirsk

Abstract

This paper describes beam extraction system for pulse linear electron accelerator ILU-14 with energy range 7.5-10 MeV and beam power up to 100 kW. The main aim of this work was to achieve the uniform dose field in radiation zone. Admissible dose nonuniformity is of no more than ± 5% along the scanning length up to 1m (if necessary, the scanning length may be reduced). Geometrical and electron-optical characteristics of all the beam channel elements were optimized after computer simulation of electron trajectories. To achieve the required nonuniformity of dose field additional electromagnets were installed. These magnets realize beam focusing and centering of the beam endwise of the channel, as well as correction of the scanning field. Control system of magnets power supply allows the online correction of electron beam.

INTRODUCTION

Radiating technologies reached now such wide application in the industry that became its separate branch. And improvement of generators of electron beams occurs at the same time to high-quality improvements of extraction devices. Questions of efficiency of radiation, i.e. efficiency of process of radiation became the main requirements at radiation of production. The nomenclature of irradiated objects considerably increased and diversified. Rigid modern requirements to uniformity of dose fields of electronic accelerators demand detailed consideration of the questions connected with operation of extraction devices. To improve radiation quality (dose uniformity) and obtain competitive advantages the new system of the beam output for the industrial accelerators of the ILU series is developed. The main requirements to this system are nonuniformity of the dose field not worse ±5 %, and also width of the beam scanning of 1 m (at energy of an electron beam up to 10 MEV). In industrial accelerators of ILU type an electron beam with duration 0.5 ms is scanned along the output window from a titanic foil (thickness of 50 microns). Uniformity or the set nonuniformity of distribution of the beam intensity along a foil is one of the most important parameters of radiating and technological complexes on ILU base. The general block diagram of the output path of the accelerator is provided on fig. 1. After accelerating structure 1 beam gets to the electron-optical channel. For control of the beam position of rather central axis of the channel input of the directing magnet 2, representing the two-coordinate corrector of electron trajectories in the range ±5sm is supposed see. For formation of the cross-section size of a beam (at initial adjustment of system without beam scanning) the quadrupole doublet 3 is provided. For control of beam parameters the graphite diaphragm 4 from which the signal will be taken off further will be located. Necessary uniformity of the output current density is offered to be reached by installation before the main beam scanning system 6 of the correction system of the scanning magnetic field 5. Also in extraction system possibility of so-called horizontal beam scanning 7 across the bell is provided. For receiving on the bell foil of a beam with identical angular characteristics, especially at big angles of scanning, it is necessary to install the additional turning devices 8 (Panovsky lenses) which transform trajectories of electrons so that a beam falls on a foil everywhere on its length at right angle. After an exit of an electron beam from a bell possibility of its transformation to bremsstrahlung by means of the converter 9 is provided.

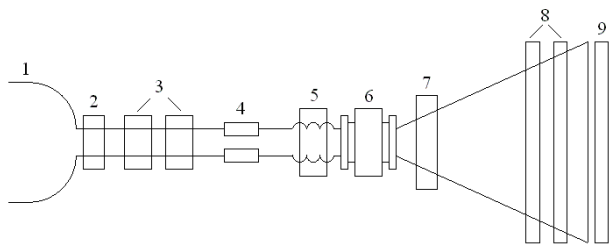

Figure 1: 1 – accelerating structure, 2 – control magnet, 3 – quadrupole doublet, 4 – diaphragm, 5 – bellows unit with correction system of scanning field, 6 – scanning chamber with scanning electromagnet, 7 – transverse beam scanning system, 8 – Panovsky lenses, 9 – converter.

BEAM SCANNING SYSTEM

It is necessary to give special attention to formation of a demanded dose field on an exit from the accelerator. First of all, it is necessary to consider influence on a form of a scanning field of the processes occurring in metal walls of the vacuum chamber of beam scanning (a bell filler).

When giving a pulse magnetic field in a metal not magnetic shield (screen) of scanning system which divides on vacuum space of a beam deviation and the scanning electromagnet which was outside, there is a reaction of the induced currents which distorts a scanning field. From [1] follows that the field inside the screen H0(t) is superposition of the influencing field H1(t) and the field H2(t) raised by currents, induced in the shield thickness by pulse of H1(t). In the same place it is deduced that the field in the screen H0(t) raised by pulse H1 (t), satisfies to the ordinary differential equation:

$$H1(t) = \frac{L}{R} \cdot \frac{dH0}{dt} + H0(t), \quad H0(0) = 0, \quad (1)$$

where L and R are inductance and active resistance of the screen.

From the equation (1) it is obvious that the field form in vacuum depends only on size of a ratio of L and R. For the designs of scanning shields in accelerators of a ILU series, the size of the relation of L/R makes size about 100 microseconds. The technique of definition of this constant is stated in [2].

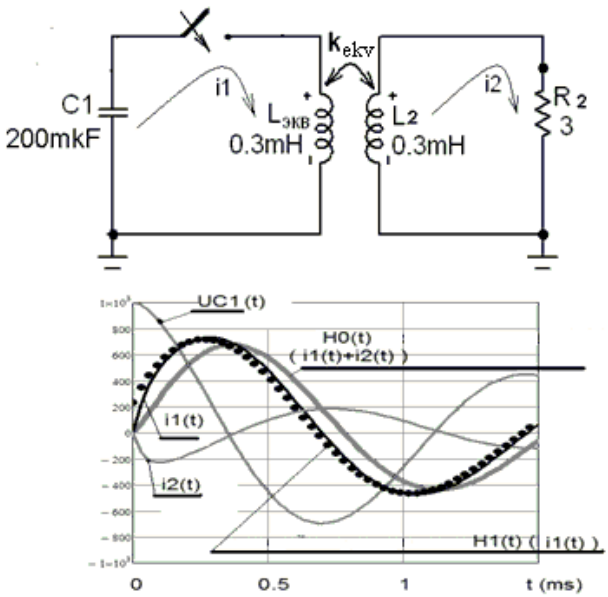

Figure 2: Calculated curves of currents and magnetic fields in the simple generator of scanning.

Let's consider work of an equivalent chain of a scanning electromagnet at the discharge on this chain of capacity. On fig. 2 the scheme of a chain and the main curves of currents, voltages, and also magnetic fields in vacuum are presented. And, continuous lines reflected results of calculation of transients for this scheme, and points showed a curve of the exciting field H1(t) found according to (1). For H0(t) we take i1(t) + i2(t). The main time regularities of influence of the closed turn of a vacuum shield on a working magnetic field are visible. It is necessary to note big attenuation of a field in vacuum H0(t) from brought active resistance of a filler R2.

The sign-variable scanning field during a pulse of a beam current should be symmetric, concerning the middle, not only on absolute amplitudes, but also on their derivatives. This circumstance considerably reduces possibilities of application of schemes of this kind because of a big difference of working amplitudes of a demanded symmetric reverse of this field.

SYSTEM OF THE SCANNING FIELD CORRECTION

For the purpose of elimination of the described effect for the scanning electromagnet supply of the accelerator ILU-14 the following scheme (fig. 3) was offered.

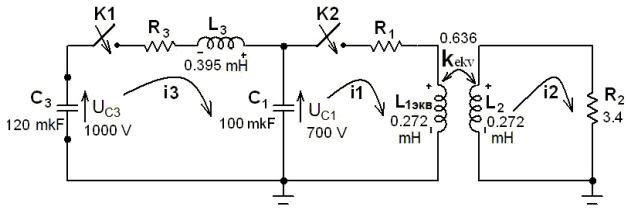

Figure 3: The scheme of a working chain of a scanning electromagnet taking into account a filler. i1, i2 and i3 are currents in contours. Keys K1 and K2 are switched on at the same time.

Presence of a correcting chain of L3 and C3 allows to achieve symmetry of a sign-variable scanning magnetic field during the beam current pulse (see fig. 4). It is necessary to note that given results were received provided that by R1=R3=0. Thus, we consider only influence of the bell filler on a resultant magnetic field in vacuum.

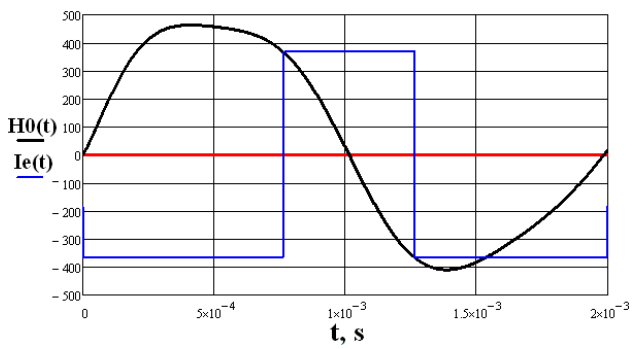

Figure 4: The diagram of a scanning magnetic field with use of a correcting power-supply circuit of a magnet. During a beam pulse (a dark blue meander) the symmetric part on amplitude of this distribution is used.

For computer modeling of electron trajectories the beam on an entrance to the output channel is set or a circle of the points, which gives the evident three-dimensional image of the beam form deformation in the plane of the output foil, or in the form of a round electron spot with really measured distribution of current density that allows to receive values of current density distribution on the exit. Calculation of movement trajectories of electrons in constant magnetic fields was carried out by means of MathCAD software. By results of this calculation the value of amplitude of a magnetic field of the scanning electromagnet necessary for a beam turn on the demanded length along the output window of the accelerator is 0.11T. On fig. 5b calculated trajectories of electrons with energy of 10 MEV are given in a way from scanning electromagnet to the extraction window of the bell. The bell height (axis Z) is 2 m.

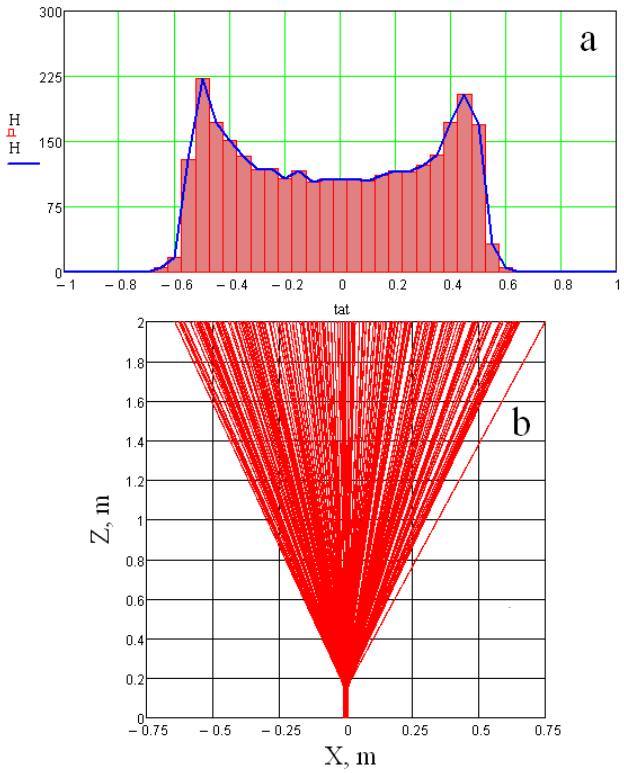

Figure 5: a – the histogram of output current density without correction, b – the scanned electron beam with energy of 10 MEV.

The power supply system of the scanning electromagnet forms a current pulse, in a form reminding piece of a sinusoid with duration of 0.5 ms and adjustable amplitude. Scanning of the beam occurs on a linear site of a sinusoid in the field of transition through zero. Speed of scanning is proportional to a derivative of a magnetic field and there can not be a constant during an acceleration cycle.

On fig. 5a the calculated histogram of the output current density distribution of the scanned beam is provided. It is visible that the current density at edges of a foil increases, and for achievement of the dose uniformity the speed of beam scanning to edges should be raised. Necessary uniformity of output current density is reached by installation before a scanning electromagnet of the system for scanning magnetic field correction. The additional correcting field leads to equalizing of beam scanning speeds along the output bell. The amplitude of the correcting magnetic field is 0.012 T.

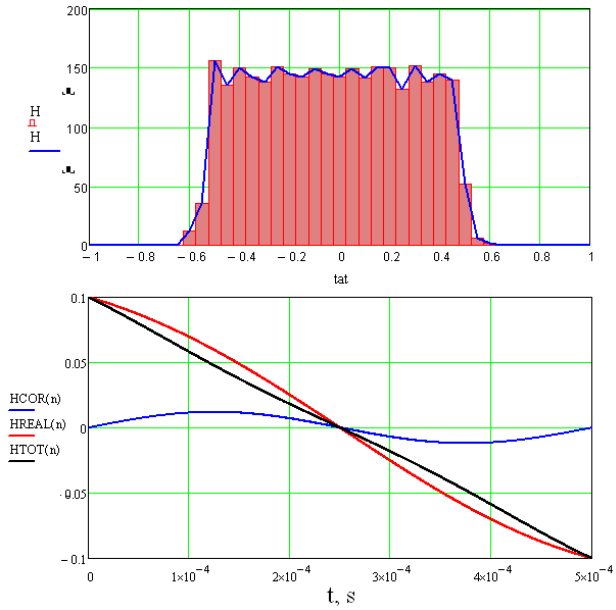

Figure 6: Distribution of output current density with necessary uniformity (at the top) and distributions of the scanning (HREAL), correcting (HKOR) and total (HTOT) magnetic fields (on the bottom).

On fig. 6 the histogram of output beam current density along the bell (the sizes are specified in meters) with use of the system of scanning magnetic field correction, and also forms of scanning and correcting fields during the beam pulse are illustrated.

RESULTS

The scanning system of the beam with energy up to 10 MEV is produced and tested. The received nonuniformity of the dose field in radiation zone was ±10%. To improve radiation quality (dose uniformity) and obtain competitive advantages the correction system of a scanning magnetic field was designed. Consequently, nonuniformity of the surface dose is reduced to ±5 %. This system will be tested within projects of sterilizing complexes at FMBC of A.I.Burnazyan (Moscow) and "Park of Nuclear Technologies" (Kurchatov, Kazakhstan).

REFERENCES

[1] Vasiliev V.V. *et al*, " Conducting covers in a pulse electromagnetic field ", Moscow, Energoatomizdat, 1982.

[2] Auslender V.L. et al, "Technique of design and calculation of extraction devices for electron accelerators", Preprint BINP 2004-27, Novosibirsk, 2004.

CHARACTERISTICS OF THE MODEL OF LINEAR ACCELERATOR BASED ON PARALLEL COUPLED ACCELERATING STRUCTURE WITH BEAM LOADING

Yu. Chernousov, V. Ivannikov, I. Shebolaev, ICKC, Novosibirsk, Russia
E. Levichev, V. Pavlov, BINP, Novosibirsk, Russia

Abstract

The 5-cavity model of linear accelerator based on parallel coupled accelerating structure (LAPCAS) with periodic permanent magnet focusing system (PPMFS) and RF-controlled three-electrode electron gun is under study. The work of the accelerator with electron beam is demonstrated. Parameters of short pulses mode are the following: electron energy – 4 MeV, pulse current – 0.3A, pulse duration - 2.5 ns; parameters of long pulses mode are the following: energy – 2.5 MeV, pulse current – 0.1A, pulse duration – (0.1 - 4) μs. Working frequency of the accelerator – 2.45 GHz. In RF-controlled mode the capture about 100 % has been demonstrated. Beam loading effect in the LAPCAS takes place. Data of observation of this effect and compensation of energy spread of accelerated electrons by delaying the moment of injection in the LAPCAS are demonstrated. The equations describing the transient process in the accelerating cavity which is powered by an external RF generator and excited by electron bunches are presented in a simplified form.

INTRODUCTION

Parallel coupled accelerating structure (PCAS) is a new type of the structures and consists of separate accelerating cavities feeding from common exiting cavity in parallel [1]. The structure is equipped with an inside installed reverse periodic permanent magnet focusing system (PPMFS). The possibility to use the PCAS in the accelerator technique demands experimental studies. Accelerating cavities of PCAS work in standing wave regime and beam loading effect – dependence of average energy of accelerated electrons on time during the pulse takes place in this structure. The methods of compensation the energy spread of accelerated electrons in the standing wave and traveling wave structures have been discussed for a long time [2-5]. Now in some installations the issue came into practical implementation [1,6,7]. One of the methods to reduce this negative effect – injection the electron pulse with delay relatively to pulse of feeding RF power, so called ∇T-method. In this paper the equations describing the transient process in the accelerating cavity which is powered by an external RF generator and at the same time excited by electron bunches in a simplified form are obtained and data of experimental observation of the beam loading characteristics, beam loading effect and compensation of energy spread in the LAPCAS by ∇T-method are represented. For experimental observation of the beam loading effect we used energy spread measurements by method of absorption in retarding metallic plates [8].

THEORY

Beam loading is defined as the energy reduction of charged particles due to their interaction with an accelerating structure [2]. Charged bunches, when passing through the structure, generate RF oscillations that decelerate the subsequent bunches. As a result average energy of accelerated beam depends on time during the pulse. To evaluate the energy spread due to the transients, it is necessary to take into account that acceleration voltage on the accelerating cavity is excited by two independent sources: the external RF generator and modulated electron beam. In the theoretical description we assume that the electron beam consists of a train of short bunches, RF pulse is an ideal step-function and that all charged particles travel with the speed of light, the difference between the frequencies of generator, cavities and moving bunches is zero.

Evaluation of complex magnitude of equivalent acceleration voltage U in the standing wave accelerating cavity, which is powered by an external RF generator and at the same time excited by electron bunches can be described, as may be shown from [5], by the following equations:

$$\tau\frac{dU}{dt}+U=U_G-U_{B0},$$

$$\tau=\frac{2Q_0}{\omega_0(1+k)},\ U_G=U_{G0}\exp(i\theta),$$

$$U_{G0}=\frac{2(kZLP_G)^{1/2}}{(1+k)},\quad U_{B0}=\frac{IZL}{(1+k)} \qquad (1)$$

where τ is the filling time constant of these evaluations; U_G is complex amplitude of equivalent acceleration voltage on the cavity, excited by the generator; U_{G0} and U_{B0} are steady-state values of amplitudes of equivalent acceleration voltage on the cavity, excited by the generator (U_{G0}) and beam (U_{B0}) correspondently, real positive quantities; ω_0 is cavities eigenfrequency; k is the coupling coefficient between the cavity and feeder line; Q_0 is the cavities unloaded Q - factor; Z is effective shunt impedance per unit length; L is the length of the accelerating cavity; P_G is the RF power which excites the cavity; $\theta-\pi$ is the phase of generator-induced oscillations relatively to beam-induced

oscillations. The load due to the current is taken into account by the term $U_{B0} = \frac{IZL}{(1+k)}$, where I is average current. The definitions of U, τ, k, Q, Z are taken from [3,4].

Then real part of U determines the energy gain U_A of the beam, is expressed in term of angle θ:

$$U_A = (U_{G0}\cos\theta - U_{B0})[1 - \exp(-t/\tau)] \quad (2)$$

In accordance with relation (2) average energy of accelerated charged particles depends on time.

Situation changes if the beam injects with delay t_B relatively to the start of RF pulse.

Total acceleration voltage after moment t_B is:

$$U_A = U_{A,G} - U_{A,B} = (U_{G0}\cos\theta - U_{BO}) + [U_{G0}\cos\theta\exp(-t_B/\tau) - U_{BO}]\times \exp(-(t-t_B)/\tau)), \quad t \geq t_B \quad (3)$$

Dependence on time disappears if:

$$U_{G0}\cos\theta\exp(-t_B/\tau) - U_{BO} = 0. \quad (4)$$

This equation determines the moment t_{B0} of beam injection:

$$t_{B0} = \tau \ln \frac{2(kZLP_G)^{1/2}\cos\theta}{IZL} \quad (5)$$

For $\theta = 0$ the same expression is obtained in [4].

If the beam injects with delay time $t_B > t_{B0}$, in accordance with equation (3) real part of equivalent voltage U_A decreases with time and correspondently average energy of the beam decreases. If $t_B < t_{B0}$, then real part of equivalent voltage U_A increases and average energy of the beam increases with time.

EXPERIMENTALS

Experimental observations of the beam loading characteristics were done on the electron accelerator, which consists of 5-cavities model of PCAS and pulsed three-electrode RF controlled DC high voltage electron gun [1]. The RF-controlled gun forms RF-modulated electron beam, which consists of a train of grouping charged bunches on the frequency 2450 MHz with duration of every bunch about 0.2 ns and with variable parameters: energy 0 - 50 keV, value of pulse current 0-0.5 A, pulse duration 0.1-5 μs. Delay time of the moment t_B of beam injection may be changed from 0 up to 5 μs. Accelerating structure feeds on the klystron KIU-111 [9]. In the experiments RF pulse duration of the klystron was 5 μs, pulsed RF power varied up to 2 MW.

Beam loading effect and application of ∇T-method for compensation of this negative phenomenon are successfully investigated on the LAPCAS. The

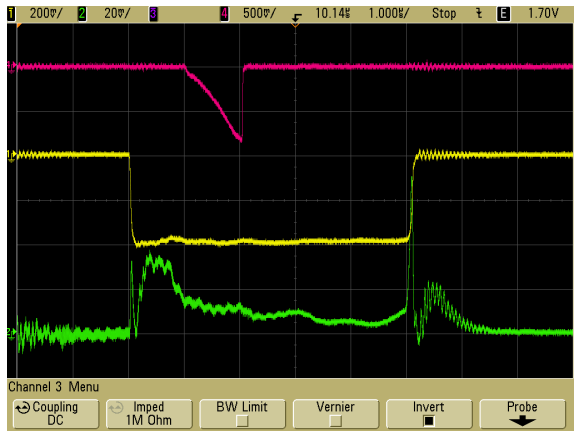

Figure 1: Delay time of electron pulse (red) is 1 μs.

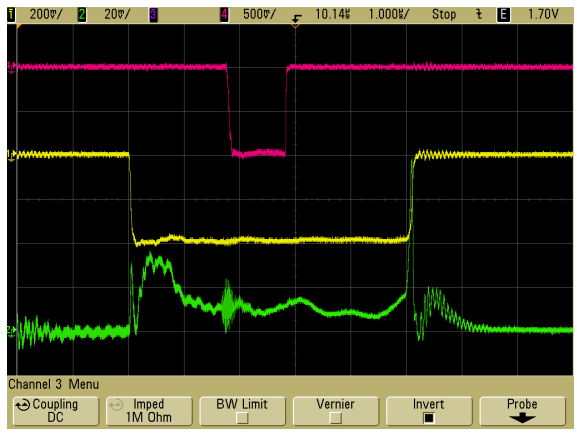

Figure 2: Delay time of electron pulse is 1.8 μs.

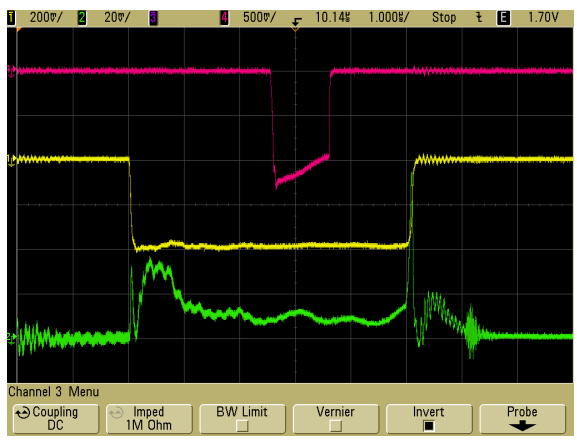

Figure 3: Delay time of electron pulse is 2.6 μs.

experimental observations of beam loading effect are performed by the following way. Pulsed electron beam of rectangular form with pulse duration of 1 μs (test pulse) with constant magnitude of injection current (0.1A) and variable delay time was injected into the accelerating structure. A Faraday cap with metal plates in front of them was installed at the exit of the accelerator. Electrons with high energy overcome the metal plates, and those

with low energy get stuck in it. Part of accelerated beam overcoming the metal plate of any thickness and electrons passed through the plate fall into the Faraday cap and pulsed current is recorded by oscilloscope. On the total thickness of retarding plates 70-80 % of accelerated electron beam is absorbed.

As one can see from the equation (3), output beam energy and consequently the magnitude of a current recorded by oscilloscope will increase during a test pulse, if $U_{G0}\cos\theta\exp(-t_B/\tau)-U_{BO}>0$.

The magnitude of a current recorded by oscilloscope will decrease during a test pulse,

if $U_{G0}\cos\theta\exp(-t_B/\tau)-U_{BO}<0$.

The magnitude of a current recorded by oscilloscope will remain a constant during a test pulse, if

$$U_{G0}\cos\theta\exp(-t_B/\tau)-U_{BO}=0.$$

In other words, the dependence of beam energy on time becomes the dependence on time of magnitude of a current from Faraday cap recorded by oscilloscope. Thereby, for experimental observation of beam loading effect we used energy spread measurements by method of absorption in retarding metallic plates [8] in pulse regime.

Pulse-energy characteristics of the accelerated beam are represented on Fig. 1-3. Curves registered by oscilloscope: 1- RF pulse of klystron (yellow); 2- reflected signal from accelerating structure (green); 4 - pulse form of accelerated beam (red). Electron pulses from injector were of rectangular form. Delay time of beam injection t_B relatively to RF pulse changed from approximately 1μs (Fig. 1) up to 2.6 μs (Fig. 3). Figure 2 represents a point on the time scale, t_{B0}=1.8 μs, where the conditions (4), (5) take place, therefore, the recorded current pulse has a rectangular shape. In this case it means that average energy of accelerated electrons does not depend on time.

CONCLUSION

The work of LAPCAS with electron beam in different regimes is demonstrated. Short pulses mode: electron energy – 4 MeV, pulse current – 0.3A, pulse duration -2.5 ns; long pulses mode: electron energy – 2.5 MeV, pulse current – 0.1A, pulse duration - 0.1-4μs. When the electron gun worked in RF-control regime the capture about 100 % was achieved. Beam loading effect in LAPCAS takes place. Method of compensation of energy spread of accelerated electrons by delaying the moment of injection in the LAPCAS gives encouraging results. The equations in the simplified form describing transients allow interpreting the experimental pulse dependences obtained by a method of retarding metallic plates in pulse regime.

REFERENCES

[1] Yu.Chernousov, V.Ivannikov, I.Shebolaev, V.Pavlov, A.Levichev. Prototype of Parallel Coupled Accelerating Structure. Proc. of EPAC 2008, p. 2737.

[2] Perry B. Wilson. High Energy Electron Linacs: Applications to Storage Ring RF Systems and Linear Colliders. SLAC-PUB-2884 (Rev.) November 1991.

[3] Zenghai Li, Roger Miller, David Farkas, Tor Raubenheimer, Huan Tang and Di an Yeremian. Beam Loading Compensation for the NLC Low Frequency LINACs. SLAC-PUB-7429, 1997.

[4] Thomas P. Wangler. *RF Linear Accelerator*. WILEY-VCH, 2008.

[5] Yu. D. Chernousov, V. I. Ivannikov, and I. V. Shebolaev, Possibility of Stabilizing the Beam Energy in Resonant Accelerator on the Leading Edge of the Microwave Pulse. Proc. of RuPAC 2006, p.324.; V .I. Ivannikov, V.M. Pavlov, Yu.D. Chernousov , and I.V Shebolaev. The Effect of Accelerating Cavity's Transients on the Particle Energy Spread. Technical Physics, Vol. 49, No. 6, 2004, p. 795. Translated Zh. Tekh. Fiz., Vol. 74. No. 6. 2004, p. 134.

[6] Abhay Deshpandea, Sakae Arakib, Masafumi Fukudab, Kazuyuki Sakauec, Nobuhiro Terunumab, Junji Urakawab, Masakazu Washioc. Generation of Long Bunch Train Using RF Gun. Proc. of LINAC2010, p. 992.

[7] Y. Yokoyama,T.Aoki, K.Sakaue ,T.Suzuki,T. Yamamoto, M.Washio, J.Urakawa, N.Terunuma, H.Hayano, S.Kashiwagi, R.Kuroda. Study on Energy Compensation by RF Amplitude Modulation for High Intense Electron Beam Generated by a Photocathode RF-Gun. Proc. of IPAC2011, p.1132.

[8] *Beta- and Gamma-Ray Spectroscopy.* Edited by Kai Siegbahn. Amsterdam: North-Holland publishing company, 1955.

[9] I.A. Frejdovich, P.V. Nevsky, V.P. Sakharov, M.Yu. Vorob'ev, E.A. Knapp, W.P. Trower, H. Yamada, A. Kleev, A.S. Alimov, V.I. Shvedunov, Yu.D. Chernousov, I.V. Shebolaev, V.I. Ivannikov, Yu.N. Gavrish, V.M. Nikolaev. Multy-Beam Klystrons with Reverse Permanent Magnet Focusing System as the Universal RF Power Sources for the Compact Electron Accelerators. Proc. of RuPAC 2006, p.100.

NIIEFA ACCELERATORS FOR INDUSTRY AND MEDICINE

M.F. Vorogushin#,
D.V. Efremov Scientific Research Institute of Electrophysical Apparatus, Saint Petersburg, Russia

Abstract

The D.V. Efremov Institute (NIIEFA) is a leading enterprise in Russia involved in designing and manufacturing of applied and medical charged particle accelerators, as well as electrophysical systems based on these accelerators. Since the foundation of the Institute, we have designed, manufactured and delivered to Russian customers and abroad more than three hundred accelerators of different types, in particular, cyclotrons, high-frequency linear electron accelerators, high-voltage accelerators and neutron generators. The activities of the Institute in the field of accelerating engineering encompasses all the stages of an accelerator manufacturing, starting from R & D works to manufacturing, installation, adjustment and maintenance of the equipment delivered.

NUCLEAR MEDICINE

Among the present-day methods of medical examination, the radionuclide diagnostics presents the most complete information on available pathologies. The method is characterized with a high sensitivity, the shortest possible time needed for analysis and reliability of the data obtained. A single-photon emission computer tomograph (SPECT) is an apparatus the most widely used for examination of great masses of population. This apparatus uses radiopharmaceuticals labeled with short-lived isotopes with the half-life period from several hours up to 2-3 days. The clinical experience gained over a number of years demonstrates that in about 20% of cases more accurate positron-emission diagnostics is needed, which applies ultra-short-lived isotopes with the half-life from two up to one hundred and ten minutes. Radio-isotopic examinations allow cardio-vascular and oncologic diseases, the death rate from which is the main factor determining the age of a human life, to be detected at very early stages. Cyclotron is the most proper accelerator allowing necessary ultra and short-lived isotopes to be produced in the most cost-effective way.

NIIEFA has been involved in designing and production of cyclotrons since the day of its foundation. More than forty different models of cyclotrons have been delivered to Russian customers and abroad, and the majority of these machines have been operated until now. Recently, a series of compact cyclotrons has been designed specially for production of medical isotopes [1]. The main parameters of these cyclotrons are given in Table 1.

Specific features of these cyclotrons are: the external injection of hydrogen negative ions, beam extraction by stripping negative ions on carbon foils, the main electromagnet of shielding-type with the vertical median plane, the same principle of construction of the RF-power supply system, vacuum system and automatic control system.

Table 1: Main Parameters of Cyclotrons for Medicine

Parameters	CC-12	CC-18/9	MCC-30/15
Accelerated ions	H^-	H^- / D^-	H^- / D^-
Ion energy, MeV	12	18/9	18…30 / 9…15
Extracted beam current, μA	50	100/50	200/70
Electromagnet:			
- pole diameter, cm	90	115	140
- supply power, kW	5	7	12
- mass,t	10	20	41
Frequency of RF oscillations, MHz	76.4	38.2	40.68
RF generator power, kW	15	20	25
Energy consumption, kW	30	70	100

To give an access to in-chamber components, the iron core is made as a fixed part and a movable part. The movable part is fixed on a support and can be moved apart for a distance up to 800 mm.

The CC-12 compact cyclotron is intended for production of ultra short-lived isotopes directly in medical diagnostic centers. The CC-18/9 cyclotron (Fig. 1) allows both ultra short-lived isotopes and short-lived isotopes to be produced. The CC-18/9 machines are successfully operated in PET centers in Turku (Finland), Saint-Petersburg and Snezhinsk (Tchelyabinsk district), Russia.

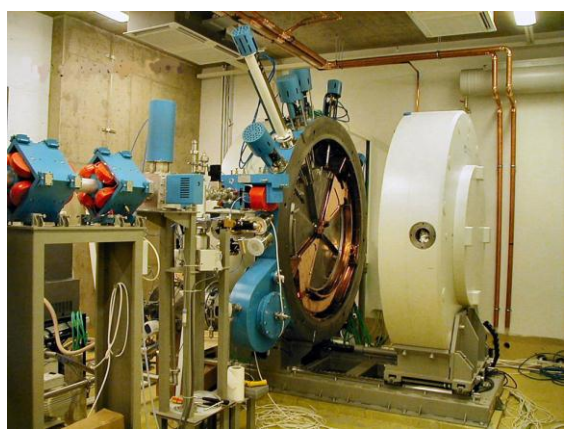

Figure 1: The CC-18/9 cyclotron installed in Turku (Finland).

#vorogushin@luts.niiefa.spb.su

The MCC-30/15 cyclotron with the variable ion energy provides production of ultra short-lived, short-lived and long-lived isotopes for nuclear medicine. Two charge-exchange devices are installed on the cyclotron for the beam extraction into beamlines. A standard set of the beamline equipment is: matching, switching and correcting electromagnets, quadrupole lens doublet, beam scanners, Faraday cup and necessary vacuum equipment.

The MCC-30/15 cyclotron together with the equipment for two beamlines has been delivered to the University of Jyvaskula, Finland and has been in operation since 2010 (Fig. 2). Preliminary works on organization of serial production of medical cyclotrons are now underway in NIIEFA.

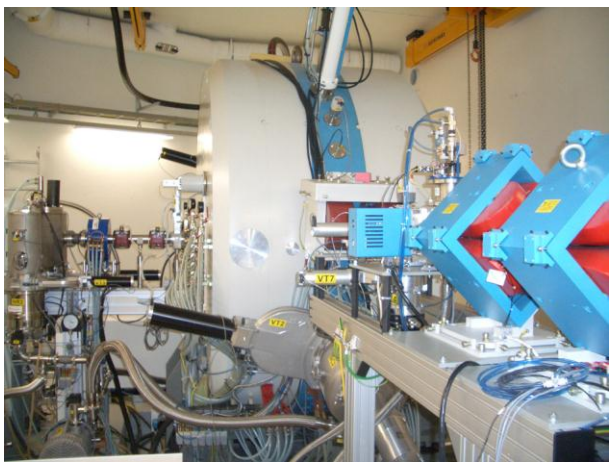

Figure 2: The MCC-30/15 cyclotron installed in the University of Jyvaskula (Finland).

RADIOTHERAPY AND NEUTRON THERAPY

The D.V.Efremov Institute is the only national designer of linear electron accelerators for radiation therapy, and therefore designing and production of electrophysical equipment for medicine is one of priority fields of its activity. Over the years of the Efremov Institute existence, several generations of medical accelerators have been designed and manufactured. About one hundred machines have been delivered to oncologic clinics of Russia and CIS countries.

In the framework of international cooperation with the “Philips Medical Systems. Radiotherapy” firm (Great Britain), a small-scale production of SL-75-5MT accelerators for radiotherapy was organized; up to 15 machines per year were produced. The SL-75-5MT accelerator is a Russia-made version of the “Philips” accelerator (up to 60% of Russian component parts), it is intended for X-ray radiation therapy with an energy of 6 MeV in the static and arc modes. About sixty machines have been manufactured and delivered to clinics of Russia.

In compliance with international standards, after ten years of operation medical accelerators should be either subjected to updating or replaced. To meet these requirements, additional medical equipment is required, the cost of which can be several times more than the cost of the accelerator itself. In this connection, recently a new medical accelerator «ELLUS-6M» with an electron energy of 6 MeV have been designed in the Efremov Institute (Fig. 3) with the following additional equipment:

- multi-leaf collimator to form the X-ray therapeutic beams maximally corresponding to the shape of a tumor;
- translator, an automatic control system used to transfer digital data from the treatment planning system to the control console of the accelerator;
- device for the detection of the X-ray radiation passed through the body of a patient and the table top and for forming the portal images;
- modified patient-support system.

Figure 3: The «ELLUS-6M» accelerator in the N.N. Petrov Institute of Oncology, St.Petersburg.

The «ELLUS-6M» accelerator is equipped with a computer control system compatible with all additional medical equipment. The accuracy of the irradiator rotation velocity setting, the grid modulator of the electron source, which ensures ten-fold variation of the irradiation dose by changing the pulse length, allow the dose rate to be controlled depending on the rotation angle (the IMRT mode).

The accelerator is equipped with the treatment planning system, laser pointers and dose field analyzer with a double-channel measurement system on the basis of diamond detectors. The accelerator with the additional medical equipment has been delivered to the N.N. Petrov Scientific Research Institute of Oncology (St. Petersburg) where starting since 2011 it undergoes medical and operational life tests. After successful completion of the tests, the «ELLUS-6M» accelerator can find wide application including the replacement of obsolete accelerators SL-75MT and cobalt apparatus “Rocus”.

Nowadays, the accumulated clinical experience has demonstrated that up to 30% patients with severe radioresistant forms of malignant tumors need radiation therapy treatment using neutron ionizing radiation.

The 14 MeV neutrons necessary for radiation therapy can be produced on comparatively low-cost and small-sized neutron generators on the basis of high-voltage accelerators. The NG-12-I neutron generator designed and manufactured in NIIEFA was used in the system of the Ural Center of Neutron Therapy. After updating the generator specially for neutron therapy of malignant tumors, it provides the neutron yield up to $3 \cdot 10^{12}$ n/s [2].

By now, more than two thousand patients with tumors localized in the head and neck regions have received treatment. In opinion of oncologists, radiation therapy in combination with the neutron beam is highly effective. The majority of patients (79%) demonstrated the complete resorption of tumors and in 76% of cases complete remission was observed. The results obtained provide solid grounds to consider promising the introduction of similar facilities into clinics of Russia.

NON-DESTRUCTIVE TESTING

The most important line of activities of NIIEFA in the field of accelerating engineering is designing and construction of systems for non-destructive testing of large-scale products based on linear accelerators with energy ranging from 3 to 15 MeV. NIIEFA has delivered more than thirty similar machines both to industrial enterprises in Russia and abroad. New accelerators, UEL-10-D and UEL-6-D, have been designed and manufactured especially for non-destructive inspection of products of atomic, chemical and shipbuilding industries.

Radiation characteristics of these machines are as follows: energy of accelerated electrons is 10/6 MeV and maximum average dose rate 1m from target on the central axis is 30/10 Gy/min. The asymmetry of the X-ray field is no more than 5%.

The UEL-10-D accelerator, 2040×950×950m^3 in size and 1160 kg in weight, is mounted on a trolley of a bridge crane using a special yoke. This yoke allows the position of the irradiator to be changed relative to an object under inspection: from 180º (rightwards) to 135º (leftwards) in the horizontal plane and from 45º (upwards) up to 95º (downwards) in the vertical plane. The irradiator is made as a support frame of aluminum profile. In contrast to previous models, all the equipment is housed inside the irradiator including the high-voltage power supply system consisting of a high-voltage rectifier and pulse magnetron modulator (Fig. 4).

Different defects, such as voids, cracks and foreign inclusions and their localization can be detected by radiographic, radioscopic and tomographic methods [3].

In the radiography, the X-ray beam passed through an object inspected is recorded on the X-ray film. An advantage of this method is a possibility for inspection of objects with a thickness of up to 600 mm for steel. Quality of the image obtained meets the requirements of the international ASTM E142 standard. Standard film size is 3000×4000 mm. For products of the aforementioned thickness, linear accelerators are the only available tool, which provides a required quality of inspection.

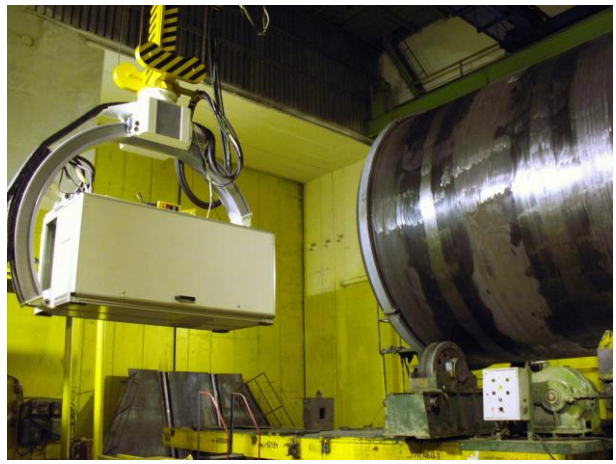

Figure 4: The UEL-10-D accelerator at the Izhorskie Zavody, St. Petersburg.

In radioscopy and tomography, an object under inspection is scanned layer-by-layer by a fan-shaped X-ray beam. A line of scintillation detectors is used instead of the X-ray film. A shadow image of a defect is obtained on the monitor of the operator workstation in the real-time mode.

Compared to the radiographic inspection, the radioscopic method offers higher efficiency and lower operating costs. In the radioscopy, a standard set of the linear accelerator equipment is supplemented with the following (Fig. 5): beam collimation system, detection system, system for positioning an object under inspection, operator workstation with a software.

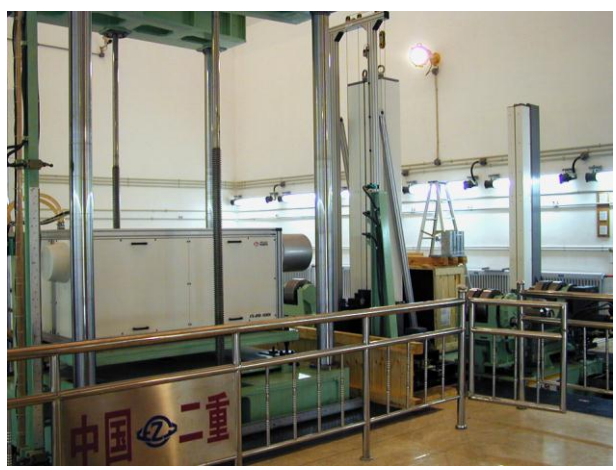

Figure 5: The UEL-15-D accelerator installed in China.

High degree of spatial resolution allows radioscopic systems to be used for inspection of large-scale vehicles and containers without their opening to expose either arms or contraband goods. For this purpose, linear accelerators of the LINAC-2(4) model with an energy in

the range from 2 up to 4 MeV have been designed and manufactured in NIIEFA. The accelerators are made with local radiation shielding. Figure 6 shows a LINAC-4 accelerator functioning as a part of the SMITH HEIMAN system (Germany) intended for customs inspection [4].

Figure 6: The LINAC-4 accelerator in the SMITH HEIMAN system, Germany.

HIGH-VOLTAGE ACCELERATORS FOR RADIATION PROCESSING

High-voltage charged particle accelerators are ranked high in the ine of the accelerating equipment designed and manufactured in NIIEFA. By now, more than one hundred and thirty high-voltage electron and ion accelerators for various purposes have been delivered to Russian customers and abroad. In NIIEFA first high-voltage accelerators were designed on the basis of electrostatic generators. The maximum proton energy attained 10 MeV. About thirty similar machines intended for research in the field of nuclear physics, particles' injection into cyclic accelerators and ion implantation were manufactured. Many of these accelerators have been updated and have been in successful operation till nowadays, for example in the Federal Nuclear Center in Germany, the University of Helsinki and in the Institute of Nuclear Research, Kazakhstan.

Further, radiation processing of different materials and products with an electron beam to modify their molecular structure and impart new properties becomes one of the most promising fields of practical application of high-voltage accelerators with a charged particle energy of up to 1 MeV.

To introduce radiation processing on industrial enterprises, a series of high-voltage accelerators with an electron beam power of up to 50 kW has been designed in NIIEFA. A typical accelerator of this series is the "ELECTRON-10" (Fig. 7), which consists of a high-voltage generator, electron source, accelerating structure and irradiation field forming system. The high-voltage generator is made on the basis of a single-phase transformer - rectifier, Power is supplied from an ac 3-phase mains 380 V, 50 Hz. Two extraction windows oppositely located and covered with metal foil serve to extract an electron beam into the atmosphere. Such a design ensures the double-sided irradiation of a material for one passage. The automatic control system is made on the basis of an industrial computer.

Figure 7: The «Electron-10» accelerator at the plastic materials production plant, Izhevsk.

The main parameters of the accelerator are: the energy in the 500÷750 kV range, maximum current of accelerated electrons – 70 mA, non-uniformity of the current linear density along the scanning length of 1200 mm is not more than 5%. Accelerators of this series are equipped with a compact local radiation shielding and can be installed together with the equipment of rtechnological lines in conventional rooms. The running hours per year are five thousand hours, which meets the requirements for industrial equipment.

More than fifty such accelerators have been delivered. The machines were used for commercial production of roofing, shrink polymer tape for protection of underground gas and oil lines against corrosion, foamed polyethylene and polymer tape with an adhesive layer [5].

A recent advance of NIIEFA in the field of high-voltage accelerators on the basis of three-phase transformer-rectifier is an «ELECTRON 23» with an electron beam power of up to 400 kW and an energy of 1 MeV.

An important field of application of high-voltage accelerators is the activation analysis. The method is used to determine the element composition of a substance by irradiating it with fast or thermal neutron fluxes (14 and 2.5 MeV) with subsequent measurement of the induced gamma activity of irradiated samples.

The most easily available source of neutrons for these purposes is facilities constructed on the basis of high-voltage ion accelerators. 14 MeV neutrons are produced as a result of the D-T reaction under interaction of deuterium ions accelerated up to 150-300 keV with tritium of a metal-tritium target. The D-D reaction produces neutrons with an energy of approximately 2.5 MeV. More than sixty neutron generators producing neutron fluxes with an intensity of up to 10^{13} n/s have been designed and manufactured in NIIEFA.

RF ACCELERATORS FOR RADIATION PROCESSING

Several models of linear accelerators with the electron energy ranging from 3 up to 15 MeV and average beam power up to 15 kW have been designed and manufactured in NIIEFA for high-energy radiation processing. The accelerators are equipped with horn scanning chambers. Thickness of objects under processing depends on the electron energy; the velocity and throughput depend on the beam power. To generate a directed X-ray beam, an accelerator is equipped with a tungsten-nickel target.

More than fifteen accelerators of the UEL-8-8S model with an energy of 8 MeV and beam power of 5 kW are operated in Russia and abroad, in Poland, Hungary, China and France. In addition to electron beam processing of products of irregular configuration, these machines are also used for the element analysis on the basis of photonuclear reactions. Construction of such systems allowed the use of a highly effective method of the activation analysis to be pioneered at a number of mines. The method is used for detecting ore samples for the content of various chemical elements, up to fifty in number, including Au. The time needed for the analysis of one sample for the content of aurum is less than 22 seconds, and the throughput is one million of analysis per year.

The aforementioned systems operate at a mining – and-processing integrated works in Navoi, Uzbekistan, in the analytic service of geological field parties in Batogai town, Yakutia. For the “in-line” processing of products in standard industrial premises, a 3 MeV UELV-3-3S accelerator with a beam power of up to 3 kW equipped with a local radiation shielding has been designed.

Figure 8: The UELR-10-10S accelerator installed in Beijing, China.

The UELR-10-10S accelerator (Fig. 8) has been designed and manufactured in NIIEFA specially for commercial sterilization centers to be used for processing of disposable medical utensils. Typical penetration depth of electrons is up to 40 mm. Characteristics of the accelerator are as follows: electron energy is 8 MeV, nominal average beam power is 10 kW, radiation field size is 800×20 mm^2 at a distance of 200 mm from the extraction window foil and uniformity along the scanning length of 5%. The accelerator can be operated in the long-term mode: three shifts with a one-hour interval between shifts.

CONCLUSION

Technical characteristics of the accelerating equipment designed and manufactured in NIIEFA are on a par with their foreign analogs and in some cases are even superior to their competitors. Taking into account expenditures for transportation, customs duties, intermediary firms, warranty/after-warranty servicing (especially in case of no foreign service centers), delivery of spare parts, etc ., the total cost of the equipment is much lower.

Nowadays, the demand for applied accelerators round the world increases rapidly. Proper activities towards marketing, promotion and patent right protection as well as the organization of serial production of the accelerating equipment being at present in ever-growing demand can ensure the competitiveness of national projects.

REFERENCES

[1] M.F. Vorogushin, A.P. Strokach, O.G. Filatov, “Status and DevelopmeAt of accelerating Equipment in NIIEFA”, VANT series “Electrofizicheskaya Apparatura, #5(31), p. (2010).

[2] G.G. Voronin et al., “Neutron Therapy System based on the NG-12I Neutron Generator”, Proceed. of the XI International Conference on Charged Particle Accelerators Applied in Medicine and Industry”, St. Petersburg, October 2005, p.382 (2005).

[3] B.Yu. Bogdanobich, M.F. Vorogushin et al., “Remote radiation control”, v.2. Radiation Control Systems, Mashinostroenie, p 284 (2012).

[4] M.F. Vorogushin, “Electrophysical Systems based on Charged Particle Accelerators”, Proceedings of the XIX Russian Particle Accelerator Conference, Dubna, October 2004, p. 13 (2004).

[5] V.P. Maznev et al., “Experience on operating high-voltage accelerators designed in NIIEFA on industrial facilities intended for polimer materials modification,” RuPAC-2010, Protvino, Russia, September-October 2010, Proceed., p. 343, http://acceleonf.web.cern.ch/RuPAC-2010

FLNR HEAVY ION CYCLOTRONS FOR INVESTIGATION IN THE FIELD OF CONDENSED MATTER PHYSICS INDUSTRIAL APPLICATIONS

B. N. Gikal, Joint Institute for Nuclear Research, Dubna, Russia

Abstract

Applied research on heavy ion beams are carried out in many scientific centres of the world. Some of the developed technologies are successfully used in industry, for example, a well-known method of track membranes production using heavy ion beams, which as a rule have an energy from 1 to 3.5 MeV/nucleon. At FLNR several specialized accelerators have been created for this purpose.

Since 1983 a complex based on the IC-100 cyclotron for industrial manufacturing of track membranes operates at the JINR Flerov Laboratory of Nuclear Reactions (Dubna, Russia). The modernization in 2003 equipped the cyclotron with a superconducting ECR ion source as well as with an axial injection system. High intensity heavy ion beams of Ne, Ar, Fe, Kr, Xe, I, W have been accelerated to an energy of 1.2 MeV/nucleon.

The DC-60 cyclotron with smooth ion energy variation was designed by FLNR for the research center at L.N. Gumilev Euroasian State University in Astana (Kazakhstan). The cyclotron equipped with an ECR ion source accelerates ions from Carbon to Xenon. The energy of the extracted beams can be varied from 0.35 up to 1.7 MeV/nucleon.

In 2009-2010 a cyclotron complex for a wide spectrum of applied research in the field of nanotechnologies (template technologies, track membranes, surface modification, etc.) was designed at the Flerov Laboratory of Nuclear Reactions. This complex includes a specialized DC-110 cyclotron, which produces high intensity beams of accelerated Ar, Kr, and Xe ions with a fixed energy of 2.5MeV/nucleon. The DC-110 cyclotron is at the commissioning stage now.

The accelerated ion beams of U400 and U400M cyclotrons (FLNR) have been used for several years already by the Russian Space Agency (Roscosmos) for investigation of radiation resistance of electronic devices. For these experiments ions with atomic masses of 4÷209 and an energy of 3÷6 MeV/nucleon are used. Now a specialized channel and a facility for carrying out these investigations on the beams of ions with energies of 25-55 MeV/nucleon is being mounted.

IC-100 CYCLOTRON

In 1985, at the Laboratory of Nuclear Reactions of Joint Institute for Nuclear Research, the IC-100 cyclic implanter of heavy ions was developed [1, 2]. The cyclotron was designated for acceleration of ions from $^{12}C^{2+}$ to $^{40}Ar^{7+}$ with a fixed energy of ~1.2 MeV/nucleon at acceleration at the fourth harmonic of the high voltage system and ~0.6 MeV/nucleon for acceleration at the sixth harmonic. A PIG type internal ion source was used at this accelerator; the mentioned source determined the mass range of accelerated ions. For more efficient application of the complex and for industrial production of track membranes, it was proposed to switch to irradiation of films with heavier ions [2].

In the course of the upgrade performed in 2003–2005, the IC-100 implantation complex was equipped with a system of beam axial injection from an external superconducting ECR ion source (Fig. 1). This provided a possibility of obtaining intense beams of highly charged ions of Xenon, Iodine, Krypton, Argon, and other heavy elements of the Periodic Table [4]. The launching and the adjustment of systems of the IC-100 cyclotron were performed using $^{86}Kr^{15+}$ and $^{132}Xe^{23+}$ beams. The intensity of accelerated and extracted beams is ~2μA. $^{40}Ar^{7+}$ beams with a current of more than 2μA, $^{56}Fe^{10+}$ beams with a current of 0.3μA, $^{127}I^{22+}$ beams with a current of up to 0.25μA, $^{132}Xe^{24+}$ beams with a current of ~0.6μA, $^{182}W^{32+}$ beams with a current of ~0.015μA, and so on were also accelerated.

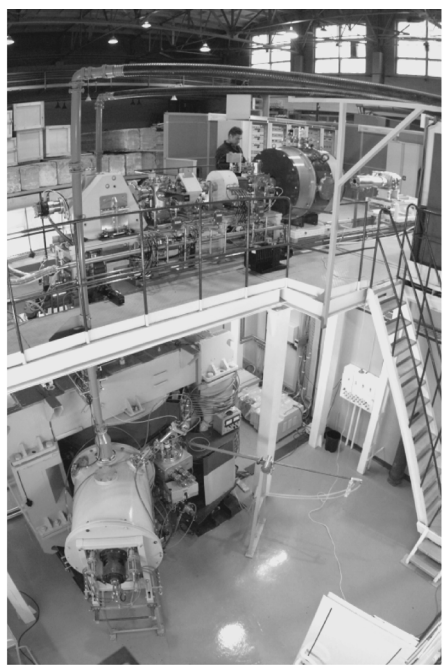

Figure 1: General view of the IC-100 cyclotron.

DC-60 CYCLOTRON

A specialized accelerating facility based on the DC-60 cyclotron was built by the Flerov Laboratory of Nuclear Reactions in collaboration with the Institute of Nuclear Physics (Almaty, Kazakhstan) for the Interdisciplinary Scientific Research Center of the Gumilev Eurasian

National University (Astana, Kazakhstan). The facility, based on the heavy ion cyclotron DC-60, is capable of providing intense heavy ion beams ranging from Lithium to Xenon in the energy range of 0.35–1.7 MeV/nucleon. The facility is supplied with a (10–25)×Z kV (Z – the ion charge) low energy beam channel as well. Heavy ions are produced by the Electron Cyclotron Resonance Ion Source (ECR) (Fig. 2). The whole facility was designed, built, and put into operation over the period of 2004–2006 [3], [4]. Main parameters of the DC-60 cyclotron are shown in Table 1.

Table 1. Main parameters of DC-60

ION BEAM INJECTOR	**ECR ion source + axial injection system**
MAGNET	
Magnet pole diameter	1.62 m
Cyclotron magnetic field	1.45 T - main mode 1.25÷1.65 T - magnetic field variation
Weight of magnet	~ 100 tons
Magnet power	67 kW
Correction coils: - radial coils - azimuth coils Total power	 5 sets 2 sets 1 kW
RF SYSTEM	
- frequency - harmonic number - dee voltage - RF power	11.00 ÷ 17.5 MHz 4 and 6 50 kV 20 kW
Pressure in cyclotron vacuum chamber	$(1\div2)\cdot10^{-7}$ Torr

Main accelerated ion beam parameters

Ions	**Li ÷ Xe**
Mass to charge ratio A/Z	6 ÷ 12
Accelerated ion energy	0.35 ÷ 1.7 MeV/nucleon
Beam intensity	$6\cdot10^{13}$ - $1\cdot10^{12}$ pps
Discrete ion energy change	Due to A/Z ratio
Smooth energy variation with respect to nominal one	-30 % / +20% Due to magnetic field variation

Low energy ion beam parameters

Ions	**He ÷ Xe**
Mass to charge ratio (A/Z)	2 ÷ 20
Ion energy from ECR source	10 ÷ 20 keV/charge
Discrete ion energy change	Due to change of A/Z
Smooth ion energy variation	Due to extracted potential variation in ECR source

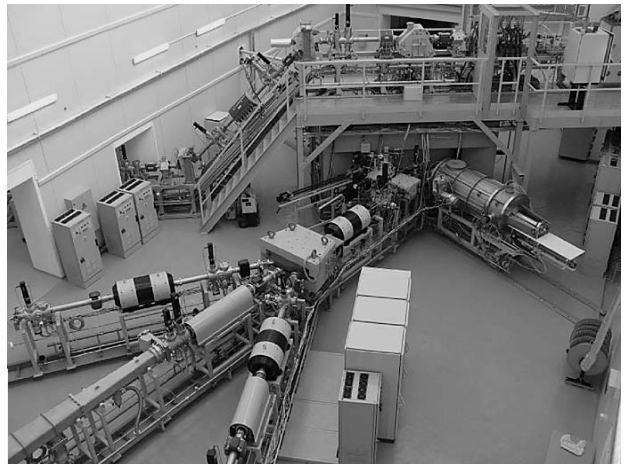

Figure 2: Photo of DC-60 cyclotron facility.

DC-110 CYCLOTRON

The project of the DC-110 cyclotron facility for applied research in nanotechnologies (track pore membranes, surface modification of materials etc) has been designed by the Flerov Laboratory of Nuclear Reactions of the Joint Institute for Nuclear Research (Dubna) [5]. The facility includes an isochronous cyclotron DC-110 for acceleration of intense Ar, Kr, Xe ion beams with a 2.5 MeV/nucleon fixed energy (Table 2). The cyclotron is equipped with a system of axial injection and with an 18 GHz ECR ion source. The cyclotron with a 2m diameter magnet pole creates in the working gap a magnetic field of 1.67 T. The RF system operates at a fixed frequency of 7.75MHz. The extraction system is equipped with an electrostatic deflector.

Ions of $^{40}Ar^{6+}$, $^{86}Kr^{13+}$ and $^{132}Xe^{20+}$ are chosen for acceleration in the cyclotron because they have a mass/charge ratio close to 6.667, 6.615 and 6.6 respectively. It allows realizing an acceleration mode on a practically fixed RF system frequency and with a fixed magnetic field level. Variation of ions energy and change of acceleration mode are not envisaged in this cyclotron. The cyclotron complex is equipped with two channels and two facilities for irradiation of polymeric films. The accelerator provides a possibility of preparing one of the facilities for irradiation while the second facility is being used for film irradiation. It raises considerably the efficiency of equipment. The DC-110 cyclotron is at the commissioning stage now (Figs. 3,4).

Table 2. Basic parameters of DC-110 cyclotron.

Accelerated ions	$^{40}Ar^{6+}$	$^{86}Kr^{13+}$	$^{132}Xe^{20+}$
Mass to charge ratio of accelerated ion, A/Z	6.667	6.615	6.6
Ions energy, MeV/n	2.52	2.52	2.52
Magnetic field, T	1.683	1.67	1.666
RF frequency	7.753	7.753	7.753

Number of Acceleration Harmonic	2	2	2
Planned intensity of the extracted beams	12μA (2 pμA)	13 μA (1 pμA)	10 μA (0.5 pμA)

Figure 3: The DC-110 cyclotron.

Figure.4: The facility for irradiation of polimer films at the DC-110 cyclotron

SINGLE-EVENT EFFECTS (SEE) TESTING AT FLNR CYCLOTRONS

The Russian Space Agency (Roscosmos) carries out investigations of single-event effects (SEE) in electronic devices using ion beams of U400 and U400M cyclotrons of the Flerov Laboratory of Nuclear Reactions [6]. U400 cyclotron delivers beams of ions with atomic masses of 4÷209 at energies of 3÷29 MeV/nucleon [7]. U400M cyclotron [7] was intended for acceleration of ion beams in two modes:

- acceleration mode of high energy ions - 19–3 MeV/nucleon (mass to charge ratio of accelerated ions A/Z = 2.8 – 5),
- acceleration mode of low energy ions - 5–10 MeV/nucleon (mass to charge ratio of accelerated ions A/Z = 7– 10).

Both options are used for testing of electronic devices. A beam channel of low energy ions is now in operation (fig. 5). Ions of O, Ne, Ar, Fe, Kr, Xe, Bi with an energy of 3÷6 MeV/nucleon are available to users. At the end of 2012 the installation of the channel will be finished for testing at high energy ion beams. Beams of ions from C up to Xe with energies from 25 to 53 MeV/nucleon will be available for carrying out experiments.

REFERENCES

[1] B.N.Gikal, S.N.Dmitriev et al., "IC-100 Accelerator Complex for Scientific and Applied Research ". ISSN 1547-4771, Physics of Particles and Nuclei Letters, Vol. 5, No. 1, pp. 33–48. © Pleiades Publishing, Ltd., 2007

[2] B. N. Gikal et al., "Upgrading of IC-100 Cycle Implantator,"Preprint OIYaI R9-2003-121 (Dubna, 2003).

[3] B. Gikal et al., "Project of the DC-60 Cyclotron with Smoothly Ion Energy Variation for Research Center At L. N. Gumilev Euroasia State University in Astana (Kazakhstan)," in Proc. of the XVII Cycl. Conf. andTheir Applications (Tokyo, Japan, 2004,), pp. 205–207.

[4] B.N.Gikal, S.N.Dmitriev et al., "DC-60 Heavy Ion Cyclotron Complex: The First Beams and Project Parameters", ISSN 1547-4771, Physics of Particles and Nuclei Letters, 2008, Vol. 5, No. 7, pp. 642–644. © Pleiades Publishing, Ltd., 2008.

[5] B.N.Gikal, G.G.Gulbekyan, S.N.Dmitriev et al., "The project of the DC-110 heavy ion cyclotron for industrial application and applied research in the nanotechnology field" Physics of Particles and Nuclei Letters, Vol. 7, No. 7(163), pp. 891–896. 2007.

[6] V. A. Skuratov, V.S. Anashin, A.M.Chlenov, V.V. Emeliyanov, B. N. Gikal, G.G. Gulbekyan, I.V. Kalagin, Y.A. Milovanov, Y.G. Teterev, V. I. Kazacha, "Roscosmos Facilities for SEE Testing at U400M FLNR JINR Cyclotron". Proceedings of RADECS 2011 PJ-8, pp.756-759, 2012.

[7] B. Gikal, I.Kalagin, G. Gulbekyan, S. Dmitriev, "Status of the FLNR JINR cyclotrons". Proceedings of PAC09, Vancouver, BC, Canada FR5REP099, pp. 5011-5013.

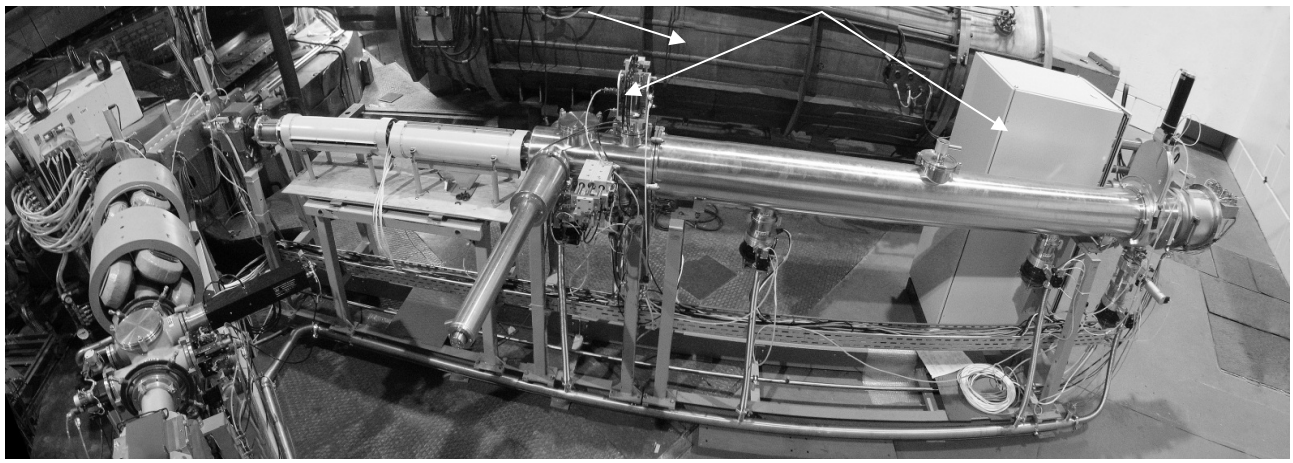

Fig. 5. General view of the ion beam transport line and experimental set up for SEE testing at U400M cyclotron.

IRRADIATION FACILITIES AND COMPLEXES OF INRP RFNC-VNIIEF

V.F.Basmanov, S.V.Vorontsov, V.S.Gordeev, S.A.Gornostaj-Pol'ski, A.V.Grishin, A.V.Grunin, A.A.Devyatkin, N.V.Zavyalov, V.F.Kolesov, G.A.Myskov, S.T.Nazarenko, V.T.Punin, V.A.Savchenko, I.G.Smirnov, A.V.Tel'nov, FSUE RFNC-VNIIEF, Sarov, Russia

Abstract

There are presented in the review the facilities and complexes that were created and are applied in the Institute of Nuclear and Radiation Physics (INRP) RFNC-VNIIEF to simulate under laboratory conditions the effect of NM penetrating radiation on the special-purpose objects. There is given a brief description of the design and characteristics of different-type electron accelerators, pulsed nuclear reactors (PNR) as well as two irradiation complexes PUL'SAR and LIU-10M-GIR2 that are located in the adjacent halls.

INTRODUCTION

Within several decades there was being created in INRP RFNC-VNIIEF a specialized stock of irradiation facilities on the base of electron accelerators, PNR and complexes aimed at carrying out - under laboratory conditions - system researches of radiation resistance of armament and defense technology (A and DT) standard objects against the effect of NM penetrating radiation.

According to state standards there is performed certification of experimental facilities as test equipment – simulating facilities for B and BT testing as to radiation effect of NM, power generating systems and space.

IRRADIATION COMPLEX PUL'SAR

The multi-purpose irradiation complex PUL'SAR [1,2] that has been under operation since 1991, possess widest test potentialities in factor-by-factor and joint loadings for laboratory elaboration and resistance tests of B and BT against NM penetrating radiation.

The leading facility of the complex is a high-power pulsed linear induction accelerator of electrons LIU-30 [3-5]. Into the complex structure there is also included a booster reactor BR-1M [6] aimed at generation of gamma-neutron radiation - both independently and jointly with accelerator LIU-30 [7]. In order to provide more precise simulation of penetrating radiation effect, into the complex there are included: pulsed electron accelerators STRAUS-2 and ARSA and generator of X-radiation pulses ILTI-1. The typical chart of PUL'SAR facilities arrangement is given in Fig.1 while the basic characteristics of the facilities are available in Table 1.

Fig.2 gives the chart of LIU-30 accelerating system of which is evident that it is produced of 36 sequentially connected modules with self-contained supply and independent control of each module. Into accelerator structure there are also incorporated a transportation channel and output device with a target ensuring the required characteristics of electron beam and bremsstrahlung field.

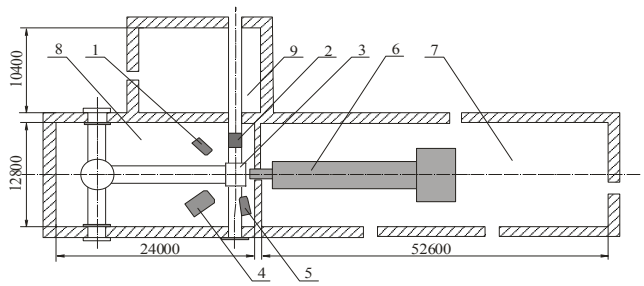

Fig. 1. Chart of PUL'SAR irradiation complex facilities arrangement. 1 – accelerator ILTI-1; 2 – booster-reactor BR-1M; 3 – object under irradiation; 4 – accelerator STRAUS-2; 5 – accelerator ARSA; 6 – accelerator LIU; 7 – accelerator hall; 8 – irradiation hall; 9 – reactor hall.

Table 1. Irradiation complex PUL'SAR

Facility	Radiation characteristics
LIU-30	$P_{bs}^{max} = 1{,}5\cdot10^{13}$ R/s in ∅ 11 cm, $P_{bs}^{1M} = 5\cdot10^{11}$ R/s in ∅ 60 cm, $E_{bound.}$ = 4, 15, 25, 40 MeV, $\tau_{ти}$ = (5-25) ns
BR-1M	$\Phi_n^{max} = 10^{15}$ n/cm^2 in ∅ 10 cm, $\Phi_n^{1M} = 5\cdot10^{12}$ n/cm^2, D_γ^{max} = 160 kR, D_γ^{1m} = 1,1 kR, W_0 = 11 MJ, $\tau \geq 55$ μs
STRAUS-2	$P_{bs}^{max} = 10^{12}$ R/s in ∅ 5 cm, $P_{bs}^{1m} = 10^{9}$ R/s in ∅ 80 cm, $E_{bound.}$ =3 MeV, τ_{bs} = (18-25) ns
ILTI-1	$P_{uhr}^{max} = 3\cdot10^{10}$ R/s in ∅ 5 cm, $P_{uhr}^{1m} = 5\cdot10^{7}$ R/s, $E_{bound.} \leq 700$ keV, τ_{bs} = 40 ns
ARSA	$P_{bs}=3\cdot10^{10R}$P/s in ∅10 mm, $E_{bound.} \leq 1$ MeV, τ=10 ns

where $P_\gamma^{1m}(P_{bs}^{1m})$, $D_\gamma^{1m}(D_{bs}^{1m})$, Φ_n^{1m} – dose rate, dose of gamma-radiation, bremsstrahlung and neutron fluence at a distance of 1m from facility at the area with diameter ∅.

Each module of the accelerator channel contains one block of four inductors on radial lines (RL) with water insulation possessing common accelerating tube 2 (see Fig. 2). Each inductor has two radial lines formed by a central disc electrode and grounded toroidal screen disconnected on the internal diameter. The energy in the radial line is stored at their electric capacitance charging ~ 850 ns from five-cascade pulse voltage generators (PVG) produced using Arkadiev-Marx circuit. Into the accelerator structure there are included 72 PVGs, their total energy store being ~1,5 MJ. At closing the RL gap by controlled switches of trigatron type 3, located uniformly by azimuth, there are formed at the inductors output the pulses of accelerating voltage of alternate polarity. The acceleration of high-current electron beam takes place within the first voltage pulse ~ 0.8 MV/block amplitude and 30 ns duration at

half-height. To switch all radial lines there are used 2432 switches turned on with nanosecond accuracy according to the prescribed time program.

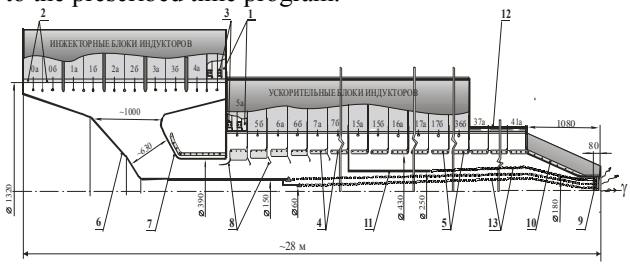

Fig. 2. Configuration of LIU-30 accelerating channel with additional cathode and focusing system, where 1 – radial lines; 2 – accelerating tube; 3 - switches; 4 – drift tubes; 5 – solenoid coils; 6 – basic two-emitter cathode; 7 – anode electrode of injector blocks; 8 - annular protective diaphragm; 9 – multilayered target; 10 – focusing system; 11 – additional (second) cathode; 12 – transportation channel; 13 – high-current electron coaxial beams; 0a, 0b, 1a ... 36b – numbers of injector and accelerating semi-blocks.

The voltage of each two inductors is concentrated in accelerating gaps formed by drift tubes 4. Inside the tubes there are placed solenoids 5 forming a magnetic field with induction ~ 0.5 T on the axis for the sake of stability and accelerating electron beam keeping from radial expansion. A 6-MJ capacitor bank serves as a source of magnetic field energy in the accelerator channel and output device.

The formation of hollow electron beam and its injection to the accelerating system is realized with the aid of a cylindrical foil-free magneto-insulated diode formed by cathode 6 and anode 7 summing up the voltage of four injector blocks of inductors. The beam increases energy when passing through 64 accelerating gaps and drifts to the distance of 4.2 m to target 9 of the output assembly or focusing section 10 (see Fig.2).

The LIU-30 facility uses the operation modes with the boundary energy of electrons equal to 4, 15, 25 and 40 MeV. The decrease of pulse duration is implemented through its front deceleration by intrinsic electromagnetic fields of the beam. At the accelerator output there are produced bremsstrahlung pulses of 4 ns duration at half-height while the bremsstrahlung dose is 1.5 kR at a 1 meter distance from the target and dose rate - $3 \cdot 10^{11}$ R/s.

With the aid of additional cathode 11 there is realized in accelerator LIU-30 the mode of two bremsstrahlung pulses formation per one startup of the facility. Fig.3 gives the configuration of accelerator tube with two cathodes. The diameters of emitting edges of the first cathode are 60 mm and 150 mm, while for the second cathode it is – 250 mm. In this case the dose of bremsstrahlung at a 1 meter distance from the target constitutes 300 R for the first pulse and 2.2 kR for the second one. The interval between the pulses can vary from 0.1 μs to 1.5 μs.

As a result of experimental researches in bremsstrahlung dose rate increase through beam compression at the output from the accelerator there are obtained: maximal dose rate of bremsstrahlung ~ $1.5 \cdot 10^{13}$ rad/s and dose ~ 240 krad (TLD) in a spot of ~ 100 cm^2 area and radiation pulse duration - 16 ns [8].

A pulsed reactor with metal core BR-1M (booster-reactor) is included to complex PUL'SAR [6, 7]. In a hall designed for joint operation with other facilities of complex PUL'SAR the center of BR-1M core can be arranged within the limits of 3 meters from the central axis of the hall (see Fig. 1).

At independent operation reactor BR-1M is placed in a hall with the following dimensions (14×10×8) m^3. The object under testing can be arranged in any point of the hall as well as in a container of the central channel with the dimensions: ∅9.4x30 cm. The original design of the BR-1M core made it possible to achieve record parameters of fission pulse for fast pulsed nuclear reactors with metal core and essentially increase the resource of fuel elements what will give the possibility to use the facility within at least 25 years and realize all promising programs of researches.

Movable accelerators of electrons STRAUS-2 and ILTI-1 are aimed at simulating sequential in time effects of two or three pulses of NM gamma-radiation at their joint operation with accelerator LIU-30. Accelerator STRAUS -2 is created basing on a five-cascade double stepped line with water insulation the external diameter being equal to 1.3 m [9,10].

A small accelerator ARSA is aimed at simulating the effect of pulsed gamma-radiation on semiconductor devices and electronics; it also can operate jointly with other facilities of the complex.

The modes of joint functioning of the complex electrophysical facilities make it possible to form the required fields of loading on separate devices of large objects to study the functioning of protective systems and serviceability recovery of articles B and BT. At microsecond intervals between the radiation pulses of the facilities there can be provided the accuracy of LIU-30 synchronization with STRAUS-2 not worse than 10 ns, while with ILTI-1 ~ 50 ns.

IRRADIATION COMPLEX LIU-10M-GIR2

The irradiation complex LIU-10M-GIR2 was put into operation in 1994. It was created on the base of linear induction accelerator LIU-10M, pulsed nuclear reactor GIR2 and high-current pulsed electron accelerator STRAUS-2 that is also widely used for independent tests both in the mode of bremsstrahlung pulses generation and those with the use of electron beam put to the atmosphere. Into the complex there is also included a small pulsed accelerator of electrons ARSA. The chart of the complex facilities arrangement is presented in Fig.3, while the basic characteristics of the facilities are given in Table 2.

Accelerator LIU-30-10M [12] is produced on the base of the developed in VNIIEF stepped forming lines, the wave processes in which increase several times the output accelerating voltage as compared to the charging voltage of the line. The accelerating system consists of injector,

16 standard accelerating modules incorporating one inductor, electron beam transportation channel 4 meters long and output device with a target assembly. The dimensions of the accelerating system without the transportation channel are as follows (12×3.5×2.4) m^3. The diameter of inductors is 1.1 m, the length – 0.58 m. The number of switches in the forming lines is 341. The maximal energy store in 18 Arkadiev-Marx generators is 184kJ. The acceleration and transportation of the beam is in the longitudinal guiding magnetic field with the induction of 0.5T. The energy store of the magnetic field capacitor bank is 0.65 MJ.

At joint operation of LIU-30 and STRAUS-2 accelerators with different time intervals the accuracy of synchronization constitutes ±10 нс, ±2, ±10 и ±100 μs.

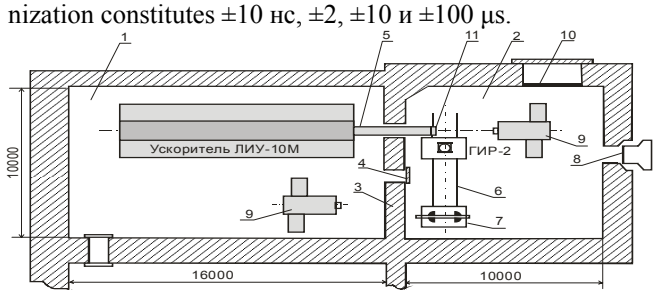

Fig. 3. Chart of LIU-10M-GIR2 complex facilities arrangement. 1,2 – accelerator and irradiation halls; 3 – protective wall; 4 - gate; 5 – beam transportation channel; 6 – reactor rail gage; 7 – core biological shielding; 8 – sliding hatch; 9 – two possible places of STRAUS-2 accelerator arrangement; 10 – gate opening; 11 – output device of LIU-10M.

Table 2. Irradiation complex LIU-10M-GIR2

Facility	Radiation characteristics
LIU-10M	$P_{bs}^{max}= 4\cdot10^{12}$ R/s in ∅8 cm, $P_{bs}^{1m}=4\cdot10^{10}$ R/s in ∅55 cm, $E_{bound.}\leq$ (20÷25) MeV, τ_{bs}=(10÷20) ns
GIR2	$\Phi_n^{max}=10^{14}$n/cm^2 in ∅30cm, $\Phi_n^{1m}=3\cdot10^{12}$n/cm^2, D_γ^{max}=60 kR, D_γ^{1m}=3 kR, W_0=7 MJ, $\tau\geq$300 μs
STRAUS-2	$P_{bs}^{max}=10^{12}$ R/s in ∅5 cm, $P_{bs}^{1m}=10^{9}$ R/s in ∅80 cm, $E_{bound.}$=3 MeV, τ_{bs}=(18-25) ns
ARSA	$P_{bs}=3\cdot10^{10}$ R/s in ∅10 mm, $E_{bound.}\leq$ 1 MeV, τ=10ns

Reactor GIR2 (reactor gamma-source) is a pulsed reactor with metal core and neutron reflector (see Table 1). The irradiation process on GIR2 can be realized only inside the core in the hall with the following dimensions: (10×10×8) m^3. The maximal fluence of neutrons with the energy of >0.1 MeV beyond the "neutron window" is $1.1\cdot10^{14}$ n/cm^2, beyond the reflector – $1.5\cdot10^{13}$ n/cm^2. The dose of accompanying γ-radiation is 40 and 60 kR, correspondingly.

The use of booster mode of the complex operation makes it possible to generate 200-J fission pulses of GIR2, pulse width 1...2 μs and high – up to 10 pulses per session – pulse repetition rate.

ELECTRON ACCELERATORS

The researches in radiation resistance are also performed in INRP on direct-action pulsed electron accelerators RIUS-5 and RIUS-3B [13].

To simulate the effects of gamma-radiation dose in armament and defense technology (A and DT) articles there are applied linear resonance accelerators of electrons LU-50, LU-10-20 and LU-7-2 [14, 15].

The characteristics of accelerator LU-50 are as follows: energy of accelerated electrons - 55 MeV; average current of electrons – 0.24 mA; pulse current – 10 A; average energy of bremsstrahlung quanta ~6 MeV; pulse duration - 10 ns; bremsstrahlung exposure rate up to 3.3 kR/s at a distance of 1 meter from the target at the area ∅ 0.18m the heterogeneity being no worse than 30%. The average beam power is 10 kW.

The characteristics of accelerator LU-10-20 are as follows: regulated energy of accelerated electrons is (5÷9) MeV; average current– 1.3 mA; pulse duration – 3.5 μs; pulse repetition rate - 10÷1000 Hz; power of electron radiation absorbed dose near the output window – up to 5 Mrad/s; bremsstrahlung exposure rate at a 1 meter distance from the target at the area ∅ 0.2 m the heterogeneity being no worse than 30% - up to 500 R/s. The average power of electron beam is 10 kW. The accelerator irradiates the objects with the dimensions up to 700x750x2000 mm.

The characteristics of accelerator LU-7-2 are as follows: energy of electrons is 6.5 MeV; pulse duration – 4.5 μs; average power of electron beam – 2kW, average bremsstrahlung exposure rate – up to 250 R/s at the area of 800cm^2 the heterogeneity being no worse than 30%; pulse repetition rate - 600 Hz.

In order to develop the stock of testing equipment in RFNC-VNIIEF there are carried out the works on the creation of a multi-terra-watt facility GAMMA aimed at producing high-power 2-MeV bremsstrahlung pulses at the area of up to 1m^2. It is assumed that the facility will consist of several 2-MeV modules [16].

As a result of computation and experimental works performed there was created and is now successfully functioning the first module of the facility – high-current pulsed accelerator of electrons – GAMMA-1 [1].

The STRAUS-R pulsed accelerator (overall dimensions 4.7×2.2×2.4 m^3) aimed at roentgenographic researches and operating in the mode of electron beam focusing on the target, refers to a series of accelerators on stepped lines [17]. It is also used to study radiation resistance in the mode of bremsstrahlung pulses generation: boundary energy of electrons – 3.5 MeV, pulse amplitude of beam current - 55 kA, current pulse duration at half-height - 60÷65 ns, bremsstrahlung dose on the output flange - 11 kR, while at a distance of 1 meter from the target - 36 R the diameter of irradiated spot being 9 and 100 cm, correspondingly, at bremsstrahlung pulse duration at half-height – (45÷50) ns [18].

PULSED NUCLEAR REACTORS

Today there are 6 pulsed nuclear reactors in INRP: BIR-2M, BR-1M, BR-K1, BIR-2M, GIR2, BIGR [6,7]. Being different in design, fuel composition and basic parameters these facilities can be divided to three groups.

Into the first group there are included the reactors with metal core BIR-2M, BR-1M, BR-K1 and GIR2 that are characterized by short pulse and comparatively low energy release. The fuel of these reactors represents an alloy of highly enriched uranium with molybdenum; it has high strength properties and provides operability of the core elements under pulsed heating followed by occurrence of considerable mechanical stresses.

To the second group there can be referred reactor VIR-2M which core represents solution of uranium salt in usual water.

The third group includes reactor BIGR with the core of unique high-temperature ceramic fuel in the form of compressed homogeneous mixture of dioxide of highly enriched uranium and graphite

Basic pulse characteristics of the enlisted PNR are presented in Table 3.

Table 3. Characteristics of RFNC-VNIIEF pulsed nuclear reactors

Reactor	BIR-2M	BR-1M	BR-K1	GIR2	VIR-2M	BIGR
Core material	U+6%Mo alloy	U+9%Mo alloy	U+9%Mo alloy	U+9%Mo alloy	UO_2SO_4+ H_2O	UO_2+C ceramic
Fuel mass, kg	121	176	1511	178	7.1(104 l)	833
Core dimensions, cm	∅22x21.7	∅27x27	∅62x75	∅30	∅55x63	∅76x67
Irradiation cavity, mm	∅40	∅100	∅308x360	-	∅142,∅300	∅100
Energy release, MJ	3	11	30	7	60	280
Half-width, μs	55	53	1200	300	2600	2000
Φ, 10^{14}n/cm^2 >0.1MeV in the cavity on the surface of the core	5 0.6	10 3.5	5.1	1	7 1	70 8
Dγ, 10^3 Gy in the cavity on the core surface	1 0.06	2 0.5	0.65	0.6	5 0.5	30 2.4

The reactors are equipped with different experimental devices making it possible to change the relation of neutron and gamma components of ionizing radiation in order to extend the potentialities of methodology of armament and defense technology (A and DT) testing. Below is given a brief description of the specified reactors excluding those considered before – BR-1M and GIR2.

Reactor BIR-2M (fast pulsed reactor, modified) is a typical representative of PNRs with metal core. The core components are produced of alloy of highly enriched (85% by ^{235}U) uranium with molybdenum (6 mass %). Initially the reactor (BIR-1) was put into operation in 1965. In 1970 the reactor was displaced to a special-purpose building, updated and called BIR-2. After its equipping with automated systems SUZ (System of Monitoring and Safety Provision) and IIS (Integrated Information System) on the base of mini-computer, the BIR-2M reactor was put into operation in 1991.

Reactor BIR-2M is a basic facility of the created in VNIIEF branch center of neutron measurements (OBNI). On the reactor there were obtained and certified the reference neutron field OP-2, neutron source OI-R-17 and source of thermal neutrons OI-T-22.

Reactor BR-K1 (booster reactor “Kaskad”, version 1) is a pulsed reactor with metal core. The core material is an alloy of enriched (36% by ^{235}U) uranium with molybdenum (9 mass %). The reactor was put into operation in 1995 and represents a multi-purpose nuclear-physical facility aimed both at testing the elements of the conceptual project of two-section booster reactor “Kaskad” and at realizing different irradiation experiments.

The shape of reactor core represents a hollow cylinder with the following overall dimensions: length - 75 cm, external diameter – 62 cm. The size of the internal cavity is as follows: length - 36 cm, internal diameter– 30.8 cm. By analogy with reactor BR-1M, the core of reactor BR-K1 is of a circular structure: it is divided to discs (blocks) while the discs – to coaxial rings. The core blocks are put to a hermetic casing of stainless steal filled with helium. The distinguishing feature of reactor BR-K1 is a horizontal alignment of the core what ensures convenient loading of samples to the central cavity and considerable size of the cavity for irradiation.

Reactor VIR-2M (water pulsed reactor) is a pulsed reactor with a solution core using salt solution (uranyl sulphate) of highly enriched (90% by ^{235}U) uranium in water as fuel. The volume of fuel solution is 104 l, uranium mass - ~ 7.1 kg. The fuel solution is filled up to a hard cylinder tight case of stainless steel (height - 2 м, Ø0.68 m, the wall thickness 65 mm). In the case bottom there is a hemispherical channel (PSK) its internal radius being 300 mm. The central channel (CC) with the internal diameter 142 mm and six channels for control rods (absorbing rods of lithium hydride) placed uniformly along the circumference 360mm in diameter are welded on the case head (cap).

As a rule, irradiation is realized in two experimental channels – central and PSK - as well as in any point of the bottom hall (10×10×2.5) m^3 in the field of PSK radiation. The irradiated objects can also be placed into auxiliary experimental channels. The levels of reactor radiation in these channels are approximately 10 times lower than in

CC. The operation on static power up to tens of kilowatts is also possible. Reactor VIR-2M is fitted up with a shock table what makes it possible to simulate if necessary the effect of air-shock wave (ASW) with maximal overload 15 arbitrary units ~1s after n-γ-radiation pulse.

Reactor BIGR (fast pulsed graphite reactor) put into operation in 1977 is a pulsed reactor with hard neutron spectrum most powerful in the world. It has got a shape of a hollow cylinder with the following dimensions by fuel: height - 67 cm, external diameter - 76 cm, internal diameter - 18 cm. The reactor core consists of elements which shape is similar to fuel rings of reactor BR-1M. The core is divided into 3 blocks: immobile block, block of coarse adjustment. A steel tube is used as a pulsed block. The core is put into a hermetic casing filled with helium.

Irradiation is possible in the central channel of the container (diameter – 10 cm, height – 550 cm) and outside the core in a hall with the following dimensions: $(11.5\times10\times8)m^3$. Due to a high level of residual gamma-radiation the admittance to the hall is forbidden, thus, the irradiated objects are delivered to the core (from the opposite sides) remotely on the special trucks.

SUZ (System of Monitoring and Safety Provision) of the facility provides a means for generation in the automated mode of pulses on delayed neutrons of different shape including rectangular ones. This mode serves to simulate effects of NM radioactive products. The power in this case can vary from 0.5 до 500 MW, while duration - from 0.5 to 100 s.

The reactor is equipped with a pneumatic test–shock table UIS-5 what makes it possible to simulate the air shock wave as well as complex effect of ionizing radiation and air shock wave. The accelerated mass is up to 300 kg, overloads – up to 1500g, time of load ≥5 ms.

CONCLUSION

Today INRP RFNC-VNIIEF possesses a unique stock of electron accelerators and pulsed nuclear reactors as well as two special irradiation complexes to simulate under laboratory conditions the effects of NM penetrating radiation, power generating systems and space on the special-purpose objects. This ensures carrying out under laboratory conditions of system researches of В и ВТ standard objects radiation resistance against the effect of NM penetrating radiation. The works on keeping test and mastering new levels of effect are being constantly performed on the facilities. There are also carried out the works on creation of multi-terra-watt irradiation facility GAMMA.

REFERENCES

[1] N.V.Zavyalov, V.S.Gordeev, V.A.Savchenko et al. Simulating and irradiation complexes and facilitiesof RFNC-VNIIEF. p.165 //65 anniversary of VNIIEF. Part 1. Sarov: FSUE «RFNC-VNIIEF», 2011-335 p.

[2] V.T.Punin, V.A.Savchenko, N.V.Zavyalov et al. High-power linear induction accelerators of electrons and irradiation complexes on their base for radiation researches // Proc. RFNC-VNIIEF Sarov. No 1. 2001. P. 356-363.

[3] A.I. Pavlovskii, V.S. Bossamykin, V.A.Savchenko et al. Linear accelerator with radial lines - LIA-30// 9th Intern. Conf. on High Power Particle Beams, BEAMS-92, USA, Program Abstracts 1992. P. 205.

[4] A.I.Pavlovskii, V.S.Bossamykin, A..I.Gerasimov et al. High-power linear pulsed electron beam accelerator on radial lines LIU-30 // Instruments and experimental technique (PTYe). 1998. № 2. P.13-25.

[5] V.S.Bossamykin, A.I.Gerasimov, V.S.Gordeev. Iron-free linear induction accelerators of electrons as high-power generators of bremsstrahlung short pulses // Collected papers. RFNC-VNIIEF Sarov. 1997. P. 107-133.

[6] Yu.B.Khariton, A.M.Voinov, V.F.Kolesov et al. VNIIEF pulsed reactors (review)// VANT. Ser.: Physics of nuclear reactors. -1996. No 2. p. 3-12.

[7] V.F.Kolesov. Aperiodic pulsed reactors. V.1, 2. Sarov: RFNC – VNIIEF, 2007.

[8] V.T. Punin, N.V. Zavyalov, V.F. Basmanov et al. Generation of bremsstrahlung fields of higher than 10^{13} rad/s intensity in the mode of LIA-30 electron beam focusing// 15-th Intern. Conf. on High-Power Particle Beams, BEAMS-2004, Saint-Peterburg, RF. 2004. Abstracts. P. 53.

[9] V.S. Bossamykin, V.S. Gordeev, A.I. Pavlovskii et al. STRAUS-2 electron pulsed accelerator// Proc. 9-th IEEE Pulse Power Conf. Albuquerque, USA. 1993. P. 910-912.

[10] V.S.Gordeev, G.A.Myskov, V.O.Filippov, V.Ya.Averchenkov. Investigation of characteristics of pulsed electron accelerator STRAUS-2 // Proc. of RFNC-VNIIEF. No1. 2001. P. 402-407.

[11] S.L.Ehlyash, A.I.Aleksandrin, Ye.N.Donskoj et al. Accelerator ARSA as a small source of nanosecond pulses of electron and X-ray radiation // Physics and technology of pulsed sources of ionizing radiation for investigation of high-speed processes. Collected papers of scientists of nuclear centers in Russia № 5. Sarov. 1996. P. 229 - 237.

[12] V.S.Gordeev, G.A.Myskov, V.O.Filippov, I.V.Viktorov. Results of LIU-10M accelerator investigations // Proc. of RFNC-VNIIEF. Sarov. No. 5. 2003. P. 176-181.

[13] V.A.Tsukerman, N.I.Zavada, K.F.Zelenskii et al. Direct-action accelerators developed in VNIIEF within 1963-1992.// Physics and technology of pulsed sources of ionizing radiation for investigation of high-speed processes. Collected papers of scientists of nuclear centers in Russia № 5. Sarov. 996. P. 97.

[14] N.V.Zavyalov, Yu.A.Khokhlov, V.I.In'kov et al. Commercial linear accelerator of electrons LU-10-20//VANT. Ser.: Nuclear Physics researches. No 2, 3(29, 30). Khar'kov. 1997. P. 39-41.

[15] I.V.Shorikov, N.V.Zavyalov, Yu.A.Khokhlov et al. A small linear accelerator of electrons for gammagraphy of large-size objects // Proc. of RFNC-VNIIEF. Sarov. No 3. 2002. P. 142.

[16] V.S. Gordeev, G. A. Myskov, Ye.S.Mikhajlov, D.V.Laptev. Design of a highPower pulsed accelerator of electrons // Proc. of RFNC-VNIIEF. Sarov. No 3. 2002. P. 176-183.

[17] V.S. Gordeev, G. A. Myskov, Ye.S.Mikhajlov, D.V.Laptev. Design of accelerator STRAUS-R// Proc. of RFNC-VNIIEF. Sarov. No 4. 2003. P. 178-183.

[18] V.S. Gordeev, G. A. Myskov, V.F. Basmanov et al. Pulsed Electron Accelerator STRAUS-R// 15-th Intern. Conf. on HighPower Particle Beams, BEAMS-2004, SaintPeterburg, RF. 2004. Abstracts. P. 108.

TECHNIQUE AND INSTRUMENTATION FOR BUNCH SHAPE MEASUREMENTS

A.V. Feschenko, Institute For Nuclear Research, Moscow 117312, Russia

Abstract

Bunch shape is one of the most important, interesting but difficult to observe characteristics of a beam in ion linear accelerators. Different possibilities of bunch shape measurements are considered but the emphasis is put on the Bunch Shape Monitors (BSM) developed in INR RAS. The operation of BSM is based on coherent transformation of a longitudinal structure of a beam under study into a transverse distribution of a secondary electron beam through rf scanning. BSM characteristics found both by simulations and experimentally are presented. Modifications of BSM are described. Some experimental results of bunch observations are demonstrated.

INTRODUCTION

A longitudinal distribution of intensity in bunches $I(\varphi)$ or $I(z)$ as well as more complicated functions additionally dependent on transverse coordinates and time are meant by a bunch shape. The main requirement for bunch shape measurements is phase resolution. In ion linacs for typical bunch phase durations ranging from several degrees to several tens of degrees the resolution of 1° looks adequate. The corresponding temporal resolution, for example for 400 MHz, equals to 7 picoseconds. Small dimensions along the beam line, small beam distortion, wide range of measurements in beam intensity and sufficient one in phase, small power consumption and sufficient lifetime are of importance as well.

In ion beams, as opposite to electron ones, an attempt to extract information on bunch shape through beam electromagnetic field results in aggravation of phase resolution due to large longitudinal extent of the particle field to say nothing of the frequency response range of a beam monitor. The problem can be overcome if one localizes a longitudinal space passing through which the bunch transmits information on its shape. This approach can be implemented if a longitudinally small target is inserted into the beam and some kind of radiation due to interaction of the beam with this target is detected.

Different kinds of radiation are used or proposed to be used: Cherenkov radiation [1], detached electrons in case of H-, including photo-detachment by a laser beam [2-4], high energy electrons (δ-electrons) [5], X-rays [6]. Electrons obtained due to residual gas ionization are also used [7,8], the space of their generation being localized by electron collimation and separation in energy.

However low energy secondary electrons are used most extensively. The distinctive feature of these electrons is a weak dependence of their properties both on the type of primary particles and on their energy. Due to this features the detectors can be used for almost any ion beam. Among the characteristics of low energy secondary emission, influencing the parameters of the bunch shape monitor, one can mark out initial energy and angular distributions as well as time dispersion or delay of the emission. Time dispersion establishes a fundamental limitation on the resolution of the detector. The value of time dispersion for metals is estimated theoretically to be about $10^{-15} \div 10^{-14}$ s [9], which is negligible from the point of view of bunch shape measurements. The experimental results of time dispersion measurements give not exact value but its upper limit. It was shown that the upper limit does not exceed $(4\pm2)\cdot10^{-12}$ s [10].

Operation of bunch shape monitors with low energy secondary electrons is based on coherent transformation of a time structure of the analyzed beam into a spatial distribution of secondary electrons through rf modulation. The first real detector is described in [11]. In this detector the electrons emitted from the thin strip target are accelerated by electrostatic field and simultaneously modulated in energy by rf electric field. Further energy analysis in a magnetic field enables to spatially separate the electrons with different energies, each point of the spatial distribution corresponding to a particular point of the longitudinal distribution of the analyzed beam. The detector described in [12] uses the same principle except for the feature that the processes of electrostatic acceleration and rf modulation are separated in space. Both the above detectors use rf modulation in energy or in other words a longitudinal modulation. Another possibility is using a transverse scanning. The electrons are modulated in transverse direction and deflected depending on their phase. Spatial separation is obtained after a drift space. In the first proposal of the bunch shape detector with transverse modulation of low energy secondary electrons, made in the early sixties [13], a circular scan with the help of two rf deflectors is foreseen. The circular scan provides a band of measurements equal to a full period of the rf deflecting field. However the bunches in linear accelerators are normally much shorter than the period and instead of a circular scan one can use a linear one thus twice loosing the phase range of measurements but essentially simplifying the detector.

BSM WITH TRANSVERSE SCANNING

Principle of Operation

The BSM operation principle has been described in detail earlier [14÷16]. Briefly it can be repeated with the reference to fig. 1. The series of bunches of the beam under study crosses the wire target 1 which is at a high negative potential ($U_{t\,\mathrm{arg}}$ about -10 kV). The target represents a tungsten wire of 0.1 mm diameter. Interaction of the beam with the target results in emission of low energy secondary electrons. The electrons are

accelerated by electrostatic field and move almost radially away from the target. A fraction of the electrons passes through input collimator 2 and enters rf deflector 3 operating at a frequency equal to or multiple of the linac accelerating field frequency. Deflection of the electrons at the exit of the rf deflector depends on their phase with respect to deflecting field. Downstream of the drift distance the electrons are spatially separated and their coordinates are dependent on phase of the deflecting field. Temporal structure of the analyzed ion beam is initially transformed into that of secondary electrons and then into spatial distribution of the electrons. The intensity of the electrons at a fixed coordinate is proportional to the intensity of the primary beam at a fixed point along the bunch. These electrons are separated by output collimator 4 and their intensity is measured with electron detector 5. Adjusting the deflecting field phase with respect to accelerator rf reference, one can obtain a longitudinal distribution of charge in the bunches of the analyzed beam.

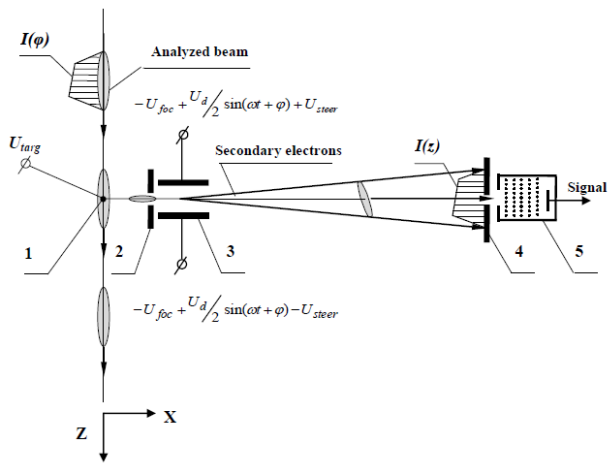

Figure 1: Principle of operation of Bunch Shape Monitor (1 - target, 2 - input collimator, 3 - rf deflector combined with electrostatic lens, 4 - output collimator, 5 – electron collector).

Main Parameters

The most important characteristic of BSM is its phase resolution. We define phase resolution by a simple relation $\Delta\varphi = \Delta Z / nZ_{\max}$, where $Z_{\max}$ is the amplitude of electron displacement at collimator 4 plane, n is a harmonic number of the deflecting field with respect to the fundamental bunch array frequency and ΔZ is a full width at a half maximum of the electron beam at the collimator 4 for zero phase duration bunches of the analyzed beam. To decrease ΔZ and hence to improve the resolution the electron beam must be focused. In the first BSM [14] a separate electrostatic lens located between the input collimator and the rf deflector was used. Later rf deflector was combined with electrostatic lens [17] by additionally applying focusing potential U_{foc} to the deflector electrodes (fig.1). This solution enabled to bring the deflector nearer to the input collimator thus decreasing temporal structure distortions and to improve deflector stability by reliably suppressing multipactoring. To steer the electron beam additional potential difference U_{steer} is also applied between the deflector electrodes. Evidently the size of the collimator should not exceed ΔZ. Otherwise the size of the collimator is to be used in the above formula instead of electron beam size ΔZ.

The value of maximum displacement $Z_{\max}$ can be both calculated and found experimentally [15]. As for the ΔZ value, its finding is not a trivial task. To find the value of ΔZ for the purpose of phase resolution evaluation both theoretical and experimental data are used. Initially focusing properties of the detector can be found experimentally using thermal electrons. Heating the wire target made of tungsten, it is possible to visually observe the thermal electron beam on the phosphor covering the front surface of the plates of collimator 4 through the viewing port. The size of the focused beam of secondary electrons can be measured by adjusting the steering voltage U_{steer} for the turned off rf deflecting field. After that computer simulations can be done to find the value of ΔZ for real parameters of the low energy secondary electrons taking into account a real spatial distribution of the deflecting field. Sometimes instead of full width at a half maximum a double rms size is used.

The simulations are done with the following assumptions. Bunches of the primary beam are considered to have a δ-function type longitudinal distribution. The target is an ideal cylinder with no surface roughness. Deceleration of primary electrons in target material is not taken into account. Initial energy of secondary electrons is distributed within the range of 0÷30 eV according to a typical for secondary emission distribution function [9]. Initial angles with respect to the emitting surface are randomly distributed within the hemisphere. The delay of emission is randomly distributed within the range of $(0\div6)\cdot10^{-12}$ s.

To simulate electron motion from target 1 to input collimator 2 three models have been examined: coaxial line model, wire and plane model and a model with a real 3D geometry. Due to concentration of the electric field in the vicinity of the target the influence of the outer boundaries in not essential and all the three models give approximately the same results. The fields in the deflector are calculated in a quasi-static approximation.

The example of typical behaviour of phase resolution versus deflecting voltage for different input collimator sizes is presented in fig. 2. The calculations are done for the frequency of 352.2 MHz. Because of displacement of the trajectories of those electrons, which pass through the output collimator, off the deflector axis due to rf deflecting field the electrons are defocused and the value of ΔZ increases with increasing of the deflecting voltage. As a result the resolution changes rather slowly within a wide range of the deflecting voltages. The effect depends on electron beam size in the deflector which depends on the input collimator size.

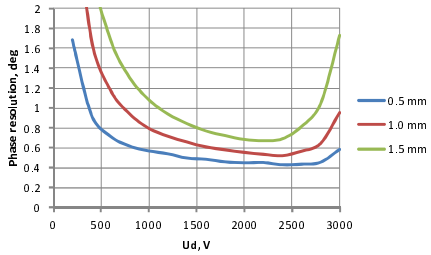

Figure 2: Dependence of phase resolution on deflecting voltage for different input collimators.

Another important characteristic is an ability of measuring small intensities. This feature is especially important for longitudinal halo measurements. Using a secondary electron multiplier as an electron beam detector 5 (fig.1) enables the measurements to be done within 5 orders of intensity magnitude.

The limitation of BSM use for high intensities is due to two reasons. The first one is target heating. In case of tungsten target before its destruction the overheating is manifested as arising of thermal electron current. A bunch substrate increasing within the beam pulse is observed when bunch behaviour within the beam pulse is measured [16].

The second limitation is effect of space charge of the analysed beam.

Influence of Analyzed Beam Space Charge

Influence of electromagnetic field of the analyzed beam on bunch shape measurement accuracy has been estimated and analyzed elsewhere by several authors including the author of this report [18-23].

The influence of the electromagnetic field of the analyzed beam results in two effects: deterioration of phase resolution and appearance of a specific error which we call phase reading error. Deterioration of phase resolution results in a loss of a fine longitudinal structure and phase reading error distorts the shape of the measured function. Both effects depend on many parameters and vary along the bunch. As opposite to the phase resolution which is influenced by many factors the phase reading error is due only to electromagnetic field of the analyzed beam.

We use two models for the analysis of bunch field influence for two utmost cases. The first model is suitable for relatively long bunches. Boundary conditions are supposed to be kept constant while the bunch passes the BSM chamber. The fields are found by multiple solving of Poisson equation in the beam frame for fixed bunch positions as the bunch passes the chamber. Electrostatic fields found in the beam frame produce both electric and magnetic components in the lab frame. The field effecting secondary electrons is represented as a superposition of electromagnetic field of the bunch and an unperturbed electrostatic field due to target HV potential. In case of short bunches the charge distribution providing invariability of target potential has no time to be formed. Electrostatic fields of the bunch in the beam frame are found by Poison equation multiple solving for boundary conditions with the target absence. The field effecting secondary electrons is found similarly to the first model as a superposition of electromagnetic field of the bunch and an unperturbed electrostatic field due to HV potential applied to the target. The considerations on applicability of the models are given in [22].

Figures 3 and 4 demonstrate a behavior of phase resolution and phase reading error along the bunch of H^- beam for the two models. In both cases the target position is at the beam center.

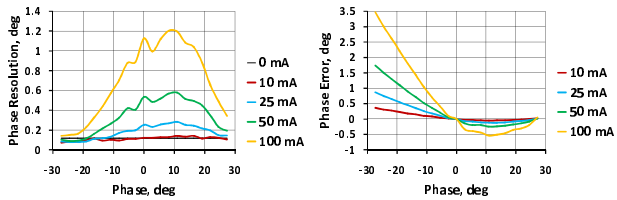

Figure 3: Resolution and phase reading error for the following beam parameters: W=3 MeV, σ_x=2.6 mm, σ_y=2.6 mm σ_φ=13° (Model 1).

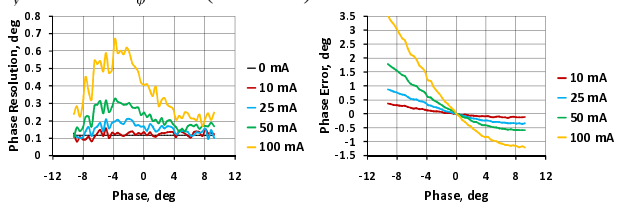

Figure 4: Resolution and phase reading error for the following beam parameters: W=200 MeV, σ_x=1.2 mm, σ_y=1.2 mm σ_φ=2.1° (Model 2).

Experimental data available [22] demonstrate applicability of BSM for the measurements at high peak currents, but do not reveal the measurement errors and are not straightforward ones. The only directs experiment confirming negligibility of the errors was done with the 20 mA beam [15]. The measurements were done for the full beam and for the beam collimated at the BSM entrance. No difference in the measured distributions was observed.

MODIFICATIONS OF BUNCH SHAPE MONITOR

Additionally to the basic detector above described there are three BSM modifications: BSM for H^- beams, Bunch Length and Velocity Detector (BLVD) and Three Dimensional Bunch Shape Monitor (3D-BSM).

BSM for H- minus Beams

In case of H^- beam a fraction of the detached electrons after interaction with the BSM target gets into the secondary electron channel of BSM and the detected signal represents a superposition of signals due to low energy secondary electrons and the detached electrons [24]. The effect has been analyzed in [25]. The energy of the detached electrons differs from that of low energy secondary electrons so the two groups of the electrons can be effectively separated. BSM for H^- beam includes

additional element – bending magnet located between the output collimator and the electron detector.

Bunch Length and Velocity Detector

BLVD is a BSM, which can be mechanically translated along the beam line [26-29]. In this detector a time of flight method of energy measurements is implemented. The translation results in a shift in phase of the observed distribution. Measuring the value of the translation and the value of the shift one can find an average velocity of the beam. The accuracy of bunch shape measurements for this detector is the same as for normal BSM. Special procedure of velocity measurement enables to decrease systematic error to ±0.1%. Total error of velocity measurements is typically within ±(0.3÷0.4)%.

Three Dimensional Bunch Shape Monitor

3D-BSM is aimed to measure a three dimensional distribution of charge in bunches [30,31]. Due to high strength and concentration of electric field near the wire target the electrons move almost perpendicular to its axis with very small displacement along the wire in the area between the target and the input collimator. Additional slit perpendicular to the target installed outside the beam enables to separate the secondary electrons emitted from a fixed coordinate along the wire. For fixed position of the wire and fixe position of the additional slit the intensity of the electrons passed through the slit is proportional to beam intensity at the fixed transverse coordinate. The phase distribution of the separated electrons is measured in the same manner as in basic BSM. Moving the target and the slit and each time measuring longitudinal distribution one can obtain a three dimensional distribution of charge in bunches.

INR ACTIVITY IN DEVELOPMENT AND FABRICATION OF BUNCH SHAPE MONITORS

The first BSM with transverse scanning of low energy secondary electrons has been developed and built in INR in the eighties and the first measurements has been done in 1988 during commissioning of INR linac. Since that time BSMs of various modifications have been developed and built for several accelerators including SSC Linac (four BSMs), CERN Linac-3 (one BLVD), CERN Linac-2 (two BSMs, one 3D-BSM), DESY Linac-3 (two BSMs, one BLVD), JHP-RFQ (one BLVD), SNS Linac (eight BSMs), CERN Linac-4 (one BSM), J-PARC Linac (three BSMs).

It should be noted that the detectors of this type have also been developed in other laboratories [32-34].

MAIN BSM SYSTEMS

The main BSM systems are rf system, HV system, electron detection system and control system.

RF System

The system includes rf deflector, rf amplifier and phase shifter. Depending on bunch lengths and BSM design features both fundamental bunch array frequency and higher harmonics are used. There is a variety of deflector types used in BSMs. For the deflector combined with the electrostatic lens the most suitable are the cavities based on coaxial or parallel wire lines. HV potentials are applied to the deflector electrodes at zero points of rf electric field. Typical value of rf power required for deflector excitation is near 10 W. Phase of the deflecting field is normally adjusted from pulse to pulse and the most suitable are voltage controlled electronic phase shifters.

HV System

The system is intended to supply HV potentials to the target and electrostatic lens as well as to secondary electron multiplier. Typical value of target potential is −10 kV. To provide BSM tuning with thermal electrons a filament source is foreseen at HV target potential. To provide steering of the electrons an adjustable voltage difference of several hundred volts must be superimposed on focusing potential.

Electron Detection System

Secondary electron multipliers are most widely used. In this single channel system only one phase point is detected for a fixed phase setting hence multiple beam pulses are required for bunch shape measurement. The detection system of 3D-BSM [31] uses 30-channel electron collector thus enabling the measurement of the whole longitudinal distribution to be done per single beam pulse. This possibility also exists in BSM described in [33, 34] where the electrons are detected with micro channel plate, phosphor screen and CCD camera.

Control System

In principle any type of control system can be used. However the most recent our developments are based on LabView platform with the use of National Instruments control modules.

DEMONSTRATION OF MEASUREMENT RESULTS

Here just for demonstration we confine ourselves with basic BSM or its modification for H^- beam with a single channel for electron signal detection. Normally different phase points are measured for different beam pulses and the signal is digitized within the beam pulse. It is implied that bunches are reproducible from pulse to pulse though can vary within the beam pulses. Bunch shape measurements can be used for restoration of longitudinal emittance, setting of accelerating field parameters, longitudinal beam matching etc. However the data directly obtained from BSM represent no more than a two dimensional function of phase and time. If the measurements are done with increased gains of secondary

electron multiplier a longitudinal halo and bunch tails can be observed after stitching together the pieces of the measured functions. The examples of such a data reported in [35] are shown in fig. 5, 6.

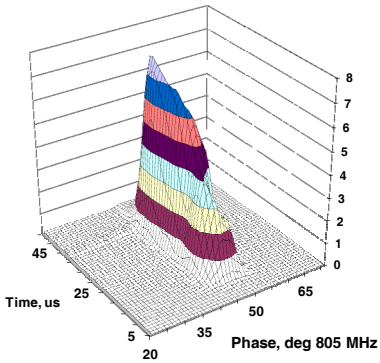

Figure 5: Typical BSM experimental data.

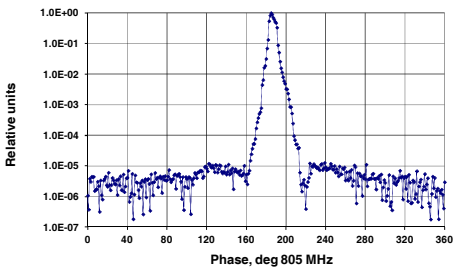

Figure 6: Longitudinal profile combined from several measurements with gains ranging within 3500.

ACKNOWLEDGMENT

Bunch Shape Monitors are being developed in INR since eighties. Many people contributed in this work for such a long period and it s not an easy task to list all of them. Nevertheless the author would like to express acknowledgment to those who made enormous contribution during the resent years: Victor Gaidash, Yuri Gotovtsev, Yuri Kisselev and Alexander Mirzojan.

REFERENCES

[1] Johnson, Kenneth W. USA Patent, 250-639, No.3873839.
[2] A.S.Artiomov at al. IEEE Part. Acc. Conf., May 6-9, 1991, San Francisco, p.1573.
[3] S. Assadi, Proc. EPAC 2006, Edinburgh, Scotland, UK, pp.3161-3163.
[4] Y. Liu et al. Proc. PAC2011, New York, USA, pp.1433-1437.
[5] A.M.Tron. Collection “Accelerators” No.15.,Atomizdat, Moscow, 1976, pp.77-80 (in Russian).
[6] P. N. Ostroumov et al. Proc. PAC2009, Vancouver, BC, Canada, pp.751-753.
[7] P. Forck et al. Proc. EPAC 2004, Lucerne, Switzerland, pp.2541-2543.
[8] P. Forck, C. Dorn. Proc. DIPAC 2005, Lyon, France, pp.48-50.
[9] Bronstein, I.M., Fraiman, B.S. Secondary Electron Emission, Moscow, Nauka, 1969 (in Russian).
[10] Ernst E.W., H.Von Foerster. JAP, 1955, v.26, No.6, pp.781-782.
[11] Witkover, R.L. NIM, 1976. V.137, No.2, pp.203-211.
[12] A.M.Tron, A.V.Feschenko. Proc. of the 8th All Union Meeting on Particle Accelerators, v.2, Dubna, 1981, pp. 125-129 (in Russian).
[13] I.A.Prudnikov et al. USSR invention license, H05h7/00, No.174281 (in Russian).
[14] A.V.Feschenko, P.N.Ostroumov. Proc. of the 1986 Linear Acc. Conf., Stanford, 1986, pp.323-327.
[15] A.V.Feschenko, P.N.Ostroumov. Proc. of the Workshop on Advanced Beam Instrumentation, KEK, Tsukuba, Japan, April 22-24, 1991, p.236-245.
[16] A.V.Feschenko. Proc. PAC2001, Chicago, USA, pp.517-521.
[17] A.V.Feschenko et al.. Proc. of the EPAC-3,Berlin, Germany, 1992, v. 2, pp. 1073-1075.
18] V.Vorontsov, A. Tron. Proc of the 10th All-Union Workshop on Part. Acc. Dubna 1986, V.1, pp.452-455 (in Russian).
[19] A.Tron, I.Merinov. Proc. of the 1997 PAC, Vancouver, 1997, V.2, pp.2247-2049.
[20] E.McCrory et al Proc. of the XVIII Int. Linear Acc. Conf., Geneva, 1996, pp.332-334.
[21] A.V.Feschenko, V.A.Moiseev. Proc. of XX Int. Linac. Conf., Monterey, Ca, 2000, pp.178-180.
[22] V.A.Moissev, A.V.Feschenko. Proc. of XVII the Workshop on Particle Accelerators, Protvino, Russia, 2000, pp.271-274 (in Russian).
[23] A.V. Feschenko, V.A. Moiseev. Proc. IPAC’10, Kyoto, Japan, pp.1065-1067.
[24] A. Mirzojan et al. Voprosy Atomnoi Nauki i Tekhniki. V. 4,5 (31,32), Kharkov, 1997, pp. 92-95 (in Russian).
[25] A.Denisov, A.Feschenko, A.Aleksandrov. Proc. of PUPAC2008, Zvenigorod, Russia, pp.298-300.
[26] Ostroumov, P.N. INR Preprint-812/92, May 1993 (in Russian).
[27] Yu.V.Bylinsky et al. Proc. of the EPAC-94, London, 1994, v. 1. pp.1702-1704.
[28] A.V.Feschenko et al. Proc of PAC1997, Vancouver, Canada, 1997, pp.2078-2080
[29] A.V.Feschenko et al. Proc. of the XIX Int. Linear Acc. Conf., Chicago, IL, 1998. pp.905-907.
[30] S.K.Esin, A.V.Feschenko. Proc. of XIV Workshop on Particle Accelerators, Protvino, Russia, 1994, v. 2, pp.17-20 (in Russian).
[31] S.K.Esin, et al. Proc. of the XVIII Int. Linear Acc. Conf., 1996, Geneva. pp.193-195.
[32] A.Feschenko, E.McCrory, C.Schmidt. Proc. of the 1992 Linear Acc. Conf., Ottawa, Ontario, Canada, v. 2. pp. 662-664.
[33] N. Y. Vinogradov et al. Proc. of LINAC2002, Gyeongju, Korea, 2002, pp. 61-63.
[34] N.E Vinogradov et al. Nucl. Instrum. Meth A 526, p. 206 (2004).
[35] Alexander V. Aleksandrov et al. Proc. of PAC07, Albuquerque, New Mexico, USA 2007, pp.2608-2610.

BEAM DIAGNOSTIC INSTRUMENTATION FOR THE NSLS-II BOOSTER *

O.I. Meshkov, BINP, Novosibirsk, Russia; NSU, Novosibirsk, Russia
V.V. Smaluk, BINP, Novosibirsk, Russia

Abstract

For a successful commissioning and for effective operation of the NSLS-II Booster a number of beam parameters should be measured in real-time mode. The main parameters and features of the diagnostics of the NSLS-II booster are briefly described. The diagnostics will be applied as well as during booster commissioning as well as during routine operations.

List of diagnostics

Six fluorescent screens (beam flags) are used for Booster commissioning and troubleshooting. The beam closed orbit is measured using electrostatic BPMs with turn-by-turn capability. The circulating current and beam lifetime are measured with DCCT. The fill pattern is monitored with FCT. The betatron tunes are measured with a set of two pairs of striplines, the first pair is for excitation and the second one – for beam response measurement. Visible synchrotron radiation is used for observation of the beam image during ramp and for emittance measurement. (Fig.1)

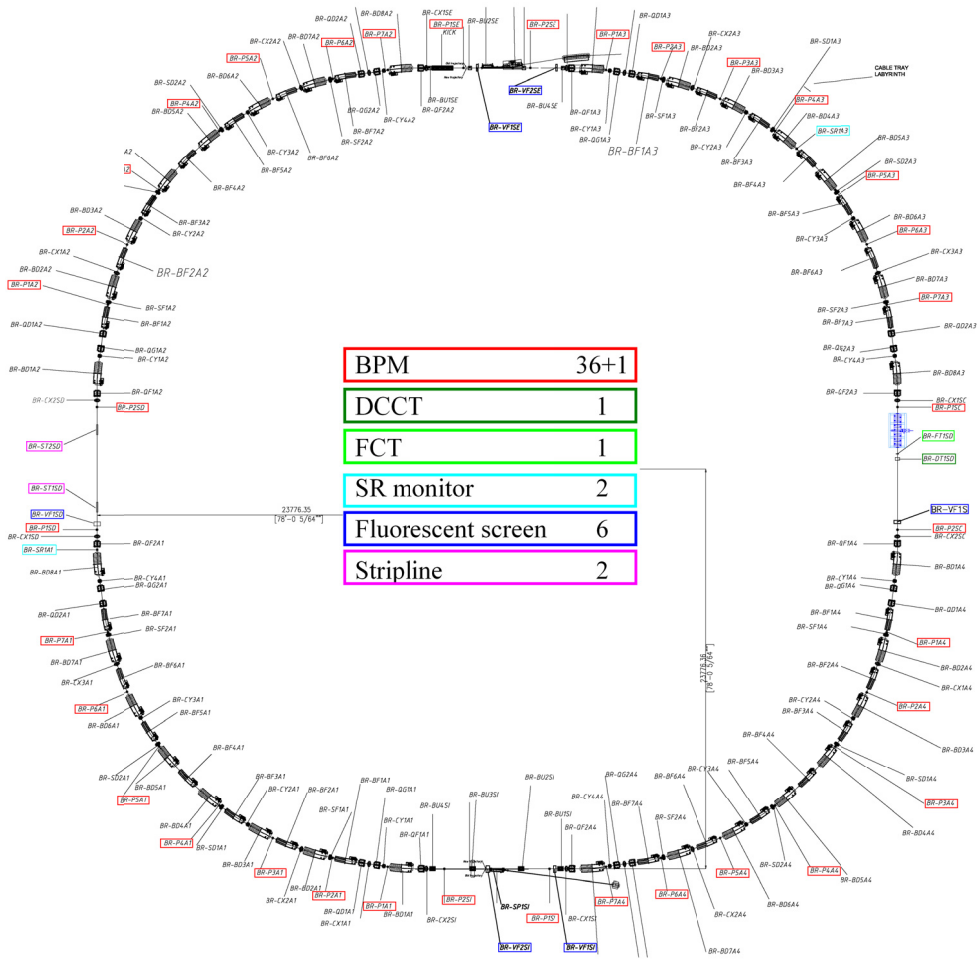

Figure 1. Layout of Booster beam diagnostic

The supplied equipment and subsystem components are durable and capable of operating in the accelerator environment (with the presence of EMI, radiation, vibration, etc.). The schematic layout of the Booster is shown in Fig. 1, the beam diagnostic instruments are marked. The beam diagnostic instruments are listed in

Table 1: Booster beam diagnostic instruments.

Diagnostic device	Number
BPM	37
DCCT	1
FCT	1
SR monitor	2
Fluorescent screens (Beam flags)	6
Stripline	2
Tune measurement system	1

Beam Position Monitors

To provide the accuracy of orbit measurement, which is sufficient for good orbit correction, it is recommended to use at least 4 BPMs per one period of betatron oscillation. One more BPM will be installed between the extraction septum magnets. Therefore, total number of BPMs is 37. Each BPM consists of four RF pickup electrodes connected to vacuum-tight feedthroughs with a characteristic impedance of 50 Ω.

Two types of BPM have been designed. The 1st-type BPM has an elliptical cross-section 41×24 mm, the button electrodes are placed at an angle of 45 degrees relative to the horizontal axis, total number is 28. The 2nd-type BPM has an elliptical cross-section 60×21 mm, the button electrodes are placed at an angle of 30 degrees relative to the horizontal axis, total number is 9.The BPM electronics should provide turn-by-turn beam position measurements and the beam orbit measurement. The vacuum-tight feedthrough with mounted button electrode and SMA plug is produced by MPF Products [1]. This part of BPM is exactly the same as for NSLS-II beam transport lines.

DC Current Transformer

A DC Current Transformer is used to measure the beam current, lifetime and injection efficiency. A Bergoz New Parametric Current Transformer (NPCT) [2] has been chosen. The device should provide the following specifications:

Beam current range	0-50 mA
Resolution	<5 μA/Hz$^{1/2}$
Bandwidth	DC to 10 kHz
Output voltage range from	–10 V to 10 V

The In-Flange NPCT-CF4.5"-60.4-120-UHV-C30-H with radiation-tolerant sensor will be installed at the Booster. The In-Flange version of the transformer is mounted in the vacuum chamber between two flanges, has short axial length, includes a ceramic gap vacuum-brazed on kovar.

Fast Current Transformer

A fast current transformer is used to measure individual bunch charges (intensity) and filling pattern. To fulfill the Specifications, the wideband current transformer Bergoz FCT-WB-CF6"-60.4-40-20:1-UHV-H [3] has been chosen

Bergoz In-flange.FCT is a wideband current transformer designed to be bolted in place as part of the accelerator vacuum chamber. Its purpose is to observe the beam longitudinal profile or waveform up to the highest possible frequency allowed by the current transformer bandwidth.

Table 2: Specifications of Bergoz FCT

Turns ratio	20:1
Sensitivity (nominal)	1.25 V/A
Rise time (typ.)	200 ps
Droop	<6 %/μs
Upper cutoff frequency -3 dB (typ.)	1750 MHz
Lower cutoff frequency -3 dB	<9.5 kHz
Position sensitivity (on axis)	0.2 %/mm
L/R time constant (min.)	17 μs
Max. charge/pulse (pulses <1 ns)	0.4 μC
Max. peak current (pulses >1 ns)	400 A
Max. r.m.s. current (f > 10 kHz)	1.4 A

Fluorescent Screens

The beam flag consists of an integrated system of components that can be reconfigured and interchanged, whereby Cerium-doped Yttrium Aluminum Garnet (YAG:Ce) screen can be easily taken out of a UHV-compatible body. Typical resolution of the fluorescent screen is about 50 μm. The YAG plates are produced by Crytur Company [4] (Czech Republic).

The screen is placed inside a cylindrical volume and move inside and outside of the vacuum chamber. The CCD-camera is placed outside the median plane of the accelerator and is radiation-protected with the lead shield. The screen can move between two fixed positions, inside and outside of the vacuum chamber.

The CCD camera GC1290 [5] (Allied Vision Technology, USA) will be used for the beam image registration. To move the beam flag, the pneumatic drive DSNU-25-80-PPS-A [6] (FESTO Company, Holland) is used.

Synchrotron Radiation Monitor

The synchrotron radiation (SR) monitor provides routine measurements of transverse beam profiles and

beam sizes with spatial resolution better than 50 μm in each plane. The synchrotron radiation monitor consists of a metallic mirror placed inside the vacuum chamber, light output window, image formatting optics and a CCD camera. Two ports of SR output are proposed; the first one is located in the 3rd arc, the second one is close to the diagnostic straight section.

Tune Measurement System

The tune measurement system should provide measurement of the betatron tunes in the range of ±0.5 (in units of the revolution frequency) around the design working point. The measurements have to be performed for a single bunch charge of 100 pC and for a train of 150 bunches with 10 pC/bunch for each injector cycle without any data drop. The tunes should be available to the injector control system during whole energy ramp duration T_R between the beam injection and extraction with at least 20 time steps. The system should have an ability of magnifying the tune range of interest and providing sampling of every booster ramp (Tab. 3).

Table 3: Parameters of the tune measurement system

Tune measurement error	less than 0.0005
Time of a single measurement (ν_x and ν_y) (measurement mode)	~4 ms
Time of one scanning in full frequency range (search mode)	500 ms

Budker Institute has a large experience in development and usage of tune measurement systems. A tune measurement system, similar to the described below, has been implemented for the Siberia-2 storage ring at Kurchatov Institute (Moscow, Russia).

The system is able to perform tune measurements using two methods.

The kicking method is the main one. The beam is excited by radio frequency (RF) pulses with the frequency close to $f_B = (1 + \nu_{x,y})f_0$, where f_0 is the revolution frequency, $\nu_{x,y}$ – is the fractional part of the horizontal (vertical) tune. Duration of the RF pulse is 100-500 μs.

The second method of tune measurement is based on white noise beam excitation. To excite the betatron oscillations, white-noise signal is used instead of RF pulses. Total number of measurements during the Booster energy ramp is 128 (64). The measurements of horizontal and vertical tunes are performed simultaneously.

Striplines

Two identical sets of four 50-Ohm striplines are used. One set is a kicker for beam excitation; another one is a pickup for measurement of a beam response signal..

The stripline electrodes used for kick are mounted at the angle of 45° relative to the horizontal plane using a BINP-made 50 Ω/450°C vacuum-tight feedthrough for SMA plug with bearing capacity Characteristic impedance of the stripline is close to 50 Ω. The length of stripline is 450 mm, which is about 3λ/4 (λ is the wavelength) at RF frequency of 499.68 MHz.

Design of Interface Between Booster Diagnostics System and Booster Control System

Booster Diagnostics control subsystem will conform to NSLS-II control system standards. It will be EPICS-based and the preferable operating systems for IOCs are RTEMS (Real-Time Executive for Multiprocessor Systems) and Linux. The diagnostics controls pursue the utilization of commercial off-the-shelf hardware to reduce cost as well to achieve better reliability.

Conclusion

A list of typical problems of the accelerator physics related to the measurements of beam parameters can be conventionally divided into three stages.

1. Commissioning: passing of the beam in transport lines; measuring of the beam emittance and matching it with the accelerator acceptance; observation and correction of the beam trajectory at the first turn closing; beam monitoring during adjustment of injection and capture by the accelerating RF-field.
2. Operative control for a regular work. At this stage routine measurement and correction of the following beam parameters are necessary: circulating current and lifetime; filling pattern; closed orbit; betatron and synchrotron frequencies; chromaticity; longitudinal and transverse beam sizes.
3. Accelerator physics tasks necessary for the optimization of the machine operation: measurement and correction of magnet lattice functions; study of nonlinear beam dynamics; research of collective effects and suppression of instabilities; analysis of external beam-perturbing factors.

We believe that the diagnostics described above are adequate for solving of all these problems.

REFERENCES

[1] http://www.mpfpi.com/2010catalog_coaxial-5.5.pdf
[2] http://www.bergoz.com/index.php?option=com_content&view=article&id=35&Itemid=48
[3] http://www.bergoz.com/index.php?option=com_content&view=article&id=23&Itemid=28
[4]http://www.crytur.cz
[5] http://www.alliedvisiontec.com/emea/products/cameras/gigabit-ethernet/prosilica-gc/gc1290.html
[6] http://www.festo.com/cat/en-us_us/data/doc_enus/PDF/US/DSNU-ISO_ENUS.PDF

HIGH-VOLTAGE ACCELERATORS INTENDED TO PRODUCE CONTINUOUS AND PULSE NEUTRON FLUXES

D.A. Solnyshkov#, G.G. Voronin, A.V. Morozov, N.P. Mikulinas, A.N. Kuzhlev, V.D. Shiltsev, D.V. Efremov Scientific Research Institute of Electrophysical Apparatus, Saint Petersburg, Russia

Abstract

Recently, in NIIEFA a series of high-voltage accelerators intended to produce continuous and pulse neutron fluxes with a yield of 10^{10}-10^{12} n/s has been designed. The facilities designed can be used for operation in the continuous, microsecond and nanosecond modes, in any combination. In the pulse microsecond mode, ion currents of up to 100 mA with pulse lengths ranging from 2 up to 100 μs can be obtained on target. In the nanosecond mode, the accelerator produces an ion beam current of up to 5 mA with a pulse length in the range of 2-30 ns.

Over the last years the interest towards pulse neutron generators is growing due to continuation of research in the field of nuclear physics using time-of-flight methods. One more reason of such interest is that the development of high-effective systems for the detection of fissionable substances, explosives, drugs and poisons is a currently central issue. R & D works have been carried out in NIIEFA to design and build neutron generators, which produce neutron fluxes of high-intensity in the continuous operating mode and, in addition, will be capable of producing neutron fluxes in a wide range of the pulse repetition rate and pulse length.

The NG-12-2 neutron generator [1] is a high-voltage accelerator of deuterium ions with an acceleration voltage of 300 kV and a beam current of deuterium atomic ions of up to 15 mA.

The general view of the NG-12-2 neutron generator is shown in figure 1.

Figure 1: The NG-12-2 Neutron Generator Installed in the Institute of Nuclear Physics and Chemistry, CAEP, China.

#d-soln@luts.niiefa.spb.su

The ion injector is installed in a high-voltage terminal of the accelerator and consists of an ion source with initial beam forming system, analyzing 90^0 electromagnet, autonomous vacuum system, electric power supply and control systems. The ion source is of an ECR type with a four-electrode ion beam forming system [2]. Spatial and angular characteristics of the beam at the accelerating tube input are controlled with a double-focusing analyzing electromagnet and electromagnetic solenoid lens.

The ion optical system of the accelerator was designed so that to obtain at the accelerator output in the switching magnet plane a deuterium ion beam with a current of up to 20 mA, an emittance and regular divergence values required for its further transport towards the target. A 45^0 electromagnet serves for the beam switching to two beamlines. The first of them is intended for the operation in the continuous and pulsed microsecond modes. An ion beam with a pulse length of 10-100 μs and pulse repetition rate up to several kHz is produced by the microwave discharge modulation in the ion source. The second is designed for the production of ion pulses with the 1-2 ns length on a stationary target. Such pulses are produced in a beamline, which consists of a beam chopper, klystron particle buncher, target device and beam focusing and measuring system. The system of nanosecond pulse forming is described in detail in [3]. The length of the beamline is about 6 m.

Thus, the neutron generator described in the paper allows a beam of atomic ions with a current of up to 15 mA and beam diameter of 20 mm to be obtained on a rotating target of 230 mm diameter. In the pulsed mode, a pulse length can be 10-100 μs and current amplitude of up to 20 mA. In the second beamline, a peak ion current of 10 mA with a pulse length of 1.7 ns was obtained. The pulse repetition rate can be set to 1, 2, 4 MHz; a mode is provided when it can be smoothly varied in the 1-100 kHz range.

The generators of the NH-12-2 model can be successfully operated at large research centers. However, there exists a demand for less expensive generators with lower neutron yield but also equipped with auxiliary systems to widen the fields of possible applications.

The NG-11I neutron generator is designed for a neutron yield of 5×10^{11}n/s in the continuous operating mode. It is equipped with a system for production of pulse neutron fluxes in the microsecond range by modulating the ion source discharge. The generator is a deuterium ion accelerator with an acceleration voltage of 180 kV and atomic ion beam current on target up to 5 mA. An ECR ion source is also used in the accelerator. An electromagnetic analyzer mounted behind the accelerating

tube serves for the mass separation of the ion beam and its simultaneous switching between two beamlines. This makes much simpler the design of the injector and the whole accelerator. The ion-optical system of the accelerator with the main focusing element being an adjustable input lens of the accelerating tube serves to form a beam with parameters required for its transport to the target in the continuous operating mode and its modification in the beamline, in which a nanosecond pulse is produced. The latter is completely similar in design to the beamline of the NG-12-2 neutron generator. The NG-11I generator is shown in Figure 2.

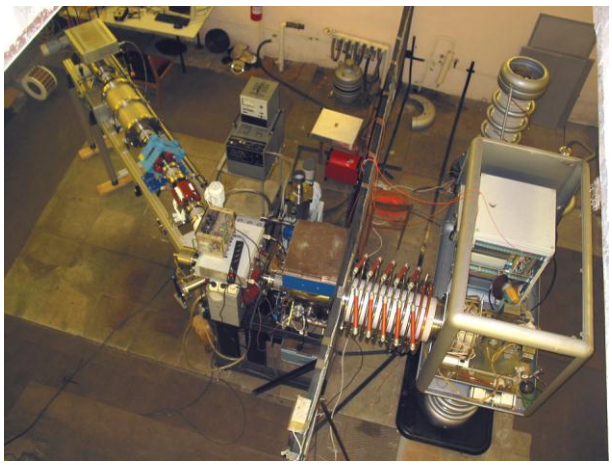

Figure 2: The NG-11I neutron generator at a test facility.

One more generator, the NG-11I-1, with a yield of 2×10^{11} n/s has been developed on the basis of duoplasmatron ion source, which allows shorter beam current pulses, compared to the ECR source, to be obtained in the microsecond mode. This is very important for certain applications. Figure 3 shows the general view of the NG-11I-1 neutron generator.

Figure 3: The NG-11I-1 Neutron Generator at a Test Facility in the MIPHI.

A deuterium ion beam produced by the duoplasmatron is accelerated up to 180 keV, separated with a 90^0 electromagnetic analyzer and directed towards the target through a beamline. The atomic ion beam current on target is up to 3 mA both in the continuous and microsecond pulse modes. To produce nanosecond pulses, a system similar to that of the NG-12-2 generator is used with minor modifications in power supply systems of the beam chopper and buncher.

Nowadays, the designing of the NG-10 neutron generator has been finished and works on its manufacturing have been started. This machine is designed to work as a reference source of a neutron flux and neutron flux density. The accelerator is designed for obtaining a stable current of an atomic deuterium ions on target up to 500 μA with the acceleration voltage smoothly controlled in the 120-150 keV range. The generator can be operated both in continuous and pulse modes. The current amplitude of the atomic deuterium ions is 1mA, pulse length can be varied from 2 up to 100 μs, pulse repetition rate can be controlled from single pulses to 20 kHz.

Works to increase the neutron flux intensity are in progress. For the neutron generator with a yield of 5×10^{12}-10^{13} n/s, an ECR ion source with a current of up to 100 mA and pulse lengths in the 10-200μs range has been designed. The source has been successfully tested at a test facility in NIIEFA.

The control systems of the designed generators are based on industrial computers, which provide control of the accelerator parameters, keep the parameters within a selected range, inform the operator on the current state of the main sub-systems and switch the accelerator off in case of an emergency. The power supply sources of the accelerators operate at a frequency of 20 Hz, which allowed their overall dimensions to be significantly decreased and the stability of operation to be increased. High-voltage systems are controlled via fiber-optical communication channels.

In conclusion, four neutron generators have been designed and built over the last years in NIIEFA. These machines can satisfy a demand of research centers for a sufficiently wide range of applications. Different configurations of these accelerators can be provided and output parameters can be varied on request.

REFERENCES

[1] G.G. Voronin et al., “The NG-12-2 Neutron generator”. Proceed. of the 11th International Conference Applied Charged Particle Accelerators in Medicine and Industry, St. Petersburg, October 2005, p. 278 (2005).

[2] G.G. Voronin, D.A. Solnyshkov et al., Nucl.Instr. and Meth., In Phys. Res., V. 161-163 (2000), p.1118.

[3] G.G. Voronin et al., “Accelerator for Production of Beams in Continuous and Pulse Operating Modes”, 20th Russian Conference on Charge Particles Accelerators, September 2006, BINP, Novosibirsk, Russia.

THE CC1-3 CYCLOTRON SYSTEM

V.G. Mudrolyubov#, I.N. Vasilchenko, Yu.N. Gavrish, A.V. Galchuck, S.V. Grigorenko, V.I. Grigoriev, M.T. Kozienko, L.E. Korolev, A.N. Kuzhlev, Yu.I. Stogov, V.I. Ponomarenko, A.P. Strokach, S.S. Tsygankov, V.D. Shiltsev,
D.V. Efremov Scientific Research Institute of Electrophysical Apparatus, Saint Petersburg, Russia
Nebojsa Neskovic, Petar Belicev, Aleksandar Dobrosavljevic, Velibor Vujovic,
The Vinca Institute of Nuclear Sciences, Belgrade, Serbia

Abstract

A CC1-3 cyclotron system has been designed to be installed in the Vinca Institute of Nuclear Sciences, Belgrade, Serbia. This system will be operated in the laboratory of nuclear-physical methods of the elemental analysis. The system includes a compact cyclotron and a system for beam shaping with specified energy characteristics. The cyclotron ensures the acceleration of negative hydrogen ions up to energy in the range from 1 to 3 MeV and a beam of protons is extracted by stripping on a thin carbon foil. The beam-shaping system ensures the beam of protons with a spectrum width not more than 0.1%. The main unit of the beam-shaping system is a magnetic analyzer with a bending angle of 270º. To date, the equipment of the cyclotron system has been manufactured and tests have been carried out on test facilities in the D.V. Efremov Institute. Installation will be performed in 2012.

The CC1-3 cyclotron system has been designed at the D.V. Efremov Scientific Research Institute of Electrophysical Apparatus (NIIEFA), St. Petersburg with an active participation of specialists from the Vinca Institute of Nuclear Sciences, Belgrade, Serbia. The system will ensure effective technological facilities necessary to carry out analytical research in the Vinca Institute, in particular RBS, PES, NRA и PIXE spectroscopies. Strict requirements are imposed for parameters of accelerated proton beams: the energy range should be from 1 to 3 MeV, spectrum width no more than 0.1%, accuracy of energy setting not worse than 1 keV and current ranging from 10 to 100 nA.

To attain the aforementioned parameters, we have chosen the version of the system consisting of a compact cyclotron with a beam-forming system (Fig. 1) and systems of power supply, automatic control, vacuum pumping and water cooling.

The compact cyclotron is intended to accelerate negative hydrogen ions. An extraction by stripping on a thin carbon foil allows a proton beam with a final energy up to 1-3 MeV to be delivered. The current of the extracted beam of protons is 20 μA. The cyclotron comprises the following units and elements: an electromagnet with a vacuum chamber, resonance system, probes and stripping device, external injection system and high-frequency generator.

#Mudrolubov_VG@luts.niiefa.spb.su

The beam-forming system is designed to ensure beam parameters, which are not typical for cyclotrons. The beam-forming system includes a matching magnet and switching magnets, doublet of quadrupole lenses, correcting electromagnets and magnetic analyzer.

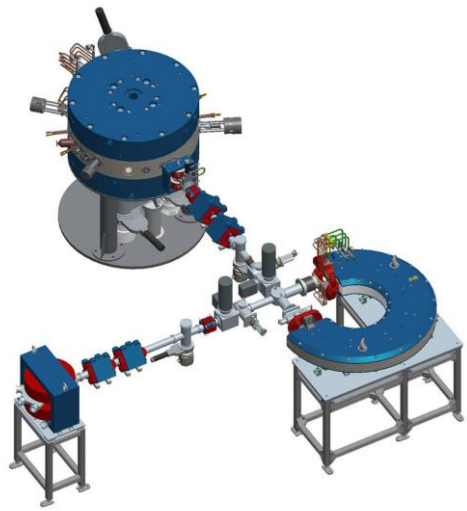

Figure 1: The compact cyclotron CC1-3 with a beam-forming system.

The major part of the cyclotron is a four-sector shielding-type electromagnet (Fig. 2). The electromagnet is 1400 mm in dia, pole diameter is 600 mm and average induction is 0.98 T. Gap hills/values are 50/100 mm. The maximum acceleration radius for the 3 MeV energy is 250 mm. The power consumption of the magnet is 5.2 kW; its mass is 6.5 tons. The upper beam of the magnet can be moved upward up to 500 mm.

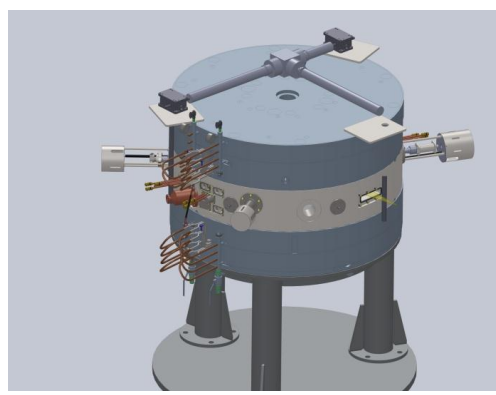

Figure 2: The magnet of the cyclotron.

The vacuum chamber of the cyclotron (Fig. 3) consists of a casing and two covers. The casing is a hollow thick-walled cylinder of carbon steel, which simultaneously is a part of the iron core. Pole pieces of the magnet with welded rings of stainless steel are the covers of the chamber. Such a structural concept provides necessary mechanical strength of the chamber and also forms a type of a volume to improve pumping of the vacuum chamber. A cryogenic pump, vacuum chamber of the matching magnet, RF power in-feeding device, AFT trimmer, stripping device and probes are fastened to flanges of the vacuum chamber casing.

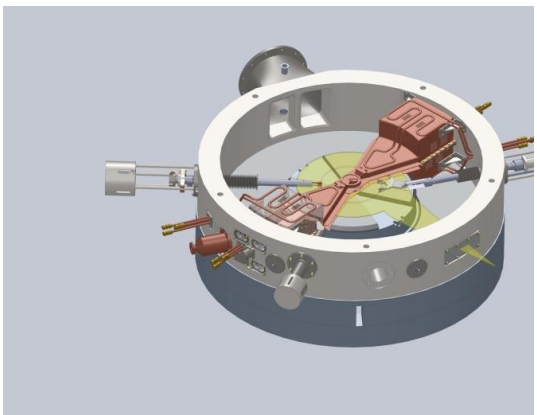

Figure 3: The vacuum chamber with resonance accelerating system, stripping device and probes.

The resonance accelerating system is located completely inside the vacuum chamber volume and is fixed to a side surface of the vacuum chamber casing. The system consists of two mirror-symmetrical quarter-wave resonators. An inner conductor of each resonator consists of a dee and a stem. The dees in the vicinity of the magnet axis are galvanically coupled. An outer conductor of the system is claddings of the magnet and vacuum chamber valleys as well as plates connecting the upper and lower claddings of chamber. The side surfaces of the valley claddings follow the shape of the side surfaces of the magnet sectors and serve as dummy dees. The system is equipped with an inductive RF power in-feeding device, AFT trimmer and RF-probe. Stems, dees and claddings are cooled with water. The central part of the dees is made removable and it is cooled by thermal contact with the dees. The operating frequency of the resonance system is 59.7 MHz and it corresponds to the 4^{th} harmonic of the revolution frequency for hydrogen ions. The design power of active losses in each resonator is 1.6 kW at an RF voltage amplitude of 25 kV.

The high-frequency generator consists of a control and stabilization module and RF-power amplifier. The main parameters of the high-frequency generator are as follows: operating frequency – 59.7 MHz, frequency stability – 1.10^{-7}, phase stability – ±0.5°, output power – 5 kW and accelerating voltage amplitude stability – 10^{-3}. Generator triode 3CW5000A7 is used in the power amplifier. The RF power is transmitted to the resonance system through a flexible coaxial feeder.

Three versions of a negative ion beam generation are considered in the technical project: radial or axial inner sources and an external injection system. Stringent requirements are imposed on the energy spectrum of the accelerated ion beam and current stability, therefore the last version of the aforementioned has been chosen. The external injection system is located under the electromagnet. The system consists of a source of negative ions with an ion-optical system for the beam additional acceleration and focusing, differential pumping chamber, two electrostatic lenses, spiral inflector and an ancillary equipment. The ion beam current at the injector output is 0.5 mA, ion energy is 11.5 keV, calculated normalized emittance is not more than 0.3 π mm·mrad.

The cyclotron is equipped with two probes designed for removal of the maximum beam power of 60 W. The probes have similar connection dimensions, electrical and water connectors. A remote drive ensures radial travel of the probes from the minimum allowed position of ~ 100 mm to the position when the probes are outside the acceleration area. The stripping device is equipped with a drive, which allows one of three charge-exchange foils to be quickly installed to the working position and also the foil radius and angle of location to be varied. The charge-exchange foil is a carbon film of 0.2 μm thickness with a glue substrate. We were not sure if this foil would suit us as 1 MeV ions lose ~15 keV when passing through the foil. In this connection, pilot samples of this foil were manufactured and tested on the operating cyclotron CC-18/9 with an ion energy of 1-2 MeV. Simultaneously, a technique for fabrication of foils with a smaller thickness has been developed and tried out, which will allow energy losses to be reduced and reliability of the stripping device to be increased.

The major part of the beam-forming system is an analyzer, which consists of an analyzing magnet (Fig. 4) and two collimators installed at the inlet and outlet of the analyzing magnet vacuum chamber. The analyzing magnet ensures a bending angle of 270° with a bending radius of 600 mm. To expand the potentialities of the beam-forming system, three fixed dimensions of the input and output slits of 0.5, 1 and 2 mm are provided. The design energy resolution behind the output slit is not worse than 0.05%.

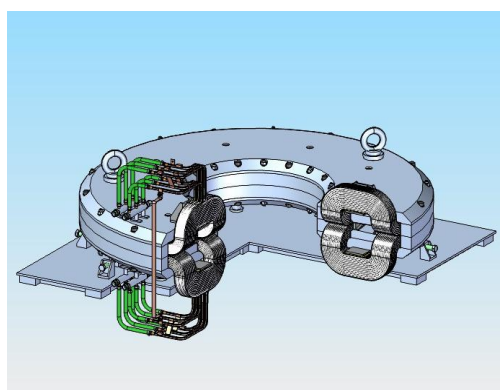

Figure 4: The analyzing magnet.

The matching magnet is intended to make coincident the axis of the extracted beam with the ion guide axis. A doublet of quadrupole lenses focuses the beam to the input slit of the analyzer. The switching magnet specifies the beam bending angle for its further transport, either 0° or ±15°. To measure the beam parameters when it is transported to targets, the beam transport system contains the following diagnostic means: beam profile monitors (scanners), which are used to measure the beam profile in horizontal and vertical planes, and Faraday cups to measure the beam current.

The power supply system is intended to supply electric power to the cyclotron equipment. The maximum installed power of the equipment is 40 kW. The system consists of a power switchboard, two power supply racks for magnets and lenses and two power supply racks for the external injection system as well as power supply units for step motors and the mechanism moving upward the upper beam of the magnet.

The automatic control system is of distributed architecture. It consists of Mitsubishi and Fastwel IO controllers and computers, each being responsible for the control of one or several sub-systems of the cyclotron. The main unit of the control system is an industrial (host) computer, which inquires slave controllers and transmits the information acquired to computers of the operator's workstation; receives commands from the operator's workstation and performs their arbitration and distribution. Data exchange is realized via network interfaces of three types: the Ethernet, an upper level network, the ProfiBus DP and RS-485, low-level networks.

The Ethernet networks the host Mitsubishi controller, which is responsible for the control, interlock and signaling sub-system, host computer, computers of the operator's workstation, computer of the beam current measuring system and an industrial computer, which controls the RF system.

The ProfiBus DP links the host controller, controllers of devices of the cyclotron, and beam-forming system, vacuum system, power switchboard, power supply racks of the external injection system, water cooling system as well as control units of the power supply system of magnets and lenses. The RS-485 networks the host computer, vacuum measuring units and controllers of turbomolecular pumps as well as the computer of the beam current measuring system and drivers of step motors of devices for measuring the beam current density. In addition, the RS-485 links the controller of the cyclotron and beam-forming system devices with drivers of step motors of probes and the stripping device.

The vacuum system contains a cryogenic pump used in the vacuum chamber of the cyclotron, four turbomolecular pumps for the external injection system and beam-forming system, mechanical dry pumps, gate valve, valves, leak valves and pressure gages to measure low and high vacuum.

The equipment of the cyclotron will be cooled with distilled water circulating in the water-cooling loop of the cyclotron building. Four water distribution boards are used to distribute cooling water to remove the heat released by the heat-loaded components and units of the cyclotron, to control pressure and stabilize water flow rates.

At present, the equipment has been designed, manufactured and tested at test-facilities of the D.V. Efremov Institute. Installation of the system is planned to have been finished by the end of 2012.

ACCELERATION TECHNIQUE DEVELOPED AT JINR FOR HADRON THERAPY

E.M. Syresin, Joint Institute for Nuclear Research, Dubna, Russia

Abstract

The JINR activities are aimed on the construction of accelerators for proton and carbon ion therapy. JINR-IBA have developed and constructed the proton cyclotron C235-V3. The cyclotron will be delivered in the first Russian hospital center of the proton therapy in Dimitrovgrad in 2012.

The project of the medical carbon synchrotron was developed in JINR. The project goal is accumulation of the superconducting Nuclotron technology at construction of the medical carbon synchrotron. Accelerated ^{12}C ion beams are effectively used for cancer treatment.

The PET is the most effective way of tumor diagnostics. The intensive radioactive ^{11}C ion beam could allow both these advantages to be combined. JINR-NIRS collaboration develops formation of a primary radioactive ion beam at intensity on the tumor target of 10^8 pps for the scanning radiation.

A superconducting cyclotron C400 has been designed by the IBA-JINR collaboration. This cyclotron will be used for radiotherapy with proton, helium and carbon ions. Its construction was started in 2010 within the framework of the Archarde project (France).

The interaction between delta electrons and DNA molecules is one of the important processes in the hadron therapy. The formation of low energy electrons and DNA ions are presented for the KEK electrostatic storage ring with the electron target developed by JINR-NIRS collaboration.

PROTON CYCLOTRON C235-V3

The JINR-IBA collaboration has developed and constructed the C 235-V3 proton cyclotron for Dimitrovgrad hospital proton center. The C235–V3 cyclotron, superior in its parameters to the IBA C235 medical proton cyclotron, has been designed and manufactured by the JINR-IBA collaboration. This cyclotron is a substantially modified version of the IBA C235 cyclotron.

Modification of the extraction system is the main aim of the new C235-V3 cyclotron [1-2]. The main feature of the cyclotron extraction system is a rather small gap (9 mm) between the sectors in this area. The septum surface consists of several parts of circumferences of different radii. The septum thickness is linearly increased from 0.1 mm at the entrance to 3 mm at the exit. The proton extraction losses considerably depend on the septum geometry. In the septum geometry proposed by JINR, where the minimum of the septum thickness is placed at a distance of 10 cm from the entrance, the losses were reduced from 25% to 8%. Together with the optimization of the deflector entrance and exit positions it leads to an increase in the extraction efficiency to 80%. The new extraction system was constructed and tested at the IBA C235 cyclotron. The experimentally measured extraction efficiency was improved from 60% for the old system to 77% for the new one.

One of the nearest goals is to modify the sector spiral angle at R>80 cm for improving the cyclotron working diagram and reducing of coherent beam losses at acceleration. The coherent beam displacement z from the median plane is defined by the vertical betatron tune Q_z: $z \propto Q_z^{-2}$. At $Q_z \cong 0.2$ the coherent beam displacement corresponds to 7 mm and at the free axial oscillation amplitude of 2-3 mm can cause beam losses due to reduction of the sector gap in the C235 cyclotron. An increase of the vertical betatron tune from $Q_z \cong 0.2$-0.25 to $Q_z \cong 0.4$ in C235-V3 permits the coherent losses at proton acceleration to be reduced by a factor of 3-4.

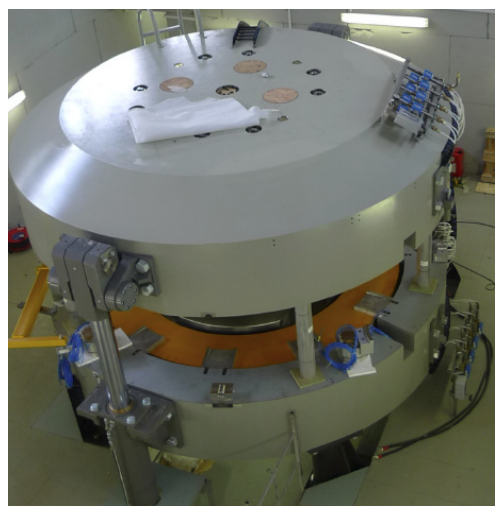

Figure 1: Cyclotron C235-V3 in JINR engineering center.

SUPERCONDUCTING SYNCHROTRON FOR CARBON THERAPY

A project of the medical superconducting synchrotron (Fig. 2) dedicated for the carbon therapy has been designed in JINR [3]. The basis of this medical accelerator is the superconducting JINR synchrotron – Nuclotron [4]. The Nuclotron type straight dipole magnets [4] were adopted for the optic of the medical synchrotron and beam delivery system. The

superconducting magnets permit to reduce the accelerator electrical consumption, the size and weight of the accelerator and the carbon gantry.

The superconducting electron string ion source is planed to use for $^{12}C^{4+}$ injection in the carbon linac. The compact IH linac will apply as synchrotron injector.

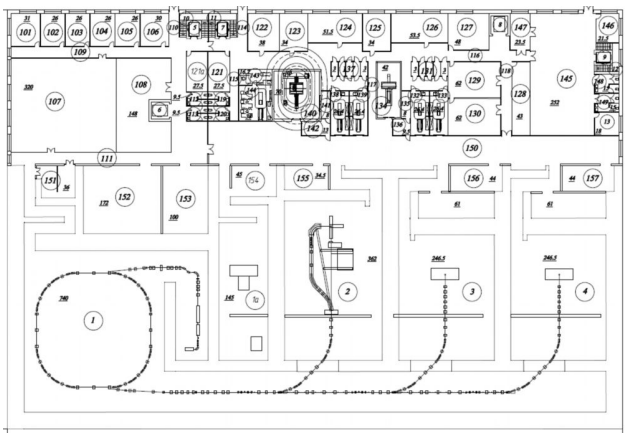

Figure 2: Layout of the carbon therapy hospital center on the basis of superconducting synchrotron.

The FODO structure is more preferable for injection and extraction schemes and corrections of the closed orbit distortions. The synchrotron magnetic system [3] consists of 4 superperiods, which involves 8 straight dipole magnets, 8 quadrupole lenses and multipole correctors. The maximum magnetic field in dipole magnets corresponds to 1.8 T. The multiturn injection is realized at fulfilling of the horizontal acceptance during 10-15 ion turns. The stored beam intensity is equal to 10^{10} ions C^{6+} per pulse. The working point corresponds to betatron tunes $Q_{x,z}$ ≈3.25. Nonlinear 3 order resonance $3Q_x=10$ is used for slow beam extraction. The intensity of extracted beam is equal to 10^9 pps.

The beam delivery system [3] consists of following sections: the extraction section; the foil section provided equal beam emittances in both transverse planes; the accommodation section; the section for beam delivery in the cabin; the section of beam transportation between the medical cabins; the isocentric gantry; the channel with fixed beam position cabin. The beam delivery system should provide the fixed transverse beam sizes in the gantry isocenter. These sizes do not depend on the gantry rotation angle, the extracted ion energy, emittance of the extracted carbon ion beam.

The extracted carbon beam has non symmetric horizontal and vertical emittances, the vertical emittance is few times larger horizontal one. A special scattering foil is installed in the beam delivery system to provide both equal horizontal and vertical beam emittances. The accommodation section is used to provide same optical beam characteristic in the vertical and horizontal directions at exit. It accommodates the beam optic to the gantry for any its rotation angles. The section for beam delivery in cabin consists of the chopper, the achromatic bend and 2 triplets. The chopper involves 4 dipole magnets. The beam is pick-upped by an absorber trap, when dipoles switch off. The beam is transported in the channel when magnets switch on. The section of beam transportation between cabins has the horizontal betatron phase shift 2π and vertical one π. The optic of the isocentric gantry is achromatic at beam transportation to the tumour target. The gantry optic provides equal horizontal and vertical beta functions and zero alpha-function on the tumor target. The parameters of gantry optic is adjusted to obtain the equal vertical and horizontal beta and alpha functions at the gantry entrance at variation of extracted beam emittances and sizes.

The JINR-IBA collaboration develops superconducting cyclotron C400 and carbon gantry in frame work of Archade project [5]. This gantry is planed to use in JINR carbon synchrotron complex. The gantry provides rotation around the patient on an angle $0\text{-}180^0$. The positioner also rotates together with patient on an angle $180^0\text{-}360^0$. The main gantry superconducting dipole magnet has aperture 20×20 cm at magnetic field homogeneity of 10^{-4}. The magnetic field rate corresponds to 1 T/min. The magnet is cooled by 4 He-free criocoolers. The distance from dipole magnet exit to isocenter corresponds 2 m.

FORMATION OF PRIMARY RADIOACTIVE CARBON ION BEAMS

Accelerated ion beams of the positron-emitting ^{11}C isotope (half-lifetime is about 20 min) were first used at NIRS-HIMAC for cancer therapy applications. The use of the ^{11}C ion beam could allow both these advantages to be combined because this beam could be simultaneously used both for cancer treatment and for on-line positron emission tomography. Verification of the radiation dose in the tumor target will be carried out simultaneously with cancer treatment.

In the ISOLDE scheme the ^{11}C isotope is produced through the nuclear reaction $^{14}N\ (p,\alpha)^{11}C$ in the target chamber filled with N_2 gas. The nitrogen gas target also contains 5% of H_2 to produce $^{11}CH_4$ molecules. The Electron String Ion Source [6] is one of the promising ion sources for generation of the positron-emitting $^{11}C^{4+}$ ion beam at the intensity of $6\cdot10^9$ pps. The charge capacitance of the Krion-2 ion trap is $6\cdot10^{10}$ elementary charges. As was shown experimentally [6], adjusting the electron energy, injection time, and time of ion confinement, one can get up to 50 % of C^{4+} in the total ion beam pulse extracted from the source. So, the existing ion source Krion-2 could produce around $2\cdot10^9$ C^{4+} particles per pulse at an optimized ion conversion efficiency. The maximum number of C^{4+} ions produced per pulse in Krion-2 corresponds to $4\cdot10^9$. The further increase of ion intensity in Krion-2 is restricted by electron string capacity at magnetic field 3T. The developed in JINR new ESIS Krion-5T with magnetic field 5-6T will produce $6\cdot10^9$ $^{11}C^{4+}$ ions per pulse.

The radioactive carbon beams are planed to use for the HIMAC raster scanning irradiation. According to the this therapy requirements, the ion source should produce C^{4+} ion beams with the intensity of $6 \cdot 10^9$ particles per pulse and pulse width of 0.1 ms. The project number of ions produced in the ring per injection-extraction cycle and applied for the scanning irradiation corresponds to $2 \cdot 10^9$ particles. Maximum number of extracted ions is equal 10^8 pps at HIMAC raster scanning.

SUPECONDUCTING CYCLOTRON C400 APPLIED FOR CARBON THERAPY

Carbon therapy is the most effective method to treat the resistant tumors. A compact superconducting isochronous cyclotron C400 was designed by JINR-IBA collaboration [5]. This cyclotron will be used for radiotherapy with protons, helium and carbon ions. The $^{12}C^{6+}$ and $^{4}He^{2+}$ ions will be accelerated to the energy of 400 MeV/amu and H_2^+ ions will be accelerated to the energy 265 MeV/amu and protons will be extracted by stripping.

Three external ion sources will be mounted on the switching magnet on the injection line. The $^{12}C^{6+}$ ions are produced by a high performance ECR at the injection current of 3 μA.

The design of the C400 magnetic system was based on its main characteristics: four-fold symmetry and spiral sectors; deep-valley concept with RF cavities placed in the valleys; elliptical pole gap is 120 mm at the center decreasing to 12 mm at extraction; accelerate up to 10 mm from the pole edge to facilitate extraction; pole radius is 187 cm; hill field is 4.5 T, valley field is 2.45 T; magnetic induction inside yoke is less 2-2.2 T; the magnet weight is 700 tons and the magnet yoke diameter is 6.6 m; the main coil current is 1.2 MA. The sectors have following parameters: the initial spiral law with parameter Nλ=77 cm with increasing spiral angle to the final radius with parameter Nλ~55 cm; the sectors azimuth width is varying from 25° in the cyclotron center to 45° at the sectors edge; axial profile is the ellipse with 60/1874 mm semi-axis, at the final radii the ellipse axial profile is cut by the planes at the distance z= ± 6 mm. The optimized sector geometry provides vertical focusing Q_z~0.4 in the extraction region.

Extraction of protons is supposed to be done by means of the stripping foil. It was found that 265 MeV is the energy of protons for 2-turns extraction..

It is possible to extract the carbon beam by means of one electrostatic deflector (which is located in valley between sectors) with a 150 kV/cm field inside. Septum of the deflector was located at the radius 179.7 cm for tracking simulation. The extraction efficiency was estimated as 73% for the septum with increased (0.1 – 2) mm thickness along its length**.** The extraction of the carbon and proton beams was realized by the separate channels. It is possible to align both beams into one direction just before the energy degrader. Both beams have a spot with $\sigma_{x,y}$<1 mm at this point. Transverse emittances are equal to 10 π mm·mrad and 4π mm·mrad for the extracted carbon beam.

FORMATION AND INTERACTION OF ELECTRONS AND BIOMOLECULAR IONS IN ELECTROSTATIC STORAGE RING

The basis of hadron therapy is the modifying action of carbon ion or proton beams on biological structures. In the case of carbon therapy, ions cause double strand DNA breaks due to direct ionization, and delta electrons produced in this case result in the DNA ionization along their trajectories. Most delta electrons have energy under 30 eV; ions and protons produce about 10^5 secondary electrons. Below we discuss the results of experiments related to the interaction between low energy electrons and bimolecular ions produced in the KEK electrostatic storage ring [7]. The KEK electrostatic ring with a perimeter of 8.1 m was first used to store different bimolecular ions, including ions of DNA molecules with a mass of up to 60000 u. The maximum ion energy is 30 keV/Z. A special electron target was developed for investigating the interaction between low energy electrons and biomolecular ions in the electrostatic storage ring in the framework of the JINR–NIRS-KEK collaboration [7]. The maximum energy of the target electrons is 100 eV, the maximum electron current is equal to 2 mA, and the length of the electron–ion interaction region is equal to 20 cm.

The cross section of the interaction between target electrons and ions of DNA molecules (oligonucleotide d(AAA)) has a maximum for a relative electron and ion energy of 4.5 eV. The peak in the cross section of the electron interaction with DNA ions is determined by the contribution of sugar–phosphate breaks and dissociative recombination and electron capture dissociation.

REFERENCES

[1] E.M. Syresin et al, IPAC11, S-Sebastian, 2706, (2011).
[2] E.M. Syresin et al, Particle and Nuclei Letters, v.8, 635 (2011).
[3] E. Syresin et al, Particle and Nuclei Letters, v.9, 328 (2012).
[4] A.A. Smirnov, A.D. Kovalenko, Particle and Nuclear Letters, v.1, 11 (2004).
[5] Y. Jongen, G. Karamysheva, E.Syresin et al., NIM A 624, 47 (2010).
[6] D.E. Donets, E.D. Donets, E.E. Donets, E.M. Syresin et al, J. of Applied phys., v.3, 56 (2010).
[7] T. Tanabe, K. Noda, and E. Syresin, NIM A 532, 105 (2004).

PROSPECTS FOR INTRODUCTION OF HOME-MADE EQUIPMENT FOR RADIONUCLIDE DIAGNOSTICS

A.P. Strokach#, M.F. Vorogushin, A.V. Stepanov, O.G. Filatov
D.V. Efremov Scientific Research Institute of Electrophysical Apparatus, Saint Petersburg, Russia

Abstract

The radionuclide diagnostics allows the most of diseases to be diagnosed at a very early stage and therefore it has received much attention over the last years. The current concept of the radionuclide diagnostics advancement takes into account Russia geographic and demographic features, and supports the introduction of the home-made equipment into practice. As a basis, the concept assumes the establishment of regional diagnostic centers at large hospitals in each Russian Federal district. Each such a center should be equipped with a cyclotron of the CC-18/9 model, modules for radiopharmaceuticals' synthesis, single-photon emission (SPECT) and positron (PET) scanners. The yield of radiopharmaceuticals' production will satisfy the needs of such a center and of 30-35 SPECT-"satellites" located in diagnostic departments of hospitals situated up to 1000 km from the center. In future, autonomous PET- centers, each equipped with specialized CC-12 cyclotrons, modules for radiopharmaceuticals' synthesis and with 3-4 PET scanners can be established on the basis of these diagnostic departments. The implementation of the Federal Targeted Program on the serial production of cyclotrons and SPECT will require 5-6 years to increase the number of the people examined per year up to 1.0-1.2 million.

Nowadays in Russia the radionuclide diagnostics based on the use of radioactive isotopes is beyond the reach of the majority of people. In accordance with the program of the Ministry of Health and Social Development of the Russian Federation in force at present, three large federal medical high-technology centers are to be built in Dimitrovograd, Obninsk and Tomsk; PET-centers and radionuclide therapy departments are to be built in Krasnoyarsk, Nizhniy Novgorod and Novorossisk. The higher yield of radioisotopic products should be provided in Moscow, Obninsk and Tomsk.

The suggested construction of federal high-tech medical centers in the vicinity of the nuclear-power industry facilities offer definite advantages due to the location of the sources of radioactive products close to consumers. However, there are serious disadvantages connected with necessary staffing these federal centers with a qualified medical and technical personnel and a large volume of capital construction. It is sufficient to note that thousands of patients and accompanying persons from all regions of the Russian Federation will come to these center,s and all these people will need a place to live in. For example, Dimitrovgrad or Obninsk, towns with a population of 100-120 thousand people, will have to accommodate tens of thousands of people per year who need diagnostics and treatment. In this context, a developed infrastructure is needed including hospitals with medical and auxiliary personnel, hotels, public catering, transport, etc. The total number of tomographs functioning in three federal centers will be much lower than it is required for Russia in compliance with the world standards.

So, this program does not take into account geographic and demographic features of our country and in view of large volumes of necessary capital construction, including residential housing, and serious staff problems, the delivery of modern therapies to the majority of people will be postponed for an indefinite period of time. There are grounds to suppose that an expensive import equipment will be purchased to equip these centers, and interests of the national manufactures will be completely ignored.

NIIEFA in cooperation with other organizations can manage to completely equip radionuclide diagnostic centers mostly with home-made equipment by analogy with the operating PET center in the Russian Research Center for Radiology and Surgical Technologies, Pesochnyi, St. Petersburg [1].

In NIIEFA the designing of a new series of cyclotrons, the CC-12, CC-18/9 and MCC-30/15, has been finished and prototypes of these machines have been manufactured (digits here denote the design energy of proton/ deuterium ion beams). When designing these machines, the following innovations were realized: the acceleration of negative hydrogen ions generated by an external source and extraction of beams of accelerated protons and deuterons by recharging on thin carbon foils. Three CC-18/9 and one MCC-30/15 cyclotrons have been manufactured and put into operation. These machines are used for production of a wide set of ultra short-lived and short-lived radionuclides used in medicine for PET and SPECT diagnostics. The CC-18/9 and MCC-30/15 cyclotrons also produce short-lived radionuclides for the contact radiation therapy. The CC-12 cyclotron specialized only in production of ultra short-lived radionuclides is nowadays under tests at a test facility in NIIEFA.

A prototype of the double-detector single-photon emission computerized tomograph "EFATOM" has been designed and manufactured [1]. After successful technical and clinical tests, the "EFATOM" was put on the list of the medical equipment allowed to be produced in Russia.

So, prototypes of the major equipment, cyclotrons and tomographs, to be used in the present-day radionuclide diagnostics have been designed and manufactured in

#strokach@luts.niiefa.spb.su

NIIEFA. A Federal Targeted Program on the serial production of cyclotrons and single-photon tomographs has been approved, which allows the problem of centralized supplies of competitive home-made equipment to medical institutions of Russia to be successfully solved.

Nowadays, the State Corporation "ROSATOM" is conducting negotiations with a number of firms on the joint production of PET tomographs, radiopharmaceuticals synthesis and packing modules and protective boxes.

Taking into account vast territories of Russia and comparatively short half-life of the radionuclides used for diagnostics, it is reasonable to build regional centers for the radionuclide diagnostics in each federal district of Russia [2]. This will allow a decentralized production of short-lived radiopharmaceuticals and location of SPECT and PET tomographs proportionally to the population density. These centers should be established on the basis of large medical institutions (medical scientific and therapeutical centers, republican, regional and municipal hospitals, oncologic dispensaries), which have a well-developed local infrastructure. In these institutions, diagnostics of cardiological, oncological and neurological patients is a routine practice and they are staffed with qualified medical and technical personnel experienced in diagnostics and treatment of similar diseases.

Each of the regional centers of the radionuclide diagnostics shall be equipped with a cyclotron of the CC-18/9 type, radio-chemical laboratory with radiopharmaceuticals synthesis and quality control modules and two types of tomographs, SPECT and PET. The centers can be equipped with home-made equipment on a centralized basis. The radiopharmaceuticals for PET and SPECT tomography will be produced in these centers, and examinations of patients will be carried out. Alongside with positron and single-photon isotopes produced on cyclotrons, comparatively long-lived "reactor" isotopes will be also used for these purposes. In addition to the own needs, each center can provide functioning of up to 30-35 SPECT- "satellites" located in republican, regional and district hospitals located at a distance of up to 1000 km from the center. After the identification of a disease, therapy to patients will be administered in the hospitals, which have functioning rooms of the radionuclide diagnostics. To equip such rooms all over the country, the total number of SPECT needed is estimated to be 325-330 apparatus.

In future, up to 50-60 autonomic PET centers can be established in largest hospitals on the basis of similar rooms of the radionuclide diagnostics. Such a PET center shall include the following equipment: CC-12 cyclotrons, modules for ultra-short-lived radiopharmaceuticals synthesis and positron scanners. Yields of the radiopharmaceuticals produced on a CC-12 cyclotron provide functioning of 2-3 PET scanners located in the vicinity of each cyclotron. Over the whole country, the number of functioning scanners can reach up to 120-140 apparatus.

The aforementioned number of regional and autonomic centers will bring the radionuclide diagnostics in RF within the reach to all levels of the country population, and the situation will be similar to countries with developed economy. In 5-6 years, the scale of examinations will be 1.0-1.2 millions patients per year.

Thus, to reach the world level in medical services, 130-140 PET scanners and 320-330 SPECT scanners, 10 cyclotrons of the CC-18/9 model, 50-60 cyclotrons of the CC-12 model and 3-4 machines of the MCC-30/15 should be introduced to the national clinics and hospitals. The MCC-30/15 cyclotrons are used for large-scale production of various radionuclide products, for medicine included. [3].

In view of qualified personnel, raduonuclide products available in federal regions, scales and limited terms for the introduction of new equipment, it is reasonable to start practical implementation of the program in the Federal Northwestern District as the most ready for this purpose. We think that installation of single-photon tomographs in St. Petersburg (in several hospitals and dispensaries), Kaliningrad, Arkhangelsk, Cherepovets, Vologda, Murmansk, Petrozavodsk, Syktyvkar, Velikiy Novgorod, Pskov and Severodvinsk will be sufficient to provide the population of the Federal Northwestern District with modern medical diagnostic apparatus. For this purpose in large hospitals of the aforementioned cities and towns, rooms for isotopic diagnostics equipped with SPECT and other necessary equipment should be established in accordance with a standard plan. Simultaneously, hospitals should be re-equipped, as far as possible, with new medical equipment, staffed with qualified attending personnel and provided with a storage bank of data on the health level of the RF population.

In compliance with the effective world standards, the Northwestern Federal District should be equipped with up to 34 SPECT and up to 13 PET tomographs. At present, there are 12 and 4 functioning apparatus, respectively, all in St. Petersburg.

Ready radiopharmaceuticals labeled with I-123, Ga-67, In-111, Tc-99m and other isotopes will be supplied to new diagnostic rooms from St. Petersburg (produced on the CC-18/9 cyclotrons and three MGC-20 cyclotrons), Gatchina and Sosnovyi Bor (Mo-99/Tc-99m reactor generators).

Personnel training can be organized in the Russian Research Center for Radiology and Surgical Technology (RRC RCT), where functions a large system consisting of two cyclotrons, target devices, modules of radiopharmaceuticals' synthesis and quality control. It should be noted that home-made equipment is also applied. The RRC RCT provides their own needs and, in addition, regularly supplies ultra short-lived radiopharmaceuticals to St. Petersburg and short-lived radiopharmaceuticals to Moscow.

The RRC RCT is one of the leading medical centers in Russia, and it can promptly and effectively deliver consultation services for the patients in the Northwestern District.

In conclusion we should to draw attention to a profound economical and social effect to be produced by the introduction of the nuclear medicine methods into the national Healthcare Service as the state of health, higher quality of life and larger life span of millions of people are concerned.

The suggested concept of the radionuclide diagnostics advancement on the basis of regional centers established in each Federal district fits well into the existing today organization of medical services to the population of the Russian Federation. The concept gives proper weight to geographic and demographic features of the country, and within the shortest time and in the most cost-effective way will allow the majority of the RF population to be provided with modern medical diagnostics and subsequent therapy mostly using the home-made medical equipment

The main customer of the new production for medicine is the state. Therefore, in the case of expansion of a high-tech equipment production in Russia, the expenditures of the state budget for purchasing medical equipment abroad will be substantially reduced. An additional saving can be obtained due to the use of the PET-center standard plan designed by the State Corporation "ROSATOM".

The production of the high-tech home-made equipment for the nuclear medicine will result in a larger number of worksites and higher qualification level of the personnel; will give an impetus to progress in adjacent fields of science and engineering. So this will stimulate higher technological development of our country.

REFERENCES

[1] M.F. Vorogushin, A.P.Strokach, O.G.Filatov, "Status and Development of Accelerating Equipment in the D.V. Efremov Institute", VANT, Seriya "Electrofizicheskaya Apparatura", St. Petersburg, "Izdatelstvo Yanus" Ltd, 2010, #5(31), pp.5-11.

[2] A.V. Stepanov, M.F. Vorogushin, "System for the Radionuclide Diagnostics", RuPAC-2008, Zvenigorod, Russia, September-October, 2008.

[3] P.V. Bogdanov, M.F. Vorogushin, A.V. Galchuk, V.G. Mudrolubov, A.P. Strokach, "MCC-30/15 cyclotron – parameters, adjusting works and their results", RuPAC-2010, IHEP, Protvino, Russia, September -October, 2010, Proceed. Volume, p.408 http://accelconf.web.cern.ch/accelconf

METHOD OF STATE AND ALIGNMENT MONITORING FOR CRYSTAL DEFLECTORS OF RELATIVISTIC IONS*

A. Gogolev#, S. Uglov, TPU, Tomsk, Russia
A. Taratin, JINR, Dubna, Russia

Abstract

The calculations of the parametric X-ray radiation (PXR) characteristics produced by 158 GeV/u Pb nuclei in silicon crystal deflectors were carried out. The PXR intensity at the maximum angular distribution was about 4 ph/Pb/sr, which should allow to monitor the state and the orientation of the deflector by means of the observation of the PXR spectrum characteristics.

INTRODUCTION

Systems of relativistic particle beam steering based on the use of channeling effect are widely applied in leading research centers of Russia and foreign countries. It was experimentally shown that with use of short crystals one can obtain extracted beams with intensity of ~ 10^{12} protons/cycle with efficiency of ~ 85% [1].

The radiation resistance of crystals is one of important characteristic in the applications of crystals for beam control of accelerator. Estimation of the limit value of the particle flux through the crystal before its destruction has been obtained in the experiments carried out at CERN (Switzerland) and BNL (USA) and is equal to ~ $2 \cdot 10^{20}$ protons/cm^2. Silicon crystals with efficiency $80 \div 85\%$ reliably provide the extraction up to 10^{12} particles per cycle duration of $1 \div 2$ seconds. When intensity of beam is about 10^{13} protons the crystal loses the capability to deflect the particles [2].

An operative control is required in the case of using crystal deflectors for the accelerator intensive beam collimation. The control should allow to conclude about the state and alignment of the crystal collimator relative to the beam halo.

In paper [3] we were proposed concept a method of exploiting parametric PXR as a monitor of deflector quality and orientation. PXR is emitted in directions satisfying the Bragg condition when relativistic charge particles are incident on a crystal and its properties strongly depend on kinematics of process [4-6]. Since its first observation [7] one studied using electron beams of different energies [8, 9]. The first experiment with the aim of PXR observation from heavy charged particles was carried out on the 70 GeV proton beam at IHEP [10]. After that PXR has been successfully observed from 5 GeV protons and 2.2 GeV/u carbon nuclei in a silicon crystal on the external beams of the Nuclotron at LHE JINR [11, 12]. Recently, PXR produced by 400 GeV/c protons in silicon deflector has been observed [13].

*Work supported by Russian Foundation for Basic Research grant 12-02-16130 and the GK #14.B37.21.0912
#gogolev@tpu.ru

The aim of this paper is to calculate the spectral and angular characteristics of the PXR from silicon deflectors when relativistic Pb nuclei are passing through them.

SIMULATION

The layout of numerical experiment is similar to work [13]. Fig. 1 shows the layout in the horizontal plane for the experiments with quasi-mosaic (QM) and strip (ST) silicon crystals. A beam of Pb nuclei with energy 158 GeV/u entered a crystal in the collimation geometry so that it is parallel to the deflecting planes, which are the (111) and (110) crystallographic planes for the QM and ST crystals, respectively.

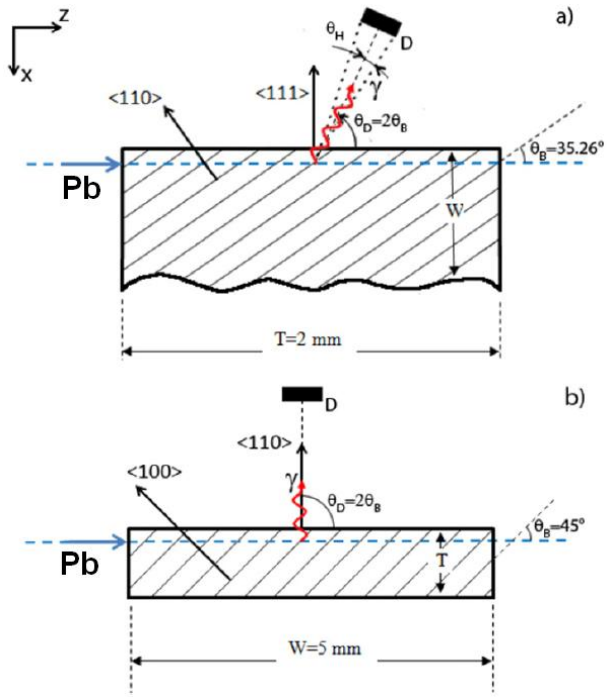

Figure 1: The simulation scheme details: (a) for quasi-mosaic crystal, (b) for strip crystal.

Simulation was carried out for a Gaussian incident beam with the cross-section σ = 1,0x0,7 mm^2 and σ = 10,7x7,8 μrad^2 divergence. A beam of Pb nuclei crossed the crystal with an offset of 0,7 mm depth in the QM case and in the centre in the ST case.

PXR is generated by particle field when it crossing a set of the crystallographic planes. PXR reflexes (110) and (100) in the case of (a) and (b) shown in Fig. 1, respectively, was calculated.

The energy of PXR photons is determined in the following way:

$$E_n = n\frac{2\pi\hbar c}{d}\frac{\beta\sin\theta_B}{1-\beta\sqrt{\varepsilon}\cos\theta_D\cos\theta_y} \quad (1)$$

where n is the diffraction order, d is the interplanar distance, $\beta=v/c$ and ε is the dielectric constant of the target material ($\varepsilon = 1-(\omega_p/\omega)^2 \approx 1$, ω is the frequency of PXR photons, ω_p is the plasmon frequency), θ_B is the Bragg angle, θ_D and θ_y are the radiation registration angles. θ_D is the angle between the projection of the radiation direction and momentum in the diffraction plane. θ_y is the angle between projection of the radiation direction on the diffraction plane and the radiation direction. The diffraction plane is determined by the particle momentum and by vector normal to the crystal planes, its figure plane in Fig.1.

According to the formula (1) PXR photons energy of the reflex (110) for detection angle ($\theta_D=2\theta_B$) 70.52° is equal to 5.59 keV and to the reflex (100) for detection angle 90° is equal to 6,46 keV. The distance between the crystal and screen D was 117 and 200 mm in case QM and ST crystal, correspondently. The calculations of PXR characteristics have been performed according to the PXR kinematic theory [14], which describes well many experimental results. In the simulation a crystal considered as a set of the straight samples and PXR yield from all crystal can be presented as superposition of separate contributions from each sample. It should be noted that the PXR intensity must increase with the charge number Z of the particle as Z^2 therefore the PXR intensity from nuclei much more then from proton. The dependence on particle charge was experimentally observed in [11] with a large error.

Fig. 2 presents the simulation, the results of which show the difference between the intensities from Pb nuclei and protons. The intensities from Pb nuclei are more than from protons in 6724 times.

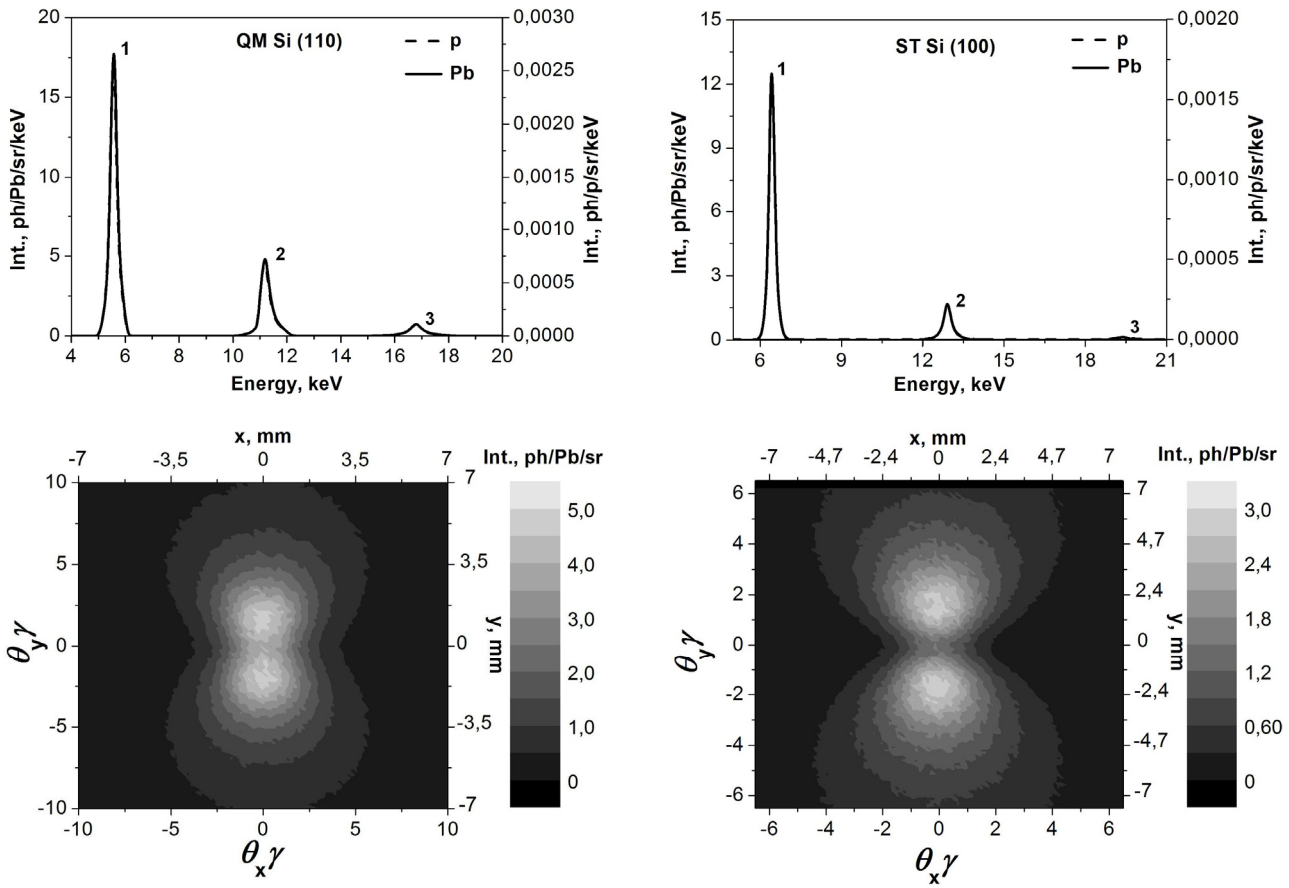

Figure 2: The spectra and angular distributions on the detector plane of the PXR from QM crystal (a) and ST crystal (b). Calculations were taking into account absorption in the crystal and the air.

CONCLUSION

The calculations of the spectral and angular characteristics of the PXR generated by Pb nuclei with an energy 158 GeV/u from planes (110) and (100) in the silicon deflectors were carried out. Expected values of the intensities are given in Table 1. As Table 1 shows intensity of PXR is about 2 ph/Pb/sr. Using a commercially available Si-PIN x-ray detector with a sensitive surface area about 10 mm^2 at a sufficiently distance from crystal about 100 cm the number of detected photons is equal to about 10^5 ph/cycle, which should allow to monitor the state and the orientation of

the deflector by means of the observation of the PXR spectrum characteristics.

Table 1: Simulation result

Reflex	Energy of maximum, (keV)	Intensity I, ph/Pb/sr	**FWHM, eV**
(220)	5.59	2.998	259
(440)	11.19	1.375	330
(660)	16.79	0.009	432
(400)	6.46	2.241	182
(600)	12.91	0.522	296
(800)	19.39	0.061	407

REFERENCES

[1] Afonin A.G. et al., Proton beam extraction by a short silicon crystal from the IHEP accelerator, (IHEP Preprint: Protvino, 2003), 49.
[2] A.G. Afonin, et al., Phys. Rev. Lett. 87 (2001) p. 094802.
[3] Gogolev A.S. et al., NIMB 266 (2008) p. 3876.
[4] M.L. Ter-Mikaelian, High Energy Electromagnetic Processes in Condensed Media, (New York: Wiley - Intersci., 1972) 300.
[5] G.M. Garibyan, Yan Shi, Zh. Eksp. Teor. Fiz. 61 (1971) p. 930.
[6] V.G. Baryshevsky, I.D. Feranchuk, Zh. Eksp. Teor. Fiz. 61 (1971) p. 947.
[7] A.N. Didenko et al., Phys. Lett. A 110 (1985) p. 177.
[8] A.V. Shchagin, X.K. Maruyama, Accelerator-Based Atomic Physics: Technique and Applications, (New York: AIP Press, 1997), 279.
[9] P. Rullhusen, X. Artru, P. Dhez, Novel Radiation Sources Using Relativistic Electrons, (Singapore: World Sci., 1998) 370.
[10] V.P. Afanasenko et al., Phys. Lett. A 170 (1992) p. 315.
[11] Yu.N. Adishchev et al., JETP Lett. 81 (2005) p. 241.
[12] Yu.N. Adishchev et al., NIMB 252 (2006) p. 111.
[13] W. Scandale et al., Phys. Lett. B 701 (2011) p. 180.
[14] H. Nitta, Phys. Rev. B 45 (1992) p. 7621.

RECENT DEVELOPMENT IN ECR ION SOURCES AT FLNR JINR

S.Bogomolov, V.Bekhterev, A.Efremov, B.Gikal, G.Gulbekian, Yu.Kostukhov, A.Lebedev, V.Loginov, N.Yazvitsky, JINR, Dubna, Russia

Abstract

In the Flerov Laboratory of Nuclear Reactions (JINR) the development of ion sources based on the plasma electrons heating at the frequency of electron cyclotron resonance (ECR) is stimulated by the necessity of the accelerator complex (U-400, U-400M and CI-100 cyclotrons) upgrading as well as by creation of the new high current cyclotrons for basic and applied research.

Several ECR ion sources have been operated in the Flerov Laboratory of Nuclear Reactions (JINR) supplying various ion species for the U400 and U400M cyclotrons correspondingly for experiments on the synthesis of heavy and exotic nuclei, using ion beams of stable and radioactive isotopes, for solid state physics experiments and polymer membrane fabrication. In this paper the new development concerned with modernization of ECR4M ion source, development of the new superconducting source DECRIS-SC2 and creation of the DECRIS-5 ion source for the DC-110 cyclotron complex will be presented.

INTRODUCTION

Main theme of FLNR JINR is super heavy elements research. From 2000 up to 2010 more then 40 isotopes of elements 112, 113, 114, 115, 116, 117, 118 were synthesized in the laboratory.

At present four isochronous cyclotrons: U-400, U-400M, U-200 and IC-100 are under operation at the JINR FLNR. Three of them are equipped with ECR ion sources. In the DRIBs project for production of accelerated exotic nuclides as ^{6}He, ^{8}He etc. the U-400M is used as radioactive beam generator and U-400 is used as a post-accelerator. Layout of FLNR accelerators complex is presented in Fig.1 [1]. Red stars indicate the location of the ECR ion sources.

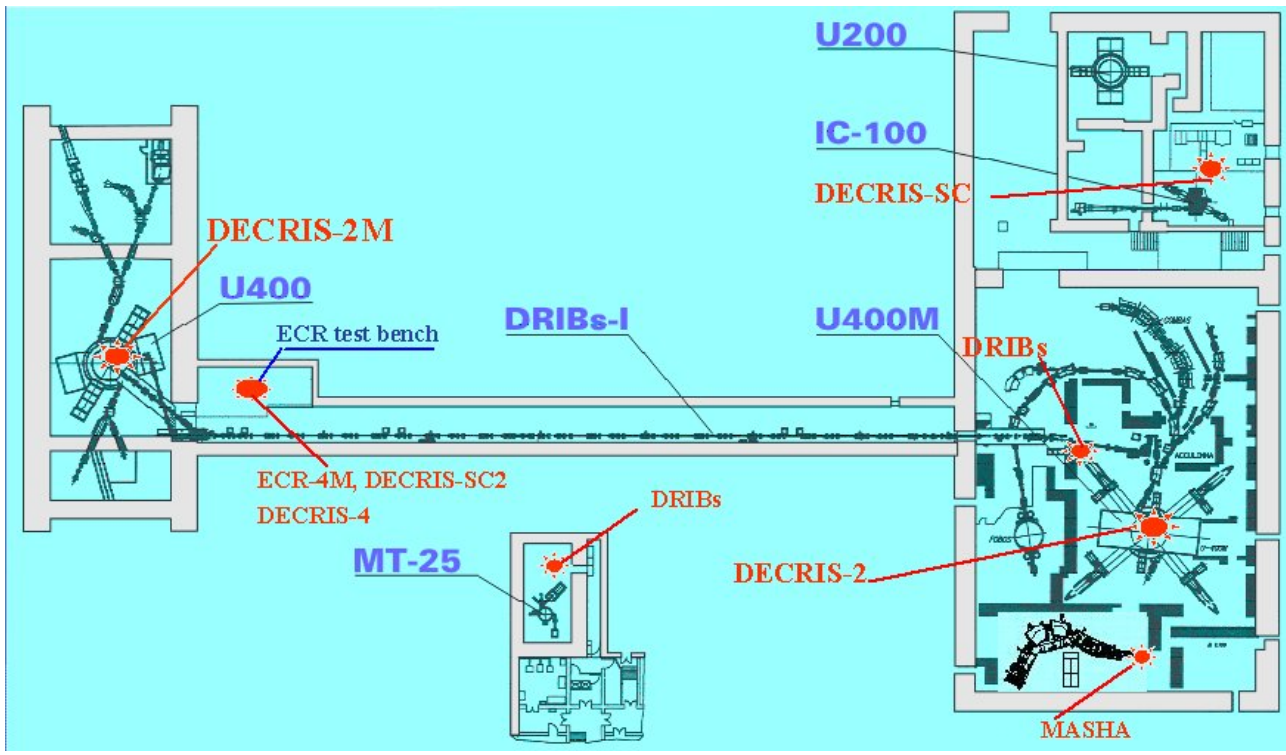

Figure 1: Layout of FLNR JINR accelerator complex. Red stars indicate the location of the ECR ion sources.

ECR4M ION SOURCE

The ECR4M source and the axial injection system were assembled and commissioned in 1996. First accelerated Ar beam was produced in November 1996 [2]. The main goal was to provide the intense beam of the ^{48}Ca ion beam for the experiments on synthesis of super heavy elements at a minimal consumption of this enriched and expensive isotope. First experiment on the synthesis of superheavy elements with the beam of ^{48}Ca was performed in November 1997. Since that about 66% of total operation time was used for acceleration $^{48}Ca^{5+,6+}$ ions for research

on synthesis and investigation of properties of new elements.

The modernization of the U400 axial injection, which included sharp shortening of the injection channel horizontal part, was performed. These changes allow us to increase the $^{48}Ca^{18+}$ ion intensity at the U400 output from 0.9 to 1.4 pμA

According to the plans of the reconstruction of the U400 cyclotron (U400R project [3]) the project of the modernization of the ECR4M source was developed and realised. This modernization include production of the higher magnetic field in the injection region by insertion an iron plug in the injection side; the increase of the plasma chamber diameter from 64 to 74 mm; waveguide UHF injection into plasma chamber. The modified magnetic structure of the ECR4M and the axial magnetic field distribution are shown at Fig.2 and Fig3 correspondingly.

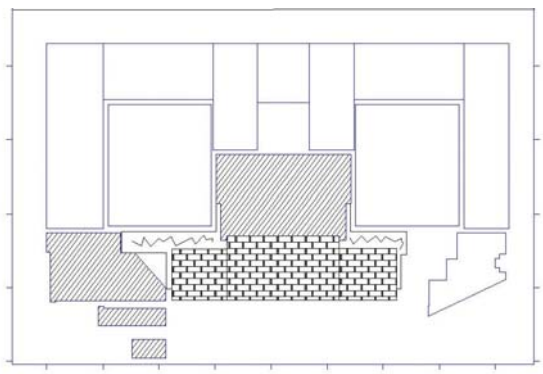

Figure 2: The modified magnetic structure of ECR4M source.

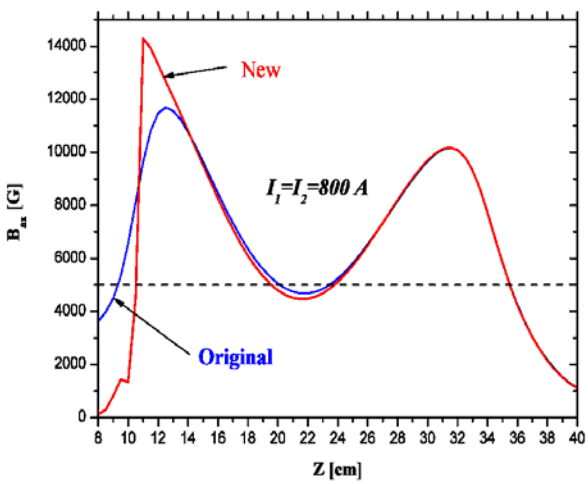

Figure 3: Axial magnetic field distribution of ECR4M source.

The modified ECR4M source was installed at the test bench, and after the tuning with Ar beam the experiments on production of Ca beam were performed. The same technique with the use of microoven and thin cylindrical Ta sheet placed inside the discharge chamber to prevent the condensation of metal at the chamber wall [4] was employed. The Ca spectrum optimized for production of Ca^{11+} is shown in Fig.4.

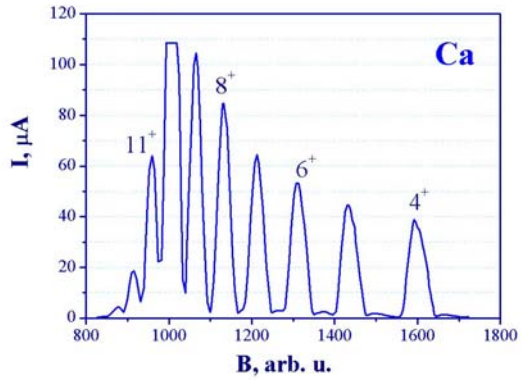

Figure 4: Calcium spectrum . The source tuning is optimized for production of Ca^{11+} ions.

After the tests with calcium beam the source was used for development of titanium beam using MIVOC method with $(CH_3)_5C_5Ti(CH_3)_3$ compound, first used by Jyvaskyla group [5]. The aim of these experiments is the production of intense ^{50}Ti ion beam for research on synthesis of superheavy elements.

During the experiments up to 80 μA of Ti^{5+} and up to 70 μA of Ti^{11+} ion beams were produced at different source tuning. Fig. 5 shows the titanium spectrum with the source tuning optimized for production of Ti^{11+} ions. The spectrum is obtained at the UHF power level about of 300 W.

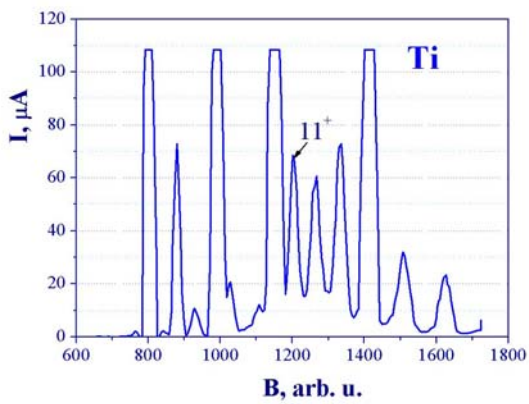

Figure 5: Titanium spectrum. The source tuning is optimized for production of Ti^{11+} ions.

DECRIS-SC2 ION SOURCE

Using the experience obtained during construction and operation of the DECRIS-SC [6] source the new source DECRIS-SC2 was developed [7]. The source is planned to be used at the U-400M cyclotron aiming the production of more intense ion beams in the mass range heavier than Ar. For ECR plasma heating the existing microwave system (14 GHz) will be used. Taking this into account the magnet system of the source was designed with the minimum magnetic field about of 0.4 T, maximum

magnetic field about of 1.4T and 1.9T in the injection and the extraction side correspondingly.

The design of the superconducting magnet system of the new source differs essentially from the previous source. To decrease the weight and dimensions of the system it was decided to produce the vacuum vessel from chromium plated soft steel, so it will simultaneously serves also as a magnetic yoke. The main parameters of the source are listed in the Table 1. The axial magnetic field distribution at different coils currents setting is shown at Fig. 6. The current of the middle coil was adjusted to keep the minimum constant. The radial magnetic field distribution is shown at Fig. 7.

Table 1: Main parameters of the DECRIS-SC2 ion source

UHF frequency	14 GHz
Injection side magnetic field	1.9 T
Extraction side magnetic field	1.4 T
Radial magnetic field	1.05 T
Hexapole structure (NdFeB)	24 sectors
Plasma chamber diameter	74 mm
Plasma chamber length	300 mm
Max. extraction voltage	30 kV

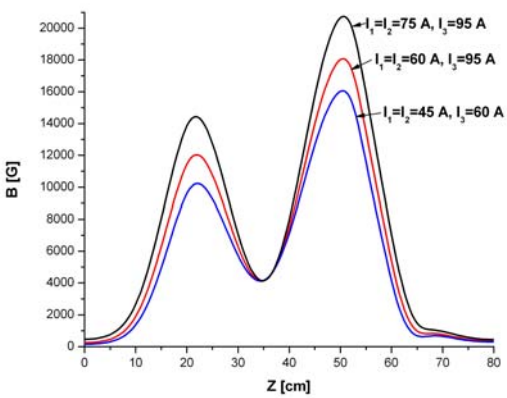

Figure 6: Axial magnetic field distribution of the DECRIS-SC2 source.

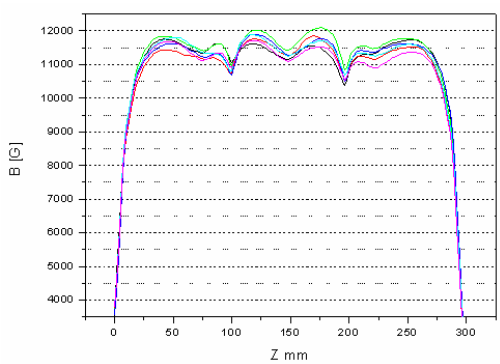

Figure 7: Radial magnetic field distribution of the DECRIS-SC2 source.

The source was tested at the test bench for production of gaseous ions from oxygen to xenon. For commissioning the traveling wave tube amplifier (TWTA) with the maximum output power of about 600 W was used to feed UHF power directly into the plasma chamber through the standard rectangular waveguide. With the one gap extraction system and a stainless steel puller the source can work without discharge at 25 kV. The transmission efficiency right until the Faraday cup installed after the analyzing magnet was estimated with an oxygen beam in the range of 40%–60% for the extraction voltage varied from 15 to 25 kV.

Generally, the operation of the DECRIS-SC2 ion source was very stable and reproducible. Biased disc and mixing gas effect were actively adopted to maximize the ion beam production. Fig. 8 shows the argon spectrum with the source tuning optimized for production of Ar^{11+} ions. The results obtained with the DECRIS-SC2 source during the tests are summarized in Table 2.

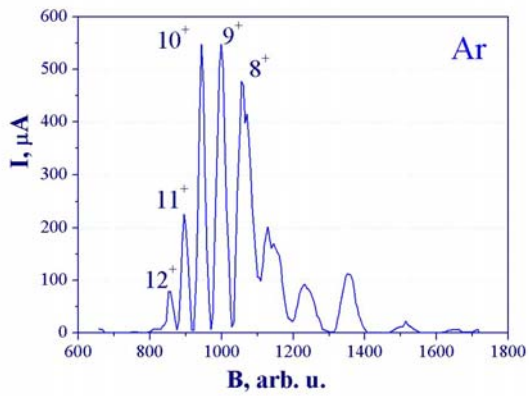

Figure 8: Argon spectrum. The source tuning is optimized for production of Ar^{11+} ions.

Table 2: Ion yields from the DECRIS-SC2 ion source

Ion	O	S	Ar	Kr	Xe
5+	920				
6+	820				
8+			880		
9+		265	680		
11+		90	250		
12+			120		
15+				250	
17+				150	
30+					~ 1

DECRIS-5 ION SOURCE FOR DC-110 CYCLOTRON COMPLEX

The project of the DC-110 [8] cyclotron facility to provide applied research in the nanotechnologies (track pore membranes, surface modifcation of materials, etc.) has been designed by the Flerov Laboratory of Nuclear Reactions of the Joint Institute for Nuclear Research (Dubna). The facility includes the isochronous cyclotron

DC-110 for accelerating the intensive Ar, Kr, Xe ion beams with 2.5 MeV/nucleon fixed energy. The cyclotron has 2m pole diameter, and to provide the energy of 2.5 Mev/nucleon the accelerated ions should have the mass to charge ratio about of A/Z = 6.6, that is $^{40}Ar^{6+}$, $^{86}Kr^{13+}$ and $^{132}Xe^{20+}$. The parameters of the source are determined mainly by required intensity of $^{132}Xe^{20+}$ ion beam (≥150 μA), and are listed in the Table 3.

Table 3: Main parameters of the DECRIS-5 ion source

UHF frequency	18 GHz
Injection side magnetic field	2.2 T
Extraction side magnetic field	1.35 T
Radial magnetic field	1.15 T
Hexapole structure (NdFeB)	36 sectors
Plasma chamber diameter	80 mm
Plasma chamber length	300 mm
Max. extraction voltage	30 kV
Maximal power consumption	160 kW

The magnetic system for creation of the axial magnetic field can be realized with copper coils, or with superconducting coils. In case of copper coils the power consumption of the magnetic system will be about of 150 kW, with superconducting coils – about of 10 kW. Taking into account the operating conditions (industrial operation) the use of copper coils was chosen.

Description of the source

The magnetic structure of the source is composed by three independent copper coils. The injection and extraction coils are enclosed in soft iron yokes. Soft iron plug is placed inside the discharge chamber. The scheme of the magnetic structure, and calculated axial magnetic field distribution are shown in the Fig. 9 and Fig. 10 correspondingly.

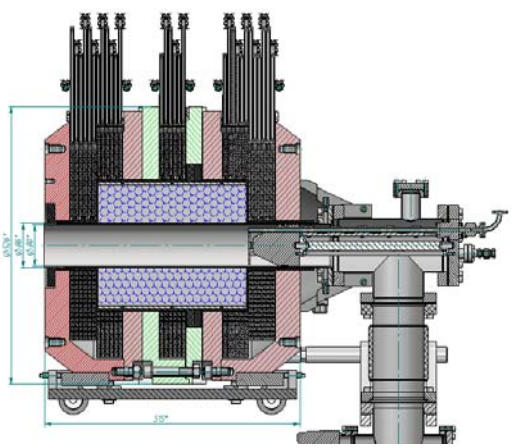

Figure 9: The scheme of magnetic structure of the DECRIS-5 ion source.

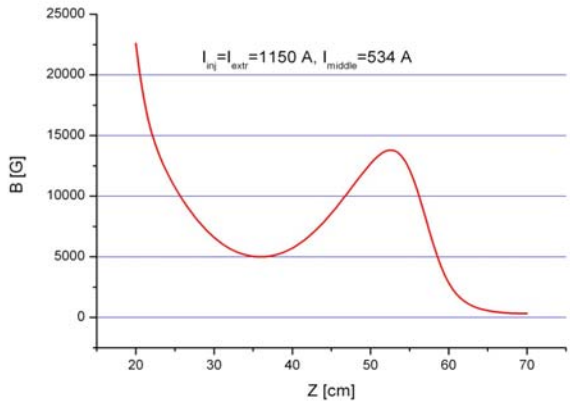

Figure 10: Axial magnetic field distribution of the DECRIS-5 ion source.

The maximal current of the power supplies for the injection and extraction coils is 1200 A, for the middle coil – 800 A. The power consumption of the coils is about 150 kW.

The radial magnetic field distribution is shown in the Fig. 11.

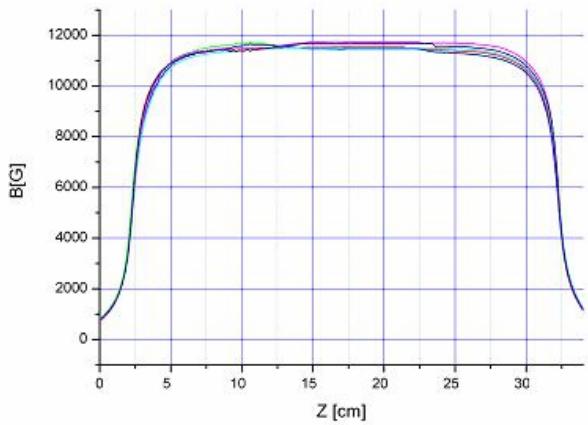

Figure 11: Radial magnetic field distribution of the DECRIS-5 ion source.

The stainless-steel plasma chamber of the source is made as a water-cooled double wall tube. The internal diameter of the plasma chamber is 80 mm. On the injection flange there are mounted soft iron plug, water cooled standard waveguide, gas feeding tubes. Biased electrode is mounted on the soft iron plug and is not cooled, as well as soft iron plug. The working gases (Ar, Kr, Xe) and support gas (O_2) are fed into the source chamber by two double channel piezoelectric valves.

The source is equipped with three electrode extraction system. The plasma electrode aperture is 10 mm in diameter, its position can be changed while the source is open. The negatively biased extraction electrode is water cooled, and position of the whole assembly can be adjusted manually without breaking vacuum.

Results of the test

The test of the source was performed during December 2011 – February 2012. For the test the source was assembled with the part of the axial injection beam line of DC-110 cyclotron (see Fig. 10). The main optical elements of the system are the analyzing magnet IM90, solenoid IS1 and two dipole correcting magnets ICM1 and ICM2. In the diagnostic box after analyzing magnet a Faraday cup, 30 mm diaphragm and luminophor screen are installed. All elements are movable with pneumatic actuators. The vacuum system provides background vacuum about of 2×10^{-8} torr in the extraction and diagnostics boxes.

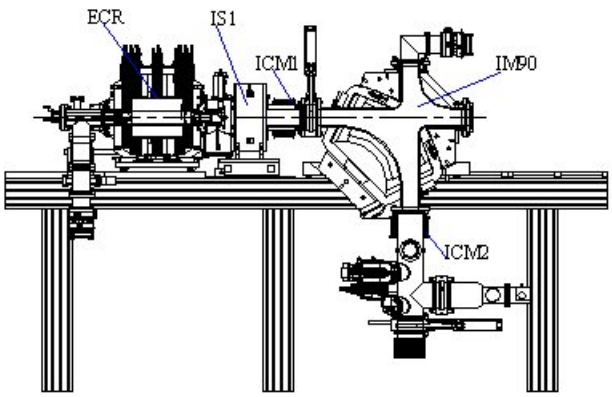

Figure 12: Axial injection system of the DC-110 cyclotron.

The ion source was tested for production of Ar, Kr and Xe ion beams. The production of required intensity of the Ar^{6+} beam (about of 100 μA) should present no problem. Therefore, to study the source performances the parameters of the source were tuned for production of higher charge states. Figure 11 shows the Ar spectr optimized Ar^{11+}. The results were obtained in the UHF power range lower than 700 W at 21÷22 kV extraction voltage.

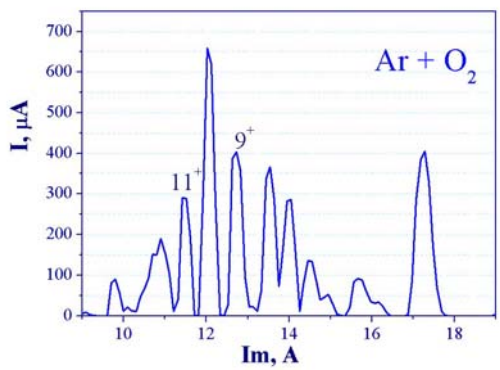

Figure 13: The Ar spectrum. The source tuning is optimized for production of Ar^{11+} ions

During the tests the operation of the DECRIS-5 ion source was very stable and reproducible. The results, obtained during the tests are summarized in Table 4.

Table 4: Ion yields from the DECRIS-5 ion source

Z	8+	9+	11+	15+	18+	19+	20+
Ar	1200	750	300				
Kr				325	182	120	70
Xe							220

SUMMARY

Over past years several types of ECR ion sources of **DECRIS** (**D**ubna **E**lectron **C**yclotron **R**esonance **I**on **S**ource) family were developed in FLNR (JINR). The progress in development of DECRIS sources is illustrated in Fig. 14.

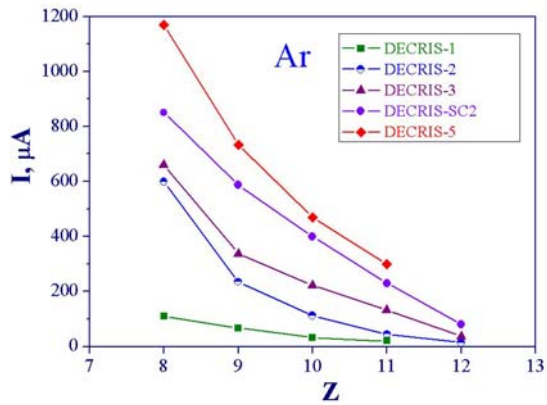

Figure 14: Comparison of Ar currents produced by DECRIS type ion sources.

REFERENCES

[1] S. Bogomolov et al. "Present Status of FLNR (JINR) ECR Ion Sources". Beam Dynamics Newsletter No. 53, December 2010, p.109 .

[2] Yu.Ts. Oganessian et al. "Axial injection system for the U-400 cyclotron with the ECR-4M ion source". JINR FLNR Scientific Report 1995 – 1996 Heavy Ion Physics. E7-97-206, Dubna 1997, p.270.

[3] G. Gulbekyan et al. "Development of FLNR JINR Heavy Ion accelerator Complex in the Next 7 Years. New DC-280 Cyclotron Project," IPAC2011, San Sebastian, Spain, September 2011, WEPS082, p. 2700 (2011); http://www.JACoW.org.

[4] V. Kutner et al. "Production of intense ^{48}Ca ion beam at the U-400 cyclotron". Rev. Sci.Instrum. 71, p.860, 2000.

[5] H. Koivisto et al. "Production of titanium ion beams in an ECR ion source" NIM B, 187 (2002), p.111

[6] A. Efremov et al. "Status of the ion source DECRIS-SC". Rev. Sci. Instr. V. 77, P.235, No.03A320, 2006.

[7] A. Efremov et al. "The preliminary tests of the superconducting electron cyclotron resonance ion source DECRIS-SC2". Rev. Sci. Instr. 83, 02A334 (2012).

[8] B. N. Gikal et al. "The Project of the DC-110 Heavy Ion Cyclotron for Industrial Application and Applied Research in the Nanotechnology Field" Physics of Particles and Nuclei Letters, 2010, Vol. 7, No. 7, p. 891.

STATUS REPOTR ON PHYSICS RESEARCH AND TECHNOLOGY DEVELOPMENTS OF ELECTRON STRING ION SOURCES OF MULTICHARGED IONS

A.Yu. Boytsov, S.V. Gudkov, D.E. Donets, E.D. Donets, E.E. Donets, A.Yu. Ramsdorf, V.V. Salnikov and V.B. Shutov, Laboratory of High Energy Physics, Joint Institute for Nuclear Research, Dubna, 141980, Russia

Abstract

Electron String Ion Source (ESIS) "Krion-2" (JINR) is the first and now only ion source of such type in the world. ESIS is a sophisticated modification of Electron Beam Ion Source (EBIS) working in a reflex mode of operation under very specific conditions. Using the results of the research and the technology development the following main results were achieved in JINR with Krion-2 ESIS during recent years: Au^{54+} ion beams with intensity $5x10^7$ particle per pulse were first produced and ion-ion cooling technology was demonstrated to prove its efficiency for a thermal ion loss reduction; Krion-2 was used for production and injection of Xe^{42+} ion beam into LINAC injector of JINR synchrotron Nuclotron, where the beam was first accelerated to relativistic energy in March 2010 [1-3].

At the present time an essential progress was achieved in construction of the new 6 Tesla ESIS, which is expected to be the full scale prototype of a highly charged ion source for NICA - the new JINR accelerator complex. It is foreseen in the NICA project that new ESIS will provide Au^{32+} beams with the ion yield about $2x10^9$ ppp. However, a project parameters of new Krion-6T(esla) ion source allow to expect production of even more highly charged states of heavy elements, up to Au^{69+} in terms of gold. In this case the new Krion-6T ESIS may be used on operating JINR "Nuclotron" facility in near future for experiments with an extracted accelerated gold ion beams on a fixed target.

INTRODUCTION

Electron string phenomenon occurs during the reflex mode of EBIS operation. The interest in the studies of reflex mode operation was motivated by an attractive possibility to decrease the power of the electron beam by a hundred times while simultaneously preserving the same ion yield. Indeed, the power of the electron beam in a direct mode can reach many hundreds of KW that provides serious technical obstacles for a successful realization.

The study of the reflex mode of EBIS operation was initiated in JINR in 1994. These research were performed with use of JINR EBIS Krion-2. The reflex mode of EBIS operation is realized by using the specially designed electron gun and electron reflector that allows multiple use of beam electrons. The electrons do not reach electron collector after one pass through the drift space of the source (1.2 m long). Usually emitter has a negative voltage of few KV, anodes and drift tube structure are at ground potential, and the reflector has negative voltage few KV lower than the emitter. As a result, the emitted electrons after one path are reflected back towards the emitter side and then are reflected again in a vicinity of the emitter and so on. The emitter and reflector are placed in a fringe magnetic field (in a region of about 1/20 of a maximal magnetic field) hence each electron reflection is accompanied by some transformation of the longitudinal electron velocity to the radial/azimuthal velocity. As a result, the electrons are accumulated in a drift tube space of the source. The stored multiply reflected electrons can be used for highly charged ions production similarly to the beam electrons.

An unknown phenomenon was unexpectedly observed in JINR in 1994, which became a key physics ingredient of the proposed EBIS development in the reflex mode of operation. It was found that under certain conditions one component pure electron plasma, which consists of the multiply reflected electrons, confined in a strong solenoid magnetic field, exhibits a stepwise increase of the confined electron plasma density in a new steady state called "electron string". The transition usually goes via an unstable pre-string state in which the electron energy spectrum expands, which further suppresses the instability.

The electron string can arise if a definite number of electrons which exceeds some threshold value is stored in the source drift tube space. This threshold value depends on various parameters such as the electron injection energy, the applied magnetic field strength, the magnetic compression of the injected electron beam and so on. Electron strings are occurred to be stable in a certain frames that allows to use them for an effective production of highly charged ions in Electron String Ion Sources (ESIS), similarly to electron beams in EBIS.

An interesting observed feature of electron strings is a high energy tail in a total electron energy distribution. For example, for electrons with injection energy 3 KeV, this tail extends up to 5 KeV , see [1] and refs therein.

HIGHLY CHARGED ION BEAMS PRODUCED WITH KRION-2

Kr and Xe Highly Charged Ions

Production of highly charged Kr and Xe ion beams has been done in a framework of preparing Krion-2 ESIS for the Nuclotron run. Nuclotron – superconducting synchrotron which includes Linac LU-20 as a part of its injection complex. LU-20 accepts highly charged ions

with charge to mass ratio q/A ≥ 1/3 which determines lower boundary of charge states for all possibly accepted ions; for example q = 28+ for ^{84}Kr and q = 41+ for ^{124}Xe. Binding energy of the external electron for Kr^{27+} ion is equal to 3,2 KeV and for Xe^{40+} ion − 3.0 KeV.

Because of technical limitations of injected electrons energy only up to 5,0 KeV the well known for EBITs energy recuperation mode was proposed and used first in Electron String Ion Source. In order to realize the method of energy recuperation, main part of the Krion-2 drift tube structure was lifted up to +1.5 KV. Electrons which are injected by the electron gun with injection energy, say, 4.5 KeV, get additional acceleration in a gap between gun anode sections (at ground potential) and first drift tube section which is at +1.5 KV potential. So, string electrons should get energy about 6,0 KeV along the ion trap. After one pass through the drift tube structure electrons decelerate down to the energy 4.5 KeV at the gap between the last drift tube section (at +1.5 KV voltage) and the reflector anode, which is also at ground potential.

As a result, accumulated string electrons, being multiply reflected from the repeller and the gun electrodes, have energy on 1.5 KeV higher at the ionization trap region. It was shown experimentally that electron strings retain all their main features under such conditions, hence energy recuperation could be efficiently used in electron string mode of ESIS operation. Moreover, electron strings with energy recuperation are stable and can be used for highly charged ions production during long confinement time.

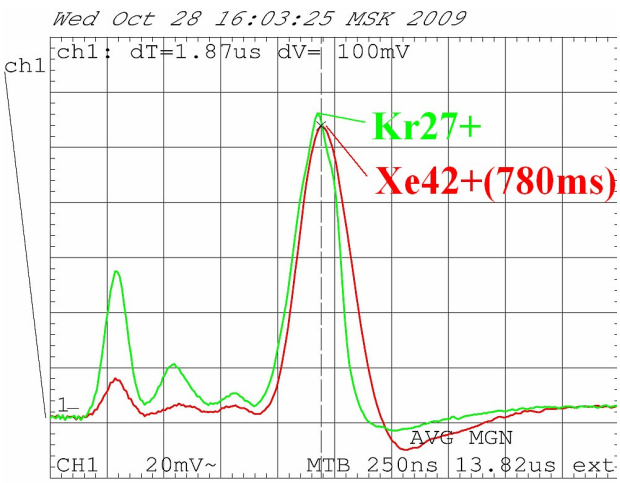

Figure 1: TOF spectra (arb. units) of Xe (natural mixture of isotopes) and Kr highly charged ions, produced with Krion-2 ESIS during 780 ms of ionization.

We used purely separated isotope ^{84}Kr in this experiments that allowed us to get enough resolution to identify definite charge states. During the experiments we did not have purely separated Xe isotope so a natural mixture of Xe isotopes was used. As a result, definite Xe charge state lines have not been resolved. We used TOF calibration based on the identified ^{84}Kr charge state lines positions. TOF spectrum for natural mixture of Xe isotopes is presented on Fig.1 together with ^{84}Kr spectrum, obtained at the same conditions. One can see that the maximum intensity corresponds to Xe^{42+} charge state. This charge state has been chosen for further acceleration by Nuclotron. Note, ionization time for Xe ions to get Xe^{42+} charge state was about 750 ÷ 950 ms that is acceptable for Nuclotron acceleration regime.

One can summarize ion yield produced by Krion-2 ESIS on HV platform of the Linac during Nuclotron run at February-March 2010 as follows:

- $^{84}Kr^{28+}$ $3.5\cdot10^7$ ions per pulse 7 μs duration,
- **$^{84}Kr^{29+}$ $3.2\cdot10^7$** ions per pulse 7 μs duration,
- $^{84}Kr^{30+}$ $3.0\cdot10^7$ ions per pulse 7 μs duration,
- $^{124}Xe^{41+}$ $3.0\cdot10^7$ ions per pulse 7 μs duration,
- **$^{124}Xe^{42+}$ $3.0\cdot10^7$** ions per pulse 7 μs duration,
- $^{124}Xe^{43+}$ $2.7\cdot10^7$ ions per pulse 7 μs duration,
- $^{124}Xe^{44+}$ $1.5\cdot10^7$ ions per pulse 7 μs duration.

Au Highly Charged Ions

The scheme of internal injection of gold atoms into the working space of the Krion-2 ESIS is based on evaporation of Au atoms from the surface of tungsten wire by pulse electric current heating. We used a gold plated tungsten wire of 0.05 mm in diameter. The wire was installed in the specially designed cell in the vicinity of the working space of the ESIS, few mm away from the axis. The cell volume was separated from the drift tube space by the stainless steel grid with 70 % transparency.

As it was noted before the electron injection energy in Krion-2 ESIS can not be more than 5,0 KeV because of technical reasons. So, Au^{51+} was a maximal charge state reachable at such conditions. There is a considerable gap in binding energies between the last electron in N-shell (2.96 KeV for $Au^{51+)}$ and the next M-shell: 4.89 KeV for Au^{52+}, 5.04 KeV for Au^{53+}5.32 KeV for Au^{54+} et cetera…

We still had no possibility to increase the electron injection energy higher than 5.0 KV, however, it became possible to overcome this limit by lifting the drift tube structure up to +1.5 KV and using the energy recuperation mode of operation.

These experiments have been done during December 2009. Electron injection energy was 4.8 ÷ 5.0 KV and the drift tube structure was lifted up to 1.5 KV as well. Typical TOF spectrum of gold ions after 1500 ms of ionization is presented in Fig.2, where mean charge state in its maximum corresponds to $Au^{54.17+}$ [1].

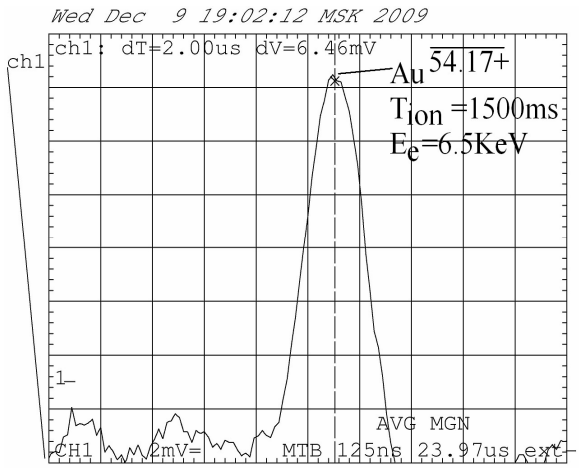

Figure 2: TOF spectrum (in arbitrary units) of the gold HCI beam extracted from Krion-2 ESIS after 1500 ms of the ionization. Mean charge state is equal to 54,17+.

In the Table 1. the parameters and the sorts of produced ions of existing ion source Krion-2 are listed.

Table 1: Krion-2 parameters and produced ions

	Fe^{24+} Nuclotron 2003	Au^{32+} stand	Au^{51+} stand 2007	Au^{54+} stand 2010	$Xe+^{42}$ Nuclotron 2010
Binding energy E_b, keV	2.05	1.21	2.96	5.32	3.07
Electron injection energy, keV	4.0	4.0	5.0	6.5	6.5
Ionization time τ, s	1.5	2×10^{-2}	1.0	1.5	1.5
Repetition rate, Hz	0.5	40	1.0	0.67	0.67
Extraction time t, 10^{-6} s	8	8	8	8	8
N_i per pulse	1×10^8	5×10^8	1×10^8	1×10^7	3×10^7

PULSE INJECTION OF GASEOUS SPECIES IN E-STRING

A specially designed cryogenic cell has been elaborated and successfully tested for pulse injection of gaseous species. The cell consists of a cylindrical chamber which is situated in the vicinity of the working space of the ESIS, 1 cm away from the axis. The chamber is placed at 78 K temperature terminal. This provides an efficient reflection of CH_4,N_2,O_2, and CO molecules and of Ar, Kr, Xe, and possibly Rn atoms from the chamber walls. The chamber has two orifices: one is being opened in order to load the portion of working gas from the outside, and the second one is always opened and it is designed to connect the chamber with the working space of ESIS through a thin pipe of 0.5 mm diameter and of 3.0 mm length. The pipe is kept at 78 K for an efficient transportation of gases.

The key element of the cell is the copper rod of 2.5 mm diameter and of 90 mm length, located on the axis of the chamber and connected to 4.2 K terminal of the ion source. The rod is supported with thermoinsulated flanges of the cell cylinder. The rod has the sandwich-type electroinsulating-conducting layers so that the conducting one may be heated by a current pulse. The cell operates as follows. A working or coolant gas portion, transported from the outside, is frozen on the rod surface. Due to electric pulse the rod surface is heated during 1–2 ms from 4.2 K up to 40–60 K and all the frozen gas leave the rod surface. The resulting gas pressure at this temperature provides penetration of about 10^{10} molecules or atoms into the drift tube space of the ESIS during 2–5 ms. After switching off the electrical current through the conduction layer the temperature of the rod surface is relaxed down to the 4.2 K during a few milliseconds as well and all the rest gas is frozen again at the rod surface. Then the injection pulses can be repeated with necessary repetition rate.

The cell construction was simulated and optimized numerically with use of all available information about the material properties versus temperature in the range of 4.2–78 K where all these dependencies are very strong. Experimentally it was proven that for nitrogen the elaborated cryogenic cell provides pulse injection with the shortest pulse duration equal to 3 ms and for methane 5 ms [2]. The cell has been successfully tested and used for pulse injection of CH_4, N_2, Ar, Kr, and Xe in e-string of the ion source. As an example in Fig. 3, the Ar ion current pulse is presented [3].

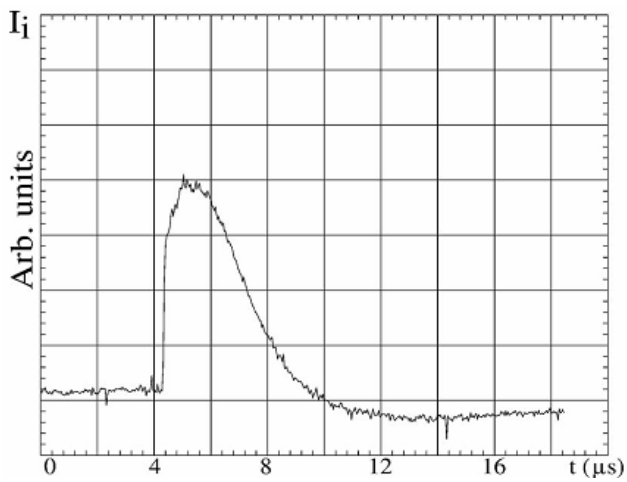

Figure 3: Ar ion current pulse obtained using the cryogenic cell.

CONVERSION EFFICIENCY OF GASEOUS SPECIES TO ION BEAM

There can be cases, when conversion efficiencies of gaseous species to ion beams are of a great importance. Conversion efficiency of radioactive $^{11}CH_4$ to $^{11}C^{4+}$ ion beam is one of the cases. Development of the cell for gas pulse injection allowed us to measure this efficiency for Krion-2 using non-radioactive methane. The efficiency appeared to be rather high, but inexplicable spread of results from 4.2% to 19% in various experiments requires a further research [3].

ION-ION COOLING

We consider ion-ion cooling technology as a powerful mean for decreasing of ion losses during ionization. There fore, we began systematic studies of the cooling with a goal to find the best coolant for various heavy ions. The first pair was Kr injected from the described above cryogenic cell and continuously injected CH_4 – the lightest coolant. In Fig. 4 we show the rather large effect of ion–ion cooling in production Kr^{27+} during 155 ms confinement [3].

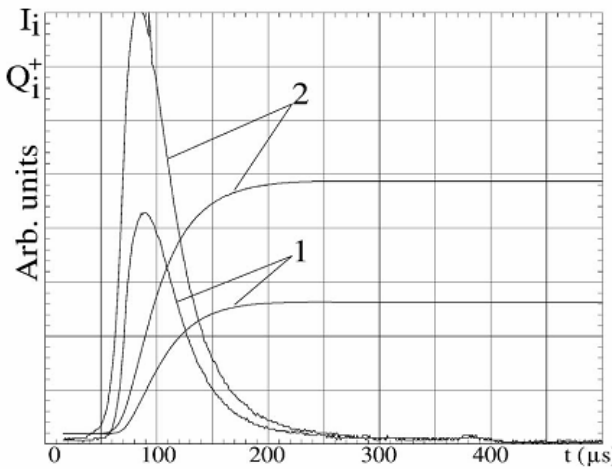

Figure 4: Kr^{27+} ion pulses: 1 – cooling "off"; 2 – cooling "on."

For Au^{51+} ions we have tried first CO, desorbing from the gold plated tungsten wire, as the gas for coolant ions. Fig. 5 illustrates the benefit of the ion-ion cooling in terms of ion yield under various time of coolant gas injection. Total ionization time is T_i=700 ms. The injection time for cooling gas, as shown on corresponding curves, T_c =150 ms, T_c =450 ms, T_c =550 ms, and T_c =650 ms.

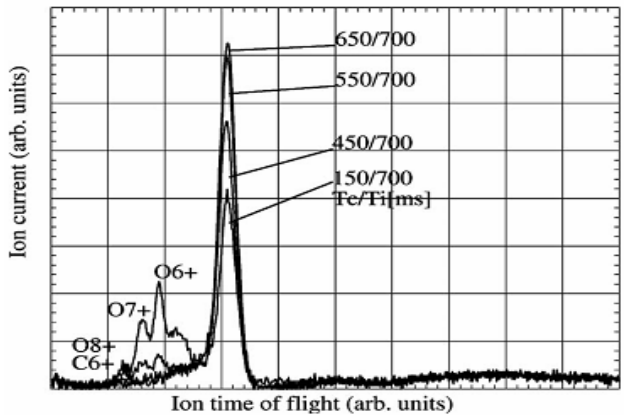

Figure 5: Au ion yield and TOF spectra for various injection time of the cooling CO gas.

The ion yield has been measured in the Faraday cup, located behind the last section of the TOF spectrometer. Because of several grids along the spectrometer only some fraction about 40% of the total ion beam was passed through the spectrometer structure and was measured. The measured fraction of ion yield is definitely proportional to the total produced ion yield. Hence Fig. 5 gives an adequate impression on a benefit of the ion-ion cooling. The total maximal number of the produced Au^{51+} ions was about 10^8 per pulse [2].

CONSTRUCTION OF NEW 6 TESLA ESIS: CURRENT STATUS

The ion source of ESIS-type, named Krion-6, is expected to be one of the ion sources JINR NICA project. Krion-6 is currently under construction with the following project parameters: 6 T superconducting solenoid of 1,2 m length and electron injection energy range of up 25.0 KeV. Expected main parameters of new ion source are presented in the Table 2.

Table 2: Krion-6 expected main parameters in terms of Au^{31+} ions, planned for NICA injector.

Working element/charge state	Au^{31+}
Expected ion yield N_i (number of $^{Au31+}$ ions in pulse)	$2\div4 \times 10^9$
Repetition rate	50 ÷ 60 Hz
Extraction time form the ESIS	$8 \div 30 \times 10^{-6}$ s
RMS emittance	0.6 π mm mrad (for 8×10^{-6} s extraction time); 0.15 π mm mrad (for 30×10^{-6} s extraction time).
Peak current in pulse	up to 10 mA

We expect to get 2 ÷ 8 times increased ion yield with our new Krion-6T ESIS in comparison to Krion-2 ESIS. Our optimistic expectations (8 times) on ion yield increase are inspired by the observed earlier ion yield N_i growth in ESIS $Ni \sim B^3$, where B is an applied solenoid magnetic field of the ion source. This almost cubic dependence on the magnetic field was measured in a range 2.8 ÷ 3.3 T with Krion-2 ESIS and we hope this growth will continue up to 6 T magnetic field as well.

The vacuum system of the source was constructed and tested. The winding device to manufacture 6 T solenoid of a perfect symmetry magnetic field was constructed and three test solenoids of 20 cm length have been manufactured to proof the manufacturing technology. We have reached 7.15 T, 7.4 T and 7.8 T maximal magnetic field correspondingly for these test solenoids, tested in a liquid helium filled cryostat. The obtained currents/magnetic fields are occurred to be just in a short vicinity (and even exceeded) of the corresponding critical currents for short pieces according to the superconducting wire manufacturer data.

The full-scale solenoid for Krion-6 facility was manufactured in JINR and its field symmetry test is done. The test was performed at room temperature with current about 100 mA. Magnetic field sensors was installed near the ends of the solenoid, where the symmetry of the field is worse than in the middle part of the solenoid. The maximal asymmetry in different azimuthal positions on the first side was 0,23%, on the second side 0.16%. This asymmetry past to the sufficient magnetic field quality needed for the ion source operation. The symmetry in the middle part is much better then at the ends.

The solenoid and a passive quench protection system were installed and cryomagnetic tests were done. Maximal reached magnetic field was 5.44 T using the current 105 A at October 04, 2012. After assembling of an active quench protection system further tests at higher magnetic field up to 6 T and more, we hope, will be possible.

As we already noted, it is foreseen in the NICA project that new ESIS will provide Au^{31+} beams with ion yield about $2x10^9$ ppp. However, a project parameters of new Krion-6T(esla) ion source allow to expect production of even more highly charged states of heavy elements, up to Au^{69+} in terms of gold. In this case new Krion-6T ESIS is planned to be used on operating JINR "Nuclotron" facility in near future for experiments with an extracted accelerated gold ion beams on a fixed target.

ACKNOWLEDGMENTS

We want to thank our colleagues from Laboratory of High Energy Physics, JINR for fruitful collaboration on various research and technological tasks related to the ion sources development: A.V. Butenko, A.R. Galimov, A.I. Govorov, I.K. Djakupov, V.M. Drobin, A.P. Dergunov, A.K. Kaminsky A.D. Kovalenko, L.V. Kutuzova, H. Malinowski, V.A. Monchinsky, S.N. Sedych, and G.V. Trubnikov. Helpful discussions with Leif Liljeby (MSL, Stockholms University), Reinard Becker (IAP, Frankfurt University; Scientific Software Service), Oliver Kester (GSI, IAP Frankfurt University), K.Noda, T. Homma, K.Katagiri (NIRS, Chiba, Japan) are greatly acknowledged. Work were supported in part by JINR-BMBF (Germany) grant "Ion source development" 2009-2012, by JINR-South Africa grant "Ion source" 2010-2012, and by RFBR Grant 11-01-00278.

REFERENCES

[1] D.E. Donets, E.D. Donets, E.D. Donets, V.V. Salnikov and V.B. Shutov,, "Production of highly charged ion beams Kr^{32+}, Xe^{44+} and Au^{54+} with ESIS Krion-2 and corresponding basic and applied studies", 2010 JINST **5** C09001; http://iopscience.iop.org/1748-0221/5/09/C09001

[2] D.E. Donets, E.D. Donets, E.E Donets, V.V. Salnikov and V.B. Shutov, "Production and ion-ion cooling of highly charged ions in Electron String Ion Source", Rev. Sci. Instrum. **80,** 063304 (2009).

[3] D.E. Donets, E.E. Donets, T. Honma, K. Noda, A.Yu. Ramsdorf, V.V. Salnikov, V.B. Shutov and E.D. Donets, "Physics research and technology development of electron string ion sources", Rev. Sci. Instrum. **83**, 02A512 (2012).

PROGRESS IN THE NEGATIVE ION SOURCES DEVELOPMENT

Vadim Dudnikov#, Muons, Inc., 552 N. Batavia Ave., Batavia, IL 60510 USA

Abstract

Recent progress in development of advanced negative ion sources was connected with optimization of cesiation in surface plasma sources (SPS). The cesiation effect, a significant enhancement of negative ion emission from gas discharges with decrease of co-extracted electron current below negative ion current, was observed for the first time in 1971 by placing into the discharge a compound with one milligram of cesium. Subsequent developments of SPS for highly efficient negative ion production caused by the interaction of plasma particles with electrodes on which the adsorbed cesium reduced the surface work-function are described. In the last 40 years, the intensity of negative ion beams has increased by cesiation up to 10^4 times from three milliamp to tens of Amperes.

INTRODUCTION

One practical result of the development of high brightness surface plasma negative ion sources with cesiation (SPS) [1-4] is the wide use of charge-exchange injection in circular accelerators for routine operation[5,6]. Now SPS are "working horses" for large accelerator complexes at ORNL (SNS Spallation Neutron Source, Oak Ridge National Laboratory), FNAL (Fermi National Accelerator Laboratory), LANSCE (Los Alamos Neutron Science Center), BNL (Brookhaven National Laboratory), RAL (ISIS proton synchrotron at the Rutherford Appleton Laboratory), DESY (Deutsches Elektronen-Synchrotron), KEK/J-PARC (Japan Proton Accelerator Research Complex), and other accelerators.

The efficiency and operational reliability of these sources have determined the productivity of these laboratories and their big machines. Many results of high energy physics were discovered using negative ion sources. The development of high brightness H^- sources was first stimulated by successful high current proton beam accumulation using charge-exchange injection [4] and further supported by the interest in particle beam weapons as part of the "Star Wars"[3,4] program. The testing of H^- beam acceleration and neutralization in space (The Beam Experiment Aboard Rocket (BEAR)) considered in [3]. Military uses and classified work caused long delays of first publications, but nonofficial communication was relatively fast. Until 1971, the main attention was concentrated on charge-exchange ion sources because there was no hope to extract more than 5 mA of H^- directly from plasma.

The cesiation effect, a significant enhancement of negative ion emission from a gas discharge with decrease of co-extracted electron current below negative ion current, was observed for the first time in 1971 by placing into the discharge a compound with one milligram of cesium at the Institute of Nuclear Physics (INP), Novosibirsk, Russia [1].

This observation, considered in review [4], was further developed and understood as on principle new surface plasma method of negative ion production. In the patent application [1] it was stated: "a method of negative ion production in gas discharges, comprising adding into the discharge an admixture of substance with a low ionization potential such as cesium, for example, for enhancement of negative ion formation".

In subsequent experiments it was demonstrated that cesium adsorption decreases the surface work function from 4-5 eV to ~1.5 eV, which enhances secondary emission of negative ions caused by the interaction of the plasma with the electrode surface and thereby enhances surface plasma generation (SPG) of negative ions. Ion sources based on this process have been named Surface-Plasma Sources (SPS). The theoretical explanation of this enhancement of negative ion emission by cesiation was presented by Kishinevsky [4]. A small admixture of cesium or other impurity with low ionization potential (ILIP) in the gas discharge significantly improves H^- production. When done correctly, a cesiated SPS works very well [1-4] . However, improper cesiation can complicate ion source operation. For example, injection of too much cesium can cause the discharge to become unstable and sparking occurs in the extractor with loss of stable ion source operation. With low cesium concentration the efficiency of negative ion production is too low. With "proper" cesiation the efficiency of negative ion production is high and extended ion source operation is stable.

Further development of SPS was conducted by collaboration of Belchenko, Dimov, and Dudnikov . The development of the first high brightness SPS for accelerators was presented in[4]. The Semiplanatron SPS with efficient geometrical focusing has been developed by the author [3]. The development and adaptation of SPS started soon after in many USA laboratories, in Europe, and in Japan. A very active program of SPS development was established in BNL by Sluyters and Prelec. BNL Symposiums for Production and Neutralization of Negative Ions and the European Workshops on Production and application of Light Negative Ions Beams were established. Physical principles of SPS operation were presented in [2-4] and were reproduced in many reviews and books. Good reviews of SPS for accelerators were presented in reports of Peters. The development of high brightness SPS by Allison's group in LANL is considered in[3]. The development of high current SPS (tens of Amperes) for thermonuclear plasma heating was conducted by teams at LBNL and in Japan which is still in progress and is used in large tokamaks and stellarators[4]. Production of polarized negative ions by

#vadim@muonsinc.com

charge-exchange with a slow negative ions in SPS has been proposed by the author and has been successfully realized in colaboration with Belov [4].

Heavy negative ion SPS for technology applications has been successful[4], but it is still necessary to improve the DC SPS for heavy negative ion production to meet the broad requirements of many industrial applications. A DC SPS for long term operation with accelerators has been developed by a BINP team[4]. Cesiated SPS with RF discharges for accelerators and for Neutral Beam Injectors (NBI) were significantly improved recently by the SNS ion source group and by the IPP (Max-Planck-Institut für Plasmaphysik) team.

FEATURES OF SPS

Many versions of SPS have been developed and optimized for different applications[2-4]. Cesium admixtures enhance negative ion formation in all types of discharges, but the most efficient negative ion production and highest beam quality is attained using an SPS that is optimized for a desired application. Some basic discharge configurations of compact SPS (CSPS) are presented in Fig. 1.

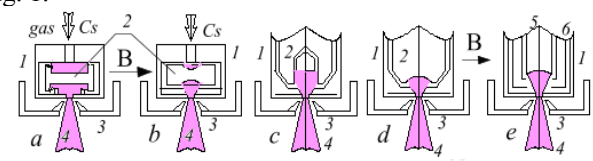

Figure 1:: Schematic diagrams of the basic versions of CSPS.: a) plain magnetron (planotron); b) magnetrons with focusing; c) Penning discharge SPS; d) semiplanotrons; e) hollow cathode SPS

Fig. 1 shows: a) plain magnetron (planotron); b) magnetrons with geometrical focusing; c) Penning discharge SPS (Dudnikov type source) was adopted for injection into ISIS; d) semiplanotron; e) hollow cathode SPS. The main components of SPS are: 1-anode (gas discharge chamber); 2-cold cathode-emitter; 3-extractor with magnetic system; 4-ion beam; 5-biased emitter; 6-hollow cathode; 7-filaments; 8-multi-cusp magnetic wall; 9-rf coil; 10-magnetic filter. The CSPS shown in Fig. 1 use a cold cathode glow discharge in a crossed *ExB* field. These CSPS have high plasma density (up to 10^{14} cm^{-3}), high emission current density of negative ions (up to 8 A/cm^2), small (1–5 mm) gap between cathode emitter (2) and a small extraction aperture in the anode (1). They are very simple, have high energy efficiency (up to 100 mA/kW of discharge) and have a high gas efficiency (up to 30%) using pulsed valves. CSPSs are very good for pulsed operation but electrode power density is often too high for dc operation. However, CSPS were successfully adopted for DC operation with emission current density ~300 mA/cm^2 in and up to 1 A/cm^2 .A different situation is typical for the large volume SPS (LV SPS) with discharge volume up to hundred of liters, presented in Fig. 2. The first LV SPS (*a*) was developed at the Lawrence Berkeley National Laboratory (LBNL). The gap between the emitter (5) and extractor aperture is very large (8–12 cm) and the plasma and gas density must be kept low to prevent negative ion destruction. In the LV SPS, hot filaments (7), RF coils (9), or microwave discharge and multicusp magnets (8) are used for plasma generation at low gas density.

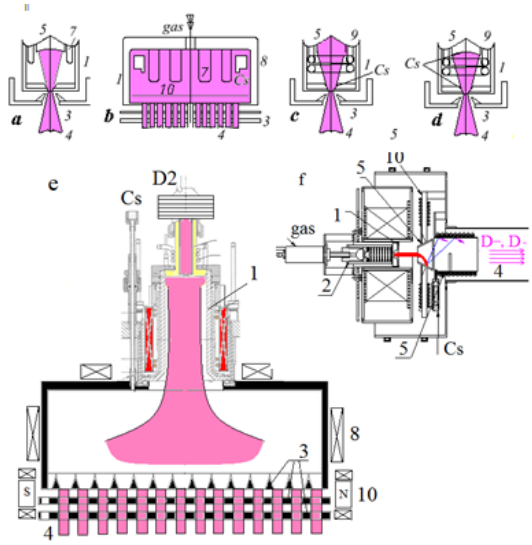

Figure 2: Schematic diagram of the basic versions of LV SPS.

LV SPS have a low power density and can be used for dc operation. Emission current density is below 100 mA/cm^2 and the brightness is not so high. LV SPS with production of negative ions on the plasma grid surface (anode production) on Fig. 2(b) were adopted for high current (up to 40 A) negative ion beam production for plasma heating by NBI. LV SPS for accelerators with RF discharges generated by solenoid internal antennae is shown in Fig. 2 (c). Some versions of LV SPS (d) with emitter (5) were adapted for heavy negative ion production. LV SPS for NBI with RF discharges generated by solenoid external antennae or by saddle antennae with longitudinal magnetic field are shown in Fig. 2 (e). Version (f) is used in polarized H^-/D^- sources.

The efficiency of negative ion formation depends very much on the catalytic property of the surface, mainly the work function. For enhanced negative ion formation in SPS, an admixture of substances with low ionization energy, such as alkaline or alkaline earth elements or compounds are used. The most efficient is the addition of cesium. Still, the surface work function and catalytic properties of the surface for negative ion formation depend on many parameters, including surface-cesium concentration, and admixtures of other compounds, such as oxides, halides, nitrides, and the surface temperature Cesiation of the first SPS used discharge heating of pellets pressed from a mixture of cesium chromate with titanium powder placed into the discharge chamber[1-3]. The next SPS generation used independently heated ovens with the similar pellets [2-4] and ovens with metallic cesium. The discharge heating of cartridges with cesiun

chromate become usable again in the RF SPS for SNS. Stable long term SPS operation can be established with very different cesium consumption parameters: from milligrams per week to grams per day. Sometimes cesiation from impurities remaining from previous operations can be enough for long term operation.

An example of the H^- beam current evolution during "self-cesiation" in a LV SPS with RF discharge driven by a saddle antenna is shown in Fig. 3 c, e.

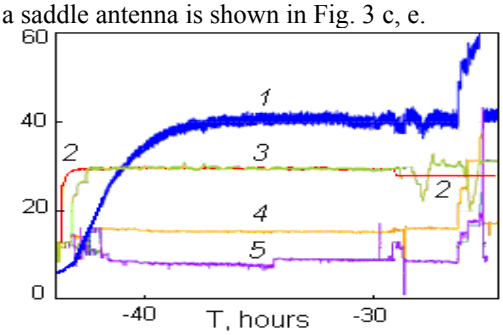

Figure 3: Evolution of H^- beam intensity of the saddle antenna RF LV SPS; 1- ion beam current; 2-gas flow; 3-collar temperature; 4-forward RF power; 5-reflected RF power.

In this LV SPS, H^- ions are produced by cesiation enhanced secondary emission from the surface around the emission aperture. Molecules of cesium containing impurities are dissociated and ionized in the discharge. The plasma has a positive ambipolar potential relative to the plasma electrode and positive Cs ions are transported to the plasma electrode by the electric field and accumulate on the surface around the emission aperture enhancing the H^- ion formation. The saddle antenna produces a higher plasma density on the axis of the discharge chamber and increases the efficiency of H^- generation.

After starting the RF discharge with RF power Prf = 24 kW, 10 Hz, 0.4 ms at magnetic field B = 250 G, the initial beam current into the Faraday cup Ifc= 8 mA grows to 42 mA during four hours without cracking the cesium ampoule as shown by curve (1) in Fig. 3.

At the same time, the extracted current (which includes electrons and back-accelerated positive ions in addition to the H^- ions measured by the Faraday cup) decreased significantly. The initial current density J~ 20 mA/cm^2 generating with a cleaned collar can be interpreted as volume generation but the increase of J up to 100 mA/cm^2 with the same RF power must be interpreted as produced by surface plasma generation (SPG) through electrode activation by the accumulation of impurities with low ionization potential (ILIP) substances on the collar ionization surface. An H^- beam current Ifc=67 mA was collected with RF power of 56 kW.

SUMMARY

Cesiation is accepted as indispensable for high intense high brightness negative ion beam production.

SPSs with cesiation are "sources of life" and "work horses" in almost all high intense proton accelerators.Operation of these accelerators were not limited or compromised by SPS operation during last 30 years. For new project as SNS were developed new SPS with a DF 6% at pulsed current ~50 mA and lifetime ~1000 hours (integrated beam lifetime IBLT up to 2.7 Ahours). Cs consumption was reduced up to ~1 mg per week. Intensity of PD SPS was increased up to 60 mA at 5% DF. However, for internal and external cyclotron injection are used Cesium-less hot cathode discharge NIS with low energy and gas efficiency. In high energy heavy ion tandem implanters are used charge exchange NIS with Mg targets. Efficiency of Semiplanotron SPS was increased to ~100 mA/kW, similar to best proton sources. Intensity of H^-/D^- beams for NBI were increased to >40 A at emission current density up to 30 mA/cm2 and electron current less than H^- current. Used for regular operation in LHD and JT-60. Acceleration up to 1 MeV under development. DC H^- beams from PD SPS was increased to 25 mA with emission current density J~100 mA/cm^2. Push button operation is developed. Improve reliability and availability of SPS, lower ownership cost and push button operation are main task of negative ion sources development now.

Improving intensity of B^- (B_2^-) beam above 1-2 mA is important for semiconductor applications.

REFERENCES

[1] V. Dudnikov, The Method for Negative Ion Production, SU patent, C1.H013/04, No 411542, Appl. 3/10/72.

[2] J. Alessi , Recent Developments in Hadron Sources accelconf.web.cern.ch/accelconf/IPAC2011/talks/frxba01_talk.pdf

[3] D. Faircloth, " Negative Ion Sources (Magnetron, Penning)"; CERN Accelerator School , Slovakia, 2012; http://cas.web.cern.ch/cas/Slovakia-2012/Lectures Faircloth Negative.pdf http://www.adams=institute.ac.uk/lectures/?scheme=1&id=55

[4] V. Dudnikov, , Rev. Sci. Instrum., 83 (2) pt. 2, 02A708(2012); 02A724 (2012).

[5] M. Reiser, "Theory and Design of Charged Particle Beams", Wiley- VCH Verlag, second edition, (2009).

[6] R. Martin,"History of the ZGS 500 MeV Booster", www.ipd.anl.gov/anlpubs/2006/05/56304.pdf

CREATING STRONGER ACCELERATOR BEAMS

Richard M. Kriske, University of Minnesota, Minneapolis, Minnesota, USA

INTRODUCTION

Many new designs for Particle Accelerators have been proposed including the ILC (The International Linear Collider and the CLIC (The Compact Linear Collider). Both the ILC and the CLIC are high energy electron-positron colliders. The CLIC seems somewhat more impressive in its ability to operate up to 3TeV, but the ILC uses the more normal means of operation as a superconducting machine. The CLIC has a more ambitious output but with a more experimental approach. Prototypes of many of the subsystems of CLIC have been constructed at CERN and around the world, but the ILC has in general been subject to a more larger review in this authors view. Of course the ILD and SiD detectors where originally designed for the ILC, but have now become appendages of the CLIC design, showing that no good idea goes to waste. There has been some debate as to the physics obtainable using e+e- colliders, but the consensus is that this is a useful idea, but as always a greater beam strength would be better. Of course the LHC (the large Hadron Collider) has a potential range from 8 TeV to 14TeV . The demand for a stronger beam can be seen from the differences and trade-offs between the ILC and the CLIC. This paper is not meant to be comprehensive in the comparison between these designs.

CLIC DESIGN

The CLIC has a broad center-of-mass range from 500Mev to 3TeV, which may be crucial for some experiments. The discovery of a particle in the 125 GeV range at the LHC may warrant a collider that can “scope” this energy range out in greater detail. The CLIC design is currently in the 500 GeV range and the 3 TeV range. In the CLIC there are drive beam accelerators. The drive beam energy is transferred to the colliding beam through RF power through waveguides. The bunch spacing is 60cm. The major design difference between the 500 GeV range and the 3 TeV range is a greater number of Klystrons, which has a greater number due to the larger beam current. A larger bunch charge and more bunches per pulse gives the 500 GeV design more luminosity. The designs are about the same length, but the 3 TeV design has a larger gradient.

ILC DESIGN

The ILC has a narrower center-of-mass range from about 500 GeV to 1 TeV, and uses superconducting klystron tubes as its construction. A large number of Tubes have to be used and this like the CLIC is a linear device.

TRADE-OFFS

The major difference between CLIC and ILC seems to be the amount of current in the beam. The CLIC claims to be able to produce 100 Amps (Is this true?) and do this because it is not technically a superconducting device (klystrons?). The ILC produces about 7milliamps, which is large compared to the average current at Fermilab.

NEW PHYSICAL IDEAS

From both designs, there could be an advantage to supplying more electons and positrons. It may be possible to use very fine nanotubes as conduits to supply the these particles. There is some evidence that the Quantum Field Theory allows for the tubes to act as springs in the Quantum Field that exists inside the klystron tubes of the Particle Accelerators. Experiments could be done to see if this is the case, and fine tubes could be attached to the klystrons. A mathematical model of this is available. It may be that it is not possible to generate and use such large currents with existing technology even if the large number of klystrons can be produced. Larger currents need to be produced, but it is this authors opinion that this can not be done without having larger sources and means for storing particles for creating larger bunch charges. Although this is without experimental evidence it may be possible to use nanotubes to store positrons, at least in very short time periods, but within the times allowed to create bunches. It is this authors opinion that the limits on these machines is going to be the storage of these particles and that research into nanotubes as storage devices may be more important than any other parameter in their construction.

CONCLUSION

Both systems seem to be designed for the same range, but neither seems to have enough klystrons available, in order to produce such large amounts of klystrons, a Japanese company has agreed to produce more sheet niobium which is needed in the production of these tubes. Both designs seem to be a little grand in their expectations of current and for that matter damage by using larger currents. Both designs lack for testing of their components, although both reports seem encouraging in their outlook. Of course both lack for funding.

REFERENCES

[1] M. Aicheler et al. (editors), A Multi-Tev Linear Collider based on CLIC Technology: CLIC Conceptual Design Report, JAI-2012-001, KEK Report 2012-1, PSI012-01, SLAC-R-985, https://edms.cern.ch/document/1234244/

[2] I., Linssen et al. (editors), Physics and Detectors at CLIC: CLIC Conceptual Design Report, 2012, ANL-HEP-TR-12-01, CERN-2012-003, DESY 12-008, KEK Report 2011-7, arXiv:1202.5940

[3] International Linear Collider Report, ILC Global Design Report and Worldwide Study. ArXiv:0709.1893v1 [hep-ph] 12 Sep 2007.
[4] P. Lebrun et al. The ClIC Programme: Towards a Staged e+e- Linear Collider Exploring the Terascale: CLIC design report. ArXiv:1209.2543 12 Sep 2012
[5] R. Kriske TIPP 2011- 2nd International Conference on Technology and Instrumentation in Particle Physics- Using Nanotubes to store Particles for future use in Particle Acclerators.

NON-GATED FIELD EMISSION ARRAY AS LOW-ENERGY ELECTRON SOURCE: EXPERIMENT AND SIMULATION

K.A. Nikiforov*, L.I. Antonova, N.V. Egorov, V.V. Trofimov,
St. Petersburg State University, St. Petersburg, Russia
V.V. Makeev, O.F. Ogurtsov, Molecular Electronics Research Institute, Zelenograd, Russia

Abstract

A non-gated NbN on Si wafer field emission arrays are studied. The I-V measurements and emission characteristics of edge-shaped cathodes in atmosphere low-voltage regime are considered. Mathematical and computer models are presented. The current density obtained from experiment was up to 384 Ampere per square centimeter in emission area 9 mm^2. Low-voltage regime (20 V) for near ($\sim$1 μm) interelectrode distance in diode configuration is discussed. High-voltage operation in high vacuum was experimentaly studied and preliminary results are discussed.

BACKGROUND

The standard emission mechanisms of the cathodes used in the accelerator electron guns are photoemission and thermionic emission. One alternative technology is field-emitter arrays (FEA) where electrons are emitted with energies close to the Fermi level. Such cathodes have potentially a lower mean transverse kinetic energy of the produced electron beam, which is mainly determined by the geometry of the electric field lines. We present first measurements on commercial field-emitter arrays in atmosphere pulsed low-voltage operation and DC high-vacuum high-voltage regime as well as numerical simulations of the electric field near the cathode surface.

There are 2 main architectures of field-emission cathodes: (i) the needle cathode, i.e. one single sharpened tip and (ii) FEA which are arrangements of field emitters on a periodically spaced lattice.

In these proceedings we consider FEA with axial-symmetric emitters of sharp edge type. The photo and SEM image in Figure 1 represent 1×1 cm cathode in pincers with NbN thin-film emitters on heavy As-doped Si wafer from JSC Mikron.

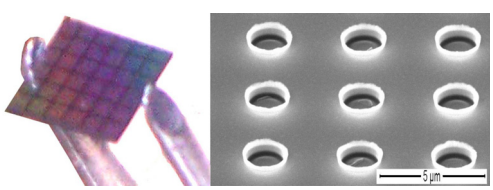

Figure 1: FEA 1×1 cm (left) with $\sim$4000000 NbN emitters (right).

* nikiforov_k@mail.ru

PULSED LOW-VOLTAGE OPERATION IN ATMOSPHERE

Experiment

An ungated NbN field-emitter array was placed at atmospheric pressure in a close-diode configuration with a planar anode with area 9 mm^2. The anode-cathode gap was set 1 μm using precision dielectric spacers shown in Figure 2.

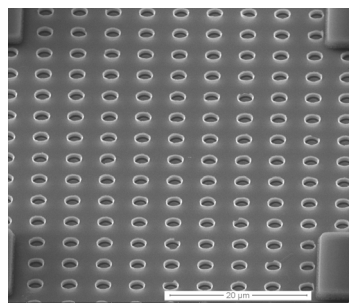

Figure 2: SEM picture of 1 μm height spacers on cathode surface.

The anode was heavy As-doped Si plate electrically isolated from ground and pressed close to cathode by probe tungsten tip of micromanipulator, 300 μs voltage pulses at low frequency was applied. A 100 Ω resistor was placed in series with the cathode and attached to a sensitive voltage meter. A schematic of the experimental configuration is shown in Figure 3.

Results

The field emission characteristics of the system are shown in Figure 3, as a function of bias voltage.

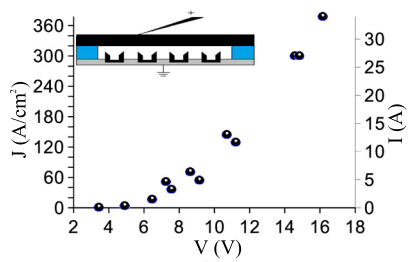

Figure 3: Field emission current and current density vs. cathode voltage. Insert: a schematic of the FEA cathode, emitters, spacers and anode used to collect the field emission.

DC HIGH-VOLTAGE OPERATION IN HIGH VACUUM

Experiment

The apparatus is shown in Figure 4. Experiments were performed in a high vacuum chamber with a base pressure of about $5 \cdot 10^{-8}$ Torr. The system is capable of applied voltages up to 15 kV. Prior to the application of high voltage, the FEA was baked at $\sim$100° C for approximately 1 hour to prevent local pressure rising during experiment.

In DC operation the limiting factor for high current emission in FEAs is the thermally induced desorption of atoms and the related contamination and sputtering problems. These well-known environmental problems can lead to current emission fluctuations by changing either the work function or the tip geometry [1]. Local pressure rise can even lead to some destructive arcs. Therefore A 100kΩ conditioning resistor was placed in series with the cathode FEA and served to protect the apparatus in case of sudden discharge of stored energy. The cathode could be horisontally moved/rotated to vary the cathode/anode gap and therefore the field gradient. A flat luminophore anode was parallel placed 1.5÷3.0 mm away from cathode FEA and large voltage (kilovolts) was applied.

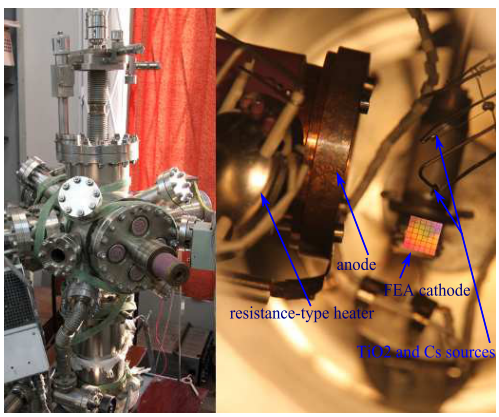

Figure 4: (left) High voltage vacuum chamber and field emission test stand used for evaluating FEA cathode, (right) anode, FEA cathode turned round in horizontal plane, resistance-type heater and TiO_2/Cs sources inside the chamber.

Results

When a FEA was initially turned on, the emission was nonuniform and the observed beamlets underwent flickering, presumably due to the diffusion of weakly bound adsorbed species. Over time, following voltage increasing, the weakly bound species were removed from the cathode and the tightly bound adsorbates performed a pseudo-random walk toward the region of highest field, the emitter edge. These adsorbates may enhance the emission by dipole lowering of the local surface-energy barrier, resonant tunneling, or other effects. Therefore emission uniformity was improved, turn-on field was decreased, and current fluctuations due to adsorbate diffusion were reduced.

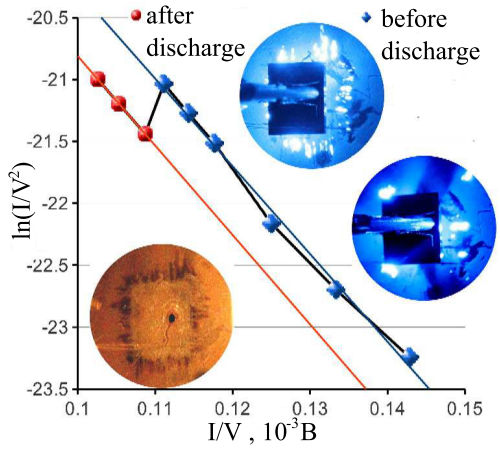

Figure 5: Fowler-Nordheim plots of emission characteristics before and after discharging. Insert: pictures of luminophore anode during and after the experiment.

Figure 5 represents the emission current measured between FEA cathode and luminophore anode when increasing DC voltage was applied. The gap between electrodes was 1.5 mm. Temporal and spacial unstability were observed again when voltage reached 9 kV and current$\sim$0.05 A. Tracks of some destructive arcs were visible on anode surface when cathode had been moved away after the experiment. Squere shaped tracks (shown in Figure 5) opposite FEA cathode edges are cased by fringe effects of electric field gain.

DISCUSSION AND NUMERICAL SIMULATION

Historically, one of the most significant barriers to the adoption of FEA technology has been the difficulty of providing uniform emission current over a large spatial extent. The emitted current is extremely sensitive to emitter properties such as geometry, work function, and surface contamination. Small fabrication variations in emitter tip radius, height, chemical composition, and crystalline orientation can result in order of magnitude differences in the emission current between tips in a FEA. Additionally, the strong electric field gradient near the cathode attracts polarizable species from the vacuum to the cathode surface. The induced dipole moment of an adsorbate can significantly lower the local surface energy barrier for emission. Also, adsorbate effects such as resonant tunneling may produce order-of-magnitude enhancements in the local emission current. The varying emission levels from tip to tip result in different local surface temperatures through Joule heating. This spread in temperature leads to fundamentally different contamination states for various tips in the ensemble.

In this section we first consider the physical explanation the law of the electric field gain on emitters according to

[2]. As it is shown in Figure 5 fringe effects play negative role in emission uniformity while gap between electrodes is relatively large (∼1 mm). Electric field gain at FEA edges is very high that does not allow rise voltage sufficient to turn on middle FEA emitters: only extreme emitters operate at FEA edges and higher voltage causes destructive (maybe explosive) effects on them. Thus maximal emission current density observed in experiment was limited by power dissipation in vacuum chamber. Moreover in case of near interelectrode distances there is not fringe effects, therefore maximal current density observed in experiment has remarkable value 384 A/cm^2 (we can not evaluate improved uniformity because the anode has not luminophore in this case, but high maximum of current values indirectly indicates this fact).

To calculate the electric field gain "zooming" algorithm has been used. According to this algorithm at the first stage the field gain is calculated over whole area of FEA under consideration using the net with the large enough pitch so only squere shape of FEA is considered. At the second stage the field is calculated more accurately over the less area including emitters and using the net with less pitch (relative to the whole area) and the boundary conditions being defined from the solution obtained at the first step.

In case of near interelectrode distance (∼1 μm, first experiment) let k_2 is protrusive emitters magnification factor of planar capacitor uniform field E_0 formed by electrodes surfaces (in smooth geometry approximation). If gap between electrodes is relatively large (∼1 mm, second experiment) electric field E_0 is additionally magnified due to fringe effects. Let k_1 is magnification factor in this case. Thus electric field in emission area is $E = k_2 E_0$ in first experiment and $E = k_1 k_2 E_0$ in second experiment.

Program complex for vacuum nanoelectronics simulations [3] based on Matlab Partial Differential Equation Toolbox has been used for calculating the value k_2. The electrostatic field calculated at the second stage has got equipotentials shown in Figure 6. The field gain of the second step has got the value which changes along the surface of the emitter's top, $\max(k_2) = 3.5$.

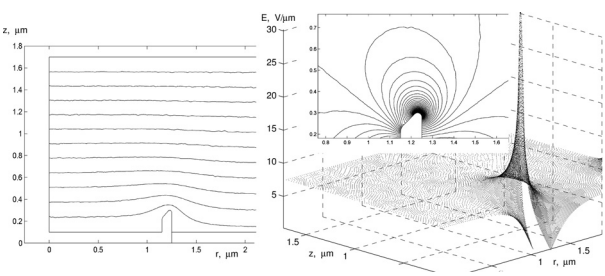

Figure 6: (left) Equipotential line plot of cylindrical field emitter cell in diode configuration at a given bias condition (only one half of cell is shown in cylindrical coordinates due to axial symmetry), (right) electric field distribution around the emitter. Insert: constant-electric field distribution contours around the top of a cylindrical emitter.

Figure 6 provides a view of the equipotential plot around the emitter, when the bias condition is set as 0 V on the cathode and 12 V on the anode. The contours around the top of emitter in Figure 6 indicate the zones at which the electric field distribution is constant. The contours that have been plotted include magnitudes of ≈5 to 30 V/μm in increments of 1 V/μm and do not denote the direction of the electric fields. The magnitude of the electric field defined by each contour scales linearly with respect to the anode voltage.

Factor k_1 has been found from finite element analysis in Comsol Multiphysics. 3D electrostatic problem has been solved in large sphere bounded domain. Electrodes were located in sphere centre. Constant-electric field distribution contours around the cathode edges are presented in Figure 7. The inner and outer countours matche the electric field of 3.5 V/μm and ≈5.5 V/μm at anode voltage 3 kV , i.e. 70% and 110% of planar capacitor field E_0 respectively: $k_1 \approx 1.1$.

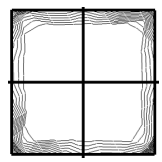

Figure 7: Constant-electric field distribution contours around the FEA cathode edges.

CONCLUSION

Preliminary results on peak current performance of field emitter array sample in atmosphere and high-vacuum during pulsed and DC operation at low- and high-voltages showed that higher values and more stable current can be emitted with anode near location at distance ∼1 μm and voltage ≤20 V. Fringe effects play negative role in emission uniformity while gap between planar electrodes and voltage are relatively large (∼1 mm and ∼10^3 V). Electric field gain in this case has got the value 110% at cathode edges. This value is quite essentially due to exponential dependence of emission current density vs. applied voltage. FEA is considered as low-energy electron source. The future work involves spherical anode compensating fringe effects.

REFERENCES

[1] P. R. Schwoebel, et al., J. Vac. Sci. Technol. B 19 (2001) 582.

[2] V. A. Solntsev, A. N. Rodionov, Solid-State Electronics 45 (2001) 853.

[3] K. A. Nikiforov, N. V. Egorov, "Program Complex for Vacuum Nanoelectronics Finite Element Simulations" TUPPB043, these proceedings.

DEVELOPMENT OF THE IBA-JINR CYCLOTRON C235-V3 FOR DIMITROVGRAD HOSPITAL CENTER OF THE PROTON THERAPY

S. Kostromin, S. Gursky, G. Karamysheva, M. Kazarinov, S. Korovkin, S. Mokrenko, N. Morozov, A. Olshevsky, V. Romanov, E. Samsonov, N. Shakun, G. Shirkov, S. Shirkov, E. Syresin, JINR, Dubna, Russia
P. Cahay, Y. Jongen, H. Nkongolo, Y. Paradis, Ion Beam Application, Louvain-la-Neuve, Belgium

Abstract

The Dimitrovgrad project, the first Russian hospital center of the proton therapy, was approved in 2010. The JINR-IBA collaboration developed and constructed the C235-V3 proton cyclotron for this center. The assembly and the beam tests of the machine were done in 2011-2012 in special experimental hall in JINR.

This cyclotron is a substantially modified version C235-V3 of the IBA C235 serial cyclotron. C235-V3 has the improved extraction system which was constructed and tested. This system allows raise the extraction efficiency up to 77% from 50% in comparison with serial C235.

Special mapping system (for B_r-component) of the magnetic field was developed and constructed by JINR for the shimming of the B_r-field in the middle plane of the cyclotron.

Tests with accelerated and extracted beam were performed in August 2012 in JINR. Beam vertical motion in the cyclotron is in the acceptable limits ($\Delta Z_{beam} \leq 3$ mm). Transmission from r=300mm to 1030 is 72% without beam cutting diaphragms. This allows reduce irradiation dose of the machine elements in comparison with serial C235. Extraction efficiency is 62%. Total efficiency of the machine is 45%. Further improvement of the parameters expected after final tuning of the cyclotron in Dimitrovgrad.

Recommendations are formulated to modify the magnetic system and reduce sensitivity of the machine to the magnetic field imperfections. Most of changes concerned with the increasing of the vertical focusing at the final radii where the aperture equals two vertical size of the beam.

PROTON THERAPY AT JINR

Dubna is one of the leading proton therapy research centers in Russia [1-2]. The synchrocyclotron (JINR Phasotron) with the proton energy of 660 MeV and current of 3 μA has been used for medical applications since 1967. The modern technique of 3D conformal proton radiotherapy was first effectuated in Russia at this center, and now it is effectively used in regular treatment sessions [1-2]. The irradiated dose distribution in 3D conformal proton therapy coincides with the tumor target shape with an accuracy of 1 mm. About 100 patients undergo a course of fractionated treatment here every year. About 880 patients were treated by proton beams during the last 12 years.

C235-V3 PROTON CYCLOTRON

Federal Medico-Biological Agency in collaboration with JINR developed the Dimitrovgrad project of the first hospital proton center in Russia. The center (Fig.1) consists of two gantry systems, a medical treatment room with a fixed beam used at the treatment angles of 0° & 60°, an eye treatment room and a PATLOG system of preliminary patient positioning. The JINR-IBA collaboration has developed and constructed the C235-V3 proton cyclotron for this center.

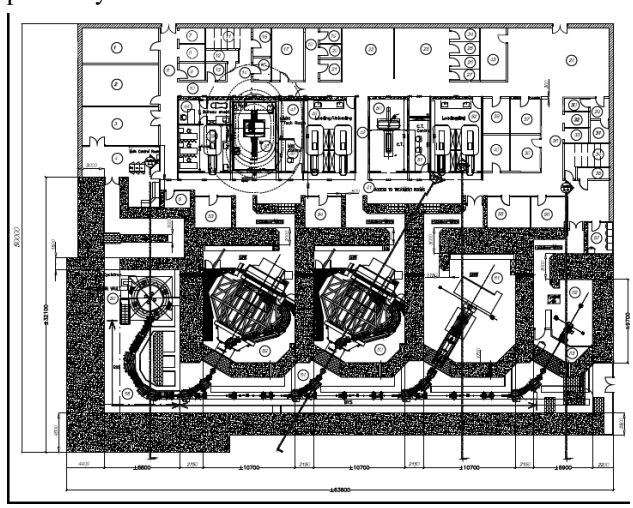

Figure 1: Layout of Dimitrovgrad proton therapy hospital center.

The C235–V3 cyclotron is superior in its parameters to the IBA C235 medical proton cyclotron. It has been designed and manufactured by the JINR-IBA collaboration. This machine is a substantially modified version of the IBA C235 cyclotron.

C235-V3 has modified extraction system [3-4]. After complete study of the beam dynamics in C235 it is clear that the beam extraction losses considerably depend on the septum of electrostatic deflector geometry. In the septum geometry proposed by JINR, where the minimum of the septum thickness is placed at a distance of 10 cm from the entrance, the beam losses on outer surface of the septum were reduced from 25% to 8%. Together with the optimization of the deflector entrance and exit positions it leads to an increase in the extraction efficiency to 80%. The new extraction system was constructed and tested at the IBA C235 cyclotron for Orsay (France). The experimentally measured extraction efficiency was

improved from 50% for the old system to 77% for the new one (Fig.2).

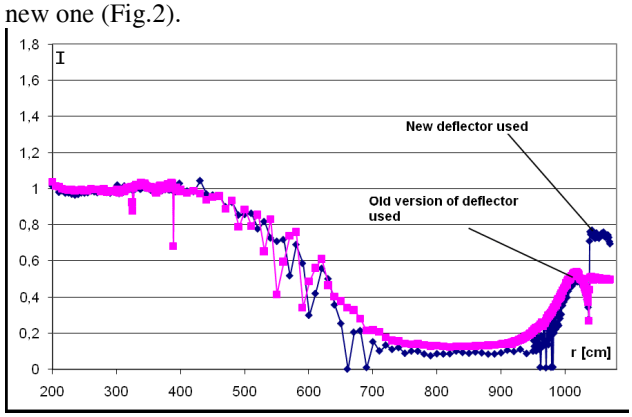

Figure 2: Circulating and extracted beam current in C235 cyclotron with old and new version of deflector.

CYCLOTRON ASSEMBY AND MAGNETIC FIELD MEASUREMENTS

The assembling of the machine started in June 2011 at JINR. A special engineering center (Fig. 3) was created at JINR in 2008-2010 for testing of the medical accelerators.

Figure 3: JINR engineering centre for the assembling and testing of the medical accelerators and equipment.

The magnetic measurements and shimming of the cyclotron magnetic field was done. The axial magnetic field mapping is based on the Hall probe technique. The special platform was designed for fabrication of all sector edges simultaneously. The accuracy of the mechanical fabrication of the sector edge surface modification is about ±20 μm. Precision geometrical measurements of the sector edges at the shimming of the magnetic field are produced by the Eclipse 3D Carl Zeiss machine. The new JINR calibration magnet applied for magnetic field up to 2.9T was implemented in the scheme of the magnetic measurements. Estimated RF-phase motion in the final magnetic field map (see Fig. 4) in the limits ±15°RF [5].

The new equipment [6] with the search coils for measurements of the average radial component $<B_r>$ of the magnetic field and for correction of the magnetic field median plane in the C235-V3 cyclotron was developed and tested at JINR.

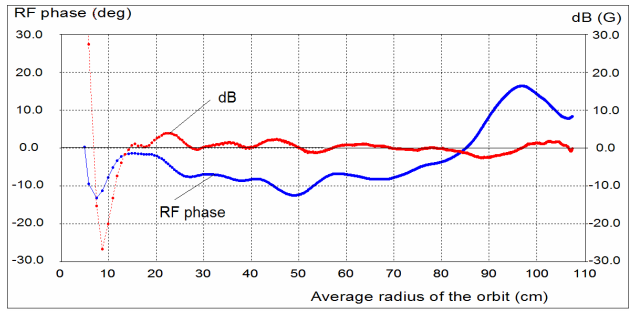

Figure 4: Difference between formed and isochronous field and integrated RF-phase shift .

The $<B_r>$ in the middle plane $z=0$ of the machine leads to vertical beam offset. This is critical for C235 cyclotrons due to small vertical gap (9mm) of the magnetic system at the extraction radii.

The $<B_r>$ measurements are based on integration of the signal from the coil during its movement in vertical direction near median plane. The measurement coil of the specified radius is moving in vertical direction from–z to +z (from median plane of cyclotron). During this motion the coil covers the cylindrical surface. The radial component magnetic flux change at this surface induces the voltage in the measurement coil and can be integrated by electronic equipment.

C235-V3 BEAM TESTS

Magnetic measurements and shimming of the magnetic field finished at June 2012. After full assembly of the all cyclotron systems tests with the circulating and extracted proton beam were performed.

The machine was finally isochronized (see Fig. 5), operating RF-frequency is 106.270 MHz, I_{mc}=760.7 A.

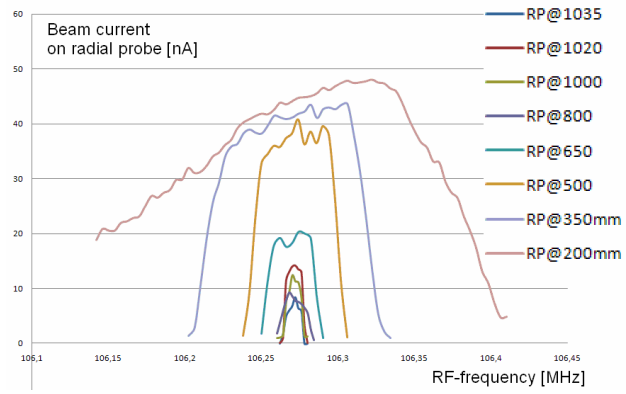

Figure 5: Smith & Garren curves at final configuration of the central plugs

Calculated beam RF-phase motion (see Fig. 6) based on Smith & Garren data (see Fig. 5) confirms that there would not be remarkable phase beam losses during the acceleration in final configuration of the magnetic system.

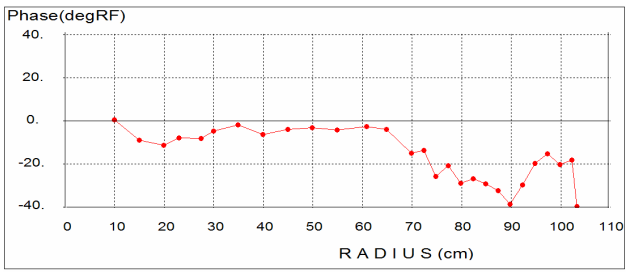

Figure 6: RF phase of the beam obtained after S&G calculations for I_{mc}=760.7 A, f=106.270 MHz

Smith & Garren procedure gives the phase slip relatively first point examined. If we shift first point to 30-40ºRF which corresponds to maximal axial focusing due to RF field, then the beam RF phase at final radii will be close to 0ºRF.

Cyclotron tested in Dubna had Q_z–drop down to 0.04 at radii of 100mm – the lowest value of IBA previous C235 machines. This was cause to weak beam vertical focusing at this region and as a consequence increased amplitude of the beam vertical motion. Correction of the vertical tune was done by shimming of the magnetic field at radii of ~100mm. Eight shims were installed symmetrically near upper and lower central plugs.

After correction of the Q_z–drop at r~100mm by increasing average magnetic field at these radii beam essentially decreased its vertical size (see Fig 7) due to more strong vertical focusing and reduced system sensitivity to a presence of the $<B_r>$ component at this place.

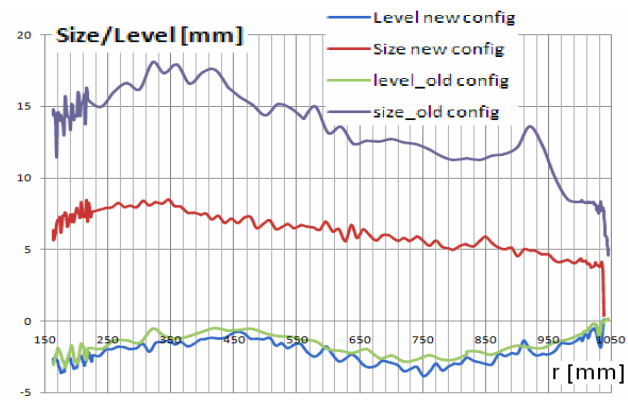

Figure 7: Parameters of the beam before and after correction of Q_z-drop at 100mm

Transmission from r=300mm to r=1030 mm is 72%. Then circulating beam was extracted by the electrostatic deflector (60kV voltage, 3mm deflector gap). Extraction efficiency is 62%. Thus, the total efficiency of C235-V3 is 45%.

Further optimization [3-4] of C235-V3 proposed by JINR is the modification of the sector spiral angle at R>80 cm which will provide larger vertical betatron tune Q_z and reduce the coherent beam losses at acceleration. The coherent beam displacement Δz from the median plane is defined by the vertical betatron tune: $\Delta z \sim Q_z^{-2}$.

At Q_z~0.2 the vertical coherent beam displacement is 2.5 mm in presence of the magnetic field radial component B_r~2G, and having free axial oscillation amplitude of 2-3 mm in the proton beam it can cause significant beam losses due to a small sector gap (9mm) in the C235. An increase of Q_z from ~0.2 to ~0.4 permits to decrease the coherent beam displacement by a factor of 4 and to reduce the proton losses at acceleration.

CONCLUSIONS

C235-V3 version of serial C235 IBA cyclotron was developed by JINR-IBA collaboration. C235-V3 has the improved extraction system. It allows raise the extraction efficiency up to 80% from 50% in comparison with serial C235.

Special mapping system (for B_r-component) of the magnetic field was developed and constructed by JINR in frame of C235-V3 tests. Tolerances to the mechanical positioning of the mapping disk are defined.

C235-V3 (for Dimitrovgrad) tests with accelerated and extracted beam were performed in JINR. Coherent beam vertical motion in the cyclotron is in the acceptable limits ($\Delta Z_{beam} \leq 3$ mm). Transmission from r=300mm to r=1030mm is 72% without beam cutting diaphragms. Extraction efficiency is 62%. Total efficiency of the machine is 45%.

Proposal for further optimization of C235-V3 magnetic system was formulated. It concerned to increase the Qz from 0.2 to 0.4 at the extraction radii which can lead to decreasing of possible losses during the acceleration.

With increased intensity of the extracted beam C235-V3 has advantages in treating of large-volume tumors using pencil scanning. At the same time C235-V3 has lower irradiation dose of the machine elements in comparison with serial C235.

REFERENCES

[1] O.V. Savchenko, J. Medical physics (2007), № 3-4.
[2] A.V. Agapov et al, Particle and Nuclei Letters, № 6 (2005), 80-86.
[3] G. Karamysheva et al, Particle and Nuclei Letters,v.7, №4 (2010) , 507-510.
[4] E.M. Syresin et al, Particle and Nuclei Letters, v.8, №4, (2011), 635-646.
[5] N. Morozov, E. Samsonov, Y. Paradis, PAP116 Magnetic Field Mapping Report, Feb., Dubna, 2012,
[6] G. Karamysheva et al, The 19th Cyclotrons Conference, Lanzhou, China, 2010, MOPCP077.

PROJECT OF LOW-ENERGY ACCELERATOR DRIVEN POWER PLANT

I.V. Kudinovich, A.A. Bogdanov, V.P Struev,
Krylov Shipbuilding Research Institute, St.Petersburg, Russia
A.G. Golovkina, D.A. Ovsyannikov, Yu.A. Svistunov,
SPbSU, St.Petersburg, Russia

Abstract

Project of low-energy accelerated driven nuclear power plant is considered. It is proposed the accelerated driven system (ads) with subcritical fast reactor, proton linac and fissile target. The main performance data of the ads: proton beam energy 300-400 MeV, accelerator average current 5ma, reactor thermal power 200mw, core effective multiplication factor k_{eff}= 0.98. The principal design features of the power plant is represented.

INTRODUCTION

The accelerator driven system – subcritical reactor driven by high power proton accelerators through a spallation target which is neutronically coupled to the core – have been proposed for addressing certain missions in advanced nuclear fuel cycles [1]. The interest is induced by a number of ADS applications in field of nuclear technologies:

- Transmuting actinides and fission products;
- Producing fissile materials;
- Power generation.

LINEAR ACCELERATOR

For transmuting and large power ADS there are needed high energy proton beams obtained in unique expensive accelerators. For ADS with reactor power 200-400 MW accelerator requirements are much less and traditional proton linac without superconductivity may be used [2].

In Fig. 1 it is shown layout of proton linac with output energy 300 MeV which can be suitable for ADS. Linac consists of multicusp ion source, 4 vane spatially homogeneous strong focusing structure (RFQ), six resonators with alternating phase focusing structure (APF DTL) and working frequency in diapason 424-433 MHz, coupled cavity linac structure (CCL). Injector, RFQ and six APF DTL resonators are LEBT system, eight resonators of CCL with working frequency in diapason 800-861 MHz are MEBT system. APF DTL structure is IH-cavity which have many cells with thick holders turned on right angle in each following cell and magnetic lenses in the drift tubes [3].

Accelerating gradients, collateral disposition of LEBT and MEBT connected by isochronous turning with help of magnetic system (270° bending magnet and focusing lenses).

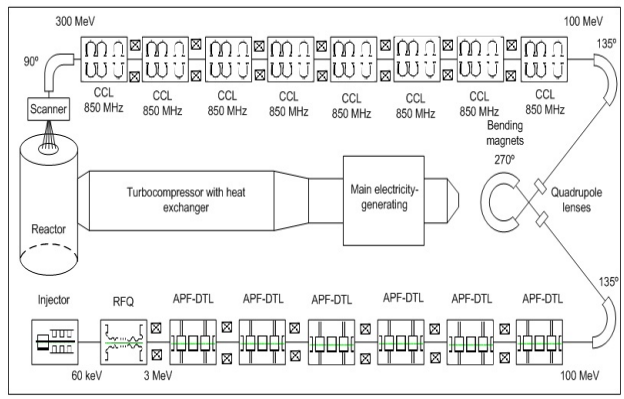

Figure.1: Layout of ADS Power Plant with proton linac.

According to results achieved at SNS accelerator in Oak-Ridge laboratory one can suppose accelerating gradients for LEBT and MEBT 4 MeV/m and 10 MeV/m accordingly [4]. Linac current adjustment can be realized by varying of pulse current repetition frequency. Main parameters of proton linac are given in Table 1.

Table.1: Main parameters of linac.

Output energy	300 MeV
Average current	up to 5 mA
Duty factor	10%
Frequency range of RFQ and DTL	424 - 433 MHz
Beam power	1,5 MW
Working frequency of CCL	805-861 MHZ
Number of RFQ	1
Number of APL-DTL resonators	6
Number of CCL modules	8

TARGET

Neutron yield from the target irradiated by charge particles depends on parameters of particle beam, target composition and it dimensions.

Characteristics of targets were defined with code Geant 4.9.5.

In case of non-fissile target materials spallation neutrons aren't multiplicated inside target and neutron source intensity is specified by leakage from target surface. In target with fissile materials spallation neutrons are multiplicated in target due to fissile processes and neutron source intensity is specified by yield of spallation neutrons inside target.

Calculated values of optimal dimensions of cylindrical non-fission targets are presented in Fig. 2, it also represents neutron yields for them.

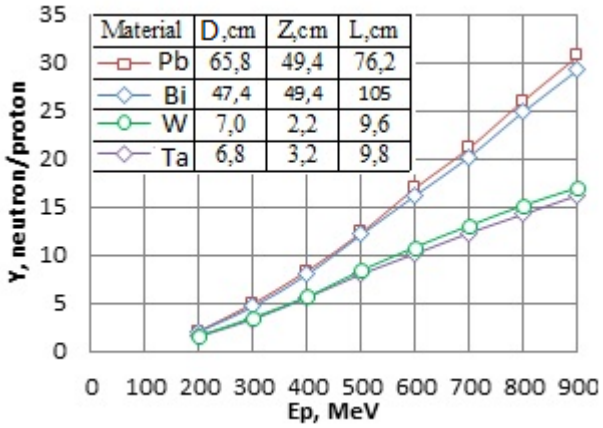

Figure 2: Neutron yield from non-fissile target with table of optimal dimensions for 300 MeV primary protons. D – diameter; L- length; Z – injection point injection point depth.

This is necessary because for small size targets a significant part of secondary particles that can induce nuclear fissions leave the target. For large size – radioactive capture of neutrons by the target plays an important role. In addition, it should be noted that since entering the beam directly at the face surface leads to the large protons and neutrons leakage, it's necessary to deepen input beam penetration point.

Calculated values of spallation neutron source (without fission process) inside uranium target are presented in Fig. 3.

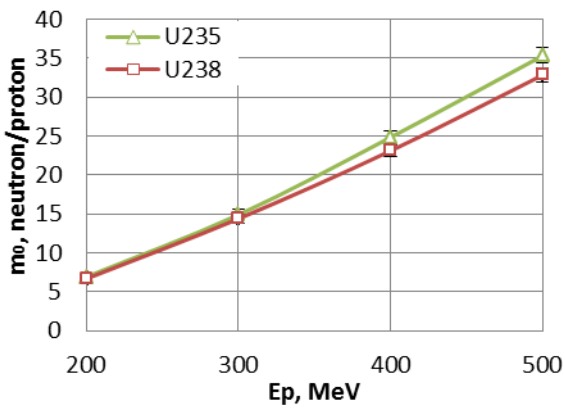

Figure.3: Spallation neutron source inside fissile target.

Obtained dimension of neutron production fissile target demonstrate that spallation source is indifferent to increasing of target diameter and leakage of spallation neutron is insignificant. For Uranium target irradiated by 300 MeV protons the leakage of spallation neutrons is less than 5% for target with diameter 32 cm (3 λ_{in}).

For ADS with 300 MeV proton beam should be used fissile target with diameter $D = 3\lambda_{in}$, which produce m_0=*15* spallation neutron in fissile material.

Design of target with tube irradiated elements is shown at Fig. 4. Structure of irradiated element allows to implement fissile material in form of tablets, powder etc. The diameter of target is 40 - 60 cm depending on void fraction of fissile material.

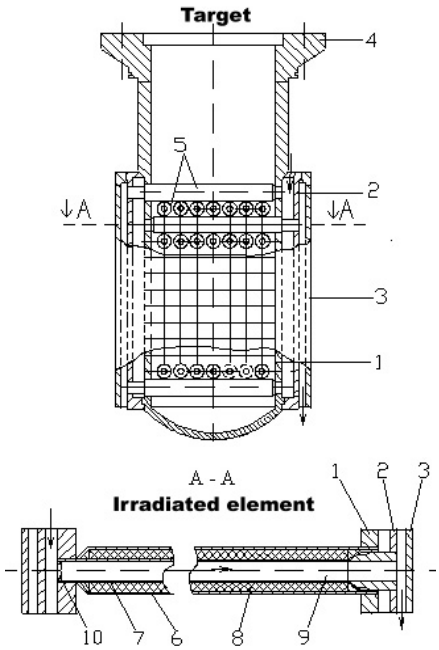

Figure.4: Target. 1, 2, 3 – vessel with channels for coolant; 4 – vacuum ion guide; 5 - irradiated elements; 6, 7 – shells of irradiated element; 8 - fissile material; 9 - coolant channel; 10 – throttle.

SUBCRITICAL REACTOR

The intensity of electronuclear neutron source is defined as

$$S = \frac{I_p m_0}{e}$$

I_p – accelerator current, m_0 – spallation neutron yield per primary particle, e – charge of primary particle.

For gas cooled target with fissile material UN and structural material W spallation neutron source m_0=*12 n/p* and intensity S=4,2·10^{17}n/s for I_p=*5mA*.

Thermal power of sub-critical reactor with external neutron source spatial distribution similar to fission neutron one (reference neutron source) is evaluated as

$$N_T = S_0 \cdot \frac{k_{эф}}{1 - k_{эф}} \cdot \frac{1}{\nu} \cdot E_f$$

where S_0 - intensity of reference neutron source, $k_{\text{eff}} < 1$ – multiplication factor, ν – mean number of neutrons per fission, E_f – energy released per fission.

To maintain constant power rate of ADS over reactor operation period with decreasing k_{eff} it's necessary to increase accelerator current. Reactivity reduction as a result of nuclear fuel burning and reactor poisoning is about 8% for thermal-neutron reactor and 1- 3% for fast-neutron reactor. Thus, in ADS with fast neutron reactor accelerator current variety during the operation period is significantly less than in one with thermal-neutron reactor. Consequently, using fast core in ADS is more preferable.

It is possible to increase reactor power locating external neutron source in the center of the core and hence decrease neutron leakage.

High-temperature gas-cooled fast neutron reactor (HTGR) with helium coolant is proposed as sub-critical reactor for ADS. The design of this reactor is shown in Fig. 5.

The thermal power of sub-critical core with fissile target($S=4,2\cdot10^{17}$ *n/s*) is equal 400MW at $k_{eff}=0,98$ and 200 MW at $k_{eff}=0,96$.

ADS POWER PLANT

The ADS is comprised of a sub-critical high-temperature gas-cooled reactor (HTGR), a linear proton accelerator and a single-circuit gas-turbine installation. Gas-turbine installation efficiency is 20%. With accelerator energy consumption of linac equal to 15 MW the effective electrical output of ADS is 25 MW.

ADS layout and its main characteristics are shown in Fig. 5 and in Table 2. It is possible to place installation in protected container with diameter 10 m and length 30 m.

Table 2: Main characteristics of accelerator driven power plant.

Effective output:	25 MW(el.)
Linac:	
-current	0,5 mA
- proton energy	300 MeV
Target (D)	UN+W (0,4 m)
Reactor:	Fast HTGR
- Thermal power,	200 MW
- Core DxH,	1,6x1,5 m
- k_{eff}	0,98 - 0,96
- fuel	UN
-coolant (P; T_{in}; T_{out})	He(10MPa; 230^0C; 900^0C)
Gas-turbine efficiency	20%

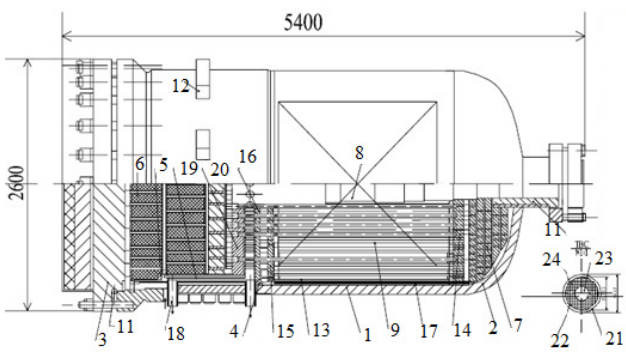

Figure.5: Design of high temperature gas-cooled reactor. 1-vessel; 2 – bottom; 3 – closure head; 4 – core shroud; 5 – fuel assemblies holder; 6 – upper shield; 7 – edge shields; 8 – target; 9 – core; 10 – nozzle ofion guide; 11 – sealing; 12 – reactor vessel fixing elements; 13 – core shroud shell; 14, 15, 16 – core plats; 17 – shield; 18 – output gas nozzle; 19, 20 – fuel assemblies holder shell, plate; 21, 22, 23 – fuel assemblies' tubes; 24 – cylindrical fuel elements.

CONCLUSION

Present-day reactor and accelerator technologies allow to create low energy accelerator driven power plant with electrical output 25 MW.

A promising option of a small-size electronuclear power plant can be based on linear high-frequency proton accelerator, fissile target and sub-critical fast reactor.

REFERENCES

[1] OECD Nuclear Energy Agency, "Accelerator-driven systems (ADS) and fast reactors (FR) in advanced nuclear fuel cycles. A comparative study," Tech. Rep. number, Nuclear Development, NEA/OECD, Les Moulineaux, France, 2002.

[2] Yu.A. Svistunov, M.F. Vorogushin, I.V. Kudinovich. The Feasibility of Low-Energy Electronuclear Power Plant // Proc. Of LINAC08, Victoria, BC, Canada, 2008, pp. 217-219

[3] Yu.A. Svistunov, S.A. Minaev, S.A. Silaev. Modelling and Testing of APF Cavity RF Field // Proc. of workshop BDO-95, St.Petersburg, Russia, 1995, pp.130-13

[4] N. Holtkamp. Status of the SNS Project // Proc. of PAC03, Portland, Oregon, pp.11-15

HIGH VOLTAGE ELV ACCELERATORS FOR INDUSTRIAL APPLICATION (FAMILY OF ACCELERATORS AND TENDENCY OF DEVELOPMENT)

N.K. Kuksanov, Y.I. Golubenko, P.I. Nemytov, R.A. Salimov,S.N. Fadeev, A.V. Lavruhkin, A.I. Korchagin, D.S. Kogut, A.V. Semenov, BINP SB RAS, Novosibirsk, Russia

Abstract

Budker Institute of Nuclear Physics Siberian Branch of Russian Academy of Science (SB RAS) continue its activity in the development and manufacturing of electron accelerators of the ELV-type for their use in the industrial and research radiation-technological installations. The ELV-type accelerators were designed with use of the unified systems and units enabling thus to adapt them to the specific requirements of the customer by the main parameters such as the energy range, beam power, length of extraction window, etc.. INP proposes a series of electron accelerators of the ELV-type covering the energy range from 0.3 to 2.5 MeV with a beam of accelerated electrons of up to 400 mA and maximum power of up to 400 kW. The design and schematic solutions provide the long term and round-the -clock operation of accelerators under the conditions of industrial production processes. The ELV accelerators are especially popular accelerators not only in Russia, but in China, Korea, and etc.

INTRODUCTION

Radiochemical technologies with the use of electron accelerators as ionizing radiation sources were generally developed in the early sixties. By recent, they had strongly consolidated in world industrial production and, thereby, confirmed their efficiency as well as their uniqueness. The technological processes with the use of electron beams for polymer radiation modification, stimulation or initiation of chemical reactions, smoke purification, waste waters treatment, grain disinfection, etc., are widely used in modern industry. A lot of accelerators are installed and operated in different science and research centers and applied-research laboratories. That leads to growth of radiation-modified goods production and development of new matters and technologies, where electron beams are used to obtain new and, sometimes, unique properties.

Budker Institute of Nuclear Physics (BINP) of Siberian Branch of Russian Academy of Sciences is one of the world leaders in the development, design, manufacture and application of electron accelerators of different series (such as DC accelerators of continuous action based on high-voltage rectifier, high-frequency accelerators, pulsed accelerators), the accelerated electron energy and power of which are much more. ELV-series accelerators are some of them. Their compact size and high functional quality allowed BINP to stand as a leading institution at industrial accelerators market as in Russia and abroad.

DESIGN OF ACCELERATOR

ELV high voltage power source is cascade generator with parallel inductive coupling. The rectifier column is installed inside the primary winding. The primary winding is supplied with frequency converter on IGBT transistors. The operation frequency is near 400 Hz. The coil of secondary winding has maximum induced voltage

Figure 1. ELV-8 accelerator.

on its ends 20 kV. This voltage is rectified with the voltage doubling circuit. Thus, the output voltage of the rectifying section is 40 kV. The rectifying sections are connected either in series. The rectifier section column is terminated with the high voltage electrode inside of which there is the injector control unit. The accelerating tube are located inside the column of high voltage rectifier.

All these elements are installed inside of pressure tank filled with SF6. Due to these circumstances ELV-accelerators are the most compact among the devices of this class. Accelerator is equipped with gas system that allow to recovery SF6 during service and maintenance. The vacuum system components and extraction device are fixed to the bottom of the tank. Electrons emitted by the cathode, placed on the upper end of the accelerating tube, have the total energy eU0 on the output of the

accelerating tube. Passing through the vacuum system they reach the extraction device where they are homogeneously distributed along the foil by the scanning electromagnets and then extracted into air. The beam is scanned in 2 directions along and across the foil window. The irradiated material is transported under the frame of the extraction window. Due to special electronics device the beam raster position on extraction window is monitored by oscilloscope.

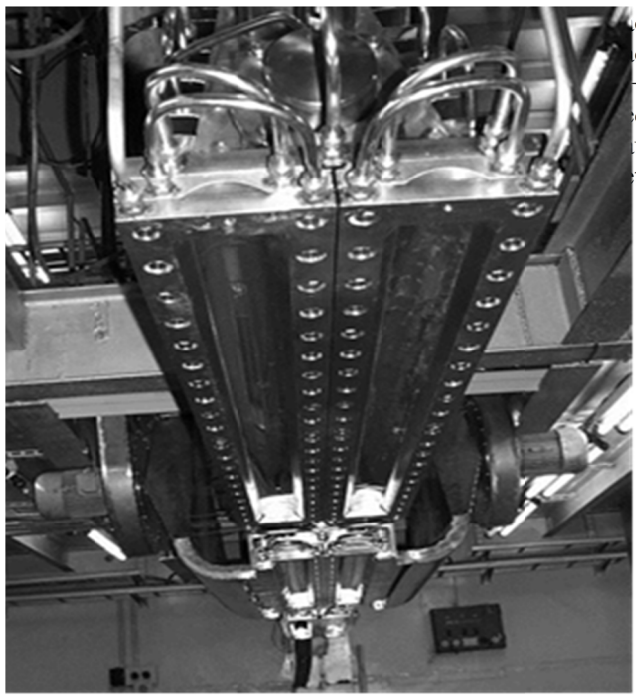

Figure 2. Double window extraction device of ELV-12 accelerator.

CURRENT STATUS

Market conditions and growing demands for modified materials forms the industrial manufacturers needs in more powerful and effective electron accelerators enabling to increase the volume of production without compound and expensive inputs for change all equipment. Table 1 and 2 shows accelerator parameters of last 38 contracts.

Table 1			
Energy, MeV	1 or less	1,5	2,5
Amount	14	14	10

Table 2				
Power, kW	100	70	50	20 (mobile)
amount	14	1	1	2

As it is shown in Tables 1, 2 the needed accelerators are distributed enough evenly starting from 1 MeV by energy in accordance with maximum energy. Most of them are of 100 kW power. That is why, at present, the development of ELV model range goes towards increase of accelerators power within the range of 1.0…1.5 MeV. Earlier, we can obtain 100 kW at 1.0 MeV with maximal current 100 mA and 2.0 MeV with maximal current 50 mA. There was redesigned ELV-4 accelerator and appeared 3 new models with maximal energy 1.0, 1.2, 1,5 MeV and maximal current 100, 83 and 67 mA accordingly. Those accelerators designed in new dimension type extend power and energy range of earliest models enabling the following:

− production of more powerful electron beams, which accurately satisfy existing production needs, taking into account present and new industrial technologies;

− modification and/or replacement of accelerator equipment without changing the existing technological auxiliaries such as rewinding lines, take up &payoff units, etc.

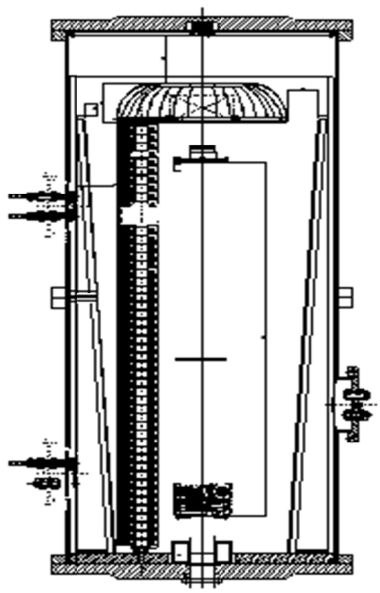

Figure 3: Structure and dimensions of ELV4-1,2 accelerators.

Another important direction in development of accelerators is adaptation of accelerator complexes to present technological equipment and their integration with industrial technologies. So, to increase production efficiency in accordance with the customers' needs, the scanning and beam extraction systems were modified. The length of extraction window was increased from 1600 mm up to 2000 mm (see Figure 5). This enabled to irradiate two and more types of products.

Figure 4. Modification of extraction window.

Other examples of integration allowing improvements in productive efficiency are information-measuring complex on visualization of accelerator current parameters and technological irradiation process (Fig.6) and under-beam transportation system developed in BINP.

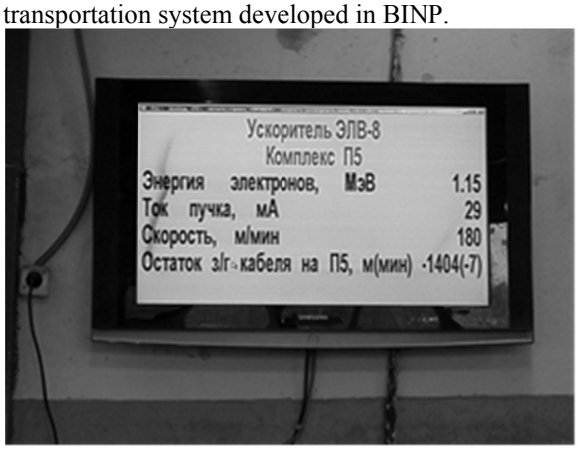

Figure 5. Parameters of accelerator ELV operation.

Concerning the high power ELV-12 400 kW accelerator for environmental application: it continues operation and proves advantage of EB technologies but during 5 years we have no orders for such accelerators.

Figure 6. Irradiation hall of 400 kW accelerator.

There was developed movable accelerator. This project was made together with our collaborator from South Korea EB-TECH. Accelerator together with radiation shielding was installed inside trailer. Main reason of this installation is demonstration of EB treatment. Extraction device is adapted for treatment the flow of gas or liquid substances. EB-TECH already replaced this accelerator in Saudi Arabia and made demonstration experiments.

ELV accelerators are used practically in all technologies where electron beam is needed. 140 accelerators were delivered in 12 countries. The most of them are under operation until now. The oldest operating accelerator has age 32 years.

Figure 7. Movable accelerators.

This work was is supported by the Ministry of Education and Science of the Russian Federation.

REFERENCES

[1] N. Kuksanov, S. Fadeev, Y. Golubenko, D. Kogut et al, «High Power ELV Accelerators for Industries Application» // Proceeding of RuPAC-2010, Protvino, Russia, 2010

[2] S. Fadeev, Salimov R., et al, "Underbeam equipment to expand technological capabilities ELV accelerators", Proceedings of the X International Workshop on the Application of Charged Particle Accelerators in industry and medicine, St. Petersburg, October 1-4, 2001. 68. See also Bulletin "Radteh - Eurasia", Novosibirsk, 2002. p. 8.

[3] N. Kuksanov, S. Fadeev, et al, BINP SB RAS, Novosibirsk, “The development of the model range and the improvement of the performance accelerators”, VANT №3 March 2012, p. 15 (1996); http://vant.kipt.kharkov.ua

VITA BASED NEUTRON SOURCE - STATUS AND PROSPECTS *

S. Taskaev#, V. Aleynik, B. Bayanov, A. Kuznetsov, A. Makarov, I. Sorokin, M. Tiunov,
BINP SB RAS, Novosibirsk, Russia,
A. Bashkirtsev, I. Schudlo, Novosibirsk State Tehnical University, Russia,
M. Kamkin, D. Kasatov, Novosibirsk State University, Russia

Abstract

At the BINP, a pilot epithermal neutron source is now in use. It is based on a compact Vacuum Insulation Tandem Accelerator (VITA) and uses neutron generation from the reaction ^{7}Li(p,n)^{7}Be. Generation of neutrons was established and *in vitro* experiments were held. Most recent investigations on the facility are related with: i) studying of the dark currents and breakdowns, ii) analyzing and suppressing the high intensity dark currents, iii) measuring the intensity and the spectra of the X-ray radiation, iv) optimization of the H^- beam injection into the accelerator, v) placing and calibrating the new charge-exchange target. The results of these studies are discussed in the present work. Investigations resulted in increasing of mean current of the proton beam in stable mode (from 0.1 – 0.7 to 1.5 – 2 mA). In the nearest future new experiments are planned, including *in vitro* tests, blistering investigation, spectrum and flux measuring for neutrons and gamma, calculating the dose absorbed by phantom. Different ways of providing additional stability to the accelerator, of increasing the current of the proton beam are discussed in this work, as well as the ways of creating the therapeutic beam and strategies of applying the facility for clinical use.

INTRODUCION

Presently, Boron Neutron Capture Therapy (BNCT) [1] is considered to be a promising method for the selective treatment of malignant tumours. The results of clinical trials, which were carried out using nuclear reactors as neutron sources, showed the possibility of treating brain glioblastoma and metastasizing melanoma incurable by other methods [2, 3]. The broad implementation of the BNCT in clinics requires compact inexpensive sources of epithermal neutrons. At the BINP the source of epithermal neutrons based on 2 MeV Vacuum Insulation Tandem Accelerator (VITA) and neutron generation through ^{7}Li(p,n)^{7}Be reaction was proposed [4] and realized. Although the accelerator is designed to obtain a 5 mA proton beam, but in the experiments carried out in 2008-10 we usually got the proton beam currents of hundreds of microamperes, and occasionally for a short time – a few milliamps. Such a current was enough to demonstrate the generation of neutrons [5] and monochromatic gamma-rays [6], to carry out initial *in vitro* investigations [7], but it is clearly not sufficient for the thorough BNCT research and other applications. This paper presents the results of experiments carried out after the IPAC-2011 [8], aimed at increasing the current of the proton beam and improving the stability of the accelerator. We also discuss plans of works and strategies of applying the facility for clinical use.

*Work is supported by Ministry of Education and Science of RF
taskaev@inp.nsk.su

VITA

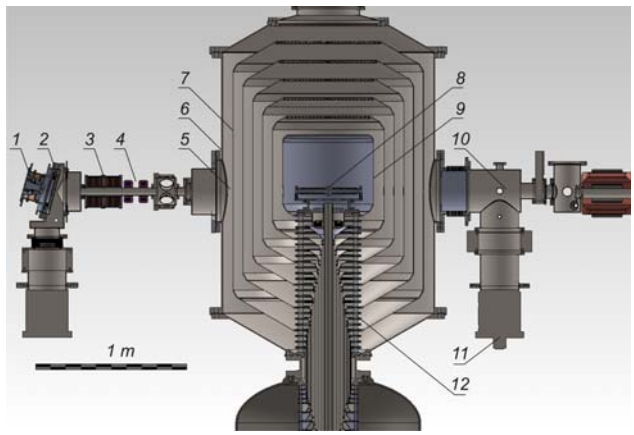

Figure 1: High-current vacuum insulation tandem accelerator. 1 – H^- ion source, 2 – diaphragm, 3 – magnetic lenses, 4 – corrector, 5 – a temporary location of the beam detector, 6 – accelerator, 7 – electrodes, 8 – high voltage electrode, 9 – stripper, 10 – high energy beam transport, 11 – turbo molecular pumps, 12 – insulator.

General view of the accelerator is shown in Fig. 1. Negative hydrogen ions are injected and accelerated up to 1 MeV by potential applied to the electrodes, then H^- turn into protons in the stripping target and at last the protons are accelerated up to 2 MeV by the same potential. Pumping of the gaseous stripping target is carried out by cryogenic and turbomolecular pumps through the jalousies. The potential of the high-voltage and five intermediate electrodes is supplied by a high-voltage source through the insulator which has a resistive divider.

DARK CURRENTS

The accelerator has a high electric field in the electrode gap – about 25 kV/cm, and a large total area of the electrodes – tens of square meters. In such a system in the electrode gap dark currents of different nature must inevitably occur, which may have a significant impact on the potential distribution along the accelerating channel.

When training the accelerator, at the time of voltage increasing, a dark current is recorded. It is associated with the appearance of micro-discharges, accompanied by

desorption of adsorbed gases on the surface of the electrodes. Usually within an hour of training the value of the dark current decreases from the typical values of 100 – 300 μA to ten microamperes and then to few microamperes.

In a series of experiments in order to increase the H^- beam current the apertures of electrodes were increased from 20 to 58 mm, except for the high-voltage electrode, in which the diameter of the hole was still 20 mm. This change resulted in frequent registration of dark current of high intensity – up to 3 – 4 mA. Flowing of such a current compared to the standard training mode led to a nearly 100-times increase in radiation. The latter fact assumed high energy of electrons which is possible when the current flows not in the gap between adjacent electrodes but, for example, between the case of vacuum tank and the high-voltage electrode. This assumption was confirmed by measuring the X-ray spectrum by BGO-spectrometer: the maximum of the spectrum was shifted from 120 to 400 keV [9]. It was found that when the aperture of the channel increases, the electric field on the sharp edge of the cathode part of diaphragm mountings increases by 20% – up to 51 kV/cm, which leads to increased emission of electrons directly into the acceleration channel. To prevent the occurrence of this phenomenon the aperture of the channel has been reduced and sharp edges of diaphragm mountings has been rounded. This study shows the danger of exceeding the electric field strength of 50 kV/cm. Earlier in [10] we found that the 70 kV/cm electric field leads to dramatic increase of field emission current in the high-voltage gap.

BEAM INJECTION

Negative ion beam with energy of 21 keV and current of 5 mA is created by surface-plasma source with Penning discharge and hollow cathode. After turning at an angle of 15 degrees the peripheral part of the beam is cut off by 28mm cone diaphragm and the rest center of the beam enters into the transport channel. Then the divergent beam is focused by two magnetic lenses and can be shifted by corrector for subsequent precise input into the accelerator. VITA is characterized not only by a high rate of acceleration, but also by a strong entry electrostatic lens between the cover of the accelerator and the first accelerating electrode. To study the influence of the lens and to optimize H^- beam injection the 22-channel detector has been produced and installed at the entrance of the accelerator. Beam detector is mounted directly on the first electrode of the accelerator. Using the detector we have measured the dependence of the relative maximum beam current density on the focusing magnetic lenses current. It has been determined that the best agreement with the numerical calculation is achieved by assuming the full compensation of the space charge in the transport channel and setting the transverse ion temperature equal to 1 eV at the plasma boundary of the ion source. This study described in detail in [11] resulted in better focusing of the beam required for acceleration of the beam without significant losses.

STRIPPER

To increase the current a new stripping target has been made. It is designed as a cooled tube having length of 400 mm and internal diameter of 16 mm, with argon gas valve in the middle. Previously we used a tube with diameter of 10 mm.

Negative ion beam with energy of 21 keV was injected into the accelerator with the high-voltage electrode potential of 800 kV. When there was no gas supply in the stripping target the Faraday cylinder at the exit of the accelerator registered negative current. This current was the current of negative hydrogen ions, which were first accelerated and then decelerated. When the stripping target is filled with argon it exchanges negative hydrogen ions into protons. When the thickness of the target is $0.29\ 10^{16}\ cm^{-2}$ the number of appeared protons is comparable to the number of negative hydrogen ions and detected current becomes equal to zero. Registration of the moment of the current transition from negative to positive with changing argon pressure has become a useful direct diagnostics of stripping target thickness. Also the thickness of the target is indirectly characterized by the residual gas pressure, because the experimentally measured dependence of the residual pressure on the amount of supplied argon is linear in operating range of parameters. With a further target density increase there is a growth of output current and its saturation. When injected H^- current is around hundreds of microamps the dependence measured experimentally is in good agreement with the calculated one (Fig. 2, [12]). However, when the injected current is around few milliamps there is some reduction in the proton current in the saturation region with increasing gas supply. It is planned to investigate this effect in detail in the near future.

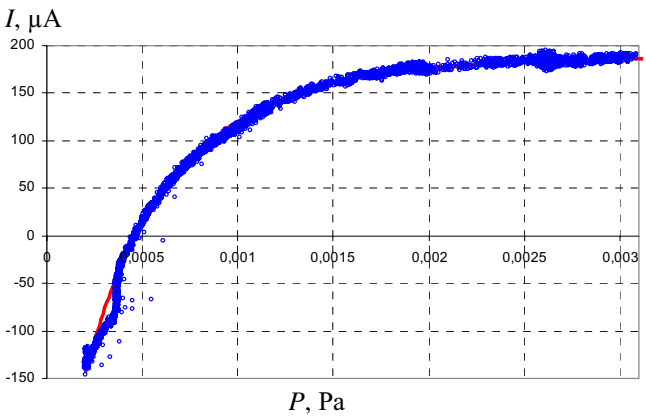

Figure 2: Measured and calculated (solid line) dependence of the detected output current of the accelerator on the residual gas pressure.

RESULTS AND PROSPECTS

The above-described investigations allowed us to move to a long stable operation with a much higher average current – 1.5 – 2 mA instead of previously achieved 0.1 – 0.7 mA. This current provides the possibility of measuring neutron spectrum by the time-of-flight technique, carrying out *in vitro* and *in vivo* studies and developing other techniques for BNCT. Numerical simulation is used to optimize beam forming unit for epithermal neutrons and, in addition to the standard mode with a 2.5 MeV proton beam, there are determined 2 more acceptable modes: i) at the near-threshold energy of 1.95 MeV, which is characterized by low activation of the lithium target and the facility, and ii) orthogonal at 2.5 MeV, characterized by high therapeutic dose rate – up to 3 Sv/min @ 10 mA [13]. Discovered modes allow changing in the design of installation for hospitals, which can make it more attractive. [14]

Also on the facility it is possible and it is planned to carry out the investigations of i) testing the method of fast detection of explosives and narcotics by resonance absorption of monochromatic gamma rays, ii) measuring the cross section and the spectrum of α-particles from neutronless thermonuclear reaction $^{11}B(p,\alpha)2\alpha$, iii) dating of rock formation (apatite) by inducing the fission of uranium nuclei contained in the rock, iv) forming monochromatic beam of epithermal neutrons for calibration of dark matter detector.

REFERENCES

[1] G. Locher, Am. J. Roentgenol. Radium Ther. 36 (1936) 1.
[2] H. Hatanaka, Basic Life Sci. 54 (1990) 15.
[3] H. Hatanaka and Y. Nakagawa, Int. J. Radiat. Oncol. Biol. Phys. 28 (1994) 1061.
[4] B. Bayanov, et al., NIM A 413 (1998) 397.
[5] A. Kuznetsov, et al., Tech. Phys. Lett. 35 (2009) 346.
[6] A. Kuznetsov, et al., NIM A 606 (2009) 238.
[7] L. Mostovich, et al., Bulletin of Experimental Biology and Medicine 151 (2011) 264.
[8] S. Taskaev, et al., IPAC-2011, San Sebastian, Spain, Septemper 2011, THPS079, p. 3615 (2011); http://www.JACoW.org.
[9] I. Sorokin, et al., "X-ray Radiation of the High-Voltage Elements of the Tandem-Accelerator with Vacuum Insulation", MOPPA030, these proceedings.
[10] G. Dimov, et al., Atomic Energy 94 (2003) 155.
[11] A. Makarov, et al., "Optimization of the Negative Hydrogen Ion Beam Injection into the Tandem Accelerator with Vacuum Insulation", WEPPD038, these proceedings.
[12] A. Kuznetsov, et al., "Calibration Testing of the Stripping Target of the Vacuum Insulated Tandem Accelerator", WEPPC057, these proceedings.
[13] E. Kashaeva, et al., "Regimes of therapeutic beam shaping from an accelerator neutron source", XV Int. Congress on Neutron Capture Therapy, Tsukuba, Japan, September 2012 (in press).
[14] V. Kanygin and S. Taskaev, "New design of medical facility for BNCT based on VITA neutron source", XV Int. Congress on Neutron Capture Therapy, Tsukuba, Japan, September 2012 (in press).

APPLICATION OF SMALL-SIZED VACUUM ACCELERATING TUBES FOR NEUTRON CONTROL OF INCREASING DEBIT OF OIL WELLS BY ACOUSTIC INFLUENCE OF THE FORMATION*

A. E. Shikanov, B.Yu. Bogdanovich, A.V Ilyinsky, D. R. Khasaya#, A. Nesterovich, D.D. Ponomarev, E. Shikanov, MEPhI, Moscow, Russia

Abstract

The report presents experimental studies results of the possibility using the technique of neutron "labeled" reagent (NaCl) for monitoring of the acoustic effect (AE) results in the oil reservoir to increase oil production debits. These obtained data allow us to estimate the effectiveness of acoustic influence the method on managed oil reservoirs in conjunction with the equipment which pulsed neutron-neutron ray logging based on vacuum accelerator tubes that implements the method of neutron "labeled" reagent. The proposed instrumental set ensures reliable process control stimulation of oil from the reservoir and the allocation of layers to abnormal filtration and capacitive properties and their subsequent development.

MANUSCRIPT

One of the most effective methods of cleaning fluid productive zone recovery in oil well is AE at her longitudinal ultrasonic pressure wave. In the pores of the reservoir fluid-filled productive, there are transient oscillatory micro streams. With sufficient intensity ultrasonic wave cleaning these areas contribute microstreams productive fluid extraction from the above contaminants. [1]

The effectiveness of the AE direction in oil reservoirs can be improved by controlling the parameters of the processes occurring before and after AE in oil reservoirs and selecting intervals stimulation oil. Measurements of changes in the formation of these processes are made remotely through a metal pipe casing, which requires the use of transparent methods of control.

The most effective is the pulsed neutron-reagent method. It allows the monitoring of changes in the formations chlorine containing fluid during its displacement pumped reagent containing solution. The specified control is pulsed neutron method based on the measurement of the lifetime of thermal neutrons in the formation, depending on the composition of the substance contained in the pores. This structure defines the process of formation in the reservoir and the well resulting deceleration,thermalization and diffusion of the field of thermal neutrons, falling in time exponentially.

The time variation of the decrement recession thermal neutron density characterizes the content of chlorine in the reservoir due to its abnormally high radiative capture cross section. This solves the problem of determining water contact due to shortage of chlorine in the oil-rich part of the formation and the presence of excess reagent in a solution in water due to its mineralization. Lack of formation water or hydrocarbons in the reservoir also affects the damping rate of the neutron density decline, which is proportional to the total cross section of neutron absorption.

In implementing the method of pulsed neutron-neutron logging (PNNL) with the reagent before and after AE in the reservoir in the study area creates a pulsed periodic field of fast neutrons emitted by the accelerating tube (AT), the result of passing on its target nuclear reaction T(d, n) ^{4}He. After slowing down neutrons to thermal velocities begins the process of decay of the neutron density. In this case, the decline of the spatial density of neutrons occurs exponentially with a decrement proportional to the total neutron absorption cross-section [2]. Measuring the density of a neutron decay detector is filled with 3He, which proceeds in the amount of nuclear reaction ^{3}He (n, p) T, followed by analysis of the time spectrum known methods used in experimental nuclear physics. [3]

The measurements were carried out using hardware methods complex AIOC-43 (development VNIIA named by N.L.Duhov) [4] on the basis of compact pulsed neutron generator [5] and multi-channel time analyzer [3].

Upon command from the ground control unit through the correctional system is launched neutron emitter in a repetitively pulsed mode. As a result of the interaction of fast neutrons generated in the target vacuum accelerating tube, in the study of the geophysical environment shapes the field of thermal neutrons.

The detection system converts this field into analog electrical signals that are in well telemetry system are converted into digital information that is sent in geophysical well logging cable telemetry unit to the ground. In this unit, this information is decoded and formatted as a series of files, coming to a computer. The computer is processing the information on the two-component processing algorithms logging signal [3,6]. The result depends decrement Depreciation thermal neutron density λ of the depth of the test bed.

If the acoustic impact inflow of hydrocarbon fluid, it will be recorded a significant decrease in the decrement recession thermal neutron density, since this reduces the concentration of nuclides detected. In the case of failure of the process of acoustic impact or fill water reservoir effect of changing the decrement will be less significant.

Equipment complex consists of ground control unit (geophysical station), which controls the change of geophysical instruments (instrument pulsed neutron

*Work supported by Shikanov A.E. and Khasaya D.R.

#damir_hasaya@rambler.ru

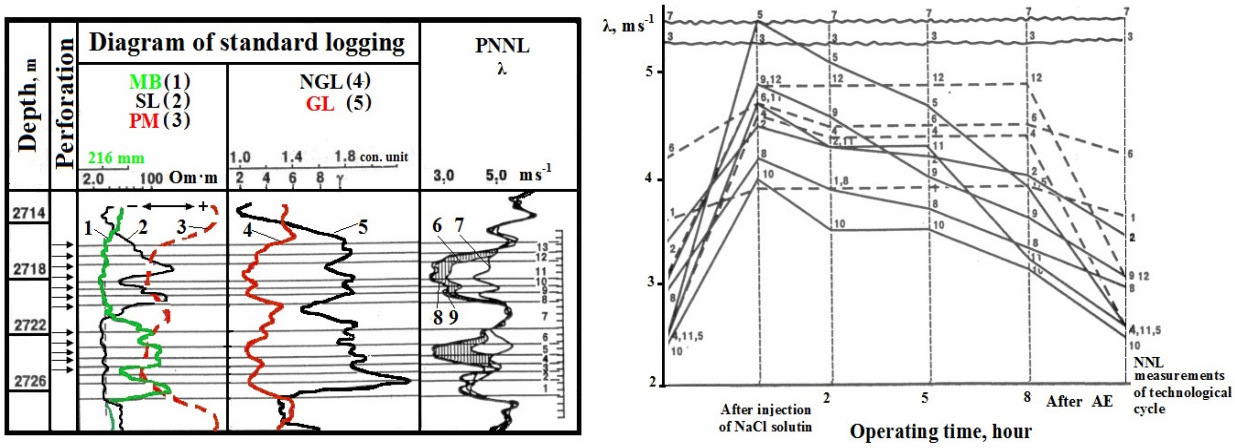

a) b)

Figure 1: a) Diagram of experiment results in the well by the method of neutron-"labeled" substance and directional acoustic stimulation (right vertical scale numbers are seams); b) Temporary change of decrement λ in layers in the process of technological cycle measurements on well PNNL.

generator and the device acoustic action), depending on the work performed. Replacement geophysical instruments lowered into the well through the valve by tubing to the oil reservoir. Geophysical studies were conducted at the perforations seams.

Measurements were carried out by the method of PNNL after the first injection of the labeled solution, then after 8 hours of recovery (recovery of productive hydrocarbons) and finally after AE in the monitoring section of the reservoir interval. Recording was performed with PNNL lifting speed of 40 m / h The main interpretive the-damping constant λ the thermal neutron density calculated from the measurements of PNNL with a special program of processing two-logging signal. The working solution was used standard technical NaCl solution with density 1180 kg/m3.

During the experiment in a well on the above method were performed as follows:

a) Background recording PNNL, followed by treatment in the test signal logging intervals;

b) injection into the well of the solution, the subsequent recording and signal processing PNNL;

c) a record PNNL after an 8-hour work strata;

d) issued by AE in layers and subsequent recording and processing of PNNL

Fig.1-a. shows the resulting experimental logs. In the first two fragments are standard geophysical logging chart:

MB - measurement of borehole diameter (caliper), SL-side logging (logging type of resistivity recovery wells), PM-potential measurement spontaneous polarization, depending on the lithology of the borehole that is logged on the potential difference between two spaced electrodes (probes) NGL - neutron-gamma logging (measurement of the intensity of the secondary γ-radiation produced by irradiation of rock neutron source rocks in the well-GC γ-ray logging (recording the intensity of natural γ-radioactivity of rocks in the well).

In the third figure shows a fragment PNNL diagram illustrating the change control of the damping decrements the density of thermal neutrons in the process of the work in the well to intensify the flow of oil and the breakdown of oil reservoir (1 ÷ 13) in the depth of their location, different filtration properties collectors.

Layers are divided by differences of λ, the decrement values obtained by comparing the results of the correlation of background measurements with measurements after: a) push into the layers of the labeled solution, and b) an eight-hour working out of the directional acoustic stimulation. Dedicated strata characterized by different dynamics, the degree of absorption and impact of the labeled solution. When comparing the background diagrams and control charts in separate cycles of measurement established that error definitions are usually random and can be up to 2% to a thickness of 1m. When comparing the results of measurements in different cycles observed small (up to 5%) differences of values of the damping decrement of thermal neutrons due to various backfilling. This distortion is additive and can be easily removed by comparing diagrams to support layers - noncollector, with obviously unchanging properties on the damping decrement of thermal neutrons. The data obtained were evaluated λ changes of reservoir properties of the layers:

- No change in λ push NaCl solution into the formation and development of the eight layers indicates the absence of the connectivity in the well
- In layers 4, 6, 12, minor changes compared to the decrement using NaCl solution in the formation and development of a marker of poor reservoir properties of these layers.

- In layers 5 and 8, with a mean change in the decrement using NaCl solution in the formation and development of their shows low filtration properties of reservoirs.

The data obtained by the interpretation of the definition of reservoir formation properties marked layers 4, 5, 6, 8, 9,11,12. There has been directed acoustic impact on these layers and then measuring PNNL control effectiveness to develop recovery after AE

Fig.1-b. shows changes in reservoir mapping λ decrement in the time interval of work on the well. The ordinate values are laid decrement recession thermal neutron density λ for various spans and technological cycles of pulsed neutron-reagent method (x-axis). In this case, layers with different numbering have different reservoir properties.

The results of correlation comparing the measured values of λ before and after the directional acoustic effects using a solution of the reagent NaCl suggest cleaning processes reservoirs of oil reservoirs. This is a group with a lower reservoir properties - layers 4, 5, 8, and to the development of reservoirs 9,10,11.

The data obtained with the use of reagent AE indicate the intensification of treatment reservoirs containing oil. This is a group with lower reservoir properties (zones 4, 5, 6, 9, 10, 12), which were not used 8 hours working out well.

Factor increasing the adaptability of this technique is the possibility of its combination with traditional events in the wells, requiring the use of chlorine-containing substances. For example, the killing of a well solution NaCl, CaCl during repair works, hydrochloric acid treatment beds, etc.

For solving complex problems stimulation and detail inhomogeneous cut oil layer on the dynamics of processes of filtration displacement and the involvement of the oil reservoir (thickness h> 0,2 m) with different reservoir properties.

REFERENCES

[1] Kuznetsov O.,L., Efimova S.,A, "The use of ultrasound in the oil industry," Moscow, "Nedra", 1983

[2] Shimelevich Y.,S, Cantor S.,A.,Shkolnikov A.,S., Popov N.,V., Ivankin V.,P., Cedars A.,I., Miller V.,V.,Polyachenko A.,L., Physical basis of pulsed neutron techniques for wells. , Nedra, 1976, p.122-130.

[3] Bogdanovich B.,Y., Nesterovich A.,E.,Shikanov A.,E.,Vorogushin M.,F.,Svistunov Y.,A., Remote radiation control with linear accelerators. V.2. Radiation monitoring systems. M., Mechanical Engineering, 2012, p. 284.

[4] Amur A.,G.,Kurdyumov I.,G., Titov I.,A., Hassan T.,S., Shipunov M.,V., Apparatus pulsed neutron-neutron logging for use in modern technology for wells. Sat Materials of the International Scientific Conference "Portable neutron generators and technologies based on them," Moscow, VNIIA them. NL Spirit, 2005, p. 253 - 255.

[5] Bessarabian J.,G., Bogolyubov E.,P., Kurdyumov I.,G.,Simagin B.,I.,Shikanov A.,E.,Downhole neutron emitter. Instruments and Experimental Techniques, № 5, 1994

[6] Startsev A.A., Fedyna E.A., Shikanov A.E. Appl. Radiat. Isot.Vol.48, No.10-12, 1997, p.1329-1330.

PROJECT OF THE RADIOISOTOPE FACILITY RIC-80 (RADIOACTIVE ISOTOPES AT CYCLOTRON C-80) IN PNPI

V.N. Panteleev, A.E. Barzakh, L.Kh. Batist, D.V. Fedorov, A.M. Filatova, V.S. Ivanov, K.A. Mezilev, F.V. Moroz, P.L. Molkanov, S.Yu. Orlov, Yu. M. Volkov, PNPI, NRC Kurchatov Institute, Gatchina, 188300, Russia
E.K. Dyakov, I.B. Savvatimova, RISPA "LUCH", Podolsk, 142100, Russia

INTRODUCTION

It is well known that the main sources for production of the radioactive nuclides are thermal neutrons reactors and accelerators of charged particles. Since in the last years new reactors were not constructed (in Russia the only reactor which construction has been finished in 2011 was the PIK reactor at PNPI in Gatchina) on the front place go the accelerators of the charged particles - cyclotrons, as the most safe and reliable technological installations. The list of cyclotron radio nuclides is much longer and more varied, than ones got on reactors. Cyclotron radio nuclides can be used both for diagnostics and for therapy. As to cyclotrons used in Russia for radioisotope production, mostly they have the energy of bombarding particles lower than 30 MeV, therefore the variety of nuclides produced with these installations is limited. The cyclotron of NRC "Kurchatov institute" is at present time the only working cyclotron with the energy of external proton beams of 30 MeV. As a result only there the isotope ^{123}I can be produced with the high radionuclide purity from a xenon target.

At INR of RAS (Troitsk) the powerful linear accelerator is in operation - Moscow meson factory. At 160 MeV proton beam branch the laboratory, which has the installation for irradiations of targets was created for production of medical radio nuclides [1]. This installation is one of the largest in the world in respect of beam energy accumulated in production of radio nuclides and providing a possibility to produce practically the whole list of accelerator radio nuclides. The essential disadvantage of this method is that the usage of the accelerators of such kind is very expensive and the production cost of medical radio nuclides by that method is considerably higher than by means of cyclotron with the proton energy up to 80 MeV.

SCHEME OF THE DESIGNED INSTALLATION RIC-80 (RADIOACTIVE ISOTOPES ON CYCLOTRON C-80)

In PNPI NRC KI (Gatchina) the project of the radioisotope facility RIC-80 (Radioactive Isotopes at cyclotron C-80) is being developed [2]. In fig. 1 the layout of RIC-80 installation is presented. The proton beam energy at the target will be of 40-80 MeV and the intensity up to 200 μA. This cyclotron is intended for production of a wide spectrum of medical radio nuclides for diagnostics and therapy and also for a treatment of ophthalmologic diseases by irradiations of a malignant eye formation. The cyclotron is located in the right side of experimental hall (ground floor) of the PNPI synchrocyclotron.

The outgoing proton beam is directed down to the underground floor and traced in the horizontal direction. After that the beam can be directed to one of target stations: a) the isotope mass-separator target by the 37 degrees clockwise deflection from "zero" beam direction; b) the target station by "zero" deflection and c) the target station by the 34 degrees counterclockwise deflection. The mass-separator with its target as the first target station will allow getting the separated isotopes of a high purity, which are implanted into a corresponding collector from which they can be easily extracted. Target stations will be equipped with special devices to download highly radioactive targets into protection containers to transport them safely to special storage places or to hot cells for the after-treatment and production of corresponding pharmaceutics.

ESTIMATED YIELDS OF RADIO NUCLIDES EXPECTED TO BE PRODUCED AT RIC-80 FACILITY

RIC-80 facility is unique being the largest in Russia cyclotron facility in respect of beam energy accumulated in production of radio nuclides and providing enough high energy of bombarding particles (proton energy of 80 MeV). It gives an opportunity to produce sources of a high activity within practically the whole list of radio nuclides produced at accelerators. In table 1 calculated activities of radio nuclides are shown, which are planned to be obtained at RIC-80 facility.

It is necessary to emphasize that the activities of radioisotopes are shown for production in the target. The actual activities extracted out of target material can be less because of incomplete extraction of produced radioisotopes.

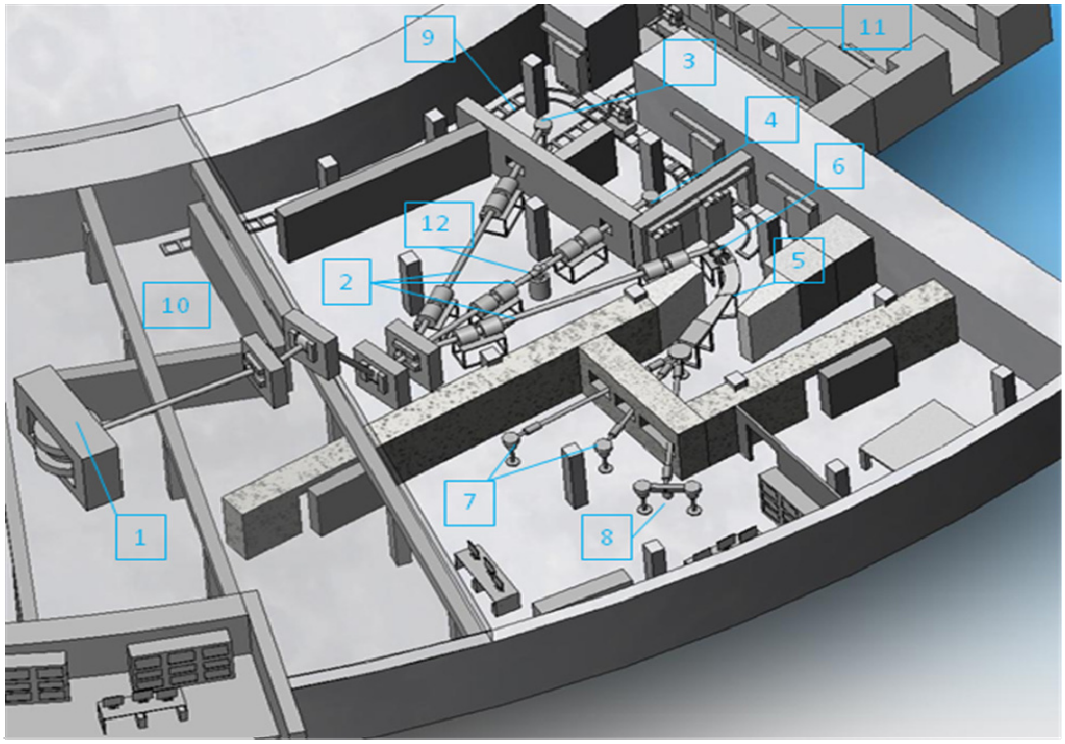

Figure 1: Layout of RIC-80 radio isotope complex. 1 – Cyclotron C-80, 2 – proton beam tubes, 3, 4 – target stations for radiochemical production of medical isotopes, 5 – mass-separator for production of medical isotopes of a high purity, 6 – target station of mass-separator, 7 – collecting stations for separated radio nuclides, 8 – detector stations for obtained radio nuclide purity measurement, 9 – transportation system for activated targets to special storage places or to hot cells, 10 –storage place for irradiated targets, 11 – hot cells, 12 – pneumatic rabbit station.

Table 1: Yields of some radionuclides planned to be obtained at RIC-80 facility with proton beam energy of 40-80 MeV and current of 100 μA.

Isotope	Half life	Target	Irradiation time interval (h)	Target Activity (Ci)
^{68}Ge	270.8 d	Ga	240	2
^{82}Sr	25.55 d	Rb	240	10
^{111}In	2.8 d	Cd	25	24.7
^{123}I	13.27 h	Te	5	10.4
^{124}I	4.17 d	Te	25	9.3
^{201}Tl	3.04 d	Tl	25	9.2
^{223}Ra	11.4 d	Th	240	7.3

For appropriate target developments the test experiments with target prototypes are performed presently at the synchrocyclotron in operation at PNPI for effective production of the listed nuclides.

Possibilities of the radionuclides production at RIC-80 installation are not exhausted by the list of isotopes provided in Table 1. The unique parameters of the C-80 cyclotron allow produce the broad nomenclature of radioisotopes, which are at present under discussion in corresponding publications as very perspective for diagnostics and therapy. The comparison of used for many years isotopes with new isotopes, which are under discussion and used in clinical tests brings us to a conclusion on trends to use more short-lived radionuclides to aim the diagnostics and therapy that significantly reduces the radiation rate for patients.

ON-LINE MASSES-SEPARATOR AT RIC-80 INSTALLATION TO OBTAIN MEDICAL ISOTOPE BEAMS OF THE HIGH PURITY

The production and study of radioactive isotopes by ISOL systems (Isotope Separator On-Line) is one of the fundamental directions of nuclear physics, as well as study of astrophysical processes in laboratory conditions. The main problem – the extraction and isotopic separation produced radio nuclides is under successful solution for 40 years already by means of ISOL installations at beams of different bombarding particles - protons, neutrons and heavy ions. Such on-line systems like ISOLDE (CERN,

Switzerland) [3], ISAC (TRIUMF, Canada) [4], IRIS (PNPI, Gatchina) [5] under operation on-line at proton beams, allow to obtain at present more than 2000 separated isotopes of almost all elements of the Periodic system. Produced radioactive isotopes of half-life from several milliseconds to several thousand years are used in nuclear physics study, in solid state physics and in the radiation medicine.

On the base PNPI synchrocyclotron the single ISOL facility in Russia - IRIS (the Investigation of Radioactive Isotopes at Synchrocyclotron) is under operation, where radioactive isotopes of many elements are produced and investigated. At IRIS for more than thirty years different target-ion devices for production and studies of a very wide range of radioactive isotopes are developed and used. For the time of the facility operation more than 300 nuclei have been investigated and 17 of them have been identified for the first time. For the period since 2000 new target devices of high efficiency have been designed, which have been used for production of more than 50 radionuclides from areas of β^+, β^- и α decay. For nuclear physics studies radioactive isotopes of Mn, Fe, Co, Ni, Ga, Rh, Pd, Rb, Cd, In, Sn, Sb, Te, I, Cs, Tl, Pb, Bi, Po, At were produced using the targets made of a high density uranium mono carbide [6]. Liquid metal targets and a high temperature refractory metal targets have been used to produce radioisotopes of alkaline metals - Li, Rb, Cs and also isotopes of rare earth elements - Sm, Eu, Gd, Tm, Yb [7]. New developments and 35 years of experience in operation of IRIS installation will be used for the new ISOL system construction on-line with the beam of a high current C-80 cyclotron for production of intensive beams of medical radionuclides of a high purity.

The products formed inside a target material get out of target container kept at high temperature (1800-2200°C) by the diffusion-effusion process into an ion source, where the ionization occurs. Ions, going out of ionizer, are formed by the field of extraction electrode into a beam of ~ 2 x 10^{-2} radians divergence. Going through a focusing lens, ion beam is converted into a parallel and gains the energy of 30 keV. Later the beam of mono energetic ions enters the magnet-analyser, where the mass separation occurs. Beams of radioactive ions separated by masses enter the switchyard chamber and after that they go along vacuum ion guide tubes to the experimental hall, where they are implanted into corresponding collectors. Sources of radio nuclides obtained without any carrier and admixtures are measured in time of the accumulation process for the determination of their purity and activity rate by means of α, β and γ detectors installed close to collectors, where the radioactive ion beams are implanted. Coming from aforesaid one, the mass-separator method possesses the following values:

- allows to obtain very pure beams of isotopes of many elements;
- several separated radionuclides can be accumulated simultaneously;
- the implantation depth of tens Å allows to use very fine organic substrates that can significantly simplifies the production process of pharmaceutics.
- the method of the radioactive ions implantation allows to obtain the unique generators of radioactive noble gases;
- the target can be used many times and does not require reconstruction;
- beside a number of relatively long-lived nuclides, mass- separator on-line at accelerator or reactor allows to obtain a lot of new "short-lived" radioactive isotopes ($T_{1/2}$ = from several minutes to several hours for diagnostics;
- process of the diagnostics can be realized "on-line" in medical laboratories, which are based on installations produced a big variety of short-lived mass-separated radioactive nuclides of a high purity.

The efficiency of the mass-separator method on the production of different nuclides varies in the range from some to ninety percents. So one of the main goals is the development of new highly efficient target - ion source devices specially suited for production of radionuclides with a high current medicine accelerators.

CONCLUSIONS

RIC-80 facility project will give an opportunity to use both the traditional radiochemistry method for the extraction of produced nuclides and the innovative mass-separator method, which will allow obtaining radionuclides of a high purity directly at the collector of the mass-separator, providing herewith an unique possibility to produce short-lived radioactive nuclides. By means of the advancement into a short half-life area the number of radionuclides in use (half-life from about some minutes to some hours) can be significantly extended. The corresponding studies of target materials and target – ion source device prototypes for RIC-80 facility were started in 2010 in the beam of PNPI synchrocyclotron.

REFERENCES

[1] Zhuikov, B.L. et al., Radiochemistry, 53, 66 (2011).
[2] V. N. Panteleev et al., absracts ici7, Moscow 4-8 Sept., 2011, p. 35.
[3] U. Koster et al., Nucl. Instrum. and Meth. B 204 (2003) 347-352.
[4] P. Bricault et al., Nucl. Instrum. and Meth. B 204 (2003) 319-324.
[5] E. Ye. Berlovich et al., Izvestiya Akademii Nauk SSSR, Ser. Fiz., 1976. V.40. P. 2036.
[6] A. Andrighetto et al., Nucl. Instrum. and Meth. B 204 (2003) 267-271.
[7] V.N. Panteleev et al., Eur. Phys. J. 26, 147-150 (2005).

TRANSFORMATION OF BEAMS IN THE PLASMA LENS AND INVESTIGATION OF Z-PINCH DYNAMICS*

A.Drozdowskiy, N.Alexeev, S.Drozdowskiy, A.Golubev,
Yu.Novozhilov, P.Sasorov, S.Savin, V.Yanenko. ITEP, Moscow, Russia

Abstract

The plasma lens can carry out sharp focusing of ion beam with considerable reduction sizes of focal spot. At those stages of the plasma discharge at which the magnetic field is nonlinear, formation of other interesting configurations of beams is possible. The report presents the results of studies transformation the Gaussian beam into hollow one and into beam with homogeneous spatial distribution. The discharge current distributions obtained by numerical calculation ensure the experimental beam transformations. Thus possibility of the research of the plasma discharge dynamics by means of relativistic ions beams is shown. The plasma lens represents the universal device for scientific and technical applications in particular for irradiation of medical objects.

INTRODUCTION

The ion beam focusing in the plasma lens is carried out as shown in Fig.1. The discharge current produces an azimuthal magnetic field. The ions are injected along the lens axis, and the radial Lorentz force focuses the ion beam [1].

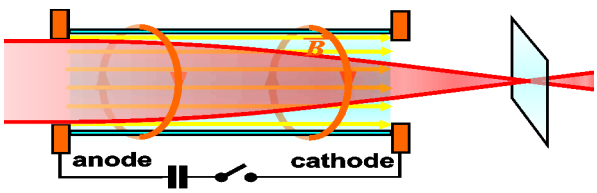

Figure 1: Ion focusing in a plasma lens.

The focusing properties of plasma lenses depend on the current density distribution along the radius of the plasma discharge. The current distribution across the tube changes significantly during the discharge. Therefore, plasma lens, in general, is nonlinear. Uniform current distribution exists for a limited time, so the plasma lens, as a device for sharp focusing, operates for about 1 μs or less. As a non-linear focusing device, the plasma lens can be used to produce beams of special shape.

The studies of possibility of use of a plasma lens were carried out at ITEP both for sharp focusing, and for formation of tubular beams and beams with homogeneous distribution of density [3,4]. Researches were carried out of ion beams of carbon and iron with energy 200-300 Mev/a.e.m.. Duration of an impulse of a current of the plasma was 5 and 20 μs, and the duration of an impulse of a current of an ion beam – 0.3 μs . Sizes of a discharge tube: length – 10 cm, diameter – 2 cm. Pressure of gas (argon) before a discharge impulse was of 0.5-10 mbar.

Z-PINCHS DYNAMIC RESEARCH

Research of that implosion of plasma and mechanisms of penetration into it a magnetic field - is a fundamental scientific problem. The understanding of the mechanisms defining distribution of a current in plasma is absolutely necessary for thermonuclear synthesis, lasers in the field of XUV and a soft X-ray, transportation of powerful laser beams, focusing of powerful beams of ions, etc.

Active corpuscular diagnostics, based on application of special beams of fast atoms and ions, have considerable development. The main problems of use of that technique - limited transparency of plasma for beams. Therefore the beams of relativistic energy is necessary for plasma researches. The systematic researches z-pinchs by means of relativistic ion beams weren't carried out yet. Meanwhile in a plasma lens Z-pinches creation in a wide interval of parameters is possible: with a current to 0.5 MA at duration of impulses of 1-30 microsec.

We developed a numerical technique of receiving distribution of currents and self magnetic fields in the plasma lens, adequate to the configurations of an ion beams received experimentally. Some results of this work are presented in [4].

The results of experimental researches of influence of a plasma lens on a beam of ions with gauss distribution of density at various stages of development of the plasma discharge are shown on fig. 2. The each column of the figure corresponds to a certain moment of time after the beginning of the plasma discharge: 0.5, 1.7 and 8.5 μs. On the first line of the figure the distributions of ion beam density are shown. On the second line of the figure the experimental distributions self magnetic field in lens z-pinch are shown. On the third line of the figure the modeling distributions self magnetic field in lens z-pinch are shown.

* Work supported by the *Russian Federal Ministry of Education and Science*, and by the Russian Foundation for Basic Research

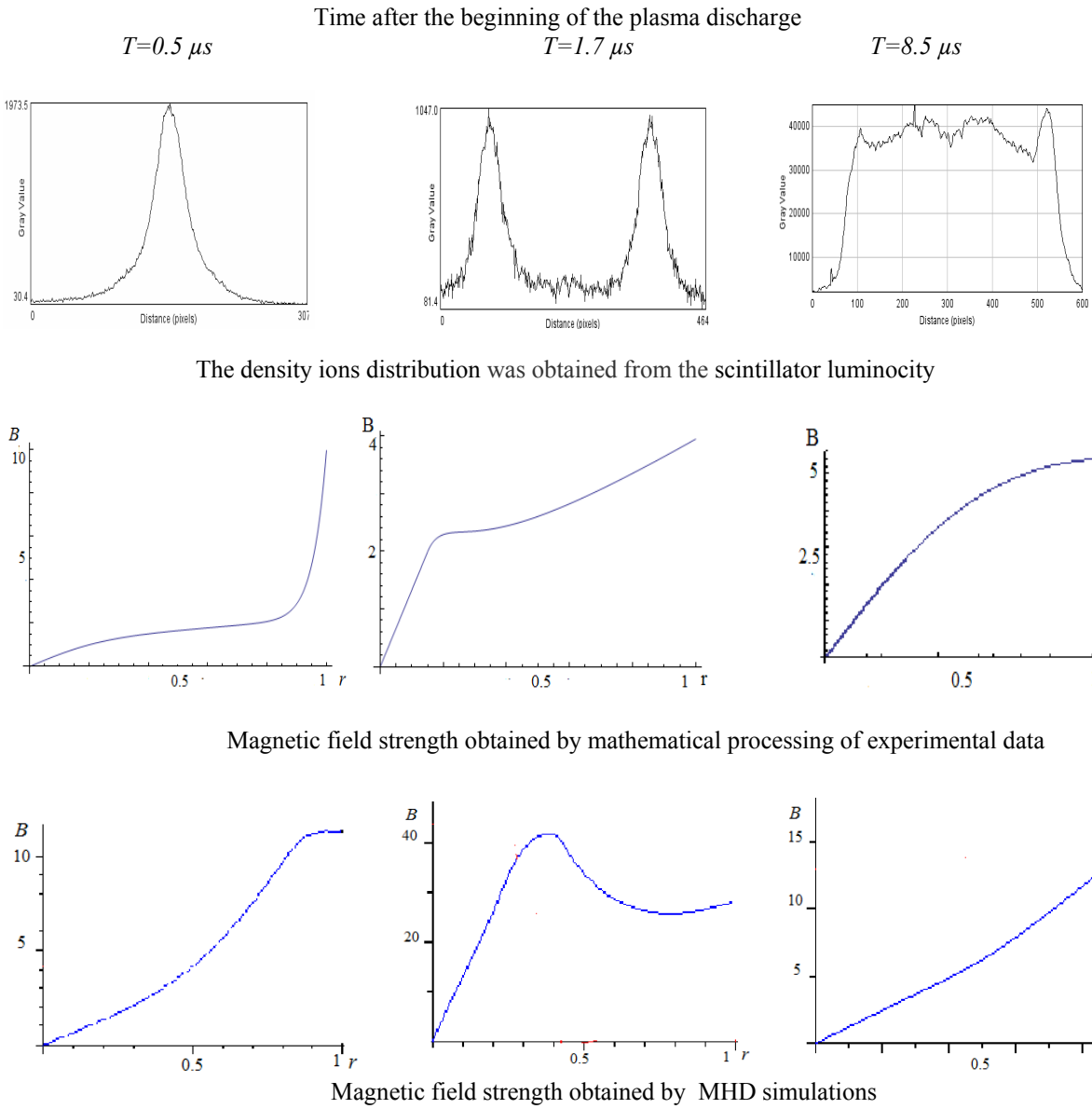

Figure 2. The results of experimental researches of influence of a plasma lens on a beam of ions and comparison of self magnetic fields B of z-pinch, defined from experimental data and MHD theoretical modeling: the distributions of ion beam density (first line); the experimental distributions self magnetic field in lens z-pinch (seconde line); the MHD modeling distributions self magnetic field in lens z-pinch (third line). Here strength of a magnetic field B is given in kG, distance from an axis r - in cm.

COMPARISON OF THE EXPERIMENTAL RESULTS AND MHD SIMILATIONS OF Z-PINCH DYNAMICS

The beam diagnostics gives important information concerning spatial distribution of electric current across the discharge of the investigated type. This causes a question about correspondence of these data with the theory of Z-pinches as well as with results of mhd-simulations. To clarify this question we used the one-dimensional MHD code NPINCH. It adopts all dissipative processes in plasma and was successfully used for simulation of capillary discharges of different types. See Refs. [5,6].

One of the main questions that should be answered concerns a role of evaporation from inner wall of the discharge insulator tube, which interacts with discharge plasma, ionization of these vapors and engaging of this new plasma in the discharge. Preliminary very rough estimations show that the present discharges are close to the threshold of the evaporation. The method of inner

wall evaporation description, used in Refs. [5,6], was tested there and in other publications for fast capillary discharges with typical current rise time of the order of 0.1 μs, when the evaporation threshold was surely overcame. In the present case the typical discharge time is 10-100 times longer. For this reason it is not so obvious in advance that the same simplified method can be applicable for these discharges also.

Let us consider at first discharges with the typical current ~ 150 kA and its half period ~ 5 μs. Under assumption that there is no evaporation, dynamics of plasma in such discharge would be characterized by detachment of plasma from the discharge tube inside wall at the very beginning of the discharge and to unreal strong compression of the plasma at the axis. Such strong compression would lead to strong implosion of the whole current to a very thin pinch. This contradicts apparently to experimental data and, in particular, to the data about field distribution across the discharge. See Fig. 2 (line 2) for t = 1.7 μs. This apparent and strong contradiction means that more or less smooth distribution of the current over the whole discharge including the outermost parts of it is possible only if there is a significant evaporation from inner walls of the discharge tube. Mass of plasma formed from the vapors that joints the discharge should be comparable with the initial mass of argon inside the tube. Our next step is to include evaporation of inner wall material and plasma formation from these vapors into our MHD simulation. We use the same method for description of this evaporation as previously in publications mentioned above. We assume that the whole heat flux from the discharge plasma toward the walls is spent for formation of new plasma. Thus we neglect completely initial period of the discharge when the wall surface is heated up to sufficiently high temperature ~ 1000° K and the energy of the discharge that was spent to this latent heating. Results of such simulations are presented in Fig 2 (line 3).

Our simulations show that radial current distribution changes dramatically after taking into account the evaporation. Considerable part of the whole current stays in outer parts of the discharge including very close vicinity of the wall. Magnetic field distribution becomes qualitatively similar to that takes place in the experiment. About 60% of the total current flows in the central region of the discharge that occupies about 15% of its cross-section. The rest of the current flows mainly in outer regions of the discharge. As a result we may conclude that the experimental data indicate to a considerable role of new plasma formed from evaporated material of the walls.

Turn now to the longer discharges with ~ 20 μs half-periods and about ~ 60 kA peak currents. In this case there is no plasma detachment from the walls even, if we neglect evaporation from the walls. As a result current is distributed across the whole cross-section more or less uniformly even without taking into account wall evaporation. As a result there is no rough contradiction of our simulations without the evaporation with the experiment. It is in contrast to the previous case. Thus there are no apparent arguments for existence of evaporation in this case. Nevertheless more detailed analysis of radial current density distributions says that there is a bump of experimental current density that does not correspond to simulations. We may conclude that wall evaporation plays probably some role in this case also. It appears however we cannot simulate unlimited evaporation with the lagrange code NPINCH for such long lived discharges. The reason of this situation is that this hydro-code cannot to take into account kinetics of phase transitions that is necessary to describe considerable discontinuity of electric conductivity between hot dielectric and plasma. However we have presently no suitable code without this disadvantage. Such code should be likely an Euler one.

CONCLUSION

The plasma lens can carry out not only sharp focusing of ion beam with considerable reduction of focusing spot. At those stages of the plasma discharge at which the magnetic field is nonlinear, formation of other special configurations of beams is possible. The plasma lens provides transformation the Gaussian beam into hollow one and into beam with homogeneous spatial distribution. The plasma lens essentially represents the universal tool for preparation of beams for the decision of scientific and applied technical problems, in particular for irradiation of medical objects and as a possible variant of a terminal lens for realization of inertial thermonuclear synthesis.

The discharge current distributions obtained by numerical calculation ensure the experimental beam transformations. Thus possibility of the research of the plasma discharge dynamics by means of relativistic ions beams is shown.

REFERENCES

[1] D.H.H. Hoffmann et al., Nucl. Instr. Methods Phys. Res., Sect. B 161-163, (2000), p. 9.
[2] B.Yu. Sharkov et al., Nucl. Instr.Meth. A464 (2001), p. 1-5.
[3] A. Drozdovskiy et al., International Particle Accelerator Conference IPAC'08, July, 2011, http://web.cern.ch/accelconf/, WEPC074.
[4] A. Drozdovskiy et al., Physics of Particles and Nuclei Letters, 2012, Vol. 9, No. 4-5, pp. 356-359.
[5] N.A. Bobrova, S.V.Bulanova, T.L.Razinkova, P.V. Sasorov, Physics of Plasmas, **22,** 387 (1996).
[6] P. Vrba, N.A. Bobrova, P.V. Sasorov, M. Vrbova, J. Hubner, Physics of Plasmas, **16**, 073105 (2009).

EXCITATION OF THE FOCUSING WAKEFIELDS BY A RELATIVISTIC BUNCH IN ISOTROPIC CAPILLARY DISCHARGE PLASMA*

R.R. Kniaziev#, KhNU them. V.N. Karazin, Kharkov, Ukraine
G.V. Sotnikov, NSC Kharkov Institute of Physics and Technology, Kharkov, Ukraine

Abstract

The present paper offers research of wake waves by the relativistic electron bunch in the capillary tube filled with plasma. Analytical expressions for the electromagnetic field component with approaching "hard" bunches have been obtained. Numerical calculations of the appearing fields for capillary tubes samples have been made. The transversal and axial structure of wake fields in the slowing structure with plasma in the transport channel has been researched in detail. The regimes in which focusing of the accelerated bunch is clearly seen have been studied. The results of numeric PIC modeling of fields in the structure under consideration have been provided.

INTRODUCTION

One of the promising ways of accelerating by wake fields excited by relativistic electron bunches uses plasma, created by the same bunches [2] or by external sources, as the slowing medium [1]. The capillary discharge can be used as an external source [3, 4]. The capillary tube is the slowing structure, therefore eigen waves of dielectric structure, modified by the presence of plasma in the transport channel, as well as plasma waves are excited in the tube channel when electron bunches are travelling in it. Below we research the influence of electrodynamic properties of the capillary tubes material on wake waves excitation.

NUMERICAL CALCULATIONS

For the cylinder all-over bunch having the radius r_b and the length L_b, and with homogeneously distributed density of particles:

$$n(r_0, t_0) = \frac{Q/e}{\pi L_b r_b^2}\left[\Theta(t_0) - \Theta(t_0 - L_b / v_0)\right]\Theta(r_b - r) \ , \quad (1)$$

where Q is bunch charge, -e is electron charge.

Final expressions for the wake field components were presented in the paper [5]. Here are the results of the wake field calculations. For our calculations we choose the dielectric waveguide with dimensions presented in the Table 1, with the dielectric tube made of fused silica. In the same table electron bunch parameters are given. Plasma parameters are given in Table 2. The results of calculations for plasma with such parameters are shown in Figures 1-2.

Table 1: Dielectric structure (Fused silica).

Parameter	Value
Outer radius of dielectric tube	0.6 mm
Inner radius of dielectric tube	0.5 mm
Relative dielectric constant, ε	3.75
Bunch energy	5 GeV
Bunch charge	3 nC
Bunch length L_b (box charge distribution)	0.2 mm
Bunch radius r_b (box charge distribution)	0.45 mm
Density of drive bunch electrons, n_b	$1.47 \cdot 10^{14}$ cm^{-3}
Vacuum wavelength of 1st radial mode of the vacuum DWA	~1 mm
Vacuum wavelength of 2nd radial mode	~0.3 mm
Vacuum wavelength of 3rd radial mode	~0.16 mm

Table 2: Parameters of the plasma

Plasma density	$4.41 \cdot 10^{14}$ cm^{-3}
Plasma wavelength	1.59 mm
Radius of plasma	0.5 mm

Fig.1 shows axial distribution of the axial force, acting on the probing particle. It follows from the dependence, given in Fig. 1, that we can ensure acceleration of charged particles with their simultaneous radial focusing by placing the testing bunch at some distance from the drive bunch head. As it can be seen in the Figure, the radial force almost harmoniously depends on the axial coordinate with the period of approximately 0.16 cm, i.e. the Langmuir wave makes the greatest contribution into the radial force. At the same time, its contribution into the axial force, accelerating test particles, is predominantly small. The axial force is predominantly determined by the eigen modes of the dielectric waveguide; its complex behavior from the axial coordinate is caused by excitation several radial modes of the dielectric waveguide. For the used in analytical calculations parameters of the dielectric waveguide, bunch and plasma, the focusing force amplitude is approx. 300MeV/m, which equals the focusing magnetic field induction ~1T.

* The research is supported in part by STCU, project №. P522.
# RKniaziev@gmail.com

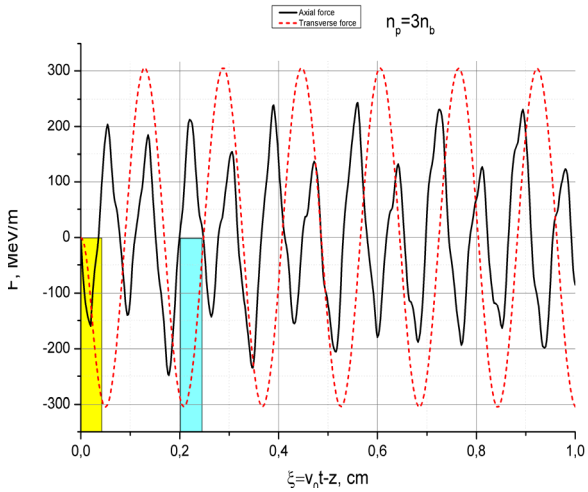

Fig.1: Analytical code. Plasma-filled transport channel, plasma density $n_p = 3n_b$. Axial profile of the axial force (black line) and axial profile of transverse force (red line) at the distance r = 0.45 mm from waveguide axis. Drive bunch (yellow rectangular) moves from right to left. Cyan rectangular shows possible location of test (accelerating) bunch.

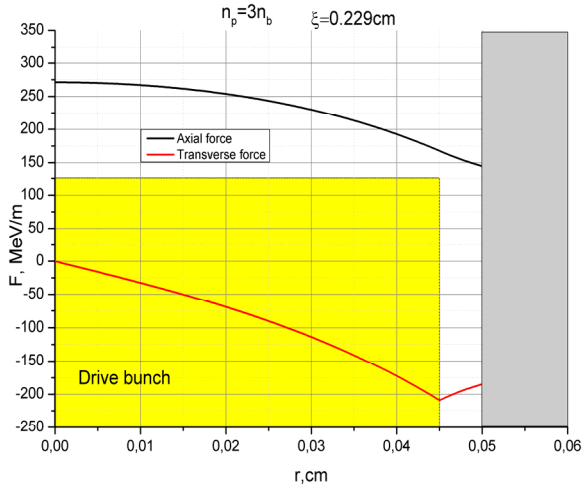

Fig. 2: Analytical code. Plasma-filled transport channel, plasma density $n_p = 3n_b$. Transverse profile of the longitudinal (black line) and transverse forces (red line), acting on a test particle, located at a distance of 0.23 cm from the head of the drive bunch.

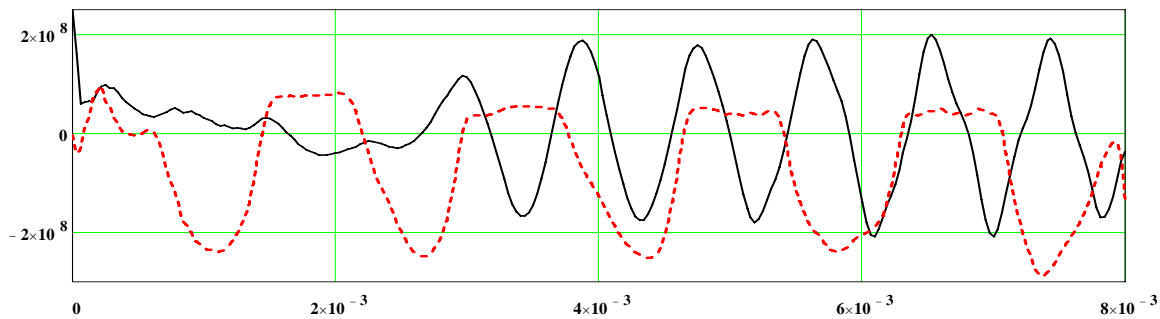

Fig.3: OOPIC simulations of plasma-filled transport channel, plasma density $n_p = 3n_b$. Axial profile of the axial force (black line) and axial profile of transverse force (red line) at the distance r=0.45mm from waveguide axis. Drive bunch (yellow rectangular) moves from left to right, travel time t=26.7psec. Distance (x-axis) is measured in m, forces (y-axis) are in eV/m.

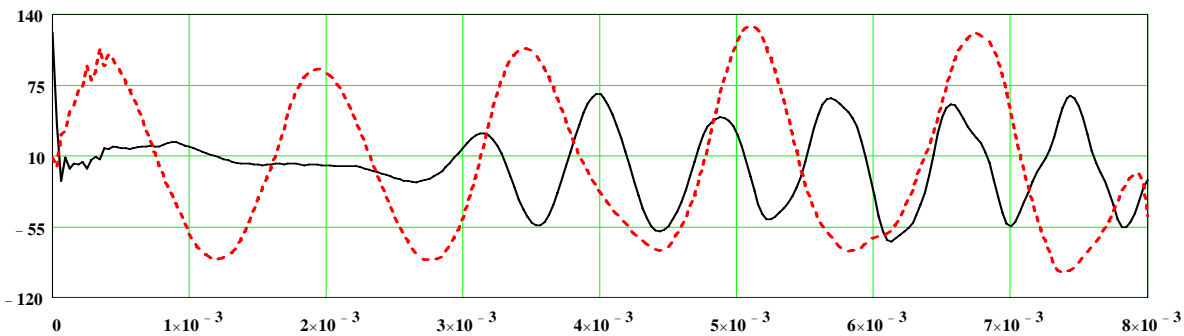

Fig.4: OOPIC simulations of plasma-filled transport channel. Drive bunch charge is 1nC. Axial profile of the axial force (black line) and axial profile of transverse force (red line) at the distance r=0.45mm from waveguide axis. Drive bunch (yellow rectangular) moves from left to right, travel time t=26.7psec. Distance (x-axis) is measured in m, forces (y-axis) are in MeV/m.

Fig. 2 shows the radial dependence of axial and transverse forces, acting on the test particle, placed in the first of the maximums of the accelerating field, at the distance of 0.23 cm behind the drive bunch head. The axial force changes insufficiently in the transport channel

cross section, while the radial force remains focusing along all the channel section.

The results, presented in Fig. 1-2, obtained through analytical expressions [5], are true for the approximation of linear plasma $n_b \gg n_p$ (overdense regime). Another extreme case $n_b \ll n_p$ (underdense or blowout regime), with a focusing provided by plasma ions, remaining in the transport channel after plasma ions have been pushed out of it by the intense drive bunch. In order to verify the analytical theory applicability [6], we have made full numeric simulation of wake fields excitation in the plasma dielectric structure under investigation. For calculations we used both our own PIC code and OOPIC code realized for Linux [7]. The results of modeling, made with both codes, coincide well.

Fig. 3 shows the results of the numeric modeling with the use of OOPIC code of wake fields behavior in the slowing environment. Comparison of the curves in Fig.3 with corresponding curves in Fig. 1 confirms acceptable coincidence of the results of PIC modeling at self-consistent account of the plasma dynamics and analytical results. The accelerating and focusing fields coincide quite well. The greatest difference is observed in defocusing areas of the wake field. This difference can be explained for by the pushing out of plasma electrons to the dielectric surface and the appearance of the local under dense plasma area. This explanation is confirmed by the results of the OOPIC modeling for the bunch with the charge decreased by 3 times, with the plasma electrons loss being much smaller. Fig. 4 shows axial distribution of the accelerating and focusing forces for the drive bunch with the charge 1nC. As it followed from Fig. 4. we observe a more exact correspondence with the analytical calculations (taking into account the normalization for the bunch charge), given in Fig.1.

CONCLUSIONS

Research of wake fields excited by the electron bunch in the plasma dielectric waveguide shows that filling up of the dielectric waveguide vacuum transport channel with isotropic plasma of a definite density results in the set up of the focusing wake field which accelerates a witness bunch. The uncovered mechanism of the test bunch focusing in terms of plasma density as well as other parameters of the dielectric waveguide has been optimized. Optimal regimes for the accelerated bunch focusing in the drive bunch wake fields have been found. The results obtained at complete numeric modeling with taking into account a non-linear plasma particles dynamics coincide accurately enough with the theoretical calculations in a definite range of the plasma density and the drive bunch density ratio.

The authors are grateful to Manuylenko O.V. and Markov P.I. for the opportunity to compare the PIC modeling and the analytical results.

REFERENCES

[1] P. Chen, J. M. Dawson, R.W. Huff, and T. Katsouleas, Phys. Rev. Lett. 1985. V.54, No.7. P. 693-696.

[2] M. J. Hogan, C. D. Barnes, C. E. Clayton et.al., Phys. Rev. Lett. -V.95, 054802(2005).

[3] L. C. Steinhauer, W. D. Kimura., Phys. Rev. ST – Accelerator sand Beams. V.9 , 081301 (2006).

[4] A. Butler, D. J. Spence, and S. M. Hooker, Phys. Rev. Lett. V.89, 185003(2002).

[5] G.V. Sotnikov, R.R. Kniaziev , “Focusing of Accelerated Particles by Wakefields of a Drive Bunch in a Plasma-dielectric Waveguide, IPAC2012, New Orleans, Louisiana, WEPPP003, ISBN 978-3-95450-115-1, p. 2723 http://accelconf.web.cern.ch/AccelConf/IPAC2012/papers/weppp003.pdf

[6] [6] J.B. Rosenzweig, B. Breizman, T. Katsouleas, and J.J. Su, Phys. Rev. A44, R6289 (1991).

[7] [7] http://www.txcorp.com/products/OOPIC_Pro/

NONLINEAR THEORY OF EXCITATION OF AN AXIALLY ASYMMETRIC WAKEFIELD IN DIELECTRIC RESONATOR*

K. V. Galaydych#, G. V. Sotnikov
Kharkov Institute of Physics and Technology, Kharkov, Ukraine
I. L. Sheynman, LETI (ETU), Saint-Petersburg, Russia

Abstract

A nonlinear self-consistent theory of excitation of an axially asymmetric wakefield by relativistic electron bunches in cylindrical dielectric resonator with a vacuum channel for the charged particles transportation through the resonator is constructed. The formulated nonlinear theory allows investigating numerically the nonlinear effects such as increasing of the transverse bunch size, and head-tail beam breakup instability, which occurs if an electron bunch in the structure is misaligned.

INTRODUCTION

The dielectric wakefield accelerator is one of the modern trends of acceleration schemes, which can provide high-accelerating gradient for future colliders. But besides for high output energy of an accelerated bunches high demands are made on their quality, the same, for example, as low emittance. No loss of current under acceleration of the bunch are also desirable. This information about the bunch can not be obtained using assumption of the absence of reverse influence the excited field on the dynamics of electron bunches. In this paper we present nonlinear self-consistent theory of wakefield excitation in a dielectric–lined resonator by an electron bunches. The previous theoretical investigations on wakefield excitation in dielectric–lined structures, have been done for longitudinally unbounded structures [1]–[4]. In cited papers was noted, that it is necessary to taking into account the contribution of higher multipole modes to the total transverse field. A presented complete bunch–excited electromagnetic field includes all azimuthal modes, which allows calculating transverse wakefield in order to investigate bunch deflection problems.

STATEMENT OF THE PROBLEM

Consider cylindrical metallic resonator with inner radius b, partially filled with isotropic material with dielectric constant ε, containing on-axis vacuum channel of radius a which allows charged particles to pass through. We suppose that the end walls of the resonator are closed by metal grids transparent for charged particles and nontransparent for an excited electromagnetic field. Consider an electron bunch, injected into the resonator and moving along a line parallel to the axis of the resonator.

The electron bunches will be described in terms of macroparticles, therefore the charge density ρ and the current density $\mathbf{j}$ will be written as:

$$\rho = \sum_{p\in V_R} q_p \delta\left(\mathbf{r}-\mathbf{r}_p(t)\right),\ \mathbf{j} = \sum_{p\in V_R} q_p \mathbf{v}_p(t)\delta\left(\mathbf{r}-\mathbf{r}_p(t)\right), \qquad (1)$$

where q_p is the charge of the macroparticle, $\mathbf{r}_p$ and $\mathbf{v}_p$ are its time-dependent coordinates and velocity, respectively. The summation in Eq. (1) is carried out over the particles being in the resonator volume V_R.

FIELD SOLUTION

We introduce the solenoidal $\mathbf{E}^t$ $\mathbf{H}^t$ and the potential $\mathbf{E}^l = -\nabla\Phi$ fields defined as

$$\mathrm{div}(\varepsilon\mathbf{E}^t) = 0,\ \mathrm{div}(\mu\mathbf{H}^t) = 0,\ rot\mathbf{E}^l = 0, \qquad (2)$$

which are given by Maxwell's and Poisson equations:

$$rot\mathbf{E}^t = -\frac{\mu}{c}\frac{\partial\mathbf{H}^t}{\partial t},\ rot\mathbf{H}^t = \frac{\varepsilon}{c}\frac{\partial\mathbf{E}^t}{\partial t} + \frac{4\pi}{c}\mathbf{j}, \qquad (3)$$

$$\Delta(\varepsilon\Phi) = -4\pi\rho \qquad (4)$$

The solenoidal $\mathbf{E}^t$ and potential $\mathbf{E}^l$ electric fields are mutually orthogonal [5] and satisfy the boundary conditions, making their tangential components vanish on the metal walls of the resonator.

First we solve the equation (4) for the potential in the vacuum channel and dielectric. In cylindrical coordinate Eq.(4) rewrites as:

$$\frac{1}{\varepsilon r}\frac{\partial}{\partial r}\left(r\varepsilon\frac{\partial\Phi}{\partial r}\right) + \frac{1}{r^2}\frac{\partial^2\Phi}{\partial\varphi^2} + \frac{\partial^2\Phi}{\partial z^2} = -\frac{4\pi}{\varepsilon}\rho \qquad (5)$$

Eq.(5) should be complemented by boundary conditions consisting in that the potential Φ on the resonator metal walls becomes zero

$$\Phi(z=0) = \Phi(z=L) = \Phi(r=b) = 0, \qquad (6)$$

*The research is supported in part by STCU, project №. P522.
#kgalaydych@gmail.com

and continuity of the potential and radial component electric induction vector

$$\Phi(r=a-0)=\Phi(r=a+0),\ \left.\frac{\partial\Phi}{\partial r}\right|_{r=a-0}=\varepsilon\left.\frac{\partial\Phi}{\partial r}\right|_{r=a+0.} \quad (7)$$

By using the expansion by eigenfunctions method Eq. (5), with boundary conditions (6) and (7), can be solved. Finally, we obtain the potential in the form

$$\Phi(\mathbf{r},t)=\sum_{m=0}\sum_{n=1}\sum_{l=1}\frac{4\beta_m R_{mn}(r)\sin k_l z}{L\left(k_l^2+\kappa_{mn}^2\right)\left\|R_{mn}\right\|^2}\times \\ \times\sum_{p\in V_R} q_p R_{mn}(r_p)\cos m\left(\varphi-\varphi_p\right)\sin k_l z_p. \quad (8)$$

In the above (and below in paper) n, m, and l enumerate, respectively, radial, azimuthally and longitudinal indexes. Radial eigenfunctions $R_{mn}(r)$ and their norm have the form:

$$R_{mn}(r)=\begin{cases}\mathrm{J}_m(\kappa_{mn}r),\ 0\le r<a\\ \mathrm{J}_m(\kappa_{mn}a)\mathrm{Z}_m(\kappa_{mn}r)/\mathrm{Z}_m(\kappa_{mn}a),\ a\le r\le b\end{cases} \quad (9)$$

$$\left\|R_{mn}\right\|^2=\frac{a^2\left(1-\varepsilon\right)}{2}\left(1-\frac{m^2}{\kappa_{mn}^2a^2}\right)\mathrm{J}_m^2(\kappa_{mn}a)+ \\ \varepsilon\frac{\mathrm{J}_m^2(\kappa_{mn}a)}{\mathrm{Z}_m^2(\kappa_{mn}a)}\frac{2}{\pi^2\kappa_{mn}^2}\frac{1}{\mathrm{Y}_m^2(\kappa_{mn}a)}+\frac{a^2}{2}\left(\mathrm{J}_m'(\kappa_{mn}a)\right)^2\left(1-\frac{1}{\varepsilon}\right), \quad (10)$$

where $\mathrm{Z}_m(\kappa r)\equiv\mathrm{J}_m(\kappa r)-\mathrm{J}_m(\kappa b)\mathrm{Y}_m(\kappa r)/\mathrm{Y}_m(\kappa b)$, J_m and Y_m are , respectively, Bessel function and Neumann function of order m; $k_l=\pi l/L,\ (l=0,1,...)$ are the longitudinal eigenvalues; $\beta_{m=0}=1,\ \beta_{m\ne0}=2$. Radial eigenvalues κ_{mn} satisfies the equation

$$\varepsilon\mathrm{J}_m(\kappa a)\mathrm{Z}_m'(\kappa a)=\mathrm{Z}_m(\kappa a)\mathrm{J}_m'(\kappa a), \quad (11)$$

and can be found numerically.

The solenoidal parts of the electromagnetic field can be determined by expanding the required fields into solenoidal fields of the empty dielectric resonator [5]. Let us write down the fields $\mathbf{E}^{\mathrm{t}}$ and $\mathbf{H}^{\mathrm{t}}$ in the form:

$$\mathbf{E}^{\mathrm{t}}=\sum_s A_s(t)\mathbf{E}_s\left(\mathbf{r}\right),\quad \mathbf{H}^{\mathrm{t}}=-i\sum_s B_s(t)\mathbf{H}_s\left(\mathbf{r}\right). \quad (12)$$

The functions $\mathbf{E}_s$ and $\mathbf{H}_s$, which describe the spatial structure of solenoidal fields, satisfy the Maxwell sources-free equations.

By using the orthonormality conditions of eigenwaves

$$\int_{V_R}\varepsilon\mathbf{E}_s\mathbf{E}_{s'}^*dV=\int_{V_R}\mu\mathbf{H}_s\mathbf{H}_{s'}^*dV=4\pi N_s\delta_{ss'} \quad (13)$$

one can obtain the differential equations for calculation the expansion coefficients $A_s(t)$ and $B_s(t)$

$$\frac{d^2A_s}{dt^2}+\omega_s^2A_s=-\frac{dR_s}{dt},\ \frac{d^2B_s}{dt^2}+\omega_s^2B_s=-\omega_sR_s, \quad (14)$$

where $R_s=\frac{1}{N_s}\sum_{p\in V_R}q_p\mathbf{v}_p(t)\mathbf{E}_s^*[\mathbf{r}_p(t)]$.

Eigenfields, which satisfy the source–free Maxwell equations and electromagnetic boundary conditions can be written as:

$$\begin{cases}E_{r,s}=e_{r,s}(r)e^{im\varphi}\sin k_lz,\\ E_{\varphi,s}=-ie_{\varphi,s}(r)e^{im\varphi}\sin k_lz,\\ E_{z,s}=e_{z,s}(r)e^{im\varphi}\cos k_lz,\end{cases}\quad\begin{cases}H_{r,s}=h_{r,s}(r)e^{im\varphi}\cos k_lz,\\ H_{\varphi,s}=ih_{\varphi,s}(r)e^{im\varphi}\cos k_lz,\\ H_{z,s}=h_{z,s}(r)e^{im\varphi}\sin k_lz,\end{cases} \quad (15)$$

Then function R_s transforms to the expression

$$R_s=\frac{1}{N_s}\sum_{p\in V_R}q_p\left(v_{pr}e_{r,s}(r_p)\sin k_lz_p\cos m\varphi_p+\right. \\ v_{p\varphi}e_{\varphi,s}(r_p)\sin k_lz_p\sin m\varphi_p+v_{pz}e_{z,s}(r_p)\cos k_lz_p\cos m\varphi_p- \\ \left.i\left[v_{pr}e_{r,s}(r_p)\sin k_lz_p\sin m\varphi_p+v_{p\varphi}e_{\varphi,s}(r_p)\sin k_lz_p\cos m\varphi_p+\right.\right. \\ \left.\left.v_{pz}e_{z,s}(r_p)\cos k_lz_p\sin m\varphi_p\right]\right). \quad (16)$$

The functions describing the transverse structure of the solenoidal fields have the form:

$$e_{r,s}(r)=\frac{k_s}{k_l^2-\varepsilon k_s^2}\left(\frac{m}{r}h_{z,s}+\frac{k_l}{k_s}\frac{de_{z,s}}{dr}\right), \\ e_{\varphi,s}(r)=i\frac{k_s}{k_l^2-\varepsilon k_s^2}\left(\frac{k_l}{k_s}\frac{m}{r}e_{z,s}+\frac{dh_{z,s}}{dr}\right), \\ h_{r,s}(r)=\frac{\varepsilon k_s}{\varepsilon k_s^2-k_l^2}\left(\frac{m}{r}e_{z,s}+\frac{k_l}{\varepsilon k_s}\frac{dh_{z,s}}{dr}\right), \\ h_{\varphi,s}(r)=i\frac{\varepsilon k_s}{\varepsilon k_s^2-k_l^2}\left(\frac{k_l}{\varepsilon k_s}\frac{m}{r}h_{z,s}+\frac{de_{z,s}}{dr}\right), \quad (17)$$

where transverse structure of the axial components $e_{z,s}(r)$ and $h_{z,s}(r)$, through which all others components can be expressed, defines as follows:

$$e_{z,s}(r)=\begin{cases}\mathrm{J_m}(k_{v,s}r)/\mathrm{J_m}(k_{v,s}a),0\le r<a\\ \mathrm{Z_m}(k_{d,s}r)/\mathrm{Z_m}(k_{d,s}a),\ a<r\le b\end{cases} \\ h_{z,s}(r)=\begin{cases}C_s\mathrm{J_m}(k_{v,s}r)/\mathrm{J_m}(k_{v,s}a),\ 0\le r<a\\ C_s\Phi_{\mathrm{m}}(k_{d,s}r)/\Phi_{\mathrm{m}}(k_{d,s}a),\ a<r\le b,\end{cases} \quad (18)$$

where

$$C_s=-\frac{k_s^2k_lm(\varepsilon-1)}{k_{v,s}^2k_{d,s}^2aD_s},\ D_s=\frac{k_s}{k_{v,s}}\frac{\mathrm{J}_m'(k_{v,s}a)}{\mathrm{J}_m(k_{v,s}a)}-\frac{k_s}{k_{d,s}}\frac{\Phi_m'(k_{d,s}a)}{\Phi_m(k_{d,s}a)},$$

Eigenfrequencies ω_s are determined from the dispersion equation

$$\left(\frac{1}{k_v^2}-\frac{1}{k_d^2}\right)^2\frac{k_l^2m^2}{a^2}-\left[\frac{k}{k_v}\frac{\mathrm{J}'_m(k_va)}{\mathrm{J}_m(k_va)}-\frac{k}{k_d}\frac{\Phi'_m(k_da)}{\Phi_m(k_da)}\right]\times$$
$$\left[\frac{k}{k_v}\frac{\mathrm{J}'_m(k_va)}{\mathrm{J}_m(k_va)}-\frac{\varepsilon k}{k_d}\frac{\mathrm{Z}'_m(k_da)}{\mathrm{Z}_m(k_da)}\right]=0, \quad (19)$$

where $k_s=\omega_s/c$ are the wave numbers, $k_{v,s}^2=\omega_s^2/c^2-k_l^2$, $k_{d,s}^2=\varepsilon\omega_s^2/c^2-k_l^2$ are the transverse wave numbers, respectively, in vacuum channel and in the dielectric;
$\mathrm{Z}_m(k_dr)\equiv \mathrm{J}_m(k_dr)-\mathrm{J}_m(k_db)\mathrm{Y}_m(k_dr)/\mathrm{Y}_m(k_db)$,
$\Phi_m(k_dr)\equiv \mathrm{J}_m(k_dr)-\mathrm{J}'_m(k_db)\mathrm{Y}_m(k_dr)/\mathrm{Y}'_m(k_db)$.

Taking into account the expressions for the transverse structure of the solenoidal fields (17) and (18) we can write down the expressions for the norms N_s:

$$N_s=\frac{ak_s^2(\varepsilon-1)}{k_{v,s}^3k_{d,s}^2}\frac{\mathrm{J}'_m(k_{v,s}a)}{\mathrm{J}_m(k_{v,s}a)}\left(k_s^2C_s^2+k_l^2\right)+$$
$$\frac{k_s^2a^2}{2k_{v,s}^2}(1+C_s^2)\left[\left(1-\frac{m^2}{k_{v,s}^2a^2}\right)+\left(\frac{\mathrm{J}'_m(k_{v,s}a)}{\mathrm{J}_m(k_{v,s}a)}\right)^2\right]+$$
$$\frac{k_s^2\varepsilon C_s^2}{k_{d,s}^2}\left[\frac{2}{\pi^2k_{d,s}^2}\left(1-\frac{m^2}{k_{d,s}^2b^2}\right)\frac{1}{\left(\Phi_m(k_{d,s}a)\mathrm{Y}'_m(k_{d,s}b)\right)^2}-\right.$$
$$\left.\frac{a^2}{2}\left\{\left(1-\frac{m^2}{k_{d,s}^2a^2}\right)+\left(\frac{\Phi'_m(k_{d,s}a)}{\Phi_m(k_{d,s}a)}\right)^2\right\}\right]+$$
$$\frac{k_s^2\varepsilon^2}{k_{d,s}^2}\left[\frac{2}{\pi^2k_{d,s}^2}\frac{1}{\left(Z_m(k_{d,s}a)\mathrm{Y}_m(k_{d,s}b)\right)^2}-\right.$$
$$\left.\frac{a^2}{2}\left\{\left(1-\frac{m^2}{k_{d,s}^2a^2}\right)+\left(\frac{\mathrm{Z}'_m(k_{d,s}a)}{\mathrm{Z}_m(k_{d,s}a)}\right)^2\right\}\right]-$$
$$2k_sk_lmC_s\left(\frac{\varepsilon}{k_{d,s}^4}-\frac{1}{k_{v,s}^4}\right), \quad (20)$$

For all of the components of the solenoidal electric and magnetic field the results are:

$$E_r(\mathbf{r},t)=\sum_{m=0}\sum_{n=1}\sum_{l=1}\beta_m e_{r,s}(r)\sin k_lz\times$$
$$(\mathrm{Re}\,A_s(t)\cos m\varphi-\mathrm{Im}\,A_s(t)\sin m\varphi)$$
$$E_\varphi(\mathbf{r},t)=-\sum_{m=0}\sum_{n=1}\sum_{l=0}\beta_m e_{\varphi,s}(r)\sin k_lz\times \quad (21)$$
$$(\mathrm{Im}\,A_s(t)\cos m\varphi+\mathrm{Re}\,A_s(t)\sin m\varphi)$$
$$E_z(\mathbf{r},t)=\sum_{m=0}\sum_{n=1}\sum_{l=0}\beta_m e_{z,s}(r)\cos k_lz\times$$
$$(\mathrm{Re}\,A_s(t)\cos m\varphi-\mathrm{Im}\,A_s(t)\sin m\varphi)$$

$$H_r(\mathbf{r},t)=\sum_{m=0}\sum_{n=1}\sum_{l=0}\beta_m h_{r,s}(r)\cos k_lz\times$$
$$\left(\mathrm{Im}\,B_s(t)\cos m\varphi+\mathrm{Re}\,B_s(t)\sin m\varphi\right)$$
$$H_\varphi(\mathbf{r},t)=\sum_{m=0}\sum_{n=1}\sum_{l=0}\beta_m h_{\varphi,s}(r)\cos k_lz\times \quad (22)$$
$$\left(\mathrm{Re}\,B_s(t)\cos m\varphi-\mathrm{Im}\,B_s(t)\sin m\varphi\right)$$
$$H_z(\mathbf{r},t)=\sum_{m=0}\sum_{n=1}\sum_{l=1}\beta_m h_{z,s}(r)\sin k_lz\times$$
$$\left(\mathrm{Im}\,B_s(t)\cos m\varphi+\mathrm{Re}\,B_s(t)\sin m\varphi\right)$$

The self-consistent dynamics of bunch particles is described by relativistic equations of motion in the electromagnetic fields excited by bunches:

$$\frac{d\mathbf{p}_p}{dt}=q_p\left(\mathbf{E}+\frac{1}{m_pc\gamma_p}\mathbf{p}_p\times\mathbf{B}\right),\qquad \frac{d\mathbf{r}_p}{dt}=\frac{\mathbf{p}_p}{m_p\gamma_p}, \quad (23)$$

where $\gamma_p^2=1+\left(\mathbf{p}_p/m_pc\right)^2$.

CONCLUSIONS

In present work a system of self-consistent equations describing the dynamics of excitation both an azimutally uniform and nonuniform modes of wakefield, excited by relativistic electron bunches in a dielectric resonator, are obtained.

An bunch–excited fields are presented in the form of superposition solenoidal and potential fields. The solenoidal electromagnetic fields are presented by an expansion of the required fields into solenoidal fields of the empty dielectric resonator. The potential field is presented by the eigenfunction expansion method. The dispersion equation for determination of eigenfrequencies and the equation for eigenvalues are obtained, eigenwaves, eigenfunctions and their norms are found.

The analytical expressions of an excited fields, that take into account both longitudinal and transverse dynamics of bunch particles are derived.

Along with the equations of motion they provide a self-consistent description of the dynamics of generated fields and bunches.

REFERENCES

[1] M. Rosing and W.Gai, Phys. Rev. D. 42 (1990) 1819.
[2] King-Yuen Ng, Phys. Rev. D. 42 (1990) 1829.
[3] A.M. Altmark et al., Techn. Phys. 78 (2008) 103
[4] W. Gai et al., Phys. Rev. E. 55 (1997) 3481.
[5] L. A. Vainstein, *Electromagnetic Waves*, (Moscow: Radio i Sviaz, 1988), 440.

A COAXIAL TWO-CHANNEL DIELECTRIC WAKEFIELD STRUCTURE FOR TWO-BEAM ACCELERATION EXPERIMENTS AT SLAC*

G.V.Sotnikov[1,2#], T.C. Marshall[3,2], J.L. Hirshfield[2,4], , S.V. Shchelkunov[4]

[1]NSC Kharkov Institute of Physics and Technology, Kharkov, Ukraine
[2]Omega-P, Inc., New Haven Connecticut, USA
[3]Columbia University, New York City, USA
[4]Yale University, New Haven, Connecticut, USA

Abstract

Results of analytical and numerical investigations of a coaxial dielectric wakefield accelerator structure (CDWA) for experiments at FACET (SLAC) on two-beam acceleration are presented. For these experiments it is proposed to use ~1THz structure with two nested silica cylindrical shells having these diameters: outer shell, OD = 2mm, ID = 1mm; inner shell OD = 360μm, ID = 100μm. A conventional CDWA structure is energized by an annular drive bunch travelling in the annular vacuum channel. Our analytical studies prove clearly that an annular drive bunch can be substituted by a solid bunch having the same charge. For the simulation we used the SLAC drive bunch parameters: energy is 23 GeV, charge is 3nC, axial RMS size is 20μm, transverse RMS size is 10 μm. This bunch sets up at the central channel axis an accelerating gradient of ~1 GeV/m.

INTRODUCTION

The use of wakefields produced by a relativistic "drive bunch" charge moving inside a dielectric-lined channel to accelerate a following "witness" bunch has promise for making a linear Collider with gradient ~ 1-3GeV/m [1,2], and has received modest attention for the past 25 years [3-5]. More recently, there is experimental evidence [6], consistent with theoretical expectation [7], that certain dielectric materials can withstand the brief (nsec) pulses of high intensity radiation associated with passage of a drive bunch through the dielectric structure. Drive bunches having relativistic energy and charge of several nC can produce a train of THz wakefields having intensity > 1GeV/m in a hollow coaxial dielectric structure of mm-scale transverse dimension [8]. This, together with the use of a smooth-bore structure (DWA) that can accelerate positrons or electrons, has recommended the concept for further study as an "advanced" linear Collider accelerator module. The simplest structure, a hollow cylindrical dielectric tube with an outer metallic surface, in which the drive and witness bunches travel the same path, is unfortunately afflicted with stability problems, and its transformer ratio (**TR**) is no larger than 2. In order to avoid these problems, other structures, such as a wide rectangular channel lined with dielectrics [9] that is excited by a sheet beam, or a coaxial two-channel structure that is excited by an annular bunch, have been proposed and studied [8,10,11] computationally and analytically.

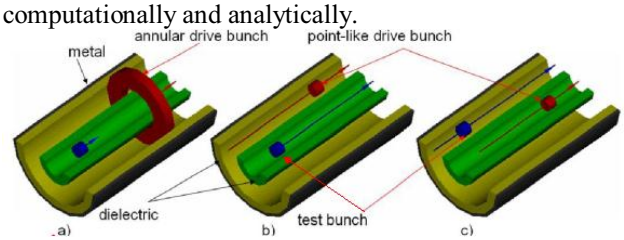

Figure 1: The CDWA structure excited in three different ways by a drive bunch (red), to accelerate a witness bunch.

We have planned at FACET (SLAC) proof-of-principle experiments E-207 to test a mm-scale THz CDWA. Because SLAC cannot provide at present a drive bunch of annular shape we propose to substitute such a bunch by a solid bunch having the same charge. In what follows, we shall show that a solid drive bunch will establish the same wake fields we wish to study. Furthermore, we shall show how we may obtain information from this study whereby the data can be compared with theoretical simulations obtained with the CST STUDIO code. This is possible because of the reciprocity principle [12].

We will consider three regimes of operation of the CDWA (see Fig.1): a) conventional CDWA; b) the CDWA with a point-like drive bunch that moves in the annular channel while the witness bunch accelerates along the central channel axis, c) "inverse" CDWA when the structure excited by a solid drive bunch that moves along the central channel axis while the witness bunch samples its wakefield as it moves along the annular channel. Certain of these field components are simply related, as we shall establish in the next section. This allows us to study regimes b) and c) at FACET, and relate the measurements made there to the desired operation with an annular drive bunch, conventional regime a).

CDWA UNIT FOR E-207 EXPERIMENTS

Parameters of CDWA structure under investigation are listed in Table 1. The CDWA structure with similar parameters will be tested at SLAC.

Table 1: Parameters used for THz CDWA

Frequency of dominant mode (E_{04})	473 GHz
External diameter of outer coaxial cylinder	2.0 μm
Inner diameter of outer coaxial cylinder	1.0 μm
External diameter of inner coaxial cylinder	0.36 mm

* Supported by the US Department of Energy, Office of High Energy Physics, Advanced Accelerator R & D.
#sotnikov@kipt.kharkov.ua

Inner diameter of inner coaxial cylinder	0.1 mm
Relative dielectric constant ε	3.75
Bunch axial RMS dimension σ_z	20 μm
Outer drive bunch diameter (annular bunch)	0.83 mm
Inner drive bunch diameter (annular bunch)	0.53 mm
Point-like bunch transverse RMS size σ_r	10 μm
Bunch energy	23 GeV
Bunch charge, Q_{drive}	3 nC

In Fig.2 are shown axial profiles of axial wakefields for the conventional regime of CDWA operation when the structure is excited by an annular drive bunch traversing the annular vacuum channel. The maximum accelerating

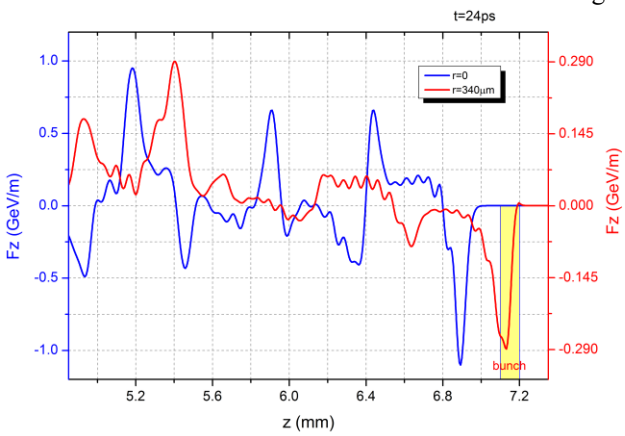

Figure 2: Longitudinal force axial profile at the center of the annular vacuum channel (red line) and at the central channel axis (blue line) in the case of conventional CDWA [8]. Yellow rectangle shows the location of the drive bunch particles.

gradient in the central channel is 0.95 GeV/m, average decelerating force on drive bunch particles is 0.2 GeV/m, so the transformer ratio for this device is ~5.

The longitudinal component of force acting on a witness bunch for the three ways of excitation of the structure is given in Fig. 3. The component $F_z(z)$ is the same at corresponding locations where the witness bunch resides. The witness bunch in either of these cases would experience an accelerating force ~ 0.95 GeV/m if located at z ~ 5.18mm. This figure shows convincingly that an annular drive bunch can be replaced by a point drive bunch located in the annular channel, as we must do at FACET. Understanding is provided from analytic theory [8] where it is found that the on-axis longitudinal wakefield amplitude depends on an integral over the eigenfunctions $e_{zn}(r_0)$, where n is the radial index and r_0 is the location of an element of drive bunch charge. It turns out that the eigenfunction is nearly constant across the radius of the annular channel, so the integral is insensitive to the transverse bunch charge profile.

Furthermore, each azimuthal mode amplitude is proportional to the modified Bessel function $I_m(\kappa r)$

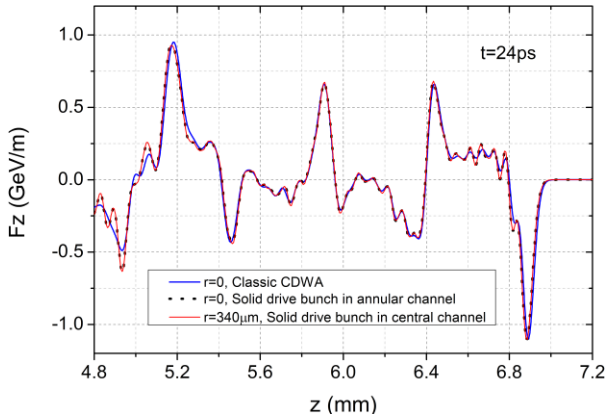

Figure 3: Axial profile of wakefield registered by witness bunch for three regimes of operation of the CDWA: a) blue line - conventional CDWA; b) black dots - solid drive bunch is in the annular channel, c) red line - "inverse" CDWA .

where κ is the transverse wavenumber and m is the Bessel function order. For regions close to the axis with $\kappa r \ll 1$, $I_m(\kappa r) \sim (\kappa r)^m$. Thus the only contribution is from the symmetric monopole term which is valid for the on-axis field from a point bunch and generally true for an annular bunch.

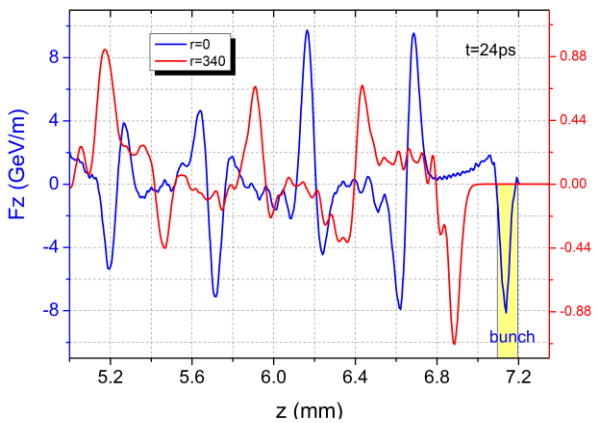

Figure 4: Longitudinal force axial profile at the center of the annular vacuum channel (red line) and at the central channel axis (blue line) in the case of "inverse" CDWA.

In Fig.4 are shown axial profiles of axial wakefields for the "inverse" CDWA. From Fig.4 it follows that the axial field along the central channel is then approximately one order of magnitude larger (~10 GeV/m) in comparison with excitation regime b), but the maximum wakefield in the annular space is again 0.95 GeV/m at z= 5.18mm, the same field that a point drive bunch located in the annular channel sets up in the central channel. This provides evidence that a reciprocity principle is governing "Green's function" excitation in a two-channel structure (for regimes (b) and (c), the source and the observation point are interchanged). This is key to linking the FACET experimental results to data that apply to the annular drive bunch operation.

In Fig. 5 we show maps of the radial wakefield $E_r(r,z)$

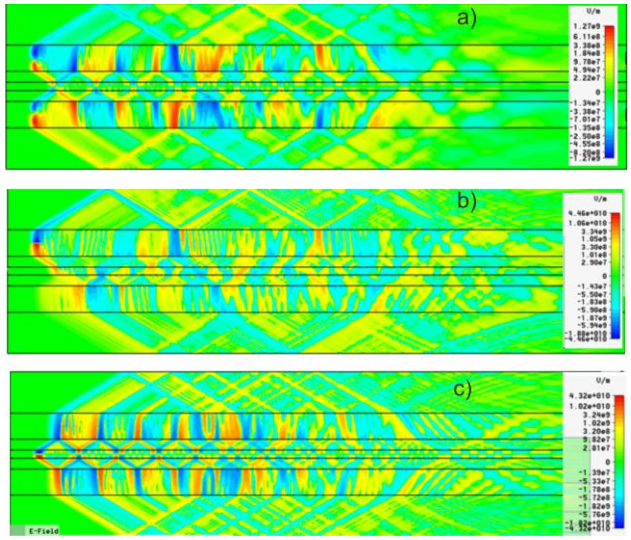

Figure 5: Transverse wakefield component $E_r(r,z)$ map for three operation regime (see Fig.1). Bunch moves right to left, length shown is 7.5mm. Note color scale changes.

for the three drive bunch cases shown in Figs. 1. We point out an interesting situation that applies to the fields at the outer surface when the drive bunch moves in the central channel: the fields at the metallic surface of the unit are modest here, unlike the case of the single-channel device [6] where high fields occur that can destroy the metallic coating.

DATA EXPECTED AND INTERPRETED

It is impossible to obtain data for the experiment E-207 by measuring the energy change of a witness bunch, at least insofar as FACET is presently structured. However, we can obtain and interpret the following data. We shall begin by observing the overall amount of THz radiation emitted by the device when the point drive bunch moves, respectively, in the annular channel and in the central channel. The intensity of the radiation, which scales as Q_{drive}^2, is proportional to the drag force exerted on the drive bunch by the wakefields it sets up. The ratio of the THz radiation signals for the two point drive bunch locations therefore provides the ratio of drag forces [for drive bunch in the central channel] / [for drive bunch in the annular channel], which is predicted by theory (in the ratio, calibration factors of the THz radiation diagnostic cancel) to be 4.0 for a unit with central channel ID = 150microns, and 5.3 when the central channel ID = 100microns. If we use the CST code to determine the energy loss of the electrons over a fixed distance of travel to determine this ratio, the 150micron channel ratio is 3.7 and the 100micron channel ratio is 5.7, a satisfactory check. Next, one can determine the energy loss of the drive bunch as it moves along the central channel. For the given bunch charge and channel diameter, we expect the average drag force to be ~ 5GeV/m, so the energy loss of the drive bunch should be $\leq$ 1.5% of its initial energy for a 6cm long unit, an amount that is within the capability of the FACET energy analyzer to measure. (At present the radial dimensions of the FACET drive bunch are somewhat too large to permit this measurement, but it is likely that the performance can be improved in the future). Now, combining this measurement with the THz measurement, we can infer the drag force of the drive bunch when it is located in the annular channel. This will permit us to compute the longitudinal component of wakefield in the central channel that is set up by the point drive bunch in the annular channel—and that, as we have shown in previous section, is the same as the longitudinal wakefield set up there by the annular bunch. In this way we can largely characterize the performance of this THz CDWA structure as it may operate in the future when it is excited by a high energy annular drive bunch (however, the energy of the drive bunch need be only ~ 5 GeV).

CONCLUSION

Our theoretical studies and numerical simulations show that for the wakefield experiments with our CDWA at FACET, an annular drive bunch can be replaced by a point-like drive bunch that travels in the annular vacuum channel or the central vacuum channel. Axial wakefields registered by the witness bunch travelling in the opposite vacuum channel will be the same as in the case of a conventional CDWA when the annular drive bunch traverses the annular channel. Simulated bunch motion for regimes b) and c) shows that the drive bunch will move with tolerable distortion a distance ~6-8 cm (the length of our unit for SLAC experiments). Data obtained from experiments with point-like bunches will allow us to draw conclusions about the accelerating gradient and transformer ratio in the case of a conventional CDWA.

REFERENCES

[1] V.D. Shiltsev, "High energy particle colliders: past 20 years, next 20 years and beyond", arXiv:1205.3087 [physics.acc-ph].
[2] W. Gai, J.G. Power, and C. Jing, J. Plasma Physics (2012), 78, pp. 339-345.
[3] W. Gai, et.al, Phys. Rev. Lett. **61**, 2756 (1988).
[4] E. Chojnacki, W. Gai, P. Schoessow, and J. Simpson, Proc. PAC 1991; IEEE, P. 2557 (1991).
[5] T-B. Zhang, et.al, Phys. Rev. **E56**, 4647 (1997).
[6] M. Thompson, et.al, Phys. Rev. Lett. **100**, 214801 (2008).
[7] P. Sprangle, et.al, Phys. Rev. **E55**, 5964 (1997).
[8] G.V. Sotnikov, T.C. Marshall, and J.L. Hirshfield, Phys. Rev. STAB, **12**, 061302 (2009).
[9] A. Tremaine, J. Rosenzweig, and P. Schoessow, Phys. Rev. **E56** 7204 1997).
[10] T.C. Marshall, G.V. Sotnikov, and J.L. Hirshfield, AIP Conf. Proceedings **1299**, 336 (2010), eds. S. Gold and G. Nusinovich.
[11] G.V. Sotnikov, T.C. Marshall, J.L. Hirshfield, and S.V. Shchelkunov, Ibid, p.342.
[12] G.V.Sotnikov, J.L. Hirshfield, T.C. Marshall, ,S.V. Shchelkunov. "A reciprocity principle for wakefields in a two-channel coaxial dielectric structure" in Proc. of IPAC2012, New Orleans, Louisiana, USA, May 25-30, 2012, paper WEPPP003, p. 2726-2728.

ENERGY SPREAD DECREASING IN LINEAR MODE OPERATING LASER PLASMA WAKEFIELD ACCELERATOR

S.M. Polozov
National Research Nuclear University - Moscow Engineering Physics Institute, Moscow, Russia

Abstract

Laser plasma wakefield acceleration (LPWA) [1] is one of most popular novel methods of acceleration. The LPWA is very perceptively because the accelerating gradient in plasma channel can be a number of orders larger than in metal structures. But the LPWA has two serous disadvantages as very high energy spread and low part of electrons trapped into acceleration. The energy spectrum better than 10 % does not observed anyone in simulations or experiments. Bunching before injection into plasma channel will discuss to decrease the energy spread and to enlarge the electron trapping efficiency.

INTRODUCTION

A number of ideas for increasing the rate of the energy gain have been discussed in the last few decades. Among others, the acceleration of electrons in a modulated plasma channel was proposed by Ya.B. Feinberg in the 1950's [2]. Possible schemes for the plasma wakefield acceleration (PWA) differing in ways of modulating the plasma channel were developed later. The first one uses a high energy (tens of GeV) beam of particles to form a plasma wave and accelerate a fraction of the injected particles or a probe beam [3]. Another method is the laser plasma wakefield acceleration (LPWA) [1], in which a laser pulse is used to create a plasma wave. The modulation period of the accelerating field (the wakefield) is $L_w=\lambda_w/2=\pi c/\omega_p$, were c is the speed of light in vacuum, $\omega_p=(4\pi e n_0/m)^{1/2}$ is the plasma frequency, e end m are the elementary charge and mass, and n_0 is the electron density in plasma. Using two lasers with close frequencies ($\Delta\omega \sim \omega_p$) was also suggested for enhancing the accelerating gradient even further. The advantage of the PWA technique vs. conventional accelerators is obvious: the accelerating gradient in a plasma channel can reach hundreds of GeV/m and hence the accelerator can be very compact. This statement does not at present include high power lasers with powers up to 10^{22} W/cm^2, which are necessary for LPWA, although significant progress is happening in this area with the introduction of fiber lasers. The idea is very popular at present and a number of international collaborations are working on analytical and experimental demonstration of PWA. Large scale projects based on PWA are being discussed now. These include electron-positron colliders, X-FELs and medical facilities. However, the step from a novel acceleration technique to routinely operating facilities has not been made yet. LPWA has two serious disadvantages: a very high energy spread of the accelerated electrons and only a small fraction of electrons is captured into the process of acceleration. An energy spectrum better than 10 % has not yet been demonstrated either in simulations or experimentally. A beam with such a wide energy spread can not be used for the majority of applications including medical and particle physics as the beam can not be transported efficiently.

BEAM DYNAMICS IN LPWA

Considering LPWA, two regimes are distinguished: the underdense plasma, in which $\pi^2 r_l^2/\lambda_p >> a_0^2/2\gamma_l$, (quasi linear regime) and the non-linear regime with $\pi^2 r_l^2/\lambda_p << a_0^2/2\gamma_l$. Here r_l is the laser spot size, $a_0=eA/W_0$ normalized laser intensity, $\gamma_l=(1+a_0^2/2)^{1/2}$. The electron beam dynamics is different in the two regimes. Both regimes, however, experience the high energy spread and low capturing. Conventional accelerators experienced similar problems in the past, where they were solved by bunching the beams using klystron or waveguide type bunchers, and later by producing short bunches with photocathodes. Making a bunch shorter than the accelerating field modulation period L_w in a plasma channel does not seem to be viable. However, pre-modulation (bunching) of the electron beam can still be used as discussed below.

A few methods for improving the energy spread in the non-linear regime have been proposed. The first is to use two plasma stages with constant but not equal plasma densities and a transient stage with exponentially varying plasma density between them for the beam modulation [4, 5]. The second is so-called ponderomotive injection using two synchronized laser pulses [6]. Two lasers can also excite a beat wave in the plasma, which is then used for bunching in the third method [7]. These methods improve the energy spread to about 3 % for a 1 GeV beam. Still, this number is too high for many applications. The electron capturing efficiency also remains problematic. All the methods described above apply to the non-linear regime. However, the linear LPWA mode is also interesting for practical use. The rate of the energy gain can still be very high, while the laser power requirements are comparatively moderate, meaning that compact, laboratory scale facilities could be designed for accelerating electron beams to hundreds of MeV. Studies of the linear LPWA regime have been conducted at LBNL and INFN LNF and showed that electrons can be accelerated to 1 GeV with an energy spread of 6-10 %. Below two possible bunching schemes can be proposed to decrease the energy spread and improving the number of electrons captured by the plasma wave in the linear LPWA mode.

BEAM PRE-MODULATION SCHEMES

The code for electron beam dynamics simulation in LPWA channel was designed and two possible beam pre-modulation schemes were studied. The plasma channel is divided into two stages in the first scheme. The plasma density is varying in the first, pre-modulation stage, and is constant in the second, the main accelerating stage. The following assumptions are made for simulation: the beam is injected externally, the amplitude of the electric field does not vary on the scale of the time of flight, the plasma is cold, linear and collisionless, the space charge field of the injected electrons is much lower than the plasma wakefield, the beam motion is 1D. The beam dynamics can be studied analytically and numerically in a way similar to how it is done for electron RF linacs. Functions $\omega_p(\xi)$ and $E(\xi)$ describe dependencies of the plasma frequency and accelerating field on the longitudinal coordinate $\xi = 2\pi z/\lambda_l$. A variable similar to the wave velocity in a conventional accelerator is introduced $\beta_v(\xi) = \left(1-\hat{\omega}_p^2(\xi)\right)^{1/2}$, where $\hat{\omega}_p(\xi) = \omega_p(\xi)\lambda_l/2\pi c$ is the normalized plasma frequency and λ_l laser wavelength. The equations of motion for an electron in a plasma channel in Cauchy form then are:

$$\frac{d\gamma}{d\xi} = \hat{e}(\xi)\sin\varphi,$$
$$\frac{d\varphi}{d\xi} = \left(1-\hat{\omega}_p^2(\xi)\right)^{-1/2} - \left(1-1/\gamma^2\right)^{-1/2}, \quad (1)$$

where $\hat{e}(\xi) = eE(\xi)\lambda_l/2\pi W_0$ is the normalized amplitude of the longitudinal accelerating field in the plasma channel and γ is Lorentz factor. Hamiltonian formalism can be applied to the above equations for studying the beam-wave system and the standard energy balance equation written. Injection conditions can thus be analyzed analytically. In contrast to conventional accelerators, the phase velocity and amplitude of the accelerating field are not independent variables, but functions of the plasma electron density $n_0(\xi)$ and are related as $E = mc\omega_p/e$. Therefore, optimizing the parameters of the plasma channel is a complex problem in LPWA. The linearity condition for the plasma wave can be expressed as $E(\xi)\sqrt{k(\xi)} = E(\xi=0)\sqrt{k(\xi=0)}$, and hence the amplitude of the accelerating field only depends on the longitudinal coordinate. Here $k(\xi)$ describes the plasma wave number in the longitudinal direction.

The beam dynamics in the main accelerating stage of the plasma channel is considered to be similar to the beam dynamics in waveguide or resonator accelerators with a phase velocity β_v=1. Strictly speaking, this is only true for LPWA with a zero-field channel in which n_0=0 (in case the plasma is absent). However, the phase velocity must be close to 1 ($\beta_v \to 1$) for an efficient acceleration, and at least for underdense plasma we can approximate β_v=1. Simulations were first done to find the optimal phase size and energy spread for the injection into the accelerating stage. Electrons previously bunched in the modulating stage can be accelerated to an energy of about 200 MeV with an energy spread $\Delta\gamma/\gamma \approx 4\%$ providing the initial phase size and energy spread are $\Delta\varphi \approx \pi/2$ and $\Delta\gamma/\gamma < 25\%$ respectively. The choice of plasma (and accelerating field respectively) distribution in a modulation stage was the following step of simulation.

At first, using the RF linac analogy again, we borrow a function conventionally used for waveguide type bunchers for the field distribution in the first stage of plasma channel:

$$E(\xi) = E(\xi=\xi_b) + [E(\xi=0) - E(\xi=\xi_b)]\times \times\left[1-\sin^m(\pi\xi/2\xi_b)\right], \quad (2)$$

where ξ_b is the normalized length of the bunching region. A number of modulation stage configurations were simulated and the optimal parameters chosen. The beam can be modulated using distribution (2). The resulting energy spread is 4 % with the capturing coefficient reaching 40-45 % front-to-end. Higher capturing (up to 70 %) with a wider energy spread, or better energy spectrum with a lower capturing coefficient (about 20-25 %) can be achieved with different injection conditions of the pre-modulated beam. In general though, these results do not agree well with the single-particle simulations: a phase size lower than (0.7-0.8)π has not been observed with field distribution (2) after pre-modulation.

For those reasons, a different bunching scheme consisting of a number of short plasma sub-stages (several λ_l long each) separated by drift gaps was considered. This configuration resembles a multigap klystron type buncher. The plasma density distribution in the sub-stages can be simulated using standard functions (step, Gauss, etc.). The step function was chosen for the simulation. The accelerating field distribution in the bunching part is shown in Fig. 1a. The $\Delta\varphi$ and $\Delta\gamma/\gamma$ necessary for an efficient acceleration can be achieved with $E(\xi=\xi_b)/E(\xi=0)$ =0.85 and a low value of the accelerating field in the bunching part $\hat{e}(\xi=0)$ =0.009 for an injection energy W_{in}=10 MeV (see Fig. 1b).

The beam is accelerated in the main plasma stage with $\hat{e}(\xi=0)$ =0.033. It has $\Delta\gamma/\gamma \le 4$ % at the output while accelerating from 12 to 108 MeV (the channel length $z_{ch} = 1000\lambda_l$, see beam distribution in the (φ, γ) phase plane in Fig. 2a and energy spectrum in Fig. 2b). Note that the energy spread decreases with energy increase as in the conventional accelerator and it is equal to $\Delta\gamma/\gamma \le 2.8$ % at 205 MeV ($z_{ch} = 2000\lambda_l$, Fig. 2c and 2d) and $\Delta\gamma/\gamma \le 1.3$ % at 520 MeV ($z_{ch} = 5000\lambda_l$, Fig. 2e and 2f). In Fig. 2 the beam parameters after the pre-modulation stage are shown as red points, after the main stage as blue ones. In Fig. 3 the energy spread (a) and the part of electrons captured by the plasma wave (b) are shown as the function of output energy.

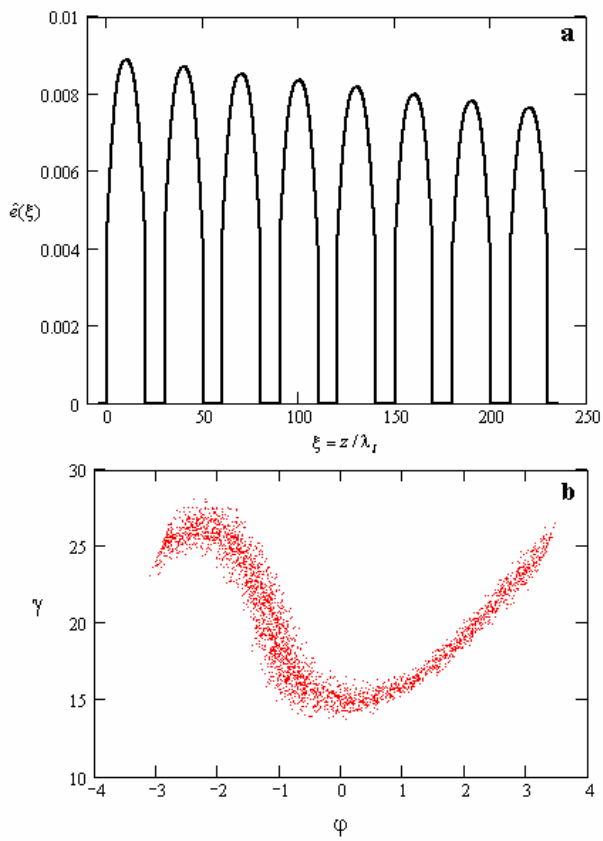

Fig. 1. The accelerating field distribution in the bunching part (a) and modulated beam after first channel stage (b).

CONCLUSION

Two possible beam pre-modulation schemes discussed to decrease the energy spread for the linear laser plasma wakefield acceleration mode. The bunching scheme consisting of a number of short plasma sub-stages (several λ_I long each) separated by drift gaps is preferable. The low energy spread electron bunch can be accelerated to hundreds of MeV. The part of externally injected electrons captured in to acceleration is very high. Note that the part of accelerated electrons decreases with the beam energy increase due to loses from resonant beam-field interaction.

REFERENCES

[1] T. Tajima, J.M. Dowson. Phys. Rev. Lett., 1979, v. 43, 4, p. 267.
[2] Y.B. Feinberg, Sov. Atomic Energy, 1959, v. 6, p. 431.
[3] M.J.Hogan et al., Phys. Rev. Lett., 2005, v.95, 054802-1-4.
[4] S.V. Bulanov et al. Physics of Plasmas, 2008, 15, 073111.
[5] S.V. Bulanov et al., Phys. Rev. E, 1998, 58, R5257.
[6] E.Esarey et al. Phys. Rev. Lett., 1997, 79, 2682.
[7] D. Umstadter et al., Phys. Rev. Lett., 1996, 76, 2073.

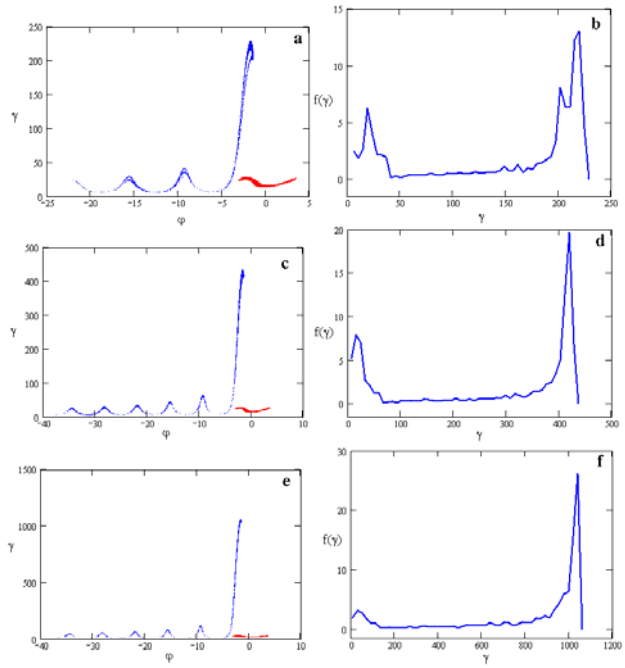

Fig. 2. The beam distribution in the (φ, γ) phase plane and energy spectrum for different output energies.

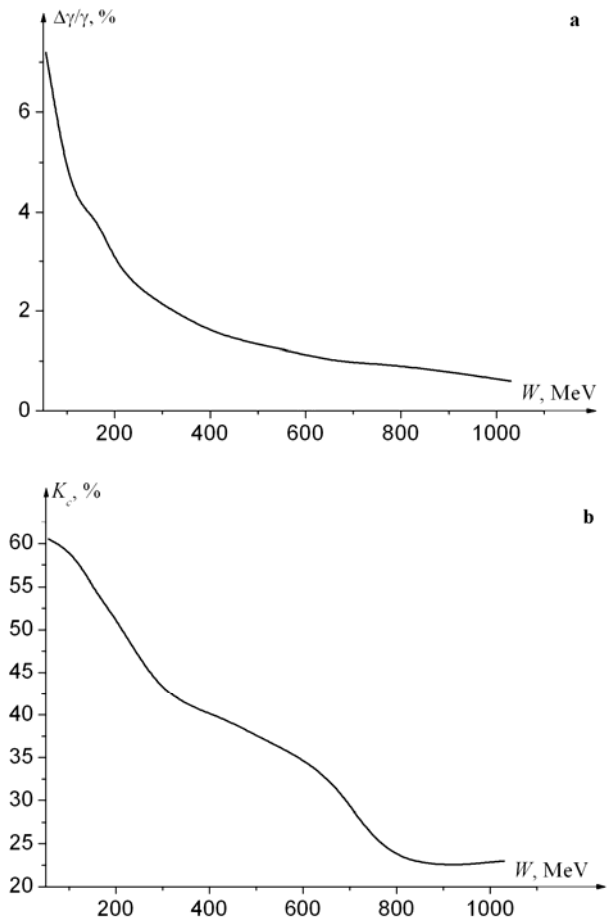

Fig. 3. The bunch energy spread (a) and the part of captured electrons (b) as the function of output energy.

LASER-WAKEFIELD ACCELERATION WITH EXTERNAL BUNCH INJECTION AT REGAE*

J. Grebenyuk† and K. Floettmann, DESY, Hamburg, Germany
T. Mehrling and J. Osterhoff, University of Hamburg, Germany

Abstract

We present particle-in-cell simulations with the code OSIRIS [1] for future laser-plasma wakefield experiments with external bunch injection at the REGAE accelerator at DESY. The topics of particular interest are: emittance evolution of electron bunches and longitudinal bunch compression inside the wakefield. Results show significant transverse emittance growth during the injection process, if the electron bunch is not matched to its intrinsic betatron motion inside the wakefield. In addition, when externally injected at the zero-field crossing of the laser-driven wake, the electron bunch may undergo significant compression in longitudinal direction and simultaneously be accelerated due to the gradient in the accelerating field. This mechanism would allow for production of high-energy, ultra-short (on the order of one femtosecond) bunches at REGAE.

EXTERNAL BUNCH INJECTION AT REGAE

Laser-plasma acceleration (LPA) is a technology which exploits large electric wakefields created by high-intensity laser pulses in plasma. Such wakes support field gradients which are many orders of magnitude larger than in conventional accelerators and can be used to accelerate particle bunches over short distances. Experiments demonstrated GeV energy gain in centimeter distances [2, 3]. Nevertheless, the energy increase in a single LPA module is limited by energy depletion of the laser pulse. Further energy gain is thus possible by placing LPA modules one after another, i.e. by staging [4], or by using a stronger laser for wakefield generation. LPA might potentially develop into a technology to be used for driving compact and brilliant X-ray sources, and possibly particle colliders. Thus achieving a beam quality sufficient for these demanding applications is of crucial importance.

The injection process of electrons into a plasma wake in the wave-breaking regime is sensitive to fluctuations in laser and plasma parameters, and difficult to manipulate. Our aim is to inject externally accelerated and phase-space tailored beams from a conventional accelerator into a laser-driven wake for full control over the electron-trapping process. These experiments will open numerous opportunities for probing wakefields and exploring fundamental properties of laser-plasma interaction and electron acceleration. Moreover, external injection experiments are of crucial importance for exploring the concept of staging. The aim of external injection is to place electron bunches with a length much shorter than the plasma wavelength, λ_p, and a transverse extent much smaller than the laser spot size in the phase-region of the wake which is both focusing and accelerating.

The Relativistic Electron Gun for Atomic Exploration (REGAE) is a linear accelerator at DESY which produces 2 to 5 MeV velocity-grouped electron bunches of 10-15 fs RMS length, ∼1 pC charge, 3-5 μm RMS width, and 0.3 mm mrad emittance. Originally designed for femtosecond electron diffraction experiments, the REGAE injector will be used together with a high-intensity laser and a plasma target for LPA external injection experiments.

EMITTANCE EVOLUTION

External controlled injection is a direct way to study bunch emittance evolution in LPA. Minimising emittance growth during the acceleration process is crucial for most applications. Emittance growth in LPA was earlier investigated in [5, 6, 7]. The transverse trace-space emittance, $\epsilon = \sqrt{\langle x^2\rangle \langle x'^2\rangle - \langle xx'\rangle^2}$ [8], is a figure of merit for the transverse beam quality, where x is the transverse particle position, $x' = p_x/p_z$ is the ratio of transverse and longitudinal particle momenta and $\langle Y^k\rangle = \sum_i^N (Y_i - \overline{Y})^k/N$ the k-th central moment of a discrete variable Y. We consider an electron bunch with transverse properties defined by the emittance ϵ and the Courant-Snyder parameters (CSP)[9] :

$$\beta = \frac{\langle x^2\rangle}{\epsilon}, \qquad \gamma = \frac{\langle x'^2\rangle}{\epsilon}, \qquad \alpha = -\frac{\langle xx'\rangle}{\epsilon}. \quad (1)$$

Combining emittance definition and (1) yields the relation between these parameters, $\beta\gamma = 1 + \alpha^2$.

While being accelerated, the individual particles perform transverse betatron oscillations with a betatron frequency ω_β. Due to the particle oscillations, the ellipse with area $\pi\epsilon$, defined by the CSP (1), $\gamma x^2 + 2\alpha xx' + \beta x'^2 = \epsilon$, rotates according to the single particle trajectories in trace space. Since the transverse field and ω_β are ξ-dependent ($\xi = z - ct$ is a co-moving variable, where z is the longitudinal coordinate, c is the speed of light and t is time), the individual longitudinal slices of the bunch oscillate at different frequencies which leads to a betatron-oscillation phase mixing during the acceleration process, as illustrated in Fig. 1. Slice ellipses develop a tilt with respect to each other which increases the projected area and hence causes emittance growth. Emittance growth due to this mechanism can be suppressed by matching the transverse properties of the electron beam to the intrinsic electron betatron motion in the plasma wake [10, 5]. Expressing the matching con-

* Work supported by the Helmholtz Alliance "Physics at the Terascale" and a grant of computing time by the Juelich Supercomputing Centre on JUGENE under project id HHH09.
† julia.grebenyuk@desy.de

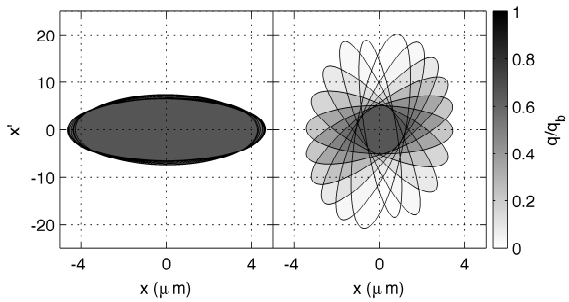

Figure 1: Ellipses representing bunch slices from PIC simulation C2 (see below) at position $z = 0.72$ mm (left) and $z = 2.10$ mm (right). The gray-scale of the ellipse was chosen according to the ratio of the charge in a slice q and total bunch charge q_b.

ditions in terms of the CSP in the relativistic limit gives

$$\beta_m \simeq \frac{c}{\omega_\beta}\,, \qquad \gamma_m = \frac{1}{\beta_m} \simeq \frac{\omega_\beta}{c}\,, \qquad \alpha_m = 0\,, \quad (2)$$

so that particle oscillations follow the ellipse defined by the CSP of the beam.

3D PIC simulations were performed to study emittance growth. Laser, bunch and plasma parameters listed above correspond to expected experimental conditions at REGAE. Electron bunches with an initial normalised emittance of $\epsilon_{n,\mathrm{init}} = 0.3\,\mu$m propagate collinear to laser pulse of 5 J energy, $\tau_0 = 25$ fs FWHM pulse duration, $\lambda_0 = 800$ nm central wavelength, and a peak-normalised vector-potential of $a_0 = 1.8$. The Rayleigh-length of the laser is long compared to the betatron length and the waist of the pulse is 50 μm FWHM, where the transverse profile is a Gaussian and the temporal profile is a symmetric polynomial. Electron beams have a charge of 1 pC, mean energy of 5.5 MeV an energy spread of 32.5 keV, RMS length of 10 fs, and an RMS transverse size of 3μm. The charge is sufficiently low to neglect space-charge forces as well as beam loading at the accelerating and focusing phase of the plasma wave. The plasma target has a flat-top longitudinal profile with an electron density of $n_0 = 10^{17}\mathrm{cm}^{-3}$.

We compare PIC simulations with different sets of CSP that result from different focussing geometries of the same electron beam:

- *matched case (CM)*: beam with matched CSP;
- *miss-matched case (C1)*: beam with matched beta function at focus but with miss-matched focal position;
- *miss-matched case (C2):* beam with miss-matched beta function but matched focal position.

Fig. 2 depicts the emittance evolution during acceleration for the three mentioned cases. If matched, the bunch ellipse will not oscillate after injection and the emittance will not grow. For the non-matched cases the betatron phase is completely mixed at $z \approx 3.5$ mm and emittance growth is saturated at that position.

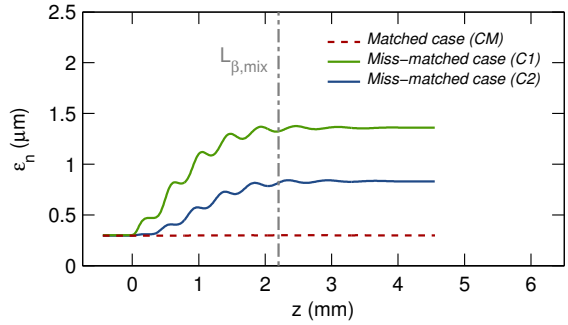

Figure 2: Evolution of the normalised emittance $\epsilon_n = \epsilon\bar{p}_z/m_e c$ in PIC simulations for the three considered cases. The total betatron-phase mixing length relative to the initial position is indicated by the dash-dotted line.

The consequences of the presented simulations for multi-stage acceleration are discussed in the following. We derive the propagation distance during which the betatron phase of a bunch becomes completely mixed. Assuming the bunch with the length L_b and the relativistic gamma-factor γ_b is injected and fixed to the maximum accelerating field phase of a quasilinear plasma wave driven by a laser pulse with a spot diameter on the order of λ_p, we find an expression for the total betatron-phase mixing length:

$$L_{\beta,\mathrm{mix}} \simeq \frac{\lambda_p}{a_0}\sqrt{\frac{8\pi\gamma_b}{k_p L_b}}\,. \quad (3)$$

where $k_p = c/\omega_p$ is a plasma skin depth. This suggests that total betatron phase mixing occurs within $\leq$1 m scale stages for electron energies of up to one TeV for a plasma density of $10^{17}\,\mathrm{cm}^{-3}$, 3 μm long bunches and a laser pulse with $a_0 = 2$. This might introduce the necessity to include beam-matching sections upstream of each plasma-accelerator section with fundamental implications on the design of staged laser wakefield accelerators.

BUNCH COMPRESSION

Ultra short bunches are of high interest for coherent X-ray generation and ultrafast pump-probe experiments. The longitudinal electric field in the laser-driven wake has a ξ-dependence and can be used for simultaneous acceleration and compression of the externally injected electron bunch. The accelerating force in longitudinal direction acting on the front part of the bunch is weaker than at the back part, such that after propagation in the plasma wake the bunch can undergo significant size reduction. The compression of the bunch in the wakefield was analytically analysed in [12, 13] and was proposed to minimise energy spread growth in multi-staged LPA. Bunch compression occurs in LPA if the following conditions are fulfilled:

- the bunch should experience the strongest negative gradient of the accelerating force, i.e. to be injected at the maximum of the wakefield potential (at the zero-field crossing);
- low initial bunch energy to ensure maximum change in

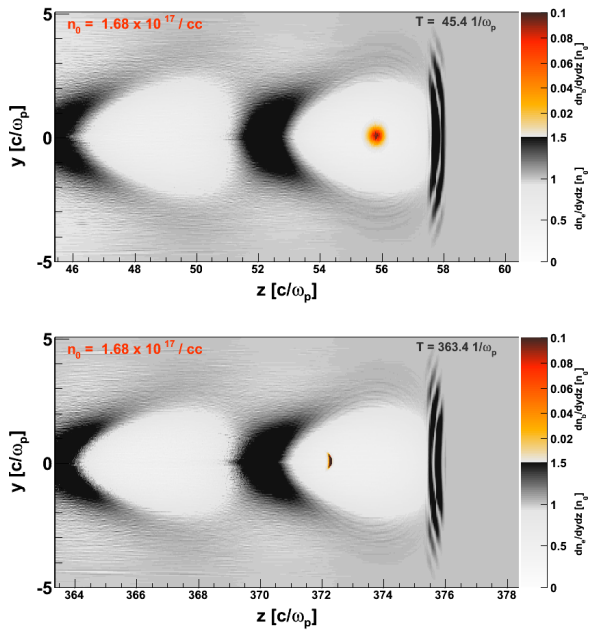

Figure 3: Plasma and externally injected bunch charge densities from PIC simulations at an early position (top) and after 8 mm of propagation inside plasma (bottom). Significant reduction in longitudinal size is observed.

velocity between the front and the back of the bunch;
• sufficiently low initial bunch charge, i.e. the electron-number density in the bunch should be smaller than the plasma density, $n_e \ll n_p k_p^{-3}$, to avoid space-charge effects;
• initial length of the bunch should be much smaller than λ_p. For sufficient compression the bunch length should not exceed k_p^{-1} [12];
• initial transverse size of the bunch should be significantly smaller than the laser-spot size in order to ensure constant transverse accelerating fields along the bunch.

Current studies focus on investigating the effect of longitudinal bunch compression by means of 2D PIC simulations. The compression factor depends on the gradient of the longitudinal field, therefore a more intense laser-pulse is advantageous. In the following, simulations in homogeneous plasma of $n_0 = 1.68 \times 10^{-17}$ cm^{-3} density are presented with a laser of $a_0 = 5$, $\lambda_0 = 800$ nm, $\tau_0 = 25$ fs FWHM, waist $w_0 = 24$ μm RMS. An electron bunch with the same parameters as listed in the previous section, was externally injected into a wake on the laser axis at the zero-field crossing. The transverse properties of the beam were matched to the intrinsic betatron motion to suppress emittance growth [10]. Fig. 3 shows the plasma charge density together with the externally injected electron bunch in the initial and final position of propagation inside the plasma. It can be seen that strong compression occurs after 8 mm distance. The final bunch length was 1.2 fs RMS (which corresponds to a compression factor of 8.3), energy of 37 MeV with relative energy spread of 6%. Bunch energy grows steadily during propagation while the absolute energy spread saturates when the bunch reaches the point of maximal compression, which leads to a steady reduction of the relative energy spread. This suggests that acceleration to higher energies would reduce the relative energy spread even more, though this would require laser guiding in a parabolic plasma channel for acceleration over longer distances.

One of the crutial factors for efficient bunch compression is injection at exactly or near to the zero-field crossing. Injection phase scans showed that strong compression still occurs if the bunch is injected within ∼10 fs from its optimal injection phase. This puts strong restrictions on the synchronisation between the laser and electron-injection system. The level of synchronisation at REGAE experiments is expected to be ∼10 fs RMS which should allow for the experimental observation of bunch compression. Furthermore, space-charge effects were studied by injecting bunches of higher charge density. Simulations showed that compression did not occur for charges of 5 pC and above.

SUMMARY

PIC simulations matching future experimental conditions of LPA experiments at REGAE were performed and two major topics are covered in present studies: electron-bunch emittance growth and bunch compression. It was shown that the emittance of externally injected electron beam grows if the beam parameters are not matched to the intrinsic betatron length in the plasma wake. If matched, the emittance remains constant during the acceleration process. We also presented the mechanism of longitudinal bunch compression due to the gradient in the longitudinal field inside the plasma wake. This effect is sensitive to the injection phase, initial bunch energy, energy spread, length and charge.

REFERENCES

[1] R.A. Fonseca *et al.*, Lect. Notes Comput. Sci. **2331**, 342 (2002).
[2] W.P. Leemans *et al.*, Nat. Phys. **2**, 696 (2006)
[3] C.G.R. Geddes *et al.*, Phys. Rev. Lett. **100**, 215004 (2008)
[4] W. Leemans and E. Esarey, Phys. Today **62**, 44 (2009).
[5] A. G. Khachatryan *et al.*, Phys.Rev. STAB **10**, 121301 (2007)
[6] P. Michel *et al.*, PRE **74**, 026501 (2006)
[7] R. Assmann and K. Yokoya, NIMA **410**, 544 (1998)
[8] K. Floettmann, Phys. Rev. STAB **6**, 034202 (2003)
[9] E. Courant and H. Snyder, Ann. Phys. **3**, 1 (1958)
[10] T. Mehrling *et al.*, *Transverse emittance growth in staged LWFA*, submitted to PRSTB (2012).
[11] W. Rittershofer *et al.*, Phys. Plasmas **17**, 063104 (2010).
[12] N. E. Andreev, S. V. Kuznetsov, I.V. Pogorelsky, Phys. Rev. STAB **3** 021301 (2000)
[13] N. E. Andreev and S. V. Kuznetsov, Trans. on Plasma Science, **28**, 4 1211 (2000)

WAKEFIELD PRODUCED BY A SMALL BUNCH MOVING IN COLD MAGNETIZED PLASMA ALONG THE EXTERNAL MAGNETIC FIELD*

S.N. Galyamin#, D.Ya. Kapshtan, A.V. Tyukhtin,
Saint Petersburg State University, Saint Peterburg, Russia

Abstract

Plasma wakefield acceleration (PWFA) is a promising tool for acceleration of charged particles to high energies at relatively small lengths. Knowledge about the structure of the electromagnetic field produced by the driver bunch in plasma plays the essential role for the realization of this accelerating scheme. Constant external magnetic field which can be used for focusing the driver bunch affects the field structure essentially because plasma acquires both anisotropy and gyrotropy. However, the field in the latter case has not been practically investigated until present. Here we study the field produced by point charge and small bunch moving in cold magnetized plasma along the external magnetic field. We note the singular behavior of some components of the wave field produced by point charge near the charge trajectory. We also analyze the influence of the external magnetic field and bunch size on the field components.

INTRODUCTION

Cherenkov radiation in a cold magnetized plasma has been investigated for the first time in the early fifties [1], but the detailed analysis of the electromagnetic field structure in this situation has not been performed until present. However, this question is of essential interest in the context of wakefield acceleration method [2] and especially plasma wakefield acceleration (PWFA) method [3], which has achieved a 40 GeV/m gradient for now [4]. Outcomes of the present paper concerning the peculiarities of the electromagnetic field of small bunch moving in the considered medium can be used for further development of PWFA technique.

We consider cold electron plasma under the external magnetic field H_{ext} described by permittivity tensor [5]

$$\hat{\varepsilon} = \begin{pmatrix} \varepsilon_1 & -i\varepsilon_2 & 0 \\ i\varepsilon_2 & \varepsilon_1 & 0 \\ 0 & 0 & \varepsilon_3 \end{pmatrix}, \qquad (1)$$

$$\varepsilon_1 = 1 - \frac{\omega_p^2}{\omega^2 - \omega_h^2},\ \varepsilon_2 = \frac{-\omega_p^2 \omega_h}{\omega(\omega^2 - \omega_h^2)},\ \varepsilon_3(\omega) = 1 - \frac{\omega_p^2}{\omega^2}, \qquad (2)$$

where $\omega_p^2 = 4\pi N e^2/m$ is a plasma frequency (N is an electron density, e and m are an electron charge and a mass respectively), $\omega_h = |e|H_{ext}/(mc)$ is a "gyrofrequency" and c is the light speed in vacuum.

*Work is supported by Saint Petersburg State University, the Dmitry Zimin "Dynasty" Foundation and Russian Foundation for Basic Research (Grant No. 12-02-31258).

galiaminsn@yandex.ru

FIELD OF POINT CHARGE

The electromagnetic field generated by point charge q moving with constant velocity $\upsilon = \beta c$ along H_{ext} in (1) is given in the ultrarelativistic case $\gamma >> 1$ (γ is Lorentz factor) for $\zeta < 0$ ($\zeta = z - \upsilon t$) and $|\zeta| >> c/(\gamma\omega_p)$ by the following formula

$$H_\varphi = \int_{\omega_p}^{\omega_\Sigma} h_\varphi(\omega) J_1(\rho s_e) \sin(\omega\zeta/\upsilon) d\omega \qquad (3)$$

for the azimuthal magnetic component (the cylindrical frame with z axis coinciding with H_{ext} is used) and by similar ones for the rest of components [1, 6]. Here

$$h_\varphi = \frac{qc\beta}{\omega_p^2 \omega_h} \frac{\omega_h^2 - \omega^2}{\sqrt{\omega^2 - \omega_c^2}} \left[\frac{\omega^2}{c^2} \left(\varepsilon_2^2 - \varepsilon_1^2 + \frac{\varepsilon_1}{\beta^2} \right) + \varepsilon_1 s_e^2 \right] s_e, \qquad (4)$$

$$s_e^2 = \frac{(\beta^2 - 1)(u - u_1)(u - u_3)(u - u_4)}{\beta^2 c^2 (u - u_2)},\ u = \sqrt{\omega^2 - \omega_c^2}, \qquad (5)$$

$$\omega_c^2 = \omega_p^2 - \omega_h^2 [1 - \beta^2]^2/(4\beta^2),\quad \omega_\Sigma = \sqrt{\omega_p^2 + \omega_h^2}, \qquad (6)$$

$$u_{1,2} = \frac{\omega_h(1 \mp \beta^2)}{2\beta},\ u_{3,4} = \frac{\omega_h \beta}{2} \mp \frac{1}{2\beta} \sqrt{\frac{\omega_h^2}{4} - \frac{\omega_p^2 \beta^2}{1 - \beta^2}}. \qquad (7)$$

Two analytical approaches have been applied to calculation of (3). First one gives the field representation in the far-field zone within the Cherenkov cone $\rho s_{e1,2} >> 1$, $|\zeta| > \zeta_{\min}(\rho)$:

$$H_\varphi \approx \left[-h_\varphi(\omega_{s1}) \sin(\rho s_{e1} - \omega_{s1}|\zeta|/\upsilon) / \sqrt{s_{e1}|s''_{e1}|} + h_\varphi(\omega_{s2}) \cos(\rho s_{e2} - \omega_{s2}|\zeta|/\upsilon) / \sqrt{s_{e2}|s''_{e2}|} \right] / \rho, \qquad (8)$$

where $s_{e1,2} = s_e(\omega_{s1,2})$, $\omega_{s1,2}$ are solutions of $ds_e/d\omega = |\zeta|/(\rho\upsilon)$, $\zeta_{\min}(\rho) = \rho\upsilon s'_{e\min}$, $s'_{e\min} = ds_e(\omega_{s0})/d\omega$, ω_{s0} is solution of $d^2 s_e/d\omega^2 = 0$. In the special case of $\gamma >> 1$ and $\omega_h << \omega_p$ one obtains:

$$\omega_{s0} \approx \omega_p \left[1 + \omega_h^2/(8\omega_p^2) \right],\quad s'_{e\min} \approx 4\omega_p^2/\omega_h^2. \qquad (9)$$

For $|\zeta| >> \zeta_{\min}$ we have

$$\omega_{s1}^2 \approx \omega_p^2 + \left[\rho\omega_p^2/(2|\zeta|\sqrt{\omega_h}) \right]^{4/3}, \qquad (10)$$

$$\omega_{s2}^2 \approx \omega_p^2 + \left[\omega_h - \left[\rho\omega_p\omega_\Sigma/(2|\zeta|\sqrt{\omega_h}) \right]^{2/3} \right]^2. \qquad (11)$$

Formula (8) predicts the beating behavior of the field.

Another approach describes the field in the vicinity of the charge motion line behind the charge [6]:

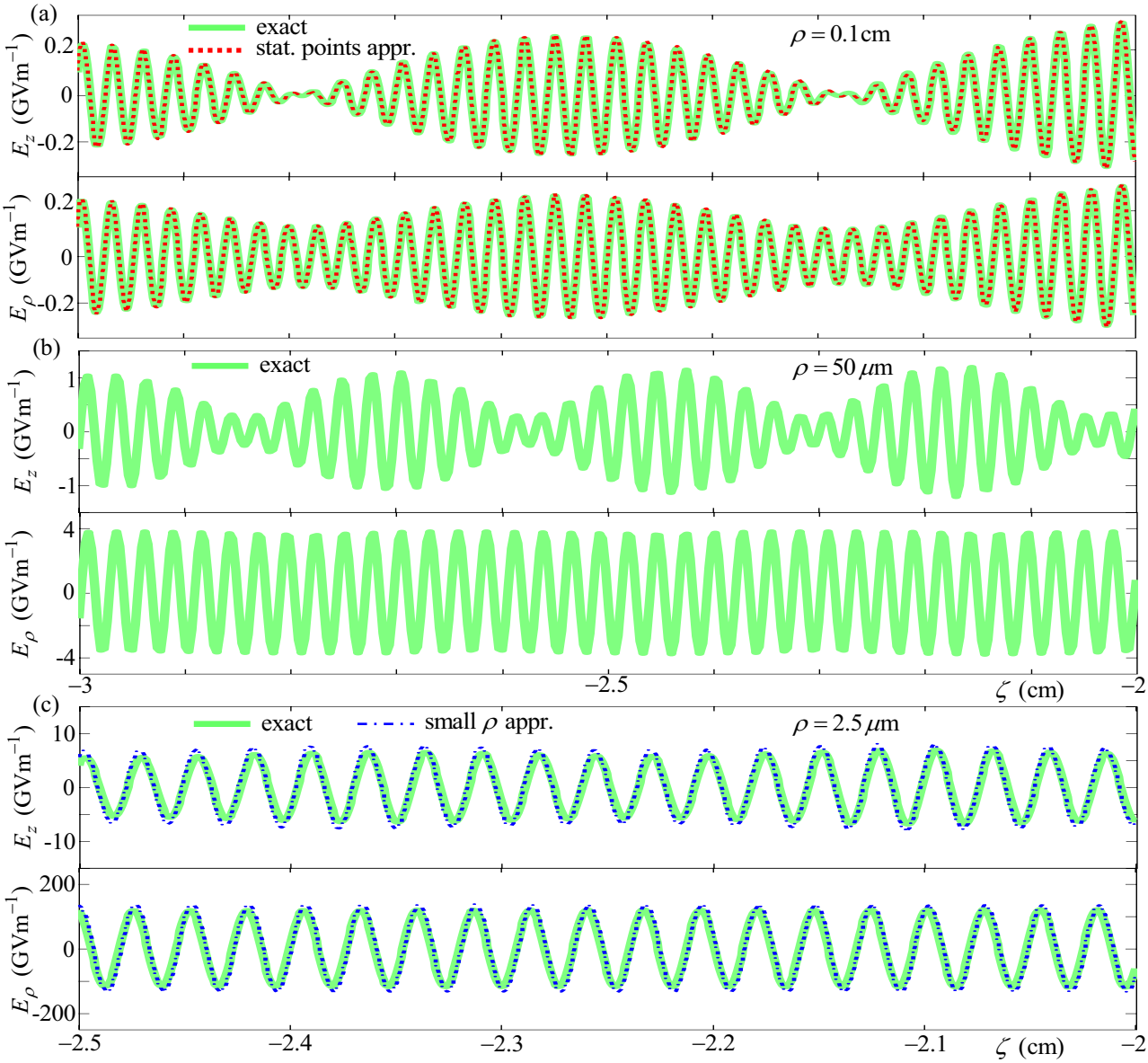

Figure 1: Field of point charge calculated with the use of exact numerical approach (solid green line), stationary point approach (dashed red line) and small ρ approximation (dash-dotted blue line). Plot (a) corresponds to the far field zone, plot (b) corresponds to the middle zone, while plot (c) corresponds to the zone of small values of ρ. Calculation parameters are: $q = -1$ nC, $\omega_p = 2\pi \times 10^{12}\,\mathrm{s}^{-1}$, $\omega_h = 0.5\omega_p$ ($B_{ext} \approx 18$ T), $\gamma = 22$.

$$E_\rho \approx E_{\rho 0}\sin\left(\omega_\Sigma \zeta/\upsilon\right),\ E_z \approx E_{z0}\cos\left(\omega_\Sigma \zeta/\upsilon\right),\quad H_z \approx H_{z0}\sin\left(\omega_\Sigma \zeta/\upsilon\right), \tag{12}$$

$$E_{\rho 0} = 2q\omega_p^2(\upsilon\omega_\Sigma\rho)^{-1},\ E_{z0} = 2q\omega_p^2\upsilon^{-2}\ln\left(\rho\omega_p/c\right),\quad H_{z0} = 2q\omega_p^2\omega_h(\upsilon c\omega_\Sigma)^{-1}\ln\left(\rho\omega_p/c\right). \tag{13}$$

As one can see, E_ρ possesses strong inverse proportional singularity, while E_z and H_z possess weaker logarithmical ones. The rest of components vanishes $\sim \rho\ln\rho$ as $\rho \to 0$. Moreover, all components behave harmonically with frequency ω_Σ. Possibilities of decreasing the orthogonal electric component and enlarging the longitudinal magnetic one by increasing the external magnetic field have been shown in [6].

Along with two aforementioned analytical approaches an effective numerical algorithm has been developed for computation of the field components for arbitrary distance from the charge. Figure 1 shows the dependence of the longitudinal and orthogonal components of the electric field on ζ for different offsets ρ from the charge trajectory. For relatively large offset (Fig. 1,a) the total field calculated numerically is in a good agreement with that calculated via the stationary point approach (8). Both components are of the same magnitude, and the beating behavior is brightly expressed. For relatively small offset

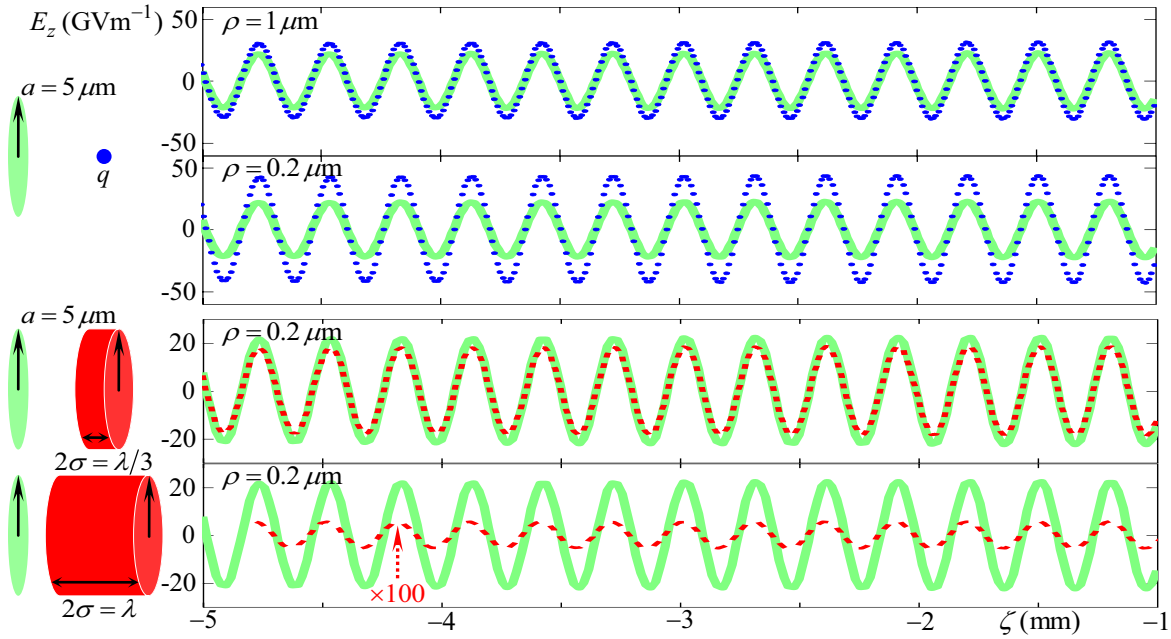

Figure 2: Fields produced by point charge (dotted blue line), thin disc (solid green line) and cylindrical bunch (dashed red line) versus ζ for $q = -1\text{nC}$, $\omega_p = 2\pi \times 10^{12}\,\text{s}^{-1}$, $\omega_h = 0.14\omega_p$ ($B_{ext} = 5\,\text{T}$), $\gamma = 22$ and $\lambda = 2\pi\beta c/\omega_\Sigma = 300\,\mu\text{m}$.

(Fig. 1,c) the total field calculated numerically is again in a good agreement with that calculated via small ρ approximation formulas (12). Both components behave harmonically at frequency ω_Σ and E_ρ is about one order larger compared with E_z. The region of middle offsets (Fig. 1,b) cannot be covered by any of discussed analytical approximations. Here E_z component is steel in the beating regime, while E_ρ is already in the harmonic one; magnitudes of components are comparable.

FIELD OF FINITE BUNCHES

As was shown, field components (12) have singularities on the charge trajectory. Therefore, the analysis of the small bunch field near the line $\rho = 0$, which is of most interest in the context of PWFA, requires accounting the finite size of the bunch. We can easily calculate the field of different bunches using the field of the point charge (12) as the Green function. This approach is based on computing the convolution integral with analytical functions and therefore requires neither expensive numerical simulation suites nor a large amount of computer resources.

Figure 2 compares fields produced by point charge, charged disc and charged cylinder. For relatively large ρ (comparable with the disc radius) the longitudinal electric field produced by point charge practically coincides with that produced by charged disc. With decrease in ρ the difference becomes essential. Moreover, short cylinder (in the wavelength $\lambda = 2\pi\beta c/\omega_\Sigma$ scale) produces the field which practically coincides with that of disc. The field of long cylinder is several orders smaller compared with the field of disc which is explained by non-coherency of the fields produced by separate particles of the long bunch.

CONCLUSION

In this paper we have analytically described the field of a small bunch moving in a cold electron plasma along the external magnetic field both in the far-field zone and in the vicinity of the bunch trajectory. We have suggested the combined numerically-analytical method for computation of wakefields produced by small (in the orthogonal direction) bunches of arbitrary shape and charge distribution which can be applied to improvement of PWFA technique. Moreover, we have shown that the use of longitudinally magnetized plasma provides certain advantages for this scheme, such as focusing action of the external magnetic field (which can be additionally enhanced by the longitudinal magnetic component of the wakefield) and suppressing of the transversal electric field which causes the bunch spreading.

REFERENCES

[1] A.G. Sitenko and A.A. Kolomensky, Sov. Phys. JETP 30 (1956) 511.
[2] W. Gai *et al.*, Phys. Rev. Lett. 61 (1988) 2756.
[3] C. Joshi and T. Katsouleas, Phys. Today 56 (2003) 47.
[4] C. Joshi and V. Malka, New J. Phys. 12 (2010) 045003.
[5] V.L. Ginzburg, *The propagation of electromagnetic waves in plasma*, (London: Pergamon, 1964).
[6] S.N. Galyamin *et al.*, "Cherenkov Radiation from a Small Bunch Moving in a Cold Magnetized Plasma," IPAC'12, New Orleans, May 2012, WEPPP024, p. 2775 (2012). http://www.JACoW.org

PARAMETER OPTIMIZATION OF A RECTANGULAR DIELECTRIC BASED WAKEFIELD ACCELERATING STRUCTURE

S. Baturin, A. Altmark, I.L. Sheynman, St.Petersburg Electrotechnical University "LETI", Saint-Petersburg, Russia
A. Kanareykin, St.Petersburg Electrotechnical University "LETI", Saint-Petersburg, Russia and Euclid Techlabs LLC, Gaithersburg, MD USA

Abstract

In this talk, we present the algorithm and simulation results of a single mode wakefield parametric study of the rectangular dielectric based wakefield accelerating structure. Analytical solutions of wakefield generation in rectangular dielectric structures have been studied in order to achieve optimal relations between the geometrical parameters and dielectric constant of the structure, and the drive beam parameters like bunch charge and bunch length. Optimization has been carried out for maximization of the accelerating gradient in the single LSM_{11} mode approximation.

INTRODUCTION

In this paper we consider dielectric based wakefield acceleration technology [1-4] as one of the most promising for the development of the high gradient accelerating structures to be used for the next generation of linear colliders [5] and future X-ray FELs [6].

It is assumed that dielectric lined structures will be excited by a high intensity electron beam (e.g., the CLIC collider project [7,8]) for generating high power X-band, mm-wave or THz radiation. This type of electromagnetic wave generation is essential for avoiding the need to develop high power upper GHz/THz sources and coupling components that are able to sustain and transmit into the structure GW-level power in the same frequency ranges [2-4].

An accelerating structure with dielectric loading is a dielectric waveguide with an axial vacuum channel for beam propagation. The dielectric is surrounded by a conducting metal wall [1-4]. Recent experiments have proved that the dielectric based structures can sustain accelerating gradients in excess of 100's of MV/m [8,9] and GV/m [3] in the upper GHz and THz frequency ranges respectively.

For example, a high current (up to 100 nC) short (1–2 mm) relatively low energy (15–100 MeV) electron bunch in this type of a structure can generate Cerenkov wakefields with a longitudinal field magnitude up to 100-300 MV/m in the X - Ka band frequency ranges [9]. A 3 nC charge and 30 μm long bunch from the 23 GeV FACET/SLAC accelerator generates 1-10 GV/m wakefields in the THz range [3,10]. These wakefields are used for accelerating a less intense but high energy electron bunch propagating behind the drive bunch at a distance corresponding to the accelerating phase of the E_z field [11]. Dielectric based structures provide in addition to a high accelerating gradient the control over the frequency spectrum of the structure by introducing additional ferroelectric layers [12,13] as well as the possibility of using new promising microwave/THz materials (such as diamond and sapphire) with unique breakdown strength and thermoconductive properties [14]. Cerenkov radiation generated by a relativistic electron bunch in a rectangular waveguide with a transverse, inhomogeneous dielectric layers has been analyzed in [15], where a modification of the transverse operator method was used. In [15], the Sturm–Liouville second order operator with an alternating sign weight function was considered. This approach makes it possible to obtain a complete analytic solution for eigenmodes and to solve the problem of Cerenkov wakefield generation in a rectangular accelerating structure with a composite dielectric loading in the most general form [15].

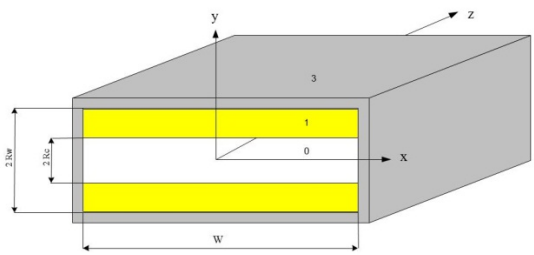

Figure 1: A rectangular dielectric based accelerating structure.

Below, we present the analytical solution for wakefield generation in the rectangular dielectric structure to optimize relations between both the geometrical parameters and dielectric constant of the structure, and the beam parameters for two specific user facilities, the Argonne Wakefield Accelerator (AWA) and the FACET facility at SLAC.

ANALYTICAL APPROXIMATION

We consider an ultrarelativistic Gaussian electron bunch passing along the central axis of a rectangular DLA (dielectric loaded accelerating) structure presented in Fig.1.

Let us take into account first the symmetric accelerating LSM mode ($H_y = 0$), which corresponds to the first asymmetric eigenfunction of the transverse $\hat{T}_E$-operator of the wave equation [15]. We introduce dimensionless parameters as follows:

$$p_1 = \frac{R_w}{R_c},\ p_2 = \frac{R_c}{w}. \quad (1)$$

Here R_w is the outer half height of the waveguide, R_c is the vacuum gap half height, and w is the width of the waveguide.

We assume here that the condition $\omega^2 << \gamma^2 \beta c (\pi / w)^2$ is fulfilled for the frequency of the mode under consideration. In this case the dispersion relationship for the LSM symmetric modes presented in [15] can be written as:

$$\cot(X) = X \frac{\tanh(\pi p_2)}{\varepsilon(p_1 - 1)\pi p_2}. \quad (2)$$

The axial electric field E_z for this approximation is given by the following expression:

$$E_z = \frac{4\pi Q}{w^2} \frac{\pi^2 p_2}{S(p_1,p_2)^2 + (\pi p_2)^2} \frac{\varepsilon}{\varepsilon - 1} \frac{1}{p_1 - 1} \times$$
$$\times \left[\frac{\cos(X)}{\sinh(\pi p_2)} \right]^2 \frac{4X}{\sin(2X) + 2X} \times \quad (3)$$
$$\times \exp\left(-\frac{\sigma_z^2}{2w^2} \frac{S(p_1,p_2)^2}{p_2^2} \right)$$

Here

$$S(p_1,p_2) = \frac{1}{\sqrt{\varepsilon - 1}} \sqrt{\frac{X^2}{(p_1 - 1)^2} + (\pi p_2)^2}, \quad (4)$$

Where σ_z is the bunch length, and Q is the bunch charge.

The mode frequency can be calculated as

$$f = \frac{c}{2\pi w} \frac{S(p_1,p_2)}{p_2} \quad (5)$$

Now we maximize E_z using the expression (3) by varying p_1, p_2 and w for the given beam parameters and dielectric constant value ε. The optimal structure dimensions have been simulated for the FACET and AWA accelerator parameters. The corresponding parameter optimization results are presented below.

OPTIMIZATION FOR THE AWA BEAM

Let us consider the AWA beam parameters: bunch length $\sigma_z = 1.5$ mm, bunch charge $Q = 20$ nC, and transverse bunch size $\sigma_r = 0.5$ mm. The vacuum gap half-height has to satisfy $R_c > 3\sigma_r$ to be able for the bunch to pass through the structure with no significant beam loss.

An additional analysis that has been carried out (Fig. 2) shows that the optimal dielectric constant of the dielectric loading material should be within the range that corresponds to the diamond dielectric constant. This leads to additional terms for the maximization procedure for $R_c > 1.5$ mm. We chose the dielectric constant as $\varepsilon = 5.7$, which corresponds to a diamond like material that exhibits specific advantages by comparison with the cordierite and alumina ceramics previously used for DLA applications [4,16].

Maximization of E_z according to expression (3) for the given parameters leads to:

$$R_c = 1.5 \text{ mm},\ R_w = 2.33 \text{ mm},\ w = 11.1 \text{ mm}. \quad (6)$$

Optimization of the AWA structure geometry was carried out numerically. The wakefield magnitude was found $E_z = 24.3$ MV/m or 1.22 MV/m/nC for the accelerating mode frequency $f = 36.2$ GHz. The maximum charge of a single AWA bunch can be up to 120 nC [2,9] giving the upper gradient limit of ~ 150 MV/m in the single mode approximation.

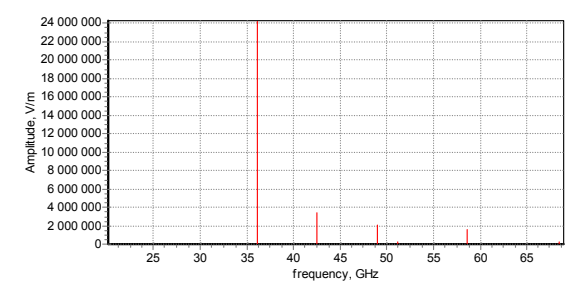

Figure 2: E_z field spectrum distribution for the AWA bunch parameters and structure geometry corresponding to expression (6).

The corresponding amplitude-spectrum distribution for the parameters (6) is presented in the Fig. 2. One can see that the AWA bunch wakefield is nearly monochromatic for the optimized structure parameters. This gives an additional opportunity for the more precise bunch phasing in multibunch wakefield accelerating methods [17].

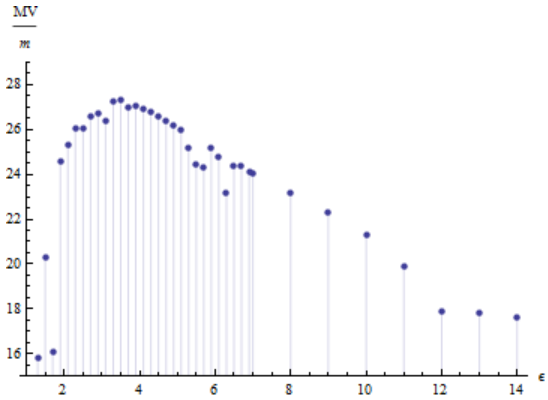

Figure 3: Result of the E_z field maximization (3) for the AWA beam parameters for different values of the dielectric constant of the DLA structure material.

OPTIMIZATION FOR THE FACET BEAM

In this section we consider the FACET beam parameters [4,16]: bunch length $\sigma_z = 30\ \mu$m, bunch charge $Q = 3$nC, transverse size $\sigma_r = 30\ \mu$m. Following the same approach as for the AWA structure above one can use $R_c > 3\sigma_r$ or $R_c > 100\ \mu$m. For the dielectric layer we considered diamond as in the AWA case. Due to the small transverse and longitudinal dimensions of the FACET beam it could be considered as a potential driver for a terahertz radiation source based on dielectric structure.

Maximization of (3) for the FACET beam parameters leads to:

$$R_c = 100\ \mu\text{m},\ R_w = 112\ \mu\text{m},\ w = 406\ \mu\text{m}. \qquad (7)$$

With the wakefield amplitude $E_z = 2.7$GV/m or 0.9GV/m/nC and frequency $f = 1.32$ THz. The maximization was performed numerically.

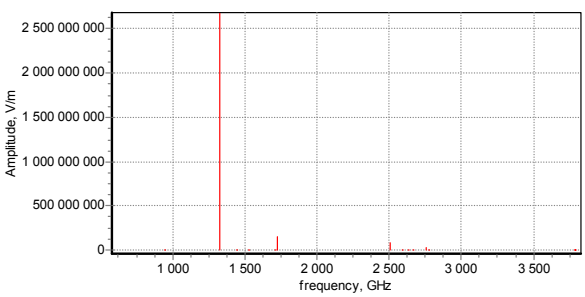

Figure 4: Full E_z field amplitude-spectrum distribution for the structure parameters (7) and FACET beam.

CONCLUSION

We considered a new algorithm for the single mode longitudinal wakefield magnitude maximization of rectangular dielectric based wakefield accelerating structures. Analytical solution of the wakefield generated in rectangular dielectric structures are presented. The optimal relations between both the geometrical parameters and bunch charges and lengths were found. We have shown that theoretical predictions of the wakefield maxima are quite promising for both AWA and FACET beam parameters that are 1.22 MV/m/nC at 36 GHz and 0.9 GV/m/nC at 1.3 THz respectively. Multibunch acceleration schemes are to be considered as well. It should be noted that the results presented here open new possibilities for considering the DLA structures designed for the AWA and FACET beams as new narrow band high power terahertz sources.

REFERENCES

[1] W.Gai, P. Schoessow, B. Cole, R. Konecny, et al., Phys. Rev. Lett. 61, 2756 (1988).
[2] W.Gai, AIP Conf. Proc. 1086, 3 (2009).
[3] M.C. Thompson et al., Phys. Rev. Lett., 100 , 214801 (2008).
[4] A.D. Kanareykin, J. Phys.: Conf. Ser. 236, 012032 (2010).
[5] C Jing, S. Antipov, A. Kanareykin, P. Schoessow et al. Proceedings PAC'11, 2279 (2011).
[6] C.Jing, A. Kanareykin, J.G. Power, A. Zholents. Proceedings IPAC'11, 1485, (2011).
[7] R. Tomás. Phys. Rev. ST Accel. Beams 13, 014801 (2010).
[8] C. Jing, S.P. Antipov, A. Kanareykin, P. Schoessow et al. Proceedings PAC'11, 315 (2011).
[9] M. Conde, S. Antipov, W. Gai, R. Konecny. Proceedings IPAC'10, 4425, (2010).
[10] J.Rosenzweig, G.Travish , M.Hogan, P. Muggli. Proceedings IPAC'10, 3605, (2010).
[11] S.Antipov, C.Jing, A.Kanareykin, V.Yakimenko et al. Appl. Phys. Lett. 100, 132910 (2012).
[12] A. Altmark, A. Kanareikin, and I. Sheinman, Tech. Phys. 50, 87 (2005).
[13] C. Jing, A. Kanareykin, J. G. Power, M. Conde et al. Phys. Rev. Lett. 106, 164802 (2011).
[14] A.Kanareykin. AIP Conference Proceedings, 1299, 286 (2010).
[15] S. Baturin et al., Journal of Technical Physics, 57 №5, 683-692 (2012).
[16] A. Kanareykin et al., Proceedings of IPAC2012, New Orleans, Louisiana, USA, 2819 (2012).
[17] A.M. Altmark, A.D. Kanareykin, Technical Physics Letters, 36 №3, 207-210 (2010).

AN ANALYTICAL APPROACH TO SOLUTION OF SELF-COORDINATED BEAM DYNAMICS IN DIELECTRIC WAKEFIELD ACCELERATING STRUCTURES*

I. Sheynman#, LETI (ETU), Saint-Petersburg, Russia

Abstract

Self-coordinated transverse dynamics of the high current relativistic electronic bunches used for generation of wake fields in wakefield accelerating structures with dielectric filling is investigated. An analytical approach to solution of self-coordinated beam dynamics is developed.

INTRODUCTION

Wakefield acceleration in a dielectric wakefield waveguide structures is one of the most intensively developed direction among new methods of particle acceleration. Linear accelerators are considered also as sources of sequence of electronic bunches for the free electron laser, which is considered now the major candidate for creation of ultra short impulses (of attosecond range) X-ray radiation. Waveguide structures with dielectric filling excited by a high current electronic bunch were investigated intensively for the last years [1] – [5]. The main purpose is of prospects of their use as high gradient linear accelerators.

One of the main problems in realization of the wakefield method is keeping of an intensive electronic bunch in the channel of a wave guide and prevention of subsidence of particles on its wall. In this regard, a key task in the wakefield method of acceleration is modeling of the self-coordinated movement of a relativistic electronic bunch passing through dielectric structure in fields of Vavilov-Cherenkov created by it.

In recent years in tasks of the analysis of self-coordinated dynamics of relativistic electronic bunches in wakefield accelerating structures methods of direct numerical modeling where developed. These methods are «particle – particle» and «particle – grid». These methods allow on the set parameters of accelerating structure and an initial condition of a bunch to simulate process of its movement. The results of calculations are determination of flight range of the bunch to a contact to them accelerating structure walls, emittance of the bunch, and also transferred or received by bunch energy of particles.

Shortcomings of these methods are considerable duration of calculations for ensuring accuracy of calculations, insistence to volume of random access memory and productivity of computer system. Let us note also that at change of parameters of the bunch and of accelerating structure complete recalculation of a problem of the bunch movement is necessary.

For design of accelerating structures, solutions of problems of optimization in which the structure and bunch parameters maximizing efficiency of accelerating process are determined are necessary. The solution of similar tasks based on direct numerical modeling of dynamics demands repeated carrying out numerical calculations. Creation of the analytical description of self-coordinated dynamics of the bunch allowing direct parametrical research of process in this regard is of interest.

BEAM DYNAMICS EQUATIONS

The description of movement of the electronic bunch was carried out on the basis of the equations of relativistic dynamics [3]:

$$F_r = d\left(m_e V_r \gamma\right)/dt ,$$

where

$$F_r = F_{focus} - eq\sum_{n,m}\Big[\psi_{F_r\,n,m} I_n'\left(k_{r\,n,m} r(\zeta,t)\right)\cdot$$

$$\cdot\int_0^{\zeta} f(\zeta_0)\sin\left(k_{z\,n,m}\left(\zeta-\zeta_0\right)\right) I_n(k_{r\,n,m} r(\zeta_0,t))d\zeta_0\Big],$$

$r(\zeta,t)$ is a bunch deflection from waveguide axes, $\zeta = z - vt$ is a distance behind the bunch, F_f is a focusing force, e and m_e are charge and mass of electron, q and γ are charge and relativistic factor of the bunch, $k_{z\,i,j}$ and $k_{r\,i,j}$ are longitudinal and radial components of wave vector, $\psi_{E_z\,i,j}$ and $\psi_{F_r\,i,j}$ are coefficients of series, depending of geometry and wave guide filling permittivity, $f(\zeta_0)$ is a function describing longitudinal charge distribution, $I_n(x)$ are modified Bessel function of n-th order.

The task of the description of macroparticle movement is self-coordinated: the mutual provision of particles in ensemble influences a field created by particles which, in turn, leads to change of their position. Let's consider an analytical method of the solution of the integro-differential equation of self-coordinated dynamics at the following simplifying assumptions:

1. Let's consider that the charge of the bunch is distributed evenly in the longitudinal direction, thus $f(\zeta_0) = 1/l$, where l is a length of the bunch.

*Work supported by the Russian Foundation for Basic Research and the Ministry of Education and Science of the Russian Federation in the framework of the Federal Program "Human Capital for Science and Education in Innovative Russia" for 2009–2013.

#ishejnman@gmail.com

2. Let's neglect change of size of a relativistic factor over time $\gamma(t)=\gamma_0$.

In considered case $k_{r\,i,j}r(\zeta,t)<<1$, in rejecting field at small deviations of the bunch from the wave guide axis the overwhelming contribution is brought by the 1st azimuthal mode $i=1$. Nonlinear component of a force is negligible. Thus, it is possible to consider that the force operating on charges in the radial direction, depends on r linearly $I_1(kr)\approx kr/2$, $I_1'(kr)\approx 1/2$.

In case the contribution of one of modes is overwhelming, and the others can be neglected, the equation essentially becomes simpler:

$$\frac{\partial^2 r(\zeta,t)}{\partial t^2}-B\int_0^{\zeta}\sin\left(k_z\left(\zeta-\zeta_0\right)\right)r(\zeta_0,t)d\zeta_0=\frac{F_f}{\gamma_0 m_e}.$$

To reduction of the received integro-differential equation to the integrated equation we will apply Laplace's transformation on time. The received integrated equation has the known decision received on the basis of transformation of Laplace on longitudinal coordinate.

Expressing the image of required function, and finding the original Laplace's return transformation by image decomposition in a Laurent series, we receive for lack of focusing force $F_f=0$:

$$r(\zeta,t)=r_0+v_{r0}t+$$
$$+\sum_{n=0}^{\infty}\left[\frac{\left(k_z\zeta\right)^{2n+2}}{(2n+2)!}\sum_{m=0}^{n}\left[\binom{n}{m}\frac{(-1)^m\left(t\sqrt{B/k_z}\right)^{2(n-m+1)}}{(2n-2m+2)!}\cdot\right.\right.$$
$$\left.\left.\cdot\left(r_0+\frac{v_{r0}t}{2n-2m+3}\right)\right]\right],$$

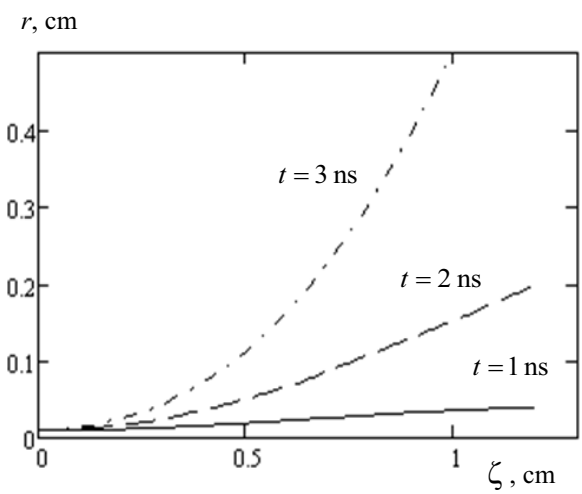

Figure 1: Characteristic dependences $r(\zeta)$ for the different moments of time.

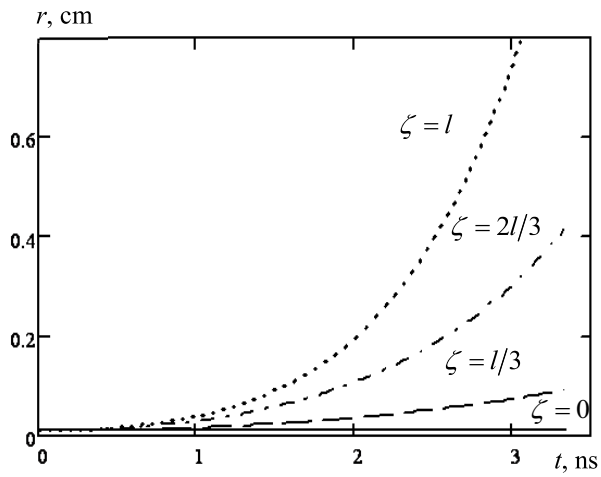

Figure 2: Radial bunch charge distribution for constant initial deflection of the bunch.

In Fig. 1, 2 for the purpose of an illustration of the received decision if $B=6.365\cdot10^{20}$ м$^{-1}\cdot$с$^{-2}$, $k_z=260$ м$^{-1}$, $r_0=0.01$ см, dependences $r(\zeta)$ for the different moments of time and $r(t)$ for the various ζ are given. A head – tail instability leads to growing deflection of the backward part of the bunch.

Comparison of the received analytical expression was carried out with numerical modeling of bunch dynamics by a method of macroparticles based on the BeamDynamics program. Comparative calculations were made at the following parameters of a waveguide and a bunch: $R_c=0.5$ cm, $R_w=0.634$ cm, $\varepsilon_1=16$, $W=16$ MeV, $Q=100$ nC, $l=6\sigma=1.2$ cm, $r_0=0.01$ cm, $v_0=0$.

The BeamDynamics program realizes modeling of Gaussian distribution of the bunch charge [3]. The bunch with the Gaussian profile of charge distribution exponentially suppresses excitation of high modes of the waveguide that allows its comparison to analytical calculation of dynamics of a homogeneous bunch taking into account only one main mode. Program finishing was made after a contact by the bunch of a wall of the vacuum channel. Results of comparison are presented on Fig 3. The dotted line shows radius of the channel of accelerating structure. Thus range of flight of the bunch to a contact of the waveguide wall in analytical and numerical calculations practically coincided and made $L=86$ cm.

As the charge of a Gaussian bunch is concentrated near its center, influence of radial forces created by it near the head of the bunch is expressed weaker, than in case of the homogeneous bunch. At the same time on a tail of the Gaussian bunch influence of radial forces is expressed stronger.

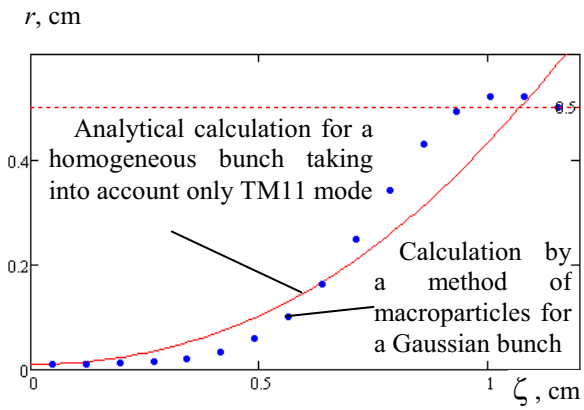

Figure 3: Comparison of analytical dependence to numerical calculation by a method of macroparticles.

BEAM DYNAMICS WITH FOCUSING

Significant amplitude of own rejecting fields generated by high current bunch affecting his tail, emphasizes focusing system necessity. To keep the high current beam is appropriate to use a rigid focusing system based on FODO focusing [4, 5].

The period of the radial force of the focusing system can be approximated by the harmonic dependence for taking part a potential "sagging" between quadruple lenses:

$$F_f = -k(z)r = -ec\frac{\partial B(z)}{\partial r}r = -ecr\frac{B_0}{2R_w}\cos\frac{2\pi z}{L_s}.$$

Such dependence may be written as

$$F_f = -g_1 r(\zeta,t)m_e\gamma_0\cos\kappa(\zeta+vt),$$

To simplify the beam dynamics equation let us consider that restoring force is linear increasing with deflection from waveguide axis without alternating sign component.

$$F_f = -g_0 r(\zeta,t)m_e\gamma_0,$$

where $g_0 = g_1/4$.

Solving such integro-differential equation by Laplace transform method, we receive:

$$r(\zeta,t) = r_0\cos\left(\sqrt{g_0}t\right)+$$

$$\frac{r_0}{a^2}\sum_{n=1}^{\infty}\left\{\frac{(k_z\zeta)^{2n+2}}{(2n+2)!}\sum_{j=0}^{n-1}\left[\frac{j+1}{a^j}\sum_{m=0}^{(n-j-1)}\binom{n}{m}\frac{(-1)^{m+j}\tau^{2(n-m-j-1)}}{(2(n-m-j-1))!}\right]\right\}+$$

$$+r_0\cos\left(t\sqrt{g_0}\right)\left(\frac{\cos(\lambda\zeta)-1}{(a+1)^2}+\frac{k_z\zeta\sin(\lambda\zeta)}{2\sqrt{a}(a+1)^{3/2}}\right)-$$

$$-\frac{r_0 t\sqrt{g_0}}{2(a+1)}\sin\left(t\sqrt{g_0}\right)\left(\cos(\lambda\zeta)-1\right),$$

where $\tau = t\sqrt{B/k_z}$, $a = g_0 k_z/B$, $\lambda = k_z\sqrt{\frac{a+1}{a}}$.

Characteristic dependences $r(\zeta)$ for the different distances of bunch flight with focuser were presented on Fig. 4.

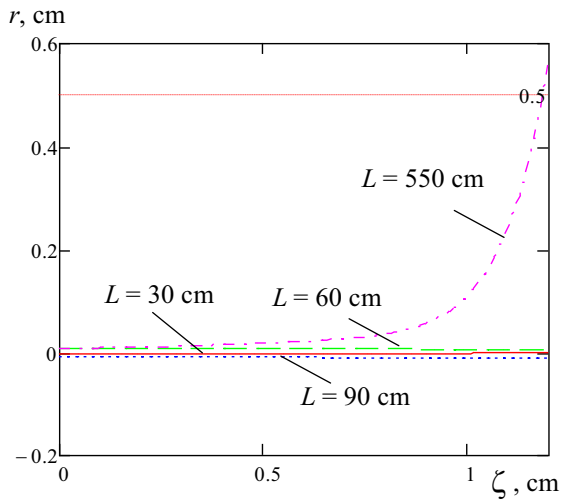

Figure 4: Characteristic dependences $r(\zeta)$ for the different distances of bunch flight with focuser.

It is visible that the bunch flight range significantly increases under the influence of the focuser.

CONCLUSION

Offered methods of analytical calculation of self-coordinated dynamics of bunches in wakefield accelerating structures open prospects for development of solving new optimization tasks of accelerators for physics of high energy and perspective sources of radiation in THz range of frequencies.

REFERENCES

[1] I. L. Sheinman and A. D. Kanareykin, Technical Physics, 53 (2008) 10, pp. 1350–1356.

[2] Manzhirov A.V., Polyanin A.D., *Directory on the integrated equations: Decision methods*, (Moscow: Publishing house «Factorial Press», 2000). 384.

[3] I. L. Sheinman and A. D. Kanareykin, "Numerical and Analytical Methods of Modelling of Bunch Dynamics in Dielectric Filled Accelerating Structures," MOPPA010, these proceedings.

[4] Thomas P. Wangler. RF Linear Accelerators. Wiley-VCH, 2008.

[5] Pavlov V. M. Linear accelerators. Part II: Dynamics of particles in linear accelerators. Novosibirsk University. Novosibirsk, 1999.

NUMERICAL AND ANALYTICAL METHODS OF MODELLING OF BUNCH DYNAMICS IN DIELECTRIC FILLED ACCELERATING STRUCTURES*

I. Sheynman#, LETI (ETU), Saint-Petersburg, Russia,
A. Kanareykin, Euclid TechLabs, LLC, Solon, Ohio, USA
G. Sotnikov, NSC/KIPT, Kharkov; Omega-P, Inc., New Haven

Abstract

RF waveguide structures are a basis for development of new generation of accelerators on the basis of a wakefield method of the charged particle acceleration, and also free electron lasers. Numerical and analytical calculation methods of Vavilov-Cherenkov radiation generated by relativistic electronic bunches in wave guides with dielectric filling, and also self-coordinated bunch dynamics in own and external fields are considered.

INTRODUCTION

The modern accelerating technique is in search of new methods for ensuring progress in the field of experimental physics of high energy. The developed technologies of dielectric wakefield acceleration of electrons on Vavilov-Cherenkov effect are one of the most perspective directions of creation of high gradient structures of modern linear accelerators for high energy physics [1].

Linear accelerators are considered also as sources of sequence of electronic bunches for the free electron laser which is considered now the major candidate for creation of ultra short impulses (of attosecond range) X-ray radiation. Waveguide structures with dielectric filling (Fig. 1) excited by a high current electronic bunch were investigated intensively for the last years [1] – [5]. The main purpose is of prospects of their use as high gradient linear accelerators.

For linear accelerator the achievement of high accelerating fields in structure where the electronic bunch gained energy ~GeV at extremely short distances is necessary. Increase of wake fields is reached on the basis of increase in a charge of generating bunch creating a wakefield wave, and also optimization of the geometrical sizes and a material of filling of accelerating structure. However along with accelerating fields the high current bunch generates the considerable rejecting fields leading to a bend of the bunch and its deviation from an axis of wave guide structure. In this regard one of the main problems in realization of the wakefield method is control of an intensive electronic bunch in the channel of the wave guide and prevention of subsidence of particles on its wall.

*Work is supported by the Russian Foundation for Basic Research and the Ministry of Education and Science of the Russian Federation in the framework of the Federal Program "Human Capital for Science and Education in Innovative Russia" for 2009–2013.
#ishejnman@gmail.com

Key task in the wakefield acceleration method is modelling of the self-coordinated movement of a relativistic electronic bunch passing through dielectric structure in Vavilov-Cherenkov fields created by it.

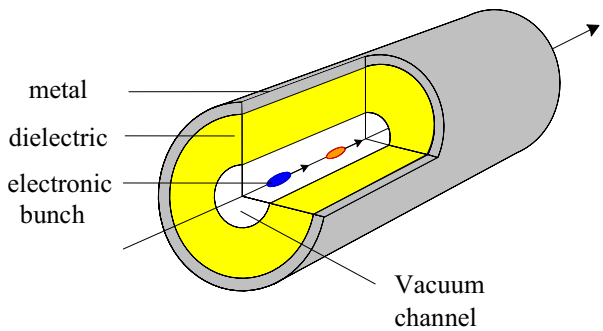

Figure 1: Wakefield waveguide structure.

To research of bunch dynamics the numerical approaches based on modelling of electronic bunches by a method of macroparticles are applied. The method of macroparticles is based on splitting of phase volume of a bunch into a large number of not being crossed elementary volumes; movement of each is identified with movement of one macroparticle with a total charge and mass of particles entered into this volume.

BEAM DYNAMICS EQUATIONS

The description of movement of an electronic bunch was carried out on the basis of the equations of relativistic dynamics [3]:

$$F_z = -eE_z = m_e\, d\left(V_z\gamma\right)/dt\,, \qquad F_r = d\left(m_e V_r\gamma\right)/dt\,,$$

where

$$E_z = q\sum_{n,m}\Big[\psi_{E_{z\,n,m}} I_n\left(k_{r\,n,m} r(\zeta,t)\right)\cdot$$

$$\cdot\int_0^{\zeta} f(\zeta_0)\cos\left(k_{z\,n,m}\left(\zeta-\zeta_0\right)\right) I_n(k_{r\,n,m} r(\zeta_0,t))\,d\zeta_0\Big],$$

$$F_r = F_{focus} - eq\sum_{n,m}\left[\psi_{F_{r\,n,m}} I_n'\left(k_{r\,n,m} r(\zeta,t)\right)\cdot\right.$$
$$\left.\cdot\int_0^{\zeta} f(\zeta_0)\sin\left(k_{z\,n,m}(\zeta-\zeta_0)\right) I_n(k_{r\,n,m} r(\zeta_0,t))d\zeta_0\right].$$

where $r(\zeta,t)$ is a bunch deflection from waveguide axes, $\zeta = z - vt$ is a distance behind the bunch, F_f is a focusing force, e and m_e are charge and mass of electron, q and γ are charge and relativistic factor of the bunch, $k_{z\,i,j}$ and $k_{r\,i,j}$ are longitudinal and radial components of wave vector, $\psi_{E_{z\,i,j}}$ and $\psi_{F_{r\,i,j}}$ are coefficients of series, depending of geometry, wave guide filling permittivity and initial charge place, $f(\zeta_0)$ is a function describing longitudinal charge distribution, $I_n(x)$ are modified Bessel function of n-th order.

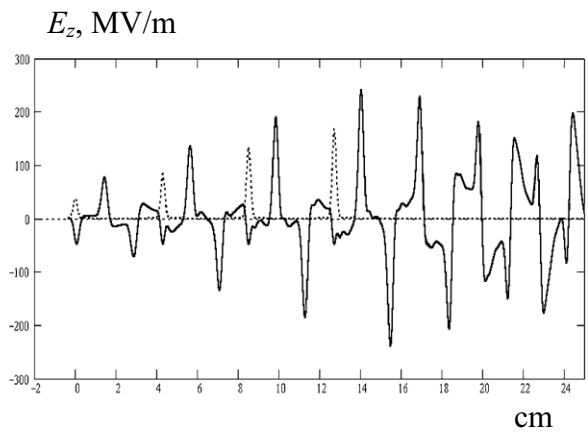

Figure 2: Longitudinal field structure behind four bunch train.

The task of the description of movement of macroparticles is self-coordinated: the mutual provision of particles in ensemble influences a field created by particles which, in turn, leads to change of their position.

Complexes of the BBU'3000 and BeamDyn programs were developed for the solution of the equations of self-coordinated dynamics of a relativistic electronic bunches, allowing to model movement of system of the bunches consisting of a chain of accelerating driver bunches and the accelerated bunch. Also the approximate analytical method of calculation of self-coordinated dynamics of the bunch was developed, presented in the separate bench report [7] at this conference.

Determinative influence on speed and accuracy of the bunch dynamics calculation on each step of algorithm is rendered by procedure of calculation of fields created by ensemble of particles, and procedure of definition of new position of particles under the influence of the found forces.

In the BBU'3000 program [4] calculation of the fields created by ensemble of particles, is carried out by summation of fields of a large number of macroparticles into which three-dimensional bunches with the set function of a charge spatial distribution break. In the BeamDyn [5] program for calculation of radial dynamics, according to [3], it is supposed that the charge is concentrated in the centre of cross-section distribution of the bunch. Longitudinal and radial fields turn out by integration of the function describing a radiation field in a point of z, r from the dot charge being in a point with coordinates of z_0, r_0 convoluted with function of the charge distribution on length of the bunch. On each time step dependence of radial shift of particles of the bunch of r_0 on z_0 which is used for field calculation is known. Its longitudinal splitting into a chain of macroparticles is made for definition of radial shift of the average line of the beam $r(\zeta,t)$. On the basis of integration of the equations of movement there are coordinates of macroparticles along the average line of the bunch during the subsequent moment of time, and then this discrete sequence is interpolated for obtaining again functional dependence.

For definition of new positions of particles in algorithms of bunch dynamics calculation numerical methods of the solution of the dynamics equations are traditionally used. They are transfer of the equations to a difference form with accuracy of the decision of the 1st order [3] and method of Runge-Kutta of the second and the fourth orders [4, 5]. Now the analytical solution of the particle dynamics equations under the influence of constant force [6] in which coordinates and speeds of a particle are received based on expressions:

$$z = z_0 + \frac{c}{a^3}\left[aa_z(\gamma_1-\gamma_0) + \gamma_0\left(a_r^2\beta_{z0} - a_z a_r \beta_{r0}\right)\ln|\delta|\right],$$
$$r = r_0 + \frac{c}{a^3}\left[aa_r(\gamma_1-\gamma_0) + \gamma_0\left(a_z^2\beta_{r0} - a_r a_z \beta_{z0}\right)\ln|\delta|\right],$$
$$\beta_z = \xi/\gamma_1\ ,\ \beta_r = \eta/\gamma_1\ ,$$
$$\delta = \frac{a^2 t + \gamma_0\left(a_z\beta_{z0} + a_r\beta_{r0}\right) + a\gamma_1}{\gamma_0\left(a_z\beta_{z0} + a_r\beta_{r0} + a\right)},$$

where $a = \sqrt{a_z^2 + a_r^2}$, $a_z = -eE_z/(m_e c)$, $a_r = F_r/(m_e c)$, $\xi = a_z t + \beta_{z0}\gamma_0$, $\eta = a_r t + \beta_{r0}\gamma_0$, $\beta_z = v_z/c$, $\beta_r = v_r/c$, $\gamma_0 = \left(1 - \beta_{z0}^2 - \beta_{r0}^2\right)^{-1/2}$ is an initial relativistic factor, $\gamma_1 = \sqrt{1+\xi^2+\eta^2}$.

Comparison of efficiency of algorithms shows that for calculations of dynamics it is the most preferable to use the algorithm based on the exact analytical solution of the movement equation of a relativistic particle under the influence of constant force, providing a prize till speed of calculation in 2-4 times in comparison with numerical methods of the differential equations of movement solving.

On fig. 3 as an example radial distribution of a charge and energy distribution in bunches at the moment of a contact by the bunch of wall of the wave guide is shown.

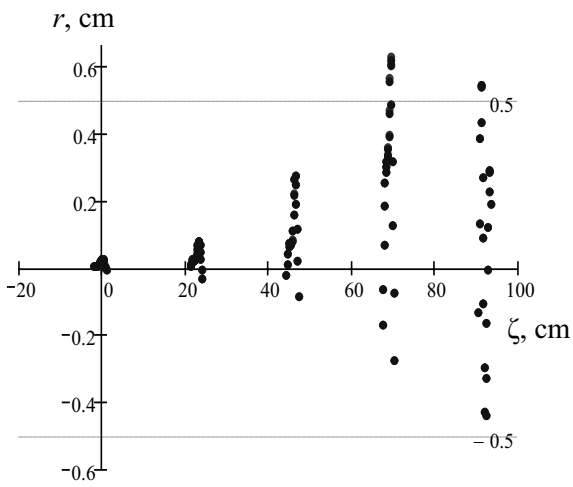

Figure 3: Radial macro particles displacement.

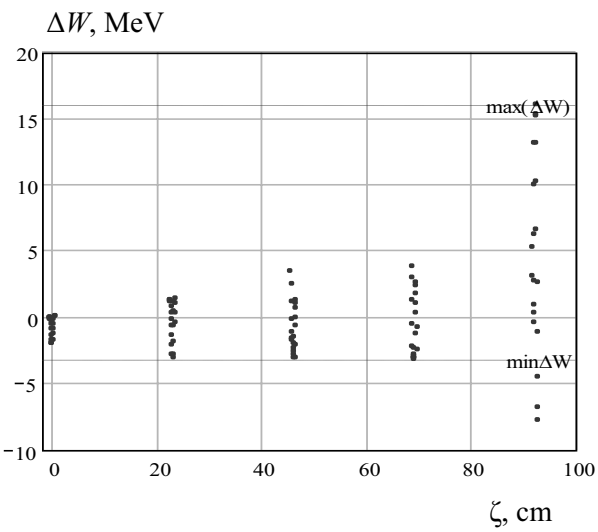

Figure 4: Macroparticle energy distribution.

CONCLUSION

The methods of calculation of Vavilov-Cherenkov radiation fields presented in this work and self-coordinated dynamics of bunches in wakefield accelerating structures open prospects for development of new generation of accelerators for physics of high energy and perspective sources of radiation in THz range of frequencies intensively mastered now.

REFERENCES

[1] Gai W., Schoessow P., Cole B., Konecny R.et al. Phys. Rev. Lett. 61, 2756 (1988).

[2] A. M. Altmark, A. D. Kanareykin, and I. L. Sheinman, Technical Physics, 50 (2005) 1, pp. 87–95.

[3] King-Yuen Ng. Single-Bunch Beam Breakup in a Dielectric-Lined Waveguide / Proceedings XVth International Conference on High Energy Accelerators (FERMILAB-Conf-92/212), Hamburg, Germany, July 20-24, 1992.

[4] P. Schoessow, A. Kanareykin, C. Jing, A. Kustov, A. Altmark, and W. Gai Beam Dynamics Simulation Platform and Studies of Beam Breakup in Dielectric Wakefield Structures. AIP Conf. Proc. 1299, pp. 262-267, 14th Advanced Accelerator Concepts Workshop, 13–19 June 2010, Annapolis, (Maryland)

[5] I. L. Sheinman and A. D. Kanareykin, Technical Physics, 53 (2008) 10, pp. 1350–1356.

[6] I. L. Sheinman and A. D. Kanareykin, Izvestia CPbETU, 6 (2010), p. 10-14.

[7] I. L. Sheinman, "An Analytical Approach to Solution of Self-coordinated Beam Dynamics in Dielectric Wakefield Accelerating Structures," MOPPA009, these proceedings.

OPTIMIZATION OF LASER RADIATION PRESSURE ACCELERATOR FOR ION GENERATION

G. Dudnikova#, ICT SB RAS, Novosibirsk, Russia
D. Gorpinchenko, ICM&MG SB RAS, Novosibirsk, Russia
C.S. Liu, T.C. Liu, R. Z. Sagdeev, X. Shao, J.J. Su, UMD, College Park, MD, USA

Abstract

Compact laser-driven accelerators are an attractive alternative for monoenergetic proton and ion generation in conventional RF accelerator because the particle acceleration electric fields can reach tens GV/cm, which allows reduction of the system size. The scheme for generating quasi-monoenergetic proton with Radiation Pressure Acceleration (RPA) has the potential of leading to table-top accelerators as sources for producing 50-250 MeV protons. Theoretical and computational studies of ion energy scaling of RPA are presented. 2D and 3D PIC simulations are performed to study limitations of energy gain due to Rayleigh-Taylor instability and how is the Rayleigh-Taylor instability suppressed by density fluctuations or inhomogeneities of targets. Energy transfer efficiencies and qualities of accelerated proton beams are discussed.

INTRODUCTION

One of the most attractive applications of ultra-short superintense laser pulses is connected with the development of new methods of accelerating charged particles. The generation of high energy particles, both electrons and ions, when strong electromagnetic radiation interacts with a plasma is a well known phenomenon. However it is necessary to find the plasma and radiation parameters that optimize this process. Thick targets with thicknesses ranging from a few to tens of laser wavelengths were employed in early studies of ion acceleration. and the target normal sheath acceleration (TNSA) was the predominant mechanism leading to the production of multi-tens MeV ion beams but with wide energy spectra [1, 2]. Recently, the scheme of laser radiation pressure acceleration (RPA) of ultra-thin target shows promising aspect of efficient quasi-monoenergetic proton generation [3-5]. In the RPA scheme, a circularly polarized, high power, short pulse laser is focused on a suitable ultra-thin foil, which leads to the acceleration of the whole foil. The RPA focuses on increasing the efficiency of acceleration and producing monoenergetic protons. The scheme for generating quasi-monoenergetic proton with RPA has the potential of leading to table-top accelerators as sources for producing monoenergetic 50 - 250 MeV protons suitable for widespread dissemination for cancer therapy and other applications such as fast ignition in laser fusion. In comparison to the conventional TNSA-scheme, the conversion efficiency with the RPA scheme is estimated to be more than 40 times higher. During the RPA of a ultra-thin foil, the laser ponderomotive force sweeps all electrons in the foil forward until the electrostatic force on the electrons due to the ions left behind balances the ponderomotive force on electrons at a distance D. These electrons form a charged layer and their electrostatic force now accelerates the ions left behind. When the thickness of the target, Δ, is equal to this distance of maximum charge separation, we obtain optimal thickness $D = \Delta$, at which the electrons are pushed to the rear end of the target and the space charge force balances the ponderomotive force $eE = F_P(\Delta)$ on the electrons. In the limit of the normalized laser amplitude $a_0 = e|E|/(m\omega c) >> 1$, we obtain the thickness as

$$\Delta \cong \frac{4\pi}{\lambda_L}\left(\frac{c}{\omega_p}\right)^2 a_0 = \frac{\lambda_L}{\pi}\left(\frac{\omega}{\omega_p}\right)^2 a_0 \qquad (1)$$

where m and e are the electron mass and charge, λ and ω are the laser wavelength and angular frequency, ω_p is the electron plasma frequency, E is the electric field amplitude, a_0 is the dimensionless laser amplitude. To minimize the wave tunneling through the target, $\Delta > c/\omega_p$ should be satisfied.

In RPA, high intensity circularly polarized laser light with a high contrast ratio accelerates the ultra-thin foil with radiation pressure, and the foil has a definite, optimal thickness. It must be sufficiently thin so that

- The ponderomotive force of the laser radiation accelerating the electrons in the foil is balanced by the electric force due to ions at the outer edge of the thin foil.
- The mass of the thin foil must be sufficiently light so that the whole foil is accelerated by the laser radiation pressure in the short duration of the order of ion plasma period. In this case, protons are subject to both the electric force of the electron layer accelerating them forward, and the inertial force pulling them back in an accelerated frame. The balance of these two opposing forces forms a trap for the ions in real and phase spaces.
- These stably trapped protons and electron layers form a self-organized double layer. The laser radiation pressure accelerates this double layer as a whole, with protons trapped in it.

#gdudnikova@gmail.com

However, the time for monoenergetic ion acceleration with RPA is limited by the duration in which the double layer can maintain its overdense properties, which can be lost due to the development of the Rayleigh-Taylor instability (RTI), which is one of the most important instabilities arising when a thin plasma foil is accelerated by the radiation pressure of an intense laser [6]. It poses a limit on the time a foil can be accelerated before it loses its monoenergetic properties.

Recent experiments and simulations have demonstrated effective CO_2 laser acceleration of quasi-monoenergetic protons from thick gaseous hydrogen target (of thickness tens of laser wavelength) via hole boring and shock accelerations [6]. Laser pulse can compress the target to form a shock and accelerate it as a whole, in the light-sail fashion, with the protons trapped in it. The proton acceleration is thus a combination of the RPA and the shock acceleration, with the RPA being the dominant acceleration mechanism at the later stage.

In this paper, we present the results of computer simulation of ion acceleration based on RPA scheme for generating quasi-monoenergetic protons, potentially suitable for medical applications such as particle therapy, and present recent advances in the studies of energy scaling of RPA. We propose a scheme of combining the laser radiation pressure acceleration (RPA) with the shock acceleration by irradiating lasers on thin gaseous targets, with thin gas targets thickness of a few laser wavelengths. Laser can compress it to form a shock and to accelerate it as a whole, in the light-sail fashion, with the protons trapped in it. Thus proton acceleration is a combination of radiation pressure acceleration and shock acceleration, with the RPA being the dominant acceleration mechanism at later stage. Ion acceleration is examined on the base of 2D and 3D, relativistic, electromagnetic, particle-in-cell (PIC) codes UMKA2D3V and MANDOR. These codes are massively parallel and designed for achieve high performance on modern supercomputers.

SIMULATION SETUP AND RESULTS

To demonstrate the proposed acceleration scheme, we performed a series of PIC simulations with CO_2 laser irradiated on a thin gas target with the dimensionless laser amplitude a_0=5-10.The incident laser is a circularly polarized plane wave with a longitudinal profile of $10T_L$ rising time, $280T_L$ flat top, and $10T_L$ falling time, where T_L is the laser period. The rising and falling time slope is of sine-quared shape. Target thickness varying from 1.5 λ to 15 λ. The target density n_0 varies from $5n_c$ to $40n_c$ where n_c is the critical density.

The light pressure may compress plasma and generate shock waves that lead to acceleration of ions due to reflection by shock front (monoenergetic component in ion spectra are produced). Snapshots of proton density distribution and the proton energy spectra are shown in Figure 1. During the first 40 T_L--70 T_L, the compression in shock formation is observed, and a compressed electron-proton layer is formed with enhanced density as high as 180 n_c within a region of sub-wavelength scale. The laser radiation pressure is able to accelerate this thin electron-proton layer formed around the over a distance of 3λ during 40 T_L and to generate the quasi-monoenergetic protons with energy gain of about 4 MeV and acceleration gradient of 1.3 GeV/cm. The quasi-monoenergetic proton beam is finally destroyed due to RTI, and the target becomes broadened and transparent with laser light leaking through the low density region.

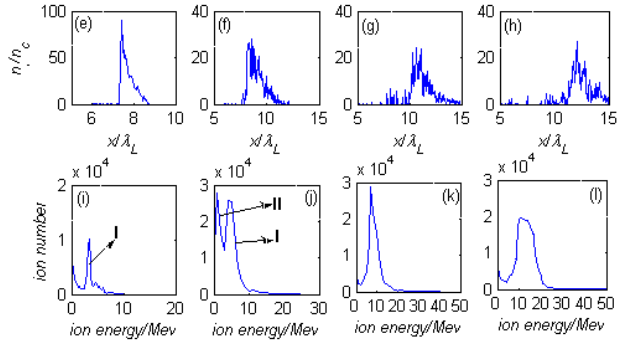

Figure 1: 2D PIC simulation results of the proton density distribution (the upper row) and the proton energy spectra (the lower row) with the normalized incident laser intensity a_0=10, the maximum plasma density n =30 n_c, and the plasma thickness l_s = 2.5 λ. From the left column on, the snapshots are at the times t = $30T_L$, $50T_L$, $70T_L$, and $80T_L$, respectively. Part I is the shock reflected protons, part II is the shock front I.

The usual nonlinear development of the RTI is to generate fingers of high and low densities at the most unstable mode with wavelength comparable to the laser wavelength (Figure 2). During the growth of the RTI, small ripples on the surface of foil grow exponentially and these fine structures in the transverse direction perpendicular to laser propagation will be converted to large amplitude perturbations with wider transverse periodical structure, i.e. density blobs. During the development of the RTI, the filamentation of the plasma density will produce regions of low density plasma, transparent to laser radiation. The laser can no longer be reflected effectively by the plasma mirror, and the acceleration stops.

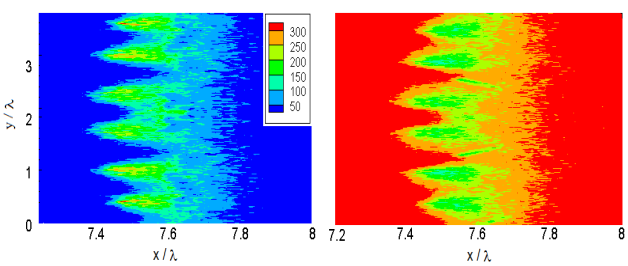

Figure 2: Ion (left) and electron density distribution in the stage of RT instability.

A direct consequence of RTI-induced transparency and the proton energy spectra broadening is the limitation on the achievable quasi-monoenergetic proton energy or brightness of the particle beam for a given laser power.

By defining quasi-monoenergetic particle as particles having energy spread of half maximum particle flux within 20 percent of the energy of peak flux, we studied the scaling of quasi-monoenergetic proton energy vs. normalized incident laser amplitude (Figure 3). In this study, the foil density changes linearly with incident laser amplitude and the foil thickness was chosen to be optimal thickness (Eq. (1)). In the non-relativistic limit, the attainable quasi-monoenergetic ion energy is

$$E_{non-rel} \approx 2(\pi \frac{m_e}{m_i} \frac{a_0 t_s}{T_L})^2 m_i c^2 \qquad (2)$$

where t_s is the occurrence time of maximum quasi-monoenergetic ion energy. The scaling indicates that with flat ultra-thin targets of optimal thickness, the quasi-monoenergetic proton energy can be ~ 250 MeV for normalized incident laser amplitude a_0=25, corresponding to 2 PetaWatt laser power. Also, the quasi-monoenergetic proton energy is adjustable by changing the incident laser power.

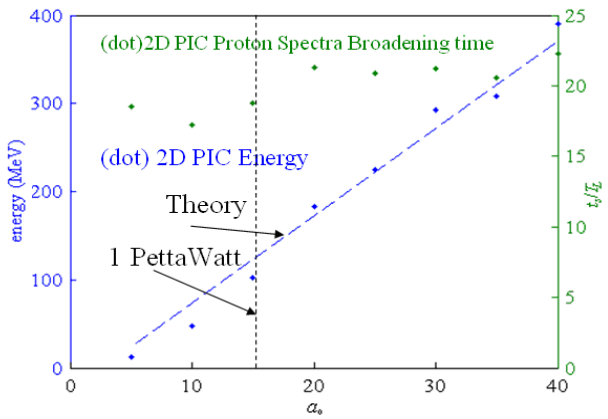

Figure 3: Scaling of quasi-monoenergetic proton energy vs. normalized incident laser amplitude as obtained from PIC simulation (blue dot) and theory (blue dashed curve). Green dots indicate the time when the proton spectra start to broaden and deviate from our definition of quasi-monoenergetic (a_0=15).

On the other hand, this scaling is still theoretical since in real applications, it is hard to have solid target made of pure hydrogen; particle energy spread being less than 10 percent of the peak flux energy is more desirable; and using sub-PetaWatt laser is more practical for commercialization and maintaining high repetition rate. Therefore, there are needs for research on laser proton accelerator using practical target and suppressing and remediate the RTI needs for research on laser proton accelerator using practical target and suppressing and remediate the RTI.

Figure 4 shows the dependence of the energy of quasi-monoenergetic protons on the gas target peak density and the incident laser energy in laser-thin gas target acceleration. The simulations use the same spatial profile of gas target density as that in Figure 1 with different peak gas target density and laser power.

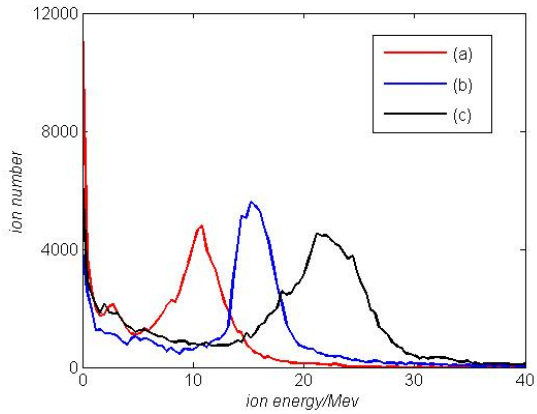

Figure 4: The proton energy spectrum obtained with different incident laser and plasma parameters. The simulation parameter of line (a) is normalized laser amplitude a_0 = 5, gas target thickness l_s = 2.5 λ_L, peak gas target density n_0 = 20 n_c, line (b) is a_0 = 10, l_s = 2.5 λ_L, n_0 = 20 n_c, and line (c) is a_0 =10, l_s = 2.5 λ_L, n_0 = 30 n_c.

Changing the incident laser amplitude from a_0 = 5 to a_0 = 10 increases the energy of quasi-monoenergetic proton from ~ 10 MeV to 16 MeV. Further increase of peak gas density from n_0 = 20 n_c to n_0 = 30 n_c also helps further increases the energy of quasi-monoenergetic proton to 22 MeV.

REFERENCES

[1] P. Mora, Phys. Rev. Lett. 90, 185002 (2003).
[2] Y. T. Li, Z. M. Sheng, et al., Phys. Rev. E 72,066404 (2005).
[3] B. M. Hegelich, B. J. Albright, et al. , Nature (London) 439, 441 (2006).
[4] T. Esirkepov, M. Borghesi, S.V. Bulanov, et al., (2004), Phys. Rev. Lett. 92, 175003 (2004).
[5] T.V. Liseikina, A Macchi, App. Phys. Lett. 91, 17502 (2007).
[6] F. Pegoraro and S.V. Bulanov, Phys. Rev. Lett. 99, 065002 (2007).
[7] C. A. J. Palmer, N. P. Dover, I. Pogorelsky, et al., Phys. Rev. Lett. 106, 014801 (2011).

PROPOSAL OF LASER ION BEAM ACCELERATOR FOR INERTIAL FUSION

F. Scarlat, Valahia University of Targoviste, Targoviste, Romania
A. Scarisoreanu, INFLPR, Bucharest-Magurele, Romania

Abstract

The inertial nuclear fusion with laser beams, relativistic electron beams, ion beams, micro-particle beams and superconducting projectiles has been analytically investigated and numerically calculated by various authors along years and nowadays. Starting from the record laser peak power of 1.25 PW and radiation peak intensity of 100 EW per square centimeter produced at LLNR using the chirped pulse amplification (CPA) laser technology as well as from ELI Nuclear Physics - laser system, 3 APPOLON 10 PW (150 J / 15 fs) (http://www.eli-np.ro/) proposed to be realized, this paper presents the principle and the configuration of a compact ion accelerator operated by an optical laser in an ultra-relativistic regime, for the inertial confinement fusion. Ions acceleration is based on the acceleration mechanism named "Radiation Pressure Acceleration". By the application of this mechanism the calculations for the physical parameters of an ion accelerator operated by laser were made. Calculation results are also presented in this paper.

INTRODUCTION

Fusion by inertial confinement (ICF) represents an alternative energy source to the nuclear fission energy, hydraulic energy, wind energy, etc. That can be achieved by means of a thermonuclear target (TN) consisting of a capsule housing the fusion fuel located in the centre of a spherical cavity surrounded by a pusher and an ablator.

The fusion fuel may be deuterium (D) and tritium (T) since the nuclear fusion reaction of the two has the most probable efficient section.

The fusion with inertial confinement of D-T is developing on the irradiation of the TN target with particle beams of a certain energy followed by the ablation of the surface material outside the target, the acceleration and compression of the capsule for igniting the fuel core and burning which is spread fast through the compressed fuel.

The fusion of both light nucleus to high temperature and density generates the 17.6 MeV thermonuclear energy by the reaction: D + T → n (14.1 MeV) + α (3.5 MeV). This energy is absorbed by the reactor blanket and converted in thermal energy that is transformed in electric energy by classic methods and techniques.

The TN target containing 1 g D-T produce TN energy of 340 GJ. A fusion reactor with inertial confinement can produce 1.25 GW (electric) with 40 % thermal efficiency with a consumption of 10 mg of DT per second. From the produced electric energy, 1 GW goes to consumer and 36 GW is used for the driver supply.

At present, worldwide, there are more powerful facilities under construction, such as "The National Ignition Facility (NIF) at LLNL [1] and "The Laser Megajoule" (LMJ) in France [2].

There are also programs for light ion accelerators, e.g.: p, ^{12}C and heavy ion accelerators e.g.: $^{55}Fe \rightarrow U$, as drivers for inertial confinement fusion. This drivers are by types: induction accelerator, linear accelerator, synchrotron [3, 4, 5].

The construction of a 10 PW (150 J / 15 fs) laser system in Bucharest – Magurele led to the elaboration of some programs for the application of the laser beam generated by the laser [6].

One of such applications proposed in the paper, is the use of the laser radioation beam generated by APPOLON 10 PW system to accelerate the ions for to be used as drivers for the conventional ICF or hot-spot ignition with spherical configuration [7].

LASER ION ACCELERATOR

Requirements for ICF

One of the requirements for ICF is represented by the DT fuel capsule compression. Since the fuel mass depends on fuel density square inverse, one may chose a smaller mass capable to generate a managing energy output. Choose the inertial fusion parameter $\rho R = 2.8$ g/cm^2 for the burn-up efficiency $\Phi = \rho R / (\rho R + 6\ \text{g/cm}^2) = 0.32$, where ρ is the fuel density and R is the target radius [8].

For the fuel mass $M = 10^{-3}$ g, the density of the compressed fuel is $\rho = ((4\pi / 3)(\rho R)^3 / M)^{1/2} = 300$ g/cm^3. The required specific energy to compress this mass is given by the Fermi-Dirac internal specific energy $\varepsilon_{FD} = 3 \times 10^5 \rho^{2/3}$ J/g $= 1.35 \times 10^7$ J/g. The compression energy for $\alpha_C = 2$ is $E_C = \alpha_{cf}\ \varepsilon_{FD} M = 0.027$ MJ [9].

The energy per gram required to heat a DT plasma at 8.6 keV, which is twice the ideal ignite temperature, is $E_H = 1$ MJ. If 2% of the fuel mass is kept for central hot spot, the energy required to heat this mass would be about 0.02 MJ.

The total energy required for compression and ignition would be about 0.05 MJ. The driver energy required to assemble energy for the plasma efficiency with $\eta_P = 10$ % is equal with 0.5 MJ, resulting in G = 200.

The fusion energy for 1 mg DT with burning efficiency by 32 % is equal with $E_{DT} = \varepsilon_{DT} \Phi M = 3{,}4 \times 10^{11}$ J/g $\times 0.32 \times 10^{-3}$ g = 100 MJ, where $\varepsilon_{DT} = 17.6$ MeV/5amu is the energy specific to DT fuel per reaction. A nominal 100 MW fusion power plant would consume 1 mg / s of DT.

Driver Requirements

There are several major reasons to use the ion beams for irradiating the TN targets, directly or indirectly. The first one is the distribution of the absorbed dose deep in the heavy ion beam where towards the end of the range, Gray absorption peak is occurring, like in Figure 1 [10].

One may choose the energy of the heavy ion so that Gray peak should fall on the DT capsule. Also, one may realise the uniform distribution of the absorbed dose on the capsule circumference with the direct and indirect driven alternative.

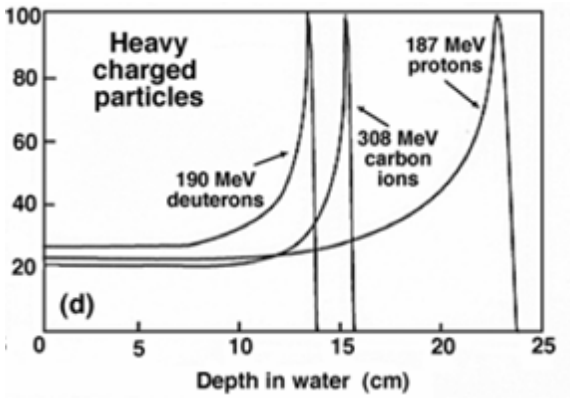

Figure 1: Depth dose in water.

A second reason is that, with the indirect driven alternative the beam has the required intensity for the generation of X-rays in hohlraum. Finally, another reason consists in the high repetition frequency f = 10 Hz, of the driver.

The parameters required for the DT combustible firing and burning are presented in Table 1 [11].

Table 1: Driver requirements

Parameters	Values
Energy beam	1 – 3 MJ
Heavy ion energy	10 - 20 GeV
Peak beam power	100 - 400 TW
Average beam power	150 MW
Deposition characteristics	10^6 - 10^8 J/g
Driver Efficiency	20-30 %
Focusing	< 2 mm at 5 to 10m
Pulse repetition rate	1 - 15 Hz

PRINCIPLES OF ACCELERATOR OPERATION

Considering that in the end APPOLON shall provide 10 PW output power [12], we have been thinking to use the beam in steps in order to carry-out some experiments related to the heavy ion acceleration for ICF. The idea which is the basis of the heavy ion accelerator with laser consists in the selection of the parameters for the lasers with the power ranging between 1 PW and 10 PW in ultra-relativistic operation regime. The ultra-relativistic regime (URL) is defined for $a_0 = 10^2 \div 10^5$. This regime corresponds to the generation of electric charged particles (electrons, protons, heavy ions, muons, mesons etc) [13].

Ion accelerations to MeV/u level can be made by the "Target Normal Sheath Acceleration" (TNSA) mechanism [14], while for GeV/u level the "Radiation Pressure Acceleration' (RPA) mechanism can be used, theoretically introduced [15] and firstly experimentally observed to 5 x 10^{19} W/cm^2 intensity [16, 17].

In this work the RPA acceleration method has been adopted because according to this method, the accelerated ion energy is proportional with laser radiation intensity [18, 19]. TNSA acceleration method allows the ion to acquire energy proportional with the square root of the laser radiation intensity and with a poor efficiency of about 1 % that needs huge lasers. The RPA mechanism has some advantages: ion energy does not depend on its charge, efficiency is up to 10 – 20 % and the neutral beam made-up of ion and electrons is accelerated like an all, the ion bunches has like solid-state densities (10^{22}/cm^3 - 10^{23}/cm^3) that are about 10^{14} times dense than ion bunches from the classic accelerators (10^8/cm^3) [20-25].

Proposal of an Ion Accelerator

An ion accelerator has, as a main component, the APOLLON laser having intensities about 10^{24} W/cm^2. The laser beam is optically divided in n under-beams. In this work, take n = 4; 2 of them are in the 1 quadrant (on x and y axis) and the other 2 are in the 3 quadrant (on –x and –y axis).

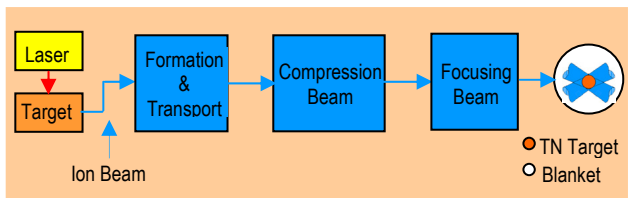

Figure 2: Scheme of an ion accelerator.

The scheme of a beam line with the ion accelerator from four identical lines is shown in Figure 2. The laser beam is focused on a solid metallic target.

At the interaction with this target a ion beam is generated by TNSA or RPA acceleration mechanism which is farther getting into the classic chain of formation and transport, the longitudinal compression of the beam and next, the focusing of the accelerated ion beam on the TN target which is located inside the reaction chamber or the Blanket, in case of Inertial confinement energy production reactor. All these operations are developing outside the reaction chamber. Inside the reaction chamber, there is a device to homogenize the beam at the level of the TN target spherical surface.

The proposed scheme is substituting the standard accelerator (linac, induction linac or synchrotron) with a laser with the power P ranging between 1 PW and 10 PW and an ion solid target.

The ion accelerator controlled by APPOLON laser with operation in URL regime has the physical parameters calculated by means of the RPA method [18] and are presented in Table 2.

Table 2: Parameters for laser, target and electron beams

Laser: circular polarized	**Values**
Pulse energy, W [J]	195
Peak power, P [PW]	9,7
Wavelength, λ [μm]	0.8
Radiation intensity, I [W/cm ^{2}]	1.37×10^{23}
Conversion efficiency, χ ξ[%]	8.65
^{192}Ir Ion beam	
Heavy ion energy, E_i [GeV]	2
Nucleon energy, E_u [MeV]	10
Dimensionless pistoning parameter, ξ	2.2×10^{-3}
Total number of ions, N	5.4×10^{10}
^{192} Ir Target	
Focal spot area, A_t [μm^2]	7.1
Thorium foil thickness, d_t [nm]	207

CONCLUSIONS

The proposal of a heavy ion accelerator for inertial confinement fusion is based on the characteristics of the ELI Nuclear Physics project which is to be implemented in Magurele-Bucharest. As a result, the accelerator consists of the laser beam and the ion target. The ion acceleration is based on the 'Radiation Pressure Acceleration' mechanism.

It was considered that ions are the proper most particles for the fast ignition of the DT capsule due to Gray peak which occurs at the end of the ion range in the irradiated substance.

The calculation examples given in the text are grounded on the experimental data obtained with the lasers operating in non-relativistic regime and on the numerical simulations around the adimensional amplitude of the lasers $a_0 = 1$, published in specialized magazines.

In order to carry-out a complex project of an accelerator as driver for the inertial confinement fusion it is still necessary to have further data resulted from the studies regarding the heavy particle acceleration in RPA regime, the conversion efficiency, the target geometry and the atomic stopping power of dense ion beams in the substance.

REFERENCES

[1] C. Haynam, R.A. Sacks, E. I. Moses, K. Manes, S. Haan, L. Spaeth, Applied Optics, 47 (2008) 10.

[2] J. Ebrardt, "The Laser Megajoule Project: progressing towards fusion", ISTC Workshop, Moscow, November 2008;http://www.istc.ru/istc/istc.nsf/va_WebResources/Events_1/$File/Ebrardt.pdf

[3] S. Humphries Jr., "Charged Particle Accelerators for Inertial Confinement Fusion", PAC1991, p. 6-10 (1991); http://epaper.kek.jp/p91/PDF/PAC1991_0006.PDF

[4] I. Hofmann, "Inertial Fusion with Accelerators", EPAC'96, Sitges, June 1996, TUZ01A, p. 255 (1996), http://accelconf.web.cern.ch/accelconf/e96/PAPERS/ORALS/TUZ01A.PDF

[5] M. Roth, A. Blazevic, M. Geisel, T. Schlegel, T.E. Cowan, M. Allen, J.C. Gauthier, P. Audebert,, J. Fuks, J. Meyer-ter-Vehn, M. Hegelich, S. Karskh, A. Pukhov, "Energetic ions generated by laser pulse: A detailed study on target properties", Phys. Rev. STAB. 5 (2002) 061301.

[6] The Scientific Case of ELI Nuclear Physics - Bucharest Magurele, Romania, The ELI Nuclear Physics Experiment working group, Editors: Dietrich Habs, Martin Groß, Nicolae Marginean, Florin Negoita, Peter G. Thirolf, Matthias Zepf, Draft version: May 2010 (2010); - http://www.eli-np.ro/documents/Scientific_Case.pdf

[7] J.D. Lindl, "Development of the indirect-drive approach to inertial confinement fusion and the target physics basis for ignition and gain", Phys. Plasmas, 2 (1995)11.

[8] J.H. Nuckolls, R.O. Bengerter, J.D. Lindl, W.C. Med, Y.I. Pan, „High Performance Inertial Confinement Fusion Targets", UCRL, Laser Program Annual, 2 (1977) 4-15-19.

[9] M. Tabak, J. Hammer, M.E. Glinsky, W.L. Kruer, S.C. Wilks, J. Woodworth, E.M. Cambell, M.D. Perry, R.J. Mason, "Ignition and high gain with ultrapowerful lasers", Phys. Plasmas, 1 (1994)5.

[10] E.B. Podgorsak, *Radiation Physics for Medical Physicist*, (Springer Verlag Berlin Heidelbeg, 2006), 12.

[11] W.B. Herrmannsfeldt, *The development of heavy ion accelerators as drivers for inertially confined fusion*, LBL 9332, SLAC 221, UC 21, 1979.

[12] ELI-NP, The 11th Conference on nucleus-nucleus collisions, San Antonio, Texas, May 27th – June 1st, 2012; http://cyclotron.tamu.edu/nn2012/Slides/Parallel/NFD1/ELI-NP_NN2012.ppt#325,1,Slide 1

[13] F. Scarlat, R. Minea, A. Scarisoreanu, "Relativistic Optical Laser as FEL Injector", 33rd International FEL Laser Conference, Shanghai, August 2011, MOPC15 (2011).

[14] S.C. Wilks, Phy. Rev. Lett. 103 (2009)245009.

[15] A.P.L. Robinson et al., Plasma Phys. Control. Fusion 51 (2009)024004.

[16] A. Henig et al., Phys. Rev. Lett. 103 (2009)245009.

[17] T. Tajima, D. Habs and X. Yan, Laser acceleration of ions for Radiation Therapy, RAST 2 (2009)221.

[18] P.G. Thirolf, D. Habs, M. Gross, K. Allinger, J. Bin, A. Henig, D. Kiefer, W. Ma and J. Schreiber, „Laser ion Acceleration: Status and Perspectives for Fusion", EPJ Web Conferences 17,11001 (2011).

[19] V. Bulanov, E.Yu. Ekhkina, T.Zh. Esirkepov, I.N. Inovenkov, M. Kando, F. Pegoraro and G. Korn, "Unlimited Energy Gain in the Laser-Driven Radiation Pressure Dominant Acceleration of Ions", Phys. Plasmas, 17 (2010)063102.

[20] A. Macchi et al., Phys. Rev. Lett. 94 (2005)16.

[21] O. Klimo et al., Phys. Rev. STAB, 11 (2008)031301.

[22] A.P.L. Robinson et al., New J. of Phys. 10 (2008)013021.

[23] X.Q. Yan et al., Phys Rev. Lett. 100 (2008)13.

[24] A. Andreev, J. Limpouch, J. Plasma Physics 62 (1999)2.

[25] D. Habs et al., Appl. Phys. B 103 (2011) 501.

DYNAMICS OF $^{197}AU^{+78}$ IONS GENERATED IN RECOMBINATION WITH COOLING ELECTRONS IN THE NICA COLLIDER

A.V. Eliseev, O.S. Kozlov, A.B.Kuztnetsov, I.N. Meshkov, A.O. Sidorin, A.V. Tuzikov, A.V. Philippov, JINR/VBLHEP, Dubna, Russia

Abstract

In the NICA Collider [1], recombination of original $^{197}Au^{+79}$ ions with cooling electrons in the electron cooler will lead to generation of $^{197}Au^{+78}$ ions. Dynamics of these ions in the energy range 1 – 4.5 GeV/u when the ion beam is bunched with RF voltage (collision mode operation) is considered in this report. It is shown that some part of 78+ ions can be involved into synchrotron motion when other part suffers a chaotic motion regime. Most of these ions circulate in vacuum chamber until further recombination into the charge state of $^{197}Au^{+77}$ and then leave the Collider acceptance very fast. The evolution in time of the ion distribution over the Collider aperture is presented

INTRODUCTION

Longitudinal motion of a multi-component ion beam can be in synchronism with an accelerating field when the revolution period T does not depend on the charge and mass of the ion in any moment of time. In differential form this condition is:

$$\frac{\Delta T}{T} = \frac{\Delta R}{R_0} - \frac{\Delta\beta}{\beta} = 0 \qquad (1)$$

Variation of the average radius R can be expressed as follows:

$$\frac{\Delta R}{R_0} = \alpha\left[\gamma_0^2\frac{\Delta\beta}{\beta_0} - \frac{\Delta\left(Z/W_r\right)}{Z_0/W_{r0}}\right] \quad , \qquad (2)$$

The relative velocity and momentum deviations of the beam components are:

$$\frac{\Delta\beta}{\beta_0} = -\frac{\alpha}{1-\alpha\gamma^2}\frac{\Delta\left(Z/W_r\right)}{Z_0/W_{r0}}, \quad \frac{\Delta p}{p_0} = \frac{\alpha\gamma^2}{1-\alpha\gamma^2}\frac{\Delta\left(Z/W_r\right)}{Z_0/W_{r0}} \quad (3, 4)$$

Where α is the ring compaction factor, β, γ – relativistic parameters, Z – particle charge, W_r – rest energy, index zero corresponds to the main component of the beam.

All the particles can be accelerated if aperture allows. As for collider operating at constant energy the particles not involved in synchrotron regime circulate in vacuum chamber as well.

In electron cooler of the NICA collider the ions of Au^{+79} after successive recombination with electrons will transfer into Au^{+78}, Au^{+77} and so on. The ions in different charge states, involved into synchrotron motion will arrive to the detector sites simultaneously. This may contort physical experiments and hamper the feedback steering of the main beam. The ions forming coasting beam will create an unwanted noise.

PHASE SPACE MOTION OF IONS WITH DIFFERENT CHARGE STATE

RF Bucket Parameters

The bunch length in the NICA collider is chosen to be 0.6 m (rms) independently on the energy. The relative momentum spread (σ_p) is linearly proportional to relativistic gamma and varies from $6\cdot10^{-4}$ at 1 GeV/u to $1.7\cdot10^{-3}$ at 4.5 GeV/u [2]. The bucket height keeps ~3.7 σ_p regardless energy. Shift of the synchronous energy between Au^{+79}, and Au^{+78} (centres of corresponding buckets) and the bucket height are represented in the Fig.1 as functions of the particle energy.

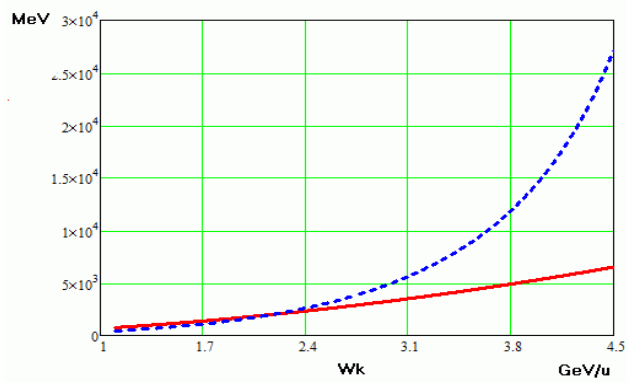

Figure 1: Bucket height (red) and energy shift between synchronous Au^{+79} and Au^{+78} (blue) vs. particle energy.

The buckets of the different charge states are moving apart in the phase plane with the energy increase. Graphically the situation is illustrated by the Fig. 2.

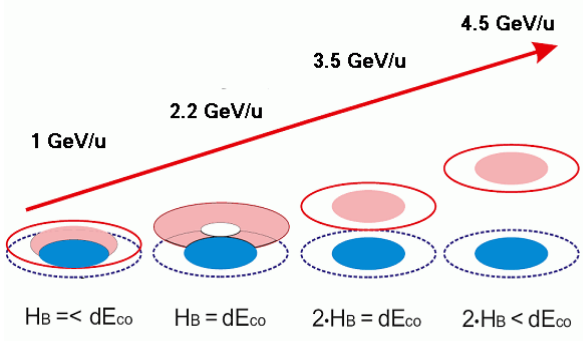

Figure 2: General scheme of buckets Au^{+79} (blue) and Au^{+79} (red) allocations in longitudinal phase space.

Thus new formed ions of Au^{+78} can find themselves either inside or outside the bucket in the energy range from 1 to 3.5 GeV/u and outside the bucket only in the range 3.5 ÷ 4.5 GeV/u. Particles inside the bucket are

involved in synchrotron motion and move in the phase plane within the envelope surrounding the new orbit. Particles outside the bucket follow flow lines parallel to the dispersion orbit.

Non-synchronous (Chaotic) Motion of Particles after their Recombination with e⁻

The dispersion orbit is the trajectory of the initially synchronous Au^{+79} after its recombination with a cooling electron and turning out outside the new bucket. The radial shift of the orbit is equal to:

$$\Delta R = \frac{\Delta Z}{Z_0} D_x. \quad (5)$$

Where D_x is the dispersion function and ΔZ is the charge variation.

Trajectories of other particles are parallel to the dispersion orbit. Their position above or below depends on their momentum at the moment of recombination. An ion will survive in collider's vacuum chamber if its trajectory doesn't exceed the radius of aperture in the place of the dispersion maximum. The vacuum chamber radius in the horizontal plane is ± 0.06 m. Figure 3 shows that coasting beam within aperture limits contains not only ions of Au^{+78} but ions of Au^{+77} as well, number of which increases with energy. Scrapers with proposed position at radius of 4 cm at maximums of dispersion are necessary for clearing out the ions Au^{+77}.

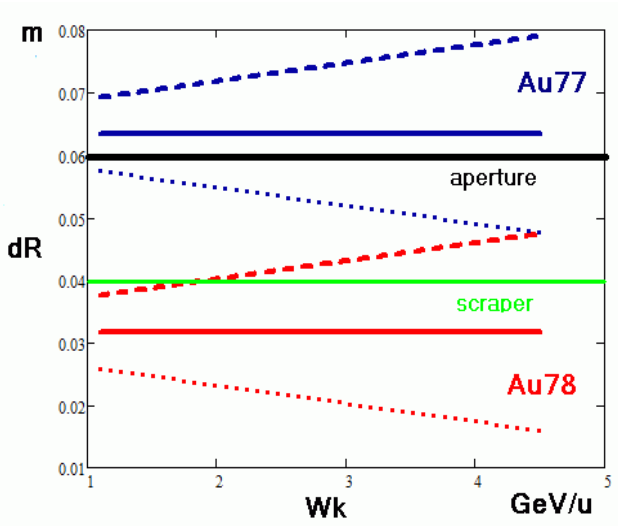

Figure 3: Coasting beam of Au^{+78} and Au^{+77}. Radial shifts of their orbits (solid lines) and envelopes (dashed and dotted lines) in maximum of dispersion.

Au^{+78} Ions Involved in Synchrotron Motion

Buckets of Au^{+78} and Au^{+79} overlap in energy range 1 ÷ 3.5 GeV. Thus newly recombined ion can found itself within its bucket and can move in the envelope near the new orbit. As opposed to the trajectories of chaotic motion the trajectories of the particles involved into synchrotron motion always cross the dispersion orbit. It means that synchronous particle will be the last one lost on aperture of scraper. The orbit displacement from the center of the vacuum chamber increases with energy growth. The position of the orbit and envelope at maximum of the dispersion value for the Collider parameters is shown in the Fig. 4.

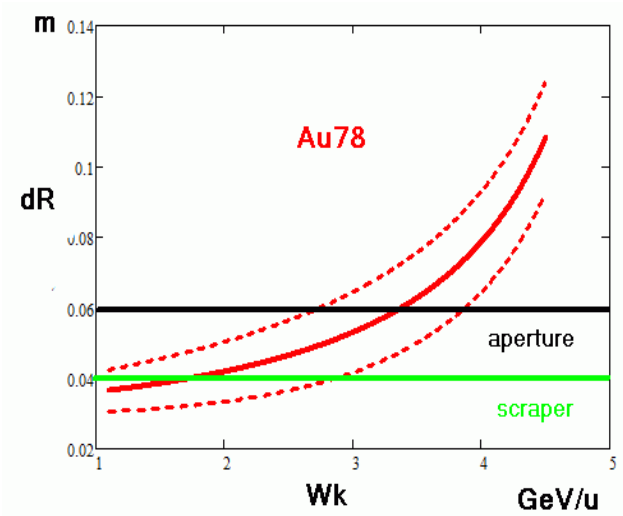

Figure 4: Particles Au^{+78} involved in synchrotron motion. Radial shift of their orbit and envelope in maximum of dispersion from the central orbit (Au^{+79})

The orbit of Au^{+78} crosses the radius of scrapers position at energy of 1.7 GeV/u. Thus the multi-turn synchrotron motion is possible below this energy only. Here the particle life-time is less than the half of the synchrotron period. At 2.8 GeV/u lower limit of the envelope crosses scraper "position". Over this energy the synchrotron motion is impossible in principal.

Upper limit of the envelope exceeds the radius of scrapers starting from the minimum collider energy. It means that ions of Au^{+78} moving in the vicinity of the separatrix will be lost on scraper at the energy above 1 GeV/u.

The simulations of Au^{+78} motion have been done using ESME code [3] at different ion energies. The result of the simulations is shown in the Fig. 5. At 1 GeV/u multi-turn synchrotron motion is possible only for particle in the inner part of the bucket. At 1.6 GeV/u the simulation shows that only small number of particle is trapped inside the bucket.

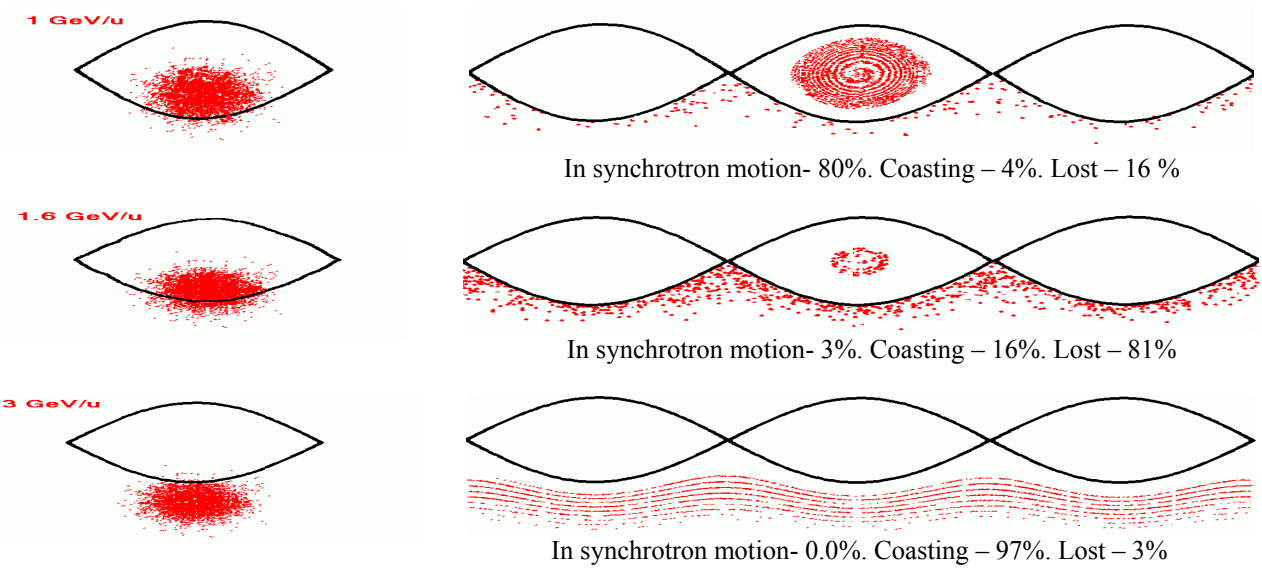

Figure 5: ESME simulation of Au^{+78} motion in longitudinal phase space at 1.0, 1.6, 3.0 GeV/u

.

INTENSITY OF THE RECOMBINED IONS

The ratio of recombined particles involved in synchrotron motion, in coasting motion and lost on scrapers depends on the energy. Scrapers eliminate all ions with charge state starting from Au^{+77}. The ratio depends on cross sections of two reactions: $Au^{+79} + e^- \rightarrow Au^{+78}$ and $Au^{+78} + e^- \rightarrow Au^{+77}$. Estimations presented in [4] show that the second cross-section exceeds the first one by about factor of 10. In this case the total proportion of Au^{+79} and Au^{+78} will have the time dependence shown in the Fig. 6.

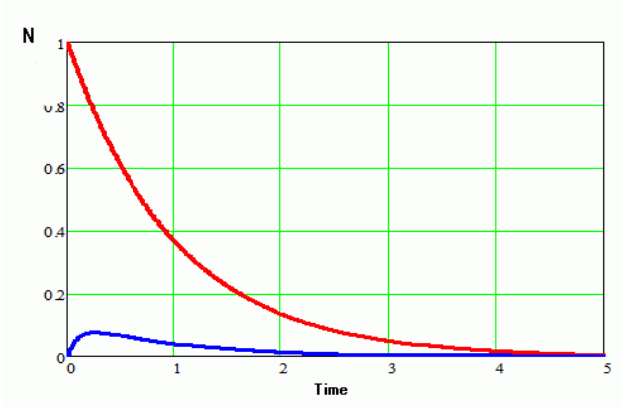

Figure 6: Change of number of ions Au^{+78} (blue) and Au^{+79} (red) in time (in number of characteristic times).

Stationary ratio of $N(Au^{+78})/N(Au^{+79})$ is inversely proportional to the ratio of the cross-sections.

CONCLUSIONS

- Ions Au^{+79}, Au^{+78}, Au^{+77} can circulate in the Collider vacuum chamber.
- Scrapers positioned at R=4 cm in maximums of dispersion function will remove Au^{+77} ions.
- Coasting ions of Au^{+78} will survive till further recombination to Au^{+77} take place.
- Part of the Au^{+78} ions involved in synchrotron motion will be cleared by scrapers. Number of ions lost by this way depends on energy.
- Ions Au^{+78} involved in synchrotron motion will be seen by the detector simultaneously with ions Au^{+79}. Ratio of their intensities can be calculated by multiplying ratio of cross sections of reaction ($Au^{+79} + e^- \rightarrow Au^{+78}$ and $Au^{+78} + e^- \rightarrow Au^{+77}$) by the portion of Au^{+78} involved in synchrotron motion.
- Number of ions Au^{+78} survived in synchrotron motion is negligible at energy above 1.6 GeV/u.

REFERENCES

[1] I. Meshkov, Status of NICA Project, these proceedings.
[2] A. Eliseev et al., "Storage, Acceleration and Short Bunched Beam Formation of 197Au79+ Ions in the NICA Collider", these proceedings.
[3] http://www-ap.fnal.gov/ESME.
[2] A. Philippov et al., "Influence of the Effect of Bare Gold Nuclei Recombination in Electron Cooling System on Working Regime of NICA Collider", these proceedings.

COLLIDER OF THE NICA ACCELERATOR COMPLEX: OPTICAL STRUCTURE AND BEAM DYNAMICS

O.Kozlov, A.Eliseev, H.Khodzhibagiyan, S.Kostromin, I.Meshkov, A.Sidorin, G.Trubnikov,
JINR, Dubna, Russia

Abstract

The Nuclotron-based Ion Collider fAcility (NICA) [1] is a new accelerator complex being constructed at JINR. It is aimed to collider experiments with ions and protons and has to provide the ion-ion (Au^{+79}) and ion-proton collision in the energy range of 1÷4.5 GeV/u and also polarized proton-proton (5÷12.6 GeV) and deuteron-deuteron (2÷5.8 GeV/u) collisions. Two collider rings are designed and optimized to achieve the required luminosity at two interaction points (IP). Providing the intense ion beam life time the space charge effects were considered. Beam accumulation scheme and scenario of collider operation in collision mode with application of electron beam or stochastic cooling methods were proposed.

INTRODUCTION

The goal of the NICA project is construction at JINR of the new accelerator facility that consist of [1]: cryogenic heavy ion source of Electron String type (ESIS), source of polarized protons and deuterons, the existing linac LU-20 of Alvaretz type, a new heavy ion linear accelerators RFQ-DTL, a new superconducting Booster-synchrotron placed inside the decommissioned Synchrophasotron yoke, the existing proton and heavy ion synchrotron Nuclotron, the new system of beam transfer channels, and two new superconducting storage rings of the collider. NICA collider lattice development [2] has many necessary aspects of the design. The collider should operate in the energy range for Au-ions of 1÷4.5 GeV/u, with the average luminosity about $1\cdot10^{27}$ cm^{-2} s^{-1}. The ring should work with the different particle species (Au^{+79}, protons and deuterons). Collider must fit into JINR infrastructure and has a certain circumference limitation. The collider lattice is based on the technology of super-ferric magnets developed in VBLHE, JINR [3]. Such a dipole magnet with up to 2 T bending field operates with hollow composite NbTi cable at 4.5 K. The collider optics optimization includes the certain effects which set some constraints on the lattice parameters: luminosity lifetime limitation by intrabeam scattering in a bunch (IBS); space charge tune shift, threshold of microwave instability; slippage factor optimization for efficient stochastic cooling; maximum required RF voltage amplitude.

Collider operation at fixed energy without acceleration of the injected from the Nuclotron beam is considered. Beam storage at some optimum energy and slow acceleration in the collider (at field ramp rate < 1 T/s) is presumed as a reserve option. The maximum energy of the experiment is determined by the Nuclotron maximum magnetic rigidity of 45 T·m. In this paper we discuss only the most developed heavy ion mode of facility operation and the $^{197}Au^{+79}$ ions as the reference particles.

LATTICE STRUCTURE

Together with the physical effects the another technical constraints were taken into account in lattice optimization: ring circumference, number of the dipole magnets in arc, convenience of the beam injection into the ring. The FODO optics with 12 periods is a principal choise for arc structure. Two arcs and two long straight section form the collider racetrack shape and correspond exactly to two Nuclotron circumferences. The rings are vertically separated (32 cm between axes) and use "twin aperture" superconducting magnets (dipole and quadrupoles) [2]. This lattice has a large efficiency of stochastic cooling at 4.5 GeV/amu. But the luminosity of 10^{27} cm^{-2} s^{-1} could be reached in the wide energy range. The convenient injection scheme could be realized through the arc dipole-empty cell.

Table 1: Collider Ring and Beam Parameters

Ring circumference, m	503.04		
Gamma-transition, γ_{tr}	7.091		
Betatron tunes, Q_x/Q_y	9.44/9.44		
Chromatisity, $\xi_{x,0}/\xi_{y,0}$	-33/-28		
Max. number of bunches	23		
Rms bunch length, m	0.6		
β-function in the IP, m	0.35		
FF lenses acceptance	40π mm mrad		
Long. acceptance, Δp/p	±0.010		
Ion energy, GeV/u	1.0	3.0	4.5
Ion number per bunch	2.75e8	2.4e9	2.2e9
Rms Δp/p, 10^{-3}	0.62	1.25	1.65
Rms emittance, hor/vert, (unnorm), π·mm·mrad	1.1/ 1.01	1.1/ 0.89	1.1/ 0.76
Luminosity, $cm^{-2}s^{-1}$	1.1e25	1e27	1e27
IBS growth time, s	190	700	2500

FODO-cell geometry is set up with the fixed lengths of magnetic elements and spaces. In Fig. 1 the scheme of 11.96 m cell is shown. There are four rectangular dipole magnets per cell (80 magnets per ring), two quadrupoles [3], multipole correctors and BPMs. The maximum field in dipoles of 1.8 T and gradient in quadrupoles of 23 T/m are chosen to possibly avoid the saturation effects in iron yokes at higher energies. Multipole corrector includes the several types of windings – dipole (orbit correction),

quadrupole (tuning), skew quadrupole (coupling correction), sextupole (chromaticity correction).

Arc comprises 12 FODO cells (90^0 phase advance per cell). The last 1.5 cells realize the horizontal dispersion suppressor (the effective quadrupole gradient (3 families) tuned by the nearby quadrupole corrector).

Long straight sections are matched to the arcs, contain the insertion devices, produce the betatron tune variation and vertical the beam separation and final focusing in IPs.

Ring general parameters are given in Table 1 and assembly for one of the rings is shown in Fig. 2. Two rings are separated vertically. Counter circulating beams must see the same optics to adjust the same betatron tunes ($Q_{x,1}=Q_{x2}$, $Q_{y,1}=Q_{y,2}$). Thus 2-aperture quadrupoles should have the opposite connections for upper and bottom rings in arcs and long straights, but the final focus triplets should have the antisymmetric connections with respect to IPs. The corresponding β and dispersion functions over half of the ring are pictured in Fig. 3. In antisymmetric scheme the uncorrected vertical dispersion approximately cross zero at IPs.

A chromaticity correction includes 4 families of sextupole correctors (focusing and defocusing). Sextupoles in each family are located in 180^0 betatron phase advance for the compensation of their nonlinear influence on the dynamic aperture (DA). The dependence of the collider tune on Δp/p is shown in Fig. 4 before and after chromaticity correction. At the slightly negative corrected chromaticity $\xi_{x,y}=-1.5$ sextupole setting (maximum strength of 130 T/m^2) the corresponding estimated DAs (for several 1000 turns) are pictured in Fig.5 for the maximum energy 4.5 GeV/u without and with expected nonlinearities in dipoles [3]. In these cases they are large enough compare to the ring acceptance. But DA studies require more detailed and sophisticated simulation in 3D with the beam space charge for the very large turn numbers.

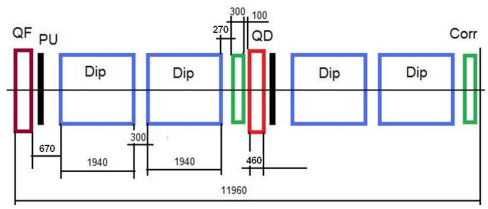

Figure 1: Arc periodic cell.

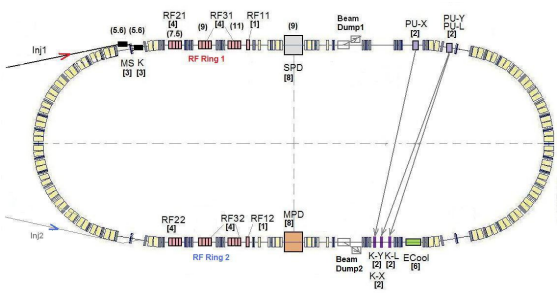

Figure 2: Ring assembly. Stochastic cooling system location for one ring, electron cooling and RF systems location for both rings are shown.

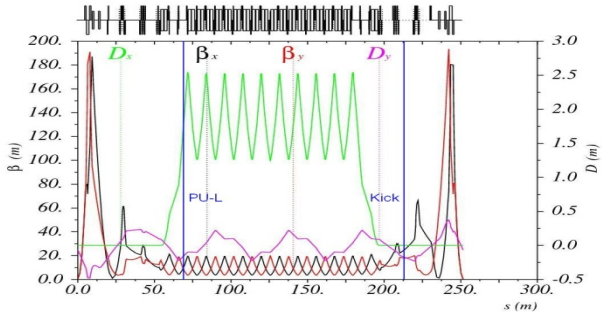

Figure 3: β-functions and dispersions for half a ring.

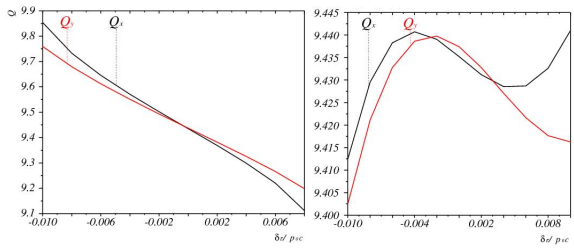

Figure 4: Tune dependence on momentum offset before and after chromaticity correction.

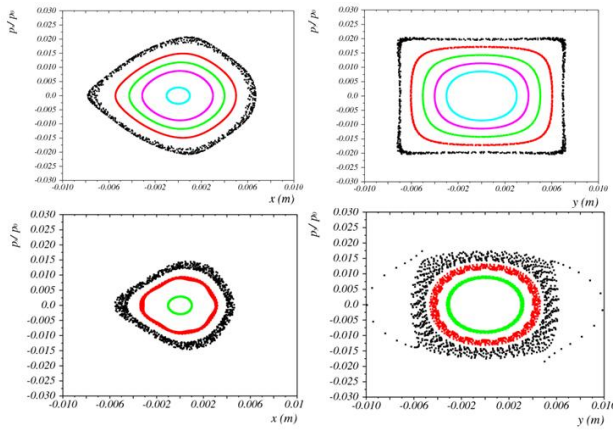

Figure 5: Horizontal and vertical DAs at IP, 4.5 GeV/u: top – chromaticity correction, bottom – chromaticity correction and b_2 dipole errors.

LONGITUDINAL DYNAMICS

To achieve desirable bunch parameters for collision, three RF systems are needed in the collider: one broadband type for ion accumulation and two narrow-band systems for the bunch formation [6].

RF1 – the first collider RF system of Barrier Bucket type serves for ion accumulation. Rectangular pulses at 5 kV of amplitude and phase duration π/6 are able to accept particles with relative momentum deviation of ±0.01. Phase distance between the pulses is π. The accumulation length is the half of the collider perimeter, one perimeter of Nuclotron. After accumulation of a required ion number the barrier voltage is switched off and the beam becomes coasting. *RF2* provides the required number of bunches in the collision mode. In presence of cooling the emittance and bunch length continue to decrease. It will be switch on until the bunch length reduces enough to fit

the RF3 acceptance. The maximum RF2 voltage amplitude of 100 kV has some reserve for operation. *RF3* is the principal system of the collider. It keeps the collision regime. The bunch momentum spread is the result of equilibrium of two processes – intra beam scattering and cooling and varies with energy as shown in Fig. 6. At harmonic number 69 the bucket size is still large enough ($\pm 6\sigma_s$ in length and $\pm 4\sigma_p$ in height) and maximum voltage is still at reasonable value (Fig. 6).

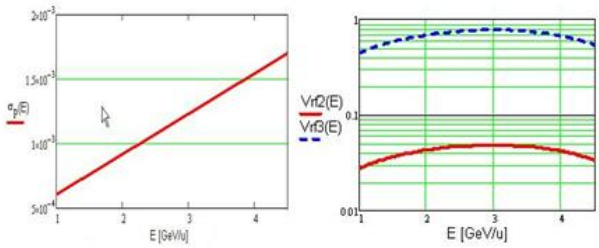

Figure 6: R.m.s. momentum spread (σ_s=0.6m), and RF2 and RF3 amplitude (in MV) vs ion collision energy.

COLLIDER LUMINOSITY AND REGIMES

The collider design has to provide the project luminosity (beam life time) and its maintenance during long time of experiment performance. Beam intensity is limited by beam space charge effects, which can be estimated by "tune shift criteria" [6]: the total tune shift $\Delta Q_{total}=\Delta Q_{Las}+2\xi$ (Laslett and 2 beam-beam) that could not exceed the limit of 0.05. The main problem of the NICA collider is suppression of intrabeam scattering (IBS) in the intense ion beam. For this purpose both electron beam and stochastic cooling methods are proposed. The first situation is the achievement the equilibrium between the cooling and space charge when the space charge reaches the resonant value $\Delta Q_{total} = 0.05$. This is called "Space Charge dominated regime". At this regime the maximum luminosity is obtained with the maximum beam emittance. For some reasons the luminosity can be limited, for example by the value $1\cdot10^{27}$ cm^{-2} s^{-1}. In that case one can reoptimized beam intensity and emittance to keep ΔQ_{total} below the limit. It also decreases the cooling force providing the equality between IBS and cooling rates. The corresponding regime of the collider operation is called "IBS dominated regime".

For NICA parameters IBS dominated regime can be used at energies above 3 GeV/u where ΔQ_{total} <0.05. At that energy range the stochastic cooling is proposed to use. The choosing stochastic cooling system bandwidth from 3 to 6 GHz provides the cooling time two-three times shorter than IBS times. At lower energies below 3 GeV/u the application of electron cooling is preferable.

CONCLUSION

The collider lattice concept – "2 Nuclotrons" circumference with 12 cell FODO structure in the arcs has been chosen. The ring meets the requirements of tunes adjustment in the dispersion free sections, large transversal and momentum acceptances, location of number of the insertions, vertical beam separation in interaction region, maximum total voltage of RF stations (≤1MV).

The collider rings of the NICA accelerator complex have the particular operating features described in this report: SC and IBS dominated regimes. The application of the cooling methods is only way to realize the required collider luminosity parameters. The proposed cooling scenario includes: electron beam cooling in the energy range from 1 to 3 GeV/u can provide short cooling times at the SC dominated regime; the stochastic cooling technique is more preferable in the range 3÷4.5 GeV/u where luminosity $1\cdot10^{27}$ cm^{-2} s^{-1} can be obtained in IBS dominated regime (Fig. 7).

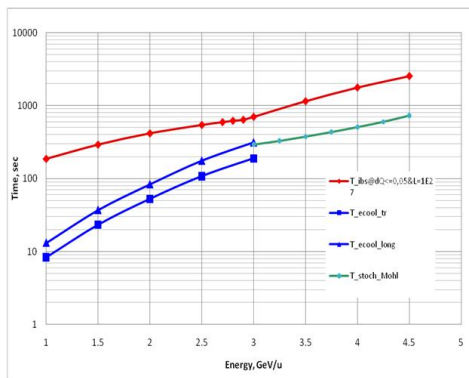

Figure 7: IBS growth times in the IBS dominated regime, electron cooling times (<3 GeV/u) and stochastic cooling time (≥3 GeV/u).

REFERENCES

[1] G.V. Trubnikov et al., "Project of the Nuclotron-based Ion Collider fAcility (NICA) at JINR", RuPAC'10, Protvino, September 2010, TUCHB02, p. 17 (2010).

[2] O.S. Kozlov et al., "Design of the NICA Collider rings", IPAC'11, San Sebastian, May 2011, TUPZ005, p. 1807 (2011).

[3] H.G. Khodzhibagiyan, "Status of the Design and Test of Superconducting Magnets for the NICA Project", these proceedings, THAOR03.

[4] S. Nagaitsev, "Intrabeam scattering formulas for fast numerical evaluations", Physical Review Special Topics – Accelerators and Beams, 8, 064403, (2005).

[5] A. Eliseev et al., "Storage, Acceleration and Short Bunched Beam Formation of 197Au79+ Ions in the NICA Collider", these proceedings, MOBCH01.

[6] O. Kozlov et al., "Space Charge Effects in the NICA Collider Rings", HB2012, Beijing, September 2012, THO1B04, to be published.

LOCALISATION OF THE RF BREAKDOWN IN THE PARALLEL COUPLED ACCELERATING STRUCTURE

Yu. Chernousov, V. Ivannikov, I. Shebolaev, ICKC, Novosibirsk, Russia
A.Barnyakov, A. Levichev, V. Pavlov, BINP, Novosibirsk, Russia

Abstract

Parallel coupled accelerating structures (PCAS) [1,2] with parallel RF power feeding of accelerating cavities have some features and advantages vs. conventional TW - traveling wave and SW - standing wave structures with sequential (serial) RF power feeding. Parallel feeding of accelerating units - individual cells or accelerating substructures provides normal regime acceleration of the beam by all cells and minimizes the RF power flows via coupling slots and determines individual behavior of each cell in the regime of RF breakdown. These features can be used for developing low energy linear accelerators as well as high gradient accelerating structures. The experimental data of the breakdown regimes in the PCAS are presented in this paper.

INTRODUCTION

The main idea of the PCAS is the feeding of accelerating cells in parallel from the rectangular waveguide [1,2]. Parallel feeding of accelerating units – individual cells or accelerating substructures, provides normal regime of acceleration of the beam by all cells [1], minimizes RF power flows via coupling slots, and as shown in this paper, determines individual behavior of each cell in the regime of breakdown and minimizes absorbed RF energy in each accelerating cavity. These inherent characteristics and features of the PCAS are helpful for developing of low energy linear accelerators [1-3] and as noted in the papers [1,2,4] can be used to overcome difficulties when elaborating a high gradient accelerating structures.

A breakdown violates normal work of the accelerator, destructs the surface of the cells. The damage accumulates and as a result the RF property of separate cells and accelerating structure changes. Numerous investigations are devoted to study of this phenomenon [5-9]. The phenomenon is rather complicated and the processes involved are not clear yet. Nevertheless in recent years some evidence has been found that the RF power flow in particular determines the maximum sustainable gradient in an accelerating structure [6,7]. Using a parallel feeding in the PSAC handles and solves the issue of high level of RF flows in the structure.

Feeding line delivers electromagnetic energy to accelerating sells of the PCAS, it works on TW [1,2,4] or SW [2,3] mode. In the case of TW-mode it is difficult to provide the necessary amplitude and phase distributions of microwaves along the accelerating structure. For these goals it is necessary to employ variable coupling coefficient of cells with feeding line [1,2,4] which reduces advantages of the PCAS. The most straightforward means to solve this problem seems to be the use of SW-mode in the feeding RF line. This mode gives π-phase shift between the accelerating cavities as well as provides required amplitude distribution of an accelerating field along the structure [2,3]. The experimental data of the breakdown in the PCAS [3] which consists of an individual accelerating sells feeding via common exciting cavity – segment of rectangular waveguide working in the SW regime are given below.

EXPERIMENTAL SETUP

A conceptual scheme of PCAS is shown in Fig.1. The Accelerating (Accel.) Cavities are fed in parallel by common Exciting Cavity connected to feeding RF Power line thru Input Diaphragm. Exciting Cavity is shorted at

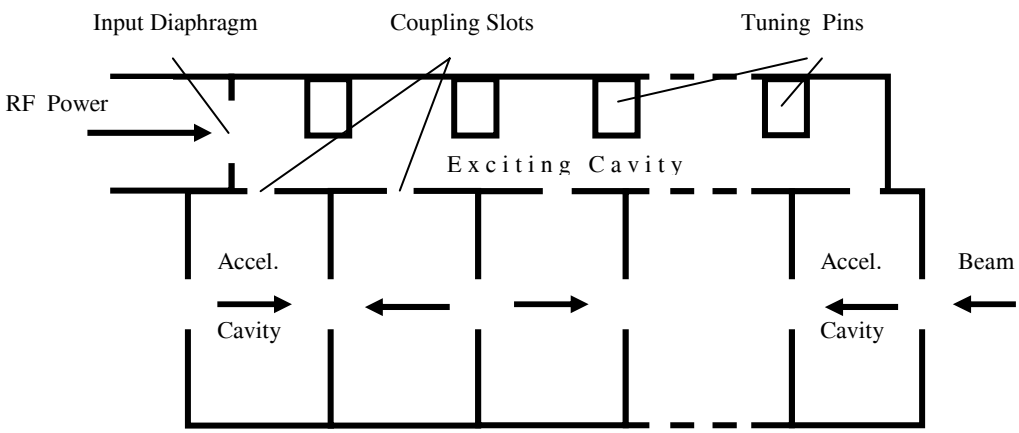

Figure.1: Conceptual scheme of the PCAS

the ends a segment of rectangular waveguide operating on TE_{10N-1} – like SW mode, N – quantity of accelerating cavities. It is loaded by Tuning Pins to reduce the wavelength. Due to the Pins in the Exciting Cavity standing wave with period of $\lambda_0/2$ is settled, where λ_0 is the wavelength of accelerating frequency in the free space. The distance between the neighboring Coupling Slots is also $\lambda_0/2$. Therefore accelerating cavities are excited by the transversal component of the magnetic field of exciting cavity with a phase shift π, which provides regime of acceleration of electron bunches with velocity of light C by all accelerating cavities.

RF power delivers to all accelerating cavities by individual Coupling Slots in parallel. This feeding system minimizes RF power flows via all Coupling Slots as well as optimizes stored RF energy in every sell of PCAS.

The Coupling Slots of all accelerating cavities are under the identical conditions. Due to the parallel connection all accelerating cavities can be considered as one equivalent cavity. Thus the accelerating structure can be described as a system of two coupled cavities [10] – exciting cavity and common accelerating cavity. In such a system the coupling coefficient between cavities (first and second) can be varied over a wide range. Employing exiting cavity installed in front of the accelerating cavities permits to decrease the sizes of the coupling slots [11].

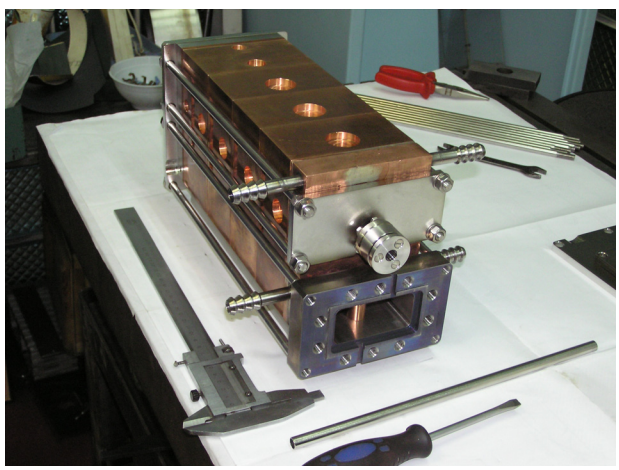

Figure 2: 5-cavity model of PCAS.

The experiments in the regime of breakdown were done on the experimental model of PCAS shown in Fig.2. Model contains 5 accelerating sells [3].

MESURMENT OF BREAKDOWN

Experimental data characterizing the breakdown processes during RF processing are represented in Fig. 3a-3c. Measured value of RF power was 1.6 MW, calculated amplitude of surface electric field reached up to 0.7 MV/cm. Incident, reflected RF power and stored RF energy in the fifth accelerating cavity were measured at the experiments. In Fig.3 one can see signals: incident RF power (F1) – yellow; reflected RF power (F3) – blue; RF signal from fifth accelerating cavity, proportional to stored energy in them (F4) – green. In normal regime (without breakdown) all signals are of the proper form, without any singularity. Incident RF power (F1) has rectangular form. Reflected RF signal (F3) characterizes transients in the system of two coupled cavities – accelerating and exciting cavities. Signal (F4) with exponential form represents stored energy in the fifth cavity.

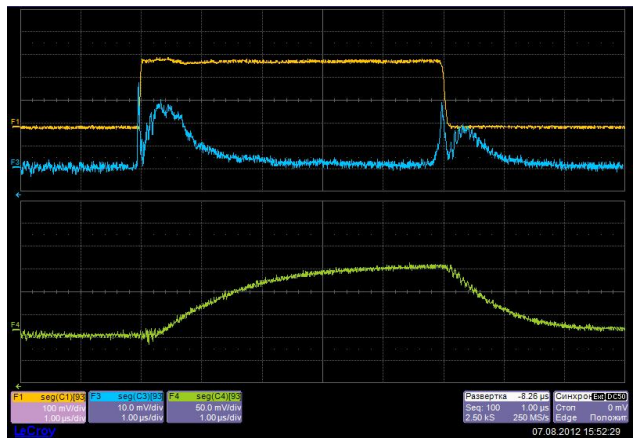

Figure 3a: Regime without breakdowns.

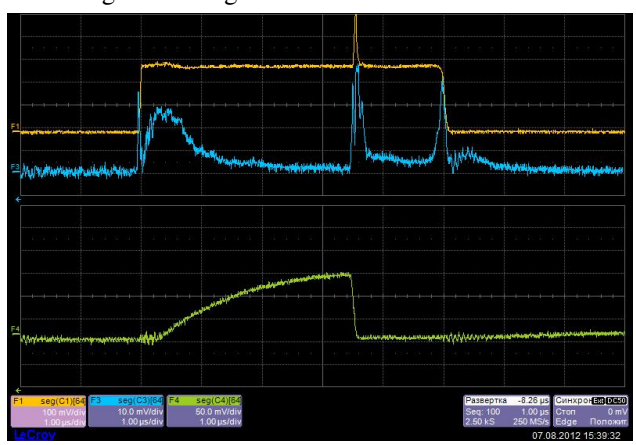

Figure 3b: Breakdown in the 5-th accelerating cavity.

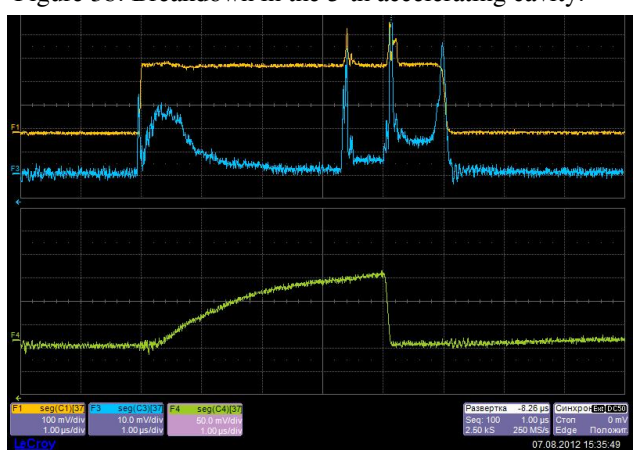

Figure 3c: Regime with breakdowns in several accelerating cavities. F1 – RF power from klystron, 1.6 MW, pulse duration 5 μs; F3 – reflected signal; F4 – stored RF energy in 5-th accelerating cavity.

The processes change under breakdown. If a breakdown takes place in the single accelerating cavity, a

part of the stored RF energy dissipates in this cavity, some fraction radiates to exciting cavity and then thru Input Diaphragm to external RF Power line. As a result on the reflected signal one can see short pulse burst - Fig.3b, line (F3). Let's note that there are no sizeable reflections from accelerating structure which could affect the RF generator. So, PCAS almost doesn't ″notice″ the breakdown in the separate cavity. In Fig.3c behavior of the system when the breakdowns take place almost simultaneously - during one RF pulse in some accelerating cavities – a very rare event is shown. In this case accelerating cavities are disconnected one by one, reflected RF signal increases – Fig.3c, line (F3).

THE SUM OF OBSERVATIONS AND DISCUSSION

At high level of RF power breakdowns occur in the well-established SW and TW structures as well as in accelerating cavities of PCAS. In the case of SW accelerating structure in the regime of breakdown the reflection coefficient becomes close to unit and almost all incident RF power of the generator is reflected [4]. Nevertheless total RF energy stored in the whole structure can dissipate in the cavity where breakdown takes place. For the case of TW in the regime of breakdown the reflection coefficient remains close to zero and RF energy, stored in the structure, and almost all RF power of the generator feeding the accelerator dissipates in the cavity with breakdown.

Character of processes at the regime of breakdown in the PCAS seems to be as follows. Breakdown process in the PCAS localizes in a single accelerating cavity. If a breakdown occurs in some cavity, stored RF energy dissipates and amplitude of RF field in this cavity decreases. The neighboring accelerating cavities are isolated one from another by Exiting Cavity, therefore stored RF energy and amplitude of RF field remains invariable in them. The breakdown in the separate cavity does not change the property of accelerating structure on the whole. Electron beam accelerates almost up to its previous energy. Only one cavity where breakdown occurs is eliminated of this regime. External RF generator ″sees″ the exciting cavity of PCAS with practically constant amplitude. After the breakdown RF field and stored energy in the accelerating cavity restore with time constant $\tau \sim Q/\omega$, where Q is quality factor of the cavity and ω is the frequency of accelerating field. Let's note that additional reflection from the structure practically doesn't arise.

CONCLUSIONS

Parallel feeding of accelerating cavities in the PCAS determines individual behavior of each cell in the regime of breakdown. Breakdown process in the PCAS localizes in a single accelerating cavity. If a breakdown occurs in an accelerating cavity of PCAS, stored RF energy of this cavity dissipates only in this cavity.

Breakdowns occur in the accelerating cavities with sequential (serial) RF power feeding violates normal work of the accelerator, destructs the surface of the cells. In the case of PCAS a breakdown does not change acceleration regime in the accelerating structure. RF energy destroying the surface of accelerating cavity of PCAS due to breakdowns, as compared to SW and TW structure with sequential RF power feeding is at least N times less, where N is a quantity of accelerating cavity of the structure. Therefore the damages are alike smaller.

Certainly the method of feeding of accelerating sells in parallel from a rectangular waveguide [1,2] will help to create the robust high gradient accelerating structures [4].

REFERENCES

[1]. V.I. Ivannikov, Yu. D. Chernousov, I. V. Shebolaev Parallel-Coupled Accelerating Structure. JTPh,1986, V.56, N12, p.2407. (In Russian).

[2] O.N. Brezhnev, P.V.Logatchev, V.M.Pavlov, O.V.Pirogov, S.V.Shiyankov, Yu.D.Chernousov, V.I.Ivannikov, I.V.Shebolaev. Parallel-Coupled Accelerating Structures, Proc. of LINAC2002, p.215.

[3] Yu.Chernousov, V.Ivannikov, I.Shebolaev, V.Pavlov, A.Levichev. Prototype of Parallel Coupled Accelerating Structure. Proc. of EPAC 2008, p. 2737.

[4] J.Neilson, S.Tantawi and V.Dolgashev. Design of Feed System for Standing-Wave Accelerating Structures. Proc. of LINAC2010, p.235.

[5] R.H. Miller, R.M. Jones, C. Adolphsen, G. Bowden, V. Dolgashev, N. Kroll Z. Li, R. Loewen, C. Ng, C. Pearson, T. Raubenheimer R. Ruth, S. Tantawi, J.W. Wang. Room Temperature Accelerator Structures for Linier Colliders. Proc. of PAC2001, p.3819

[6] S. Döbert, A. Grudiev, G. Riddone,M. Taborelli, W. Wuensch, R. Zennaro, S. Fukuda, Y. Higashi, T. Higo, S. Matsumoto, K. Ueno, K. Yokoyama, Adolphsen, V. Dolgashev, L. Laurent, J. Lewandowski, S. Tantawi, F. Wang, J. W. Wang. High Power Test of a Low Group Velocity X-Band Accelerator Structure for CLIC. Proc. of LINAC08, p.930.

[7] Faya Wang, Chris Adolphsen, and Christopher Nantista. Performance Limiting Effects in X-Band Accelerators. Phys. Rev. STAB. 14, 010401 (2011).

[8] Lisa Laurent, Sami Tantawi, Valery Dolgashev, Christopher Nantista, Yasuo Higashi, Markus Aicheler, Samuli Heikkinen, and Walter Wuensch. Experimental Study of RF Pulsed Heating. Phys. Rev. STAB. 14, 041001 (2011).

[9] Roark A. Marsh, Michael A. Shapiro, Richard J. Temkin, Valery A. Dolgashev, Lisa L. Laurent, James R. Lewandowski, A. Dian Yeremian, and Sami G. Tantawi. X -Band Photonic Band-Gap Accelerator Structure Breakdown Experiment. Phys. Rev. STAB. 14 , 021301 (2011).

[10] Yu. D. Chernousov, V. I. Ivannikov, I. V. Shebolaev, A. E. Levichev, and V. M. Pavlov. Bandpass Characteristics of Coupled Resonators. J. of Communications Technology and Electronics, 2010, Vol. 55, No. 8, p. 863. In Russian: Radiotekhnika i Elektronika, 2010, Vol. 55, No. 8, p. 923.

[11] Yu. D. Chernousov. Excitation Method of Acceleration Structure. Patent RU № 2427112 C1, Bul.23, 2011.

RF ANTENNA LEAD

A.Barnyakov, A.Levichev, V.Pavlov, BINP SB RAS, Novosibirsk, Russia
Yu.Chernousov, V. Ivannikov, I. Shebolaev, ICKC SB RAS, Novosibirsk, Russia

Abstract

RF antenna lead is described. This lead is used for RF power input to high voltage electrodes. The device consists of receiving and transmitting antennas realized as symmetrical parts of coaxial cavity with dielectric disk between the parts. Main operating characteristics are the following: high voltage is over 60 kV, coefficient of transmission S_{21} at the operating frequency is over 0.97, bandpass is over 70% (at the level of S_{21} = -3dB). The scheme of device, the principles of operation and measured results are presented in the paper.

INTRODUCTION

Antenna leads for the supply of RF signals into isolated high-voltage electrodes are used in the microwave and accelerator technology [1-3].

RF antenna lead was developed for current management of high voltage gun for electron accelerator. The operating frequency is 2450 MHz. The lead must have both high breakdown strength and low microwave losses.

The requirements for the device are following:

1) the transmission coefficient at the operating frequency of 2450 MHz must be more than 0.85;
2) the reflection coefficient at the operating frequency must be less than 0.1;
3) the breakdown voltage must be not less than 60 kV;
4) the leakage currents must be less than 10 μA;
5) the bandwidth of the transmission coefficient on the level -3 dB should be not less than 30 MHz;
6) the power flux density at 1 m from the lead should not exceed 10 μW/cm^2.

DESIGN AND PRINCIPLE OF OPERATION

Figure 1 shows the scheme of the lead. The lead presented consists of two symmetrical parts of coaxial half-wave resonator. The resonator is spitted along the perpendicular to the longitudinal axis plane of symmetry and solid dielectric disk is located between the halves.

The operating scheme is following. Microwave signal from a generator feeds the resonator by coaxial line. The excited mode of electromagnetic field is *TEM*-type. Taking into account the dielectric disk, the cavity length is chosen so that the resonator length fits a half of wavelength.

According to the structure of the *TEM* mode standing wave, the radial electric field has maximum at the location of the dielectric disc; angular components of the magnetic field, longitudinal currents on the inner and outer conductors of the coaxial line have minimum.

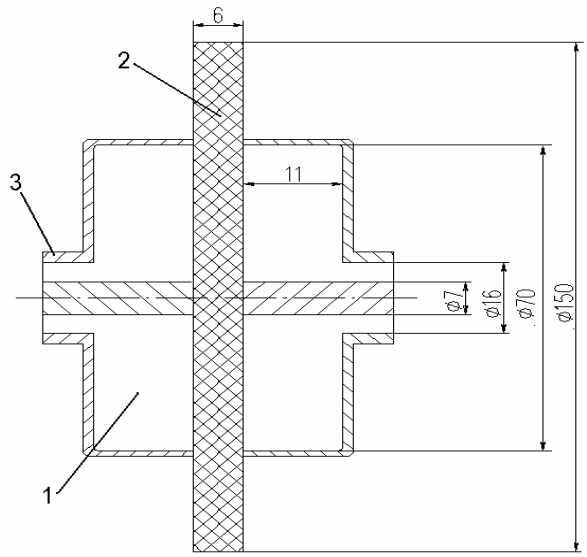

Figure 1: RF antenna lead design: 1 – half of coaxial resonator, 2 – dielectric disk, 3 – coaxial feed line.

The gap of coaxial line, which is set between the dielectric insulating discs, does not rupture the longitudinal currents and does not violate the cavity field structure. For these reasons, the reflected and radiated waves are not formed and the microwave signal passes the cavity without losses.

The breakdown strength of the device is determined by the breakdown voltage of the insulating dielectric. In our case, the dielectric material is formed from ceramics VG-4. The ceramic parameters at the operating frequency of 2450 MHz are following: the relative dielectric constant is 9.6, dielectric loss tangent is $<5\cdot10^{-4}$, the breakdown voltage is >150 kV/cm.

NUMERICAL SIMULATION

Ansoft HFSS [4] was used to calculate the basic characteristics of the device. Sizes of the resonator and thickness of dielectric disk were varied. The purpose of the calculations was to minimize the transfer attenuation and the amplitude of the reflected wave at the operating bandwidth in terms of the transmission coefficient S_{21} = -3dB. Also, the internal losses and radiation losses into the environment at the operating frequency were minimized.

Figure 2 shows the near field at a distance of 1 m from the lead (Y-axis coordinate is directed along the resonator axis). To calculate the characteristics of the device, the following parameters of the microwave signal were used: pulse duration – 5 μs, duty cycle – 1000, pulse power – 1 kW and frequency – 2450 MHz.

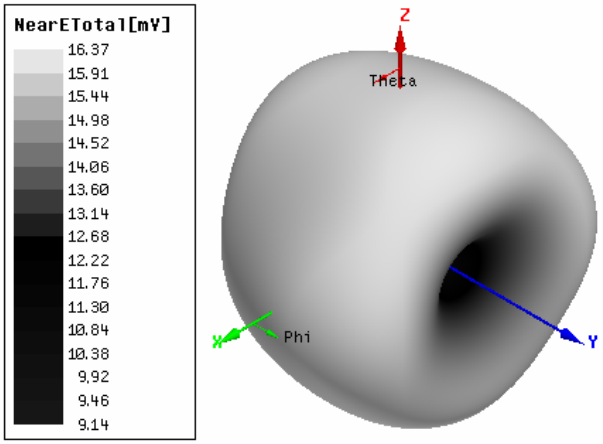

Figure 2: The flow of the electric field vector at a distance 1 m from the lead.

The amplitude-frequency characteristics of the calculated lead are shown in Figure 3.

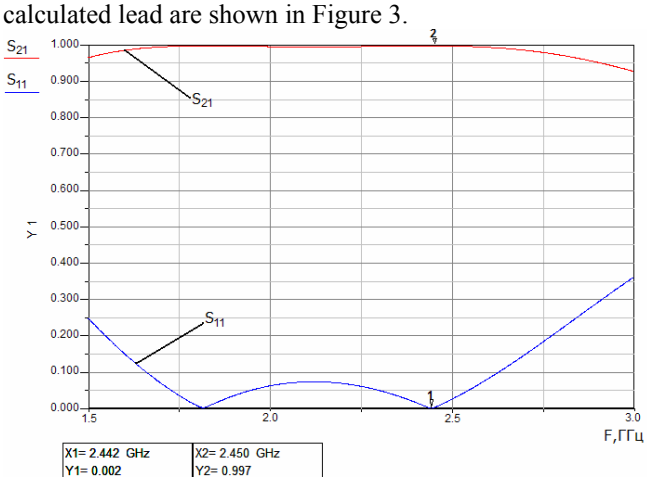

Figure 3: Dependence of the reflection coefficient S_{11} and the transmission coefficient S_{21} on frequency.

The transmission coefficient at the operating frequency is $S_{21} = 0.997$ and the reflection coefficient is $S_{11} = 0.002$.

To estimate the value of RF field radiation from device to environment we can use the following expression. The level of radiation power into the environment is equal to [5]:

$$P_r = P\left[1 - \left(S_{21}^2 + S_{11}^2\right)\right] \quad (1)$$

where P is the power in supplying line.

Taking into account the near field (Fig.2) one can see that the intensity distribution is close to a spherically uniform one, so the power density can be estimated by the equation:

$$p_r = \frac{P_{rad}}{S_{sph}}, \quad (2)$$

where $S_s = 4\pi R^2$ is area of a sphere which are limited the volume around the device, R is the radius of the sphere. Taking into account (1), S_{21}=0.997 and S_{11}=0.002 the losses of RF power radiation at the operating frequency does not exceed 0.5% of the generator power. The density of the pulsed flux power calculated by (2) at a distance 1 m from the antenna is equaled to 0.042 mW/cm^2. The density of the average flux power is 0.042 μW/cm^2.

Figure 1 shows the geometry of the main elements of the device corresponding to the characteristics obtained in numerical simulation. These dimensions were used in manufacturing of the device.

MEASUREMENTS

The reflection and transmission coefficients of manufactured device were measured in a wide range of frequencies. The leakage currents were measured with applying voltage of 60 kV. The maximum of the leakage current was 10 μA. Under high voltage the current quickly increased and the breakdown occurred.

Figure 4 shows the measured bandpass characteristics. The reflection coefficient at the operating frequency is 0.098 and the transmission coefficient is 0.976.

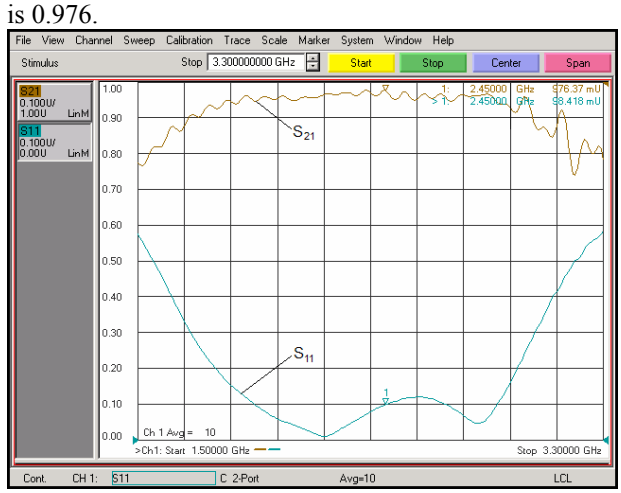

Figure 4: The transmission S_{21} and reflection S_{11} coefficients in a wide frequency range.

The bandwidth at attenuation level -3 dB is more than 1800 MHz (73%). Figure 5 shows a comparison of measured and calculated transmission characteristics of the device. Near the operating frequency the difference between measured and calculated values is less than 3% and the unevenness of the experimental curve is about 1.5%.

The level of radiated power calculated by (1) is not more than 6%. Accordance (2) the flux density of radiated power at the distance of 1 m from the lead is 0.48 μW/cm^2.

Table 1 lists the main parameters to be met by the device, the results of calculation and measured results of the device developed.

Differences between measured and calculated characteristics are present due to non-ideal RF components such as connectors, cables and transitions that introduce additional reflections and attenuations. In simulation, the effect of insulating plexiglas body around the device was not taken into account.

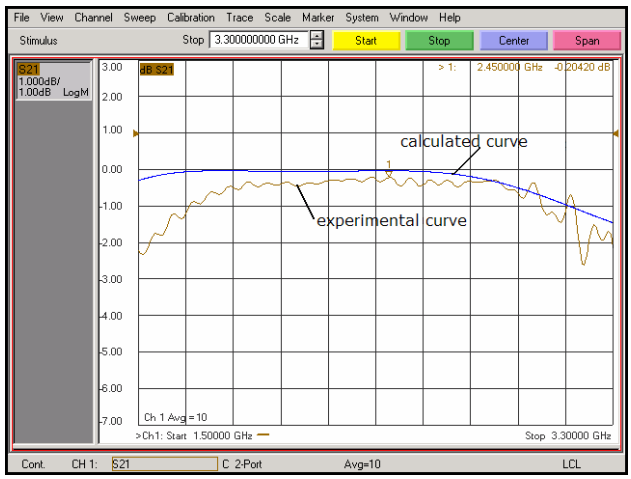

Figure 5: Frequency dependence of the transmission attenuation (S_{21}, dB). Comparison of calculated and experimental curves.

Also deviations from the actual geometry such as, for example, rounding sharp edges and corners of the electrodes of the resonator were not taken into account. The unevenness of transmission curve is probably due to the presence of standing waves in the measuring cables.

Table 1: Main parameters of RF lead

Parameter	Require-ment	Calcu-lation	Experiment
Breakdown voltage, kV	>60	>60	>60
Leakage current, μA	<10	-	<5
Transmission coefficient S_{21} at 2450 MHz	>0.85	>0.997	>0.97
Reflection coef-ficient S_{11} at 2450 MHz	<0.1	<0.002	0.098
Bandpass (at level S_{21}= -3 dB), MHz	>30	>1800	>1800
Radiation den-sity at 1 m dis-tance, μW/cm^2	<10	<0.05	<0.5

CONCLUSIONS

RF antenna lead was developed and designed by numerical simulation. Device parameters satisfy all requirements. The experimental results show good agreement with calculations and confirm high dielectric strength, low RF losses with wide bandpass. The device (Fig.6) is used in the injection current control of three-electrode electron gun to study parameters of the accelerator with parallel coupled accelerating structure [6].

This work is supported by the Ministry of Education and Science of the Russian Federation (grants №14-740-11-0836).

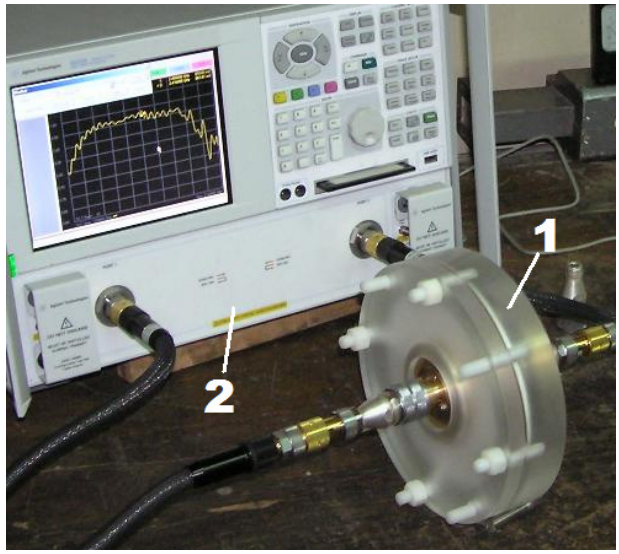

Figure 6: RF antenna lead. The measuring stand: 1 – the lead, 2 – measuring circuits Agilent N5230A.

REFERENCES

[1] A.S. Bogomolov. Pulsed electron injector. A.s. №438357. Publ. in BI, 1975, № 47, p.170.

[2] A.S. Bogomolov, E.M. Zacutov. Three-electrode electron gun with a grounded anode and the microwave grid modulation of the beam. PTE, 1973, № 3, p.23.

[3] R. J. Becker et al. 1-GHz Modulation of a High-Current Electron Gun. Nucl. Instrum. Methods. A307, (1991), p.543.

[4] HFSS. Users Guide., Ansoft Corporation, Pittsburgh, 1999.

[5] D. Mattei, L. Young, E.M.T. Jones. Microwave filters, matching circuits and circuits of coupling. M: Sviaz, 1971.

[6] A.E. Levichev, V.M. Pavlov, V.I. Ivannikov, I.V. Shebolaev, Yu.D. Chernousov. Prototype of Parallel Coupled Accelerating Structure. Proceedings of EPAC 2008, JACoW publication, pp. 2737-2739.

MULTIPACTOR DISCHARGE IN THE ELINAC ACCELERATOR

M.A.Gusarova, I.I.Petrushina, National Research Nuclear University "MEPhI", Moscow, Russia
V.L. Zvyagintsev, TRIUMF, Vancouver BC, Canada

Abstract

This paper concerns numerical simulations and experimental investigation of multipactior discharge in accelerating cavities and the feeding waveguide section of the eLINAC accelerator. The threshold values of the accelerating gradient and of the input power, at which the discharge may occur in these structures, have been obtained experimentally and compared to predictions of numerical simulations. The issues of the influence of secondary emission yield on a discharge growth were also considered.

INTRODUCTION

TRIUMF has recently embarked on the construction of ARIEL, the Advanced Rare Isotope Laboratory [1]. The superconducting electron linear accelerator (eLINAC) was developed under this project. It will be used as a photo-fission driver for the production of short-living rare isotopes. The TRIUMF eLINAC layout with the construction phases is shown in Fig. 1. The elliptic 9-cell accelerating cavities were developed in the TRIUMF laboratory [2] based on the well-known TESLA cavities [3]. The cavity will accelerate 10 mA current up to energy of 10 MeV. Two input CPI couplers [4] with an average operating power of about 60 kW are used for each cavity.

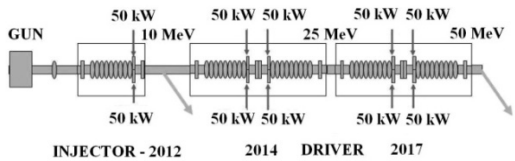

Figure 1: TRIUMF eLINAC layout

Each 9-cell cavity will operate with an acceleration gradient of E_a = 10 MV/m. It is quite safe goal for production. This class of cavities achieved operation gradients of 25-30 MV/m. However, it is necessary to study this structure with respect to the probability of multipactor discharge.

Multipactor discharge (secondary electron discharge) is the undesirable resonant particle number growth in the vacuum space of the RF structure. It may lead to a series of negative effects. The electron avalanche could consume RF power and limit level of the accelerating field. The electron bombardment may cause an overheating of the structure and a quench effect, when the material becomes normal conducting. Therefore, multipacting investigations are important for the RF structure development.

MULTIPACTING SIMULATIONS FOR THE 1-CELL ELLIPTIC TEST CAVITY

The Simulation Results

The investigations were carried out for the elliptic 1-cell superconducting Niobium TESLA cavity. The cavity model and main geometry parameters are shown in Fig. 2 and Table 1.

The special code for multipacting simulations Multp-M has been used [5]. The dependence of secondary particle count vs. accelerating gradient (considering the transit-time factor TTF = 0.52) was obtained for different secondary electron yields (SEY) which correspond to the various methods of the surface treatment (Fig. 3).

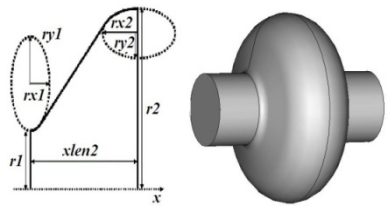

Figure 2: The 1-cell cavity geometry.

Table 1: Main geometry parameters of the 1-cell cavity

xlen2, MM	r1, MM	r2, MM	rx1, MM	ry1, MM	rx2, MM	ry2, MM
56.7	39	103.3	9	12.8	42	42

The generalized plot for the accelerating gradient in the range of 0-30 MV/m is shown in Fig. 4. The main peak of particle growth is obtained at low levels of the accelerating field. The influence of the SEY is insignificant for this kind of calculations; the dependence is the same and the difference is only in the height of the main peaks.

Stable multipacting trajectories of order 2-4 were obtained in the range of 2.6 - 6.3 MV/m and 27.9-35.5 MV/m of the accelerating gradient for over 40 RF periods. The stable 1-2 order multipacting trajectories are obtained in a range of 6.3 – 27.9 MV/m of the accelerating gradient. The latter are the most dangerous.

The direct multipacting simulations were performed in order to find the structure areas which undergo multipacting.

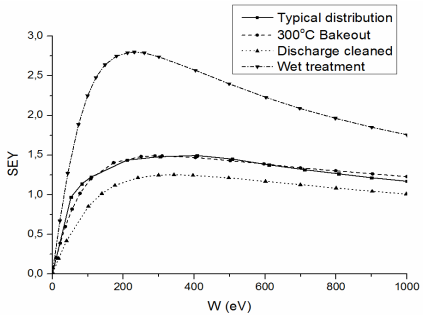

Figure 3:SEY for Nb(various methods of treatment)

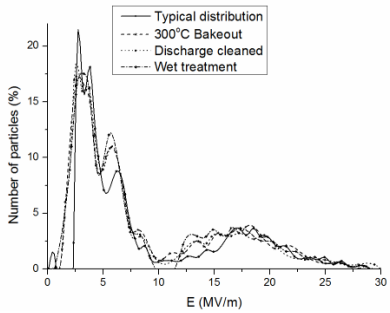

Figure 4: The number of secondary electrons in the cavity as a function of the accelerating gradient for different SEY.

The results show that the exponential increase in particle number is obtained in the range of 2.6 – 24 MV/m of the accelerating gradient. This growth indicates the probability of multipacting. Multipacting occurs in the equatorial region of the accelerating cavity. Various SEYs influence the rate of an electron avalanche formation.

THE EXPERIMENTAL RRESULTS

The 1-cell superconducting cavity tests were performed by the Canadian laboratory TRIUMF. The geometry of this cavity is shown in Fig. 2 and the vertical installation (facility) for the cavity testing is depicted in Fig. 5. Two series of experiments for various methods of the cavity treatment were done. The dependence of cavity quality Q_0 vs. accelerating gradient E_a is shown in Fig. 6. These experimental data were obtained during the conditioning of the structure.

The cavity quality factor reached $1.4 \cdot 10^{10}$ at the operating temperature 2 K and an accelerating gradient up to16 MV/m. The results showed that the cavity is capable to provide the specified operating parameters: value of the cavity quality factor was about 10^{10} at operating accelerating field of 10 MV/m. The line marked by a star in Fig. 6 corresponds to a power dissipation of 1.1 W in the 1-cell cavity. This value corresponds to the nominal value of the dissipation 10 W in the 9-cell accelerating structure. Intersection of this line with Q-curve shows value of accelerating gradient which can be obtained in the 9-cell cavity with the same degree of treatment as the tested one. The value of this field is 9 MV/m. This parameter can be improved by further conditioning of the cavity. However, it was not possible due to the power limit for the test input coupler.

Figure 5: Vertical stand for 1-cell testing.

The conditioning will be done after the test input coupler modification. Multipactor discharge was obtained at levels of the accelerating field above 11 MV/m. Multipacting limited the accelerating gradient without field emission (radiation).

The Q-curve shows that the quality factor starts to decrease at a field level of about 6 MV/m. Possible reason of the quality decrease is stable multipacting in this case. Presumably, multipacting appeared in the regime which was close to the stationary one.

Comparing the experimental Q-curves with the simulation results, one can make the conclusion that the reason of the quality factor decrease in the first series of measurements was stable multipactor discharge. An initial stage of the quality factor decrease corresponds to the accelerating field region in which dangerous 1st and 2nd order multipacting trajectories are obtained numerically.

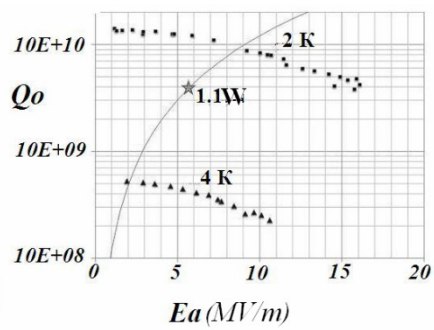

Figure 6: The quality factor as a function of the accelerating gradient

THE 9-CELL ACCELERATING STRUCTURE

Multipacting simulations were performed for the 9-cell superconducting accelerating cavity which was developed by TRIUMF laboratory for the eLINAC [2].

Multipacting occurs in the equatorial region of the elliptic cavities at lower levels of the accelerating field in comparison to the 1-cell structure. Stable multipacting trajectories of order 2-4 were obtained in the range of 1.32 - 3.08 MV/m of the accelerating gradient over 40 RF periods. The stable 1-2 order multipacting trajectories are obtained in a range of 3.08 – 17.16 MV/m of the accelerating gradient.

INPUT COUPLER

Multipacting simulations were performed for the CPI input coupler [4]. The ceramic window is the most dangerous part of the input coupler, which may undergo multipacting. Overheating due to multipactor discharge may lead to serious structural damage of the window.

The simulations were performed for the "cold" ceramic window area. The input coupler consists of the coaxial line with diameters of the outer and inner conductors d_{out} = 62 mm, d_{in} = 28.8 mm (an area between the "warm" and "cold" windows) and the conical transition part, which contains the ceramic window and the coaxial line with diameters d_{out} = 62 mm, d_{in} = 22.8 mm (an area between the window and the cavity). The simulations have been carried out in two steps: firstly for the coaxial lines and then for the conical part containing the ceramic window.

The dependence of secondary particle count vs. power for two kinds of the coaxial lines were obtained. Multipacting appears in the coaxial line with a smaller gap between the outer and inner conductors at lower transmission power levels (above 15 kW). This power level for the coaxial line with a bigger gap is above 49 kW. The motion of the particles has been investigated in detail. The simulation results showed that the stable trajectories at power levels of about 60 kW are high order multipactor trajectories, which are not so dangerous as 1st or 2nd order trajectories in the cavities.

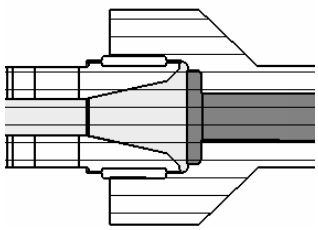

Figure 7: The coupler geometry

However, the multipactor trajectories were obtained on a surface of the ceramic window at power levels of about 50 kW being the most dangerous.

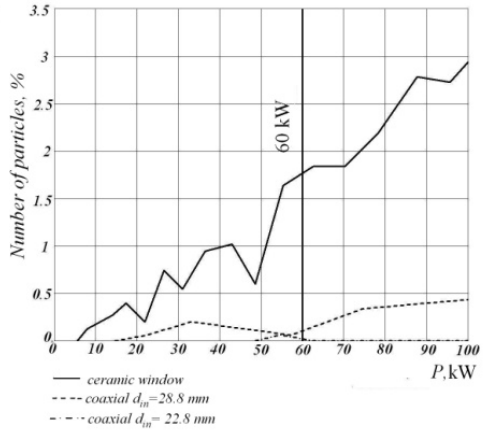

Figure 8: Number of particles as a function of the power.

REFERENCES

[1] L. Merminga et al., "ARIEL: TRIUMF's Advanced Rare Isotope Laboratory", Proceedings of IPAC2011, San Sebastian, Spain, September 4-9, WEOBA01, p 1917-1919, 2011

[2] V. Zvyagintsev et al., "Nine-Cell Elliptical Cavity Development at TRIUMF ", SRF 2011, Proceeding of SRF2011 Conference, Chicago, USA, July 25 - 29, 2011, MOPO020.

[3] B. Aune et al., "Superconducting TESLA cavities" Phys. Rev. ST Accel. Beams 3, 092001 (2000) ,

[4] V. Veshcherevich, I. Bazarov, S. Belomestnykh, "A High Power CW Input Coupler for CORNELL ERL Injector Cavities", SRF 2009, p 722-725, 2009

[5] M.A. Gusarova et al., "Multipacting simulation in accelerator RF structure", Nuclear Instrument and Methods in Physics Research A, 599. P. 100-105, 2009

176 MHZ SOLID STATE MICROWAVE GENERATOR DESIGN

A. Smirnov, A. Krasnov, K. Nikolskiy, N. Tikhomirova, E. Ivanov, S. Polikhov
Siemens Research Center, Moscow, Russia
O. Heid, T.Hughes, Siemens AG, Erlangen, Germany

Abstract

This paper concerns the R&D work upon design of a compact RF amplifier to be used for linear accelerators. The machine under development will operate at 176 MHz with output power of 25 kW in continuous wave regime. It consists of 50 push-pull PCB modules (approx. 500W output power each), connected in parallel to several radial filter rings, which both allow class-F operation and combine the power from the modules, delivering it to a single 50 Ohm coax cable. The CST simulations and the design of 324 MHz test prototype are presented.

INTRODUCTION

High power RF sources are important elements for most of linear accelerators that have found growing number of applications in physics and medicine.

The main benefits of the generator under development will be its smaller size, perspective of lower cost, better reliability and higher efficiency, achieved with class-F operation, compared to conventional RF power sources like klystrons. The solid-state microwave power modules based on SiC vJFET transistors arranged in parallel push-pull circuits, will be designed on PCB boards.

All modules will be connected to a power combiner with common output 50 Ohm coaxial cable.

This generator is planned to be a predecessor to the 'big' 324 MHz machine with pulsed RF output power of 3 MW.

RF POWER MODULES

We have designed and manufactured compact RF power modules with one pair of SiC transistors arranged in circlotron topology [1] as shown on Fig.1.

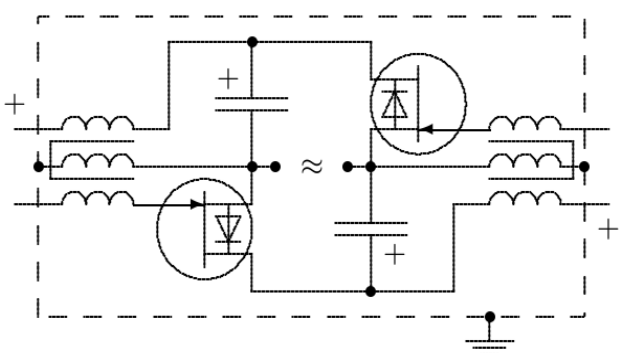

Figure 1: Parallel push-pull circuit

The manufactured module layout is presented on Fig.2. We used Rogers 4003C with ε=3.55 as a substrate material. The transistors are fed with 180^0 phaseshift, provided with external balun. The module provides maximum available gain of 18.9 dB at output power of 2.0 kW and with supply voltage of 150 V.

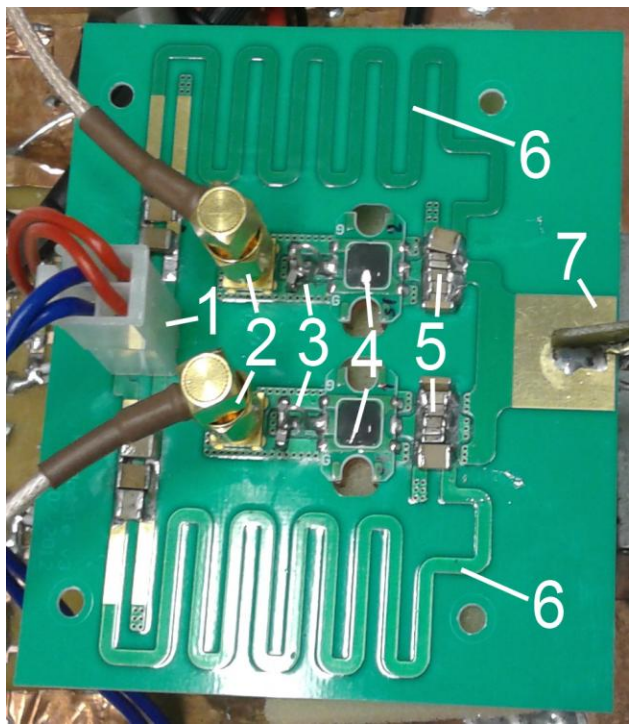

Figure 2: RF power module (heat sink is not shown):
1 – DC supply voltage; 2 – RF inputs; 3 – input matching circuit; 4 – SiC transistors; 5 – DC-blocking capacitors; 6 – quarter-wavelength lines; 7 – symmetric output stripline

Each transistor will be mounted on a water-cooled heat-sink with a sinter paste, as shown on Fig. 3, which can dissipate up to 300 W average thermal power.

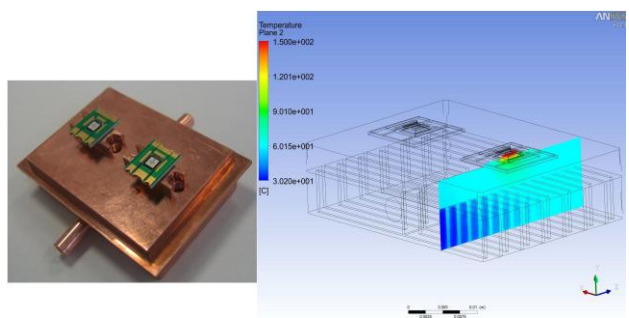

Figure 3: Transistor package mounted on a water-cooling module with temperature distribution

POWER COMBINER

In [2], a possibility of parallel power combining with use of a resonant cavity was shown. In this work, we present a non-resonant power combiner concept based on a stepped coaxial line, shown on Fig 4. It benefits in avoidance of energy storage and thus in lower power dissipation.

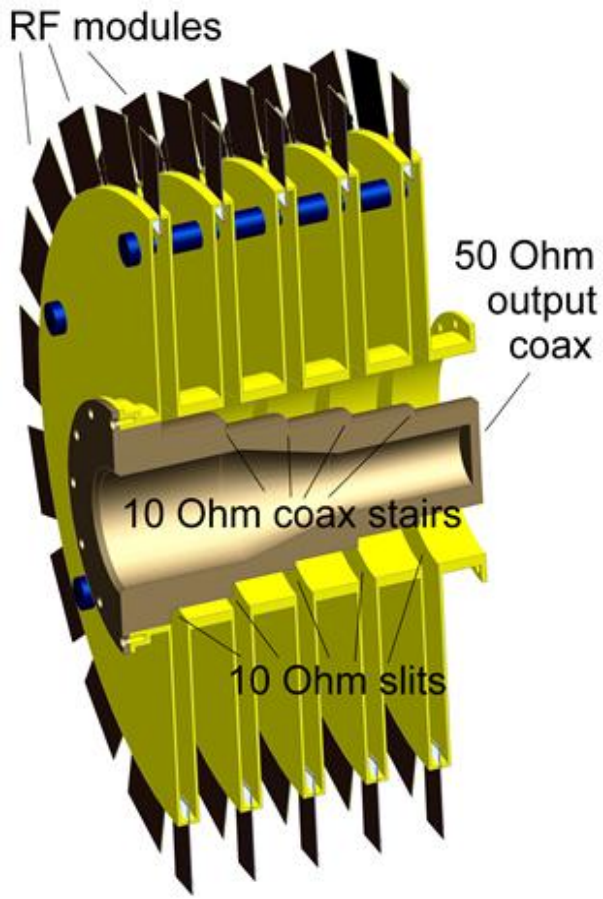

Figure 4: Stepped-line power combiner

The inner conductor represents sequence of coaxial segments with impedances from 10 to 50 Ohm with 10 Ohm steps. The whole number of modules can be distributed among 5 rings that are mounted on the outer conductor of the coaxial cable and feed it through 5 circumferential slits, each ring having output impedance of 10 Ohm.

Due to the offsets between the rings the drive amplifier must provide the phase shift between the groups of RF modules hooked up to each ring. Meanwhile, the distance between the first and the last slits must not exceed quarter-wavelength to avoid the resonance in the coaxial cable.

Each ring has to be surrounded with metal housing that introduces high shunt inductance which will serve to reduce the power leakage.

RADIAL FILTER

In combination with a suitable resonant load, the RF module can operate in class-F mode at very high efficiencies (over 85%). In an ideal class-F operation, current and voltage are shifted in phase by 180^0, the output voltage waveform having square shape and the drain current being sine-like. A filter at the drain of the transistor with the proper values of input impedances at fundamental frequency and at odd harmonics is required to shape the waveforms [3]. The shaping minimizes the overlap of the voltage and current waveform which reduces power dissipation in the transistor and increases the efficiency.

Henceforth, we consider the third harmonic filter only. Even harmonics are shorted inside each RF module.

The input impedance constraints for the filter are as follows:

let

$$Z_{module}^{1}=R^{1}+jX^{1}$$
$$\text{and } Z_{module}^{3}=R^{3}+jX^{3}$$

be the output series impedances of a single RF power module at fundamental frequency and at the third harmonic respectively. Since we need to extract the power at fundamental with high efficiency and to reflect the third harmonic back in-phase, the input impedance Z_{filter} has to

- compensate the imaginary part at both frequencies;
- provide power dissipation in the load higher than in the transistors by a factor of 10 (~90% efficiency);
- behave as an open-circuit at odd harmonic

or

$$Z_{filter}^{1}=10R^{1}-jX^{1}$$
$$\text{and } Z_{filter}^{3}=500R^{3}-jX^{3}$$

at the fundamental frequency and the third harmonic respectively.

We design the filter which fulfills these two complex constraints using four λ/16 transmission lines (four segments) with different line impedances. We calculate the line impedance of each filter segment using scattering matrix approach, taking into account that the filter eventually acts like an impedance transformer of the load R_{load}; see Fig. 5.

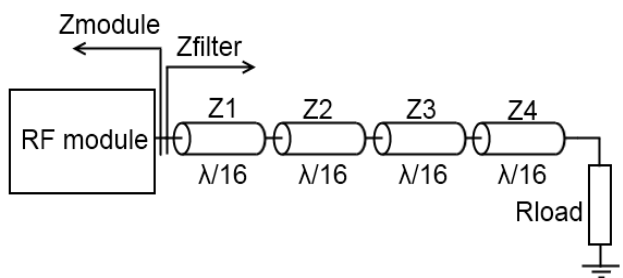

Figure 5: Filter schematics

The preferable concept of the filter design is to use segments formed from radial transmission lines, driven with non-dispersive TEM-like wave. This leads to a filter

that serves to a plurality of the RF modules connected in parallel through horn antennae as shown on Fig.6.

We use CST Microwave Studio to optimize the filter interior shape in order to get desired input impedance values at the antennae tips, to which the modules are connected.

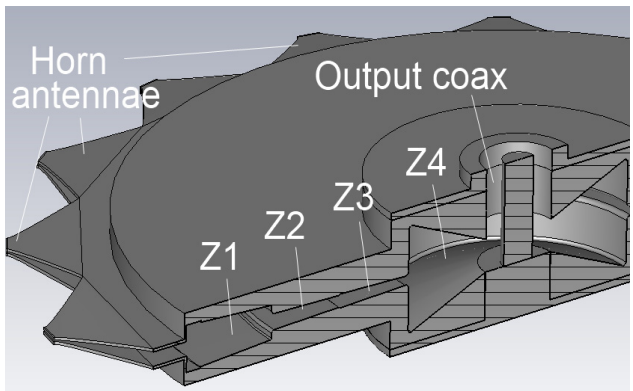

Figure 6: Radial filter CST model

The numerical simulations showed that the radial filter made of copper will dissipate 4.5 times less power than in case of using stripline-based filters connected to the output of each RF module individually. This filter geometry can be easily embedded inside every ring of the power combiner.

Test prototype

In order to verify the CST predictions we have designed one filter ring with 16 horn antennae (see Fig. 7), which is currently under manufacture.

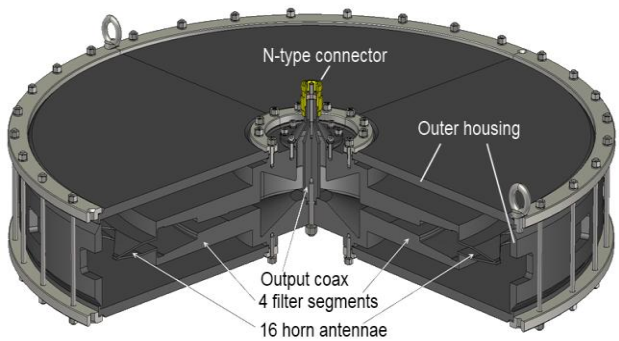

Figure 7: Test prototype CST model

SUMMARY

We have described our preliminary design of the basic RF generator components. The next steps will improve the RF modules' performance in terms of output power and gain; reduce the size of the power combiner by shortening each filter segment and by tuning each horn antenna shape to make it work as the first filter segment itself.

REFERENCES

[1] R. Irsigler, M. Back, O. Heid, Th. Kluge, J. Sirtl, "Compact Solid State RF-modules for Direct Drive RF-Linacs", IPAC2011, San Sebastian, Spain

[2] O. Heid, T. Hughes, "Compact Solid State Direct Drive RF Linac Experimental Program", HB2010, Morschach, Switzerland

[3] F. H. Raab, "An introduction to class-F power amplifiers", RF Design, vol 19, no. 5m pp. 79-84, May 1996

STATUS OF INR DTL RF SYSTEM

A.V.Feschenko, A.I Kvasha, V.L.Serov, INR RAS, Moscow

Abstract

INR Linac is in regular operation since 1993. The accelerator incorporates DTL and DAW structures operating at 198.2 MHz and 991 MHz correspondingly. Initially two types of high power vacuum tubes specially designed for INR DTL (GI-54A for final amplifier and GI-51A for intermediate amplifier) were used in the RF power system. However production of these tubes has been stopped resulting in a need of DTL RF system upgrade. The main goal of the last upgrades is replacement of the old tubes by modern ones as well as development and implementation of series crowbar system. Replacement of the tubes is not an easy task, because new tubes have to be installed in the old structures. The results and the experience of INR DTL RF system upgrade are presented.

INTRODUCTION

Last time information on the status of INR DTL RF system has been presented eight years ago [1]. Since then several significant upgrades have been done in the DTL RF system including the series crowbar system implementation [2,3] and replacement of powerful grid tubes in both intermediate power amplifier (IPA) and final power amplifier (FPA). Since 1993 up to now grid tubes GI-51A and GI-54A have been in operation in IPA and FPA, correspondingly. However, at the beginning of the nineties manufacture of the above tubes at CSC "SED.-SPb" (former name – Electron Device Mfg. Corp. "Svetlana") has ceased and INR DTL RF system operation continued only due to the earlier plentiful supplies. At the same time the new grid tube GI-71A ("Katran") [4] was developed and designed in the CSC "SED-SPb" as the alternative to GI-54A. The requirement for GI-71A was to keep the dimensions and the anode-grid capacity C_{ag} about the same as for GI-54A in order to avoid essential reworking of the anode-grid cavity.

GI-71A tubes have been tested in the final power amplifiers of INR DTL RF system for ten years. Now they are installed in four of five FPA, including the most powerful amplifier for the third drift tube cavity.

Replacement of GI-51A (tetrode) by GI-57A (triode) appeared to be more complicated task and additional investigations were required.

RESULTS OF THE SERIES CROWBAR SYSTEM LONG TERM OPERATION

The series crowbar system (SCS) has been described earlier [2, 3]. At that time the system was in operation for 700 hours only. By now it is in operation for more than 5000 hours. The system cuts off anode HV pulse in case of discharges or sparking in IPA or FPA. One should note that the SCS can be realized only for vacuum tube modulators, which is the case in INR DTL RF system. Now the modulator is intended for three purposes:

1. Generation of the anode high voltage pulses for IPA and FPA tubes.
2. Control of the anode voltage with the aim of stabilization of the accelerating field amplitude.
3. Protection of IPA and FPA grid tubes in case of sparking or discharges inside of the tubes.

There are two main reasons of crowbar system activation.

The first one is due to HV breakdowns in the anode-grid cavity. Neither in IPA nor in FPA blocking capacitors are used for separation of HV and RF circuits. HV is applied to the central conductor of the coaxial cavity at the node of RF electric field. The voltage between the central conductor and the ground is a superposition of the anode pulse voltage and the cavity RF one. RF voltage is an order of magnitude higher than the anode voltage and the probability of RF breakdown is not negligible. The RF breakdown initiates HV breakdown, and, as a result, the full discharge of modulator storage device capacitors. The activated series crowbar system cuts off the modulator pulse thus preventing discharge of the capacitors and excessive local energy dissipation.

The second reason is breakdown or sparking in the grid tube directly. We have no possibility to preliminary age new tubes so there are numerous breakdowns for several days after installing new grid tubes in RF amplifiers. Earlier each sparking inside the tube resulted in interruption of accelerator operation for 10-15 minutes. New series crowbar system enables to diminish the interruptions to a few sec only. As a result we have got a possibility to age tubes during accelerator operation and have essentially decreased beam interruptions.

INTERMEDIATE POWER AMPLIFIER

Utilization of new grid tube GI-57A in IPA instead of GI-51A was not a trivial task not only due to different sizes of the tubes but also due to different modes of operation: GI-51A has operated with common cathode and GI-57A is foreseen for common grid operation.

Changing of the tube resulted in a need of additional calculation of the anode-grid cavity electrodynamics. Eigen mode frequencies as well as field distributions have been calculated and analysed. Special attention was paid to field distribution in the loop area as well as to higher modes that could be excited.

The model of the anode-grid cavity is shown in Fig.1.

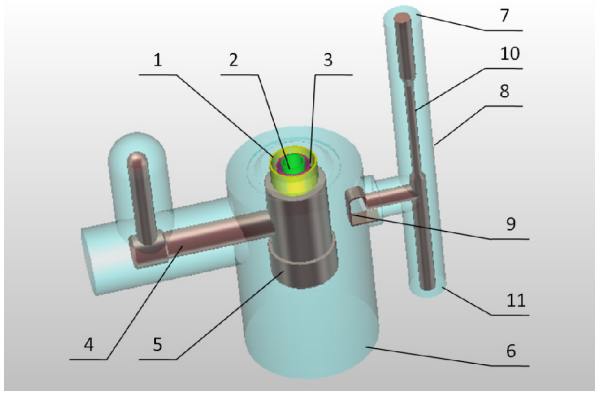

Figure 1: Model of the IPA anode-grid cavity.

The following designations are used: 1,2 and 3 - cylindrical electrodes of anode, grid and ceramic seal of the tube; 4 - unit for supplying high voltage pulse and cooling water to anode; 5 - nozzle at central conductor of the coaxial cavity, which can be moved by several millimetres; 6 – outer conductor of the cavity; 7 – RF power output; 8 – short-circuited coaxial line with moving piston 11; 9 – loop; 10 – λ/4 transformer.

Unit 8 along with λ/4 transformer 10 and moving piston 11 is aimed to properly transform the 50 Ohm load impedance to the loop and to the anode-grid gap.

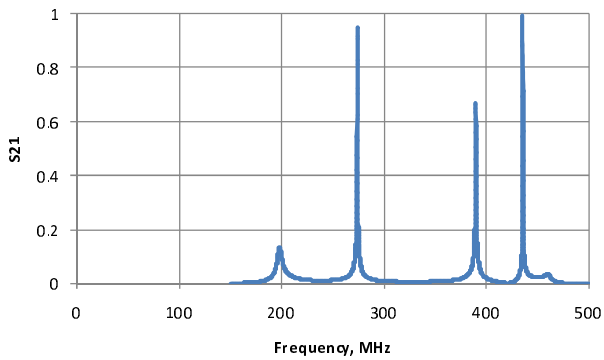

Figure 2: IPA anode-grid cavity frequency spectrum.

The geometry and the dimensions of the tube electrodes in the model do not exactly correspond to those of the real tube. The dimensions of tube electrodes were varied in the model to obtain the same operating mode frequency as in real installation. It has been verified that changing the configuration of tube electrodes with corresponding trimming of the dimensions to maintain resonant frequency does not result in observable change of RF field distributions in the main volume of the cavity except the neat tube area.

Typical IPA cavity frequency spectrum is shown in fig.2. The first f_{01} and the third f_{02} lines are of special interest. The first one is the operating frequency and the third one is very close to the second harmonic of the operating frequency. The line f_{02} can be excited by the second harmonic of the anode current.

Distributions of electric and magnetic fields at frequency f_{01} are presented in fig. 3 and 4.

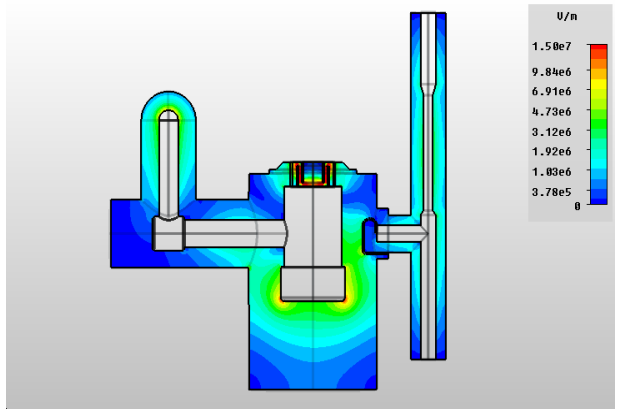

Figure 3: Distribution of electric field.

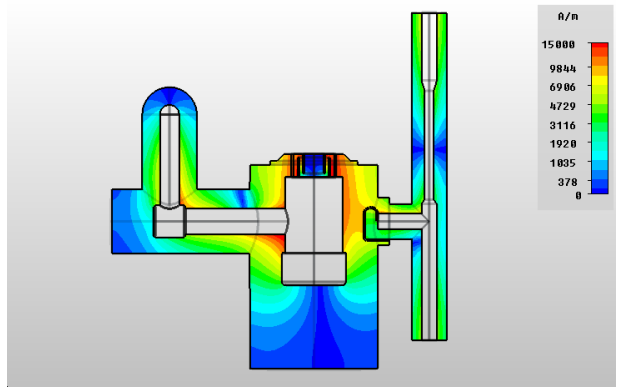

Figure 4: Distribution of magnetic field.

Analysis of the distributions as well as other results of simulations enables to formulate some conclusions and recommendations. Coupling loop is located in the region of about maximum magnetic field and there is no need to move it. Electric field between the central conductor nozzle and the bottom of the cavity is very week and, hence, frequency tuning by means of bottom displacement is ineffective. Anode-grid cavity tuning procedure includes tuning the resonant frequency as well as the equivalent resistance of anode-grid gap R_{oe} in order to maximize power transmitted to the output [5]. These adjustments are not independent and can be done with nozzle 5 and shortening piston 11. Frequency mode f_{02} has a maximum electric field in a loop-central conductor area. Adjustment of the nozzle position as well as the cavity bottom position in order to shift resonant frequency f_{01} of the operation mode simultaneously shifts the frequency f_{02}. For some positions the exact relation $f_{02}=2 \cdot f_{01}$ is obtained thus resulting in effective excitation of f_{02} mode by the second harmonic of anode current which is dangerous from the point of view of breakdowns.

COMMON OPERATION OF IPA WITH TUBE GI-57A AND FPI WITH TUBE GI-71A

Installation of tubes GI-57A and GI-71A was done in several stages. At the first stage tubes GI-71A were only installed in FPA of the less powerful RF channels for the first and the fifth DTL cavities (nominal power 1÷1.2

MW). Long-term successful operation enabled to proceed further modernization. At the second stage tube GI-71A only was installed in RF channel for the forth DTL cavity and several problems have been revealed. To obtain the nominal power near 2 MW anode voltage had to be increased by 3÷4 kV. Local overheating of the coaxial line from IPA to FPA was also observed.

The next stage was installation of GI-57A in IPA instead of GI-51A in the forth RF channel. Though GI-57A is a triode, whereas GI-51A is a tetrode, the value of IPA output power has increased for the same input power. Nominal power at the output of FPA was obtained for smaller anode voltages and anode and grid currents of FPA thus indicating improvement of FPA efficiency. The tandem of GI-57A and GI-71A operated in the forth RF channel for 6000 hours. Though the problems of breakdowns in the coupling loop area of IPA and overheating of the coaxial line from IPA to FPA have not been overcome generally positive results of operation as well as the lack of tubes GI-54A for FPA enabled to proceed to the next stage – installation of GI-57A and GI-71A in the most powerful channel (2.5 MW) for the third DTL cavity.

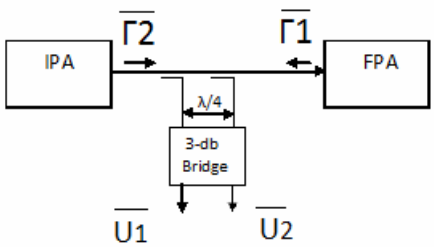

Figure 5: Directional coupler for matching measurement

In the second RF channel all the above listed problems notably increased. Due to absence of circulators between IPA and FPA breakdowns in IPA and overheating in coaxial line could be due to bad matching with FPA. To verify this version the simplest directional coupler has been installed between IPA and FPA (fig. 5). If loop sizes and lengths of cables from loops to bridge are identical, then $U_1 = kU_{inc}(1+\overline{\Gamma}_1\overline{\Gamma}_2)\overline{\Gamma}_1$ and $\overline{U}_2 = k\overline{U}_{inc}(1+\overline{\Gamma}_1\overline{\Gamma}_2)$, where U_{inc} - amplitude of the incident wave. In this case the value of reflection can be found as $\Gamma_1=U_1/U_2$. After retuning of FPA cathode-grid cavity (by changing of short circuit coaxial cavity length) the value of the reflection coefficient Γ_1 has been decreased by a factor of 2÷3 and the situation has been noticeably improved.

Figure 6 demonstrates experimental behavior of output power (upper curve), anode current of GI-57A (middle curve) and anode current of GI-71A (lower curve) versus anode voltage, kV. The anode voltage is common for the two tubes. The FPA output was connected to powerful matched terminator.

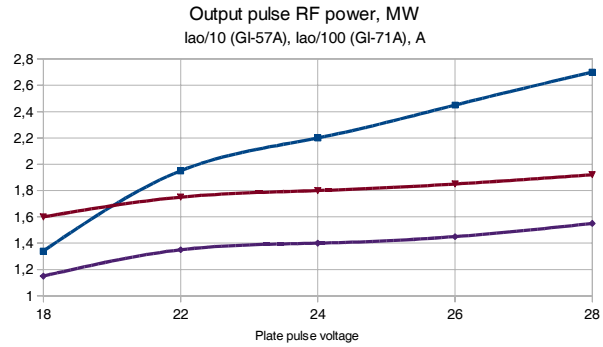

Figure 6: Experimental dependencies of FPA output power and anode currents of GI-57A and GI-71A.

CONCLUSION

The most significant INR DTL RF system upgrades for the last eight years were development and implementation of the series crowbar system as well as replacement of powerful grid tubes in the intermediate and final power amplifiers. The modernization not only decreased the problem of the tubes deficiency but also increased the efficiency of RF channels. Installation of new tubes in the next in power RF channel #2 is scheduled for the end of this year.

REFERENCES

[1] A.I.Kvasha “Linac Moscow Meson Factory DTL RF System Upgrade”, Linac 2004, (THP54), Lubeck, Germany, p.733.

[2] A.I.Kvasha. V.L.Serov "Development of the INR DTL RF System Crowbar Operation", RUPAC2008, Dubna, p.218.

[3] A.I.Kvasha, Yu.M.Lopatnikov "Results of the INR DTL series crowbar system testing", Journal "Problems of Atomic Science and Technology", series "Nuclear Physics Investigation" (54), #3, 2010, p.13-17.

[4] A.I.Kvasha, etc., "A new 200MHz Powerful Pulse Triode for the Output Power Amplifier of DTL RF System", PAC2001, Chicago, (MPPH318), p.1222.

[5] A.I.Kvasha “Numerical calculation of vacuum tube power amplifier mode of operation”, Journal "Problems of Atomic Science and Technology", Series "Nuclear Physics Investigation" (58), #3, 2012, p.29-33.

INVESTIGATION OF INR DTL RF SYSTEM OPERATION AT 100 HZ REPETITION RATE

A.N.Drugakov, A.V.Feschenko, A.I.Kvasha, A.N.Naboka,V.L.Serov, Institute For Nuclear Research, Moscow 117312, Russia

Abstract

INR Linac has been operating with 50 Hz beam repetition rate so far. Increasing the repetition rate up to 100 Hz is of importance as it results in doubling of the beam intensity. To solve the task several accelerator systems have to be modernized but the most critical one is DTL RF system (up to 100 MeV). The problems related to DTL RF system repetition rate increasing are described. One of the problems is a 50 Hz modulation of a 100 Hz RF pulse sequence. Though the instabilities of accelerating field due to the modulation are reduced by the feedback systems, nevertheless investigation of the effect and its minimizing is of importance. The analysis of the effect is given and the results of experimental studies are presented. Other problems to be overcome to increase the repetition rate are mentioned as well.

INTRODUCTION

Operation with the repetition rate of 100 Hz was foreseen by initial design of INR linac [1]. However since commissioning for more than twenty years accelerator operated with 50 Hz repetition rate satisfying requirements of beam users. Recently the goal of doubling of the repetition rate has been formulated with the aim of increasing the beam intensity and efficiency of the accelerator. Several problems have to be solved: increasing of the repetition rate of HV proton injector, commissioning of beam pulse separation system [2] etc. However the most complicated task is related to RF system of the accelerator. The accelerator consists of low energy part (100 MeV, DTL, 198.2 MHz) and high energy part (600 MeV, Disk and Washer structure, 991 MHz). Initial tests of RF equipment with 100 Hz repetition rate revealed modulation of rf field pulses with 50 Hz frequency. One of the origins of the effect was found to be biperiodic triggering of rf equipment. Accelerator clocking pulses are coupled to one of the mains phases and a 100 Hz sequence is generated at zeroes of 50 Hz voltage. Due to distortions of sinusoidal waveform the clocking pulses were not equidistant thus resulting in a different levels of charging of pulse forming lines used to generate HV pulsed for klystrons (high energy part) and power grid tubes (low energy part). Special measures taken to provide exact periodicity of 100 Hz series enabled to eliminate the effect for high energy part but appeared to be ineffective for low energy part. Further study showed that the main reason of the effect in low energy part is using of AC current for directly heated cathodes of power grid tubes.

DTL RF SYSTEM

DTL RF system includes seven RF channels: one for RFQ and six for five accelerating cavities, one of them being a spare channel. A simplified block diagram of one RF channel is shown in fig. 1. The channel represents a four stage amplifier (K1÷K4) with two anode pulse modulators MB and M1.

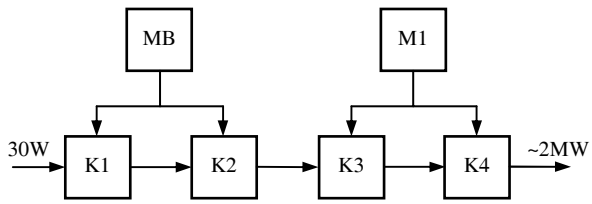

Figure 1: Block diagram of DTL RF channel.

Both amplifier stages and pulse modulators use power grid tubes. The upgrade of DTL RF system with replacement of grid tubes is under way now [3]. The type of grid tubes used in RF channels at present is given in table 1.

It will be shown that the mode of cathode heating (direct or indirect) is essential for 100 Hz operation. It is listed in table 2 for all the types of tubes used in DTL RF system.

Table 1: Type of grid tubes

Unit	RF channel						
	RFQ	1	2	3	4	5	6
K1,K2	GS-31B	GS-31B	GS-31B	GS-31B	GS-31B	GS-31B	GS-31B
K3	GI-51A	GI-51A	GI-51A	GI-57A	GI-57A	GI-51A	GI-51A
K4	GI-54A	GI-71A	GI-54A	GI-71A	GI-71A	GI-71A	GI-54A
MB	GMI-34A	GMI-34A	GMI-34A	GMI-34A	GMI-34A	GMI-34A	GMI-34A
M1	GMI-44A	GMI-44A	GMI-44A	GMI-44A	GMI-44A	GMI-44A	GMI-44A

Table 2: Mode of cathode heating

Tube	GS-31B	GI-51A	GI-57A	GI-54A	GI-71A	GMI-34A	GMI-44A
Directly heated cathode		*	*	*	*		*
Indirectly heated cathode	*					*	

50 HZ MODULATION OF 100 HZ RF PULSE SEQUENCE

After switching the RF channels from 50 Hz mode to 100 Hz mode of operation a 50 Hz modulation of RF channel output power and hence of the envelopes of RF fields in DTL cavities was immediately revealed. As an example Fig. 2 demonstrates a screen view of oscilloscope with the envelopes of RF field in DTL cavity

#5 and modulator M1 output pulses. The 100 Hz series represents a superposition of two 50 Hz trains shifted in time by 10 ms.

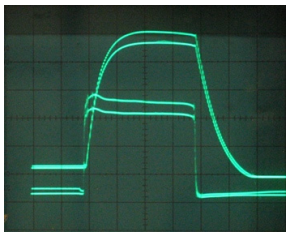

Figure 2: Typical envelopes of RF field in accelerating cavities (upper beam) and stages K3-K4 anode pulses (lower beam). Horizontal scale – 100 μs/div.

This information is routinely available for operator and the first explanation of RF field modulation was corresponding modulation of modulator M1 pulses. Several effects were considered as the reason of modulator pulses biperiodicity but the most realistic appeared to be 50 Hz modulation of cathode-grid bias in the M1 modulator tube GMI-44A. The cathode of the tube is a directly heated one and is powered from two phases of the mains. Filament voltage modulates cathode-grid bias, the magnitude of modulation being different for different point along the cathode. This effect is specific for tubes with directly heated cathodes and must be absent for tubes with cathodes heated indirectly. This statement is confirmed by observations of RF power at the output of stage K2. Neither modulator MB nor stages K1 and K2 use tubes with directly heated cathodes (Table 2). As a result no power modulation at the output of K2 is observed.

The duration of RF pulses is equal to 400 μs, which is appreciably smaller than the period of 50 Hz mains. In this case the bias is almost invariable within the beam pulse, its value being dependent on the modulator triggering delay with respect to the mains. Figure 3 demonstrates RFQ modulator M1 pulses for two delays with respect to the mains. The left picture corresponds to triggering at the maximum of filament AC voltage and the right one - at zero. One can see that proper triggering delay effectively minimizes the effect of modulator pulses biperiodicity.

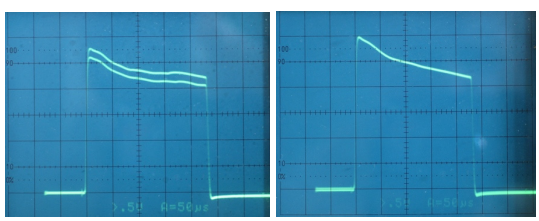

Figure 3: Modulator pulses for different delay with respect to the mains.

Initially the filaments of the modulator tubes were powered from different phases of the mains. To remove modulation of the pulses we have powered the filaments of all the modulator tubes from the same phases of the mains and have triggered modulators at a zero point of AC filament voltage.

One should note that the pictures presented in Fig. 2 and Fig. 3 were observed with no modulator pulse stabilization and no saturation of the tube. In reality both measures are used thus decreasing the effect. Fig. 4 demonstrates the same pulses as in Fig. 3 but with modulator tube input saturation as well as stabilization of the pulse flat top.

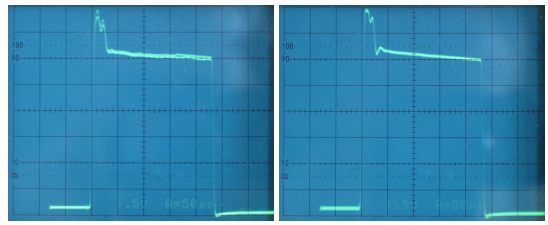

Figure 4: Effect of modulator tube input saturation and stabilization of the pulse flat top.

Minimization of modulator pulses biperiodicity resulted in decreasing of 50 Hz modulation of RF channels output power but not to complete elimination of the effect. An assumption was done on existence of similar effect of the bias modulation in the RF tubes, also with directly heated cathodes, used in K3 and K4 stages (Table 1, 2). The effect is not related to the tube GI-54A as its cathode is heated with a current supplied from the 12-phase rectifier with minor pulsations.

The filaments of the tubes GI-71A are power from two phases of the mains similarly to the modulator tube GMI-44A. In RF channels #1 and #3 adjustment of the filament power is done by changing the voltage with induction regulators and in channels #4 and #5 - by thyristor phase control. In order to minimize bias modulation in the tubes GI-71A their filaments have been switched to be powered from the same phases of the mains as modulator tubes GMI-44A. Filament voltages of GI-71A and GMI-44A for RF channel #4 are presented in Fig.5. The modulator is triggered when the filament voltage is near zero.

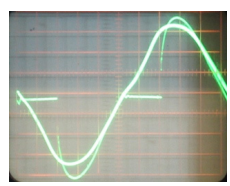

Figure 5: Filament voltages of GI-71A and GMI-44A for RF channel #4.

Unlike GMI-44A and GI-71A the filaments of the tubes GI-51A and GI-57A are powered from one phase of the mains. In this case exact phasing of their filament voltages with those of GMI-44A and GI-71A is impossible and the minimum possible phase difference equals 30°. Adjustment of the heating power is done with bidirectional triode thyristor phase control. It turned out that for the nominal heating power the thyristor is closed when the GMI-44A filament AC voltage crosses zero, which is demonstrated in fig. 6. In this case the RF modulator is triggered when the distortion of the cathode-grid bias is small.

The above described measures resulted in essential reduction of the effect of accelerating field modulation in all DTL cavities. Figure 7 demonstrates a dependence of deviations of the amplitudes of even and odd pulses of the 100 Hz series of the RF field in the anode-grid cavity of K4 stage of channel #5 versus delay with respect to the phase of the mains. One can see that the value of deviation is close to zero within the delay range of 3÷7 ms. Similar behavior of pulse modulations was also obtained for RF fields in all accelerating cavities. The middle of the above range of 5 ms was selected as a reference for triggering of all the accelerator equipment. As an example Fig. 8 demonstrates the envelope of RF field in DTL cavity #2 as well as modulator M1 pulse. No visible modulation can be observed.

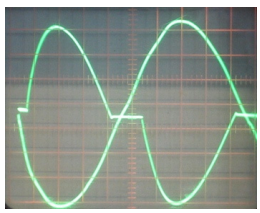

Figure 6: Filament voltages of GI-51A and GMI-44A for RF channel #2.

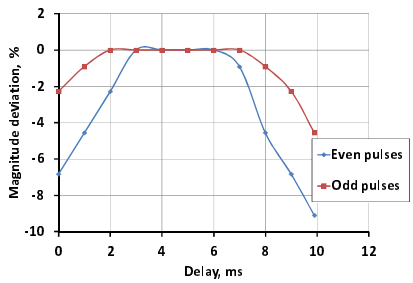

Figure 7: Deviation of even and odd pulses of RF field in anode-grid cavity vs delay.

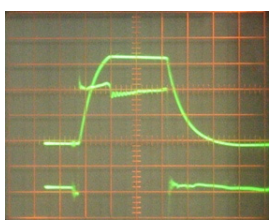

Figure 8: Envelope of accelerating field in DTL cavity #2 (upper beam) and modulator M1 pulse.

ADDITIONAL PROBLEMS

Additionally to the above described problem several other problems must be solved to implement a 100 Hz mode. Among them the most important are:

Doubling of Average RF Power

Doubling of the repetition rate results in doubling of RF power dissipating at grid and plate of powerful vacuum tubes GI-57A and GI-71A, anode-grid and cathode-grid resonators of RF power amplifiers, coaxial transmitting lines between K4 and drift tube cavities, numerous RF junctions etc.

Increasing the Cavity Warm-Up Time After Switching Off the RF Power Due to Breakdowns or Other Reasons

DTL cavity resonant frequency control is done by means of drift tube cooling water temperature control. Water temperature is varied by changing the electric heater power and the flow of water through heat exchanger. Before switching RF power on the drift tubes have to be warmed up to the resonance temperature and after switching on the temperature of cooling water has to be decreased to maintain the cavity drift tube temperature invariable. The value of water temperature decresing depends on the cavity and amounts to several degrees at 50 Hz repetition rate. In case of unexpected switching RF power off the temperature of the drift tubes goes down to water temperature in 10÷15 s. Subsequent switching RF power on is possible only after warming up the whole amount of water to the cavity temperature. The warm up time is proportional to the temperature change and one can show that this change in its turn is proportional to the average RF power. For 100 Hz repetition rate the warm up time increases up to 20÷30 minutes thus essentially decreasing availability of the accelerator beam.

Increasing of High Voltage in the Pulse-Forming Lines of the Modulators M1

In pulse modulator M1 plate voltage supply of GMI-44A is realized by means of a pulse forming line (PFL) as storage device. The PFL consists of 20 cells with time discharge 400 μs and impedance ρ = 24 Ohm. The DC load of the PFL is near 200 Ohm and, hence, it operates with partial discharge [4]. A recovery time of PFL charge is determined by HV rectifier parameters (choke inductance and internal resistance) and full capacity of AFL and is near 30 ms. As follows from measurements, at 100Hz repetition rate rectifier HV value has to be increased at 4-5 kV.

CONCLUSION

The problem of 50 Hz modulation of 100 Hz RF pulse series in DTL RF system of INR linac has been investigated. The solution found enables to essentially eliminate the problem providing the base for further activity in increasing the intensity of INR linac. Several other problems exist and their contributions in accelerator operation at 100 Hz repetition rate require additional studies.

REFERENCES

[1] B.P.Murin et al. Linear Ion Accelerators. Atomizdat, Moscow, 1978, V.1,2.
[2] N.I.Brusova et al. Beam Pulse Separation System of INR Linac, WEPPC003, these proceedings.
[3] A.V. Feschenko et al. Status of INR DTL RF System, MOPPA022, these proceedings.
[4] A.I.Kvasha. V.L.Serov "Development of the INR DTL RF System Crowbar Operation", RUPAC2008, Dubna, p.218.

X-RAY RADIATION HIGH-VOLTAGE ELEMENTS OF THE TANDEM ACCELERATOR WITH VACUUM INSULATION

I. Sorokin #, A. Bashkirtsev, A. Ivanov, D. Kasatov V., A. Kuznetsov, S. Taskaev, V. Chudaev,
BINP SB RAS, Novosibirsk, Russia

Abstract

In Institute of Nuclear Physics SB RAS the epithermal neutron source is entered into operation based on the tandem – accelerator with vacuum isolation. There was evaluated the accelerating installation components of a x-ray field causing dark current and breakdowns in accelerating gaps. The estimated account of equivalent doze capacity on different distances from the accelerator in the protected hall and behind its limits is made.

The experimental measurements were carried out and the study results of the doze capacity dynamics are submitted, depending on change of a dark current in tandem accelerating gaps at a complete working voltage 1 MV without a beam. The spectrum of x-ray radiation is experimentally measured. It is experimentally revealed and the occurrence of powerful X-ray radiation is investigated at substantial growth of the aperture of the accelerating channel. The design changes of installation for prevention of occurrence of powerful X-ray radiation are offered and realized.

The carried research allows setting necessary parameters for designing medical installation on the basis of an accelerator - tandem with vacuum isolation with the purpose of realization in oncological clinics neutron-capture therapy of malignant tumors.

INTRODUCION

In the BINP, the prototype of epithermal neutrons source in an innovative high-current tandem accelerator with vacuum insulation has been proposed [1] and constructed [2]. It is attractive to be accommodated in oncological clinics for carrying out boron neutron capture therapy of malignant tumors.

In the high-voltage vacuum components of the installation, electrons of auto emission and discharge origin, which are the basic elements of the parasitic "dark" current [3] and are accelerated in a vacuum gaps, emit X-rays after braking at the electrodes, which is the main source of radiation hazard in operation without the accelerated charged particles beam. The study of the unused X-ray field of the installation and the method to reduce its radiation hazard to an acceptable level is an urgent task, as the accelerator is being developed for medical purposes.

EXPERIMENTAL MEASUREMENT OF X-RAYS LEVELS ON THE INSTALATION

For operational monitoring of X-ray radiation levels around the experimental installation and for its biological defense, tandem is equipped with automatic radiation monitoring system (provided services) [4], developed in BINP.

Dose rate measurements of photon radiation in the system are carried out by four detecting units (Fig. 1),

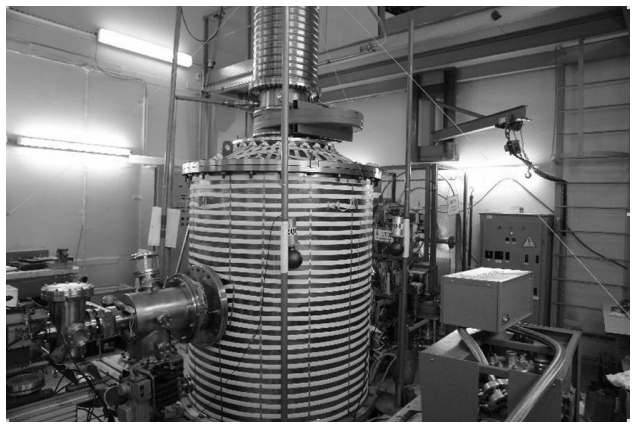

Fig. 1. Placement detection units around the accelerator.

Fig.2. Detection unit dose power of photon radiation.

based on the spherical ionization chambers (Fig. 2) with an air-filling 0.85 liter volume and with a thickness of polyamide wall about 1.1 mm, coated with a thin layer colloidal graphite.

Using the organic dielectric, as a wall material, can reduce overall dimensions and weight of the detector and can help to avoid significant deterioration in the camera's sensitivity to low-energy radiation. The dynamic range of the detector is - 1 ÷ 12 000 mcSv/h.

To determine the uniformity level of X-ray radiation in the azimuth plane, around the accelerator at a distance of

1 m from the external surface of the tank there were placed four detection units through 90°. After the data record, all the blocks were shifted by 45° and measurements were repeated. To filter out the values, clearly associated with the breakdown and pre-breakdown currents, which can be determined by voltage divider indications of the high-voltage source and the insulator, by a sharp deterioration of the residual vacuum in the tandem, by a throws of dark current I and X-ray dose power D (Fig. 3)[5].

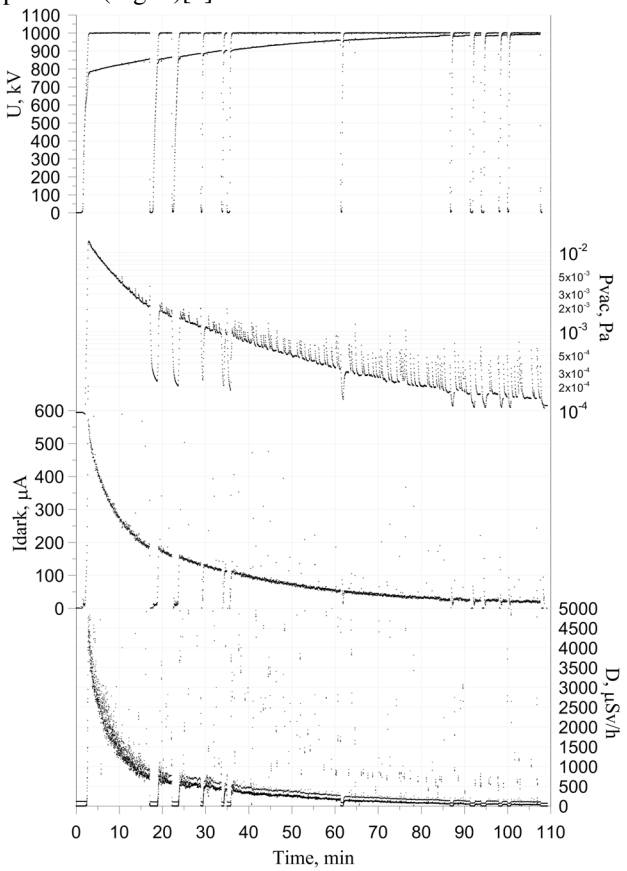

Fig.3. Typical graphics of the voltage, vacuum, dark current and dose X-rays with the 4 detectors on time.

The results of X-rays measurements in all the experiments were processed by using the software implemented algorithm of statistical data processing.

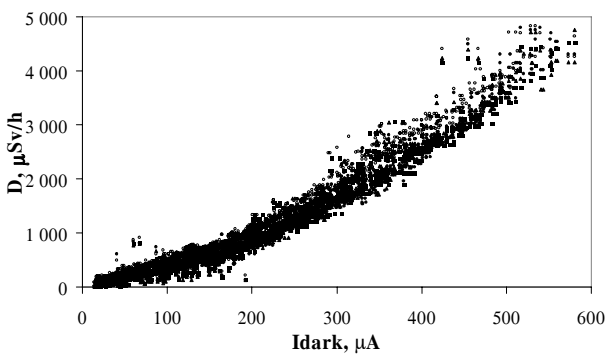

Fig. 4. Dependence of X-rays on the value of the dark current.

Fig. 4 shows the dependence of the X-ray power dose of all four detectors on the dark current. It can be seen, that with good accuracy the radiation power is proportional to the dark current. Fig. 5 shows the average measured values from three consecutive experiments for the dark current values I = 300 ± 10 mA and the voltage on the high-voltage electrode 1 MV. It can be seen, that the radiation can be considered uniform within 20%, which means a relatively uniform distribution of dark currents on the electrode surfaces.

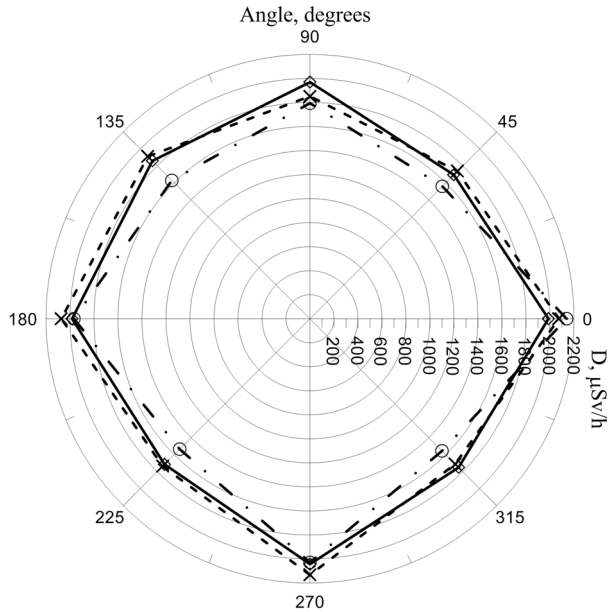

Fig.5. Angular distribution of the X-ray radiation accelerator.

The measurement results of the X-ray intensity by sensors, located at 2, 3.3 and 4.2 m from the center of the accelerator in the horizontal plane at the center height of the accelerator, are in agreement with the calculated, assuming a point source, with an accuracy ~ 8%. This result confirms the relatively even distribution of dark currents on the electrode surface.

The experiments have showed, that for training time ~ 1 ÷ 2 hours, the level of X-ray field is greatly reduced. Thus, at a distance of 2 m from the accelerator, X-ray dose is reduced from 1000 mcSv/h to ~ 10 mcSv/h. The vacuum value of ~ 10^{-4} Pa. Dynamics of changes in the dark current showed that the main cause of its occurrence is the gas desorption from the tank and electrode surfaces. To reduce output time to a safe level of the X-ray radiation it is necessary to increase the vacuum pumping speed.

ENERGY SPECTRUM OF X-RAY RADIATION

With using BGO-spectrometer, installed inside the protected room at a distance of 6.3 m from the center of the accelerator, the X-ray energy spectrum was measured (Fig. 6). At the moment of the spectra measurement, the residual gas pressure was 4 10-4 Pa, dark current value

was 65 ± 3 mA, and the ionization chamber registered the dose 34 ± 4 mcSv/h at the distance of 4 m. This spectrum confirmed well the initial data point, that achieved electron energy must not exceed the value of 200 keV, determined by the difference in potential between adjacent electrodes accelerating gaps.

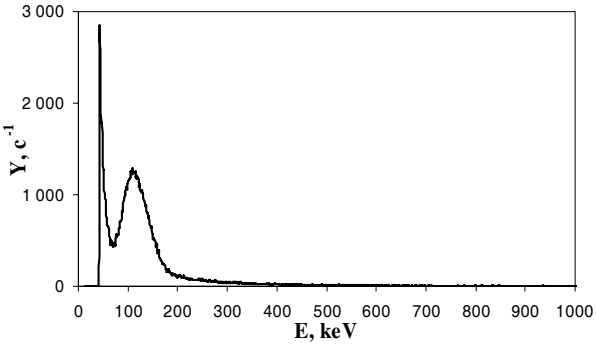

Fig. 6. Measured energy spectrum of X-rays.

THE DARK CURRENT OF GREAT INTENSITY AFTER INCREASING APERTURE ACCELERATING CHANNEL

Following an increase in the aperture of the accelerating channel up to 58 mm there was recorded the dark current 3 - 4 mA [6] with a much greater intensity of radiation than dark currents studied in [3] and described above. In [6] it is found that increasing the diameter of the aperture increases the electric field strength at the sharp edge of the cathode frame hole of the mounting aperture. Electrons, emitted from the sharp edge, pass directly into the acceleration channel. The measured energy spectrum of the X-ray emission during the flow of the current high intensity is shown in Fig. 7. It can be seen that the distribution shifted to larger values of the photon energy, which confirms the conclusion made in [6], that the emitted electrons enter the accelerating channel and accelerated up to full voltage. It should be noted, that in comparison with the conditions of the experiment, described in [3], the diameters of the intermediate electrode diaphragms, which are the accelerating channel of the negative hydrogen ions, are not 58 mm, and gradually decreasing: 43, 43, 35, 30, 25 and 20 mm, which, perhaps, explains the lower value of the current - about 1 mA.

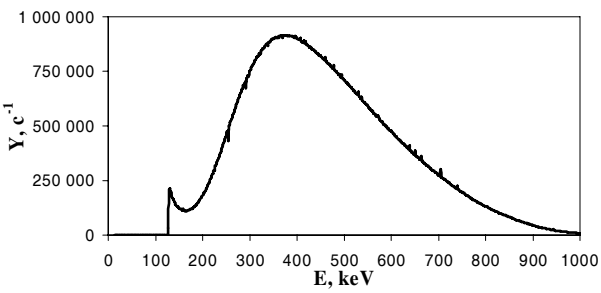

Fig. 7. Measured energy spectrum of the X-ray emission during the flow of the dark current great intensity.

RESULTS AND PROSPECTS

While accelerator training the X-rays dose at different azimuths, heights and distances was experimentally measured. It is found out that the radiation can be considered azimuthally uniform and decreases quadratically with the distance from the center of the accelerator. It is determined, that during accelerator training, the dose rate at a distance of 2 m from the accelerator does not exceed 1000 mcSv/h, and by the end of the training in 1 - 2 hours decreases to about 10 mcSv/h. Behind the existing 122-centimeter concrete wall of radiation-protected room, which houses the accelerator, the dose rate is below the sensitivity limit of the dosimetric devices.

BGO-spectrometer measured the spectrum of X-rays, characterized by energies below 200 keV to 120 keV maximally. This spectrum confirms the assumption, that during the training of the accelerator, the radiation source is dark currents in interelectrode gaps caused by auto electron emission from the surface of the vacuum tank and the accelerating electrodes.

The emergence of powerful radiation at a significant increase in the aperture of the accelerating channel is experimentally observed and studied. The measured X-ray spectrum contains photons with significant energy, up to the energy corresponding to the full voltage of the accelerator. It was determined that the emergence of intense radiation is due to dark current, flowing directly in the accelerating channel and arising with the resulting increase in the aperture of the channel due to the sharp edge hole of the cathode part mounting frame diaphragm. The design of the accelerator has been amended to prevent currents and, as a consequence, high-power radiation.

This study allows setting the required parameters for the design of medical installation based on a tandem accelerator with vacuum insulation to conduct neutron capture therapy of malignant tumors in oncological clinics.

The authors thank V.V. Extra for performing mounting, adjustment and startup of ACPM.

REFERENCES

[1] B. Bayanov, et al. NIM A 413/2-3 (1998) 397-426.
[2] A. Kuznetsov, et al., Tech. Phys. Lett. 35 (2009) 346.
[3] V. Aleynik, A. Ivanov, A. Kuznetsov, I. Sorokin. Preprint BINP 2011-19. Novosibirsk, 2011.
[4] V. Barkova, O. Koryabkin, A. Repkov, V. Chudaev. Proceedings of the Ninth Union Conference on Charged Particle Accelerators, 2, Dubna, 1985, p. 318.
[5] A. Bashkirtsev, A. Ivanov, D. Kasatov, et al., Medical Physics, №2 (54), 2012.
[6] V. Aleynik, A. Kuznetsov, I. Sorokin et al. Preprint BINP 2012-2. Novosibirsk, 2012.

RESIDUAL ACTIVITY IN HEAVY-ION ACCELERATORS AS BEAM-LOSS LIMITING FACTOR

V. Chetvertkova, E. Mustafin, I. Strasik, GSI, Planckstrasse 1, 64291 Darmstadt, Germany

Abstract

Residual activity is one of the main beam-loss limiting factor in high-energy proton accelerators. In order to ensure 'hands-on' maintenance 4 h after the shutdown, the losses of proton beam should be kept below 1 W/m. It has been shown in our previous publications that the beam-loss criteria for heavy-ion machines may be established by rescaling the '1 W/m criterion' for protons into a similar 'n W/m' criteria for different heavy ions. For protons the scaling factor is obviously 1. Scaling factors for other ions depend on the charge number of the ion and on the beam energy. For example, for U ions with energy E = 200 MeV/u the scaling factor is 60, i.e. 60 W/m losses of U beam are tolerable from the 'hands-on' maintenance point of view, whereas for U ions with E=1 GeV/u the scaling factor is just 5. In the present paper we show that this scaling factor concept has natural limits of applicability. In the case of very low beam energies or in the case of long-term accumulation of the residual activity, the tolerable beam-loss criteria cannot be obtained by simple rescaling of the '1 W/m criterion' with one single number.

INTRODUCTION

An energetic heavy ion penetrating into a bulky target typically destroys several target nuclei. Therefore the total residual activity of the target is usually dominated by the radioactive fragments of the target nuclei and has negligible contribution from the projectile fragments. As it was shown in [1] the relative number of produced radioisotopes in this case does not depend on the type of bombarding heavy ion projectile at the energy range from 200 AMeV to 1 AGeV, and the evolution of the induced radioactivity has the same time dependence for protons and all heavy ion beams. This allows rescaling the whole radioactivity evolution curve from proton induced activity to any heavy ion beam induced activity just by one number. For example, this number is 1/60 in the case of rescaling the 1-GeV-proton induced activity into the activity induced by 200 MeV/u U beam [1]. This means that the well known 1 W/m tolerable beam loss limit for proton accelerators can be rescaled to 60 W/m tolerable loss limit for a 200 MeV/u U beam machine.

This rescaling concept works only for the case when the number of created target fragments considerably exceeds the number of projectile fragments stopped in the bulky target. One could expect a violation of this concept for example in the case of low-energy heavy ion machines. Indeed, low energy heavy ions have very short ranges in a bulky target and do not develop any considerable shower of projectile fragments. Therefore, the interactions with primary projectiles play more important role compared to the production of isotopes via the secondary particles.

The other limit of the simple rescaling concept to be checked is the accumulation of the long-lived isotopes: the long-lived isotope inventory may be different than the short-lived isotope inventory studied in [1].

COMPARISON OF TOTAL ACTIVITIES INDUCED BY PROTON AND URANIUM BEAMS

To study the extremes, let's compare the total activity induced by 1 W beams of protons and U ions lost into a bulky target (a cylinder 20 cm in diameter and 60 cm long, like in [1]) made of Cu.

In order to study the long-term accumulation of isotopes and their following decay, the irradiation time and the consecutive 'cooling-down' time were chosen to be 20 years each. All calculation of the activity were done using FLUKA code [2].

As it is shown in Table 1 the evolution of the total activity has the same time dependence for both p and U beams in the case of high energy beams E=500 and 1000 MeV/u. Indeed, the ratio of the normalised activities (shown in the columns denoted as U/p in Table 1) is within about 30% spread. The normalisation of the activity is done to the end of irradiation (i.e. to the activity at time point 20 years).

Table 1: Time evolution of the total activity for 500 and 1000 MeV/u p and U beams

year	Activity, Bq, 500 MeV/u			Activity, Bq, 1 GeV/u		
	p	U	U/p	p	U	U/p
1	8.2E+9	7.2E+8	0.99	9.3E+9	1.8E+9	0.97
2	8.7E+9	7.6E+8	0.99	9.9E+9	1.9E+9	0.96
5	9.2E+9	8.1E+8	0.99	11E+9	2.0E+9	0.91
10	9.8E+9	8.7E+8	1.00	11E+9	2.2E+9	1.00
20	9.9E+9	8.8E+8	1.00	11E+9	2.2E+9	1.00
21	1.7E+9	1.5E+8	0.99	2.1E+9	3.9E+8	0.93
22	1.2E+9	1.2E+8	1.13	1.6E+9	3.0E+8	0.94
25	7.5E+8	7.6E+7	1.14	1.1E+9	1.9E+8	0.86
30	4.7E+8	4.8E+7	1.15	7.0E+8	1.3E+8	0.93
40	2.6E+8	2.7E+7	1.17	3.9E+8	7.4E+7	0.95

The same shape of the time evolution of the activities for both p and U beams indicates in the case of high-energy beams that the total activity is dominated by the same isotopes, i.e. by the isotopes produced from the target nuclei by the secondary projectiles.

The time evolution of the total activity has a different behaviour in the case of low energy p and U beams. As it is shown in Table 2 only the accumulation of the activity

during the irradiation (i.e. up to the time point 20 years) is the same for both beams (within a spread of 5%). The time evolution of the activity during 'cooling-down' is very different. Indeed, the ratio of the normalised activities U/p may be a factor of 4 in the case of 100 MeV/u beams and as big as a factor of 9 in the case of 50 MeV/u beams. In order to understand this difference let's analyse the isotope inventory more closely.

Table 2: Time evolution of the total activity for 50 and 100 MeV/u p and U beams

year	Activity, Bq, 50 MeV/u			Activity, Bq, 100 MeV/u		
	p	U	U/p	p	U	U/p
1	2.1E+9	7.0E+7	0.97	3.1E+9	1.3E+8	0.98
2	2.1E+9	7.2E+7	0.90	3.3E+9	1.3E+8	0.92
5	2.2E+9	7.4E+7	0.95	3.4E+9	1.4E+8	0.96
10	2.2E+9	7.8E+7	1.00	3.5E+9	1.5E+8	1.00
20	2.2E+9	7.9E+7	1.00	3.5E+9	1.5E+8	1.00
21	8.3E+7	8.6E+6	3.00	3.4E+8	2.6E+7	1.78
22	4.8E+7	7.6E+6	4.58	2.2E+8	2.2E+7	2.33
25	2.3E+7	6.0E+6	7.15	1.2E+8	1.7E+7	3.31
30	1.4E+7	4.4E+6	9.20	7.4E+7	1.2E+7	3.78
40	8.2E+6	2.7E+6	8.94	4.0E+7	7.2E+6	4.20

The isotopes contributing into the total activity at the time point 40 years is presented for 50 and 1000 MeV/u p and U beams in Table 3 and Table 4. The half-lives of the isotopes are presented in column denote as $T_{1/2}$ and given in years. The activities of the isotopes are presented in the column denoted Activity and given in Bq.

Table 3: Dominating isotopes contributing to the total activity of Cu target irradiated by 50 and 1000 MeV/u beams of U ions

50 MeV/u			**1000 MeV/u**		
Element	**$T_{1/2}$**	**Activity**	**Element**	**$T_{1/2}$**	**Activity**
H-3	12.33	1.72E+6	H-3	12.33	4.39E+7
Ni-63	100.11	7.51E+5	Ni-63	100.11	2.05E+7
Co-60	5.27	1.29E+5	Co-60	5.27	4.39E+6
Ba-133	10.5	9.25E+3	Fe-55	2.73	5.66E+5
Ar-42	32.9	5.91E+3	Ti-44	64.81	2.87E+5
Gd-148	74.6	5.28E+3	Sc-44	0.0004	2.23E+5
Pm-145	10.7	4.79E+3	Ar-39	268.99	1.59E+5
K-42	0.0014	4.66E+3	Ar-42	32.91	2.96E+4
Tb-157	71.0	3.27E+3	Ni-59	80004	2.68E+4
Si-32	28.8	2.99E+3	Si-32	132	2.43E+4
Sr-90	28.8	2.48E+3	K-42	0.00	2.33E+4
Ar-39	269.0	2.33E+3	Bi-207	31.55	1.98E+4
P-32	0.04	2.27E+3	P-32	0.04	1.85E+4
Y-90	0.0073	1.97E+3	Pb-210	22.30	1.79E+4

One may notice that the contribution of heavy fragments of U ions is very minor and therefore cannot influence the time evolution of the total activity.

The main contribution comes from the fragments of the target nuclei, namely from H-3 and Ni-63. The ratio of the activity of H-3 to the activity of Ni-63 is about the same (about a factor of 25) in the case of U beam of E=1000 MeV/u, p beam of E=1000 MeV and U beam of E=50 MeV/u. But in the case of p beam of energy 50 MeV the isotope Ni-63 is dominating over the isotope H-3 by a factor of 4. These isotopes have different half-lives and this makes the difference in the time evolution of the total activity.

Table 4: Dominating isotopes contributing to the total activity of Cu target irradiated by 50 and 1000 MeV protons

50 MeV			**1000 MeV**		
Element	**$T_{1/2}$**	**Activity**	**Element**	**$T_{1/2}$**	**Activity**
Ni-63	100.11	5.69E+6	H-3	12.33	2.85E+8
H-3	12.33	1.26E+6	Ni-63	100.11	1.11E+8
Co-60	5.27	1.13E+6	Co-60	5.27	2.07E+7
Fe-55	2.73	9.94E+4	Ti-44	64.81	4.64E+6
Ni-59	80004	4.09E+4	Sc-44	0.0004	3.60E+6
Co-57	0.7445	4.82E-1	Fe-55	2.73	3.09E+6
Mn-54	0.8555	9.10E-2	Ar-39	267	2.38E+6
Zn-65	0.6691	5.32E-2	Ni-59	80004	1.32E+5
Co-58	0.1940	1.3E-23	Ca-41	102993	8.40E+3
Co-56	0.2117	9.0E-24	Cl-36	300989	2.30E+3

CONCLUSION

The rescaling concept of [1] works well for the activity with the domination of the short-lived isotopes even for low energies of the ion beams and but it fails in the case of accumulation of long-lived isotopes. The reason for the violation of the concept is not the contribution of the heavy fragments created from the heavy ion projectiles. The main reason is the difference in the production rates of major contributing isotopes H-3 and Ni-63 from the interaction of protons with the target Cu nuclei at different energies.

REFERENCES

[1] I. Strasik, E. Mustafin, and M. Pavlovic "Residual activity induced by heavy ions and beam-loss criteria for heavy-ion accelerators", PRST-B 13, 071004 (2010)

[2] A. Fasso, A. Ferrari, J. Ranft, and P. R. Sala, Reports No. CERN-2005-10, No. INFN/TC_05/11, and No. SLAC-R-773 (2005).

STUDY OF DYNAMICAL APERTURE OF NICA COLLIDER WITH ACCOUNT OF MAGNETIC FIELD ERRORS AND COULOMB EFFECTS

A.Ye. Bolshakov, P. R. Zenkevich, ITEP, Moscow, Russia

Abstract

By use of MADX code beam dynamics in NICA collider has been studied. NICA collider has comparatively small kinetic ion energies (1.5-4.5 *GeV/u*) that results in essential one beam Coulomb effects. These effects are simulated by set of "BEAM-BEAM" elements with appropriate chosen strength and location. Moreover it was taken into account beam-beam interaction, system of chromaticity correction and influence of systematic and random errors of the magnetic field. The simulation results are given and discussed.

Coulomb Forces

In collider Coulomb forces result in effect of "beam-beam" interaction. In linear approximation shift of the betatron tune because of the effect is defined of so named "beam-beam parameter", which for symmetrical Gaussian beams is defined by

$$\xi = -r_i \frac{N_b}{4\pi\beta^2\gamma\varepsilon}\frac{1+\beta^2}{2} \qquad (1)$$

Here the classical ion radius $r_i = \frac{Z^2 r_p}{A}$ (r_p - classical proton radius, A and Z are atomic and charge ion numbers), β, γ – relativistic, N_b is the number of ions per bunch, ε is r.m.s beam emittance. Non-linear kick in the interaction point results in appearance of a set of non-linear resonances (see, for example, [1]). Let us use model of "frozen beam", which is assumed that this effect does not influence on a particle distribution in a phase space. In MADX code [2] this effect is described by special element (Beam-Beam element) located in the interaction point. NICA collider has comparatively small kinetic energy (1.5-4.5 GeV) and therefore there are essential "one beam" Coulomb forces, which result in shift of the betatron tune (Laslett tune shift)

$$\Delta Q = -\frac{r_i N_b}{4\pi\beta^2\gamma^3\varepsilon}F_b \qquad (2)$$

Here we assume that the beams have Gaussian distribution. The bunching factor $F_b = \frac{C_{ring}}{\sqrt{2\pi}\sigma_s}$, where C_{ring} is the ring circumference, σ_s is r.m.s. longitudinal size of a bunch. Dependence of the tune shift with longitudinal coordinate z tune shift

$$\Delta Q(z) = \Delta Q \cdot \exp\left(-\frac{z^2}{2{\sigma_s}^2}\right) \qquad (3)$$

Periodical oscillations of the tune shift because of the synchrotron oscillations result in crossing of high order betatron resonances. Coulomb shift due to simultaneous action of both effects (for two interaction points) $\Delta Q_c = \Delta Q + 2\xi = -\frac{N_b r_i}{4\pi\beta^2\gamma\varepsilon}\left[\frac{F_b}{\gamma^2} + (1+\beta^2)\right]$. In choice of machine parameters we assumed that $|\Delta Q_c| \le 0.05$. Then maximal beam intensity

$$N_b^{max} = 4\pi\beta^2\gamma\frac{|\Delta Q_c|}{\frac{F_b}{\gamma^2}+(1+\beta^2)}\frac{\varepsilon}{r_i} \qquad (4)$$

In high energy region (3-4.5 *GeV*) in NICA collider the intensity is limited by IBS and $N_b^{max} = 2.4 \cdot 10^9$ ions [3]. Let us mark that for equal tune shifts Coulomb effect due to the beam-beam interaction is more dangerous than one-beam one. Thus for given intensity the most dangerous point in high energy region corresponds to $E = 3\ GeV$. In low energy region (1.5-3 *GeV*) the intensity is defined by Eq. (3) and the most dangerous point corresponds to the lowest energy ($E = 1.5\ GeV$). In this report we choose for simulations point $E = 3\ GeV$.

Code for numerical simulations

Simulations are made using MAD-X code with account of the following factors:

1) Chromaticity correction system, which is corrected machine chromaticity and chromaticity due to sextupole errors in the collider magnets.
2) Systematic errors and random errors in the collider magnets. Systematic errors are accepted same as in paper [4] (these errors are given at Table 1). Random errors correspond r.m.s. value equal to 1/3 from systematic errors. For simplification we take into account only one set of random errors.
3) Beam-beam Coulomb forces with two similar interaction points.
4) One-beam Coulomb forces.

Table 1: Systematic errors in the magnets

$\frac{1}{BR}\left(\frac{d^2B_y}{dx^2}\right)$ m^{-3}	$\frac{1}{BR}\left(\frac{d^4B_y}{dx^4}\right)$ m^{-5}	$\frac{1}{BR}\left(\frac{d^6B_y}{dx^6}\right)$ m^{-7}
-0.027	76.312	-1.489E5
$\frac{1}{BR}\left(\frac{d^8B_y}{dx^8}\right)$ m^{-9}	$\frac{1}{BR}\left(\frac{d^{10}B_y}{dx^{10}}\right)$ m^{-11}	$\frac{1}{BR}\left(\frac{d^{12}B_y}{dx^{12}}\right)$ m^{-13}
-2.669E10	-7.507E14	-6.616E18

Calculations are made in "thin lens approximation" in order to provide a simplecticity [5]. The synchrotron motion is simulated by inclusion in lattice the cavity with voltage 1 *MV*. Initial distribution in phase space is assumed to be Gaussian one, number of macro particles is 20000-300000, number of turns 1000-5000. Influence of "one beam" Coulomb forces is taken into account by use of "beam-beam" non-linear lenses located in the centers of all lattice elements (such method was used earlier in [6]). Beams in the "beam-beam" elements are assumed to be in one direction, which allows us to describe correctly Lorentz force. Dependence of space charge force on

longitudinal distance z is reached by variation of strength this "beam-beam" lenses with z according to Eq. 3.

Dynamical aperture (DA) analysis is made in space of transverse invariants E_x, E_y, where $E_x = \gamma_x x^2 + 2\alpha_x \dot{x}x + \beta_j \dot{x}^2$, $E_y = \gamma_y y^2 + 2\alpha_y \dot{y}y + \beta_j \dot{y}^2$ (here x, y are transverse coordinates, $\dot{x}, \dot{y}$ are corresponding derivatives on variable s, $\alpha_j, \beta_j, \gamma_j$ are Twiss parameters). The beam has the following parameters: 1) number of particles per bunch $N_b = 2.4 \cdot 10^9$; 2) ion energy $E = 3\ GeV$; 3) r.m.s. beam sizes in longitudinal space $0.6m \times 1.2 \cdot 10^{-3} \frac{\Delta p}{p}$; 4) r.m.s. beam emittances in the transverse space $\varepsilon_x = \varepsilon_y = 10^{-6}\ m$.

Numerical results

Results of numerical simulations of particle trajectories are shown at Fig. 1. Calculations are made for the following bunch parameters: $\sigma_s = 0.6\ m$, $\sigma_p = 0.00125$, harmonic number $q = 72$, $V = 1\ MV$, synchrotron period $\tau_{sinchr} \approx 170 \cdot \tau_{rev}$. Number of macroparticles N_{part}=300000, number of turns N_{turn}=1000. All effects are taken into account (factors 1+2+3+4). The lost particles are marked by black points. We see from the plot that picture is very complicated.

As the first step of treatment of Fig.1 we have found for given horizontal invariant E_x value of vertical invariant E_y corresponding to the lowest value for lost particles. Typical results of such treatment are plotted at Fig.2.

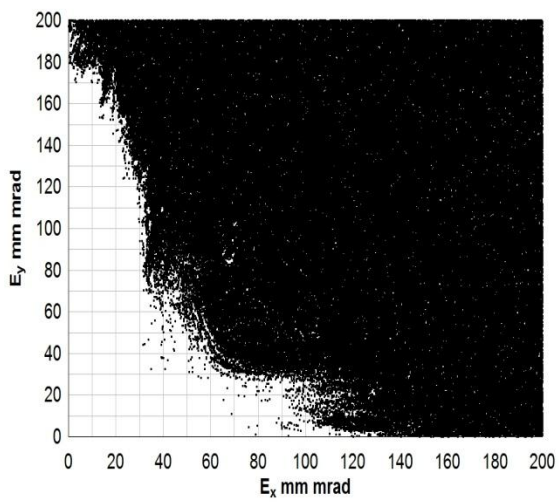

Figure 1: Results of numerical simulations of particle trajectories. Number of macroparticles N_{part}=300000, number of turns N_{turn}=1000.

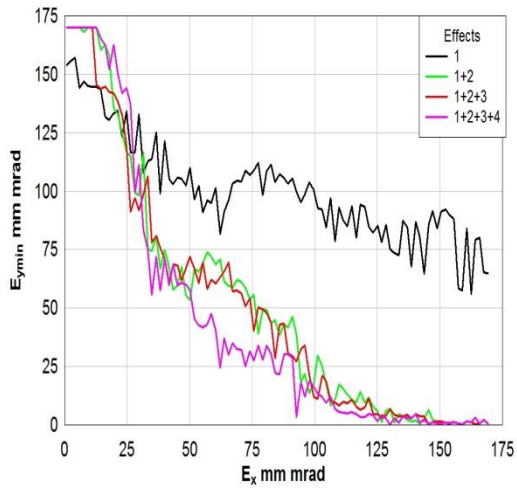

Figure 2: Dependence of minimal value of E_y on E_x for lost particles. Number of macroparticles N_{part}=20000, number of turns N_{turn}=1000.

In NICA the narrowest point is located in final focus lenses where chamber is circular that corresponds to equation $r^2 = x^2 + y^2 \le a^2$ (a is the chamber radius). Let us introduce parameter $E = E_x + E_y$; then avoiding by difference between beta functions we obtain the following condition of particle loss: $E = E_x + E_y \ge \frac{a^2}{\beta_{max}}$. We see that minimal value E_{min} of parameter E determines particle survival. Dependence of E_{min} on parameter $\mu = (\frac{\Delta p}{p})^2 / (\frac{\Delta p}{p})_{max}^2$ (here $(\frac{\Delta p}{p})_{max}$ is the separatrix half-width on momentum deviation) is given at Fig. 3 (parameter μ with good accuracy is proportional to longitudinal invariant).

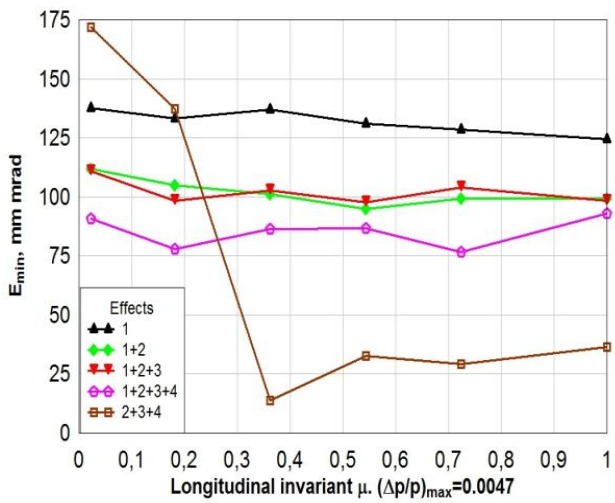

Figure 3: Dependence of E_{min} on parameter $\mu = (\frac{\Delta p}{p})^2 / (\frac{\Delta p}{p})_{max}^2$. Number of macroparticles N_{part}=20000, number of turns N_{turn}=1000.

We see from the plot that beam-beam interaction only weakly affects on DA; the more important effect is one-beam Coulomb interaction. Another important result is the sharp diminishment of DA with increase of μ in absence of the chromaticity correction system. Moreover we have studied dependence of E_{min} on number of turns N_{turn} ; results are presented at Fig. 4.

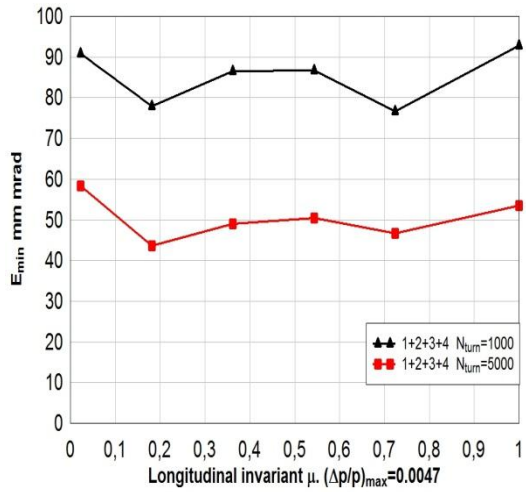

Figure 4: Dependence of E_{min} on parameter $\mu = (\frac{\Delta p}{p})^2/(\frac{\Delta p}{p})_{max}^2$. Number of macroparticles N_{part}=20000, number of turns is marked at the plot.

Discussion

We see from Fig.4 that dependence on particle number is strong. Significant diminishment of DA with number of turns shows that accepted method of results treatment has some indefinity. In fact we observe that there are particles separated from basic massive of lost particles [Fig.4]. Number of these particles increase with number of turns. This effect is connected with very complicated mechanism of particle losses in for bunched beams, which includes a lot of processes: 1) adiabatic particle capture during resonance crossing [7,8]; 2) modulational diffusion, i.e. diffusion due to random jumps of invariant because fast resonance crossing (see for example [9]); 3) some "rare" processes (for example, Arnold diffusion [9]). It is possiblewe should take into account only "basic massive" neglecting these particles. Nevertheless in a frame of this method we could make the following conclusions:

- In absence of the chromaticity correction the dynamical aperture is sharply decreased with increasing of longitudinal invariant.
- Main sources of DA reduction in presence of the chromaticity correction circuit are magnetic field errors and one-beam Coulomb forces; beam-beam interaction influence is smaller.

REFERENCES

[1] E. Keil, "Beam-beam dynamics", Report CERN/ISR-TH/72- 7, (1972).

[2] H. Grote and F. Schmidt, MAD-X, An Upgrade from MAD8 , CERN-AB-2003-024 ABP.

[3] I. N. Meshkov, "NICA Project at JINR **",** 11 International Meeting on Beam Cooling and Related Topics, Ukraine, Alushta, 2011.

[4] O Kozlov, private communication, JINR, 26.11.2011.

[5] W. Herr, "*P*article tracking with M*AD*-X including *L*HC beam-beam interactions" LHC Project Note 344, CERN, May 25, 2004.

[6] V.V. Kapin, A.Ye. Boshakov, P.R. Zenkevich, "Influence of Beam Space Charge on Dynamical Aperture of TWAC Storage Ring , XXI Russian Particle Accelerator Conf.), Sep. 28 - Oct.3, 2008, Zvenigorod, Moscow region,pp.399-401; http://accelconf.web.cern.ch/accelconf/r08/papers/FRCAU03.pdf

[7] A. W. Chao, M. Month, Particle Trapping during Passage through a High-Order Nonlinear resonance

[8] G. Franchetti and I. Hofmann, Particle Trapping by Nonlinear Resonances and Space Charge , NIM, A-261, p. 195-202, 2006.

[9] .J. Lichtenberg, . A. Lieberman, Regular and Stochastic Motion, Springer, N.Y., 1983.

EFFECT OF GOLD NUCLEI RECOMBINATION IN ELECTRON COOLING SYSTEM ON BEAM LIFETIME IN THE NICA COLLIDER

O.S. Kozlov, A.B. Kuznetsov, A.V. Tuzikov, A.V. Philippov#
Veksler and Baldin Laboratory of High Energy Physics, JINR, Dubna, Russia
I.N. Meshkov, Dzhelepov Laboratory of Nuclear Problems, JINR, Dubna, Russia

Abstract

On the basis of experimental data the production of the ions Au^{78+} and Au^{77+} as a result of step-by-step radiative recombination of bare nuclei on free electrons in the NICA Collider electron cooling system is presented. The influence of Au^{78+} ions on the luminosity lifetime is discussed. The optimum working cycle of the NICA Collider is described.

LUMINOSITY LIFETIME

The NICA Collider working cycle will consist of the following modes: collision mode during time T and reloading mode during time ΔT. The average luminosity $\langle L(T)\rangle$ can be estimated using the following formula:

$$\left\langle L(T)\right\rangle = \frac{\int_0^T L(t)\,dt}{T+\Delta T}. \qquad (1)$$

For the round beams the peak luminosity L_{max} can be calculated in accordance with the formula:

$$L_{max} = \frac{N^2}{4\pi\varepsilon_\perp \beta^*} F_{coll} f_{HG}\left(\frac{\sigma_s}{\beta^*}\right). \qquad (2)$$

Where N is the bunch intensity; $\varepsilon_\perp$ is the transverse unnormalized rms emittance; β^* is the beta function in the interaction point; σ_s is the rms value of the longitudinal beam size; F_{coll} is the collision repetition frequency and factor f_{HG} is define the hour glass effect. When the emittance and bunch length are stabilized by electron cooling (we assume that the cooling power is adjusted for exact compensation of the beam heating due to intrabeam scattering process) the luminosity lifetime is determined by the bunch intensity variation only:

$$\frac{1}{L}\frac{dL}{dt} = 2\frac{1}{N}\frac{dN}{dt}.$$

During the collision mode the ion losses lead to decrease of the total beam intensity by the value ΔN (in each ring of the NICA Collider). Thereafter one needs to provide debunching of the beam, injection of a few portions of the ions from the Nuclotron and beam bunching to prolong the collisions. The time ΔT required for these procedures can be estimated approximately to $\Delta T = 250$ s [3]. In this estimation the beam preparation time that describes the full period of time required for the beam debunching and adiabatic capturing in the NICA Collider (in the estimations below we used rather optimistic value of 10 s).

Maximizing the average luminosity (1) we can obtain optimum duration for the collision mode of the NICA Collider operation.

More powerful process leading to the ion losses during the collisions is the radiative recombination (RR) of gold ions on free electrons in the NICA Collider electron cooling system i.e.:

$$\frac{1}{L}\frac{dL}{dt} \propto -\frac{2}{\tau^{RR}}. \qquad (3)$$

Here τ^{RR} is the characteristic time of the bunch intensity variation due to RR process.

In this case the average luminosity (1) can be written as follows:

$$\left\langle L(T)\right\rangle = \frac{\tau^{RR}}{T+\Delta T(T)}\cdot\frac{1-e^{-2T/\tau^{RR}}}{2}\cdot L_{max}. \qquad (4)$$

Resume all that was said above the information about beam intensity kinetics is needed.

BEAM INTENSITY KINETICS DUE TO RR PROCESS

The analysis of Au^{79+} bare nuclei and Au^{78+}, Au^{77+} ions beam formed in the NICA Collider electron cooling system in energy range of 1÷4.5 GeV/u has shown (Fig. 1) that most of the Au^{77+} ions will be lost at the vacuum chamber aperture $r_x = 60$ mm during approximately 1.8 μs (one revolution period). The amount of surviving Au^{77+} ions increases with beam energy but does not exceed 5% at 4.5 GeV/u. In this case for our goal it is sufficient to consider RR process of Au^{79+} bare nuclei into Au^{78+} ions. The ions of lower charge states can be neglected because they lost on vacuum chamber aperture at the first turn in the NICA Collider ring after their generation.

Therefore the set of kinetic equations describing formation of Au^{78+} ions owing to RR process of Au^{79+} bare nuclei on free electrons in the NICA Collider cooling system can be written as follows:

#philippov@jinr.ru

$$\begin{cases} \dfrac{dN_{79}}{dt} = -\dfrac{N_{79}}{\tau_{79}}, \\ \dfrac{dN_{78}}{dt} = -\dfrac{N_{78}}{\tau_{78}} + \dfrac{N_{79}}{\tau_{79}}(1-\delta_{78}), \\ N_{79}(0) = N_{79,0}, \quad N_{78}(0) = 0. \end{cases} \tag{5}$$

The closed orbits of Au^{79+} bare nuclei and ion beams Au^{77+}, Au^{78+} are shown on Fig. 1.

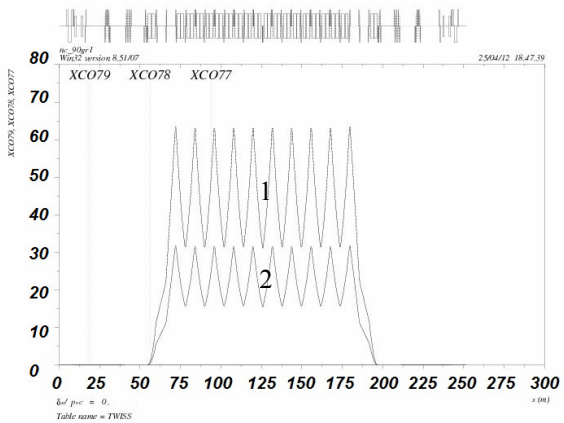

Figure 1: Closed orbits of ion beams 1 — Au^{77+} and 2 — Au^{78+}; the closed orbit of Au^{79+} bare nuclei coincides here with abscissa axis.

The analytical solution of equations set (5) can be written as follows:

$$N_{79}(t) = N_{79,0}e^{-t/\tau_{79}},$$
$$N_{78}(t) = N_{79,0}(1-\delta_{78})\frac{\tau_{78}}{\tau_{78}-\tau_{79}}\left(e^{-t/\tau_{79}} - e^{-t/\tau_{78}}\right). \tag{6}$$

Here N_{78} and N_{79} the beam intensities of Au^{78+} ions and Au^{79+} nuclei. Symbols τ_{78} and τ_{79} designate the RR times of Au^{78+} ions and Au^{79+} bare nuclei; $\delta_{78} \le 1$ designate loss factor of Au^{78+} ions on vacuum chamber wall due to the beam dynamics during a time less than the betatron oscillations.

With using (6) the effective RR time τ^{RR} in (4) can be found from following:

$$\tau^{RR} = \frac{\tau_{79}}{\delta_{78} + x\tau_{79}/\tau_{78}} \cdot (1+x), \quad x = \frac{N_{78}}{N_{79}}. \tag{7}$$

For further estimations in (7) we used the values for RR time τ_{79} and ratio τ_{79}/τ_{78} (~ 10) based on experimental data [2].

RESULTS AND CONCLUSION

The dependencies of lost factor δ_{78} as function of beam energy E was taken from the results of article [1]. These dependencies were calculated for two particle distributions in the bunch, i.e. Gauss and Kapchinsky-Vladimirsky (homogeneous charge density) ones. Below this results are shown in Fig. 2. The ion beam emittance $\varepsilon_\perp = 1.1$ π·mm·mrad was taken into account.

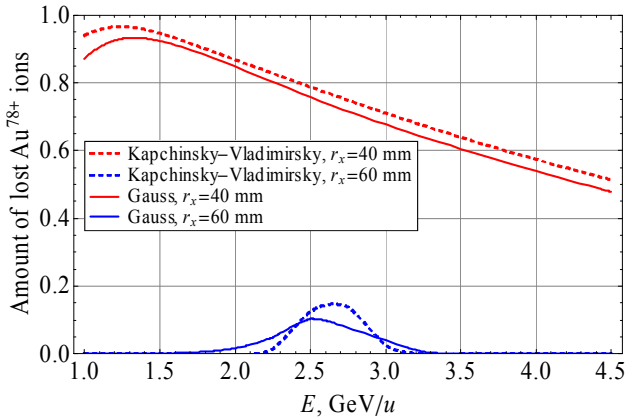

Figure 2: Loss factor δ_{78} of ion beam Au^{78+} as function of beam energy E.

Variation of the vacuum chamber aperture from $r_x = 40$ mm up to $r_x = 60$ mm leads to insignificant variation of the loses factor δ_{78} (about 10÷15%) so the influence of ion losses on beam intensity kinetics is small (Figs. 3-5 below). On Figs. 3-5 N/N_0 is ratio of beam intensity to initial value; t/τ_{79} is the time in units of RR time of Au^{79+} bare nuclei; $T_{\perp,e}$ and I_e transverse temperature of electron beam and electron beam current correspondingly; τ_{cool} is the cooling time [1].

As a conclusion we can say the following:

- RR process of Au^{79+} bare nuclei on free electrons in the NICA Collider electron cooling system leads to formation of Au^{77+} and Au^{78+} ion beams;
- For vacuum chamber aperture $r_x = 60$ mm the number of surviving ions Au^{77+} does not exceed 5% at 4.5 GeV/u;
- In contrary Au^{78+} ions have significantly long lifetime; for improving the vacuum conditions the special collimators (catchers) to clean the vacuum chamber from the charge-exchanged beam of Au^{78+} ions can be installed. For vacuum chamber aperture $r_x = 40$ mm the analysis of (4) gives us the average luminosity values shown in Table 1 at $T = \tau^{RR}$. The reloading time is the same for all these energies and equal approximately to $\Delta T \approx 250$ s [3].

Table 1: The NICA Collider electron cooling parameters for optimal working regime at peak luminosity $L_{max} = 10^{27}$ cm^{-2}·s^{-1}.

E, GeV/u	I_e, A	$T_{\perp,e}$, eV	$\tau^{RR}/\tau^{cool}/\tau^{IBS}$, s	L/L_{max}
1	0.3	2	1000/140/186	0.4
3	1.3	2	1070/680/702	0.4
4.5	1.5	2	1800/2400/2540	0.4

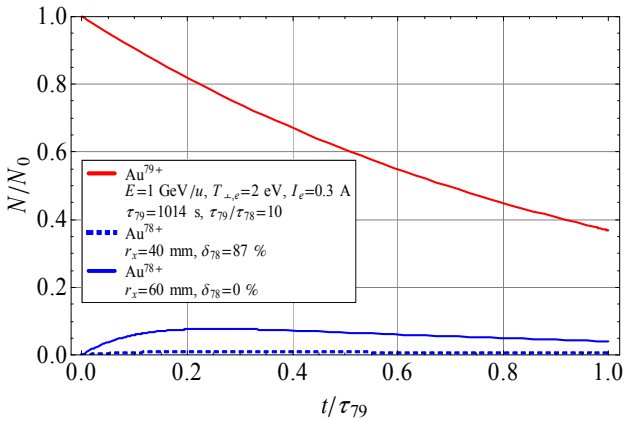

Figure 3: Solution (6) for beam energy E = 1 GeV/u.

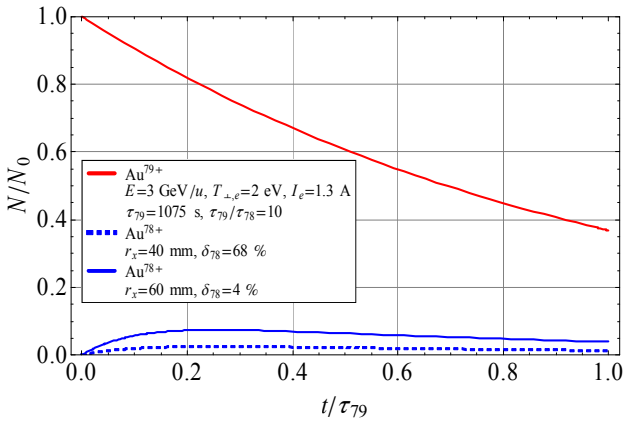

Figure 4: Solution (6) for beam energy E = 3 GeV/u.

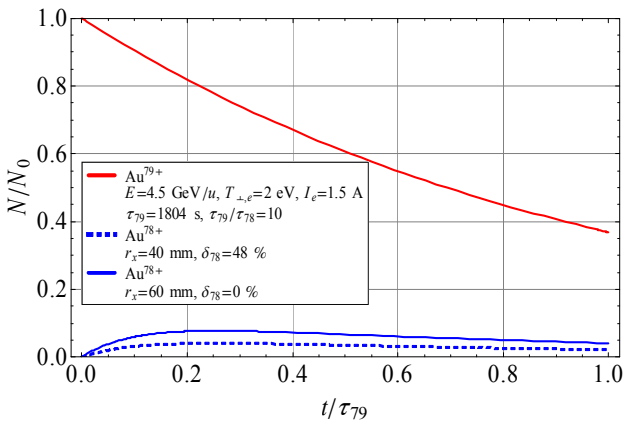

Figure 5: Solution (6) for beam energy E = 4.5 GeV/u.

REFERENCES

[1] A.V. Eliseev et al. Dynamics of $^{197}Au^{78+}$ Ions Generated in Recombination with Cooling Electrons in the NICA Collider. RuPAC2012, St. Petersburg, September 2012. MOPPA016, these proceedings.

[2] A.V. Philippov et al. Radiactive Recombination of Heavy Bare Nuclei and Ions in Electron Cooling System. COOL2011, Alushta, September 2011. THCOB01, p. 48; http://accelconf.web.cern.ch/accelconf/COOL2011/papers/thcob01.pdf

[3] I.N. Meshkov. Status of NICA Project. RuPAC2012, St. Petersburg, September 2012. MOXCH03, these proceedings.

PROGRESS IN NICA BOOSTER DESIGN

A.Butenko, H.Khodzhibagiyan, V.Mikhaylov, I.Meshkov, G.Trubnikov, A.Tuzikov, A.Valkovich, A.Sidorin, JINR, Dubna, Russia

Abstract

NICA is a new accelerator complex being under design and construction at Joint Institute for Nuclear Research in Dubna. A few changes in NICA booster ring design took place over the last half a year.The most significant one is making use of DFO doublet optical structure instead FODO lattice studied previously. Based upon this new optics the injection and extraction systems were proposed. Both "One time, many turn" and "Many times, one turn" schemes of injection are presented here. Fast extraction system (to inject beam to Nuclotron) is mentioned too. Optimal arrangement of the closed orbit correction system (correctors,BPMs) was found. Chromaticity correction system with relatively small reduction in dynamical acceptance is paid attention to.

INTRODUCTION

The NICA/MPD project [1] started at the Joint Institute for Nuclear Research (JINR) in Dubna in 2007. The goal of the project is to carry out experimental studies of the hot and dense strongly interacting quantum chromodynamics matter and light polarized ions. The NICA accelerator complex will consist of two injector chains, a new 600MeV/u superconducting booster synchrotron, the existing superconducting synchrotron – Nuclotron [2], and the new superconducting collider consisting of two rings each of about 503 m in circumference. The report presented is to describe the latest results of the R&D efforts in NICA booster ring design.

OPTICAL STRUCTURE OF THE BOOSTER RING

One of the most significant developments in the overall design of the booster ring is the choice of DFO-doublet-based lattice. In previous reports FODO lattice was considered as the most possible solution for the ring.

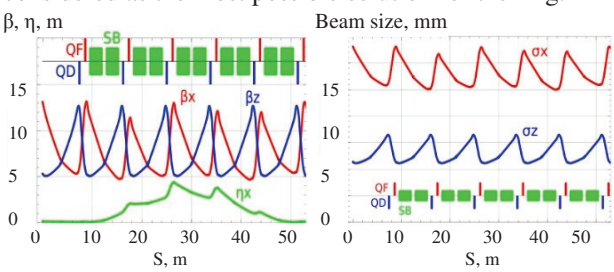

Figure 1: Optical functions and envelopes in the ring.

Optical structure of the booster ring has periodicity and has four super periods. Each of them has 5 regular DFO periods and one period having no bended magnets in it. Regular period includes couple of lenses (defocusing and focusing ones) and couple of bended dipole magnets. Schemes of both regular DFO period and straight section are presented at the Fig.1.

Table 1: Main parameters of the Booster ring

1. Main Parameters		
Energy of injection, MeV		6.2
Maximum energy of the Au+32 ions,MeV/amu		600
Magnetic rigidity, T·m	at injection	2.2
	maximum	600
Circumference, m		211.2
Coulomb intensity limit, part/cycle		5×10e9
Transition energy, GeV/amu		4.5
2. Lattice and Magnetic Elements		
Number of superperiods		4
DFO-type periods		24
Dipole magnets		40
Quadrupole lenses		48
Magnetic field in dipole magnets, T		1.8
Gradient in F/D-lenses, T/m		24.7/-24.2

Lattice functions in one super period are presented at Fig.1 Envelope functions of the beam corresponding to the physical acceptance of the vacuum chamber (Ex=123π mm mrad, Ey=66 π mm mrad) and energy spread (estimated to be ~5×10e-3) are shown at the Fig.1. Main parameters of the optical structure of the booster ring are given at the Table 1.

INJECTION AND EXTRACTION SCHEMES

njection system for the booster ring with new DFO optics was developed. By now, three major injection schemes are at the table: “one time, many turns”, “many times, one turn” and “one time, one turn”.

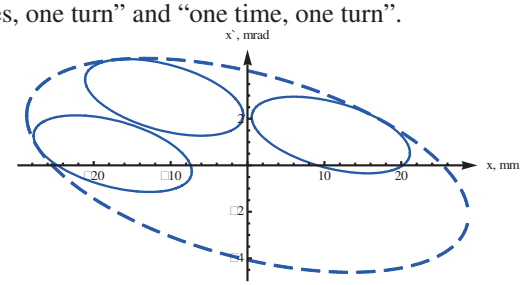

Figure 2: “One time, many turns” injection scheme in phase space.

Fig.2 gives an appearance of the "three turns" injection in phase space. The phase advance corresponding to the circumference of the ring separates small ellipses.Phase space shown at the Fig.2 is depicted for the betatron motion around closed orbit with the local bump introduced.

Local bump necessary for the proper "one time, many turns" scheme operation is presented at Fig.3. For the comparison, the local bump in "one time, one turn" approach is depicted at the Fig.4. The overall layout of the injection system is given at Fig.4.

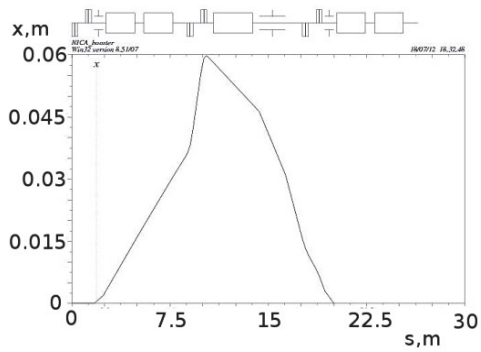

Figure 3: Local bump for the beam injection over three turns.

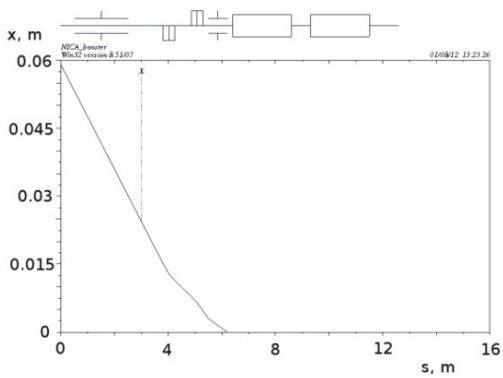

Figure 4: Local bump for the single beam injection over one turn.

Position of the injection plates to be used for the creation of the local bump was chosen in such a way as to have no significant reduction of dynamical acceptance at the new orbit. The behaviour of the envelope function for the injected beam during the first three turns is depicted at the Fig.5.

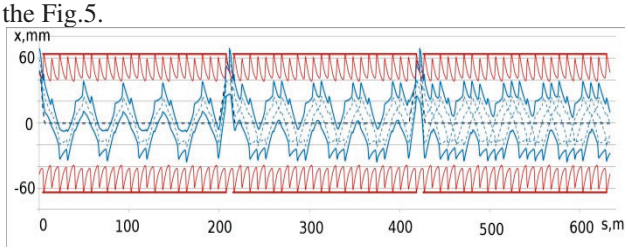

Figure 5: Envelope function of the stored beam during the injection (three turns)

The behaviour of the injected and stored beam near the first straight section is given at the Fig.6.

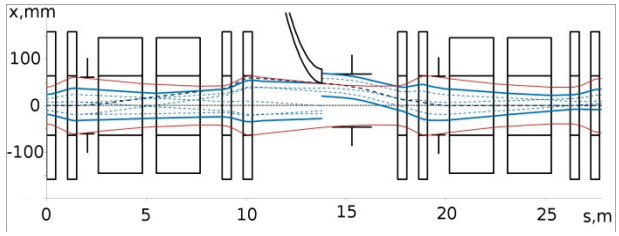

Figure 6: Envelope functions of the stored and injected beam during the injection (first straight section of the ring).

Main parameters of the deflection plates are given in the Table 2.

Table 2: Main parameters of the deflection plates.

	Voltage, kV	E-field, kV/cm	Deflection angle, mrad
IK1	35.4	2.9	5.5
IK2	18.2	-1.6	-8.5
IK3	58	4.6	8.8

The emittance of the beam coming from the linac is anticipated to be 10 π mm mrad. With the system described here the emittance of the beam immediately after the injection is estimated to be 117 π mm mrad.

As for the fast extraction system there are three options to proceed: with horizontal kicker, vertical kicker and "skew" kicker. The one with vertical kicker is considered as the most possible for the actual realisation. In this configuration the extraction system consists of vertical kicker and three lambertson magnets. Length of the kicker is 2.5 m, magnetic field is 0.1T.
Envelope functions in x,y-directions for the last scenarioare given at the Fig.7,8.

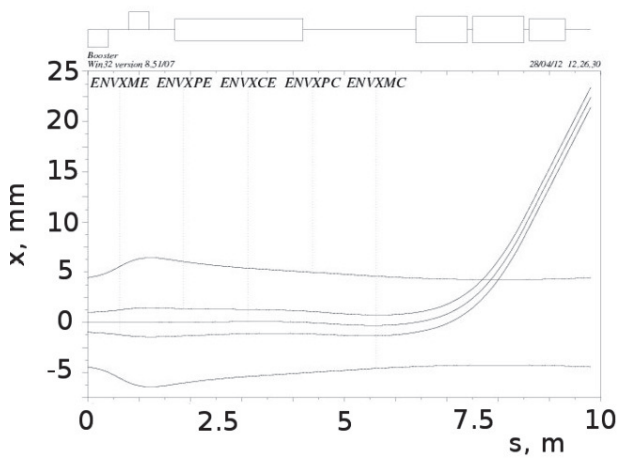

Figure 7: Fast extraction of the beam in x-direction.

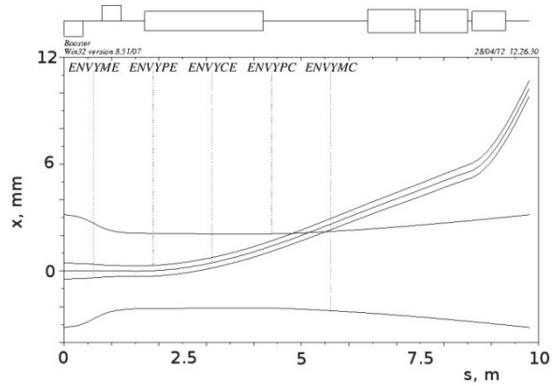

Figure 8: Fast extraction of the beam in y-direction.

ORBIT CORRECTION SYSTEM

Orbit correction system of the Booster ring was developed with rather standard means provided by MAD-X program [1].Typical orbit distortion with lenses shifted in the transverse direction with Gaussian law of the distribution (in average at 2mm) is shown at the Fig.9.

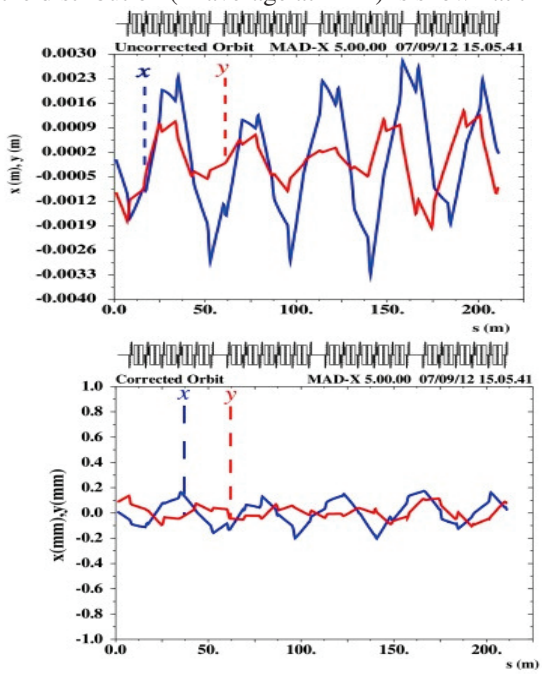

Figure 9: Closed orbit before and after correction.

CORRECTION OF THE NATURAL CHROMATICITY

Fig. 12 shows the variant of sextupoles arrangement to be implemented in the ring. The phase advance between focusing and defocusing sextupoles is approximately equal to an even number of π (0×π). In the case of booster ring it is zero. The phase advance between two sextupoles of the same sign is odd multiple of π (1×π). Fig.13 gives one an impression of how a dynamical acceptance got reduced due to the nonlinearity introduced.

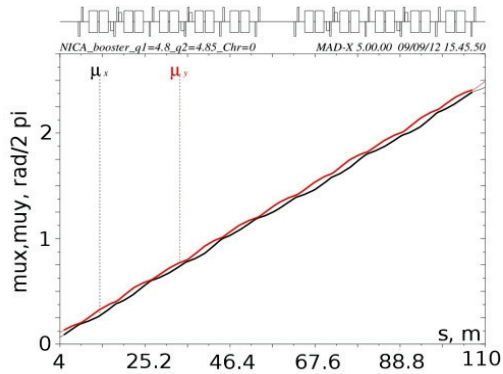

Figure 12: Betatronphase advance in the booster ring with sextupoles implemented.

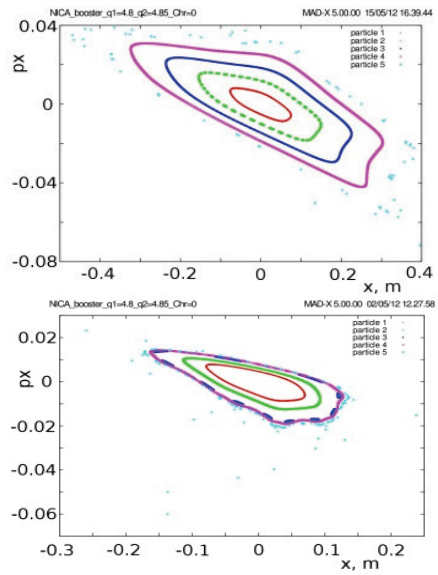

Figure 13: Dynamical acceptance with correct and wrong sextupoles arrangement (in terms of phase advance).

CONCLUSIONS

A few changes and developments in the NICA Booster ring design are described. The most significant ones are related to the development of the injection/extraction systems for the new DFO doublet lattice model of the ring. Other points of progress are the first steps towards the development of the closed orbit correction system and therefore deciding upon where dipole correctors and beam position monitors are to be located in the ring. Along with the closed orbit correction system chromaticity correction system is proposed. The system is designed in such a way as to minimize the reduction of the dynamical acceptance due to the nonlinearity introduced.

REFERENCES

[1] MAD-X computer code.
Available:http://mad.web.cern.ch/mad/

[2] Nuclotron - based ion collider facility.
Available:http://nica.jinr.ru/

DEVELOPMENT OF STOCHASTIC COOLING TECHNIQUE FOR NICA PROJECT

N. Shurkhno#, A. Kobets, I. Meshkov, V. Seleznev, A. Sidorin, G. Trubnikov, JINR, Dubna, Moscow region
R. Stassen, IKP, FZ Juelich, Germany

Abstract

Joint Institute for Nuclear Research (JINR) initiated the creation of a new and unique heavy-ion collider – Nuclotron-based Ion Collider Facility (NICA), which is planned for commissioning in 2016. The luminosity in the colliding beams of gold ions is expected to reach 10^{27} $cm^{-2}s^{-1}$. By estimations the luminosity will be mainly determined by the intra-beam scattering effect. To suppress this, a cooling system should be used. For the medium and high-energy heavy ions such as at NICA collider, stochastic cooling will be more efficient than electron cooling, so that system will be used in the collider. It was decided to construct a prototype stochastic cooling system, which can be tested at the Nuclotron in an early stage of the NICA project. A longitudinal stochastic cooling system was constructed in 2011. The report presents first experimental measurements and further developments of the stochastic cooling system.

INTRODUCTION

JINR is in the initial phase of constructing the NICA collider [1] for which both longitudinal and transverse stochastic cooling systems are obligatory. We are developing the stochastic-cooling system of NICA at the existing Nuclotron superconducting synchrotron at JINR. So, we gain experience of stochastic cooling in a NICA-specific environment [2]. The prototypes has been designed and tested during the years 2010 and 2011. The experiment with this constructed stochastic cooling system was carried out in November 2011. In the course of the experiment, longitudinal Schottky noise and beam transfer function were measured and the optical notch-filter was tested. Since experiment the scheme of the system was significantly developed and improved. The results of the experiment as well as new system design will be discussed below.

EXPERIMENT SETUP AND RESULTS

Main parameters of the accelerator and the cooling system are summarized in Table 1.

Table 1: Parameters of cooling system

Circumference, m	251.5
Ions	Deuterons, C6+
Energy, GeV/u	0.5-4
Rev.frequency, MHz	1.13
Number of particles	10^9
Momentum spread, Δp/p	10^{-3}
Ring slip factor	0.0322
System bandwidth, GHz	2 - 4

The first step of the realization of the stochastic cooling experiment was longitudinal cooling of coasting beam. The dispersion value is too small in the section, where the pick-up is placed, so Palmer method cannot be implemented. Instead a scheme with a notch filter was installed. The octave band of 2-4 GHz was chosen for that system. The scheme of the system is shown in Fig. 1.

Slot ring couplers, developed and produced at FZ Juelich [3], were used for pick-up as well as for kicker. Both structures have identical design – an assembly of 16 rings with 8 electrodes each. Longitudinal coupling impedance of each ring is 9 Ohms. The pick-up is placed in a cryostat at 10 K, while the kicker is placed at room temperature. Each output of pick-up has a 34 dB low-noise pre-amplifier. The outputs are then combined together. The optical notch-filter [4, 2] was adjusted for 2 GeV deuteron beam; the notch depth was not less than 35 dB.

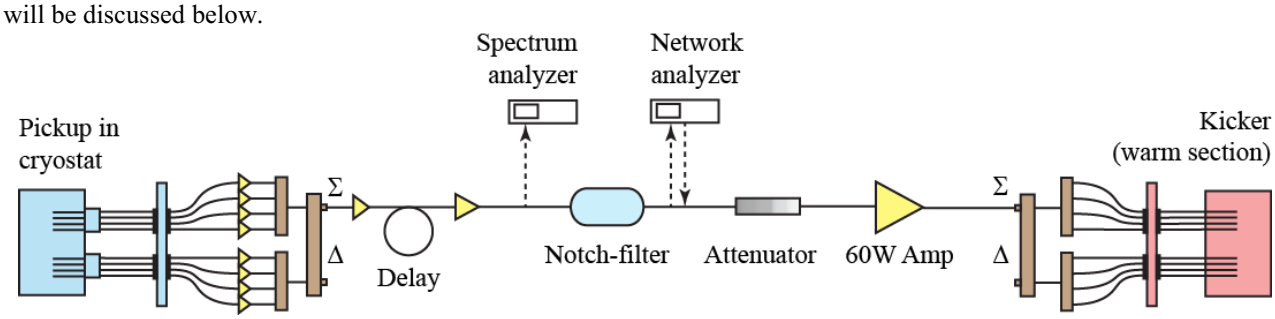

Figure 1: The scheme of stochastic cooling system in experiment.

#shurkhno@physics.msu.ru

At first, longitudinal Schottky noise for deuterons at 2 GeV was measured. The bands were observed over the whole bandwidth, allowing the estimation of revolution frequency, momentum spread and form of beam distribution function. Figure 2 shows measured signals of a deuteron beam at 2.5 GHz.

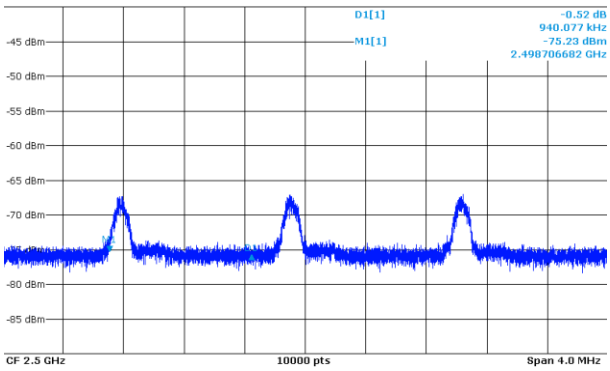

Figure 2: Longitudinal Schottky noise of coasting beam of deuterons (10^9 particles, 2 GeV/n), measured at 2.5 GHz.

The calculated momentum deviation at each harmonic corresponds to the nominal value of 10^{-3}, as well as the revolution frequency of about 1.3 MHz.

The notch-filter was then inserted before the spectrum analyzer to make sure it works properly. Figure 3 demonstrates the work of the notch-filter, as it cancels the harmonics of revolution frequency, while its delay line is being adjusted.

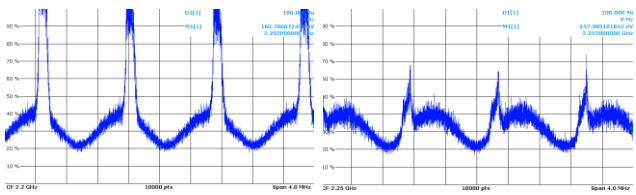

Figure 3: Longitudinal Schottky noise after notch-filter with imprecisely (left) and more precisely (right) adjusted delay line.

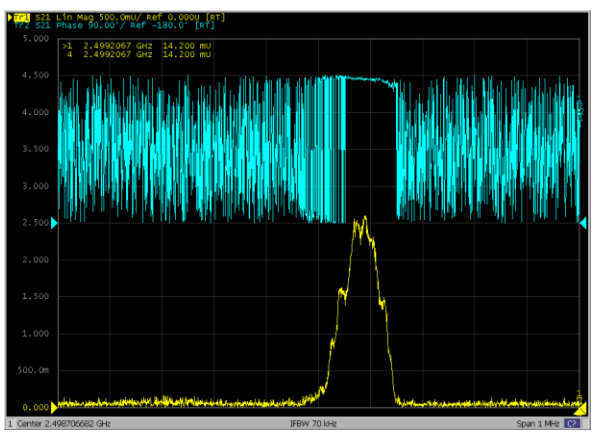

Figure 4: Amplitude (bottom) and phase (top) responses during BTF-measurements.

The next step was to measure the beam transfer function at different harmonics to adjust the system delay (open-loop measurements). The long branch of the notch-filter was broken to take into account the device delay only. One measurement at 2.5GHz is presented in Fig. 4.

The top curve represents the phase response, bottom the amplitude response. There were also observed double peaks, which nature was quite unclear during the experiment. While previous results guarantee the parts of the system from PU to main amplifier works properly, positioning and functionality of the kicker should be tested again.

NEW SCHEME DESIGN

The stochastic cooling system at the Nuclotron is considered as a prototype for NICA, so further development of the system is necessary for NICA. This upgrade includes new schemes for signal handling at pick-up and kicker, a new optical delay line and an improved notch-filter. The scheme of combining the outputs of the pick-up is shown in Fig. 5.

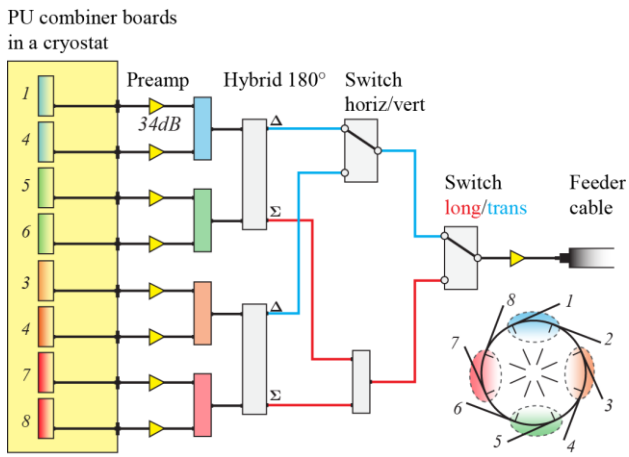

Figure 5: Scheme of combining pick-up outputs.

Eight outputs are first combined in four pairs in vertical and horizontal planes. Then utilizing two switches it is possible to get a vertical, horizontal or longitudinal signal. Kicker input signals are similarly handled except pre-amplifiers.

The delay lines and the notch filter were also revised. The delay lines for the system delay between pickup and kicker is now included in the optical notch filter, because fibers have negligibly small attenuations and dispersion. See the scheme of delay lines and notch-filter in Fig. 6. Both system and notch-filter delays include nanosecond-delay switches, ranging from 0.5 ns to 15.5 ns, and precise delay modules with 0-550 ps delay range and 0.01 ps accuracy. Using a variable delay allows adjusting the cooling system to specified beam energy in a fairly wide range. An attenuator in the short branch of the filter compensates the attenuation of the long branch, while an attenuator in the long branch is required to break the circuit for open-loop measurements.

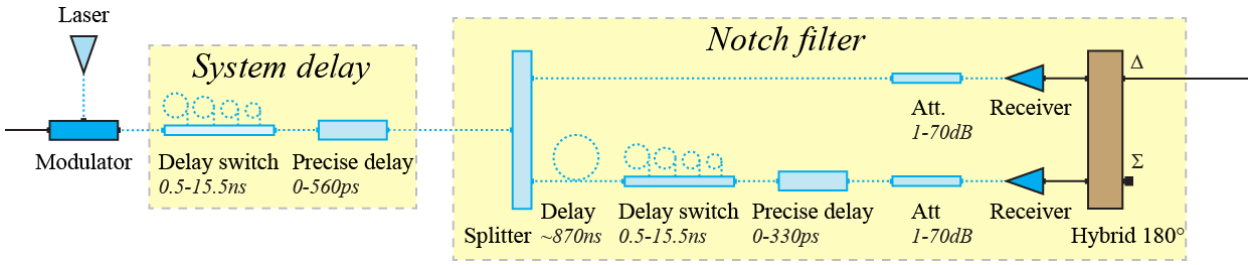

Figure 6: Optical delay line and notch-filter.

The new scheme also includes switches for open-loop measurements.

PERSPECTIVES

The new scheme has been assembled in the test laboratory and measured component by component, and proved to be properly working. Closer to the run pick-up and kicker positioning will be checked again. Extensive simulations of beam evolution during cooling with the new scheme convince that in principle cooling effects can be seen in each cooling direction (longitudinal and transversal). For reference, the result of cooling for proton beam (intensity 10^9, momentum deviation 10^{-3}) with notch-filter scheme is shown in Fig. 7. Simulation for deuterons gives approximately the same result within 60s. During the following run it is planned to measure transverse and longitudinal Schottky noises, perform open-loop measurements and subsequently try different working modes of the new system.

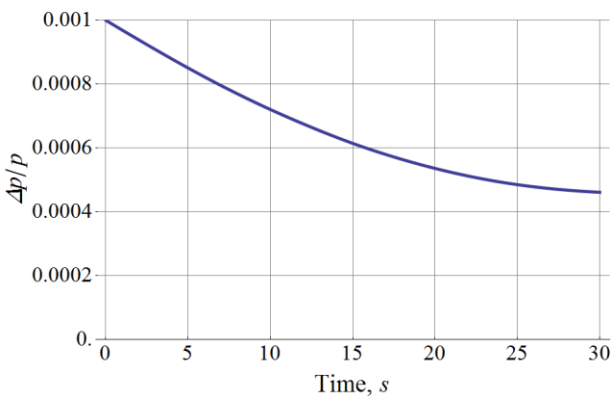

Figure 7: Simulation of momentum spread evolution during cooling. Protons at 3.5 GeV, 10^9 particles, notch-filter method.

ACKNOWLEDGMENT

We would like specially thank Lars Thorndahl, Takeshi Katayama, Hans Stockhorst, Fritz Caspers and Valery Lebedev for many fruitful discussions and great help in theoretical investigations.

This work is supported by FRRC.

REFERENCES

[1] A.N.Sisakian et al. XXIII Int. Symposium. on Lepton and Photon Interactions at High Energy, LP07, Daegu, Korea. (2007).

[2] I. Meshkov et al., "Stochastic cooling system for Nuclotron", RuPAC'10, Protvino, Russia, 2010, TUPSA016, p.74.

[3] R. Stassen et al., "Recent developments for the HESR stochastic cooling system", Proceedings of COOL 2007, Bad Kreuznach, Germany, THAP13, p. 191.

[4] U. Bechstedt et al., "Optical notch filter for the stochastic cooling system of COSY", PAC, New York, 1999, p. 1701.

LEPTA PROJECT: TOWARDS POSITRONIUM

E.Ahmanova, V.Kaplin, V.Karpinsky, V.Lokhmatov, I.Meshkov, V.Pavlov, A.Rudakov, A.A.Sidorin, S.Yakovenko, JINR, Dubna
A.Kobets#, JINR, Dubna and Institute of Electrophysics and Radiation Technologies, NAS of Ukraine
M.Eseev, JINR, Dubna and M.V.Lomonosov Pomor State University, Russia

Abstract

The project of the Low Energy Positron Toroidal Accumulator (LEPTA) is under development at JINR. The LEPTA facility is a small positron storage ring equipped with the electron coolin system. The project positron energy is of 2 – 10 keV. The main goal of the facility is to generate an intense flux of positronium atoms – the bound state of electron and positron.

Storage ring of LEPTA facility was commissioned in September 2004 and was under development up to now. The positron injector has been constructed in 2005 ÷ 2010, and beam transfer channel – in 2011. By the end of August 2011 experiments on electron and positron injection into the ring have been started. The recent results are presented here.

LEPTA RING DEVELOPMENT

The Low Energy Particle Toroidal Accumulator (LEPTA) is designed for studies of particle beam dynamics in a storage ring with longitudinal magnetic field focusing (so called "stellatron"), application of circulating electron beam to electron cooling of antiprotons and ions in adjoining storage electron cooling of positrons and positronium in-flight generation.

For the first time a circulating electron beam was obtained in the LEPTA ring in September 2004 [1]. First experience of the LEPTA operation demonstrated main advantage of the focusing system with longitudinal magnetic field: long life-time of the circulating beam of low energy electrons. At average pressure in the ring of 10^{-8} Torr the life-time of 4 keV electron beam of about 20 ms was achieved that is by 2 orders of magnitude longer than in usual strong focusing system. However, experiments showed a decrease of the beam life-time at increase of electron energy. So, at the beam energy of 10 keV the life time was not longer than 0.1 ms. The possible reasons of this effect are the magnetic inhomogeneity and resonant behaviors of the focusing system.

Positron Transfer Channel

The channel is aimed to transport positrons extracted from the trap of the injector (see below) and accelerate them up to 10 keV (maximum) in electrostatic field in the gap between the trap and the channel entrance. The designing and manufacturing of the channel elements was completed in 2010(Fig. 1).

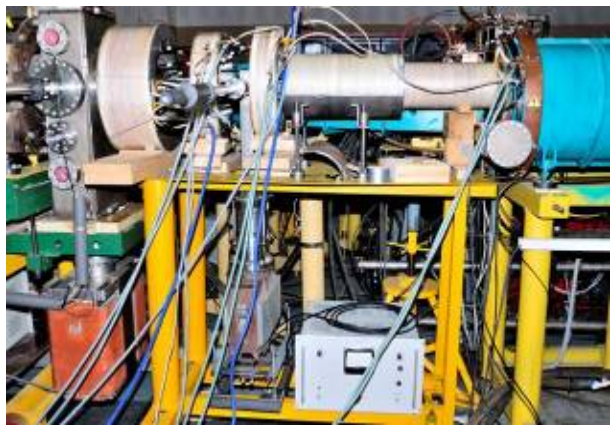

Figure 1. The transfer channel.

Circulating e+ Beam Detector

For fine tuning of the trajectory and control of circulating positron beam aperture probe based on semiconductor gamma detector has been designed (Fig.2). Fabrication of the probe is in progress.

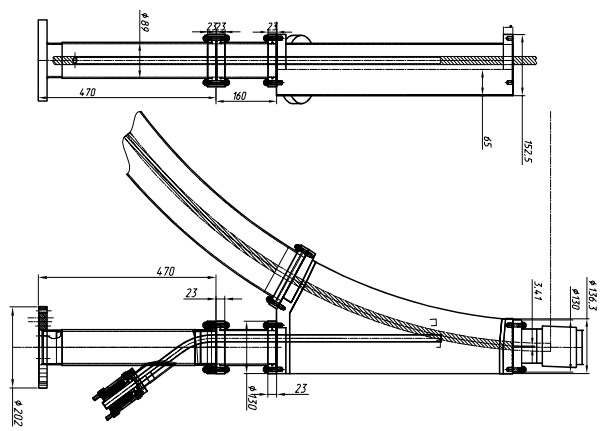

Figure 2. The circulating e^+ beam detector.

THE POSITRON INJECTOR

In summer 2010 the slow positron source and the trap have been assembled. The first attempts of slow positron storage were performed (Fig.3) and stored positrons were extracted to the collector.

kobets@jinr.ru

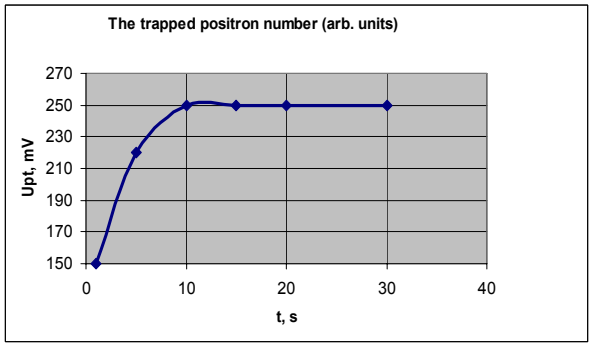

Figure 3: The trapped positron number vs storage time. Rotating wall(RW)=0,5V.

Upt is the amplitude of the signal from the phototube (PT), RW amplitude is equal to 0.5 V.

Manufacturing and assembling of the transfer channel from injector to the ring were completed by the end of July 2011. The test of the channel was performed in August 2011, first with test electron beam and later with positrons. Test electron gun was installed at the entrance of positron trap (Fig.4).

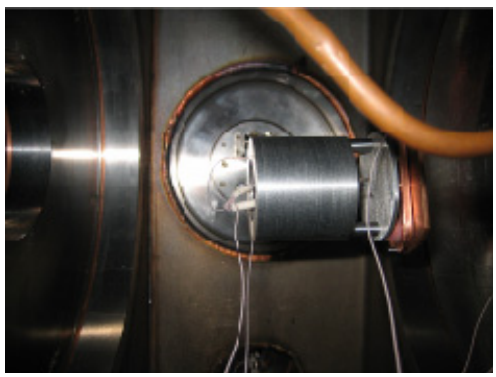

Figure 4. The test electron gun.

The ring was disassembled and luminescent screen was placed inside the kicker chamber. The beam images of electron beams both from the test gun and electron gun of the electron cooling system were obtained on the screen (Fig.5). After that positrons were injected into the ring at facility parameters optimized with electron beam.

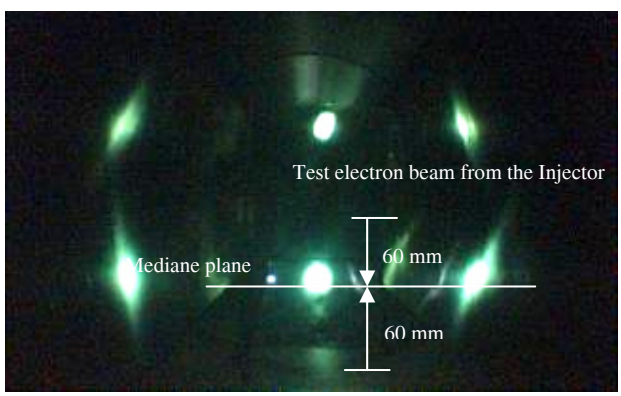

Figure 5. Two beams on luminescence screen.

The registration of positron transportation through the channel and septum section of the ring to the luminescence screen was performed using for e^+ registration a NaI scintillation counter in counting mode.

The vacuum conditions in the accumulation space of the positron trap have been improved by the application of a cryogenic screen that was designed, manufactured, mounted and tested (Fig.6). It has effected in an increase of stored positron life time by three times.

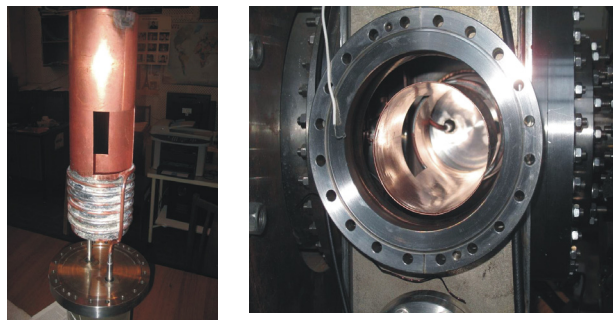

Figure 6. The cryogenic screen.

For magnetic field optimization its measurement and numerical simulations have been produced (Fig.7).

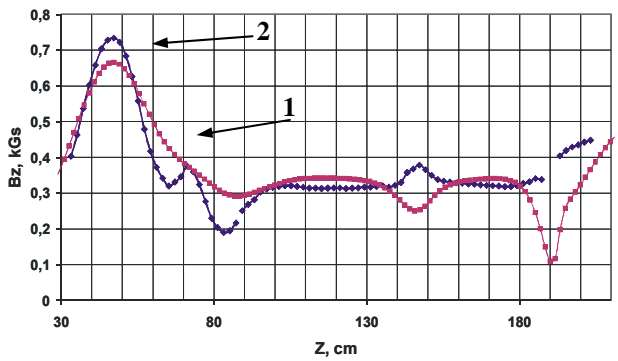

Figure 7. Magnetic field in the transfer channel: 1) B_z(z) at the channel axis (simulation); 2) B_z(z) at r=4 cm (experiment).

During the spring-summer 2012 the experiments on optimization of positron accumulation in the trap and positron injection into the ring have been performed.

We have found in the experiments that quantity of slow positrons rises up by 30% if temperature of neon layer is increased from 6,5 to 7,2 K after the positron source freezing completion.

For tuning of positron trajectory in the ring we have used scintillation counter operated in analog signal mode. The positrons extracted from the trap, passed through the transfer channel and after completion of single turn were shifted to the vacuum chamber wall (Fig.8). Finally, single turn regime of positron extraction/injection has been found and optimized.

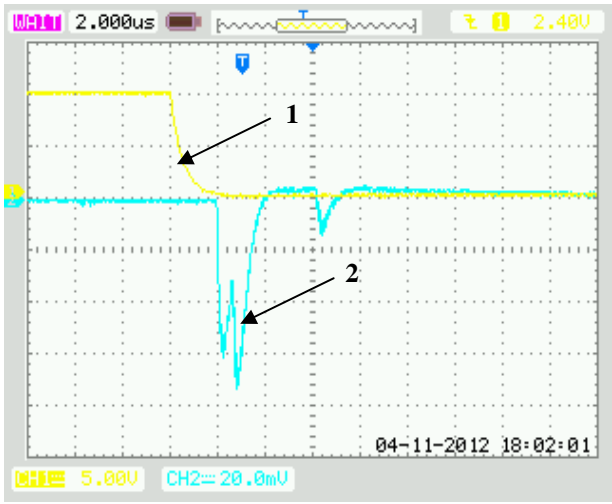

Figure 8. Analog signal from phototube: 1) potential of the trap exit electrode; 2) phototube pulse.

CONCLUDING REMARKS

The development of the LEPTA project is approaching the stage of experiments with circulating positron beam. All main elements of the ring and the injector are ready and have been tested.

All works supported by RFBR, grant №09-02-00084.

REFERENCES

[1] A.Kobets, et. al., Status of the LEPTA project, Proc. of COOL'05 AIP Conference Proceedings, 2006, v.821, p.95-102

[2] M. Amoretti et al., The ATHENA antihydrogen apparatus, Nucl. Inst.Meth. Phys. Res. A 518 (2004) 679-711

[3] C.M.Surko, R.G.Greaves, Radial compression and inward transport of positron plasmas using a rotating electric field, Phisics of plasmas, 8 (2001), 1879-1885.

COMPRESSION AND CONFINEMENT OF POSITRON CLOUDS IN THE SURKO TRAP OF LEPTA FACILITY*

E. Ahmanova, A. Kobets, I. Meshkov, A. Rudakov, S. Yakovenko, JINR, Dubna, Russia
M. Eseev#, A. Vititnev, NAFU, Arkhangelsk, Russia

Abstract

A bunch of positrons confined in a cylindrical Penning-Malmberg trap can be compressed radially by applying a rotating asymmetric dipolar electric field. An explanation of this effect presented in the report is based on the solutions of particle 3D dynamics equations in the fields of the trap taking into account the positron collisions with a neutral buffer gas. The result agrees well with experimental data obtained at the positron injector of LEPTA facility at JINR. Essential feature of the compression process is resonant character of applied rotating field and coincidence its frequency with the frequency of longitudinal positron bouncing in the trap.

INTRODUCTION

The LEPTA facility consists of the source of positrons, the trap and storage ring for generating positronium stream [1]. The Penning-Malmberg trap operates in pulsed mode, accumulating positrons from the source. At accumulation is important to increase the number of the storage particles and clouds in the lifetime of the trap and optimized parameters for this accumulation. It is important to ensure the uniformity of the longitudinal, in relation to the axis of the trap, the magnetic field required pressure of the buffer gas (nitrogen), the distribution of confining potential (see Fig. 1).

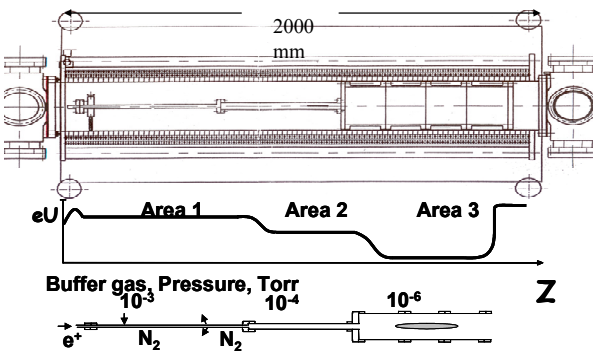

Figure 1: The scheme of the trap. Longitudinal section. Injector accumulated particles to the left in Figure.

In the Surko trap the rotating electric field (the RW-field) created by the electrodes of discontinuous (see Fig. 2). This can significantly improve the accumulation of particles [2,3]. The trap scheme is shown in Figure 1. Previously presented the optimal parameters of accumulation of particles in the trap [4]. Mechanism of action of the rotating field on the accumulation of particles has been discussed. There are different approaches to explain this effect [3,5,6]. For further consideration is the formulation of hypotheses about the need to consider context of longitudinal and transverse motion of the particles in the trap to explain the effect of the rotating field. Will also present experimental verification of the hypothesis.

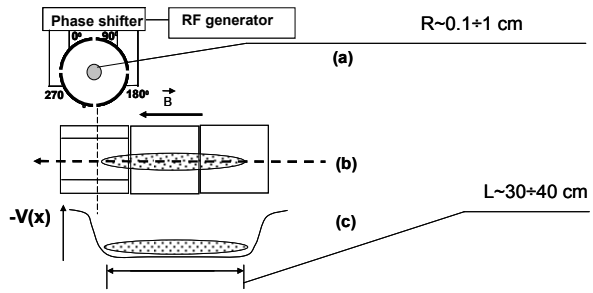

Figure 2: "Rotating wall" (RW) technique: rotating electric field at the trap entrance.

3D-DYNAMICS OF PARTICLE

What is the mechanism for increasing the lifetime confinement and focus particle clouds the use of RW field?

3D-hypothesis

Consider the field and the forces acting in the transverse and longitudinal section of the trap on the particle (see Fig. 3). This is **B** – the longitudinal magnetic field (axis z), $\mathbf{E}_R$ – the field of the space charge of the particle cloud, $\mathbf{E}_\omega$ – the rotating wall field, $\mathbf{E}_{b,r}$, $\mathbf{E}_{b,z}$ – transverse and longitudinal component of the field locking electrode traps.

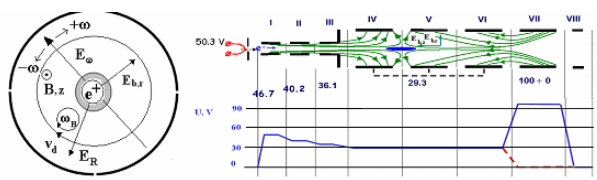

Figure 3: Field distribution in the trap in the longitudinal and transverse section.

Previously, we and other authors have noted the good agreement of the resonance frequency of the RW field f with the drift frequency in the transverse direction $f_{drift} = cE / B$. Some studies indicated agreement with the longitudinal bounce frequency f. This allowed us to assume that the effect of compression and increase the lifetime of clouds stored particles is observed in agreement longitudinal and transverse 3D-motion of the

*Work supported by grants RFBR №09-02-00084, FCP№14.A18.21.1302.
#m.eseev@narfu.ru

particles. Phase entry of the particle in the rotating field is defined as a transverse drift, and longitudinal motion. As shown below, the particles trapped in the correct phase RW-field has a focusing effect, offsetting the particle scattering by inhomogeneities of the magnetic field traps.

The Equations of Motion of the Particles and the RW Field Effect

Rotating field work effectively only with the concurrence of the longitudinal and transverse movements. The action of the buffer gas (nitrogen) can be approximated to shine viscous friction $F_{fr} = -k \cdot V$, where k – friction coefficient, V – particle velocity. As the result, the equations of motion can be written as:

$$m\ddot{\mathbf{r}} = e\left(\mathbf{E}_R + \mathbf{E}_b + \mathbf{E}_\omega\right) + \frac{e}{c}\left[\mathbf{V}\times\mathbf{B}\right] - k\mathbf{V},$$

where e, m - the charge and mass of the particles. In the projections, we have

$$\begin{cases} \ddot{x} = \dfrac{\omega_p^2}{2}\left(x - x_c\right) + \dfrac{\omega_z^2}{2}x + \dot{y}\omega_c - A_\omega\left(z - Z_0\right)\cos[\omega\cdot t] - K\dot{x} \\ \ddot{y} = \dfrac{\omega_p^2}{2}\left(y - y_c\right) + \dfrac{\omega_z^2}{2}y - \dot{x}\omega_c + A_\omega\left(z - Z_0\right)\sin[\omega\cdot t] - K\dot{y} \\ \ddot{z} = -\omega_z^2 z - K\dot{z} \end{cases}$$

Where $K = k/m$, $A_\omega = eU_\omega/\left(2mR_0Z_0\right)$, $U(z,r) = U_0\left(z^2 - r^2/2\right)/\left(2d^2\right)$, $\omega_z = \sqrt{eU_0/md^2}$ - bounce frequency, $\omega_p = \sqrt{4\pi ne^2/m}$ - plasma frequency, $\omega_C = eB/(mc)$ - cyclotron frequency, U_0 – well depth of accumulation, $d^2 = \left(Z_0^{\,2} - R_0^{\,2}/2\right)/2$.

The longitudinal motion - oscillations:

$$z \approx z_0\cos[\omega_z t + \varphi_0].$$

Transverse motion in a strong magnetic field - fast cyclotron rotation with frequency $\omega_+ \approx \omega_c$ and the slow rotation of the magnetron frequency $\omega_- \approx \left(\omega_p^2 + \omega_z^2\right)/2\omega_c$. Movement goes in the projections:

$$x_+ = r_+\sin[\omega_+ t + \Phi],\ y_+ = r_+\cos[\omega_+ t + \Phi],$$
$$x_- = r_-\sin[\omega_- t + \Phi],\ y_- = r_-\cos[\omega_- t + \Phi].$$

Transmits power RW-field of the moving charge $P(t) = e\mathbf{E}_\omega\left(\dot{\mathbf{r}}_+ + \dot{\mathbf{r}}_-\right)$:

$$P(t) = mA_\omega(r_+\omega_+\sin\left[\{\omega - \omega_+\}t + \Phi\right] +$$
$$+ r_-\omega_-\sin\left[\{\omega - \omega_-\}t + \Phi\right])$$

(Φ - phase entry of the particle in the RW-field). If $\omega = \omega_- = 2\pi f_{drift}$, then $\bar{P}_- = mA_\omega r_-\omega_-\sin[\Phi]$, and $r_-(t) = r_-(0) - A_\omega t\left(\omega_+ - \omega_-\right)$ for $\Phi = \pi/2$. We see focusing to the axis of the trap effect of the RW-field.

EXPERIMENTAL VERIFICATION OF THE 3D-HYPOTHESIS

We checked (June 2012) the dependence of the resonance frequency of the rotating field of the bounce frequency $f_Z = \omega_Z/2\pi \approx \upsilon_\parallel/2L$ ($\upsilon_\parallel$ - the longitudinal velocity), changing the length of the accumulation. The length of the accumulation is manipulated by controlling the confining potential at the electrodes V-VIII (see Fig. 3). In this case, we have changed the frequency of the rotating field and observed it will change in the number of accumulated particles at different points in time (see Fig. 4). This dependence shows that the maximum number of stored particles for each length of accumulation is reached at the specific frequency RW-field. This resonance frequency increases with decreasing length of storage. We also determined the dependence of the lifetime of the cloud of particles accumulated on the RW-field frequency for different lengths of accumulation. (see Fig. 5). Analysis of the dependences shows modifies the lifetime and resonant frequency of the RW-field at different lengths of storage. Possible to observe several peaks lifetime at multiple frequencies (see Fig. 5 a). Another interesting result: the accumulation does not occur if the area of accumulation is only within the RW-field. That is, the particles must be in the rotating field is not all the time, and select the phase of entry into this field. This supports the hypothesis about the relationship of the longitudinal and transverse motion of the particles in the trap with the frequency of the rotating field. For greater clarity, the longitudinal evaluation of the bounce frequency of and agreement to the resonant frequency of the rotating field for various lengths of storage were presented in the Table 1.

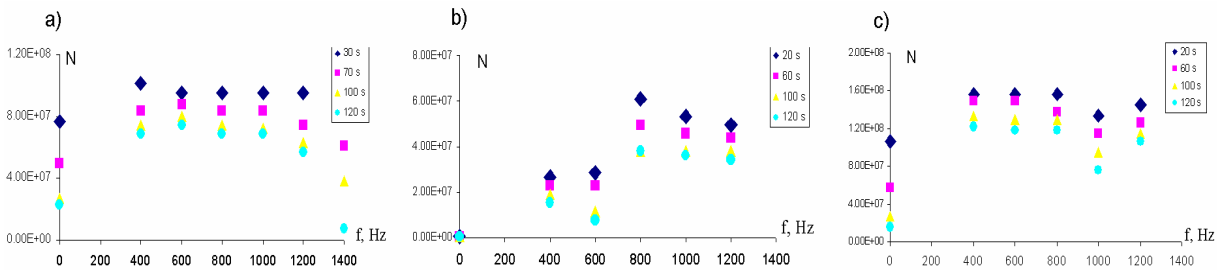

Figure 4: The dependence of the number of particles accumulated on the frequency of the rotating field for different lengths of accumulation: a) L=72 cm, b) L=48 cm, c) L=32 cm.

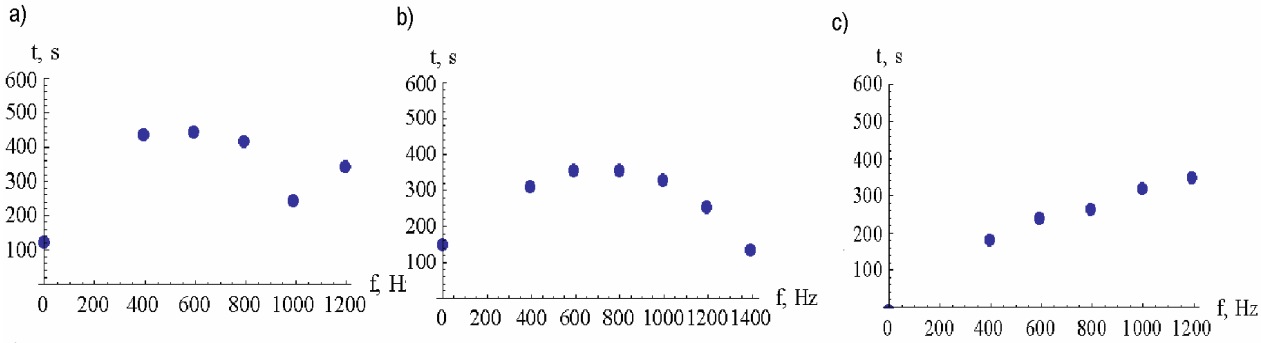

Figure 5: The dependence of the lifetime of a cloud of particles accumulated on the frequency of the rotating field for different lengths of accumulation: a) L=72 cm, b) L=48 cm, c) L=32 cm.

Table 1: Relationship with the length of the accumulation of frequencies.

Length of accumulation, L, cm	**Bounce frequency,** f_Z, kHz	**Resonance RW frequency,** f, kHz
72	600	600
48	850	800
32	1200	>1100

SUMMARY AND OUTLOOK

- The optimal parameters, which significantly increase the lifetime of the cloud and compress the accumulated particles.
- Proposal the 3D-hypothesis on the relationship RW frequency field, the frequency of the longitudinal motion and frequency drift motion.
- Resolved the 3-dimensional equations of motion of particles in the trap and show the focusing effect of the rotating electric field. Particles for the RW-mechanism work should not always be in the RW field, and at the right time, "dive" under its action necessary phase.
- Communication of the resonance frequency RW field and the bounce frequency of the longitudinal motion has been confirmed experimentally.

Further development of methods compression and storage of the positron clouds in the trap will improve the injection positron [7,8] in the storage ring LEPTA facility.

ACKNOWLEDGMENT

The work was supported under the grant RFBR №09-02-00084 and the Federal Program "Scientific and Educational Research Staff of Innovative Russia" SC № 14.A18.21.1302.

REFERENCES

[1] E. Akhmanova et al. Particles and Nuclei, Letters, 7 (2010) 502.
[2] X.-P. Huang et al. Phys. Rev. Lett., 78 (1997) 875.
[3] J.R. Danielson and C.M. Surko, Phys. Plasmas, 13 (2006) 055706.
[4] M.K. Eseev et al. “Methods for optimization of the dynamics of the storage of positrons in the Surko trap”, COOL’11, Alushta (Ukraine), September 2011, WECOB01, p. 81 (2011); http://www.JACoW.org.
[5] R.G. Greaves and J.M. Moxom Phys. Plasmas, 15 (2008) 072304.
[6] D.P. van der Werf et al. New Journal of Phys. 14 (2012) 075022.
[7] E.V. Akhmanova et al. Particles and Nuclei, Letters, 9 (2012) 373.
[8] A.G. Kobets et al., “Lepta project: towards positronium”, TUPPB005, these proceedings.

TRANSFER CHANNEL FROM BOOSTER TO NUCLOTRON AT THE NICA FACILITY

G. Filatov#, I. Meshkov, V. Mikhaylov, A. Sidorin, N. Topilin, G. Trubnikov, A. Tuzikov,
JINR, Dubna, 141980, Russia

Abstract

In the last years the Nuclotron-based Ion Collider fAcility (NICA) project is developed at Joint Institute for Nuclear Research (JINR), Dubna, Russia. Important elements of the NICA are two synchrotrons: Booster and Nuclotron. Connection between these synchrotrons is provided with the transfer channel for heavy ions at energy of 600 MeV/u. The transfer channel includes a stripping station and charge separation system. General goal of the optic design is to minimize emittance at the exit of the channel. Magnetic system of the channel will be constructed using magnets of the Nuclotron type.

INTRODUCTION

The NICA project [1] aims to construct the new accelerator facility for colliding beam experiments. The first stage of the project is experiments on heavy ion beams particularly gold ions. Goals of the transfer channel between Booster synchrotron and existing Nuclotron are the following: the beam transport with minimum ion losses and minimum increase of the beam emittance; ion stripping to a maximum charge state (the goal charge of the beam) and the separation of parasitic charge states. The design parameters of the ion beam are given in Table 1.

Table 1: Design parameters of the beam

Sort of ions	
before stripping station	Au^{31+}, Au^{52+}, Au^{65+}
after stripping station	Au^{79+}
Maximum energy of ions, MeV/u	685
Maximum magnetic rigidity of ions, T m:	
before stripping station	25
after stripping station	11
Ion number	$2 \cdot 10^9$

The channel has some features considered in the physical design of the channel:

- complex 3D geometry which proposes the installation of tilt bending magnets;
- presence of the striping station and the necessity of the separation of parasitic charge states;
- different magnetic rigidities of ions before and after the striping station;
- wide ranges of momentum spread values, horizontal and vertical emittances at the entry of the channel;
- increase of the beam emittance in the channel because of ion stripping and betatron coupling;
- mismatch of the beam parameters with lattice functions of Nuclotron.

Old version of physical design of the channel has been presented in early works [2, 3]. New schemes of the beam extraction from Booster and the beam injection into Nuclotron are applied that impact on the channel geometry. Also, the new lattice of the channel is designed considering minimization of transverse emittances after the beam injection into Nuclotron.

LATTICE OF THE TRANSFER CHANNEL

The geometry and the magnetic system of the channel are mainly defined by the mutual position of Booster and Nuclotron. These synchrotrons have different radii and vertical positions of their median planes. The vertical distance between median planes of the synchrotrons is 3.76 m. The beam is extracted from Booster in both directions. The horizontal extraction angle is 120 mrad, the vertical extraction angle is 30 mrad. The beam is injected into Nuclotron in the vertical plane at an angle of 350 mrad. The beam in the channel is transported in the horizontal and vertical directions simultaneously. The total length of the channel is 23.2 m. Its azimuthal size is 45°, which corresponds to the beam injection through one Nuclotron octant from the point of extraction from Booster.

The channel consists of 5°tilt sector bending magnets and 7°quadrupoles, 2 of which are tilt ones. Magnetic elements of the beam are superconductive with an iron yoke. One quadrupole has the opportunity to reverse a polarity. Vacuum chamber of the channel has a circle cross section with a diameter of 60 mm.

The stripper station is situated inside the Booster yoke. Parasitic charge states after stripping is separated by the optical system of the channel and then a superconductive Lambertson magnet.

General view of the Booster-Nuclotron channel and a view from above are given in Fig. 1, 2. Vertical profile of the channel is shown in Fig. 3 (the profile means a side view of the linearized channel so it differs from any lateral view of the channel itself). Lattice of the channel is presented in Fig. 4, where BM1-BM5 — bending magnets, Q1-Q7 — quadrupoles, LM — Lambertson magnet, Str — stripping station. Main parameters of the magnetic elements are given in Table 2.

#filatov.jinr@mail.ru

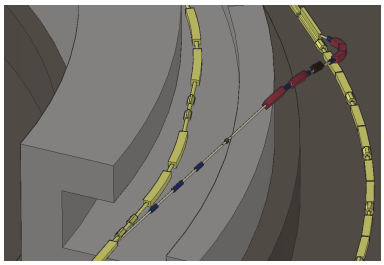

Figure 1: General view of Booster-Nuclotron channel.

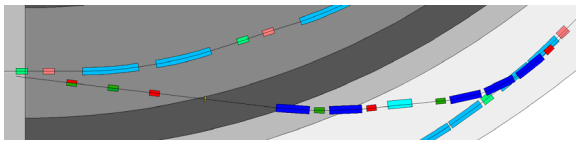

Figure 2: A view of the channel from above.

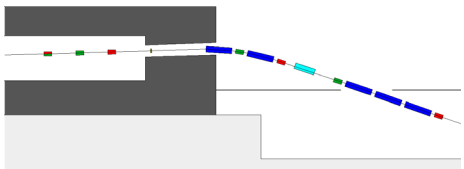

Figure 3: Vertical profile of the channel.

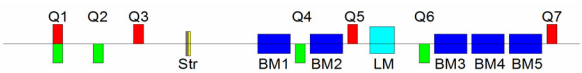

Figure 4: Lattice of the channel.

Table 2: Main parameters of the magnetic elements

Magnetic element	Effective length, м	Max. magnetic field (gradient), T (T/m)
BM1-BM5	1,312	1,8
LM	1	1,5
Q1, Q3	0,4	27
Q2	0,6	27
Q4-Q7	0,4	12

OPTIMIZATION OF OPTICAL SYSTEM OF THE CHANNEL

The beam is transported from Booster to Nuclotron with increase of longitudinal and transverse emittances. The main reasons behind the growth are the following:

- multiple scattering and energy straggling of the beam ions at the stripping target;
- a coupled motion in tilt bending magnets;
- a mismatch of the beam at the exit of the channel with lattice functions of Nuclotron.

Significant growth of the beam emittance causes decrease of NICA collider's luminosity, so minimization of the emittance growth in the channel is a necessary requirement for parameter definition of the channel optical system.

The optical system of the channel has to provide separation of parasitic charge states appearing after stripping and their extraction to a dump system because of high beam intensity.

So, criteria of optimality for a tuning of the channel optical system are:

1) minimality of horizontal and vertical emittances of the beam after their dilution by filamentation in Nuclotron (longitudinal emittance growth depends only on properties of the stripping target and is not taken into account in the optimization);

2) full separation of Au^{78+} ions from the Au^{79+} beam.

The values of the beam emittance at the entry of the channel may vary over a wide range because Booster has features such as: 1) different methods of the beam injection, and 2) the electron cooler system. Optical system of the channel must satisfy the criteria of optimality defined above for all the possible initial values of momentum spread, horizontal and vertical emittances.

The optimization of the optical system of the channel is the minimization of the corresponding objective function, arguments of which are gradients of magnetic field in quadrupoles. Minimization is performed by numerical methods.

Simulations have been carried out for initial values of momentum spread, horizontal and vertical emittances in the following ranges: from 0.01 to 1.8 π·mm·mrad for horizontal emittance $\varepsilon_{x,0}$; from 0.01 to 0.14 π·mm·mrad for vertical emittance $\varepsilon_{y,0}$; from $7 \cdot 10^{-5}$ to $3 \cdot 10^{-4}$ for momentum spread $\sigma_{p,0}$. 125 μm Carbon film was considered as the stripping target. The simulation results are shown that longitudinal emittance growth is not greater than 10%, that is acceptable. Values of horizontal and vertical emittances after their dilution in Nuclotron ($\varepsilon_{x,Nucl}$ and $\varepsilon_{y,Nucl}$) are less than 1.5π·mm·mrad and 0.9 π·mm·mrad, respectively. It should be noted that vertical emittance of the beam increases for any values of $\varepsilon_{x,0}$ and $\varepsilon_{y,0}$ while horizontal emittance decreases for $\varepsilon_{x,0} > 0,5$ π·mm·mrad. It is explained by betatron coupling in the channel. Variation of initial momentum spread does not influence essentially on transverse emittances.

Ranges of optimal gradients in the channel quadrupoles are given in Table 3. Contour plots of horizontal and vertical emittances $\varepsilon_{x,Nucl}$ and $\varepsilon_{y,Nucl}$ depending on initial values are presented in Fig. 5.

Table 3: Parameters of quadrupoles in the channel.

Quadrupole	Gradients (min/max), T/m
Q1	-11.8 / 22
Q2	-26.5 / -9.7
Q3	20.8 / 25.2
Q4	-10.1 / -6.4
Q5	5.3 / 9.5
Q6	-8 / -5.1
Q7	5 / 6.8

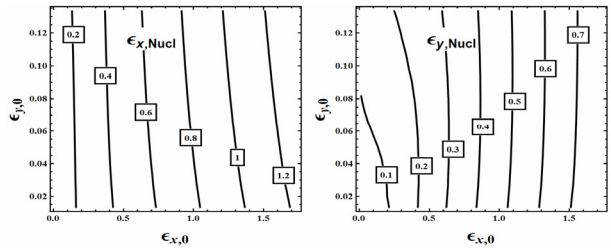

Figure 5: Contour plots of horizontal (left) и vertical (right) emittances after their dilution in Nuclotron. All values are given in π·mm·mrad.

BEAM DYNAMICS SIMULATION

Simulation of the beam dynamics in the channel has been fulfilled for different initial values of the beam emittances. Results have shown that the chosen aperture of the vacuum chamber allows transporting the ion beam with 100% efficiency.

The results of the beam dynamics simulation for $\varepsilon_{x,0}$ = 1.8 π·mm·mrad, $\varepsilon_{y,0}$ = 0.14 π·mm·mrad and $\sigma_{p,0} = 3 \cdot 10^{-4}$ are given in Fig. 6-8. The optical functions of the beam $\beta_{x,y}$ and $D_{x,y}$ are shown in Fig. 6. Envelopes of the beam $a_{x,y} = 2.45\sigma_{x,y}$ are in Fig. 7. Fig. 8 shows evolution of the RMS beam emittances $\varepsilon_{x,y}$ along the channel (including the beam emittance growth due to the injection of the mismatched beam into Nuclotron that is shown as a leap at the plot end).

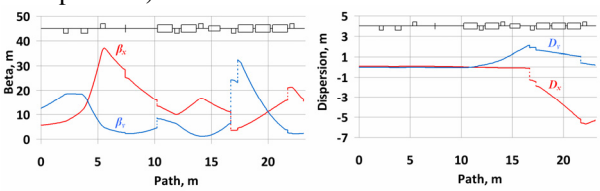

Figure 6: The optical functions of the beam.

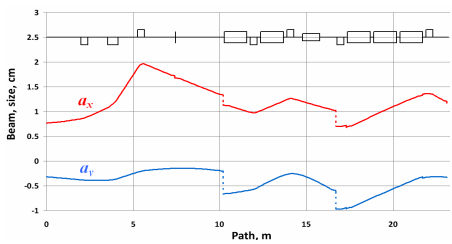

Figure 7: The beam envelops along the channel.

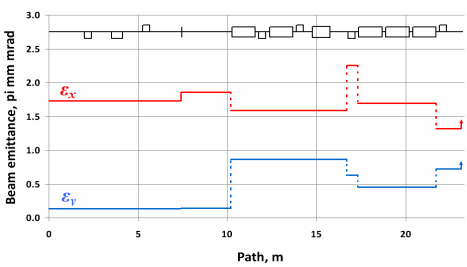

Figure 8: Evolution of the beam emittances.

As the channel does not lie in one plane, coordinates x and y means transverse coordinates of local reference system spanned by the accompanying tripod of the reference trajectory of the beam. Ox is an axis directed at a minimal angle to the horizontal plane. Rotations of the local reference system are used in the beam dynamics simulations because magnetic elements are installed at different angles to the horizontal plane. The rotations are shown as dashed gaps of the plot in Fig. 6-8.

CHARGE STATE SEPARATION

A composition of the ion beam after the stripping station is defined by its stripping efficiency. The stripping efficiency for Au^{31+} at the energy of 580 MeV/u (that corresponds to the Booster maximum magnetic rigidity) is estimated to be not less than 80%, so ions of parasitic charge states (mainly Au^{78+}) after stripping can reach about 20% of the beam intensity.

A section of the channel with bending magnets BM1-BM2 and quadrupoles Q4-Q5 is used for the separation of the parasitic charge states. Lambertson magnet carries out a final extraction of Au^{78+} ion beam.

The trajectories and envelops of Au^{79+} and Au^{78+} beams in the separation section are given in Fig. 9.

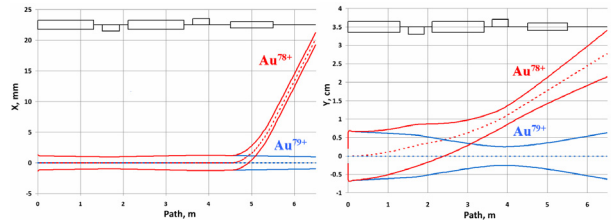

Figure 9: The separation of Au^{78+}ion beam.

CONCLUSION

The geometry and the lattice have been chosen in frame of the conceptual project of the Booster-Nuclotron channel. The optical system parameters have been optimized to provide the ion beam transport with a minimal emittance growth and full separation of parasitic charge states. Requirements for the aperture of the vacuum chamber and the magnetic elements of the channel are defined by means of the beam dynamics simulations. Design and parameters of the magnets are similar to the Booster ones, which prototypes were constructed and tested at JINR.

REFERENCES

[1] A.Sidorin, A.Kovalenko, I.Meshkov, G.Trubnikov, Project of the Nuclotron-Based Ion Collider Facility (NICA) at JINR. Proceedings of IPAC'10, Kyoto, Japan, 2010, pp.693-695.

[2] A.Tuzikov, V.Mikhaylov, Booster-Nuclotron Beam Line for NICA Project. Physics of Particles and Nuclei Letters, 2010, Vol. 7, No. 7, pp.478-482.

[3] O.Kozlov, A.Eliseev, I.Meshkov, V.Mikhaylov, A.Sidorin, N.Topilin, G.Trubnikov, A.Tuzikov, Transport beam lines for NICA accelerator complex. Proceedings of IPAC2011, San Sebastian, Spain, 2011, pp.3526-3528.

SNOP – BEAM DYNAMICS ANALYSIS CODE FOR COMPACT CYCLOTRONS

V.L. Smirnov, S.B. Vorozhtsov, JINR, Dubna, Russia

Abstract

The SNOP program complex intended for particle dynamics simulations in a compact cyclotron from the injection line to the extraction system is described. The main features of the SNOP are usage of 3D electric and magnetic field maps, beam space charge effect calculation, and analysis of the beam losses on the structure elements of the facility under consideration. The optimal usage of modern computer capabilities and graphic libraries for visualization is a key issue in the SNOP development. The beam dynamics modeling results for various cyclotrons are presented.

INTRODUCTION

Recently, compact cyclotrons are widely used for solution of fundamental and applied problems. Noticeable expenses that are needed for the design and operation of the cyclotrons impose stringent requirements on the accuracy of the simulations conducted to select the facility parameters and to assess the beam dynamics peculiarities. There are a number of available codes such as TRANSPORT [1], MAD [2], TRACE3D [3], and COSY [4] based on the matrix formalism for the design and study of beam-optics systems. Some of them include detailed beam space charge calculations. However, none of these codes provides a full description of the peculiarities of beam dynamics in a compact cyclotron. The other group of the programs is prepared for special accelerating facilities [5, 6]. It is problematic to use these codes for the beam dynamics analysis in the cyclotron as a complete setup, from the injection line to the extraction system. This situation appeals to preparation of programs that can be easily applied to any cyclotron facility, operate with 3D (spatial) electric and magnetic field maps, take into account the beam space charge effects, and most effectively use resources of modern computers. The program complex SNOP that is produced at JINR and intended for simulation of beam dynamics in a compact cyclotron complies with all the above-mentioned requirements. The SNOP is a qualitative extension of the CBDA code described in [7].

PROGRAM COMPLEX DESCRIPTION

The main features of the SNOP are usage of 3D electric and magnetic field maps, beam space charge effect calculation, and analysis of the beam losses on the structure elements of the facility under consideration. The optimal usage of the modern computer capabilities is a key issue in the SNOP development.

Complex Structure

The program complex is convenient to use due to its user-friendly interface (see Fig. 1). The SNOP is structured in such a way that there are dedicated blocks responsible for real units in the beam transport line and accelerator itself. There are also separate menus to control parameters of acceleration particles and setting parameters for the equation of particle motion including beam space charge effects.

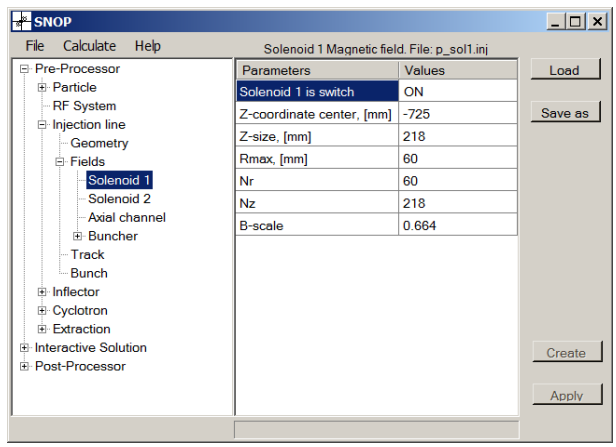

Figure 1: SNOP main window.

The program complex shell permits one to control parameters of the electromagnetic devices for the beam acceleration and focusing, such as the dee electrode, solenoid, electrostatic inflector, magnetic and electrostatic quadrupole, magnetic channel, electrostatic deflector, and main, trim and harmonic coils.

The SNOP shell is prepared in such a way that it is possible to modify available parameters without editing any files manually.

The tooling for the magnetic field analysis permits full-size calculations of the magnetic field characteristics. The mean magnetic field, flutter, betatron tunes, amplitudes of radial oscillations, etc can be calculated using analytical formulas and closed equilibrium orbit computation.

There is a possibility of using such systems as MathCAD and AutoCAD, with which data exchange can be carried out. MathCAD is applied at the initial data generation and for analysis of the results. AutoCAD permits one to specify geometry of the objects when calculating particle losses and to depict the positions of the accelerated and lost particles against the background of the real geometry of the facility (see Fig. 2).

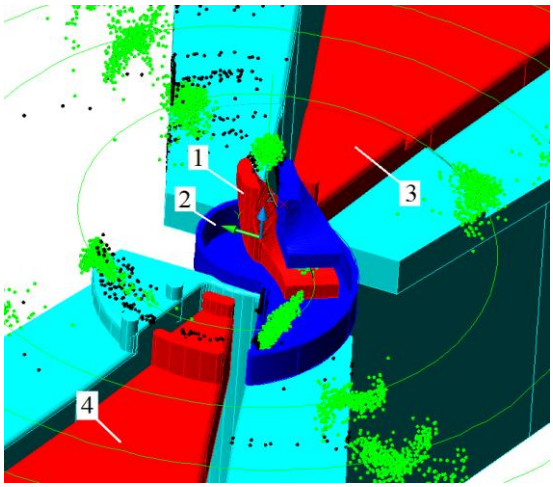

Figure 2: AutoCAD visualization of the central region of a cyclotron: (1) inflector, (2) inflector RF shield, (3) dee 2, (4) dee 1.

The SNOP allows using graphical libraries for visualization of the calculated results. This makes t possible to plot on the screen some physical process that happen in the facility simultaneously with the simulation progress. The simultaneous motion of a set of the macroparticles can be visible against the background of the chosen geometrical structure of the facility under investigation to understand an impact of various selected parameters of the acceleration regime on the particle behavior.

Equations of Particle Motion

The Cartesian coordinate system is used in the program complex as most generally applicable to definition of electromagnetic fields of the structure elements. The SNOP calculates trajectories of macroparticles in the electromagnetic fields, solving a complete system of the equations of motion without any simplification. It uses the classical fourth order Runge-Kutta method to solve the system of the equations.

Usage of the Electromagnetic Field Maps

The SNOP supports beam dynamics calculations using 3D (spatial) maps of electric and magnetic fields. Import of the field maps calculated in the OPERA/TOSCA program [8] is an option provided. For user's convenience there is a possibility of analytical field distribution for some of the structure elements at the stage of initial selection of the facility parameters. Along with application of the static field maps there is a possibility of using time-dependent electromagnetic fields, e.g., buncher and acceleration dee fields.

Calculation of Beam Space Charge Effects

There are two possibilities of considering particle self-fields in the SNOP: direct calculation of the Coulomb particle interactions and the PIC (Particle-In-Cell) method [9]. The latter is one of the methods used to solve a certain class of partial differential equations. In this method, individual particles in a Lagrangian frame are tracked in continuous phase space, whereas moments of the distribution such as densities and currents are computed simultaneously on Eulerian (stationary) mesh points. A larger number of macroparticles in the calculation is ensured by application of the PIC method compared to the former method.

Particle Losses on the Structure Elements of the Facility

In the SNOP there is a possibility of detecting loss of particles when they cross the surfaces of the accelerator structure elements. One of the options is description of the structure geometry by analytical surfaces. This permits fast estimation of the particle losses in the facility regions where this geometry input is valid. For more accurate calculation of losses the geometry can be imported from the CAD program with sufficiently detailed presentation of the mechanical model. It can be used in those parts of the facility where the geometry is more complex and cannot be described by analytical surfaces. Fast algorithms for determining the particle intersection with the surfaces of the bodies are used to decrease the required computer time for the calculations in the SNOP. The graphical capability of the program complex permits visualization of the lost particles on various surfaces of the facility.

BENCHMARKING

As was mentioned above, the predecessor of the SNOP is the CBDA code. The results obtained with the CBDA were many times cross-checked with such well known programs as Trace3D and SPUNCH and were confirmed by the experiments with the beam at the RIKEN AVF Cyclotron (Japan).

Let us consider some examples of the SNOP application to the modeling of newly developed and operational accelerating facilities.

The HITFiL cyclotron (IMP, China) [10] is under construction to be employed as an injector to a synchrotron for hadron therapy of tumors. The synchrotron should accelerate carbon ions with the energy 400 MeV/nucl. The cyclotron is designed to accelerate $^{12}C^{5+}$ ions up to the energy 7 MeV/nucl.

As the starting point, the preliminary cyclotron technical project was adopted. The main purpose of the simulations was analysis of the beam dynamics and overall functioning of the injection, acceleration, and extraction systems. The results of the simulations were taken as a basis for modification of practically every element of the machine in the final version of its technical project. Estimation of the overall beam transmission efficiency through the whole cyclotron was a key issue of the study.

The activity was focused on substantial improvement of the extraction system functionality. The main results emerged from the calculations were substantial modernizations of the extraction system elements and,

which is most important, installation of a new element, namely, the gradient corrector of the cyclotron fringe field along the extracted beam trajectory. The calculations showed that the proposed upgrade of the extraction system would lead to drastic improvement of the extracted beam characteristics.

The corresponding calculations performed for the newly formulated machine structure (after all the modifications offered by the calculations) showed that the beam transmission efficiency through the accelerator units increased and the total transmission increased by a factor ~5 times (see Fig. 3).

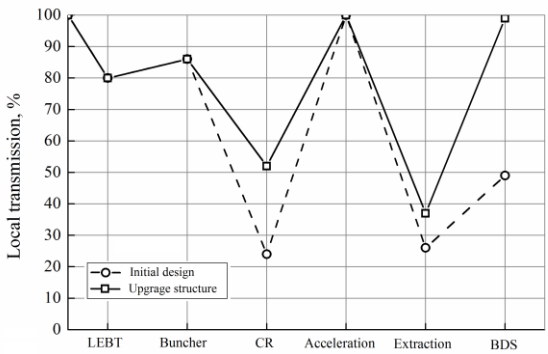

Figure 3: Beam transmission efficiency at various structure elements of the cyclotron.

Computer-aided modeling for the RIKEN AVF cyclotron (Japan) [11] was also performed. As one of the results, a new method was emerged [12] to substantially suppress particle energy spread in a compact cyclotron. The viability of the method was demonstrated experimentally by the beam tests. The new inflector geometry and the optimized central electrode structure have been formulated for the upgrade of the AVF cyclotron.

The SNOP was applied to multicomponent beam (15 various ions) dynamics simulations of the FRIB Front End line [13]. Space charge calculations were performed with 10^6 macroparticles.

The recent application of the SNOP was modeling of the NIRS-930 cyclotron [14]. Computer representation of the machine was prepared, including the area from the axial injection line to the outlet window of the cyclotron. A comparison of the calculations with the experimental data shows that the constructed model agrees with the reality very well. Here one of the key points is the beam transmission efficiency though the cyclotron (see Table 1).

Table 1: Transmission, %

	Calculation		Experiment
Range	No space charge effects	Space charge effects included.	
Central region	35	31	29
Acceleration	89	85	89
Extraction	52	49	49
Total	16	13	12

Optimization of the operational parameters for typical beams in the whole performance area of NIRS930 is the next step in the simulations, which is expected to improve the transmission through the cyclotron and the beam quality.

CONCLUSIONS

The program complex SNOP is a convenient tool for the beam dynamics analysis in a compact cyclotron. The SNOP is user-friendly and permits conducting calculations for a wide class of facilities. It is handy for construction of the computer model of a cyclotron. The program complex is very useful and has a high potential for computer simulations of accelerators.

The SNOP was applied for the beam dynamics analysis in a number of operational and projected accelerator facilities with favorable comparison to the beam measurements.

REFERENCES

[1] K.L. Brown, The ion optical program TRANSPORT. Technical Report 91, SLAC, 1979.
[2] F. Christoph Iselin, "The Mad Program Reference Manual," CERN, LEP Division November 1, 1984.
[3] K.R. Crandall, TRACE 3-D Documentation, Report LA-11054-MS, Los Alamos, 1987.
[4] M. Berz, COSY INFINITY, Version 8 User's Guide and Reference Manual, MSU, 1999.
[5] J. J. Yang, A. Adelmann, M. Humbel, M. Seidel, and T. J. Zhang, "Beam dynamics in high intensity cyclotrons including neighboring bunch effects: Model, implementation, and application", Phys. Rev. Special Topics - Accelerators and Beams 13, 064201, 2010.
[6] E. Pozdeyev, Ph.D thesis, Michigan, State University, 2003.
[7] E.E. Perepelkin and S.B. Vorozhtsov, "CBDA – Cyclotron Beam Dynamics Analysis Code", Proc. 21st Russian Particle Accelerator Conference, 2008, pp.40-42.
[8] Cobham CTS Limited, 24 Bankside, Kidlington, Oxfordshire OX5 1JE, UK.
[9] Yu.N. Grigoryev, V.A. Vshivkov, M.P. Fedoruk, Numerical particle-in-cell methods. Theory and applications. VSP, 2002.
[10] B. Wang et al.. "Computer Design of a Compact Cyclotron", Physics of Particles and Nuclei Letters, 2012, Vol. 9, No. 3, pp. 288–298., 2012.
[11] S. Vorozhtsov, V. Smirnov, and A. Goto, "Modification of the Central Region in the RIKEN AVF Cyclotron for Acceleration at the H=1 RF Harmonic", Proc. 19th Int. Conf. on Cyclotrons and their Appl., Lanzhou, 2010.
[12] S.B. Vorozhtsov and V.L. Smirnov. "The method of decreasing of the energy spread of the beam in a cyclotron". Patent application, RU 2455801, № 19 (II), p. 490, 01.02.2011.
[13] L. T. Sun et al. "Low energy beam transport for facility for rare isotope beams driver linear particle accelerator", Rev. Sci. Instrum., 83, 02B705, 02B705, 2012.
[14] S. Vorozhtsov, V. Smirnov, A. Goto, S. Hojo, T, Honma, K. Katagiri, "Quantitative Simulation of NIRS-930 Cyclotron", Proc. Int. Particle Accelerator Conference, New Orleans, 2012.

RF SELF–CONSISTENT ELECTRON BEAM DYNAMICS SIMULATION IN THZ GENERATOR BASED ON PHOTOINJECTOR AND CHERENKOV DECELERATING SYSTEM

T.V. Bondarenko, S.M. Polozov, O.A. Tatsyuk,
National Research Nuclear University Moscow Engineering Physics Insitute, Moscow, Russia

Abstract

The generator of high intensity monochromatic radiation in sub-mm range is currently under R&D at the Department of Electrophysical Facilities of MEPhI. This generator is based on photoinjector and irradiating Cherenkov capillary. It is necessary to have high brightness electron beam for generation of monochromatic radiation in this type of structure. Such beam can be produced by photocathode and accelerated to energy of several MeV using short structure with high acceleration efficiency. Irradiating capillary represents as metal tube with inner radius of the radiation wavelength order and covered with dielectric layer or made of corrugated waveguide. It is important to study the self-consistent dynamics of the beam during the acceleration as the current pulse is equal to several A, i.e. the beam dynamics should be studied considering both RF (radiation) and Coulomb components of self-field of beam. Another problem is to study the electron beam dynamics and fields irradiated by it in decelerating structure in the absence of external fields. The scheme of irradiating facility, its operation mode and high-current beam dynamics simulation results in accelerating structures are presented.

INTRODUCTION

The generators of high intensity monochromatic radiation in sub-mm range are highly demanded nowadays and developed for a number of research centers and applied tasks. One of the applications is cargo inspection system that demands high power THz radiation and working mode with repetition rate about tens of Hz.

High radiation power can be generated using large accelerator (linear or synchrotron) and free electron laser (FEL) but such facilities are not compact. Traditional vacuum (e.g. traveling wave tubes) and solid state (OLED, resonant tunnel diodes) generators doesn't provide the power level higher than 1 W.

THz radiation generation can be obtained using Cherenkov or Smith-Purcell radiation capillary channels and photoinjector accelerating system [1].

The important problem is investigation of self-consistent beam dynamics, mathematical model development and high current relativistic beam dynamics simulation during the acceleration and going through the irradiating structure.

In common case it is necessary to solve the motion equation together with Maxwell's equations. But sometimes we can replace the solution of Maxwell's equations (this is a quite complicated task) by the solution of Poisson's equation (for example, if we are looking for the solution of motion equation for intensive non-relativistic ion beams) or excitation equation (in case of ultrarelativistic beams, when we can neglect the Coulomb component of self-field of the beam). But for some tasks we have to consider both quasi static Coulomb component of self-field and RF radiation field of the beam.

The developed model considers full self-consistent field (both Coulomb component and radiation field), induced by beam in structure.

The key feature of the model is external field absence in irradiating structure.

FACILITY SCHEME

The coherent Cherenkov radiation can be generated using short and well collimated electron bunches with ps or sub-ps duration and 100-200 μm transverse size. Such bunch can be formed using a photocathode and compact accelerating system providing high accelerating gradient. The laser system in photogun is proposed to generate a series of short laser pulses which irradiate photocathode placed in the sidewall of an accelerating system. It was proposed to separate the accelerating structure into two sections (Fig. 1).

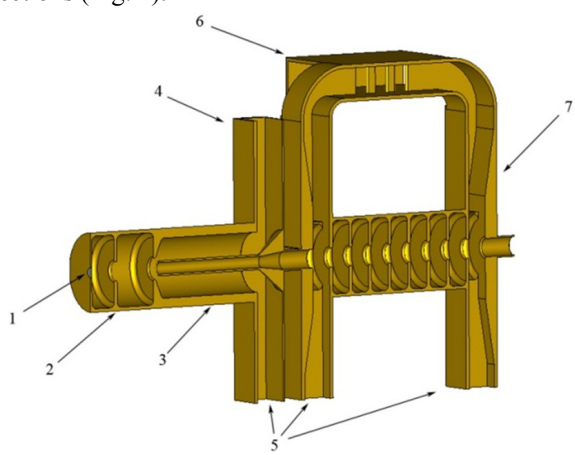

Figure 1: Accelerating system: 1 – photocathode, 2 – 1.6 cell structure, 3 – coaxial wavetype transformer, 4 – power input, 5 – vacuum ports, 6 – directional coupler, 7 – travelling wave resonator structure.

The first accelerating system is based on 1.6-cell disk loaded waveguide (DLW) and provides maximum accelerating fields on the cathode surface. After that the bunch (or bunch packet) should be accelerated in the

second structure to the energy of several MeV. Second accelerating structure is traveling wave structure based on traveling wave resonator principle (TWR) [2]. After acceleration bunch should be injected into special irradiating capillary channel where electromagnetic radiation will be induced under the Cherenkov principle.

Two types of capillary channel can be used in the proposed generator. First one is conducting (copper) capillary tube coated inside by dielectric. The slow-wave structure can also be made as a metal corrugated channel or a grating surface. Both decelerating systems have transverse sizes compared with the wavelength of generated radiation (0.1-1 mm) and a length of several cm.

HIGH CURRENT BEAM DYNAMICS

Space Charge Field

Space charge field (Coulomb component of self-field of beam) calculation is proposed to be carried out using "large particles" method [3]. The main point of this method is the following. During bunching or emission processes beam is formed into separate bunches which follow each other with some period. We consider the area with length of few periods (usually 1-3). Into the bunch area we involve spatial grid. Bunch represents as a large number (N>>1) of particles with limited size. According to three dimensional model particles are divided into rectangular parallelepipeds of the same size.

If we know beam current density and size of large particle, we can find its charge. Then the solution is reduced to three tasks. The first one is to find charge density distribution on the grid. Then the Poisson equation

$$\bar{U}_c = -\bar{\rho}_c / \varepsilon_0$$

is solved using Fast Fourier Transformations (FFT) and, finally, the components of electric self field of the beam are defined by potential differentiation.

Large particle method has few varieties, which differ from each other by charge distribution way in cells of spatial grid. For modeling beam dynamics CIC (Clouds in Cells) method was used. Here charge of each particle is spread to the nearest nodes of grid with corresponding "weight coefficients".

Beam Loading Simulation

In this фкешсду based on electro dynamical theory excitation simulations were carried out for accelerating structures on standing and traveling waves in case when the duration of current pulse is many times smaller than filling time of structure with RF power (short electron pulse from photocathode case).

More details about excitation calculation theory can be found in book of Prof. E. S. Masunov [4].

Beam Dynamics Simulation In 1st Accelerating Section Considering Beam Loading

After formation beam is accelerated in 1st accelerating section represented as 1.6 cell structure and accelerates beam on standing wave on π mode.

Main electro dynamical parameters for 1st accelerating section are shown in Table 1.

Table 1: Main electrodynamics parameters for 1st accelerating section.

Section length (m)	0,072
β_v	0,9
Wave length (m)	0,1
Efficient shunt impedance (MΩ/m)	50
Q factor	13000

Initial particles phases during injection into the 1st section are chosen from the point of max efficiency of acceleration. Main parameters used in the simulation are shown in Table 2:

Table 2: Main parameters used in the simulation.

Wave length (m)	0,1
Section length (m)	0,072
Attenuation parameter w	0
Initial phase duration of current pulse	0,02
Initial dimensionless amplitude of electric field	2,544

Motion equations were used to simulate beam dynamics considering beam loading in 1st section are the following:

$$\frac{dA}{d\xi} = A\left(\frac{d}{2d\xi}(lnR_n) - w\right) - \frac{2B}{N}\sum_{n=1}^{N} I_0\left(\frac{2\pi}{\beta_v}\sqrt{1-\beta_v^2}\eta_n\right)cos\psi_n$$

$$\frac{d\psi_i}{d\xi} = 2\pi\left(\frac{1}{\beta_v} - \frac{1}{\beta_{\xi.i}}\right) + \frac{2B}{AN}\sum_{n=1}^{N} I_0\left(\frac{2\pi}{\beta_v}\sqrt{1-\beta_v^2}\eta_n\right)sin\psi_n$$

$$\frac{d\gamma_i}{d\xi} = Acos\psi_i$$

where B characterizes beam-structure coupling,

$$B = \frac{eJ_0\omega R_{sh}\lambda^2}{4W_0 QLV_{gr}}$$

N – number of particles in bunch, $\xi = z/\lambda$ - dimensionless longitudinal coordinate, $\tau = \omega t$

$$A_z = (e\lambda / m_0c^2)E_z$$

As a result of beam dynamics simulation in 1st section the dependence of average energy of all particles as a

function of longitudinal coordinate is presented at Figure 2.

Preliminary studies shows that pulse beam current equal to 1 A is necessary for THz generator operation. According to Fig. 2 beam with beam current equal 1 A is accelerated to the energy of 1.33 MeV. We assume this energy as injection energy for 2nd accelerating structure. Output phase duration of current pulse after 1st accelerating structure equals 0.0016.

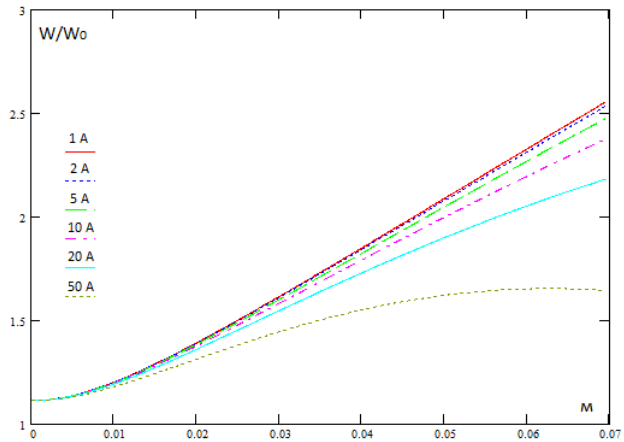

Figure 2: Average energy of all particles as a function of longitudinal coordinate with different beam currents.

Beam Dynamics Simulation In 2nd Accelerating Section Considering Beam Loading

After 1st accelerating section beam is moving to the 2nd accelerating section is presented as an 8 cell structure and accelerates beam on traveling wave with negative dispersion on π/2 mode.

Table 3: Main electrodynamics parameters for 2st accelerating section.

Section length (m)	0,2
β_v	1
Wave length (m)	0,1
Series impedance (MΩ/m)	70

Motion equations used to simulate beam dynamics considering beam loading in 2st section are:

$$\frac{dA}{d\xi} = A\left(\frac{d}{2d\xi}(lnR_n) - w\right) - \frac{2B}{N}\sum_{n=1}^{N} I_0\left(\frac{2\pi}{\beta_v}\sqrt{1-\beta_v^2}\eta_n\right)cos\psi_n$$

$$\frac{d\psi_i}{d\xi} = 2\pi\left(\frac{1}{\beta_v} - \frac{1}{\beta_{\xi.i}}\right) + \frac{2B}{AN}\sum_{n=1}^{N} I_0\left(\frac{2\pi}{\beta_v}\sqrt{1-\beta_v^2}\eta_n\right)sin\psi_n$$

$$\frac{d\gamma_i}{d\xi} = Acos\psi_i + Acos\left(\frac{\xi}{\beta_{ph}} + \tau\right)$$

$$\frac{d\tau}{d\xi} = \frac{1}{\beta_{ph}}$$

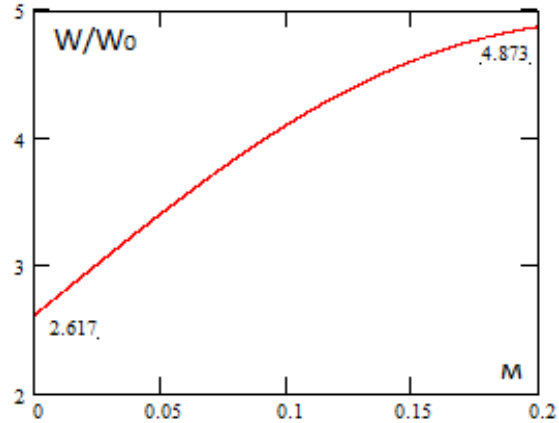

Figure 3: Lorenz factor value as a function of coordinate in 2nd accelerating structure for beam current value of 1 A

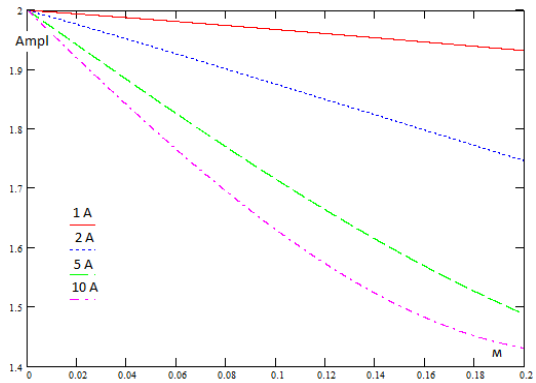

Figure 4: Accelerating field amplitude as a function of coordinate considering different beam current during the acceleration in 2nd accelerating structure.

SUMMARY

The generator of high intensity monochromatic radiation in sub-mm range was discussed with an emphasis on beam dynamics investigation in accelerating sections considering full self-field of the beam.

Mathematical model for high current beam dynamics calculation considering both Coulomb and radiation field was developed.

Beam loading simulation was carried out in 1st and 2nd accelerating sections. Figure 2 shows output beam energy after 1st accelerating section for different beam current values. As a working beam current we choose 1 A. Output energy after 1st accelerating section is equal to 1.33 MeV. According to Figure 3 the output energy after 2nd accelerating section is equal to 2.44 MeV.

REFERENCES

[1] A. V. Smirnov, A High Performance, FIR Radiator Based on a Laser Driven E-Gun, ISBN 978-1-60456-720-5, 2008.
[2] J. L. Altman, Microwave circuits, Van Nostrand Co., 1964.
[3] A.S. Roshal, Charged particles modeling, Moscow, Atomizdat, 1979. (in Russian)
[4] E.S. Masunov, Beam loading effects, Moscow, MEPhI, 1999. (in Russian)

RF QUADRUPOLE FOCUSING LATTICES

A.S. Plastun, T.V. Bondarenko,
NRNU MEPhI, Moscow, Russia

Abstract

Spatial homogeneity of a conventional RFQ allows estimating parameters of the lattice easily. Hybrid-RFQ structures with spatially periodic RFQ lenses are more complicated in respect of beam dynamics. Transverse stability of beam motion is defined by lattice parameters. Basically parameters of RF focusing lattices are influenced by longitudinal emittance of a bunch in contrast to static focusing lattices. The paper presents a method which allows evaluating parameters of a very wide class of RF and static quadrupole lattices. Transverse acceptance and acceleration rate could be determined. The method is useful to compare Hybrid-RFQ structures with a conventional RFQ.

INTRODUCTION

The main parameter of periodical focusing lattices is acceptance. It is extremely important for high intensity beams. It is known from the Hill`s equation theory that the acceptance A of any periodical lattice can be defined as [1]:

$$A = \frac{\gamma}{c}\omega_{r\,\min}a^2 , \qquad (1)$$

γ –Lorentz factor, c – the speed of light, $\omega_{r\,min}$- minimum frequency of transverse oscillations of a particle, a – aperture radius of a focusing channel. Another lattice parameter, which describes transverse motion of particle, is a phase advance μ.

$$-1 < \cos\mu < 1 \qquad (2)$$

should be performed to provide stability of transverse motion. The phase advance can be represented as

$$\mu = \int_{t}^{t+T_f} \omega_r(t)dt , \qquad (3)$$

where $\omega_r(t)$ – frequency of transverse oscillations of a particle, t – time, T_f – the period of time for which a particle passes one period of focusing lattice. Thus phase advance μ means the averaged frequency of transverse oscillations for one period.

The accelerating structure of ion linac can be studied with quasi-static approach usually. Estimations for transverse motion of particles in static periodical lattices are generally performed by matrix method or smooth approximation. However range of application of these methods for RF focusing lattices is limited. There is an experience of application of these methods for a conventional RFQ and spatially periodic quadrupole focusing [1]. The limitation consists of low phase advance $\mu << 2\pi$, thin lens approximation and simplicity mainly for FODO lattices [1]. Unfortunately transverse motion of particles in a Hybrid-RFQ is too complicated to be considered by these methods [2].

The focusing lens of a Hybrid-RFQ is too long to use thin lens approximation in the scale of focusing period. Strength of RF focusing lens dependent on time and long focus length don't allow us to use smooth approximation easily.

The paper presents a method which allows studying a very wide class of RF and static quadrupole lattices.

HYBRID-RFQ

A Hybrid-RFQ structure is combined from accelerating gaps and RF quadrupole lenses [3]. Simplified scheme of the structure and its placement with respect to the first RFQ section are shown in Figure 1.

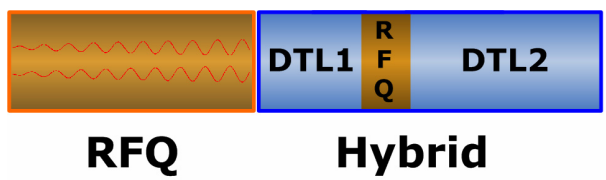

Figure 1: Scheme of Hybrid-RFQ structure.

Focusing regions are formed by vanes with quadrupole symmetry - RFQ-lenses [4]. This part of Hybrid-RFQ structure acts as a conventional triplet of quadrupole lenses. Required focusing strength of RFQ-lenses is defined by distance from axis to vanes.

THE METHOD

The method proposed in this paper is based on several stages:

1. RFQ lens is approximated by electrostatic thin lens with effective gradient $G_{ef} = G_{ef}(\psi, \beta_z)$ dependent on arriving phase ψ and particle velocity β_z. Arriving phase ψ is phase of RF field when a particle arrives at an entrance of RF lens.
2. Effective gradient of the lens and RF defocusing effects of accelerating gaps forms a lattice gradient function $G_{lat} = G_{lat}(z, \psi, \beta_z)$ as a "rectangular" function.
3. Smooth approximation [5] is used to describe the transverse motion of a particle in the gradient G_{lat}. An effective potential function U_{eff} is defined.
4. Study of effective potential function U_{eff} is carried out.

Stage 1 (Lens approximation)

Focusing effect on transverse motion of a particle along the RFQ lens can be described by expression in Cartesian coordinates:

$$\frac{d\beta_x}{dz} = -\frac{qG(z)x}{\beta_z W_0}\cos(\omega t + \psi), \quad (4)$$

$\beta_x = v_x/c$ – transverse component of particle velocity, q – particle charge, $\beta_z = v_z/c$ – longitudinal component of the particle velocity, W_0 – rest energy of a particle, $\omega = 2\pi f$ – frequency of RF field. Let us equate the effect of RF lens to effect of static lens:

$$\int_0^{L_{lens}} G(z)x(z)\cos\left(\omega\frac{z}{v_z} + \psi\right)dz = G_{ef}(\psi,\beta_z)xL_{lens}, \quad (5)$$

where L_{lens} – lens length. The effective gradient can be presented as a series:

$$G_{ef}(\psi,\beta_z) = \sum_{n=0}^{\infty}\sum_{m=0}^{\infty} G_{1,n,m}\beta_z^n\cos(m\psi) + G_{2,n,m}\beta_z^n\sin(m\psi). \quad (6)$$

Stage 2 (Effective lattice gradient)

RF field of accelerating gaps sequence can be written as:

$$E_x = -E_1 I_1(kr)\frac{x}{r}\sin\varphi, \quad (7a)$$

$$E_y = -E_1 I_1(kr)\frac{y}{r}\sin\varphi, \quad (7b)$$

$$E_z = E_1 I_0(kr)\cos\varphi, \quad (7c)$$

where E_1 – amplitude of accelerating harmonic, $r^2 = x^2 + y^2$ – radial coordinate. $I_0(kr)$, $I_1(kr)$ – modified Bessel functions, $\varphi = kz - \omega t$ – phase of RF field when particle passes the center of an accelerating gap.

$$k = \frac{2\pi}{\beta_s\lambda} = \frac{\omega}{v_s}, \quad (8)$$

where $\beta_s = v_s/c$ is a velocity of the synchronous particle, λ – wavelength of RF field. Defocusing effect of RF gaps:

$$\frac{d\beta_x}{dz} = \frac{-qE_1 I_1(kr)}{2\beta_z W_0}\frac{x}{r}\sin\varphi. \quad (9)$$

At paraxial approximation:

$$I_1(kr) \approx k\frac{r}{2}. \quad (10)$$

Thus

$$\frac{d\beta_x}{dz} = \frac{-qE_1 kx}{4\beta_z W_0}\sin\varphi. \quad (11)$$

Finally the equation of particle transverse motion in the lattice can be written as:

$$\frac{d\beta_x}{dz} = -\frac{qG_{lat}(z,\psi,\beta_z)}{\beta_z W_0}x, \quad (12)$$

here

$$G_{lat}(z,\psi,\beta_z) = \begin{cases} G_{ef}(\psi,\beta_z), z \in RFQ\ lens \\ -\frac{E_1}{4}k\sin(\psi - \Delta\psi), z \in DTL \end{cases}, \quad (13)$$

and $\Delta\psi = \psi - \varphi$ is a phase difference between the entrance of RFQ lens and center of the gap.

Figure 2 shows the lattice gradient function $G_{lat}(z,\psi,\beta_z)$ along the focusing period of a Hybrid-RFQ as a sum of RFQ focusing effect of lens and defocusing effect of accelerating gaps.

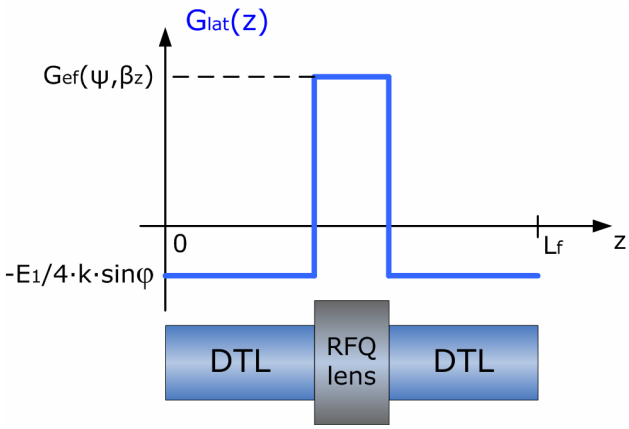

Figure 2: Lattice gradient along the focusing period L_f of a Hybrid-RFQ.

In the case of more detailed analysis we should consider $E_1 = E_1(\beta_z)$. The proposed method allows us to take this dependence into account easily.

Stage 3 (Smooth approximation)

According to the smooth approximation method the component of effective potential function U_{eff} corresponds to the longitudinal motion of a particle can be presented as:

$$U_{eff}^* \approx -\frac{qE_1}{m_0}\left[I_0(kr)\cos\varphi + \varphi\sin\varphi_s\right]. \quad (14)$$

The total 3D effective potential function is:

$$U_{eff}(x,y,z) \approx -\frac{qE_1}{m_0}\left[I_0(kr)\cos\varphi + \varphi\sin\varphi_s\right] + \\ + \frac{q}{m_0}\frac{a_0}{2}x - \frac{1}{2}\left(\frac{q}{m_0}\right)^2 \sum_{n=1}^{\infty} \frac{a_n^2 + b_n^2}{\left(\frac{2\pi n}{L_f}\right)^2}(x^2 + y^2). \quad (15)$$

Here

$$a_0 = a_0(\psi, \beta_z), \\ a_n = a_n(\psi, \beta_z), \quad (16) \\ b_n = b_n(\psi, \beta_z),$$

are coefficients of the Fourier-series of G_{lat}-function

$$G_{lat}(z, \psi, \beta_z) = \\ = \frac{a_0}{2} + \sum_{n=1}^{\infty} a_n \cos\left(\frac{2\pi n}{L_f} z\right) + b_n \sin\left(\frac{2\pi n}{L_f} z\right). \quad (17)$$

Stage 4 (Effective potential study)

Motion equations in the smooth approximation can be written as:

$$\frac{d^2x}{dt^2} = -\frac{\partial U_{eff}}{\partial x}, \\ \frac{d^2y}{dt^2} = -\frac{\partial U_{eff}}{\partial y}, \\ \frac{d^2z}{dt^2} = -\frac{\partial U_{eff}}{\partial z}. \quad (18)$$

The averaged frequency of transverse oscillations can be calculated as:

$$\left\langle \Omega_x^2 \right\rangle = \frac{1}{x}\frac{\partial U_{eff}}{\partial x}, \quad (19)$$

and transverse phase advance is:

$$\mu = \left\langle \Omega_x^2 \right\rangle T_f. \quad (20)$$

Figure 3 presents the results of the particle tracking simulation. Trajectories in real field and obtained by smooth approximation are shown. Smoothed trajectory is close enough to the "real" one. The phase advance of oscillation corresponds to the calculated one. It is about to 60° at period length of 2.1m. The lattice acceptance can be estimated with (1) for a given aperture. Energy gain is calculated with (7c).

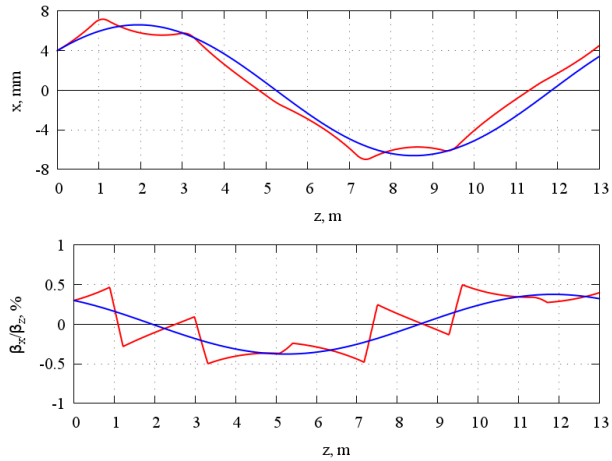

Figure 3: Trajectories of transverse particle motion through the Hybrid structure without accelerating gaps. Red - trajectory in real field, blue - trajectory calculated with the smooth approximation.

CONCLUSION

The method of RF quadrupole focusing studying has been proposed. It has been applied to Hybrid-RFQ analysis. Both averaged frequency of particle oscillations and transverse phase advance have been estimated. The agreement between "real" and "smooth" particle motions has been shown.

The method allows us to compare any types of focusing easily. It gives some advantages for RF focusing analysis. Lattice parameters can be estimated. Nonlinear effects can be studied with proposed method.

ACKNOWLEDGMENT

Authors thank S.M. Polozov for his valuable suggestions and discussions.

REFERENCES

[1] I.M. Kapchinskiy, “Theory of Resonance Linear Accelerators”, Moscow (1982) (in Russian)
[2] A.S. Plastun, S.M. Polozov, “Beam Dynamics Simulation in DTL with RF Quadrupole Focusing”, Proceedings of IPAC-2011, p.2625, San Sebastián, Spain
[3] P.N. Ostroumov and A.A. Kolomiets, “New Concept for Acceleration of Slow, Low-Charge-State Heavy Ion Beams”, Proceedings of the 2001 Particle Accelerator Conference, Chicago
[4] A.S. Plastun, S.M. Polozov, “RF Quadrupole Focusing Drift Tube Linac RF Design”, Problems of atomic science and technology, Kharkov, Ukraine (2011)
[5] L.D. Landau, E.M. Lifshitz, “Mechanics”. Volume 1 (Course of Theoretical Physics), Moscow (2007)

ANALYTICAL APPROACH FOR BEAM MATCHING

V.S. Dyubkov*, S.M. Polozov, NRNU MEPhI, Moscow, Russian Federation

Abstract

Charge particle beams transportation with small cross-sections and low energies is an actual problem for a gantry. That beams are used actively for isotope therapy. Beam emittance is its quality factor, and it should be matched with a facility channel acceptance. The method for beam dynamics analysis in lattice is developed in terms of non-coherent particle oscillation study. Nonlinear beam dynamics is investigated by using this method. It is shown that this technique allows one to realize effective beam emittance control. Analytical results obtained are verified by means of numerical simulation.

INTRODUCTION

One of the most interesting problems of accelerator engineering to date are the design and development of high-performance high-current compact systems for an injection and acceleration of low-velocity heavy-ion beams. This problem as well as others cannot be solved without taking into account problem solution on beam emittance matching with an acceptance of an accelerator channel. Effective acceptance evaluation for the resonance accelerator channel depends on a mathematical model used for describing a beam dynamics. Effective acceptance evaluation of the resonance accelerator channel was performed previously on basis of charged particle beam oscillation as a whole [1] – [4], that is under the assumption of coherent oscillations of individual particles. It is of particular interest to consider a model, which is taking into account non-coherent particle oscillations in the beam, and analyse results based on it.

BEAM DYNAMICS

It is difficult to analyse a beam dynamics in a high frequency polyharmonic field. Therefore, we will use one of methods of an averaging over a rapid oscillations period, following the formalism presented in [1] – [4]. One first expresses RF field in an axisymmetric periodic resonant structure as Fouriers representation by spatial harmonics of a standing wave assuming that the structure period is a slowly varying function of a longitudinal coordinate z

$$E_z = \sum_{n=0}^{\infty} E_n I_0\left(k_n r\right) \cos\left(\int k_n\, dz\right) \cos\omega t,$$

$$E_r = \sum_{n=0}^{\infty} E_n I_1\left(k_n r\right) \sin\left(\int k_n\, dz\right) \cos\omega t,$$

where E_n is the nth harmonic amplitude of RF field on the axis; $k_n = (1+2n)\pi/D$ is the propagation wave number for the nth RF field spatial harmonic; D is the resonant structure geometric period; ω is the RF frequency; I_0, I_1 are modified Bessel functions of the first kind.

As it was stated above, we will take into account non-coherent particle oscillations in the beam being accelerated. To this end, one introduces a notion of a reference particle, i.e. a particle moving on the channel axis. A magnetic force can be neglected for low-energy ions. We will assume that $dr/dz \ll 1$. Then, one passes into the reference particle rest frame. There is a differentiation over longitudinal coordinate in the beam motion equation. Thus, the motion equation together with an equation of particle phase variation can be presented in a view of a system of the first order differential equations as follows

$$\begin{cases} \dfrac{d\Gamma}{d\xi} = e_z(\xi, 0, \tau^*) - e_z(\xi, \rho, \tau), \\ \dfrac{d\beta_r}{d\xi} = \beta_z^{-1} e_r(\xi, \rho, \tau). \end{cases} \tag{1}$$

Here we introduced the following dimensionless variables: $\Gamma = \gamma^* - \gamma$; γ^* and γ are the Lorentzs factors for the reference and given particles respectively; $\xi = 2\pi z/\lambda$ is dimensionless longitudinal coordinate; $e_{z,r} = eE_{z,r}Z\lambda/2\pi m_0 c^2$; e is the elementary charge; Z is a charge state of an ion; λ is a wave length of RF field; m_0 is an ion rest mass; c is the light velocity in free space; $\beta_{z,r}$ is normalized velocity component.

Let us introduce a new dynamical variable $\psi = \tau - \tau^*$ ($\tau = \omega t$, τ^* is a normalized motion time of the reference particle at the laboratory coordinate system). Note, that

$$\frac{d\psi}{d\xi} = \beta_s^{-3}\Gamma, \tag{2}$$

β_s is normalized synchronous particle velocity, s is the field harmonic number.

Suppose that $|\beta_z - \beta_s| \ll 1$ one can obtain

$$\frac{d^2\psi}{d\xi^2} + 3\varkappa\frac{d\psi}{d\xi} = \frac{1}{\beta_s^3}\frac{d\Gamma}{d\xi} \tag{3}$$

upon differentiation of Eq. 2. The second equation of Eq. 1 can be rewritten as

$$\frac{d^2\delta}{d\xi^2} + \varkappa\frac{d\delta}{d\xi} = \frac{e_r}{\beta_s^3}, \tag{4}$$

where $\delta = \rho/\beta_s$, $\rho = 2\pi r/\lambda$, $\varkappa = \ln'_\xi \beta_s$.

* vsdyubkov@mephi.ru

On averaging Eq. 3 and Eq. 4 over rapid oscillation period one can present the motion equation in the smooth approximation with the restrictions mentioned above in the following matrix form

$$\ddot{\Upsilon} + \Lambda\dot{\Upsilon} = -L\Phi_{\text{ef}}, \qquad (5)$$

where the dot above stands for differentiation with respect to the independent longitudinal coordinate and

$$\Upsilon = \begin{pmatrix}\psi\\ \delta\end{pmatrix}, \qquad \Lambda = \begin{pmatrix}3\varkappa & 0\\ 0 & \varkappa\end{pmatrix}, \qquad L = \begin{pmatrix}\frac{\partial}{\partial\psi}\\ \frac{\partial}{\partial\delta}\end{pmatrix}.$$

Now, ψ and δ mean its averaged values. Φ_{ef} plays role of an effective potential function (EPF) describing a beam interaction with the polyharmonical field of the system subject to the incoherent particle oscillations.

For example, we consider there are two spatial harmonics at the linac. One of it is the synchronous harmonic with $s = 0$, and another one is the nonsynchronous (focusing) with $n = 1$. In this case we have

$$\begin{aligned}\Phi_{\text{ef}} = {} & \frac{e_0}{2\beta_s}\left[I_0(\delta)\sin(\psi+\varphi^*) - \psi\cos\varphi^* - \sin\varphi^*\right]\\ & + \frac{e_0^2}{64}\left[I_0^2(\delta) + I_1^2(\delta) - 1\right]\\ & + \frac{5e_1^2}{256}\left[I_0^2(3\delta) + I_1^2(3\delta) - 1\right]\\ & - \frac{e_0^2}{32}\left[I_0(\delta)\cos\psi - 1\right] - \frac{5e_1^2}{128}\left[I_0(3\delta)\cos\psi - 1\right]\\ & - \frac{e_0e_1}{32}\left\{\left[I_0(\delta) + I_0(3\delta)\right]\cos(\psi+2\varphi^*) - 2\cos 2\varphi^*\right\}\\ & + \frac{e_0e_1}{32}\left\{\left[I_0(\delta)I_0(3\delta) + I_1(\delta)I_1(3\delta)\right]\cos 2(\psi+\varphi^*)\right.\\ & \left. - \cos 2\varphi^*\right\},\end{aligned}$$

where $e_n = eE_nZ\lambda/2\pi\beta_s^2m_0c^2$.

To define eigenfrequencies of small system vibrations, EPF is expanded in Maclaurins series

$$\Phi_{\text{ef}} = \frac{1}{2}\Omega_{0\psi}^2\psi^2 + \frac{1}{2}\Omega_{0\delta}^2\delta^2 + o(\Upsilon^{\text{T}}\Upsilon),$$

and the coefficients in which are given by

$$\Omega_{0\psi}^2 = -\frac{e_0}{2\beta_s}\sin\varphi^* - \frac{e_0e_1}{16}\cos 2\varphi^* + \frac{e_0^2}{32} + \frac{5e_1^2}{128},$$

$$\Omega_{0\delta}^2 = \frac{e_0}{4\beta_s}\sin\varphi^* + \frac{3e_0e_1}{64}\cos 2\varphi^* + \frac{e_0^2}{128} + \frac{45e_1^2}{512}.$$

NUMERICAL SIMULATION

The analytical results obtained above were used to investigate the beam matching possibility at the linac output. The beam was the unbunched 2.5 keV/u lead ions Pb^{25+} with charge-to-mass ratio is equal to 0.12. Self-consistent beam dynamics simulations were conducted by means of a modified version of the specialized computer code BEAMDULAC-ARF3 based on CIC technique to calculate beam self-space-charge field. Computer simulation was carried out for the linac structure under the following parameters: $\lambda = 8.88$ m, system length is equal to 2.5 m, channel aperture is equal to 5 mm; input and output values of the equilibrium particle phase are equal to $-\pi/2$ and $-\pi/6$ respectively, synchronous harmonic maximal value at the axis is equal to 16 kV/cm, $e_1/e_0 = 9$. The equilibrium particle phase linearly increases at the bunching length (1.75 m) and plateaus further. Note that the variation of the synchronous harmonic amplitude against longitudinal coordinate (at 1.75 m) was calculated by using the technique described in [1]. Initial beam radius and current were 1 mm and 5 μA respectively. This parameters guarantee a positivity of the eigenfrequency of the small transverse tunes and, therefore, provide beam matching at the linac output. The output beam energy and current transmission coefficient were 100 keV/u and 85% respectively.

4D beam phase volume projection onto $(\psi, \dot{\psi})$ phase plane together with phase paths calculated in keeping with Eq. 5 at linac output is shown in Fig. 1. There are channel longitudinal acceptance in conservative approximation (curve 1) as well as channel dynamical acceptance in Fig. 1 too.

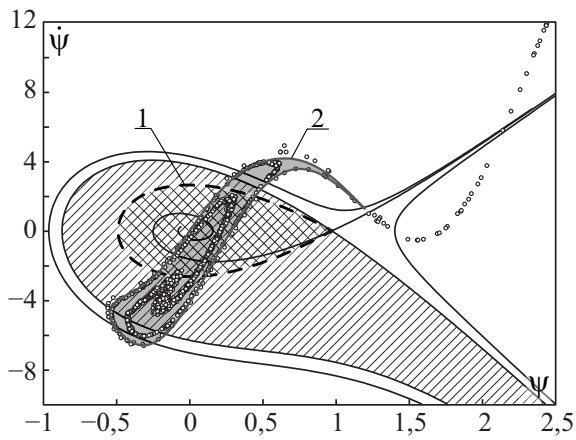

Figure 1: 4D beam phase volume projection and phase paths.

The size of beam envelope and transmission are shown in Fig. 2 and Fig. 3 respectively. The output beam radius is nearly 1.5 times greater than the input one because of this fact. This result is acceptable. It is clear that main linac parameters choice based on proposed technique is rather efficient to realize beam envelope (emittance) control.

SUMMARY

Beam dynamics model with regard for particles non-coherent oscillations was made. Effective acceptance evaluation in terms of this model was evaluated. The necessary restrictions on the linac parameters were imposed to make beam matching at the output. The numerical simulations of the self-consistent low-velocity heavy-ion beam dynamics confirmed the analytical results obtained.

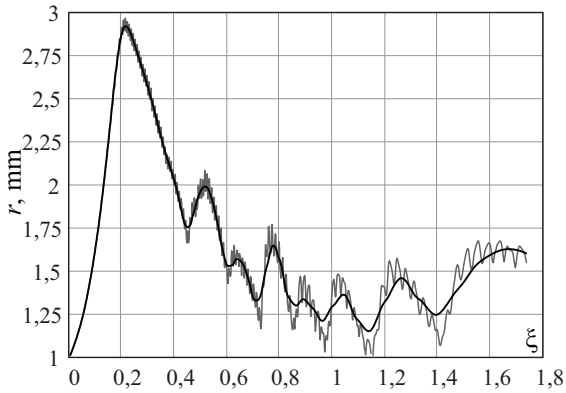

Figure 2: Beam envelope.

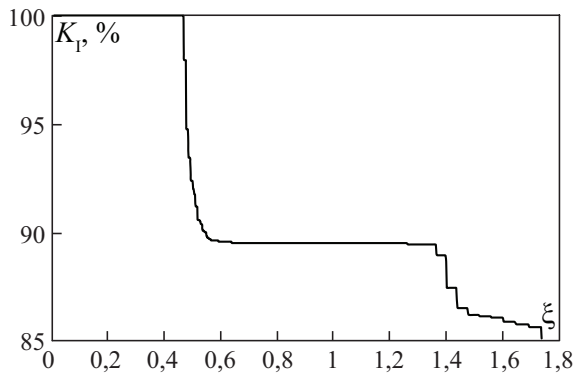

Figure 3: Current transmission.

REFERENCES

[1] V.S. Dyubkov and E.S. Masunov, International Journal of Modern Physics A, 24 (2009) 843.

[2] E.S. Masunov and N.E. Vinogradov, Zhurnal Tekhnicheskoi Fiziki, 71 (2001) 79.

[3] E.S. Masunov and S.M. Polozov, Zhurnal Tekhnicheskoi Fiziki, 75 (2005) 112.

[4] E.S. Masunov and V.S. Dyubkov, Problems of Atomic Science and Technology, 3 (2008) 166.

SEARCH OF THE MOTION INTEGRAL AT LINAC WITH RF FOCUSING

V.S. Dyubkov*, S.M. Polozov, NRNU MEPhI, Moscow, Russian Federation

Abstract

The problem of the effective linac design is of interest to many fields of science, industry and medicine. It is well known that nonsynchronous harmonics of RF field (RF undulator) are focusing the low-energy particles. Analytical beam dynamics investigation can be carried out by means of the averaging method over the rapid oscillations period (the so-called smooth approximation) in the oscillating fields. Motion equation is presented in the form of the Hamilton's equations. Motion integrals are sought by means of Poincare mapping.

INTRODUCTION

The problem of the effective low-energy linac design is of interest to many fields of science, industry and medicine (e.g. nuclear physics, surface hardening, ion implantation, hadron therapy). There are a few problems that lead to beam instabilities at linacs. Nonlinear effects are the most important among it. Certain nonlinear problems of accelerator physics are both important for successful operation of accelerator and interesting as problems in their own right. In this paper we consider nonlinear interaction between beam particles and a field of accelerator structure. In order to accelerate the low-energy ion beams one of the following fruitful rf focusing types can be used: alternating phase focusing (APF), radio frequency quadrupoles (RFQ), focusing by means of the nonsynchronous wave field as well as the undulator rf focusing. Each of mentioned focusing types has its advantages as well as disadvantages. For example, we consider axially symmetric Wideröe type structure with the rf focusing by the nonsynchronous harmonics [1], [2].

BEAM DYNAMICS

It is difficult to analyse a beam dynamics in a high frequency polyharmonic field. Therefore, we will use one of methods of an averaging over a rapid oscillations period, following the formalism presented in [1] – [3]. One first expresses RF field in an axisymmetric periodic resonant structure as Fouriers representation by spatial harmonics of a standing wave assuming that the structure period is a slowly varying function of a longitudinal coordinate z

$$\begin{aligned} E_z &= \sum_{n=0}^{\infty} E_n I_0\left(k_n r\right) \cos\left(\int k_n\, dz\right) \cos\omega t, \\ E_r &= \sum_{n=0}^{\infty} E_n I_1\left(k_n r\right) \sin\left(\int k_n\, dz\right) \cos\omega t, \end{aligned} \tag{1}$$

where E_n is the nth harmonic amplitude of RF field on the axis; $k_n = (1+2n)\pi/D$ is the propagation wave number for the nth RF field spatial harmonic; D is the resonant structure geometric period (depends on z implicitly); ω is the RF frequency; I_0, I_1 are modified Bessel functions of the first kind.

We shall assume the beam velocity (the one-particle approximation) differs from one of the field harmonic phase-velocities strongly except the synchronous harmonic of rf field, the gap-to-gap spacing of rf structure along the beam axis being defined as $D = \beta_s \lambda\,(s+0.5)$, where s denotes the synchronous harmonic number, β_s is the normalized velocity of the synchronous (equilibrium) particle.

It is convenient to introduce the nondimensional variables $\widehat{\mathbf{\Omega}} = (\xi;\varrho)$ and τ as

$$\widehat{\mathbf{\Omega}} = 2\pi \mathbf{R}/\lambda, \quad \mathbf{R} = \big(z;r\big), \quad \tau = \omega t, \tag{2}$$

then one can write the second Newton's law

$$\frac{d^2\widehat{\mathbf{\Omega}}}{d\,\tau^2} = \widehat{\mathbf{e}}\Big(\tau, \widehat{\mathbf{\Omega}}\Big), \tag{3}$$

where $\widehat{\mathbf{e}} = q\mathbf{E}\lambda/2\pi mc^2$, q and m are charge and mass of a particle.

The particle path in the rapidly oscillating field (1) we search as a certain sum of a some slowly varying term and a rapidly oscillating one. We assume that the amplitude of the rapid velocity oscillations is much smaller than the slowly varying velocity component for the smooth approximation to be employed.

On averaging Eq. 3 over rapid oscillation period one can present the motion equation in the smooth approximation with the restrictions mentioned above in the following form of the Hamilton's equations

$$\frac{d\,\mathbf{\Omega}}{d\,\tau} = \frac{\partial\,\mathcal{H}}{\partial\,\mathbf{\mathcal{P}}}; \qquad \frac{d\,\mathbf{\mathcal{P}}}{d\,\tau} = -\frac{\partial\,\mathcal{H}}{\partial\,\mathbf{\Omega}}, \tag{4}$$

where $\mathbf{\mathcal{P}}$ and $\mathbf{\Omega}$ are the canonically conjugate variables, the canonical coordinates being selected in such a way that the origin in a phase space is an equlibrium point, i.e. $\mathbf{\Omega} = (\overline{\widehat{\mathbf{\Omega}}} - \widehat{\mathbf{\Omega}}_s)/\beta_s$ and the beam-wave system Hamiltonian is

$$\mathcal{H}\left(\mathbf{\mathcal{P}}, \mathbf{\Omega}\right) = \frac{1}{2}\mathbf{\mathcal{P}}^2 + U_{\text{ef}}(\mathbf{\Omega})\,. \tag{5}$$

Here $U_{\text{ef}}(\mathbf{\Omega})$ is the Effective Potential Function which describes the low-energy beam interaction with the polyharmonical field of the system. The EPF depends solely on the averaged variable $\mathbf{\Omega} = (\zeta;\eta)$.

* vsdyubkov@mephi.ru

EPF can be written as $U_{\rm ef} = U_0 + U_1 + U_2$ [1], introducing notations

$$
\begin{aligned}
U_0 &= -\frac{1}{2} e_s \left[I_0(\eta) \sin(\varphi_s + \zeta) - \zeta \cos\varphi_s - \sin\varphi_s \right];\\
U_1 &= \frac{1}{16} \sum_{n\neq s}^{\infty} \frac{e_n^2}{\nu_{n,s}^2} w_{n,s}^{(0)}(\eta) + \frac{1}{16} \sum_{n=0}^{\infty} \frac{e_n^2}{\mu_{n,s}^2} w_{n,s}^{(0)}(\eta);\\
U_2 &= \frac{1}{16} \sum_{\substack{n\neq s \\ k_n + k_p = 2k_s}}^{\infty} \frac{e_n e_p}{\nu_{n,s}^2} \Big[w_{n,s,p}^{(1)}(\eta) \cos(2\zeta + 2\varphi_s) \\
&\quad + 2\zeta \sin 2\varphi_s - \cos 2\varphi_s \Big] \\
&\quad + \frac{1}{8} \sum_{\substack{n\neq s \\ k_n - k_p = 2k_s}}^{\infty} \frac{e_n e_p}{\nu_{n,s}^2} \Big[w_{n,s,p}^{(2)}(\eta) \cos(2\zeta + 2\varphi_s) \\
&\quad + 2\zeta \sin 2\varphi_s - \cos 2\varphi_s \Big],
\end{aligned}
\tag{6}
$$

where $e_i = \widehat{e}_i/\beta_s$, $\nu_{n,s} = (k_n - k_s)/k_s$, $\mu_{n,s} = (k_n + k_s)/k_s$, $\iota_{n,s} = k_n/k_s$. n, s, $p \in \mathbb{N}_0$, φ_s is the synchronous particle phase, the functions of the dimensionless transverse coordinate being defined as

$$
\begin{aligned}
w_{n,s}^{(0)}(\eta) &= I_0^2(\iota_{n,s}\eta) + I_1^2(\iota_{n,s}\eta) - 1;\\
w_{n,s,p}^{(1)}(\eta) &= I_0(\iota_{n,s}\eta) I_0(\iota_{p,s}\eta) - I_1(\iota_{n,s}\eta) I_1(\iota_{p,s}\eta);\\
w_{n,s,p}^{(2)}(\eta) &= I_0(\iota_{n,s}\eta) I_0(\iota_{p,s}\eta) + I_1(\iota_{n,s}\eta) I_1(\iota_{p,s}\eta).
\end{aligned}
\tag{7}
$$

POINCARÉ MAPPING

Most of accelerator design is based on the paraxial approximation and the resultant linearized equations. In order to investigate nonlinear beam particle interaction with the linac field we study the particle motion in the potential (6) by means of numerical simulations. For example, linac parameters presented in [1] were used to this purpose.

It is well known that chaotic particle motion can appear even in Hamiltonian systems with a few degrees of freedom, including potential (6), due to property of nonlinear systems to separate originally close particles trajectories in the restricted space exponentially fast. For sufficiently large perturbation strength, which appears far from linac axis or near it in the case of strong field (see (1)), the particle motion can be chaotic. It is unacceptable for accelerator operation because the particles go to sufficiently large amplitude that they are lost. Of some interest is the problem of finding the largest regular Kolmogorov-Arnold-Moser curve, as that defines the dynamic aperture inside which linac operation is at least potentially possible.

We plotted numerically a few Poincare section under linac parameters mentioned above. There are three Poincare sections, calculated for $\mathcal{H} = \mathcal{H}_{\rm sep}$ and $z = 0, z = L_{\rm gr}, z = L$ in Fig. 1, Fig. 2 & Fig. 3 respectively, where $L_{\rm gr}$ and L are the field amplitude increasing length and the linac total length. Based on the presented pictures one can define the dynamic aperture readily. As one can see there is no additional isolating motion integral (the so called third motion integral) in the given case. Furthermore, three qualitatively different types of motion are observed. The qualitative features are that for all time particle representation points either lie on regular closed smooth curves or lie on islands, jumping from one to other, or follow chaotic trajectories, jumping around erratically.

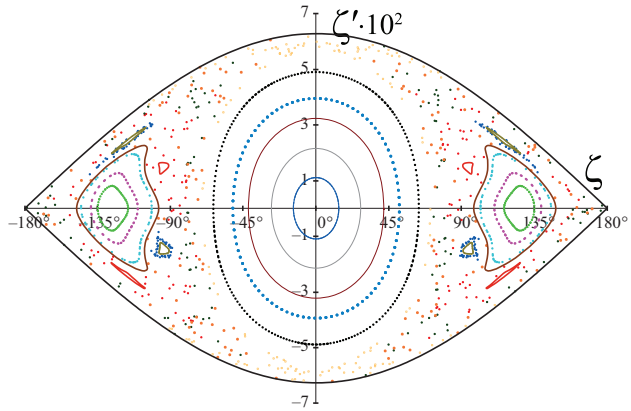

Figure 1: Poincaré sections at linac input.

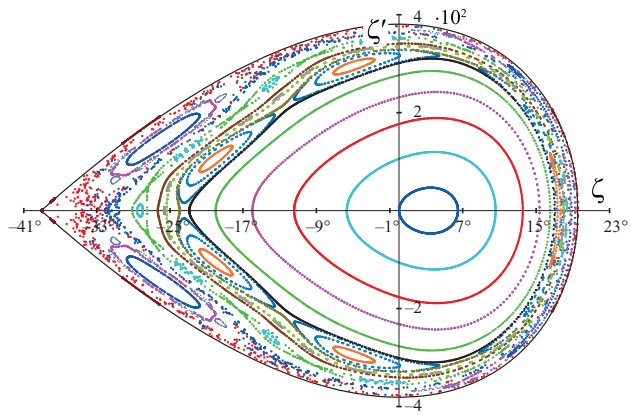

Figure 2: Poincaré sections at the end of bunching part.

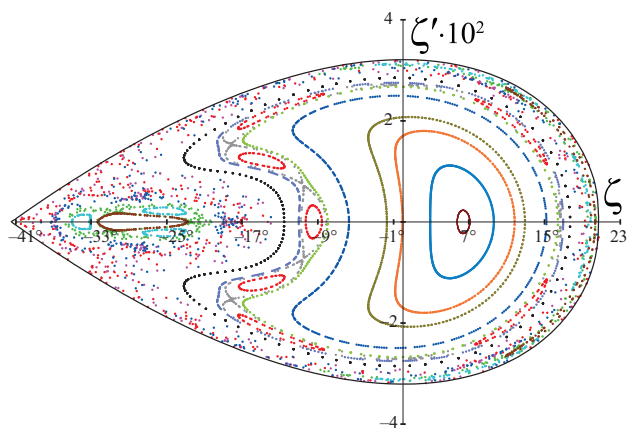

Figure 3: Poincaré sections at linac output.

SUMMARY

Analytical beam dynamics investigation is carried out by means of the averaging method over the rapid oscillations period. Motion equation is presented in the form of the Hamilton's equations. Additional (third) motion integral is not found by means of Poincare mapping for linac parameters presented in [1]. Three qualitatively different types of motion are observed.

REFERENCES

[1] V.S. Dyubkov and E.S. Masunov, International Journal of Modern Physics A, 24 (2009) 843.

[2] E.S. Masunov and N.E. Vinogradov, Zhurnal Tekhnicheskoi Fiziki, 71 (2001) 79.

[3] E.S. Masunov and V.S. Dyubkov, Problems of Atomic Science and Technology, 3 (2008) 166.

DEPENDENCE ON BETATRON OSCILLATIONS OF THE ANGULAR VELOCITY

O.E. Shishanin, Moscow State Industrial University

Abstract

Study of the topic, along with other factors necessary to understand the role of electron oscillations in the formation of the synchrotron radiation. The above-mentioned problem is considered by the author in various periodic magnetic fields. Emergence of the correction terms to the angular velocity of storage rings is also discussed.

At first let us take an axially-symmetric magnetic field as the most extensively studied. In the neighborhood of equilibrium orbit the magnetic field is chosen as

$$H_x = H_y = 0, H_z = br^{-n},$$

where b is the constant, $r = \sqrt{x^2 + y^2}$, n is the field gradient $(0 < n < 1)$. If $rot\bar{H} = 0$ one can concede that the potentials in cylindrical coordinates take the form

$$\Phi = 0, \quad A_r = A_z = 0,$$

$$A_\varphi = \frac{b}{r^{n-1}(2-n)}[1 + \frac{n(2-n)}{2r^2}z^2],$$

where φ is the azimuth angle. The relevant Hamiltonian $\mathcal{H}$ for electron can be written as

$$\sqrt{m^2c^4 + c^2p_z^2 + c^2p_r^2 + \frac{1}{r^2}c^2p_\varphi^2 + e^2A_\varphi^2 + 2ec\frac{A_\varphi}{r}p_\varphi}.$$

One of the Hamilton equations is

$$\dot{\varphi} = \frac{\partial\mathcal{H}}{\partial p_\varphi} = \frac{1}{\mathcal{H}}(\frac{c^2}{r^2}p_\varphi + \frac{ec}{r}A_\varphi),$$

where p_φ is the integral of motion.

Let us denote a small variable by $\rho = r - R$, where the equilibrium radius R can be deduced on condition that linear in ρ terms for Hamiltonian are absent (parabolic approximation). This gives

$$R = (\frac{2-n}{1-n}\frac{cp_\varphi}{eb})^{\frac{1}{2-n}}.$$

Restricting our selves to terms $\rho^2/R^2, z^2/R^2$, we can obtain the angular velocity as

$$\dot{\varphi} = \omega_0(1 - \frac{\rho}{R} + \frac{3-n}{2}\frac{\rho^2}{R^2} + \frac{n}{2}\frac{z^2}{R^2}), \qquad (1)$$

where $\omega_0 = ceH_0/E$ is the frequency, energy E is the constant, $H_0 = b/R^n$. The well-known asymptotics for oscillations have the form

$$\rho = A\cos(\sqrt{1-n}\omega_0 t + \chi), z = B\cos(\sqrt{n}\omega_0 t + \psi), \quad (2)$$

where A and$B$ are, respectively, the amplitudes of radial and axial vibrations, χ and ψ are the initial phases. Total velocity $v = \beta c$ is also constant and

$$v = R\omega_0\sqrt{1 + (1-n)\frac{A^2}{R^2} + n\frac{B^2}{R^2}}.$$

Expressions (1) and (2) made it possible to solve the synchrotron radiation problem [1] for given magnetic field. In such a case it has been found an essential influence of vertical oscillations on the spectral and angular properties of radiation in agreement with experiment. Here we can take only the linear terms and the accuracy was limited by decision (2).

Taking into account for oscillations the quadratic terms one can obtain nonlinear equations

$$\ddot{\rho} + (1-n)\omega_0^2\rho = \frac{\omega_0^2}{2R}[(1-n)(3+n)\rho^2 + n(1+n)z^2],$$

$$\ddot{z} + n\omega_0^2 z = n(1+n)\omega_0^2 z\frac{\rho}{R}.$$

Resolving them by the iterated method we can find, for example, an expression for radiation intensity [2] in a given approximation

$$W = W_0[(1 - \frac{n^2}{2})\frac{A^2}{R^2} - n\frac{3 - 2n + n^2}{2(1-n)}\frac{B^2}{R^2}],$$

where intensity for homogeneous magnetic field

$$W_0 = \frac{2}{3}\frac{ce^2}{R^2}\frac{\beta^4}{(1-\beta^2)^2}.$$

Clearly formula (1) may be also derived from equation

$$\frac{d}{dt}(r^2\dot{\varphi}) = -\frac{e_0}{mc}r(\dot{z}H_r - \dot{\rho}H_z),$$

where the constant of integration is defined as $\omega_0 R^2$.

In studies of radiation in the straight section accelerators we expanded in a power series the transverse components of magnetic field or gradient. Here an electron revolves on orbit consisting of N periods, where one element of the system includes a bending magnet of length $a = 2\pi R/N$ and free gap of length l. The length of entire orbit will be

$$2\pi R + Nl = 2\pi R_0,$$

where $R_0 = (1+k)R$ is the averaged radius, $k = l/a$. After expansion in a series we can put $n(\tau) = f(\tau)n$, where $\tau = N\varphi$ and the discrete function

$$f(\tau) = \frac{1}{1+k}[1 + \frac{2(1+k)}{\pi}\sum_{\nu=1}^{\infty}\frac{\sin\nu\tau_1}{\nu}\cos\nu(\tau - \tau_1)]$$

with $\tau_1 = \pi a/(a+l)$. This operator $f(\tau)$ is 1 on the section with the magnetic field and 0 in the free gap.

The equation for the vertical oscillations of electron in the linear approximation can be put into the form

$$\frac{d^2z}{d\tau^2} + \frac{(1+k)^2}{N^2} n f(\tau) z = 0. \quad (3)$$

Solution of Eq. (3) may be sought as a series [3], where n/N^2 is the small parameter. In the long run it will be a superposition of sinusoids and cosine curves with modulated amplitudes.

For the radial vibrations one can substitute in Eq. (3) n by $1-n$. These radial oscillations are small compared with the radius and have only a negligible impact on the radiation properties. In this connection it may be assumed that a particle moves along a circle with radius R_0, and the guiding magnetic field H can be averaged over the entire length of the period. Because of the magnetic field components take the form

$$H_z = H_0[\frac{1}{1+k} - \frac{\rho}{R} n f(\tau)], H_r = -H_0 \frac{z}{R} f(\tau), \quad (4)$$

where already $\rho = r - R_0$. The angular velocity of this motion can be represented by the expression

$$\dot{\varphi} = \frac{\omega_0}{1+k}[1 - \frac{\rho}{R_0} + \frac{3}{2}\frac{\rho^2}{R_0^2} + \frac{n}{R^2}\int (z\dot{z} - \rho\dot{\rho}) f(\tau) dt]. \quad (5)$$

Coefficient $1/(1+k)$ here is due to the straight sections.

For the FODO model $(n > 1)$ the focusing and defocusing segments have length a and are separated by field free section of length l. Then the orbit length of N elements is

$$2\pi R + 2Nl = 2\pi R_0.$$

Expanding $n(\varphi)$ in a Fourier series, we get

$$n(\tau) = \frac{4n}{\pi} \sum_{\nu=0}^{\infty} \frac{\sin(2\nu+1)\tau_2}{2\nu+1} \cos(2\nu+1)(\tau - \tau_2),$$

where $\tau_2 = \pi a/(2(a+l))$. In this case one can use the Eq. (3) and suppose that the parameter n/N^2 is else small. The guiding magnetic field will be more properly as

$$H_z = H_0[\frac{a}{a+l} + \Phi_1(\tau)],$$

where

$$\Phi_1 = \frac{2}{\pi} \sum_{\nu=1}^{\infty} \frac{\sin 2\nu\tau_2}{\nu} \cos 2\nu(\tau - \tau_2).$$

Then in Eq. (5) we must add the correction

$$\frac{\omega_0}{1+k} \int \frac{\dot{\rho}}{R}(1 + \frac{\rho}{R})\Phi_1(\tau) dt.$$

For storage rings we shall restrict our consideration to the case of the triplet achromat lattice [4]. It has the defocusing quadrupole of length a_1, then focusing quadrupoles of a long and bending magnet of length d lie on each side. The total run of lattice is

$$L = a_1 + 2(a + d + l_1 + l_2 + l_3),$$

where l_i is the length of free shifts. Let us denote the magnetic field of dipole by $B_z = B$, the lens constant by g, the small radial vibrations by x instead of ρ. The transverse components of magnetic field are

$$H_z = \frac{2d}{L} B - \Phi_2(\tau) g x + H_{ad}, \quad H_r = -\Phi_2(\tau) g z,$$

where

$$\Phi_2(\tau) = \frac{2a - a_1}{L} + \frac{2}{\pi} \sum_{\nu=1}^{\infty} \frac{(-1)^\nu}{\nu} \cdot$$

$$[2 \sin\tau_3 a \cos\tau_3(2l_1 + a + a_1) - \sin\tau_3 a_1] \cos\nu\tau,$$

with $\tau_3 = \pi\nu/L$.

Besides the part of guiding field is

$$H_{ad} = \frac{4B}{\pi} \sum_{\nu=1}^{\infty} \frac{1}{\nu} \sin\tau_3 d \cos\tau_3(d + 2l_3) \cos\nu\tau,$$

which disappears after averaging. Eq. (5) is complemented by expression

$$\omega_q \frac{2a - a_1}{2L} (\frac{z^2}{R_0^2} - \frac{x^2}{R_0^2})$$

and $n\omega_0 f(\tau)/((1+k)R^2)$ is replaced by $\omega_q \Phi_2(\tau)/R_0^2$, where $\omega_q = e_0 g R/(mc), k = (L - 2d)/(2d)$.

The vertical oscillations are described by linear equation

$$\frac{d^2z}{d\tau^2} + \frac{C}{N^2} \Phi_2(\tau) \cdot z = 0, \quad (6)$$

where $C = (1+k)\omega_q/\omega_0$. Note that parameter $C/N^2 >> 1$ and the quest of solution is a challenging task. It should also be pointed out that the expressions (3) and (6) is the Hill equations.

The used procedures are first of all stipulated by a necessity to investigate the synchrotron radiation characteristics in accelerators. Formulas (1) and (5) illustrate that $\dot{\varphi}$ is different in the various points of particle trajectory. Thus it was established that the angular velocity of particle is defined by the structure of concrete magnetic system. Proposed approach can be developed further and move to nonlinear problems.

REFERENCES

[1] V.Ch.Zhukovsky and O.E.Shishanin, JETP 34(1972)729.

[2] V.Ch.Zhukovsky and O.E.Shishanin, Izvestia Vuzov, Fizika, 3(1978)149, (in Russian).

[3] O.E.Shishanin, JETP 90(2000)725.

[4] H.Wiedemann, Particle Accelerator Physics, Springer, 2007.

COOLING OF ELECTRON BEAMS

V. Khoruzhiy, Kharkov Institute of Physics and Technology, Kharkov, Ukraine

Abstract

We considered cooling of electron beams in synchrotrons (storage rings) using gyro-oscillator by the example of gyromonotron as part of cyclic accelerator at straight-line portion. Gyromonotron is a simplest gyro-oscillator for converting energy of transversal beam energy to oscillation of electromagnetic energy. Cooling of electron beams due to synchrotron radiation (radiative "cooling") is ineffective not only for energy W<50 MeV (low level of synchrotron radiation), but for high relativistic energies too, when positive radiative losses for cooling of a beam were prevailed by another increasing negative force named as Ternov-Sokolov effect (beam radius and emittance growth take place as result of quantum fluctuations of electron trajectories in accelerators). Hence, under high energies (starting from some hundreds MeV) synchrotron radiation is source not only focusing radiative cooling force, but defocusing force too due to recoil effect of electrons under radiation high energy quantum. Using gyromonotrons give possibility to increase maximal beam energy in synchrotrons through cooling of electron beam for prevention beam particles losses due to Ternov-Sokolov effect.

INTRODUCTION

We proposed cooling of electron beams in synchrotrons [1-3] (storage rings [4, 5]) using gyromonotron [6-12] for converting energy of transversal beam energy to oscillation of electromagnetic energy. A gyromonotron is a simplest gyro-device from possible variants (gyrotron, gyromonotron, gyro_BWO) for this purpose. A gyromonotron is cylindrical resonator placed into solenoid's longitudinal magnetic field. We suggest effective cooling of electron beam for energy of one less 50MeV (low level of synchrotron radiation [13, 14]) and especially for energy W of electron beam more than some hundreds MeV, when starts action quantum fluctuations of macroscopic electron trajectories in accelerators (Ternov-Sokolov effect[15-17]). Analytical expression for Ternov-Sokolov effect is

$$W_0 > mc^2 (2\pi mcR / h)^{1/5}$$

where $h / 2\pi$ is reduced Planck constant, R is synchrotron's radius.

Expression for W_0 can be rewritten in a more convenient form for electrons

$$W_0(MeV) > 151.82(R)^{1/5}$$

where radius dimension is [R]=meter.

Quantum fluctuations (recoil of electrons) lead to growth of emittance through additional particles divergence, hence, as result, growth beam dimensions. As result, high energy electron beams have upper limit for synchrotrons energy despite all efforts for focusing one. For former LEP collider maximal beam energy was achieved approximately 100GeV for each beam (electron and positron). We proposed cooling of electron (positron) beams in synchrotrons by gyromonotron as part of cyclic accelerator (storage ring) at straight-line portion for multiple passing the same bunches. Gyromonotron converts energy of transversal movement electrons (positrons) into RF oscillation under corresponding longitudinal magnetic field for constancy of cyclotron frequency. Relativistic cyclotron frequency approximately has to equal RF frequency in synchrotron during accelerating process.

BASIC EXPRESSIONS

The gyromonotron is a HF oscillator for cm and mm band of wavelength. Electron (positron) beams with nonzero transversal velocities are used for excitation electromagnetic wave in resonator nearly cut off frequency. No transversal velocities mean no exciting of electromagnetic waves at all (in gyromonotron). Energy of transversal motion of electron beam converts into energy of electromagnetic wave during multiple passing the same bunches with synchrotron's RF frequency f_0 through gyromonotron nearly cut off frequency $f_{cut\ off.}$ (f_0 - $f_{cut\ off.}$>0). Output window is absent. We choose frequency $f_{cut\ off.}$ (and corresponding wavelength λ) as minimal frequency (H_{111} mode) for gyromonotron's resonator with length L. As well known [18], frequency $f_{cut\ off.}$ of H_{111} mode provides possibility to determine radius of the resonator

$$R = 1.841 / \sqrt{(2*\pi / \lambda)^2 - (\pi / L)^2};$$

$$R \approx \lambda / (2*1.71) \quad for \quad L^2 >> (\lambda / 2)^2$$

We assumed above that resonator's length is

$$L / (2*R) > 1$$

for exciting of H_{111} mode.

Then it is possible for gyromonotron's solenoid to determine longitudinal magnetic field

$$H_{Z0}(kOe) \simeq 10.7 * f_0 / c$$

for low relativistic beam's energy (dimension $[c / f_0] = cm$).

For gyromonotron's operation at given frequency f_0 its needed realization of condition for relativistic cyclotron frequency

$$n * \Omega_{c.rel} / (2*\pi) \approx f_0;\ n = 1, 2...$$

For phase focusing is needed

$$f_0 - n*\Omega_{c.rel} / (2*\pi) > 0 .$$

A value n>1 is applicable under high energy beam.

For effective operation of installation is needed for H_{111} mode frequency of gyromonotron's oscillation have to be nearly cut off frequency approximately, for example, $f_{cut\,off} \approx 0.975 f_0$ .We consider radio frequency f_0=350MGHz (former LEP collider), cut off frequency $f_{cut\,off}$ =340MHz, wavelength $\lambda = 88.2\,cm$. Then, for sufficiently long resonator, gyromonotrn's radius is R=25.8cm, length of resonator for H_{111} mode is L>51.6cm and strength of nonrelativistic longitudinal magnetic field is $H_{Z0} \simeq 0.125\ kOe$. Conservation relativistic cyclotron frequency takes place under $H_{Z,REL} = \gamma H_{Z0} / n$, where γ is beam relativistic factor. Under $\gamma >> 1$ we have possibility to reduce longitudinal magnetic field using harmonics of cyclotron frequency n>1. Superconducting (SC) gyromonotron's solenoid in stored rings may be used for Top Up operation with constant stored beam current and energy [19].

CONCLUSIONS

Cooling of electron beams in synchrotrons (storage rings) using gyromonotron as device for converting energy of transversal motion of a beam into oscillation of electromagnetic energy is additional device for reducing transversal velocities of beam particles together with synchrotron radiation (radiative losses) for beam energies W> W_0. We suppose dominant role of beam cooling due to gyromonotron under high energies will cause neutralization of essential increasing of beam divergence due to quantum fluctuations of macroscopic electron trajectories. That emittance growth problem is main restriction of synchrotron for further growth of beam energy $W \geq 100\,GeV$ for future, for example, electron-positron collider.

REFERENCES

[1] Veksler, V. I. "A new method of accelerating relativistic particles", Comptes Rendus (Doklady), Acad. Sci. U.S.S.R. V. 43, No. 8, 329-331, 1944.

[2] E. M. McMillan, "Synchrotron a proposed high energy accelerator", Phys. Rev. Lett., **68**(1945), 143.

[3] E.D. Courant, M.S. Livingston and H.S. Snyder, "The Strong-Focusing Synchrotron -A New High Energy Accelerator", Phys. Rev. **88** (1952), 1190.

[4] Gerard K. O'Neill, "Storage-Ring Synchrotron: Device for High-Energy Physics Research", Physical Review, Vol. 102 (1956); pages 1418-1419.

[5] Matthew Sands "The Physics of electron storage rings. An introduction", Preprint SLAC-121, UC-28, (ACC), 1970.

[6] Twiss R.Q. "Radiation transfer and the possibility of negative absorption in radio astronomy"// Austral. J. Phys. 1958. V. 11, No 4.

[7] Gaponov A.V. "Interaction of non-straight electron beams with electromagnetic waves in feed lines".(in Russian)// Izv.VUZov. Radiofizika. 1959, V. 2, No. 3, pp. 450-462; Gaponov, A.V. Addendum. Izv. VUZ. Radiofiz. V . 2, 2, 836, (1959).

[8] J. Schneider "Stimulated emission of radiation by relativistic electrons in a magnetic field". //Phys. Rev. Lett., 1959, Vol. 2, No. 12, P. 504.

[9] Pantell R.H. "Electron beam interaction with fast waves" // In: the Proc. Symp. on Millimeter waves. Polytechnic Inst. of Brooklin, N.Y.: Politechnic Press, 1959. V. 9. P. 301.

[10] Pantell R.H. "Backward-wave oscillattions in an unloaded waveguide" // In: the Proc. IRE. 1959. V. 47, No 6. p. 1146.

[11] V. L. Bratman, N. S. Ginzburg, G. S. Nusinovich, M. I. Petelin, and P. S. Strelkov, "Relativistic gyrotrons and cyclotron autoresonance masers" Int. J. Electron. V. 51, pp.541-567, 1981.

[12] V. Khoruzhiy "Phase portrait of bunched beam under profiling guiding magnetic field at coaxial gyro BWO", 2008, Int. Crimean Conference "Microwave & Telecommunication Technology" pp. 207-208 (CriMiCo'2008)

[13] F. R Elder, A. M. Gurewitsch, R. V.; Langmuir, H. C., Pollock, "Radiation from Electrons in a Synchrotron", Physical Review, vol. 71, Issue 11, pp. 829-830 (1947)

[14] J. L. Hirshfield and G. S. Park "Electron-Beam Cooling by Stimulated Synchrotron Emission and Absorption", Phys. Rev. Lett. V. 66, # 18 (1991) pp.2312-2315.

[15] A. A. Sokolov and I. M. Ternov, "On the quantum theory of electron radiation" .(in Russian) Zh. Eksp. Teor. Fiz. V.25, pp. 698 – 712, 1953.

[16] A. A. Sokolov and I. M. Ternov, "To movement of fast electrons in magnetic field". (in Russian), Doklady Akademii Nauk, 1953, v. 92, pp. 537 – 540.

[17] Sokolov A A, Ternov I M Relyativistskiî Élektron (Moscow: Nauka, 1983) [Translated into English as Radiation from Relativistic Electrons (New York: American Institute of Physics, 1986)]

[18] L.A. Vainshtein, "Electromagnetic Waves" [in Russian], Publ. house "Sovetskoe Radio", Moscow, 1957

[19] L. Emery, M. Borland, Top Up operation experience at the advanced photon source, Proceedings of the 1999 Particle Accelerator Conference, New York, pp. 200-202, 1999.

THE PARAMETERS EXTRACTED BEAMS IN RECIRCULATOR SALO

I.S. Guk, S.G. Kononenko, F.A. Peev, A.S. Tarasenko National Science Centre "Kharkov Institute of Physics and Technology", Kharkov, 61108, Ukraine

Abstract

Optimization of recirculator SALO magnetic structure has allowed to refine essentially beam parameters in points of a leading-out of particles. Beam parameters on an inlet and an exit of the basic channels of an extraction of particles from recirculator are given in article. Calculations are spent taking into account nonlinear field components of dipole and quadrupole magnets of the accelerator.

INTRODUCTION

The recirculator SALO project envisages an extraction of electrons in several experimental halls [1]. As it has been shown in paper [2], nonlinear field component of dipole and quadrupole magnets can exert on recirculator beam parameters appreciable influence. Channels of beam transportation contain enough large number of dipoles and quadrupoles. Therefore beam characteristics can change on these channels under the influence of the same causes. By means of program code MAD X [3] lateral dimensions of beam in extraction points from recirculator and on an exit of beam transportation channels have been counted. Magnitudes sextupole component field of dipole magnets of the injection channel and the first ring of recirculation were are taken from papers [4, 5]. They have been measured in these publications on prototypes of magnets which will be used in recirculator SALO. Dipole magnets of the second recirculation ring and output channels were not produced yet. Because these magnets window type it is natural to assume that the sextupole component of the field of the magnets will not exceed the values measured for the first ring magnets [4]. Octupole component of the value of the quadrupole lenses was calculated based on data from the literature [2].

These data were used for the numerical simulation of the particle dynamics in the recirculator. Sextupole component is taken into account in the description of the dipole. Octupole field component simulated thin lens on the entrance and exit of the quadrupole. The figures present the results of modeling the movement of 3000 electrons through the recirculator magnetic structure.

BEAM PARAMETERS

Location of the main beam channels on the recirculator shown in Fig. 1.

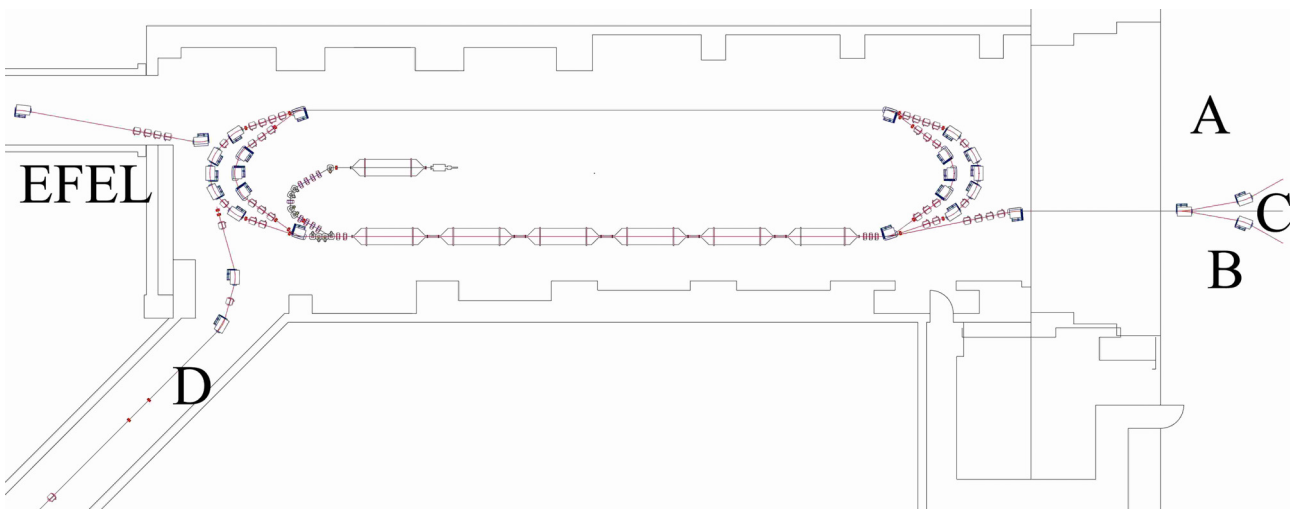

Figure 1: Beam output channels on SALO recirculator.

In channels A, B and C the beam with energy from 60 to 750 MeV [1, 6] can be extracted. For beam formation on channels A and B four quadrupole and two dipole magnets are used (one dipole magnet on the channel C). The electrons with energy to 270 MeV can be received in these halls with use of injection magnetic system and the magnets which are a part of channel magnetic system [3]. To produce a beam with energy of up to 490 MeV it is necessary to use magnetic system of the first ring of recirculation. For obtaining the maximum energy also magnetic system of the second ring of recirculation is used. Thus the bunch will pass accelerating structure three times. The cross-section of a bunch on an entrance to the transportation canal at the maximum energy of 730 MeV is presented on fig. 2. On fig. 3 distribution of particles on an exit from the channel B at distance of 26 m from input point for the same energy is presented.

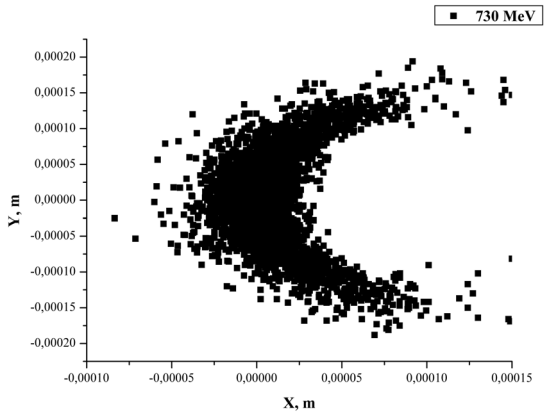

Figure 2: Beam cross-section on an input in the B channel.

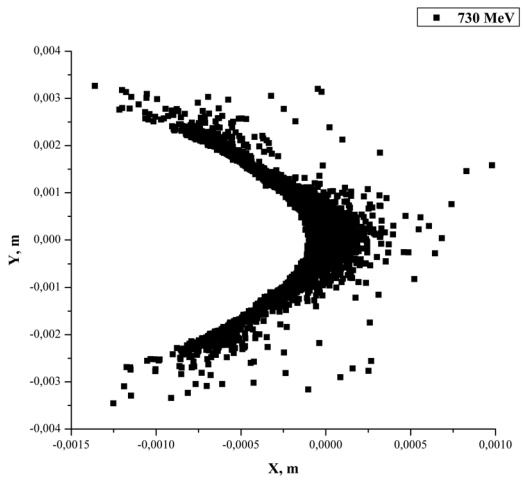

Figure 3: Beam cross-section on exit the B channel.

Distributions of particles in phase space x, x' and y, y' for the same point are presented on fig. 4 and fig. 5.

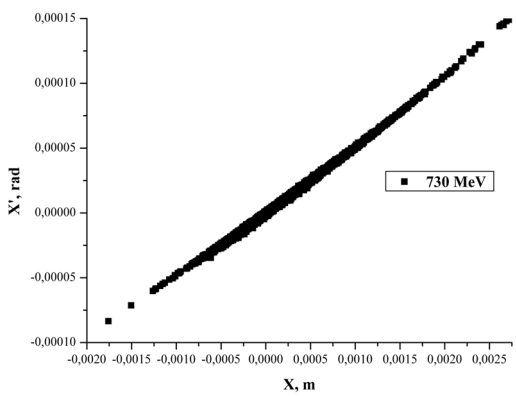

Figure 4: Distribution of particles in phase space x, x' on a channel B output.

Channels A, B and C are intended for experiments with beams of polarized and unpolarized electrons. On the channel C free electron laser installation is possible.

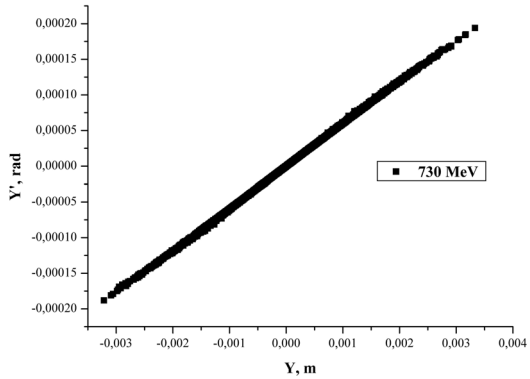

Figure 5: Distribution of particles in phase space y, y' on a channel B output.

In the EFEL channel the electrons with energy to 240 MeV can be extracted with use of the first five magnets of the first ring of recirculation. The beam with the maximum energy to 490 MeV is extracted to the canal in case of the switched-off magnets of the second arch of the second ring of recirculation. The beam on this channel can be created by eight quadrupoles and two dipole magnets. Cross distribution of particles on an input in the channel and on an output from it at distance of 66 m is presented on fig. 6 and fig. 7. The EFEL channel is supposed to be used for operations with beams of electrons and photons.

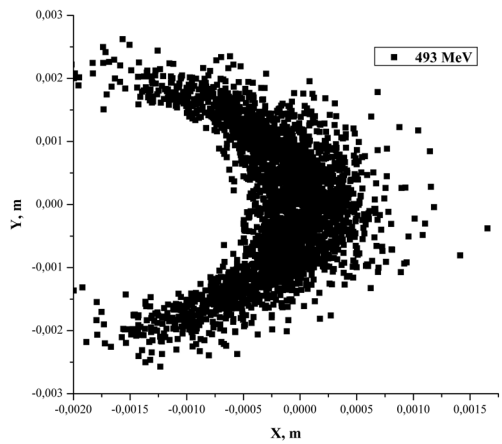

Figure 6: Beam cross-section on an input in the FEEL channel.

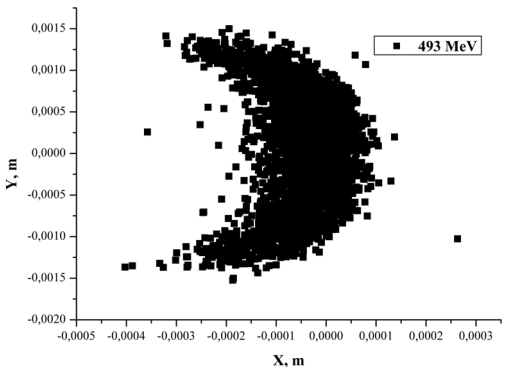

Figure 7: Beam cross-section on an exit the FEEL channel.

The electrons with the maximum energy of 490 MeV can be sent to the channel D if to switch on three magnets of the second arch (see fig. 1). The beam cross-section on an input to this canal is provided on fig. 8.

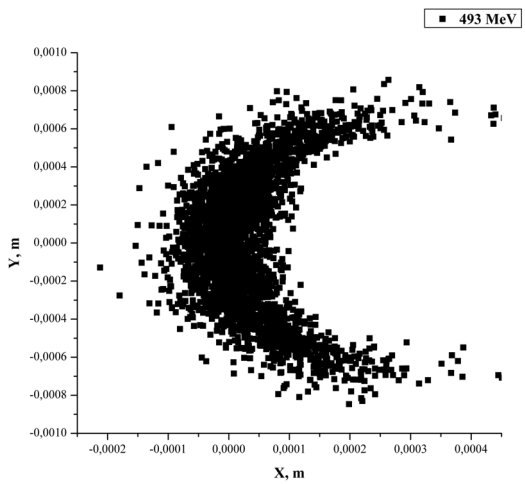

Figure 8: Beam cross-section on an input in the D channel.

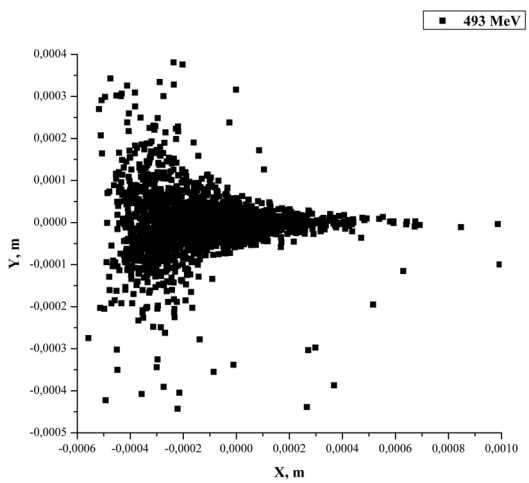

Figure 9: Beam cross-section on exit the D channel.

For beam framing on this channel two dipole magnets and five quadrupole lenses are used. On fig. 9 distribution of particles in a beam at distance of 76,8 m from entry point is presented. The channel D is supposed to be used for operations with beams of electrons and photons.

The carried-out calculations showed that non-linear components of a field of dipoles and quadrupoles influence distribution of density of electrons on an exit of channels. However the beam sizes thus change slightly.

CONCLUSION

Results of these researches give the chance to simulate interaction of electron beams with targets in the experimental halls.

REFERENCES

[1] I.S. Guk, A.N. Dovbnya, S.G. Kononenko, F.A. Peev, A.S. Tarasenko and J.I.M. Botman , “Recirculator SALO project in NSC KIPT ” EPAC’08, Genoa, Italy, June 2008, WEPP082 , p. 2710 (2008); http://www.JACoW.org.

[2] I.S. Guk, S.G. Kononenko, A.S. Tarasenko, Problems of atomic science and technology, Series: Nuclear Physics Investigations, № 3 (79) (2012) 137.

[3] MAD - Methodical Accelerator Design; http://mad.home.cern.ch/mad.

[4] X. Boling, J. I. M. Botman, A. T. A. M. Derksen, H. L. Hagedoorn, A. H. Kemper, C. J. Timmermans, “Magnetic Performance of the EUTERPE Ring Dipole” EPAC1994, London, June 1994, p. 2232 (1994); http://www.JACoW.org.

[5] I. S. Guk, A. N. Dovbnya, S. G. Kononenko, V. N. Lyashchenko, A. Yu. Mytsykov, B. P. Romas’ko, A. S. Tarasenko, and V. A. Shcherbinin. Physics of Particles and Nuclei Letters, Vol. 9, No. 4–5 (2012) 410.

[6] A.N. Dovbnya, V.B. Ganenko, I.S. Guk, S.G. Kononenko, A.S. Tarasenko, The Journal of Kharkov National Univesity, No. 784, Physical series “Nuclei, Particles, Fields”. Issue 4/36/. (2007) 74.

INVESTIGATION OF PHASE TRAJECTORIES OF PARTICLE MOTION IN A SYNCHROTRON NEAR THE NONLINEAR RESONANCE OF THIRD ORDER

Yu.A.Bashmakov
P.N.Lebedev Physical Institute, Leninsky Prospect 53, 119991 Moscow, Russia

Abstract

The nonlinear resonance of third order plays an important role in the particle dynamics in circular accelerators, colliders and storage rings and is widely used for slow extraction of particles from synchrotrons. Consideration is carried out in the canonical variables X, Y which at a given accelerator azimuth are simply related to the angle and the deviation of the circulating particles relative to the equilibrium orbit. The problem is reduced to the construction of the phase trajectories, which are the curves of the third or fourth order and determine the type of the motion near the resonance under consideration. The construction of the phase trajectories is performed by the Klein's perturbation method. The influence on the particles dynamics of octupole component of the magnetic fields is investigated.

INTRODUCTION

The problems of nonlinear dynamics play an important role in different fields of modern physics such as elementary particle physics, nuclear physics, plasma physics, quantum electronics and, certanly, in the particle accelerators physics [1]. The nonlinear resonance excitation is wiedly used for particle extraction from circular accelerators [2], the nonlinear resonances action determines dynamical aperture of large circular accelerators and storage rings. One of the most important problems in nonlinear oscillations study is construction of the trajectories of representive points on phase plane and stable motion regions finding.

BASIC THEORETICAL STATEMEMTS

When considering a particle motion in a circular accelerators it is convenient to replace longitudinal coordinate s by so called generalized azimuth ϕ

$$\phi = 2\pi\frac{s}{R_0},$$

where $R_0 = \Pi/2\pi$, and Π - accelerator perimeter.

The equation of one-dimensional particle motion in an accelerator in the presence of a perturbation has the form

$$\frac{d^2x}{d\phi^2} + \nu_x^2 x = \epsilon F\left(\phi, x, \frac{dx}{d\phi}\right), \qquad (1)$$

where x is the transverse displacement of the circulating particle with respect to the equilubrium orbit, ν_x is the betatron oscillation frequency, ϵ is small positive parameter, $\phi = \int \frac{ds}{\nu_x \beta(s)}$, $\beta(s)$ is the betatron function. The function $F\left(\phi, x, \frac{dx}{d\phi}\right)$ is periodic with respect to ϕ function with period equal to 2π. Taking the smallness of the perturbation into acount the solution of the equation (1) can represented in the form, that it has for the homogeneous equation, but now with the amplitude a and the phase ψ depending on the azimuth ϕ [3].

$$x = a(\phi)\cos(\nu_x\phi + \psi(\phi)). \qquad (2)$$

The amplitude a and phase ψ are subjected to the following equations

$$\begin{aligned}\frac{da}{d\phi} &= A(a,\psi),\\ \frac{d\psi}{d\phi} &= \Psi(a,\psi).\end{aligned} \qquad (3)$$

Canonical variables

For further analysis it is convenient to move to the new variables X and Y [4]

$$X = a\cos\psi, \qquad Y = -a\sin\psi. \qquad (4)$$

At a given accelerator azimuth variables X, Y are connected in a simple way with the angle and the displacement of the circulating particle with respect to equilibrium orbit. In these variables equations (3) take the canonical form

$$\begin{aligned}\frac{dX}{d\phi} &= \frac{\partial H}{\partial Y},\\ \frac{dY}{d\phi} &= -\frac{\partial H}{\partial X},\end{aligned} \qquad (5)$$

where $H(X,Y)$ is the Hamiltonian. Such change of the variables and use of the Hamiltonian allow to make a descriptive analysis of the particles motion on the phase plane (X,Y). Curves on which the particles move are determined by the equation $H(X,Y) = const$. From the conditions

$$\begin{aligned}\frac{dX}{d\phi} &= \frac{\partial H}{\partial Y} = 0,\\ \frac{dY}{d\phi} &= -\frac{\partial H}{\partial X} = 0,\end{aligned} \qquad (6)$$

the postions of the specific points on the phase plane are determined.

Resonance terms In a special case the nonlinear field F appearing in the equation (1) can be represented in the following way

$$F = x^l \cos(m\phi), \tag{7}$$

l, m – integer. The substitution of (2), (7) in equation (1) and subbsequent expansion of the function F into a Fourie series causes resonance terms appearance. Resonance condition takes the form

$$\nu_x = \frac{m}{l+1}. \tag{8}$$

THIRD ORDER RESONANCE

The third order resonance $\nu = q/3$ is exited by a suitable q harmonic of the quadratic (sextupole $l = 2$) magnetic field $F(\varphi, x, dx/d\varphi) = -A_2 x^2 \cos q\varphi - Bx^3$. Here the constant component of qubic (octupole $l = 3$) magnetic field B playing an important role in circular accelerators is keeping.

In this case the Hamiltonian can be represented in a normal form [5] and can be written as [4].

$$H = \frac{A_2}{16}(Y^3 - 3X^2Y) + \frac{1}{2}\left(\nu_x - \frac{q}{3}\right)(X^2 + Y^2) + \frac{B}{2}(X^2 + Y^2)^2. \tag{9}$$

By analogy with high energy physics [6] for further analysis of the phase trajectories we introduce the new designations

$$\begin{aligned} s &= Y - \sqrt{3}X + \frac{2\sqrt{3}}{3}X_0, \\ t &= Y + \sqrt{3}X + \frac{2\sqrt{3}}{3}X_0, \\ u &= Y - \frac{\sqrt{3}}{3}X_0, \end{aligned} \tag{10}$$

where $X_0 = 8\sqrt{3}(\nu_x - q/3)/3A_2$, and in accordance with the sign of the tune shift $\delta = (\nu_x - q/3)$ it takes positive or negative value. Taking into account (10) one can cast (9) in the form

$$s \cdot t \cdot u + \frac{8B}{A_2}(X^2 + Y^2)^2 = \frac{16}{A_2}H - \frac{4}{9}X_0^3. \tag{11}$$

In general, this is the equation of the fourth order curve. In the absence of the constant component of the cubic nonlinearity of the magnetic field ($B = 0$) it defines a curve of the third order. Phase trajectories are given by the equation

$$s \cdot t \cdot u = \eta, \tag{12}$$

where $\eta = 16H/A_2 - 4X_0^3/9$ – constant. By analogy with electrostatics value η can be called charge [7]. Then the entire phase plane is divided into two areas: one carrying a positive charge of $\eta > 0$, and the other carrying a negative charge of $\eta < 0$ [9]. The boundary between these regions is separatrix

$$s \cdot t \cdot u = 0, \tag{13}$$

on separatrix $H = \frac{\sqrt{3}}{36}A_2X_0^3$. The solution of this equation is given by family of three straight lines:

$$s = 0, \quad t = 0, \quad u = 0, \tag{14}$$

forming the equilateral triangle at its intersection. The vertexes of this triangle determine the position of three unstable fixed points

$$\begin{aligned} 1)\quad X &= 0, & Y &= -\tfrac{2\sqrt{3}}{3}X_0; \\ 2)\quad X &= -X_0, & Y &= \tfrac{\sqrt{3}}{3}X_0; \\ 3)\quad X &= X_0, & Y &= \tfrac{\sqrt{3}}{3}X_0. \end{aligned}$$

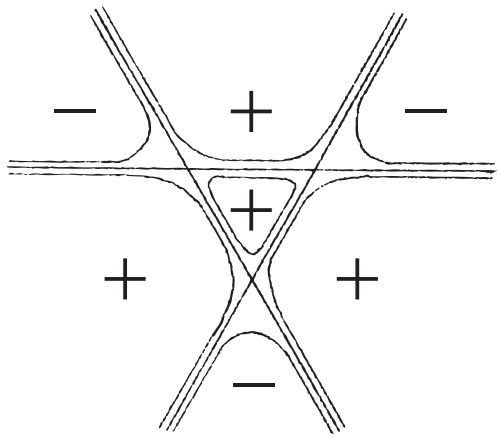

Figure 1: Schematic view of the phase trajectories near to the resonance of third order. Distribution of charge is shown. $B = 0$.

The separatrix divides the phase plane into regions of stable and unstable motion. Let us examine the nature of the phase curves. First of all it should be noted that each of the straight lines (14) divides the plane into two half-plane with positive or negative values of the corresponding variables s, t, u. According to this fact the sign of the $s \cdot t \cdot u$ product in (12) is determined. The phase trajectory bild-up may be performed in "the small variation method" explained by F. Klein [8]. For a small values of η, such that $|\eta| \ll |X_0^3|$ the corresponding phase trajectories are close to the separatrix in the region defined by the sign of η. It opens up a opportunity of graphical construction of phase trajectories on the basis of qualitative analysis [9] (fig. 3).

The phase curves farthest from the separatrix are close to the fixed points. In the central area there are the closed curves containing the stable singularity. If $X^2 + Y^2 = R^2 \gg X_0^2$ the phase curve distance from the separatrix decreases as η/R^2. When B is not equal to zero at the large distances from the center of the coordinate system ($R^2 \gg X_0^2$) term in (11) proportional to $(X^2 + Y^2)^2$ dominates and defines the sign of the left side of the equation keeping it constant everywhere outside of some central area with a large enough radius. This leads to the coalescence of the separatrix branches. Moreover there is the connection of the branches limiting the sectors with η opposite in the sign to B.

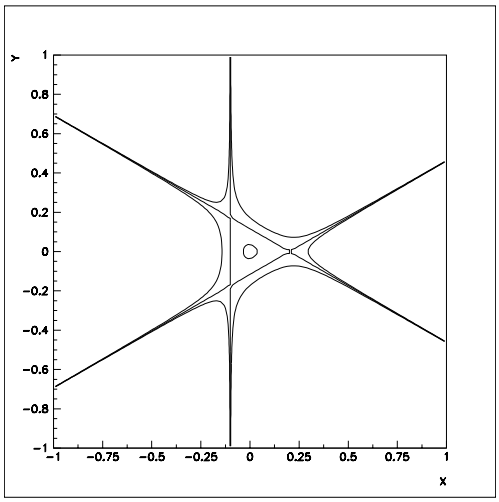

Figure 2: Phase trajectories close to the resonance of third order, $B = 0$.

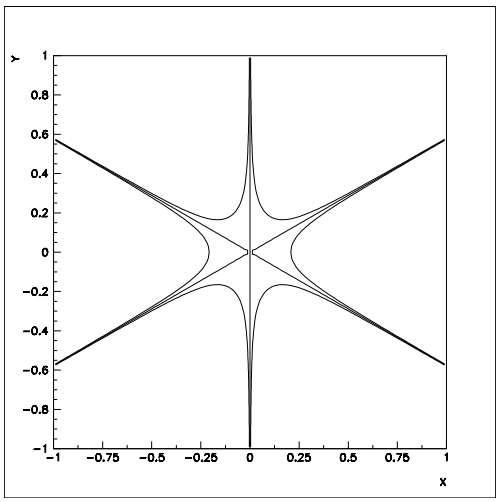

Figure 3: Phase trajectories at the resonance of third order, $B = 0$.

REFERENCES

[1] Lee S. Y. Accelerator Physics. World Scientific, 2004 596 p.

[2] Bashmakov Yu.A., Belovintsev K.A., Karpov V.A. An extraction of electrons from a synchrotron on fourth resonance.EPAC'90, June 12-16, 1991. Proc. 2nd Euroipean. Particle Accelarator Conf., Editions Frontiers, V. 2. p. 1601.

[3] Bogolyubov N.N, Mitropolskii Yu.A. Asimptoticheskie metody v teorii nelineinykh kolebanii. . 1963.

[4] Bashmakov Yu.A., Belovintsev K.A. Dynamics of Particles in Slow Extraction from the Pakhra Synchrotron with Resonances of 3/4 and 2/3. (In Russian) LEBEDEV-72-105, Jul 1972. 44 pp.

[5] Arnold V.I. Mathematical Methods of Classical Mechanics (2ed Springer, 1989)

[6] Beresteskiy V. B., Lifshitz E. M., Pitaevskii L. P. Relyatevistic quantum theory. p. 1. –.: 1968. 480 p.

[7] Kolmogorov A.N., Fomin S.V. Elementa of the function theory and functional analysis. M:. 1968. 496 p.

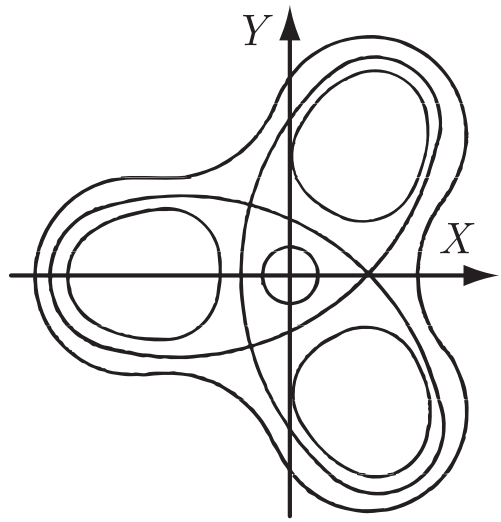

Figure 4: Phase trajectories close to the resonance of third order, $B \neq 0$.

[8] Klein F. Higher geometry M. 1939. 450 p.

[9] Bashmakov Yu.A., Phase trajectory analysis at the nonlinear resonances. PAC'91, San Francisco, May 6-9, 1991, Proc. 1991, IEEE Part. Accel. Conf., 1991. V. 3. P. 1684-1686.

MULTY FREQUNCY STORED ENERGY RF LINAC

V.G.Kurakin, P.V.Kurakin, Lebedev Physical Institute, Moscow, Russia

Abstract

Due to beam loading, accelerating gradient in rf linac is reduced in time if the energy acquired by charged bunches is not compensated by external generator that feeds the linac. Since the bunch energy gain in this mode of operation correlates strongly with bunch number, the energy spectrum of total bunch train might be corrected in order to suppress this additional spectrum widening. This spectrum control might be achieved with the rf cavity that operates at frequency shifted relative the main one in such a way, that any new bunch sees the cavity field in the appropriate phase correlated with bunch number. The first bunch traverses correcting cavity in field node while the last one in the phase, where the energy acquired by this bunch is equal to resulting bunch train energy spread arising from beam loading effect. Measures for suppression of non coherent bunches spectrum widening are suggested leading to insertion additional cavity excited at frequency shifted relative the main and adjacent frequencies.

INTRODUCTION

In RF linac, that might be represented as RF cavity and a train of charged bunches traversing the cavity, the bunches increase their energy due to the work of electric force of electromagnetic field inside the cavity. If the energy being carried out of cavity is compensated by external RF generator one has steady state acceleration. In this case, any new bunch from the bunch train acquires the same energy while traversing the cavity. In stored energy mode, external rf generator is used to excite cavity – to produce definite level of rf field before acceleration takes place while charged bunches get energy from the power stored in the cavity. Any new bunch carries away some portion of stored electromagnetic energy thus resulting in reduction of this energy and hence in corresponding reduction of the field level. The total bunch train is found to have energy spread after acceleration, its width being the function of the train charge accelerated. This seems to be the main shortcoming of stored energy mode of linac operation that limits this method for many applications.

In this paper, we discuss the possibility to avoid or compensate partially this spectrum widening for coherent motion.

QUALITATIVE ESTIMATIONS AND THE MAIN IDEA

The energy W stored inside rf cavity

$$W = QP/\omega \tag{1}$$

where Q is the cavity quality factor and ω stands for cavity eigen frequency, while P is the power dissipated in cavity walls. Any bunch from bunch train carries out of cavity the portion of energy

$$\Delta w = qU = ITU = IT\sqrt{PR}\,. \tag{2}$$

Here q, U, I, T denote bunch charge, accelerating voltage, average beam current and RF field period respectively, R is real part of cavity shunt impedance. After acceleration bunch train consisting of N bunches, reduction of accelerating gradient can be estimated as

$$\Delta U = \frac{\Delta E}{e} = \pi N I \frac{R}{Q} \tag{3}$$

Depending on relation between cavity time constant $\tau = 2Q/\omega$ and beam pulse duration t bunch energy drops down as linear function of time for the case $t << \tau$. This linear energy fall down might be eliminated by the accelerating gap with linear dependence of gap voltage on the number of the bunch entering the gap, the difference between the energy gain of the last bunch and the first one being equal to the energy spread defined by the formula above. A cavity on the beam path that is excited at frequency that differs from the main one by the value defined below provides necessary spectrum correction, and fig,1 serves to illustrate such a correction.

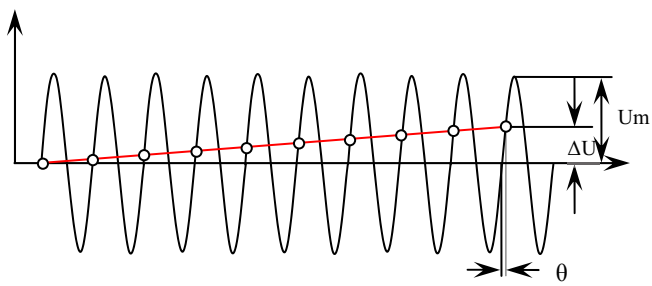

Fig.1 Spectrum correction

It can be calculated from fig.1 that $\theta = \Delta E / eU_m$. From the other hand

$$\theta = \omega(N-1)(T_1 - T_2) = 2\pi(N-1)\frac{\Delta\omega}{\omega}\,. \tag{4}$$

It follows from these two expressions that

$$\frac{\Delta\omega}{\omega} = \frac{\Delta E}{2\pi e U_m (N-1)}\,. \tag{5}$$

Taking into account formula (3)for cavity voltage reduction after all bunches acceleration one arrives at the next formula for the frequency of correcting cavity

$$\frac{\Delta\omega}{\omega} = \frac{I}{2U_m}\frac{R}{Q} \tag{6}$$

While deriving this expression, we supposed that $\Delta U << U_m$.

THE VOLTAGE INDUCED IN A CAVITY BY CHARGED BUNCHES TRAIN

To calculate the field radiated in a cavity by charged bunches traversing this cavity, we will follow standard method described in details in ref. [1]. In this method, vector potential $\vec{A}(\vec{r},t)$ where $\vec{r}$ is radius-vector of a bunch and t denotes time is represented in the form of eigen functions $\vec{A}_\lambda(\vec{r})$ series expansion

$$\vec{A}(\vec{r},t)=\sum_\lambda g_\lambda(t)\vec{A}_\lambda(\vec{r})\,. \tag{7}$$

$$\Delta\vec{A}_\lambda(\vec{r})+\kappa_\lambda^2\vec{A}_\lambda=0 \tag{8}$$

$$\frac{d^2g_\lambda(t)}{dt^2}+\frac{\omega_\lambda}{Q_\lambda}\frac{dg_\lambda(t)}{dt}+\omega_\lambda^2 g_\lambda(t)=\int_V\vec{j}(\vec{r},t)\vec{A}_\lambda(\vec{r})dV\,. \tag{9}$$

Here eigen frequencies of cavity modes $\omega_\lambda=c\kappa_\lambda$, c – light velocity, $\vec{j}$ - excitation current density, V- cavity volume, Q_λ - cavity mode quality factor. It is supposed that eigen functions are normalized by the condition

$$\int_V A_\lambda^2=\mu_0c^2=1/\varepsilon_0\,. \tag{10}$$

Electric and magnetic fields are expressed in terms of following expressions of eigen functions and expansion coefficients

$$\vec{E}_\lambda=-\frac{dg_\lambda}{dt}\vec{A}_\lambda,\ \vec{H}_\lambda=\frac{1}{\mu_0}g_\lambda rot\vec{A}_\lambda \tag{11}$$

For the main mode of pill box form (cylindrical resonator in Russian notation) [2]

$$A^z=\frac{c}{\omega\,a\sqrt{\pi\varepsilon_0L}}\frac{\nu_l}{a}\frac{J_0(\nu_1\frac{r}{a})}{J_1(\nu_1)} \tag{12}$$

In our analysis, we ignore the losses in cavity walls considering time interval of interest mach less cavity time constant $\tau=Q/\omega$. We also consider charge bunches to have point size. Under these assumption we have

$$\frac{d^2g(t)}{dt^2}+\omega^2g(t)=\int_V q\vec{v}(\vec{r},t)\delta(x,y,vt)\eta(vt)\eta(L-vt)\vec{A}(\vec{r})dV\,, \tag{13}$$

where all values are taken for the main mode, q,v,L denote bunch charge, its velocity and cavity length respectively, while δ and η stand for delta function and step function respectively. Making all substitutions we have

$$\frac{d^2g(t)}{dt^2}+\omega^2g(t)=F(t)\,, \tag{14}$$

$$\text{where } F(t)=\frac{2qvc\,\nu_1}{\omega a^2J_1(\nu_1)\sqrt{\pi\varepsilon_0L}} \tag{15}$$

for $0<t<L/v$ and $F(t)=0$ for $t>L/v$. (16)

We assume that at the moment t=0 bunch enters the cavity. The solution of this equation that satisfies initial conditions $g(0)=\dot{g}(0)=0$ (corresponding equal to zero magnetic and electrical components of induced field) can be represented in the form [3]

$$g(t)=\frac{2qvc\,\nu_1}{\omega^3a^2J_1(\nu_1)\sqrt{\pi\varepsilon_0L}}\sin\frac{\omega L}{2v}\sin(\omega t-\frac{\omega L}{2v}) \tag{17}$$

for $t>L/v$.

According to the formula (12) cavity electric field

$$E=-\dot{g}A=-\frac{2qvc^2\nu_1^{\,2}J_0(\nu_1\frac{r}{a})}{\omega^3a^4\pi\varepsilon_0LJ_1^{\,2}(\nu_1)}\sin\frac{\omega L}{2v}\cos(\omega t-\frac{\omega L}{2v}) \tag{18}$$

If the bunches from a bunches train traverses a cavity tuned to ω_2 with a frequency ω_1, the electric field that excites k-th bunch is

$$E_k=-\frac{2qvc^2\nu_1^{\,2}J_0(\nu_1\frac{r}{a})}{\omega_2^{\,3}a^4\pi\varepsilon_0LJ_1^{\,2}(\nu_1)}\sin\frac{\omega_2L}{2v}\times\cos\left[\omega_2t-\frac{\omega_2L}{2v}-2\pi(k-1)(\frac{\omega_2}{\omega_1}-1)\right] \tag{19}$$

and the n-th bunch radiates its own field and moves in the field induced by all previous bunches:

$$E^\Sigma=-\sum_{k=1}^{n-1}\frac{2qvc^2\nu_1^{\,2}J_0(\nu_1\frac{r}{a})}{\omega_2^{\,3}a^4\pi\varepsilon_0LJ_1^{\,2}(\nu_1)}\sin\frac{\omega_2L}{2v}\times\cos\left[\omega_2t-\frac{\omega_2L}{2v}-2\pi(k-1)(\frac{\omega_2}{\omega_1}-1)\right] \tag{20}$$

Summation on all bunches gives [4]

$$E^\Sigma=-\frac{2qvc^2\nu_1^{\,2}J_0(\nu_1\frac{r}{a})}{\omega_2^{\,3}a^4\pi\varepsilon_0LJ_1^{\,2}(\nu_1)}\sin\frac{\omega_2L}{2v}\times\cos\left[\omega_2t-\frac{\omega_2L}{2v}-\pi(n-2)(\frac{\omega_2}{\omega_1}-1)\right]\times\sin\left[(n-1)\pi\left(\frac{\omega_2}{\omega_1}-1\right)\right]\frac{1}{\sin\pi(\frac{\omega_2}{\omega_1}-1)} \tag{21}$$

To find out the energy that the n-th bunch looses in the field radiated in the cavity by all previous bunches one has to integrate the last expression over cavity length.

$$U_{lost}=-\frac{2qvc^2\nu_1^{\,2}}{\omega_2^{\,3}a^4\pi\varepsilon_0LJ_1^{\,2}(\nu_1)}\sin\frac{\omega_2L}{2v}\times\frac{\sin\left[(n-1)\pi\left(\frac{\omega_2}{\omega_1}-1\right)\right]}{\sin\pi(\frac{\omega_2}{\omega_1}-1)}\frac{\sin\frac{\omega_2L}{2v}}{\frac{\omega_2}{2v}}\cos\left[\pi(n-2)(\frac{\omega_2}{\omega_1}-1)\right] \tag{22}$$

It is taken into account that the n-th bunch enters the cavity in the phase $2\pi(n-1)(\omega_1/\omega_2-1)-\omega l/2v$ relative the voltage induced by the first one and in the phase $\pi(n-1)(\omega_1/\omega_2-1)-\omega L/2v, n>2$ relative total induced voltage.

BEAM ENERGY SPECTRUM CORRECTION

Let us consider the simple rf linac consisting of two accelerating cavities. The first one operates at frequency ω_1 that coincides with the bunches repetition rate while the second one is tuned to frequency ω_2. The n-th bunch from bunches train traverses the cavity assembly loosing the energy (with the account of $\pi n(\frac{\omega_1}{\omega_2}-1)<<1$)

$$U_{lost}(n)=\frac{2qvc^2\nu_1^{\,2}(n-1)}{\omega_1^{\,3}a_1^{\,4}\pi\varepsilon_0 LJ_1^{\,2}(\nu_1)}\frac{\sin^2\frac{\omega_1 L_1}{2v}}{\frac{\omega_1}{2v}}+$$
$$\frac{2qvc^2\nu_1^{\,2}(n-1)}{\omega_2^{\,3}a_2^{\,4}\pi\varepsilon_0 LJ_1^{\,2}(\nu_1)}\sin\frac{\omega_2 L}{2v}\frac{\sin\frac{\omega_2 L_2}{2v}}{\frac{\omega_2}{2v}} \quad (23)$$

Thus, we have linear dependence of the energy lost with bunch number, and this energy lost might be compensated with linear growth of the accelerated voltage of the second cavity if the following condition takes place:

$$U_2(t)=U_{20}\sin(\omega_2 t), U_{20}>>U_{lost},$$
$$U_{20}\times 2\pi(\omega_2/\omega_1-1)=U_{lost}(2), \quad (24)$$

and $\omega_2 t=-L_2/2v$ corresponds to the moment when the first bunch enters the second cavity.

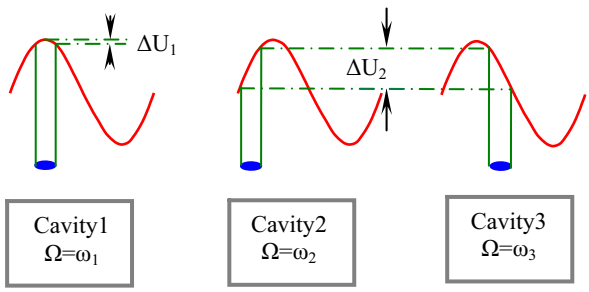

Fig2. Elimination of additional energy spread in sequence of two correcting cavities

Two frequency rf accelerator method just described may result in additional energy spread of individual bunch as in can be seen from fig.3. The bunch positions on sine wave of correction voltage corresponds to large value of $\frac{dU_2}{dt}$ that results in large difference of accelerating gradients of end bunch particles. Three frequency scheme with additional cavity installed on beam path after the first correcting and operating at frequency $\omega_3<\omega_1$ so that

$$U_3(t)=U_{20}\sin(\omega_3 t), U_{20}>>U_{lost},$$
$$U_{20}\times 2\pi(\omega_3/\omega_1-1)=-0.5U_{lost}(2), \quad (25)$$
$$U_{20}\times 2\pi(\omega_2/\omega_1-1)=0.5U_{lost}(2)$$

is free of the shortcoming mentioned. Indeed, the bunch head moves at higher field level than its centre and the tail while traversing the first correcting cavity. In the second correction cavity instead one has quite opposite case that is bunch tail acquires the same energy as its head in the first correction cavity. Thus, in configuration described all bunch particles acquire the same energy after passing consequently two correction cavities.

To provide periodical mode of operation, the relation $T_{rep}=\frac{n\times 2\pi}{\omega_1}=\frac{m\times 2\pi}{\omega_2}$ has to be satisfied. Here m and n are integer numbers, T_{rep} - the period of bunches trains sequence.

DDS (Direct Digital Synthesis) technique might be used to provide necessary frequency relation, their phasing and stability. The details are the subject of separate paper.

CONCLUSION

Due to beam loading, additional energy spread of accelerated bunch train arises in a stored energy linac. It has been shown that this coherent energy spread widening might be eliminated with additional cavities on beam path, tuned to slightly different frequency relative to the main part of rf accelerator. The effect of spectrum correction takes place due to phase slip of successive bunches from bunches train in correcting cavities installed on beam path. The undesired incoherent energy spread widening can be eliminated by adding additional correcting cavity, both correcting cavities being detuned by the values with opposite signs.

The method described might be used in rf superconducting linacs in short current pulse mode.

REFERENCES

[1] V.M.Lopukchin. Excitation of electromagnetic oscillations and waves by electron flows. Gostekchizdat, 1953. 324 pp., in Russian.
[2] O.A.Kolpakov, V.I.Kotov. Jurnal tekchnicheskoy Fiziki, v. 34, No8, pp. 1387-1391, in Russian
[3] V.V.Stepanov. Kurs differencialnikch uravneniy, Moscow, KomKniga, 2006. 468 pp., in Russian.
[4] Gradshtein, Rygik. Tablitsi integralov, summ, ryadov I proizvedeniy, in Russian.

SIMULATION OF HOLLOW ION BEAM FORMATION LINE

H. Barminova, N. Alexeev, A. Golubev, T. Kulevoy, A. Sitnikov, T. Tretyakova
ITEP, Moscow, Russia

Abstract

Heavy ion beam may be used for the matter extreme state creation [1], a forming line must satisfy to certain requirements on beam brightness, spot size and focus position. The original method of hollow ion beam formation - wobbler system - was proposed to deposit the beam energy at cylindrical target [2]. To verify wobbler parameters the beam dynamics simulation was carried out by means of two codes – "Transit", that is a modified code "DINAMION" [3], and G4Beamline [4]. The results obtained are discussed.

INTRODUCTION

Intense heavy ion beam is an effective tool to create matter extreme states in laboratory conditions. The advanced experiments in high energy density physics require the cylindrical target irradiated by the hollow beam [1]. The wobbler system [2] allows to shape such a hollow beam. Preliminary system simulation has illustrated the feasibility of the method [5]. In paper presented the beam dynamics simulation is carried out in order to consider some nonlinear effects that may influence on the beam spot size and focus position.

ITEP WOBBLER SYSTEM DESCRIPTION

A layout of the wobbler system for hollow beam formation line in ITEP (ITEP TWAC project) is based on the system layout for GSI FAIR project [2]. The ITEP wobbler system consists of two four-cell RF-cavities and focusing triplet of quadrupole magnetic lenses. RF-cavities deflect the beam in x- and y-directions. The phase shift between RF-fields in first and second cavities is chosen so that the particle with zero deflection in the first, x-cavity, gains the maximum deflection in the second, y-cavity, and vice versa.

The general requirements for layout were the target size satisfaction and the beamline length limitation in case of the real initial parameters of ITEP beam. In Fig.1 designed layout of the ITEP wobbler system is shown.

The asymmetric quadrupole magnetic triplet follows by the second cavity, the triplet focusing the beam on the target. In this project the target assume to be irradiated from one side.

The whole length of the system is about 8 m, and it is sufficient length under conditions of the ITEP experimental area limitation.

The structure of the channel as well as preliminary parameters of beamline elements are shown in Table 1.

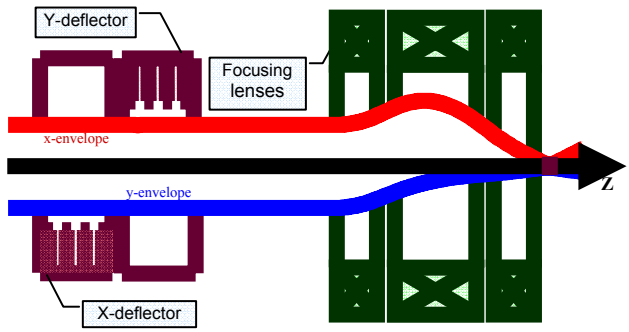

Figure 1: A principal layout of ITEP wobbler system.

Table 1: System structure.

Element	Field value	Element length, mm	Aperture radius, mm
Drift	-	800	100
Wobbler X	1.5 MV/m	4*368	100
Drift	-	184	100
Wobbler Y	2.5 MV/m	4*368	100
Drift	-	800	100
1st magnetic quadrupole lense	15.3 T/m	400	100
Drift	-	160	100
2nd magnetic quadrupole lense	-16.3 T/m	800	100
Drift	-	160	100
3rd magnetic quadrupole lense	18.8 T/m	400	100
Drift	-	~ 900	100

PARTICLE DYNAMICS SIMULATION

The first simulation was carried out for ions Co^{27+}_{59} by means of "Transit-DINAMION" code, developed in ITEP [3]. The beam parameters taken for simulation are close to the real beam parameters in ITEP project. For cobalt ions the beam energy was taken 450 MeV, the pulse duration – 120 ns. Energy spread was varied between 1% and 0.1%. Maximum beam intensity per pulse – $2*10^{12}$ particles. Normalized effective x-emittance (4 rms) was 8 π mm mrad, and normalized effective y-emittance was the same. Initial radius of the beam (at the entrance to the first cavity) was 40 mm.

As far as concerns the wobbler parameters, the resonant frequency of both cavities was 297 Mhz, the shift between RF-fields in cavities used in our simulation was $\pi/2$. For ITEP project it is practically sufficient to use four-cell cavity so the field mode chosen was H_{114}.

The results obtained are shown at Fig. 1-4. The values of the outer and inner radii of the target were 2.1 mm and 0.6 mm respectively. One can see the beam focus after third lens from Fig.1, where x- and y-envelopes are presented.

Simulation with and without beam space charge shows that own space charge weakly affects on the spot size (see Fig.2-4), but it leads to the focus position displacement. For cobalt ion beam with 450 MeV energy and with intensity equal to $2*10^{12}$ particle per pulse this displacement was about 10 mm [5]. Nonzero beam emittance is found to affect on the shape of the final ring (at the target), but the energy maximum position is the same. In this simulation the particle distribution was supposed to be Gaussian in both transverse planes. Longitudinal distribution has been assumed uniform.

For the simplicity the beam was assumed to have axial-symmetric shape and zero divergence angle at the entrance to the wobble system (the preliminary forming optics system is not considered here).

To verify the system parameters and to take into account the possible aberrations and some other nonlinear effects simulation was carried out by means of G4Beamline code [4], developed by Tom Roberts, Muons Inc. The dynamics of the equivalent proton beam was simulated in order to minimize the time of simulation. The system parameters were re-calculated in according to charge-mass ratio. The simulation results coincide with the results of the previous simulation in whole, if we neglect the fringe field of the lens. The lens fringe field existence leads to lens effective length decreasing and to the beam focus displacement along the longitudinal axes.

The error in the lens magnetic field gradient equal to 0.1% leads to significant beam defocusing, so it is very important to transit the beam in the “linear” area of the channel.

During simulation we didn’t consider nonlinear effects in RF-cavities assuming the cavity aperture essentially more than the beam radius for 95% of the particles and the field harmonic characteristic spatially stable along the cavity axis. But it would be interesting to take into account these complicated effects for two deflecting cavities with the field phase shift**.**

CONCLUSIONS

Wobbler system allows to obtain the focused hollow beam on the target with size and position required.

Simulation of the wobbler system have shown that parameters of the system should be chosen with nonlinear effects in the lenses and in the cavities taken into account because of the beam focus displacement.

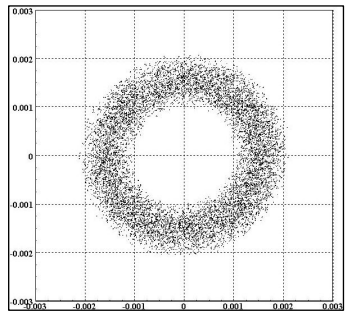

Fig.2. Cross-section of the particle distribution on the target (with zero own space charge).

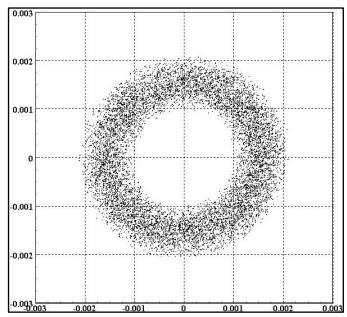

Fig.3 Cross-section of the particle distribution on the target (with nonzero own space charge).

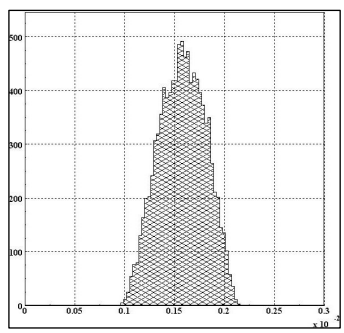

Fig.4. Particle radial distribution on the target.

REFERENCES

[1] V.E. Fortov, D.H. Hoffman, B. Yu. Sharkov, NIM A415 (1998) 20
[2] S. Minaev et al, NIM A620 (2010) 99-104
[3] DYNAMION – Multiparticle code for beam dynamics simulation. Manual. A. Kolomiets et al.
[4] G4Beamline – http://g4beamline.muonsinc.com
[5] S. Minaev et al, In Proc. PAC’11, New York, USA, THP041

MATHEMATICAL MODEL OF BEAM DYNAMICS OPTIMIZATION IN TRAVELING WAVE

A.D. Ovsyannikov, A.Y. Shirokolobov, SPbSU, Saint-Petersburg, Russia

Abstract

In works by B.I. Bondarev, A.P. Durkin, A.D. Ovsyannikov mathematical model of optimization of charged particles dynamics in RFQ accelerators was proposed. In this paper a new mathematical model of optimization of particle dynamics in traveling wave is considered. Joint optimization model of program and disturbed motions is investigated.

INTRODUCTION

In works [1] mathematical model for optimization of RFQ structure was suggested. Transverse and longitudinal motions were investigated separately. But characteristics of transverse motion were considered and analyzed at the stage of longitudinal motion optimization. In particular restrictions were imposed on defocusing factor.

In this paper other model of longitudinal motion based on the selection of program motion (synchronous particle motion) and beam of charged particles (movements in deviations from program motion). This model has been tested for RFQ structure.

Phase of synchronous particle and intensity of accelerating field are considered as control parameters (functions). It should be noted that in paper [1] those parameters also were considered as controls, but mathematical model of optimization was different from the model proposed in this paper.

PROBLEM STATEMENT

Let us investigate the problem of control of longitudinal dynamics of beam in waveguide accelerator as a problem of joint optimization of synchronous particle motion and ensemble of trajectories [3]. As control functions let us choose the laws of changing of dimensionless parameter of the amplitude of the accelerating wave $\alpha(\xi)$ [5] and synchronous phase $\varphi_s(\xi)$ along the structure.

Adopt the following notation $u_1 = \alpha(\xi), u_2 = \varphi_s(\xi)$, where functions $u_1(\xi),\ u_2(\xi)$ are *controls*.

Let the phase of the particle is given by [1]

$$\varphi = \omega \int_0^z \frac{dz}{v(z)} - \omega t + \varphi_s. \tag{1}$$

Under *program motion* (synchronous particle motion) we mean a solution of the system

$$\frac{d\gamma_s}{d\xi} = -\alpha(\xi)\sin\varphi_s,$$
$$\varphi_s = u_2(\xi)$$

with initial condition

$$\gamma_s(0) = \gamma_{s0}.$$

Here γ_s — reduced energy of synchronous particle.

Phase of the beam particles, according to (1) will be considered in the deviation of the phase of the synchronous particle:

$$\widehat{\varphi} = \varphi - \varphi_s.$$

Considering that the longitudinal velocity of the synchronous particle coincides with the phase velocity of the wave, i. e.

$$\beta = \beta_s = \frac{\sqrt{{\gamma_s}^2 - 1}}{\gamma_s}, \tag{2}$$

obtain controlled dynamical system described by the system of ordinary differential equations

$$\frac{d\gamma_s}{d\xi} = -u_1(\xi)\sin(u_2(\xi)), \tag{3}$$
$$\frac{d\gamma}{d\xi} = -u_1(\xi)\sin(\widehat{\varphi} + u_2(\xi)), \tag{4}$$
$$\frac{d\widehat{\varphi}}{d\xi} = 2\pi\left(\frac{\gamma_s}{\sqrt{\gamma_s^2 - 1}} - \frac{\gamma}{\sqrt{\gamma^2 - 1}}\right) \tag{5}$$

with initial conditions

$$\gamma_s(0) = \gamma_{s0}, \tag{6}$$
$$\gamma(0) = \gamma_0, \quad \widehat{\varphi}(0) = \widehat{\varphi}_0. \tag{7}$$

Here $\xi \in T_0 = [0, L]$ — independent variable; $(\gamma_0, \widehat{\varphi}_0)^T \in M_0, \gamma_s \in \Omega_x \subseteq R^1$; $(\gamma, \widehat{\varphi})^T \in \Omega_y \subseteq R^2$ — vector of system variables; $(u_1, u_2)^T \in U \subseteq R^2$ — 2-dimensional vector-function of control; L — constant value.

It is assumed that the sets of Ω_x and Ω_y — are open, set U and set of positive measure $M_0 \subset \Omega_y$ — are compact.

We also assume that the admissible controls $u = u(\xi)$, $\xi \in T_0$, constitute a class of piecewise smooth on the interval $[0, L]$ functions with values in a compact set U. By piecewise smooth functions we mean functions, which derivatives have only a finite number of discontinuities of the first kind.

Equations (3)–(5), where $\widehat{\varphi}$ — phase in deviations from the synchronous phase, and γ — complete reduced energy, convenient when considering optimization problems. But in the future equations in deviation of energy of the synchronous particle will be considered.

THE EQUATION OF THE SEPARATRIX

Choose as dynamic variables, the phase difference of asynchronous and synchronous particle and the difference of the reduced energy

$$\psi = \varphi - \varphi_s, \quad p_\psi = \gamma - \gamma_s.$$

Subtracting equation (3) from (4),

$$\frac{dp_\psi}{d\xi} = -u_1(\xi)\big(\sin(\psi + u_2(\xi)) - \sin(u_2(\xi))\big).$$

Take the derivative with respect to the coordinate of value and make the substitution $\xi = z/\lambda$. Given that $\omega = 2\pi c/\lambda$, $\upsilon = \upsilon_s$, $\frac{\upsilon_z - \upsilon_s}{\upsilon_s} \approx \frac{1}{{\gamma_s}^2}\frac{p_\psi}{p_s \upsilon_s}$ [2], we obtain a system of first order equations describing the dynamics of the longitudinal motion:

$$\frac{dp_\psi}{d\xi} = -u_1(\xi)\big(\sin(\psi + u_2(\xi)) - \sin(u_2(\xi))\big), \quad (8)$$

$$\frac{d\psi}{d\xi} = \frac{2\pi}{\sqrt{(\gamma_s^2 - 1)^3}} p_\psi. \quad (9)$$

From equations (8), (9) we obtain an equation describing the separatrix of the beam in the phase plane ψ, p_ψ [2]:

$$p_\psi = \pm\sqrt{\frac{\sqrt{({\gamma_s}^2 - 1)^3}}{\pi}}\sqrt{V(-\pi - 2u_2) - V(\psi)},$$

where function

$$V(\psi) = -u_1(\xi)\big(\cos(\psi + u_2(\xi)) + \psi\sin(u_2(\xi))\big)$$

is analogous to the potential energy.

FUNCTIONALS

In accordance with the objectives of optimizing we shall consider the following functionals:

$$I_1(u) = \int_{M_{L,u}} \left(a\left(\frac{\gamma_L}{\gamma_{sL}} - 1\right)^2 + b(\widehat{\varphi}_L - \bar{\varphi}_L)^2 \right) d\gamma_L d\widehat{\varphi}_L, \quad (10)$$

$$I_2(u) = \int_0^L \int_{M_{\xi,u}} h(q, \bar{q}) d\widehat{\varphi} d\gamma d\xi, \quad (11)$$

where

$$h(q, \bar{q}) = \begin{cases} (q - \bar{q})^2, & \text{if} \quad q > \bar{q}; \\ 0, & \text{if} \quad q \leqslant \bar{q}, \end{cases}$$

Here $\widehat{\varphi}_L, \gamma_L$ — phase and reduced energy of disturbed motion at the output of accelerator correspondingly, $\gamma_{sL}, \bar{\varphi}_L$ — reduced energy of synchronous particle and average phase of disturbed motion at the output of accelerator, $q = H(\psi, p_\psi)$ — value of the Hamiltonian of the particles beam system (4), (5), which is given by

$$H(\psi, p_\psi) = V(\psi) + \frac{\pi}{\sqrt{(\gamma_s^2 - 1)^3}} {p_\psi}^2,$$

and $\bar{q}$ — value of Hamiltonian corresponding to the separatrix.

We will consider the minimization of functional (10), (11) by controls $(u_1, u_2)^T$.

Optimization will be performed by the gradient methodon the basis of variation of the [3–6], which is a linear combination of the above functional, equipped with weighting coefficients.

NUMERICAL RESULTS

Software tool for considered problem was implemented in Matlab as a unit of the BDO-RFQ 1.6 system, developed by the department of theory of control systems of electrophysical equipment in SPbSU.

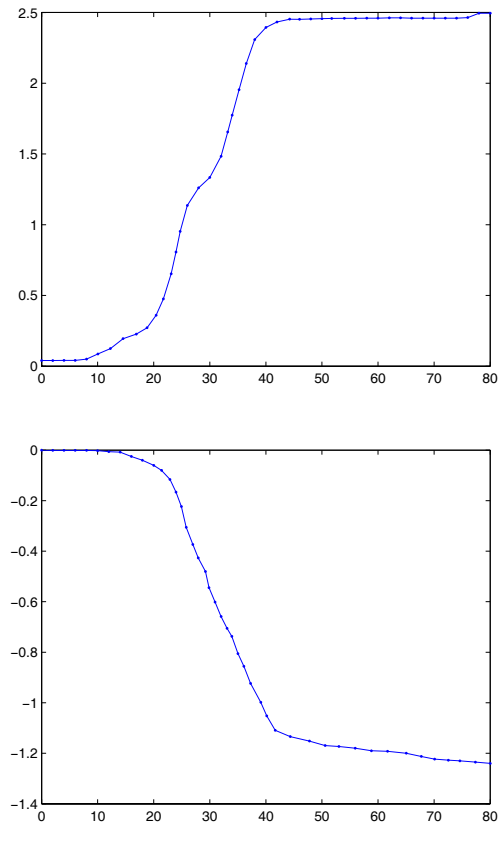

Figure 1: The change of reduced amplitude of intensity (upper plot) and phasesynchronous particle (lower plot) after optimization

Initial controls $u_1 = \alpha(\xi)$ and $u_2 = \varphi_s(\xi)$ were defined by 40 points and interpolating between them with splines.

The calculations were carried out for the structure with the following parameters: injection energy — 80 keV, ac-

celerating wave length — 1 cm, length of structure — 80 cm.

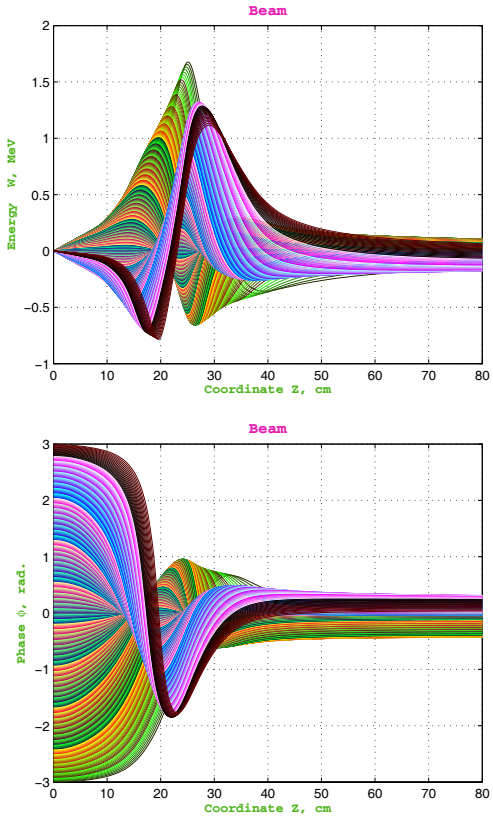

Figure 2: The relative deviation of the energy of the beam particles (upper plot) and the phases of the beam particles (lower plot)

The solution was carried out in two stages. At the first stage capture coefficient equal to 0.95 was achieved. At the second stage the width of the energy and phase spectra was minimized at the output of accelerator.

Numerical optimization was performed on 500 particles uniformly located in between the phases of -3 to 3 rad., which corresponds to obtained coefficients of capture. This resulted in the controls $\alpha^{(1)}(\xi)$ and $\varphi_s^{(1)}(\xi)$ (Fig. 1). These controls allow the output structure with the energy spread 28%and the width of the phase spectrum 0,73 rad. (Fig. 2). The average energy at output of structure is 5,6 MeV.

It should be noted that all of the particles were in the acceleration mode. It is seen in Fig. 3, since the separatrix limits the capture of particles into the acceleration mode.

CONCLUSION

In this paper a mathematical model to optimize the beam dynamics in the accelerator with traveling wave was developed. The separatrix equation was used for the construction of mathematical optimization model of beam dynamics.

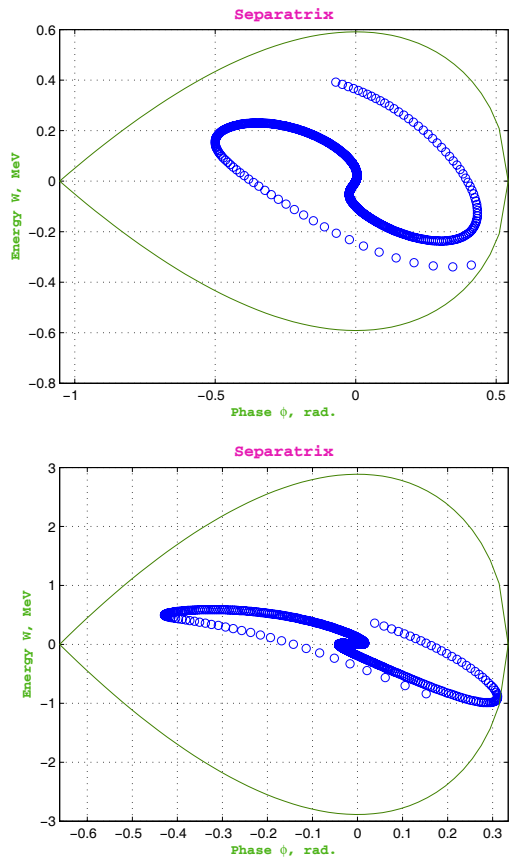

Figure 3: Separatrix and energy-phase distribution of the particle beam at the output of buncher (upper plot) and output of structure (lower plot)

REFERENCES

[1] B. I. Bondarev, A. P. Durkin, A. D Ovsyannikov. New Mathematical Optimization Models for RFQ Structures // Proceedings of the 18-th Particle Accelerator Conference, New York, USA, 1999. P. 2808–2810.

[2] I. M. Kapchinsky. Theory of linear resonance accelerator, Moscow, Energoizdat, 1982 , 310 p.

[3] A. D. Ovsyannikov. New approach to beam dynamics optimization problems // Proceedings of the 6-th international computational accelerator physics conference, Darmstadt, Germany, 2000.

[4] D. A. Ovsyannikov. Mathematical Methods of Optimization of Charged Partical Beams Dynamics // Proceedings of European Partical Accelerator Conf., Barselona, Spain, Vol.2, 1996, pp. 1382–1384.

[5] D. A. Ovsyannikov. Modeling and Optimization of Charged Particles Beam Dynamics, Lenigrad, 1990, p. 312.

[6] D. A. Ovsyannikov. Modeling and Optimization Problems of Charged Particle Beams Dynamics // Proceedings of the 4th European Control Conference, Brussels, 1997, pp. 390–394.

CALCULATION OF TOLERANCES AND STATISTICAL TEST

Y. Yelaev, SPbSU, Saint-Petersburg, Russia

Abstract

In the paper mathematical methods of tolerance determination of different parameters of accelerating and focusing structures are considered. The determination of tolerances is based on the analytical representation of variation of functional characterizing the beam dynamics. Method of statistical analysis of calculated tolerance values is represented. The purpose of the work is to determine the maximum possible deviations of the real (actual) parameters from nominal, when the qualitative structure function satisfies to the required modes.

INTRODUCTION

In the design of any kind of system, whether is it a linear accelerator or some other system, the nominal (rated) values of parameters are determined. The system must satisfy the specified criterion of the quality according to these parameteres. But accelerator of any type is a very difficult complex structure. It is almost impossible, and sometimes not economical to provide in accelerator the equality of actual parameters values with their nominal values. Deviations from the rated values influence on the quality of the system functioning and cause deviations from the specified quality criterion. These deviations can have a negative impact.

In this work the analytical and statistical method of tolerance determination is considered on the example of the longitudinal motion of charged particles in an accelerator with drift tubes. Thus, the maximum possible deviations of the real (actual) parameters from nominal are found when the qualitative structure function satisfies to the required modes. The statistical analysis of the getting results is carried out.

PROBLEM STATEMENT

In the paper we consider the problem of tolerances calculation for the dynamics of longitudinal motion of charged particles in an accelerator with drift tubes. The equations describing this process have the following form [1], [2]

$$\begin{aligned} \frac{d\varphi}{d\xi} &= \frac{2\pi\gamma}{\sqrt{\gamma^2-1}}, \\ \frac{d\gamma}{d\xi} &= \alpha(\xi)\cos(\varphi), \end{aligned} \tag{1}$$

where $\alpha(\xi)$ — the stepwise function defined on the interval [0, L],

$$\alpha(\xi) = \alpha^i, \quad \xi \in [\mu_{i-1}, \mu_i], \quad i = \overline{1,m}.$$

Here $0 = \mu_0 < \mu_1 < \ldots < \mu_m = L$, m — fixed non-negative integer. Further, we consider tolerances determination only of parameters μ_i, which are coordinates of the drift tubes. We introduce into consideration the functional characterizing the quality of the system functioning according to the μ_i parameters

$$I(\mu) = \int_{M_{L,\mu}} \left(a(\frac{\gamma_L}{\bar{\gamma}} - 1)^2 + b(\varphi_L - \bar{\varphi})^2 \right) d\varphi_L d\gamma_L. \tag{2}$$

Here $\bar{\varphi}$, $\bar{\gamma}$ — average energy and phase, $M_{L,\mu}$ — beam cross-section of paths depending on μ parameters.

The nominal values of the parameters are known, and they are $\mu_0 = (\mu_{01}, \ldots, \mu_{0m})$. It is necessary, according to the given value of $\triangle > 0$, to determinate the tolerances $\triangle_i > 0$, $i = \overline{1,m}$, such that

$$|\triangle I| = |I(\mu_0 + \triangle\mu) - I(\mu)| \leq \triangle,$$

where $|\triangle\mu_i| \leq \triangle_i$, $\triangle\mu = (\triangle\mu_1, \ldots, \triangle\mu_m)$, and realize statistical analysis of the tollerances value.

ALGORITHM OF THE TOLERENCE ESTIMATE

We assume that the deviations from the nominal values of the parameters are small and that the changes within the tolerances bands are linear. So the total increment of the functional I can be changed by its variation [3]

$$\delta I \approx \sum_{i=1}^{m} \left(\frac{\partial I(\mu_0)}{\partial \mu_i} \right) \triangle\mu_i. \tag{3}$$

There are two basic principles for the determination of the tolerances: the principle of equal influences and the principle of equal tolerances [4]. The sense of principle of equal influences is that the change of each input parameter affects the same way on the output value. So we obtain the formula for the calculation of tolerance:

$$\triangle_i = \triangle(m^{-\frac{1}{2}}) \left| \frac{\partial I(\mu_0)}{\partial \mu_{i0}} \right|^{-1}, \quad i = \overline{1,m}. \tag{4}$$

The sense of principle of equal tolerances is that the all tolerances are equal, i. e. $\triangle_i = \bar{\triangle}, i = \overline{1,m}$. So we

obtain the formula:

$$\bar{\triangle} = \triangle \left(\sum_{i=1}^{m} \left(\frac{\partial I}{\partial \mu_{i0}} \right)^2 \right)^{\frac{1}{2}}, \quad i = \overline{1,m}. \tag{5}$$

For the tolerance calculation we use the following equation [5]

$$\frac{\partial I(\mu)}{\partial \mu_i} = -\int_{M_{\mu_i,\alpha}} (\alpha_i \psi_2 \cos(\varphi(\mu_i)) - \\ -\alpha_{i+1}\psi_2 \cos(\varphi(\mu_i)))dx_{\mu_i}. \tag{6}$$

Find the ψ_1 and ψ_2 solving the system of differential equations

$$\frac{d\psi_2}{d\xi} = \frac{2\pi\psi_1}{(\gamma^2-1)^{\frac{3}{2}}}, \\ \frac{d\psi_1}{d\xi} = \alpha(\xi)\sin(\varphi)\psi_2 \tag{7}$$

with initial conditions

$$\psi_2 = -\frac{2a}{\bar{\gamma}}\left(\frac{\gamma(L)}{\bar{\gamma}} - 1\right), \\ \psi_1 = -2b(\varphi(L) - \bar{\varphi}), \tag{8}$$

where $\bar{\gamma}, \bar{\varphi}$ — average energy and phase.

STATISTICAL ANALYSIS OF THE TOLERANCE VALUE

After calculations the tolerances were found for each $\mu_i, i = \overline{1,m}$ parameter of the accelerating structure. The structure must function with the required characteristics within tolerances bands. We realize statistical analysis to evaluate the behavior of accelerating structure within tolerances bands.

Assume $\mu_i, i = \overline{1,m}$ are normal random variables with a standart deviation σ_i and mathematical expectation $M[\mu_i] = \mu_{i0}, i = \overline{1,m}$. Set aside the cross-correlation of random variables $\mu_1, \ldots, \mu_m$. Remind that $\mu_{i0}, i = \overline{1,m}$ are nominal (rated) parametres of the system. Acording to the three sigma rule, normal random variable possesses the values in the interval $[\mu_{i0} - 3\sigma, \mu_{i0} + 3\sigma]$ with a probability $0,997$. It is necessary, that all possible values of the parameter μ_i (i. e. all its possible deviations) were within the tolerances bands. In this case the satisfactory system functioning is provided. Thus, the boundary of the tolerance zone must be equal to three sigma, i. e. $\triangle_i = 3\sigma_i$ therefore $\sigma_i = \frac{\triangle_i}{3}$. Model normal distribution for each random value with mathematical expectation $M[\mu_i] = \mu_{i0}$ and standart deviation $\sigma_i = \frac{\triangle_i}{3}$. As a result, all possible values of each $\mu_i, i = \overline{1,m}$ parameter must be in the range of tollerance zone.

Statistical modeling can be realized the following way:

- Generate the values of the random variables $\mu_1, \ldots, \mu_m$.
- Model the dynamics of the longitudinal motion with the new values of the control parameters $\mu_i, \ldots, \mu_m$. Find the functional I corresponding to this dynamics. Also it is suggested, that this functional is a random variable.
- After the implementation N of these experiments we get a sample of the functional values $(I_1, \ldots I_N)$. Find the standart deviation [6]

$$\sigma_I = \sqrt{\frac{1}{N}\sum_{i=1}^{N}(I_M - I_j)^2}. \tag{9}$$

Here I_M — mathematical expectation.

If the standard deviation σ_I is less than the initially specified deviation $\triangle$ of the functional, the tolerances can be increased. Thus, the tolerances zones can be expanded, until σ_I and $\triangle$ are not comparable. Vice versa if σ_I more than $\triangle$, the tolerances bands are reduced.

RESULTS

Based on the principle of equal influences, calculation of the tolerances was realized, and statistical analysis was implemented. We considered, the case where the two parts of the functional (2) are equal to the result. So the weight coefficients have the following meaning $b = 1, a = 2,929e+006$. Were found the tolerances, according to which the functional deviation shall not exceed 5%, it is equivalent to $\triangle I \leqslant 1,110e-008$.

Statistical analysis of the tolerances values showed that the standard deviation of the functional $\sigma_I = 2,8838e-010$ is approximately 0,129%, which is significantly less than 5%. So we can expand the tolerances bands. By increasing the tolerances in 5.9 times, we received the following results $\sigma_I = 7,9668e-009$, which is about 3,6% (see Fig. 1).

Similarly, we considered cases where functional had another weighting coefficients. Statistical analysis showed that the tolerances can be increased by several times. Measure of the tollerance' increase depends on the type of functionals.

CONCLUSION

In the work method of the tolerances determination was investigated on the example of the longitudinal motion of charged particles in an accelerator with drift tubes. Statistical analysis of the tolerances values was carried out. The same method can be applied to any other accelerating and focusing structure, in which the dynamics of the particles is described by the differential equations. Nowadays, there are many works

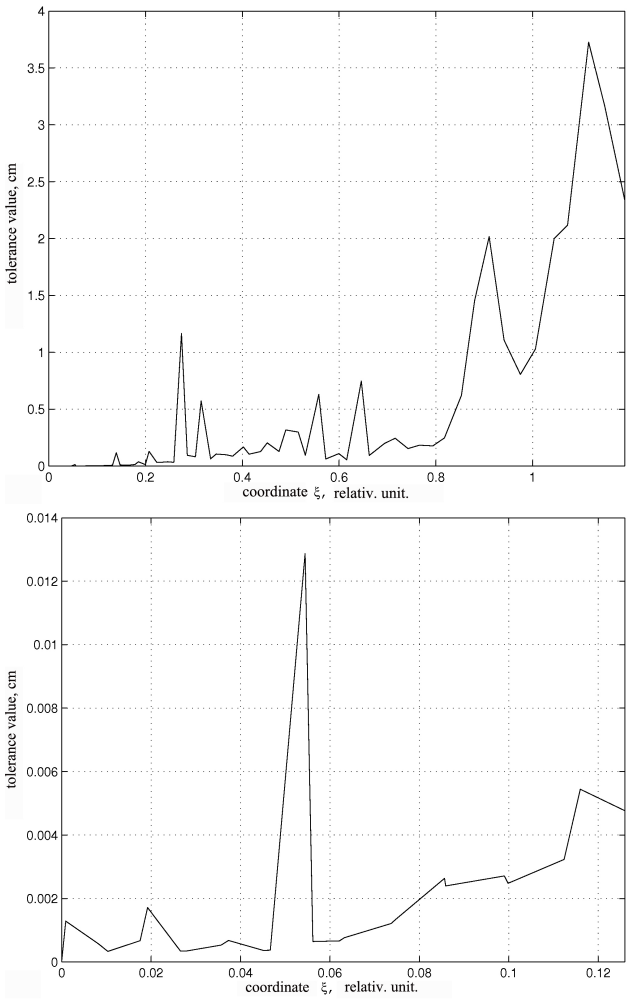

Figure 1: Values of the tolerances.

devoted to beam dynamics optimization. In some of them [1, 7–14] the methods and approaches of finding functional variation were considered. These methods can be used for the tolerance determination.

REFERENCES

[1] D. A. Ovsyannikov, *Modeling and optimization of charged particle beam dynamics*, (Leningrad, 1990, p. 312).

[2] I. M. Kapchinsky, *Theory of linear resonance accelerator*, (Moscow, Energoizdat, 1982, p. 310).

[3] A. P. Durkin, A. A. Kovalenko, D. A. Ovsyannikov, "Theory of tolerances calculation for parameters of focusing systems," Technical Physics 1991, T.61, Issue 7.

[4] E. N. Rosenwasser, R. M. Yusupov, *Sensitivity of control systems,* (M. 1986, p. 463).

[5] O. I. Drivotin, D. A. Ovsyannikov, Yu. A. Svistunov, M. F. Vorogushin, "About computational tolerances problem in accelerating structures," Proc. of the first international workshop BDO — St.Petersburg, (1994).

[6] V. E. Gmurman, *Theory of probability and statistics,* (Moscow High School, 2003, p. 479).

[7] Y. A. Svistunov, A. D. Ovsyannikov, "Designing of compact accelerating structures for applied complexes with accelerators," 2010 Problems of Atomic Science and Technology (2), pp. 48-51.

[8] A. D. Ovsyannikov, D. A. Ovsyannikov, A. P. Durkin, S.-L. Chang, "Optimization of matching section of an accelerator with a spatially uniform quadrupole focusing," 2009 Technical Physics 54 (11), pp. 1663-1666.

[9] A. D. Ovsyannikov, D. A. Ovsyannikov, M. Yu. Balabanov, S.-L. Chung, "On the beam dynamics optimization problem," 2009 International Journal of Modern Physics A 24 (5), pp. 941-951.

[10] D. A. Ovsyannikov, A. D. Ovsyannikov, M. F. Vorogushin, Yu. A. Svistunov, A. P. Durkin, "Beam dynamics optimization: Models, methods and applications," 2006 Nuclear Instruments and Methods in Physics Research, Section A: Accelerators, Spectrometers, Detectors and Associated Equipment 558 (1), pp. 11-19.

[11] A. D. Ovsyannikov, "Transverse motion parameters optimization in accelerators," Problems of Atomic Science and Technology, Number 4(80), pp. 74-77, (2012).

[12] D. A. Ovsyannikov, A. G. Kharchenko, "On numerical methods of optimization in the problem of charged particle beams control" Vestnik Sankt-Peterburgskogo Universiteta. Ser 1. Matematika Mekhanika Astronomiya, (4), pp. 56-58, (1991).

[13] D. A. Ovsyannikov, "Mathematical Methods of Optimization of Charged Partical Beams Dynamics". Proceedings of European Partical Accelerator Conf., Barselona, Spain, Vol.2, pp.1382-1384, (1996).

[14] D. A. Ovsyannikov, "Modeling and Optimization Problems of Charged Particle Beams Dynamics", Proceedings of the 4th European Control Conference, Brussels, pp. 390-394, (1997).

MATHEMATICAL MODEL OF BEAM DYNAMIC OPTIMIZATION

V.V. Altsybeyev, SPbSU, Saint-Petersburg, Russia

Abstract

We treat here the process of simulation of charged particle dynamics using so called hybrid system. Hybrid system is a system with continuous and discrete parts, described by differential and difference equations, respectively. In this case new mathematical model of beam dynamics optimization is suggested. The main parameters of optimization are: coefficient of particle capture in the acceleration mode, phase and energy spectra of particles at the exit of the accelerator, the transverse beam characteristics, etc. Optimization was carried out for the drift tubes accelerator.

INTRODUCTION

At present time design of accelerators with accelerating field focusing become important [1–6]. Such a focusing in RFQ accelerators being established, but APF focusing still requires development. For various problems of accelerator physics it is necessary to use a different mathematical models [4, 6–10]. Often it is necessary to build several models, taking into account their hierarchy. For example, it is interesting to consider the model "square wave" approximation of the accelerating field in DTL [5] to optimize its parameters. Such a model allows us to construct a well implemented on a computer optimization algorithm. In this paper, an attempt to optimize APF accelerator of deuterons was considered. Similar problems are discussed, especially in [6]. APF structure considered, as well, in the papers [1, 2], where the selection of the parameters of accelerators was made by using stability diagramm.

MATHEMATICAL MODEL OF OPTIMIZATION

"Square wave" approximation of the accelerating field in DTL allows to accept the following mathematical model of optimization, in which the dynamics of the beam is described by the so-called hybrid system of equations having a continuous (1) and discrete part (2) whith initial conditios (3).

$$\dot{x} = f_1(t, x, u), \quad t \in [\mu_{i-1}, \mu_i), \tag{1}$$

$$x(\mu_{i+1}) = f_2(\mu_i, x(\mu_i), v_i), \quad t \in [\mu_i, \mu_{i+1}), \tag{2}$$

$$x(0) = x_0 \in \overline{M}_0, \tag{3}$$

$$i = 2k + 1, \quad k = 0, \ldots, N - 1.$$

Let us consider beam quality functional. We consider the problem of its minimizing for the admissible controls.

$$I = \sum_{i=0}^{2N} \int_{M_{\mu_i,u}} \varphi(x(\mu_i), \mu_i) dx_{\mu_i} + \int_{M_{T,u}} g(x_T) dx_T \to min. \tag{4}$$

The variations of functional (4) can be written as

$$\delta I = -\sum_{k=0}^{N-1} \Bigg(\int_{\mu_{2k}}^{\mu_{2k+1}} \int_{M_{t,u}} \big(\psi(t)^T \Delta_u f_1(t, x, u) + \lambda(t, x) \Delta_u \mathrm{div}_x f_1(t, x, u)\big) dx_t dt + \int_{M_{\mu_{2k+2},u}} \big(\psi(\mu_{2k+2})^T \Delta_u f_2(\mu_{2k+1}, x(\mu_{2k+1}), v_{2k+1}) + \lambda(\mu_{2k+2}, x(\mu_{2k+2})) \Delta_u J(\mu_{2k+1})\big) dx_t \Bigg). \tag{5}$$

Where ψ and λ are satisfying the following equations

$$\psi(\mu_{i+1} + 0) = \psi(\mu_{i+1} - 0) + \frac{\partial \varphi(x(\mu_{i+1}), \mu_{i+1})}{\partial x}, \tag{6}$$

$$\psi(\mu_i) = J(\mu_i) \Big(\frac{\partial}{\partial x} f_2(\mu_i, x(\mu_i), v_i) \Big)^T \psi(\mu_{i+1}) + \lambda(\mu_{i+1}) \left(\frac{\partial J(\mu_i)}{\partial x} \right)^T + \frac{\partial \varphi(x(\mu_i), \mu_i)}{\partial x}, \quad t \in [\mu_{i+1}, \mu_i), \tag{7}$$

$$\frac{d\psi}{dt} = -\Big(\frac{\partial}{\partial x} f_1(t, x, u) + E \mathrm{div}_x f_1(t, x, u) \Big)^T \psi - \lambda \left(\frac{\partial \mathrm{div}_x f_1(t, x, u}{\partial x} \right), \quad t \in [\mu_i, \mu_{i+1}). \tag{8}$$

$$\lambda(\mu_{i+1} + 0) = \lambda(\mu_{i+1} - 0) + \varphi(x(\mu_{i+1})), \tag{9}$$

$$\lambda(\mu_i) = J(\mu_i) \lambda(\mu_{i+1}) + \varphi(x(\mu_i)), \quad t \in [\mu_{i+1}, \mu_i), \tag{10}$$

$$\frac{d\lambda}{dt} = -\lambda \mathrm{div}_x f_1(t, x, u), \quad t \in [\mu_i, \mu_{i+1}). \tag{11}$$

$$\lambda(T, x(T)) = -g(x_T), \tag{12}$$

$$\psi(T, x(T)) = -\left(\frac{\partial g(x_T)}{\partial x} \right)^T. \tag{13}$$

So, analitical representation of variation of functional (4) was obtained.

NUMERICAL OPTIMIZATION

Consider APF deuteron accelerator, consisting of three focusing periods of simple structure with law of changing of synchronous phase, shown in Fig .1. In this case equation (1)–(2) can be written as

$$\frac{d\varphi}{d\xi} = \frac{2\pi\gamma}{\sqrt{\gamma^2-1}},$$
$$\frac{d\gamma}{d\xi} = \alpha(\xi)cos(\varphi), \quad \xi \in [\mu_{i-1}, \mu_i);$$

$$\varphi(\mu_{i+1}) = \varphi(\mu_i) + (\mu_{i+1}-\mu_i)\frac{2\pi\gamma}{\sqrt{\gamma^2-1}},$$
$$\gamma(\mu_{i+1}) = \gamma(\mu_i), \quad \xi \in [\mu_i, \mu_{i+1}).$$

Here $\varphi = \omega t$ is a particle phase, γ is a Lorentz factor, $\alpha(\xi)$ is a function of accelerating field distribution. Based on variation (5) and equations (6)–(13) the optimization algorithm was built. For accelerator optimization the following functionals were used

$$I_1 = \int_{M_{T,u}} \left(a\left(\bar{\varphi} - \varphi_T\right)^2 + b\left(\frac{\gamma_T}{\bar{\gamma}} - 1\right)^2 \right) d\varphi_T d\gamma_T,$$

$$I_2 = cF\left(\sum_{i=0}^{2N} \int_{M_{\mu_i,u}} kcos(\varphi(\mu_i)) d\varphi_{\mu_i}\gamma_{\mu_i}\right),$$

$$F = \begin{cases} (I - I_{cond})^2, & I < I_{cond}, \\ 0, & I > I_{cond}, \end{cases}$$

$$I = I_1 + I_2.$$

Here a, b, c, I_{cond} are positive constants; k is parameter, that describes a difference of an accelerating field at the gap bound. In an optimization problem of the longitudinal motion it is appropriate to consider parameters, which can provide transverse motion. The functional I_2, that limiting focusing factor, is corresponds to that aim. Functional I_1 evaluates the quality of the beam at the output of the accelerator. Initial conditions of beam are shown in Fig. 2, Fig. 3. Results of the numerical simulation and optimization are shown in Fig. 5–Fig. 6.

CONCLUSION

The paper proposes the mathematical model of beam dynamics optimization in DTL. Optimization was carried out for APF structure. Numerical calculations showed that the optimization of the longitudinal motion including a focusing factor provides APF structure, but simultaneously transverse and longitudinal motion must be optimized. The resulting model can be viewed as the first step, which allows to get an initial approximation of linac paremeters. Later, in particular, the model of approximation field by first of the Fourier harmonics was considered. Also, space charge of the beam was taken into account. Also an effective approach for the optimization was the consideration of the longitudinal dynamics in the equivalent traveling wave.

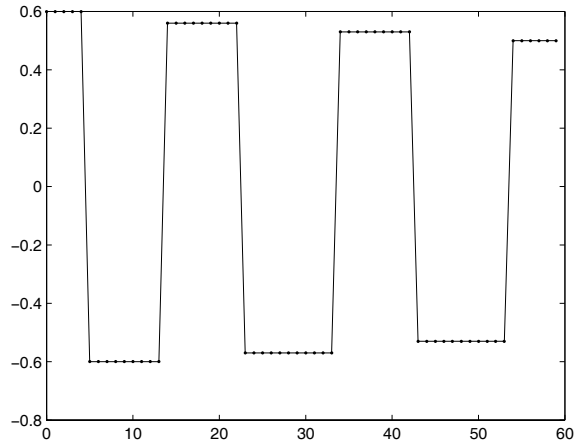

Figure 1: Synchronous phase

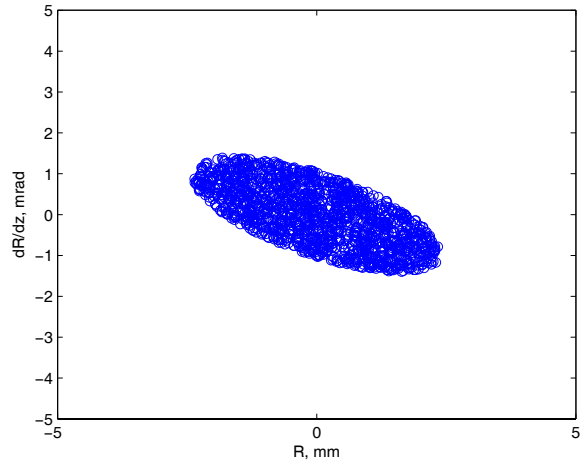

Figure 2: Input transverse emittance

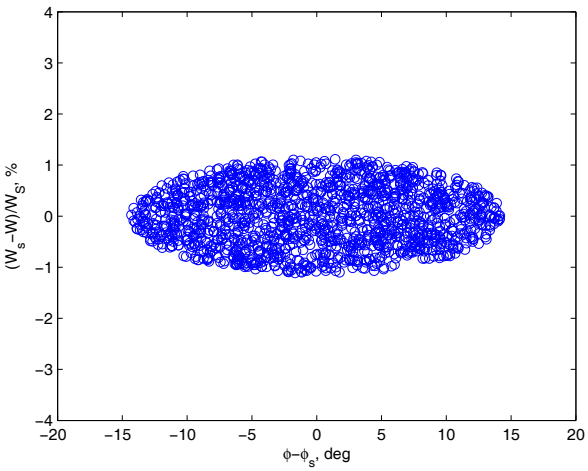

Figure 3: Input longitudinal emittance

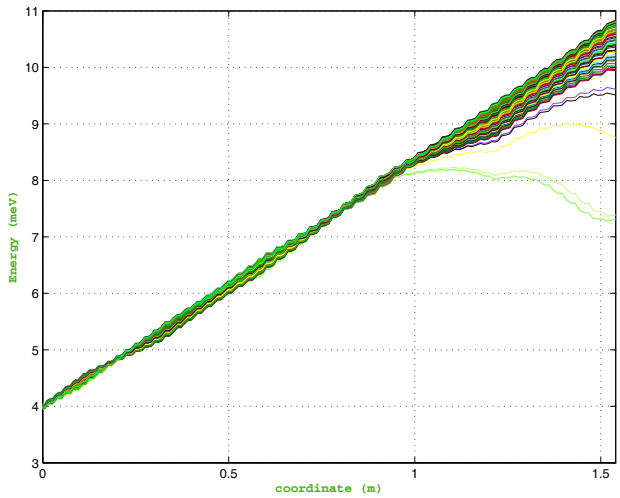

Figure 4: Energy trajectory before optimization

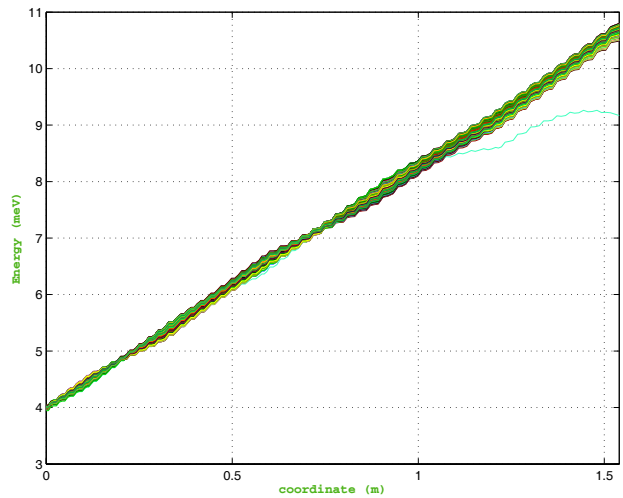

Figure 5: Energy trajectory after optimization

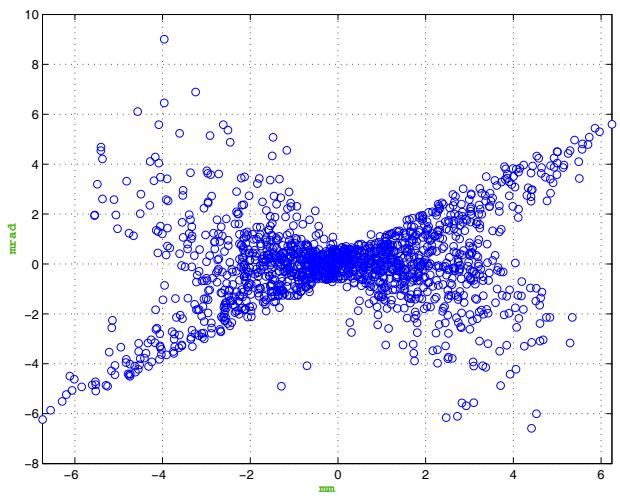

Figure 6: Output transverse emittance

REFERENCES

[1] V.V.Kapin, S.Yamada, Y.Iwata, "Design of APhF-IH Linac for a Compact Medical Accelerator," National Institute of Radiological Sciences, 2003, JAPAN.

[2] Kapin V.V., Nesterovich A.V. "Feasibility of alternative phase focusing for a chain of short independently-phased resonators," Proceedings of RuPAC-2010, Protvino, Russia.

[3] Kushin V.V. "On improving the phase-alternating focusing in linear accelerators," Nuclear Energy, 1970, .29, N2.

[4] D.A. Ovsyannikov, A.D. Ovsyannikov, M.F. Vorogushin, Yu.A. Svistunov, A.P. Durkin, "Beam dynamics optimization: Models, methods and applications," 2006 Nuclear Instruments and Methods in Physics Research, Section A: Accelerators, Spectrometers, Detectors and Associated Equipment 558 (1), pp. 11-19.

[5] I.M.Kapchinsky, *Theory of linear resonance accelerator*, (Moscow, Energoizdat, 1982), pp. 130-165.

[6] D.A.Ovsyannikov, *Modeling and Optimization of Charged Particles Beam Dynamics*, (Lenigrad, 1990, p. 312).

[7] Y.A. Svistunov, A.D.Ovsyannikov "Designing of compact accelerating structures for applied complexes with accelerators," 2010 Problems of Atomic Science and Technology (2), pp. 48-51.

[8] A.D. Ovsyannikov, D.A. Ovsyannikov, S.-L. Chung, "Optimization of a radial matching section," 2009 International Journal of Modern Physics A 24 (5), pp. 952-95.

[9] A.D. Ovsyannikov, D.A. Ovsyannikov, M.Yu. Balabanov, S.-L. Chung, "On the beam dynamics optimization problem," 2009 International Journal of Modern Physics A 24 (5), pp. 941-951.

[10] P. Snopok, C. Johnstone, M. Berz, D.A. Ovsyannikov, A.D. Ovsyannikov, "Muon Collider interaction region simulation and optimization," 2005 International Conference on Physics and Control, PhysCon 2005, Proceedings 2005, art. no. 1513993, pp. 278-281.

DEVELOPMENT OF THE OBJECT-ORIENTED PROGRAM IN C ++ FOR SIMULATION OF BEAM DYNAMICS IN ACCELERATOR INJECTION SYSTEMS

S.A. Kozynchenko *, Saint-Petersburg State University, Saint-Petersburg, Russia

Abstract

In this paper the program for simulation and optimization of beam dynamics in injection systems is considered, which at the same time allows the choice of parameters of the accelerating-focusing system. This permits designing the injection system during optimization process, taking into account the required output characteristics of the beam. The given program is based on Win 32 API dialog boxes and is developed in standard C++, using parallel programming tools based on the MPI-1.

INTRODUCTION

At present both in Russia and abroad, more attention is paid to design and creation of the accelerator complexes which provide generating the high-precision ion beams. When developing an accelerator complex, the injection system design is of importance, because it largely determines the output characteristics of the beam. For the design of such systems it is necessary to carry out numerical simulation and optimization of beam dynamics in the electro-magnetic fields. To reduce the calculation time for beam dynamics, the external fields in each step of optimization are usually approximated by analytical expressions, obtained for the simplified model of the real system under consideration. In order to design the accelerating structures providing high- precision ion beams, it is necessary to optimize the beam dynamics in the fields to be closed to real ones. In this paper, the program for simulation and optimization of beam dynamics in injection systems is considered, which at the same time allows the choice of parameters of the accelerating-focusing system. This permits designing the injection system during optimization process, taking into account the required output characteristics of the beam. Examples of such problems will be considered in the next section. The given program is based on Win 32 API dialog boxes and is developed in standard C++, using parallel programming tools based on the MPI-1.

SOME PROBLEMS OF MODELING AND OPTIMIZATION OF BEAM DYNAMICS IN THE INJECTION SYSTEMS OF ACCELERATORS.

Following D.A. Ovsyannikov [1], the dynamics of the beam in the external field, taking into account the beam space charge, is described by integro-differential equaions:

$$\begin{cases} \frac{dX}{dt} = V, \\ \frac{dV}{dt} = \frac{1}{m_p} f_1\left(t, X, \varphi\left(X, u\right)\right) + \\ \qquad \frac{1}{m_p} \int\limits_{M_{t,u}} f_2\left(t, X, V, \xi\right) \rho\left(t, \xi\right) d\xi = f_3\left(t, X, V, u\right), \\ X\left(t_0\right) = X_0, \quad V\left(t_0\right) = V_0, \quad \left(X_0, V_0\right) \in M_0, \end{cases} \tag{1}$$

$$\frac{\partial \rho\left(t,\eta\right)}{\partial t} + \frac{\partial \rho(t,\eta)}{\partial \eta} f\left(t,\eta,u\right) + \rho\left(t,\eta\right)\, div_{\eta} f\left(t,\eta,u\right) = 0 \tag{2}$$

$$\rho\left(t_0,\eta\right) = \rho_0\left(\eta\right). \tag{3}$$

Here $t \in [t_0, T]$ — the independent variable (time); parameters t_0, T are fixed; m_p, — the mass, $X(t) \in R^3$ — the position, $V(t) \in R^3$ — the velocity of a charged particle, respectively; $u = (u_1, u_2, ..., u_p) \in D$ — vector of control parameters, where $D \subset R^p$ — limited and a closed set; $\eta = (X, V) \in R^6$ — the position of the charged particle in the phase space; $\varphi = \varphi(X, u) \in C^2(G)$ — potential of the external field, where $G \subset R^3$ — limited and open set; function $f_1\left(t, X, \varphi\left(X, u\right)\right)$ describes the force, defined by external field; the choice of the function $f_2\left(t, X, V, \xi\right)$ defines the vay of modeling of the Coulomb interaction of charged particles; vector-function $f\left(t, \eta, u\right) = \left(V\left(t\right), f_3\left(t, \eta, u\right)\right)$; $\rho(t, \eta)$ — density distribution of particles due to the system (1); $\rho_0\left(\eta\right)$ — given charge density in the space M_0 at the moment t_0, where $M_0 \subset R^6$ — bounded closed set of measure zero; $M_{t,u} = \left\{X = X\left(t, X_0, u\right), V = V\left(t, V_0, u\right) : \left(X_0, V_0\right) \in M_0\right\}$ — image of the set M_0, due to system (1) under the vector u a the moment t.

For a given vector u the potential of the external electrostatic field φ, defined and continuous in $\bar{G}$, is a solution of the Dirichlet problem for the Laplace equation:

$$\begin{cases} \Delta\, \varphi\left(x, u\right) = 0, \quad x \in \mathrm{G}, \\ \varphi\left(x, u\right)|_{\Gamma_G(u)} = \varphi_0\left(x\right), \end{cases} \tag{4}$$

where $\Gamma_G\left(u\right)$ — piecewise smooth boundary of G, $\varphi_0\left(x\right)$ – known function.

On the cross-sections of the beam trajectories, the functional characterizing the beam dynamics is introduced. We consider the problem of finding the vector of controls $u^0 \in D$, delivering an extremum to the functional under the restrictions on the beam output energy, the particle losses, the max- imum radius of the beam, the potentials of the electrodes, the value of the functional, and some others.

* Sergey_Kozyntchenko@hotmail.com

Consider the problem of minimizing the growth of the beam emittance. The quality functional that characterizes the growth of beam emittance at the output of the injection system, is given in the form:

$$\begin{cases} I(u) = \dfrac{0.5\sqrt{\tilde{D_x^T}\tilde{D_{x'}^T} - \tilde{K_{xx'}^T}^2} + 0.5\sqrt{\tilde{D_y^T}\tilde{D_{y'}^T} - \tilde{K_{yy'}^T}^2}}{0.5\sqrt{\tilde{D_x^0}\tilde{D_{x'}^0} - \tilde{K_{xx'}^0}^2} + 0.5\sqrt{\tilde{D_y^0}\tilde{D_{y'}^0} - \tilde{K_{yy'}^0}^2}}, \\ x' = v_x/v_z, \qquad y' = v_y/v_z, \end{cases} \tag{5}$$

where

$$\begin{cases} \tilde{D_x} = \frac{1}{mes(M_{T,u})} \int_{M_{T,u}} x^2 \rho(t, \eta_T)\, d\eta_T, \\ \tilde{D_{x'}} = \frac{1}{mes(M_{T,u})} \int_{M_{T,u}} x'^2 \rho(t, \eta_T)\, d\eta_T, \\ \tilde{K_{xx'}} = \frac{1}{mes(M_{T,u})} \int_{M_{T,u}} xx' \rho(t, \eta_T)\, d\eta_T. \end{cases} \tag{6}$$

The coefficients $\tilde{D_y}$, $\tilde{D_{y'}}$, $\tilde{K_{yy'}}$ are calculated using formulas similar to (6). $mes(M_{T,u})$ measure of $M_{T,u}$. Consider the problem of finding of the $u^0 \in D$, which minimizes the function (5) under given constraints.

Consider the problem of matching the beam at the output of the injection system. The quality functional is given as:

$$I(u) = \int_{M_{T,u}} \Phi_1(x_T, x'_T)\, \Phi_2(y_T, y'_T), \tag{7}$$

where Φ_1, Φ_2 — given functions with compact support, defined on sets $G_1 = \{(x_T, x'_T) : S_1(x_T, x'_T) < 1\}$, $G_2 = \{(y_T, y'_T) : S_2(y_T, y'_T) < 1\}$. Where $x'_T = v_{xT}/v_{zT}$, $y'_T = v_{yT}/v_{zT}$; $S_1(x_T, x'_T) = 1$ and $S_2(y_T, y'_T) = 1$ — ellipses describing the accepance of the linear accelerator in planes xx' yy' respectively; x, y, z – cartesian coordinates of the point X.

THE PROGRAM FOR MODELING AND OPTIMIZATION OF BEAM DYNAMICS IN INJECTION SYSTEM OF AN ACCELERATOR

Let us consider the computer program designed for solving the nonlinear problems of simulation and optimization of the beam injection systems for non-relativistic beams in the form (1)–(7). The program is written in the standard C++ at Visual C++ 2010 integrated development environment (IDE), using Win32 API and object-oriented programming, and it is intended for the use on personal computers. In this program, a scheme with two threads is applied, with functions of Win32 API being used for working with these threads. The primary thread is mainly used for the output (incl. graphical) of simulation and optimization results, whereas the secondary one is intended for performing calculations. The thread interaction is accomplished using global variables. Mostly, we consider the injection systems consisting of the electrodes in the form of thick disks of arbitrary cross-section with given potentials. As the components of the vector u, such physical (design) parameters of the accelerating system are chosen, whose changes affect the design and, consequently, the field that determines the beam dynamics. So, the program consists of the following interacting parts:

- The graphical user interface (GUI), developed on the basis of modal dialog windows and intended for displaying and editing the parameters, selecting the type of the problem to be solved, methods of modelling the fields, beam dynamics, and optimization, as well as numerical and graphical output. Displaying the results of modelling of beam dynamics is carried out online at the main application window using the methods of the class template **GClass**. The graph output is performed to several dialog windows.
- The unit for calculating the three-dimensional field of the set of electrodes. The main classes developed for the unit are as follows:
  - **Electrode** — classes intended to describe the set of electrodes;
  - **ElStaticField3D** — class developed without usage of parallel computing and intended for simulation of electrostatic fields by the finite-difference method in domains with complex geometry (solving the boundary value problems of type 4));
  - The base classes for ones considered above.
- The unit for calculating the self field of the beam. The main classes included in this unit are as follows:
  - **CylRingBeamModel** — class in which the analytical algorithms of computing the beam Coulomb field are used. It is used a model of the beam in the form of a cylinder with constant radius, as well as a set of charged coaxial hollow circular cylinders;
  - **EFPoisson3D** — class designed to solving the boundary value problems for the Poisson equation by the finite-difference method in domains with complex geometry;
  - **EFPoisson3Dpbc** — class designed for solving the boundary value problems for the Poisson equation by the finite-difference method in a round metal tube with periodic boundary conditions at the ends;
- The unit of modelling of three-dimensional beam dynamics in injection systems. The main classes developed for this unit are as follows:
  - **ChargeDistr** — class intended for modelling of the initial distributions of the beam;
  - **BeamDynamNoMPI** — class intended for modelling of the beam dynamics in external field with taking into account the own beam charge, not using the parallel computing;

  - **BeamDynamMPI** — class designed for modelling of the beam dynamics, which uses the parallel computing based on MPI-1. The number of parallel processes is 5. The zero process is used for the calculation of the external field, forming the initial data for the beam, computing the beam self field and passing the results to corresponding processes, as well as for receiving the results of modelling of dynamics from other processes;
  - The classes which are basic to the above. To model the external fields, the unit 2 is used. Consideration of the beam self field is accomplished by the method of "large" particles, as well as using the unit 3;

- Optimization unit. To optimize the beam dynamics in injection systems by the Box-Wilson method under the different number N of control parameters, the class template BoxWilsonN has been developed. It uses the linear model for the description of the response surface in the factor space. Under calculating the components of the gradient vector at each step of the Box-Wilson method with a full factorial design, the number of computational experiments is equal to $2N$. For simulation of beam dynamics, the unit 4 is used. If the calculations at the points where the experiments are performed are carried out in parallel then the total number of processes may consist $5 \cdot 2^N + 1$ $5 \cdot 2^N + 6$.

CONCLUSION

The developed program has shown its efficiency for modelling and optimization of beam dynamics in injection systems, as well as under calculations and analysis of the external fields and the self field of the beam.

REFERENCES

[1] D.A. Ovsyannikov *Modelling and optimization of charged particle beam dynamics*, (Leningrad, 1990), 312.

INVESTIGATION OF PROGRAM AND PERTURBED MOTIONS OF PARTICLES IN LINEAR ACCELERATOR

Irina D. Rubtsova#, Elena N. Suddenko, SPbSU, Saint-Petersburg, Russia

Abstract

Beam control model for program and perturbed motions with interaction account is realized. Quality functional gradient is obtained.

BEAM DYNAMICS EQUATIONS

The problem under study is longitudinal beam dynamics control in linear waveguide electron accelerator. Let coordinate axis Oz be aligned the waveguide symmetry axis. Accelerating wave fundamental mode in device axis neighborhood is described by the expression [1, 2]:

$$E_z(z,t) = E_0(z)\sin\left(\omega\int_0^z \frac{d\eta}{v_{ph}(\eta)} - \omega t + \varphi_0\right).$$

Here z is longitudinal coordinate, t is the time, $\omega = \frac{2\pi c}{\lambda}$, c is velocity of light; λ, $E_0(z)$, $v_{ph}(z)$ and φ_0 are correspondingly wavelength, intensity amplitude, phase velocity value and initial phase of accelerating wave fundamental mode.

Longitudinal beam dynamics equations are as follows [2]:

$$\frac{d\xi}{d\tau} = \frac{p}{\sqrt{1+p^2}},$$
$$\frac{dp}{d\tau} = -\alpha(\xi)\sin\varphi - \frac{e\lambda}{m_0c^2}E_z^{(\rho)}(\xi\lambda),. \qquad (1)$$
$$\varphi(\tau) = 2\pi\int_0^{\xi(\tau)}\frac{d\eta}{\beta_{ph}(\eta)} - 2\pi\tau + \varphi_0.$$

Independent variable $\tau = \frac{ct}{\lambda}$ is introduced to be analogue of time to provide convenient Coulomb field account; $\xi = \frac{z}{\lambda}$; $p = \frac{mv_z}{m_0c}$; m_0 and m are correspondingly rest mass and relativistic mass of electron, v_z is particle velocity longitudinal component; $\alpha(\xi) = \frac{e\lambda E_0(\xi\lambda)}{m_0c^2}$; e is absolute value of electron charge; φ is particle phase; $E_z^{(\rho)}(\xi\lambda)$ is longitudinal component of Coulomb field intensity (integral representation of this field is given hereinafter in Eq. 5); $\beta_{ph}(\xi) = \frac{v_{ph}(\lambda\xi)}{c}$.

#rubtsova05@mail.ru

The problem of beam control in such a system was treated by Dmitry Ovsyannikov [2] as trajectory ensemble control problem; $\alpha(\xi)$ and $\beta_{ph}(\xi)$ were assumed to be control functions.

PROGRAM AND PERTURBED MOTIONS CONTROL

To continue the research, let us describe beam evolution in terms of program motion and the ensemble of perturbed motions. This approach was suggested by Alexander Ovsyannikov and successfully applied for beam control in RFQ structures [3, 4, 5, 6, 7]. The same approach was used for longitudinal beam dynamics investigation in traveling-wave linear accelerator [8] without Coulomb field account. The idea is to describe the controlled process as a combination of program motion (i.e. the motion of assigned particle) and perturbed motions ensemble (with respect to program motion). Assigned particle is the object with special dynamics equations; its initial position coincides with bunch centre and its velocity coincides with accelerating wave phase velocity $v_{ph}(z)$. Parametrized function $\varphi_a(\xi,\boldsymbol{\theta})$ (where $\boldsymbol{\theta}$ is control parameters vector) characterize the phase of assigned particle; $\varphi_a(\xi,\boldsymbol{\theta})$ is assumed to be control function instead of $\beta_{ph}(\xi)$, which is expressed in terms of assigned particle impulse. Consequently, initial control may be constructed with due account of requirements on program motion and provide rather high quality of controlled process even at optimization start. In particular, $\varphi_a(\xi,\boldsymbol{\theta})$ mathematical form may be chosen to follow synchronous phase variation tendency observed for "good" beam dynamics. Besides, different mathematical descriptions and simultaneous optimization of program motion and the ensemble of perturbed motions provide additional possibilities of beam dynamics optimization by means of control action upon assigned particle and upon beam particles.

In this paper simultaneous optimization approach is applied to time-dependent beam dynamics model with particle interaction account. This model is derived on the base of Eq. 1.

Let coordinates and characteristics of assigned particle have index "a". Program motion is described by the equations:

$$\frac{d\xi_a}{d\tau} = \frac{p_a}{\sqrt{1+p_a^2}},$$
$$\frac{dp_a}{d\tau} = -\alpha(\xi_a,\boldsymbol{\theta})\sin\varphi_a(\xi_a,\boldsymbol{\theta}). \quad (2)$$

Beam dynamics is described by equations for perturbations of particle motions with respect to program motion:

$$\frac{d\tilde{\xi}}{d\tau} = \frac{\tilde{p}+p_a}{\sqrt{1+(\tilde{p}+p_a)^2}} - \frac{p_a}{\sqrt{1+p_a^2}},$$
$$\frac{d\tilde{p}}{d\tau} = -\alpha\left(\tilde{\xi}+\xi_a,\boldsymbol{\theta}\right)\sin\varphi(\tau) + \alpha(\xi_a,\boldsymbol{\theta})\sin\varphi_a(\xi_a,\boldsymbol{\theta}) -$$
$$-\frac{e\lambda}{m_0c^2}E_z^{(\rho)}\left(\lambda\cdot\left(\tilde{\xi}+\xi_a\right)\right), \quad (3)$$
$$\varphi(\tau) = 2\pi\int_0^\tau H\left(p_a(\nu),\tilde{p}(\nu)\right)d\nu + \varphi_0,$$
$$H(x,y) = \frac{x+y}{\sqrt{1+(x+y)^2}}\cdot\frac{\sqrt{1+x^2}}{x} - 1.$$

Here $\tilde{\xi} = \xi - \xi_a$, $\tilde{p} = p - p_a$. Programmed control is introduced to be vector of parameters: $\mathbf{u}(\tau) = \boldsymbol{\theta}$.

Based on beam dynamics simulation experience the following parameterization of functions $\alpha(\xi,\boldsymbol{\theta})$ and $\varphi_a(\xi,\boldsymbol{\theta})$ is suggested:

$$\alpha(\xi,\boldsymbol{\theta}) = \theta_1 arctg(\theta_2\xi+\theta_3)+\theta_4,$$
$$\varphi_a(\xi,\boldsymbol{\theta}) = \frac{-\pi/2\cdot\left(arctg(\theta_5(\xi-\theta_6))+arctg(\theta_5\theta_6)\right)}{arctg(\theta_5(L/\lambda-\theta_6))+arctg(\theta_5\theta_6)} \quad (4)$$

Here L is accelerator length. We construct $\varphi_a(\xi,\boldsymbol{\theta})$ to follow synchronous phase variation tendency noted for "good" beam dynamics: $\varphi_a(\xi,\boldsymbol{\theta})$ is assumed to have small negative value in bunching part of the device and monotone decrease until $-\pi/2$ in accelerating part. Due to mathematical form of expressions Eq. 4 there exists some compact $U \subset R^6$ of parameters values providing "rather good" beam evolution. Choosing initial control $\boldsymbol{\theta}_0 \in U$ we obtain "rather good" beam dynamics at optimization start and may improve beam quality using search in the compact U.

Control process quality criterion is introduced as linear combination of two integral functionals. The first functional characterizes program motion and estimates the square of difference between the assigned particle exit energy and required exit energy. The second functional characterizes the behavior of perturbed motions ensemble and presents integral measure of beam trajectories perturbation with respect to program trajectory. Mathematical form of these functionals is given by Eq. 7, 8. The problem is formulated to minimize the criterion.

MATHEMATICAL OPTIMIZATION MODEL

The control problem under study belongs to the class introduces by following mathematical model. Controlled process is described by integro-differential equations:

$$\frac{d\mathbf{x}}{dt} = \mathbf{f}(t,\mathbf{x},\mathbf{u}),$$
$$\frac{d\mathbf{y}}{dt} = \mathbf{F}\left(t,\mathbf{x},\mathbf{y},\int_0^t h(\tau,\mathbf{x}(\tau),\mathbf{y}(\tau))d\tau,\mathbf{u}\right) =$$
$$= \mathbf{F}_1\left(t,\mathbf{x},\mathbf{y},\int_0^t h(\tau,\mathbf{x}(\tau),\mathbf{y}(\tau))d\tau,\mathbf{u}\right) + \quad (5)$$
$$+\int_{M_{t,\mathbf{u}}}\mathbf{F}_2(t,\mathbf{x},\mathbf{y},\mathbf{z}_t)\rho(t,\mathbf{z}_t)d\mathbf{z}_t,$$
$$\frac{d\rho}{dt} = -\rho(t,\mathbf{y})div_{\mathbf{y}}\mathbf{F}\left(t,\mathbf{x},\mathbf{y},\int_0^t h(\tau,\mathbf{x}(\tau),\mathbf{y}(\tau))d\tau,\mathbf{u}\right).$$

Initial conditions are as follows:

$$\mathbf{x}(0) = \mathbf{x}_0,\ \mathbf{y}(0) = \mathbf{y}_0,\ \rho(0,\mathbf{y}(0)) = \rho_0(\mathbf{y}_0),\ \mathbf{y}_0 \in M_0.$$

Here $t \in T_0 = [0,T]$ is independent variable, T is fixed value; $\mathbf{x} \in R^n$ and $\mathbf{y} \in R^m$ are phase vectors; $\mathbf{u} = \mathbf{u}(t)$ is programmed control; $M_0 \in R^m$ is compact set of initial $\mathbf{y}$ values; $M_{t,\mathbf{u}} = \{\mathbf{y}_t = \mathbf{y}(t,\mathbf{x}(t),\mathbf{y}_0,\mathbf{u}(t)),\ \mathbf{y}_0 \in M_0,\ \mathbf{x}(0) = \mathbf{x}_0\}$ is t-cutset of trajectory ensemble $M_{\mathbf{u}} = \{\mathbf{y}(t,\mathbf{x}(t),\mathbf{y}_0,\mathbf{u}(t)),\ \mathbf{y}_0 \in M_0, \mathbf{x}(0) = \mathbf{x}_0, t \in T_0\}$; $\rho(\tau,\mathbf{y})$ is ensemble phase density defined upon $M_{\mathbf{u}}$; $\rho_0(\mathbf{y}_0)$ is initial phase density.

Main suppositions are: n-vector function $\mathbf{f}(t,\mathbf{x},\mathbf{u})$ and scalar function $h(t,\mathbf{x},\mathbf{y})$ are continuous and have continuous partial derivatives; m-vector functions $\mathbf{F}_1(t,\mathbf{x},\mathbf{y},v,\mathbf{u})$ and $\mathbf{F}_2(t,\mathbf{x},\mathbf{y},\mathbf{z}_t)$ have, in addition, continuous second-order derivatives; $\rho_0(\mathbf{y}_0)$ is nonnegative continuous function. Control function $\mathbf{u}(t)$ belongs to class D of piecewise-continuous on T_0 r-dimensional vector-functions assuming values in compact $U \subset R^r$.

Control process quality is estimated by values of functional [7]:

$$I(\mathbf{u}) = I_1(\mathbf{u}) + I_2(\mathbf{u}), \tag{6}$$

$$I_1(\mathbf{u}) = \int_0^T \Phi_1\big(t, \mathbf{x}(t), \mathbf{u}(t)\big)dt + g_1\big(\mathbf{x}(T)\big), \tag{7}$$

$$I_2(\mathbf{u}) = \int_0^T \int_{M_{t,\mathbf{u}}} \Phi_2\big(t, \mathbf{x}(t), \mathbf{y}_t, v(t), \mathbf{u}(t)\big)\rho(t, \mathbf{y}_t)d\mathbf{y}_t dt + \\ + \int_{M_{T,\mathbf{u}}} g_2(\mathbf{y}_T)\rho(T, \mathbf{y}_T)d\mathbf{y}_T. \tag{8}$$

We suppose Φ_1, Φ_2, g_1, g_2 to be nonnegative continuously differentiable functions.

In special case under study $\mathbf{x}(t, \mathbf{x}_0, \mathbf{u})$ describes program motion; $\{\mathbf{y}(t, \mathbf{x}(t), \mathbf{y}_0, \mathbf{u}(t)),\ \mathbf{y}_0 \in M_0\}$ present perturbed motions ensemble; $\mathbf{u}(t) = \boldsymbol{\theta}$, $n = m = 2$; $r = 6$; $v(t) = \int_0^t h(\tau, \mathbf{x}(\tau), \mathbf{y}(\tau))d\tau$ presents the phase of particle (see Eq. 3); the integral $\int_{M_{t,\mathbf{u}}} \mathbf{F}_2(t, \mathbf{x}, \mathbf{y}, \mathbf{z}_t)\rho(t, \mathbf{z}_t)d\mathbf{z}_t$ describes particle interaction [2]. Function $\mathbf{F}_2(t, \mathbf{x}, \mathbf{y}, \mathbf{z})$ is determined by interaction account model. In particular, disk beam model is used and $\mathbf{F}_2(t, \mathbf{x}, \mathbf{y}, \mathbf{z})$ is given by special series [9, 2]. Functional $I_1(\mathbf{u})$ estimates program motion quality and functional $I_2(\mathbf{u})$ estimates the quality of perturbed motions ensemble.

QUALITY FUNCTIONAL GRADIENT

Quality functional derivatives with respect to control parameters are obtained as follows:

$$\frac{\partial I}{\partial \theta_k} = \int_0^T \left(\frac{\partial \Phi_1}{\partial \mathbf{u}} - \psi^* \frac{\partial \mathbf{f}}{\partial \mathbf{u}}\right)\frac{\partial \mathbf{u}}{\partial \theta_k}dt + \\ + \int_0^T \int_{M_{t,\mathbf{u}}} \left(\frac{\partial \Phi_2}{\partial \mathbf{u}} - \boldsymbol{\mu}^* \frac{\partial \mathbf{F}_1}{\partial \mathbf{u}}\right)\frac{\partial \mathbf{u}}{\partial \theta_k}\rho(t, \mathbf{y}_t)d\mathbf{y}_t dt, \quad k = \overline{1, r}. \tag{9}$$

Auxiliary vector functions $\boldsymbol{\psi}(t, \mathbf{x})$ and $\boldsymbol{\mu}(t, \mathbf{y})$ are defined on trajectories $\mathbf{x}(t, \mathbf{x}_0, \mathbf{u})$ and $\{\mathbf{y}(t, \mathbf{x}(t), \mathbf{y}_0, \mathbf{u}(t)),\ \mathbf{y}_0 \in M_0\}$ correspondingly and satisfy special systems of integro-differential equations. The symbol * signifies transposition of vector.

NUMERICAL RESULTS

Numerical beam dynamics investigation was realized for the device with following characteristics: initial beam energy is $W_{inject} = 40\ keV$; accelerating wavelength is $\lambda = 0.1\ m$; accelerator length is $L = 7.8\ m$; beam current is $I = 3\ A$.

Optimization fulfilled has provided beam exit characteristics improvement: phase spread has descended by a factor of 1.7, average reduced energy has increased from 8.9 until 10.1. In addition, capture coefficient has grown from 92% until 98%.

REFERENCES

[1] I.M. Kapchinskiy, *Theory of Linear Resonance Accelerators*, (Moscow, Energoizdat, 1982), 239.

[2] D.A. Ovsyannikov, N.V. Egorov, *Mathematical Modelling of Electron and Ion Beams Forming Systems*, (SPb.: St. Peterb. Univ. Press, 1998), 276.

[3] B.I. Bondarev, A.P. Durkin, A.D. Ovsyannikov, "New Mathematical Optimization Models for RFQ Structures," IEEE Particle Accelerator Conference, New York, 1999, Proceedings, 4, pp. 2808-2810 (1999).

[4] D.A. Ovsyannikov, A.D. Ovsyannikov, I.V. Antropov, V.A. .Kozynchenko, "BDO-RFQ Code and Optimization Models," 2005 International Conference on Physics and Control (PhysCon 2005), Proceedings, Art. No 1513994, pp. 282-288 (2005).

[5] D.A. Ovsyannikov, A.D. Ovsyannikov, M.F. Vorogushin, Yu.A. Svistunov, A.P. Durkin, "Beam Dynamics Optimization: Models, Methods and Applications," Nuclear Instruments and Methods in Physics Research, Section A: Accelerators, Spectrometers, Detectors and Associated Equipment, 558 (1), 2006, pp. 11-19.

[6] A.D. Ovsyannikov, D.A. Ovsyannikov, M.Yu. Balabanov, S.-L. Chung, "On the Beam Dynamics Optimization Problem" International Journal of Modern Physics A 24 (5), 2009, pp. 941-951.

[7] A.D. Ovsyannikov, "Charged Particle Beam Control with Interaction Account", SPb.: St. Peterb. Univ. Bulletin, Ser. 10: Applied Mathematics, Computer Science, Control Processes, 2009, No 2, pp. 72-81.

[8] L.V. Vladimirova, A.D. Ovsyannikov, I.D. Rubtsova, "On Electron Beam Control in Travelling-Wave Linear Accelerator", The Problems of Mechanics and Control Processes, Issue 22: Dynamics, Optimization, Control (Ed. By D.A. Ovsyannikov), SPb.: St. Peterb. Univ. Press, 2004, P. 82-91.

[9] V.V. Zhuk, S.V. Minaev, D.A. Ovsyannikov, I.D. Rubtsova, M.A. Skopina, "On Coulomb Field Modelling for Axial-Symmetric Charged Particle Beam", Leningrad, Leningrad Univ. Press, 1987, No 638-B87, 23.

COMPARISON OF MATRIX FORMALISM AND STEP-BY-STEP INTEGRATION FOR THE LONG-TERM DYNAMICS SIMULATION IN ELECTROSTATIC FIELDS*

A. Ivanov†, Saint-Petersburg State University, Russia

Abstract

An approach based on matrix formalism for solving differential equations is described. Effective in sense of performance matrix formalism can be tested with less efficient, but accurate traditional algorithm of numerical simulation based on the Runge-Kutta scheme. In both cases the symplectic version of the algorithms are used. The results coincide to analytical calculations, but some disagreements have been identified. The approach implementation is demonstrated in the problem of long-term spin dynamics in electrostatic fields.

INTRODUCTION

Particles dynamics in electromagnetic fields is described by Newton-Lorentz equation. This system of ordinary differential equations can be solve by appropriate numerical methods. In this research two approaches are developed. Firstly, for step-by-step integration a symplectic Runge-Kutta scheme is used. As second approach a mapping algorithm based on matrix formalism [1] is implemented.

In the EDM search COSY Infinity [2] is also used. COSY Infinity is known as a very powerful instrument for particle tracking in electromagnetic fields. The key idea of this research is to develop another high-performnce approach for simulation of spin-orbital dynamics. Both Matrix Formalism and COSY Infinity allow to simulate spin-orbital motion of millions of particles. So these methods can be verified by each other. At present, in the EDM search the MPI (Message Passing Interface) version of the COSY Infinity program is installed on a supercomputer with 310^5 processors. For matrix formalism code we can use OpenMP or OpenCL for running tasks on clasters in St.Petersburg State University (e.g. GPU accelerators).

Due to the fact that one of the tasks in JEDI is examination of spin dynamics in electrostatic fields [3], in this paper magnetic fields are not considered. But all described techniques can be used in common case of electromagnetic fields without modifications.

In the article particle dynamics is considered in 9-dimensional space. A state of dynamic system is described as $(x,\ x',\ y,\ y',\ S_x,\ S_y,\ S_s,\ dv,\ t)$ vector, where x, x' and y, y' are transverse and vertical displacement and velocity respectively; $S_x,\ S_y,\ S_s$ are components of spin vector in curvilinear coordinate system (see Fig. 1); $dv = \Delta v/v_0$ is deviation of the initial particle velocity; t is time variable. Note, that a state vector depends on arc length s, which is chosen as an independent variable.

* Work performed under JEDI collaboration (Juelich Electric Dipole Moment Invenstigations)

† 05x.andrey@gmail.com

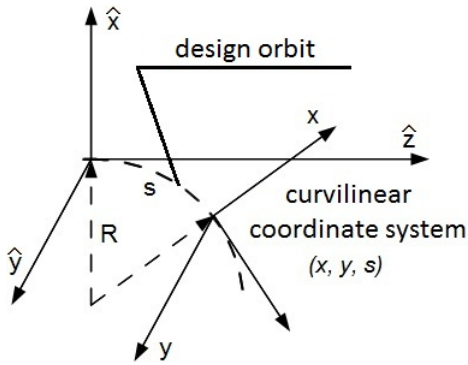

Figure 1: Curvilinear coordinate system.

The mathematical models that used for description of partical motion and spin dynamics are presented in [4]. In this article only numerical approaches are considered.

STEP-BY-STEP INTEGRATION

The Newton-Loretz (particle motion) and BMT (spin dynamics) equations can be written as following system

$$\begin{aligned} \frac{d}{ds}X &= F(s, X), \\ \frac{d}{ds}v_0 &= 0, \end{aligned} \tag{1}$$

where $X = (x, x', y, y', S_x, S_y, S_s, dv, t)$.

This allows us to use classical step-by-step integration methods to solve this system. Article [5] provide both symplectic Runge-Kutta integration schemes, and the algorithm for it derivation up to the 12 order. For the current research a symplectic 2-stage Runge-Kutta scheme of 4 order was implemented.

Table 1: 2-stage 4-order implicit Runge-Kutta scheme

$b_1 + \tilde{c_1}$	$b_1/2$	$b_1/2 + \tilde{c_1}$
$b_1 - \tilde{c_1}$	$b_1/2 - \tilde{c_1}$	$b_1/2$

$$b_1 = 1/2,\ 2b_1\tilde{c_1}^2 = 1/12$$

According to this scheme (Table 1), the solution of the equations (1) can be presented in iterative form

$$\begin{aligned} \mathbf{X}_{n+1} &= \mathbf{X}_n + h\textstyle\sum_{j=1}^{2} b_j \mathbf{F}(s + hc_j, \mathbf{X}^{(i)}), \\ \mathbf{X}^{(i)} &= \mathbf{X}_n + h\textstyle\sum_{j=1}^{2} a_{ij} \mathbf{F}(s + hc_j, \mathbf{X}^{(i)}). \end{aligned}$$

This integration method provide a symplectic solution by choosing of the corredponded coefficients a_{ij}, b_j, c_j.

MATRIX FORMALISM

As mapping approach matrix formalism is used. It allows to present the solution as set of numerical matrices and operations of multiplication and addition only.

Matrix form of ODE

Under the assumptions of $F(0, X_0) = 0$ the system (1) can be presented in the following form [6]

$$\frac{d}{dt}X = \sum_{k=0}^{\infty} P^{1k}(t)X^{[k]}, \quad (2)$$

where $X^{[k]}$ is kronecker power of vector X, matrices P^{1k} can be calculate as

$$P^{1k}(t) = \frac{1}{(k)!}\frac{\partial^k F(t, X_0)}{\partial (X^{[k]})^T}, \quad k = 1, 2, \ldots$$

Solution of system (2) can be written in form

$$X = \sum_{k=0}^{\infty} R^{1k}(t)X_0^{[k]}. \quad (3)$$

Elements of matrices R^{1k} are depended on t and can be calculated in symbolic mode [6]. But such algorithms are quite complex. In this paper a numerical implementaton of it is used. In this case matrices R^{1k} are evaluated in the specific time and presented as numerical matrices.

Symplectication

The relation (3) can be presented as map transformation

$$X = R \circ X_0. \quad (4)$$

This map R is symplectic if

$$M^* J M = J, \forall X_0, \quad (5)$$

where $M = \partial X / \partial X_0$ and M^* is the transponse of M, E is identity matrix,

$$J = \begin{pmatrix} 0 & E \\ -E & 0 \end{pmatrix}. \quad (6)$$

Relation (5) in case of numerical matrices R^{1k} leads to a system of equations

$$a_0 + A_1 \mathbf{X_0}^{[1]} + \cdot + A_k \mathbf{X_0}^{[k]} = 0,$$

where A_i is a numerical vector. Note that this equation must be satisfied for any X_0. It means that the coefficients of each polynom are equal to zero and in this way appropriate corrections of the elements of the matrices R^{1k} can be found.

Map concatenation

Imaging we have two numerical serial maps that corresponds to the different systmes of ordinary differential equations

$$X_1 = \sum_{k=0}^{k_1} R_1^{1k}(t)X_0^{[k]},$$

$$X_2 = \sum_{k=0}^{k_2} R_2^{1k}(t)X_1^{[k]}.$$

Substituting X_1 to the equation for X_2 we obtain

$$X_2 = \sum_{k=0}^{k_1 \cdot k_2} \tilde{R}_2^{1k}(t)X_0^{[k]}.$$

As you can see the resulting map has order $k_1 \cdot k_2$. But we can use terms of order not higher than $max(k_1, k_2)$

SIMULATION OF ELECTROSTATIC STORAGE RING

Electrostatic storage ring consist of elements with different electric field distribution. In this research quadrupole lenses, cylindrical deflectors and drifts are used. The orbital motion and spin dynamics of the particle are described in [4]. Using these equations it is possible both serial tracking in each elements by step-by-step integration method and to build matrix form for each lattice element and concatenate it. In this research the 3 order of nonlinearity for resulting map is used. Moreover additionally correction of elements of matrices R for symplectic condition satisfying is completed. This symplectication procedure is performed once for map.

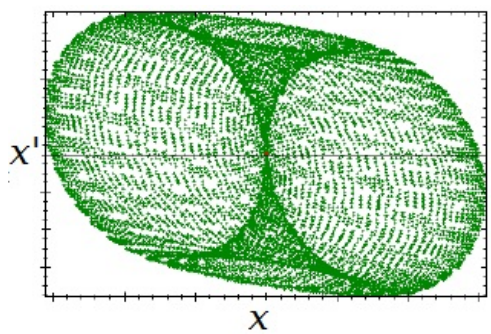

Figure 2: Step-by-step integration.

COMPARISON AND RESULTS

Comparing the results of calculations through single element good coincidence in computational model between matrix formalism approach and step-by-step integration was found out. However different approaches, methods of symplectication and so on introduces the calculation errors for the whole ring. In the article it proposed to use the comparison based on behavior of particles in predefined test cases.

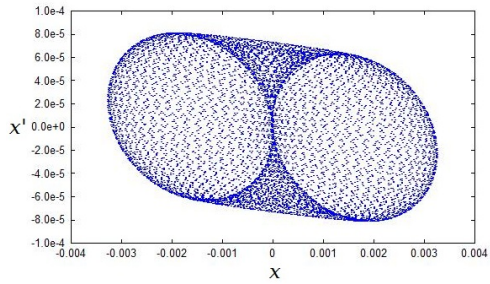

Figure 3: Matrix formalism

In Fig. 2 and 3 transverse plane of a particle (lattice with RF cavity) is presented. In these figures a particle motion with kinetic energy deviation in 310^{-4} and zero transverse displacement is shown. The similar correspondens in orbital motion of particles in longitudinal planes are also obtained.

For a numerical comparison spin coherence time (SCT) is used. SCT is the time of incogerent spin rotation on 2π rad, that is equal to the time during which the RMS spread of the spin orientation of all particles in the bunch reaches one radian.

Table 2: SCT, sec

Case	MF	Tracking	COSY Infinity
RF = OFF			
$\Delta x = 3mm$, $\Delta k/k = 0$	1980	1418	3292
$\Delta x = 0mm$, $\Delta k/k = 10^{-4}$	0.301	0.243	323
RF = ON			
$\Delta x = 0mm$, $\Delta k/k = 10^{-4}$	5813	5260	7316
$\Delta x = 0mm$, $\Delta k/k = 310^{-4}$	653	639	774

In Table 2 SCT in sec for different numerical approaches is shown. MF means mapping approach based on Matrix Formalism, tracking column corresponds to the step-by-step integration and COSY Infinity is a program for beam dynamics simulation based on map building by differential algebra concept. The results of simulation showed good agreement beetwen matrix formalism approach and step-by-step integration. SCT that was evaluated in COSY Infinity program differs from these results. It can be caused by different mathematical models, reference orbit designing and etc. Note, that for tracking approach and matrix formalism the same mathematical description of particle motion and spin dynamics was used.

CONCLUSION

The tracking approach is devoted to the high precesion step-by-step integration. On the other hand there are exist mapping algorithms for beam dynamic simulation. Such methods allows to build map corresponded to the dynamic system. Matrix formalism is a high performance approach for ordinary differential equations solving. Comparison of these two numerical methods shows good correspondes between them. So the matrix formalism can be succesfully used for long-term beam dynamics simulation.

We also plan to modify the given approaches for the direct calculation of the effect of EDM, fringe fields, etc., without significantly reducing of the calculation performance.

ACKNOWLEDGMENT

The author would like to thank Yu. Senichev for problem formulation, D. Zyuzin for comparative calculations on COSY Infinity and special thanks for my scientific supervisor S. Andrianov, in particular, for explanation of the matrix formalism concept.

REFERENCES

[1] M. Kosovtsov, S. Andrianov, A. Ivanov, "A Matrix Presentation for a Beam Propagator including Particles Spin," IPAC2011, San Sebastian, Spain, WEPC116, P. 2283-2285. 2011

[2] M. Berz, "Computational Aspects of Design and Simulation: COSY Infinity," NIM A298, p. 473 (1990).

[3] Yu. Senichev, M. Berz, R. Maier, D. Zyuzin, "Alternating spin aberration electrostatic lattice for EDM ring," IPAC2012, New Orleans, USA, TUPPC070, P. 1332-1334. 2012.

[4] A. Ivanov, "Particle tracking in electrostatic fields with energy conservation," ICAP2012, Rostock, Germany, WEP06 (2012).

[5] W. Oevel, M. Sofroniou, "Symplectic Runge-Kutta schemes II: classification of symmetric methods," `http://citeseerx.ist.psu.edu/viewdoc/summary?doi=10.1.1.46.5060`

[6] S. Andrianov, "Particle beams control systems dynamic modelling" (in Russian), SPBSU, St.Petersburg, Russia, 2004.

SOME PROBLEMS OF BEAM SLOW EXTRACTION*

S. Andrianov†, SPbSU, SPb, Russia

Abstract

In this paper we discuss some problems of modeling of beam slow extraction systems. It is known that similar type of beam extraction is used for different kind of circular accelerators. Among the most important requirements for such systems is necessary to mention the time uniformity of the extracted beam. There exist the following two key causes. The first of them is induced by time discontinuity of the corresponding steering electrical currents, and the second cause is induced by an beam inertia which usually connected with beam feedback mechanism, which is usually used for temporal smoothing of the corresponding magnetic (and electrical) fields. In the base of our approach we put the matrix formalism for Lie algebraic tools, which allows us to analyze different kind of the time discontinuity cause.

INTRODUCTION

The objectives of modeling long-term (multi-turn) evolution of particles in circular accelerators various purposes to make demands not only the adequacy of mathematical tools and related software, but taking into account the possibility of control actions necessary for the implementation of corresponding scenarios. For example, in the problems of beam particles extraction from the accelerator it is necessary not only to ensure particles extraction satisfying to some certain criteria are met but also to provide quality control for extraction system. Consideration of real (not ideal) conditions should provide an existence of instability of control systems on one side and not the "ideal" in the extraction system itself. As to the quality of the beam in modern accelerators makes more and more demanding, it is very important to develop adequate mathematical models, effective software products. Besides it is very important also to develop an uniform data-processing system, which provides support for a given extraction mode. Obviously, a required step for the creation of such a complex must be provided a predictive modeling of possible deviations as control beam and the beam characteristics from the program scenario. Under the program characteristics we mean a set of control parameters (characterized, first of all, the beam transport system itself and provides stability of the beam during an extraction process) and the extraction system, which provide the required extraction characteristics.

It is well known that the energy and intensity rise of modern accelerators also requires increasing of the slow extraction duration. Just this increasing demands much of hard requirements on the uniformity of the temporal structure of the extracted beam. These demands are caused by, first of all, a beam inertia (see further), and the feedback systems limitations. That is why the methods are needed that allow to realize effective numerical experiments to determine the degree of influence of various factors on the temporal structure of the extracted beam, and propose suppression mechanisms for unwanted effects using global optimization methods and symbolic computation that allow for parametric optimization of beam systems.

A THEORETICAL MODEL

To track the dynamics commonly used the well-known Poincaré sections method. In the case of periodic motion the one turn map generates a discrete map – a Poincaré map. This generated map can be written in the form of an operator equation for k-th turn – $\mathcal{M}_k$:

$$\mathfrak{X}_{k+1} = \mathcal{M}_k \circ \mathfrak{X}_k, \qquad (1)$$

where $\mathfrak{X}_k$ is a phase set occupied by beam particles on the k-th turn. In the case of $\mathcal{M}_k = \mathcal{M}_{k+1}, \forall\, k \geq 1$ we will speak about a periodical map. We should note that the support of periodic motion is a standard problem for most circular accelerators. In the case of the slow or fast beam extraction this periodic evolution is disturbed by introducing an additional magnetic (or electric) field, which is a time-varying field and provide the required extraction process. In this paper, the operator equations (1) is replaced by the matrix equations according to the matrix formalism [1]

$$\mathbb{X}_{k+1} = \sum_{i=1}^{\infty} \mathbb{M}_k^{1i} \mathbb{X}_k^j,$$

where $\mathbb{M}_k^{1i}$ are matrices corresponding to aberrations of i-th order, and $\mathbb{X}_k^j$ is a matrix constructed from all Kronecker degrees of all phase vectors $\mathbf{X}_k$ of j-th order ($k = \overline{1, N}$, where N is particles number). It should be noted that in the case of an infinite series equation preserves the very important properties of symplectic and energy conservation law (for stationary fields).

However, these are two very important properties violated in termination of the series, which leads to disruption qualitative and quantitative behavior of the beam. Therefore, in this paper we use the process of symplectification matrices [1] until the desired order of nonlinearity and the law energy conservation [3]. It should be noted that the property of symplecticity is universal, which is satisfied for all Hamiltonian systems, while the law energy conservation is connected with the Hamiltonian function, which is

*Work supported by Federal Targeted Program "Scientific and Scientific-Pedagogical Personnel of the Innovative Russia in 2009-2013" (Governmental Contract no. p 793)

† sandrianov@yandex.ru

a complete energy of the particle. In other words, the corresponding conditions depend on the phase coordinates of the particles and the type of the Hamilton function. Following to methods used in classical mechanics (see, eg, [2]), in beam physics we need every time to adjust to phase coordinates of the particle. That is why this approach can be applied only search of the reference trajectory. In this paper, we investigate the influence of the nonconservation of energy on the characteristics of the extracted beam in the case of well-known problem of slow extraction. It should be noted that the transfer of the described technology to the modern system does not cause fundamental difficulties because physics of the extraction process is preserved.

COMPUTATIONAL EXPERIMENTS

For computational experiments we use both analytical and numerical presentation of the matrices $\mathbb{M}^{11}$ and $\mathbb{M}^{12}$ (we confine ourselves to by second order of nonlinearities). The symplecticity and energy conservation properties is embedded the corresponding algorithm for correction of elements for $\mathbb{M}^{12}$ (see, i.e. [1]). The matrices $\mathbb{M}^{11}$ and $\mathbb{M}^{12}$ are considered as sums of two additional matrices $\mathbb{M}_1^{1k}$ and $\mathbb{M}_2^{1k}$ ($k = 1, 2$). The matrices $\mathbb{M}_1^{11}$, $\mathbb{M}_2^{11}$ fit to linear effects of regular evolution and the shift to the resonance frequency correspondingly. The matrices $\mathbb{M}_1^{12}$ and $\mathbb{M}_2^{12}$ correspond to nonlinearities of the basic field and to nonlinear effects generated by sextupoles properly (see, i. e. [4]).

The computational experiments are provided in several steps. The first step corresponds to resonance progress. This corresponds to phase ellipse transformation to some more complex figures (see on the fig. 1 a)–d)).

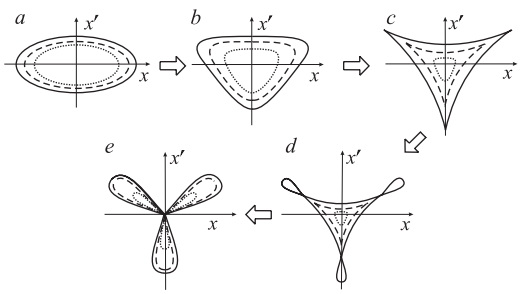

Figure 1: The sequences of phase ellipse in the process of slow phase portrait deformations in the process of an approach the resonance.

Some series of computational experiments were realized for different velocities of resonance progress. The corresponding results demonstrate some very interesting results. For some fixed location Belonging to different layers of the initial phase ellipse extracted particles reach the septum-magnet at the same time (see fig. 2) – one can see the effect of layers mixing. The corresponding analysis of this effect demonstrates also that there is a central part of the initial phase beam portrait, the particles of which are not extracted (see fig. 3). We also investigated the time variations of extracted beams in the presence of additional oscillations in additional terms in the linear and quadratic terms of the equations of motion. The corresponding computational experiments were realized for different frequency and amplitude characteristics. As a correction action we considered some feedback pulses supplied with reverse polarity with respect to the sign of the derivative of rise/fall of the amplitude of oscillations of the beam generated by periodic interference in the power system. In this study we also obtained some interesting results, demonstrating beam inertia depending on the amplitude and action time of the feedback impulse (see, e. g, Fig. 4,5).

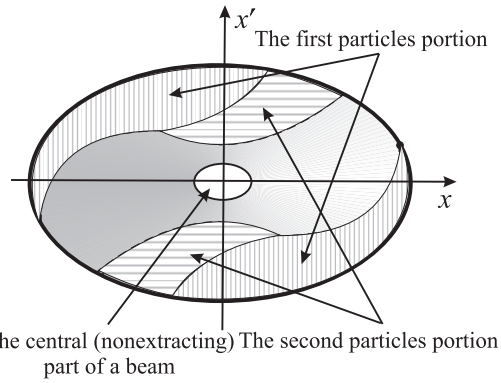

Figure 2: Initial phase coordinates of particles in $\{x, p_x\}$ extracted from the accelerator.

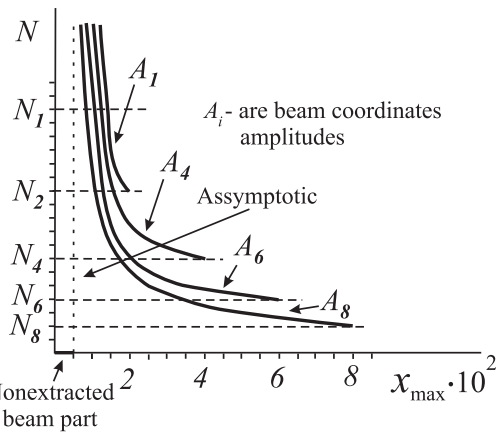

Figure 3: The dynamics of the particles extraction for the case of a fixed magnetic field index at the resonance value.

The amplitude of the peak intensity of the extracted beam from the impulse amplitude are clearly defined nonlinear character (see, Fig. 6 and 7).

CONCLUSION

As a result of numerical experiments we obtained some interesting results on assessing the impact of various factors on some the extracted beam characteristics. These results allow us to do some conclusions concerning to some procedures correction of undesirable effects. On the basis of these data we deduced some conclusions for the possible

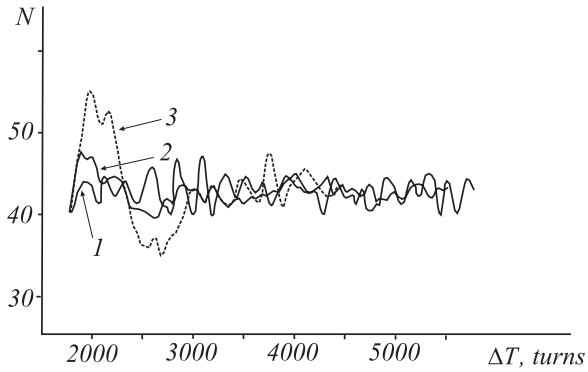

Figure 4: Inertial properties of the beam for different amplitudes of the feedback impulse with the amplitude $k_s = 10^{-5}$: 1 – $\Delta T_1 = 0$, 2 – $\Delta T_2 = 7 \cdot 10^{-5}$, 3 – $\Delta T_3 = 2 \cdot 10^{-4}$.

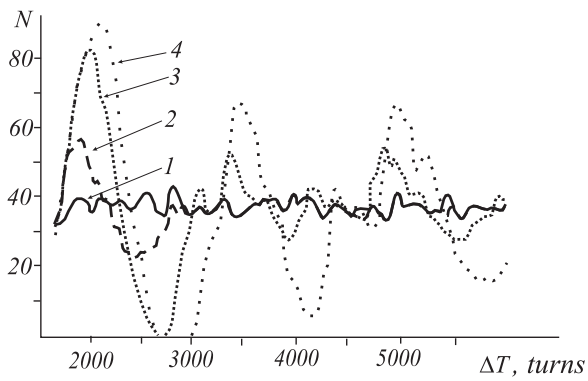

Figure 5: Inertial properties of the beam for different amplitudes of the feedback impulse with the amplitude $k_s = 3 \cdot 10^{-5}$: 1 – $\Delta T_1 = 0$, 2 – $\Delta T_2 = 7 \cdot 10^{-5}$, 3 – $\Delta T_2 = 2 \cdot 10^{-4}$, 4 – $\Delta T_3 = 3.5 \cdot 10^{-4}$.

correction procedures for unwanted effects. The effectiveness of the computational process is ensured by used matrix formalism. Indeed this mathematical methods allows us to use of parallel and distributed computational resources in the frame of proposed concept of "Virtual Accelerator" [5]. All necessary computational processes are realized using some parallel and distributed technologies on the base of the cluster of virtual machines in Saint Petersburg State University.

In the conclusion the author thanks his students and graduate students who assisted in carrying out computational experiments.

REFERENCES

[1] Andrianov S.N. Dynamical Modeling of Beam Control Systems. SPb. SPbSU. 2004 (in Russia).

[2] Zhong G., Marsden J.E., Lie-Poisson Hamilton-Jacobi theory and Lie-Poisson. Physics Letters. V. 133. No. 3. 1988. P. 134–139.

[3] Ivanov A., Andrianov S. Matrix Formalism for Long-Term Evolution of Charged Particles and Spin Dynamics in Electrostatic Fields. Will be appear in Proc. of Intern. Computational Accelerator Conf. 19–25 Aug. 2012. Rostock. Germany.

[4] Chernikov V.I., Issinsky I.B., Kozlov O.S., Mikhailov V.A., Novikov S.A. Status of the Nuclotron Slow Extraction System. Dubna, JINR, 1995.

[5] Andrianov S.N., Ivanov A.N., Podzyvalov E.A. A LEGO Paradigm for Virtual Accelerator Concept. Proc. of ICALEPCS2011, Grenoble, France, 2011. P. 728-730.

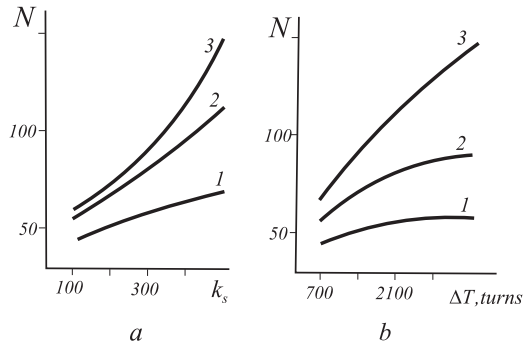

Figure 6: The dependence of amplitude of the extracted beam intensity peaks of the amplitude of the impulse – a) and the length of the impulse – b).

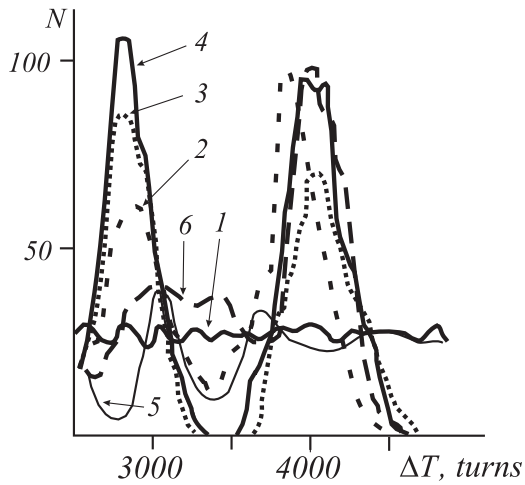

Figure 7: Influence of feedback on the impulse intensity of the extracted beam.

DEGENERATE SOLUTIONS OF THE VLASOV EQUATION

O.I. Drivotin, St.-Petersburg State University, St.Petersburg, Russia

Abstract

The present report deals with degenerate solutions of the Vlasov equation. By degenerate solution we mean a distribution which has a support of dimension smaller than dimension of the phase space. Well known example is the Kapchinsky-Vladimirsky (KV) distribution, when particles are distributed on the 3-dimensional surface in the 4-dimensional phase space.

We use covariant formulation of the Vlasov equation developed previously [1]. In traditional approach, the Vlasov equation is considered as integro-differential equation with partial derivatives on phase coordinates. For the covariant formulation of the Vlasov equation, we use such tensor object as the Lie derivative. According to the covariant approach, a degenerate solution is described by differential form which degree is equal to the dimension of its support.

Main attention is paid to the KV distribution, which is described by the differential form of the third degree. It is demonstrated that the KV distribution satisfies to the Vlasov equation in covariant formulation.

This work has theoretical as well as practical significance. Presented results can be applied for description and simulation of high-intensity beam.

PHASE SPACE AND PARTICLE DISTRIBUTION DENSITY

Consider a domain D in 4-dimensional space-time and a system of smooth spacelike 3-dimensional surfaces filling the domain D. Introduce a continuous parameterization of that surfaces and system of continuously differentiable one-to-one mappings of those surfaces to some selected surface. Let as call the selected surface a configuration space associated with this foliation of the space-time.

If we specify some reference frame, then we can take the layers of simultaneous events for this reference frame as that surfaces, and the time t a parameter. In this case, the configuration space is the configuration space associated with the reference frame.

When time passes, particles move from one layer to another, but we can examine dynamics of particle ensemble in 3-dimensional configuration space. Let us consider tangent bundle of the configuration space as the phase space. Denote by q a position in the phase space.

If there exists some kind of symmetry, we can pass to a phase space of dimension less than 6. Denote the dimension of the phase space by K.

We shall consider various types of distributions. In the simplest case, consider continuous charged media occupying a domain G_0 in the phase space instead of set of discrete particles. Take a family of subdomains $\{G\}$, $G \subset G_0$, with smooth boundaries for which their characteristic functions are defined:

$$\chi_G(q) = \begin{cases} 1, & q \in G, \\ 0, & q \notin G. \end{cases}$$

Let us call differential form of $K-$th degree

$$n = n_{1\ldots K}(q) dq^1 \wedge \ldots \wedge dq^K \tag{1}$$

the particle distribution density in the phase space (or phase density), if for each subdomain G

$$\int\limits_{G_0} \chi_G(q) n(q) = N_G. \tag{2}$$

Here N_G is the number of particles in G, which in this model may be not integer.

Consider the space of functions $f(q)$ for which $\int_{G_0} f(q)\omega(q)$ exists for any form of $K-$th degree $\omega(q)$ from given class. Let us call such functions integrable and denote by $\mathcal{F}$ their space. For some form $\omega(q)$, define a linear functional on $\mathcal{F}$ by the rule

$$< \omega, f >= \int\limits_{G_0} f(q)\omega(q), \quad f \in \mathcal{F}. \tag{3}$$

Then definition (2) can be written as

$$< n, \chi_G >= N_G. \tag{4}$$

Let us consider now the discrete model of point-like particles. In the frames of this model each particle is represented by a point in the phase space. Let us introduce the linear functional $\delta(q)$ on $\mathcal{F}$:

$$< \delta(q), f >= f(q), \quad f \in \mathcal{F}. \tag{5}$$

The measure $\mu_D =< \delta(q), \chi_D >$ is usually called the Dirac measure. Therefore, let us call the functional (5) the density of the Dirac measure. Let us call a linear combination of functionals (5)

$$< \sum_i \alpha_i \delta(q_{(i)}), f >= \sum_i \alpha_i f(q_{(i)})$$

such that for each subdomain G the equality (4) holds the phase density. It is easy to see that in this case $\alpha_i = 1$, and $q_{(i)}$ are particle positions in the phase space, $i = \overline{1, N}$ where N is the total number of particles:

$$n(q) = \sum_{i=1}^{N} \delta(q_{(i)}). \tag{6}$$

In this case, the density (6) is described by a scalar function, which is a differential form of 0 degree.

Consider also the model that can be regarded as intermediate case between the model on continuous media and the model of point-like particles. Assume that particles are continuously distributed on some oriented $p-$dimensional surface S in the domain G_0. We shall describe distribution density in this case by a differential form of $p-$th degree defined on the surface. This form depends on orientation of the surface, which is given by a set of $K-p$ vectors.

A form of $p-$th degree $\sigma(q)$ defined on a p-dimensional oriented surface S specifies a functional on $\mathcal{F}$:

$$< \sigma(q), f >= \int\limits_S f(q)\sigma(q).$$

In this case, call such form

$$n(q) = \sigma(q) \tag{7}$$

that the condition (4) holds the phase density.

COVARIANT FORMULATION OF THE VLASOV EQUATION

As particles moves, their density depends on time. In particular, points and surfaces for the cases (6) and (7) also moves.

According to Vlasov, assume that particle dynamics is determined by an external electromagnetic field and by the self electromagnetic field, which is created by the media being used as the model of a particle ensemble. For continuous models (1), (7), we assume that particle density has sufficiently small components to neglect the collision integral.

The particle dynamics equations define vector field w in the domain D_0 of the phase space. If right hand sides of the dynamics equations are continuously differentiable, then there exist integral lines, unique for each point and each instance of time. Time can be taken as a parameter for integral lines. In the simple case, when the phase space is associated with an inertial frame, the vector field w is defined by particle dynamics equations

$$\frac{dx}{dt} = v, \quad \sum_{i=1}^{3} g_{ik}(\frac{d}{dt}\gamma v)^i = \frac{e}{m}(E_k + \sum_{i=1}^{3} B_{ki}v^i), \tag{8}$$

$k = 1, 2, 3$. Here e and m are charge and mass of a particle, γ is reduced energy (in nonrelativistic case $\gamma = 1$), g_{ik} are components of the metric tensor.

The covariant form of the Vlasov equation is [1]

$$n(t + \delta t, F_{w,\,\delta t}q) = F_{w,\,\delta t}n(t, q). \tag{9}$$

Here $F_{w,\,\delta\lambda}$ denotes Lie dragging along vector field w by parameter increment δt.

For example, consider continuous model of maximal dimension. Let the phase density is differential form of maximal degree. For simplicity, assume that n is continuously differentiable on t as a parameter. Then the Vlasov equation can be written in the form

$$\frac{\partial n}{\partial t} = -\mathcal{L}_w n(t, q). \tag{10}$$

Additionally assume that $\overline{n} = n_{1\ldots K}(t, q)$ is continuously differentiable on phase coordinates, consider nonrelativistic particles, and take Cartesian coordinates. Then the equation (10) means that the single component of the phase density satisfies to the equation

$$\frac{\partial \overline{n}}{\partial t} + \sum_{i=1}^{6} w^i \frac{\partial \overline{n}}{\partial q^i} = 0.$$

CYLINDRICAL BEAM IN LONGITUDINAL MAGNETIC FIELD

Consider nonrelativistic uniformly charged cylindrical beam in uniform longitudinal magnetic field. Assume that all particles have the same longitudinal velocity. Such beam can be described by four-dimensional particle distribution in the phase space of the transverse motion. Integrals of the particles transverse motion are

$$M = r^2(\dot{\varphi} + \omega_0),$$

$$H = \dot{r}^2 + \omega^2 r^2 + M^2/r^2.$$

Here r, φ, z are cylindrical coordinates, $\omega_0 = eB_z/(2m)$, $\omega^2 = \omega_0^2 - e\varrho_0/(m\varepsilon_0)$, e, m are charge and mass of the particles, ϱ_0 is spatial density of the particles inside the beam cross-section, ε_0 is electric constant, B_z is longitudinal component of the magnetic flux density [2, 3]. In this case, magnetic flux is equal to $\Phi = \int B_{r\varphi}\, dr \wedge d\varphi$ [4]. Hence, $B_z = B_{r\varphi}/r = \text{const}$ and $\omega = \text{const}$.

Take φ, phase of a particle trajectory θ, M, and H as coordinates in the phase space. At first, consider the Brillouin flow. In this case $\varrho = m\omega_0^2\varepsilon_0/e$ and $\omega = 0$. Therefore, particles can move only on the surface $M = 0$, $H = 0$. The Vlasov equation in this case can be written in the form

$$\frac{\partial n_{\varphi\theta}}{\partial t} = \frac{d\varphi}{dt}\frac{\partial n_{\varphi\theta}}{\partial \varphi} + \frac{d\theta}{dt}\frac{\partial n_{\varphi\theta}}{\partial \theta}.$$

One can see that $n_{\varphi\theta} = \text{const}$ satisfies to the Vlasov equation. It means that the particles are evenly distributed on azimuthal angle φ and on phases of their trajectories θ. As particle trajectories in this case are circles, such distribution means rigid rotation of the beam as a whole around its axis.

Consider well known Kapchinsky-Vladimirsky distribution. Let particles are located on the 3-dimensional surface $H = \omega^2 R^2$, and are evenly distributed on M in segment $M \in [-\omega R^2/2, \omega R^2/2]$, on azimuthal angle φ, and on phases of their trajectories θ [2, 3]: $n_{M\varphi\theta} = \text{const}$. It is easy to see that it is a stationary solution of the Vlasov equation, which in this case has the form

$$\frac{\partial n_{\varphi\theta M}}{\partial t} = \frac{dM}{dt}\frac{\partial n_{\varphi\theta M}}{\partial M} + \frac{d\varphi}{dt}\frac{\partial n_{\varphi\theta M}}{\partial \varphi} + \frac{d\theta}{dt}\frac{\partial n_{\varphi\theta M}}{\partial \theta}.$$

Show that spatial density of particles is uniform in the beam cross-section. Trajectories of the particles can be found from equation of their motion: $\ddot{r} = -\omega^2 r^2 + M^2/r^2$. Integrating it, we obtain

$$r = 2^{-1/2} R\sqrt{1 - 4\mu^2 \cos(2\theta)}, \quad \theta = \omega t + \theta_0$$

where $\mu = M/(\omega R^2)$. Passing to the Cartesian coordinates $x = r\cos\varphi$ and $y = r\sin\varphi$, we get

$$n_{xyM} = \frac{n_{\varphi\theta M}}{D}, \quad D = \frac{\partial x}{\partial\theta}\frac{\partial y}{\partial\varphi} - \frac{\partial x}{\partial\varphi}\frac{\partial y}{\partial\theta} = \frac{r^2\mu\sin 2\theta}{4}.$$

Expressing θ through r one can get

$$\sin 2\theta = \frac{\pm\sqrt{1 - \mu^2 - (1 - 2r^2/R^2)^2}}{\sqrt{1-\mu^2}}.$$

Then $D = R^2\sqrt{q^2 - q^4 - \mu^2}$ where $q = r/R$. For particles which trajectory passes through point with given r, maximal value of $|M|$ is $M_{\max} = \omega r R\sqrt{1 - r^2/R^2}$. Integrating on M and passing to the variable μ we obtain

$$n_{xy} = \alpha \int_0^{q^2 - q^4} \frac{d\mu}{\sqrt{q^2 - q^4 - \mu^2}} = \text{const}$$

where $\alpha = \text{const}$. Hence, specifying the phase density as mentioned above, we obtain the KV distribution.

KV DISTRIBUTION FOR BEAM IN TRANSVERSE ELECTRIC FIELD

Consider particle distribution in the phase space of the transverse motion. Transverse Cartesian coordinates x, y and corresponding components of velocity $\dot{x}$, $\dot{y}$ can be taken as coordinates in the phase space. The KV (microcanonical) distribution is the distribution for which particles lie on the surface of the $4-$dimensional ellipsoid, and density in the configuration space is uniform inside corresponding ellipse.

Assume that this ellipsoid is specified by the matrix

$$\begin{pmatrix} B^x & 0 \\ 0 & B^y \end{pmatrix}, \quad B^{x,y} = \begin{pmatrix} (R_{x,y})^{-2} & 0 \\ 0 & (V_{x,y})^{-2} \end{pmatrix}.$$

Let introduce coordinates $\varphi_x, \varphi_y, \theta$, on the surface of the ellipsoid:

$$x = R_x\cos\varphi_x\cos\theta, \quad \dot{x} = V_x\sin\varphi_x\cos\theta,$$

$$y = R_y\cos\varphi_y\sin\theta, \quad \dot{y} = V_y\sin\varphi_y\sin\theta.$$

Take the distribution density on the surface of the ellipsoid in the form

$$n = n_{\varphi_x\varphi_y\theta}\, d\varphi_x \wedge d\varphi_y \wedge d\theta.$$

Find such $n_{\varphi_x\varphi_y\theta}$ that density in the configuration space be uniform inside ellipse $x^2/R_x^2 + y^2/R_y^2 = 1$. Expressing density component in coordinates $x, y, \dot{y}$, we can obtain

$$n_{\varphi_x\varphi_y\theta} = n_{xy\dot{x}} R_x R_y V_x |\sin\varphi_y||\cos\theta|\sin^2\theta.$$

Integrating on admissible values of $\dot{x}$ we have

$$n_{xy} = \int_{-\dot{x}_{\max}}^{\dot{x}_{\max}} n_{xy\dot{x}}\, d\dot{x} =$$

$$= \int_{-\dot{x}_{\max}}^{\dot{x}_{\max}} \frac{n_{\varphi_x\varphi_y\theta}\, d\dot{x}}{R_x V_x |\sin\theta|\,|\cos\theta|\sqrt{R_y^2(1 - (\frac{x}{R_x})^2 - (\frac{\dot{x}}{V_x})^2 - y^2}}.$$

Hence, if

$$n_{\varphi_x\varphi_y\theta} = n_0 |\sin\theta|\,|\cos\theta|, \tag{11}$$

the spatial distribution is uniform.

If beam is propagating in linear transverse electric field: $E_x = kx$, $E_y = -ky$, then it can be shown that θ is the motion integral. So, the density (11) satisfy to the Vlasov equation, which in this case takes form

$$\frac{\partial n_{\varphi_x\varphi_y\theta}}{\partial t} = \frac{d\varphi_x}{dt}\frac{\partial n_{\varphi_x\varphi_y\theta}}{\partial\varphi_x} + \frac{d\varphi_y}{dt}\frac{\partial n_{\varphi_x\varphi_y\theta}}{\partial\varphi_y} + \frac{d\theta}{dt}\frac{\partial n_{\varphi_x\varphi_y\theta}}{\partial\theta}.$$

CONCLUSION

As it is demonstrated, the covariant approach works for description of degenerate solutions of the Vlasov equation. The advantage of this approach is that it can be used when the coordinates are curvilinear. Such approach can be also used for description of the matter distribution in relativity theory.

REFERENCES

[1] O.I.Drivotin, Proc. of the 2011 Int. Particle Accelerators Conf (IPAC'2011) (San-Sebastian, 2011), accelconf.web.cern.ch/accelconf /IPAC2011/papers/wepc114.pdf

[2] O.I.Drivotin, D.A.Ovsyannikov, *Nucl. Instr. Meth. Phys. Res.*, A 558, pp. 112-118, (2006).

[3] O.I.Drivotin, D.A.Ovsyannikov, *Int. J. Modern Phys.*, A 24 (5), pp. 816-842, (2009).

[4] O.I. Drivotin, "Mathematical Basics of the Field Theory", Publ.Company of St.Petersburg State Univ., St.Petersburg, 2010 (in Russ.).

TRANSVERSE DYNAMICS OF A RING BEAM IN A COAXIAL TWO-CHANNEL DIELECTRIC WAVEGUIDE

A. Altmark, Electrotechnical University, Saint-Petersburg, Russia
A. Kanareykin, Electrotechnical University, Saint-Petersburg, Russia and EuclidTechlabs LLC, Gaithersburg, MD,USA

Abstract

The most critical issue of wakefield accelerating schemes is transformer ratio (maximum energy gain of the witness bunch/maximum energy loss of the drive bunch) which cannot exceed 2 in collinear wakefield accelerator with use of Gaussian bunches. We observe new scheme of wakefield acceleration in collinear two-channel waveguide, where accelerating field created by electron bunch with annular charge distribution passing in vacuum layer. This radiation is used for acceleration of witness beam which passing through central vacuum channel. These vacuum areas separated by dielectric tube. Transformer ratio for this scheme can be much greater than 2.

The main problem of wakefield accelerators is transverse beam dynamics of the driver bunch, because of high value of its charge and low energy of the particles. We present results of the beam dynamics calculation of the annular drive beam by "macroparticle" method based on analytical expressions for Cerenkov radiation. The upgraded BBU-3000 code has been used for calculation of the beam dynamics in coaxial dielectric wakefield accelerating structures. It is shown that dynamics depends on radial and azimuthally structures of HEM modes excited by the drive beam there. Initial beam imperfections to the beam dynamics was carried out.

INTRODUCTION

A new application of microwave and THz Cherenkov radiation has been proposed and studied in the last decade to be used for high energy physics colliders and X-ray FELs, the Dielectric Wakefield Accelerator, or DWA [1-3].

In a general sense, a high gradient is desirable for a TeV level linear collider design because it can reduce the total linac length and hence the cost. Recently a high energy linear collider based on a short rf pulse (~22 ns flat top), high gradient (~267 MV/m loaded gradient), high frequency (26 GHz) dielectric two beam accelerator scheme has been proposed. The major parameters of a conceptual 3-TeV linear collider based on a DWA have been developed and are presented in reference [4].

X-ray free-electron lasers (FELs) are expensive instruments and the accelerator contributes the largest portion of the cost of the entire facility. Using a high-energy gain dielectric wakefield accelerator instead of a conventional accelerator may facilitate reduction of the facility size and significant cost savings. It has been shown that a collinear dielectric wake-field accelerator can accelerate low charge and high peak current electron bunches to a few GeV energy with up to 100 kHz bunch repetition rate [5].

Dielectric loaded accelerator (DLA) structures using various dielectric materials [6] and excited by a high current electron beam or an external high frequency high power RF source have been under extensive study recently [1-3]. The basic wakefield RF structure is very simple - a cylindrical, dielectric loaded waveguide with an axial vacuum channel is inserted into a conductive sleeve. Following at a delay adjusted to catch the accelerating phase of the wakefield is a second electron (witness) beam. The witness beam is accelerated to high energy by the wakefield produced by the drive beam [1].

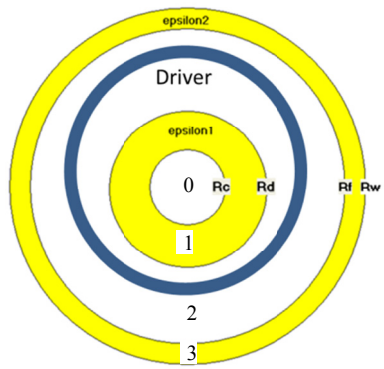

Figure1. Wakefield acceleration by ring driver beam in coaxial cylindrical waveguide

A series of proof of principle experiments have been successfully performed at Argonne's Advanced Accelerator providing accelerating gradient in the range exceeding 100 MV/m at X-band [1-3,6]. THz wakefields of ~ GV/m magnitude range have been successfully generated by the UCLA-SLAC collaboration as well [7].

Energy transfer efficiency from the drive to witness bunches is a critical issue for wakefield acceleration techniques. The transformer ratio R is defined as the ratio of the maximum energy gain of the witness bunch to the maximum energy loss of the drive bunch. There are two major classes of wakefield accelerator geometries, collinear and two beam. For a collinear wakefield accelerator, R is less than 2 under very general conditions: linear media; a relativistic, longitudinally symmetric drive bunch; and identical paths through the system of both drive and witness beams [8-9]. A number of techniques have been proposed to overcome the transformer ratio limitation. Some of the methods that can be employed to obtain R>2 for the dielectric based accelerator include: a triangular longitudinal drive bunch profile [8]; a train of Gaussian drive bunches of progressively increasing

charge (ramped bunch train) [10-11]; and use of a proton drive beam so that the particles can change positions within the bunch during deceleration [12].

Another way to achieve high transformer ratio is by designing separate drive and witness beam lines with different shunt impedances. This technique has been considered in [13] for all-metal structures and initially proposed for dielectric based high gradient accelerator in [14], where a multichannel structure with an annular drive beam propagating through a coaxial outer vacuum channel and a witness beam through a central channel has been considered.

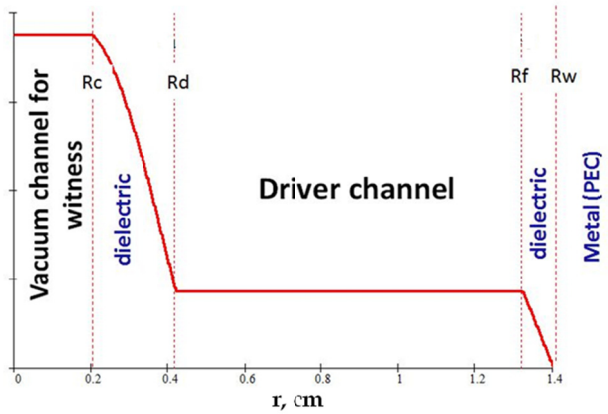

Figure 2. Accelerating TM01-mode field of the structure presented in Fig.1.Transformer ratio =4.5.

Recently the coaxial scheme [14] was considered again for high-gradient wakefield acceleration, and detailed analytical studies for this type of coaxial dielectric-loaded structure have been presented [15-17]. Transformer ratio values as large as R=4.5 were predicted, Fig. 2.

In [16], the coaxial scheme initially proposed in [14] has been considered for the THz frequency range and for the SLAC FACET drive bunch parameters. The structure geometry correspond to THz frequency range wakefields (~ 0.1 mm witness beam aperture) and can be found in reference [16].

ANALYTIC RESULTS AND COMPARISON WITH NUMERICAL SIMULATIONS

The coaxial geometry proposed in [14] for transformer ratio enhancement of the dielectric based wakefield structures is considered here for GHz Ka-band [15] and THz acceleration [16-17]. At the same time, dynamics of the beam in structure-based wakefield accelerators leads to beam stability issues not ordinarily found in other machines. In particular, the high current drive beam in an efficient wakefield accelerator loses a large fraction of its energy in the decelerator structure, resulting in physical emittance growth, increased energy spread, and the possibility of head-tail instability for an off axis beam, all of which can lead to severe reduction of beam intensity [18]. Beam breakup (BBU) effects resulting from parasitic wakefields provide a potentially serious limitation to the performance of dielectric structure based wakefield accelerators as well [18-19].

Correspondingly, the transverse stability of the annular driver beam can be a critical issue for a coaxial high transformer ratio DWA [17]. We report on beam breakup study results for the coaxial Ka-band DWA currently planned to be tested at Argonne Wakefield Accelerator (AWA). Recently we have developed a particle-Green's function beam breakup code (BBU-3000) that allows rapid, efficient simulation of beam breakup effects in advanced linear accelerators [19]. The goal of this work is foremost to design mitigation techniques for BBU and to test these concepts as part of an ongoing series of experiments at ANL/AWA, BNL/ATF and SLAC/FACET.

The coaxial, two-channel DLA structure of figure 1 has an inner vacuum region "0" ($r < a$) for the witness beam and an outer vacuum region "2" ($b < r < c$) for the drive beam. The drive beam used to excite the DLA is azimuthally asymmetric; this is necessary to excite dipole modes which cause beam instabilities. In this paper, we will concentrate on the dipole wakefield excitation due to a non-uniform ring of electrons.

BEAM DYNAMICS SIMULATIONS

BBU-3000 represents an approach to beam dynamics computations which is complementary to the usual electromagnetic PIC (Particle in Cell) approach.

Table 1. Parameters of the coaxial waveguides used in the transverse beam dynamic analysis.

#	Rc, cm	Rd, cm	Rf, cm	Rw, cm	ε_1	ε_2	f, GHz (TM_{02})
1	0.2	0.60	1.00	1.40	4.76	4.76	13.84
2	1e-5	0.06	1	1.4	24	4.76	23.89

Table 2. Parameters of the annular drive beams used in the transverse beam dynamic analysis

#	Q, nC	σ_z, cm	σ_r, cm	offset, cm	R, cm	W, MeV
1	10	0.2	0.01	0.02	0.8	10
2	10	0.2	0.01	0	0.8	10
3	50	0.1	0	0.8	-	14
4	10	0.1	0.01	0.41	-	15

Particle pushing is done in the same fashion as a PIC code but the wakefields caused by the charged particles are computed using the known analytic expressions for the Green's functions in a dielectric tube [18]. Details of the scalar code for the Gaussian shaped beam have been published elsewhere [19]. Here we focus on the recent work on the annular electron beam simulation.

It should be noted that for the annular beam the offset value is limited in comparison with ordinary Gaussian beam because of intrinsic large diameter (relatively to a witness beam aperture) of a vacuum channel of the coaxial DWA structure. Consequently, the beam dynamics of the annular drive beam will be dominated by dipole

mode fields, or HEM modes with ν=1 with the field structure presented in figure 3. In this paper, the beam breakup of the annular driving bunches has been studied with respect to its both azimuthal and radial asymmetries.

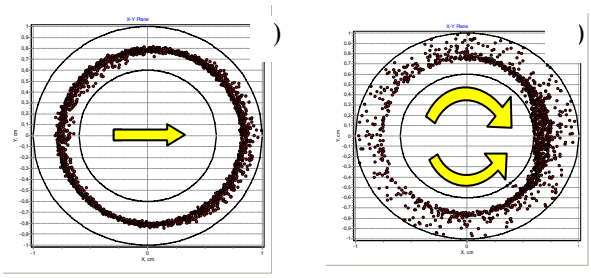

Figure 3. Beam dynamic simulations of an annular beam passing through coaxial dielectric wakefield structure presented in figure 1, region 2: (a) azimuthally symmetric beam with offset (table 1, structure #1; table 2, beam # 1); (b) azimuthally symmetric beam with no offset (table1,structure # 1; table 2, beam # 2).

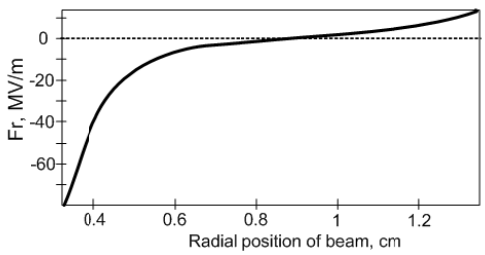

Figure 4. Transverse deflecting field vs. radial position of the Gaussian beam in region 2 for the structure # 1 of table 1, for the beam # 3 of table 2.

Fig. 3 shows the results of BBU300 simulation for the azimuthally symmetric annular beam with offset and the beam with no offset but with azimuthal charge asymmetry. One can see radial deflection for the azimuthally symmetric beam caused by center of mass shift (offset of the beam) while the azimuthal deflection is still compensated by the charge density symmetry. At the same time, the azimuthal asymmetry generates F_θ components strong enough to increase dramatically the charge density along the line of structure center – maximum of charge density distortion, Fig.3. Fig. 4 presents the transverse deflecting field vs. radial position of the beam particle: one can see the flat region where there is no force increase. Fig. 5 presents simulation results for the gaussian beam passing through coaxial structure of Fig. 1. Note strong deflection to both inner and outer dielectric surfaces.

SUMMARY

The software effort is based on development of the BBU-3000 code upgrade. A number of new features have been incorporated including a coaxial cylindrical dielectric based structure capabilities. The results of the simulations show that the contribution to the transverse deflecting field in coaxial waveguide for annular beam is made by both azimuthally and radial forces. The sign of radial force is changed when along radial coordinate in the drive beam channel.

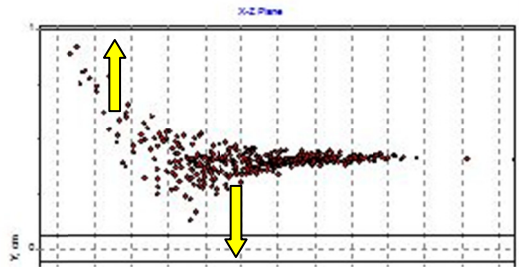

Figure 5. Beam dynamic simulations of an gaussian beam passing through coaxial structure presented in Fig.1, structure # 2 of table1, beam # 4 of table 2.

REFERENCES

[1] W.Gai, et al. Phys. Rev. Lett. **61**, 2756 (1988)
[2] W.Gai, AIP Conference Proceedings **1086**, 3 (2009)
[3] A. Kanareykin Journal of Physics, Conf. Ser., **236**, 012032 (2010)
[4] C.Jing, A.Kanareykin, J.G.Power, A.Zholents Proc. IPAC'11, 1485 (2011)
[5] C.Jing, S.Antipov, A.Kanareykin et al. Proc. PAC'11, New York, NY, 2279 (2011)
[6] A. Kanareykin, AIP Conf. Proc., **1299**, 286 (2010)
[7] M. Thompson et al., AIP Conf. Proc. **877**, 903 (2006)
[8] K. L.Bane, P.Chen, and P. B. Wilson, SLAC Report No. SLAC-PUB-**3662**(1985)
[9] J. G.Power, W.Gai, and P. Schoessow, Phys. Rev. E **60**, 6061 (1999)
[10] E.Laziev, V.Tsakanov, and S.Vahanyan Proceedings EPAC'88. IEEE, 523 (1988)
[11] C.Jing, A.Kanareykin, J. G.Power, M.Conde et al., Phys. Rev. Lett. **98**, 144801 (2007)
[12] J. B.Rosenzweig, P.Schoessow, B.Cole, W.Gai et al. Phys. Rev. A **39**, 1586 (1989)
[13] Voss G.A. and Weiland T. 1982 DESY M-82-10
[14] R.Keinigs, M.Jones,Proc. 7th Int. Conf. High-Power Part. Beams, Beams'88, Karlsruhe, Germany, **864**, (1988)
[15] W. Liu and W.Gai, Phys. Rev. ST Accel. Beams **12**, 051301 (2009)
[16] G. V.Sotnikov, T. C.Marshall, and J. L. Hirshfield Phys. Rev. ST-AB **12**, 061302 (2009)
[17] G.V. Sotnikov and T.C. Marshall. Phys.Rev.ST-Accel.Beams**14**,031302 (2011)
[18] W.Gai, A.Kanareykin, A.Kustov and J. Simpson Phys. Rev. E **55**, 3481 (1997)
[19] P.Schoessow et al., Proc. AAC'10, AIP Conference Proceedings, N.Y, **1299**, 262 (2010).

COMPUTER SIMULATION OF THE ELECTRON BEAM ENERGY SPECTRUM MEASUREMENT BY THE MAGNETIC ANALYZER METHOD BASED ON SCANNING SYSTEM OF THE STERILIZATION INSTALLATION

P. A. Bystrov, M. A. Alekseev, N. E. Rozanov, MRTI RAS, Moscow, Russia

INTRODUCTION

Currently, there is a demand for the sterilization of medical products using radiation technology, including the use of accelerated electron beams. To meet this demand sterilizing devices are being developed. Such a device, with a compact local radiation shielding, was created in the Moscow Radiotechnical Institute [1]. This installation is based on a linear high-frequency accelerator working on a standing wave, with the focusing of electron beam by the radial component of the electric microwave field [2].

Energy spectrum of accelerated electron beam is one of the important characteristics that define the efficiency of sterilizing installation. The task to create the electron beam with the optimal spectrum for the accelerator with relatively short grouping part has not been yet stated. So the form of the spectrum is defined by physical mechanisms of the beam accelerating process, and it is still, in general, has satisfied the basic requirements.

While working on increasing the efficiency of sterilizing installation, there is a need for a physical-mathematical model of processes in systems of output the beam into the atmosphere and scanning system for the sterilization of the objects. Such model that uses the information about the electron beam from the calculations of acceleration process of the beam [3] was created [4]. Perfection of this model requires the establishment of correspondence between calculated energy spectrum and real spectrum of the beam.

This paper describes a method for measuring the characteristic, which allows restoring the energy spectrum of the beam in one of the regimes of operation of the accelerator of the sterilization installation. It is based on the method of magnetic analyzer, implemented on the basis of scanning system of the electron beam of the installation. This method does not require the use of additional equipment, and this fact is important one for installation with local radiation shielding. Result of measurement is the dependence of the beam current, deflected by a transverse magnetic field, which falls in the region of the induction current sensor, on the value of deflecting magnetic field. With the computer code "BEAM SCANNING" [4], specially modified for this purpose [5], the simulation of processes in the scanning system in the regime of measuring of this characteristic was performed. It is shown that the important factors which influence the form of curve of the measured characteristic are the reflections of the beam electrons from the walls of the funnel of the scanning system and the non uniform distribution of the magnetic field in the direction of the scanning. In this case, the calculated dependence of the current in the induction sensor on deflecting magnetic field is consistent with the experimental dependence, and the restored form of the energy spectrum corresponds to the calculated beam spectrum in a particular regime of operation of the accelerator.

THE SCHEME OF MEASURMENT THE CHARACTERISTICS FOR RESTORING THE ELECTRON BEAM ENERGY SPECTRUM

Fig. 1 shows the measurement scheme, which in its time was conventionally called "scheme of spectrum measurement at the edge of the funnel".

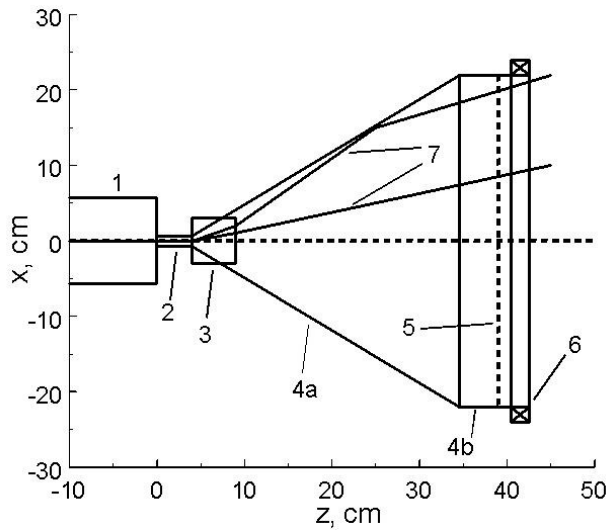

Figure 1: The scheme for measurement the characteristics for restoring the electron beam energy spectrum. 1 - end of the accelerating structure, 2 - drift tube, 3 - the area of the transverse deflecting magnetic field of scanning system, 4 - the funnel of the scanning system (a - cone part, b - rectangular part), 5 - titanium foil, 6 - inductive sensor for measure the beam current, 7 - some electron trajectories.

The electron beam emerging from accelerating structure passes the short length drift tube and appears in the location of an electromagnet that is creating a transverse magnetic field of the beam scanning system of the sterilization installation. Passing region of the

magnetic field, the beam experiences its impact of deflection (in the plane of the figure). Some of the electrons falls within the induction sensor, a part - is landed on the walls of the funnel. Inductive sensor is in fact a pulse transformer in which the primary "winding" is a part of the beam, that passes the sensor, and from the secondary "winding" the signal is taken. At relatively low magnetic fields the entire beam reaches the end of funnel, passes the titanium foil of thickness 50 microns separating the vacuum part of the system from the atmosphere, and falls into the inductive sensor completely. In this regime, inductive sensor detects a current equal to the beam current at the output of the accelerator. The current value is determined by the oscillogram of a signal from the induction sensor. Measurements were performed in single-pulse regime for beam pulses up to 6 microseconds. The current value was determined by the value on the "plato" of the oscillogram. The particles of different energies are deflected on different angles, either reaching the walls of the funnel, or being registered by the induction sensor.

In Fig. 2 the measured dependence of the current registered by inductive sensor (I_{is}) on the value of the deflecting magnetic field (B) is shown.

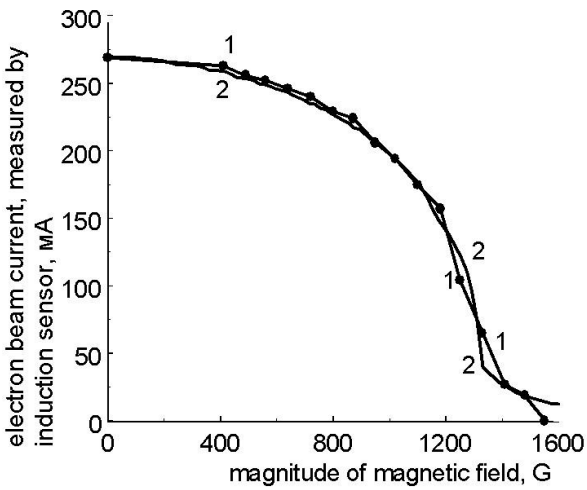

Figure 2: The dependencies of the electron beam current, measured by the induction sensor, on the magnitude of deflecting transverse magnetic field. Curve 1 - the measured dependence, 2 - calculated curve.

As follows from the figure, the experimental curve can be divided into three parts - for small, medium and large magnetic fields. At relatively small fields one can see a slow decline of current in induction sensor, which is explained by the gradual loss of low-energy electrons on the funnel walls. At moderate values of the magnetic field a pace of decline of current noticeably increases. It is explains by the "landing" of a lot of high-energy electrons on the walls of the funnel. Finally, at high magnetic fields it is seen slowing of the decrease of the measured current depending on the field. As shown below, this part of the experimental curve is due to the presence of the reflection effect of strongly deflected electrons from the walls of the funnel, leading to penetration of the electrons in the region of the induction sensor, even at high magnetic fields. This dependence allows restoring the energy spectrum of the electron beam.

THE ENERGY SPECTRUM OF THE ELECTRON BEAM

Energy spectrum - is the dependence of the energy beam current density on the energy, i.e., dependence on energy (E) of the small fraction of the current (dI), created by the electrons with energies in the small interval between E and $E+dE$: dI/dE. The integral of the spectrum over the energy (from zero to infinity) is equal to the total current of the beam. Sometimes, instead of the absolute value of the current fraction dI the normalized current is used, for example, normalized to the injected beam current. In this case, the integral over the energies of this normalized spectrum is equal to coefficient of capture of the beam into the acceleration regime. The energy spectrum of the electron beam is one of the most important characteristics that determine the effectiveness of the sterilization installation. Calculations of the spectrum were performed repeatedly, and, through a variety of computer codes. In Fig. 3 the energy spectrum of the beam calculated by using "DINA-TIME" computer code from the software package "DINA" [3] is shown.

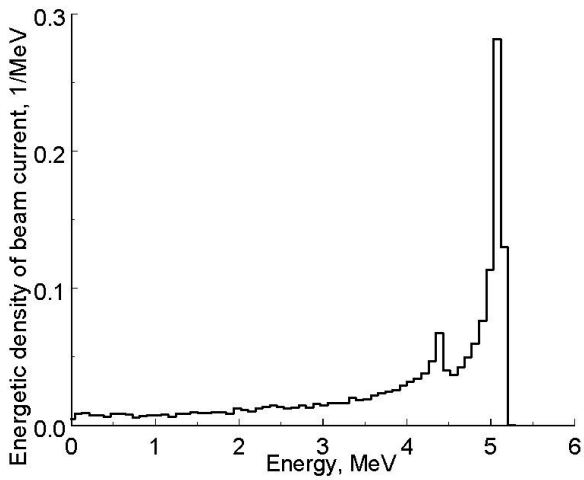

Figure 3: The energy spectrum of the electron beam: the dependence of the energetic density $d(I/I_{inj})/dE$ of the beam current, normalized to the injection current I_{inj}, on the energy E.

It has a number of features. First, one can see a long enough low-energy "tail" extending to lower energies down to very small values. It is the presence of the “tail” that gives a very strong contrast of the average energy in spectrum to the most probable energy and to the maximum energy in the energy spectrum. Second, the spectrum has a sharp peak at the energy corresponding to the most probable energy. Third, there is a very sharp drop in the interval from the most probable energy to the maximum energy in the energy spectrum.

COMPUTER SIMULATION OF THE MEASUREMENT PROCESS AND RESTORING OF THE ELECTRON BEAM ENERGY SPECTRUM

A simple way to restore the energy spectrum from the measured curve $I_{is}(B)$ could be a method based on its differentiation. Indeed, it is easy to verify that the derivative $dI_{is}(B)/dB$ is proportional to the energy density of the beam current dI/dE, called by the spectrum of the beam. In this method, energy is calculated by using the value of the uniform magnetic field, according to the formula for the trajectory of a single electron. However, this method may be used only if a number of conditions are fulfilled. These include: small radius of the beam and its transverse velocity at the exit of the accelerator, the weak expansion of the beam due to scattering on the foil of the end of scanning system, the uniformity of the magnetic field, and the lack of reflection of electrons from the walls of the funnel. The last two factors do not allow using this method.

To model the processes occurring in the measurement of the above-described experimental curve $I_{is}(B)$, the computer code "BEAM SCANNING" [4] was used. The code uses an information about the accelerated beam from calculations of acceleration processes, creates three-dimensional distribution of the three components of the magnetic field of the deflecting magnet, allows accounting processes due to hysteresis [6] in the ferromagnetic elements of the scanning system, and the scattering on the titanium foil, calculates the dynamics of electrons in the "6-microsecond" bunch during the process of scanning, calculates the distribution of radiation dose in an sterilizing object.

A detailed investigation of the possible reasons of appearing of the part of the experimental curve with a relatively slow decline in current of the sensor for high values of the deflecting magnetic field showed the following. The most important of these are the presence of effect of electron reflection from the funnel walls and the nonuniformity of the field of the magnet in the direction of the deflection (x-coordinate). To model the first effect the code "BEAM SCANNING" was modified [5]. Now, it simulates the reflection of electrons from the inner surface of the funnel, with the use of the reflection coefficients for current, electron energy losses, distributions of reflected electrons on the angles of refraction, etc. [7], and also takes into account the loss of the beam while passing the output titanium foil [8]. The distribution of the deflecting magnetic field on the x and z directions in the calculations were taken from measurements in real magnet installation.

Calculated dependence is shown on Fig. 2. One can see a good agreement of the measured dependence (curve 1) and the calculated curve (2). Thus, at low magnetic fields one can see a slow decline of the current, which is explained by the gradual “landing” of low-energy electrons on the funnel walls. At moderate values of the magnetic field the rate of decline of sensor current noticeably increases - both in the calculation and in the experiment. It is connected with the "landing" a lot of high-energy electrons on the wall of the funnel. Finally, at high magnetic fields it is seen slowing of decline of sensor current with the field.

In calculation of the dependence, shown on Fig. 2, the information about the particles of the beam was used. This information was obtained as a result of modelling of the beam acceleration by using the code "DINA-TIME" (see above, including, energy spectrum of the beam on Fig. 3). Acceleration regime in these calculations was chosen on the basis, in particular, the need to obtain the best fit of the experimental curve and calculated curve in Fig. 2. And this accordance, as can be seen, has been reached. This means that the energy spectrum of the electron beam in the same regime, which gave the experimental curve in Fig. 2, corresponds to the calculated spectrum shown in Fig. 3. Also, the acceleration regime in the experiment described above corresponds to the regime that was founded in calculation of acceleration and which gives the electron beam with the mentioned above spectrum..

REFERENCES

[1] V.M. Belugin et al, “Compact electron linacs for radiation technology systems,” Proceedings of the 2001 Particle Accelerator Conference, 2001.V. 4. P. 2515-2517.

[2] V.M. Belugin et al, “Self-shielded electron linac accelerators for radiation technologies,” Physical Review Special Topics - Accelerators and Beams, 2009, V. 12, Issue 9 (090101), P. 1-8.

[3] N.E. Rozanov, “Computer codes DINA for calculation of high-current beam dynamics in linear accelerators,” Proceedings of Moscow Engineering Physics Institute "Science Session-2003", (MEPhI, Moscow, Russia, 2003), P. 167-168.

[4] P.A. Bystrov and N.E. Rozanov, “The methodology and the computer code BEAM SCANNING for calculating the processes in the scanning system of electron beam with a broad energy spectrum,” Problems of atomic science and technology, Kharkov Institute of Physics and Technology, Ukraine, 2012, No 4, p.87-91.

[5] P.A. Bystrov and N.E. Rozanov, “The methodology and the computer code BEAM SCANNING for calculating processes in the scanning system of the electron beam of the sterilization installation,” Nuclear Physics and Engineering, 2012, to be published.

[6] P.A. Bystrov, “Accounting of the hysteresis of ferromagnetic elements in the development of beam scanning system," Nuclear physics and engineering, 2011, V.2, Number 5, p.441-444.

[7] V.P. Mashkovich, Protection against ionizing radiation, (Moscow: Energoatomizdat, 1982)

[8] M.P. Svinyin, Calculation and design of high-voltage electron accelerators for radiative technology, (Moscow: Energoatomizdat, 1989)

MEASUREMENT OF BEAM PARAMETERS IN THE VEPP-5 DAMPING RING USING BETATRON OSCILLATIONS DECOHERENCE*

K. Astrelina†, A. Petrenko, Budker INP SB RAS, Novosibirsk

Abstract

The measurement of beam parameters during the commissioning of VEPP-5 Damping Ring is presented. Coherent betatron oscillations of the 380-MeV electron beam were induced by a fast kick. Electrostatic beam position monitors were used to obtain the turn-by-turn transverse beam position data. The form and behavior of the envelope of oscillations are determined by the beam parameters, chromaticity and nonlinear detuning. The values of beam emittance $\epsilon = 1.5 \cdot 10^{-8}$ m·rad, energy spread $\delta = 3.6 \cdot 10^{-4}$ and beam length $\sigma_l = 1.5$ cm have been obtained from the analysis of the beam envelope, nonlinear detuning and chromaticity measurements. The results are in a good agreement with theoretical predictions which were made for calibrated model of the Damping Ring.

INTRODUCTION

VEPP-5 Injection Complex is designed for the production of intense high-quality electron and positron beams [1]. Damping Ring stores the electron and positron beams of 510 MeV which are injected from the Linac. These beams are to be used at the electron-positron colliders at BINP and plasma wake field acceleration (PWFA) facility [2]. The necessary requirements to the produced beams are of $2 \cdot 10^{10}$ particles in the bunch, emittance of ($\epsilon_x = 2 \cdot 10^{-8}$ m·rad, $\epsilon_y = 0.5 \cdot 10^{-8}$ m·rad with the rate of the beam accumulation 10^{10} positrons per second.

At the present moment Injection Complex and its Damping ring are under commissioning. Currently the electron beam with energy 380 MeV has been stored in the Damping Ring; the experiments with positron beam injection and storage are planned for October 2012.

There are 17 electrostatic beam position monitors (BPMs) in the Damping Ring. Each monitor can record the transverse coordinates of beam centroid over 32000 turns or less. Turn-by-turn measurements from BPMs can be used for the storage ring optics measurements as well as indirect beam parameters measurements. The envelope of coherent betatron oscillations is influenced by the energy spread, transverse and longitudinal beam sizes and emittances. Therefore, the analysis of oscillation envelopes [3] or synchrotron spectra [4] can yield these beam parameters.

This simple technique was used during the Damping Ring commissioning with electron beams and will be used for positron beams.

* Work supported by the Ministry of Education and Science of the Russian Federation, RFBR (grant N 09-02-00594)

† K.V.Astrelina@inp.nsk.su

BETATRON OSCILLATION ENVELOPE

Transverse betatron beam oscillations induced by fast inflector kick. For low enough beam intensity betatron particle motion is independent for the all particles in the beam. Single particle turn-by-turn transverse position may be written as

$$x(t) = \sqrt{2I\beta}\cos(2\pi \int_0^t \nu(t)dt + \psi_0), \qquad (1)$$

where β – beta-function at the point of BPM location, ψ, I – action-angle coordinates [3].

Initially kicked beam behaves like a single particle (coherent oscillations) but because of betatron tune spread the decoherence is developed in several thousands of turns and the beam centroid oscillations amplitude decreases due to detuning of betatron oscillations.

There are two main sources of tune spread: chromaticity and amplitude-dependent tuneshift

$$\nu = \nu_0 + \delta\xi + aI, \qquad (2)$$

where $\delta = \Delta p/p_0$, ξ – chromaticity, a is the constant describing amplitude-dependent tuneshift. Assuming that the initial beam distribution is Gaussian in longitudinal and transverse planes one can express the position of beam centroid as:

$$< x(t) >= \sqrt{2\beta I(t)}\cos(\psi(t) + \psi_0) \qquad (3)$$

where

$$I(t) = \frac{1}{1+\theta^2}\exp\left(-\frac{Z^2}{2}\cdot\frac{\theta^2}{1+\theta^2}\right)\cdot \cdot\exp\left(-2\left(\frac{\xi\delta}{\nu_s}\right)^2\sin^2(\pi\nu_s t)\right) \qquad (4)$$

$$\psi(t) = 2\pi\nu_0 t + \frac{Z^2}{2}\cdot\frac{\theta}{1+\theta^2} + 2\arctan\theta.$$

Here $Z = \sqrt{2I_{max}/\epsilon}$ – kick strength, $\theta = 2\pi a\epsilon t$, ν_s - synchrotron frequency. One can see that the form of the oscillation envelope depends on two values $\xi\delta$ and $a\epsilon$. Amplitude-tune dependence contributes as the main damping of the oscillations amplitude; chromaticity modulates the envelope with synchrotron frequency. Given the values of ξ and a from preliminary measurements, one can deduce energy spread and beam emittance by fitting the formula (Eq. 4) to the envelope by varying ϵ and δ.

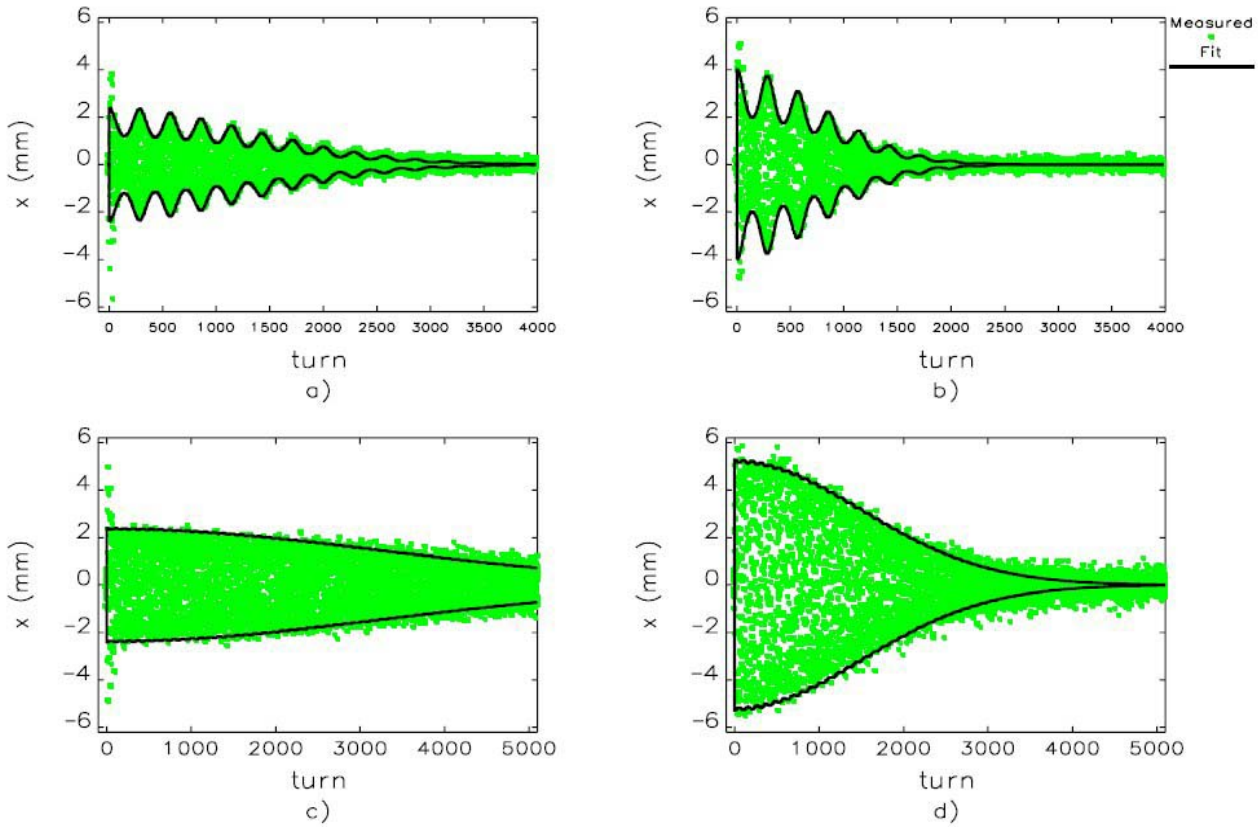

Figure 1: Horizontal betatron oscillations after the kick (green dots) and envelope fit (black solid line) calculated from Eq. 4. At the two upper plots (a,b) the turn-by-turn measurements were performed for the machine with natural chromaticity ($xi = -6.0$). At the bottom plot the chromaticity is compensated with sextupoles.

Beam length is deduced from energy spread and synchrotron frequency

$$\sigma_l = \frac{\alpha_p c}{2\pi f_0 \nu_s}\delta$$

where α_p - momentum compaction factor, L - machine circumference, f_0 - revolution frequency.

The technique is valid for low-current beams when the beam - vacuum chamber interactions can be neglected.

BEAM TILT DUE TO CHROMATICITY

It is interesting to note that chromatic decoherence results in beam tilt developed in the plane of oscillations. Beam synchrotron oscillations can be presented in the form

$$\delta = \delta_0 \cos(2\pi\nu_s t + \psi_s), \quad (5)$$

where δ and ψ_s – amplitude and phase of oscillations. Then longitudinal position of particle may be written as

$$s(t) = s_0 \sin(2\pi\nu_s t + \psi_s)$$

where $s_0 = \delta_0 L\alpha_p/(2\pi\nu_s)$.

Adding Eq. 5 to (1) and (2) one obtains

$$x(t) = \sqrt{2I\beta}\cos(\psi_0 + \\ + 2\pi\int_0^t (\nu_0 + aI + \xi\delta_0\cos(2\pi\nu_s t + \psi_s))dt) \quad (6)$$

After the half of synchrotron oscillation period ($t_0 = 1/(2\nu_s)$) the particle position is

$$x = \sqrt{2I\beta}\cos\left(\psi_0 + \frac{\pi(\nu_0 + aI)}{\nu_s} - \frac{2\xi\delta_0}{\nu_s}\sin\psi_s\right)$$

Since the longitudinal particle position at the same time is $s(t_0 = 1/(2\nu_s) = -s_0\sin(\psi_0)$ there is a correlation between transverse and longitudinal position of particle in the beam:

$$x = \sqrt{2I\beta}\cos\left(\psi_0 + \frac{\pi(\nu_0 + aI)}{\nu_s} + \frac{4\pi\xi}{L\alpha_s}s\right) \quad (7)$$

This correlation is preserved for the several turns around t_0 because the synchrotron oscillations are slow. Betatron oscillations are much faster so one can choose a turn with s-independent phase addition equal to $\pi/2 + \pi n$. Then

$$x \sim \sqrt{2I\beta}\sin\left(\frac{4\pi\xi}{L\alpha_p}s\right) \quad (8)$$

For the Damping Ring ($L = 27$ m, $\xi = 6.0$, $\alpha_p = 0.028$, $s \sim 1$ cm) one can replace the sine function with its linear approximation:

$$x \sim \sqrt{2I\beta}\frac{4\pi\xi}{L\alpha_p}s \qquad (9)$$

Therefore, the beam tilt depends only on kick amplitude and chromaticity.

The effect of beam tilt is described in details in [5] where it was used to generate very short x-ray pulses. Beam tilt can also be used to modulate the beam in the Damping Ring with a collimator for the plasma wake-field acceleration experiment.

EXPERIMENT IN DAMPING RING AND RESULTS

The results of two series of measurements and beam envelope fits are displayed at the Fig. 1. The first pair of data sets (1a, 1b) was recorded with the natural chromaticity in the Damping Ring $\xi = -6.0$ and different kick strengths. At the other data sets (1c, 1d) chromaticity was corrected with sextupoles. In the Fig. 1a, 1b the form of envelope chromatic modulation allows us to find the energy spread. In the Fig. 1c, 1d the beam emittance can be found from the decoherence envelope. Combined fitting of two data series with different kick strengths and chromaticity gives energy spread $\delta = 3.6 \cdot 10^{-4}$ and emittance $\epsilon = 1.5 \cdot 10^{-8}$ m·rad (with 5% accuracy).

The equilibrium length of the beam with measured energy spread is $0.4 - 1.5$ cm.

This result is in a the good agreement with the design prediction of equilibrium beam parameters for low-intensity beams. For the design beam with $2 \cdot 10^{10}$ particles, the parameters δ and ϵ will have a factor of 2 bigger values due to beam heating by the intrabeam scattering.

CONCLUSION

The theory of betatron oscillations decoherence was applied to the VEPP-5 Damping Ring electron beam. For the beam with energy 380 MeV the measured energy spread is $3.6 \cdot 10^{-4}$, emittance is $1.5 \cdot 10^{-8}$ m·rad and bunch length 1.5 cm which is close to the design parameters.

ACKNOWLEDGMENTS

The authors are grateful to D.V. Pestrikov for the idea of experiment, as well as N.S. Dikanskiy and P.V. Logachev for their help with the Damping Ring commissioning.

REFERENCES

[1] V. Anashin et al. "Damping Ring for Injection Complex VEPP-5" preprint. Budker Institute of Nuclear Physics. Novosibirsk, 1995.

[2] Petrenko A.V. et al. "The Facility of 500 MeV Plasma Wake-Field Acceleration Experiments at Budker INP". Proceedings of Advanced Accelerator Concepts 2010, Annapolis, MD, USA (2010), p. 467-471

[3] R.E. Meller, A.W. Chao et al. "Decoherence of Kicked Beams". SSC-N-360. 1987.

[4] T. Nakamura, K. Soutome et al. "Chromaticity for energy spread measurement and for cure of transverse multi-bunch instability in the SPRING-8 Storage Ring". PAC'01, proceedings.

[5] W. Guo et al. "Generating picosecond x-ray pulses in synchrotron light sources using dipole kickers". Phys. Rev. ST Accel. Beams 10, 020701 (2007).

SIMPLIFIED BEAM LINE WITH SPACE CHARGE COMPENSATION OF LOW ENERGY ION BEAM

A. Dudnikov#, Budker Institute of Nuclear Physics, SB RAS, Novosibirsk, Russia

Abstract

Simplified beam line for low energy Ion implantation is considered. Compensation of the space charge of high perveance, low energy ion beam in beam lines for ion implantation and isotope separation has been investigated. Different mechanisms of the compensating particle formation such as ionization by the beam, secondary emission of electrons and negative ions, electronegative gas admixture, and external plasma sources are discussed. Advanced space charge compensation increases an intensity of low energy ion beam after analyzer magnet up to 3–4 times. Space charge compensation of positive ion beam by admixture of electronegative gases and damping of the beam instability are discussed. Up to 6 mA of $^{11}B^{+}$ ions with energy 3 keV, 11 mA with 5 keV, and 18 mA with 10 keV have been transported through an analyzer magnet of a high current implanter with space charge compensation by electronegative gases

INTRODUCTION

Ion implantation is the largest commercial application for particle accelerators. Several thousand ion implanters are used for semiconductor circuits fabrication. Most difficult task of ion implantation is high dose implantation of ion with lowest energy. Now for the high-current implanters are used the beam-line (BL) shown in Fig. 1 [1]. Implanters energy is up to 40 or 80 kV, but they have been optimized for sub-1 keV implants, where space charge forces have a dominant effect. The beam line uses a couple of deceleration stages that allow the beam to be transported mainly at higher energies. It is also designed to produce a broad beam at the wafer to maximize the cross section and to minimize the space charge forces at the final implant energy. The wafer is scanned across the ribbon beam in one direction. This beam line is very long, complex and expansive. Due to the complex interactions between the ion beam and the magnetic field applied for beam expansion, this approach creates severe technical, practical, and process related problems that increase the total production cost of such equipment and lead to more complicated operation procedures for carrying out the ion implantation. In particular, the beam path through this system is relatively long, and at low energies and high beam currents it becomes increasingly difficult to control the uniformity of the ion beam and the angular variation within the beam with the precision required by certain commercial processes. Recently were proposed some simplified beam lines for production the same broad ribbon beam as in [1] directly after analyzing magnet [2-4].

Schematic of these BL is shown in Fig. 2. Main feature of this BL is very large magnet aperture along magnetic field for production of ribbon beam with width up to 300 mm .

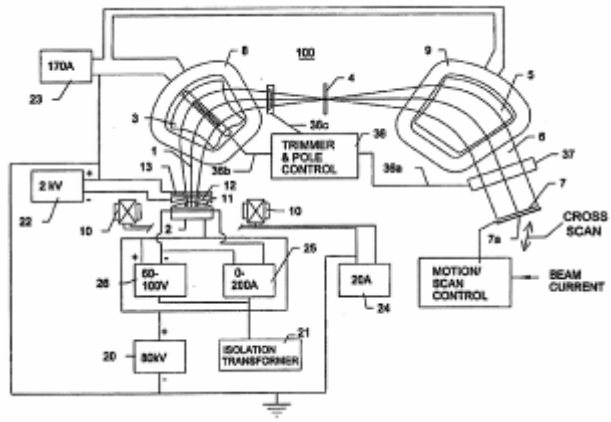

Figure 1: Schematic of high current low energy implanter from [1].

For transportation of low energy heavy ion beam through analyzer magnet is important to have a very good space charge neutralization (SCN) to avoid a beam divergency and particle loss. The space charge compensation energy of low energy ion beam was tested in the simplified beam lines described below.

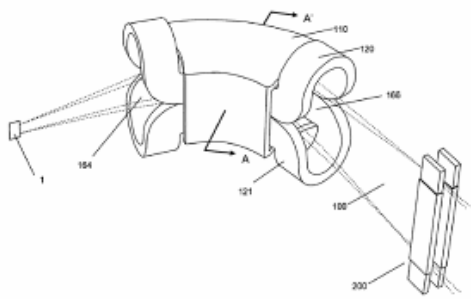

Figure 2: Beam line of implanter with a large vertical aperture. 1-ion source; 100-extended robbon iom beam; 110 magnet; 12, 1210-saddle type coils; 200-multipole beam corrector.

EXPERIMENTAL IMPLANTERS

In first experiments was used the high current ion implanted VESUVII-8M with modified Bernars type ion sources adopted for separation of Rubidium isotopes from RbCl salt. Schematic of the experimental device is shown in Fig. 3. A gas delivery systems (9-14) and plasma sources (16) were used for improved space charge compensation of ion beam generated by ion source (2) and analyzed by magnet (1) with uniform field and vertical edge field focusing.

#Andreidud@gmail.com

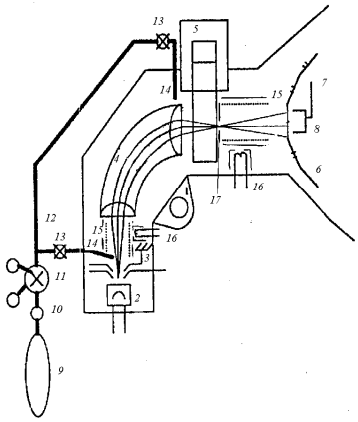

Figure 3: Diagram of implanter VESUVII-8 with improved space charge compensation [4].

With emission slit 2x40 mm an Rb+ ion beam intensity was higher than estimated space charge limit of beam line (40 cm Lamoure radius, 90° bending magnet). But with Ar gas injection the ion beam signal on collector (8) was very noisy, when with admixture of BF_3 gas the beam become stable and mass resolution was improved. It was hypotheses that generation of negative ion can be important for stable space charge compensation.

Further testing of space charge compensation with electronegative gases were conducted in the experimental implanter shown in Fig. 4.

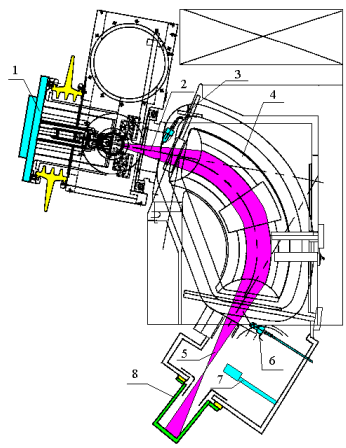

Figure 4: Schematic of implanter with large aperture and enhanced space charge compensation. Ion beams from discharge in BF3 gas.

In almost all previous investigations of SCN of positive ion beams it has been assumed that the compensating particles are electrons [1-5]. However, in the environment of isotope separation and ion implantation where the complex halide and hydride molecules with high electron affinity are often used as working gases, there is a high probability of negative ion formation. In this situation SCN by negative ions could be significant. Indeed, the SCN by negative ion could be the determining factor for productive operation of large scale ion beam industry, but so far this circumference has not been investigated. Before, this possibility has been discussed in [4-7] and some new results will be presented.

A possibility to improve SCN by negative ions was tested in beam line shown in Figs. 3 and 4 with a magnetic scanner and magnetic suppression of secondary electrons in the beam collector after mass analyzer. For production of high perveance ion beams modified Bernas source with two filaments and small anode made from W wire has been used [8-9]. In this configuration drift of ions in crossed fields to the emission slit is improved. In ion source with two filaments is possible to optimize cathode material recycling for periodic restoring of cathodes and increase of lifetime. The high temperature of small anode and ion bombardment of chamber wall prevents from the flakes formation. Three electrode extractors with precise moving electrodes have been used for beam formation. For low energy beam extraction a high voltage on the suppression electrode (up to -20 kV for 3 keV) was used. Production of high energy neutrals and negative ions in the extractor gap and on the suppressor surface is important for enhance of residual gas ionization and improved space charge neutralization. In a "standard" mode of operation with a strong acceleration- deceleration, low gas density and low noise of discharge in ion source are typically a strong instability of ion beam after analyzer as shown in Fig.5.

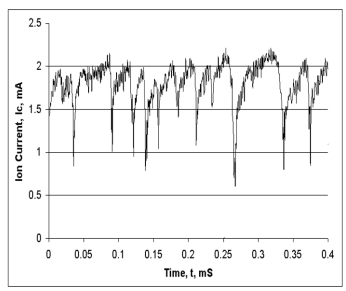

Figure 5: Oscilloscope track of ion beam after analyzer magnet with instability.

It is typically a relaxation type of oscillation. Beam intensity increases up to critical level, this drives instability, loss of SCN, drop of intensity and then this cycle repeats. It was observed, that with electronegative gases in ion sources, such as BF_3, RbCl, CF_4 it is possible to suppress beam instability by increasing gas injection into the source. This instability was not damped by increase of noble gas density such as Ar, or Kr.

Improved SCN and damping of instabilities could be related to adding of negative ions into the beam instead of free electrons.

For enhance negative ion formation in ion beams an injection of electronegative heavy molecules with high electron affinity into the ion beam is proposed. Negative ions in ion beam are formed by collision of electrons with molecules and by bombardment of electrodes surfaces by beam and plasma particles. With the use of negative ion for positive ion beam SCN it is possible to create

overneutralization, as in the negative ion beam with SCN by positive ions. For low energy ion beam overneutralization discharge plasma and electronegative heavy gas molecules are injected into the beam. For minimization of electric field influence on the beam SCN is used the shielding of beam through grid.

A typical beam line for ion beam production, formation, transportation, separation, scanning, collimation and utilizing consist of the ion source, extraction system, analyzer magnet with mass resolving system, scanner magnet, collimator magnet and end station for the material processing by ion beam. Very good space charge neutralization is necessary in the all parts of ion beam transportation. The strongest space charge forces defocused beam directly after extractor because of multicomponent, high perveance beam is extracted from ion source plasma. The intensity of one component ion beam after analyzer could be considerably lower, but the space charge neutralization of this beam is also important for prevention of the loss of beam intensity and quality. For the prevention of the compensation particles extraction from the beam to the ion source by the electric field of extraction voltage is used a suppression electrode with negative voltage between ion source and grounded extraction electrode reflecting compensating particles into the ion beam.

For improved space charge neutralization electronegative gas is injected into the beam after extraction. A tunnel- shielding around the beam is used to increase electronegative gas utilization and for beam-plasma shielding from electric field. Reflectors made from transparent mesh and negatively biased electrodes can be used for increase of the neutralizing particles lifetime. Gas control systems is used for optimization of the electronegative gas flux.

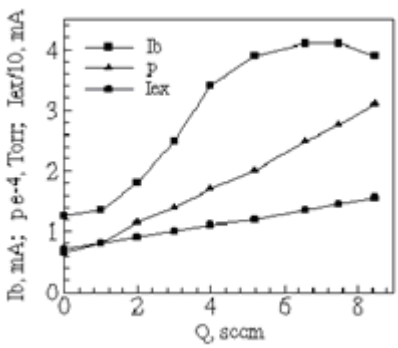

Figure 6: Ion beam current of 3 kV $^{11}B^+$ beam after analyzer magnet versus neutralizing electronegative gas CF_4 flux.

Ion beam neutralization by negative ions is the most important for low energy beams because the cross section of electron production during gas ionization by low energy heavy ions is very low, really zero. An effect of electronegative gas admixture to the 3 keV beam of B^+ demonstrated in Fig.6. Ions of $^{10}B^+$, $^{11}B^+$, F^+, BF^+, BF_2^+,.. was extracted from the 2x90 mm^2 slit of ion source with discharge in the BF_3 gas. Separated beam of $^{11}B^+$ was registered after 14x80 mass- slit of analyzer magnet by magnetically suppressed collector. Optimized fluxes of electronegative CF_4 gas was injected into the tunnel around the beam after extractor and after analyzer. Ion beam current of 3 keV $^{11}B^+$ versus full flux of electronegative gas presented in Fig. 6.

With increase of gas flux the beam intensity increases from 1.3 mA up to 4.2 mA. With increase of gas density an improvement of focusing by neutralizing the repulsing space charge force and attenuation of beam by charge exchange loss of ions is observed. For real improvement a beam transportation- separation electronegative gas should have a high probability of negative ion formation but low cross section for charge exchange for ions of beam

Ion beam instability was dumped by admixture of optimized (Q.>3 sccm) electronegative gas density as shown on Fig.7.

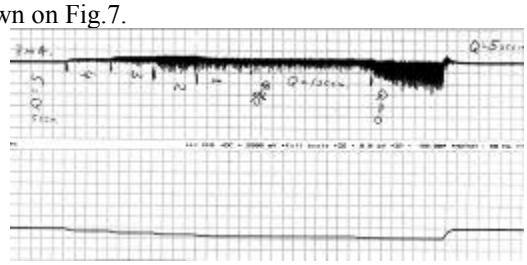

Figure 7: Ion beam current after analyzer with dumping of the beam instability by injection of electronegative gases.

SUMMARY

Space charge neutralization with different plasma sources has been tested: a hollow cathode discharge, RF discharge in the magnetic basket, combination of RF and DC discharge in magnetic field. With all discharges a deep SCN and a low potential of insulated bombarded surface have been reached.

REFERENCES

[1] N. White, et al., patent US 5,350,926, 1997.
[2] N. White, et al., patent US 7,902,527 B2, 2011.
[3] M. Aoki et al., patent US 5,350,926, 1998.
[4] A. Dudnikov, Patent RU 2105368, 1968.
[5] A.Dudnikov, V.Dudnikov, and A.Malinin, 1998. International Congress on Plasma Physics, P2.233, p.467, Prague, Czech Republic, 1998.
[6] A.Dudnikov; V.Dudnikov, Rev. Sci. Instrum. 73, 723 (2002).
[7] G. Gammel et al., Patent US 6,891,173 B2, 2005.
[8] V. Dudnikov; G..Dudnikova, Rev. Sci. Instrum. 73, 726 (2002).
[9] V. Dudnikov et al., Patent US 6,184,532, 2001.

LOW ENERGY COOLER FOR NICA BOOSTER

M. Bryzgunov, A. Bubley*, V. Panasyuk, V. Parkhomchuk, V. Polukhin, V. Reva,
BINP SB RAS, Novosibirsk, Russia

Abstract

Low energy cooler for NICA project is being currently designed at BINP in collaboration with JINR. From the point of view of its features it is similar to previous low energy coolers manufactured at BINP, i.e. equipped with variable electron beam, electrostatic bending, high precision solenoid etc. The article describes some technical solutions applied to the cooler design.

INTRODUCTION

NICA is abbreviation of one of the most challenging recent Russian project in high energy physics [1]. It is going to be largest heavy ion collider ever been built in Russia. It contains a number of complicated systems and subsystems. One of them is heavy ion booster which is located at the existing hall of former synchrophasotron, and new magnetic elements sit inside old giant iron yokes [2]. Low energy cooler is quite important element of the booster which provides sufficient improvement of the ion beam quality.

Main specifications of the cooler are listed below:

ions type	p+ up to $^{197}Au^{31+}$
electron energy, E	1,5 ÷ 50 keV
electron beam current, I	0,2 ÷ 1,0 Amp.
energy stability, $\Delta E/E$	$\leq 1\times10^{-5}$
electron current stability, $\Delta I/I$	$\leq 1\times10^{-4}$
electron current losses, $\delta I/I$	less than 3×10^{-5}
longitudinal magnetic field	0,1 ÷ 0,2 T
inhomogeneity of the field, $\Delta B/B$	$\leq 3\times10^{-5}$
transverse electron temperature	≤ 0,3 eV
ion orbit correction:	
displacement	≤ 1,0 mm
angular deviation	≤ 1,0 mrad
cooling section length (effective),	1940 mm

The requirement for vacuum condition in not very strict (10^{-11} mbar), on the other hand the cooler is the only 'warm' element, since all magnets of the booster are superconductive. This leads to some difficulties in design of junctions of different types of elements.

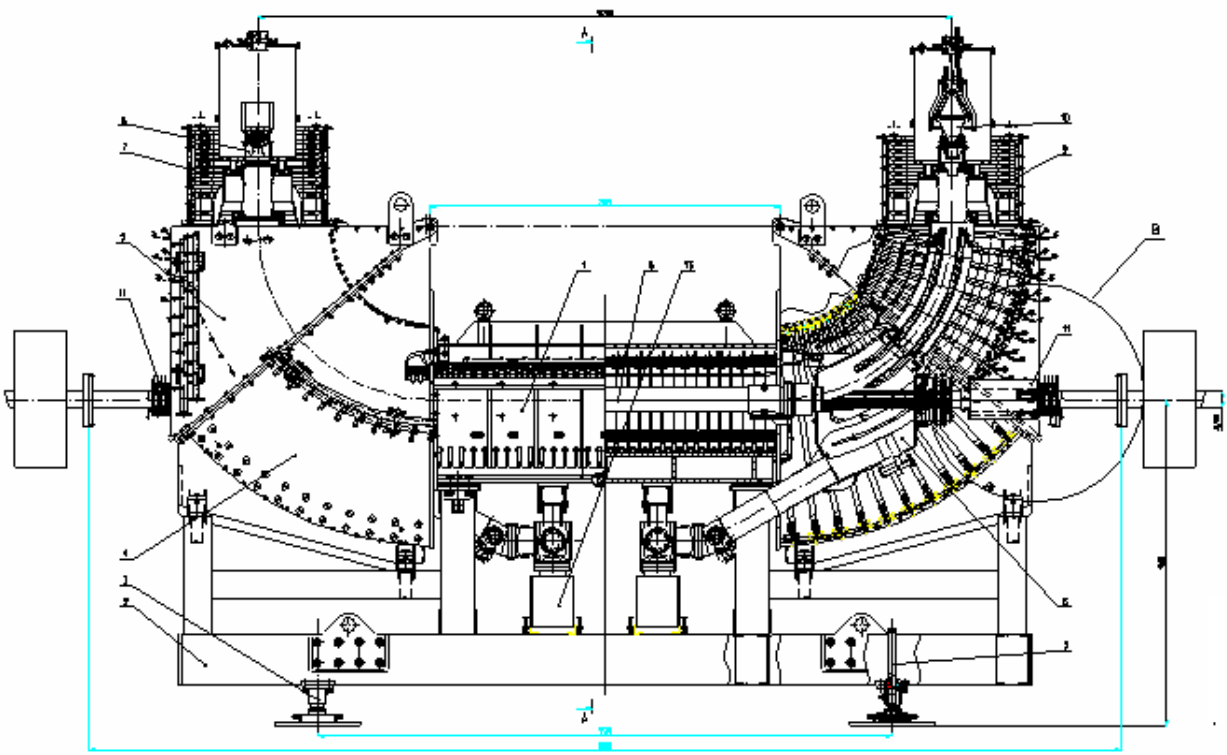

Fig.1 The general layout of the cooler.

COOLING TIME SIMULATIONS

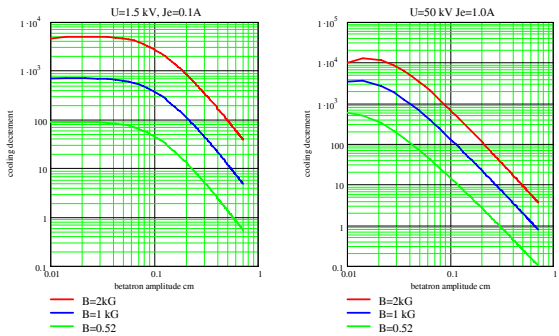

Fig. 2. Comparison of the cooling process for different energies of the electron beam 1.5 kV on the left, 50 kV on the right (electron current 0.1 A).

One can see that it is possible to achieve the cooling time better than 1s for gold ($^{197}Au^{31+}$) ion beam with the emittance of 5 mm×mrad, either for low and high energies. Strong magnetic field, required for the fast cooling, may cause some problems for low energy cooling. This should be studied after the booster optics and magnetic correction is complete.

ELECTRON GUN AND COLLECTOR

The electron gun design is based on the slightly changed gun previously used for CSRe,CSRm [3] and LEIR coolers. The only difference is the four-sector control electrode (fig.3) with separate feeding of all sectors via additional feedthroughs. This small change, nevertheless, opens a new possibility for non-axially modulation of the electron beam profile, which could be used in some applications [4].

One more perspective is to use the gun as 3D kicker [6].

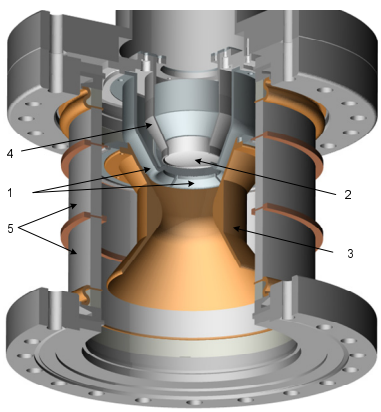

Fig.3 The sketch of the electron gun with four sectors control electrode. 1 – four-sector control electrode, 2 – oxide cathode, 3 – anode, 4 – cathode housing, 5 – ceramics.

Since the electron gun of the cooler is embedded in longitudinal magnetic field, its characteristics depend on field strength. Emissive ability of oxide cathode (2) is about 0.5 A/cm^2, so the maximum possible current is about 3A for 29 mm cathode diameter. Another important characteristic of the gun is the electron transverse temperature, which entirely determines cooling process. One of the tasks for cooler's electron guns design is keeping the transverse temperature as low as possible.

The scheme of the collector is shown on fig. Passing the accelerating tube (1) the electrons go through pre-collector electrode (2) and suppressor (3), after that enter the collector (4). The suppressor electrode forms electrostatic barrier, which catches low energy secondary electrons inside the collector. Its potential is chosen near the cathode potential. Primary electrons slow down quite strongly, and secondary electrons, loosing a part of their energy due to interaction with collector inner surface, are reflected back to collector quite effectively. Pre-collector electrode forms a 'surface' of the potential barrier. Usually it is equal to the collector potential (because of symmetry), but might differs. The coils and magnetic screen generate required shape of magnetic field to distribute the electron flux over collector internal surface [5].

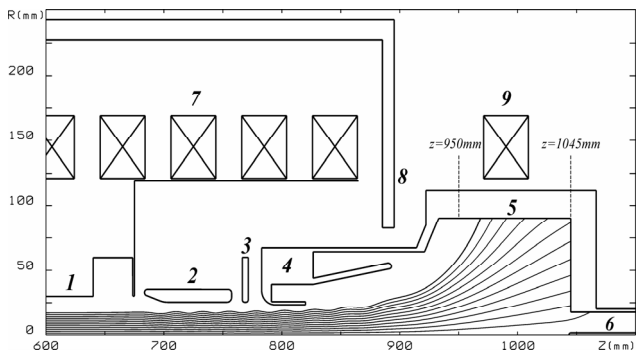

Fig.4. Collector scheme. 1 - accelerating tube, 2 - pre-collector electrode, 3 – suppressor, 4 - collector entrance, 5 - internal surface, 6 - pumping tube, 7 and 9 - coils for longitudinal field, 8 – magnetic screen.

ELECTROSTATIC BENDING

The effectiveness of electron collectors designed at BINP is about $10^{-3} \div 10^{-4}$ that doesn't provide required electron current losses, which is very important for heavy ion rings. To improve the situation the electrostatic bending proposed to be used. Since all reflected electrons are captured with the collector in a presence of the electrostatic drift compensation, current losses are extremely low (tree orders of magnitude less than without it) [8]. On the other hand, the electrostatic plates attract low energy ions originated from residual gas ionisation. This is also quite important to reduce undesirable losses. For example, special electrostatic plates had to be installed at COSY cooler to avoid this [9].

MAGNET SYSTEM

The magnet system of the cooler is similar to other low energy coolers design. The only difference is rather strict requirement for the field homogeneity at cooling section, which is typical for the high energy cooling systems. So some technical solutions of the COSY cooler are going to be applied [9]. Probably, in-vacuum field measurement system has to be installed [7], which is undesirable due to its complicity in operation and an extra space along the ring is required for the measurement equipment.

ACKNOWLEDGMENT

Authors thank the JINR team for the fruitful discussions in all aspects of the Cooler design.

REFERENCES

[1] G. Trubnikov, N. Agapov, V. Alexandrov, et.al., Project of the Nuclotron-Based Ion Collider Facility (NICA) at JINR, Proceedings of IPAC'10, Kyoto, Japan, MOPD011, pp. 693-695.

[2] A. Butenko, V. Volkov, A. Eliseev, et.al., booster synchrotron for the accelerating complex NICA, JINR publication, in Russian.

[3] Bubley, A. Goncharov, A. Ivanov, et al., The Electron Gun with Variable Beam Profile for Optimization of Electron Cooling, Proceedings of EPAC 2002, Paris, France. http://accelconf.web.cern.ch/AccelConf/e02/PAPERS/WEPRI049.pdf

[4] M. Bryzgunov, A. Bubley, A. Ivanov, V. Parkhomchuk, V. Reva, A. Kruchkov. Electron gun with variable beam profile for COSY cooler. Proceedings of COOL'11 // Alushta, Ukraine, September 2011.

[5] M.I.Bryzgunov, A.V.Bubley, V.A.Chekavinskiy, et al. Electron collector for 2 MeV electron cooler for COSY. Proceedings of COOL'11 // Alushta, Ukraine, September 2011.

[6] V.V. Parkhomchuk, V.B. Reva, A.V. Ivanov, Electron Beams as Stochastic 3D Kickers, proceedings of COOL 07, Bad Kreuznch, Germany.

[7] V.N. Bocharov, M.I. Bryzgunov, A.V. Bubley, V.G. Cheskidov, M.G. Fedotov, V.V. Parkhomchuk, V.B. Reva. System of Measurement of magnetic field line straightness in solenoid of electron cooler for COSY. Proceedings of COOL'11 // Alushta, Ukraine, September 2011.

[8] V.Bocharov, A. Bubley et. al., HIRFL-CSR electron cooler commissioning, Nuclear Instruments and Methods in Physics Research A 532 (2004) 144-149

[9] N. Alinovsky, A.M. Batrakov, T.V. Bedareva, et al. The first commissioning results of the high voltage magnetized cooler for COSY. Proceedings of COOL'11 // Alushta, Ukraine, September 2011.

THE KICKER PARAMETERS ESTIMATION FOR LONGITUDINAL INSTABILITY DAMPING OF THE BEAM AT SR STORAGE RING "SIBERIA-2"

A. Smygacheva, A. Vernov, V. Korchuganov
NRC Kurchatov Institute, Moscow, Russia

Abstract

The coupled-bunch instabilities can limit a maximum beam current and lead to a beam loss in some cases at the storage ring "Siberia-2". To cure this problem we have to develop a longitudinal feedback (LFB) system based on a high impedance kicker. In the article a result of the high order mode (HOM) spectrum measurements and the main kicker parameters are presented. Besides, an interaction of the beam with three cavities is considered theoretically.

INTRODUCTION

The RF system of the Kurchatov Institute Synchrotron Radiation storage ring "Siberia-2" consists of three cavities (181 MHz). Each of them has two HOM tuners. The fundamental mode in the cavities is tuned by feedback loops in accordance with a beam loading and temperature changes. The HOM frequencies are not controlled automatically.

Due to a shunt impedance and a quality factor of HOMs are high, the beam-cavity interaction leads to the instability and the beam loss as the result. It is not possible to reduce the HOM influence on the beam motion due to unavailability of the HOM automatic controller and an additional waveguide load for the HOM-damping. To suppress coupled-bunch instabilities we'll plane to establish the longitudinal feedback system at the storage ring. For example of the longitudinal kicker, a model of the DUKE kicker cavity will be taken.

LONGITUDINAL MOTION

For estimation of the HOM influence on the beam motion it is convenient to consider a circulating electron beam. Each bunch of the beam, represented as macroparticle, performs the small dipole synchrotron oscillations

$$\ddot{\varphi} + 2\alpha\dot{\varphi} + \omega_s^2\varphi = 0,$$

where ω_s is the synchrotron frequency, α is the growth rate. The stability synchrotron motion is determined by a sign of the growth rate, which consist of

$$\alpha = \alpha_{rad.} + \alpha_{rf} + \alpha_{kick.},$$

$\alpha_{rad.}$ is the synchrotron radiation growth rate, α_{rf} is the instability growth rate due to HOMs, $\alpha_{kick.}$ is the growth rate of the LFB system. If the growth rate, α, is positive, the longitudinal motion is stable. The sign of α_{rf} is depend on whether the Robinson stability condition is satisfied [1].

The radiation damping is small to compensate the harmful HOM influence. The necessary damping is set by the LFB system. The coefficients of α_{rf} and $\alpha_{kick.}$ [2] are expressed as

$$\alpha_{rf} = -\frac{e}{2T_0E_0}\alpha_c \sum_{p=1}^{+\infty} \frac{2I_p^2}{I_0}\frac{p\omega_0}{2\omega_s}(Z_r^+ - Z_r^-),$$

$$\alpha_{kick} = \frac{1}{2}f_0\frac{V_{kick}}{\Delta E},$$

where f_0 - the revolution frequency, E_0 - the beam energy, α_c - the momentum compaction factor, I_0 - the average beam current, I_p - the harmonic beam current, V_{kick} - the kicker voltage, ΔE - the maximum energy oscillation amplitude, $Z_r^+ \, u \, Z_r^-$ - the real parts of the HOM impedance at $p\omega_0 + \omega_s$, $p\omega_0 - \omega_s$ frequencies, respectively.

In our case at the storage ring there are three cavities, then α_{rf} has additional terms under the sum

$$\alpha_{rf} = -\frac{e}{2T_0E_0}\alpha_c \sum_{p=1}^{+\infty} \frac{2I_p^2}{I_0}\frac{p\omega_0}{2\omega_s}[(Z_r^+ - Z_r^-)\cdot (1 + \cos\omega_s\tau_{12} + \cos\omega_s\tau_{13}) + (-2Z_i^0 + Z_i^+ + Z_i^-)\cdot (\sin\omega_s\tau_{13} + \sin\omega_s\tau_{12})].$$

where τ_{12} and τ_{13} - the time of the bunch passage from the first cavity to the second and the third, respectively. If to take into account the parameters of the high order mode of all cavities are the same and the passage time is small, then the HOM influence on the beam motion is increased in three.

To damp the instabilities, the energy kick should be applied to each bunch of the beam. The necessary output kicker voltage is limited by the amplifier power [3]

$$V_{kick} = \sqrt{2P_{out}R_{sh}},$$

where P_{out} - the maximum output power of the amplifier, R_{sh} - the effective shunt impedance of the kicker cavity.

We should take into account a RF power loss between the amplifier and the LFB kicker, a group delay, a nonlinearity of the phase and gain of the LFB system, to calculate the kicker voltage. Hence, the estimated amplifier power should be taken larger, then it is necessary in practice [4].

MEASUREMENTS

The RF cavities of "Siberia-2" have bimetal walls, 7 mm of the stainless steel and 8 mm of the copper. The design of the RF cavity is presented in Fig. 1. Each of them has a water cooling channel located in a surface layer of the steel. In the design there are two operating mode frequency tuners (1), two HOM tuners (2), a inductive RF probe for the gap voltage measurements (3), a coaxial input power coupler (4) and a flange for the vacuum pump (5). The cavities operate in the TM_{010} mode.

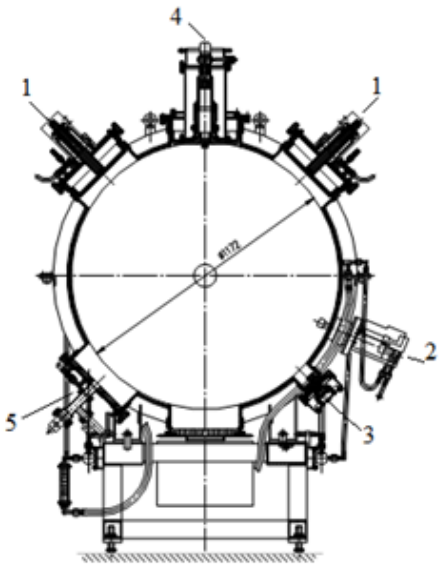

Fig. 1: Design of the RF cavity of "Siberia-2".

To found the most dangerous HOMs the field spectrum measurements were made with a wideband (up to 13.5 GHz) spectrum analyzer. The experiments were conducted at the energy 450 MeV and 2.5 GeV with a different distribution of the bunches. For measurements the signals from coupling loops in the cavities were used. The picture of the field spectrum of each cavity is given in Fig. 2.

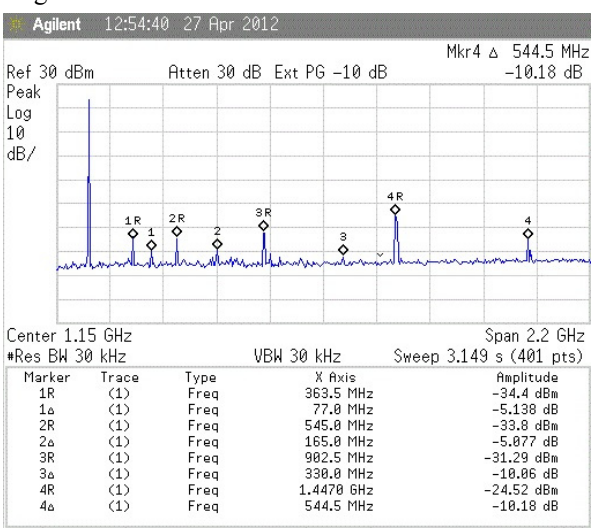

a.

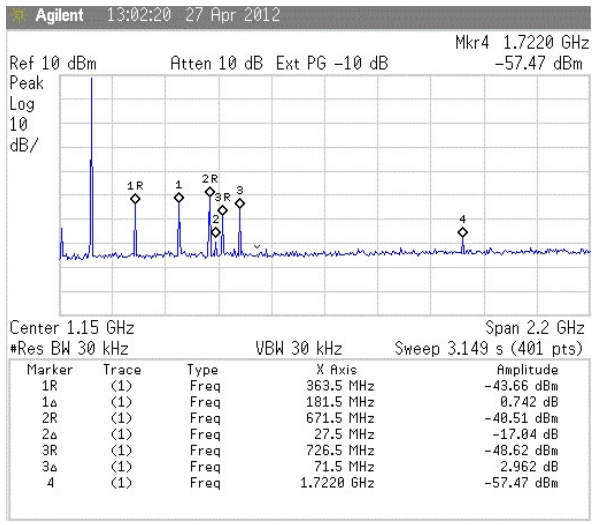

b.

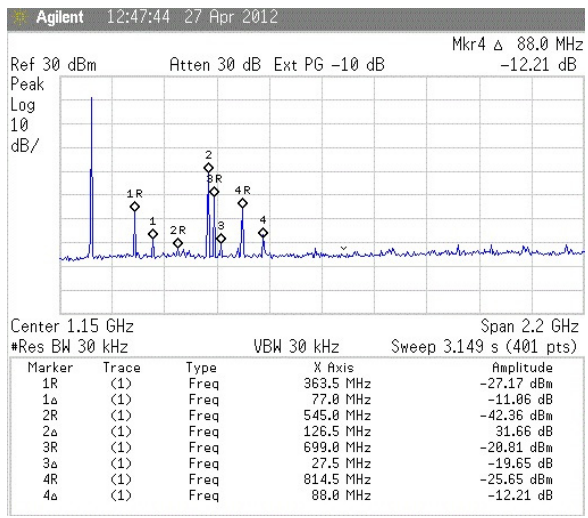

c.

Fig. 2: The field spectrum in cavities: a. - the first, b. - the second, c. - the third. The electron beam energy is 2.5 GeV, the total beam current is 39.45 mA.

The coupled-bunch instabilities limit the beam intensity. It depends on a kind of the coupled mode some bunches loss the particles on the vacuum chamber walls. It is illustrated in Fig. 3. To cure this problem we need to establish the LFB system.

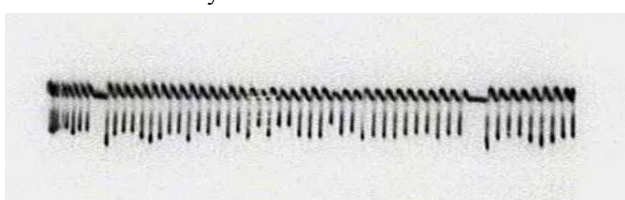

Fig. 3. The circulating electron beam of the 36 bunches.

The measurements allowed to found a constant set of HOMs, generated by the different distribution beam, and an independence of the frequency spectrum from the energy. The comparison of the results with cool

measurements of the cavities allowed to determine the most strong HOMs in the frequency range from 300 MHz to 1600 MHz.

LONGITUDINAL KICKER

To estimate the necessary kicker parameters we took the model of the DUKE kicker as an example. It was re-simulated by means of a special program. The kicker has a frequency $5.25f_{RF}$, a quality factor - 10.6, a bandwidth - 90 MHz. The calculation gave the value of the effective shunt impedance about 1255 Ω for the aluminum walls of the kicker and the transit time factor is 0.698.

To define the amplifier power, we have calculated the instability growth rate due to HOMs.

The parameters of the storage ring "Siberia-2" are given in Table 1.

Table 1: The storage ring parameters

Energy, MeV	450
Operating energy, GeV	2.5
Beam current, mA	300
Revolution frequency, MHz	2.415
RF frequency, MHz	181.125
RF voltage, kV	380
Synchrotron frequency, kHz	24.6
Number of bunches	75
Momentum compaction factor	0.0104

The calculations were performed for the Gauss bunches, interacting with the found set of the most harmful HOMs of all cavities. The results, according to a bunch length, are given in Table 2. For "Siberia-2" at 450 MeV, a dependence of the bunch length of a single-bunch current can be calculated as

$$\sigma_p\ [ps] \approx 54.5 \cdot I_b^{1/3}\ [mA],$$

where I_b is the single-bunch current.

Table 2: The instability growth rate

I_b, mA	σ_p, ps	α_{rf}, 1/c
4	86.5	736.8
12	124.8	729.4
20	148.0	696.1

The LFB system will be designed for a total multi-bunch current of 300 mA. It should be effective for a wide range of bunch length. Hence, to damp the HOM influence of three cavities the power amplifier of 200 W is enough for the beam current of 300 mA and a bunch length of 148 ps.

CONCLUSIONS

To study the beam-cavity interaction the dipole synchrotron bunch oscillation model was used. The influence of HOMs of the RF cavity was calculated. The basic kicker parameters estimation was presented. To damp the longitudinal instabilities for the presented kicker model we'll plane to take two power amplifier of 100 W.

REFERENCES

[1] A. Hofmann, "Beam instabilities", CERN Accelerator School 95-06, 1996.

[2] M. Basseti et al., "DAΦNA longitudinal feedback", in: Proceeding of the EPAC1992, Berlin, Germany, 1992.

[3] W.Z. Wu et al., "Development of a bunch-by-bunch longitudinal feedback system with a wide dynamic range for the HIGS facility", Nucl. Instr. and Meth. A, Vol 632, p. 32-42 (2011); www.elsevier.com.

[4] M. Lonza, "Multi-bunch feedback systems", Elettra Synchrotron Light Laboratory, Trieste, Italy.

[5] R. Bailey, Proceedings of the CAS-CERN Accelerator School: RF for accelerators, Ebeltoft, Denmark, 8-17 June 2010, CERN-2011-007.

STUDY OF PROTON INJECTOR BEAM TRANSVERSE PHASE SPACE VARIATIONS DURING ACCELERATING VOLTAGE PULSE

A.S.Belov, O.T.Frolov, E.S.Nikulin, V.P.Yakushev, and V.N.Zubets,
Institute for Nuclear Research of RAS, Moscow, 117312, Russia

Abstract

The proton injector of INR RAS linac provides a pulsed beam with the following parameters: current – 100÷120mA; duration – 200 μs; pulse repetition rate – 50 Hz; energy of ions – 400 keV. The results of numerical calculations and experimental studies of beam phase space variations during injector high voltage pulse are presented. It is shown that these variations are caused by instabilities of both beam current and accelerating tube intermediate electrode potential. Instability of beam current has been minimized by using of noiseless mode of operation for the pulsed duoplasmatron and by stabilization of ion source discharge current. The high voltage pulse stability has been improved and is now better than ±0.1%. For the most part of beam pulse duration a transverse normalized emittance for 90% of beam current has been measured to be of 0.09π cm·mrad and variations of the emittance are in limits of ±4% value.

INTRODUCTION

INR RAS linear accelerator proton injector is operated regularly from the end of 80-ies. And the work on its improvement is in progress all the recent years. The basic conditions of beam loss minimization in linac are as more as possible smaller transverse emittance and stability of beam phase portrait position. After installing a new expander cup isolated from duoplasmatron the beam transverse normalized emittance of 0.076π cm•mrad for 63% of central part of the 115 mA beam has been measured at the injector output in noiseless mode and 0.2π cm•mrad for 90% of the beam, respectively [1].

A number of measurements and numerical simulation of injector ion beam formation and transport to the linac LEBT input have been performed. Significant changes in the beam phase portrait position/shape have been found as a result of calculations and beam emittance measurements. In the past two years the injector structure has undergone further modifications which have improved qualitative characteristics of the beam.

NUMERICAL SIMULATION

Numerical simulation using Trak and TriComp SpaceCharge package developed Field Precision LLC has been conducted. Schematic drawing of the proton injector is shown in Fig.1. A beam of hydrogen ions is generated in duoplasmatron type ion source. The beam is accelerated and focused in two-gap accelerating tube by the electric fields between the ion source focusing electrode, intermediate and output (grounded) accelerating tube electrodes.

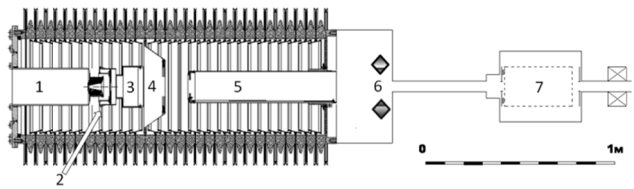

Figure 1. Schematic drawing of the proton injector:
1 - ion source, 2 – extracting electrode, 3 - focusing electrode,4 - intermediate electrode, 5 - grounded electrode, 6 – steering magnet, 7 – diagnostics box.

Simulation have shown that changing of the intermediate electrode potential by a value less than 1% already leads to significant changes in beam properties at the injector output. The example of calculations result is shown in Fig. 2.

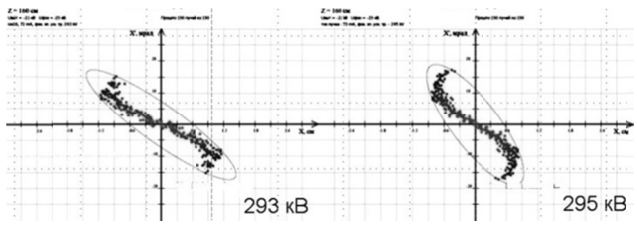

Figure 2. The influence of intermediate electrode potential value on position/shape of the injector output beam phase portrait. Intermediate electrode potential equals 293 kV and 295 kV.

Agreement between simulation and measurement is particularly evident when considering the various aberrations of beam. One of the aberration types studied is shown Fig.3.

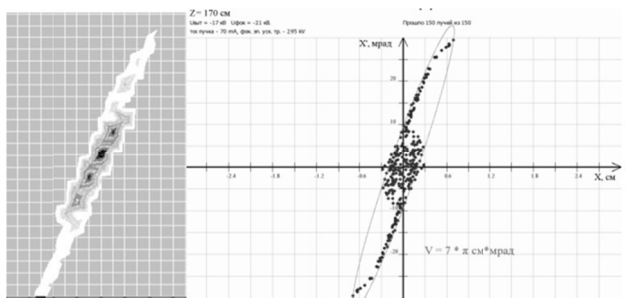

Figure 3. One of the phase portrait aberration types studied when transporting hydrogen ions beam
(left - measurement, right - simulation)

STRUCTURAL CHANGES AND RESULTS

It has found that the causes of observed position/shape phase portrait changes during high voltage injector pulse are mainly the intermediate electrode potential changes and instability of proton beam current.

To reduce the intermediate electrode potential changes during high voltage pulse the compensated high voltage divider has been installed at the injector accelerating tube. Initially a chain of the 28 680pF×20kV capacitors has been mounted in parallel to the existing water resistive divider. Later another chain of seven 200pF×20kV capacitors has been added at initial part of the accelerating tube from high voltage electrode to intermediate one.

To increase the stability of the beam current during the pulse and pulse-to-pulse stability the transistor stabilized arc modulator (instead of the thyristor unit based on artificial line) with ±0.5% discharge current stability along the pulse has been developed and placed in operation.

As a result, the stability of the beam current pulse plateau has been increased (Fig.4). Beam emittance for 63% of the 115mA beam has been measured of 0.07π cm•mrad and 0.17π cm•mrad for 90% of the beam.

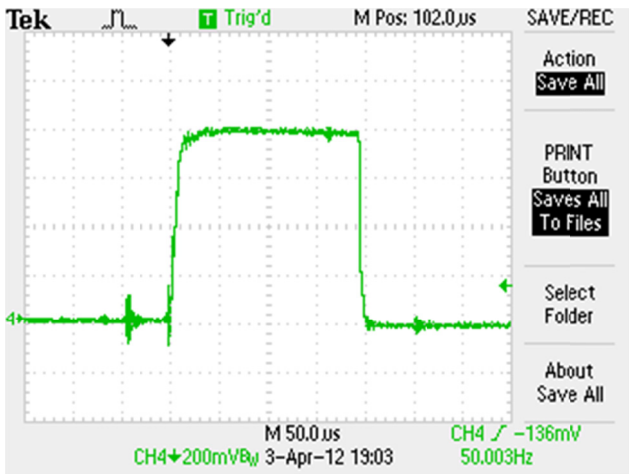

Figure 4. Ion beam current shape at injector output.

Studies of changes of the phase portrait parameters during 200 µs accelerating voltage pulse have been carried out. Duoplasmatron arc modulator has produced a 25 µs duration beam supplying into the injector with multiple of 25 µs different delays relative to beginning of the high voltage pulses .

It has found that the beam phase portrait turns through an angle of $\Delta\xi \approx 14°$ during 200 µs pulse length. This angle is twice smaller than before installation of the compensated divider and the stabilized discharge current modulator [2].

In recent times some efforts have been made to improve the injector accelerating voltage stabilization:

- characteristic impedance of the high voltage pulse generator artificial line has been reduced thus increasing current in the capacity-diode stabilizer;
- high frequency component of the capacity-diode stabilizer current has been filtered;
- a part of saw-shaped voltage amplitude with greater degree of linearity than earlier has been used when compensating the pulse plateau slope.

Some of emittance measurement results are shown in Fig.5, 6.

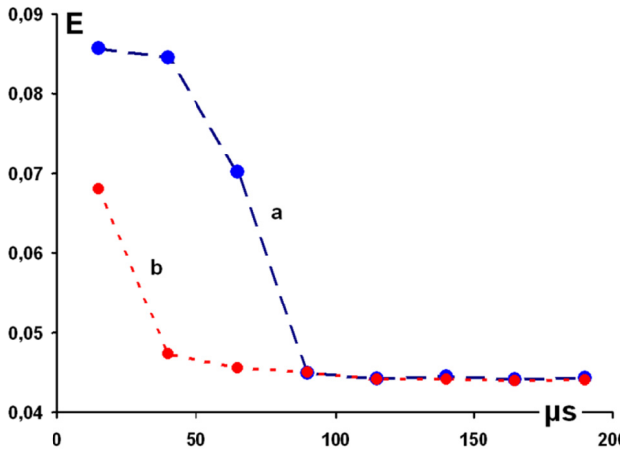

Figure 5. A 25 µs duration beam emittance dependence on multiple of 25 µs different delays along high voltage pulse when installing transistor arc modulator:

a) non-compensated divider;
b) compensated divider and improved accelerating voltage pulse plateau stabilization.

Results of the accelerating voltage pulse plateau stability improvements are shown in Fig. 7.

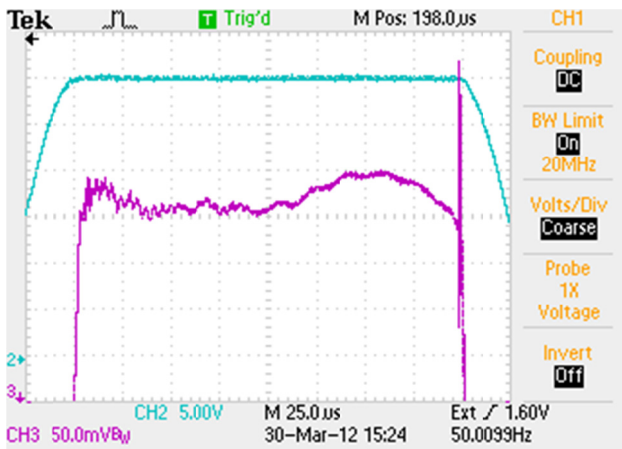

Figure 7. The accelerating voltage pulse shape: upper curve - total amplitude (30 V), lower curve - top of the pulse.

From our measurements it follows that stability of the accelerating voltage pulse plateau is now better than ±0.1% instead of the previous ±0.2% value. Emittance of 100÷105 mA beam for 63% of the beam has remained at the same values and, in fact, is now close to a value of beam emittance in the first few tens of microseconds. For the greater part of the injector pulse beam length, namely

for $\tau = 25 \div 200\mu s$, its value does not exceed 0.05π cm•mrad and for 90% of the beam emittance has reduced to 0.09π cm•mrad. It should be noted particularly that rotation of axis of ellipse described by the phase portrait has decreased to $\Delta\xi = 10°$.

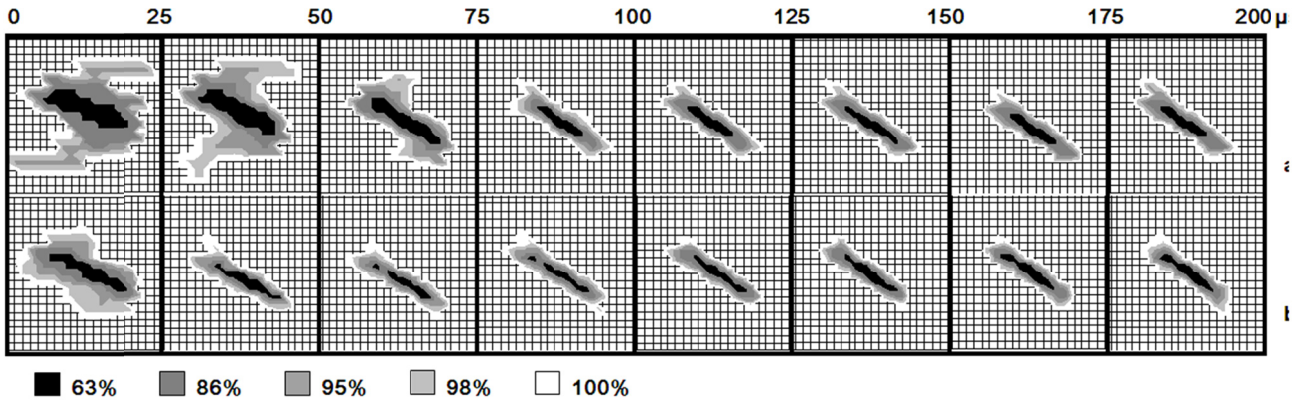

Figure 6. The beam phase portraits when scanning along high voltage injector pulse duration:
a) non-compensated divider;
b) compensated divider and improved accelerating voltage pulse plateau stabilization.

CONCLUSIONS

Due to installation of the accelerating tube compensated divider, stabilizing of duoplasmatron discharge current and improvements conducted to increase accelerating voltage stability the beam emittance and rotation of the phase portrait during beam pulse have been decreased.

Both compensated accelerating tube divider high voltage shape and beam current shape have become close to trapezoidal one with flat plateau throughout injector pulse. Stability of ion beam current throughout the injector pulse and pulse-to-pulse stability have been improved.

A satisfactory agreement of beam parameters measurements and numerical simulation has been achieved.

ACKNOWLEDGMENTS

We'd like to thank A.V.Feschenko and V.L.Serov for useful discussions, L.P.Nechaeva, N.I.Semenov and A.V.Turbabin for help in design and construction of the apparatus, Yu.V.Kiselev and A.N.Drugakov for participation in emittance measurements.

REFERENCES

[1] A.S.Belov et al. Study of the INR RAS Linac Pulsed Duoplasmatron. Proc. of RUPAC-2010, Protvino, Russia,pp.289-291, http://www.accelconf.web.cern.ch/accelconf/r10/papers/thchb01.

[2] A.S.Belov et al. The INR of RAS Proton Linac Injector Beam Study // Problems of atomic science and technology. Series "Nuclear Physics Investigations" http://vant.kipt.kharkov.ua›ARTICLE/VANT_2012_3/article_2012_3_44.pdf

SECOND-ORDER CORRECTION IN THE ISOCHRONOUS MODE OF THE COLLECTOR RING (CR) AT FAIR

S. Litvinov, C. Dimopoulou, A. Dolinskii, O. Gorda, F. Nolden, M. Steck, H.Weick
GSI, Darmstadt, Germany

Abstract

A challenge for nuclear physics is to measure masses of exotic nuclei up to the limits of nuclear existence which are characterized by low production cross-sections and short half-lives. The large acceptance Collector Ring (CR) [1] at FAIR [2] tuned in the isochronous ion-optical mode offers unique possibilities for such measurements. However, the mass-measurement resolution is inversely proportional to the transverse emittance. In order to reach a resolving power of 10^5 the transverse beam emittance would have to be limited up to 10 mm mrad in both planes, which drastically reduces the transmission of the exotic nuclei. We demonstrate here that the negative influence of the transverse emittance on the mass resolution can be significantly reduced by a proper second-order correction.

Isochronous Mode of the CR

The Collector Ring of the FAIR project is a symmetric, achromatic ring with two arcs, two straight sections and a total circumference of 221.5 meters. It is designed for operation at a maximum magnetic rigidity of 13 Tm. The CR will be operated in three ion-optical modes, two of them providing fast pre-cooling of either antiprotons or radioactive ion beams [1]. In the third mode (isochronous optics) the CR will be operated as a Time-Of-Flight (TOF) spectrometer for the mass measurement of exotic very short-lived nuclei ($T_{1/2} > 20\mu s$) produced and selected in flight with the Super-FRS fragment separator [3]. This technique for mass measurements has been developed at the ESR at GSI [4]. An advantage of this method is that a large number of nuclei can be measured in one experimental run.

The relative change of revolution time T due to different mass-to-charge ratio m/q and velocity v of the stored ions circulating in the ring is [5]:

$$\frac{\Delta T}{T} = \frac{1}{\gamma_t^2} \cdot \frac{\Delta(m/q)}{(m/q)} + \left(\frac{\gamma^2}{\gamma_t^2} - 1\right)\frac{\Delta v}{v} - \frac{dT}{T}, \quad (1)$$

where γ is the relativistic Lorentz factor and γ_t is the transition energy of the ring. The isochronous condition is reached when $\gamma = \gamma_t$. It means, the second term in Eq. (1) vanishes and T defines the m/q. The resolution depends on the width of the time dT. Effects of nonlinear field errors, fringe fields of magnets, closed orbit distortion and transverse emittance negatively act on dT. Their influence has been investigated in [5].

Ions with different m/q are separated in time if their mean time separation ΔT is larger than the full time width of the beam.

$$\Delta T > dT. \quad (2)$$

Influence of Transverse Emittance

For good adjustment of γ_t the largest contribution to dT comes from the second-order geometric aberrations. In order to distinguish their influence, we consider a beam of one species in the ideal isochronous ring without higher-order field errors, fringe fields and closed orbit distortions. Only pure betatron motion exists. For such a ring the time spread is directly related to the transverse emittance ($\varepsilon_{x,y}$) [5]:

$$\left(\frac{dT}{T}\right)_{Emitt.} \approx \frac{1}{4}\left(\varepsilon_x <\gamma_x^{\text{Twiss}}> + \varepsilon_y <\gamma_y^{\text{Twiss}}>\right), \quad (3)$$

where $<\gamma_{x,y}^{\text{Twiss}}>$ are the Twiss parameters averaged over the whole circumference of the ring.

Thus, from Eqs. (1, 3) one can derive the mass resolving power depending on the beam emittance [5]. For the CR, where acceptance is 100 mm mrad in both planes, the limit of the mass resolving power is about 10^4, which is insufficient for precise mass measurements. Therefore, in order to reach the necessary resolving power of 10^5 the transverse emittance would have to be limited to 10 mm mrad in both planes. As a result, the transmission of the ions into the ring would be reduced drastically.

Revolution Time in Second-Order

However, the mass resolving power can be improved using second-order corrections and keeping the transverse emittance large. Let us assume a beam of one species circulating in the ring turn by turn. We observe it in the symmetry plane of the ring where the phase-space ellipse is upright ($\alpha^{\text{Twiss}} = 0$) and this condition is restored after each turn.

Statistical uncertainty gets reduced with increasing number of revolutions, and for accurate mass measurements it is essential to measure the revolution time of the particle over many turns. Therefore, the relative revolution time deviation between an arbitrary and the reference particle can be expressed in terms of the initial coordinates as a Taylor

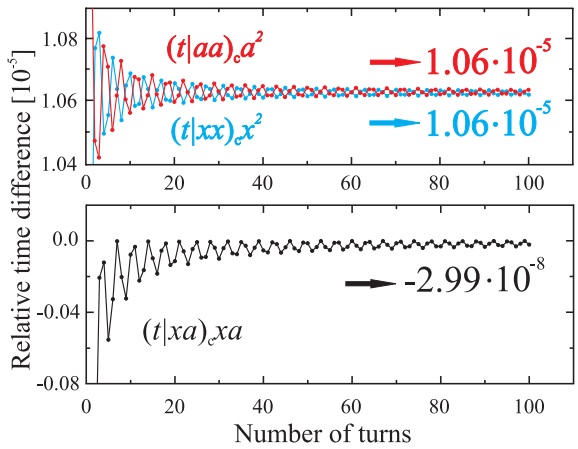

Figure 1: Evolution of the relative second-order geometric aberrations as a function of the number of turns in the CR. The aberrations $(t|xx)_c x^2$, $(t|xa)_c xa$, $(t|aa)_c a^2$ are marked in blue, black and red colors, respectively. The inserted numbers show the limit over many turns.

series in a second-order approximation [6, 7]:

$$\frac{dT}{T} = \frac{T - T_0}{T_0} = (t|x)_c x + (t|a)_c a + (t|\delta)_c \delta + (t|xx)_c x^2 + \\ + (t|xa)_c xa + (t|aa)_c a^2 + (t|yy)_c y^2 + (t|yb)_c yb + \\ + (t|bb)_c b^2 + (t|x\delta)_c x\delta + (t|a\delta)_c a\delta + (t|\delta\delta)_c \delta^2, \quad (4)$$

where (x, y) are the transverse coordinates and (a, b) their derivatives with respect to the longitudinal coordinate s. The index c stamps for the coefficients normalized by the total time-of-flight $t = nT_0$, where n is the number of turns. The fractional momentum deviation δ is given by $p = p_0(1 + \delta)$. T_0 and p_0 are the revolution time and the momentum of the reference particle, correspondingly.

In the first-order achromatic ring the first-order transverse matrix elements $(t|x)$ and $(t|a)$ simultaneously vanish [7, 8]. The necessary condition to be an isochronous ring in the first-order is $(t|\delta) = 0$ i.e. $\gamma = \gamma_t$. The second-order isochronous condition is fulfilled when $(t|\delta\delta) = 0$, which can be corrected with one family of sextupole magnets installed in a dispersive section of the ring. The mixed aberrations $(t|x\delta)_c x\delta$ and $(t|a\delta)_c a\delta$ usually do not contribute much to the revolution time. Their influence is negligible and we can skip them here.

Therefore, only the second-order geometric aberrations in time of Eq. (4) are significant. Without correction their contribution corresponds to the right part of Eq. (3) i.e. the transverse emittance. For simplicity we inspect only the horizontal plane, the arguments for the vertical plane are the same.

Geometric Aberrations and Chromaticity

The matrix elements $(t|xx)$, $(t|xa)$ and $(t|aa)$ can be expressed for the achromatic ring as [7, 9]:

$$(t|xx) = \lambda \cdot [(x|x)(a|x\delta) - (a|x)(x|x\delta)], \quad (5)$$
$$(t|xa) = \lambda \cdot [(x|x)(a|a\delta) - (a|x)(x|a\delta)], \quad (6)$$
$$(t|aa) = \lambda \cdot [(x|a)(a|a\delta) - (a|a)(x|a\delta)], \quad (7)$$

where λ is a constant with the dimension of inverse velocity. The coefficients in Eqs. (5-7) correspond to the terms of the transfer matrix M, which for the full circumference can be expressed by the betatron functions $\beta(s), \alpha(s)$ and the betatron phase advance $\mu(s)$:

$$M = \begin{pmatrix} \cos\mu & \beta \sin\mu \\ -\frac{1}{\beta}\sin\mu & \cos\mu \end{pmatrix} \equiv \begin{pmatrix} (x|x) & (x|a) \\ (a|x) & (a|a) \end{pmatrix}, \quad (8)$$

Due to the oscillatory character of betatron motion the coefficients $(t|xx)_c$, $(t|xa)_c$, $(t|aa)_c$ fluctuate with the number of turns and after many revolutions average out (see Fig. 1). The aberration $(t|xa)_c xa$ becomes negligible. $(t|xx)_c x^2$ and $(t|aa)_c a^2$ aberrations become equal at a constant value, which can be explained by the mirror symmetry [10].

The terms $(x|a\delta)$ and $(a|x\delta)$ are connected via [9]:

$$(x|a\delta)(a|x) = (x|x)(a|a\delta) - (a|x\delta)(x|a) + (x|x\delta)(a|a). \quad (9)$$

Combining Eqs. (5, 7-9) we obtain:

$$(t|aa) + \beta^2 (t|xx) = \frac{\lambda\beta}{sin\mu}[(x|x\delta) + (a|a\delta)]. \quad (10)$$

On the other hand the relative natural chromaticity ξ_{1x} can be written as (see appendix):

$$\xi_{1x} = -\frac{1}{4\pi Q_{0x} sin\mu} \cdot [(x|x\delta) + (a|a\delta)], \quad (11)$$

where Q_{0x} is the tune of the ring. Therefore, combining Eqs. (10, 11) one gets:

$$(t|aa) + \beta^2 (t|xx) = -4\pi\lambda\beta Q_{0x}\xi_{1x}. \quad (12)$$

The β is constant at the symmetry point and due to $\alpha^{\text{Twiss}} = 0$ it can be expressed as $\beta = x/a$ and $\pi\varepsilon_x = \pi xa$. Then Eq. (12) can be written as:

$$(t|aa)a^2 + (t|xx)x^2 = -4\pi\lambda\varepsilon_x Q_{0x}\xi_{1x}. \quad (13)$$

In general, due to the mirror symmetry two chromatic matrix coefficients coincide in the achromatic ring: $(x|x\delta) = (a|a\delta)$ [11]. The natural chromaticity can be corrected using one family of sextupole magnets and therefore, we can reach a regime where the $(t|xx)$ and $(t|aa)$ contribution vanishes and in the limit of many turns the isochronous ring turns into a second-order achromatic system [12, 13].

Monte-Carlo Simulation

To check the analytic derivation described above a dedicated Monte-Carlo simulation has been performed with the program MOCADI [14]. In this program an ion-optical system is described by third-order transfer matrices which have been calculated with the GICOSY code [15].

In the simulations we have used a beam of 10^5 particles of one species with transverse emittance of 100 mm mrad

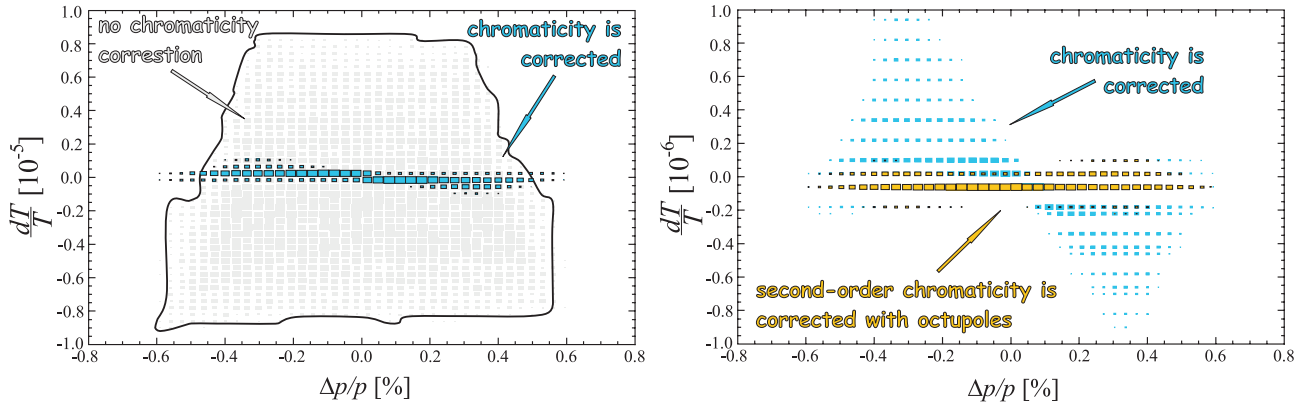

Figure 2: The revolution time spread as a function of the momentum deviation.

in both planes circulating 100 turns in the CR. The dependence of the revolution time spread on the momentum deviation in the ring has been calculated.

At first, we have corrected only the second-order isochronicity with one sextupole family (grey distribution in Fig. 2). Then, the natural chromaticity $\xi_{1x,y}$ with two additional sextupole families has been corrected (blue distribution in Fig. 2).

Moreover, applying the octupole magnets in the same manner as sextupoles, we have corrected third-order isochronicity ($(t|\delta\delta\delta) = 0$) and second-order chromaticity ($\xi_{2x,y}$) with three octupole families (yellow distribution in Fig. 2).

The broad grey time distribution in the left picture of Fig. 2 is governed by the large transverse emittance and corresponds to about $1.7 \cdot 10^{-5}$ in time resolution (or about $2 \cdot 10^{-4}$ of mass resolving power). By correcting in addition the natural chromaticity (blue distribution in the left picture of Fig. 2) the influence of the transverse motion is significantly reduced and a resolution of up to $dT/T \approx 2 \cdot 10^{-6}$ (or $m/\Delta m \approx 2 \cdot 10^{5}$) in the full momentum acceptance range can be achieved. Applying in addition the octupole correction (see the yellow distribution on the right picture in Fig. 2) one can reach a resolution of up to $dT/T \approx 3 \cdot 10^{-7}$, which corresponds to the mass resolving power of about 10^6.

Appendix

The phase advance μ can be expanded with respect to δ as [16]:

$$\mu = \sum_{n=0}^{\infty} \mu_n \delta^n, \quad \text{or} \quad cos\mu = \sum_{n=0}^{\infty} \chi_n \delta^n. \qquad (14)$$

Since $\cos\mu$ is the trace of the transfer matrix M (see Eq. 8), which can also be expanded with respect to δ one can obtain $\chi_n = 0.5 \cdot \mathrm{Tr}(M_n)$, where M_n is:

$$M_n = \begin{pmatrix} (x|x\delta^n) & (x|a\delta^n) \\ (a|x\delta^n) & (a|a\delta^n) \end{pmatrix}, \; n = 0,\ 1,\ 2,\ 3, .. \quad (15)$$

Thus, from Eqs. (14,15) one can extract the phase advance described in matrix coefficients and correspondingly obtain the chromaticity:

$$\xi_x = \frac{1}{\delta} \cdot \frac{\Delta Q}{Q_0} = \frac{\Delta\mu}{2\pi\delta Q_0} = \frac{1}{2\pi Q_0} \sum_{n=1}^{\infty} \mu_n \delta^{n-1}. \qquad (16)$$

REFERENCES

[1] A. Dolinskii et al., EPAC Proceedings, 572-574 (2002).

[2] FAIR Baseline Technical Report, GSI, Darmstadt, 2006, http://www.fair-center.de

[3] H. Geissel et. al., NIM B204, 71-85 (2003).

[4] M. Hausmann et. al., NIM A 446, 569-580 (2000).

[5] A. Dolinskii et al., NIM A 574, 207-212 (2007).

[6] D. C. Carey, "The optics of charged particles beams", Harwood Academic Publisher, New York (1987).

[7] M. Yavor, "Optics of Charged Particle Analyzers", Advances in Imaging and Electron Physics vol. 157, Elsevier Inc., 2009.

[8] H. Wiedemann "Particle Accelerator Physics I (Basic Principles and Linear Beam Dynamics)", Springer-Verlag, Berlin, Heidelberg, New York (1998).

[9] H. Wollnik, "Optics of charged particles", Academic Press, Florida (1987).

[10] M. Yavor, Private Communications.

[11] B. Erdelyi et al., Physical Review Special Topics - Accelerators and Beams 10, 064002 (2007).

[12] K. L. Brown, PAC Proceedings, 3490-3492 (1979).

[13] D. C. Carey, NIM 189, 365-367 (1981).

[14] N. Iwasa et al., NIM B 126, 284-289 (1997), http://www-linux.gsi.de/∼weick/mocadi/

[15] H. Wollnik et al., AIP Proceedings, 177, 74-85 (1988), http://www-linux.gsi.de/∼weick/gicosy/

[16] M. Takao et al., Physical Review E 70, 016501 (2004).

THE MOTION OF IONIC FLUX IN AN ELECTRON LAYER

A.S.Chikhachev, Yu.A. Kovalenko
All-Russian Electrotechnical Institute,
111250, Moscow, Russia

Abstract

An acceleration of ion flux in an electronic layer is studied beam in electron layer are studied. The layer is created by electrons that move in transverse electric field and are confined by self-generating magnetic field. It is shown that from such one can extract heavy ions with the velocities up to ion-sound velocity.

INTRODUCTION

The process of extraction of ions from plasma is very important in terms of experiment. A great number of theoretical studies are dedicated to this process. The paper [1] shows that ions leave plasma at velocities which are in excess of ionic sound velocities.Under conditions close to be actual environment when the temperature of electrons is above that of ions ($T_e >> T_i$), the number of ions being accelerated turns out to be exponentially small. The paper [2] deals with the process of accelerating ions in a non-stationary problem. The paper [3] discloses that a transition layer in the plasma-vacuum system appears out to be infinitely large. The paper [4] considers equilibrium conditions with the presence of an electron flow that is directed in line of an ionic flux. This paper deals with equilibrium states when a non-zero flow of electrons is perpendicular to across an ionic flux.

IONIC FLUX STATES IN AN ELECTRON LAYER

Let us assume that at $x = 0$ there is given an ionic flux with a negligible ($\sim v_{Ti}$) initial velocity v_0. We consider 1-D problem where physical quantities are independent of coordinates y and z. The magnetic field has only one component $B_z = -\frac{dA_y}{dx}$, where A_y is a component of a $4-D$ potential. This a magnetic field is induced by the electron flow along the y axes. The electrons move in the x, y plane under the action of electric end magnetic fields with $v_z^{(e)} \equiv 0$. We describe ensemble of electrons by means of a collisionless kinetic equation. A solution of this equation may be form of an arbitrary function of motion integrals: energy H and generalized momenta $P_y = p_y - \frac{e}{c}A_y(x)$ and $P_z = p_z$. Here p_y, p_z - are components of an electron momentum. We take a distribution function in following form:

$$f(\vec{p},\vec{r}) = \Psi(H, P_y, p_z) = \kappa\frac{\sigma(H_0 - H)}{\sqrt{H_0 - H}}\delta(P_y - p_0)\delta(p_z), \quad (1)$$

where $\sigma(x)$- is Heaviside function: $\sigma(x) = 1, x > 0; \sigma = 0, x < 0$. The Hamiltonian $H = \frac{p_x^2}{2m} + \frac{p_y^2}{2m} + \frac{p_z^2}{2m} - e\Phi$, m - is the mass of an electron,$-e$ - is a charge, $\Phi(x)$ -is a potential of electric field. The distribution of type (1) leads to a compact description of the complicated physical situation.

The calculated density of electrons is as follows:

$$n_e = \kappa\int\frac{dH}{\sqrt{H_0 - H}}\frac{1}{\sqrt{H + e\Phi - \frac{1}{2m}(p_0 + \frac{e}{c}A_y(x))^2}}. \quad (2)$$

One can get:

$$n_e = n_0\sigma(H_0 + e\Phi - \frac{1}{2m}(p_0 + \frac{e}{c}A_y)^2), \quad (3)$$

where $n_0 = \pi\kappa\sqrt{H_0}$ and the current density j_y takes the following form:

$$j_y = -\frac{e}{m}\int p_y f d\vec{p} = -\frac{e}{m}(p_0 + \frac{e}{c}A_y(x))n_e. \quad (4)$$

Let us introduce dimensionless variables:

$$\frac{e\Phi}{H_0} = \phi, \xi = \frac{x}{l_0}, l_0 = \sqrt{\frac{H_0}{4\pi n_0 e^2}}, a(x) = \frac{e}{p_0 c}A_y(x).$$

The density of ions specified by hydrodynamical equations: $n_i = \frac{\Gamma_i}{v_i}$ where Γ is density of ionic flux, v_i is velocity of ions.If M -is the mass of ions, v_0- initial velocity then $n_i = \frac{\Gamma_i}{\sqrt{v_0^2 - \frac{2e\Phi}{M}}}$.

The equation for components of $4-D$ potential will transform to the following form:

$$\frac{d^2\phi}{d\xi^2} = \sigma\left(1 + \phi(\xi) - \frac{p_0^2}{2mH_0}(1 + a(\xi))^2\right) - \frac{\nu_i}{\sqrt{u_0^2 - 2\phi(\xi)}}, \quad (5)$$

where $\nu_i = \Gamma_i/(n_0 v_s), v_s = \sqrt{H_0/M}, u_0 = v_0/v_s,$

$$\frac{d^2a(\xi)}{d\xi^2} = \frac{H_0}{mc^2}(1+a(\xi)) = \varrho^2(1+a(\xi)), \varrho = \sqrt{H_0/mc^2}. \quad (6)$$

Let us examine the condition $1 + \phi - \frac{p_0^2}{2mH_0}(1 + a)^2$, that defines boundaries of the electron layer. Assume that $\phi(0) = 0$, then

$1 + \phi - \frac{p_0^2}{2mH_0}(1 + a)^2 < 0$ with $\xi < 0$. Let us have $\frac{p_0^2}{2mH_0} = 1$ and write a general solution of the equation (6) can be written in the following form: $a = -1 + \alpha\sinh(\varrho\xi) + \beta\cosh(\varrho\xi)$, where constants α and β are defined by physical conditions. If $\beta = 1$, the it turns out that electrons may be localized only at $\xi > 0$, i.e. $\xi = 0$ is a boundary of the layer. The value of H_0 fulfils a role of temperature of the electron ensemble.For a characteristic quantity of this temperature, $50eV$ may be taken. Then

the parameter $\varrho = 0.01$. Let us write a condition that is to be met by the boundary value of $\xi = \xi_{max}$ for the electron layer: $1+\phi(\xi_{max})-(\cosh(\varrho\xi_{max})+\alpha\sinh(\varrho\xi_{max}))^2 = 0$. This condition depends on the type function $\phi(\xi)$. If ions fall into a layer with zero initial energy, their maximum energy can not be greater then H_0, that is, the ions may be accelerated only to energy that is less than or equal to the temperature of electrons. Let us consider a solution of equation (6) in the region of the layer, assuming that $\frac{p_0^2}{2mH_0} = 1$ and $\phi_0 = 0, u_0 = 0$. A solution to these values given in Fig.1.

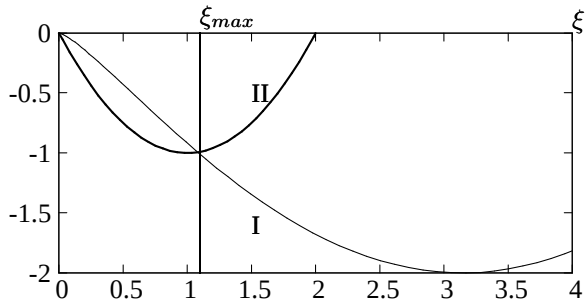

Fig.1 Curve I is a solution for potential $\phi(\xi)$ with $u_0 = 0, \phi_0' = 0, \nu_i = 1$, curve II shows a relationship of the form $-1 + (\cosh(0.01\xi) - 100\sinh(0.01\xi))^2$.

At these conditions ions are accelerated from the zero energy at $\xi = 0$ to the energy $W \sim H_0$ at $\xi = \xi_{max} \sim 1.1$. Then the ions are accelerated by a field defined by the potential an external electrode.

Let us next examine the situation when the initial energy of ions is equal to H_0, with $u_0 = \sqrt{(2)}$. In this case the coefficient α can be of substantially lesser xalue, say $\alpha = 10$ A relevant solution is presented in Fig.2.

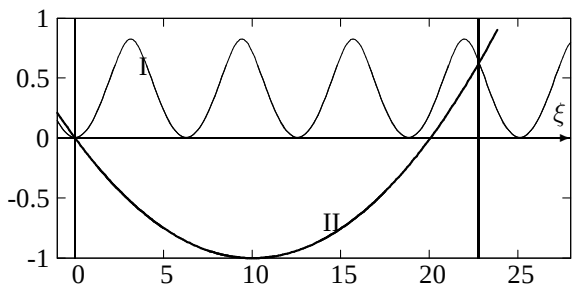

Fig.2 Curve I depicts the dependence of the potential on ξ, with $u_0 = \sqrt{(2)}, \nu_i = 1,$; curve II depicts the dependence $-1 + (\cosh(0.01\xi) - 10\sinh(0.01))^2$.

The dependence of the potential on the coordinate is of an oscillative nature according to which the ions are at first deaccelerating from energy h_0 to energy $\sim 0.2H_0$ in the peak of potential.

The oscillations take place near points the relationship of quasineutrality $n_i = n_e$ is met. Upon achieving the point $\xi = \xi_{max} \approx 22.8$, the ions are accellerating in the electric field to the energy specified by an external electrode having a potential that is dictated by a self-consistent solution for the field.

Thus, in the model being considered there are no restrictions on the extraction of ions having velocities that are less than ionic sonic velocities. This section deals with a situation when there is a non-zero flow of electrons. However, in contrast to paper [4] the direction of electronic flow here is not in line with the ionic flux and directed across this flux.

THE PLASMA-VACUUM MODEL WITH SHARP BOUNDARY

Let us consider a situation when electrons occupy a half-space $x < 0$. We take the solutions of equation (6) at $p_0 = 0$. These solutions are reasonable if they decrease $x \to -\infty$. Then $A_y(x) = C_0\exp(2\kappa\xi)$. Let us assume that C_0 complies with the following relationship: $e^2C_0^2/2mH_0c^2 = 1$. The equation for the dimensionless potential $\phi(\xi)$ takes the following form:

$$\frac{d^2\phi(\xi)}{d\xi^2} = \sigma(1 + \phi(\xi) - \exp(2\kappa\xi)) - \frac{\nu_i}{\sqrt{u_0^2 - 2\phi(\xi)}} \quad (7)$$

Next we show a particular solution (7) at $\kappa = 0.01, \nu_i = 1, \phi(0) = 0, \phi'(0) = 0$. Upon achieving the point $\xi = \xi_{max} \approx 22.8$, the ions are accellerating in the electric field to the energy specified by an external electrode having a potential that is dictated by a self-consistent solution for the field.

In Fig.3, the dependencies of potential (curve I) and of ionic density (curve II) on the coordinate are shown. The electron density takes the form of a step.

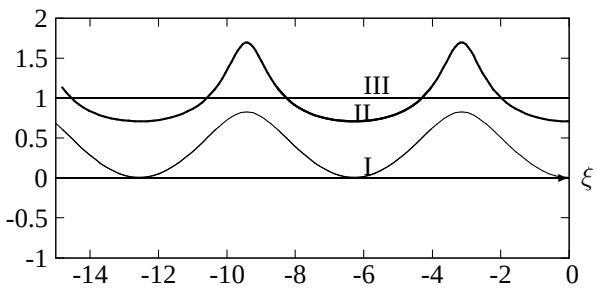

Fig.3.Curve I is dependence of the potential on the coordinate, curve II is dependence of ionic density on the coordinate. The electron density takes the form of a step: 1 with $\xi < 0$ and 0 in the region of $\xi > 0$ (III).

Thus, in the above considered cases - when there is an electron layer kept by a self-generated magnetic field and when electrons occupy a half-space - the ions with relatively low velocities (less then ionic sonic velocities) can leave the region of quasi-neutral plasma and obtain further acceleration in the field induced by the external electrode.It is essential to note that in the both above cases there is a non-zero flow of electrons that is perpendicular to an ionic flux.

REFRENCES

[1] Riemann K.-U., J.Phys.D: Appl.Phys. 24 (1991) 493-519
[2] H.E.Barminova, A.S,Chikhachev, Review of Scientific Instruments, 2012, **83**,02B505.
[3] Sternberg N., Godyak V.,IEEE Transactions on Plasma Science,Vol.35, N5, October 2007,pp.1341-1349.
[4] Yu.A.Kovalenko,T.V.Chernyshev,A.S.Chikhachev, Izvestiya RAS, series ”Energetika”, 2011,No4, pp.24-28.

ANGIOGRAPHY X-RAY MONOCHROMATIC SOURCE BASED ON RADIATION FROM CRYSTALS

Yu.A. Bashmakov, Lebedev Physical Institute of RAS (LPI), Moscow, Russia and National Research Nuclear University (MEPhI), Moscow, Russia
T.V. Bondarenko, Siemens LLC, Moscow, Russia and National Research Nuclear University (MEPhI), Moscow, Russia
S.M. Polozov, National Research Nuclear University (MEPhI), Moscow, Russia
G.B. Sharkov, Siemens LLC, Moscow, Russia

Abstract

Nowadays angiography has become one of the most commonly used medical procedures. However the X-ray tubes are mostly used in angiography imaging systems. The problem that encounters in using X-ray tubes is low monochromaticity due to bremsstrahlung while angiography imaging requires quasimonochromatic energy spectrum for better image quality and lower dose rate obtained by the patient. The use of the monocrystaline target at the medical electron LINAC can be one of the possible ways to obtain the monochromatic X-ray radiation. This type of X-ray generator will provide monochromatic radiation with photon energy dependent on the electron beam energy. The X-ray generation mechanism, possibilities of monocrystal usage as an X-ray source for angiography and requirements for beam parameters are discussed.

INTRODUCTION

Angiography nowadays is the state of the art medical imaging technique used to visualize the inside, or lumen, of blood vessels and organs of the body, with particular interest in the arteries, veins and the heart chambers. This method is traditionally done by injecting a radio-opaque contrast agent into the blood vessel and imaging using X-ray based techniques.

X-ray sources in angiography applications are based on X-ray tubes. These sources are well explored and provide high rates of radiation intensity. In X-ray tubes the source of the radiation is tungsten rotating anode that is irradiated by the electron beam from the thermal cathode. The main drawback of the tube is wide bandwidth of the generated radiation spectrum provided by two principles: fluorescence and bremsstrahlung. The low energetic part of the X-ray is cut-away by the alumina or beryllium filter.

Angiography principle lies in using a contrast medium that allows to clearly identify the agent in the patient body. A medical contrast medium is a substance used to enhance the contrast of structures because of the high rates of mass attenuation coefficient for X-ray radiation in specific narrowband peak e.g.: at 33.1 keV for iodine contrasts, 37.4 keV for barium and 50.2 keV for gadolinium. All bands of radiation spectrum from X-ray tube that differs from the agent attenuation energy peak penetrating patient is less attenuated by the contrast agent and therefore will degrade the clearness of the contrasted part of the image and leads to the unnecessary high dose rate delivered to the patient.

There are several methods of eliminating undesirable spectrum parts of the radiation. The most widespread is usage of X-ray tubes with filters like beryllium windows to suppress the low energy spectrum part that is absorbed in the skin and is the most harmful for the patient. Another method lies in the utilization of X-ray fluorescence method: radiation obtained from the X-ray tube illuminates the fluorescent target and irradiates the characteristic lines. The disadvantage of this method is low level of radiation intensity [1].

Another idea is based on using of the inversed Compton scattering principle. The light beam from the laser is counter-propagated against an electron beam produced by a linear accelerator. X-ray photons are generated by inverse Compton scattering that occurs as a consequence of the "collision" that occurs between the electron beam and IR photons generated by the laser. The disadvantage of this method is concerned in necessity for terawatt laser pulses with ps duration [2].

CHANNELLING RADIATION

The method of obtaining of the narrow-band X-rays lies in utilizing the principle of so called channeling radiation from crystals [3].

Channeling radiation is emitted by relativistic electrons passing through single crystals along a direction of high symmetry. The radiation is forward directed into a narrow cone with an angle of emission $\Theta \sim \gamma^{-1}$.

There are two different types of channeling dependent on the electron track – axis channeling and planar channeling. In the first case electron captured in the channel is moving along the crystal axis and experience the influence of the axially-symmetrical coulomb field of the crystal axis. In the planar channeling the particle is forced by the fields of the atoms situated on the crystalline plane.

The mechanism of channeling radiation can be described in two principal ways: classical physics model and quantum mechanics.

Electrical field formed between the crystallographic planes forming the channel can be characterized with an averaged potential $U(x)$ where x is transversal offset from the channel central plane. As a rule $U(x)$ is smooth,

even and periodical function with period of $2d$: $U(-x)=U(x)$, $U(x+2dk)=U(x)$, where $2d$ is the channel width, k - integer number. Potential value on the border of the channel can be labeled as $U(|x|=d)=U_0$. Potential describing the electron channeling phenomenon is often called "reversed parabola" [4]. With fine accuracy it can be expressed as follows:

$$U(x)=U_0\left(2\frac{x^2}{d^2}-\frac{x^4}{d^4}\right), \quad |x|\le d \tag{1}$$

In this field the particle with charge e, energy $\mathcal{E}$ and rest mass of m perform small transversal harmonic oscillations relative to channel central plane. The magnitude of the oscillations is much less then channel width ($x_m << d$) and the period of the oscillations can be expressed as:

$$\Omega_n=\sqrt{2}\Omega_0, \quad \Omega_0=\frac{c}{d}\sqrt{\frac{2eU_0}{\mathcal{E}}}, \tag{2}$$

here $\gamma=\mathcal{E}/mc^2=(1-\beta^2)^{-1/2}$ is reduced particle energy, $\beta=v/c$, v - particle velocity. It is obvious that the frequency of transversal oscillations is reduced with energy gain as $\sim\gamma^{-1/2}$ [5, 6].

Let us mention that the frequency of large transversal oscillations $x_m\sim d$ depends on their amplitude. Therewith in particle motion Fourier harmonic expansion appears higher harmonics of the fundamental frequency and the particles motion becomes anharmonic. This fact is significant for investigation of the radiation spectral characteristics

Radiation frequency of k-harmonic propagating with angle θ to the central plane of the channel in dipole approximation for ultra-relativistic motion ($\gamma >> 1$) can be written as:

$$\omega_k=\frac{2k\Omega\gamma^2}{1+\theta^2\gamma^2}, \quad (\theta << 1,\ \gamma >> 1) \tag{3}$$

Radiation frequency achieves its maximum at the zero angle: $\omega_k=2k\Omega\gamma^2$.

Based on mentioned equations maximum energy for 9 MeV electron channeling relative to (110) plane of the diamond crystal estimation value of the radiated X-ray photons can be obtained. For this case maximum value appears to be $\hbar\omega=5.90$ keV that qualitatively matches with experimental results [7].

Power of radiation losses of electron due to channeling radiation is defined by the equation:

$$P=\frac{2e^4<E^2>\gamma^2}{3m^2c}, \tag{4}$$

here $<E^2>$ is the mean square of electrical field along the particle trajectory.

ANGIOGRAPHY APPLICATION

Benefits provided by exploiting the channeling radiation principle consist in ability to change the X-ray energy and in the monochromaticity of the radiation.

The point is that in the case of using the X-ray tube X-ray spectrum is wide due to bremsstrahlung and K-lines of any used anodes are situated in 5 keV or more from attenuation peaks of contrast agents. In case of channeling X-ray the radiation peak can be moved directly to the attenuation peak of the agent.

The drawback of the channeling X-ray radiation is presence of the radiation background spreading from low energy level of several keV to the energy of electron beam. This radiation caused by the bremsstrahlung is still present because of electron scatter at the atoms of the crystal lattice. The radiation level is quite low, but integral radiation of all radiation bandwidth gives quite large contribution to the overall intensity.

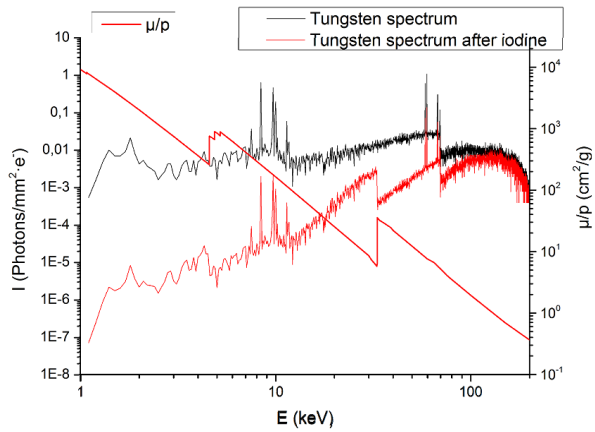

Fig. 1. Spectrum of X-ray tube with tungsten anode, spectrum after iodine contrast agent and iodine mass attenuation coefficient.

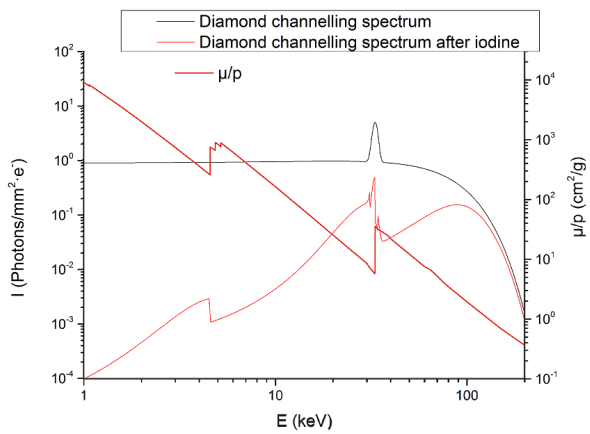

Fig. 2. Spectrum of channelling X-ray obtained from diamond crystal with 21 MeV electron beam, spectrum after iodine contrast agent and iodine mass attenuation coefficient.

The figure 3 shows the principle of image obtaining with the electron channeling mechanism. The irradiated

object contains contrast agent. In the right part of the picture the intensity of the radiation versus the transverse coordinate is presented. The highest values of intensity correspond to the imaged part of the object without contrast. As the contrast medium has high attenuation coefficient on the photon energy adjusted to the radiated X-ray energy, the image part corresponding to the contrast agent is irradiated with the X-ray of lower intensity. Obtained image contrast is the higher the higher is attenuation coefficient of the contrast agent. For example if X-ray source with 33.1 keV photons energy is used – attenuation coefficient would be 35.8 cm^2/g and in case of X-ray tube with tungsten anode (59.5 keV) the attenuation coefficient would be 5 times less – 7.5 cm^2/g.

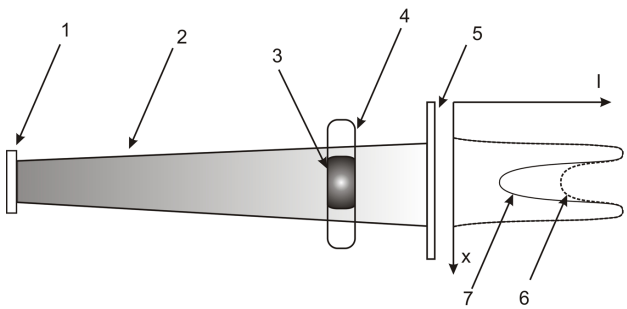

Fig. 3. Angiography image obtaining principle: 1 – X-ray source, 2 – X-ray radiation, 3 – contrast agent , 4 – investigated object, 5 – detector, 6 – intensity curve in case of X-ray intensity peak doesn't match attenuation coefficient peak of the contrast agent, 8 – intensity curve in case of X-ray intensity peak match attenuation coefficient peak of the contrast agent.

SCHEME OF THE FACILITY

The facility scheme for channeling radiation generator is constructed on the requirements for the specific types of X-ray radiation. For instance the radiation demanded for operation with the iodine medium contrast should have the energy of 33.1 keV to fit the iodine mass attenuation peak. To realize this requirement electron beam with the energy of approximately 21 MeV is required, so the electron accelerator should be used to achieve this energy level.

Channeling mechanism of X-ray generation occurs when electron travels near one of the crystal planes. The largest levels of X-ray intensity are obtained in case of (110) axis. According to this crystal must be precisely set relative to the electron beam with the goniometer having at least two axis of adjustment. Goniometer with the monocrystal must be placed inside the vacuum chamber in order to eliminate the beam scattering in the air.

Due to presence of critical angle in channeling mechanism, electrons in the beam should have angle divergence less than critical angle. Beam of this quality can be obtained with LINACs or microtrons without focusing systems.

After the interaction with the crystal electron beam should be deflected from the X-ray propagation direction. This can be made by a magnetic deflector. The deflector is turning the electron beam to the beam load that can be based on Faraday cup to produce the measurements of beam parameters and rectify the beam energy.

As the radiation obtained from the crystal contains bremsstrahlung background – some kind of filtering system should be organized to eliminate it. The low frequency bremsstrahlung can be suppressed by the beryllium windows that are opaque to the X-ray radiation with energy below about 10 keV. X-ray windows cannot suppress the high energy radiation. To eliminate the high energy tail filters like multilayer mirrors or mosaic crystals can be applied [8].

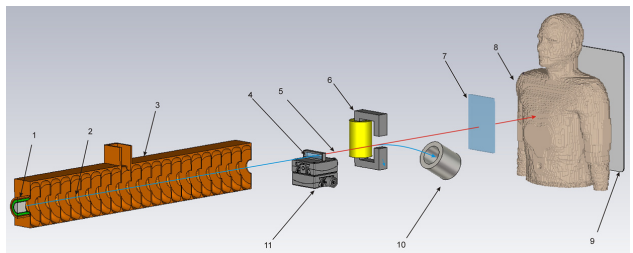

Fig. 4. Principal scheme of monocrystal based X-ray source: 1 – electron gun, 2 – electron beam axis, 3 – accelerating structure, 4 – crystal, 5 – X-ray radiation, 6 – magnet deflecting system, 7 – X-ray radiation filter, 8 – patient body, 9 – X-ray detector, 10 –beam dump, 11 – goniometer.

CONCLUSION

Principle of X-ray generation using the electron channelling through the crystal was considered. Possibility of utilizing the principle of electron channelling radiation in crystals for generating X-ray radiation was investigated. One of the possible applications of obtained X-ray radiation – angiography was discussed. Principal scheme of the estimated facility has been presented.

REFERENCE

[1] P. Schardt, E. Hell, D. Mattern, patent US 6141400, 2000.
[2] F.E. Carroll, R.H. Traeger, M.H Mendenhall, patent US 6332017 B1, 2001.
[3] Lindhard J., Kgl. Dan. Vid. Selsk. Mat.-Fys. Medd., 34, No. 14, 1965
[4] S.B. Dabagov, N.K. Zhevago, Rivesta del nuovo cimento, Vol. 31, N. 9, 2008, p. 491-529.
[5] D.F. Alferov, Yu.A. Bashmakov, P.A. Cherenkov "Radiation from relativistic electrons in a magnetic undulator" 32, 1989, p. 200–227.
[6] Bashmakov Yu.A., Bessonov E.G., On certain features of particle radiation in natural undulators-crystals, Rad. Eff. 1982. V. 66, p. 85-94.
[7] J. Freudenberger, H. Genz, L. Groening, et al., Nuclear Instruments and Methods in Physics Research B 119, 1996, p. 123-130.
[8] P. Baldelli, et al., Nuclear Instruments and Methods in Physical Research A 518, 2004, p. 286-388.

PROGRAM COMPLEX FOR VACUUM NANOELECTRONICS FINITE ELEMENT SIMULATIONS

K.A. Nikiforov*, N.V. Egorov,
St. Petersburg State University, St. Petersburg, Russia

Abstract

The program complex in MATLAB intended for vacuum nanoelectronics simulations is described. Physical and mathematical models, computational methods and algorithms of program complex are presented. Electrostatic simulation of electron transport processes is discussed under electron massless approximation; current function method and Matlab PDE Toolbox finite element solutions are used. Developed program complex is able to simulate diode and triode structures with complicated submicron geometry, current-voltage characteristics, calculate electric field distribution, estimate electric line interaction. The modelling results by the example of two different triode structures are presented. Matlab stand-alone application with graphical user interface for demonstration purposes is presented.

INTRODUCTION

The development of a new accelerator electron gun with the lowest possible emittance is actual important problem. Due to the recent advances in nanotechnologies and vacuum nanoelectronics, a field-emitter array (FEA) based gun is a promising alternative for thermionic or photocathode technologies. Indeed, several thousands of microscopic tips can be deposited on a 1 mm diameter area. Electrons are then extracted by a grid layer close to the tip apex and maybe focused by a second grid layer or anode several micrometer above the tip apex. Although simple diode system is sufficiently to start electron emission, triode configuration with field emitter as cathode, extractor electrode as gate and distant anode as collector is used for many applications. It is necessary to perform computer simulations for design and development of various types FEAs. First of all we'll say a few words about emission nanostructures by the example of wich we'll demonstrate wide possibilities of programmes writen in Matlab. The first one is FEA Spindt-type nanotriode from the company SRI Inc. A schematic of triode cell from is shown in Figure 1.

The second one is the FEA cathode with NbN sharp-edged cylindrical emitters from JSC Mikron. The SEM image in Figure 2 represents NbN thin-film emitters on heavy As-doped Si wafer.

PROGRAM COMPLEX

The device modeling is broken traditionally into two different projects. The first is to model the fields and particle motions within the device to verify the design parameters and to locate design possible problems before fabrication. The second project is to model the operation of the device and its electrical interaction with an external circuit.

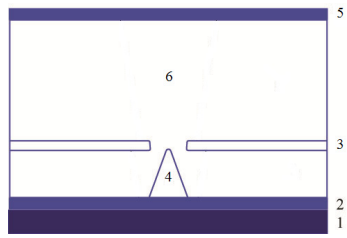

Figure 1: Vacuum nanotriode cell: 1 – wafer, 2– cathode layer, 3 – gate layer electrode, 4 – Mo emitter tip, 5 – anode, 6 – vacuum channel.

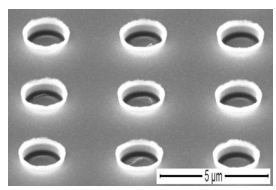

Figure 2: SEM picture of FEA cathode with NbN sharp-edged cylindrical emitters (diode/triode operation is possible).

Electron trajectories

In zero order approximation emitted electron trajectories are supposed to coincide with electric field force lines. This approach is known as electron massless approximation and used for electrostatic simulation of vacuum emission micro/nanoelectronic devices. In vacuum micro/nanoelectronics due to strong dependency of emission current density upon electric field strength the main part of electron current is formed on areas with maximum surface field. On the other hand due to potentiality of electrostatic field the larger field strength is, the smaller force lines curvature will be and the more adequate electron massless approximation will be. Figure 3 represents visualization example of trajectories simulation for Spindt triode nanostructure.

Electric field distribution

Due to axial symmetry of considered FEAs cells we use Matlab two-dimensional static field finite element analysis code (functions from Partial Differential Equations Tool-

* nikiforov_k@mail.ru

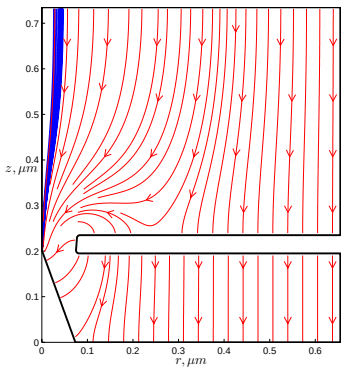

Figure 3: Electron trajectories (blue) and electric force lines for Spindt-type triode cell.

box) to model the electric field profiles in the device for various design variations and applied voltages. The code calculates the electrostatic potential and electric field in neglect of space charge in a volume defined by metallic boundaries and filled with vacuum or dielectric. Examples of simulation results are shown in Figure 4 and Figure 5 for second nanostructure sample.

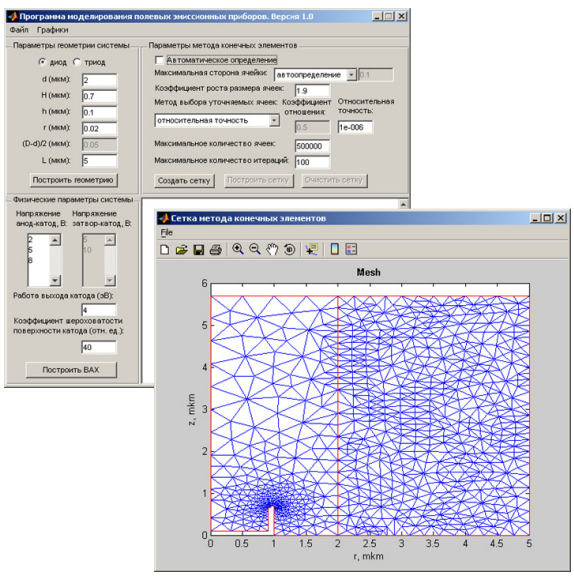

Figure 4: Graphical user interface of the programm, (left) main window, (rigth) adaptive finite element mesh in domain corresponding to the second nanostructure.

Current-voltage characteristics

Trajectory analysis in massless approximation is performed by introducing the current function ψ, well known in hydrodynamics. The physical meaning of current function ψ: it is constant along the force lines of electric field, and the vector flux of the electric field intensity between two force lines (surfaces in 3D case because of axial symmetry) is equal to the difference of relevant values of current function ψ [1]. Comments are given in Figure 6.

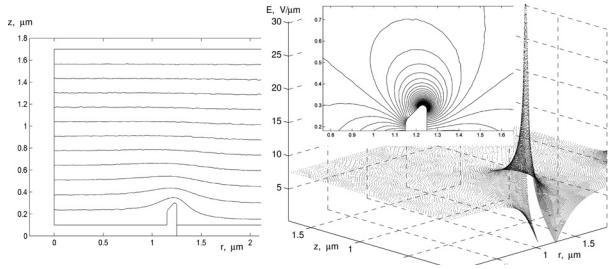

Figure 5: (left) Equipotential line plot of cylindrical field emitter cell in diode configuration at a given bias condition (only one half of cell is shown in cylindrical coordinates due to axial symmetry), (right) electric field distribution around the emitter. Insert: constant-electric field distribution contours around the top of a cylindrical emitter.

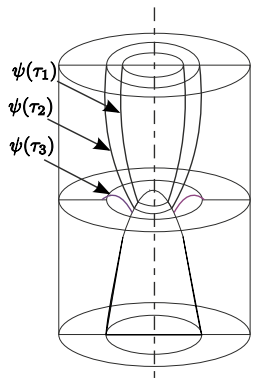

Figure 6: Force lines crossing the cathode at points τ_1 and τ_2 make a beginning at anode, $\psi(\tau_1)$ and $\psi(\tau_2)$ are corresponding values of current function; electron current flows to anode along these force lines. $\psi(\tau_3)$ corresponds to force line, connecting cathode and gate electrode, so electron current flows to gate.

ψ distribution over calculation domain is defined in cylindrical coordinates as

$$\psi_i(\tau) = \psi_{0i} + 2\pi \int_0^{\tau} r(\tau')\mathbf{E}(\tau')\mathbf{n}d\tau', \qquad (1)$$

$$E = \frac{1}{2\pi r}\frac{d\psi_i(\tau)}{d\tau}, \qquad (2)$$

where r – cylindrical coordinate, τ – local variable on boundary i, ψ_{0i} – start value of ψ-function on boundary i, $\mathbf{E}$ – electric field strength, $\mathbf{n}$ – boundary normal vector.

There is functional dependence $I(\psi)$ for electron current I inside surface ψ=const, as it is shown in Figure 7. Thus

$$\frac{dI(\psi)}{d\psi} = \xi(\psi), \qquad (3)$$

and in the presence of emission current flow along given force line:

$$\xi(\psi) = \frac{2\pi r j(E)}{d\psi/d\tau}, \qquad (4)$$

else:

$$\xi(\psi) = 0, \tag{5}$$

where $j(E)$ is defined by known Fowler-Nordheim equation.

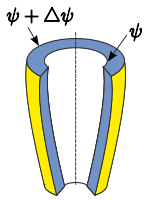

Figure 7: Limit $\frac{I(\psi+\triangle\psi)-I(\psi)}{\triangle\psi}$ when $\triangle\psi \to 0$ is equal to current density along ψ force line.

In second project using the modeling data from the first one, operating characteristics of considered vacuum nanostructures are calculated. The model supplies current-voltage characteristics, including the effects of grid leakage current. The Fowler-Nordheim equation gives current density from the electric field near the cathode surface. Knowledge of the trajectories allows determination of the grid and anode current densities from the cathode current. Device integral currents are determined by numerical surface integration.

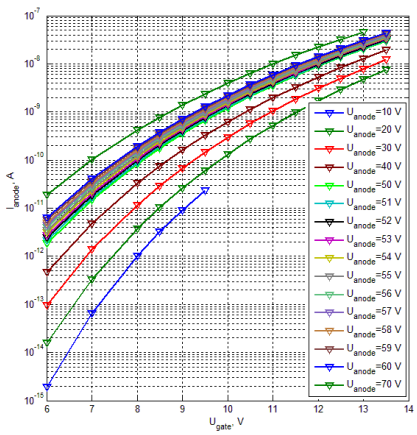

Figure 8: Anode current vs. gate voltage characteristics for triode-type emission nanostructure.

CONCLUSION

Programming with Matlab opens wide possibilities of the development of the complex program intended for vacuum nanoelectronics simulations. Matlab stand-alone application with graphical user interface was used to investigate electric field effects in real FEA nanostructures [2].

REFERENCES

[1] N. I. Tatarenko, A. Yu. Vorobyev, Technical Digest of the 17th International Vacuum Nanoelectronics Conference (2004) 278.

[2] K. A. Nikiforov et al., "Non-gated Field Emission Array as Low-Energy Electron Source: Experiment and Simulation" FRBOR03, these proceedings.

THE KNIFE-EDGED FIELD EMITTER MATHEMATICAL MODELING

E.M. Vinogradova, M.G. Fomenko, SPbSU, Saint Peterburg, Russia

Abstract

Numerous nano-scale electronic devices are based on the field emitters such as carbon nanotubes. The field emitters are extensively applied in the various domains of an instrument engineering. In the present work the problem of a field emission cathode as the knife-edged field emitter mathematical modeling is solved. The supposed shapes of the emission diode system with the field emitter are the lune's type (as a cathode) and the infinitely thin spherical segment (as an anode). The effect of the space charge is neglected. The boundary – value problem for the Laplace equation in the toroidal coordinate system is presented. To solve the electrostatic problem the variable separation method is used. The potential distribution is represented as the series with respect to Legendre functions. The boundary conditions and the normal derivative continuity conditions lead to the linear algebraic equations system relative to the series coefficients. In this way the distribution of the potentials for the whole region of the considered electro-optical systems was obtained.

INTRODUCTION

Field emitters (FE) have unique parameters for industrial applications in the domain of vacuum micro- and nano-electronics — scanning electron microscopy, x-ray sources, emission displays, parallel e-beam lithography, etc. FE are manufactured of various materials with different morphologies [1–4].

In the present work the rotationally symmetric knife-edged field emitter mathematical modeling is under investigation (see Fig.1).

PROBLEM BACKGROUND

It is presented the solution to Laplace's equation for the axisymmetric diode systems: cathode is simulated by two spherical segments with the toroidal top (lune's type), an anode modeled by thin spherical segment (see Fig.2).

To solve the rotationally symmetric electrostatic problem the variable separation method is employed. The toroidal coordinate system (α, β, φ) is used.

The parameters of the problem are as follows:

$\beta = \beta_1$ $(0 \le \alpha \le \alpha_1)$ — the surface of anode;

$\beta = -\beta_2$, $\beta = 2\pi - \beta_3$ $(0 \le \alpha \le \alpha_0)$ and

$\alpha = \alpha_0$, $(\beta_2 \le \beta \le 2\pi - \beta_3)$ — the surface of tip;

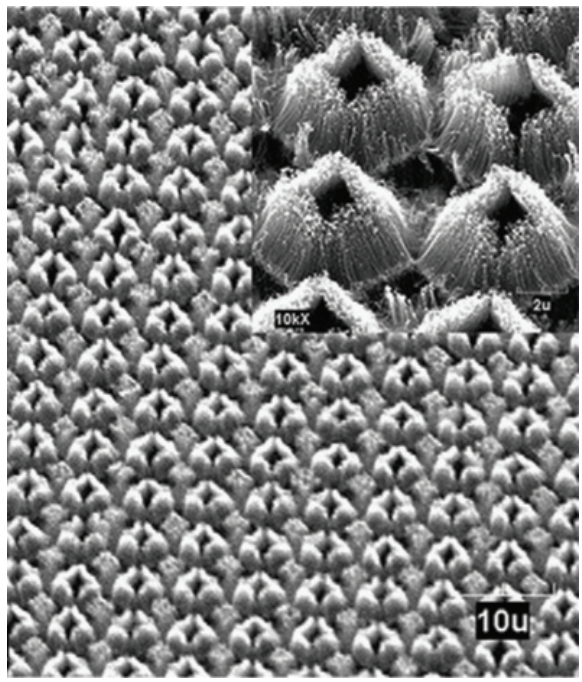

Figure 1: SEM images for aligned and patterned carbon nanotube emitters [1].

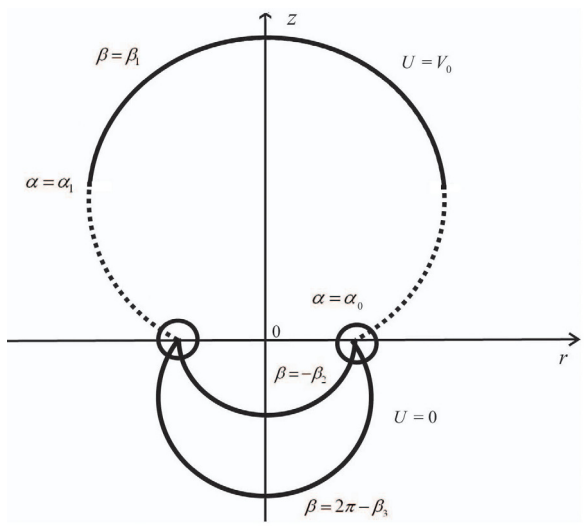

Figure 2: Schematic diagram of the diode systems based on a knife-edged field emitter.

$U(\alpha, \beta_1) = V_0$ $(0 \le \alpha \le \alpha_1)$ — the boundary condition on anode.

The potential of the tip is assumed to be zero without the loss of general character of the problem.

MATHEMATICAL MODELING AND CALCULATION

The potential distribution $U(\alpha,\beta)$ satisfies the Laplace equation. Thus, it is necessary to solve the following boundary – value problem

$$\begin{cases} \triangle U(\alpha,\beta)=0, & \\ U(\alpha,\beta_1)=V_0, & 0\le\alpha<\alpha_1; \\ U(\alpha,-\beta_2)=0, & 0\le\alpha<\alpha_0; \\ U(\alpha,2\pi-\beta_3)=0, & 0\le\alpha<\alpha_0; \\ U(\alpha_0,\beta)=0, & \beta_2\le\beta\le 2\pi-\beta_3. \end{cases} \quad (1)$$

In order to solve the boundary – value problem (1), the entire region of the diode system is split into 3 subregions with the potential distribution $u_i(\alpha,\beta)$ as

$$U(\alpha,\beta)=\begin{cases} u_1(\alpha,\beta), & -\beta_2<\beta<\beta_1, \\ & 0\le\alpha<\alpha_0; \\ u_2(\alpha,\beta), & \beta_1<\beta<2\pi-\beta_3, \\ & 0\le\alpha<\alpha_0; \\ u_3(\alpha,\beta), & -\beta_2<\beta<2\pi-\beta_3, \\ & \alpha_1\le\alpha<\alpha_0. \end{cases}$$

Designate

$$W\left(-\tfrac{1}{2}+\eta_n,\alpha,\alpha_0\right)= \\ =P_{-\frac{1}{2}+\eta_n}(\cosh\alpha)\,Q_{-\frac{1}{2}+\eta_n}(\cosh\alpha_0)- \\ -P_{-\frac{1}{2}+\eta_n}(\cosh\alpha_0)\,Q_{-\frac{1}{2}+\eta_n}(\cosh\alpha),$$

where $P_{-\frac{1}{2}+\eta_n}(\cosh\alpha)$, $Q_{-\frac{1}{2}+\eta_n}(\cosh\alpha)$ — Legendre functions of the first and second kind.

The potential distribution functions $u_i(\alpha,\beta)$ can be represented as series [5,6]

$$u_1(\alpha,\beta)=\sqrt{\cosh\alpha+\cos\beta}\times \\ \times\sum_{l=1}^{\infty}A_l\frac{\sinh(\beta+\beta_2)\tau_l}{\sinh(\beta_1+\beta_2)\tau_l}P_{-\frac{1}{2}+i\tau_l}(\cosh\alpha), \quad (2)$$

$$u_2(\alpha,\beta)=\sqrt{\cosh\alpha+\cos\beta}\times \\ \times\sum_{l=1}^{\infty}A_l\frac{\sinh(2\pi-\beta_3-\beta)\tau_l}{\sinh(2\pi-\beta_3-\beta_1)\tau_l}\times \\ \times P_{-\frac{1}{2}+i\tau_l}(\cosh\alpha). \quad (3)$$

$$u_3(\alpha,\beta)=\sqrt{\cosh\alpha+\cos\beta}\times \\ \times\sum_{n=1}^{\infty}B_n\sin\eta_n(\beta+\beta_2)\times \\ \times\frac{W\left(-\frac{1}{2}+\eta_n,\alpha,\alpha_0\right)}{W\left(-\frac{1}{2}+\eta_n,\alpha_1,\alpha_0\right)}, \quad (4)$$

where

τ_l — the roots of equations $P_{-\frac{1}{2}+i\tau_l}(\cosh\alpha_0)=0$,

$\eta_n=\dfrac{\pi n}{2\pi+\beta_2-\beta_3}$.

Using the boundary conditions (1) and the continuity conditions for the potential distribution functions on the curves separating the subregions, we obtain equations of the form

$$u_1(\alpha,\beta_1)=\begin{cases} V_0, & 0\le\alpha<\alpha_1, \\ u_3(\alpha,\beta_1), & \alpha_1\le\alpha<\alpha_0, \end{cases} \quad (5)$$

$$u_3(\alpha_1,\beta)=\begin{cases} u_1(\alpha_1,\beta), & -\beta_2\le\beta<\beta_1, \\ u_2(\alpha_1,\beta), & \beta_1\le\beta<2\pi-\beta_3. \end{cases} \quad (6)$$

Substituting the potential distribution functions (2) and (4) into equation (5), we can write

$$\sqrt{\cosh\alpha+\cos\beta_1}\sum_{l=1}^{\infty}A_lP_{-\frac{1}{2}+i\tau_l}(\cosh\alpha)= \\ =\begin{cases} V_0, & 0\le\alpha<\alpha_1; \\ \sqrt{\cosh\alpha+\cos\beta_1}\left(\sum\limits_{n=1}^{\infty}C_n\sin\eta_n(\beta_1+\beta_2)\times\right. & \\ \left.\times\dfrac{W\left(-\frac{1}{2}+\eta_n,\alpha,\alpha_0\right)}{W\left(-\frac{1}{2}+\eta_n,\alpha_1,\alpha_0\right)}\right), & \alpha_1\le\alpha<\alpha_0, \end{cases}$$

and after some transformations we arrive the first system of linear algebraic equations relative to coefficients A_l, B_n:

$$A_l=\sum_{n=1}^{\infty}B_nT_{l,n}+R_l, \quad (7)$$

where

$$T_{l,n}=(N_l)^{-1}\int_{\alpha_1}^{\alpha_0}P_{-\frac{1}{2}+i\tau_l}(\cosh\alpha)\times \\ \times\frac{W\left(-\frac{1}{2}+\eta_n,\alpha,\alpha_0\right)}{W\left(-\frac{1}{2}+\eta_n,\alpha_1,\alpha_0\right)}\times \\ \times\sin\eta_n(\beta_1+\beta_2)\sinh\alpha\,d\alpha, \quad (8)$$

$$R_l=V_0(N_l)^{-1}\times \\ \times\int_0^{\alpha_1}\frac{P_{-\frac{1}{2}+i\tau_l}(\cosh\alpha)}{\sqrt{\cosh\alpha+\cos\beta_1}}\sinh\alpha\,d\alpha, \quad (9)$$

$$N_l=\int_0^{\alpha_0}\left(P_{-\frac{1}{2}+i\tau_l}(\cosh\alpha)\right)^2\sinh\alpha\,d\alpha. \quad (10)$$

Using the expansions of potential distribution functions (2,3,4) as well as equation (6), we can write

$$\sqrt{\cosh\alpha_1+\cos\beta}\sum_{n=1}^{\infty}C_n\sin\eta_n\left(\beta+\beta_2\right)=$$

$$=\begin{cases}\sqrt{\cosh\alpha_1+\cos\beta}\sum\limits_{l=1}^{\infty}A_l\dfrac{\sinh\left(\beta+\beta_2\right)\tau_l}{\sinh\left(\beta_1+\beta_2\right)\tau_l}\times\\ \times P_{-\frac{1}{2}+i\tau_l}\left(\cosh\alpha_1\right), & -\beta_2\le\beta<\beta_1;\\ \sqrt{\cosh\alpha_1+\cos\beta}\sum\limits_{l=1}^{\infty}A_l\dfrac{\sinh\left(2\pi-\beta_3-\beta\right)\tau_l}{\sinh\left(2\pi-\beta_3-\beta_1\right)\tau_l}\times\\ \times P_{-\frac{1}{2}+i\tau_l}\left(\cosh\alpha_1\right), & \beta_1\le\beta<2\pi-\beta_3,\end{cases}$$

and after some transformations we arrive the second system of linear algebraic equations relative to coefficients A_l, B_n:

$$B_n=\sum_{l=1}^{\infty}A_lS_{n,l}, \qquad (11)$$

where

$$S_{n,l}=\frac{2}{2\pi-\beta_3+\beta_2}P_{-\frac{1}{2}+i\tau_l}\left(\cosh\alpha_1\right)\times$$
$$\times\left(\frac{-\tau_l}{\tau_l^2+\eta_n^2}\frac{\sin\pi n}{\sinh\tau_l\left(2\pi-\beta_3-\beta_1\right)}+\right.$$
$$+\frac{\tau_l}{\tau_l^2+\eta_n^2}\sin\eta_n\left(\beta_1+\beta_2\right)\times \qquad (12)$$
$$\times\Big(\coth\tau_l\left(\beta_1+\beta_2\right)+$$
$$\left.+\coth\tau_l\left(2\pi-\beta_3-\beta_1\right)\Big)\right).$$

CONCLUSION

In this work the problem of the axisymmetric diode system with a field emission cathode as the knife-edged field emitter mathematical modeling is considered. The cathode is simulated by two spherical segments with the toroidal top, an anode modeled by thin spherical segment. To solve the rotationally symmetric electrostatic problem the variable separation method is employed.

The distribution of electrostatic potential (2–4) is calculated over the entire domain of the diode system. The solution of the boundary value (1) is reduced to solving the system of linear algebraic equations (7–12).

REFERENCES

[1] Hongzhong Liu, Yongsheng Shi, Bangdao Chen et al., "Effect of patterned and aligned carbon nanotubes on field emission properties," Vacuum 86 (2012) 933-937.

[2] P.Y. Chen, T.C. Cheng, J.H. Tsai, Y.L. Shao "Space charge effects in field emission nanodevices," Nanotechnology, 20 (2009) 405202 (9pp).

[3] D.S.Y. Hsua, J. Shaw, "Integrally gated carbon nanotube-on-post field emitter arrays," Appl. Phys. Let. 80 (2002) 1. 118-120.

[4] V.I. Kleshch, A.N. Obraztsov, E.D. Obraztsova "Modeling of Field Emission from Nano Carbons," Fullerenes, Nanotubes and Carbon Nanostructures, 16 (2008) 384388.

[5] N.N. Mirolubov et al., *Methods of calculating the electrostatic fields*, (Moscow: Vysshaja shkola, 1963), 209.

[6] E.M. Vinogradova, N.V. Egorov, M.G. Mutul, Che-Chow Shen "Calculation of electrostatic potential of the diode system based on a sharp-edged field cathode," SPb, Vestnik SPbSU, Series 10: Appl. mathematics, informatics, procceses of control. 1 (2007) 29-37.

THE FIELD CATHODES WITH THE EFFECT OF SPACE CHARGE MODELING

M. Makarova, E. M. Vinogradova, Saint-Petersburg State University, Saint-Petersburg, Russia

Abstract

This work is devoted to the question of the effect of space charge on the field electron emission. The electrostatic potential distributions for the diode emission systems are calculated. The diode systems, which can be readily constructed, are generally used for the characterization of field emission properties of novel materials. They have some effective applications in vacuum nano- and microelectronics. In this work the plane diode emission system and cylindrical diode emission system are investigated. The solutions of Poisson's equation for the electrostatic potential distribution are received for the boundary-value problems. The right side of Poisson's equation is assumed to be the piecewise constant function. The charge conservation law and the energy conservation law are used. One and two dimensional cases are investigated.

INTRODUCTION

Currently there are great interest in research and practical applications of the field electron emitters, where emission occurs from a nanoscale inclusions of conducting material, carbon nanotubes and fibers, protrusions of nanometer size. Microfabricated field emission arrays (FEAs) have been studied extensively both theoretically and experimentally. FEAs are considered as excellent candidates for use as electron sources operating with high efficiency, high currents for vacuum electronic applications.Much effort has been directed towards the commercial applications of FEAs, including their use as electron sources in various types of visualization equipment, including lithography, x-ray sources, microscopes, high-power microwave amplifiers, transistors and especially for generation high-brightness flat panel displays [1, 2, 3].Field emission diodes and triodes are the most commonly used device architectures for FEAs. The diode structure, which can be readily constructed, is generally used in laboratories for the characterization of field emission properties of novel materials [1].

Electron field emission from a single emitter is a barrier tunneling, quantum mechanical process that can be described by the Fowler-Nordheim equation. At high emission current densities, however, the space charge caused by the cathode may affect the current densityvoltage characteristics predicted by the Fowler-Nordheim theory [1, 4, 5]. This work is devoted to the investigation of the effect of space charge on the field electron emission. Plane diode emission system and cylindrical diode emission system are considered.

MATHEMATICAL MODELING AND CALCULATION

Plane Diode Emission System

The problem is to calculate electrostatic potential distribution in the region between the electrodes of the plane diode emission system. This is a simple case of the electrode configuration of diode system [6]. At first a one-dimensional case was studied. Potential distribution is described by the Poisson's equation

$$\triangle \bar{U}_p(z) = -\bar{\rho}_p(z) \tag{1}$$

with following boundary conditions:

$$\bar{U}_p(z_1) = 0, \quad \bar{U}_p(z_2) = V. \tag{2}$$

Function $\bar{U}_p(z)$ is the potential distribution; $\bar{\rho}_p(z) = \frac{\bar{\rho}_d^*(z)}{\varepsilon_0}$, where $\bar{\rho}_d^*(z)$, is the space charge density, ε_0 is the vacuum dielectric constant. Function $\bar{\rho}_p(z)$ is unknown. In our work we assumed that these function is a piece-wise constant function

$$\bar{\rho}_p(z) = \begin{cases} \widetilde{\rho}_1^1, & z \in [R_1 = z_1, R_2), \\ \widetilde{\rho}_2^1, & z \in [R_2, R_3), \\ \dots \\ \widetilde{\rho}_N^1, & z \in [R_N, R_{N+1} = z_2]. \end{cases}$$

where N is the number of parts for which the region between the electrodes is divided. Solution of (1) with boundary conditions (2) is

$$\bar{U}_p(x,z) = \sum_{s=1}^{k-1} \widetilde{\rho}_s^1 \bar{P}_{s_1}(x,z) + \sum_{s=k+1}^{N} \widetilde{\rho}_s^1 \bar{P}_{s_2}(x,z) + \\ + \widetilde{\rho}_k^1 \bar{P}_k(x,z) + \bar{L}_p(z),$$

where $\bar{P}_{s_1}, \bar{P}_{s_2}, \bar{P}_k, \bar{L}_p$ is a several known functions, $\widetilde{\rho}_i^1$ is unknown values. To find these values we considered the equations

$$\mathrm{div}\vec{j_p} = 0, \tag{3}$$

$$\frac{1}{2} m \vec{V_p}^2 = -e\bar{U}_p(z), \tag{4}$$

where $\vec{j_p}$ is a current density, $\vec{V_p}$ is a speed of the electrons, e is the electron charge. Eq. 3 is the current continuity equation, Eq. 4 is the energy conservation law. Combining these equation gave

$$\bar{\rho}_p(z)\sqrt{\bar{U}_p(z)} = A = \mathrm{const},$$

where constant A can be determined from the boundary condition at the anode, $A = \widetilde{\rho}_N^1\sqrt{V}$. From the each interval (R_s, R_{s+1}) was chosen for one z_s^* and was written the system of equations

$$\vec{F}_p^1 = \vec{0}, \tag{5}$$

where $\vec{F}_p^1$ is a vector-function,

$$\vec{F}_p^1 = \begin{pmatrix} \widetilde{\rho}_1^1\sqrt{\bar{U}(z_1^*)} - \rho_N\sqrt{V} \\ \widetilde{\rho}_2^1\sqrt{\bar{U}(z_2^*)} - \rho_N\sqrt{V} \\ \vdots \\ \sqrt{\bar{U}(z_N^*)} - \sqrt{V} \end{pmatrix}.$$

System Eq.5 is a system of algebraic nonlinear equations; it was solved by numerically using Newton's method.

Next the two-dimensional case was studied. Field that arises in the region between the electrodes, is described by the Poisson's equation

$$\triangle U_p(x,z) = -\rho_p(z). \tag{6}$$

Simplification was done: the length of the diode system for the x-axis is much greater than the distance between the electrodes. Therefore $\rho_p(z)$ depends only of x. Function $\rho_p(z)$ is unknown. We have assumed that these function is a piece-wise constant function with "pieces" $\widetilde{\rho}_i^2, i = \overline{1,N}$. The boundary conditions

$$U_p(0,z) = V\frac{z-z_1}{z_2-z_1}, \qquad U_p(x_1,z) = V\frac{z-z_1}{z_2-z_1},$$
$$U_p(x,z_1) = 0, \qquad U_p(x,z_2) = V$$

for Eq. 6 was imposed. Solution of the boundary problem for the Poisson's equation was obtained as

$$U_p(x,z) = \sum_{s=1}^{k-1}\widetilde{\rho}_s^2 P_{s_1}(x,z) + \sum_{s=k+1}^{N}\widetilde{\rho}_s^2 P_{s_2}(x,z) + \\ + \widetilde{\rho}_k^2 P_k(x,z) + L_p(z).$$

where $P_{s_1}, P_{s_2}, P_k, L_p$ is a several known functions, $\widetilde{\rho}_i$ is unknown values.

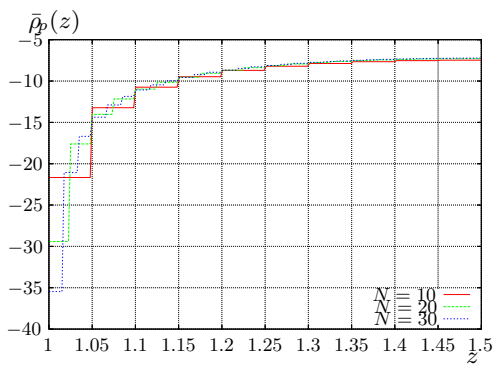

Figure 1: Space charge density, plane diode, one-dimensional case

To find them current continuity equation and energy conservation law were used. In this case according with configuration of the system current density and speed of electrons can be considered depending only of z. Potential distribution U_p can be regarded with a fixed value of x. So

$$\rho_p\sqrt{U_p(x^*,z)} = \widetilde{\rho}_N^2\sqrt{V}. \tag{7}$$

Using Eq.7 was formed a system of equations for finding the unknowns $\widetilde{\rho}_i^2$ as in a previous case. It was solved by numerically using Newton's method.

Cylindrical diode emission system

Electrodes of these diode system are two axisymmetric cylinders. In one-dimension case equation

$$\triangle\bar{U}_c(r) = -\frac{\bar{\rho}_c(r)}{\varepsilon_0}$$

with boundary conditions

$$\bar{U}_c(r_1) = 0, \quad \bar{U}_c(r_2) = V.$$

was solved. Function $\bar{\rho}_c(r)$ was regarded as piece-wise constant function. Solving of these problem can be derived as

$$\bar{U}_c(r) = \sum_{s=1}^{k-1}\hat{\rho}_s^1\bar{C}_{s_1}(r) + \sum_{s=k+1}^{N}\hat{\rho}_s^1\bar{C}_{s_2}(r) + \\ + \hat{\rho}_k^1\bar{C}_k(r) + \bar{L}_c(z).$$

where $\bar{C}_{s_1}, \bar{C}_{s_2}, \bar{C}_k, \bar{L}_c$ is a known functions. To find the unknown $\hat{\rho}_i^1$ current continuity equation and energy conservation law were used. Through the equation

$$r\bar{\rho}_c(r)\sqrt{\bar{U}_c(r)} = r_2\hat{\rho}_N^1\sqrt{V}.$$

the system of nonlinear algebraic equations for the unknowns was composed. To solve these system Newton's method was applied. During the consideration of the two-dimensional case it was supposed that the length of this system is much greater than the distance between the cylinders. Then the function $\rho_c(r) = \frac{\rho_c^*(r)}{\varepsilon_0}$ can be regarded as depending only of r.

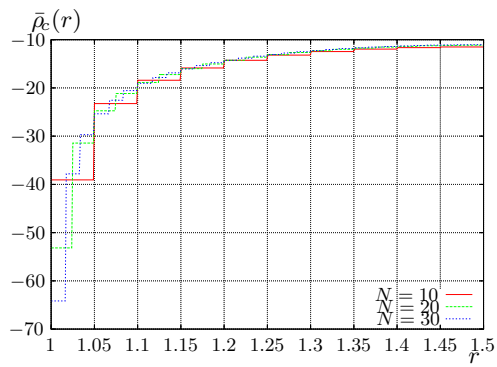

Figure 2: Space charge density, cylindrical diode, one-dimensional case

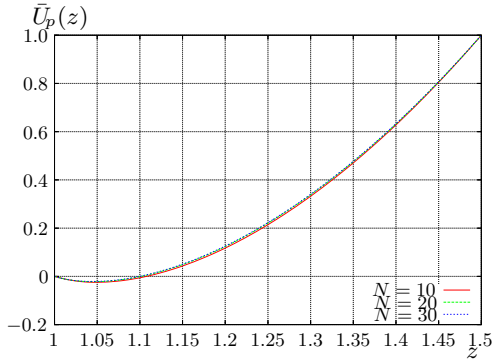

Figure 3: Potential distribution, plane diode, one-dimensional case

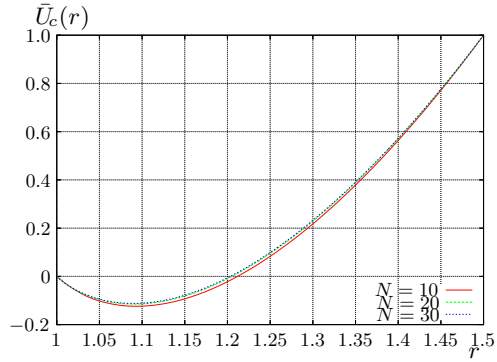

Figure 4: Potential distribution, cylindrical diode, one-dimensional case

At the boundaries of the system was set the following conditions

$$U_c(r,0) = V\frac{\ln\left(\frac{r_1}{r}\right)}{\ln\left(\frac{r_1}{r_2}\right)}, \qquad U_c(r,z_1) = V\frac{\ln\left(\frac{r_1}{r}\right)}{\ln\left(\frac{r_1}{r_2}\right)},$$
$$U_c(r_1,z) = 0, \qquad U_c(r_2,z) = V.$$

Function $\rho_c(r)$ is unknown piece-wise constant function.

The potential distribution was obtained as

$$U_c(r,z) = \sum_{s=1}^{k-1} \hat{\rho}_s^2 C_{s_1}(r,z) + \sum_{s=k+1}^{N} \hat{\rho}_s^2 C_{s_2}(r,z) + \\ + \hat{\rho}_k^2 C_k(r,z) + L_c(r),$$

where C_{s_1}, C_{s_2} and C_k can be defined in explicit form by Bessel function. System of equations for calculation $\hat{\rho}_i^2$ was obtained as in the previous tasks.

RESULTS

Calculations were done using the program that was written on C++. The following parameters were used:
$z_1 = 1, \quad z_2 = 1{,}5, \quad x^* = 0{,}5\,l, \quad l = 100, \quad V = 1$ — for the plane diode emission system;
$r_1 = 1, \quad r_2 = 1{,}5, \quad z^* = 0{,}5\,l, \quad l = 100, \quad V = 1$ — for the cylindrical diode emission system. Parameter l is the length of the diode system.

The Fig. 1 and Fig. 2 shows the space charge density at different values N for the plane and cylindrical diodes correspondingly. Can be seen that in both cases the approximation converge to a function that describes the space charge density in a region between the electrodes. Herewith the space charge density tends to infinity near the cathode. Calculations show that the density of the space charge for one- and two-dimensional cases differ by no more than in fourth decimal place.

The space charge becomes the reason potential drop especially in the region near the cathode. As shown in Fig.3 and Fig. 4 the potential near the cathode is negative. When the anode voltage reduced potential also had a negative values. Comparison distribution potential values for one- and two-dimensional cases shows that the difference in the fifth decimal place (for any fixed values of the second coordinate in the two-dimensional cases).

CONCLUSION

In this paper was considered the problem of modeling the diode emission system with regard to space charge. Poisson's equation with the boundary conditions was solved in one- and two-dimensional cases for the plane and cylindrical diode emission systems. The solution in all cases was obtained analytically. Calculations showed that the piecewise constant approximation converges to a function that describes the distribution of the space charge density in the space between the electrodes. The space charge density tends to infinity near the cathode. Calculations of the electrostatic potential showed that the space charge causes the fall of potential.

REFERENCES

[1] P.Y. Chen, T.C. Cheng, J.H. Tsai and Y.L. Shao. Space charge effects in field emission nanodevices, Nanotechnology, 2009. Vol. 20, p. 1– 9

[2] Pierangelo Gröning, Pascal Ruffieux, Louis Schlapbach, Oliver Gröning. Carbon nanotubes for cold electron sources, Advanced Engineering Materials, 2003. Vol. 5, no. 8. p. 541 – 550

[3] Fursey G.N., Petrik V.I., Novikov D. Low-threshold field emission from carbon nanoclusters obtained by cold destruction of graphite, Jurnal Tehnicheskoi Fiziki, 2009. Vol. 79, no. 7. p. 122 – 126 (in russian)

[4] Fowler R.H., Dr. Nordheim L. Electron Emission in Intense Electric Fields, Proceedings of the Royal Society of London,1928. Vol. 119, no. 781, p. 173 – 181

[5] Rukin S.N., Tsyranov S.N. The influence of space charge on the process of subnanosecond current interruption in high-power semiconductor diodes, Jurnal Tehnicheskoi Fiziki, 2009. Vol. 79, no. 11, p. 30 – 35 (in russian)

[6] Kellin N.S.,Tolmachev A.I. The influence of the space charge and initial speed of the electrons on potential distribution in a plane diode, Jurnal Tehnicheskoi Fiziki, 2012. Vol. 82, no. 4. p. 86 – 89 (in russian)

[7] A. Rokhlenko, J. L. Lebowitz. Stability and properties of stationary state of one dimensional space charge limited current, Journal of Applied Physics, 2012. Vol. 111, p. 013301-1 – 7

THE TRIODE-TYPE SYSTEM ON THE BASIS OF THE FIELD EMITTER MODELING

Televnyi D. S, Vinogradova E. M., Saint Petersburg State University, Russia

Abstract

The mathematical model of a cylindrical triode-type system on the basis of the field emitter is under consideration. The internal area of the system is filled of two different dielectrics. Effect of space charge is not considered. The field emitter is modeled by a charged filament of finite length, which located on the system's axis. The modulator has a form of a circular diaphragm. The Poisson equation with the given values of potentials at the electrodes is solved. The variable separation method is used to determine distribution of electrostatic potential. An unknown function of the charge density is approximated by a piecewise constant linear function. The problem of finding unknown coefficients in the potential eigenfunction expansion is reduced to the linear algebraic equations system. Numerical calculations emitter's forms are represented.

INTRODUCTION

Vacuum electronic devices based on the field emission are used in many areas of scientific research. Particularly in the development of new high-precision devices as an electron microscopes, flat panel displays, systems of surface diagnostics, devices of micro- and nano-electronics [1]. The main characteristics of these devices are small dimensions and low consumption of power for efficient operation. The field cathode makes it possible to generate emission of electrons at low values of the potentials in the system. The high current density provided by the small radius of curvature of the tip and does not require in consumption energy for heat the emission region. To improve the emission characteristics into the system usually include an additional electrode called as a modulator. This modulator allows to change the field close by the emitter within a wide range, with a low value of the potential [2].

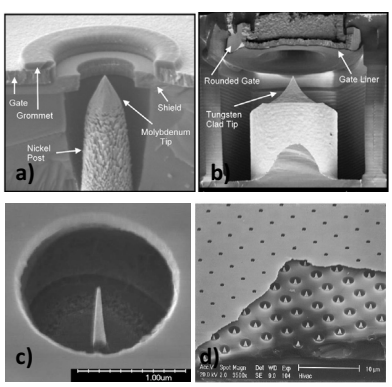

Figure 1: Pictures of cells triode-type systems based on field-emitter.

FORMULATION OF THE PHYSICAL PROBLEM

Consider a cylindrical triode-type system which consists of a substrate on which the field cathode is situated, the modulator in the form of a flat diaphragm and an anode (Fig. 2). The internal part of the system is filled by two different dielectrics with dielectric constants ε_1 and ε_2. One of them serves as a casing of dielectric shell. There is a tip on the axis of the system. This tip is modeled by charged filament which length is z_0. It is assumed that the cross geometrical dimensions of the field cathode are much smaller than the cross dimensions of the system. Cathode has a zero potential, the modulator's potential is V_1 ,the anode's potential is V_2. The main task consists in finding of potential distribution in the triode-type system with a field tip. (System's section with the axial symmetry)

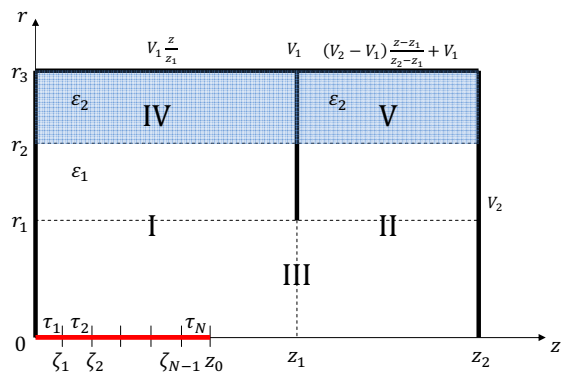

Figure 2: System's section with the axial symmetry.

FORMULATION OF THE MATHEMATICAL PROBLEM

The function of potential distribution must satisfy the Poisson's equation with considering an axial symmetry of the system

$$\triangle U(r,z) = -\frac{\rho(r,z)}{\varepsilon_0}, \tag{1}$$

with boundary conditions

$$\begin{aligned} &U(r,0) = 0, \quad r \in [0, r_3], \\ &U(r,z_1) = V_1, \quad r \in [r_1, r_3], \\ &U(r,z_2) = V_2, \quad r \in [0, r_3], \\ &U(r_3,z) = V_1\frac{z}{z_1}, \quad z \in [0, z_1], \\ &U(r_3,z) = \frac{V_2 - V_1}{z_2 - z_1}(z - z_1) + V_1, \quad z \in [z_1, z_2], \end{aligned} \tag{2}$$

where $\rho(r,z)$ is volume density of the charge created by a charged filament.

The solution of the problem can be represented as a sum of two solutions — i.e. solutions of the Laplace's equation with inhomogeneous boundary conditions and the solution of the Poisson's equation with homogeneous boundary conditions. The solution of the Laplace's equation was found [3] and now it requires solving the Poisson's equation with an unknown right side.

Represent the unknown function $U(r,z)$ in (1) in the form [4]

$$U(r,z)=\sum_{n=1}^{\infty}V_n(z)J_0\left(\frac{\omega_n}{a}r\right), \tag{3}$$

where $V_n(z)$ is an unknown function, a is border of region on r. Define the potential distribution in the first and third areas, because only in these areas located charged filament.

Substitute (3) into (1) and use the orthogonality property of Bessel's functions J_0 will come to an inhomogeneous second order of differential equation

$$V_n{}''(z)-\left(\frac{\omega_n}{a}\right)^2V_n(z)=$$

$$=-\frac{2}{a^2{J_1}^2(\omega_n)}\int_0^{r_0}r\frac{\rho(r,z)}{\varepsilon_0}J_0\left(\frac{\omega_n}{a}r\right)dr,$$

where r_0 is the estimated radius of the tip.

Represent the volume density as a linear function

$$\rho_s(r,z)=\frac{\tau_s}{\pi r_s^2},\quad \tau_s=Ash,\quad h=\zeta_s-\zeta_{s-1},$$
$$z\in(\zeta_s,\zeta_{s-1}],\quad s=\overline{1,N}, \tag{4}$$

where A is an unknown coefficient. At sufficiently lesser values of r_0 the integral $\int_0^{r_0}rJ_0(\frac{\omega_n}{a}r)dr\approx\frac{r_0^2}{2}$ [5]. Introduce the notation

$$\varphi(z)=\begin{cases}-\dfrac{1}{a^2J_1^2(\omega_n)}\dfrac{Ash}{\pi\varepsilon_0}, & z\leqslant z_0,\\ 0, & z>z_0,\end{cases}$$

$$V_n{}''(z)-\left(\frac{\omega_n}{a}\right)^2V_n(z)=\varphi(z). \tag{5}$$

Will try solution of equation (5) in the form

$$V_n(z)=a_n(z)\text{ch}\left(\frac{\omega_n}{a}z\right)+b_n(z)\text{sh}\left(\frac{\omega_n}{a}z\right).$$

The coefficients $a_n(z)$ and $b_n(z)$ should be determined from the equations, using the method of variation of constants

$$a_n{}'\text{ch}\left(\frac{\omega_n}{a}z\right)+b_n{}'\text{sh}\left(\frac{\omega_n}{a}z\right)=0,$$
$$\frac{\omega_n}{a}\left(a_n{}'\text{ch}\left(\frac{\omega_n}{a}z\right)+b_n{}'\text{sh}\left(\frac{\omega_n}{a}z\right)\right)=\varphi(z).$$

Determine the form of the function $V_n(z)$ by means of using homogeneous boundary conditions and considering the form (3). Obtain the potential distribution in the regions I and III in the general form

$$U(r,z)=\sum_{n=1}^{\infty}\frac{Ah}{\pi\varepsilon_0\omega_n^2J_1^2(\omega_n)}\frac{1}{\text{sh}\left(\frac{\omega_n}{a}z^*\right)}\times$$
$$\times\left[\text{sh}\left(\frac{\omega_n}{a}(z^*-z)\right)\sum_{s=1}^{m-1}s\left(\text{ch}\left(\frac{\omega_s}{a}\zeta_s\right)-\text{ch}\left(\frac{\omega_s}{a}\zeta_{s-1}\right)\right)-\right.$$
$$-m\text{sh}\left(\frac{\omega_n}{a}(z^*-z)\right)\text{ch}\left(\frac{\omega_s}{a}\zeta_{s-1}\right)+m\text{sh}\left(\frac{\omega_n}{a}z^*\right)-$$
$$-\text{sh}\left(\frac{\omega_n}{a}z\right)\times \tag{6}$$
$$\left.\times\sum_{s=m+1}^{N}s\left(\text{ch}\left(\frac{\omega_n}{a}(z^*-\zeta_s)\right)-\text{ch}\left(\frac{\omega_n}{a}(z^*-\zeta_{s-1})\right)\right)\right]\times$$
$$\times J_0\left(\frac{\omega_n}{a}r\right),\quad z\leqslant z_0,$$

$$U(r,z)=\sum_{l=1}^{\infty}\frac{Ah}{\pi\varepsilon_0\omega_n^2J_1^2(\omega_n)}\frac{\text{sh}\left(\frac{\omega_n}{a}(z^*-z)\right)}{\text{sh}\left(\frac{\omega_n}{a}z^*\right)}\times$$
$$\times\sum_{s=1}^{N}s\left(\text{ch}\left(\frac{\omega_s}{a}\zeta_s\right)-\text{ch}\left(\frac{\omega_s}{a}\zeta_{s-1}\right)\right)\times \tag{6′}$$
$$\times J_0\left(\frac{\omega_n}{a}r\right),\quad z>z_0.$$

where z_0 is border of region on z.

As a result, the distribution function of the system area considering linear approximation of density values of the charged wire is obtained. Also introduce two additional equations for the calculation of the coefficient A Using the functions (6) and (6′) set the point in which the zero equipotential will determine the length of the cathode [6].

Solving the system, which binds unknown coefficients, define their values, and obtain a function of the potential distribution in the entire system.

THE NUMERICAL RESULTS

The program is written on the basis of theoretical calculations. This program serves to solve the system which has to do with unknown coefficients. In the calculation of following parameters were used: $r_1=0.5$, $r_2=0,75$, $r_3=1$, $z_1=0.5$, $z_2=1$, $\varepsilon_1=1$, $\varepsilon_2=4.7$, $V_1=1$, $V_2=1$. The length of the charged wire is $z_0=0.4$. The infinite sums were limited by the number 35, which is sufficient for the required accuracy of calculations The values of the geometric parameters and the electrostatic potential are given in relation to the respective maximum values.

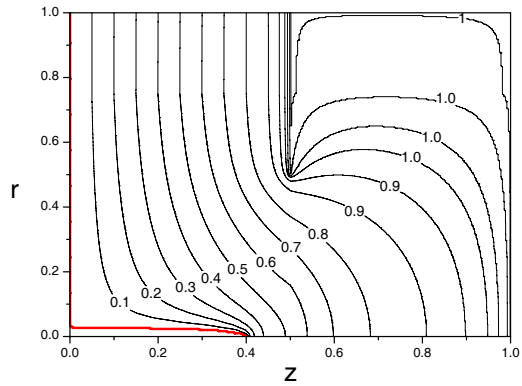

Figure 3: Graph of the potential distribution in the system area.

It is obvious that the boundary conditions is accomplished and form of the field cathode is marked in red.

On the Fig. 4 it makes clear the equipotential lines of the potential distribution close by the tip. Form of the tip is marked in red.

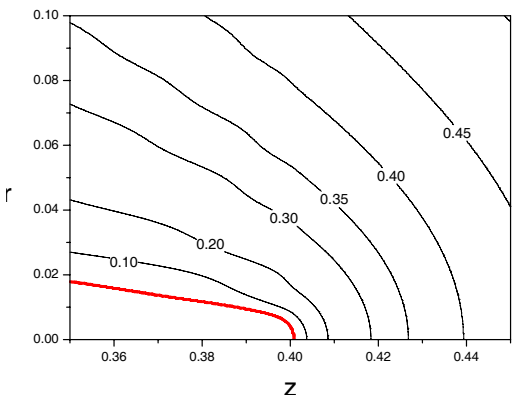

Figure 4: Graph of the potential distribution close by the tip.

On the Fig. 5 graph of the charge density is represented. This graph is calculated by the program.

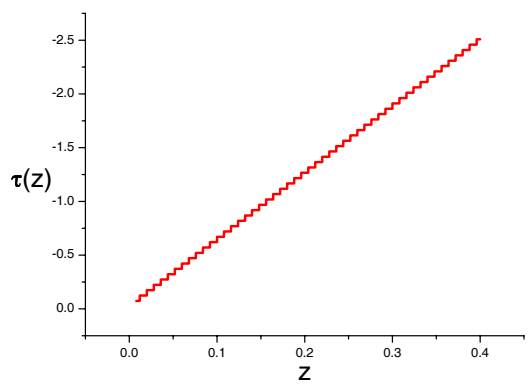

Figure 5: Graph of the charge density.

On the Fig. 6 are represented: the form of field cathode (in red denotes) and the field intensity at the axis (in blue denotes).

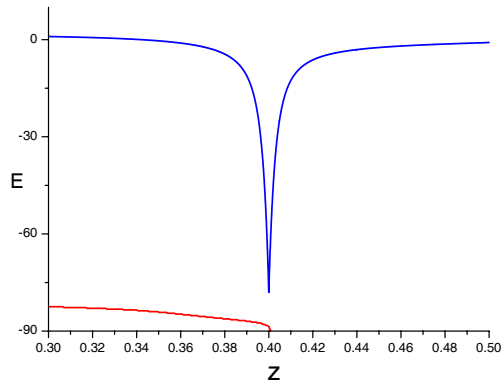

Figure 6: Graph of the field intensity on the systems axis.

It is seen that close by the tip the field intensity rapidly increases in the absolute value.

CONCLUSION

In this work consider the problem of modeling triode-type electron-optical system with a field tip. The system area is filled by two different dielectrics with different dielectric constants. The Poisson's equation is solved by approximating the charge density filaments, which is located on the axis of the system. The analytical form of the potential distribution function is obtained in the system area. According to the results of the numerical experiment the graphs of equipotential lines is represented.

REFERENCES

[1] Bargsten Johnson B., Schwoebel P. R.,Holland C. E., Resnick P. J., Hertz K. L., et al. Field ion source development for neutron generators // Nuclear Instruments and Methods in Physics Research A, 2012. Vol. 663. P. 65–74.

[2] David S. Y., Jonathan S. Integrally gated carbon nanotube-on-post field emitter arrays // Applied physics letters, 2002. Vol. 80. P. 118–120.

[3] Televnyi D. S. Calculation of the electrostatic potential in the electron-optical system with modulator // Control Processes and Stability (CPS). SPb.: publ. Unipress, 2010. P. 225–230.

[4] Mirolubov N. N. Methods of calculating the electrostatic fields. M.: publ. Vysshaja shkola, 1963. 209 p.

[5] Abramowitz M., Stegun I. Handbook of Mathematical Functions With Formulas, Graphs, and Mathematical Tables. Washington, U.S. Government Printing Office, 1979. 1037 p.

[6] Vinogradova E. M. Mathematical modeling of electron-optical systems. SPb.: publ. SPSU, 2005. 110 p.

THE MULTI-TIP FIELD EMISSION CATHODE MATHEMATICAL MODELING

N.V. Egorov*, E.M. Vinogradova, SPbSU, Saint Peterburg, Russia

Abstract

The multi-tip field cathode as the field emission cathode arrays for rectangular lattice is considered. The field emission cathodes are of interest for vacuum nano-scale electronic devices. The electrostatic potential distribution is presented for the periodic system of free-number thin tips on a plane substrate as a field emission cathode and a plane substrate as an anode. The tips shape may be various. The potential of the substrate and cathode is equal the zero, the anode's potential is equal a constant. The effect of space charge is neglected. The each tip is represented as a system of the point charges. The point charges are determined to the zero equipotential coincides with the cathode's shape. The potential distribution is found for whole region of the field emission cathode arrays. The exact three-dimensional solution to the Laplace/Poisson equation has been obtained in the Cartesian coordinate system. This solution has direct applications in three-dimensional calculations of electron trajectories in micron- and submicron-sized field-emitter arrays.

INTRODUCTION

Field emission is of great commercial interest in electronic devices. Over the last decade, carbon-based and several others nanomaterials, such as carbon nanotubes, nanotips, various zinc oxide nanostructures, have attracted considerable attention due to their unique physical, chemical, and mechanical properties [1–3]. These nanostructures as the field cathodes are applied for surface diagnostics, low-energy electron diffraction, Auger-spectroscopy, scanning tunneling microscopy and others potential applications in the areas of electron field emission [4–6].

In this work the multi-tip field cathode as the field emission cathode arrays for rectangular lattice is under investigation.

PROBLEM BACKGROUND

The solution of Laplace's equation for the electrostatic potential distribution is presented for the diode systems: the multi-tip emitter as a field emission cathode of the on a flat metal substrate (base) and a plane as an anode. Each thin tip is placed in the rectangular lattice point (see Fig.1). The tip's shape may be various. The effect of the space charge is neglected.

* egorov@apmath.spbu.ru

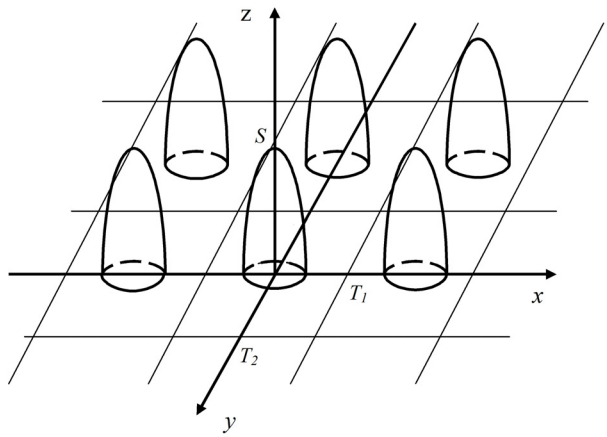

Figure 1: Illustration of a field emission cathode arrays for rectangular lattice.

To solve the electrostatic problem the variable separation method is employed. The cartesian coordinate system (x, y, z) is used.

The parameters of the problem are as follows:

$z = Z_{N+1}$ — the surface of anode;

$z = 0$ — the surface of substrate;

S — the length of tip;

$z_0(x, y)$ — the surface of tip;

T_1 — x-direction half-period;

T_2 — y-direction half-period;

$V(x, y, Z_{N+1}) = V_0$ — the boundary condition on anode;

$V(x, y, 0) = 0$ — the boundary condition on substrate.

The potential of the tip is assumed to be zero without the loss of general character of the problem.

Let us to interchange each tip influence for periodic lattice cell with a charge system q_i $(i = \overline{1, N})$ effect so that the tip surface is matched with the zero's equipotential as the virtual cathode (see Fig.2).

The parameters of the charge system are as follows:

N — the number of charges;

q_i — the values of charges;

$(0, 0, Z_i)$ — the coordinates of charges.

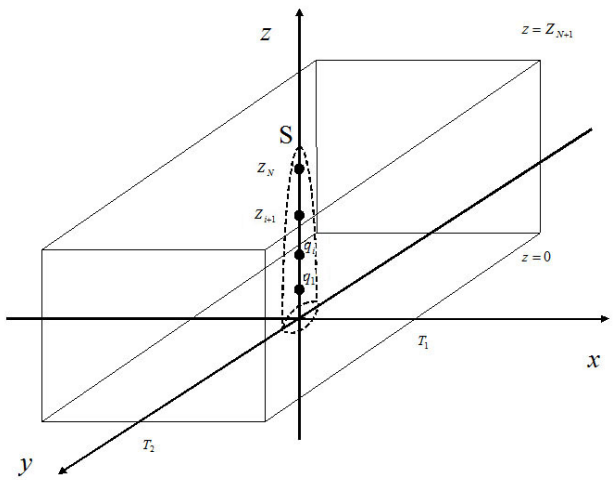

Figure 2: Illustration of a periodic lattice cell.

MATHEMATICAL MODELING AND CALCULATION

So we have to solve the boundary – value problem for the Poisson's equation

$$\begin{cases} \triangle \quad V(x,y,z) = -\frac{1}{\varepsilon_0}\rho(x,y,z), \\ \\ V(x,y,0) = 0, \\ \\ V(x,y,Z_{N+1}) = V_0, \\ \\ \left.\frac{\partial V(x,y,z)}{\partial x}\right|_{x\,=\,\pm T_1} = 0, \\ \left.\frac{\partial V(x,y,z)}{\partial y}\right|_{y\,=\,\pm T_2} = 0. \end{cases} \tag{1}$$

The potential distribution function $V(x,y,z)$ can be represented as series [7]

$$V(x,y,z) = \sum_{n=0}^{\infty}\sum_{m=0}^{\infty} v_{mn}(z)\cos\frac{\pi n x}{T_1}\cos\frac{\pi m y}{T_2}. \tag{2}$$

Function $V(x,y,z)$ (2) satisfy the boundary – value problem (1) and periodicity conditions.

In compliance with the Poisson's equation, functions $v_{mn}(z)$ are the solutions to the ordinary differential equations [8]

$$v''_{mn}(z) - \lambda^2_{mn}\, v_{mn}(z) = f_{mn}(z), \tag{3}$$

where

$$f_{mn}(z) = \frac{-1}{\varepsilon_0}\int\limits_{-T_1}^{T_1}\int\limits_{-T_2}^{T_2}\rho(x,y,z)\cos\frac{\pi n x}{T_1}\cos\frac{\pi m y}{T_2}dy\,dx,$$

$$\lambda_{mn} = \sqrt{\left(\frac{\pi n}{T_1}\right)^2 + \left(\frac{\pi m}{T_2}\right)^2},\ m \geq 0,\ n \geq 0.$$

The function $\rho(x,y,z)$ in the second member of Poisson's equation will be considered as follows

$$\rho(x,y,z) = \begin{cases} \rho_i, (|x| < \delta_1, |y| < \delta_2, |z - Z_i| < \delta_3), \\ 0,\ \ (|x| > \delta_1, \text{or}\, |y| > \delta_2, \text{or}\, |z - Z_i| > \delta_3), \end{cases}$$

$$q_i = \lim 8\rho_i\delta_1\delta_2\delta_3\ (\delta_1 \to 0,\ \delta_2 \to 0,\ \delta_3 \to 0),$$
$$\rho_i = \text{const},\ i = \overline{1,N}.$$

Designate

$$\gamma_{mn} = \begin{cases} 1, & m > 0,\ n > 0, \\ 2, & n = 0\ \text{or}\ m = 0,\ \ (m^2 + n^2 \neq 0). \end{cases}$$

Using the solutions to the equations (3) and after some transformations the potential distribution $V(x,y,z)$ can be written in an explicit form

$$V(x,y,z) = \frac{V_0}{Z_{N+1}}z + \frac{1}{\varepsilon_0 4T_1T_2}\times$$
$$\times\left(\sum_{i=0}^{k} q_i(Z_{N+1} - z)Z_i + \sum_{i=k+1}^{N} q_i(Z_{N+1} - Z_i)z\right) +$$
$$+\sum_{n=0}^{\infty}\sum_{m=0}^{\infty}\frac{\cos\lambda_{m0}\,y\,\cos\lambda_{0n}\,x}{\varepsilon_0 T_1T_2\lambda_{mn}\gamma_{mn}}\times \tag{4}$$
$$\times\left(\sum_{i=0}^{k} q_i\frac{\text{sh}\,\lambda_{mn}(Z_{N+1} - z)\,\text{sh}\,\lambda_{mn}Z_i}{\text{sh}\,\lambda_{mn}Z_{N+1}} + \right.$$
$$\left. + \sum_{i=k+1}^{N} q_i\frac{\text{sh}\,\lambda_{mn}(Z_{N+1} - Z_i)\,\text{sh}\,\lambda_{mn}z}{\text{sh}\,\lambda_{mn}Z_{N+1}}\right),$$
$$Z_k < z < Z_{k+1}.$$

The problem of determining the values of charges q_i is reduced to the solution of the system of linear algebraic equations in order that the tip surface $z_0(x,y)$ is matched with the zero's equipotential (virtual cathode) in N points $(x_l, y_l, z_l = z_0(x_l, y_l))$:

$$\sum_{i=1}^{k} q_i\, A_{il} + \sum_{i=k+1}^{N} q_i\, B_{il} = C_l, \tag{5}$$

where

$$A_{il} = \frac{1}{\varepsilon_0 T_1T_2}\left(\frac{1}{4}(Z_{N+1} - z_l)Z_i + \right.$$
$$+\sum_{n=0}^{\infty}\sum_{m=0}^{\infty}\frac{\text{sh}\,\lambda_{mn}(Z_{N+1} - z_l)\,\text{sh}\,\lambda_{mn}Z_i}{\lambda_{mn}\gamma_{mn}\,\text{sh}\,\lambda_{mn}Z_{N+1}}\times \tag{6}$$
$$\left.\times\cos\lambda_{m0}\,y_l\,\cos\lambda_{0n}\,x_l\right),$$

$$B_{il} = \frac{1}{\varepsilon_0 T_1 T_2}\left(\frac{1}{4}(Z_{N+1} - Z_i)z_l + \right.$$

$$+\sum_{n=0}^{\infty}\sum_{m=0}^{\infty}\frac{\text{sh }\lambda_{mn}(Z_{N+1} - Z_i)\text{ sh }\lambda_{mn}z_l}{\lambda_{mn}\gamma_{mn}\text{ sh }\lambda_{mn}Z_{N+1}} \times \quad (7)$$

$$\left. \times \cos\lambda_{m0}\, y_l \cos\lambda_{0n}\, x_l\right),$$

$$C_l = -\frac{V_0}{Z_{N+1}}z_l, \quad (8)$$

$$Z_k < z_l < Z_{k+1},$$

$$k = \overline{0, N},\ \ l = \overline{1, N}.$$

CONCLUSION

In this work the multi-tip field cathode mathematical modeling is considered. The Poissons equation is solved by approximating the point charges. The analytical form of the potential distribution function (4) is obtained over the entire domain of the field emission cathode arrays. The problem of determining the values of charges is reduced to the solving the system of linear algebraic equations (5–8).

REFERENCES

[1] B.B. Wang, Q.J. Cheng, X.X. Zhong, et al., "Enhanced electron field emission from plasma-nitrogenated carbon nanotips," J. Appl. Phys. 111 (2012) 044317.

[2] Qingyue Cui, Yong Huang, Ziqiang Zhu, "Syntesis and field emission of novel ZnO nanorod chains," Curr. Appl. Phys. 9 (2009) 426-430.

[3] Ming Q. Ding, Xinghui Li, Cuodong Bai et al., "Fabrication of Spindt-type cathodes with aligned carbon nanotube emitters," Appl. Surf. Sci. 251(2005) 201-204.

[4] K. Zheng, H. Shen, J. Li et al., "The fabrication and properties of field emission display based on ZnO tetrapod-liked nanostrucrure," Vacuum. 83 (2009) 261-264.

[5] R. Yabushita, K. Hata, "Newly developed high spatial resolution X-ray microscope equipped with carbon nanotube field emission cathode," Surf. and Interface Analysis. 40 (2008) 1664-1668.

[6] Y.S. Choi, "Shapes of emitter surface in field emission display," Thin Solid Films. 516 (2008) 3357-3363.

[7] N.N. Mirolubov et al., *Methods of calculating the electrostatic fields*, (Moscow: Vysshaja shkola, 1963), 209.

[8] E.M. Vinogradova, N.V. Egorov, S.L. Dolgov, "Calculation of electrostatic potential in multi-tip and single-tip field emission systems," SPb, Vestnik SPbSU, Series 10: Appl. mathematics, informatics, procceses of control. 1 (2007) 29-37.

FIRST TEST RESULTS OF RF GUN FOR THE RACE-TRACK MICROTRON RECUPERATOR OF BINP SB RAS*

V.N. Volkov#, V.S. Arbuzov, E.I. Gorniker, E.I. Kolobanov, C.A. Krutikhin, I.V. Kuptsov, G.Ya.Kurkin, V.N. Osipov, V.M. Petrov, A.M. Pilan, I.K. Sedlyarov, V.A. Scheglov, N.A.Vinokurov, BINP SB RAS, Novosibirsk, Russia

Abstract

A new electron source for the Race-Track Microtron Recuperator is being developed by BINP SB RAS. It will increase average beam current and brightness of synchrotron radiation.

Instead of the static 300kV electron gun operated now we are developing RF gun with the same energy of electrons. This RF gun consists of RF cavity with a gridded thermo cathode mounted on the back wall. RF cavity is driven by a 60 kW generator with last stage equipped by GU101A tetrode tube. Operational frequency of the cavity is 90.2 MHz. It is equal to the second subharmonic of the Microtron RF system frequency. A set of low power electronics controls amplitude of the cavity voltage and its tuner.

This system, including a diagnostics beam line, has been installed to serve as a test bench to test the RF cavity and for beam dynamics studies. In continuous regime the designed 300 kV voltages at the acceleration gap is obtained. This paper summarizes the first test results of the cavity in this configuration.

INTRODUCTION

The RF electron gun for the Race-Track Microtron Recuperator [1] operated in BINP SB RAS (Novosibirsk) is described in [2]. RF cavity of the electron gun is made on base of the Microtron accelerating cavity [3]. The layout of the RF cavity is shown in Fig.1. Only the insertion assembly (3, 5, 11) and the conic nose (4) were designed and build anew. The other parts of the existing cavity were modified to the electron gun design requirements. This cavity is manufactured at the BINP workshop where novel technologies were used widely in the manufacture process such as electron beam welding and turner's work by diamond cutting tool.

CAVITY MANUFACTURE

The cavity cylindrical wall and side walls are made of copper-stainless steel bimetal. We have selected two side walls by ultrasonic scanner for checking the quality of bonding between copper and stainless steel layers.

Assembling of the cavity was made as follows. Firstly, the conic nose (4) was welded to the left side wall (2) (see Fig. 1). Then the left side wall was welded to the cylindrical wall (1), the insertion was welded to the right wall and finally the assembly was welded to the cylindrical wall.

*Work supported by the Ministry of Education and Science of the Russian Federation; RFBR grant 11-02-91320

#V.N.Volkov@inp.nsk.su

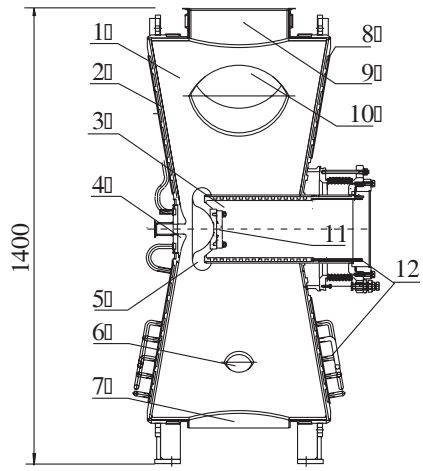

Figure 1: RF gun cavity layout. 1- cylindrical wall, 2-left side wall, 3-insertion, 4-conic nose, 5-electrode, 6-port for sampling loop, 7-vacuum pumping port, 8-right side wall, 9-RF power input port, 10-port for frequency tuning plunger, 11-vacuum cap, 12-water cooling tubes.

Conic Nose Welding

The maximum surface electric field with E_{peak}=10 MV/m is concentrated on the conic nose and on the electrode. To prevent an electric breakdown in the gap these parts were machined by diamond cutting tool using numerically controlled lathe. All other surfaces were mechanically polished by a tangle of thin nichrome wire. Then the conic nose was welded to the left wall in vacuum chamber of BINP electron beam welding installation (see Fig.2).

Welding of the Cavity

Before welding to the right wall the position of the insertion was set so that the resonance frequency of RF cavity under vacuum will be 90.2 MHz. To guarantee this the axial deformation of both discs after welding and deformation of disks under atmospheric pressure of both were accounted for. (see Fig.4). Measurement of the deformations was made only for the left disk. The other side of the cylindrical wall and all other ports were closed vacuum tight during measurements. It was presumed that deformation of the right side wall will be the same. The deformation under atmospheric pressure was measured to be 0.64 mm, welding deformation was 5.5÷7μm.

It is possible to correct the inaccuracy of the resonance frequency and cathode radial position by deformation of thin copper membrane close to the welding contact within ±0.5 mm. The cathode position is controlled by a rough tuning mechanism installed on the right side wall.

Figure 2: The left side wall with the cone nose installed into the vacuum chamber before the electron beam welding.

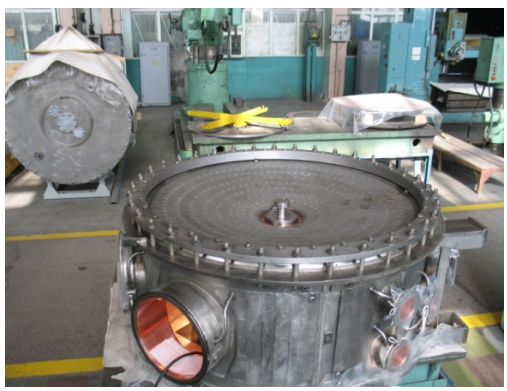

Figure 3: The left wall welding to the sidewall.

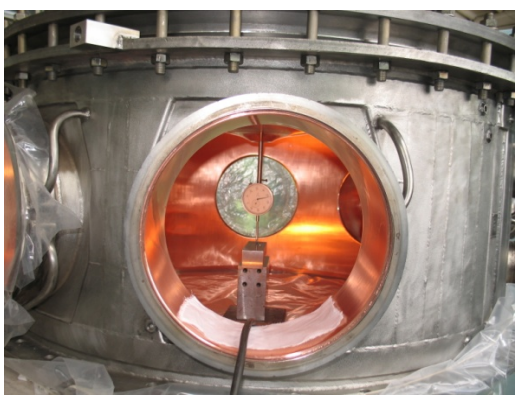

Figure 4: Measuring tool of the welding axis deformation.

Plunger Modification

Two existing plungers for frequency tuning of the cavity during operation were modified to expand the frequency tuning range up to 150 kHz. The plungers were elongated by 30 mm by a copper caps that were welded by electron beam (see Fig.5). A thin layer of titanium nitride was sputtered onto the vacuum side of plungers to prevent multipacting, using the magnetron sputtering system and technology developed at BINP [4]. Before sputtering they were cleaned for UHV requirements in ultrasonic bath with 5% detergent, rinsed with deionised water, dried with dust-free air and stored in plastic bag.

RF Power Input and Coupler

RF power input of Microtron RF cavity 180.4MHz was worked into RF power input of our project. The loop area for the coupler should be increased 3.3 times according to the calculation. The loop was cut into two segments before brazing with the ceramic insulator in a vacuum furnace. As a result the pressure to the ceramic insulator due to a thermal expansion was excluded. After the brazing the loop segments were joined again by electron beam welding.

The sampling loop was modified also. The old loop was cut off and the new one longer by 40 mm was fixed on its place by electron beam welding (see Fig. 6).

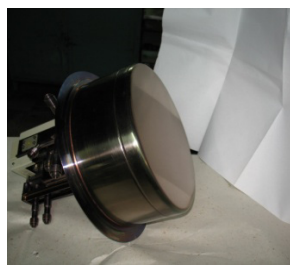

Figure 5: The modified plunger.

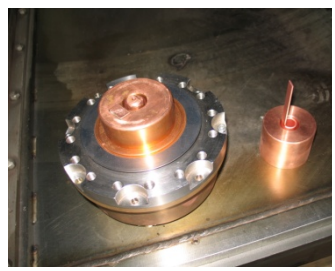

Figure 6: Sampling loop modificating components.

CAVITY PREPARATION

The cavity was tuned to resonance frequency of 90.2 MHz by adjusting the rough tuning mechanism. Then the RF power input position was adjusted by rotation to reach the VSWR of 3.21. In this case the power input will be matched during operation with a 100 mA current beam accelerated up to the energy of 300 keV. The unloaded Q-value was measured to be 25100. The sampling loop was rotated to have ~2W at 300 kV on the cavity gap and calibrated. Then RF power input and the sampler were welded to cavity ports. The all-metal gate vacuum valve with DN40 was installed at the beam pipe of the cavity and instead of the gridded cathode assembly a cap was installed.

Baking Out

Baking out under vacuum of the cavity allows to:

a) Clear out the surface from residual gas for better vacuum condition under RF; b) identify faulty components before processing under RF power. During baking out the cavity was heated to 220-240ºC with gradient of 10ºC/hr, was kept at this temperature for 70 hours and then cooled down to the room temperature with a controlled gradient (see Fig. 7). The vacuum pressure of $1.7 \cdot 10^{-7}$ Pa was obtained.

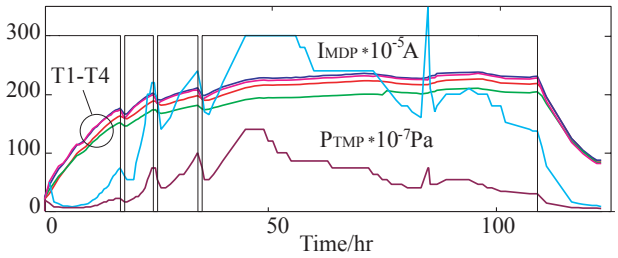

Figure 7: The baking out process. T1-T4 is temperatures of different sensors of the cavity in ºC, I_{MDP} is the current of magnetic-discharge pump, P_{TMP} is the pressure measured at the turbo molecular pump connection.

RF POWER TEST

RF Stand Layout

The 60 kW RF power generator with the tetrode GU-101A at the output stage was tested with equivalent of the load. Then it was connected with RF cavity by 100 m rigid coaxial line. The RF generator, low level control electronics were created at BINP. The RF power was measured by two methods: by directional coupler positioned on the coaxial line close to RF generator, and by a calibrated sampling loop of RF cavity.

The cavity is equipped by water cooling stand with the water flow meters and temperature sensors fixed on cavity surface.

The cavity was connected via bellows to a pumping system with rough pump, turbo-molecular pump, vacuum gauge and residual gas analyzer. In addition to RF measurements, data regarding X-ray emission, arcing were logged and used for distant control of the test regime (see Fig. 8). A fast interlock system on the vacuum controller's output switched off RF if residual gas pressure exceeded 10^{-6} mbar. After RF processing the vacuum better than $5{\cdot}10^{-7}$ mbar was obtained.

RF Power Tests

During RF processing we were raising the RF cavity gap voltage by 5-10 kV steps. Conditioning was started in pulse mode to perform RF power conditioning otherwise due to the multipacting discharge there was a deterioration of vacuum to inadmissibly low level. After several days of RF conditioning 300 kV of the gap RF voltage was reached in CW mode and was kept for a least one day without any vacuum activity. We reached 470 kV in a pulse mode.

During the testing dependency of resonance frequency on RF power was measured. Due to heating of different cavity parts the resonance frequency drifted in the range of 300 kHz when the RF power is switched on, so the plungers tuning range of 150 kHz is not sufficient. To overcome this problem we suppose to use an ancillary Master Oscillator of the control system. When the RF power is switched on and the RF cavity is warming up the ancillary Oscillator and cavity tuner are operated so that frequency of ancillary oscillator would coincide with that of the Microtron Master Oscillator. Then the system is switched to the Microtron Master Oscillator.

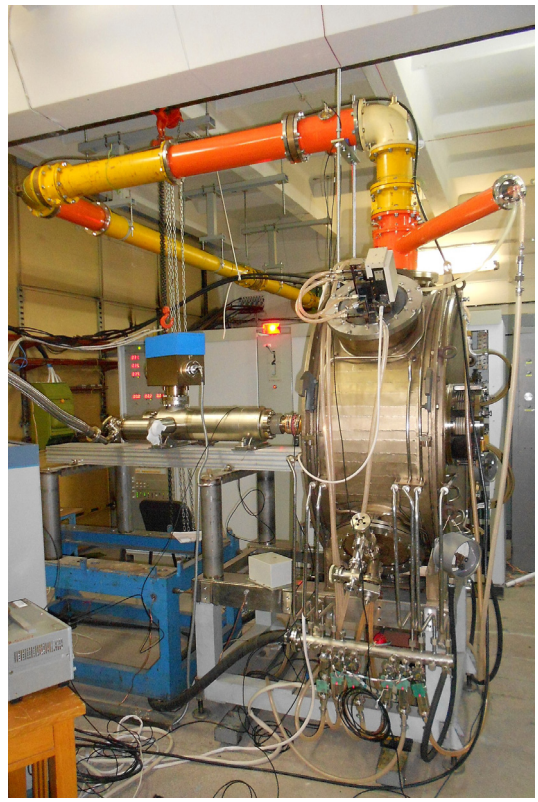

Figure 8: RF stand of the conditioning at high RF power.

During testing we compensated the total frequency drift of the cavity resonance frequency down to 100 kHz by redistribution of the water flow in different cooling channels. The maximal water flow of 12 l/min was directed to the insertion and minimal flow of about 1 l/min to the cavity cylindrical wall. The maximal temperature of about 60ºC was at the membrane connecting the insertion with right side wall. The vacuum in continuous mode was measured to be $4{\cdot}10^{-6}$ Pa.

At maximal gap voltage of 300 kV the X-ray radiation of 36 mR/hr was measured at the distance of 1.7 m from cavity.

CONCLUSION

RF gun cavity has been tested; operated gap voltage of 300 kV is obtained. Now the work with the cathode installation and beam diagnostics hardware is underway.

REFERENCES

[1] V.P. Bolotin et al. NIM A 557 (2006) p.23.
[2] V. Volkov et al., Thermionic cathode-grid assembly simulations for RF guns, PAC09, Vancouver, Canada, p.572.
[3] V.S. Arbusov et al., Accelerating RF system of microtron-recuperator for FEL, RuPAC, Dubna 2004, p. 318-320.
[4] A.N. Lukin, BINP, Novosibirsk, private communication.

THE SYSTEM OF POWER SUPPLIES, CONTROL AND MODULATION OF ELECTRON GUN FOR FREE ELECTRON LASER

E.A. Kuper, V.R., Kozak V.R.Mamkin, V.K. Ovchar, V.V. Repkov, S.S.Serednyakov,
S. V. Tararyshkin, D.A. Zverev, BINP, Novosibirsk, Russia

Abstract

The system of power supplies, control and modulation based on triode cathode-grid unit was designed for producing of pulsed electron beam for free electron laser FEL [1]. The main part of the system located inside the tank filled with SF6 gas and has -300kV potential. It's supplied through the isolated transformer and controlled through the fiber optic link with CAN interface. The GaN RF transistor in the output stage of modulator composed of hybrid assembly on the BeO ceramic plate. Pulsed output voltage of modulator can be regulated 0-120V on the load 25Ω. Time duration is <1ns. Repetition rate is 20kHz-20MHz (90MHz). Start of modulator from timer performed through the 1GHz fiber optic link.

The inverter is supplying of isolated transformer and timer for start of modulator with synchronization to RF voltage for grouping and accelerating are located in the control room. The timer ensured the compensation of the slow time shift of the electron beam relatively to RF voltage phase.

The control code was wrote on C++ language under Windows operating system using QT framework, and provide all algorithm of steering in real time with others operating programs for FEL with remote control Channel Access server from EPICS.

INTRODUCTION

For effective work of electron accelerator for Free Electron Laser (FEL) the system of power, control and modulation of triode cathode-grid unit was designed. It was designed with the high end components: GaN JFET transistors, 1GHz fiber optic link and RF micro strip transformers. The pulses on the output of modulator have very high parameters.

- Time width of pulses 1ns
- Pulse amplitude 0-120V
- Repetition rate 20kHz-90MHz
- Load 25Ω
- Part 2 of the system works at -300kV potential

SYSTEM DESCRIPTION

The system can be divided on two parts as depicted in Figure 1. The part 1 is under ground potential and provide power, control and start pulses (St) for part 2. It consists of power inverter, timer and two fiber optic converters. Power inverter has 220V input line with 50 or 60Hz. The output of power inverter is connected to input coil of isolated power transformer (300kV). Timer generates start pulses (St) with phase attached to RF voltage on the grouping resonator. The first fiber optic converter works as galvanic isolation for start pulses (St) and has 1GHz bandwidth. The second fiber optic converter works as galvanic isolation for CAN interface and has 1MHz bandwidth. The part 2 works under -300kV accelerating potential in the tank filled pressed SF6 gas (1.5 excessive bars). Figure 2 shows the total view of part 2. It consists of a cathode-grid unit, modulator, power supplies, isolated transformer, control unit CEAC124 and fiber optic converters.

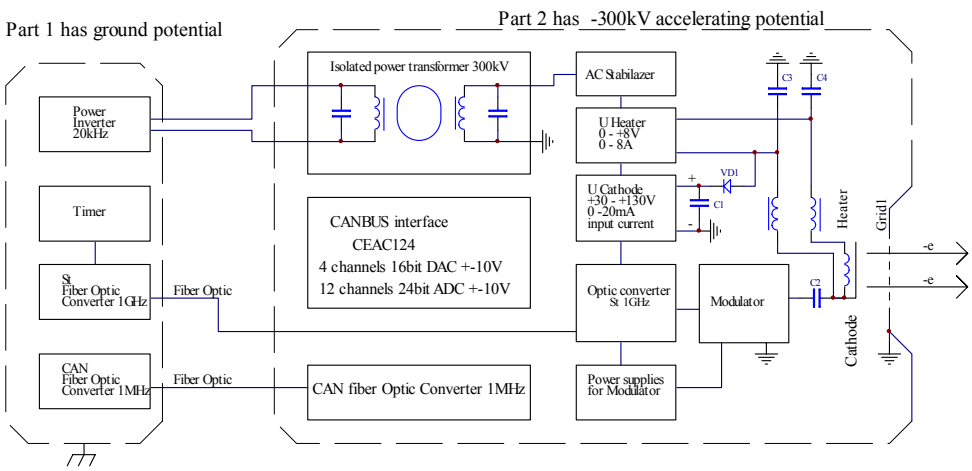

Figure 1: Block diagram of the system.

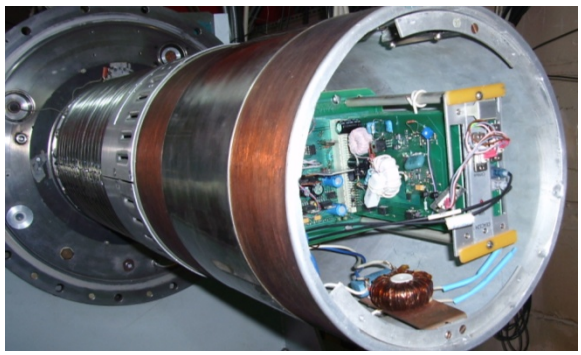

Figure 2: The part 2 works at -300kV potential.

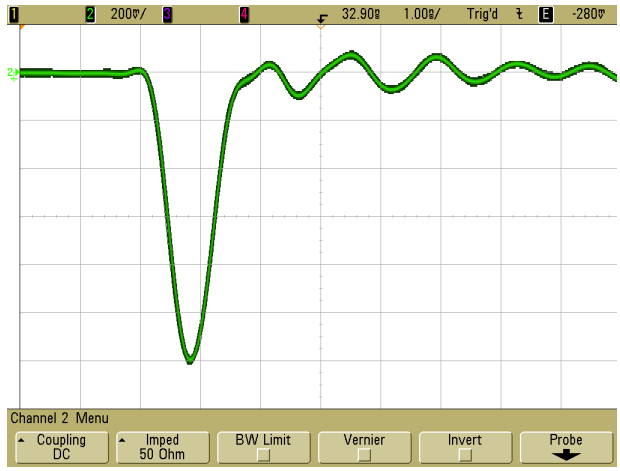

Figure 4: Modulator output pulse on 25 Ω load

Electric power for part 2 goes from power inverter through isolated power transformer (isolation voltage 300kV) to AC stabilizer and to set of power supplies. Power supplies consist of supplies for heater, cathode bias and four power supplies for modulator, control unit and fiber optic converters. For control signals isolations (300kV) we used plastic fiber optic lines with 1MHz bandwidth. For start signal isolation we used silica fiber optic line with 1GHz bandwidth. Fiber optic cables goes through vacuum tight connectors directly in the electron gun tank, filled with pressed SF6 gas. Inside tank there is sectioned isolation of these fiber optic cables along 40cm of sectioned isolators of electron gun.

MODULATOR

Figure 3 shows modulator block diagram.

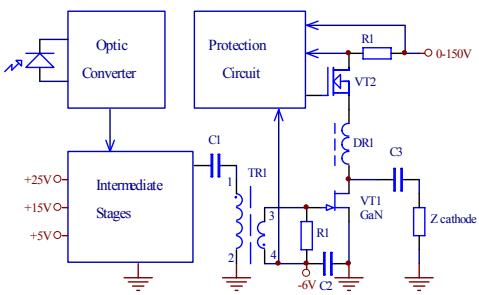

Figure 3: Modulator block diagram.

The main feature of modulator is GaN JFET RF transistor [2] in the output stage. The picture of 100 times attenuated signal from modulator output on the load 25 Ω is depicted in Figure 4. Time scale is 1ns per division. Real vertical scale of output signal is 20V per division. So we can see 1ns pulse with amplitude 120V on 25 Ω load. Repetition rate of modulator can be from 0 up to 90MHz. This modulator has very high efficiency. Only 30V from 150V of power supply dissipate in GaN transistor. GaN JFET transistors have great RF and power parameters but they have also one disadvantage. They are open when input gate voltage near 0V. It must be -6V of input gate voltage for total close these transistors. During switch on or switch off power supplies there may be uncontrolled situations when we have drain voltage but gate voltage near 0V, therefore transistor can be open and high drain current can destroy transistor. So, for reliable work of GaN JFET transistors, special protection circuit was designed. It watches for gate voltage and if this voltage to low then, this protection circuit switches on, and removes voltage from transistor drain. Also this protection circuit watches the average current of transistor drain and switches on during 1us if current more then threshold value. After 10ms protection circuit automatically switches off and restores transistor drain voltage. So, this circuit removes disadvantage of GaN JFET transistors. Pulse transformer TR1 which connected to input GaN transistor VT1 has very low output impedance 6Ω. Its construction based on strip lines and two holes RF ferrites. Optic converter accepts start signal St from timer and transmit it to intermediate stages of modulator. They are consisting of two stages with RF NPN transistors and two stages with RF MOSFET power transistors. Figure 5 shows cathode grid unit and output stages of modulator. Figure 5 shows thermo gram of modulator at 50MHz repetition rate. Alternative stile of modulator reported in [3]

SUMMARY

For output stage transistor we try many types of Si RF transistors, few SiC RF transistors and only GaN RF transistors have suitable parameters and reliability in real installation.

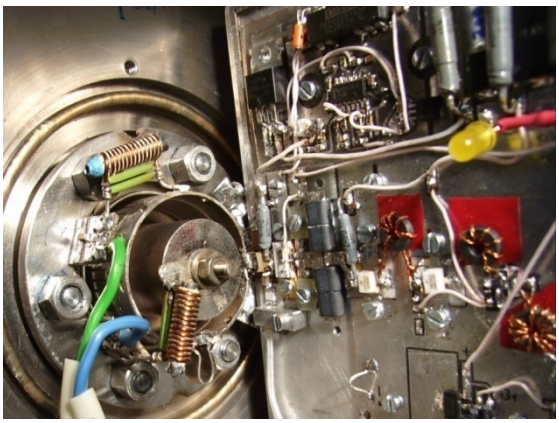

Figure 5: Cathode-grid unit and modulator.

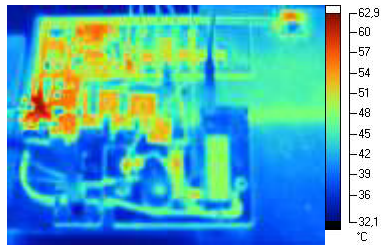

Figure 6: Thermogram of modulator.

REFERENCES

[1] ssrc.inp.nsk.su/CKP/biblio/2012/a11.doc
[2] http://www.rfmd.com/CS/Documents/RF3932DS.pdf
[3] N.A. Vinokurov. et. al. Source of High Electron Current for Injection into Accelerator. RuPAC 2006, Novosibirsk, Russia

A PS-PULSED E-GUN ADVANCED TO A T-WAVE SOURCE OF MW-LEVEL PEAK POWER

A.V. Smirnov, RadiaBeam Technologies Inc., Santa Monica, CA 90404, USA

Abstract

A coherent source based on an electron gun is considered to deliver high instantaneous power comparable to that available from a few most powerful sources operating at mm-sub-mm wavelengths. A DC or RF E-gun is integrated with a robust, compact, efficient, dismountable radiator inside the vacuum envelope. Resonant Cherenkov radiation is driven by a low-energy photoinjector operated in a custom mode combining strong over-focusing, robust slow-wave structure, and pulse sub-ps photoinjectior employing on-cathode beam modulation. Single pulse mode operation is enhanced with filed compression effect at high group velocity. The performance is analyzed analytically and numerically.

INTRODUCTION

A huge variety of applications in biology, medicine, chemistry, solid state physics, radio astronomy, homeland security, environment monitoring, spintronics, advanced spectroscopy, and plasma diagnostics need several orders higher THz peak power than it is available today for universities, middle-sized and small labs and businesses. Many of these applications are related to fast processes, emerging time-domain spectroscopy (TDS), and imaging that require short THz pulses of high intensity.

So far only a few FELs are dedicated to operate at THz frequencies. Typically such an FEL is driven by tens of MeV electron accelerator and contains an undulator and an optical cavity. The first FEL facility to provide THz radiation to users has been the UCSB-FEL (0.3-0.8mm wavelength, ~10kW power in 1-20μs pulse length). The world-largest FEL Facility at JLAB produces a broadband THz radiation [1] with 100W average and about 1MW peak power. To date the Novosibirsk FEL [2] is the most powerful coherent THz source operating at 0.12-0.24mm wavelengths and 0.3% line width to deliver 0.4kW average power and up to ~MW peak power. It comprises 20m long optical cavity, 4m long undulator driven by a 40-50 MeV e-beam accelerated in RF linac with energy recovery. The ENEA-Frascati FEL-CATS source operates in the 0.4-0.7 THz range with about 10% FWHM line width [3] in a super-radiant mode without long optical cavity. A ~1.5 kW power is measured in 5-μs macropulse at 0.4 THz (corresponding to up to 8kW peak in each 3-10 ps micropulse).

More compact, but still powerful, undulator-free, sub-mm wavelength source is considered here. The beam is microbunched on the photocathode with laser using beatwave or multiplexing technique. Important property exploited in the concept is capability of natural focusing of the intense electron beam down to sub-wavelength spot size in a conventional RF high-brightness photoinjector. These two remarkable features allow effective THz radiation resulted from interaction between high-impedance, slow-wave structure and very high-density, microbunched electron beam.

DESIGN FEATURES

The design concept of the radiator integrated into the E-gun driver is illustarted in Figure 1. The radiator can be based on periodic stricture (gratings) or dielectric (PECVD diamond). It may be circular (capillary), rectangular, or planar. The source can operate in two modes: single microbunch and train of microbunches with corresponding laser system.

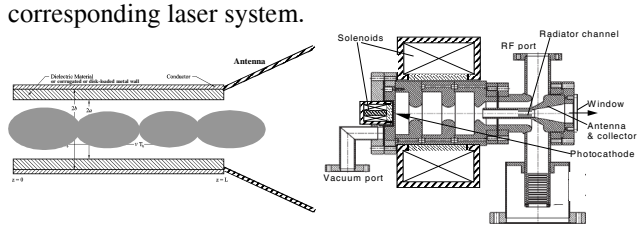

Figure 1: LEFT: THz extractor scheme (radiator). RIGHT: Schematic layout of sub-mm source based on 2-cell, pulse RF or DC-RF electron gun.

Different schemes of THz and exhaust electron beams separation and utilization are exemplified in Figure 2. Simple tapering of the radiator channel turns it into a broader spectrum source for powerful time domain spectroscopy or active "colorful" imaging for inspection and security applications.

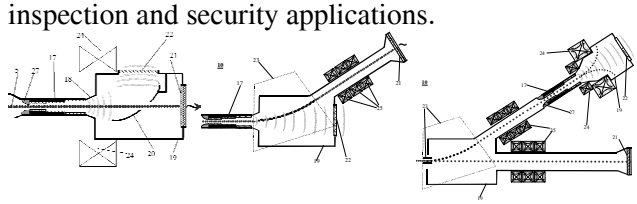

Figure 2: Schematic configurations of a combined T-X-ray source. LEFT: straight electron beam and bended THz beam. MIDDLE: bended electron beam and straight THz beam; RIGHT: alternating electron beam deflected on X-ray target or THz radiator with e-beam scattering and dumping.

A capillary channel has already been used in a number of wakefield research setups (see, e.g., [4]). It is exemplified in Figure 3, left. Radiation directivity can be enhanced with optimized shaping of the dielectric (see Figure 3, right). By sacrificing shunt impedance (see Table 1) one can make the radiator much more robust to sustain THz-field-induced stress and heat as well as beam halo

interception in a narrow channel. Such a non-circular design is shown in Figure 4.

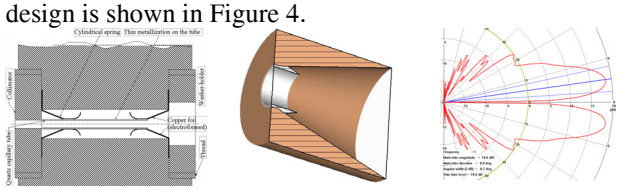

Figure 3: LEFT: Mechanical insertion of a metallized quartz capillary tube into holders (one of them is antenna). The metallization layer is limited by ~ micron to provide minimal mechanical and thermal stability (skin depth <0.1 μm at 1THz). MIDDLE: Shaped dielectric. RIGHT: Radiation diagram with improved directivity.

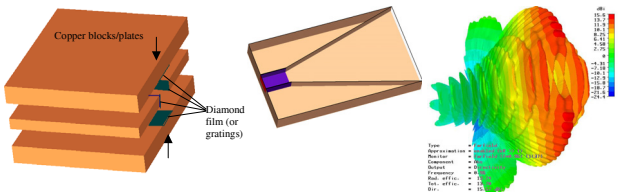

Figure 4: LEFT: Exploded view of a robust, high average power, planar radiator. MIDDLE: a cut-view of planar slot antenna attached to square diamond-coated or grated capillary tube. On the right: 3D diagram of far-field pattern radiated from the square channel.

Table 1. TM_{01} mode parameters for a capillary channel at 0.95-0.97 THz resonant frequency and different coating materials.

Material	ε	a, μm	d, μm	R/Q, kOhm/m	β_{gr}	Q/1000
Teflon	2.1	300	31	14.7	0.82	1.9
		520	26	1.07	0.89	2.4
Barium tetra-titanate	37	300	30	27.7	0.127	0.6
Sap-phire	11	300	14	18.9	0.76	1.2
SiO_2	3.8	336	19	12.4	0.83	2.1
Dia-mond	5.7	336	16	12.7	0.82	1.8
		300		8	0.83	1.7

The limits imposed by space charge 3D effects in the Cherenkov THz radiator do not allow utilizing efficiently a sub-ps laser burst carrying more than 50-100μJ energy. To overcome this limit and produce higher THz energy one can use longer laser pulses of the same energy but modulated intensity. One way to introduce THz premodulation in the long-bunch mode is photomixing. The metal photocathode (usually copper or magnesium) has to be illuminated by a laser (usually Neodymium or Sapphire laser at UV harmonic) having two (or more) lines with ~THz frequency separation. The beatwave option does not require any interaction space or ballistic drift [5]; it still possesses coherency and possibility of direct synchronization and tuning. This method was proposed for superradiant FEL [6] and Smith-Purcell FEL [7]. Two (or more) laser lines with a ~THz frequency shift can be created in different ways. Laser systems for photoinjectors a capable to deliver about 0.3-3mJ (in UV) per 5-20ps pulse using chirped pulse technology with stretcher/compressor. For a typical laser system [8] the required modification is just an addition of one mode locked tunable oscillator to provide a two-line seeding generation with appropriate frequency shift 0.67-1 THz (or 1.2-1.8nm for 744nm before frequency tripling). This frequency range is within the bandwidth of the linear regenerative amplifier (e.g., Ti:Supphire amplifier TSA-50 Positive Light) and the rest of the same laser system can be used.

The THz field induced in the channel is evaluated analytically in time domain in Figure 5 assuming a 0.6mm aperture channel having dielectric coating with ε=2.1 and 31μm thickness and a cosine squared charge distribution resulted from two-wave 0.96THz beating. Neglecting phase space dilution and debunching, detuning and transverse effects it gives bunch formfactor 0.5 and P=8.2MW peak power at I=60A beam current. To include the 3D transient beam dynamics effects PIC simulations have been performed.

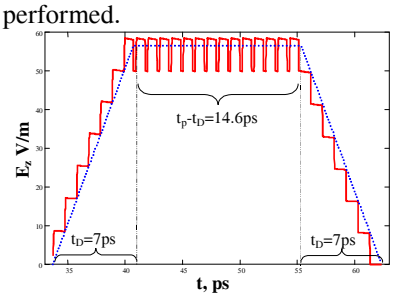

Figure 5: Field amplitude profiles calculated analytically [10] at z=L. Accelerated beam pulse length 21.6ps, L=1cm, filling time 40.7ps, drain time 7ps, formfactor=0.5, r/Q=14.7kOhm/m, Q≈1900, and β_{gr}=0.82 at f=0.96THz.

PERFORMANCE SIMULATIONS IN A BEATWAVE MODE

The setup of Figure 1(right) is used for ASTRA simulations. The required focusing is provided by both magnetostatic and RF fields of the injector given in Figure 6.

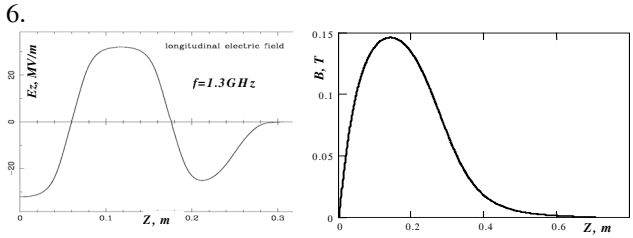

Figure 6: Longitudinal RF electric and magnetostatic field profiles used in simulations of the 2-cell RF photoelectron gun.

The result of optimized beam transport at I≈108A beam current and E_z=32MV/m cathode field is shown in Figure

7 at laser pulse length is 26 ps, bunch charge is 2nC, maximum RF electric field in the accelerating cavity is Ezmax=32 MV/m, Bzmax=1.46 kGs, and beam kinetic energy is 4 MeV. The beam waist rms radius is 110μm at Z=0.326m distance from the cathode. Unusually large laser spot on the cathode (~3mm vs. sub-mm rms radius) and magnetic field (1.46kG vs. 1kG maximum) resulted from the wavelength limit imposed on the beam waist size.

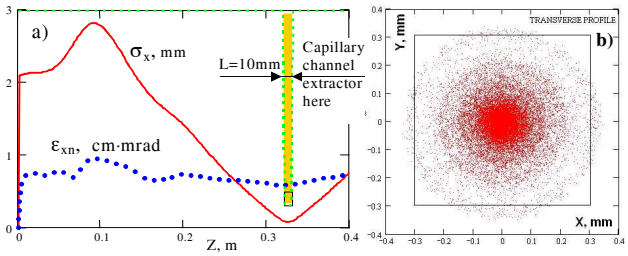

Figure 7. Beam rms horizontal (or vertical) dimension (solid curve) and normalized, transversally uncorrelated emittance (dotted line) plotted as a function of the distance from the cathode (a), and beam transverse profile at the waist (b).

Overall particle losses are 2% and 3.1% for quadratic and circular 1 cm long channels correspondingly for the same ∅ 0.6 mm minimal beam aperture and radial transverse distribution on the cathode. The most of this loss takes place in the channel entrance for the beam head and tail that can be easily collimated, whereas the bulk of the beam (between the two local waists, see Figure 8 and clip [9]) loses less than 1.4% of particles inside the channel.

Formfactor optimization and generated field results are shown in Figure 9. In our beatwave model the beam pulse compression during acceleration require Δf =0.657 THz on-cathode modulation to get the 0.958 THz resonance.

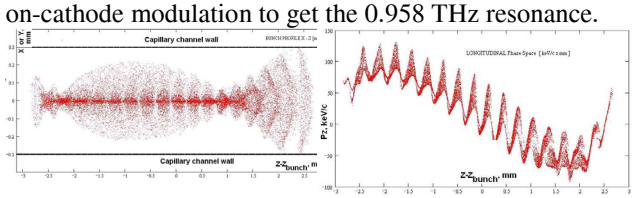

Figure 8: LEFT: Beam X-Z or Y-Z transverse profile inside the capillary channel. Modulation is produced with two-wave beating having 1.55ps period of intensity at the cathode. Laser flat-top pulse length is 26ps, the capillary channel center is positioned at z=0.326m from the cathode (see animation [9]). RIGHT: Longitudinal phase space of the microbunched beam near its waist in the capillary channel.

The beam-induced fields are calculated as superposition of radiation of each macroparticle (up to ~50,000 particles) in time domain taking into account high group velocity effects [10] resulted from large gap-to-wavelength ratio and changing formfactor: the microbunch is overfocused and its 3D shape changes rapidly in the interaction space. Peak THz power is 5.7 MW, power averaged over the pulse 1.3 MW, terahertz energy radiated by the 2nC premodulated bunch is 9 μJ.

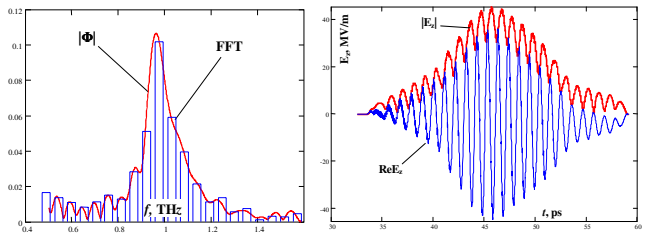

Figure 9: LEFT: Formfactor as a function of frequency at z=0.326m. RIGHT: Output longitudinal electric field amplitude and its real part.

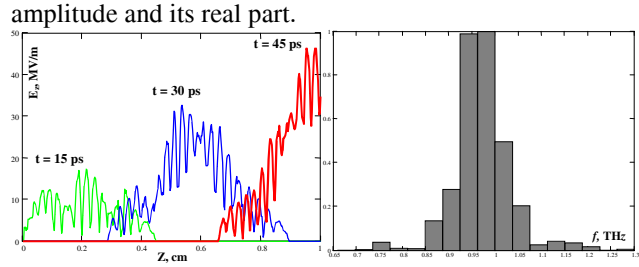

Figure 10: LEFT: Electric field amplitude profile along the capillary channel at different time moments (see animation [11]). RIGHT: Electric field spectrum corresponding to Figure 9.

ACKNOWLEDGMENTS

This work has been supported in part by the Department of Energy (DOE) under the contracts #02-07ER84877 and W21P4Q-12-C-0212. The author is grateful to Pietro Musumeci for experimental confirmation of 3D sub-mm microbunching performed at UCLA PBPL with S-band RF photoinjector.

REFERENCES

[1] http://www.usarmythz.com/THz/R+D/THz-HP-Williams.shtml
[2] www.kinetics.nsc.ru/center/public/st05.pdf
[3] Doria A.; Gallerano G.P.; Giovenale E.; Messina G.; Spassovsky I, *Phys. Rev. Lett.* V. 93 (2004) 26481.
[4] H. Badakov, et al. E-169: Wakefield Acceleration in Dielectric Structures. http://www.slac.stanford.edu/grp/rd/epac/Proposal/E169.pdf
[5] Reiche S.; Joshi C.; Pellegrini C.; Rosenzweig J.B.; Toshitsky S. Ya.; Shvets G., Proceedings of the 27th Free Electron Laser Conference, IEEE: Stanford, CA, 2005; pp 426-428.
[6] Huang Y. C. Proceedings on Joint Workshop on Laser-Beam *I*nteractions and Laser and Plasma Accelerators, NTU: Taipei, Taiwan, 2005; p 15-23.
[7] Huang Y.C.; Chang H. L; Lin Y.Y. Proceedings of the 28th Free Electron Laser Conference, Bessy: Berlin, Germany, 2006; pp 699-701.
[8] http://www.hep.anl.gov/pmalhotr/awa-new/links/laser-system.htm
[9] http://www.vimeo.com/637190
[10] Smirnov A.V., Nucl. Instrum. and Meth. 2002 NIM A 480 (2-3), 387-397.
[11] http://www.vimeo.com/637228

HIGH DUTY CYCLE ION SOURCES AT GSI AND FAIR

J. Pfister*, A. Adonin, R. Hollinger and K. Tinschert
GSI - Helmholtz Center for Heavy Ion Research, Darmstadt, Germany

Abstract

Future heavy ion experiments at GSI and FAIR demand for high current as well as highly brillant ion beams of various metallic and gaseous ions produced by the GSI accelerator facility. Therefore GSI's Ion Source Group is continously developing and operating various types of ion sources feeding the UNIversal Linear ACcelerator (UNILAC). In this contribution a status overview of operated high duty cycle ion sources including important ion source data as beam current and beam spectrum as well as future perspectives for the ion source operation for FAIR is presented.

INTRODUCTION

GSI Helmholtz Center for Heavy Ion Research is providing beams of almost every chemical element up to the heaviest stable ions like Uranium to users of the worldwide scientific community. Among others [1] two types of ion sources are dedicated for operation in the high duty cycle regime, namely the Penning Ionisation Gauge (PIG) placed at the high current injector and the Caprice-type Electron Cyclotron Resonance Ion Source (ECRIS) placed at the high charge state injector.

STATUS OF ION SOURCES

During the last years, apart from regular continuous operation of GSI's injectors, the performance of the high duty cycle ion sources has been improved. The operational results and improvements are shown in the following subsections.

Penning Ionisation Gauge - PIG

The PIG is in use for more than 30 years at GSI [2]. This type of source is the working horse especially for experiments carried out at the experimental hall of the UNILAC. Therefore the main feature is the 50 Hz operation with duty factors up to 25%. For the PIG a combination of extraction and post-acceleration is used in order to deliver the injection energy of 2.2 keV/u to the beam injected into the radio-frequency quadrupole (RFQ) for all available elements. The low energy beam transport line (LEBT) from post-acceleration towards the RFQ is about 10 m long and consist of several magnetic focussing quadrupole doublets and triplets, steerers, beam diagnostic stations (profile grids, faraday cups, beam transformators) as well as an analysing magnet for mass separation of multi-isotopic elements. Finally the beam is bend to the axis of the UNILAC via a 12.5 degrees magnetic switchyard, where also the high current beam is inclined to the linac.

The PIG is used for producing beams of gaseous as well as for metallic elements. Depending on experimentalists request development of new elements and isotopes has been done in the recent years. Most common and recent elements from the PIG source are shown in Tab. 1.

It is obvious that for metallic ions using a sputter electrode the lifetime of the source is normally not longer than a day with 25% duty cycle and reasonable currents whereas the sources with gaseous elements have lifetimes of more than just a few days. For the sputter as well as sources for gaseous elements a general refurbishment campaign is ongoing which is almost a general setup of a new source. 90% of the parts are replaced and only about 10% are carefully cleaned.

Table 1: Selections of ion beam species with corresponding beam currents in front of the RFQ.

Ion species	Intensity (eμA)	Ion species	Intensity (eμA)
$^{12}C^{+}$	300	$^{74}Ge^{4+}$	20
$^{12}C^{2+}$	60	$^{84}Kr^{3+}$	40
$^{12}C^{3+}$	73	$^{86}Kr^{2+}$	26
$^{20}Ne^{+}$	150	$^{86}Kr^{3+}$	200
$^{20}Ne^{3+}$	35	$^{92}Mo^{4+}$	5
$^{22}Ne^{+}$	200	$^{97}Mo^{4+}$	6
$^{40}Ar^{+}$	22	$^{98}Mo^{4+}$	3
$^{40}Ar^{2+}$	250	$^{124}Sn^{5+}$	8
$^{40}Ca^{+}$	80	$^{132}Xe^{5+}$	60
$^{40}Ca^{2+}$	100	$^{132}Xe^{6+}$	30
$^{40}Ca^{3+}$	50	$^{136}Xe^{3+}$	250
$^{46}Ti^{2+}$	20	$^{136}Xe^{4+}$	6
$^{50}Ti^{2+}$	70	$^{152}Sm^{3+}$	60
$^{51}V^{2+}$	55	$^{197}Au^{4+}$	500
$^{52}Cr^{2+}$	70	$^{197}Au^{7+}$	200
$^{56}Fe^{2+}$	200	$^{197}Au^{8+}$	20
$^{56}Fe^{3+}$	60	$^{208}Pb^{4+}$	100
$^{58}Ni^{2+}$	100	$^{208}Pb^{5+}$	10
$^{58}Ni^{3+}$	200	$^{208}Pb^{9+}$	20
$^{58}Ni^{4+}$	50	$^{209}Bi^{4+}$	200
$^{60}Ni^{2+}$	18	$^{209}Bi^{5+}$	300

* j.pfister@gsi.de

Electron Cyclotron Resonance Ion Source (ECRIS)

The High Charge State Injector (HLI) with its 14.5 GHz CAPRICE ECRIS had been established as an injection line for the UNILAC at GSI two decades ago. It has been in operation since then. The large number of experiments served with UNILAC beams require a great variety of highly charged ion species including isotopically enriched samples for ion beam production.

An ECRIS had been chosen as ion source for the HLI because it can work without limitation of duty cycle in CW mode as well as in different pulsed modes with enhanced intensities [3, 4]. In the ECRIS plasma long ion confinement times are possible so that very high charge states can be extracted. This makes post-acceleration avoidable and facilitates the direct injection into a compact linac consisting of an RFQ and an IH-structure. One major advantage of an ECRIS is the use of microwave injection to sustain and to heat the plasma electrons very effectively instead of using electron emitting filaments and arc discharge. So it can work over long time periods without maintenance. Furthermore ECRIS operation has a very low material consumption implying a high operation efficiency. Due to these characteristics the ECRIS turned out to be perfect for providing C^{2+}-beams for the cancer therapy project at GSI with good stability and high reliability. Patient treatment started in 1997 and initiated the concept for the dedicated Heidelberg Ion Beam Therapy Center (HIT), which took over the patient treatment in 2007.

While elements generated from gases or gaseous compounds can easily be transported into the plasma, materials in the solid state must be transformed into this state to be fed into the plasma. The method of thermal evaporation has been established and used at GSI for many years, because it resembles closely the operation with gases and provides higher intensities as the sputtering method and lower contaminations compared to the MIVOC method (Metal Ions from Volatile Organic Compounds). A sophisticated technology using resistively heated ovens was developed [5]. The effective thermal evaporation of metallic elements leads to long oven lifetime while the use of a load-lock system facilitates an easy maintenance for exchange or refilling of the oven and is perfectly adapted to the needs of long beam runs at the accelerator.

One of the frequently provided ion species is the rare isotope ^{48}Ca which is produced from highly enriched isotopic material. Fig. 1 show a charge state spectrum and the corresponding beam stability for ^{48}Ca, which is a good example for the efficiency of ion beam production. A low material consumption rate of 200 μg/h was observed for ^{48}Ca when optimized on 10+. Up to 43% of the evaporated ^{48}Ca could be analyzed behind the dipole magnet spectrometer as ions of the non-desired charge states 3+...11+ while 12.6% of the material could be provided as ion beam of the requested charge state 10+. While most of the solid elements are directly produced from the pure elemental material in some

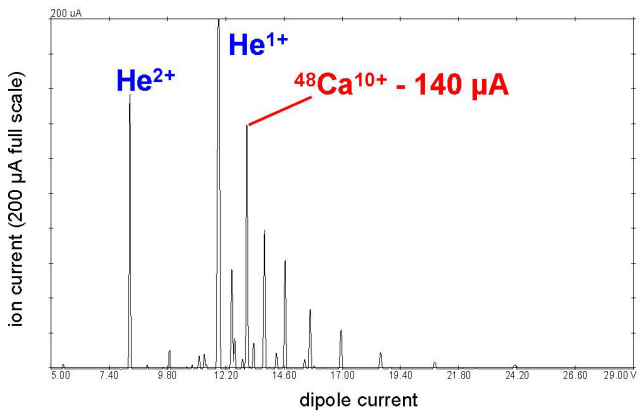

(a) charge state spectrum

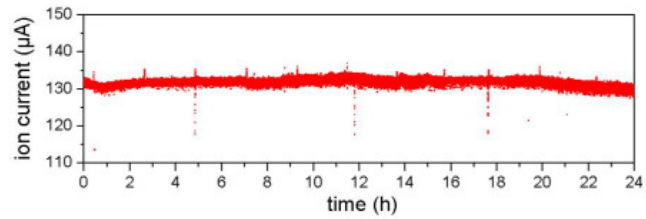

(b) intensity stability over 24 hours

Figure 1: Recorded data of ^{48}Ca. (a) charge state spectrum of ^{48}Ca + He optimized on $^{48}Ca^{10+}$, (b) intensity of the analyzed $^{48}Ca^{10+}$-beam versus time over a period of 24 hours.

cases it is necessary to evaporate compounds as ZnO or SiO. These applications in most cases are the result of dedicated development work. As the increase of available ion beam intensities is one of the most desired goals several methods have been investigated like gas mixing, the use of electron-donors, or of biased probes at the injection side of the plasma chamber. The availability of wide range microwave generators based on travelling wave tube amplifiers made it possible to apply frequency tuning and multiple frequency heating of the ECR plasma. Thus it is possible to excite different RF mode distributions in the plasma chamber which can provide more efficient microwave coupling and therefore enhanced ion beam intensities extracted from the plasma [6].

ION SOURCE DEVELOPMENTS TORWARDS FAIR

For the high current injector respectively the PIG source first steps are already undertaken in order to increase the stability while extracting higher currents out of the plasma. Due to mechanical design of the source the distance between high voltage potential and the dipole vacuum chamber is only a few milimeters. Due to this fact regular sparking was occuring in this region. By replacing the safety covers at the top end of the anode with a large insulator,

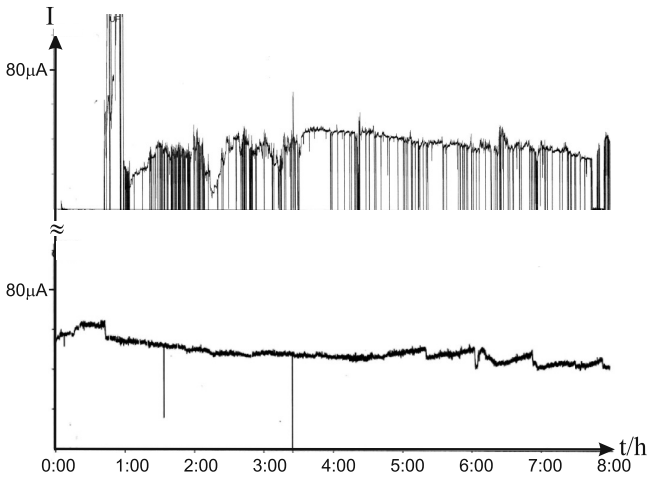

Figure 2: Top: Current vs. time plot without insulator, bottom: Current vs. time plot with insulator. Each vertical line in both graphs indicate at least one sparking event. Each plot represents a period of 8 hours.

it was possible to reduce sparking by orders of magnitude (see Fig. 2). The evaluation of remaining sparks is still ongoing. Also beam transport from the source towards the RFQ is going to be evaluated again in the near future. The long term perspective also includes an upgrade of the Penning ion source while preparing for GSI being an injector for the FAIR facility.

The requirements to ion beams for FAIR are characterized by highest beam intensities but at rather low duty cycles in pulsed operation with comparably short pulse lengths. Besides developments to expand the number of available ion species as ion beams and to improve the extraction from the ECRIS and low energy beam transport of the ion beams dedicated research will be performed towards the special requirements for FAIR. The main issue will be the optimization of pulsed modes based on investigations previously performed [4]. The pulsing is effectively achieved by modulating and switching the microwave generators by means of arbitrary waveform generators. Thus a synergy can be obtained with the optimization of the microwave-plasma coupling which is a further important issue as described above.

Multipurpose Superconducting ECR Ion Source (MS-ECRIS)

An increased microwave frequency allows for enhanced plasma densities and ion currents in an ECRIS. According to semiempirical scaling laws the electron density is directly related to the square of the microwave frequency. Considering the electron cyclotron resonance condition the increased microwave frequency requires an increase of the magnetic field. A useful frequency of 28 GHz requires magnetic flux densities above 2.2 T implying the use of superconducting magnets. In cooperation with European institutions GSI initiated a project to build a prototype of an

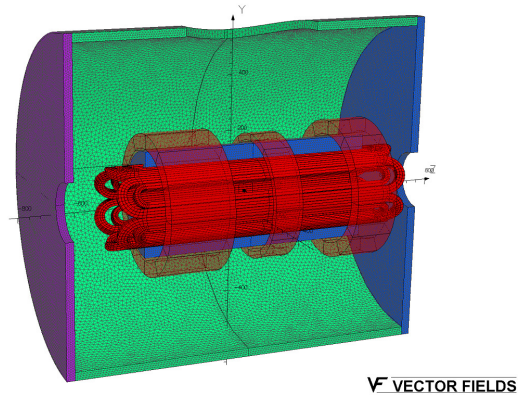

Figure 3: Model for the magnetic coil design.

advanced Multipurpose Superconducting ECR ion source (MS-ECRIS) to achieve a considerable improvement of the performances [7]. The most challenging issue is the very high level of magnetic field, so far never achieved for similar magnet systems. Therefore the realization of the magnet system for MS-ECRIS turned out to be very demanding. Its design utilizing iron collars requires a sophisticated clamping which has been subject to several modifications and is presently under investigation at the manufacturer's site [8].

CONCLUSION AND OUTLOOK

Since the FAIR project is demanding for higher intensities optimisation of the two high duty cycle injectors will be forced. First steps are already done and more of them will follow in the upcoming years. For the PIG source there is the goal of increasing extraction and transport efficiency to the RFQ, while after final tests of the magnet system production and assembly of the new MS-ECRIS will take place at GSI.

REFERENCES

[1] R. Hollinger et al., High Current Ion Sources for the FAIR Accelerator Facility, these proceedings.

[2] H. Schulte, W. Jacoby, B.H. Wolf, Development of Penning multiply charged ion sources for the UNILAC, IEEE Trans. Nucl. Sci. 23, 1042 (1976).

[3] K. Tinschert, J. Bossler, S. Schennach, H. Schulte, Rev. Sci. Instrum. 69, 709 (1998).

[4] K. Tinschert, R. Iannucci, J. Bossler, R. Lang, Rev. Sci. Instrum. 75 (5), 1407 (2004).

[5] R. Lang, J. Bossler, H. Schulte, K. Tinschert, Rev. Sci. Instrum. 71 (2), 651 (2000); R. Lang, J. Bossler, R. Iannucci, K. Tinschert, Proc. 15th Int. Workshop on ECRIS, University of Jyväskylä, Finland, 180 (2002).

[6] F. Maimone, K. Tinschert, L. Celona, R. Lang, J. Mäder, J. Roßbach, P. Spädtke, Rev. Sci. Instrum. 83, 02A304 (2012).

[7] G. Ciavola et al., Rev. Sci. Instrum. 79, 02A326 (2008).

[8] K. Tinschert et al., Rev. Sci. Instrum. 83, 02A319 (2012).

HIGH CURRENT ION SOURCES FOR THE FAIR ACCELERATOR FACILITY

R. Hollinger*, A. Adonin, J. Pfister, GSI, Darmstadt, Germany

Abstract

Vacuum arc ion sources and filament driven multi cusp ion sources are used for the production of high current ion beams of a variety of metallic and gaseous ions at the GSI accelerator facility.

For the future project FAIR (Facility of Antiproton and Ion Research) it is foreseen to provide in addition to the existing ion beams a high current proton beam from a separate linear accelerator (plinac) and an exclusive high current uranium beam from a new ion source injector.

The contribution gives an overview of the performance of the existing high current injector and presents the challenges for the future injectors for proton and uranium production.

INTRODUCTION

The GSI facility is known as an accelerator with a variety of ion species within a wide range of energy at the end of the accelerator. Two ion source platforms arranged as a "Y" deliver ion beams for the universal linear accelerator UNILAC [1] (the high charge state injector HLI equipped with an ECR is not topic of this paper). One of it is equipped with a Penning ion source the other allows the operation with MUCIS, MUCIS2010, CHORDIS, MEVVA and VARIS ion sources.

For low energy experiments (3.6-11.4 MeV/u) with high duty factor the ion source Penning [2] is used generally. With this working horse we are able to offer a multiplicity of ion species with a large range of mass over charge ratio (A/ζ) [3]. For injection into the synchrotron SIS18 for high energy experiments (up to 4 GeV/u) the ion sources MUCIS, MUCIS2010, CHORDIS, MEVVA, and VARIS are used generally at low duty factor.

The specific injection energy for the RFQ is 2.2 keV/u with its space charge limit of 0.25×A/ζ [mA]. The acceptance of the RFQ is 138π mm mrad within a maximum mass over charge ratio of 65.

The article gives an overview of ion source data and injection parameter of most important ion species generated from the high current injector. Due to the fact that experiments at GSI request a wide range of beam intensity (single particle up to 10^{11} per spill) the reached ion source intensities do not assign the physical limit, even when the ion source operates with non-enriched material.

LOW ENERGY BEAM LINE

Fig. 1 shows the low energy beam transport section (LEBT) from the high current terminal (terminal north) to the radial matching section of the RFQ [4]. The Penning terminal (terminal south) with its LEBT section is not shown here, because it is equipped with the same components.

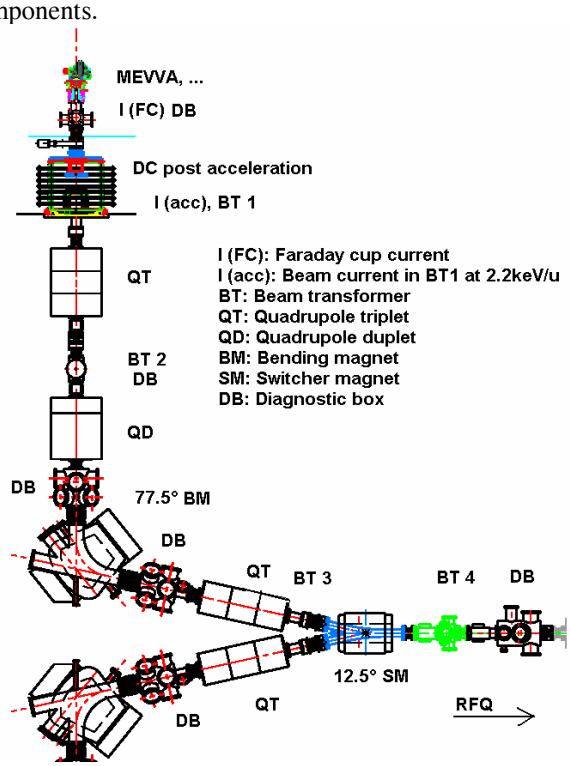

Figure 1: High current LEBT section of the UNILAC.

Close behind the ion source the LEBT section consists of a dc-post acceleration system to meet the right specific injection energy of 2.2 keV/u. In combination with the extraction system of the ion source it allows to accelerate the lightest ion species $^{1}H_{3}^{+}$ with an acceleration voltage of 6.6 kV up to $^{124}Xe^{2+}$ with 136.4 kV. A quadrupole triplet and doublet belong to the first transport section, followed by a 77.5° bending magnet for separation of the desired ion specie and charge state. The 12.5° switching magnet operates in a 50 Hz switching mode to allow the injection into the RFQ simultaneously from terminal north (max 5 Hz) and south (max 50 Hz) with two different ion species. Faraday cups, beam transformers, diagnostic grids and horizontal and vertical slits are installed to analyze the ion beam. A quadrupole quadruplet finally matches the ion beam into the RFQ.

HIGH CURRENT ION SOURCES

The ion sources MUCIS, CHORDIS, MEVVA, and VARIS are well described in the references [5-8]. All these ion sources are equipped with the same multi aperture 13-hole triode extraction system. The aspect ratio

* R.Hollinger@gsi.de

is 0.5, whereas the emission area is 0.92 cm^2. Generally high current ion sources are operated in the space charged limited extraction mode (SCLEM) compared to the emission limited extraction mode (ELEM) like an ECR ion source. Therefore, the extracted ion beam intensity is limited by the electrical field strength for a fixed geometry of the extraction system. Using special material for the extraction system (Elconite®) and preparation of the system under special conditions we reach field strengths of up to 11 kV/mm.

Filament Driven Ion Sources

The MUCIS and MUCIS2010 are filament driven volume type ion sources for gaseous ion production. Depending on the generated ion species the filament is made from tungsten or tantalum. All ion sources are equipped with up to six single filaments. The axial symmetric plasma chamber is equipped with permanent magnets for plasma confinement (cusp field Halbach configuration). The ion source operates generally with a duty cycle of 5 Hz and a pulse length of approx. 1 ms. Typical emission current densities are in the range of 30-120 mA/cm^2.

Table 1: Ion species for gaseous ion production from filament driven ion sources

ion	I_{FC} [mA/kV]	I_{ACC}/I_{RFQ}/SCL [mA]	current fraction [%] 1+/2+…
$^{1}H_3^+$	40/6.6	15/1/0.75	H_1:37, H_2:8, H_3:55
$^{2}H_3^+$	90/13.2	50/2/1.5	D_1:30, D_2:5, D_3:65
$^{14}N^+$	20/10	12/2.5/3.5	N:69, N_2:31
$^{12}CH_3^+$	30/8	12/1.2/3.75	div., C, H, CH,...
$^{14}N_2^+$	35/12	25/5.5/7	N:50, N_2:50
$^{20}Ne^+$	60/13	26/4/5	80/20 nat. mat.
$^{40}Ar^+$	65/20	42/20/10	80/20
$^{40}Ar^{2+}$	50/16	16/1.5/5	65/35
$^{80}Kr^{2+}$	60/22	28/0.15/10	17/53/29
$^{86}Kr^{2+}$	80/23	34/9/10.75	48/45/7 enriched
$^{132}Xe^{3+}$	25/18	17/0.02/11	79/18/3
$^{136}Xe^{3+}$	40/21	18/0.8/11.3	78/21/1 enriched
$^{136}Xe^{3+}$	40/21	18/0.07/11.3	78/21/1 nat. mat.

Table 1 gives an overview of ion species generated for standard operation. I_{FC} represents the ion beam current in the Faraday cup close behind the ion source with the corresponding extraction voltage. The beam current which is accelerated to 2.2 keV/u is given by I_{ACC}, the beam current in front of the RFQ by I_{RFQ}, and the space charge limit of the RFQ is given by SCL. The CHORDIS is equipped with a smaller plasma chamber compared to the MUCIS and MUCIS2010, the plasma electrode is on cathode potential, which results in a higher extracable emission current density, and the electron repeller inside the plasma chamber is electrically and not magnetically controlled compare to MUCIS type. For these ion sources the maximum charge state is one fold if the ion source is operating in the high density plasma mode. In consequence only for low plasma density operation it is possible to shift the mean charge state from one to two fold, e.g. for krypton or xenon operation.

The emittance of these low ion temperature ion sources is given by the geometry of the extraction system and the divergence angle. For all these ion sources the divergence angle is between 30 and 40 mrad, the outer diameter of the multi aperture extraction system is 20.5 mm. This results in an emittance value of roughly 500π mm mrad (320π mm mrad for the 90 % 4-rms value). The lifetime of the ion sources is limited by the lifetime of the filaments and in the range of several days (for xenon) up to weeks (for hydrogen).

Vacuum Arc Ion Sources

Vacuum arc ion sources of MEVVA and VARIS type are used for metallic ion production and for aggressive gases like oxygen. Here oxygen is used as an auxiliary gas and will be ionised in a secondary plasma process. These ion sources use a high density vacuum arc for plasma production. External magnetic fields and auxiliary gases influence the plasma production in a way that it is possible to shift the mean charge state from one fold up to four fold. Therefore, there is a wide range of ion species from these ion sources for the synchrotron injection. Table 2 summarize ion species for metallic ion production for GSI´s vacuum arc ion sources.

Table 2: Ion species for metallic ion production from vacuum arc ion sources

ion	I_{FC} [mA/kV]	I_{ACC}/I_{RFQ}/SCL [mA]	current fraction [%] 1+/2+…
$^{24}Mg^+$	80/18	28/2/6	24/62
$^{40}Ca^{2+}$	40/15	15/5/5	6/94
$^{58}Ni^+$	60/22	40/8/14.5	72/22/5
$^{58}Ni^{2+}$	60/18	17/5/7.25	8/76/16
$^{94}Mo^{2+}$	50/18	19/0.5/11.75	6/56/28
$^{100}Mo^{2+}$	50/18	19/0.5/12.5	6/56/28
$^{107}Ag^{2+}$	40/18	23/3/13.4	13/81/6
$^{142}Nd^{3+}$	80/28	32/1.5/11.8	0/4/87/9
$^{150}Nd^{3+}$	80/28	32/0.4/12.8	0/4/87/9
$^{181}Ta^{3+}$	75/24	31/7/15.1	0/0/56/35/8
$^{181}Ta^{4+}$	80/24	34/8/11.3	0/0/35/51/13
$^{197}Au^{4+}$	207/32	50/4.5/12.3	0/10/40/43/7
$^{208}Pb^{4+}$	210/32	46/6.5/13	0/0/30/65/5
$^{209}Bi^{4+}$	120/32	46/15/13	0/0/17/64/19
$^{238}U^{4+}$	150/35	55/20/15	0/0/18/67/15

A typical repetition rate for these ion sources is 1 Hz with a pulse length of 0.5 ms. The explosive ion generation process in vacuum arc ion sources results in a higher transverse energy of the ions compared to low ion temperature filament driven ion sources and therefore in a larger divergence angle. For the vacuum arc ion sources the minimum divergence angle is 90 mrad resulting in 1000 π mm rad for the total emittance and 650π mm mrad for the 90 % 4-rms value. The explosive plasma generation process defines the transverse ion energy, which strongly depends of the material. However, the relation between longitudinal and transversal energy is the same for all materials. Therefore, the emittance (divergence angle) is not a function of the material.

FUTURE INJECTORS

Uranium Injector

To meet the FAIR requirements for future ion operation it is necessary to increase the uranium beam intensity from the ion source as well as the duty factor for synchrotron injection. For RFQ injection the uranium beam intensity should be 30 mA for four fold ions within an emittance of 250π mm mrad which is an increase of the beam brilliance by a factor of 2. The repetition rate has to be increased by a factor of 4 (4 Hz). The ion source is able to deliver the requested beam intensity but we have to optimize the dc-post acceleration system to increase the beam brilliance and to reduce the beam losses in the LEBT. Therefore, it is foreseen to build up a new terminal (terminal west) between the two others with a direct two-solenoid injection scheme. To analyze the beam properties and to optimize the transport section the test injector HOSTI was build up. First experiments with a superconducting solenoid and a new compact dc post acceleration system were performed. The analyzed emittances are in the range of 250-350π mm mrad which seems to be sufficient for direct injection into the RFQ. Fig. 2 shows a possible injection scheme scenario for the future uranium injector at the test bench including the ion source, dc-post acceleration system and superconducting solenoid. A slit-grid emittance meter, Faraday cups and beam transformers are installed to analyze the beam quality.

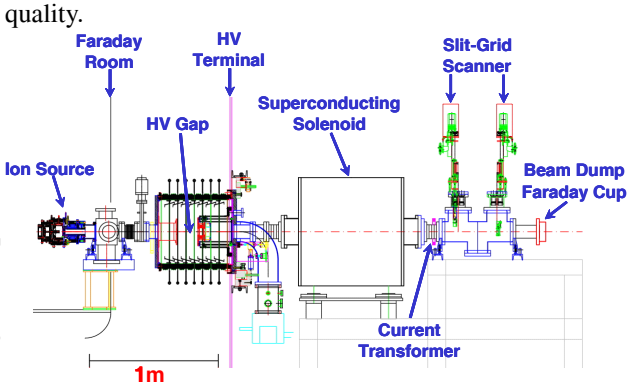

Figure 2: Injection scheme for high current uranium production

Proton Linac (p-LINAC)

The future proton LINAC is a low duty cycle machine which will serve exclusively the synchrotron SIS18. The beam energy is 70 MeV with a desired beam current at the entrance of the SIS18 of 70 mA. The pulse length is 36 µs with a repetition rate of 4 Hz. Over all the p-LINAC has a length of 33 m and working at a frequency of 325 MHz. Many collaboration partners in France (CEA, CNRS, GANIL), Slovenia (ITEC), and Germany (IAP) have their contribution to this project. For the ion source and LEBT CEA-Saclay in France take part to 100 %. The well known SILHI microwave source at CEA Saclay will be reproduced and optimized for pulse operation. For injection into the RFQ a very compact two-solenoid focussing system is foreseen. Table 3 gives an overview of the most important parameter of the ion source and LEBT.

Table 3: Ion source parameter for the p-LINAC

ion source	ECR, 3 GHz
full beam current	<130 mA @ 95keV
proton current	100 mA
proton fraction	>85 %
emittance (rms, n)	<0.3π mm mrad
duty cycle	4 Hz / ~500 µs
extraction system	single hole pentode
availability	>99 %
life time	several months

ACKNOWLEDGMENT

Many thanks to our ion source colleagues at CEA-Saclay (R. Gobin, N. Chauvin, O. Tuske, O. Delferriere) for their very professional work and for the contribution to the FAIR project.

REFERENCES

[1] U. Ratzinger, Commissioning of the new GSI high current linac and HIF related RF linac aspects, Nucl. Instrum. and Meth. in Phys. Res. A (2001) 636-645
[2] H. Schulte et al., Development of Penning multiply charged ion sources for the UNILAC, IEEE Trans. Nucl. Sci. 23, 1042, 1976
[3] J. Pfister et al., High Duty Cycle Ion Sources at GSI and FAIR, these proceedings
[4] L. Dahl et al., The Low Energy Beam Transport System of the New GSI High Current Injector, Proceedings of the 20th LINAC Conference, Monterey, 2000
[5] R. Keller et al., Multicharged ion production with MUCIS, GSI Sientific Report 1987, GSI 88-1, 360
[6] R. Keller et al., Recent results with a high-current, heavy ion source system, Vacuum 36, 833 (1986)
[7] B. H. Wolf, et al., Investigation of MEVVA ion source for metal ion injection into accelerators at GSI, Rev. Sci. Instrum. 65 (10), (1994) 3091
[8] R. Hollinger et al., Development of a vacuum ion source for injection of high current uranium ion beam into the UNILAC at GSI, Rev. Sci. Instrum. 75 (5), (2004) 1595

IMPROVING EFFICIENCY OF PLASMA GENERATION IN H- ION SOURCE WITH SADDLE ANTENNA*

V. Dudnikov#, R. P. Johnson, Muons, Inc., Batavia, IL 60510, USA
S. Murray, T. Pennisi, C. Piller, M. Santana, M. Stockli, R. Welton, ORNL, Oak Ridge, TN 37831

Abstract

Improving efficiency of plasma generation in RF H^- surface plasma source (SPS) with saddle (SA) RF antenna is considered. Several versions of new plasma generators with different antennas and magnetic field configurations were tested in the SNS small Test Stand. The efficiency of positive ion plasma generation has been improved ~4x times up to 0.18 A/cm^2 per 1 kW of RF power 13.56 MHz. A first prototype SA SPS with AlN chamber was installed in the SNS Test that achieved current of H- ions up to 67 mA with an apparent efficiency of up to 1.6 mA/kW at RF frequency 2 MHz. A new version of the RF assisted triggering plasma source (TPS) has been designed, fabricated and tested. A Saddle antenna SPS with water cooling is being fabricated for high duty factor have been tested.

INTRODUCTION

Development of a high current Surface Plasma H- ion Source (SPS) with plasma generation by RF discharge with Saddle antenna in magnetic fields is described in Refs. 1,2. A prototype of RF H- surface plasma source (SPS) with saddle (SA) RF antenna is developed. Several versions of new plasma generators with a small AlN test chamber and different antennas and magnetic field configurations were tested in the Test Stand. A prototype SA SPS was installed in the Test Stand with a larger, normal sized SNS AlN chamber that achieved peak currents of up to 67 mA with an apparent efficiency up to 1.6 mA/kW at 2 MHz RF frequency. Control experiments with H- beam produced by SNS SPS with internal and external antennas were conducted in similar conditions.

In this period main effort was concentrated on development:

1- more reliable version of the triggering plasma source (TPS);

2- improved efficiency of the plasma generators;

3- saddle antenna SPS with water cooling for high duty factor testing.

RF TRIGGERING PLASMA SOURCE

For fast igniting a powerful pulsed RF discharge at low gas density is used a separate triggering plasma gun (TPG). The hollow-anode dc glow discharge plasma gun (discharge voltage: ~600 V and current ~5 mA), designed at ORNL, has been described previously [3]. It used for injecting H_2 gas and ~20 μA of electrons into the AlN 30-70 kW discharge. It was observed that guns configured with Mo cathodes often failed to ignite after several days. In response to this issue, it was designed and developed a chamber, which is sufficient to ignite the main 2 MHz, of stable operation due to decrease a secondary electron emission.

RF assisted TPG utilizing the existing 13 MHz system. Figure 1 shows a cross-sectional view of the SA SPS with RF TPG which employs a water-cooled Al_2O_3 (Φ = 1.3 × length 10 cm) plasma chamber surrounded by a 10-turn Cu antenna. The plasma chamber integrity has been tested up to 1.2 kW of RF power with plasma. Under normal conditions (RF power: 300 W; cathode bias: −250 V; >10 SCCM H_2 flow) about 2 mA of discharge current is supplied to the cathode fabricated from W. This current is then compressed through a circular 2 mm diameter opening in the ceramic plasma chamber to a hollow anode (also fabricated from W). This gun configuration has been found to reliably ignite the main ion source plasma and has been tested coupled to an ion source over several multi-day runs on the test stand. Comparing performance to the Mo, Cu gun, the RF gun produces ~10× electron flux to the ion source with sputtering estimates suggesting ~10^3 less cathode sputtering.

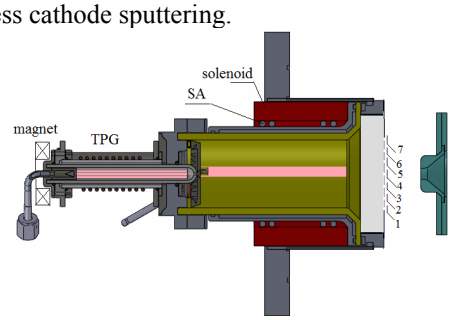

Figure 1: Drawing of the SA Plasma generator with RF TPG and plasma plate with 7 collectors opposite 7 emission apertures of 2 mm diameter (S=3.2 mm^2). Magnetic accelerator electrode is attached for producing of correct magnetic field distribution.

With attached ring permanent magnet the plasma flux from TPG was increased and the minimal gas density, necessary for TPG and pulsed discharge triggering was decreased.

IMPROVING EFFICIENCY OF PLASMA GENERATION

An external antenna source employing solenoidal antenna is under development at the SNS, which was recently described in Ref. 3. The high RF power required for the sources as well as triggering of the pulsed discharge can create problems for very long term operation.

*Work supported by Contract DE-AC05-00OR22725 and by STTR grant DE-SC0002690.
#Vadim@muonsinc.com

The total efficiency of the surface plasma produced fraction of the H^- beam is a product of the probability of secondary emission of H^- caused by plasma bombardment of the collar surface around the emission aperture, the probability of extraction of emitted H^-, and the rate of bombarding plasma flux [1]. The coefficient of secondary emission of H^- is determined by surface properties (proper cesiation) and the spectrum of the plasma particles bombarding the collar surface around the emission aperture [1].

The cesiation was improved recently, and appears to be nearly optimal. The probability of extraction of H^- emitted from the collar surface is dependent on the surface collar shape [3], which was optimized recently to improve H^- emission. The problem efficient plasma generation is being addressed by the development of new RF plasma generators with higher plasma generation efficiency and better concentration of useful plasma flux onto the internal surfaces of the collar around the emission aperture for lower RF power. In this project, we use the saddle antenna, which has its RF magnetic field transverse to the source axis, combined with an axial DC magnetic field, to concentrate the plasma on the collar where the negative ions are formed by secondary emission [1].

The strong transverse magnetic field (up to 1.6 kG) created in the collar emission aperture by permanent dumping magnets should be enough to suppress and filter out the fast electrons from the discharge plasma and to decrease the number of escaping co-extracted electrons. The gas density in the discharge must be low enough to minimize the electron stripping from the extracted H^- ions. This critical gas density is inversely proportional to the emission aperture diameter. For this is necessary to improve a TPG for reliable triggering of pulsed RF discharge at lower gas density.

Several versions of plasma generators with different antennas and magnetic field configurations were fabricated and tested in the test stand with useful plasma flux generation improvements up to 5 times by increasing the DC magnetic field.

The schematic of a large RF plasma generator with the AlN ceramic discharge chamber, prototype saddle antenna, and DC solenoid is shown in Fig. 1. The chamber has an ID=68 mm. The saddle antenna in this prototype plasma source with inductance L=1.7 μH was made from copper tube. The plasma density distribution was measured by collectors extracting the ion beam current through small emission apertures locating along a radius in the end plate attached to the end of discharge chamber as shown in Fig. 1.

The end plate had seven 2-mm diameter emission apertures which with some addition slits is comparable with surface of the SNS 7-mm diameter ion source outlet.

EXPERIMENTAL RESULTS

In previous experiments the central collector current Ic0 is increased up to 5 times from 10 mA/cm^2 to 50 mA/cm^2 as the magnetic field increased from 0 to 250 G.. The ion current density distributions for different magnetic fields are shown in Fig. 2.

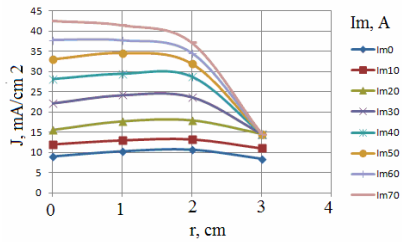

Figure 2: Radial distribution of current density of extracted positive ions for different magnetic fields (coil current I_m), as determined from the 7 collectors.

For low magnetic field (I_m up to 20A) the radial distribution of plasma density is flat. For higher magnetic fields, the plasma density inside 2 cm radius is higher. In new experiments, the saddle antenna was moved away from plasma plate back to the back flange ~ 5 cm .

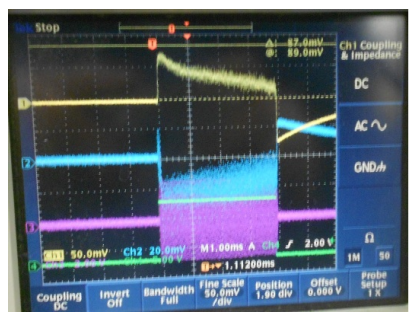

Figure 3: 1- Signal of Ic0 up to 90 mV, 0.5 A/cm^2 with RF power 3kW; 2-Ic1; 3-Antenna current 200A/div.

In result the efficiency of plasma generation was increased up to ~4x times. For plasma generation was used RF discharge with pulsed power Prf=3 kW, RF frequency f=13.56 MHz, pulses T=4 ms , repetition 5 Hz. Discharge was triggered with TPG power Ptpg=300 W, Utpg=0.2 kV, Itpg=5~mA.

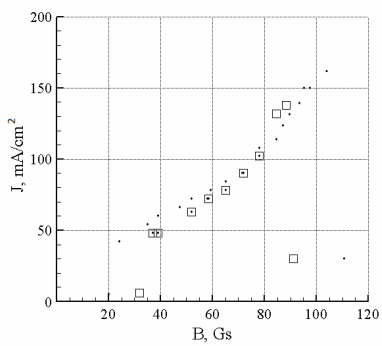

Figure 4: Emission current density Jc1(mA/cm^2) versus magnetic field B (Gauss) at gas flow Q =9.3 sccm (points) and at Q=8.8 sccm (squares) with RF power 1 kW.

The signal of ion current Ic0 from central collector 0 is shown in Fig. 3. The signal differentiation is connected with small inductance of Pearson transformer.The plasma

density observed by collectors as function of magnetic field B, gas flow Q at different collectors at RF power 1 kW are shown in Figs. 4-6. With gas flow Q=9.3 sccm pulsed discharge can be triggered at magnetic field B>25 G and can be stable supported up to B~112 G. The positive ion emission current increases from 0.004 A/cm^2 to 0.16 A/cm^2 as shown in Fig. 5 (points). With lower gas flow the pulsed discharge need higher magnetic field for triggering and can be supported up to lower critical magnetic field with lower collector maximum current as shown in Fig. 4 (squares). However, at the fixed magnetic field the emission current density increases with decrease the gas flow Q as shown in Fig. 5.

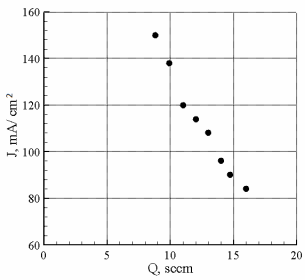

Figure 5: Emission current density Jc1(mA/cm^2) versus gas flow Q (sccm) at magnetic field B=90 Gauss with RF power 1 kW.

Ion current to four collectors (0-3) at magnetic coil current 1 and 80 A and Q=11 sccm are shown in Fig. 6. The highest emission current density Jc0=0.4 A/cm^2 up to 10 times higher than shown in Fig. 2. The current density distribution has higher pick density on the axis than distribution in Fig. 2. By this results were demonstrated than location of antenna in the divergent magnetic field can increase efficiency of plasma generation on the axis of plasma plate.

For utilization of this effect were fabricated short (5 cm) solenoid and new saddle antenna shown in Fig. 7.

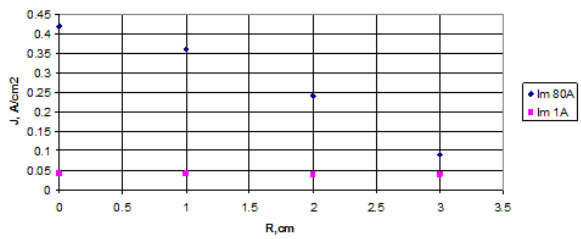

Figure 6: Ion emission current density Jc (A/cm^2) (plasma density) along the radius R (cm) at high magnetic field (blue) and at low magnetic field (pink) with RF power 3 kW.

With this design high efficient plasma production up to 0.5A/ cm^2 per 3kW RF power was reproduced. With 4.5 turns solenoidal antenna similar to SNS external antenna the plasma generation efficiency was ~4 times less with magnetic field and ~10 times less without magnetic field at RF frequency 13.56 MHz.

With RF frequency 2 MHz the pulsed discharge was not triggered without magnetic field up to 6 kW with TPG plasma. With he magnetic field the pulsed discharge was weak and the Ic1 signal was below 1 mV (~6 mA/cm^2).

In CERN replica of DESY RF sources used as proton source, the pulsed discharge is stable ignited with RF power above 20 kW. The emission current density J=240 mA/cm^2 was produced with RF power ~40 kW (~6 mA/cm^2 per 1 kW) [4].

Figure 7: Discharge chamber with a short solenoid and new saddle antenna located out of solenoid.

General design of simplified version of SA SPS with new extraction system shown in Figs. 8 has been prepared.

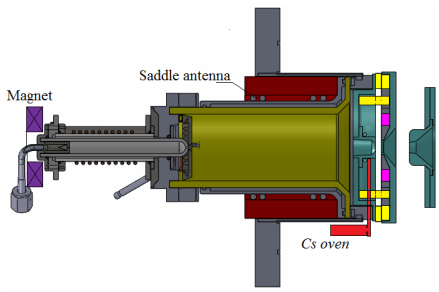

Figure 8: General design of simplified version of SA SPS with new extraction systems and cesium supply.

New version of plasma plate with H- emitting collar was designed, fabricated and assemble. The SA SPS with attached extractor is shown in Fig. 9.

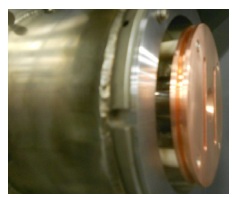

Figure 9: SA SPS with attached extractor.

REFERENCES

[1] V. Dudnikov et al., Surface plasma source with saddle antenna radio frequency plasma generator, Rev. Sci. Instrum. 83, 02A712 (2012).

[2] V.Dudnikov et al., Surface Plasma Source Electrode Activation by Surface Impurities, AIP Conf. Proc. 1390, 411 (2011).

[3] Welton R. F. et al., H- radio frequency source development at the Spallation Neutron Source, Rev. Sci. Instrum. 83, 02A725 (2012).

[4] J. Lettry et al., "High duty factor plasma generator for CERN's Superconducting Proton Linac Rev. Sci. Instrum. 81, 02A723 (2010).

LOW ENERGY CHANNEL FOR MODERNIZED LU-20

V. Alexandrov #, A. Govorov, V. Monchinsky, G. Trubnikov
JINR, Dubna, Moscow Region

Abstract

The modernization of LU-20 accelerator expects change existing electrostatic for-injector on RFQ type pre-accelerator. Low energy channel of transportation of beams is offered from three sources of ions: ESIS, LIS and SPIon - to RFQ. Parameters of channel and results of numerical modeling on fitting beams parameters with acceptance of RFQ are presented.

INTRODUCTION

The modernization of LU-20 accelerator expects change existing electrostatic for-injector on RFQ type pre-accelerator. Under this acceleration modes in the Alvarez linac must be preserved. Since at RFQ exit different energy of particles with Z/A =1 and Z/A ≤ 0.5 are required, it is expected use two separate RFQ. Modernization is conducted in 2 stages, first stage – RFQ for particles with 0.3 ≤ Z/A ≤ 0.5. A variant of low energy channel for beam transportation (LEBT) common for 3 ion sources: ESIS, LIS and SPIon – is offered.

ELEMENTS OF CHANNEL

Each source is situated on high-tension (before 150 kV) platform. The channel (Fig.1) begins from electrode with potential U0, after which a vacuum valve is fixed. In initial part of channel (IPC) the focusing electrodes with potentials U1 and U2 are located. IPC ends the tube with potential, falling off from U3 up to 0. Two solenoids, stated after initial part, form beams at the input of RFQ.

PARAMETERS OF BEAMS AND RFQ

Parameters of beams at the input in channel are given in Table 1, the input parameters of RFQ are specified in Table 2.

Table 1: Beam Parameters at IPC entrance

source, ions	Z/A	current mA	ε_n(4rms) π cm mrad	∅ beam mm	energy keV/Z
LIS, $^{27}Al^{+8}$	0.3	20	0.2	19	1
ESIS, $^{197}Au^{+60}$	0.3	10	0.15	10	19.7
SPIon, $^{2}D^{+}$	0.5	10	0.2	15	20

Table 2: RFQ Entrance Parameters

Z/A	I_{inj} mA	4rms $\varepsilon_{n\,x,y}$ π mm mrad	$\alpha_{x,y}$ rad	$\beta_{x,y}$ mm/mrad	U_{inj} kV
0.3	0	1.5	0.8818	0.0680	103
	10		0.9472	0.0721	
0.5	0	2.0	0.8818	0.0680	61.8
	20		0.9906	0.07545	

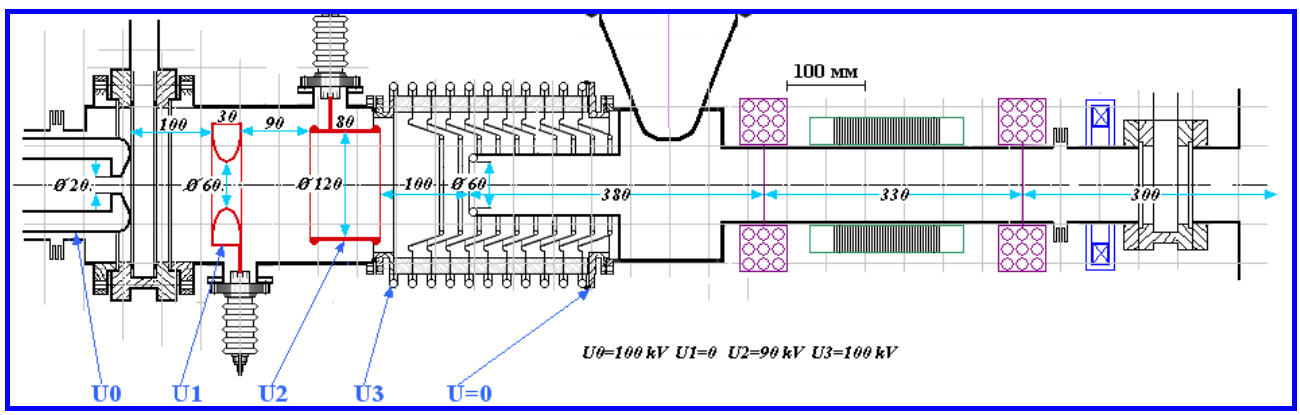

Figure 1: Schematic view of LEBT.

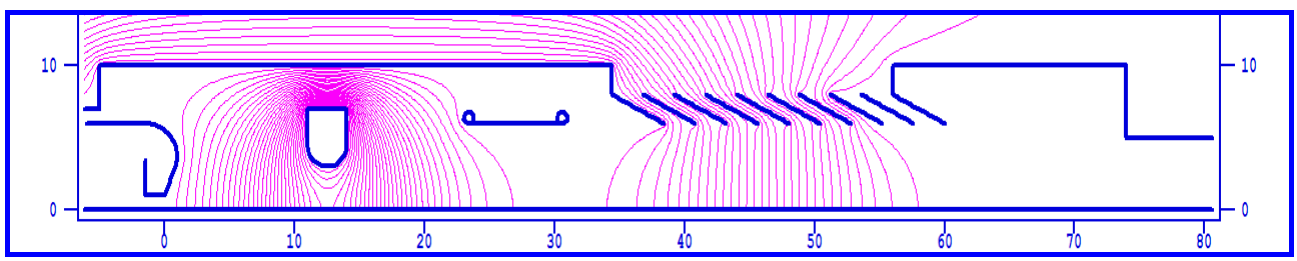

Figure 2: View of initial part of LEBT at POISSON code interface.

#aleks@jinr.ru

RESULTS OF SIMULATION

Electrostatic field inside IPC and magnetic field of solenoids are calculated by the POISSON program [1]. Optimization of channel parameters to achieve required beam parameters at the RFQ entrance was performed by MCIB04 code [2].

View of initial part of LEBT and electrical field contours at POISSON code interface is shown in Fig. 2.

LIS, $^{27}Al^{+8}$, 20 mA

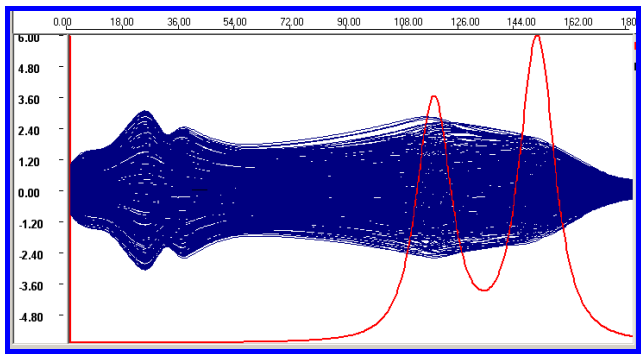

Figure 3: Ion trajectories and magnetic field.

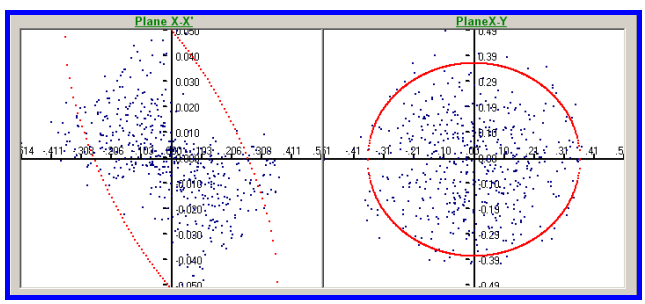

Figure 4: Phase plane and beam spot at RFQ entrance.

About 84% beam is in RFQ acceptance.

ESIS, $^{197}Au^{+60}$, 10 mA

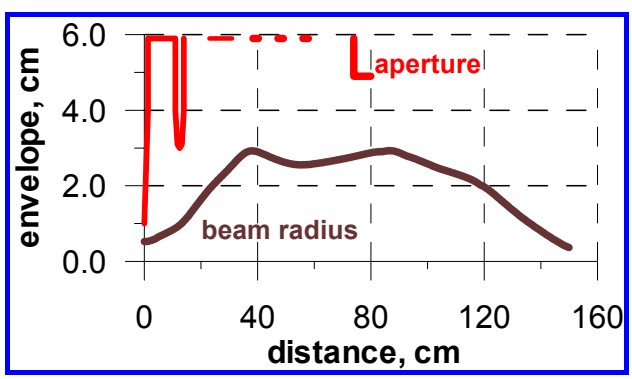

Figure 5: Beam envelope.

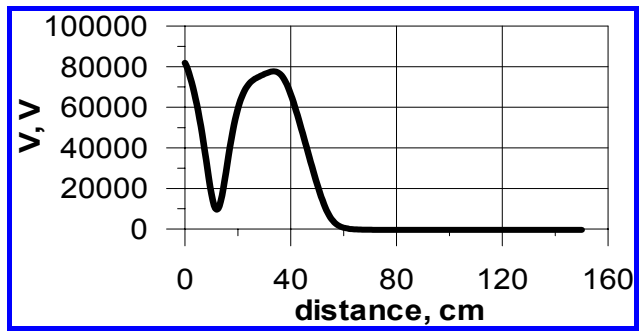

Figure 6: Potential distribution.

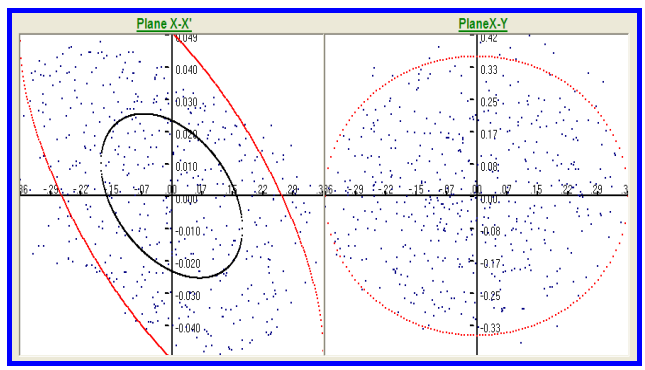

Figure 7: Phase plane and beam spot at RFQ entrance.

At RFQ entrance (z =150 см):
Emittance ε_n(4rms) = 1.3 π mm mrad,
Beam radius (2 rms) =3.4 mm,
$\alpha_{x,y}$ = 0.43 rad,
$\beta_{x,y} \cong 0.073 \div 0.074$ mm/mrad.

SPIon, $^{2}D^{+}$, 10 mA

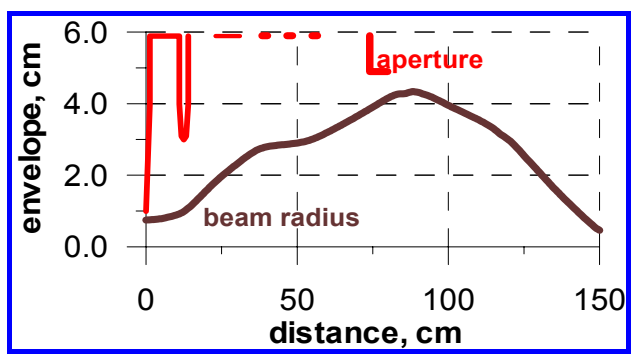

Figure 8: Beam envelope.

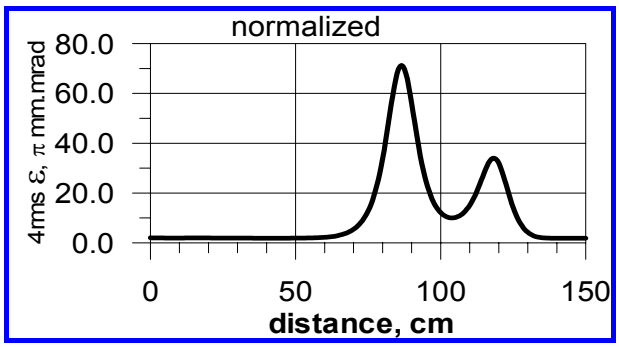

Figure 9: Normalized emittance.

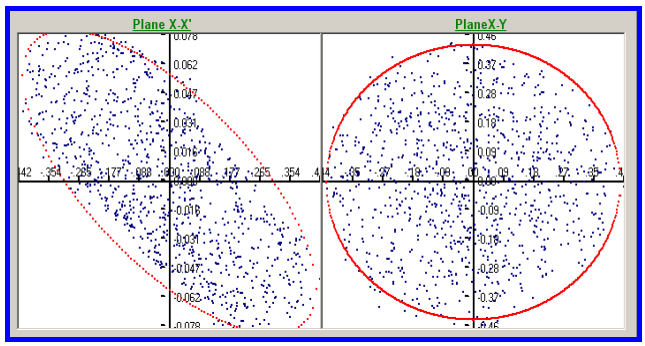

Figure 10: Phase plane and beam spot at RFQ entrance.

At RFQ entrance (z =150 см):
Emittance ε_n(4rms) = 1.84 π mm mrad,
Beam radius (2 rms) = 4 mm,
$\alpha_{x,y}$ = 0.98 rad,
$\beta_{x,y} \cong$ 0.0702 mm/mrad.

CONCLUSION

It was established that proposed variant of low energy channel is suitable for transportation of beams from three sources and injection of ions in to RFQ.
Channel length:
for SPIon and ESIS – 150 cm enough,
for LIS it needs not less than 180 cm to avoid too high fields in solenoids.

Channel Parameters For Different Ions

Deuterons, 10 mA
Potentials at energy 61.8 keV/Z:
U0=U2=U3=42.1 kV, U1=0.
Magnetic fields 4.63 and 4.38 kGs.

Gold, Z/A=0.3, 10 mA
Potentials at energy 103 keV/Z:
U0=U3= 84 kV, U2=75.6 kV, U0=0.
Magnetic fields 6.9 and 7.2 kGs.

Aluminum, Z/A=0.3, 20 mA
U0=U2=U3=100 kV, U1=0.
Magnetic fields 7.5 and 9.6 kGs.

REFERENCES

[1] F.C. Iselin and J. Niederer, The MAD Program, CERN/LEP-TH/88-38, Geneva, Switzerland, 1988.
[2] V. Aleksandrov, N. Kazarinov, V. Shevtsov, Multi-Component Ion Beam code–MCIB04, Proc. XIX Russian Particle Accelerator Conference (RuPAC-2004), Dubna, Russia, 2004, p.201.

A SIMULATION STUDY ON ACCELERATOR CAVITIES FOR A SW LINAC

N. Khosravi, University of Zanjan, Zanjan
S. A. H. Feghhi, E. Ebrahimibasabi, Department of Radiation Application,
Shahid Beheshti University, Tehran, Iran

Abstract

An on axis-coupled cavity structure has been studied using S-band microwaves at 2856MHz, suitable for industrial and research applications. It uses a bi-periodic SW structure with constant impedance that operates at π/2 mode. This structure consists of Bean-like shaped slots, placed symmetrically with respect to the accelerating axis. We compared different shapes, places and sizes of slots with respect to coupling coefficient, resonance frequency and some of cavity parameters. Sensitivity analyses of accelerating cavity on details of structure have been done and their behaviour, with respect to the resonance frequency has been investigated. According to the simulation results using SUPERFISH and CST Studio package, each accelerating cavity is capable to deliver 0.56 MeV to electrons in a 50μA beam.

INTRODUCTION

In designing of accelerator cavities for SW linacs, we should consider some figures of merit such as quality factor, effective shunt impedance and also transit time factor of cavity. This linac is intended to deliver an electron beam up to 10MeV with a Klystron power of 2MW having a pulse width of 5 μsec and a waveguide operating in the TE01 mode. And our cavity will be operated in the TM010 mode.

DESIGN CONCEPTS

Designing the cavity can be started with a simple pillbox cavity with beam holes on the end plates, adding nose cones to create a region of more concentrated axial electric field that it reduces the gap and raises the transit-time factor [1]. The optimization procedures depend on the constraints of our equipments. The nose cone, septum thickness and lower wall radius might be constrained by the technology of cavity machining. So they are known before starting our work. We should mention that Borehole radius R_b is determined from beam dynamics considerations.

Some relations can help us to find other parameters. For example, Upper wall radius, R_{co}, is determined for each cavity by[2].

$$R_{co} = L/2 - S - \Delta x \qquad (1)$$

In which L and S refer to length and septum thickness of a cavity, respectively. A small straight section Δx on the circumference of the wall cavity might be required to increase effective shunt impedance (ZT^2) slightly. This effect is more evident for larger β values than for small ones. The best value of Δx is about 10% of half-cavity length. The two remaining parameters, D and g have the strongest effect on ZT^2 and frequency [2]. Thus the Sketch of the cavity had been done. In following by sensitivity analyzing the optimization of our cavity has been performed to maximize the efficiency. using diagrams of frequency, ZT^2, Z, Quality factor etc. respect to cavity geometrical parameters[2].

Some of electromagnetic codes have been used to solve Maxwell's equation with the specified boundary conditions. In this paper SUPERFISH[3] and CST suit studio package[4] have been used for simulation of our designs.

Sensitivity analysis and benchmarking for all cavity parameters have been done. But two diagrams which are more determinative have been shown in Fig (1) and (2). Fig (1) Shows Resonant Frequency vs. Gap Length. As it is clear, there is a good agreement between CST and SUPERFISH results. The SUPERFISH results are more accurate than CST results. This discrepancy is due to different normalization coefficients, although the behavior of results in is the same in both. It can be seen in Fig (2) that these results can be coincident by varying Effective Shunt Impedance in vertical Axis. Effective Shunt Impedance is a very significant parameter in SW cavity, since it can be set to achieve a maximum value by sweeping this parameter in gap length and optimization demanded cavity [2].

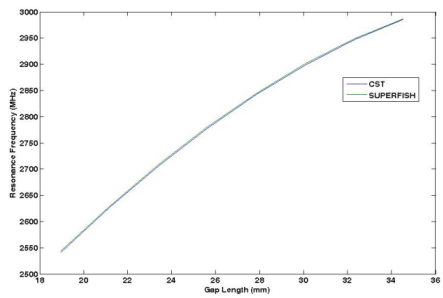

Figure 1: Resonant Frequency vs. Gap Length

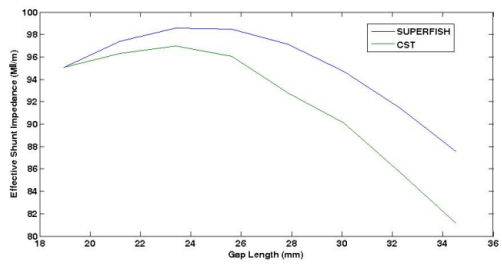

Figure 2: Effective Shunt Impedance vs. Gap Length

SIMULATION DETAILES

Both electric and magnetic field have been taken for coupling in SW cavities. These cavities are coupled by two slots in their walls. Although SUPERFISH can simulate resonance frequency in cavity by precision within 1-3% [5], but it is inefficient in simulating the geometry of these slots in three-dimensions. So the CST software with the accuracy of 5% can be useful for our propose [5]. To reduce this error, that's better to calibrate the Microwave Studio CST results by SUPERFISH.

The coupling calculations between two cavities are very important. After importing slots, it can be obtained by the equation 2 [5].

$$K_{ac} = -(1 - \frac{\omega_{\pi/2}^4}{\omega_0^2\omega_{\pi/2}^2 + \omega_{\pi/2}^2\omega_\pi^2 - \omega_0^2\omega_\pi^2})^{1/2} \quad (2)$$

In which $\omega_{\pi/2}$ is the proper accelerating mode and ω_π and ω_0 are adjacent modes. After calculating the coupling coefficient and obtaining the frequency effect of these slots on cavity, we can import ΔF to SUPERFISH. Geometrical parameters and dimensions for desirable cavity are shown in Fig (3) and Table (1) respectively

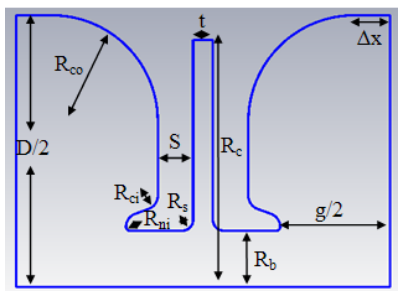

Figure 3: Geometrical Parameters.

Table 1: Geometrical Dimensions

Geometrical Parameters	Dimensions (mm)
Bore Radius (R_b)	5.0
Outer Corner Radius (R_{co})	17.5
Inner Corner Radius (R_{ci})	5.0
Outer Diameter (D)	77.257
Gap length (g)	25.649
Nose Cone Angle	20
Septum Thickness (S)	5.0
Coupling Cavity Thickness (t)	3.0
Rounding Radius (R_s)	1.5

In what follows, the coupling coefficient in different slots has been discussed.

The final parameters of desire cavity is shown in table (2)

Table 2: SUPERFISH Calculated Parameters

Figures of merit	
Transit Time Factor	0.83
Quality Factor	16616.7
Shunt Impedance	144.771 MΩ/m
Effective Shunt Impedance	100.413 MΩ/m
Maximum Electric Field	25.649 Mv/m
Kilpatrick Limitation	1.2826
r / Q	142.22 Ω
Rs * Q	233.679 Ω
Power Dissipation	23.4 kw

Different Shape of Slots

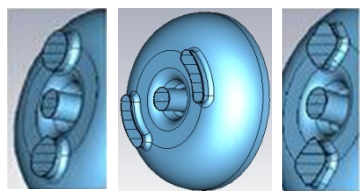

Figure 4: Circular Slot(Left),Bean Liked Slot(Center), Square Slots (Right).

Effective Shunt impedance is calculated indirectly by using the electric field and total loss that are obtained by CST and importing them to equation (3). Transit time factor is not dependent on slots, so it can be replaced from SUPERFISH results [3].

$$ZTT = \frac{E_0^2}{P/L}T^2 \quad (3)$$

Fig (4) shows the three different types of slots. As is shown in Table 3, cavity parameters have been calculated and compared for them.

Table 3: Comparing the Different Types of Slots

Cavity Parameters	Bean Like	Circular	Square
Total Loss(W)	1.786e6	1.699e6	1.694e6
Shunt Impedance (MΩ/m)	129.74	137.153	137.887
Effective Shunt Impedance (MΩ/m)	92.38	97.54	98.177
Coupling Coefficient (%)	-4.7	-0.75	-0.73
Resonant Frequency (MHz)	2824.26	2850.14	2851.4

Square or circular slots couldn't be a good replacement for coupling slots, although both of them have less power

dissipation and higher Effective Shunt Impedance than bean slots.

By choosing bean liked slots, two possible sources of inaccuracy in the performance of the cavity would arise and should be considered, that you can see them in Fig (5): first, rounding defect in the edges of slots and second, symmetrical defect.

Sensitivity Analysis of Bean Slots is shown in table (4). Note that, Asymmetric slots won't make any special problem. But its effect will influence on decreasing the accelerating field. Rounding defect doesn't have especial effect on this field, as is shown in Fig (6).

Table 4: Sensitivity Analysis of Bean Slots

Cavity parameters	Our design	With rounding defect	With symmetrical defect
Total Loss(W)	1.786e6	1.819e6	8.880e5
Z (MΩ/m)	129.74	126.1942	240.464
ZTT (MΩ/m)	92.38	89.851	171.212
Coupling Coefficient (%)	-4.7	-4.6841	-4.7369
Resonant Frequency (MHz)	2824.26	2831.1	2830.69

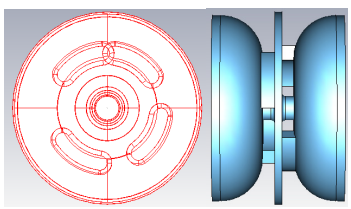

Figure 5: Asymmetric slots (left), Pointy Slots (right)

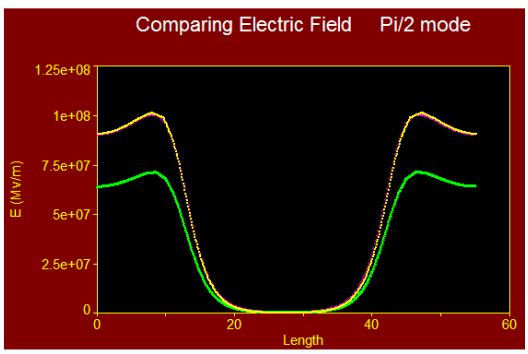

Figure 6: Electric Field in Accelerating Mode. Yellow Graph (Our Cavity), Green Graph (Symmetrical Defect) And Pink Graph (Rounding Mistakes).

Thermal Analyzing

After designing the geometry, our structure has been simulated in CST MPhysics Studio for thermal analysis. This simulation has been done by thermal conductivity of 0.024 (W/K/M) and heat capacity of 1.005 (KJ/K/Kg) in ambience air conditioning. The temperature of cavity wall was determined 300 K and boundary condition has been considered open in order to heat exchange with environment. A power source of 2MW has been considered for our system.

If roundness of the slot edge is not properly designed this part would be the hottest section in the cavity. The roundness edge of 2 mm has been selected for slots by sensitivity analysis as a function of temperature. Fig (7) shows the thermal behaviour of designed cavity, after entering a pulse of power.

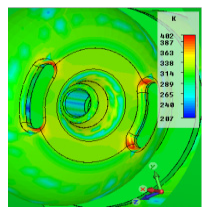

Figure 7: Thermal Analyzing of Cavity

CONCLUSION

The geometrical dimensions of an accelerating cavity in a SW linac are designed. This linac is intended to deliver an electron beam up to 10MeV with a Klystron power of 2MW.

ACKNOWLEDGMENT

The authors are deeply grateful to Mr. Khorsandi for his collaborative efforts on this research.

REFERENCES

[1] Wangler, T.P., RF Linear accelerators2008: Wiley Online Library.
[2] Joseph J. Manca, E.A.K., TM01 Mode Accelerating Cavity Optimization. LA-7323, 1978: p. 27.
[3] Laboratory, L.A.N., POISSON/SUPERFISH Reference Manual, in http://laacg1.lanl.gov/laacg/services/download_sf.phtml1987, Los Alamos National Laboratory Report LA-UR-87-126.
[4] CST Studio 2009, http://www.cst.com
[5] Leeuw, R.W., The accelerator injection chain of the electron storage ring EUTERPE. 1996.

RF DESIGN AND TUNING OF LINAC4 RFQ

A.C. France, M. Desmons, O. Piquet, CEA Saclay, France
C. Rossi, CERN, Geneva, Switzerland

Abstract

Linac4 is scheduled to deliver 160 MeV H^- beam to LHC injection chain by year 2015. The first stage of Linac4 is a 352 MHz, 3-meter long Radio Frequency Quadrupole (RFQ) accelerator [1]. It will accelerate the 70 mA, 45 keV H^- beam from the RF source up to 3 MeV energy. Fabrication of RFQ, which started in 2009, is completed [2] and tuning operations are in progress. RF controls performed at each fabrication step have shown that RFQ electrical parameters are well within bounds specified after envelope of fabrication tolerances. Tuning operations have started with adjustment of so-called quadrupole rods inserted in end plates, in order to achieve adequate voltage boundary conditions at both RFQ ends. A preliminary slug tuning test demonstrates voltage percent accuracy after a few slug tuning iterations.

RF DESIGN

Linac4 RFQ is a 3-meter long, single segment RFQ. Cross-section is kept constant over full RFQ length, in order to simplify mechanical fabrication (refer to [3] for detailed RF design). Specified voltage is constant over full RFQ length, and boundary conditions are tuned with quadrupole rods (QR) inserted in end plates, close to vane tips. Electrical parameters of RFQ however vary slightly vs. abscissa, as a consequence of vane modulations. Resulting voltage error is 10% at most, and will be easily suppressed with the 36 tuners (8 slugs and 1 RF port per quadrant). Tuners are also designed to compensate for construction errors. Envelope of fabrication tolerances may yield inter-vane capacitance errors of 2.3% (quadrupole-like errors) and/or 3.5% (dipole-like errors). The resulting tuner position range is about 34 mm, and is centered mostly "inside cavity", where tuner are efficient. To this purpose resonance frequency is set to 345.3 MHz when tuners are in flush position.

THEORETICAL BACKGROUND

A general statement is that RFQ tuning requires some bridge to be made between the 3D field maps of the desired object, and measurable quantities which are field profiles along bead-pull lines and spectra. This bridge is the 4-wire transmission line model (TLM) described in [4]. Field maps in the axial region of a 4-vane RFQ may be approximated by transverse electric-magnetic (TEM) field maps, since there the axial component of magnetic field is close to zero. These TEM field maps are assumed to be supported by a 4-wire system, whose voltage 3-vector U verifies

$$\frac{\partial}{\partial z}\left(C_Q \frac{\partial U}{\partial z}\right) + \frac{1}{c^2} L_Q U = \frac{\omega^2}{c^2} C_Q U \,, \qquad (1)$$

where z is abscissa, C_Q, L_Q are the capacitance (F/m) and inductance (H.m) matrixes, ω is the radian frequency, c is the speed of light. Quadrupole (U_Q) and dipole (U_S,U_T) components of U are related to inter-electrode voltages by $U_Q = (u_1 - u_2 + u_3 - u_4)/4$, $U_S = (u_1 - u_3)/2$, $U_T = (u_2 - u_4)/2$. Note that (1) is diagonal for a perfectly symmetric RFQ. Boundary conditions at RFQ ends in z = a,b are

$$\partial U(a)/\partial z = -s_a U(a) \,, \quad \partial U(b)/\partial z = +s_b U(b) \,, \qquad (2)$$

where s_a, s_b are 3 × 3 matrixes. The vector Sturm-Liouville (SL) operator defined after (1) and (2) is self-adjoint if and only if $(C_Q)^{-1} s_{a,b}$ are Hermitian, which is always the case since $s_{a,b} = -j(\omega/c^2) C_Q^{-1} y_{a,b}$, where $y_{a,b}$ are end-circuit admittance matrixes, and are imaginary symmetric for lossless reciprocal circuits. All TLM electrical parameters are deduced from exact 3D simulations [3], in such a way TLM is able to accurately mimic RFQ eigen-modes and eigen-functions. On the other hand, magnetic field measured along bead-pull lines are easily transformed into inter-vane voltage (eventually using simulated field maps), eigen-values $(\omega/c)^2$ are directly given by spectrum analysis, and our "bridge" is established. First-order perturbation analysis of the SL eigen-problem leads to orthogonal bases for C_Q and L_Q perturbations, which are duals of voltage eigen-basis. This important property will be applied for RF controls and for slug tuning.

RF CONTROLS

RF controls are performed at each fabrication step of each 1-meter long section: copper pieces assembly, first braze of electrodes, second braze of stainless flanges and vacuum ports. The most desirable goal would be to obtain a diagnosis of electrical properties vs. abscissa along the RFQ. This is a typical inverse problem: given voltage vector function U(z), find originating $C_Q(z)$ matrix pencil. The hard point is that U may be deduced from measured magnetic field only in small intervals, far enough from local field perturbations induced by tuners and vacuum ports. Applying sampling theory to our SL problem, a linear filter bank may be built which uses valid field samples to deliver a few spectral amplitudes estimates (6 first in present case). First-order perturbation analysis is then used to reconstruct originating perturbations. This method is of course unable to reveal strongly localized defaults; however the same procedure will be used for tuning, and these estimated perturbations are exactly the ones that will have to be cancelled by tuners. Results are displayed in Fig. 1, where successive fabrication steps are identified with color code. Typical precision of the method is ±0.003, after processing typically 5 or 6 bead-pulls. A digital "roofing" filter is also used to reduce high-frequency noise. Black traces apply to the full-length

assembled RFQ, and nicely follow individual 1-meter long sections estimates. All capacitance errors never exceed 1%, well within specifications. Note that vacuum ports positions are adjusted prior to second braze, as explained in [5]. A similar procedure is used to estimate electrical neutral position of RF dummy ports (which was not perfect after assembly, but was corrected later on as can be seen in Fig. 1, about z = 1.50 m).

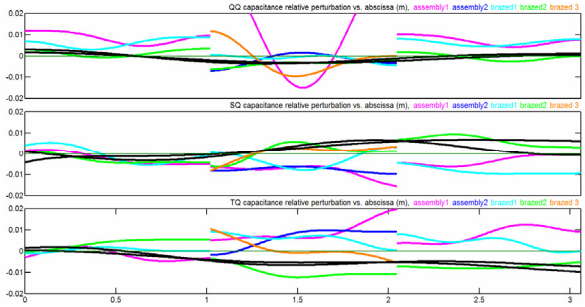

Figure 1: Reconstruction of inter-vane capacitance errors vs. abscissa along RFQ axis and fabrication step (color).

END-CIRCUITS TUNING

Coefficients of $s_{a,b}$ matrixes are estimated using the excitation set method. Several linearly independent $\{U,\partial U/\partial z\}|_{z=a,b}$ pairs are obtained upon prepositioning tuners # 04 and 06 (on either side of central RF port). End voltages and voltage slopes are derived from bead-pull measurements. Straightforward linear algebra shows that a minimum of three pairs is sufficient to recover all coefficients. Accuracy is improved upon using five pairs (as shown in Table 1) and least-square fit. The symmetry of the dipole sub-matrix $[s_{SS}\ s_{ST}\ ;\ s_{ST}\ s_{TT}]$ is also taken into account.

Table 1: Positions (in mm) of Tuners 04 and 06

excitation	quad 1	quad 2	quad 3	quad 4
f	0.0	0.0	0.0	0.0
s	+5.0	0.0	–0.5	0.0
y	+5.0	+5.0	–0.5	–0.5
t	0.0	+5.0	0.0	–0.5
x	–0.5	+5.0	–0.5	+5.0

Results of a typical measurement are displayed in Fig. 2. Left plot is a visual representation in $\{U_Q,\partial U_Q/\partial z\}$ plane; in this un-tuned case, s_{QQ} = +0.106 V/m/V (tuned value is 0, since required voltage profile is constant). Right plot is a superposition of $\{U_S,U_T\}$ and $\{\partial U_S/\partial z,\partial U_T/\partial z\}$ planes. Voltage excitations (blue circles) are easily identified (f-excitation is not exactly quadrupolar since RFQ is not tuned). Measured voltage slopes are shown with green +. Voltage slopes derived from measured voltages and estimated s-matrix are shown with purple ×. They closely track measured samples, indicating that s-matrix parameters have been properly estimated. Note also that principal axes in dipole subspace are of little importance for tuning, to the contrary of eigen-values that will determine dipole eigen-frequencies. Status of end-circuits tuning is displayed in Fig. 3. Most recent Comsol 3D simulations are shown in blue; measured values in green and red. Left plots apply to RFQ input; right ones to RFQ output. Top plots display s_{QQ} values vs. QR length; vertical bars represent ±1 standard deviation intervals (if available). Bottom plots display mean eigen-value λ_D of dipole sub-matrix vs. QR length; vertical bars represent eigen-value separation intervals. s_{QQ} tuning curves at RFQ input (in green on Fig. 3, top-left) and output (in red on Fig. 3, top-right) are measured using aluminum end-plates with adjustable rods, and closely match simulations; same conclusion applies to realized input copper plate (in red on Fig. 3, top-left). Measured λ_D closely match simulation for shorter rods, but do not follow the same slope. This apparent discrepancy likely results from ignored dispersive effects, simulated λ_D's applying to dipole mode fundamental frequency and measured values to quadrupole mode fundamental frequency. Note that $s_{a,b}$ are assumed to be independent of frequency in TLM (eigen-value dependent boundary conditions may be treated to the expense of heavy bead-pull measurements as in [6]). A definitive conclusion could be reached upon considering spectra of RFQ once tuned (eigen-frequencies being usually shifted by electrical parameters errors not compensated by tuners).

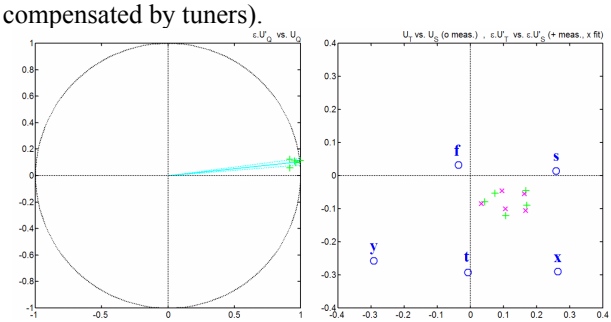

Figure 2: Example of end-circuit tuning (RFQ output).

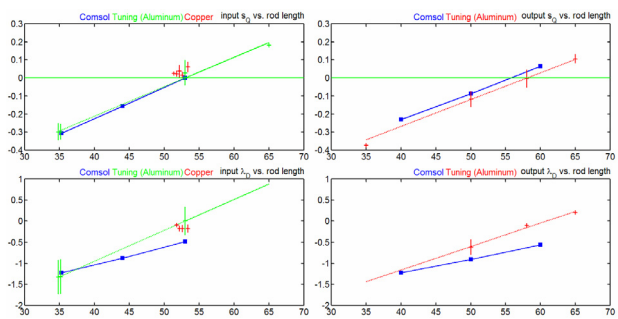

Figure 3: Summary of end-circuits tuning.

SLUG TUNING TEST

A slug tuning test has been performed with input copper plate and output aluminum plate. The closed-loop control-command tuning algorithm is sketched out in Fig. 4. A linear filter-bank derives voltage spectral components (12 in each Q, S, T subset in the present case) from valid measured samples (the controlled quantities). First-order perturbation analysis of SL operator is used to build the dual basis of tuner functions (with dim. 9 in

each subset). Measured spectral coefficients are compared to desired ones (i.e. spectral coefficients of specified voltage function in quadrupole subset, all zeroes in dipole subsets). Inverse RFQ transfer function is then applied to elaborate command parameters in each spectral channel. Transmittance of linear filter bank and normalized spectra of tuner basis functions are displayed in Fig. 5; it is seen that 8 first components are free from aliasing hence tunable.

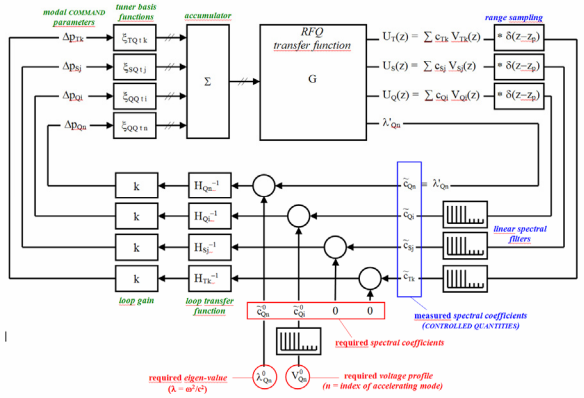

Figure 4: Tuning algorithm.

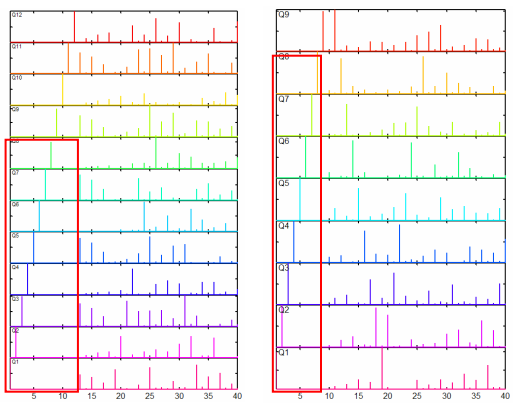

Figure 5: Transmittance of linear filter bank (left), and normalized spectra of tuner basis functions (right).

Table 2: Summary of Tuning Test Iterations

	step 0		step 5	
frequency (MHz)	345.741		351.926	
Q-component error (%)	–22.77	+18.72	–1.24	+0.77
S-component error (%)	–5.29	+8.13	–0.05	+1.29
T-component error (%)	+1.73	+7.97	–0.98	+3.06
tuner positions (mm)	0.00		+5.07	+13.42

After 5 tuning iterations, voltage errors are reduced from 23% down to a few percents (Table 2 and Fig. 6). More iterations are expected to yield better voltage accuracy and frequency match. Tuner positions vary between +5 and +13.4 mm (inside cavity), well within the [–4,+30.5] mm specification, and in agreement with small measured capacitance errors. Frequencies of dipole modes closer to accelerating Q_0 mode are given in Table 3 (acquisition step, hence accuracy, is 62.5 kHz). TLM values are derived using measured s-matrix coefficients, and assuming tuners in neutral position; quadratic frequency shifts (QFS) should theoritically be left unchanged by frequency tuning. After tuning, QFS are quite close to those derived from TLM, thus indirectly confirming our s-matrix estimates.

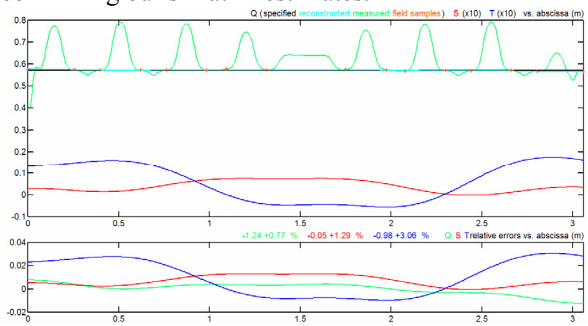

Figure 6: Voltage profile after last tuning step.

Table 3: Spectrum Analysis of Tuning Iterations

	step 0			step 5			TLM		
	f	QFS	Δf	f	QFS	Δf	f	QFS	Δf
D_0	333.38	–91.7	–12.4	339.13	–94.1	–12.8	332.56	–94.0	–13.0
D_1	339.19	–67.0	–6.6	345.00	–69.5	–6.9	338.11	–71.5	–7.5
Q_0	345.75	0.0	0.0	351.94	0.0	0.0	345.59	0.0	0.0
D_2	349.13	+48.4	+3.4	354.25	+40.4	+2.3	348.14	+42.0	+2.5
D_3	364.94	+116.8	+19.2	369.88	+113.8	+17.9	365.34	+118.5	+19.7

CONCLUSION

End-circuits tuning is now almost completed; fabrication of copper output plate is underway. End-circuits modeling is found to be satisfactory in quadrupole subspace, but deserves finer analysis in dipole subspace. A tuning test clearly demonstrates that required tuner position range is largely within specifications, in agreement with estimated inter-vane capacitance errors. Next tuning steps include: assembly of output copper plate and tuning check, tuning with dummy slugs and dummy RF ports, assembly and matching of iris coupler, fabrication and assembly of copper iris coupler, final tuning and fabrication of copper slugs.

REFERENCES

[1] C. Rossi et al., "The Radiofrequency Quadrupole Accelerator for the Linac4", LINAC'08, Victoria BC, Canada.
[2] C. Rossi et al., "Assembly and RF Tuning of the Linac4 RFQ at CERN", LINAC'12, Tel Aviv, Israel.
[3] O. Piquet et al., "The RF Design of the Linac4 RFQ" IPAC'10, Kyoto, Japan.
[4] A.C. France et al., "Un-segmented vs. Segmented 4-vane RFQ: Theory and Cold Model Experiments", IPAC'10, Kyoto, May 2010, MOPD026.
[5] C. Rossi et al., "Progress in the Fabrication of the RFQ Accelerator for the CERN Linac4," LINAC'10, Tsukuba, Japan.
[6] O. Piquet et al., "Tuning Procedure of the 6-Meter IPHI RFQ", EPAC'06, Edimburgh, U.K., MOPCH107.

BEAM PULSE SEPARATION SYSTEM OF INR LINAC

N.I. Brusova, A. Feschenko, O. Grekhov, Yu. Kalinin, V. Mikhailov, V.L. Serov, A.A. Stepanov,
INR RAS, Moscow, Russia
B.O. Bolshakov, A.V. Pozhensky, NIIEFA, St. Petersburg, Russia

Abstract

The activity for beam intensity increasing and beam use efficiency improvement is under progress in INR linac. An important stage is the development and implementation of the Beam Pulse Separation System in the accelerator intermediate extraction area (160 MeV). The system is intended for distribution the beam pulses between Isotope Production Facility (up to 160 MeV) and the Experimental Facility located downstream of the accelerator exit. The report describes the upgrade of intermediate extraction area as well as the first results of experiments with the beam.

INTRODUCTION

INR linac is a medium energy high intensity linac [1]. The accelerator includes an intermediate extraction area where the beam with the energy up to 160 MeV is extracted from the main line and is directed to isotope production facility (IPF). To extract the beam a series of two 13° bending magnets are used. The magnets are of DC type so the total beam only can be extracted. Meanwhile the intensity of the beam is sufficient to be used simultaneously for both IPF and experimental facility located downstream of the accelerator exit. Moreover, the activity of doubling the beam intensity by increasing beam pulse repetition rate from 50 Hz to 100 Hz is in progress [1,2]. That is why implementation of the mode of simultaneous operation of the accelerator for IPF and for experimental facility is of importance. A decision to develop and build a beam pulse separation system for beam distribution has been made. The system including a pulse bending magnet and a power supply has been designed and manufactured in NIIEFA [3]. The pulse magnet replaces the first DC magnet. The system can operate with the frequency up to 50 Hz providing distribution of the beam pulses between IPF and experimental facility in different ratios. In case of 100 Hz mode of accelerator operation up to 50% of the beam pulses can be directed to IPF. A DC mode of the magnet is also foreseen thus providing a full beam direction to IPF.

INTERMEDIATE EXTRACTION AREA UPGRADE

The simplified schematic of the intermediate extraction area is shown in Fig. 1. The length of the area along the main beam line is near 14 m. Besides beam extraction the purpose of the area is to match both longitudinally and transversally the beam with the subsequent structure.

In order to implement beam separation the DC bending magnet #1 was replaced by the pulsed one. To avoid distortions of the magnetic field and heating of the vacuum chamber inside the magnet the latter was replaced by the chamber made of electron-tube glass (Fig.2). Vacuum sealing of the chamber is made with the telescopic joints. For mechanical load relief the bellows are used at each of three chamber ports. To have sufficient space for chamber mounting the distance between the magnets was increased: magnet #1 was translated by 50 mm upstream of the beam and magnet #2 - towards IPF target by the same distance. After installation the flanges of the bellows were fixed with special stays to avoid load transfer to the chamber when pumping and venting the system.

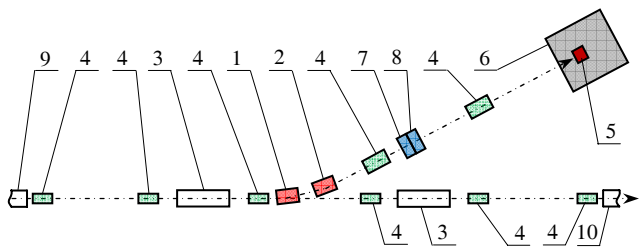

Figure 1: Intermediate extraction area (1 - bending magnet #1, 2 – bending magnet #2, 3 – two-section matching cavity, 4 – quadrupole doublets, 5 – IPF target, 6 – shield, 7 – horizontal beam corrector, 8 – vertical beam corrector, 9 – accelerating cavity #9, 10 - accelerating cavity #10).

Figure 2: Glass vacuum chamber

For beam separation the magnet #1 operates in a pulse mode meanwhile magnet #2 is turned on in DC mode. It was found that the fringe fields of magnet #2 influence the beam moving directly and result in excessive beam loss. The measurements showed that the value of B-field at the beam axis exceeds several hundred gauss and ranges along the beam line for about 40 cm. To eliminate the effect a 60 cm section of stainless steel beam pipe in the vicinity of magnet #2 was replaced by the one made of magnetic steel with the wall thickness of 6 mm. B-field decreased to the level of several gauss thus resulting in no observable influence on the beam. The view of the magnets in the extraction area is given in Fig. 3.

When operating in the beam pulse separation mode the beam matching must be done for both deflected and non deflected beams. For this purpose a separate powering of

the quads of six doublets is foreseen (two doublets upstream of the magnets, three doublets at a straight line downstream of the magnets and one doublet at the IPF line).

Figure 3: View of the magnets in the extraction area (1 – pulse magnet, 2 – DC magnet, 3 – magnetic screen).

The screen shot of the top of the pulse magnet current is shown in Fig. 4. The pulse represents a portion of a cosine function with the duration at the base of about 13 ms. Stability at the top of the pulse is within ±0.1%. Zero level of the magnetic field between the pulses in the magnet gap is less than 3 G which is smaller than the screened fringe fields of magnet #2.

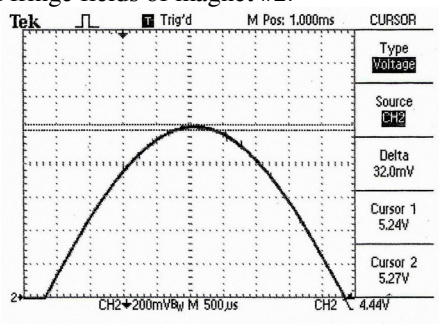

Figure 4: Current of the pulse magnet.

TESTS WITH THE BEAM

To set the beam at the top of the magnetic field pulse the magnet power supply system is triggered ~6.5 ms in advance of the injector. The tests were done with the 158 MeV 1 Hz beam. The beam was deflected to IPF. Beam position was observed with the harp installed in front of the IPF target. No beam position instability was observed. Beam losses in the extraction area and IPF line were observed as well. No increase of beam loss compared with the two magnets DC mode was revealed. The screen copy of information on beam loss is presented in Fig.5.

A smooth shape of the magnet current pulse enables a fine adjustment of deflecting field to be done by changing the delay of triggering within ± several hundred microseconds.

The system was tested for several days with 50 Hz repetition rate and nominal current.

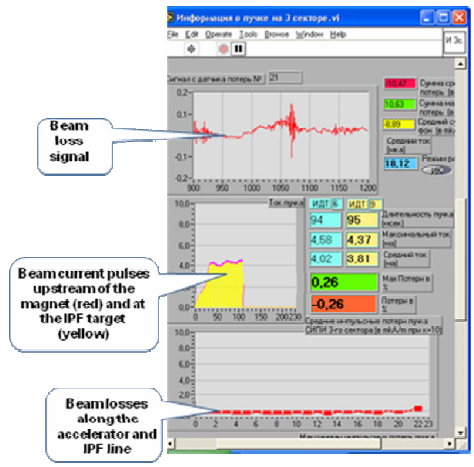

Figure 5: Information on beam loss.

CONCLUSION

Intermediate extraction area of INR linac has been upgraded with implementation of beam pulse separation system. The system has been successfully tested with nominal parameters and the first beam tests have been done.

REFERENCES

[1] A.Feschenko et al. Multipurpose Research Complex based on the INR High-intensity Proton Linac, WEYCH02, these proceedings.

[2] A.N.Drugakov et al. Investigation of INR Linac DTL RF System Operation at 100 Hz Repetition Rate, MOPPA023, these proceedings.

[3] B.O. Bolshakov et al. Power Supply System of the Pulse Bending Magnet for the Linear Accelerator Operated at the Moscow Meson Factory, WEPPC034, these proceedings.

MAXIMUM VALUE OF THE STANDING WAVE AND TRAVELLING WAVE ACCELERATING STRUCTURES ELECTRONIC EFFICIENCY

S. S. Proskin, A. P. Kulago, I. S. Shchedrin, National Research Nuclear University – Moscow Engineering Physics Institute, Moscow, Russia

Abstract

A new theoretical approach to a calculation of the standing wave and travelling wave structures electronic efficiency is described. As a result the electronic efficiency of DLWG and biperiodic structure is evaluated regarding a new definition.

INTRODUCTION

Conventional theory of linear accelerators is based on the power balance equation applied to the chosen accelerating structure: disk loaded waveguide (DLWG, working on travelling wave) or biperiodic structure.

Consider the different physically justified approaches to the issue of electron current loading in the accelerating structure. The idea of accelerating field definition forcing on accelerating electrons as algebraic sum of power source accelerating field and total decelerating field emitting by accelerating electrons [1] in chosen accelerating structure is put within this approach basis. A detailed description is reviewed in [2]. According to the ideas of electronic efficiency of DLWG and biperiodic structure are defined below.

EVALUATION OF ELECTRONIC EFFICIENCY

Consider the accelerating section of electron linac based on DLWG with relative phase velocity $\beta_{ph} = 1$. Working modes are as a rule $\theta = \pi/2$ and $\theta = 2\pi/3$. An electromagnetic field is generated by two sources. A microwave generator which supplies accelerating section produces following electromagnetic field on DLWG axis [4, 5]:

$$E_S = E_{S0}e^{-\alpha z}.$$

Where E_{S0} is the accelerating field at the input of accelerating section.

The second source which generates the electrical field is an accelerated electron beam. A summary field radiated by a series train of pointed bunches with charge q after completion of the transient processes is equal to:

$$E_S = \frac{qvR_S}{1-e^{\frac{-\pi}{Q_L}}}.$$

Where R_S – series impedance and Q_L – loaded Q factor. It should be noted that the ideal case is considered when every bunch is placed in the maximum of the total decelerating field of all bunches and in the maximum of the generator accelerating field:

$$E = E_{S0}e^{-\alpha z} - \frac{E_q}{\left(1-e^{\frac{-\pi}{Q_L}}\right)}$$

The energy obtained by every electron bunch at the exit of the accelerating section with length l equals (in terms of voltage):

$$U = E_{S0}l\frac{1-e^{-\alpha l}}{\alpha l} - \frac{E_q l}{1-e^{\frac{-\pi}{Q_L}}}.$$

Since the beam pulsed current is equal to $I_0 = q/T$ it can be written as:

$$I_0 = qc/\lambda.$$

And the expression for E_q takes the following form:

$$E_q = I_0 R_S \lambda.$$

The power of the accelerated electrons beam equals:

$$P = I_0 E_{S0} l\frac{1-e^{-\alpha l}}{\alpha l} - \frac{I_0^2 R_S \lambda l}{1-e^{\frac{-\pi}{Q_L}}}. \quad (1)$$

The electronic efficiency of the accelerating section correspondingly equals:

$$\eta = \frac{1}{P_0}\left[I_0 E_{S0} l\frac{1-e^{-\alpha l}}{\alpha l} - I_0^2\frac{R_S \lambda l}{1-e^{\frac{-\pi}{Q_L}}}\right].$$

Consider the case when the beam power is maximal and the electronic efficiency of DLWG reaches the maximal value correspondingly. Determine the accelerated beam value when $P = P_{max}$. It is necessary derivative dP/dI_0 to be equaled 0. Then using (1) get current value I_0 when $P = P_{max}$:

$$I_0 = \frac{1}{2}\frac{E_{S0}}{R_S\lambda}\frac{1-e^{-\alpha l}}{\alpha l}\left(1-e^{\frac{-\pi}{Q_L}}\right).$$

$$P_{max} = \frac{1}{2}P_0\frac{l}{\lambda}\left(\frac{1-e^{-\alpha l}}{\alpha l}\right)^2\left(1-e^{\frac{-\pi}{Q_L}}\right).$$

The dependence of the DLWG maximum electronic efficiency according to its length is presented on Fig. 1 with following parameters: $\theta = \pi/2$, iris is without rounding, $\lambda = 16.5\ cm$, $a/\lambda = 0.20$, $\alpha = 0.01492\ 1/m$ (copper), $Q_L = 3.1672$, $t/\lambda = 0.0382$.

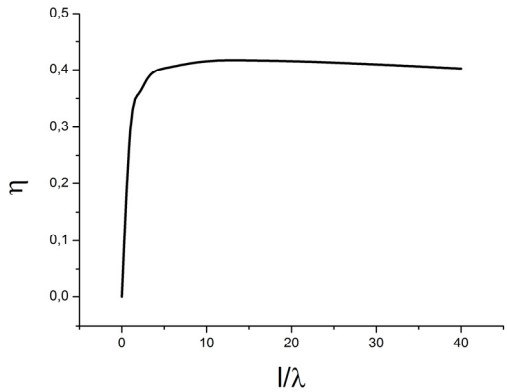

Figure 1: Dependence of DLWG electronic efficiency η from accelerating structure length

It should be noted that for the waveguide, chosen parameters the section length should not exceed 1 m. Even in this case it is desired to reach the maximum electronic efficiency. At this point the current length is $\eta = 0.45$ while the maximum η equals 0.46, when the waveguide length equals 3 m. In addition, if there are no losses in DLWG the electronic efficiency steadily increases up to $\eta_{max} = 0.50$. It is evident that the gain is not great: $l = 1\ m$ gives $\eta = 0.456$, and when $l \to \infty$ the $\eta = 0.50$.

Now consider the accelerating section of electron linac based on biperiodic system operating on standing wave [6]. Also the data of [5] are used for structures with *λ/2* period.

For the reason of simplicity, accept the approach when the section is presented in the form of a cavity with common coupling elements and with supplying waveguide [6]. It is applied here, not the energetic approach to the computation of energy, power and accelerating system electronic efficiency as well as beam parameters but the field approach when the basis for the analysis is a superposition of the accelerating field produced by the power source and the beam radiation field.

It can be written that the reflection coefficient from the load equals:

$$R_C = \frac{1-\beta}{1+\beta} = \frac{R_L - Z_0}{R_L + Z_0}.$$

According to the definition, the power incoming into the load, i.e. the BDS, can be written as:

$$P = P_S(1 - |R_C|^2) = \frac{4\beta}{(1+\beta)^2} P_S. \qquad (2)$$

On the other hand it is known that:

$$P = \frac{1}{2}\frac{U_L^2}{R_L} = \frac{1}{2}\frac{(U_L m)^2}{R_{sh}} = \frac{1}{2}\frac{U_S^2}{R_{sh}}. \qquad (3)$$

Where U_S is the voltage in BDS produced by the power source.

By comparison of (2) and (3) obtain the voltage produced by the power source in BDS accelerating section (or cavity):

$$U_S = \sqrt{\frac{8\beta}{(1+\beta)^2} R_{sh} P_S}.$$

According to Wilson theorem [7], an electron bunch has the energy loss (in terms of voltage) U_L which one equals the half of the voltage applied to the gap U_{loss}. The latter equals the result of multiplication of the electron current by the cavity shunt impedance:

$$U_{loss} = \frac{U_L}{2} = \frac{J R_{sh}}{2} = I_0 R_{sh}.$$

Where $J = 2I_0$ is the field of the harmonic periodic series of bunches with charge q and interval equaled to the wavelength.

The voltage acts on electron bunches in BDS in case when bunches are situated on maximum of the power source accelerating field and naturally on maximum of own decelerating radiation field can be written as:

$$U = U_S - U_{loss}.$$

That is:

$$U = \sqrt{\frac{8\beta}{(1+\beta)^2} R_{sh} P_S} - I_0 R_{sh}.$$

The power transferred from the power source to the beam equals:

$$P = \frac{1}{2} JU = I_0 \sqrt{\frac{8\beta}{(1+\beta)^2} R_{sh} P_S} - I_0^2 R_{sh}. \qquad (4)$$

To determine of maximum value of the electron beam power in BDS, differentiate (4) by I_0 and equate the obtained expression to 0:

$$\frac{dP}{dI_0} = \sqrt{\frac{8\beta}{(1+\beta)^2} R_{sh} P_S} - 2 I_0 R_{sh} = 0.$$

For $P = P_{max}$ it gives:

$$I_0 = \frac{1}{2R_{sh}} \sqrt{\frac{8\beta}{(1+\beta)^2} R_{sh} P_S}. \qquad (5)$$

Determine $P = P_{max}$ by substitution of (5) into (4):

$$P_{max} = \frac{2\beta}{(1+\beta)^2} P_S.$$

Correspondingly, the maximum value of electronic efficiency equals:

$$\eta_{max} = \frac{2\beta}{(1+\beta)^2}.$$

This dependence is shown on Fig. 2.

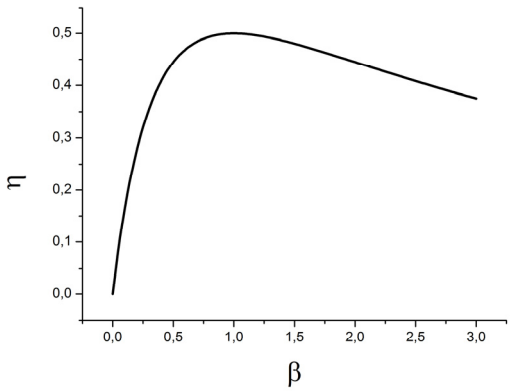

Figure 2: Dependence of biperiodic structure electronic efficiency η from coupling coefficient β.

AKNOWLEDGEMENTS

This work was accomplished under support of The Ministry of Education and Science of The Russian Federation within the program "Science and education of the innovative Russia" 2009-2013, State Contracts P433, P1222 and the program "Developing of the High School science potential" 2009-2010, scientific work number 1.49.09

REFERENCES

[1] A. P. Kulago, I. S. Shchedrin, Radiation of relativistic bunches in DLWG, II Cherenkov readings: New methods in experimental nuclear physics of elementary particles, Moscow, FIAN, 2009, pp. 48-56.
[2] S. S. Proskin, V. A. Dvornikov, I. A. Kuzmin, A. P. Kulago, I. S. Shchedrin, Study of physical processes of acceleration of electron bunches with extremal density by means of stored energy in disk loaded waveguide sections, Proceedings of IPAC2012, New Orleans, Louisiana, USA.
[3] V. V. Kudinov, V. V. Smirnov, Passing of electrons with energies of 2-8 MeV through materials and output of bremsstrahlung from these materials of different thickness (in Russian), Reference book, Moscow, MEPhI, 2005, p. 94.
[4] A. N. Lebedev, A. V. Shalnov, Foundations of accelerators physics and technology, Moscow, Energoatomizdat.
[5] O. A. Valdner, A. N. Didenko, A. V. Shalnov, Accelerating waveguides, Moscow, Atomizdat, 1973, p. 216.
[6] V. V. Stepnov, Dissertation, Moscow, MEPhI, 1986.
[7] J. W. Wang, Stanford University dissertation, SLAC, Report 39, 1989.

EXTREME DENSITY CHARGE ELECTRON BUNCHES

S. S. Proskin, A. P. Kulago, I. S. Shchedrin, National Research Nuclear University – Moscow Engineering Physics Institute, Moscow, Russia

Abstract

This paper presents untraditional approach of obtaining the DLWG limited bunch charge (LBC). The maximum energy of accelerated bunch is considered. As a result the bremsstrahlung maximum dose rate evaluation is obtained.

INTRODUCTION

Conventional theory of linear accelerators is based on the power balance equation applied to the chosen accelerating structure: disk loaded waveguide (DLWG, working on travelling wave, or biperiodic decelerating structure).

Consider the different physically justified approaches to the issue of electron current loading in the accelerating structure. The idea of accelerating field definition forcing on accelerating electrons as an algebraic sum of power source accelerating field and total decelerating field emitting by accelerating electrons [1] in chosen accelerating structure is put within this approach basis. Detailed description is reviewed in [2]. According to this idea, the maximum dose rate of bremsstrahlung from target at the exit of linear accelerator is defined within this research.

MAXIMUM DOSE RATE OF BREMSSTRAHLUNG

Consider a specific data of obtaining charges density in DLWG in order to solve an issue of designing an electron linac with output energy of 4 MeV and a bunch charge of 50 pC to obtain powerful bremsstrahlung.

According to methodic described in [2] perform a calculation of bunch charges density with modern power sources made by Mitsubishi Electric Corporation. The company produces klystrons for high energy scientific accelerators, small and middle energy accelerators with application in medicine, for airports in landing control locators.

It is important to note that a choice of power source for different accelerators should be made focusing on a serial model and a production company that has enough orders. It is desirable that the power source has a demand in different sectors of economy, for instance, in aviation, in military sector, in national security.

Back to the charge density calculation and describing main equations from [2].

The field accelerating the bunch with charge q equals:

$$E = E_{S0}e^{-\alpha z} - qcR_S \ .$$

Energy of the accelerated bunch in terms of voltage:

$$U = E_{S0}l\frac{1-e^{-\alpha l}}{\alpha l} - qcR_S l.$$

LBC value, when energy gain in terms of voltage equals 0:

$$q_{lim} = \frac{E_{S0}}{cR_S}\frac{1-e^{-\alpha l}}{\alpha l}.$$

Where E_{S0} – power source field, l – accelerating structure length, α – attenuation factor, R_S – series impedance.

The maximum dose rate absorbed in the air P_D from bremsstrahlung of accelerated electrons with bunch current equaled 1 mA and obtained on the distance of 1 m from the target with atom number Z could be defined with less than 4% tolerance by equation [3]:

$$P_D = P_{0Z}(Z) \times W^{d(Z)}.$$

Where P_D units are $Gy/(min \times mA)$, W units are MeV and a coefficient and a degree are defined by following expressions:

$$P_{0Z}(Z) = 0.144 + 7.38 \times 10^{-3} \times Z,$$

$$d(Z) = 3.19 - 6.9 \times 10^{-3} \times Z.$$

Consider a case of copper target (Z=29). $p_{0Z}(29) = 0.35802$, $d(29) = 2.9899$, $P_D = 0.358 \times W^3$.

Copper target is chosen due to simplicity of further calculations, since conversion is easy when $P_D \sim W^3$, i. e. in a degree of a whole number 3.

If consider a value of accelerated bunch pulse current I_0 (mA) then full dose rate at the exit of linear accelerator and copper target equals:

$$P_{fD} = 0.358 \times W^3 \times I_0. \quad (1)$$

Expression (1) could be written with pulse current $I_0 = qc/\lambda$:

$$P_{fD} = 0.358 \times W^3 \times q \times c/\lambda.$$

Energy in voltage term is expressed through pulse current I_0 [2]:

$$U = E_{S0}l\frac{1-e^{-\alpha l}}{\alpha l} - I_0 R_S \lambda l. \quad (2)$$

By adding expression (2) in (1) the expression for full dose rate becomes:

$$P_{fD} = 0.358\left(E_{S0}l\frac{1-e^{-\alpha l}}{\alpha l} - I_0 R_S \lambda l\right)^3 \times I_0. \quad (3)$$

If derivative of equation (3) by I_0 equals 0:

$$\frac{dP_{fD}}{dI_0} = 0.358\left(E_{S0}l\frac{1-e^{-\alpha l}}{\alpha l} - I_0 R_S \lambda l\right)^2 \left(E_{S0}l\frac{1-e^{-\alpha l}}{\alpha l} - 4I_0 R_S \lambda l\right) = 0.$$

If the first bracet is equal to 0, then dose rate tends to be zero, since charge tends to limit value and energy tends to equal zero. Equality to 0 of a second bracket corresponds following expressions:

$$I_0 = \frac{1}{4} \times \frac{E_{S0}}{R_S \lambda} \times \frac{1-e^{-\alpha l}}{\alpha l},$$

$$q_{max P_{fD}} = \frac{1}{4} \times \frac{E_{S0}}{cR_S} \times \frac{1-e^{-\alpha l}}{\alpha l} = \frac{1}{4} q_{lim}.$$

Thereby maximum dose rate could be achieved under LBC value, the charge value which would not obtain additional energy after passing accelerating structure [2]. Relation between dose rate and charge is shown on Fig. 1.

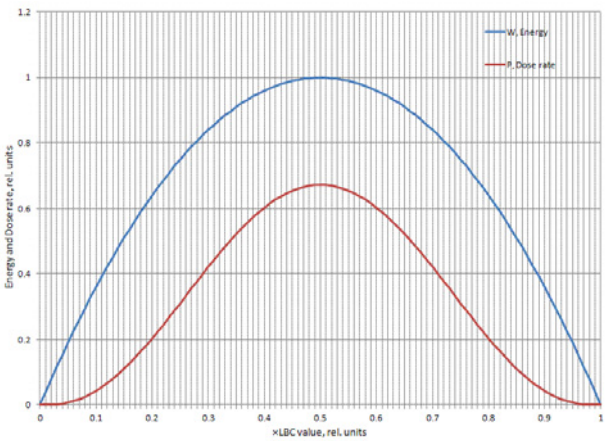

Figure 1: Energy of accelerated bunch and Absorbed Dose Rate of bremsstrahlung from tungsten target vs Bunch charge

CONCLUSION

Due to the non-traditional approach to the radiation of relativistic electron bunches, more accurate expressions of estimation of dose rate from bremsstrahlung radiated by copper target mounted at the exit of accelerating structure have been obtained. As a result, maximum dose rate is observed under limited bunch charge value. The calculation has been made for DLWG. Such approach can be used for other accelerating systems applied in linacs. If you have any questions reach me at qstpss@gmail.com please.

AKNOWLEDGEMENTS

This work was accomplished under support of The Ministry of Education and Science of The Russian Federation within the program “Science and education of the innovative Russia” 2009-2013, State Contracts P433, P1222 and the program “Developing of the High School science potential” 2009-2010, scientific work number 1.49.09

REFERENCES

[1] A. P. Kulago, I. S. Shchedrin, Radiation of relativistic bunches in DLWG, II Cherenkov readings: New methods in experimental nuclear physics of elementary particles, Moscow, FIAN, 2009, pp. 48-56.

[2] S. S. Proskin, V. A. Dvornikov, I. A. Kuzmin, A. P. Kulago, I. S. Shchedrin, Study of physical processes of acceleration of electron bunches with extremal density by means of stored energy in disk loaded waveguide sections, Proceedings of IPAC2012, New Orleans, Louisiana, USA.

[3] V. V. Kudinov, V. V. Smirnov, Passing of electrons with energies of 2-8 MeV through materials and output of bremsstrahlung from these materials of different thickness (in Russian), Reference book, Moscow, MEPhI, 2005, p. 94.

BIPERIODIC ACCELERATING STRUCTURE WITH INNER COUPLING CELLS WITH AN INCREASED COUPLING COEFFICIENT

M.A. Gusarova, I.I. Petrushina, E.A. Savin, N.P. Sobenin, National Research Nuclear University «MEPhI», Moscow, Russia

Abstract

In this article the research results of advanced biperiodic accelerating structure (BAS) re presented. This structure features increased coupling coefficient together with keeping of effective shunt impedance high value and another electrodynamics parameters.

ELECTRODYNAMICS CHARACTERISTICS

In order to characterize of accelerating cavity efficiency for low current case the effective shunt impedance per unit length is commonly used:

$$r_{\text{sh.ef}} = \left| \int_0^l E_z(z) \exp(ik_z z) dz \right|^2 \Big/ (P_{\text{loss}} l). \quad (1)$$

where $\dot{E}_z(z)$ – accelerating field electric complex amplitude; l– cavity length; P_{loss} – power losses, k_z – wave number in the z direction.

One of the most important electrodynamics characteristics for accelerating cavities is Q-factor

$$Q = 2\pi \frac{W_{stor}}{(W_{scat.res})_{T_0}} = \omega_0 \frac{W_{stor}}{P_{scat.res}}. \quad (2)$$

where W_{stor} – stored energy in magnetic end electric fields in cavity

$(W_{scat.res})_{T_0} = P_{scat.res} \cdot T_0$ – scattered energy in cavity during oscillations period, $P_{scat.res}$ – scattered power in active resistance at resonance.

Last parameter worth to be mentioned is coupling coefficient. It is defined by ratio of frequencies of π, π/2 and 0 modes

$$k = \frac{|f_\pi - f_0|}{f_{\pi/2}}. \quad (3)$$

SIMULATION MODEL

Model used for numeric simulation consists of two accelerating cells and one coupling cell between them. On Fig.1 illustrates this model with geometry parameters shown.

CALCULATION PROCESS

Each type of BAS design has been optimized on π/2 mode operating frequency both for accelerating and coupling cells.

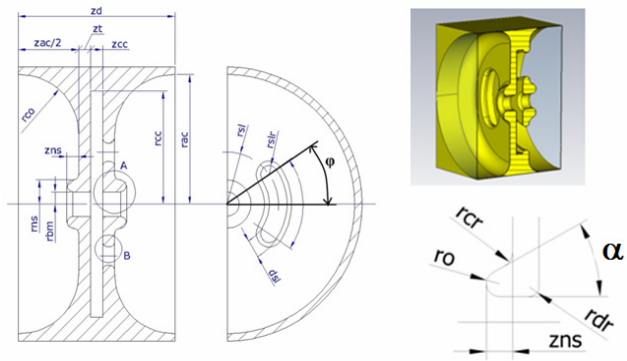

Figure 1: Structure geometry.

During researching in order to increase coupling for BAS design with inner coupling cells dual LINAC geometry was used [2]. Accelerating structure of this LINAC is designed to operate at 2856 MHz. Maximum value of coupling coefficient in accelerating section of this LINAC (with wave phase velocity equal to the 0.999c) became 10.3% instead of original 5% [1].

During the cavity optimization the following parameters remained invariable: beam pipe radius rbm, structure period zd, coupling gap thickness zt, coupling cell length zcc. The electrodynamic characteristics dependence of coupling gap radial position rsl, coupling gap width dsl, accelerating cell equator rounding rco were studied.

SWEEPING OF ACCELERATING CELL EQUATOR RADIUS

With increasing of accelerating cell equator rounding (rco) values of shunt impedance and Q-factor are increased. But this geometry change leads to coupling slots displacement – they are no longer in the maximum magnetic field region in accelerating cells and coupling cell. This results in coupling coefficient drop.

SWEEPING INNER COUPLING CELLS THICKNESS

With increasing of coupling gap thickness dsl from 9 to 13 mm angular size of coupling gap φ must be reduced from 30^0 to 25^0 to avoid coupling gaps overlapping.

In the same way radius of coupling gap middle line rsl must be reduced from 21.4 mm to 19.82 mm to place coupling gap as close to accelerating cell blend edge that leads to coupling coefficient

EXPANSION OF COUPLING CELL IN BEAM PIPE AREA

The coupling cell length zcc is expanded in the area close to cavity axis (Fig2). Simultaneously the zac/2-zns dimension is reduced by the same value t.

Cavity radius Rc was changed to place coupling slot as close to accelerating cell equator as possible while optimizing coupling cell geometry.

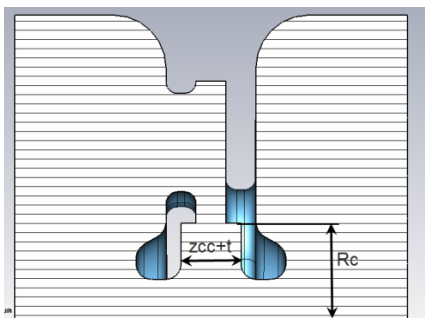

Figure 2: Coupling cell expansion.

Electrodynamic characteristics dependence on coupling gap thickness dsl for such structure geometry was studied. With dsl increase from 7 to 13 mm angular size of coupling gap φ must be reduced from 35^0 to 25^0 to avoid coupling gaps overlapping. In the same way coupling gap radial location rsl must be reduced from 25.25 mm to 23.22 mm to place coupling gap as close to accelerating cell equator as possible. This leads to coupling coefficient drop.

The structure with magnetic coupling increased by reducing diaphragm thickness zt in the coupling gaps region is the modification of geometry where coupling cell in axis region lengthened.

Rc radius value was changed while optimizing coupling cell geometry in order to place coupling gap as close to accelerating cell equator where magnetic field is maximal.

For this geometry with the following sizes: dsl=13mm, t=3.8mm, rco=7mm,φ=25^0,zt=2mm, (rcslr=1mm) with Rc value equal to 11.98 mm the coupling coefficient k=15,87% was obtained at $r_{sh.ef.}$ =80,8 MOhm/m, Q=16090, $E_{max}/E_{acc.}$=3,2.

Coupling coefficient for the model considered can be increased up to 19% by making recess in coupling gap area at the accelerating cell side (Fig 3). In the same way the effective shunt impedance will be reduced to 76 MOhm/m and Q-factor will be reduced to 14100.

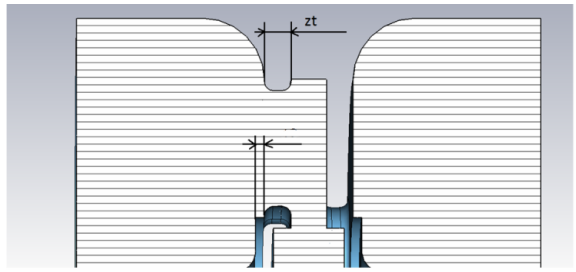

Figure 3: Coupling window recess.

ADJUSTMENT OF BEAM PIPE GEOMETRY

The coupling coefficient increases with zns rise because electrical field coupling drop. The value of effective shunt impedance has an optimum at zns=5.8 mm. The E_{max}/E_{acc} ratio increases from 3.4 to 4.5 at zns increasing in the same range.

MULTIPACTING SIMULATIONS

The electrical strength is important for the RF structure operation. Multipactor discharge is dangerous and goes along with the RF (or high-frequency) breakdown. Multipacting occurs at low levels of the electric field and is located in the coupling cells and in the areas that are close to the surface of a structure [3].

Multipacting simulations were done for four structures of the BAS with various modifications mentioned above.

The special code for multipacting simulations Multp-M was used [4].The dependence of secondary particle number vs. accelerating gradient in a wide range of latter is shown in Fig. 4.

The trajectories of the particle motion were investigated at different levels of the accelerating gradient. Multipactor trajectories were observed:

- on iris close to beam pipe from accelerating cell side (Fig. 5a) at low field strength;

Table 1: Comparison of the Results

№	1	2	3	4
$f_{p/2}$, MHz	2856.01	2855.99	2856.01	2855.94
f_{couple}, MHz	2855.96	2856	2856.01	2855.94
k,%	13	15.5	15.87	19.2
$\|B_{gr}\|$,%	19.5	22.4	22.5	26.9
$r_{sh.ef.}$, MOhm/m	81.67	76.77	80.8	75.84
T	0.81	0.81	0.77	0.81
Q	15811	15049	16088	14075
$r_{sh.ef.}$/Q, Ohm/m	5165	5101	5022	5388
E_{acc}, MV/m	51.3	50.1	53.3	52.9
E_{max}/E_{acc}	3.21	3.46	3.2	4.14
H_{max} , MA/m	0.256	0.332	0.347	0.44

• in equator areas of the coupling cell (Fig. 5b)
• on accelerating cell equator at the electric field strength levels above 9 MV/m (Fig. 5c)

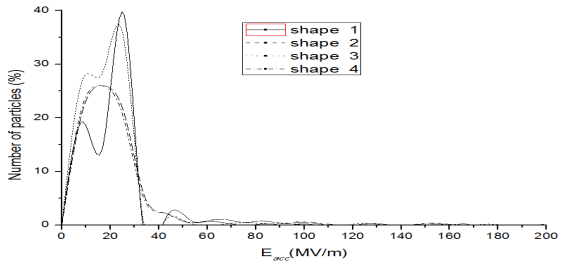

Figure 4: The number of secondary electrons in the cavity as a function of the accelerating gradient (0-200 MV/m).

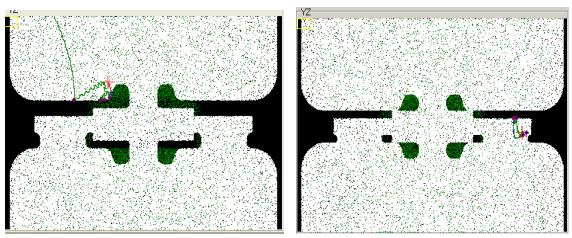

a b

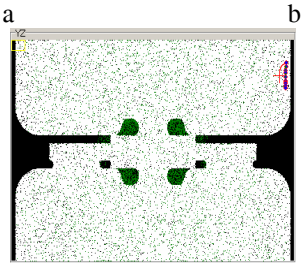

c

Figure 5: Electron trajectories in the structure at different levels of the accelerating gradient.

The results of the trajectory stability investigations in various areas of the structures are shown in Table 2.

Table 2: The results of the trajectory stability investigations in various areas of the structures: on beam pipe to iris connection area (a); in coupling cell (b); on accelerating cell equator (c).

№	a	b	c
1	~ 1.6 MV/m unstable	3–20 MV/m stable	7-20 MV/m stable
2	~0.8 MV/m stable	~ 12 MB/м stable	4.8 – 6.5 MV/m (on the blending part) stable 13.8 – 20 MV/m stable
3	1.3-2.3 MV/m stable	8 -13.8 MV/m stable	5-10 MV/m (on the blending part) stable 10 – 20 MV/m stable
4	~1 MV/m stable	5.5 – 12 MV/m stable	~15 MV/m stable

Thus, the simulation results show that:
• The first modification of the BAS with the standard coupling cell undergoes the multipacting most of all. It is obvious because the smaller the gap, the higher probability of the multipactor discharge;
• Trajectories in the coupling cell are of high order multipactor trajectories (10th and above), they are strongly twisted (curly). Electrons following these trajectories have a low probability to reach the opposite cavity wall. Consequently, such trajectories are not dangerous;
• Most of the stable trajectories are observed in accelerating cell. The motion of the particles can be described as "sliding" along the wall. The mostly apparent trajectories of this type occur in the structure shape 3.

CONCLUSION

Results of four preferred geometry types studies are given in Table 1. Geometry types are described below: 1.Geometry shown on Fig1; 2.The structure with coupling cell expansion in connection with the beam pipe area; 3.The structure with coupling cell expansion and shorter coupling cell because of expanded accelerating cell; 4. The structure with coupling cell expansion and shorter coupling cell with coupling window recess (Fig 2).

The results of multipacting simulations showed that the structure (1) undergoes the Multipactor discharge most of all. Stable trajectories were observed in areas of the coupling cell and on the walls of the accelerating cell in the range of the accelerating gradient of about 5-20 MV/m.

REFERENCES

[1] O.A.Valdner, N.P.Sobenin, at. al., "The directory about diaphragm loaded waveguides", Energoatomizdat, 1991
[2] A.A. Zavadtsev, N.P.Sobenin, et. al., "The system for cargo inspection based on dual LINAC", Devices and experimental techniques, 2011, №2, p 1-9.
[3] Paramonov V., Tarasov S, "The possibility of multipactor discharge in coupling cells of coupled-cells accelerating structures", 1998 Linac Conference, Chicago, 1998.
[4] M.A. Gusarova, S.V. Kutsaev, V.I. Kaminsky, "Multipacting simulation in accelerator RF structure", Nuclear Instrument and Methods in Physics Research A, 599. P. 100-105, 2009

USING GENETIC ALGORITHMS FOR ELECTRODE SHAPE OPTIMIZATION IN ACCELERATORS WITH RF FOCUSING

K.A. Aliev, S.M. Polozov, A.V. Samoshin#
National Research Nuclear University "MEPhI", Moscow, Russian Federation

Abstract

The drift tubes shape choice which provides the necessary distribution of the spatial RF field harmonic amplitudes is an important problem in the design of RF focusing accelerators. It is necessary to have various relationships of the main (accelerating) and the first (as main focusing) harmonics of RF field for different types of accelerators. High order harmonics should be negligible for accelerators with an external focusing, and this ratio should be E_1/E_0 = 3-5 for the efficient operation of the axially symmetric RF focusing accelerator. Thus, the distribution and harmonic amplitude's ratios at the accelerator axis which provides stable beam dynamics are always known. The drift tubes shape study problem cannot be solved directly by ordinary methods because of unknown boundary conditions belongs to a class of incorrectly defined problem. At present, this problem can be solved by using genetic algorithms (GA). For this purpose, we will define electrode's shape, and then solve the Laplace equation with boundary conditions of Dirichlet and Neumann. The necessary electrodes shape can be quickly and easily simulated using the adaptive search.

INTRODUCTION

The acceleration of high intensity low beta ion beams is one of the priority tasks of applied accelerating technology. But conventional RF low energy linacs are needed to use any external focusing elements as solenoids or quadrupole lenses to provide the beam transverse focusing. Any type of radiofrequency focusing is an alternative. It's necessary to control the spatial RF field harmonics spectrum to provide focusing condition. As an example, in axi-symmetrical RF focusing linac (ARF) [1] the base (zero order) spatial harmonic is the accelerating and high order harmonics are uses for focusing. The ratio of focusing and accelerating harmonics should be equal E_1/E_0 = 3-5 for effective beam focusing. In the other hand in RF linear undulator accelerator (UNDULAC, [2]) the acceleration is realized without synchronism with anyone of RF harmonics (beat-wave acceleration) and this ration should be equal E_1/E_0 = 0.25-0.3 for the stable beam motion. Note than in the second case the channel period can be simplest in contrast to ARF linac.

The problem of drift tubes geometry definition providing the necessary spatial RF field harmonics spectrum is not an easy task because it is an incorrectly defined problem. An other way to define the necessary electrodes geometry is to solve the analysis-syntheses problem with numerical optimization.

#avsamoshin@mephi.ru

SIMULATION MODEL

Let we consider the structure with the drift tubes (Figure 1).

Figure 1: Layout of periodic structure.

It is necessary to solve electromagnetic problems for accelerating facilities designing. In this case, it is possible to use a quasi-static approach and necessary to solve the Poisson equation in a system with a complex geometry. As stated above, the problem of electrode shapes definition for a specified field on the axis is an incorrectly defined problem. In the other hand, the problem of the field distribution simulation over the electrodes is simple, and there are many numerical methods for this simulation. For the specified field distribution we must choose the correct shape and dimensions of the electrodes, which in some cases can be a difficult problem, since changing several parameters may take a long time to find the optimal one. Therefore to solve this problem, we propose to use genetic algorithms (GA), and using one is discussed in this article.

tubeOpt console code was developed to solve this problem, which allows optimizing the accelerating structure geometry and carrying out the field calculation. tubeOpt code consists of two parts: the first electrostatic solver to find the field distribution in the cavity by numerical simulation the Laplace equation with boundary conditions of Dirichlet and Neumann, the second - a genetic algorithm which optimizes the drift tubes geometric parameters. The chosen accelerating structure has axially symmetric geometry and we can consider a quarter one (Figure 2). In this case, the following parameters will be optimized: the bore radius of the drift tube R_{in}, the external radius of the drift tube R_{out}, the bending radii R_{b1} and R_{b2} and the half-length of the tube L_{tube} (see Fig. 2).

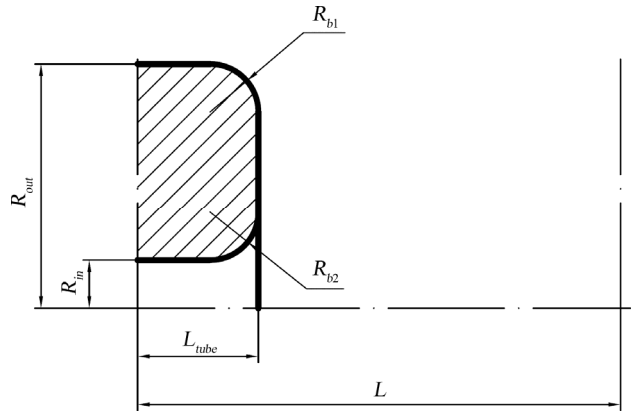

Figure 2: Layout of period structure quarter.

There are two main methods of Laplace and Poisson equations simulation. In case when the structure has a strong symmetry or consists of a several simple geometry elements (sphere, cylinder, box for example), an axis or plane symmetry coincide, the simulation area can be divided into smaller areas, where the equation can be easily solved analytically or using any simple numerical methods. The stitching of solutions can be done in case when the solutions in each area are founded and the field distribution definition in whole area is difficult. This method is called the finite volumes method. Another method is called the finite differences method. In this case, a spatial grid is imposed on the field of simulation and the solution of the electrodynamics problem can be provided on the grid. Generally a rectangular or triangular grid and their combinations are used. Obviously, the solution of differential equations on the grid is replaced by the solution of the system of finite-difference equations. This method is used in the tubeOpt code.

Genetic algorithm is a search heuristic that resembles the process of natural evolution. This heuristic can be used to generate useful solutions to optimization and search problems. GA generates solutions to optimization problems using techniques inspired by natural evolution, such as inheritance, mutation, selection, and crossover. The error between the desired and the obtained potential distribution along the accelerator axis can be selected as the fitness function and calculation carried out to minimize the error.

The tubeOpt code works using the following algorithm. At first the genetic algorithm generates a population of a few individual solutions (further individuals), i.e. combinations of the optimizing parameters that represents number of possible solutions of this problem. Each individual is evaluated to a measure of its "fitness", i.e. correspondence to the required solutions. The elite individuals have the opportunity to "reproduce" the population by crossover with other individuals from the population or undergo mutation. This leads to the appearance of new individuals, which combines some of the characteristics that are inherited from their parents. Selection of elite individuals from the previous generation replicates a new population and gets a lot of new individuals. This new generation contains more tailored individuals. The crossover of the elite individuals leads to exploration of the most promising area of the optimization space. Eventually, the population will converge to the optimal solution.

Evolution cycle continues until one of the three conditions is true: the number of generations has reached the limit, the best individual solution in the population does not change over a given number of generations, individual solutions in the population became to similar. The fitness function takes the first five harmonics variations on the axial potential. The potential on the axis is expanded into a Fourier series and compared to the ratio of the first and third harmonics, as well as minimized the variations of the second, fourth and fifth harmonics:

$$error = \sqrt{\left(\eta - \frac{U_3}{U_1}\right)^2 + U_2^2 + U_4^2 + U_5^2}.$$

We performed several numerical experiments to determine the optimal geometric parameters of the drift tubes. The results of the simulation are shown in Table 1. The optimal solution was found pending 78 generations (168 minutes). In this case, the population contains of 20 individuals, each with 5 genes (according to the optimizing parameters), the reproduction of the population set to 90%.

Table 1: tubeOpt calculation results

Population	Reproduction, %	Generations	Best solution accuracy	Runtime min
100	10	74	$4.171 \cdot 10^{-3}$	58
20	100	100	$1.7 \cdot 10^{-2}$	214
20	10	29	$4.246 \cdot 10^{-3}$	12
20	90	78	$3.798 \cdot 10^{-3}$	168
10	100	12	$2.54 \cdot 10^{-2}$	15

The optimal variant of the accelerating structure geometric parameters is presented in Table 2. Parameters are presented relative to the half-period L.

Table 2: Optimized parameters

L	L_{tube}	R_{in}	R_{out}	R_{b2}	R_{b2}
1	0.210	0.226	0.557	0.060	0.054

The potential distribution was built according to the optimized geometric of the accelerating structure (see Fig. 3). A drift tube section is shown by gray color.

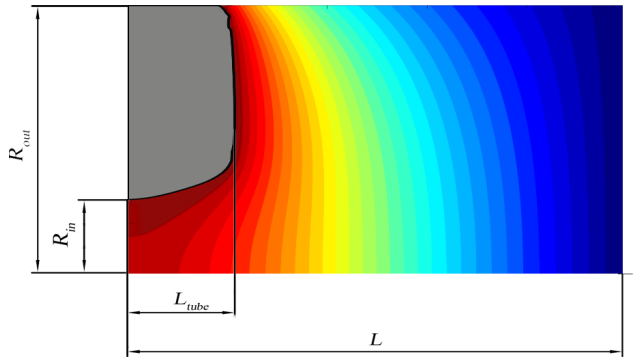

Figure 3: Equipotential surfaces obtained by tubeOpt code.

The simulated potential distribution along the accelerating structure axis was compared to the ideal distribution (Fig. 4). The figure shows the ideal distribution of the potential (red color), and the calculated potential (blue color). It can be seen that the calculated distribution is almost identical to the desired.

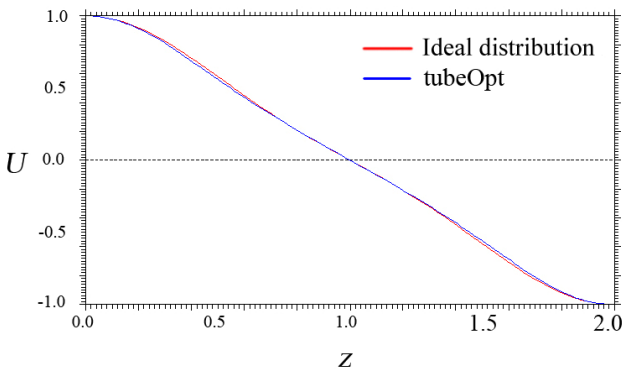

Figure 4: Calculated (blue curve) and ideal axial potential distribution (red curve).

Figure 5 shows the change of the best individual solution during evolution process. It can be seen that the optimal solution obtained sufficiently fast.

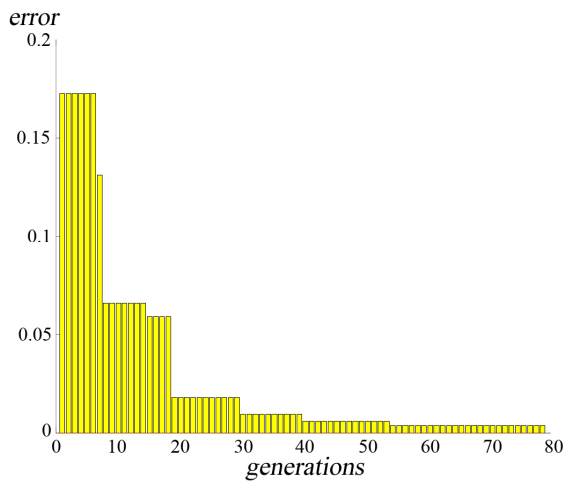

Figure 5: Optimization progress.

NUMERICAL SIMULATION VERIFICATION

Verification of the parameters provided by a well-known simulation software shows that the general view of the equipotential surfaces (see Fig. 6) is similar to the calculation result using the tubeOpt code.

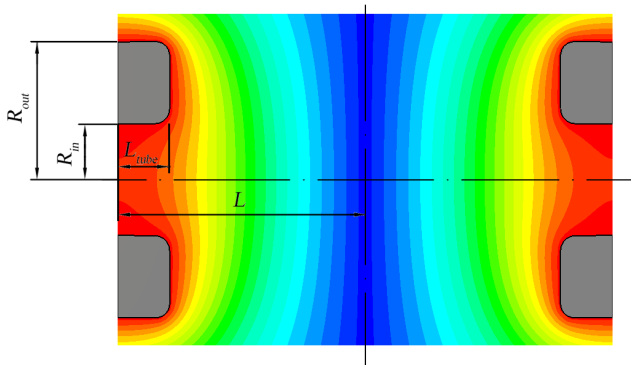

Figure 6: Sample equipotential surfaces.

We did the potential distribution comparison on the accelerating structure axis. The distribution obtained by using tubeOpt electrostatic solver (blue curve) was compared with the results of a standard electrodynamics code (red curve). It can be seen that the curves are sufficiently similar (see Fig. 7).

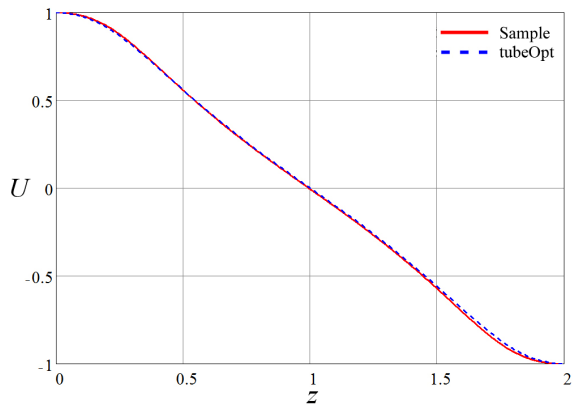

Figure 7: Comparison of the sample (red curve) and a tubeOpt (blue dotted curve) potential calculation.

CONCLUSION

It is shown that use of genetic algorithms allows to quickly and accurately optimize the accelerating structure parameters. Verification of the parameters definition by specially designed tubeOpt code shows a good agreement with the simulation by well-known codes.

REFERENCES

[1] E.S. Masunov, N.E. Vinogradov, Phys. Rev. ST Accel. Beams, 2001, No 7, 070101.
[2] E.S. Masunov, S.M. Polozov. Phys. Rev. ST AB, 11, 074201 (2008)

H-CAVITY BASED ACCELERATING STRUCTURE FOR PROTON ACCELERATOR

M.V. Lalayan, A.A. Kalashnikova, S.E. Toporkov, National Research Nuclear University "MEPhI",Moscow, Russia

Abstract

Nowadays there is a growing interest in high intensive proton sources for different types of applications: neutron sources, Accelerator-Driven Subcritical Reactors (ADSR), nuclear waste transmutation, neutron factory, etc. Different types of accelerating structures for different beam energies are developed in leading centers all over the word [2]. This paper presents the results of numerical modeling accelerating structure for low (0.01-0.04) beta range. Two operating frequencies 144 MHz and 433 MHz were analyzed in detail. The influence of geometrical sizes to the main electrodynamic characteristics was investigated to find out the optimal configuration.

CAVITY DESIGN

Today there are many projects of high current accelerator complexes one of which is BWLAP (Backward Wave Linear Accelerator of Particles). The R&D work was dedicated to the front-end part of this complex. For this purposes inter-digital H - mode (IH) resonators (see Fig. 1) consist of drift tubes, stems and pilons were chosen [3].

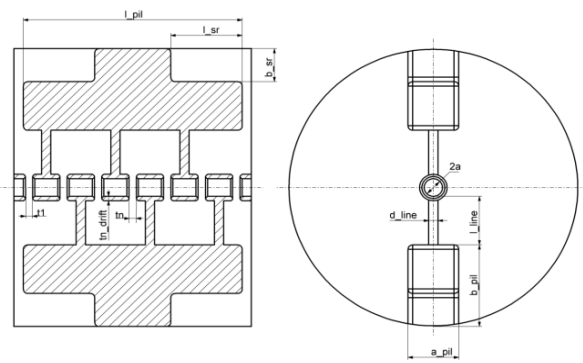

Figure 1. IH - Tank layout.

Period D of the structure is constant and it is equal to:

$$D = \frac{\beta\lambda}{2} \qquad (1)$$

as for all IH-structures working in π - mode regime.

Operating frequencies (144 MHz and 433 MHz) of front - end part were chosen according to the frequency of the main accelerator (1300 MHz). It is third (433 MHz) and ninth (144 MHz) harmonics.

Simulation Process

Since the IH - structure is periodical the first step of research process was performed on one geometric period (see Fig.2) which includes two electric periods.

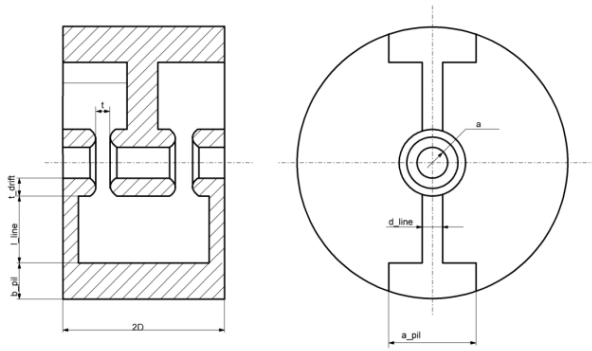

Figure 2. One period layout.

Two magnetic boundary planes were used at the opposite sides of the model to create correct field distribution. In such type of cavities electric field concentrates between drift tubes in opposite directions in neighboring gaps. Magnetic field also directed along the beam axis but it is suited at the opposite sides of the stems.

At the center of drift tubes there is a lack of electric field and presence of the longitudinal component of magnetic field. It would be the best place to locate magnetic boundary plane. Also one magnetic symmetry plane (belonging to the axis of the stems) was used to increase the accuracy.

At this stage IH - resonator demonstrated high values of shunt impedance: from 300 MOhm/m to 800 MOhm/m for different frequencies, aperture radii, accelerating gaps and geometric sizes of the stems and pilons. It should be noted that for this beam velocity range better to use lower frequency since it's got higher wavelength and higher period value. For example in case of the 433 MHz and $\beta = 0.01$ period D is equal to 3.5 mm. Such design couldn't be practically realized and they were not taken into further consideration.

Full Structure Modelling

After structure adjusting at one geometric period full tank (see fig.1) was simulated. But the field inside whole resonator isn't the same as inside one period. There is a difference of the magnetic field distribution at the central part of the resonator and at the end part of resonator. At the central part magnetic field has longitudinal component as in case with one period. At the end parts magnetic field turns around the pilon. It leads to the different field

distribution, different working frequency of the end circuits (comparing to the central part of the structure). As a result we have irregular electric field distribution along the beam axis and low efficiency of the resonator. At this stage optimizing of the electric field distribution was our main goal. To characterize the irregularity special coefficient was introduced:

$$K_{ir} = \frac{E_{\max} - E_{\min}}{E_{\min}} \cdot 100\% \quad (2)$$

The models with 7, 8 and 9 electric periods were simulated. At first all researches were performed with operating frequency equal to 352MHz. Such structures have higher period value (comparing to the 433MHz version) and lower geometric sizes (comparing to the 144MHz version). For initial investigations it was best choice between simulation time and possibility of changing geometry of the structure.

At the beginning there was not any pilon recess in the model (as one can see on fig.1). There were only gaps between end wall of resonator and pilons to make a closed flux of magnetic field around pilon. As one can see in the Table 1 structure without pilon recess has worst irregularity. But using the pilon recess didn't improve the irregularity significantly.

Table 1: Influence of the pilon geometry.

Type of modifications	K_{ir},%
Without modifications	63
Changing the gap between pilon and end wall	60
Using rectangular pilon recess	53

The next step of optimization was modification of the end cell geometry. Firstly the thickness of the end cells lying on the end wall of the resonator was changed. The irregularity became better: 39 %. Secondly the thickness of the two nearest end cells and the gap between them was changed. Employment these methods decrease the irregularity till 11%. Our main goal was noticeable field increasing at the end accelerating gaps and soft increasing at neighbor gaps. It was realized using end cells geometry described at the fig.3.

As a result irregularity is equal to 5 % with the field distribution showed at the fig.4.

All of these techniques make irregularity better but they have a negative influence on the shunt impedance value: without modifications it was equal to 250 MOhm/m; after using all this techniques it became 130 MOhm/m. But it should be noticed that increasing the amount of periods inside the tank makes the value of shunt impedance (reduced) higher.

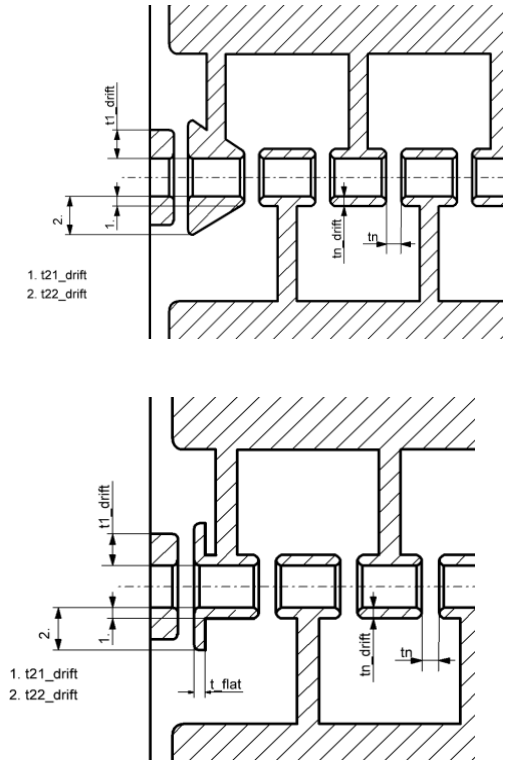

Figure 3. Different types of end cells modifications.

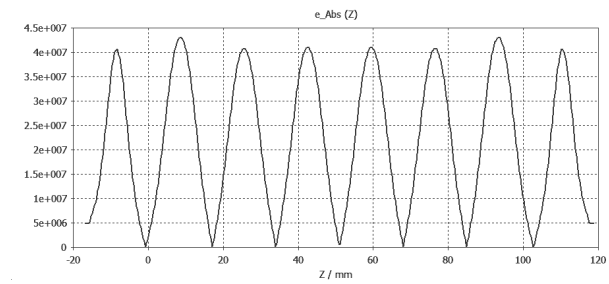

Figure 4. Field distribution after end cell modifications.

CONCLUSION

In this article the adjustment of IH-structure for low beta acceleration was presented. Two operating frequencies were considered: 144 MHz and 433 MHz. Full tank containing 7, 8 and 9 periods was modeled. Best results were obtained in the case with working frequency 144 MHz: good field flatness (better than 98%) with best values of shunt impedance for different aperture radii.

REFERENCES

[1] CST MICROWAVE STUDIO, CST, 2012, www.cst.com.

[2] An 8 GeV Superconducting Injector Linac Design Study. The Proton Driver Study II. SCRF Linac Option. G.W.Foster, W. Chou, E. Malamud. 2012.

[3] Accelerating structures. V.I. Kaminsky, M.V.Lalayan, N.P. Sobenin, M.:MEPhI 2005

MODERNISATION OF AN INITIAL PART THE MILAC HEAVY ION LINEAR ACCELERATOR

V.O.Bomko, A.P.Kobets, V.V.Panov, K.V.Pavlii, G.V.Sotnikov, B.V.Zajtsev, National Science Center "Kharkov Institute of Physics and Technology", Kharkov, Ukraine.

Abstract

New pre-stripping section (PSS-20) the MILAC heavy ion linear accelerator with the relation of their mass to charge A/q=20 is developed. That will allow to extend considerably a range accelerating ions and to increase intensity of beams. On an initial part of acceleration of ions from 6 keV/u up to 150 keV/u high capture in process of acceleration of the injected ions is provided interdigital (IH) accelerating structure with Radio-Frequency Quadrupole (RFQ) focusing. On the second part of acceleration of ions from 150 keV/u up to 1 MeV/u the highest rate of acceleration is created interdigital (IH) accelerating structure with drift tubes. Mathematical modeling geometrical and dynamic characteristics of accelerating structures pre-stripping section PSS-20 is executed. Dynamics of heavy ions in the course of acceleration is optimized.

INTRODUCTION

Main objective of investigations is development a complex on the basis of the Kharkov heavy ion linear accelerator MILAC for modeling of radioactive processes in nuclear reactor core, and also use of the accelerated heavy ions beams for investigations in the field of a nuclear physics and in the applied purposes.

Now MILAC accelerates ions from He^{+} to Ar_{40}^{3+}, i.e. ions of those elements which can be gained in ion source with mass to charge ration of A/q≤15. After the system of injection energy of ions makes 30 keV/nucleon and after acceleration in prestripping section PSS-15 - 0,975 MeV/nucleon. At such energy ions are exposed stripping, i.e. transit through a thin carbon film where their charge is incremented within and, after acceleration in the main section MS-5(DTL with quadrupole focusing) energy of ions makes 8,5 MeV/nucleon. Intensity of the accelerated beam to such energy makes 10^{9}-10^{10} particles/s and essentially decreases for ions with a mass number above 40. Such quantity of a current of the accelerated ions is caused by an out-of-date method of radio-frequency focusing on all extent prestripping section PSS-15.

The procurement problem on new prestripping section PSS-20 of the accelerated heavy ions beams with mass to charge ration of A/q≤20 with energy 1MeV/nucleon and the average beam intensity of 10^{12}-10^{13} particles/s is put.

In a Fig.1 the perspective plan of linac MILAC on which two new sites prestripping section PSS-20 is given, on first of which the accelerating structure with radiofrequency quadrupole focusing RFQ, and on second - accelerating structure with drift tubes DTL is used. On all sections of linac MILAC the interdigital H-type IH accelerating structure is used.

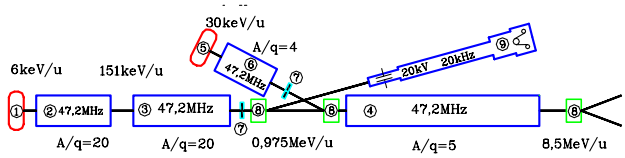

Fig. 1 Perspective plan of linac MILAC.

ACCELERATING STRUCTURE WITH RADIOFREQUENCY QUADRUPOLE FOCUSING RFQ

The accelerating structure with the radiofrequency quadrupole focusing RFQ, the offered I.M.Kapchinsky and V.A.Teplyakov [1,2], is used now almost in all existing heavy ions linacs. The basic design features and methodical workings out have been executed in many accelerating laboratories, studying of such accelerating structure in Los Alamose where all basic backgrounds for structure RFQ construction on sites of formation and an initial acceleration of high-current beams [3,4] have been created was especially intensively conducted. According to these workings out all section RFQ is divided into 4 sites: radial matcher, the phase shaper, a site of the adiabatic grouping (gentle buncher) and an acceleration site (accelerating section). However in case of acceleration of heavy ions (major A/q) the site of the adiabatic grouping demands a considerable quantity of the cells which had on major length. The problem of cutting of total length created prestripping sections PSS-20 together with injection system costs is very sharp. Besides, in a linac of heavy ions intensity of a current of a beam much more low, than in proton accelerators.

Therefore forces of a space charge are small and other plan of grouping providing higher of acceleration rate without deterioration of radially-phase characteristics of a beam can be used. Such plan of acceleration has been offered S.Yamada in which the grouping site is divided into two: prebuncher and buncher. [5]. On a site prebuncher the prompt phase compression proceeding on half of a period of phase oscillations is made. On a site buncher aspire to create high acceleration rate, without worsening thus radial and phase characteristics beam. The site booster where the peak acceleration rate is reached is entered also.

Such variant of build-up of sites prestripping section PSS-20 is developed with reference to acceleration of heavy ions with A/q=20. Thus for each of 6 sites programs of calculation of parameters of structure and characteristics beam of ions are created. Results of optimizing calculations of structure are given in [6]. In Table 1 parameters of accelerating structure and the characteristics beam on an exit of sites of section RFQ for PSS-20 accelerator MILAC are given.

Table 1: Parameters of accelerating structure RFQ for PSS-20

Parameters	Shaper	Prebuncher	buncher	booster	accelerator
Output energy W, keV/u	6	6,4	44,6	98,3	151
Cell length L, cm	1,138	1,17	3,04	4,55	5,67
Synchronous phase, deg	-87	-72,7	-29,8	-20,2	-20,2
Phase length of bunches F, deg	312,6	236,7	90,2	60,8	60,8
Modulation m	1,04 - 1,00	1,1	2,06	2,06	2,06
Aperture radius a, cm	0,7353 - 0,75	0,71	0,49	0,49	0,49
Efficiency of accelerating T	0,013 - 0	0,034	0,437	0,46	0,47
Section length Z, cm	26,19	29,84	171,04	100,29	123,65
The number of cells	23	26	99	26	24

In a Fig.2 the general view of this structure is presented and on the Fig.3 schematic view of a fragment of accelerating structure RFQ for PSS-20. In a Fig. 4 process of change of parameters along sites of accelerating structure RFQ is figured.

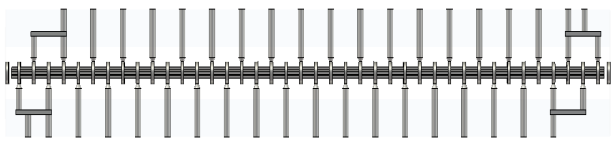

Fig. 2. The General view of structure RFQ for PSS-20

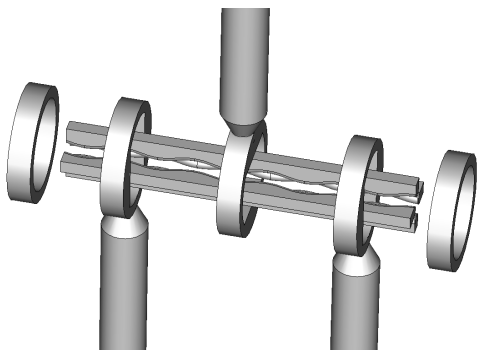

Fig. 3. Schematic view of the fragment of accelerating structure RFQ for PSS-20

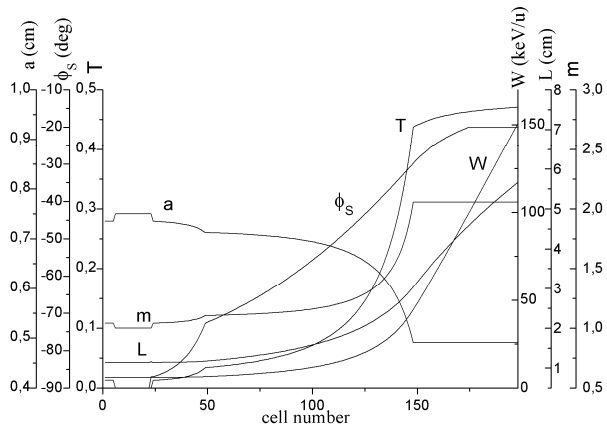

Fig. 4 Mains parameters of accelerating structure RFQ

Energy of ions on an exit from RFQ makes 151 keV/nucleon, the total length of accelerating structure RFQ is equal 451cm, the net quantity of cells - 198. It is necessary to score good characteristics of the accelerated beam of the ions, 95% providing its capture in a following site of acceleration in structure with drift tubes.

SITE OF ACCELERATING STRUCTURE PSS-20 WITH DRIFT TUBES (DTL)

On site PSS-20 with drift tubes the interdigital H-type IH accelerating structure raised on wave H_{110} is used. Prominent feature is such structure is substantial growth of a working wave length that is especially important in case of acceleration of heavy ions with high relation A/q. The economical expenditure of high-frequency power is peculiar to this structure. Besides, acceleration is carried out on π-wave that allows to gain the highest acceleration rate.

Presence of site simplifies a problem of acceleration of the ions which have gained energy 150 keV/nucleon. At a wave length λ=6,36m the length of the first period in structure with drift tubes will make 5,78cm. The longitudinal gain of the sizes of cells is carried out already in higher rate, therefore the quantity of drift tubes is reduced. Phase extent of a beam of ions after RFQ already makes nearby 20°, and its radius 4mm. It gives the chance to calculate structure of cells on considerably raised quantity of a synchronous phase that, accordingly, increments acceleration rate and lowers the factor of a defocusing of particles.

Calculation of accelerating structure with drift tubes is executed. In the course of calculation its geometrical parameters and the basic performances of a beam are spotted. In Table 2 main parameters structure are shown. The total length of structure DTL makes 422,9cm, quantity of cells - 42.

In the course of calculation of dynamics of ions phase and radial characteristics along each group of cells were spotted.

Table 2: Parameters of accelerating structure DTL for PSS-20

Parameters	Value
Input energy, keV/u	151
Output energy, keV/u	975
Mass to charge ratio, A/q	20
Operating frequency, MHz	47,2
Synchronous phase, deg	-10
Number of drift tubes	42
Cavity length,cm	422,9
Acceleration rate, MeV/m	2,9
Input beam emittance, π mm mrad	0,456
Output beam emittance, π mm mrad	0,84
Longitudinal capture, %	95
Pulsed current of accelerated ions, mA	4,5

Calculations result show that such structure in a combination with site RFQ is effective for making new prestripping section PSS-20 for linac MILAC. Total transmission along all channel PSS-20 is spotted, considering quantity of capture of an injected beam 95%. For example, for ions of nitrogen N^+ at such transmission on an exit prestripping section PSS-20 10^{13} particles/s will be gained. Considering losses on stripper foil by trusty operation of system of autoregulation RF phase, amplitude and frequency a current of ions after acceleration in the main section MS-5 to energy 8,5 MeV/nucleon will make 10^{12} particles/s.

The main objective of mathematical calculations consisted in definition of diameter of the resonator, diameter of drift tubes and a configuration of necessary updatings of the tuning devices which application provides a uniform distribution of an accelerating field along gaps of structure and operational frequency 47,2MHz.

The adjustment problem consists not only in maintenance of necessary operational frequency, but also in neutralisation of decrease of level of a field on ends resonator peculiar to H-structures. Therefore effective methods of adjustment are required, which allow to compensate the specified diversions and to reach operational frequency.

Tasks in view have been solved by the interpolation calculations which consistently joined constructive variants of devices of adjustment: diameter of the resonator, end resonant tuning elements (ERTE), and also the new inductance-capacitor tuning elements – contrivances developed in the course of investigations. Contrivances have shown high efficiency with reference to various variants of accelerating interdigital H-type IH structure - structures RFQ, DTL and others.

Adjusting devices in this case represent a construction in the form of stems which are located on the leg of drift tubes, opposite them support stick to the resonator. They form thus an additional inductance-capacitor loading which yields corresponding to depression of frequencies of cells and local increase of an electric field.

Calculation of geometrical and electrodynamic characteristics of accelerating structure was carried out in three-dimensional variant. As a result of process of consecutive definition of activity of each of tuning elements the method of mathematical modelling had been spotted geometrical parameters of all elements of accelerating structure. These investigations have allowed to gain settlement frequency 47,2MHz and to generate accelerating field.

CONCLUSION

As a result of investigations on development of accelerating structure new pre-stripping section PSS-20 for linac MILAC are created backgrounds for its construction. The design procedure of parameters of two parts interdigital H-type IH structure is developed. These structures based on radio-frequency quadrupole focusing (RFQ) and structure with drift tubes (DTL). These two structures provide both effective formation of heavy ions beam, and high acceleration rate. That will allow on the existing area with restricted length nearby 9м to accelerate heavy ions with the mass to charge ration $A/q \leq 20$ to energy 1 MeV/nucleon. Investigations on optimization of parameters pre-stripping section PSS-20 in a direction of combination of diverse sites RFQ and DTL in one resonator will be prolonged. Making such pre-stripping section considerably will raise possibilities of linac MILAC at its use in fundamental scientific investigations and in the applied purposes.

REFERENCES

[1] I.M.Kapchinsky, V.A.Teplyakov, PTE, 1970, № 2, p.19
[2] I.M.Kapchinsky, V.A.Teplyakov, PTE, 1970, № 4, p.17
[3] R.H.Stokes et al. «RF Quadrupole beam dynamics», IEEE Trans. NS-26. (1979), p.3469
[4] K.R.Crandell et al. «Quadrupole beam dynamics study», Proc of LINAC , 1979, Montauch, p.2005.
[5] S.Yamada. «Buncher section optimization of heavy ion RFQ linac». Proc. 1989 Linear Conf., Santa Fe,, LA, 9234-C
[6] V.A.Bomko et al., Heavy Ions Beams Formation In An Initial Part Of Accelerating Structures Prestripping Section The Milac Linear Accelerator, Problems of Atomic Science and Technology (VANT), Issue: Nucl. Phys. Res, #4(80), Kharkov 2012, p. 15-19.

NOVEL DTL SECTION FOR ITEP-TWAC HEAVY ION INJECTOR

V. Andreev, N.N. Alexeev, A.Kolomiets, V. Koshelev, ITEP, B. Cheremushkinskaya 25, 117218, Moscow, Russia
A. Plastun, NRNU MEPhI, Moscow , Russia

Abstract

A novel 81.5 MHz H-type drift tube (DTL) accelerating structure with RF quadrupoles following RFQ in the new injector I-4 for acceleration ions up to energy about 5 MeV/u for ITEP TWAC facility has been proposed. It is based on a combination of a DTL structure and the resonator with magnetic coupling windows. Computer simulations show that it can provide some advantages in comparison with conventional IH-DTL structure. Results of both electrodynamics and beam dynamics computer simulations of the structure as well as a new approach for beam matching RFQ and the section are presented.

INTRODUCTION

The new high current ion injector I-4 for ITEP TWAC facility is under construction [1]. The facility consists of main synchrotron accumulator U-10 with 25 MeV proton injector I-2 and booster synchrotron UK with 4 MeV ion injector I-3. It runs presently in several operation modes accelerating protons in the energy range of 0.1-9.3 GeV, ions in the energy range of 0.1-4 GeV/u and accumulating nuclei up to Cu at the energy of 200-400 MeV/u [2].

The injector I-4 have to accelerate ions with charge-to-mass ratio Z/A = 1/3 up to the energy of W = 7 MeV/u with beam current up to I = 30 mA. These parameters are required to increase the intensity of the ion beam in UK ring to reach the terawatt level of stacked beam power in storage ring U-10.

The 81.5 MHz RFQ with output energy of 1.57 MeV/u as initial part of I-4 has been successfully commissioned in 2011 [3]. The initial design of the second section (IH-DTL) was completely revised and a new design of the section has been proposed. The main goal of the new design is to provide compact, efficient and relatively inexpensive part of the injector.

The design of the accelerating channel is based on a hybrid scheme [4, 5]. A new resonant structure based on four vanes with displaced magnetic coupling windows (MCW) [6] similar to existing RFQ was proposed for second section.

The paper presents results of both electrodynamics and beam dynamics computer simulations of the new structure.

HYBRID STRUCTURE

General Injector Layout

Hybrid structure combines accelerating gaps and RF quadrupole focusing. A simplified scheme of the structure and its placement with respect to the first RFQ section is shown in Figure 1. Focusing part is formed by vanes with quadrupole symmetry. Its length is $L_q = 3\beta\lambda/2$, so focusing gradient changes its sign three times while particle passes this length. It means that this part of the hybrid structure acts as a conventional triplet of quadrupole lenses. Required focusing strength of each cell is defined by distance from axis to vanes.

TWAC injector RFQ output beam parameters allow direct injection into DTL part of the hybrid structure without any additional focusing or RF elements for matching of transverse and longitudinal beam parameters. So the design doesn't assume use any MEBT between RFQ and second accelerating section.

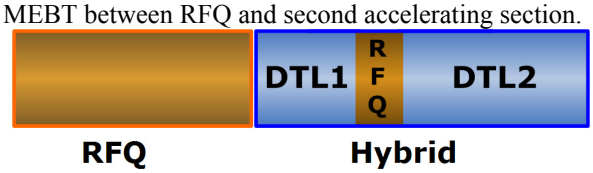

Figure 1: Simplified scheme of the hybrid structure.

Choice of the Resonator

Conventional IH and CH structures have twice lowered accelerating electric field in the space between the flanges and the tubes. In order to equalize the field distribution along the accelerating channel a new design of the resonator, using four-vane structure with displaced MCW like that was used for TWAC RFQ has been proposed. The displaced MCW structure has longitudinal electric field on the axis between the flanges and the vanes due to coaxial component of the operational mode. It allows equalizing electric field in end gaps of the CH and IH structures. Figure 2a and Figure 2b depict two 11- gap structures which have been simulated to evaluate RF parameters and choose most suitable design for second section. Varying the windows displacement and their dimensions allows very easy tuning both resonant frequency and field distribution along the structure. Normalized electric field distribution (E_{zn}) on the axis shown in Figure 3 is the same for IH and CH structures with displaced MCW.

Parameters of CH and IH structures with MCW simulated by OPERA-3d code are shown in Table 1.

Table 1: Structure parameters

Parameter	IH	CH
Inner diameter of the cavity, mm	760	880
Length of the resonator	1520	
Resonant frequency, MHz	81.5	
Frequency of nearest mode, MHz	105.1	106.2
Quality factor	17000	

Gap voltage, kV	600	
RF power losses, kW	180	320

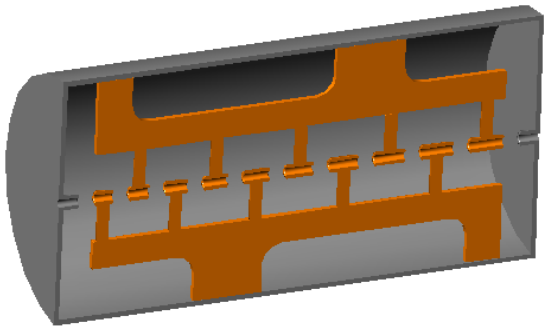

Figure 2a: IH structure with displaced MCW.

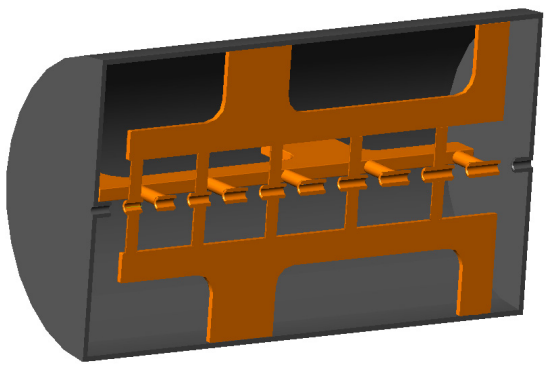

Figure 2b: CH structure with displaced MCW.

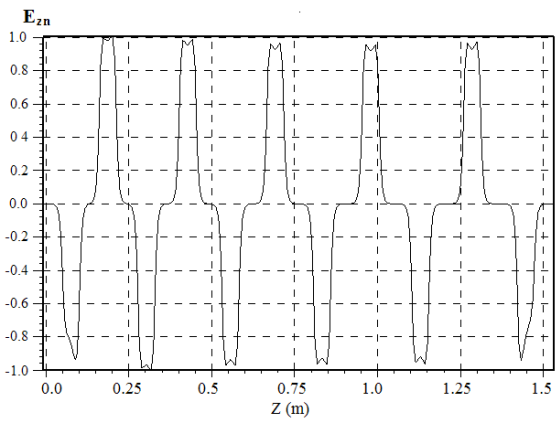

Figure 3: E_{zn} on the axis along the resonator.

IH structure has both smaller diameter and lower RF power losses in comparison with CH one. It is very important for CW operation. On other hand cross-bar structure has quadrupole symmetry that simplifies realization of the RF quadrupole focusing. Moreover, it excludes the necessity of compensation of dipole field component existing on the axis of conventional IH structure.

For low duty cycle operation (our case) excessive power losses are not very high price for listed above advantages of cross-bar cavity, taking also into account that this parameter can be improved by proper optimization of the resonator.

Second Section of the TWAC Injector

The MCW CH resonant structure with hybrid accelerating scheme was chosen for design of the TWAC second section. Its computer model is shown in Figure 4. Figure 5 shows simulated E_z field component on axis of the structure. It can be seen from Figure 5 that E_z amplitude is practically the same in all regular gaps except the gaps between drift tubes and RF quadrupole where it is two times lower owing to zero electric potential on quadrupole axis.

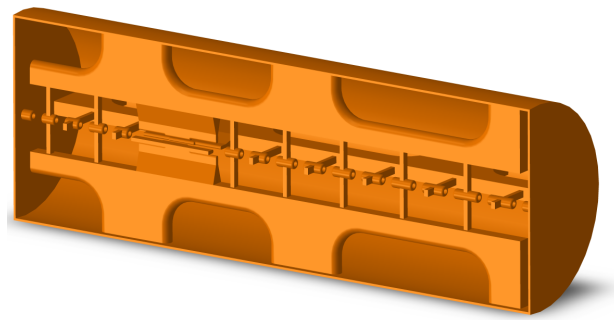

Figure 4: Computer model of hybrid accelerating structure based on four-vane cavity with MCW.

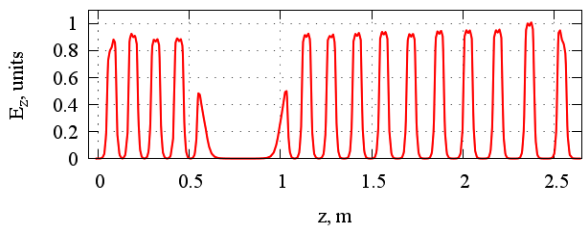

Figure 5: E_z component on axis of the structure.

Voltage V applied to RFQ vanes and drift tubes is the same in hybrid structure. It is limited only by acceptable surface field. Accelerating gap lengths are usually kept constant along the H-resonator.

Drift tube geometry is defined by several parameters. Aperture radius is determined by required transverse acceptance of the hybrid structure. Outer diameter of drift tube and rounding radius were chosen to minimize surface electric field. The gap length is optimized to achieve maximum transit time factor. Parameters of the accelerating channel are presented in Table 2.

Table 2: Parameters of the accelerating channel

Parameter	Value
Gap length, mm	50
Aperture radius, mm	12
Outer tube radius, mm	26
Inner curvature radius, mm	3
Outer curvature radius, mm	8
Maximum surface electric field MV/m	21
Gap voltage, kV	600

BEAM DYNAMICS SIMULATION

Simulation of beam dynamics in the hybrid accelerating structure was carried out by means of ITEP codes: PreRFQ, ALFIL and TRANSIT for 3D distribution of electromagnetic fields in accelerating channel. PIC solver was used for calculating particle interactions. Input energy of the second section is 1.57 MeV/u. Energy gain achieved in it is 3.33 MeV/u. Beam dynamics simulation was also carried out through the whole injector.

Simulated transverse envelopes at beam current I = 30 mA are shown in Figure 6. It confirms that RF quadrupoles provide beam focusing with the same efficiency as a triplet of conventional electromagnetic lenses.

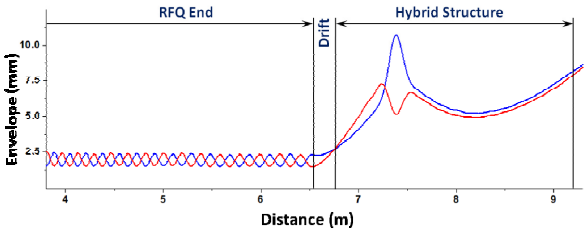

Figure 6: Simulated transverse beam envelopes. Blue line corresponds X plane, red – Y plane.

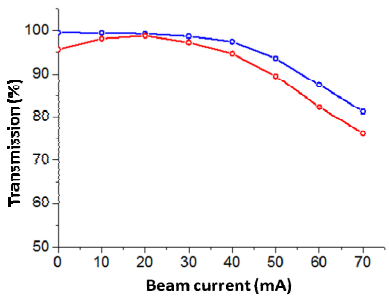

Figure 7: Calculated beam transmission in TWAC injector. Blue line represents transmission in RFQ, red line – for whole injector.

Figure 7 shows beam transmission calculated for TWAC injector linac. The transmission of the whole injector is very close to 100% for beam current of 10 – 30 mA and completely determined by RFQ section. There are only small additional particle losses in hybrid structure. Appearance some particle losses outside of the beam current range is owing to the fact that formation of longitudinal emittance in RFQ has been optimized for design beam current value I = 30 mA. Small increase of absolute value of synchronous phase in accelerating gaps can eliminate any additional particle losses in the hybrid structure.

Simulation showed negligible emittance growth in hybrid structure for both transverse and for longitudinal planes up to beam current I≅ 40 mA.

CONCLUSION

New CH-DTL section with hybrid accelerating channel following RFQ was designed for beam acceleration up to 4.9 MeV/u. Resonant structure with displaced MCW has some advantages in comparison with conventional IH and CH structures allowing very easy tuning both electric field distribution and resonant frequency.

The second section with hybrid accelerating structure allows direct beam injection from RFQ. So TWAC injector can be built without any additional MEBT.

Beam simulation carried out for whole injector shows that the new section provides acceleration up to energy required for injection into TWAC ring with transmission close to 100% for design beam current.

ACKNOWLEDGMENT

Authors thank Tatyana Tretiakova for adjustment of code TRANSIT for beam simulation of the section.

REFERENCES

[1] V. Andreev, N.N. Alexeev, A.Kolomiets, V. Koshelev, V. Kuzmichev, S. Minaev, B.Sharkov, "PROGRESS WORK ON HIGH-CURRENT HEAVY ION LINAC FOR ITEP TWAC FACILITY", Proceedings of IPAC 10, p.801, Kioto, Japan

[2] N.N. Alexeev, P.N. Alekseev, V.A. Andreev, A.N. Balabaev, V.I. Nikolaev, A.S. Ryabtsev, Yu.A. Satov, V.A. Schegolev, B.Yu. Sharkov, A.V. Shumshurov, V.P. Zavodov, ITEP-TWAC PROGRESS REPORT, Proceedings of IPAC2011, p. 2193, San Sebastián, Spain

[3] V. Andreev, N.N. Alexeev, A.Kolomiets, V. Koshelev, B. Kondratyev, A. Kozodaev, V. Kuzmichev, Y. Orlov, V. Stolbunov, T. Tretyakova, "FIRST BEAM TEST OF 81.5 MHZ RFQ FOR ITEP-TWAC", Proceedings of IPAC-2011, p.2622, San Sebastian, Spain

[4] P.N. Ostroumov and A.A. Kolomiets, "NEW CONCEPT FOR ACCELERATION OF SLOW, LOW-CHARGE-STATE HEAVY ION BEAMS", Proceedings of the 2001 Particle Accelerator Conference, Chicago

[5] A.S. Plastun, S.M. Polozov, "BEAM DYNAMICS SIMULATION IN DTL WITH RF QUADRUPOLE FOCUSING", Proceedings of IPAC-2011, p.2625, San Sebastián, Spain

[6] V.A. Andreev, G. Parisi "90^0 apart-stem RFQ Structure for Wide Range of Frequencies", Proceedings of PAC-93, Washington DC, May 1993, pp. 3124-3126 (1993)

PERFORMANCE OF THE MAGNETIC SYSTEM OF A 12 MEV UPC RACE-TRACK MICROTRON*

Yu. A. Kubyshin, J. P. Rigla, Technical Univ. of Catalonia, Barcelona, Spain
I.Yu. Vladimirov#, N.I. Pakhomov, V. I. Shvedunov, SINP, Moscow State University, Russia,
V.V. Zakharov, I.V. Chernov, Elmat-PM, Kaluga, Russia

Abstract

The design and characteristics of the end magnet of a 12 MeV electron race-track microtron (RTM) which is under construction at the Technical University of Catalonia is described. The RTM end magnet consists of four dipoles with the main field level about 0.8 T. As a source of the magnetic field a Sa-Co rare earth permanent magnet material (REPM) is used. This helps to get a quite compact design of the RTM and allows to place its magnets in a high vacuum environment of the accelerator vacuum chamber. We discuss results of numerical simulations of the tuning of the end magnets by means of special plungers and describe their engineering design which permits to assemble the magnets and fix the Sa-Co blocks without gluing. Also a method and results of the REPM blocks residual magnetization control are reported.

INTRODUCTION

The Technical University of Catalonia in collaboration with the Skobeltsyn Institute of Nuclear Physics (SINP) of the Moscow State University and CIEMAT (Madrid) is building a race-track microtron (RTM) whose main envisaged application is Intraoperative Radiation Therapy. The design of the accelerator is described in [1], the course of its development was reported in [2].

A schematic view of the RTM main unit is given in Fig. 1. It consists of electron gun (1), accelerating structure (linac) (2) with four accelerating and three coupling cavities, two end magnets (3, 4) and a horizontally focusing quadrupole (5). These elements are precisely fixed on a common rigid platform placed inside a steel box which plays the role of the vacuum chamber. The beam can be extracted from any of the four orbits with extraction magnets (6) and exits the microtron along the output trajectory (7). The main RTM parameters are listed in Table 1.

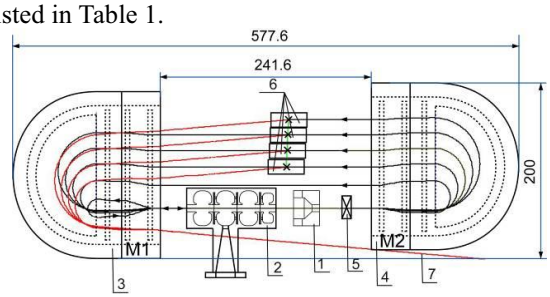

Figure 1: RTM scheme

Table 1: RTM parameters

Parameter	Value
Beam energies	6, 8, 10, 12 MeV
Operating frequency	5712 MHz
Synchronous energy gain	2 MeV
Pulsed beam current at the RTM exit	5 mA
End magnets field	0.8 T
Injection energy	25 keV
RTM head dimensions	670×250×210 mm

In all the RTM magnets as the source of the magnetic field a Rare-Earth Permanent Magnet (REPM) material is used. This allows to achieve rather compact magnetic systems which can be used inside the high-vacuum chamber.

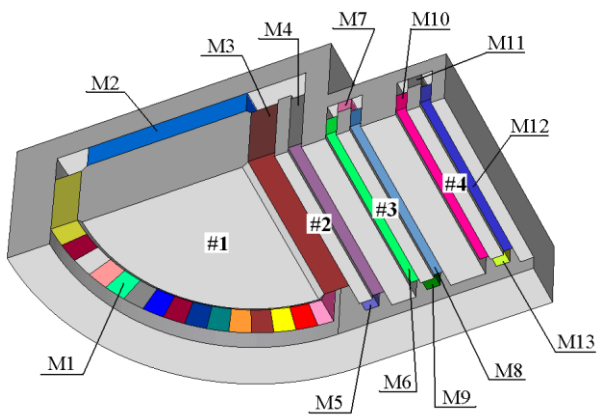

Figure 2: Geometry of the RTM end magnet used in ANSYS 3D simulations.

In the present machine with a low energy injection the end magnets, besides bending the particle trajectories by 180º, have other functions. Namely, end magnet M1 (see Fig. 1) also reflects the beam after the first acceleration back into the accelerating structure thus solving the problem of linac bypass. In addition, the beam vertical defocusing by the fringe field of the 180º bending dipole must be supressed and even converted in vertical beam focusing. All these requirements are implemented in a four-pole magnetic system described in Refs. [1], [3], its 3D geometry is shown in Fig. 2. The end magnets are symmetric with respect to the median plane and the vertical central plane, therefore from a one quarter of the magnet given in Fig. 2 the complete 3D geometry can be determined.

*Work supported by the grants 2009 SGR 1516 of AGAUR (Generalitat of Catalonia) and FPA2010-11911-E of MICINN (Spain).
e-mail: timerke@mail.ru

The system is composed by the main dipole (pole #1) responsible for the 180º bending of the beam, the inverse dipole (#2), whose field is adjusted so that an acceptable optics of the magnet is achieved, and two additional dipoles (#3 and #4) which displace the particle trajectories in such a way that the 2 MeV trajectory is reflected back into the linac. The poles are surrounded by REPM blocks (from M1 to M12) as shown in Fig. 2. In Fig. 3 the magnetic field profile in the median plane is plotted. The initial design parameters of the end magnet were calculated using the 2D POISSON code, the final optimized design was obtained from 3D simulations with the ANSYS code [4].

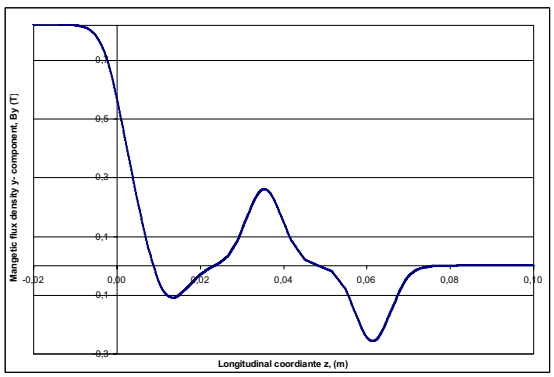

Figure 3: Vertical component of the magnetic field induction in the median plane of the 4-dipole end magnet as a function of longitudinal coordinate.

SIMULATIONS OF MAGNETIC FIELD TUNING

The main disadvantage of magnetic systems with permanent magnets is the difficulty in the adjustment of the magnetic field. A field tuning often becomes necessary in order to compensate imperfections of the magnet machining, assembling and REPM magnetization.

In the design of the 12 MeV RTM end magnets the field tuning is achieved by moving dedicated plungers through channels made in certain REPM blocks and corresponding parts of the yoke with respect to the poles. According to the design specifications the end magnets must provide the field uniformity in the good field region better than 0.075% in the main pole and 0.5% for the rest of the poles. To get a reasonable tuning range and to assure the required field uniformity it was decided to install four 10 mm diameter plungers at the main pole (#1), six 5 mm diameter plungers at the inverse pole (#2) and five 4 mm diameter plungers at the additional poles (#3, 4). The location of the plungers is shown in Fig. 4. Pole #1 plungers are moved in round channels made in the REPM blocks M2, pole #2 plungers above the M4 blocks and plungers of additional poles #3 and #4 in rectangular 5.4x5.0mm channels made in M7 and M11 blocks, respectively.

With the aim to reduce the effect of the magnetic saturation in the plungers the Vanadium-Permendur is used as the material. The design 3D simulations were performed with the ANSYS code. A detailed study of the field distribution in the median plane for different positions of the plungers was carried out. In particular, the field variation at each pole for the corresponding plungers being moved from one extreme position (plungers touch the pole) to the other one (the REPM part of the channel is free) was calculated. The obtained results are given in Table 2. The values and tolerances of the residual magnetizations of the REPM blocks were determined from the condition that for the position of the tuners corresponding to 20% of the total tuning range the nominal field profile shown in Fig. 3 must be reproduced. Also it was checked that for all the poles the field uniformity requirements are fulfilled.

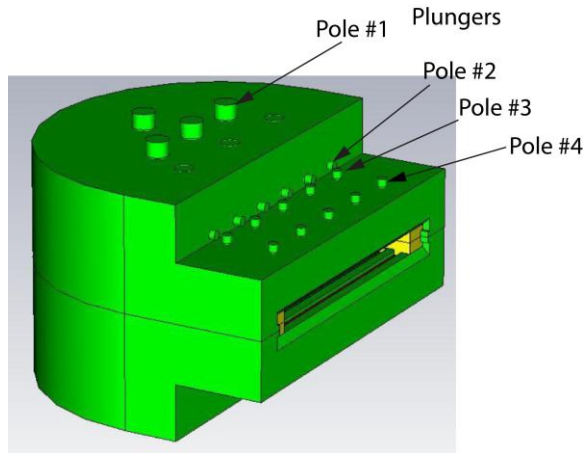

Figure 4: Position of plungers for different poles.

Table 2. Maximal variation of the magnetic field induction at each pole.

Pole number #*i*	#1	#2	#3	#4
Relative field variation $\lvert\Delta B_i / B_i\rvert$	5.2%	7.9%	5.8%	5.9%

In the ANSYS simulations it was observed that the displacement of the main pole plungers affects the magnetic field in the inverse pole and vice versa. We obtained that for the maximal displacement of the main pole plungers the field in the centre of the inverse pole changes by 3.8%, whereas the maximal displacement of the inverse pole plungers leads to a 0.2% variation of the main pole field.

MAGNETS ENGENEERING DESIGN

We use Sm-Co as an REPM material. Though it is more fragile as compared with Nd-Fe-B, it is more appropriate for operation in a high vacuum environment, for example it can be used without special coating and can be heated up to 300-400 ^{0}C for outgassing. Characteristics of the specific Sa-Co blocks used for the RTM end magnet are B_r=1.1 T, H_{CB}=820 kA/m and the temperature factor equal to -0.033 %/^{0}C.

The magnet detailed design is shown in Fig. 5. In order to decrease the outgassing the REPM blocks are fixed inside the magnetic system mechanically by means of Al insertions and parts of yoke with special tips and without using glue. The poles and the yoke made of soft magnetic steel are coated by a thin, about 10 μm, Ni layer applying the sputtering method. All dead volumes inside the magnet body have pumping out hole.

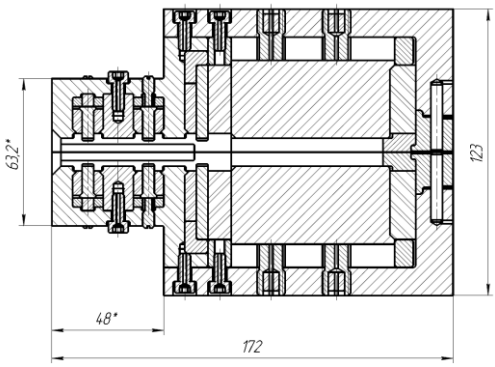

Figure 5: End magnet cross section.

The vertical component of the magnetic field in the gap between the poles must be symmetric, for this the upper and lower parts of each end magnet must be identical. This field symmetry will be controlled by measuring and adjusting to be equal the magnetic field distributions created by each of these parts separately at a plane close to the median plane in which a steel plate is placed.

REPM BLOCKS RESIDUAL MAGNETIZATION CONTROL

The value of the residual magnetization B_r induced in a specific REPM block during the production process at the factory does not necessarily coincide with the value of B_r providing the proper field in the 3D simulation. To establish the correspondence between the factory and design residual magnetizations the field distributions of two test Sa-Co blocks with dimensions 30x28x12 mm (PM1) and 72x40x11 mm (PM2) were measured and compared to results of their simulations.

The measurements were performed at an automated magnetic measurement table equipped with a precisely calibrated and temperature controlled Hall probe. The magnetic field induction component in the direction of the magnetization was measured at points of the plane situated at the distance 5 mm above the block surface at its both sides with the 3 mm step. The calculated field distributions were fitted to the measured ones by the least square method using B_r as a variable. The simulations were done assuming the uniform block magnetization.

In Figs. 6a and 6b the measured (red points) and calculated field distributions along the long block side at the central parts of PM1 and PM2, correspondingly, are shown. While for PM1 the shapes of the measured and calculated distributions are close, for PM2 a dip in the central part of the measured curve can be seen in contrast to the calculated one. This dip is explained by a non-uniform block magnetization due to its large dimensions and imperfections of the magnetization method used at the factory.

As a result of the procedure described above the following estimates of *Br* were obtained:

- PM1, side1: 0.97±0.1 T, side 2: 0.96±0.1 T;
- PM2, side1: 0.740±0.005 T, side 2: 0.787±0.005 T.

Comparing them to the value B_r = 1.09 T reported by factory the correction factors are calculated.

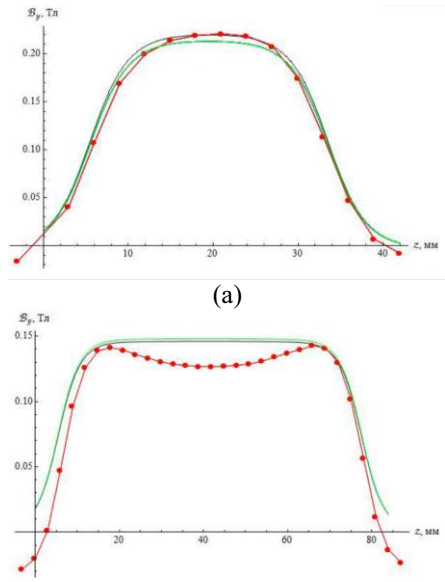

(a)

(b)

Figure 6: Field distributions along the long side of PM1 (a) and PM2 (b) obtained in the measurements (red points) and simulations for different B_r.

CONCLUSIONS

A mechanism of tuning of the field distribution in the RTM end magnets with Sa-Co permanent magnets has been suggested and simulated using the ANSYS code. The engineering design of these systems permitting their assembling without glue has been carried out. Measurements of the residual magnetization of test REPM blocks revealed a considerable difference between the value of B_r reported by factory and the ones found in the 3D simulation. This difference will be compensated by introducing a correcting factor in the magnetization procedure.

REFERENCES

[1] A.P. Poseryaev et al. “Design of 12 MeV RTM for multiple applications”, EPAC'06, Edinburgh, June 2006, WEPCH175, p. 2340 (2006).

[2] Yu.A. Kubyshin et al.” Current Status of the 12 MeV UPC Race-Track Microtron”, PAC'09, Vancouver, May 2009, WE6PFP112, p. 2775 (2009).

[3] M. Ferrer et al., ”Compact design of race-track microtron magnets”, EPAC'08, Genoa, June 2008, WEPC159, p. 2380 (2008).

[4] ANSYS Multiphysics, www.ansys.com

HIGHLY ACCURATE 3D MODELING OF THE C-80 ISOCHRONOUS CYCLOTRON MAGNETIC STRUCTURE

S. A. Artamonov, E. M. Ivanov, G. A. Riabov, N. A. Chernov, PNPI, Gatcina, Russia

Abstract

Very complicated magnetic structure with extremely high spiral angle and set of 17 correction shim types in each of 8 sectors is used in the H-minus ion isochronous cyclotron C-80. The 3D Novosibirsk code MERMAID was applied to optimize geometry of the sectors and shims in the hill and value region. A precision finite-element model allows take into account the iron non-linear effects and the detailed magnet geometry. MERMAID makes use about 20.5 millions nodes and provides magnetic field calculation accuracy in 10-20 Gs. The integral magnetic field parameters (isochronism, transversal motion frequency, H-minus ion electromagnetic dissociation) have been optimized by using the trajectory analyses. Program provides the significant reduction the time and efforts for the determination the necessary shims set in comparison with trial-and-error method.

INTRODUCTION

The isochronous cyclotron C-80 constructed at PNPI is planned to use as well for fundamental researches in nuclear physics, the solid state physics and biology, as for applied program - production of medicine isotopes for, therapy of an eye melanoma and surface forms of a cancer. As a first approximation the magnetic system of cyclotron C-80 was designed a few years ago on the basis of 2D calculations by using the POISSON program and measurements on two small models [1, 2]. The final version of C-80 magnetic structure optimized by 3D calculations with the MERMAID program was used for measurements and the field correction on the full scale magnet is presented in this report.

MAIN CALCULATION DIFFICALTIES

One of the central problems for every isochronous cyclotron is forming the radial and azimuthally magnetic field distribution. Another problem is connected with acceleration of H^- ions. To reduce the H^- dissociation losses in C-80 is used magnetic structure with very high spiral angle [3]. It is also necessary to mention the essential mathematical nonlinearity of the problem. It is to note that in isochronous cyclotron C-80 the magnetic structure is used three types of the steels. The main magnet yoke is constructed from a set of two types of the steels: steel 3 – μ_3(B) and steel 10 – μ_1(B). Poles are constructed from steel 10 – μ_1(B). Sectors, 17 correction shim types in each of 8 sectors and valleys shims are constructed from other steel 10 – μ_2(B). In the following figure it is visible that these curves μ(B) very strongly differ in a working range of magnetic fields of a cyclotron: 11000-18000 Gs. It is obvious that this creates additional computing difficulties and problems at creation of 3D model.

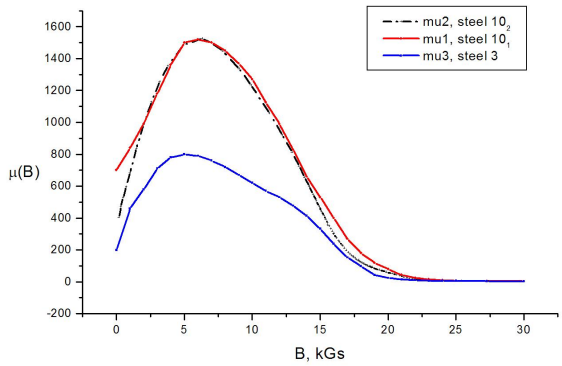

Figure 1: Permeability curves μ(B) in C-80.

PROCEDURE OF A MAGNETIC FIELD FORMATION

Procedure of the necessary magnetic field formation and selection of magnetic structure parameters for C-80 according to the program MERMAID [4] was made step by step method.

As the first step, the key parameters of magnetic system C-80 [5] were fixed. It was supposed that the geometry and height of sectors equals to 90 mm and during the further optimization is not changed. For obtaining the required isochronisms the heights of the correction sector shims have been varied. The initial heights of these shims were selected equal to 20 mm. Besides, in the course of optimization special the constrained condition was used. The amplitude of 4-th harmonic do not exceeded ~3000 Gs and the hill $B_{max} \leq 17000$ Gs near the extraction radius. Under this conditions H^- dissociation are below ≤5 % [3]. For this purpose it was introduced into the magnetic system additional valley shims. Thus formation of a demanded isochronous field is carried out only by changing iron geometry without use of corrector coils.

At the second stage 3D model of the magnetic system C-80 was developed and was constructed. It carefully describes geometry of magnet yoke, sectors (4 pairs), sector shims (17 correcting shims on each sector), and valley shims, the coils current, external boundaries. It also considers nonlinear magnetic properties used electro technical steels μ (B).

Due to high spiral angle sectors we were forced to use in calculations 1/2 magnets with the vertical

symmetry boundary conditions. The external boundary of calculated area was chosen rather far to exceed the influence on the magnetic field in working area and to correct calculation of the fringing field. The fringing field is necessary for the correct calculation of extraction beam optics. Thus, for the description of magnetic structure of C-80 in the MERMAID program it was required ~20.5 million direct prisms that allowed reaching necessary accuracy of calculation of a magnetic field ~10^{-3}—10^{-4}.

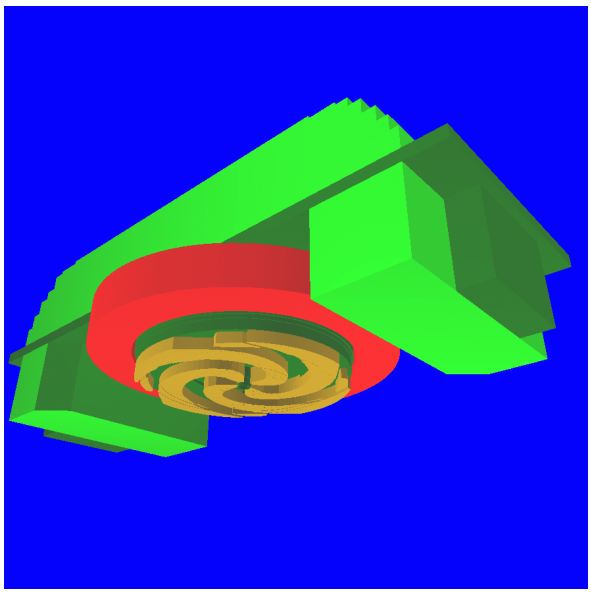

Figure 2: MERMAID model C-80.

ALGORITHM OF OPTIMIZATION

The developed computing model was used for receiving necessary spatial distribution of a magnetic field and for its subsequent analysis.

Thus procedure of the analysis of the received data across the field was divided into two complementary stages.

At the first stage the average on an azimuth magnetic field C-80 was calculated, and for obtaining other characteristics of cyclotron analytical formulas from work [6], in particular, for an isochronous field and frequencies of betathrone frequencies were used. Then various geometrical changes were made to the developed model for the purpose of receiving the minimum difference between the calculated average field and an isochronous field with control of other required characteristics of a cyclotron, and the following iteration was carried out if necessary. Such approach is rather simple, evident and fast, but it doesn't possess sufficient accuracy for an isochronous cyclotron.

Therefore periodically through some successful iterations of the first stage was made transition to the second stage where according to the calculated map of a field the full trajectory analysis of particles in the course of acceleration was carried out, and also isochronous dependence [7] was specified. I.e., at the second stage the corresponding nonlinear equations of movement were solved numerically and static equilibrium orbits in an initial magnetic field were calculated. Frequencies of betathrone oscillations were determined by these decisions, and the cycle time of an accelerated particle on each radius was calculated. Being guided by these data, there was on special procedure a new isochronous field. Then finally for this stage frequencies of betathrone oscillations in this isochronous field were defined and losses in it ions accelerated the H-minus on electro dissociation were calculated.

Then again, if it was necessary, after the analysis of results of the second stage, was made transition to the first stage where further specification of geometry of varied objects was made, leaning any more on an analytical isochronous field and frequencies of betathrone oscillations, and on an isochronous field and frequencies of the second stage. Procedure repeated until then while the discrepancy between an average and an isochronous field didn't become ~10-20 Gs. Such value just also corresponds to accuracy of calculation of an average field.

Thus the self-consistent task on optimization of magnetic structure C-80 was realized. Each time such task for decrease of number of parameters was executed with the fixed minimum gap. Thus the current of the main coils and geometry of sector tips and valley shims varied so that to receive necessary parameters of magnetic system. In total in the course of optimization the following set of gaps was considered: 146, 156, 170, 176 and 164 mm.

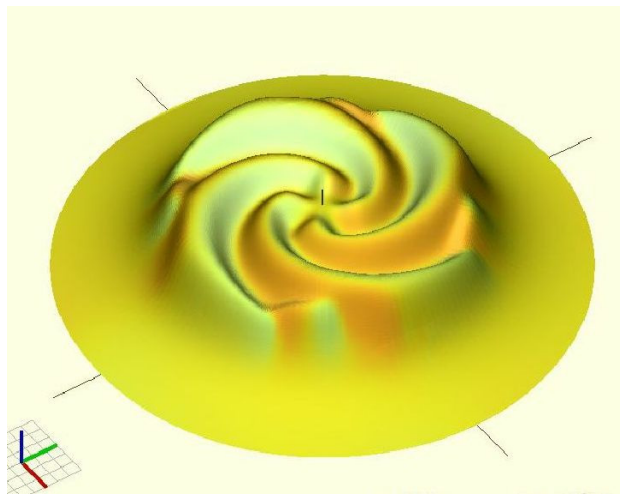

Figure 3: 3D MERMAID magnetic field for C-80.

MAIN RESULTS OF CALCULATIONS

The final version of magnetic structure of isochronous cyclotron C-80 has a minimum gap, equal 164 mm. Briefly we will enumerate the main modifications of the initial magnetic system [1,2] executed on a basis 3D simulation.

Direct sectors were continued from radius of 27 cm to radius of 40 cm, but with two turns on the fixed angles, keeping previous sector length along azimuth. It led to blocking of uncontrollable penetration of a magnetic spiral angle to the area near the central region. Thereby

growth of amplitude of the main harmonic was provided that led to stable motion of particles in this area.

The central region was changed in the spatial C-80 model so that to consider real geometry of system for axial injection. Besides, by means of a magnetic plug necessary fall of a magnetic field in the central region was created.

Angular expansion of sectors was made for reduction of quantity valley shims and for ensuring vertical stability of movement of accelerated ions near extraction radius on ~20 mm from radius of 70 cm to the final radius equal 102.5 cm.

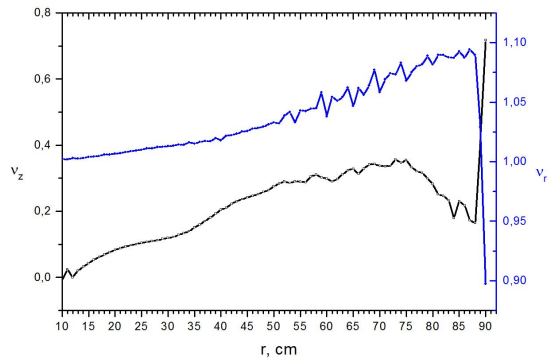

Figure 4: Vertical and horizontal frequencies in C-80.

The accepted changes of magnetic structure led as well to decrease in losses the H-minus of ions on dissociation in the course of acceleration to 2.2-2.5 %.

Finally, as a result of all-round 3D modeling the following optimum magnetic structure for cyclotron C-80 was received:

Figure 5: View of the pole tip C-80.

CONCLUSION

The careful analysis 3D data on the magnetic field, executed on the procedure which has been in detail described in [7], showed that practically all problems by constructed isochronous cyclotron C-80 to be overcome. Frequencies of betathrone fluctuations are represented rather well almost in all working area of the cyclotron. However, most likely, more careful specification of isochronous dependence of a field is required, relying on experimental measurements. Final distribution of the magnetic field was measured experimentally with 2-6 Gs precision. They are supposed to be executed after mounting of sectors in cyclotron C-80.

Then simulation 3D fields were used in trajectory calculations for the construction of extraction system of the cyclotron and the beam transport lines. Thus it is possible to confirm that the last option of magnetic structure of isochronous cyclotron C-80 meets all design requirements.

REFERENCES

[1] N.K. Abrossimov, S.A Artamonov, V.A Eliseev, G.A Riabov, "Design and optimization the magnet and magnetic structure for the 80 MeV H^- isochronous cyclotron," Proceeding of the Second International workshop: Beam Dynamics & Optimization – BDO'1995, St.-Petersburg, Russia, 1995, pp. 7-15.

[2] N.K. Abrossimov, S.A Artamonov, V.A Eliseev, G.A Riabov, "Design and modelling the spiral magnetic structure for 80 MeV H^- isochronous cyclotron", Proceeding of the XV Intern. Conf. on Cyclotron and their Application, Caen-France, 1998, pp. 518-521.

[3] N.K. Abrossimov, S.A Artamonov, V.A Eliseev, G.A Riabov, "Losses of H^- ions due to electromagnetic dissociation and their effect on selection of isochronous cyclotron magnetic structure", PNPI Research report 1994-1995, Gatchina, 1996, pp. 275-278.

[4] S.N. Andrianov, S.A. Artamonov, A.N. Dubrovin,V.A. Eliseev, "Computer simulation 3D magnetic field of PNPI isochronous cyclotron", (in Russian). Vestnik SPbSU. Ser.10. Iss. 3, 2008, pp. 12 – 23.

[5] G.A. Riabov et al., "Some design features of the 80 MeV H^- isochronous cyclotron in Gatchina," WEBOR02, these proceedings.

[6] Yu.G. Basargin, V.P. Belov, "Some problems of particle motion dynamic in cyclotrons with spatially variable fields", in: Electrofisicheskaya apparatura, (in Russian), vol. 3, Moscow, Atomisdat, 1965, pp. 3-24.

[7] S.N. Andrianov, S.A. Artamonov, "Optimal algorithm of the isochronous field constructing in accelerators with azimuthally variation", (in Russian). Vestnik SPbSU. Ser.10. Iss. 2, 2009, pp. 3 – 14.

UPDATE OF CLASSICAL CYCLOTRON U-150 MAGNETIC SYSTEM. SIMULATION AND EXPERIMENT

Yu.Alenitsky, N.Azaryan#, A.Chesnov, O.Lepkina, E.Samsonov,
I.Sedych, V.Smirnov, JINR, Dubna, Russia
I.Gulamov, Z.Shukurov, R.Umerov, Y.Uzakov, UAS, Tashkent, Uzbekistan

Abstract

Classical cyclotron U-150 located in the Academy of Sciences of the Republic of Uzbekistan, Tashkent, was developed more than 50 years ago in Efremov's institute for acceleration various particles (p, d, He). For magnetic field re-tuning the current coils are used. Nowadays U-150 is used to accelerate only protons to energy of 15-22 MeV for producing isotopes for medical or industrial applications. In order to save the electrical energy and operating simplification it is proposed to create a decreasing average magnetic field in cyclotron only by means of ferromagnetic parts. To create a negative gradient of the magnetic field steel parts are made and installed in the magnet.

Analysis of measurement results showed the possibility of production of the required isotopes in updated U-150 with power economy of about 15%. Experimental irradiation of the target showed that the created field gradient did not provide an achievement of the required proton energy at radius of 64-65 cm. To achieve required energy one correction coil is kept in operation and measured magnetic field showed a satisfactory result. For estimation of possibility of creating the required magnetic field gradient without correction by coils the simulation of the cyclotron magnetic system were done and the results of calculations and its analysis are presented in this paper.

INTRODUCTION

On Fig.1 you can see a photo of the classical cyclotron U-150 which located in Tashkent in the Academy of Sciences of the Republic of Uzbekistan. Magnetic yoke of classical cyclotron U-150 has an E-type core.

Figure 1: Cyclotron U-150 during the measurements of the magnetic field.

#azaryan@jinr.ru

One sees in Fig. 2, 3 the pole, the vacuum chamber cover and the steel rings located inside the vacuum chamber. In the gap between the poles of magnet and the vacuum chamber of cyclotron (top and bottom), which is 25 mm in height, steel discs having varying thickness along the radius were installed.

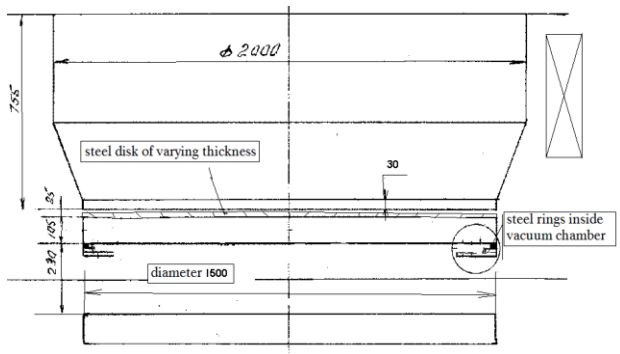

Figure 2: Size and cross section of the magnet SP-72 pole.

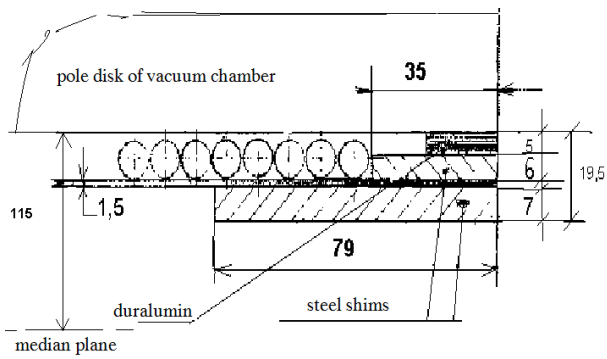

Figure 3: Cross section of the steel shims and coil located inside the vacuum chamber of the cyclotron.

Originally correction coils were included in the design of the cyclotron to provide a possibility of acceleration particles of various types. Nowadays U-150 accelerates only a proton beams and the need for using of the coils for forming of magnetic field is missing. Required profile of the magnetic field is possible to be obtained by the modification of the design of cyclotron's pole using additional iron components without the correction coils which allows saving the electric power for the operation of the cyclotron.

Overview of the modification of the magnetic system and its experimental results is presented in this write-up.

SELECTION OF THE PARAMETERS FOR MAGNETIC SYSTEM

According to the requirements specification the chosen shape of the magnetic field has to provide acceleration of the protons at the parameters of the cyclotron shown in Table 1.

Table 1: Required parameters for U-150

Operating generator frequency	15.2 – 16.0 MHz
Radius of the target position	64 cm
Voltage on the dees	100 - 110 kV
Protons final energy	22 MeV

The magnetic field during first part of simulations was assumed of the next form:

- Within radii 0 – 10 cm magnetic field is constant.
- In the range of radii of 10 – 64 cm expected decline of the magnetic field had a constant value of the field index $n = r/B \cdot dB/dr$.

Two series of calculations of the magnetic field and beam dynamics that were consistent with the different values of B_0 and n have been performed. In the first case, the value of the field at the center has been chosen so that the initial frequency of the proton revolution was ~ 200 kHz greater than the maximum possible frequency of the generator, i.e. f_0 = 16.200 MHz. For a given value of f_0 the field in the center was determined by the formula:

$$B_0 = \frac{2\pi E_0 f_0}{ec^2} = 10633\,\text{G}. \qquad (1)$$

The second series of calculations concerned to opportunity to get protons with an energy of 22 MeV on the target (r = 64 cm), since the calculations for the first series showed that the energy of the protons cannot exceed 21.5 MeV at B_0 = 10633 G. Obviously, to increase the energy at the radius of target an increase of the magnetic field is required in this place and in the center of the cyclotron as well.

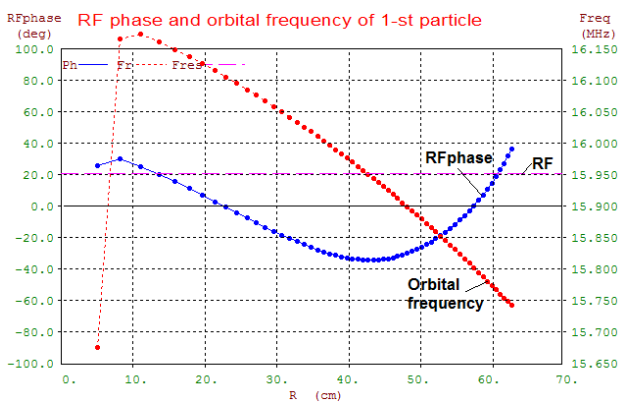

Figure 4: Results of calculation of the phase and orbital frequency of proton in magnetic field with n = -0.004 and at a voltage of 100 kV on the dees.

Dynamics calculations showed that from a set of curves of the field the best is one which corresponds to $n = -0.004$. In this case, the phase of the proton in the acceleration is in the range of ± 40 °HF. One can see in Fig. 4 the results of the phase motion in this field at dee voltage 100 kV. Frequency of the accelerating field 15.95 MHz was selected to optimize the phase motion, the energy of the central proton on the target was equal to 21.5 MeV.

Consider the results of the second cycle of calculations, which concerns the possibility of obtaining energy of 22 MeV at a radius of 64 cm. Magnetic field, which corresponds to the radius R of proton energy W, can be estimated using the following formula

$$B = \frac{\sqrt{W(2E_0 + W)}}{ecR}. \qquad (2)$$

For radius 64 cm and energy 22 MeV, this formula gives a value of 10644 G. Curves of the magnetic field passing through the R = 64 cm with a value of B_0 = 10644 G, but with different values of the index field in the range from -0.002 to -0.010 were calculated.

The results of the dynamic calculation of the acceleration of protons to an energy of 22 MeV in the magnetic fields with the values of field index -0.002, -0.004 and -0.006 have shown that if the respective frequencies of the accelerating field 16.04, 16.08 and 16.09 MHz, the protons are accelerated to 22 MeV, and their phase motion are only slightly different from that shown in Fig.4.

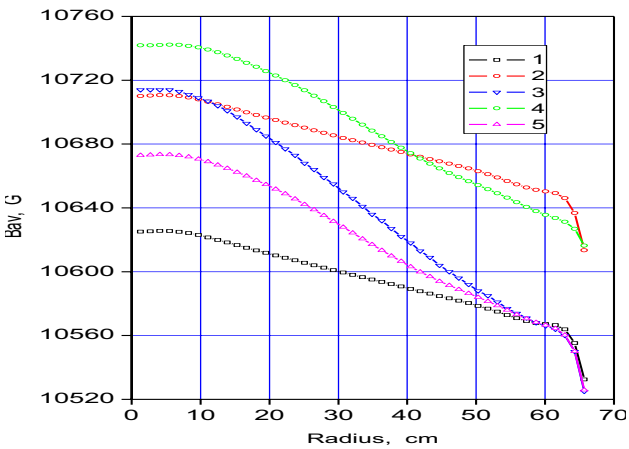

Figure 5: Five variants of calculated magnetic field, corresponding to the three disk geometry. Magnet excitation current 1 – 662.46 A, 2 – 669.21 A, 3 – 663.43 A, 4 – 667.28 A, 5 – 661.5 A.

As follows from estimation above the required decrease of the magnetic field is desirable within 0.75 – 1.1%. In Figure 5 the results of magnetic field calculation for the three types of discs are shown. At the center the discs had a thickness 13 mm, 14.5 mm and 16 mm, the thickness of the disks is reduced to 9 mm at a radius of 700 mm, a full disks radius is 750 mm. These discs placed in the gap,

provide a decline of the magnetic field along the radius by 0.5%, 1.0% and 1.5%. To obtain field decline in the range of 550-650 mm radius steel ring size 74×7 mm in thickness had to be reduced to 4 mm. Real distribution of the magnetic field corresponds to approximately constant derivative dB/dr from 10 cm to 64 cm.

EXPERIMENTAL RESULTS

As a result of simulation it was decided to form the field using the disc 1. This disk were manufactured (Fig.6) and installed in the magnet of the accelerator.

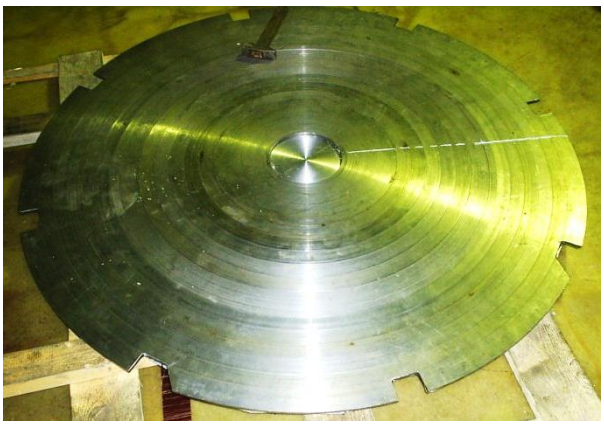

Figure 6: Steel disk for the forming of the magnetic field.

Measurements of the magnetic field showed that the decrease in the created field at target position leads to impossibility to achieve the required proton energy at radius of 64-65 cm. This fact makes impossible to irradiate the target evenly (Fig.7) causing its local overheating and an evaporation of the produced isotopes.

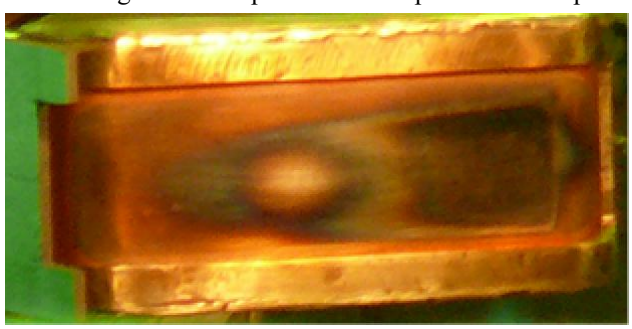

Figure 7: Target after irradiation.

Difference (Fig.8) between experimental and calculated results at radii 30-40 cm is explained by the fact that an error about 0.1 mm was made in the manufacture of discs (not counted in the calculations). The difference between the results near the radius of 60 cm is due to contradiction of drawings of the magnet (Fig.2,3) to its real design which can take place after several decades of operation. Also it can be explained by the absence of data about the B-H curve of the real material of cyclotron magnet.

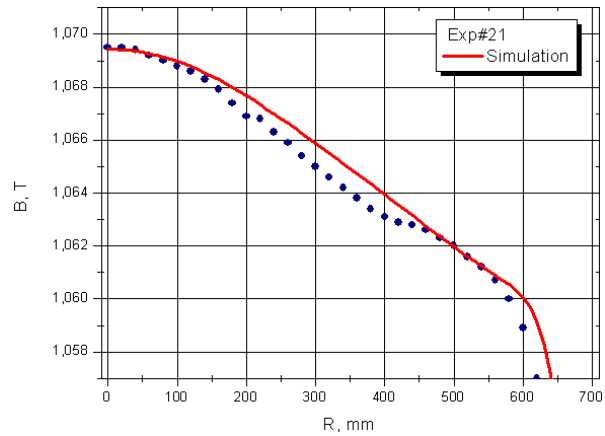

Figure 8: Calculated magnetic field in comparison with experimental measurements.

POSSIBILITY OF CORRECTION

Correction of the magnetic field at radii near the target position is possible by substitution of 6 mm outer ring by the shim of larger thickness. Calculations of the magnet with shims of different thickness were performed. To minimize the difference between simulation and experiment the following procedure were done:

- the difference of calculation results with 6 mm ring and ring with larger thickness was found;
- the resulting value of the difference was added to the experimental data.

The result is presented in Fig.9.

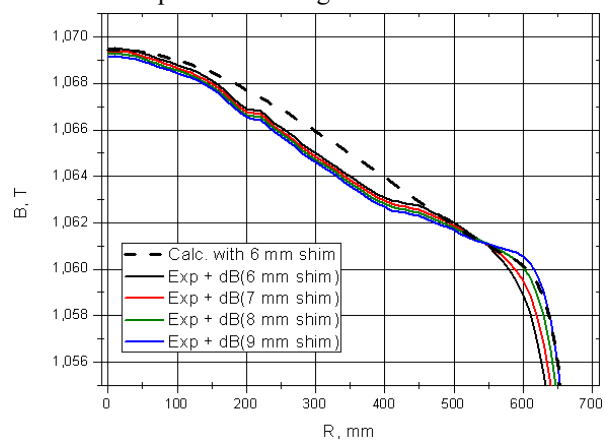

Figure 9: Calculation of the magnetic field with shims of different thickness based on experimental data.

One can see that the required magnetic field is obtained using a ring of 8-9 mm thickness.

CONCLUSSION

Nowadays cyclotron U-150 with modified magnetic system is successfully operated using only correction coils which are used for adjustment of the amplitude and phase of the first harmonic. Measured magnetic field provides energy savings of about 15%. Magnetic field correction is proposed and decision is waiting.

PULSE GENERATOR FOR THE BEAM INJECTION SYSTEM OF NICA COLLIDER

V.S. Aleksandrov, E.V. Gorbachev, N.I. Lebedev, A.V. Tuzikov, A.A. Fateev
Joint Institute for Nuclear Research, Dubna, 141980, Russia

Abstract

The new scheme of injection kicker elements distribution is described. Parameters of the circuit main elements are estimated. The system allows producing flat top of the injection pulse with high evenness. The suggested design allows building reliable and cost effective injection system satisfying the project parameters.

MAIN CHARACTERISTICS OF BUMP MAGNET

To provide one-turn injection of the ion beam in the collider NICA [1] there are two bump magnets (one piece for each ring). Bump magnet can be composed of several modules. Main requirements for the parameters of bump magnet are shown in table 1.

Table 1:. Kicker Parameters

Effective length , mm	3000
Aperture, mm × mm	55×42
Pulse duration, nsec	<900
Pulse flat top duration , nsec	≥100
Field integral, T·m	0,3
Spatial inhomogeneity of the magnetic field in the beam area,%	<5
Deviation of the field through the bunch length,%	<5

Figure 1 shows the operating aperture of the bump magnet, the envelope of the circulating beam (red), the envelope of the injected beam (blue). Blue area is the required area of "good" field.

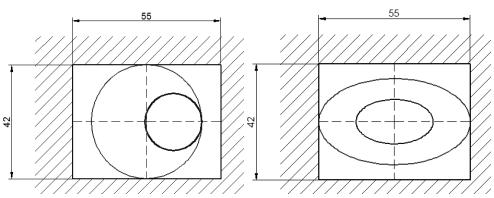

a) the kicker beginning area b) the kicker end area

Figure 1: The bump magnet aperture, the envelope of the circulating beam (outer curve), the envelope of the injected beam (inner curve).

PROJECT OF BUMP MAGNET

Several different types of magnets have been considered. The “iron-free" version of the kicker was chosen. It consists of two forward and two reverse conductors in a relatively wide-aperture vacuum chamber. Figures 2 and 3 show the position of the conductors and the distribution of magnetic fields that are optimized for the design parameters of the beam. It should be noted that the selected option almost as good as traditional ferromagnetic one in terms of energy performance, but it is much easier and cheaper to implement.

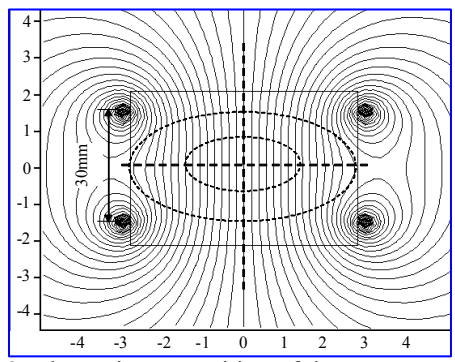

Figure 2: The optimum position of the current-carrying conductors relative to injected and circulating beams at the kicker end area .

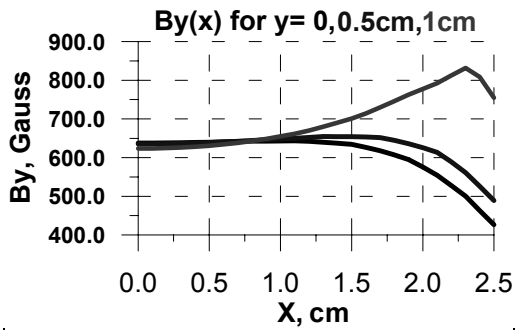

Figure 3: The distribution of the magnetic field.

PULSED POWER SUPPLY SYSTEM

Pulsed power supply is based on an capacity aperiodic discharge with the inductive load. This scheme allows to form a bell-shaped pulse. For forming the flat top of the acting impulse it is proposed to establish in the area of transportation (the best location - in the middle of the main kicker split into modules) the correcting module with a bell-shaped magnetic pulse with shorter duration, less amplitude and with opposite direction of magnetic field. Power supply circuits for main and correction magnets are shown in Figure 4. The total effect a pair of magnets is illustrated in Fig.5. To facilitate visualization the magnetic fields integrals are expressed in the normalized currents. Flatness at the top of the resulting pulse can be achieved very high, but require high precision timing switches. Besides the amplitude of

impact (the angle of deflection of the beam) is significantly reduced.

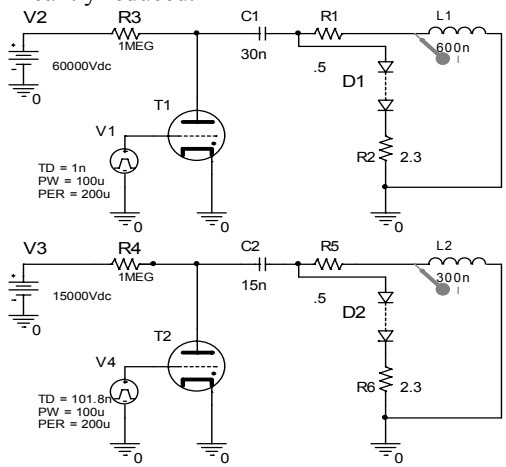

Figure 4: Kicker power supply circuits : main kicker (upper) and correcting kicker (bottom).

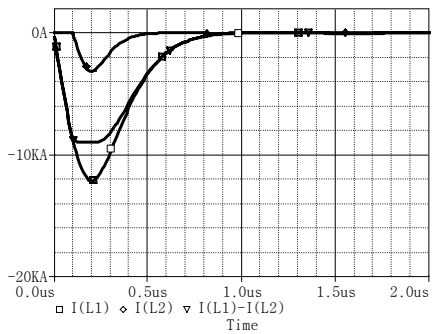

Figure 5: Normalized currents in the magnets: main, correcting and difference

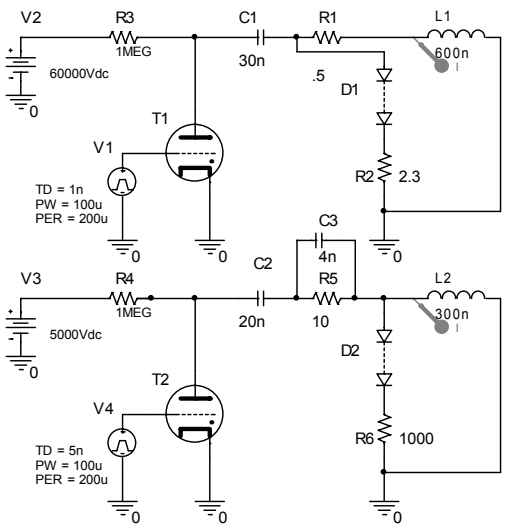

Figure6: Kicker power supply circuits for unipolar powering: main kicker (upper) and correcting kicker (bottom).

Significantly better results in the angle of deviation can be achieved by using an correcting kicker with the same direction of the field, but shifted in time. In this case, the flatness of the top will be a bit worse. One of the variants of such circuits is shown in Figure 6. The total effect a pair of magnets is illustrated in Fig.7.

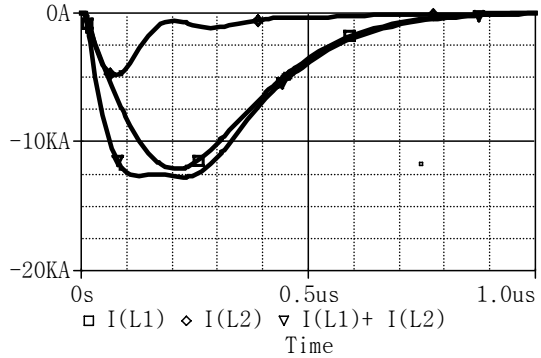

Figure 7: Normalized currents in the magnets: main, correcting and summary

BUMP MAGNET DESIGN

. The design of an experimental prototype "ironless" bump magnet module is shown in Figure 8. Bushings are located on both sides of the module, which allows using different polarities and thus reducing the voltage on external screen.

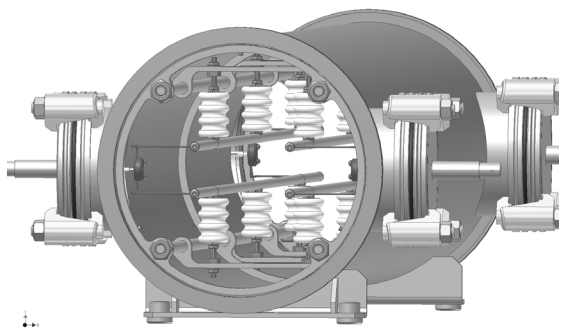

Figure 8: The design of an experimental prototype "ironless" version of bump magnet of Collider NICA

CONCLUSIONS

The proposed construction of the "ironless" bump magnet and kicker power supply circuits for the NICA Collider satisfy all the requirements of the project and efficiently use the peculiar properties of the structure and dynamics of the beam. Ease of implementation makes them preferable to traditional approaches.

ACKNOWLEDGMENT

Authors express thanks Grishanov Boris Ivanovich for seminal discussion and useful remarks.

REFERENCES

[1] Accelerating-storage complex NICA (Nuclotron-based Ion Collider fAcility). Technical design, under editing I.N. Meshkov and A.O. Sidorin. 2009. http://nucloweb.jinr.ru/nica/index1.htm

FAST KICKER

V. Gambaryan, A. Starostenko, Budker INP SB RAS, Novosibirsk, Russia

Abstract

Pulsed deflecting magnet (kicker) project was worked out in BINP (Budker Institute of Nuclear Physics). The kicker design task is: impulsive force value is 1 mT*m, pulse edge is 5 ns, and impulse duration is about 200 ns. The unconventional approach to kicker design was offered. The possibility for set of wires using instead of plates using is considered. This approach allows us to reduce the effective plate surface. In this case we can decrease effects related to induced charges and currents. In the result of modelling optimal construction was developed. It includes 6 wires (two sets in threes). Wires are 2 mm in cross-section. The magnet aperture is about 5 cm. Integral magnet length is about 1 meter. This length can be obtained by single magnet or by multiplied length of magnets array. Calculated field rise time (about 1.5 ns) satisfies the conditions. Induced current effect reducing idea was confirmed. For configuration with 3 wires pair (with cross section of 2 mm) induced current in one wire is about 10% and in the wall is about 40%. However for design with plates current is about 40% and 20% respectively. Obtained magnet construction allows controlling of high field homogeneity by changing currents magnitudes in wires. In general we demonstrated the method of field optimization. *Summary.* Optimal kicker design was obtained. Wires using idea was substantiated.

THE KICKER CONCEPT DESIGN

The kicker design should accept several requirements. The first one is vacuum chamber and kicker symmetry axis coincidences. The second one is that central angel should be about 90˚. The optimisation parameter is magnetic field homogeneity in centrally located square area (2 cm x 2 cm).

GEOMETRY OPTIMIZATION

Computer simulation was carried out for kicker's parameters optimization. Calculations were realised in FEMM and Maxwell. The central angle, the wires number and diameter was optimized.

The Number of Wires

The initial geometry is shown in Fig. 1a. The wires with fixed diameters were placed in the vacuum chamber (with the radius of 7.5 cm) at a distance of 6 cm from its centre. The wires number arranges from 4 to 20. For comparison, geometry with plates was simulated (Fig. 1b). For simulating magnetic fields, the task formulated in harmonic analysis was solved on a frequency of 200 MHz. In this task wires are parallel connected to a current source. The impressed current in three left wires is +1kA, and in three right wires is –1kA.

Simulation results allow us to obtain the follow geometry characteristic: field homogeneity, mean value of magnetic field in the centre of the magnet, and magnet impedance.

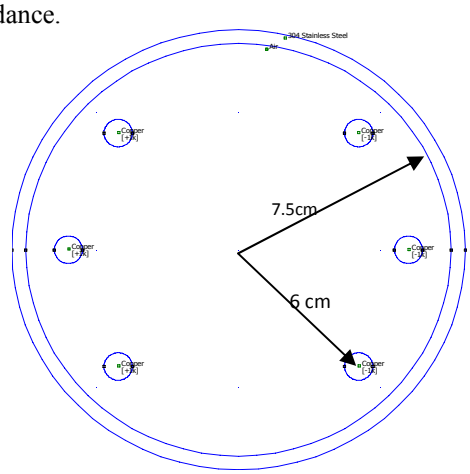

Fig. 1a: Geometry concept.

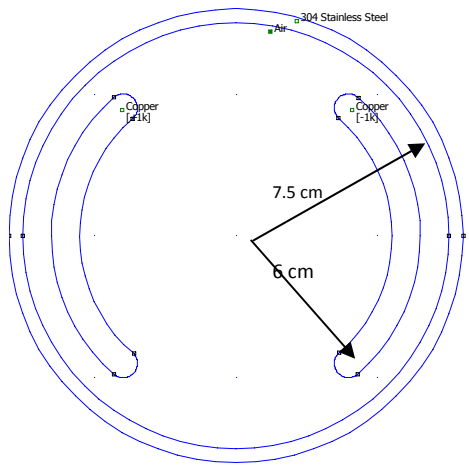

Figure 1b: Geometry with plates.

Field homogeneity is calculated according to Formula (1):

$$\delta B = \frac{B_{\max} - B_{\min}}{B_{\min}} \cdot 100\%, \qquad (1)$$

where B_{max}, B_{min} – magnetic field maximum and minimum values, respectively, determined in centrally located square area (2 cm x 2 cm).

The field homogeneity dependence on the wires number is shown in Fig. 2. Here we can see that homogeneity with using 6 wires is equal 1%, and it does not dramatically change with the wires number increase. However, the increasing number of wires leads to a lot of technical problems associated with the vacuum feedthroughs. Thus we should strive for the minimum number of wires.

The mean value of magnetic field is calculated under the same conditions as the field homogeneity. Calculation results are shown in Fig. 3. In this figure we can see that field mean value does not depend on the wires number.

Wire impedance is calculated according to energy method. To use this method two tasks were solved for the

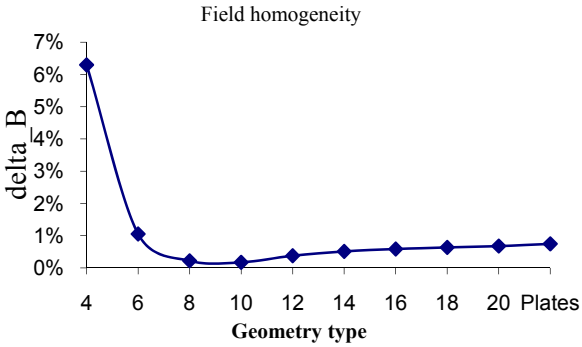

Figure 2: The dependence of field homogeneity from geometry type (total number of wires or plates).

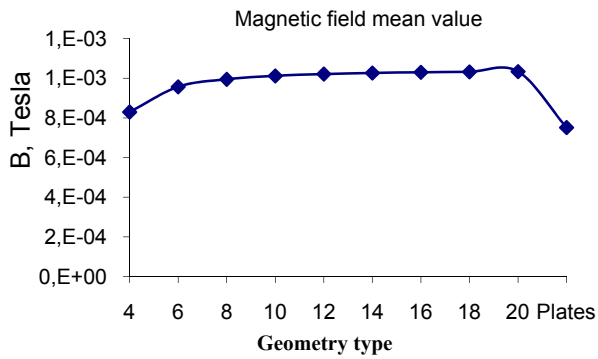

Figure 3: The dependence of magnetic field mean value from geometry type (total number of wires or plates).

different number of wires. The first problem is harmonic magnetic problem. The second problem is electrostatic problem. Energies of magnetic and electric fields can be calculated according to Eq. (2) and (3):

$$W_m = \frac{1}{2}\sum I_k \Psi_k \qquad (2)$$

$$W_e = U^2 C \qquad (3)$$

where W_m and W_e are magnetic and electric field energies, respectively, I_k and Ψ_k are current through k-conductor and flux linkage generated by I_k.

Simplified equivalent electrical circuit of the magnet is shown in Fig. 4. The magnetic field energy can also be calculated from numerical simulation of field distributions in FEMM.

If we accept both conductor groups (LI1, LI2 – first group; LI3, LI4 – second group) to have equivalent inductances and neglect magnetic field linkage between conductors, we obtain expression for energy (4).

Expressing the values C and L from (3) and (4), respectively, we can obtain the impedance (Formula 5) [1]. The obtained expression allows us to estimate the impedance of the magnet using field energies (Eq. 6).

$$W_m = \frac{1}{2} I^2 (L + L) = I^2 L . \qquad (4)$$

$$Z = \sqrt{\frac{L}{C}} . \qquad (5)$$

$$Z = \frac{U}{I}\sqrt{\frac{W_m}{W_e}} , \qquad (6)$$

where U – voltage in the electrostatic problem, I – current in the harmonic problem, W_m – magnetic field energy, W_e – electric field energy.

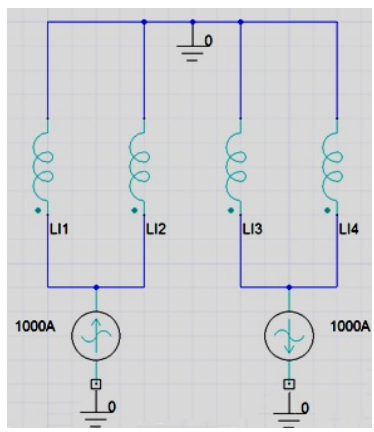

Figure 4: Simplified equivalent electrical circuit of the magnet.

Calculation results are shown in Fig. 5. We can see that if the wire number is equal 6, impedance is about 25 Ohm. So if current is 1 kA we need a modulator with an operating voltage of 25 kV.

Diameter of Wires

To determine the diameter of the wires the optimization problem was solved in Maxwell. In the initial geometry the diameter of the wires was varied. In the geometry centre a conductor with a current with amplitude of 1 A was located (Fig. 6). The dependence of the image current amplitude in each wire from its diameter was analysed.

One of the obtained dependences is shown in Fig. 6. The figure shows the dependence of the image current in

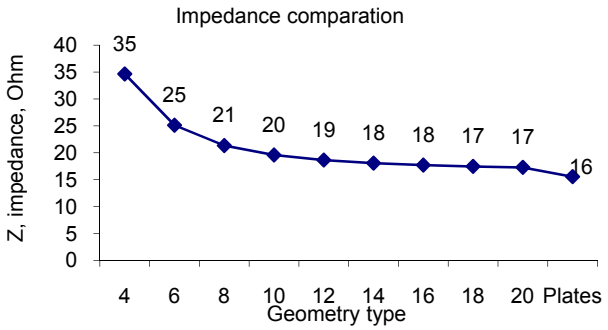

Figure 5: Impedance.

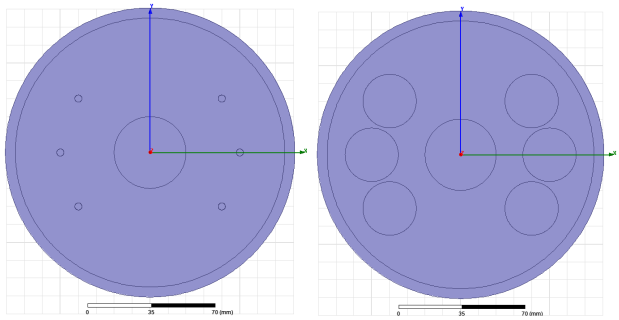

Figure 6: Image current calculation geometry (left – minimum radius, right – maximum).

the wall from the diameter of the wires. One can see that in the small diameter wires practically all the image current on the chamber walls. The plot shows that the wire diameter of 2 mm is enough.

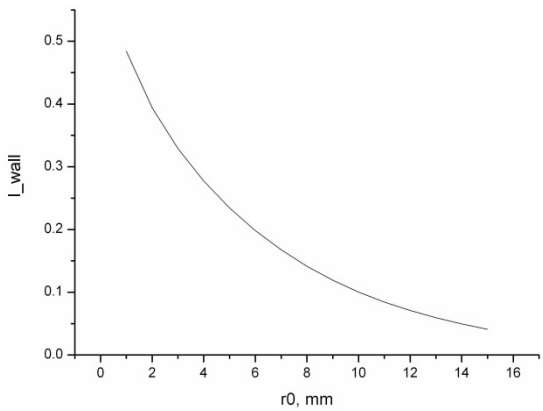

Figure 7: Image current on the wall.

Central Angle

To determine the central angle the optimization problem was solved in Maxwell. The central angle ranges from 40˚ to 140˚. The optimization goal was the maximum homogeneity of the field in the magnet middle. The value of 1 corresponds to uniform field.

The result of the optimization is shown in Fig. 8. The plot shows that the optimum angle for maximum homogeneity is 74˚.

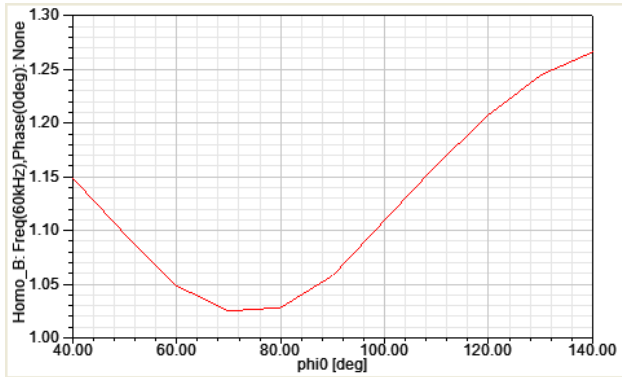

Figure 8: The central angle optimization.

SUMMARY

From these calculations we can formulate the optimal parameters in the Table 1:

Table 1. Summary result.

Parameter	Value	Unit
Total current in the conductors	1000	A
Total number of wires	6	
Central angle	74	Grad
Chamber diameter	150	mm
The distance to the centre of the wire	60	mm

REFERENCES

[1] M. T. A.W.Chao, Handbook Accelerator Physics and Engineering, Singapore: World Scientific Publishing Co. Pte. Ltd, 1999.

IMPROVEMENT OF QUADRUPOLE MAGNETS FIELD QUALITY IN SERIAL PRODUCTION *

A.A. Starostenko#, P. Burdin, T. Devyataikina, E.S. Kazantseva, T.V. Rybitskaya, B.A. Skarbo, A.S. Tsyganov, Budker Institute of Nuclear Physics, Novosibirsk, Russia

Abstract

Technology of production of quadrupole magnets for NSLSII main ring is presented in the article. Quadrupoles have laminated iron yokes and are manufactured in Budker Institute of Nuclear Physics. The technology includes the method of correction octupole and sextupole harmonics. Field quality measurements of the magnets are presented.

INTRODUCTION

NSLS-II [1], the new 3GeV 3rd generation light source, is presently under construction at Brookhaven National Laboratory. Six types of quadrupole magnets for main ring NSLSII were successfully manufactured in Budker Institute of Nuclear Physics (see fig 1). The magnets had three yoke length and use the same lamination shape. The lamination with thickness of 1 mm had two poles with a common back leg. The magnet aperture was 66 mm. One length magnets had two types of yoke side insertions. One of the types is used to accommodate X-ray extraction. The form of the insertions had no influence on the field quality, so magnet types will be referred to as "short", "middle" and "long" below.

Prescribed specification on field quality of quadrupole magnets are reviewed in the paper [2]. Magnets field quality is specified by harmonics volume. Harmonics are defined as coefficients in the Fourier expansion of the integrated radial or azimuthal component of the magnetic field (see attachment). Harmonics are well below 10^{-4} of the main field (1 "unit") at a radius of 25 mm.

Table1. Parameters

Magnets type	**9801 & 9802 (short)**	**9804 & 9807 (long)**	**9810 & 9813 (middle)**
Quantity	60	60	7
Yoke length	217 mm	415 mm	250 mm
Maximum field gradient	10.6 T/m	19.2 T/m	19.2 T/m
Ampere-turns	4.7 kA	8.6 kA	8.6 kA

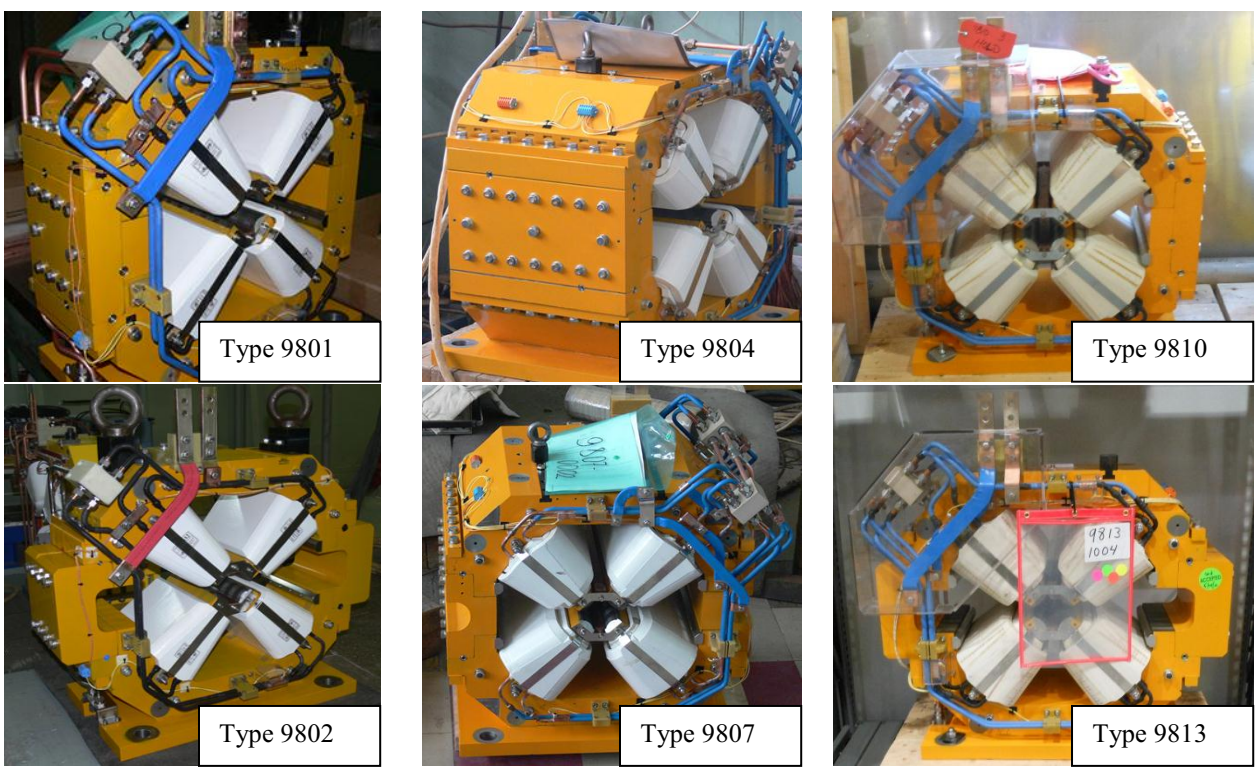

Figure 1: Quadrupole magnet types.

*Work supported by the Ministry of Education and Science of the Russian Federation (grant 14.B37.21.0784), Federal Target Program "Scientific Manpower of Innovative Russian Federation" 2009 - 2013.
#A.A.Starostenko@inp.nsk.su

MANUFACTURE TECHNOLOGY

The technology of magnets manufacturing includes high-precision lamination punching, yoke gluing in stacking fixture with movable wall, magnet assembling and tuning.

To avoid lamination shape distortion, the two stage punching was chosen. Initially rough die punched lamination blank with 6 mm allowance, and then high precision die punched final lamination. The lamination shape was monitored by measuring a pole gap of 1% samples. The deviation range for the pole gap was ±0.15 mm for lamination blanks and ±0.02 mm for final laminations. Also the lamination shape was monitored by measuring several samples of the laminations with a coordinate measuring machine. For example, the maximum deviation of the pole hyperbole shape with respect to the calculated ones was 6.5 μm, and the standard deviation of the distributions was 3.2 μm for one random lamination.

Ready lamination was stacked and glued in yoke halves with high precision. The precision was controlled by measuring pole gap along yoke. For example, measurements were carried out in twenty points along magnet axis for long yoke. Measurements of all long halves show standard deviation from average gap better then 10 μm. The volume of average gap was tuned by bar insertions (see figure 2) after magnet assembling.

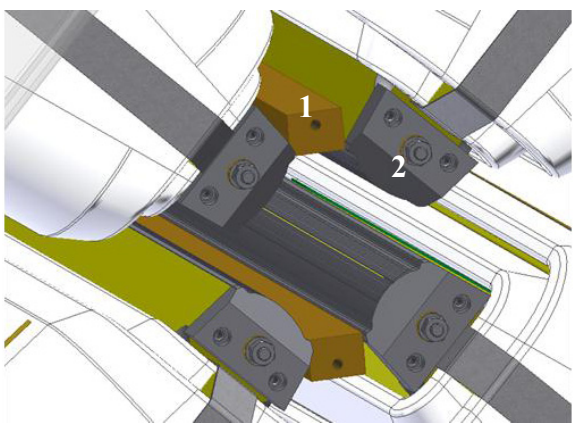

Figure 2: Magnet draft; 1 - bar insertion, 2 - nose piece.

The bar insertions had parallel surfaces and were fabricated from non-magnetic material. Its length is equal to yoke length for robust pole fixation. Width of the bar insertion was fitted to correct skew-sextupole a_3 and normal-octupole b_4 harmonics. Another advantage of using bar insertions to fix poles distance is increasing mechanical stability and therefore increasing magnetic field stability before and after magnet reassembly.

Reassembly tests were executed for all ready magnets. Typical harmonics changing was very small. For example for one random magnet #9804-0012 maximum changing was 0.15 units for harmonic b_4 (see figure 4).

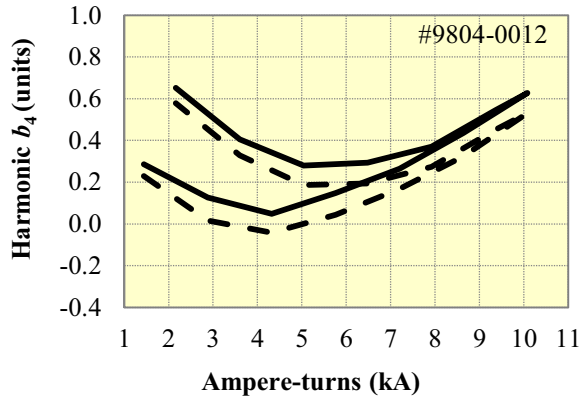

Figure 4: Measurements of harmonic b_4 dependence from current before and after reassembly.

The last elements installed on magnets were nose pieces. The nose piece was a part of pole with chamfer. Its length and height were 15 mm and 35 mm correspondingly (see fig. 1).

Nose piece fasten to yoke with stud. The fastening allow nose pieces to be shifted on 1 mm along pole face. The shift was used for corrections of sextupole, octupole and sometimes decapole harmonics. After the tuning, nose pieces got fixed by pins. One of the nose pieces well-known advantages is the integral increasing without increasing outer magnet dimensions. For long magnets the field integral was increased by 2.5 % and for middle ones by 5.1 % at design current.

Statistics for long magnets of low harmonics measurements before field tuning, and after installation of bar insertions and nose pieces, is shown on figure 4.

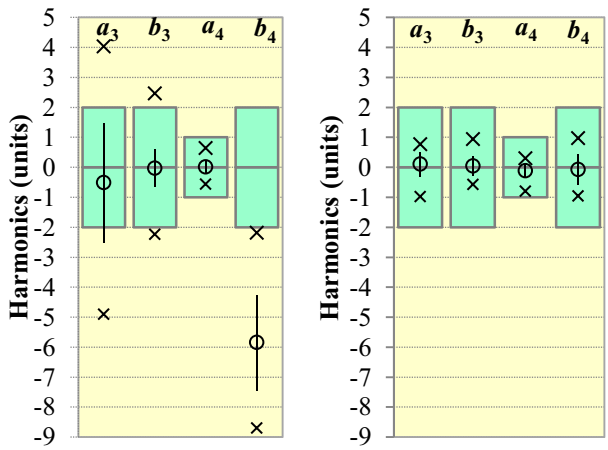

Figure 3: Statistics for 60 long magnets tuning. The circles show the mean value of each parameter, the lines give a ±sigma spread, and the x – the maximum and minimum value. Green rectangles show requirements. Left statistics show measurements before field tuning, right – after installation of bar insertions and nose pieces

Harmonic b_4 shift is the result of poles gaps understating. The understating is needed for installation and fixation of bar insertions.

All tunings are carried out under continual control of magnetic field quality by measurements. For this case, special fast and high-precision measurement stand on the base of rotating coil was developed [3].

Final measurements of harmonics amplitudes $Ampl_n = \sqrt{a_n^2 + b_n^2}$ for all magnets manufactured at BINP for NSLS-II main ring are shown on figure 6.

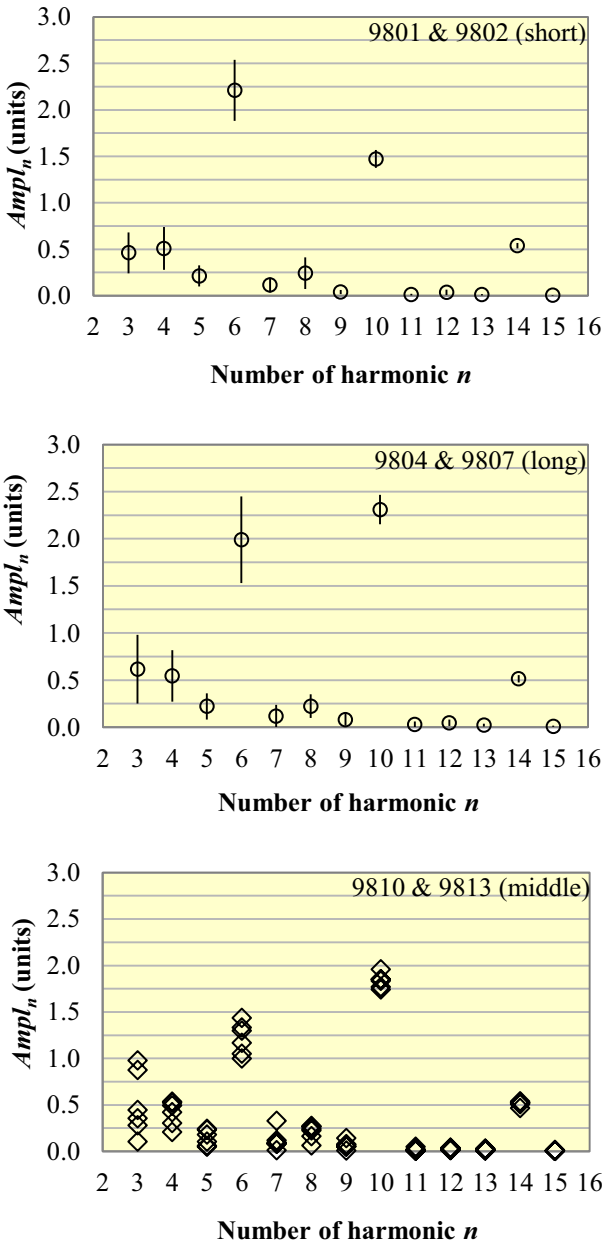

Figure 5: Statistic of magnetic field measurements for all magnet types. The circles show the mean value of each parameter, the lines give a ±sigma spread. The diamonds show volume of parameters.

CONCLUSION

The base of high field quality magnet manufacture in the described technology was high-precision lamination punching and high-precision half yoke gluing. No special control of poles gaps were exercised during magnet assembly. But assembled magnets were individually tuned, using bar insertions and nose pieces. The tuning was fast and showed good results for correction magnet fields in serial production. Bar insertions were useful not only for magnetic field correction, but also for field stability during magnet reassembly. The individual tuning of each magnet enables the manufacturing the whole series of quadrupoles with good magnetic fields. In the issue, field quality completely satisfied the prescribed specifications.

The methods elaborated can be used in further multipole magnet production.

ATTACHEMENT

The normal and skew 2n-pole integrated fields, B_n and A_n respectively, are defined as coefficients in the Fourier expansion of the integrated radial or azimuthal component of the magnetic field according to the following equations:

$$\int B_r(r,\varphi,z)dz = \sum_{n=1}^{\infty}\left[\frac{r}{r_0}\right]^{n-1}(B_n \sin n\varphi - A_n \cos n\varphi),$$

$$\int B_\varphi(r,\varphi,z)dz = \sum_{n=1}^{\infty}\left[\frac{r}{r_0}\right]^{n-1}(B_n \cos n\varphi + A_n \sin n\varphi).$$

The integrated quadrupole field is taken at $r_0 = 25$ mm.

The relative strengths of the harmonics (in "units" of 10^{-4}) in a quadrupole magnet are defined as:

$a_n = A_n/B_2$, $b_n = B_n/B_2$.

ACKNOWLEDGEMENT

We thank E. Rouvinsky for constructive remarks in the process of the technology development, P. Vobly for developing the magnetic field measurement stand and everyone who worked on this project.

REFERENCES

[1] F. Willeke, “Status of NSLS-II Project”, TUOBS3 PAC '11.

[2] J. Skaritka, "The Design and Construction of NSLS II Magnets", MO6PFP008 PAC '09.

[3] A. Tsyganov et al., “Stand for precision measurements of magnetic lenses for synchrotron radiation source NSLS-II”, WEPPC022, these proceedings.

QUADRUPOLE HARMONICS TUNING BY NOSE PIECES*

T.V. Rybitskaya#, E.S. Kazantseva, B.A. Skarbo, A.A. Starostenko, A.S. Tsyganov, Budker Institute of Nuclear Physics, Novosibirsk, Russia

Abstract

Six types of quadrupole magnets for NSLS-II main ring have been manufactured at the Budker Institute of Nuclear Physics. Some types of magnets have nose pieces on poles. Nose pieces permit the correcting of magnetic field harmonics. Corrections of octupoles, sextupoles and allowed harmonics have been implemented. Also for some magnets, corrections of amplitude of dependence sextupole harmonic from current have been implemented.

INTRODUCTION

The magnets had three yoke length (see table 1). Yoke of all magnets were glued from the same type of laminations. The lamination had two poles with a common back leg and thickness of 1 mm. The magnet aperture was 66 mm. One length magnets had two types of yoke side insertions. One of the types is used to accommodate X-ray extraction. The form of the insertions had no influence on the field quality, so magnet types will be referred to as "short", "middle" and "long" below.

Table 1. Parameters

Magnets type	**9801 & 9802 (short)**	**9804 & 9807 (long)**	**9810 & 9813 (middle)**
Quantity	60	60	7
Yoke length	217 mm	415 mm	250 mm
Maximum field gradient	10.6 T/m	19.2 T/m	19.2 T/m
Ampere-turns	4.7 kA	8.6 kA	8.6 kA

Magnets field quality is specified by harmonics volume. Harmonics are defined as coefficients in the Fourier expansion of the integrated radial or azimuthal component of the magnetic field (see attachment). Harmonics are well below 10^{-4} of the main field (1 "unit") at a radius of 25 mm.

The great labour has been applied to obtain the required field quality [2].One of the additional elements, which used to improve the field quality, was nose pieces. They were installed on middle and long magnets.

NOSE PIECES

Nose piece is a part of pole with chamfer. Its length and height are 15 mm and 35 mm correspondingly (see fig. 1). Nose piece fasten to yoke with stud. The fastening allow nose pieces be shift on 1 mm along pole face. The shift was used for corrections of sextupole, octupole and sometimes decapole harmonics.

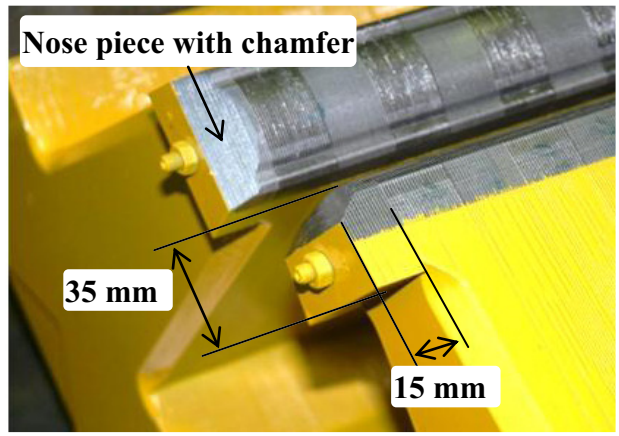

Figure 1: Nose pieces on one halve of magnet yoke.

The corrections demand the continual control of the magnet field quality. So, nose pieces position was tuned on the magnetic measurement stand [3] by iterations of tuning first then measuring the result changes. Usually three-five iteration was enough for tuning the field quality to achieve the desired result. Figure 2 shows measurements of lowest harmonics of magnet before the nose pieces installation and after the tuning. After the tuning, nose pieces got fixed by pins.

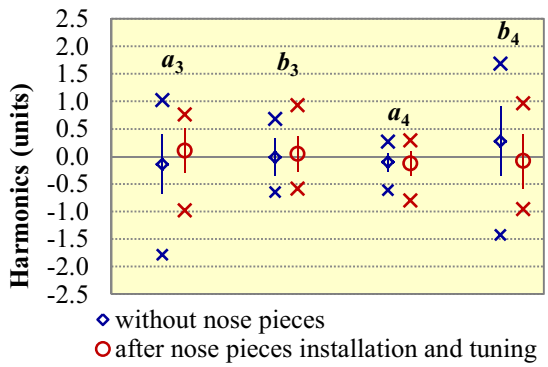

Figure 2: Statistic for 60 long magnets tuning. The circles and diamonds show the mean value of each parameter, the lines give a ±sigma spread, and the x – the maximum and minimum value.

One of the nose pieces well-known advantages is the integral increasing without increasing outer magnet dimensions. For long magnets the field integral was increased by 2.5 % and for middle ones by 5.1 % at design current.

*Work supported by the Ministry of Education and Science of the Russian Federation (grant 14.B37.21.0784), Federal Target Program "Scientific Manpower of Innovative Russian Federation" 2009 - 2013.

#T.V.Rybitskaya@inp.nsk.su

SEXTUPOLE HARMONIC DEPENDENCE OF CURRENT

In quadrupoles with yoke composed of two halves a_3 and it dependence of current can be big. The main effect observed for long magnets. First measurements of the field quality of magnet #9807-0001 show $\Delta a_3 = 4$ units in the required range 65-100% of design current.

Special parallel lamination sorting was employed to make one halve of yoke identical with the other. As a result, all magnets had less Δa_3 than first. Figure 3 shows the statistic of measurements of Δa_3 for long magnets.

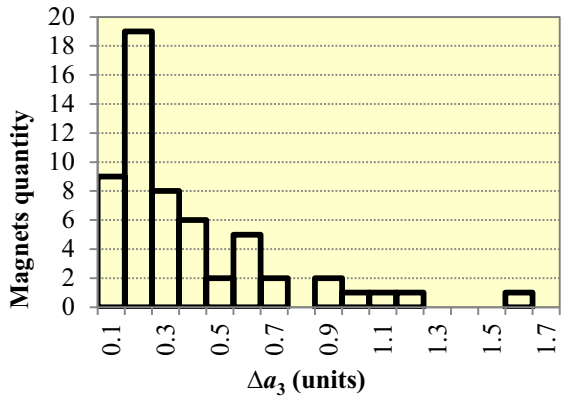

Figure 3: Statistic Δa_3 in 65÷100 % of design current range for 60 long magnets.

As experiment, an additional method of decreasing Δa_3 was checked on some magnets. The idea of this method is the shortening of length of nose piece, which are installed on one of yoke halves. Figure 4 shows example of the experiment for the magnet #9804-0009, whose top nose pieces were shortened by 0.2 mm.

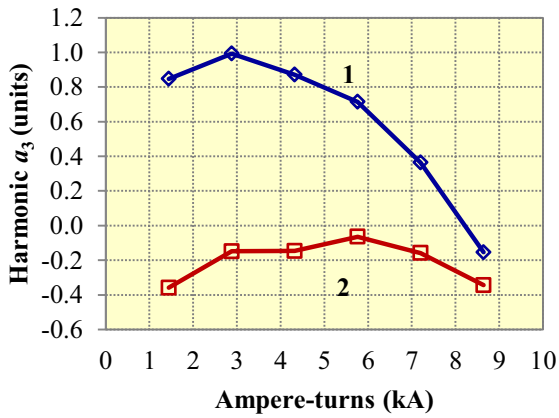

Figure 4: Measurements of harmonic a_3 dependence from full current for magnet #9804-0009: 1 - magnet without nose pieces; 2 - nose pieces were installed on magnet.

Applicability of the method is limited because shortening of some of nose pieces results in the increasing volume of a_3. To correct a_3 nose pieces were shifted after installation.

MODIFIED NOSE PIECES

The lamination profile was chosen to achieve small allowed harmonics in 2D. Immediately magnet edges in 3D increase harmonic b_6. Chamfers, which were placed on yoke ends, fitted b_6 to the required range ±3 units, but increased b_{10}. For some short magnets b_{10} goes to the boundary of requirements (see table 2).

Table 2. Statistic of allowed harmonic terms for ampere-turns 8.6 kA

Magnets type	short	long	middle
Yoke length	217 mm	415 mm	250 mm
Chamfer size	8 mm	13.5 mm	13 mm
b_6	-2.1±0.5	-1.2±0.2	-2.2±0.3
b_{10}	-2.3±0.2	-1.8±0.1	-1.5±0.1
b_{14}	-0.5±0.03	-0.5±0.02	-0.5±0.03

It was offered to modify nose pieces profile to decrease all allowed harmonics at the same time. By the instrumentality of MERMAID software [4] the profile was designed (see figure 5).

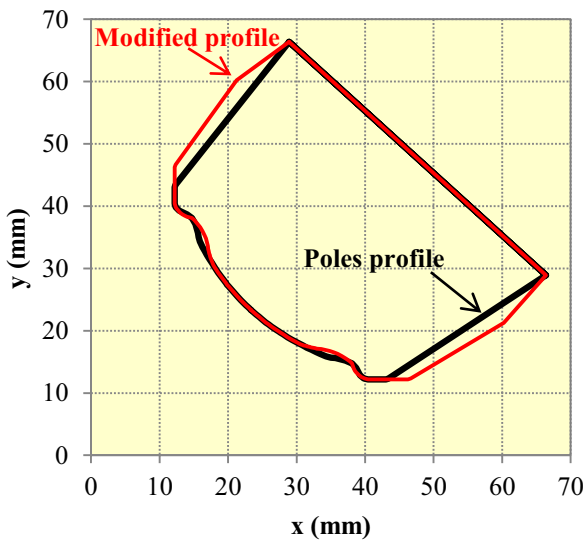

Figure 5: Nose pieces profiles

The set of nose pieces was manufactured with the calculated profile. In the experiment, the modified nose pieces were installed on magnet #9813-0001 and magnetic fields were measured. Then, usual nose pieces, which profile corresponds to yoke pole profile, were installed on the same magnet and magnetic measurements were done again.

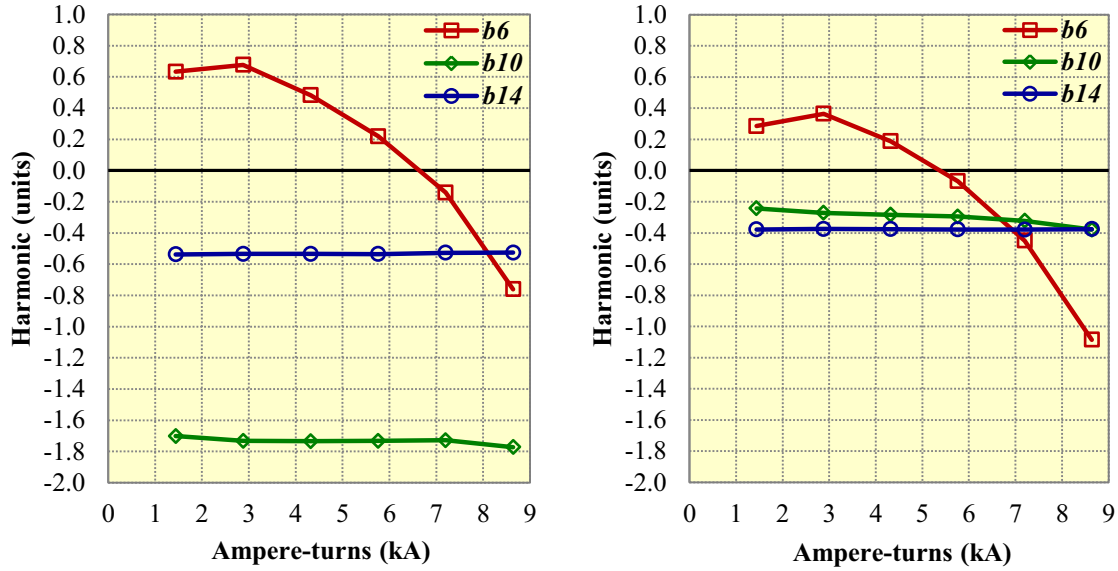

Figure 6: Measurements of harmonic terms dependence from current for quadrupole #9813-0001. Graphs show measurements for the same magnet with different nose pieces types: left – nose pieces have profile the same as yoke poles, right – nose pieces have **modified** profile.

Measurements of dependence allowed harmonics from current for this two cases are shown figure 6. Measurements show that the goal to decrease harmonic b_{10} without increasing other allowed harmonics was achieved.

CONCLUSION

Nose pieces not only increase field integral, but also can be used to make fast correction of some harmonics.

Fabricating nose pieces with profiles different from yoke poles profiles allow manufacture "good quadrupole" magnet. "Good quadrupole" means that magnet has fields with small allowed harmonics in the body of magnet and small integral field allowed harmonics simultaneously. Theoretically, yoke poles and nose pieces profiles can be fitted to achieve allowed harmonics as small as necessary at least for one current (b_6 show appreciable variation with current).

ATTACHMENT

The normal and skew 2n-pole integrated fields, B_n and A_n respectively, are defined as coefficients in the Fourier expansion of the integrated radial or azimuthal component of the magnetic field according to the following equations:

$$\int B_r(r,\varphi,z)dz = \sum_{n=1}^{\infty}\left[\frac{r}{r_0}\right]^{n-1}(B_n \sin n\varphi - A_n \cos n\varphi),$$

$$\int B_\varphi(r,\varphi,z)dz = \sum_{n=1}^{\infty}\left[\frac{r}{r_0}\right]^{n-1}(B_n \cos n\varphi + A_n \sin n\varphi).$$

The integrated quadrupole field is taken at $r_0 = 25$ mm.

The relative strengths of the harmonics (in "units" of 10^{-4}) in a quadrupole magnet are defined as:

$a_n = A_n/B_2$, $b_n = B_n/B_2$.

REFERENCES

[1] F. Willeke, "Status of NSLS-II Project", TUOBS3PAC '11.
[2] J. Skaritka, "The Design and Construction of NSLS II Magnets", MO6PFP008 PAC '09.
[3] A. Tsyganov et al., "Stand for precision measurements of magnetic lenses for synchrotron radiation source NSLS-II", WEPPC022, these proceedings.
[4] Mermaid, the 2D/3D code for magnetic design, © A.N.Dubrovin, Novosibirsk, Russia.

NONLINEAR SHUNTING AS A METHOD OF MAGNETIC FIELD CORRECTION IN QUADRUPOLE LENSES*

A. Tsyganov#, A. Batrakov, E. Kazantseva, A. Pavlenko, T. Rybitskaya, B. Skarbo, D. Shichkov, A. Starostenko, P. Vobly, Budker INP, Novosibirsk, Russia

Abstract

The quality requirements for magnetic field of elements in modern particle accelerators are high. For example, the harmonic fields quadrupole lenses main ring synchrotron source NSLS-II manufactured in BINP SB RAS must have no more than $1 \div 2 \cdot 10^{-4}$ from the field at 75% of the aperture of the lens. In the production process of magnetic lenses to adjust the fields of various methods of mechanical improvements are used, resulting in the increased time and the cost of production. The report proposes a method for precise non-destructive correction of some of the harmonics of the magnetic field of quadrupole lenses. The correction is performed using an additional element – the non-linear current shunt of coils. The report contains experimental data showing the possibilities of this method.

INTRODUCTION

In the Brookhaven laboratory, USA, synchrotron 3GeV light source NSLSII [1] is currently being constructed. For the main ring in BINP, several types of quadrupole lenses were designed and manufactured [Table1].

The magnets had three yoke length and use the same lamination shape. The lamination with thickness of 1 mm had two poles with a common back leg. The magnet aperture was 66 mm. One length magnets had two types of yoke side insertions. One of the types is used to accommodate X-ray extraction. The form of the insertions had no influence on the field quality, so magnet types will be referred to as "short", "middle" and "long" below.

Prescribed specification on field quality of quadrupole magnets are reviewed in the paper [2]. Magnets field quality is specified by harmonics volume. Harmonics are defined as coefficients in the Fourier expansion of the integrated radial or azimuthal component of the magnetic field (see attachment). Harmonics are well below 10^{-4} of the main field (1 "unit") at a radius of 25 mm.

To obtain the required field quality, many efforts were applied.

There are different tuning techniques of magnetic field during quadrupoles manufacturing. Most of these techniques require mechanical improvements.

The purpose of this article is to propose method of correction sextupole components using nonlinear shunt in power supply circuit of the quadrupole lens.

Table1. Parameters

Magnets type	**9801 & 9802 (short)**	**9804 & 9807 (long)**	**9810 & 9813 (middle)**
Quantity	60	60	7
Yoke length	217 mm	415 mm	250 mm
Maximum field gradient	10.6 T/m	19.2 T/m	19.2 T/m
Ampere-turns	4.7 kA	8.6 kA	8.6 kA

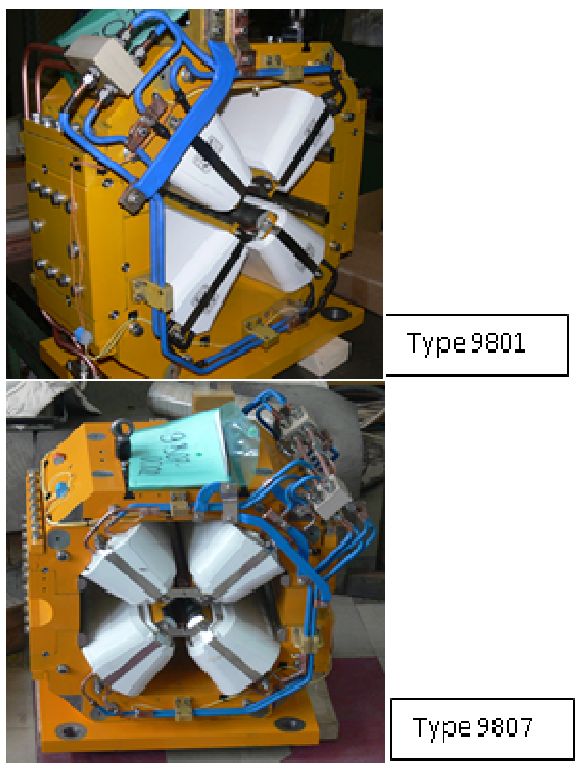

Figure 1. Two types of magnets, the experimental data are used in this article

*The work is supported by the Ministry of Education and Science of the Russian Federation (grant 14.B37.21.0784), Federal Target Program "Scientific Manpower of Innovative Russian Federation" 2009 - 2013.

A.S.Tsyganov@inp.nsk.su

CURRENT SHUNT

The quality of the magnetic field of quadrupole lenses immediately after its production may not meet the specified parameters for many different reasons. Mechanical rework of magnetic core requires significant labor costs, which forces to search the other ways of adjusting quadrupole lenses. On the basis of the practical work, the method of adjusting sextupole harmonic of a magnetic field is proposed.

This method is the addition of a current shunt of quadrupole coils. The method of the current shunt is known [3]. But in this link, shunting only single coil of quadrupole lens is mentioned.

Figure 2. The cross section of the quadrupole with an asymmetric arrangement poles relative to the horizontal axis.

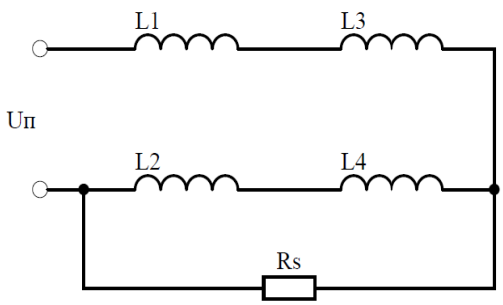

Figure 3: Scheme of shunting bottom coils of quadrupole lens. L1, L3 are top coils in quadrupole lens, L2, L4 are bottom ones. Rs is passive shunt.

Figure 2 shows the asymmetry of the poles. This means asymmetry of the magnetic field in the upper and lower gap. We can compensate this asymmetry by reducing the current in both bottom coils.

Typically, multipole coils are powered as a series circuit from a single power supply. We can change the value of currents in different coils or separate the power supply system or deliberately introduce asymmetry in quadrupole power. To do this, we need to add a current shunt to the lower coils, see Figure 3. Similarly, we can correct the asymmetry of the vertical axis if we add a shunt to side coils.

Figure 4 shows the result of the magnetic field correction. The current of shunt is ~ 0.25% of the operating quadrupole current.

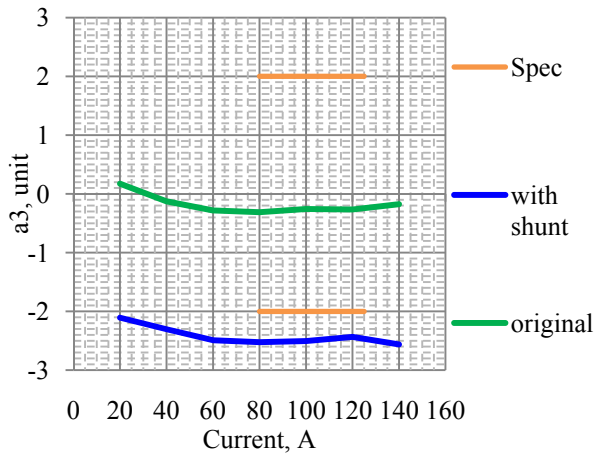

Figure 4. Result of correction of sextupole components in the magnet 9801-0015

NONLINEAR CURRENT SHUNT

Usually, customers have requirements on the harmonics value in the range of the operating current of the magnet. And if for some reason there is current dependence [4] of a sextupole component in the range of operating currents, shunting to be done must be current-dependent. An example of such a shunt may be an electrical circuit consisting of both passive components and the component of the nonlinear current characteristics, such as diodes, as shown in Figure 5. Thus, you can adjust sextupole component with complex non-linear form in the whole range of the operating current.

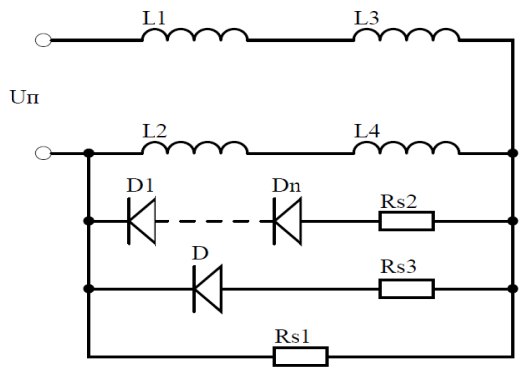

Figure 5. The general case of a non-linear shunt at the lower coils in a quadrupole lens.

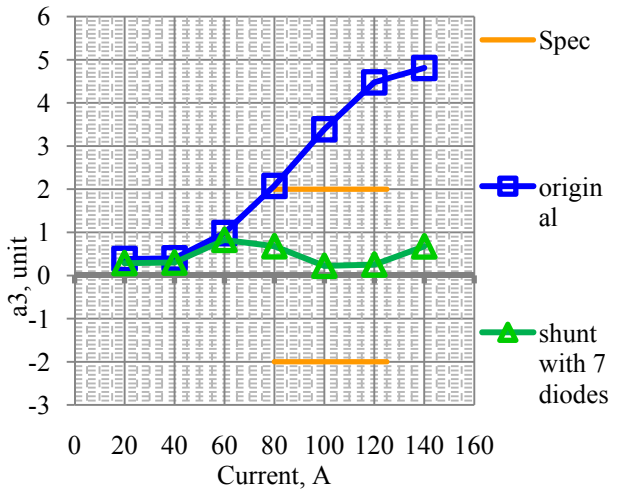

Figure 6. The correction sextupole components in the magnet type 9807.

Figure 6 shows the case of the quadrupole lens, requiring correction because the value of sextupole component in the operating current range varies from 2 to 5 units. By selecting the shunt and a number of diodes, we can adjust the lens.

In this example, the maximum current shunt is ~ 0.7% in the working range of currents.

THE METHOD OF NONLINEAR SHUNT ELEMENTS SELECTION

The possible method of selection of the nonlinear shunt elements is as follows. At first it is necessary to measure the dependence of the calibration values sextupole components of the current shunt. This function will be different for different types of the quadrupole lenses design. We measure the form of the function of sextupole components in the range of operating currents in the first measurement of the magnetic field in the custom of the quadrupole lens. On the basis of this data, the amount of necessary correction, non-linearity and calibration factor is determined by the number of non-linear elements and the value of shunt resistance.

CONCLUSION

The main advantages of this method are its simplicity and reversibility in contrast to the mechanical methods of correction. The feature of this method - the magnet is not considered as a thin lens because the method changes the magnetic field along the longitudinal axis of the lens, not locally.

This technique is not applicable or applicable only partially for the quadrupole lenses with supply voltage less than a few volts.

ACKNOWLEDGMENT

We thank everyone who worked on this project.

REFERENCES

[1] F. Willeke, “Status of NSLS-II Project”, TUOBS3 PAC '11.
[2] J. Skaritka, "The Design and Construction of NSLS II Magnets", MO6PFP008 PAC '09.
[3] Breese, Mark B. H. et al., “Measurement and correction of parasitic sextupole components in magnetic quadrupole lenses”, NIM B, Volume 47, Issue 4, June 1990, Pages 443–452.
[4] T.V. Rybitskaya et al., “Quadrupole Magnets Tuning by Nose Pieces”, WEPPC020, these proceedings.

STAND FOR PRECISE MEASUREMENTS OF MAGNETIC LENSES FIELD QUALITY*

A. Tsyganov, A. Batrakov, E. Kazantseva, A. Pavlenko, T. Rybitskaya, B. Skarbo, D. Shichkov, A. Starostenko, P. Vobly, Budker INP, Novosibirsk, Russia

Abstract

Strict requirements are imposed on the field quality of magnetic elements in today's synchrotron radiation sources. For example, magnetic field harmonics of quadrupole lenses (currently manufactured in BINP) of main ring NSLS-II, should have no more than one or two ten-thousandths parts of main harmonic at the 75% of lens aperture. The stand is designed for precise measurement of the quadrupole lenses. The well-known technique with a rotating coil was used. The design and location of coils used in the measuring shaft and the method of commutation allow to compensate for both quadrupole and dipole components of the magnetic field. This, in turn, minimizes shaft beats effect and power supply noises effect on the accuracy of the results. During measurements, the shaft is rotated without stopping, and the data received from the gauge angle and digital integrators are processed "on the fly" strictly synchronous. The measurement procedure is performed in one and a half turn of the shaft and takes six seconds. The report describes mechanical design of the stand, principle of work, parameters of the equipment, and software. Results of measurements of the quadrupole lenses synchrotron source NSLS-II are given in conclusion. The results demonstrate possibilities of the stand.

INTRODUCTION

Six types of quadrupole magnets for main ring NSLSII [1] were manufactured in Budker INP. The total quantity of magnets was 127. The high quality of magnetic field [2] was achieved by tuning directly on magnetic measurement stand. This stand was developed specially for similar task.

Requirements for MMS:

- Accuracy of magnetic field harmonics measurement is at level 10^{-5} relative to main quadrupole component.
- Short time required for one measurement with obtaining results.
- Automation of carrying out a series of measurements.
- Suitability for usage in mass production.

MECHANICAL CONSTRUCTION

All the construction is set on the girder (see Fig.1 and Fig.2). During the measurements the magnet is installed on the support, which provides the positioning of magnet in 3 coordinates. The rotating coil is installed on special supports. The rotating system is easily removable so that one can set or remove shaft in few minutes. The self-aligning shaft bearings are arranged on special steel bases, which are removable on one side due to the provided removability of shaft. Cable connections are at the both ends of shaft and they are fixed, which means that wires are rotating with the shaft. Lengths of cables were chosen for unobstructed shaft rotation of 3-4 turns in each direction.

Figure 1.Magnetic measurement stand.

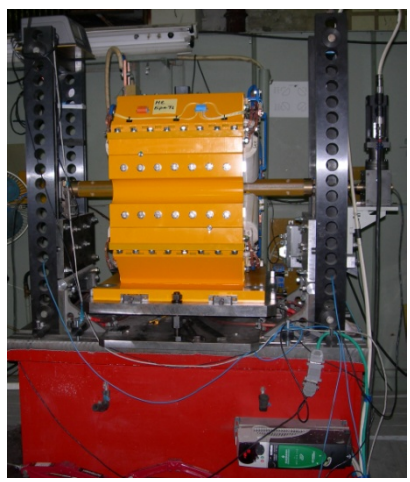

Figure 2. Mechanical construction of MMS.

The scheme of MMS interconnections is shown on Fig. 3. The integrators (VsDC3) were developed in the Budker INP [3].

MEASUREMENT SHAFT

The compensation scheme of rotating coil is shown on Fig. 4. Such connection of coils provides compensation of dipole and quadrupole components of magnetic field, so we get better signal for higher harmonics.

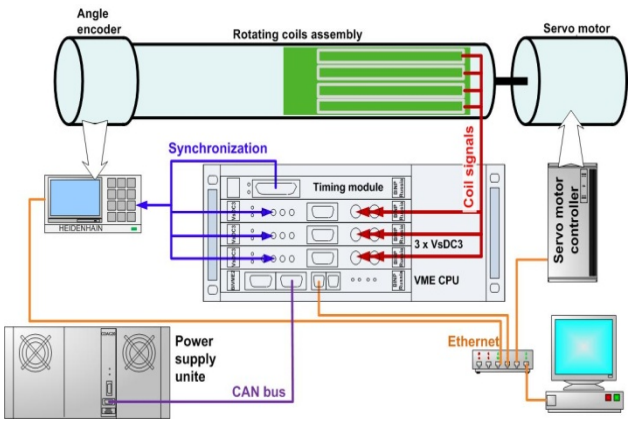

Figure 3. Interconnections of MMS.

Besides the compensation scheme consisting of 6 coils, there are 2 additional coils allowing measurement of disposition of shaft axis in relation to magnet axis. White, yellow and blue coils on Fig. 4 are responsible for the compensation scheme while black coils are responsible for the axis disposition measurements and main field integral. The coils were manufactured as multilayer printed-circuit board (see Fig.5).

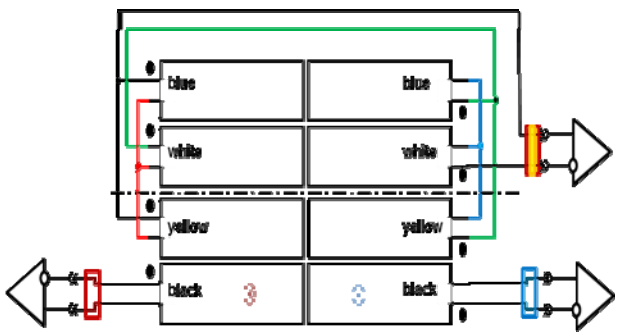

Figure 4. The compensation scheme of measurement coils.

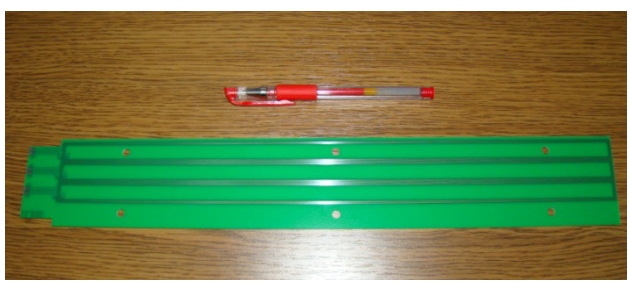

Figure 5. The printed-circuit board of measurement coils.

On the real shaft the main harmonic compensation coefficient was achieved about 5000.

SOFTWARE OF MMS

The software for MMS control consists of two parts interacting by client-server model. The server is a set of programs executed in VME controller managed by OS Linux. The client is a user application of personal computer running the MS Windows 2000/XP. Basic functions of the server part are provision of the client access to the equipment and management of measurement procedure.

To simplify the server structure and make the server easy expandable, it was decided to divide the software of VME controller into two independent services:

1. bivmeCANSrv – plays the role of Ethernet-CAN interface converter and applied for lens power supply unit control.
2. movableCoilsSrv – provides the client with access for measuring devices. This is the basic element of VME controller software.

Each of these services is realized as classic TCP-server of Linux.

In the program complex, the client is Win32 – the program with graphical user interface with the next functions:

1. Configuration of hardware;
2. Measuring, processing and providing data measured;
3. Creation and execution scripts, which allow carrying out the measurement cycle with given parameters, for example, it can be series of measurements for set of currents in lens;
4. Output of data, which assist in adjustment of lens till the alignment of lens magnetic axis with axis of measuring coils rotating;
5. Organization of measured data archive for additional data processing and reviewing.

The user interface of this program is implemented as a window with tabs, each of which is a functionally completed graphical control element used for performing one of software functions.

ALGORITHM OF MEASUREMENTS

Before measuring the operator sets the shaft in zero position by the bubble level (see Fig. 6).

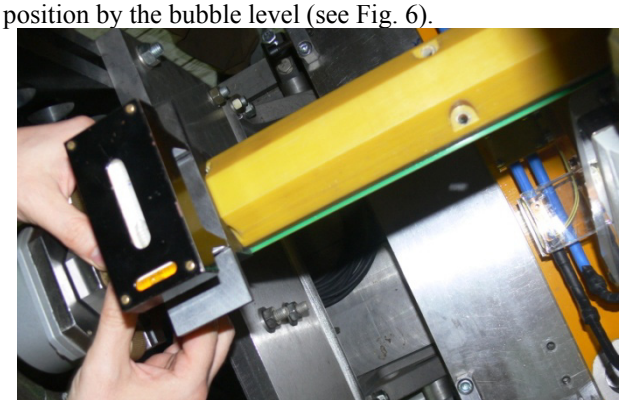

Figure 6.The shaft levelling.

Then the algorithm of measurements proceeds in the steps below:

1. The shaft begins its movement from -100 degrees in order to provide constant velocity while measuring.
2. During measurements the shaft is rotated without stopping, and the data received from the gauge angle and digital integrators are processed "on the fly" strictly synchronous. The measurement procedure is performed in one and a half turn of the shaft and takes six seconds.
3. After measurement the shaft returns to the initial position.

RESULTS

Harmonics are defined as coefficients in the Fourier expansion of the integrated radial or azimuthal component of the magnetic field. Harmonics are well below 10E–4 of the main field (1 "unit") at a radius of 25 mm. For demonstrating of precision of MMS set of 60 measurements was carried out. The results are presented below (see Fig. 7). All harmonic noise is below 0.01 unit (10E-6) except normal octupole component (b4), which is not a noise of MMS but the lens feature.

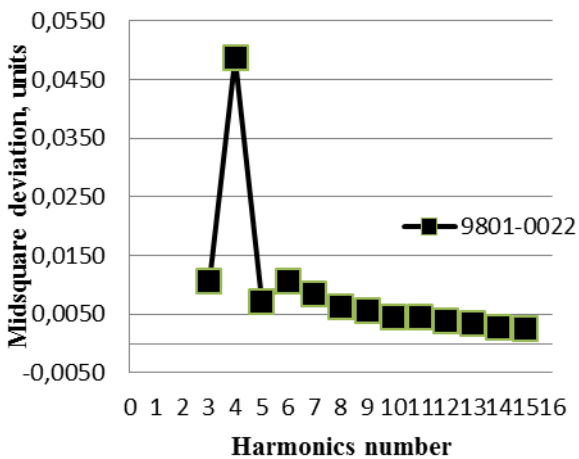

Figure 7. Statistic noise in harmonics, normal components

In order to check the stability of shaft position, the set of 30 measurements with constant current was carried out. The midsquare deviation of axes positions was about 0.7 μm (see Fig. 8).

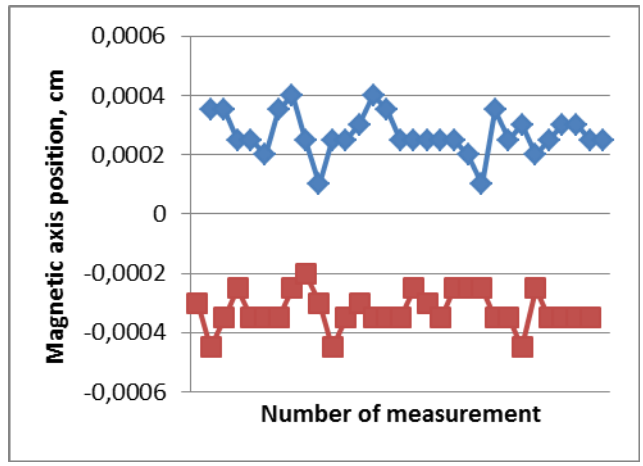

Figure 8. Axes position stability

CONCLUSION

The final parameters of MMS are:

- Precision – about $5 \cdot 10^{-6}$ on sextupole and octupole harmonic terms
- Precision – about $2 \cdot 10^{-6}$ on high harmonic

Thus, measurement precision of stand is high. At the same time the stand is relatively cheap and makes measurements very fast. The set of NSLS-II main ring quadrupole magnets (127 pcs.) were successfully tuned by this stand. Also, two similar MMS were created on the base of experience of practical work.

ACKNOWLEDGMENT

We thank Animesh Jain (BNL) for constructive remarks in the process of the stand calibration and testing, and everyone who worked on this project.

REFERENCES

[1] F. Willeke, "Status of NSLS-II Project", TUOBS3 PAC '11.
[2] J. Skaritka, "The Design and Construction of NSLS II Magnets", MO6PFP008 PAC '09.
[3] A. Batrakov et al. "Multimode digital integrators for precise magnetic measurements", WEPPD032, these proceedings

DESIGN, SIMULATION AND OPTIMIZATION OF A SOLENOID FOR ES-200 ELECTROSTATIC ACCELERATOR

M. Asgarpour, S. A. H.Feghhi, E. Ebrahimibasabi, M. khorsandi, Department of Radiation Application, Shahid Beheshti University, Tehran, Iran
N. Khosravi, University of Zanjan, Zanjan, Iran

Abstract

Solenoids have an important role from the viewpoint of focusing the beam in drift tube of charged particle accelerators. In order to optimize the beam current in ES-200, an electrostatic proton accelerator at Shahid Beheshti University (SBU), design and simulation of a suitable solenoid has been performed. The CST Studio package has been used for simulation and design. Simulation results from the CST have been validated in comparison with theoretical formula and equations. According to the results we optimized the design to have minimum lost beam current on drift tube.

INTRODUCTION

ES-200, an electrostatic proton accelerator at SBU, is a compact and portable electrostatic accelerator, which includes the basic components of a Cockcroft-Walton high voltage terminal, accelerating column, vacuum system, electromagnetic lens, drift tube, control system and etc. In this system a radio frequency ion source has been used to generate positive ions. Extraction voltage (adjustable from 0 to 5 kV) applies to the anode electrode for leading the ions to the entrance of accelerating column. Accelerating column has been composed of thirteen electrodes that can be divided into two main parts. The first part includes four electrodes for extracting, focusing and accelerating the ion beam. The second part includes nine electrodes with uniform shape which provide homogeneous field to accelerate and steer the beam. The maximum beam current on the target is about 500μA with the maximum energy of 200 keV. [1].

In order to optimize the beam current in ES-200, designing and simulation of a focusing system seems to be necessary. Magnetic lenses such as Solenoids, Quadrupoles and electrostatic lenses like Einzel lens are devices that are used as a focusing system in accelerators. In this paper, for minimizing the lost beam current on drift tube and changing the beam diameter on the target, design and simulation of the solenoid has been done by using the CST package.

DESIGN CONCEPTS

As it can be seen in Figure 1, On-axis longitudinal magnetic field for a single solenoid with the internal radii (r_1), external radii (r_2) and length of (l) is given by:

$$B=\frac{\mu_0 in}{2(r_2-r_1)}\left[x_2\ln\frac{\sqrt{r_2^2+x_2^2}+r_2}{\sqrt{r_1^2+x_1^2}+r_1}-x_1\ln\frac{\sqrt{r_2^2+x_1^2}+r_2}{\sqrt{r_1^2+x_1^2}+r_1}\right] \quad (1)$$

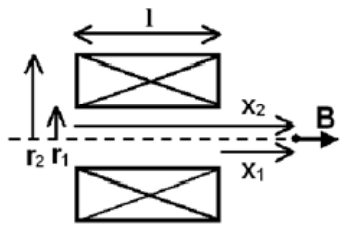

Figure 1. Solenoid in cross section view.

Where B is the magnetic field on the axis, μ_o is the permeability constant, (i) is the wire current , n is the number of turns of wire per unit length of solenoid, and x_1 and x_2 are the distances, on axis, from the ends of the solenoid to the magnetic field measurement point [2].

Some of electromagnetic codes have been used to solve Maxwell's equation with the specified boundary conditions. CST was introduced as software that analyses the structure with Finite Element Method. In this paper, CST PARTICLE STUDIO has been used to simulate charged particles travelling through electromagnetic fields [3]. Figure 2 and 3show an overview of a desired solenoid on the drift tube which was done by CST for a proton beam with energy of 200 keV (after passing through the accelerating column). The length and thickness of solenoid was considered 180 mm and 100 mm, respectively. Solenoid was set at distance of 450 mm from the end of accelerating column. Beam diameter was investigated at distance of 768.5 mm from the solenoid where the target was placed.

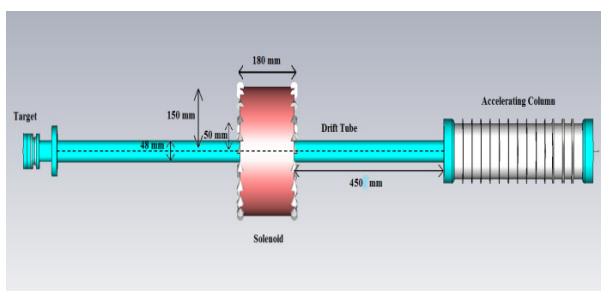

Figure 2. Simple model of a typical ES-200.

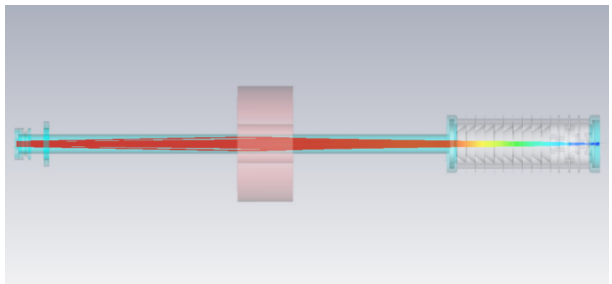

Figure 3. Focusing of the beam on the drift tube by desire solenoid in CST.

RESULTS

Behaviour of the B-field at different distances on solenoid axis has been shown in Figure 4. It can be seen that there is a good agreement between simulation results and theoretical calculations.

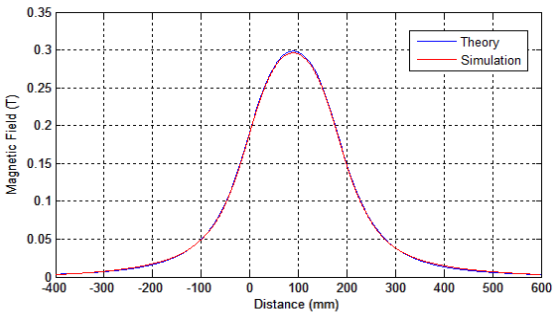

Figure 4. Simulated magnetic field by CST (red) in comparison with calculated magnetic field (blue) at different distance on the axis of solenoid

Beam diameter as a function of current has been shown in figure 5. It can be seen that an increase of the current was accompanied by a decrease of the beam diameter measured at target position. Changing the solenoid current from 0.1 to 1.8 Ampere, beam diameter was varied from 22 to 12 mm. finally the design was optimized for minimum beam loss.

CONCLUSION

In this work, for minimizing the beam current loss on drift tube and changing the beam diameter on the target, designing and simulation of a solenoid was studied. Maximum B-field was found in the solenoid centre. Changing the solenoid current from 0.1to 1.8 Ampere, the diameter of the beam can be change from 22 to 12 mm. This paper covered the basic methodologies used to obtain an identical solenoid so that it is ready to be constructed for our proton electrostatic accelerator.

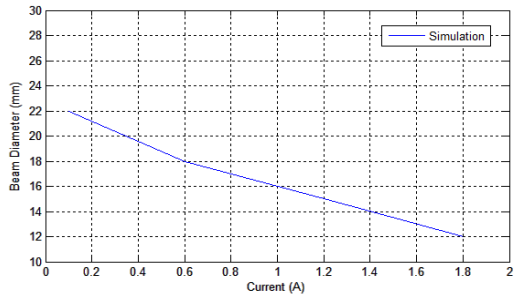

Figure 5. Beam diameter as a function of current in CST.

ACKNOWLEDGEMENT

The authors would like to convey thanks to Mr. Mohsen nikbakht for his help and support.

REFERENCES

[1] Rahighi, J., Design and Construction of a 200KV Electrostatic Accelerator, Institute of Nuclear Science and Technology, AEOI, Tehran, 2009.

[2] Makino K. et al, High-order map treatment of superimposed cavities, absorbers, and magnetic multipole and solenoid fields, Nuclear Instruments and Methods in Physics Research, A 519 (2004), 162–174. See also at http://www.netdenizen.com/emagnettest/solenoids/?solenoid.

[3] http://www.cst.com/Content/Products/PS/Solvers.aspx

[4] Terechkine, I.,Apollinari,G.,Dimorco,J., Huang,Y., Orris,D.,Page,T.,Rabehl,R., Tartaglia,M.,Tompkins,J., Focusing solenoids for the hinslinac front end., FNAl, Batavia, IL 60510, U.S.A.

CORRECTING MAGNET POWER SUPPLIES FOR THE NSLS-II BOOSTER

K.R. Yaminov, O.V. Belikov, A.S. Medvedko, V.V. Kolmogorov, A.I. Erokhin, S.R. Singatulin, S.E. Karnaev, P.B. Cheblakov, Budker INP SB RAS, Novosibirsk

Abstract

Budkers Institute of Nuclear physics builds booster for synchrotron light source NSLS-II. Booster should accelerate electrons from energy 200MeV to energy 3GeV, acceleration phase duration is 250msec, repetition rate — up to 2Hz. Booster magnet system includes 16 sextuples and 36 dipole correcting magnets powered separately. Forth-quadratant current sources for sextuples and correcting magnets have maximum output current ±6A, maximum output voltage ±100V, maximum output current ripples and long-term stability are better than 0,1% relative to 6A. In ramping mode with current slew rate up to 200A/sec time lag between setpoint and output current is not more than 1msec and can be compensated by software. Results of power supplies system tests and commissioning will be presented in paper.

INTRODUCTION

The National Synchrotron Light Source II is a third generation light source under construction at Brookhaven National Laboratory. The project includes a highly optimized 3 GeV electron storage ring, linac pre-injector and full-energy booster-synchrotron. Budker Institute of Nuclear Physics builds booster for NSLS-II. The booster should accelerate the electron beam continuously and reliably from minimal 170 MeV injection energy to maximal energy of 3.15 GeV and average beam current of 20 mA. The booster shall be capable of multi-bunch and single bunch operation. A nominal repetition rate of the booster is 1 Hz with possibility to upgrade it up to 2 Hz. Main booster parameters are presented in the Table 1.

Table 1: Main booster parameters

Parameter	Value
Beams Energy: Injection/Ejection	200MeV/3GeV
Number of periods	4
Circumference, m	158.4
Repetition rate, Hz	1(2)
Bunch number	40-150
Revolution Frequency, MHz	1.893
Synchrotron frequency, kHz	35.5/20.3 (0.2/3GeV)
Betatron tunes: *νx*/*νy*	9.65/3.41
3D Damping time, sec	16.2s to 7.7s (0.2GeV) 4.8ms to 2.3ms (3GeV)
Energy rise time, sec	0.26

SEXTUPOLES AND CORRECTING DIPOLE MAGNETS

Quadratic nonlinearity of the magnetic field at the quadrupole lenses are proposed to be tuned using 16 sextupole lenses (8 lenses to X direction and 8 – to Y one). All the lenses are identical in design and in electrical parameters. The specified parameters of sextupole lenses are presented in Table 2.

Table 2: Sextupoles parameters

Magnet	I_{max}, A	R, OHm	L, H
BR-SXV	5,6	1,2	0.104
BR-SXH	5,6	1,2	0.104

It is proposed that for the beam orbit correction 36 dipole correcting magnets will be installed in the Booster magnet system. 20 dipole correctors are for X coordinate and 16 – for Y one. The specified parameters of correctors are presented in Table 3.

Table 3: Dipole correctors parameters

Magnet	I_{max}, A	R, OHm	L, H
BR-CX	5	2	0. 4
BR-CY	5	2	0.25

POWER SUPPLIES REQUIREMENTS

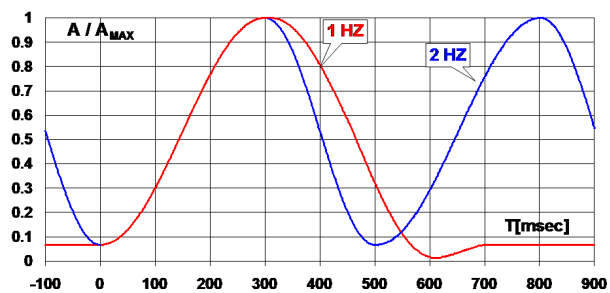

Figure 1: Magnetic field evolution during the ramp.

Cosine approximation of magnetic field evolution during the ramp for 1 and 2Hz modes is shown in Fig. 1. Sextupoles and dipole correctors are used to compensate higher harmonics caused by non-linearity of magnetic system. Therefore, power supplies should provide output voltages enough for necessary current slew rate. Output

voltage requirements for sextupoles and dipole correctors power supplies are presented in Table 4.

Table 4: Power supplies output voltage requirements

Magnet	Resistive voltage, V	Inductive voltage, V	Peak voltage, V
BR-SXH(V)	6.7	10	16.7
BR-CX	10	40	50
BR-CY	10	25	35

Power supplies for sextupoles and correcting dipole magnets should provide error better than than 0,1% relative to the I_{max} in static mode (during injection/extraction) and .better than 1% relative to the I_{max} during beam acceleration.

MPS-6 STABILIZED CURRENT SOURCE

MPS-6 stabilized current source developed earlier in BINP is used to supply sextupoles and correcting magnets of the booster.

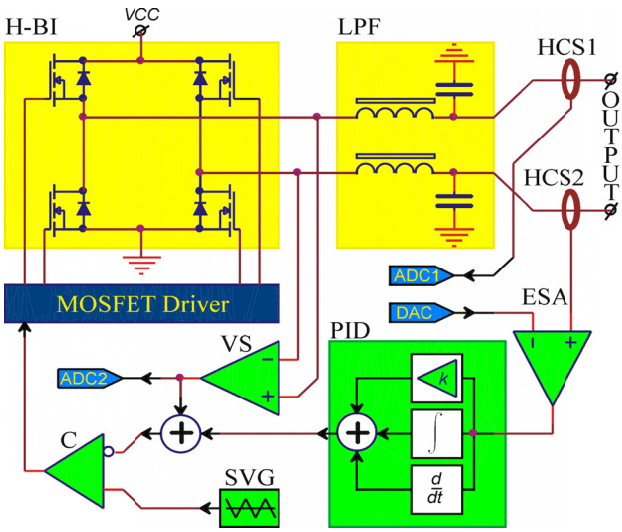

Figure 2: The MPS-6 structural scheme.

Structural scheme of the MPS-6 power supply is shown in Fig. 2. H-bridge DC/DC converter is assumed as a basis. The output current adjustment is made by pulse-width modulation operating at 50kHz frequency. There is a second-order LPF filter on the output of the bridge-inverter, providing the damping of carrier frequency by 60dB. The measurement of output current is realized by two identical contactless compensatory Hall sensors. One sensor is used in the feedback circuit, the other – as an independent measuring device for the control system. H-Bridge output voltage is used for the voltage feedback loop which is intended to dump the LPF filter. The feedback loop contains elements with differential and integral characteristics to provide necessary accuracy and dynamic characteristics. Main parameters of the MPS-6 power supply are presented in Table 5.

Table 5: Parameters of the MPS-6 current source

Parameter	Value
Output current	±6 A
Maximum output voltage	±80 V
Conversion frequency	50 kHz
Absolute error of regulation	0.1% relative to I_{max}
Output dispersion for 10hours operation	100 ppm relative to I_{max}
Output current ripples	<0.1%
Output current temperature drift	50 ppm/°K
Output current hysteresis	5 mA
Heat dissipation in the unit	<15 W

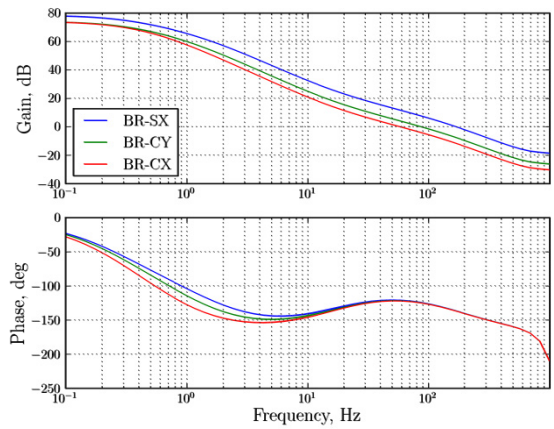

Figure 3: Open feedback loop frequency response.

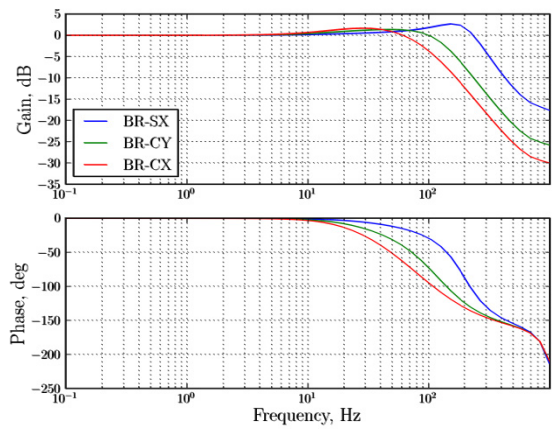

Figure 4: Closed feedback loop frequency response.

Feedback loop was optimized to meet dynamic error requirements and conserve high static parameters. Calculated frequency responses of open and closed loops are presented in Fig. 3 and Fig. 4 respectively. Simulation

shows a presence of time shift between preset and output currents. The time shift value is not more than 1msec and can be compensated by software.

The design of single-channel MPS-6 power supply is the insert module in "Euromechanics" standard (Fig. 5).

For the resistive/inductive load the output power of power supply source can be of positive and negative values. Therefore, the four-quadrant volt-ampere characteristic of current source is required for correctors and sextupoles. Such a source allows recuperation of a part of energy from a load inductance in the decreasing output current mode to the buffer capacity. It is more optimal to use common buffer capacity per several power supply channels for multichannel power supply system in frames of one multichannel module (Fig. 5). Such multichannel module can include up to 8 MPS-6 power supplies.

Figure 5: MPS-6 power supply and multichannel module with inserted units.

POWER SUPPLY CONTROLLER AND POWER SUPPLY INTERFACE

Power supply controller (PSC) and power supply Interface (PSI). were developed at BNL for the NSLS-II magnetic system power supplies control.

PSI has one or two precision 20-bit DACs, three channels of precision 16-bit ADC for each DAC, six channels of 16-bit ADC for each DAC, sixteen digital inputs, 8 digital outputs. PSI is connected to PSC via fiber-optic 50 Mbps data link. The PSI can digitize up to 10 analog signals at a 100 KHz sample rate. Up to four dual channel PSIs are used to control MPS-6 multichannel module. Three analog and two digital signals are used for each power supply.

The PSC has two major functions. The first function is to provide communication between a PSI and EPICS IOC. The second major function of PSC is to provide a large memory for storing large amount (half Gigabyte) of data. The data can be used for power supply ramping waveforms or various diagnostic data.

Transition board installed in multichannel module is used to connect each power supply with PSI For one MPS-6 it is proposed to use one DAC channel and 2 ADC channels (one – for load current measurement, the other one – for load voltage measurement), one bit of input command and one bit of output command of digital IN/OUT registers for control and monitoring of each power supply sources MPS-6.

RESULTS

Bench tests included long-term stability test, output current ripples measurement and dynamic error measurement for 2Hz sinusoidal ramp. Some results are presented below.

The diagram given in Fig. 6 presents output current drift during 7-hour long-term stability test. After warming up during 2 hour discrepancy doesn't exceed 0,02% relative to the maximum output current 6A. Temperature after warming up changes in ±1°C range. Output current ripples are given in Table 6.

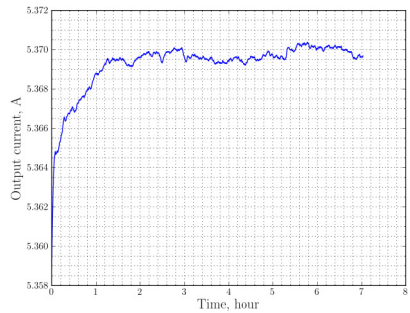

Figure 6: Output current drift during 7-hour long-term stability test.

This dynamic error for 2Hz sine output current is shown in Fig. 7. Curve 1 – is the sinusoidal ramp, curve 2 – dynamic error measured with compensated time shift, curve 3 – dynamic error without time shift compensation.

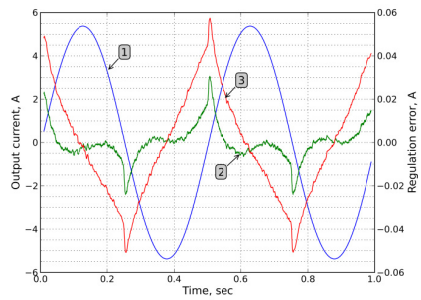

Figure 7: The dynamic error for 2Hz sinusoidal ramp.

Table 6: Output current ripples

Output current	RMS ripples, mA	RMS ripples % of I_{max}
0A	1.38	$2.3*10^{-4}$
3A	1.56	$2.6*10^{-4}$
6A	1.74	$2.9*10^{-4}$

REFERENCES

[1] O. Belikov et al. "Four quadrant power supplies for steering electromagnets for electron-positron collider", RuPAC-2008, BINP SB RAS

HIGH VOLTAGE TERMINAL IN COSY ELECTRON COOLER

V.A. Chekavinskiy, E.A. Bekhtenev, I.A. Gusev, M.N. Kondaurov, V.R. Kozak, E.A. Kuper, V.R. Mamkin, A.S. Medvedko, D.N. Pureskin, D.V. Skorobogatov, BINP SB RAS, Novosibirsk

Abstract

In Budker INP SBRAS was developed electron cooler with energy up to 2MeV for COSY accelerator (Germany). Due to restricted footprint, cooler's collector and gun parts were combined in a single acceleration system – high voltage terminal. All power and control electronics were placed in a single isolated volume, filled with SF6 gas under 4-6 atm. pressure. Electronics is controlled via wireless CAN, and powered by multistage transformer, capable of 15 kW power at 26 kHz. Wireless control is passed through dedicated optically transparent window, also served for modulated laser beam, used in electron beam diagnostic. By construction, electronics is divided on two standalone units: collector power supply and gun-filter system (SGF). SGF is built on 19" EuroPak chassis, where were placed all power modules, needed for collector and gun pipe electrodes. All power outputs were protected against overvoltage and sparks, available while cooler exploitation. In SGF there were controlled up to 40 parameters altogether. SGF inner power supply provides stable operation in wide range of input voltage, up to +/- 50% from nominal. Also included in SGF are 2 auxiliary systems, used for beam guiding and beam diagnostics.

INTRODUCTION

High Voltage Terminal (HVT) in electron cooler is intended for generating of electron cooling beam and collecting the beam back, producing thus continuous up to 3A electron current. Due to this task, it consists of:

- Gun of electron beam, including cathode, anode and 4 control grid electrodes.
- Collector of electron beam, including collector, suppressor and 2 Wien filter electrodes.

Both grid and collector bodies are encircled with a number of magnetic solenoids intended for shaping a proper magnetic field profile inside. Also measurement of the collector current and the so-called leakage current should be provided. HVT has an outer metal shielding cap with smooth rounded shape, intended for uniform voltage distribution under high voltage circumstances. Powering of HVT electronics is provided by cascade transformer, that is a part of accelerator column, with output voltage varying in wide range of 400 – 800VAC at 26 kHz frequency [2]. Accelerator column itself provides up to 2MV negative acceleration voltage, so HVT chassis ground is under this voltage too.

The electronics needed for providing power supply (P.S.) for HVT electrodes and solenoids is divided on 3 separate units. The most power consuming is collector power supply, with up to 15KW output power, therefore it was designed as standalone unit equipped with an oil force-cooling system. Another unit, housing magnetic solenoids power supplies, is situated at opposed to collector power supply side on HVT chassis. The remaining electrodes power supplies are united in the third unit, named Gun-Filter System (SGF), it is mounted on top of the second unit. Each unit was developed by the different developer; we will focus from now on mainly on SGF unit.

SGF UNIT DEVELOPMENT

SGF power supplies detailed specifications are summarized in Table 1. Besides power supplying, the following additional requirements are imposed for SGF functioning:

- Each of 4 grid electrodes can be modulated individually with 3MHz sinusoidal wave at regulated amplitude from 0 to 8Vrms.
- Computer control of the whole cooler system is based on CAN protocol.
- Collector power supply unit control requires CAN control with optic fibre transport.
- Collector and leakage current should be measured by means of voltage drop on the corresponding resistors given.
- The collector to cathode return current is passed via HVT chassis.

Table 1: SGF Power Supplies Specifications

Name	Uout, Iout	Tolerance
Anode	0…+10kV, 1,5mA	0,1%
Suppressor	-3…+5kV, 3mA	0,1%
Control grid	-3…+5kV, 3mA	0,1%
Filament	+7…+25V, 5A	1,0%
Wien filter x2	0…+30kV, 1mA	0,1%

Connections requirements

The layout of collector and gun on the HVT chassis is illustrated in Fig. 1. Note how the electron return current (shown in red colour) flows on the chassis. Taking into account that the material of chassis is stainless steel, and the current value is up to 3A, care must be taken to eliminate unexpected voltage drops in control paths, because both gun and collector electrodes (shown in blue colour) are powered from a single unit (SGF), which is electrically and mechanically connected to the same chassis. Due to high risk of damage because of high voltage breakdowns and uncontrollable discharges, all electrodes power supply's return paths must be of low impedance, that is achieved by 10kV rated coaxial cable used for all electrodes except Wien filter electrodes. Those are to power with a voltage up to +30kV, so an appropriate shielded cable could not be used. Instead, a

high resistance (1kOhm/m) unshielded cable was used, with an external flexible shield manually enveloped.

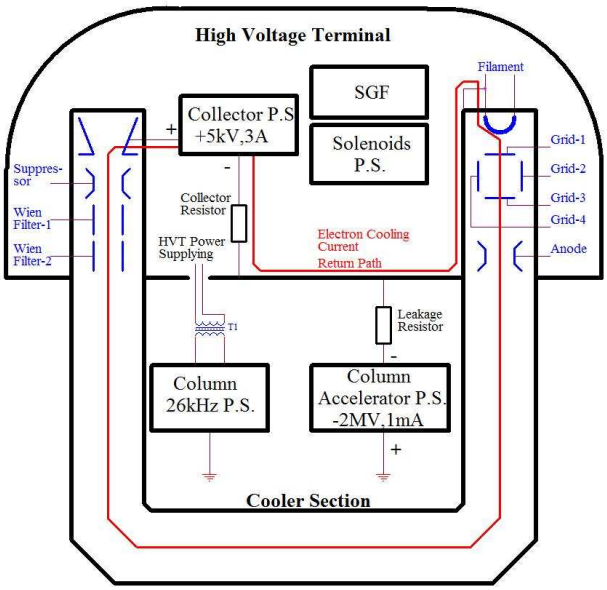

Figure 1: Position of High Voltage Terminal in COSY electron cooler.

A special attention was paid to cathode ground connection. The cathode implemented in gun is of filamentary type, with MHV-type sockets used as input pins, both isolated from ground. Since both collector return current and filament current (which are of the same order of magnitude) flow across a single pin, a special decoupling scheme was applied, using BNC T-connector and a zero resistance BNC terminator on one side of it. Furthermore, to eliminate chassis voltage drop, a phantom filament powering was implemented, withstanding up to +/-10V voltage output shift.

All high voltage electrode (except Wien filter electrodes) cables are connected to SGF face panel by means of LEMO high voltage sockets, and Wien filter cables are permanently fixed to SGF face panel. This provides more safety and reliability when routing high voltage cables in HVT.

Structural Considerations

Block diagram of SGF inner structure is shown in Fig.2. Input power AC voltage is down transformed to the value, which after rectifying is related to input voltage as follows: 400V set on control program's panel is corresponded to 40V DC of inner voltage, when no load is applied. The inner voltage is used by a number of DC/DC converters to produce all specified output voltages, along with +5V power supply for control modules. The DC/DC converters used have extra wide input voltage range of +18…+72V, it suited well to input voltage significant instability when all the system is under a load. But there can be situations, when input voltage exceeds the rated voltage. At this case, the overvoltage protection module shuts off the supplying DC/DC converters line at the level of +75V; in case of further increase to +150V level, the supplying line is forcedly shorted to ground, causing the fuse break.

Another protection channel monitors the leakage current. If this current exceeds 0,9mA, that indicates that the electron beam surely leaks to ground, anode voltage is forced to zero, and grid voltage is forced to -3kV to stop the electron current. This state is latched, and reset afterwards manually.

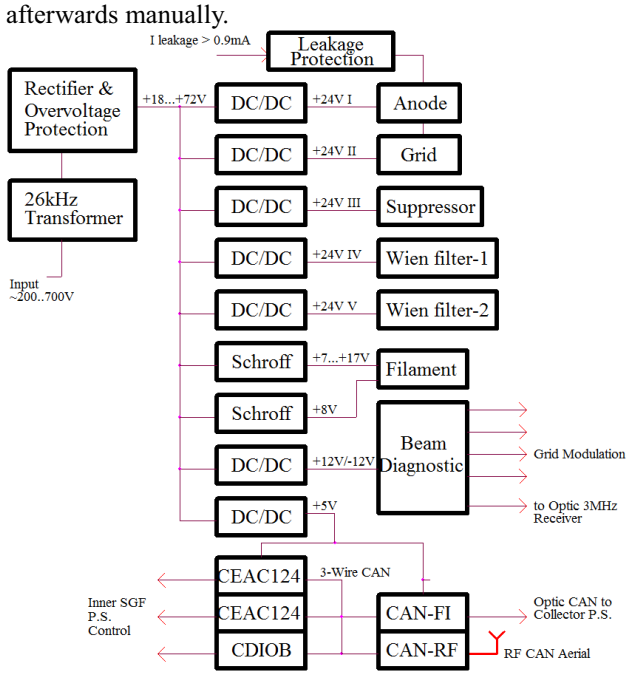

Figure 2: Block diagram of SGF.

All SGF output power supplies should have an output current control. In case of Wien filter power supplies, the MATSUSADA +30kV/1mA DC/DC converter fully satisfies this demand. At all other cases, a special schematic was used, illustrated in Fig.3.

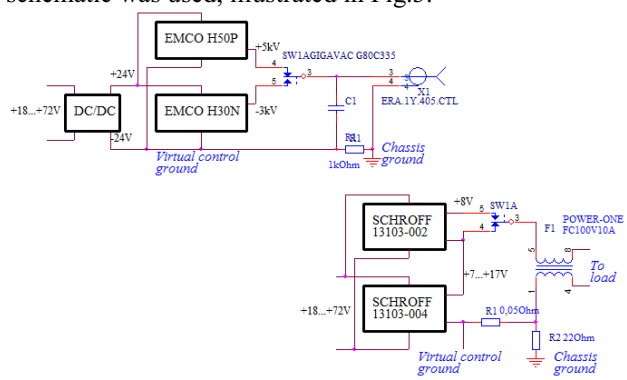

Figure 3: Output stages with current sense resistor.

On the top, the grid and suppressor output stage is shown, where two EMCO type DC/DC converters get isolated from ground +24V power supply. Positive or negative output is selected with a high voltage GIGAVAC type relay, after RC-filtering it connects to high voltage LEMO type output socket. Socket's case is mounted on grounded SGF face panel. The load current returns back across 1kOhm resistor, producing the voltage drop to measure. The similar is output stage of filament power supply, there output voltage is selected from either a

single regulated SCHROFF type DC/DC converter, or a sum of two converters; this approach gives a full +7…+25V output voltage range. High current (10A) output T-filter of POWER-ONE type effectively protects the output stage. To prevent the collector current leak into this circuit, as it was mentioned above, all output stage was isolated from ground, thus resembling phantom power supply, only single 22Ohm resistor ties negative output to ground to give the control function properly. Chassis current flow can run across this resistor, resulting in voltage shift that can be allowed up to +/-10V.

Beam Diagnostic and Control

To couple the high voltage grid power supply output and beam diagnostic outputs with four grid electrodes, a summing schematic, shown in Fig.4 is used, where 50Ohm low impedance modulator signals are decoupled with high voltage capacitors.

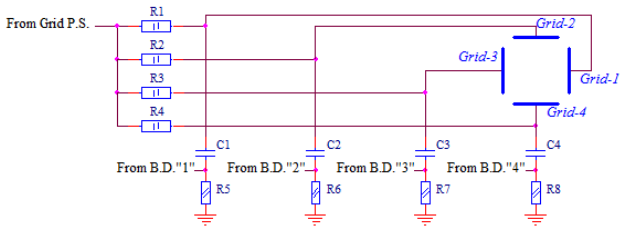

Figure 4: Feeding four grid electrodes.

Taking into account the low output impedance of grid power supply output at 3MHz frequency, channel-to-channel grid separation is better then 1%. Synchronising 3MHz signal the beam diagnostic module gets by a remote optical receiver, attached near inner shield cap window. The laser diode transmitter is situated on the matched outer shield cap window.

All the SGF control is concentrated in 3 modules: two widely used in BIMP DAC/ADC converter modules of CEAC124 type, and one CDIOB input/output register with extended functionality. These are CAN-controlled modules, so along with collector CAN-controlling it was a task to deliver CAN to HVT high voltage potential. The solution was made to use one wireless CAN module in SGF, while another wireless CAN module is fixed near the outer shield cap window. Both modules are of Agilion manufacturer. The distance of 50cm between them provides good reliability in communication. To provide the collector power supply with optic CAN, CAN-FI wired-to-optic CAN translator was used. The advanced control, provided by CEAC124 modules, gives wide opportunities to monitor all parameters of SGF modules.

Fig.5 illustrates a screenshot of the control program, where available are for every power supply: programming the output voltage, monitoring the output voltage by high voltage divider and from dedicated high voltage DC/DC converter output, monitoring the output current. Collector and leakage current values are shown in “Collector” tab. The beam diagnostic control is shown in corresponding tab too. Additionally, all inner voltage lines and temperature level inside SGF unit are monitored under “AUX PS” tab.

Figure 5: A screenshot of SGF control program.

SGF Design

For placing all the modules used in SGF, the SCHROFF EuroPak was chosen; it is the metal case with a standard 19inches wide, 6U height and 160cm depth dimensions. All the heat producing DC/DC converters were placed on the back panel, serving as heat radiator; heat dissipation of the modules is equalized by the natural convection of gas inside HVT volume. The SGF unit with all modules installed is shown in Fig.6.

Figure 6: The SGF unit front panel.

All cables except Wien filter cables are detachable. Both leakage and collector current signals are handled in a dedicated module, where low-pass filtering and clamping is applied.

RESULTS

Thorough testing of all cooler electronic systems in BINP showed that SGF unit can successfully withstand high voltage breakdowns up to 1,6MV while staying in good condition. Temperature level inside SGF unit is not exceeds 60° C at 5 days continuous cooler test under unconditioned room environment. Input voltage working span of +200V…+600V was confirmed.

REFERENCES

[1] J. Dietrich et al., “Status of 2 MeV electron cooler for COSY-Julich/HESR” PAC’11 New York, NY, USA, WEP229, p.1918-1920.

[2] V. Reva et al., “The first commission results of the high voltage magnetizied cooler for COSY” COOL’11 Alushta, Ukraine, THIOA02, p.37-42.

HIGH-VOLTAGE SOURCE WITH OUTPUT VOLTAGE UP TO 110 kV WITH OUTPUT CURRENT UP TO 100 mA

I.A. Gusev, A.S. Medvedko, A.Yu. Protopopov, D.N. Pureskin, D.V. Senkov,
BINP, Novosibirsk, Russia

Abstract

The presented report contains the description of high-voltage source with output voltage up to 110 kV and output current up to 100 mA. The source consist of the chopper with IGBT switches working with a principle of pulse-width modulation and the full H-bridge converter with IGBT switches, both working on programmed from 15 to 25 kHz frequency, and the high voltage transformer powering the four-stage multiplier with the additional capacity filter at output. The transformer and multiplier both are made in common volume separated on oil tank part with silicon oil for transformer and SF6 part for multiplier. The additional capacity filter provides low ripple and noise level in working range of output currents. A nominal output voltage of the source is 110 kV. The source can operate in normal mode with series of high-voltage breakdown in output voltage. In the high-voltage breakdown the released in load and matching circuit energy is less than 20 J at maximum operating voltage 120kV. The efficiency of system is more than 80% at the nominally output power 11 kW. The controller of the source is developed with DSP and PLM, which allows optimizing operations of the source. For control of the source serial CAN-interface is used. The description of the source and the test results are presented.

DESCRIPTION

The presented source was designed for some different applications at the BINP tasks. That was reason for some specific terms like: strong reliability to high-voltage breakdown, low energy dissipated in high voltage breakdown, low voltage ripple for maximal power operation. The energy is dissipated in components of source and in the load during the high voltage breakdown less than 30J for 110 kV operations. The basic characteristics of high-voltage source are shown in Table1.

Overview

The circuit diagram of power part of high-voltage source is shown in Fig.1. The high-voltage source consists of the 20 kHz power converter with insulated gate bipolar transistors (IGBT) as switches (part A) and high-voltage transformer with the four-stage multiplier (part B). The power converter consists of 3-phase rectifier VD1, electromagnetic (EMI) filter F1, switch SW1, rectifier's filter capacitors C1-C2, 20 kHz chopper with IGBT switch Q1, 20 kHz inverter with IGBT switches Q3-Q6, output filter circuit L2 C5 C6, and isolation transformer T1.

Table 1. Basic characteristics of high-voltage source.

Parameter	**Unit**			
		Min	**Nom**	**Max**
Output voltage	kV	10	110	120
Output current	mA	0.1	100	120
Output power	kW		11	
Voltage ripple	%			0.5
Voltage stability	%			0.2
Transient time	ms		50	
Converter frequency	kHz	15	20	25

Input Rectifier

EMI filter is used to eliminate high-frequency noise to the power line from the source. 3-phase rectifier and filter C1-C2 is used to convert input AC 3-phase voltage 380V 50Hz to DC 550-600V voltage. Contactor SW1 consists of 2 groups of contact: the first is used for soft start of converter and another is used for normal operations. First group of contacts is switched ON and the filter's capacitors C1-C2 are charged with 10A current. When the voltage on filter is up to 450 volts level the second group of contacts is switched ON and the rectifier is connected directly to 3-phase AC line.

Chopper

The chopper switch Q1 is operated with principle of pulse-width modulation on programmed from 15 kHz to 25 kHz frequency. The working frequency of inverter is the same. The operating frequency is selected depending on the characteristics of high-voltage transformer and the requirements to the spectrum of output high voltage ripple. The output voltage of chopper is changed from 10 to 450 volts DC by control circuit to obtain the required output high voltage of source.

Inverter

Full-bridge inverter Q3-Q6 converts DC voltage from chopper's capacitors C3-C4 to AC voltage with programmed from 15 to 25 kHz frequency. When the high voltage breakdown or over current is detected the inverter switches are switched OFF in 10 microseconds to protect power circuit from damage.

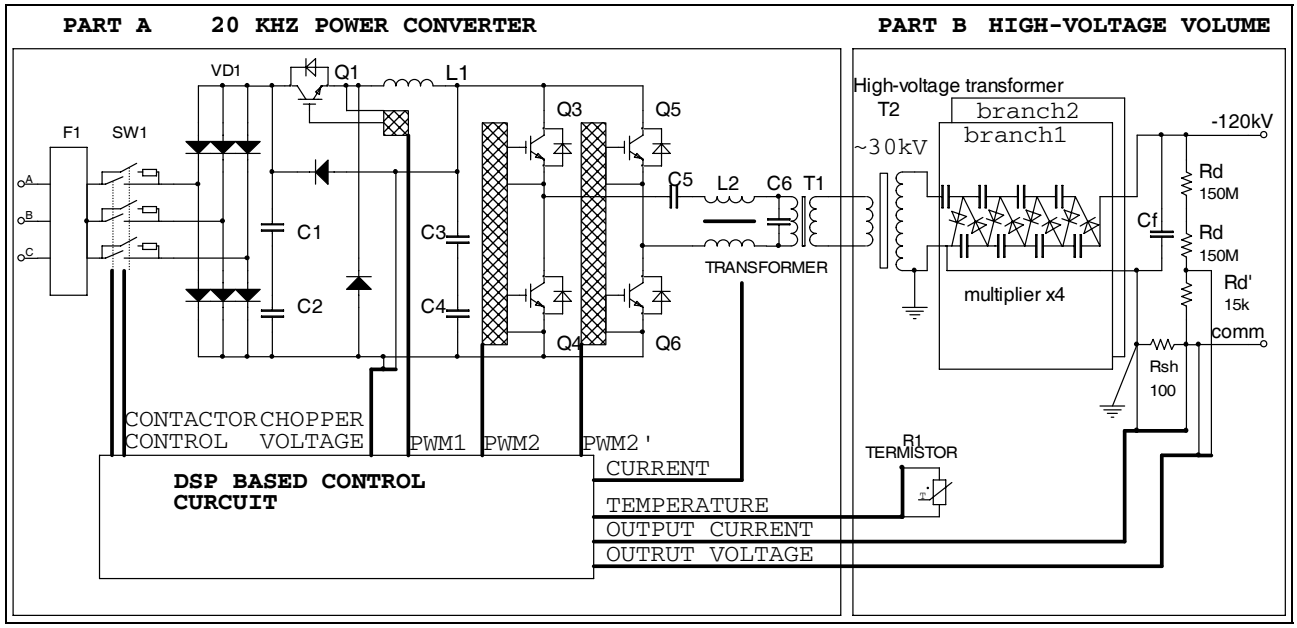

Fig.1. The high-voltage source block-diagram.

Filter Circuit

The power source must work with wide range of loads, from zero current to full load. The technical conditions for this high-voltage source are: transient process time interval must be less then 5 ms with transient overvoltage less than 20% for 110 kV operations for load switching between 1mA and 50mA (half load). The matching circuit consists of elements C5 and L2 and low pass filter L2 C6 are used for minimizing transient process and for improving efficiently of design. The matching circuit is used for protection reasons. When there is a high voltage breakdown or over current the matching circuit limits the rate of current rise in the inverter. Magnetising inductance of high voltage transformer, its capacitance calculated to primary side in parallel with C6 and the matching circuit organize low-pass filter for all high harmonics of inverters rectangular waveform voltage. That way, sinusoidal voltage is feed in the high-voltage transformer, because all high harmonics are filtered. In other case, the presence of high harmonics causes power dissipation in the coils because of skin-effect. Also this harmonics can induce the singing in the winding of high-voltage transformer and this effect increases the output zero load voltage and complicates the reduction transient over voltage.

High-Voltage Transformer and Multiplier

Sectioned high-voltage transformer consists of two high voltage sections, joined in series. The nominal output voltage of transformer is 30kV. The transformer is designed in oil-filled tank. The silicon oil [1] is used. This tank is located in the bottom part of high voltage volume. In top part of the volume is located four stage multiplier. The multiplier has two parallel connected brunches. Each brunch is the same.

The multiplier brunch is complete design and it includes multiplier, output filter capacitors, output current sensor and voltage divider resistors Rd, Rd`. Output filter capacity is chosen to decrease output voltage 40 kHz ripples less than 0.5% for full load operation. The sulfur hexafluoride (SF6) is used as insulator is this part of the high voltage volume.

Design

The converter is made in one 4U and three 6U crates in the rack of 19" Euromechanics standard. There are distilled water is used to cool IGBT switches and other elements.

The EMI-filter, input switch and input rectifier are positioned in the first 4U crate. The input filter capacitance, chopper's switches and choke are located in second crate. The chopper's capacitors, inverter and control circuit are located in the third case. And at last, there are capacitor and inductors of matching circuit located in the fourth crate.

Control Circuit

The control circuit is realised in digital signal processor (DSP), programming logic matrix array (PLM), and analogue input buffers. The control and analogue grounds are isolated from external signals and grounds and, that way, in control circuit has obtained low noise level. It allows operation with better then 0.1% accuracy. All the IGBT switches are protected from short circuit and overcurrent. The controller measured seven analogue channels with 12-bits resolution. These channels are shown in Table 2. The controller has CAN-bus interface which is used to link with an external control system. The used data rates are 125, 250 and 500Kbits in second. The protocol of CAN-bus interface is compatible with devises

produced in the BINP [2]. This controller circuit is an improved development of previous version used high voltage source [3].

Protections and Interlocks

There are two level of overcurrent protection: programmable and circuitry one. Rigid protection has a 140mA threshold level, if the output current increases up to 140mA or higher the all converter switches OFF. The programmable threshold level is tunable. If output current is higher then programmable threshold level (from 5 to 110mA) the converter first tries to limit current on this level than in case of failure all converter switches OFF. Switching OFF time is less then 50 microseconds. The converter tries to switch on output voltage after 100 milliseconds with rise speed 100V/msec. High-voltage transformer protection measures the temperature of transformer and the transformer's input current. In case the input current of transformer rises up to 250A that matter the short circuit in transformer. In this case the converter is OFF.

RESULTS

The high-voltage source was made and now it is in tests. The tests are shown high reliability, efficiency better than 85% for full load operations. The long time stability of output voltage was better than 0,2%. Voltage ripple was better than 0,5%.

Table2. Measured channels

Channel	Period	Range
Output voltage	50μsec	0-140.00kV
Output current (full range)	50μsec	0-150.0mA
Input current high-voltage transformer	50μsec	0-300A
Feedback signal	25μsec	0-3000mV
Input 3-phase voltage (r.m.s.)	1msec	0-600V
Input current (r.m.s.)	1msec	0-150A
Temperature of IGBT switches	1sec	0-70°C
Temperature of high-voltage transformer	1sec	0-100°C

REFERENCES

[1] http://www.sofex.ru/pdf/SOFEXIL-TCJ.pdf. Transformer fluid technical manual.

[2] V. R. Kozak, M. M. Romakch "The devices vith CANBUS interface for automatic control systems of physical complexes" pre-print BINP 2004-68, 2004

[3] I.A.Gusev, A.S.Medvedko, A.Yu.Protopopov, D.N.Pureskin, D.V.Senkov "High-voltage source with output voltage up to 60 kV with power current up to 1A", Proceedings of RuPAC 2010, Protvino, Russia.

3-CHANNEL CURRENT SOURCE WITH CHANNEL OUTPUT CURRENT UP TO 180 A AND OUTPUT VOLTAGE UP TO 180 V

I.A. Gusev, D.V. Senkov, A.I. Erokhin, V.V. Kolmogorov, A.S. Medvedko, S.I. Potapov, D.N. Pureskin, Budker INP SB RAS, Novosibirsk, Russia

Abstract

The presented report contains the description of 3-channel current source with channel output current up to 180 A and output voltage. Each channel can be operated and controlled independently. The source consists of 2 part. First part is charging source with capacitance bank at output. And the second part is 3 current sources powered by a capacitance bank. The charging source is converter with IGBT switches, working with a principle of pulse-width modulation on programmed from 15 to 25 kHz frequency, with high power rectifier at output. The source output voltage is up to 180 V, peak power is 40 kW and average power is 20 kW. Capacitance bank has 120 kVA storage energy. Second part contains 3 independent current sources with up to 180 A output current each. Each current source consists of H-bridge 2-quadrant convertor with MOSFET switches working on 50 kHz frequency and the output LC filter. The controllers of the sources are developed with DSP and PLM, which allows optimizing operations of the sources. The controllers are connected by internal control network for more flexibility and efficiency. The description of the source and the test results are presented.

DESCRIPTION

The presented current source was designed for supply of quadrupole magnets with 2 Hz ramping 180A current. There are three group of quadrupole magnets is used BF BD BG. That way three current sources are needed. Parameters Current scenario for quadrupole magnets is shown in Figure1. In the beginning there is a few-millisecond injection plateau - the current should be 1/15 from the maximum current and have the stability not worse than 0.05 %. It is followed by a 0.26-second controllable rise of current . The current stabilization accuracy at rising should be better than 0.1 %. Then there is a short flat-top for extraction of the particles with the fixed energy – followed by fall. The repetition period is 1 or 2 Hz.

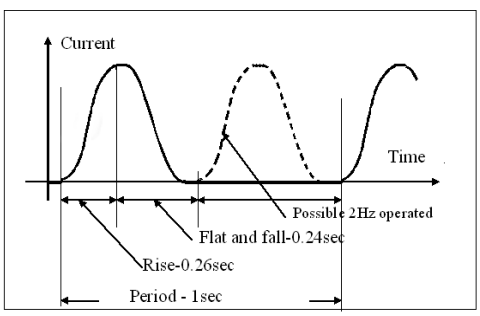

Fig.1. Current scenario.

The load parameters are the same for each channel. Load inductance is 0.14Hn. Load resistance is 0.3Om. At the specified current scenario, the average power of active losses is 2.5 kW for channel, the energy accumulated in inductance is 2 kJ. Time constant of the magnets is approximately 0.5 sec, thus, to provide the current fall during the necessary (<0.2 sec) time, the current source should be two-quadrant and the part of current from inductance at fall should be recuperated to the source buffer capacitor. The capacitance value is 0.1F per channel for 40V over voltage and 200V operating voltage. The selected diagram of power source is shown on Fig.2. The common 30kW bulk power supply with 200V output voltage and common 0.3mF capacitance bank are used. Three separate current sources are powered from capacitance bank. Each of the Output sources has their own channel of computer control via PSC and PSI controllers. Bulk Power supply is controlled current sources by local bus. The circuit with the single bulk PS and the common capacitance allows optimizing the magnet energy recuperation for asynchronous operation or for different values of maximum currents in channels.

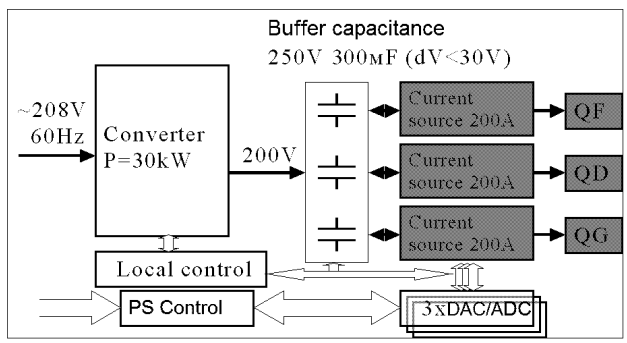

Fig. 2. Power source block diagram.

Overview

The current source circuit diagram is shown in Fig.3. The bulk power supply consists of 3-phase rectifier VD1, electromagnetic (EMI) filter F1, switch SW1, rectifier's filter capacitors C1-C2, 20 kHz inverter with IGBT switches Q1-Q4, isolation transformer T1 output rectifier circuit VD1-VD3, and the capacitance bank C4. The current sources are identical. Current source consists of input capacitance C5, 50 kHz two quadrant H Bridge with MOSFET switches Q5-Q12, filter circuit L1 C6 C7 and DCCT circuit.

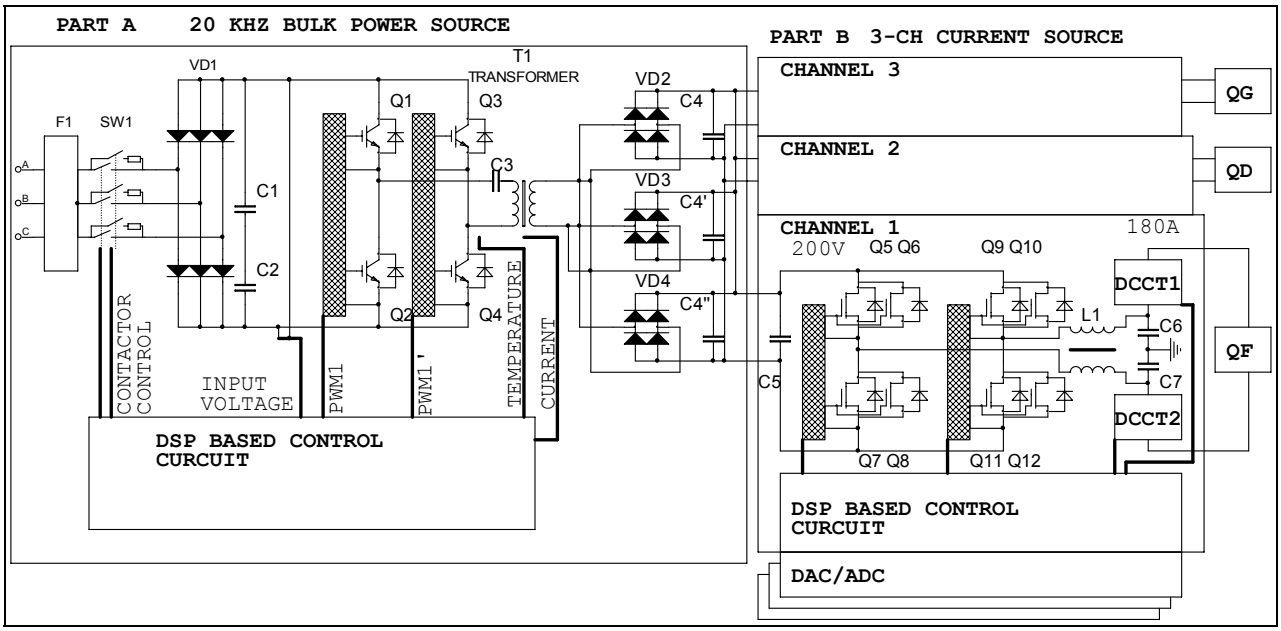

Fig.3. 3-channel current source circuit diagram.

Input rectifier

EMI filter is used to eliminate high-frequency noise to the power line from the source. 3-phase rectifier and filter C1-C2 is used to convert input AC 3-phase voltage 208V 60Hz to DC 300-350V voltage. Contactor SW1 consists of 2 groups of contact: the first is used for soft start of converter and another is used for normal operations. First group of contacts is switched ON and the filter's capacitors C1-C2 are charged with 10A current. When the voltage on filter is up to 250 volts level the second group of contacts is switched ON and the rectifier is connected directly to 3-phase AC line.

Inverter

Full-bridge inverter Q1-Q4 converts DC voltage from chopper's capacitors C3-C4 to AC voltage with programmed from 15 to 25 kHz frequency. When the short circuit or over current is detected the inverter switches are switched OFF in 10 microseconds to protect power circuit from damage.

Output rectifier

20 kHz voltage is decreased by transformer T1 from 350V down to 200V and is transmitted from three secondary windings to the rectifiers. From the rectifiers, voltage is transmitted for capacitors charging. Capacitance bank is divided on two parts. C4 0.15F capacitance is located near rectifier and another C5 48mF part is located in each current source. Voltage at the rectifier outputs is monitored. The current is already monitored at the current source input.

Current source

200 V-voltage from the converter output charges the buffer capacitor C1-C4, from which voltage is transmitted to H-bridge operating at 50 kHz frequency. The bridge is made on the doubled MOSFET transistors. The bridge operating frequency is determined by presence of the beam synchrotron oscillations zone at the frequencies from 20 to 33 kHz. So the converter operating frequency should be out of the given zone in order to avoid the ripple components with the frequencies coinciding with the synchrotron oscillation frequencies in the spectrum of output voltage frequencies.

From the MOSFET bridge output the PWM signal is sent to LC filter L1, C6, C7 filtrating a 50-kHz frequency, then, through two DCCTs, the current comes to the source output terminals. The first DCCT is used for the organizing of the feedback loop, the second one - for independent current measurement. Current source control unit compares the measurements of both DCCTs and, at difference of measurements, set the control circuit fault signal.

Design

The converter is made in one 4U and two 6U crates in the rack of 19" Euromechanics standard. Three quadrupole current sources are made in the 4U crates in the rack of 19" Euromechanics standard. There are distilled water is used to cool IGBT and MOSFET switches and other elements.

The EMI-filter, input switch and input rectifier are positioned in the first 4U crate. The input filter capacitance, inverter and Bulk PS control circuit are located in the second case. And at last, there are rectifier

circuit and capacitance bank are located in the third crate. Three current sources are located in another rack in three 4U crates

Control circuit

The bulk PS controller based is an improved development of previous version of PS controller used high voltage source [1].

The current source control circuit is realised on digital signal processor (DSP), programming logic matrix array (PLM), analogue input buffers and analogue feedback circuit. The control and analogue grounds are isolated from external signals and grounds and, that way, in control circuit has obtained low noise level. It allows operation with better then 0.01% accuracy.

All the IGBT and MOSFET switches are protected from short circuit and overcurrent. This protection has 2 levels. First level is the over current protection in driver, the switching OFF switches in case of over current and short circuit is the second level of protection. The MOSFETs has overvoltage protection too. The current source MOSFETs are switched ON if switch voltage exceeded 250V.

RESULTS

The current source was made and fully tested. The tests are shown high reliability, efficiency better than 85% for full load operations. The long time stability of output current was better than 0,1% for 8 hours. Current setup accuracy was better than 0,1% in both mode: ramp mode and continuous mode. The results of long time stability tests with ramp current scenario are shown on Fig. 4. The current was measured on the middle of ramp and on the top Plato.

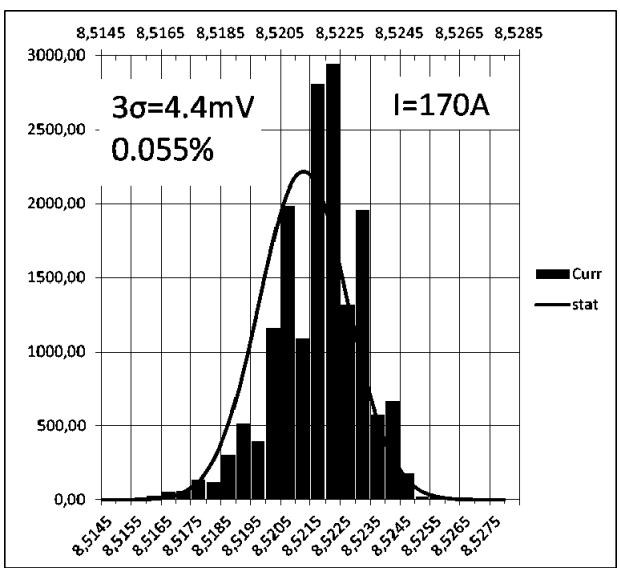

Fig 4a. Long time stability on top Plato.

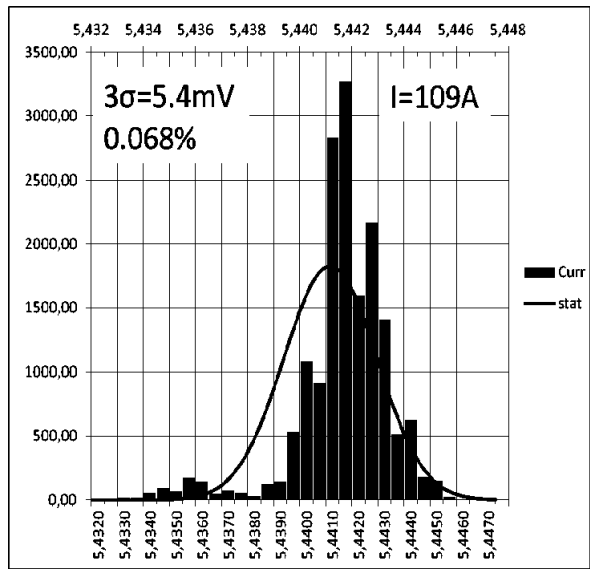

Fig 4b. Long time stability on ramp.

REFERENCES

[1] I.A.Gusev, A.S.Medvedko, A.Yu.Protopopov, D.N.Pureskin, D.V.Senkov "High-voltage source with output voltage up to 60 kV with power current up to 1A", Proceedings of RuPAC 2010, Protvino, Russia.

THE POWER SUPPLY SYSTEM FOR THE ACCELERATING COLUMN OF THE 2 MEV ELECTRON COOLER FOR COSY

D. Skorobogatov, M. Bryzgunov, A. Goncharov, I. Gusev, M. Kondaurov, V. Kozak, A. Medvedko, V. Parkhomchuk, D. Pureskin, A. Putmakov, V. Reva, D. Senkov, BINP SB RAS, Novosibirsk

Abstract

The 2 MeV electron cooler for the COSY storage ring (FZJ) is being assembled at BINP. The electrostatic accelerating column generates a high-energy electron beam. The power supply for the accelerating column of the electron cooling system consists of 33 controlled modules distributed by the accelerating potential. Each module has a precision controlled voltage source for 60 kV, 1mA and an additional supply for the solenoids of the magnetic system with a maximum current of 2.5 A. All the systems are controlled through the wireless ZIGBEE network. This report presents the structure of the power system, its parameters, and the results of tests carried out at BINP.

INTRODUCTION

In 2009-2012, BINP was involved in the creation of an electron cooler for heavy ions to be installed on the COSY accelerator of the Jülich accelerator center (Germany) [1, 2]. The main parameters of the cooler are as follows: the electron energy is 25 keV to 2 MeV and the current is up to 3 A. The energy instability will not exceed 10 ppm. Besides, the installation was designed with a proper account of limitations associated with the fact that it will be installed on an already-existing accelerator ring in an earlier-built building.

The accelerating column, where the electron beam is accelerated and recuperated, is one of the main components of the installation.

The main parameters of the accelerator column of the cooler are presented in Table 1:

Table 1: Main parameters of the accelerator column of the COSY cooler

Parameter	Units	Value
Electron energy	MeV	0.025 - 2.0
Energy instability, less than		10^{-5}
Magnetic field of the transport line	G	500
Field instability		10^{-3}
External power supply	V	600
Carrier frequency	kHz	26.2
Power consumption	kW	30-40
Total height of the column	m	3.7

To meet the requirements of the installation we had to develop a power supply system which along with precision output parameters would have high reliability in a strong magnetic field and at strong electrostatic discharges.

STRUCTURE OF THE ACCELERATING COLUMN

The structure of the accelerating column is shown in Fig. (1).

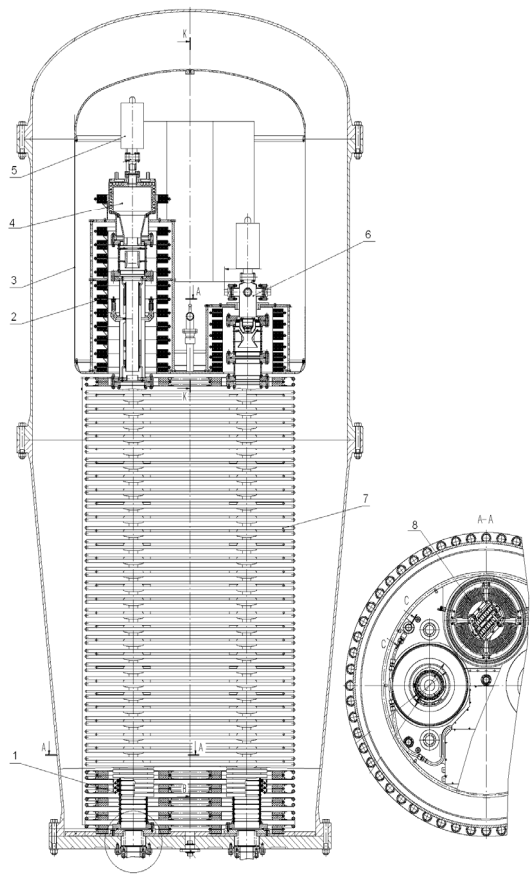

Figure 1: The structure of the accelerating column: 1 – accelerating tube; 2 – solenoid; 3 – high voltage terminal tank; 4 – collector; 5 – ion pump; 6 – electron gun; 7 – high voltage section; 8 – cascade transformer.

The accelerating column is a high-pressure tank, which is filled with SF_6, and houses accelerator tubes, high-voltage sections, cascade transformer, and high-voltage terminal. The high-pressure tank is limited in height by the existing building which houses the COSY accelerator.

The high-voltage terminal comprises an electron gun, collector, Wien filter, and various power supplies for these elements. The cascade transformer is to provide a required power for the acceleration sections and high-voltage terminal. The accelerating sections provide a voltage required for electron beam acceleration and in addition support magnetic field in the accelerating tubes.

Requirements to high voltage in the accelerator column are pretty tough: the ripple and long-term instability shall not exceed 10^{-5}. A voltage of 2 MV is generated by 33 high-voltage sections with a maximum voltage of 60 kV each. Besides the high voltage, is important to maintain the magnetic field along the accelerator tubes. The magnetic field is generated by a set of solenoids, two solenoids per accelerator section. Requirements to the power supply of the solenoids are not as stringent as to the accelerator voltage; the ripple shall not exceed 10^{-3}.

The general view of the section is shown in Fig. (2).

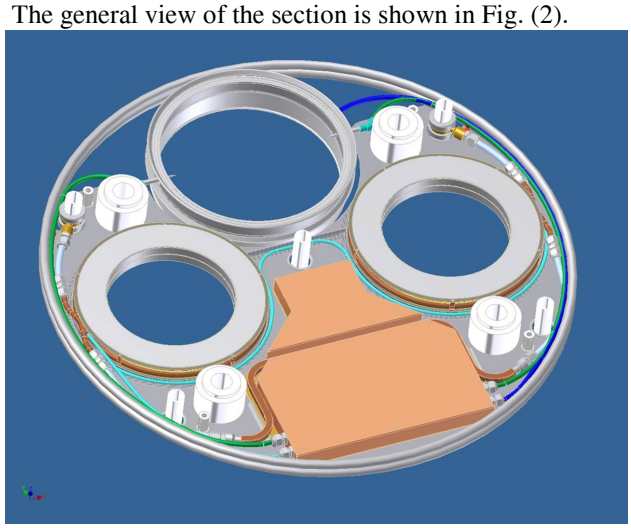

Figure 2: The general view of the section.

The high-voltage section is powered from the power-takeoff winding on the corresponding section of the cascade transformer. One section consumes no more than 350 W, about 90 W for generation of high voltage and the rest for maintenance of the magnetic field. Acceptable supply voltages vary from 100V to 250V. Externally, the section looks like a disc 40 mm high of 1000 mm in diameter, with a cut for the cascade transformer, closed with screens from above and below. The bottom screen is also a load-bearing element and supports the entire structure. Along the perimeter, the section is shielded with metal bands. A section comprises two solenoids and an electronics unit. Since the sections are arranged densely, natural cooling is rather hindered. That is why we provided an oil circulating system for cooling of the solenoids and electronics. The electronics unit is enclosed in a shielding housing, structurally divided into two parts. A general view of the unit is shown in Fig. (3).

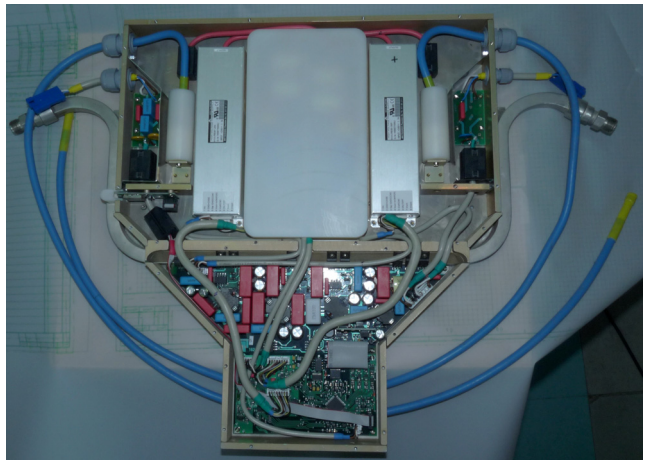

Figure 3: General view of the electronics unit of section with the shield panel raised.

The larger part of the housing is occupied by high-voltage sources and filtering and protection elements on the electrical inputs and outputs from the housing. This part also comprises a high-precision high-voltage divider for provision of feedback in the high-voltage stabilization circuits and a transceiver for communication with the controlling server by the radio frequency channel. The second part of the housing contains a power electronics board, which provides power supply to the high-voltage electronics of the solenoid, and the controller board.

KEY POINTS OF THE ELECTRONICS OF THE SECTION

From a user's point of view, the electronics of the high-voltage section is a high-precision regulated high-voltage power supply (1 mA 60 kV) and a regulated current source for powering the solenoids of the magnetic system, integrated into a single housing. The control interface is realized in a ZigBee self-organizing network based on Telegesis transceivers [3]. This network operates in the 2.5 GHz radio frequency band, which allows doing without a large number of optical lines and simplifies the mounting and maintenance of the system. The structure of the section is shown in Fig. (4).

Prior to beginning work on the accelerator column, we developed a prototype high-voltage section, on which we conducted preliminary tests of all systems of the section and debugged the feedback of the power supplies. In addition, we tested resistance to magnetic fields and electrostatic discharges. Optimal electronics shield housing was designed. In the course of high-voltage tests, different versions of passive protection in circuits external to the screened enclosure were tested, and the presence of strong magnetic fields made us use precision resistive shunts with galvanic isolation instead of current sensors based on the Hall effect.

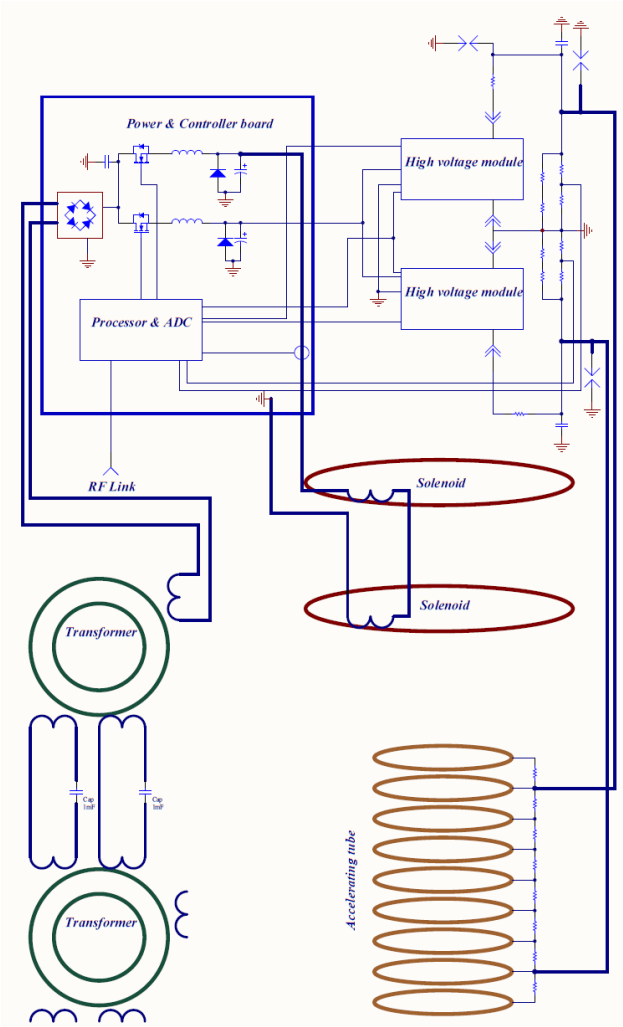

Figure 4: The structure of the section.

A set of programs with graphical interface was developed for control and monitoring of the accelerator column. The graphical interface of the program is shown in Fig. (5).

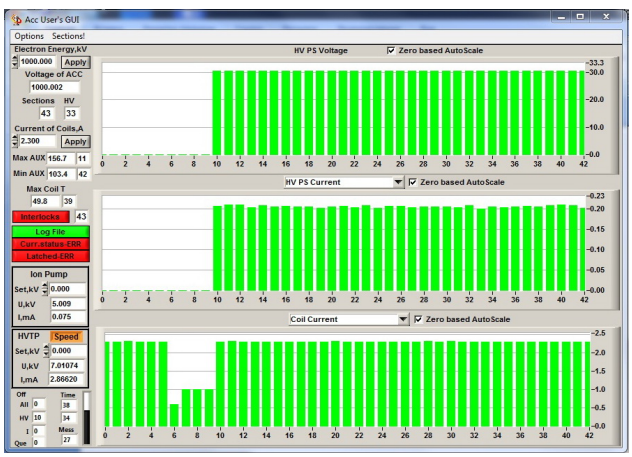

Figure 5: A screenshot of the graphical interface of the accelerator column control software. An accelerating voltage of 1 MV, a high voltage of about 200 μA, and a current in the solenoids of 2.3 A.

RESULTS

The entire electron cooling system and individual units of the installation were tested at BINP in the spring and summer of 2012. High-voltage tests were carried out at voltages in the column of up to 1.8 MW and a current in the magnetic system of up to 2.5 A.

Numerous high-voltage breakdowns at voltages of 200 kV in air and up to 1.6 MV in SF_6 at a pressure of 6 Bar allowed us to identify and eliminate trouble spots in the power supply system. The final high-voltage tests and operation of the system for approximately 5 days showed that the power supply system of the high-voltage column in general meets all the requirements of the electron cooler.

ACKNOWLEDGEMENTS

Special thanks to Alexander Semenov for the careful assembling of the sections and column.

REFERENCES

[1] J. Dietrich et al/ “Status of 2 MeV electron cooler for COSY-Julich/HESR” PAC’11 New York, NY, USA, WEP229, p.1918-1920.

[2] V. Reva et al/ “The first commission results of the high voltage magnetized cooler for COSY” COOL’11 Alushta, Ukraine, THIOA02, p.37-42.

[3] “ETRX357 ZigBee module” http://www.telegesis.com /downloads/general/ETRX35x_Product_Brief.pdf

POWER SUPPLY SYSTEM OF THE PULSE BENDING MAGNET FOR THE LINEAR ACCELERATOR OPERATED AT THE MOSCOW MESON FACTORY

B.O. Bolshakov#, A.A. Budtov, A.V. Pozhenskiy, A.V. Popov,
D.V. Efremov Scientific Research Institute of Electrophysical Apparatus, Saint Petersburg, Russia
O.V. Grechov, V.N. Michailov, V.L. Serov, A.V. Feschenko,
Institute for Nuclear Research RAS, Moscow, Russia.

Abstract

To ensure simultaneous operation of the linear accelerator in the experimental and isotope production systems, a pulse (kicker) magnet with its power supply system (pulse modulator) has been designed and manufactured in the D.V. Efremov Institute by an order of the INR RAS. The pulse magnet with its power supply system has been installed in the INR RAS and adjustment works have been performed. In the paper are described a schematic and principle of operation of the pulsed magnet and modulator deflecting a part of proton macropulses to the isotope production system. The results of the adjustment works performed are presented in the paper.

INTRODUCTION

To widen the potentialities of simultaneous operation with the beams produced by the linear accelerator operating at the Moscow Meson Factory (Troitsk town), a special pulse electromagnet(kicker magnet) with a supply system (pulsed modulator) has been designed and manufactured. The magnet pulsed at a repetition rate of 50 Hz allows a deflection of a 100-160 MeV beam of H^+ или H^- ions by 13º to a target intended for production of isotopes. The rest macropulses intended for physical experiments pass without distortion of their trajectories.

REQUIREMENTS FOR KICKER MAGNET

The kicker magnet is intended to replace the used permanent electromagnet, therefore, overall and setting dimensions should be kept the same. In addition, the magnet was supposed to operate both in the pulse and continuous modes, and a sufficiently high induction in the magnet yoke, 0.85 T, was chosen. The pulse of the current passing through the magnet is of a half-sinusoidal shape; the current pulse length is 12 ms. The pulse repetition rate is 50 Hz. When a pulse ceases, the residual magnetic field should be minimum so that the second macropulse can pass without a deflection. When a 200 ms macropulse is passing, the magnetic field non-uniformity at the half-sinusoid top is 0.05%. To keep stable 13º bending of a proton macropulse, the long-term pulse-to-pulse reproducibility of the magnetic field should not exceed this value.

#Bolshakov.BO@luts.niiefa.spb.su

Table 1: Main Parameters of the Kicker Magnet

Parameters	Q-ty
Bending angle for 100-160 MeV proton beam	13º
Pole straight section length (uniform field), mm	350
Pole width (uniform field), mm	145
Gap height, mm	60
Magnet inductance, H	0.03
Magnetic half-sine pulse length, ms	12
Winding cooling	Water

PULSE MAGNET DESIGN

As the kicker magnet is pulsed at a repetition rate of 50 Hz, to reduce the eddy current heating of the magnet yoke it was assembled of 0.35 mm- thick laminations of electrotechnical steel 3413 previously thermally treated and with insulating coating [1]. Figure 1 shows the general view of the magnet.

Figure 1: The kicker magnet at a test facility.

To reduce the edge effect along the beam axis, pole shimming is provided. To give a necessary shape to magnet poles, prior to assembly steel laminations have been milled in stacks, each of 5 sheets, at least. Thus the damage of the insulation between laminations was minimized. The direction of the electrotechnical steel rolling is perpendicular to the pole surface. All the laminations are glued with an epoxy compound under press and are tied with sheets of stainless steel.

The windings are divided into four separate coil sections. Two sections are fixed on the upper pole and other two are fixed on the lower pole. Each section is wound of a rectangular conductor 8×8 mm in cross-section; a circular channel is made inside the conductor through which the cooling water circulates.

POWER SUPPLY SYSTEM OF THE BENDING MAGNET

For the supply of the kicker magnet, a special pulse modulator has been designed and manufactured in the D.V. Efremov Institute. The output parameters of the modulator are given in Table 2. Figure 2 shows a functional diagram of the pulse modulator of the kicker magnet.

Table 2: Main parameters of the pulse modulator

Parameters	Q-ty
Magnet current maximum amplitude, A	430
Maximum amplitude of voltage across the magnet, V	3200
Power consumed by the modulator, W	36000
Recuperation current amplitude, A	3000
Pulse-to-pulse instability of the magnet current amplitude, not worse than, %	±0.05
Long-term instability of magnet current amplitude, not worse than, %	±0.05
Magnet current amplitude step, A	0.02
Pulse repetition rate, Hz	25-50
Modulator current pulse shape	Half-sine pulse
Modulator half-sinusoid pulse length, ms	12

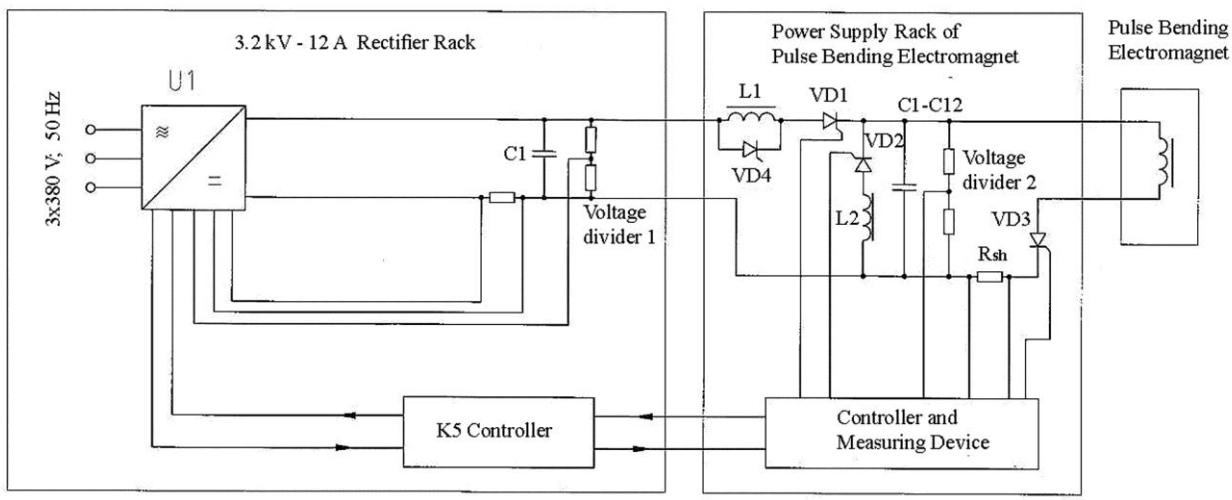

Figure 2: Functional diagram of the power supply system of the pulse bending electromagnet for the Moscow Meson Factory, the INR RAS

The pulse modulator consists of a high-voltage power supply rack-U_1 and a power supply rack of the magnet. The principle of operation of the pulse modulator is based on the discharge of a capacitor bank into a magnet inductance. Voltage for C1-C12 capacitors charging is supplied from the high-voltage power supply U1 through a charging resonant choke L1 and a unit of charging thyristors VD1. When a VD3 thyristor turns on, the magnet inductance is turned on in parallel with C1-C12 capacitors. A resonance circuit formed by these capacitors is tuned to a frequency of 42 Hz, which corresponds to the half-sinusoid length of 12 ms. On the half-period termination, capacitors recharge, the current decreases to zero and the VD3 thyristor turns off.

To recharge the capacitors, a recuperation choke L2 is turned on through a VD2 thyristor. Less than 2 minutes is sufficient to recharge the capacitors.

In response to a comparator signal, the charging choke is shunted by a VD4 thyristor. To ensure a necessary stability of the current pulse (0.05%), the pulse power supply system includes two current feedback loops.

Figure 3 shows the pulse modulator installed in the hall housing the life-support systems of the accelerator.

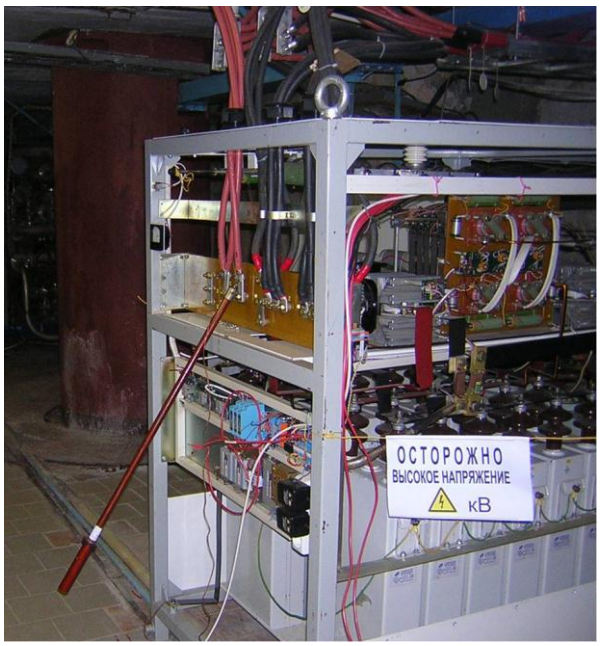

Figure 3: The power supply rack of the kicker magnet in the hall housing water and vacuum systems of the proton accelerator.

TESTS OF THE KICKER MAGNET WITH PULSE MODULATOR

The IM.103 B2-1 Hall probe was used to measure the main magnetic field on the magnet axis. The residual magnetic field was measured with the AD22151YR Hall probe. These probes provide necessary measurement accuracy. Simultaneously, the magnet current was measured with a current shunt. Signals were read on the Tektronix TDS2012 oscilloscope. The relative instability of the magnetic field amplitude and non-uniformity of the sinusoid pulse top were measured ±100 μs from the pulse top center.

At a pulse repetition rate of 50 Hz, the long-term, 4-hour, instability was less than 0.05%. Pulse-to-pulse instability was also less than 0.05%, which completely meets the performance specifications. The short-term, several-second, falls of the magnetic field amplitude outside the allowable limits were observed. However, the proton beam was switched off for these time moments, and this should not influence the accelerator operation.

The residual magnetic field after the main pulse caused an anxiety. The measurements performed demonstrated that it was lower than $5 \cdot 10^{-4}$ T, which completely meets the performance specification.

CONCLUSIONS

The kicker magnet with the pulse modulator designed and manufactured in the D.V. Efremov Institute for the linear accelerator operated in the INR RAS (the Moscow Meson Factory) meets the main technical requirements. Active losses in the pulse magnet and pulse modulator appeared to be close to design values. The used technique of the magnet yoke assembly allowed high eddy current loss to be avoided. The residual magnetic field after the main pulse was lower than we expected.

REFERENCES

[1] Electrotekhnicheskaya stal, 3413 GOST 21427.1-83 produced by NLMK.

[2] H.W. Alvestad, “Design, Fabrication, and Test of a Kicker Magnet and Modulator for the IPF Beam Line,” EPAC, 02, Paris, June 2002, p. 2382.

SYSTEM OF VACUUM MONITORING OF SYNCHROTRON RADIATION SOURCES OF NATIONAL RESEARCH CENTRE KURCHATOV INSTITUTE

N. I. Moseiko, V.N. Korchuganov, Yu.V. Krylov, L.A. Moseiko, D.G. Odintsov, B.I. Semenov, A.V. Shirokov, National Research Centre Kurchatov Institute, Moscow, Russia

Abstract

The modernization project of the vacuum system of the synchrotron radiation source at the National Research Centre Kurchatov Institute (NRC KI) has been designed and is being implemented; it includes a change in the system to high-voltage power sources for NMD and PVIG–0.25/630 pumps. The system is controlled via the CAN bus, and the vacuum is controlled by measuring pump currents in a range of 0.0001–10 mA. The system ensures a vacuum of 10–7 Pa. The status is mapped and the data collected into the archive are processed on the MS SQL Server platform. The efficiency and reliability of the vacuum system is increased by this work, making it possible to improve the main parameters of the SR source.

INTRODUCTION

The vacuum system of the SR source (synchrotron) should ensure a vacuum of 10–7 Pa. In this case, NMD-type magnetic-discharge diode pumps with a pump capacity of 0.16 m3/s and 0.4 m3/s are placed on the small ring of the synchrotron. PVIG 250/620-type vacuum-ion-getter stations with a pump capacity of 0.25m3/s/630 l/s are placed on the large ring of the synchrotron.

EQUIPMENT OF THE VACUUM SYSTEM

Works on replacing outdated DIV-6 vacuum power sources with a 5-kV output voltage, used for energizing PVIG 0.25/630 pumps (800 pieces) in the BS storage of the synchrotron, are completed. The DIV-6 sources were replaced by new VIP-27 high-voltage four-channel power sources with a 5-kV/7-kV supply voltage [3]. The use of VIP-27 sources allowed us to increase pump capacity by 30% and reduce the time it takes to bring the system (after opening the chamber) to the operating conditions of the synchrotron by 10 h.

The VIP-27 source is controlled by BUP-27 units, which also measure the output voltages (*U*P) and currents of sources (*I*P) of the pumps (which used to be measured by outdated IVA-16 units). The VIP-27 power source with the BUP-27 control unit are placed in a standard 3U Euromechanics crate (Fig. 1). For powering 80 vacuum pumps of the large ring of the SR source, twenty crates with VIP-27 power sources and BUP-27 units are used. The SQL-server of the vacuum system controls the power source of all the pumps via a common CAN bus. Data on the pump currents (*I*P) obtained by it are transmitted to the main server of the SR source.

VIP-27 High-Voltage Power Source

Let us present the main technical characteristics of the VIP-27 source (Fig. 1) designed at OOO KBST (Vyborg). The VIP-27 source ensures the following: an open-circuit voltage of 5.0 ± 0.1 kV and 7.0 ± 0.1 kV, an output voltage no smaller than 4 kV with a load current of 4 mA and a setup open-circuit voltage of 5 kV, an output voltage no smaller than 6 kV with a current load of 4 mA and a setup open-circuit voltage of 7 kV, a short-circuit current of 10 ± 1 mA, and a remote switch to the START mode from the STOP mode and the other way around.

Fig. 1. VIP-27 power source.

Physically, the VIP-27 source is fulfilled in a 19" Euromechanics standard basket with a 3U height (133 mm), 84TE width (426 mm), and 300-mm depth. The basket contains six 12TE modules of equal width (60 mm), namely, four high-voltage modules, one power-supply module, and one BUP-27 interface control/diagnostic module. The power system consumption is no higher than 150 W.

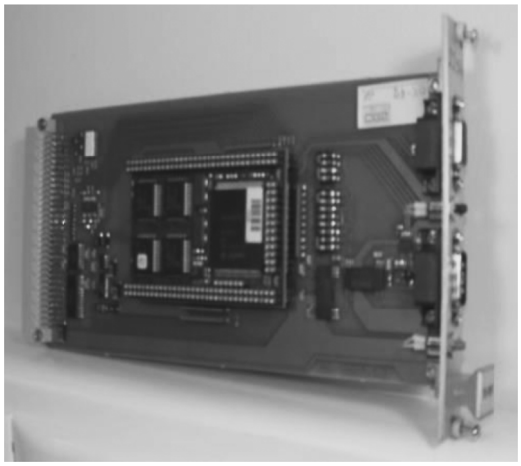

Fig. 2. BUP-27 control unit.

The BUP-27 unit is based on a mini MODUL-167 SBC computer, and it is the interface card (Fig. 2). The VIP-27 unit is intended for the control of four channels of the VIP-27source via the CAN bus. It is connected to the computer through the CAN bus or RS-232 interface. It ensures the on/off switch of each channel, the selection of the output voltage (5.0/7.0 kV) of each channel, and measurements of the amplitudes of the output voltage and current of each channel to determine the vacuum. The mini MODUL-167 of the SBC computer (further referred to as mM167) switches the channels of the VIP-27 source on and off using signals applied to output optical couplers. The output voltages and currents of the VIP-27 channels are determined with the use of the 24-bit AD7732 ADC, which measures the voltages of eight pseudodifferential signals, proportional to them. The printed circuit card of the BUP-27 controller is fulfilled in the Euromechanics constructive with a 3U height, 220-mm length, and 4TE width (20 mm) of the front panel.

SOFTWARE OF THE VACUUM SYSTEM

The software of the vacuum system includes three levels [2, 3]. The lower level is the executive program operating in the BUP-27 unit under control of the RTX-166 operational system. The database is the MS SQL Server and inquiry formatter on the server (Pentium personal computer (PC) using Windows XP). The upper operator level is the network applications (which are the SQL server clients) for mapping the status and processing the data collected into the archive. The clients of the following three types are designed in Delphi and SQL languages. The first client ensures access to a dynamically changing parameter table, in which it reads the latest measured values of selected channels (currents and voltage of vacuum pumps). After processing, the data are outputted either in graphic form or to the information panel on the PC screen, which shows the status of the vacuum system; the serviceability of the equipment; and, using variations in color and in sound signals, warns the operator about deviations from the rated value. The client of the second type processes archives and outputs currents of selected pumps for the specified time interval in tabular or graphic forms. A separate client type, operating on the server in singular form, is a program which supports connections with the BUP-27 control units and constantly (with a 5-s period) replenishes the dynamic data table with new measured data.

Database Editing

We consider in more detail the operation of the modernized vacuum system using the finalized software version [2]. All database (DB) editing facilities in the dialog mode are brought into it. Figure 3 shows one of the main windows of the DB editing program.

Fig. 3. DB editing.

There are four tables in this window, which are filled from left to right and from top to bottom. First the upper left table is filled; then the upper right, the bottom right, and the bottom left tables are filled. After the filling of the next (in turn) table, it is necessary to press the key with a green arrow. The numbers of the superperiods of the BS storage and the names of synchrotron systems on which the vacuum pumps are placed are entered into the *Segment* table of the vacuum system. The names of racks which belong to the selected segment are entered into the *Rack* table. The numbers of VIP-27 power sources are entered into the *Level* table. The names of vacuum pumps with the number of the BUP-27 control unit and the number of the channel to which each pump is connected are entered into the *Pump* table. The operating parameters of the BUP-27 channel (pump power supply On/Off; 5-kV or 7-kV power-supply setup) are also set.

The dialog DB editing method is intended to promptly change the configurations of the vacuum system,

connecting pumps to different VIP-27 power sources, BUP-27 units, and their channels. This reduces the time and resources to ensure the uninterrupted operation of the complex and multichannel vacuum system of the SR source.

TESTING OF THE VIP-27 POWER SOURCES

To test the VIP-27 power source controlled by the VIP-27 unit, a program was designed which is intended to promptly check the serviceability of all channels and determine the technical characteristics of the channels: the speed of operation and measurement errors of currents in each channel of this source by the BUP-27 unit and errors of voltages produced by the VIP-27 source to the vacuum pumps. Reference passive loads were used when the channels were tested.

Figure 4 shows the form of the VIP-27 testing program. Before the test startup, the test is intended to specify the data transmission rate via the CAN bus from 125 Kbaud up to 1 Mbaud, the number and order of BUP/VIP-27 tested channels, the interrogation period of channels of the source from 1 ms up to 10 s, and the VIP-27 unit measurement error of voltages of 0.1 V or 1 V and source currents of 0.1 μA or 1 μA. After the test startup, it allows one to select a 5-kV or 7-kV supply voltage for each channel and to switch on or off the power-supply unit of any channel.

The measurement results of current and voltages (running values, average values of the last 100 measurements, and variance) are outputted in digital and graphic form. The testing of the BUP-27/VIP-27 channels demonstrated that the equipment operates reliably; the vacuum measurement rate of the new vacuum equipment can reach 500 Hz (i.e., it is 100 times higher than older equipment); and the measurement error of 5-kV/7-kV supply voltages and currents of the source for reference passive loads does not exceed 0.1 V and 0.1 μA, respectively (when load currents reach 100 μA), at a stable temperature (a change within 5°C) in a range of (20–35)°C.

The high measurement rate and large memory of the computer of the BUP-27 unit allow one to accumulate up to 2500 sample/s in each channel for an interrogation cycle of the vacuum system. These data can make it possible to more accurately diagnose the vacuum state in channels and to more quickly find failures of the system operation and reasons for vacuum violation. The interrogation period is 100 ms; 7-kV voltages were connected in turn to 1, 2, 3, and 4 channels.

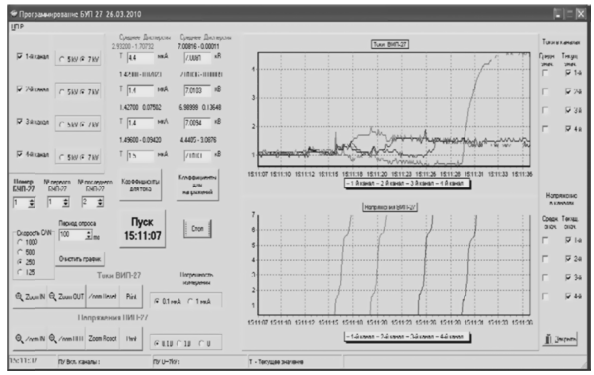

Fig. 4. VIP-27 testing program form.

CONCLUSIONS

The new system provides reliable work of all 132 vacuum pumps. As a result of our works, the throughput of pumps significantly increased and the time and resources for ensuring the uninterrupted operation of the complex and multichannel vacuum system of the SR source were substantially reduced. The increase in the efficiency and reliability of the vacuum system allowed one to improve some important parameters of the SR source such as the lifetime of electrons in the SIBERIA SR source.

REFERENCES

[1] M. Blokhov et al., "Kurchatov Synchrotron Radiation Source Facilietes Modernization," in Proceedings of RuPAC-2010, Protvino, Russia, pp. 136–140.

[2] E. Kaportsev et al., "The Expanded Program Tools for KSRS Operation with Archivatio of Data," in Proceedings of RuPAC-2010, Protvino, Russia, pp. 187–189.

[3] Y.Krylov et al., "Enhancement of Vacuum Monitoring System of KCSR Accelerator Facility," in Proceedings of RuPAC 2006, Novosibirsk, Russia, pp. 264–266.

CYLINDRICAL PHASED DIPOLES ARRAY FOR HYPERTHERMIA OF DEEP-SITUATED TUMORS

S.M. Polozov, A.M. Fadeev, V.N. Belyaev, National Research Nuclear University MEPhI, Moscow, Russia
E.A. Perelstein, JINR, Dubna, Moscow Region, Russia

Abstract

The treatment of deep-situated malignant tumors is often a difficult problem in which the purpose is to reduce the size of completely remove a tumor by using one or more modalities. The traditional methods are: radiation therapy, chemotherapy and surgery. Hyperthermia is another method which is used alone or coupled with other methods of cancer treatment. Hyperthermia is a heating of the tumor that makes it more sensitive to chemotherapy or radiation therapy and leads to it thermal damage. Temperature range for hyperthermia treatment is from 42.5 °C to 45 °C. It is important to prevent heating of healthy tissues and to produce sufficient heating at the site of a deep-situated tumor. This kind of hyperthermia is called the local hyperthermia. The electromagnetic field in 100-200 MHz frequency range is optimal for heating of deep-situated tumors. The system for local hyperthermia of cancer was simulated. This system is based on cylindrical phased array consisting of multiple dipole antennas with operating frequency 150 MHz. The electric fields and specific absorption rate distributions are calculated in cut of tissue-equivalent phantom. Shown that electric field can be focused in desirable region by means of varying of amplitudes and phases of each dipole. The advantages of using combined therapy of common hyperthermia with chemotherapy or radiation therapy are discussed.

INTRODUCTION

Hyperthermia is a good adjuvant for the common modalities such as surgery, radiation and chemotherapy. It is proved that cancer cells are dying under the heating and the main goal is to deliver heat into source of disease without damaging of nearby healthy tissues [1-3]. Also suitability of using hyperthermia combined with radiation and chemotherapy is proved [4, 5]. Efficiency required that temperature within tumor remain above 43 °C for 30 to 60 minutes, while limit temperatures in normal tissues has to be lower than 43 °C. Noninvasive heating of deep-situated malignancy is a difficult technical challenge. Electromagnetic field is more prior for creating higher level temperature in desirable volume than other methods of physical effect. High penetration ability of radiofrequency EM field into human body in comparison with other frequencies ranges makes using of radiofrequency promising for distance hyperthermia. As temperature increase occurs not at the expense of heat transfer from surface to inwards, but because of electromagnetic field absorption, danger of skin burns is decreasing. This fact makes fields in 100-200 MHz frequency range is optimal because wave length in human body is proportional with body's sizes. The thermal effect lead to lysosome activation, tissue breathing and protein synthesis inhibition, tissues pH decreasing, kariokynetic cycle modification, trans membrane transfer improvement, sensitization tumor cells to chemotherapy and growing up immunity. Moreover basic advantages of electromagnetic hyperthermia occurs on radio resistance tumors, in other words on cells with high reparation effect from radiation. First of all hyperthermia decelerates cell's reparation and secondly induces strong heat damage of zone with bad thermal sink, hypoxia zone.

PHASED DIPOLE ARRAY

Cylindrical phased dipole array is proposed for creating high level temperature inside patient body. In this paper we assume that phased array consists of eight dipole antennas arranged on an inner side of a cylindrical plastic shell. Dipoles are surrounding the patient body and the amplitude and phase of each antenna is under control of the operator as shown in Figure 1. The space between patient's body and dipoles is filled with deionized water (conductivity $\sigma \approx 0$). Hereby dipole antennas are squeezed between the high-permittivity medium inside the tank ($\varepsilon \approx 80$ for water) and the low-permittivity medium outside the tank. We assume to use flowing deionized water not for cooling only. Due to the electric field energy density ($1/2 \cdot ED$) inside the tank is higher by a factor ε (the relative dielectric constant of the medium) the E-field energy is extremely concentrated in the inner side of a tank. The frequency of operation is chosen to be 150 MHz.

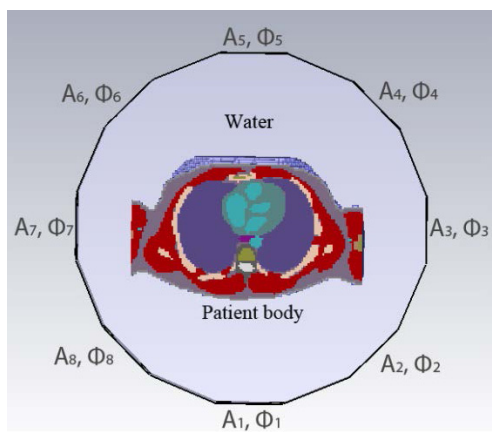

Figure 1: Patient body surrounded by phased dipoles array. Dipole antennas have amplitudes $A_1 \ldots A_8$ and phases $\Phi_1 \ldots \Phi_8$ respectively.

We have Maxvell's equations:

$$\nabla \boldsymbol{E} = i\omega\mu \boldsymbol{H}, \quad (1)$$
$$\nabla \boldsymbol{H} = -i\omega\varepsilon_c \boldsymbol{E}, \quad (2)$$

where to $\boldsymbol{E}$ and $\boldsymbol{H}$ is the complex amplitude of the electric and magnetic field correspondingly, μ is the magnetic permeability, $\varepsilon_c = \varepsilon + i\sigma/\omega$ is the complex permittivity, σ is the electric conductivity. Isolating $\boldsymbol{E}$ in (1) and (2) we have:

$$\nabla(\nabla \boldsymbol{E}) - k^2 \boldsymbol{E} = 0, \quad (3)$$

where k is the complex wavenumber $k^2 = \omega^2\mu\varepsilon + i\omega\mu\sigma$. E_j is the solution of E-field for antenna j scaled by the amplitude and phase take into account:

$$E_j = A_j E_{j0}(x,y) e^{i\Phi_j}, \quad (4)$$

where E_{j0} is the complex field for $A_j = 1, \Phi_j = 0$, and $A_k = 0$ for $j \neq k$. A time variation of the form $\exp(-i\omega t)$ is dissembled.

The specific absorption rate (SAR) or absorbed power per unit mass (W/kg) is given by:

$$SAR(x,y) = \frac{\sigma E E^*}{2\rho}, \quad (5)$$

where E is the total electric field at the point (x,y), E^* is the complex conjugate of E, σ is the electrical conductivity of tissue and ρ is the density of tissue.

E is the sum of the electric fields from each of the dipoles and the absorbed power per unit mass becomes:

$$SAR = \frac{\sigma}{2\rho} \sum_{j=1}^{8} \sum_{k=1}^{8} A_j A_k E_j E_k^* e^{i(\Phi_j - \Phi_k)} \quad (6)$$

Due to varying amplitudes and phases of dipole antennas necessary distribution of SAR is produced, in other words we can focus electromagnetic field in desirable volume (tumor) and to minimize energy absorption in healthy tissues.

RESULTS

Simulation of SAR patterns in horizontal plane with phantom filled with water is shown on Fig. 2. Four different combinations of relative phases are used. Here higher energy absorption is shown in red. As seen the maximum SAR peak moves either in horizontal or in vertical directions (amplitudes stays constant). High level of SAR around outer edge (not shown on the picture) is appeared because of the high near field neighboring with each dipole, which has little influence on heating process inside of the phantom. This temperature rise can be decreased by flowing water without any effect on heating inside the phantom. As seen, the SAR peak moves away from antenna with higher phase shift. The value of SAR is maximized when all antennas are in phase.

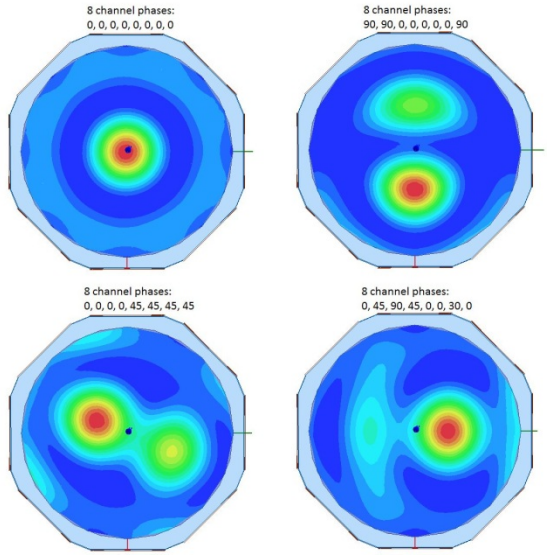

Figure 2: Results of simulation in the transverse cut for four combinations of phases. Combinations are provides movement of the SAR peak in both horizontal and vertical.

Fig. 3 shows SAR pattern in x-y plane of tissue equivalent phantom. This phantom is a primitive model of human leg with diameter 24 cm. Tumor size is 30 mm. All tissues are labeled on the picture. RMS feed power of each dipole is 0.5W. Dielectric properties of body tissues used in simulation are presented in Table 1 [6]. Phases are adjusted to focus heat onto tumor. If bottom antenna would be first and to keep count counter-clockwise, relative phases will be: $\Phi_1 = -5°, \Phi_2 = 30°, \Phi_3 = 50°, \Phi_4 = 65°, \Phi_5 = 50°, \Phi_6 = 30°, \Phi_7 = -5°, \Phi_8 = -5°$. All amplitudes still stay constant. As seen, the SAR peak is moved away from antenna 5 (relative phase 65°) as we noted above. The SAR minimum is located in bone due to low conductivity and high density in comparison with muscle tissue. Also we can decrease power absorption in outer side of phantom by using flowing water with constant cooling temperature.

Table 1: Dielectric properties of human tissues used in simulation.

Tissue	Relative permittivity	Conductivity [S/m]	Density [kg/m^3]
Muscle	62.18	0.73	1047
Fat	5.84	0.04	955
Bone	14.41	0.07	1990
Tumor	74.5	0.9	1047

For accurate simulation we have to use real body model, which will be obtained after CT or MRI scanning. SAR distribution in longitudinal cut of voxel human leg is shown on Fig. 5. All antennas are in phase, amplitudes are

equal. Maximum SAR is 1.63 W/kg with RMS feed power 0.5 W on each dipole. For hyperthermia in thorax or abdomen we have to use lower frequencies for deeper penetration of electromagnetic fields onto human body.

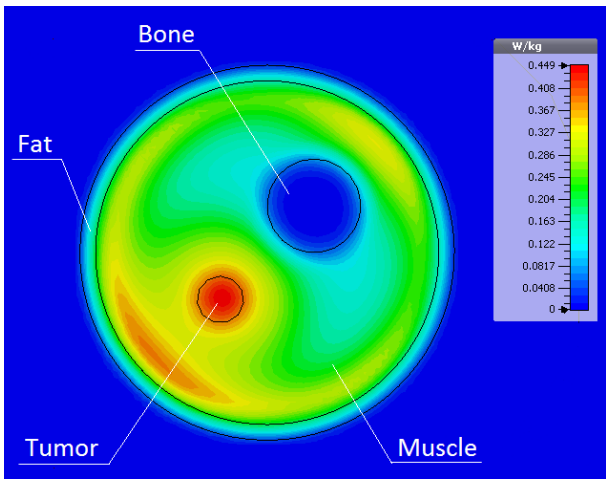

Figure 3: SAR distribution in transverse cut of phantom with adjusted relative phases. Tissues are labeled. RMS feed power of each dipole is 0.5W.

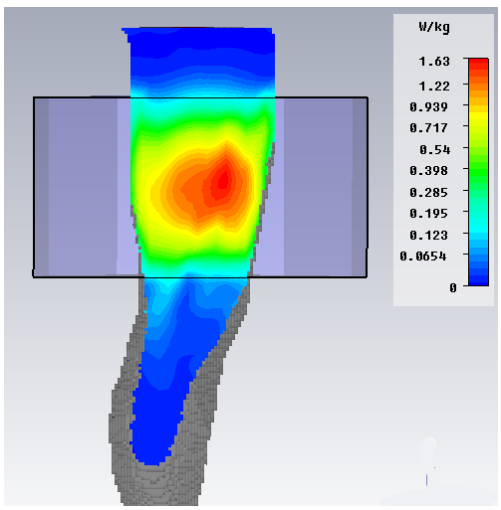

Figure 5: SAR distribution in longitudinal cut of voxel human leg. All antennas are in phase. RMS feed power of each dipole is 0.5W.

CONCLUSION

Combined therapy using the hyperthermia with the radiotherapy of the chemotherapy is very perspective methods of the cancer treatment. The efficiency of combined therapy is evaluated on practice. Cylindrical phase dipole array is proposed for electromagnetic hyperthermia of deep-situated malignancy.

As was noted above, using of voxel models is preferable for more accurate simulation. For these goals we develop software which able to produce voxel model of human body (or body parts). Further different tissues are separated and assigned to the relevant dielectric and thermal properties.

Also software for solving bio-heat transfer equation is under developing, where we have to take into account perfusion, thermal conductivity and tissue specific heat, which will be used for thermodynamic simulation, i.e. for planning of hyperthermia procedure. The bio-heat transfer equation is solved for changes in temperature [7]:

$$\rho c \frac{dT}{dt} = \kappa \cdot \nabla^2 T - \rho \rho_b c_b F (T - T_b) + \rho \cdot SAR \qquad (7)$$

where T is temperature, t is time, ρ is tissue density, κ is thermal conductivity, c is the tissue specific heat, F is the blood flow rate (perfusion), type “b” is for blood. This equation shows relate between temperature’s rise over the time in a desirable region to the heat inputs (SAR) and heat losses from thermal conduction and convection (blood flow rate).

REFERENCES

[1] M. Ardenne, Theoretische und experimentelle Grundlagen der Krebs-Mehrschritt-Therapy, Berlin, 1967.
[2] N.N. Alexandrov, N.E. Savchenko, et al., Hyperthermia and hyperglycemia in malignancy treatment, Moscow, 1980., p. 12-15 (in Russian).
[3] Leo E. Gerweck, Hyperthermia in Cancer Therapy: The Biological Basis and Unresolved Questions, Cancer Res 45, p. 3408-3414, 1984.
[4] van der Zee J. Heating the patient: a promising approach? Annals of Oncology, 13(8), p. 1173–1184, 2002.
[5] P. Wust, B. Hildebrandt, G. Sreenivasa, et al. Hyperthermia in combined treatment of cancer, The Lancet Oncology; 3(8): p. 487–497, 2002.
[6] Dielectric properties of body tissues in the frequency range 10 Hz – 100 GHz, http://niremf.ifac.cnr.it/tissprop/
[7] H.H. Pennes, Analysis of tissue and arterial blood temperatures in the resting human forearm, Journal of Applied Physiology, 1, 1948, p. 113–121.

RF POWER AND CONTROL SYSTEMS FOR PHASED DIPOLES ARRAY SYSTEM FOR HYPERTHERMIA

S.M. Polozov, A.M. Fadeev, V.N. Belyaev, A. Blinnikov, National Research Nuclear University MEPhI, Moscow, Russia
E.A. Perelstein, JINR, Dubna, Moscow Region, Russia

Abstract

Cylindrical array of independently phased dipoles is suggested for hyperthermia of deep-situated tumors as a kind of treatment of cancer coupled with other methods such as radiation therapy and chemotherapy. It was proposed to focus the maximum of electromagnetic field at the site of tumor to produce high efficiency heating of tumor and to prevent overheating of surrounding healthy tissues. That's why we use system of independently fed dipole antennas. The operating frequency is 150 MHz. The independent feeding permits us to focus electromagnetic field producing by phased array in desirable area by means of changing of amplitudes and phases of each dipole. The RF power system schematic layout for 8 independently phased dipole antennas is presented. The control system of RF power system elements is considered. The software developing to provide the choosing of amplitude's and phase's values of dipoles are discussed.

INTRODUCTION

Many clinical and experimental studies have shown promising results in using of hyperthermia coupled with radiotherapy or chemotherapy for treatment of malignancies [1-3]. Treatment requires that temperatures within tumor remain above 43 °C during 30-60 min, while maximum temperature in normal tissues have to be lower than 42°C. Cylindrical phased dipole array is proposed to produce difference between temperature in healthy tissues and tumor. Range in 100-200 MHz of electromagnetic wave produced by dipoles is prior because wave length in human body is proportional with body's sizes. Phased array consists of eight dipoles arranged on inner side of plastic shell and surrounds patient body like it shown on Figure 1. Deionized water filling space between patient and array is for cooling outer side of body and for better matching. The E-field energy is extremely concentrated in the inner side of a shell due to the electric field energy density inside the shell is higher by a factor ε (the relative dielectric constant of the medium) than outside the shell.

Phased array provides desirable distribution of electromagnetic field inside of the patient body. The specific absorption rate (SAR) or absorbed power per unit mass (W/kg) is given by:

$$SAR(x,y) = \frac{\sigma E E^*}{2\rho}, \qquad (1)$$

where E is the total electric field at the point (x,y), E^* is the complex conjugate of E, σ and ρ are the electrical conductivity and the density of tissue respectively.

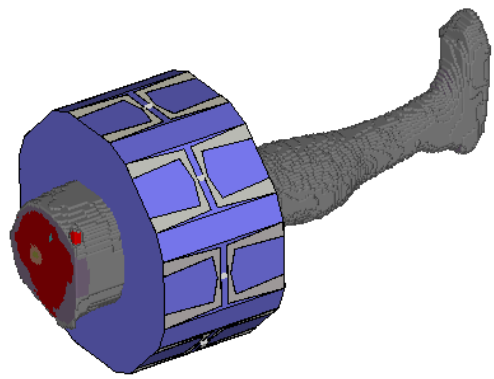

Fig. 1: Voxel model of leg inside phase array.

E_j is the E-field for antenna j scaled by the amplitude and phase take into account:

$$E_j = A_j E_{j0}(x,y) e^{i\Phi_j}, \qquad (2)$$

where E_{j0} is the complex field for $A_j = 1, \Phi_j = 0$, and $A_k = 0$ for $j \neq k$. A time variation of the form $\exp(-i\omega t)$ is dissembled.

Necessary distribution of E-field can be reached by means of independent feeding of each dipole that permits us to vary amplitudes and phases of electromagnetic field. In other words we can concentrate absorption energy of E-field and deliver therapeutic heat in tumor and at the same time prevent extra heating of normal tissues.

RF POWER SCHEME

As it was noted above, the RF power supply have to be independent for each dipole. The RF power system schematic layout is shown in Figure 2: 1 – driving generator with input signal's frequency range 100 – 300 MHz and input impedance 50 Ohm; 2 – 8-out power splitter (for example Mini-circuits ZBSC-8-82+); 3 – voltage-controlled phase shifter (Mini-circuits JSPHS-150) with frequency range 100 – 150 MHz, phase range 180°, control voltage 0 – 12 V; 4 - solid state amplifier (Mitsubishi RA60H1317M1A-101) with frequency range 135-175 MHz, output power – 60 W, supply voltage – 12.5 V, control gate voltage 12.5 V; 5 – 10 dB uni-directional coupler (Werlatone Model c7929, 100-

200MHz, 200 W, 10.0±1.0 dB Nom, 6 – load absorbed, 50 Ohms, 7 – phased array with patient body inside.

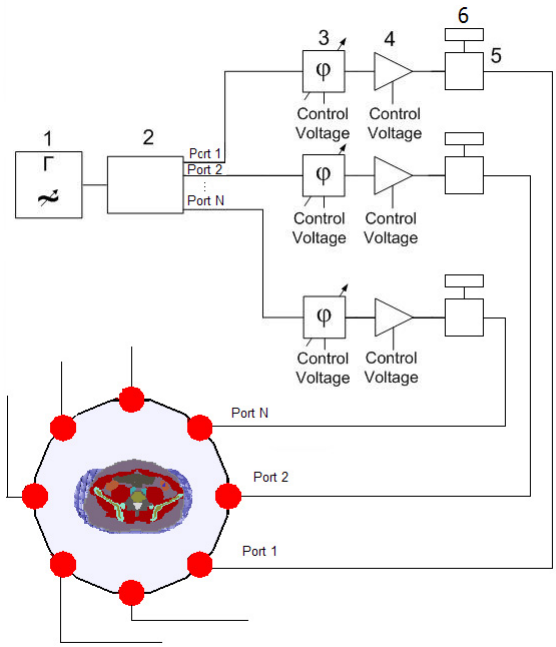

Fig.2: RF power system schematic layout.

The operating principle of such layout is the following. The RF signal at 150 MHz from signal source splits into 8 channels. Then by means of controlled 8 phase shifters and 8 solid state amplifiers we can adjust phase and amplitude of every signal. Due to these adjustments electric field focusing in the desire region is available. Directional couplers prevent reaching reflected wave to generator. Reflected wave will be absorbed by 50 Ohm load.

Modern solid state amplifiers are simple and stable in operation and can derive the necessary amplification. For example, solid state RF amplifier Mitsubishi RA60H1317M with amplify frequency range of 135-175 MHz and supply voltage 12.5 V can be used to provide the necessary RF power (to 60 W) and SAR values. The control of RF power can be realized using amplifier's gate channel which provide the turn on/off of amplifier.

CONTROL SYSTEM

RF power system control scheme is shown in Figure 3: 1 – control unit; 2, 3 – signal shaping units for amplifiers and phase shifters correspondingly. Control system of phased array is based on Arduino Mega. Arduino Mega is a microcontroller board based on the ATmega1280. It has 54 digital input/output pins (of which 14 can be used as PWM outputs), 16 analog inputs, 4 UARTs (hardware serial ports), a 16 MHz crystal oscillator, a USB connection, a power jack. Control unit gets data about amplifier's and phase shifter's values from PC and generates signals, which passing through units 2 and 3 operate amplifiers and phase shifters. Signal from 1 generates a pulse-width modulation (PWM) signal. Further signal passing through RC-filters situated in both 2 and 3 units, goes to gate pin of amplifier. Because of control voltage of phase shifter varies in 0-12 V, we have to use operational amplifier with $K_u=2.6$ in unit 3.

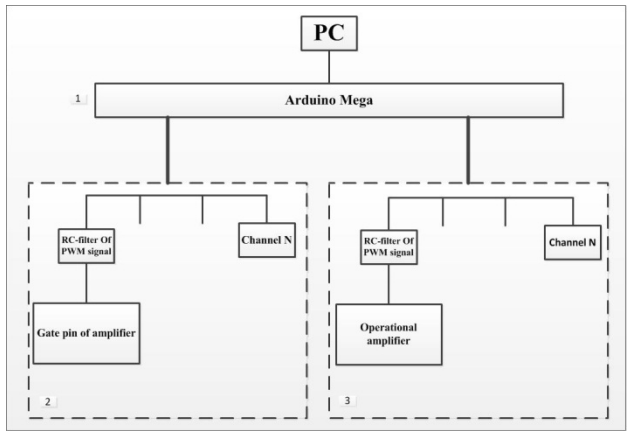

Fig.3: Control system schematic layout.

CONCLUSION

Phased dipole array is proposed for hyperthermia of oncological disease. RF dipole antennas produce difference between temperatures in tumor and healthy tissues because of ability to focus electromagnetic field in tumor side. Also different dielectric properties influence on absorption process. Focusing of E-field is achieved by varying of phases and amplitudes of each dipole, i.e. we have to use independent feeding of dipoles.

RF power system realizing this approach is discussed. Control system based on microcontroller board Arduino Mega Schematic layout is described. Also software for convenient controlling of hyperthermia phased array is developed.

REFERENCES

[1] Dewhirst M.W., Vujaskovic Z., Jones E., Thrall D. Re-setting the biologic rationale for thermal therapy. International Journal of Hyperthermia. 21(8), p.779–790, 2005.

[2] A.W. Guy, History of Biological Effects and Medical Applications of Microwave Energy, Microwave Theory Tech. 32, p. 1182, 1984.

[3] Bagshaw, M.A., Taylor, M.A., Kapp. D.E., et al., Anatomical site specific modalities for hyperthermia, Cancer Rex 44(Suppl), p. 4842-4852, 1984.

DATA PROCESSING AND QUANTITATION IN NUCLEAR MEDICINE*

E.D. Kotina, V.A. Ploskikh, St. Petersburg State University, St. Petersburg, Russia

Abstract

Accelerators of charged particles, radiation detectors are widely used in nuclear therapy and nuclear diagnostics. So there is necessity for diagnostic processing of data obtained using these devices. Nuclear diagnostics is based on analysis of radiation passing through the study object emitted from radiopharmaceuticals within the object or from external radiation source. First stage of data processing is presentation of detector signals in 2D or 3D image form. Further processing is based on mathematical modeling of processes within the investigated object. Mathematical modeling of static, dynamic and periodic processes is considered for quantitative analysis of studies in nephrology, osteology, endocrinology and cardiology. The data processing and quantitation software suite is presented. Clinical applications of the developed suite are discussed. Possibilities of software deployment in clinical centers are considered.

DATA ACQUISITION

The NM diagnostic methods study the activity distribution of object.

Nuclear imaging system consists of n_d logical detector units. Detector units need not correspond to physical detectors. Examples of detector unit are Anger camera projection bin at a particular projection angle ($n_d=n_x n_y n_\Theta$), a line of response in PET ($n_d=(n-1)n/2$, where n is a number of detector crystals). Radiation detection hardware registers emission radiation of radiopharmaceutical and forms the flow of registration events. The event carries information about detector unit and time of registration. Registration software during the time of acquisition accumulates events in a projection data array. Exact structure of the array depends on the hardware type and operating mode.

Discrete formulation of the projection problem reads:

$$p=Hx,$$

where x is a column vector of $n_x n_y n_z$ elements corresponding to activity distribution, p is projection data array and H is the system matrix. Each element H_{ij} of H is defined as the probability that emission event occurred in voxel j is detected by i-th logical detector unit.

Depending on studied process temporal nature three basic hardware operating modes can be distinguished [1, 2]:

Static. During the static acquisition it is assumed that the activity distribution function does not vary in time. The goal of static studies is to analyze spatial distribution of radiopharmaceutical.

Dynamics. During the dynamic scan several projection data arrays are formed in sequence. Dynamic studies used to analyze processes of radiopharmaceutical redistribution.

Gated acquisition. Gated acquisition is used in cardiac cycle analysis. The acquisition computer defines the number of time slots to divide the R to R interval of the patient's electrocardiogram. Electrocardiogram guides the acquisition so a projection data array is formed for each time slot.

After acquisition projection data should be corrected for various physical effects: attenuation, Compton scattering, Poisson noise, false coincidences et al.

Planar SPECT projection data is presented as sequence of 2D images. Projection data arrays of tomographic studies are subjected to reconstruction methods and presented as series of 3D data volumes.

For mathematical modeling purposes we consider these series of images as discrete representation of continuous radiopharmaceutical density distribution function $\rho(t, x)$. In 3D case the density distribution function coincides with the source activity distribution function. In 2D case the density distribution function is a projection of the source activity distribution to the detector plane.

DATA PROCESSING

Quantitative analysis is based on computation of various parameters for regions of interest (ROIs). The first step is to extract these ROIs from raw projection data.

Segmentation

In SPECT data processing various region extraction techniques are used. In most cases of static planar processing human-drawing ROI tools is the most simple and flexible method. This method also used in planar dynamic studies in conjunction with patient motion correction methods.

Specialized applications may use organ specific detection methods (fig. 1)

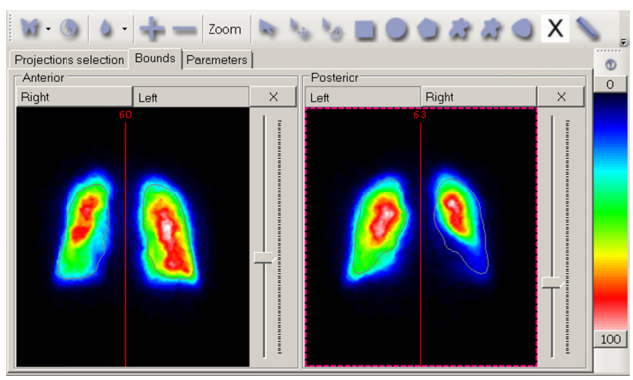

Figure 1: Automatic segmentation in lung perfusion.

*Work supported by SPbGU, grant 9.39.1065.2012

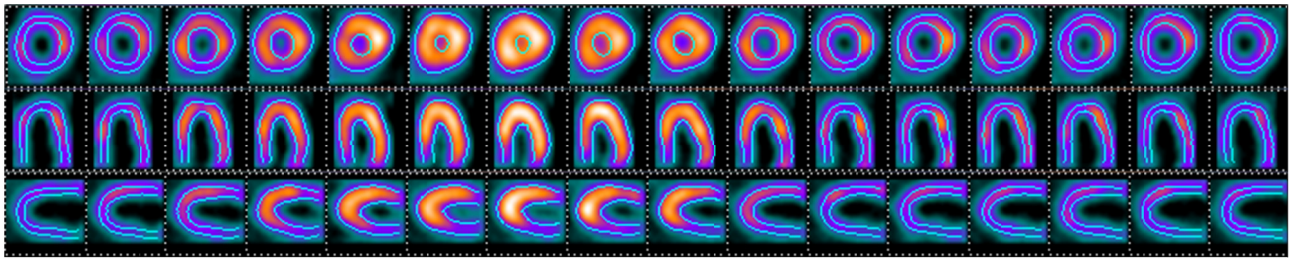

Figure 2: Left ventricle segmentation in gated SPECT.

Volume and gated segmentation techniques incorporate complex automatic and semi-automatic edge-detection algorithms based on detection of isocount surfaces, adaptive thresholds, coordinate transformations, models of mechanical motion, gradient and velocity field analysis.

Mathematical Modelling

In radionuclide studies of the functional state of organs and systems mathematical processing of data is very important. In the interpretation of the data it is necessary to know the features of transport of the radiopharmaceuticals in the study of the physiological system, knowledge of the structure and interactions of the structural elements of the system under study.

For quantitative analysis of the results of radionuclide studies of the functional state of various organs and systems mainly two approaches are presented: the calculation of the complex variety of amplitude and time parameters directly from dynamic curves constructed by regions of interest, the definition of physiologically meaningful parameters that characterize the state of the organ under investigation based on mathematical modeling [3]. Parametric imaging based on the definition of parametric (functional) transformation can also be considered as formal mathematical model of the process, in order to obtain additional diagnostic information.

Since the processing of data uses a model representation of transport indicators describing the system of ordinary differential equations

$$\begin{aligned} \dot{x} &= u(t,x,y), \\ \dot{y} &= v(t,x,y). \end{aligned} \tag{1}$$

Let us consider the following equation together with equation (1):

$$\frac{\partial \rho}{\partial t} + \frac{\partial \rho}{\partial x}u + \frac{\partial \rho}{\partial y}v = 0, \tag{2}$$

under initial condition

$$\rho(t_0,x,y) = \rho_0(x,y), \tag{3}$$

where $\rho_0(x, y)$ is given function and $\rho=\rho(t, x, y)$.

Model representation of radiopharmaceutical transport allows to set the problem of determining the velocity field of the system (1) for a given density distribution of radiopharmaceuticals.

In the case of optical flow system for the determination of the functions u, v has the form [4, 5]

$$\begin{aligned} \alpha^2 \Delta u - \rho_x^2 u - \rho_x \rho_y v &= \rho_t \rho_x, \\ \alpha^2 \Delta v - \rho_y^2 v - \rho_x \rho_y u &= \rho_t \rho_y. \end{aligned} \tag{4}$$

As a result of this approach, the problem of finding the velocity field of (1) by known density $\rho(t, x, y)$ is reduced to the solving of (4) under the corresponding boundary conditions.

The construction of the velocity field, i.e., finding functions u, v can have both intrinsic interests, giving additional visual and quantitative information, and used in various applications.

To analyze the distribution of the radiopharmaceutical in different dynamic studies different compartment models are used.

The density distribution of radiopharmaceuticals $\rho=\rho(t, x, y, z)$, which depends on the time t and space coordinates is considered. Next, for convenience we denote $x_1=x$, $x_2=y$, $x_3=z$, and, now $x=(x_1, x_2, x_3)$. It is assumed that the transport of the indicator is based on system

$$\dot{x} = f(t,x), \tag{5}$$

and the function $\rho(t,x)$ satisfies the generalized Liouville equation [6]

$$\frac{\partial \rho}{\partial t} + \frac{\partial \rho}{\partial x} f + \rho \operatorname{div} f = 0, \tag{6}$$

where $\rho=\rho(t, x)$, $f=f(t, x)$ – velocity field of the system (5).

Human organism represented by the sum of related virtual domains (compartments), with the introduction of the following notation: D_i – investigated compartment, $i=1,..,n$, where n – the number of compartments, $q_i=q_i(t)$ - function that characterizes the amount of indicators in the compartment D_i, which is determined by the formula

$$q_i(t) = \int_{D_i} \rho(t,x)\,dx. \tag{7}$$

Considering the density redistribution and, given that the integral of the density by the domain $D=\sum_{i=1}^{n} D_i$ is constant, and also taking into account that the velocity of change of indicator is directly proportional to the amount of indicators in the source compartment, we consider the equations of compartment models

$$\frac{dq_i}{dt} = \sum_{j=1}^{n} a_{ij}(t) q_j, i = 1,2,...,n. \tag{8}$$

The system of parameters $\{a_{ij}\}_{i,j=1}^{n}$ is the transport matrix size, $n \times n$. It is the desired system of unknown clinical and physiological parameters of the model. Also within the framework other mathematical models are considered.

SOFTWARE SUITE FOR SPECT

In this work program complex for data processing of radionuclide studies is considered, it is intended to perform complex tasks of mathematical SPECT data processing.

The suite could work with various sources of medical

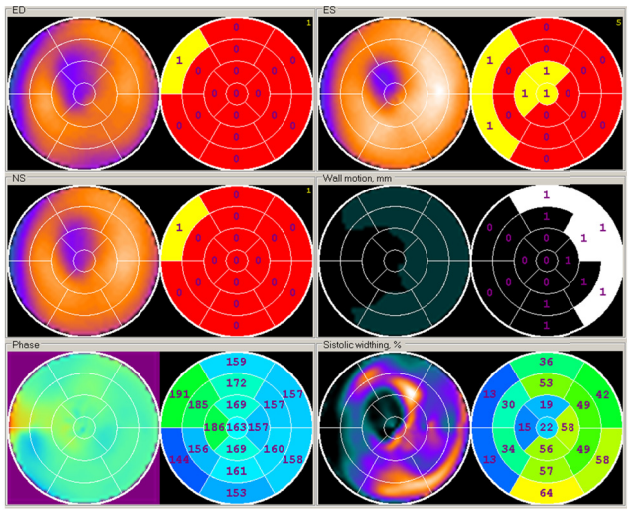

Figure 3: Myocardial perfusion polar maps.

data, based on hardware interoperation, file storages and databases. For interoperability with other software DICOM file format is supported.

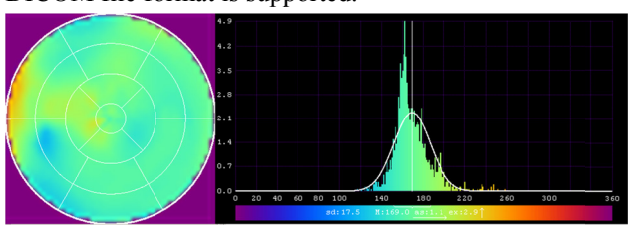

Figure 4: Myocardial perfusion phase analysis.

The designed suite makes it possible to capture and process information in static, dynamic, tomographic, and SPECT gated modes. The data processing applications provide possibility for qualitative and quantitative estimation of the results of radionuclide studies.

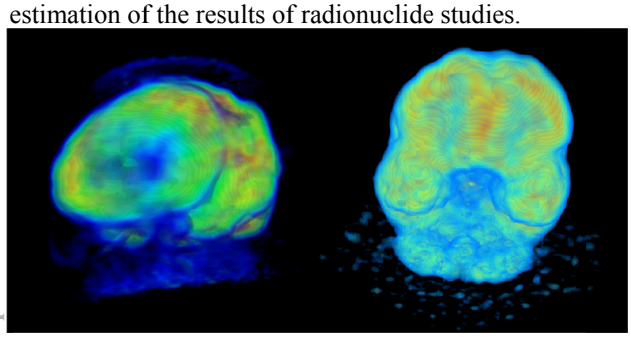

Figure 5: Volume visualization of brain studies.

Data processing of the results of radionuclide studies is performed by clinical software application modules.

The software suite incorporates specialized medical software applications which perform data processing and visualization according to established clinical protocols and methods [7]. Also applications for preliminary data processing (tomographic reconstruction and reorientation, motion correction [5], data view) are included into the suite.

The suite incorporates clinical software applications for data processing in cardiology (fig. 3, 4) [8, 9]; brain studies (fig. 5); in nephrology (fig. 6); in pulmonology (fig. 1); in osteology; in endocrinology; hepatobiliar system analysis; multifunctional application for static and dynamic data processing et al.

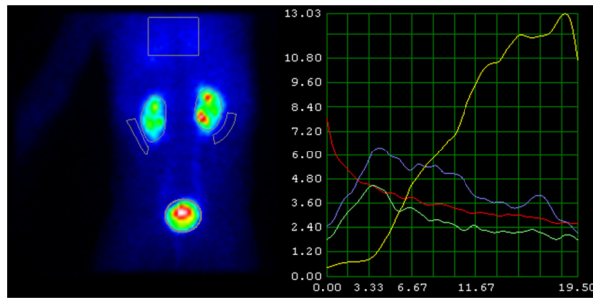

Figure 6: Dynamic nephroscintigraphy.

REFERENCES

[1] E.D. Kotina, A.I. Dzhaksumbaev, D.V. Dezhurnyuk,V.A. Ploskikh "Automated information system for radionuclide diagnostics" Vestnik of St. Petersburg University, Ser. 10, №.1, pp. 110-115, 2006.

[2] M.A. Arlychev, V.L. Novikov, A.V. Sidorov, A.M. Fialkovskii, E.D. Kotina, D.A. Ovsyannikov, V.A. Ploskikh. Two-Detector Single Photon Emission Tomograph EFATOM //Technical Physics, 2009, Vol. 54, No. 10, pp. 1539–1547.

[3] E.D. Kotina "Program complex "Diagnostics", Vestnik of St. Petersburg University, Ser.10, №2, pp. 100-113, 2010.

[4] B.K.P. Horn, B.G. Schunck Determining optical flow // Artificial intelligence. 1981. Vol. 17. Pp. 185–203.

[5] E.D. Kotina, K. M. Maximov "Motion Correction in SPECT and Planar Radionuclide Studies", Vestnik of St. Petersburg University, Ser.10, №1, pp. 29-36, 2011.

[6] D. Ovsyannikov, E. Kotina, "Reconstruction of Velocity Field", ICAP'12, Rostok, August 2012, THSCC2, (2012).

[7] Y.B. Lishmanov, V.I. Chernov et al., National guidelines for nuclear medicine, (Tomsk: STT, 2010), 686.

[8] E.N. Ostroumov, E.D. Kotina, O.R. Senchenko, A.B. Mironkov. Radionuclide methods in the cardiology clinic / / Heart. 2010, № 3. pp. 90 – 95.

[9] G. Germano et al. Quantitation in gated perfusion SPECT imaging: The Cedars-Sinai approach // Journal of Nuclear Cardiology Volume 14, Number 4; pp. 433-54. 2007.

DESIGN PARAMETERS OF BIPERIODIC ACCELERATING STRUCTURE FOR MEDICAL LINAC WITH WIDELY VARIABLE ENERGY

Yu.V. Zuev#, M.A. Kalinichenko, V.V. Terentiev
D.V. Efremov Scientific Research Institute of Electrophysical Apparatus, Saint Petersburg, Russia

Abstract

Results on the simulation of the beam dynamics in an accelerating structure with the particle energy varied from 6 to 21 MeV are presented. The structure operating in the standing wave mode consists of two weakly-coupled substructures and resonates at closed frequencies f_1 and f_2. In-phased electromagnetic field oscillations take place in the substructures at the frequency f_1, whereas anti-phased oscillations occur at the frequency f_2. Main features of the accelerating structure are electronic control of the beam energy and possibility to form narrow energy spectrum at both frequencies.

OPERATION PRINCIPLE OF THE STRUCTURE

Different methods are used to vary the energy of electrons in standing wave accelerators [1]-[3]. In the paper, we consider a biperiodic accelerating structure with inner (axial) coupling cells to be used in a medical accelerator. The method of energy variation was suggested in [4]. The accelerating structure consists of two substructures A and B with an odd (N_A and N_B) number of resonator cells tuned to the same frequency f_0. In each separate substructure, π/2-oscillations are excited at the frequency f_0. By joining substructures A and B through a small hole in a diaphragm, a structure, consisting of an even ($N_A + N_B$) number of cells, is formed to resonate at frequencies close to f_0:

$$f_1 = f_0(1 - k_{AB}/(N_A + N_B)),$$
$$f_2 = f_0(1 + k_{AB}/(N_A + N_B)) \quad (1)$$

where k_{AB} is the coupling coefficient of substructures. At the frequency f_1, in-phased π/2- oscillations occur in substructures A and B, and these oscillations are anti-phased at the frequency f_2. As a consequence, either acceleration of electrons in the substructure A and deceleration in the substructure B or acceleration in both of these substructures is possible. Switching from one mode to another is realized by change in frequency f_G of the generator, which drives the structure; this produces maximal variation of the beam energy. For “fine tuning" of the beam energy, the power of the RF generator is additionally varied.

FEATURES OF THE STRUCTURE DESIGN AND OPERATING MODE

Similar to the prototype [4], the considered structure consists of sixty six cells, N_A=39 and N_B=27. First ten (cylindrical) cells form a cascade buncher. The remaining elements are standard Ω-shaped accelerating and cylindrical coupling cells, which are uniform in size with exception for two (or four) cells located at the joint of substructures [5]. The axial length of these cells has strong influence on the beam dynamics, therefore their dimensions like the buncher cell dimensions are specially designed. The RF power is supplied to the substructure A through the wave converter cell.

In contrast to the prototype-structure [4], the resonance frequency of separate cells, f_0, has been changed from 2856 to 2998 MHz. The dependence of the input VSWR of the structure with the beam off on the generator frequency is shown in Fig. 1. Frequencies f_1 = 2997.693 MHz and f_2 = 2998.307 MHz correspond to operating modes of the structure. Fig. 2 shows an axial distribution of the amplitude of the electric field excited at the frequency f_1 in the cold structure. Practically the same field distribution was obtained in computations performed at the frequency f_2.

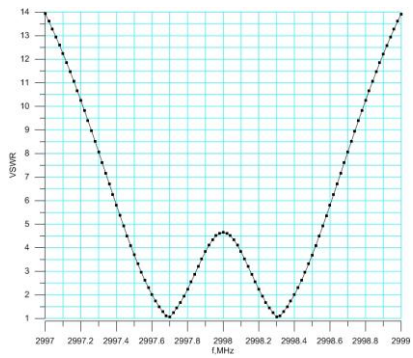

Figure 1: The dependence of the input VSWR of the structure with the beam off on the generator frequency.

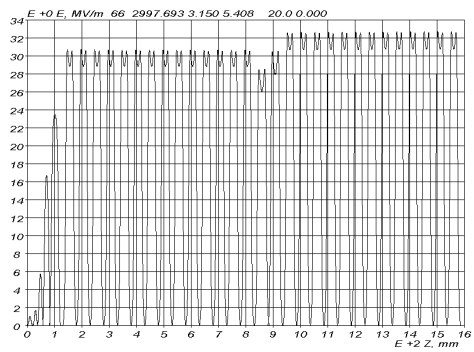

Figure 2: An axial distribution of the amplitude of the electric field excited at the frequency f_1 in the cold structure

#yuri_zuev@mail.ru

DESIGN PARAMETERS

The results of the numerical simulation of the beam dynamics are given in Fig. 3 and Table 1. Table 1 presents: the generator frequency f_G; pulse RF power P_{inp} supplied to the structure, MW; voltage standing wave ratio (VSWR) in the entrance waveguide; pulse current I_{inp} of the beam injected to the structure, mA; average particles' energy W at the structure output, MeV; beam transmission efficiency, $\eta_1 = I_{out} / I_{inp}$; fraction η_2 of accelerated particles with energies in the $W \pm 5\%$ interval and radius $R_{90\%}$ of the output beam cross-section containing 90% of current, mm.

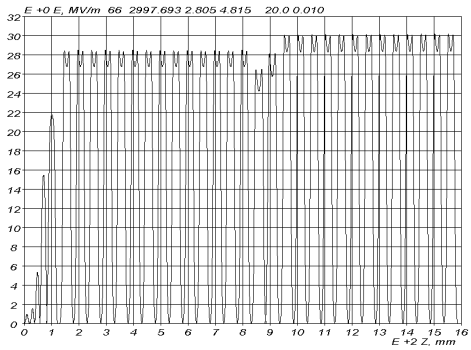

(a)

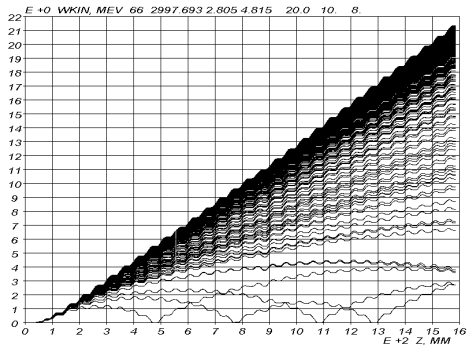

(b)

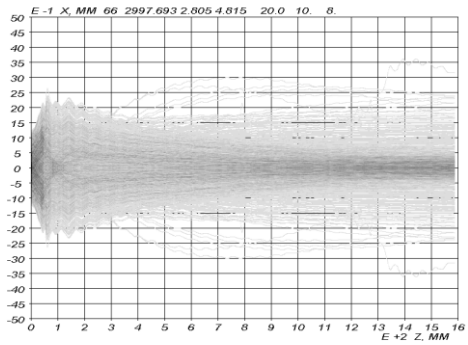

(c)

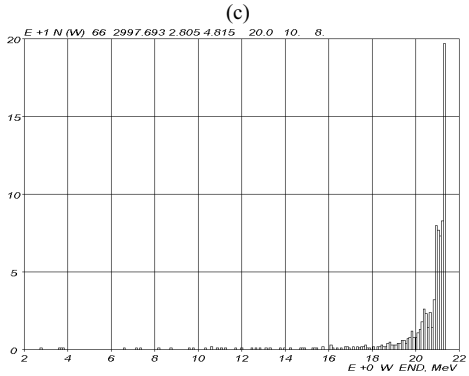

(d)

Figure 3: Computational results of the beam dynamics in the structure: to the left – the mode with I_{inp} = 10 mA and W= 21 MeV; to the right – the mode with I_{inp}= 300 mA and W = 6 MeV; (a)- distribution of the electric field amplitude on the structure axis, (b)-kinetic energy of electrons in the accelerating structure, (c)- particle trajectories, (d)- particle energy spectrum at the structure output.

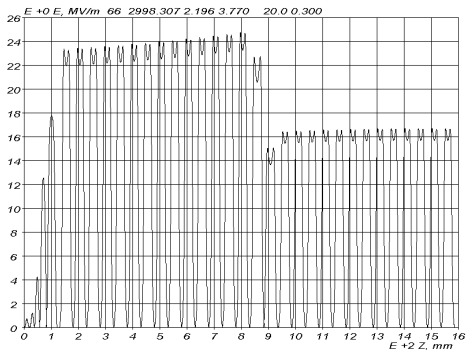

(a)

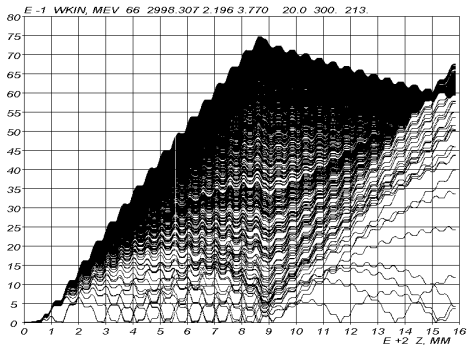

(b)

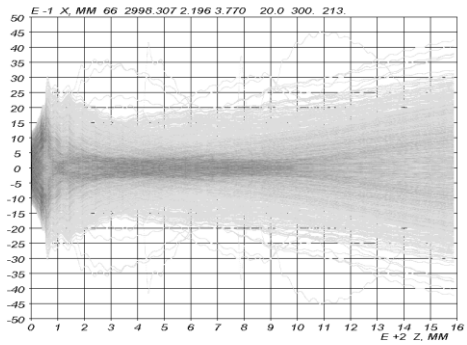

(c)

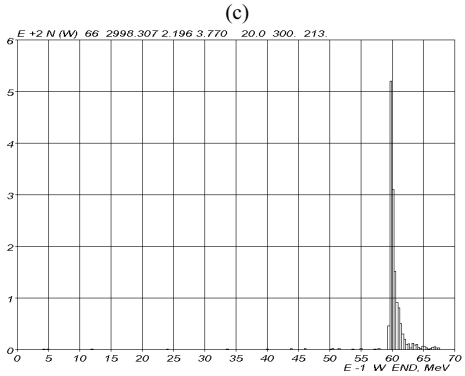

(d)

Table 1: The results of the numerical simulation of the beam dynamics

W	f_G	P_{inp}	VSWR	I_{inp}	η_1	η_2	$R_{90\%}$
21	f_1	4.9	1.039	10	0.81	0.87	1.1
18	f_1	4.7	1.191	50	0.77	0.79	1.0
18	f_1	4.1	1.041	10	0.77	0.70	1.2
15	f_1	3.4	1.042	10	0.73	0.68	1.4
12	f_1	2.9	1.042	10	0.69	0.64	1.5
9	f_1	2.6	1.042	10	0.64	0.47	1.6
6	f_2	3.7	1.073	300	0.70	0.96	2.0
6	f_2	4.9	1.009	30	0.80	0.63	2.0

All the computations have been performed for a particle injection energy of 20 keV. The presented set of output beam energies and currents corresponds to typical operating modes of the medical accelerator [6]. Data on the current transmission and output beam transverse size have been obtained assuming optimal conditions for the beam injection [7]. Transverse size of the accelerated beam is confined by the RF field of the structure; there are no external focusing elements.

To attain an energy of 6 MeV, the particle deceleration mode is used; the accelerating structure is fed at the frequency f_2 with an RF power of 3.7÷4.9 MW depending on the beam current. An increase in the beam current results in a reduced power consumption [8] and a narrower particle energy spectrum. To attain energies in a range of 9÷21 MeV and higher, the normal operating mode of the structure is used. In this case the accelerating structure is fed by pulses at the frequency f_1 with an RF power of 2.6÷4.9 MW. The average energy of particles increases with a higher RF power level, the energy spectrum narrows and the beam transverse size decreases. The widest spectrum was observed with 6, 9 and 12 MeV low-current beams. In the worst case, less than a half of the total number of accelerated particles occurs in an energy range of 9±0.45 MeV. However, it is not a problem as in medical accelerators the non-working part of the spectrum is always eliminated with a magnetic separator installed behind the accelerating structure.

CONCLUSION

The simple and reliable method of the beam energy variation used in the described structure eliminates all the problems typical for the structures equipped with mechanical means for energy variation. Change in energy proceeds by electronic circuits and takes only several milliseconds. Therefore, this method can be used in the accelerators with two energies, which operate in customs inspection systems (so-called dual-energy structures). A definite advantage of the presented structure is a balance between the energy spectrum width and the transverse size of the accelerated beam, which can hardly be attained with a large number of operating modes.

REFERENCES

[1] Patents SU1429919, SU1586502, US4286192, US5821694, US6366021, US6407505, US7491958 et al.

[2] B.Yu. Bogdanovich, A.A.Zavadtsev, D.A. Zavadtsev, V.I.Kaminskiy et al., "Electron Linac Project Based on Biperiodic Accelerating Structure with a Deep Energy Variation in the Pulsed Mode," Proc. of the Xth Int. Conf. on Applied Charged Particle Accelerators in Medicine and Industry (ICAA'01), St.Petersburg, (2001), pp.109-112.

[3] S. Hanna. "Review of Energy Variation Approaches in Medical Accelerators," EPAC08, Genoa, TUPP117, pp.1797-1799 (2008).

[4] Yu.N. Gavrish, O.L. Maslennikov, A.V. Ryabtsov, V.V. Terentyev, "New Method for Deep Electron Energy Variation in Standing Wave Linear Accelerators," Proc. of the XIth Int. Conf. on Applied Charged Particle Accelerators in Medicine and Industry (ICAA'05), St.Petersburg, (2001), pp. 311-314.

[5] Substructures *A* and *B* are joined through a diaphragm separating whole Ω- shaped cells.

[6] Modes with 18 and 6 MeV beam energies and injection currents of 50 and 300 mA, respectively, are used for photon irradiation. The rest modes given in Table 1 are applied for irradiation with electrons.

[7] Non-normalized beam emittance is not more than π 20÷25 mm× mrad and injection from the beam waist of 1.2÷1.4 mm radius for all modes excluding the 6 MeV photon mode. When injection currents are 200÷300 mA, a convergent beam with the 1.8÷2.0 mm radius and the beam envelope slope of 30 mrad is required. Injection conditions are changed to weaken the effect of the beam space charge.

[8] The reason is that a part of the RF field induced by the decelerating beam enters the substructure *A* from the substructure *B* synchronously with the generator-produced field and partially compensates for a field reduction caused by the beam loading.

POSITRON ANNIHILATION SPECTROSCOPY AT LEPTA FACILITY

P. Horodek, A. Kobets, I. Meshkov, V. Pavlov, A. Rudakov, A. Sidorin, S. Yakovenko,
JINR, Dubna, Russia

Abstract

At the moment Positron Annihilation Spectroscopy (PAS) unit is being created as a part of LEPTA project at JINR in Dubna. A slow positron beam, dedicated to creating a positronium atom in flight, will also be used for material research related to detection of point defects under the surface. For this purpose Doppler broadening of annihilation line spectrometer is being made. Basis of the method, operational principle, plans and current state of works, are all presented in this article.

INTRODUCTION

Positron Annihilation Spectroscopy method is sensitive to presence of defects in materials. Its currently highly developed measurement techniques enable detection of imperfection of crystal lattice the size of a lattice constant. Vacancies, concentrations of vacancies, pores and dislocations can be spotted in this way. Since late 1960s, when it was discovered that a positron interacts with defects, PAS method has been developing. At the moment it has got solid theoretical basis. A growing interest in this method in condensed matter research and materials engineering in recent years resulted not only in new results but also in a search for increasingly sophisticated measuring techniques. Research on monoenergetic positron beams and positron microscopy are the current trends in this department.

POSITRONS IN THE MATTER

Positron, antiparticle of an electron, coming from β^+ decay in PAS experiments is implanted into the tested sample directly after emission from isotope or into a specially formed beam.

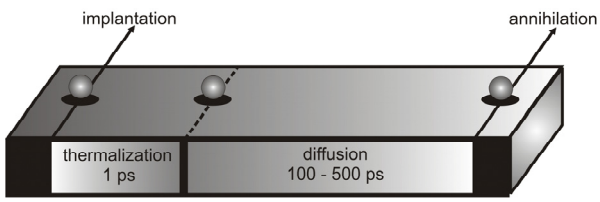

Figure 1: Stages of positron implantation into the matter.

As it possesses both energy and charge, it reacts elastically and non-elastically with ions and electrons, and to a lesser degree with phonons and impurities. Thus, after circa 1 ps it reduces its energy to thermal oscillation energy i.e. about 25 meV [1]. This stage is called thermalization. Next, anti-electron, which at this stage is in a state of thermodynamical balance with its environment starts free diffusion, which is a random walk over the area occupied by 10^7 atoms. Such state lasts from 100 to 500 ps and it ends with an encounter with an electron. The process of annihilation into two gamma quanta of energies that equal about 511 keV occurs in over 99% cases [2].

Therefore, the process of positron-electron annihilation does not occur immediately after positron appears in the matter. The fact that in different stages (schematically marked in Fig.1) it spends a certain time in the material, is significant from PAS point of view.

In the central mass system annihilation quanta are emitted in the exactly opposite direction (see Fig. 2). In a laboratory system a certain deviation from this collinearity will be observed, expressed by

$$\Delta\theta = \frac{p_\perp}{mc} \qquad (1),$$

where m is electron's mass, c is speed of light in a vacuum and $p_\perp$ is a perpendicular component of the momentum of the annihilating pair. A deviation from 180° will be bigger, the bigger momentums of a positron and an electron. The momentum additionally manifests itself in gamma quanta energies, which are changed as a result of Doppler effect

$$E_\gamma \cong mc^2 + E_B \pm \frac{p_\parallel c}{2} \qquad (2)$$

where E_b is the energy of positron-electron pair coupling and $p_\parallel$ is a perpendicular component of the pair's momentum. It is worth emphasising that positron's momentum is negligibly small in relation to electron's momentum, therefore it usually omitted in deliberations.

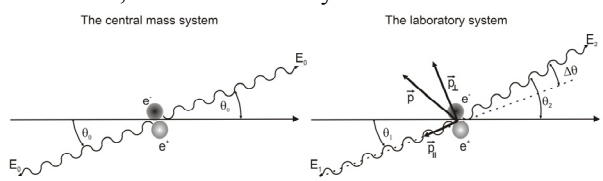

Figure 2: The annihilation processes in the two systems.

During its random walk a positron may encounter places which have a modified electron density. Those place are structural defects such as vacancies, inside of which a positron may be located. Electron density in such traps is smaller in comparison with the defect's environment. This inevitably is reflected in deviation from collinearity of annihilation quanta and in their energies, which are then respectively smaller, as well as in an average life time of a positron in a defect, which is longer than outside of it.

Observations of angular correlations of annihilation quanta, changes of energies or life times are operational basis of the three basic measuring PAS techniques. The technique of observation of Doppler broadening of annihilation gamma line is going to be more widely discussed further in the article.

THE DOPPLER BROADENING OF ANNIHILATION GAMMA LINE

Widely known in physics Doppler's phenomenon causes a change of energies of annihilation quanta according to the formula (2), which, having neglected electron's momentum and energy, can be thusly expressed

$$E_\gamma \cong mc^2 \pm \sqrt{\frac{1}{2}mc^2 E}\,. \qquad (3)$$

If the energy of an annihilating positron equals e.g. 7eV (Fermi energy for copper), then a change of energy of annihilating gamma quantum, according to the above formula, will equal 1,4 keV. Thus, the total broadening of annihilation line will equal 2,68 keV.

Observation of such broadening requires using detectors of a high energetic resolution. Currently available germanium detectors allow to take measurements with resolution equal to 1-2 keV around 511 keV energy.

Doppler broadening of annihilation line technique is used to detect concentrations of defects such as vacancies and their accumulations. A signal from annihilation of a trapped positron gives broadening of the 511 keV line accordingly smaller than the one that would occur in case of annihilation with nucleus electrons. In other words, less defected sample gives smaller broadening of the 511 keV line.

In practice, information about concentration of defects is received from analysis of the shape of annihilation line, by calculating two important parameters, called S and W. Exemplary annihilation line as well as the rule for calculating both parameters are presented in Fig. 3.

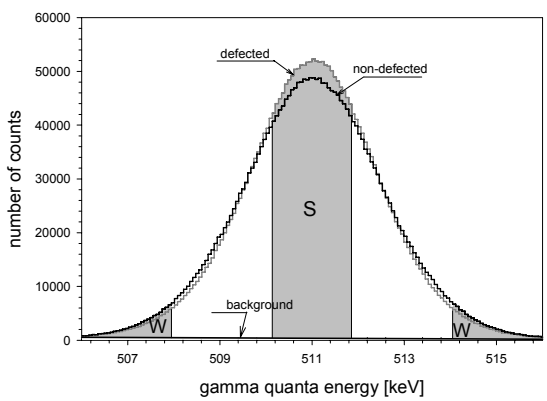

Figure 3: The annihilation lines with marked areas defining parameters S - and W - measured in stainless steel. The grey line comes from the defected (by sliding) sample, while the black line represents the non-defected sample.

S parameter defines proportion of annihilation of positrons with low-momentum electrons. It is closely related to concentration of defects in a material. It is defined as ratio of surface area under the central part of the 511 keV line to total surface area under this line. Areas are usually selected so that their ratio approximated 0,5. Bigger S parameter value means bigger concentration of defects.

The second parameter, the so called W parameter is defined as ratio of surface area under the wing part of 511 keV line to total surface area. It is related to annihilation of positrons with high-momentum electrons and it provides information about chemical environment of the defect. Value of this parameter is also selected arbitrarily – it tends to be smaller than 0.01.

Both parameters S and W are calculated after background reduction. Calculations are made by special computer software. As stated above, the analysis of results of Doppler broadening of annihilation line is based on calculating S and W parameters, changes of which provide information on changes in concentration of defects [3,4].

PAS AT LEPTA PROJECT

Since 2000 at JINR in Dubna project LEPTA has been realised. Its main aim is to acquire a positronium atom in flight [5]. A positron beam constructed for this aim can also be used for PAS.

The concept of producing the beam is the following. Positrons emitted from ^{22}Na go through a moderator, which is condensed Ne source. As a result of elastic scatterings on gas particles some electrons lose their energy. Those two types of particles are separated by the use of perpendicular magnetic fields. Fast positrons are stopped at diaphragm, while the slow ones are slaloming and are then formed into a beam and accelerated by negative potential to needed energies. Currently available beam's parameters are given in Table 1.

Table 1: General Beam Parameters

Feature	Value
activity of ^{22}Na isotope	25mCi
moderator	frozen Ne (7K) under pressure 10^{-8} Torr
longitudinal magnetic field	100 Gs
vacuum conditions	10^{-6} Pa
intensity	10^{5} e^{+}/s
energy range	1 eV ÷ 50 keV
diameter of the flux	5 mm

Positrons are implanted from the beam into the sample which has electric current applied to it. Quantum 511 keV created through annihilation is registered by a DBGL spectrometer, which scheme is shown in Fig. 4.

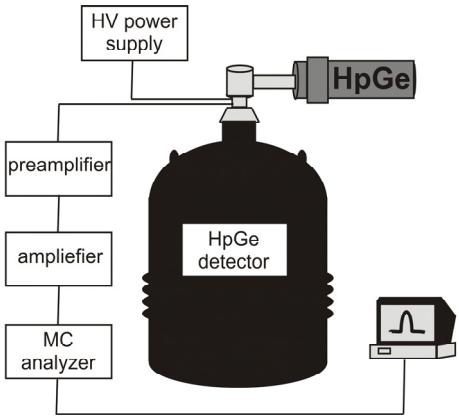

Figure 4: The scheme of Doppler broadening of annihilation gamma line 511 keV spectrometer.

It consists of HV adapter, HpGe detector, a preamplifier, a multichannel analyser and a computer Annihilation quanta are registered by a detector made by BALTIC SCIENTIFIC INSTRUMENTS. Its parameters are given in the table.

Table 2: Main Parameters of HpGe Detector

Feature	Valu
relative registration efficiency at 1.33 MeV-photon	30%
energy resolution FWHM for energy 511 keV	<1250 eV
peak to Compton ratio	58:1
energy range of detector operation intensity	40 ÷ 10 000 keV

SUMMARY

Completion date of PAS measurements unit by LEPTA project is expected to be the end of 2012. First results are predicted to be obtained at the beginning of 2013. The research is going to concern mostly materials engineering, both in metals and semi-conductors. The main research is going to include studies on the influence of surface treatment processes on the defecting of the surface layer in materials which are commonly used in industry, such as stainless steel. Furthermore, plans are made to conduct research oriented around thin layers and layers created by ion implantation. In further perspective there are plans to develop the equipment for registering two gamma quanta in a coincidence, which would significantly reduce the background in the spectrum.

REFERENCES

[1] J. Dryzek, et al., Mat. Sci. Forum 666 (2011) 10.
[2] S. Adachi, et al., Phys. Rev. Lett. 65 (1990) 2634.
[3] R. Krause-Rehberg et al., *Positron Annihilation in Semiconductors: Defect Studies*, (Berlin: Springer-Verlag Berlin Heidelberg, 2003), 18.
[4] P. Horodek, et al., Tribol. Lett. 45 (2012) 341.
[5] E. Akhmanova, et al., Phys. Part. Nucl. Lett. 9 (2012) 373.

RF PHOTOINJECTOR PARAMETERS OPTIMIZATION

T.V. Bondarenko, S.M. Polozov,
National Research Nuclear University (MEPhI), Moscow, Russia

Abstract

Sources of high-power electromagnetic radiation in THz band are becoming promising as a new method of a low activation introscopy. Research and development of accelerating RF photoinjector for THz source are reported. The photoinjector is based on disk loaded waveguide (DLW). Photoinjector consists of two accelerating structures: widespread 1.6 cell DLW structure and travelling wave resonator structure based on 9 cells traveling wave accelerating structure. The resonant models of these structures and the structures with power ports were designed. Electrodynamics characteristics and electric field distribution for all models were acquired. Electrodynamics models were tuned to the resonant frequency of 3000 MHz. Magnetic field coupling between cells of accelerating structure and optimization of the diaphragms sizes were analyzed to enlarge the structures efficiency. Diaphragms windows profiles were optimized to decrease the overvoltage on the windows edges and to eliminate the breakdown possibility.

INTRODUCTION

RF photoinjectors are accelerating structures and electron guns at the same time. The main work principle of photoinjector is based on photoemission electron generation type. Photoinjectors are used is applications that requires femto-picosecond time resolution beam such as free electron lasers that demand short bunches for generation of monochromatic radiation.

One of interesting applied usage of photoinjectors is a source of high intensity THz radiation based on Cherenkov irradiating capillary channel that can be used in the field of cargo introscopy [1]. This source implies travelling of about 5 MeV beam in the capillary with sub-mm transverse sizes.

Such facilities can be used not only in introscopy system as well as in biology, medicine, chemistry, solid state physics, radio astronomy, homeland security, environment monitoring, spintronics, advanced spectroscopy, and plasma diagnostics.

ACCELERATING STRUCTURES

The photoinjector must be formed of accelerating structure with one or two sections for achieving of the demanded beam energy, laser system for beam generation from the photocathode and focusing system for beam shape preserving.

RF power source feeding the photoinjector is based on 2.5 MW pulse power magnetron with 2.995-3.005 GHz working frequency. Hence the accelerating system must be formed of two accelerating structures – standing wave structure emitting and preliminary accelerating the electron beam and travelling wave structure proceeding acceleration to the final energy.

Accelerating structures geometry was tuned to provide advanced operating mode of the structures and from here to reach the maximum possible efficiency of the structures.

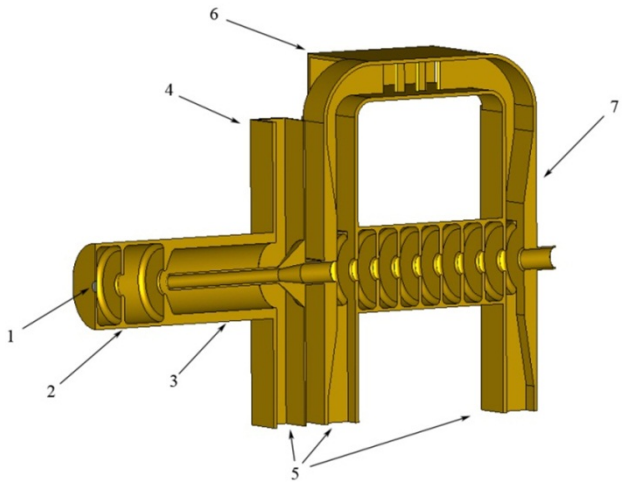

Fig. 1. General layout of accelerating system: 1 – photocathode, 2 – 1.6 cell DLW structure, 3 – coaxial wavetype transformer, 4 – RF power input, 5 – vacuum ports, 6 – directional coupler, 7 – travelling wave resonator structure.

Standing Wave Structure

1.6 cells accelerating structure was computed for 3000 MHz operational frequency. The general view of the accelerating system with MW power port is represented in Figure 2. The photocathode will be arranged in 0.6 cell's sidewall, therefore accelerating field on the sidewall's surface must be as high as possible. That is the reason of making half-cells length equal to 0.6 of full sized cell. Zero and π modes are excited in this structure, mode with μ= π phase shift per cell is the operating mode. The structure is characterized by the positive normal dispersion.

Iris profile was made rounded to eliminate the possibility of breakdown. This was done to reduce the electric field in the window's aperture because of high-rate accelerating fields in 1.6 cells accelerating structure that can lead to electrical breakdown. The ratio of iris window to the wavelength was set to 0.1. This value is a trade-off between the wish to get maximum amplitude of accelerating field and except probable beam loses on the iris. The structure performance was also increased by rounding of shells edges. The rounding radius value was chosen to provide the highest possible shunt impedance.

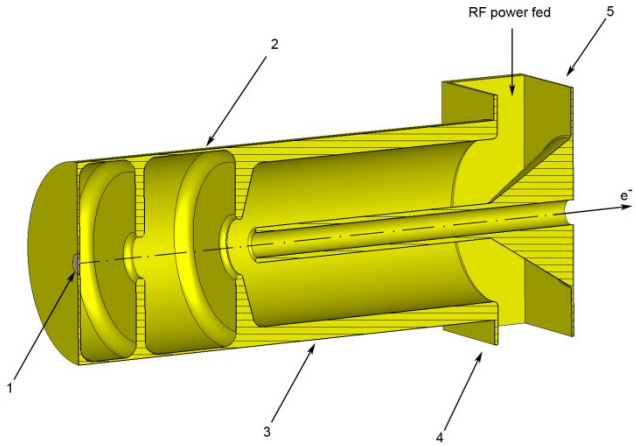

Fig. 2. 1.6 accelerating structure: 1 – photocathode, 2 - resonator, 3 – coaxial wave type transformer, 4 – vacuum port, 5 – power input.

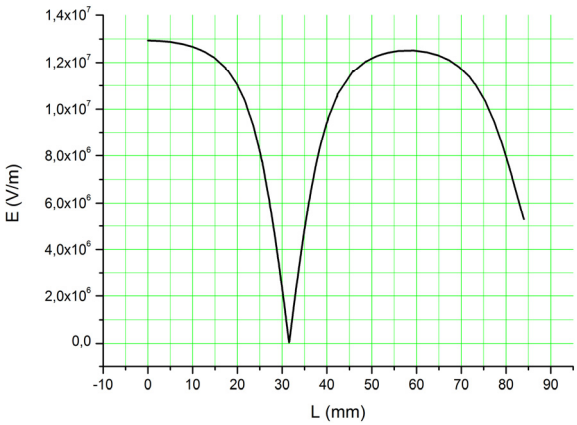

Fig. 3. Electrical field distribution in 1.6 cell structure.

Structure RF power input in organized by S-band standard rectangular waveguide with the coaxial coupler. This type of wave transformer differs from recently used RF power inputs in photoinjectors like ones in BNL Guns [2]. That type was exploiting the scheme of power input through the coupling diaphragm directly into the full-sized cell of the structure in this wise full cell was a wave transformer. RF power is fed into the structure through only one of the connected waveguides; another is used for structure field symmetry and will be applied for vacuum system and other accompanying connections. This scheme provides high level of field symmetry in the system that leads to better quality of the accelerated beam.

Travelling Wave Resonator Structure

Travelling wave resonator is a type of ordinary linear accelerator structure with some additions. Basically the accelerating wave propagating in acceleration structure is travelling wave type but the trait that makes this system a resonator is energy recuperation coming out of interlocking RF power input with output and feeding power with directional coupler (figure 2). If the length of the TWR circuit is devisable to the generator wavelength, the magnitude of electromagnetic fields in TWR reaches its maximum and magnitude of the wave incoming to the load from the ring turns to minimum [3].

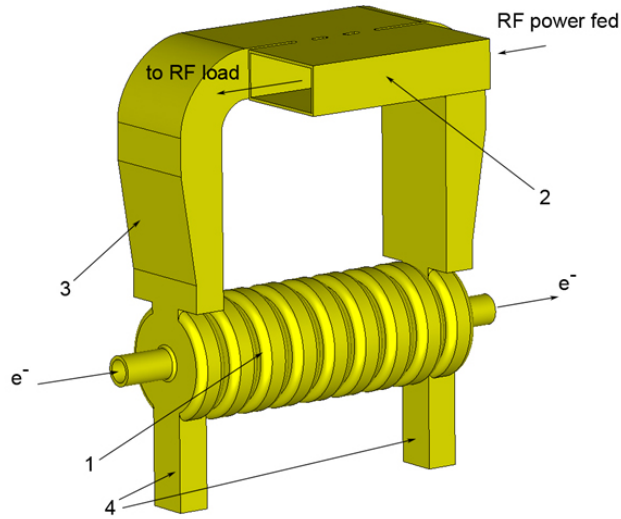

Fig. 4. Travelling wave resonator structure: 1 – accelerating structure, 2 – directional coupler, 3 – TWR ring, 4 – vacuum ports.

TWR is based on 8 cell travelling wave S-band structure with $\pi/2$ operating mode. To enhance the shunt impedance of the structure the magnetic coupling between cells was introduced into the scheme of the structure. Another way applied to increase shunt impedance is to insert a drift tube, which can help to concentrate the electric field near the axis and provide an RF-focusing of the particles [3]. By means of used drift tubes and magnetic coupling windows the shunt impedance of the system was enhanced from 54 MOhm/m to 71 MOhm/m.

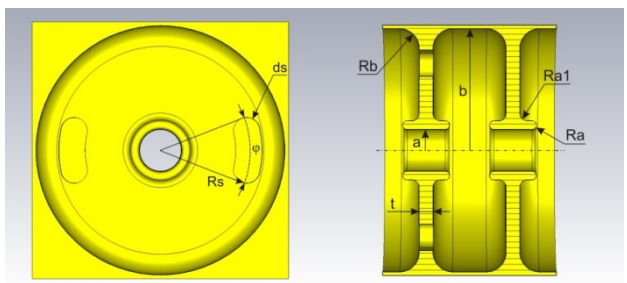

Fig. 5. DLW with magnetic field coupling cells and drift tubes

The optimal operation regime of the structure is critical mode. In this regime part of RF power is fed into the accelerating system through the directional coupler and fills in the power resistance losses in the resonators sidewalls. In this case the part of power that is not branched into the TWR ring is summed with the one from generator in the opposite phase and gives the minimal magnitude signal coming to the load. Two main parameters determining efficiency of TWR are the circuit

power attenuation factor and the directivity factor of the directional coupler.

Directional coupler with narrow or wide side coupling represents the connection of two waveguides by coupling windows with space shift of quarter wavelength between he windows irradiating in the opposite directions of jointed waveguide. Directional coupler computation included receiving of required transfer coefficient in the forward direction of jointed waveguide C and simultaneously keeping transfer coefficient in the opposite direction of jointed waveguide $|\Gamma|$ below the certain level.

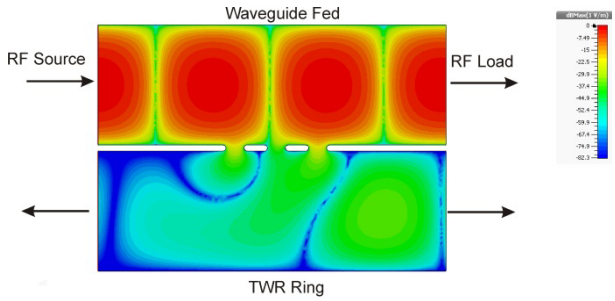

Fig. 6. Directional coupler field distribution in non-steady case.

Three coupling window model was applied to provide high directivity level of directional coupler. Enlarging the number of coupling windows doesn't improve the directivity coefficient.

Taking into account part of the signal branching in the opposite direction and intensity attenuation factor, expression for the magnitude of electrical field spreading in TWR storage ring for critical mode can be written as:

$$A_{TWR} = \pm j \frac{1}{\sqrt{1 - e^{-2\alpha_T}}} \frac{C - |\Gamma|}{C} A_{input}, \qquad (1)$$

here A_{TWR} - TWR circuit electrical field intensity magnitude, α_T - TWR ring signal intensity attenuation factor, A_{input} – RF generator signal intensity magnitude [4].

In considered case transition coefficient of directional coupler C=1.71% that equals to TWR ring decay coefficient at the 10.94 mm coupling window width, sidewall width between waveguides is 4 mm. Sidewalls width doesn't have much impact on directivity coefficient but ought to be wide enough to provide coupler ruggedness. Transfer coefficient in the opposite direction of TWR ring equals Γ=-55.5dB. Thus directivity coefficient of directional coupler is D=23dB. Using the formula (1) power in TWR multiplies 9 times vs. input power level and field intensity – 3 times vs. input power level.

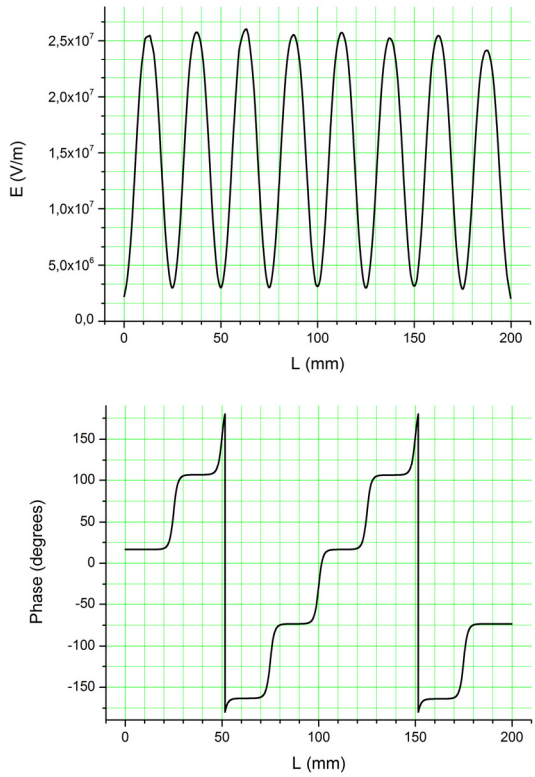

Fig. 7. Travelling wave resonator structure electrical field distribution (upper) and phase distribution (lower).

CONCLUSION

RF accelerating system was investigated and modeled for high-power THz generator. RF accelerating system is based on two accelerating sections: 1.6 cell standing wave structure with coaxial power input and travelling wave section based on travelling wave resonator.

Both structures are fed by 2.5 MW magnetron working on the frequency of 3 GHz. Updates made for the structures include coaxial power input in 1.6 cell structure and drift tubes and magnetic coupling windows in TWR structure. These changes in structures models enlarged the system efficiency.

REFERENCES

[1] Yu.A. Bashmakov, T.V. Bondarenko, S.M. Polozov, et al., Problems of Atomic Science and Technology. Series: Nuclear Physics Investigations, 3 (79), 2012, p. 53-57.

[2] D. T. Palmer, R.H. Miller, X.J. Wang, et al., SLAC–PUB–7420, May 1997.

[3] S.V. Kutsaev, N.P. Sobenin, A.Yu. Smirnov, et al., Nuclear Instruments and Methods in Physics Research A, 636 (2011) 13–30.

[4] J. L. Altman, Microwave circuits, Van Nostrand Co., 1964.

OPERATIONAL EXPERIENCE WITH 55 MEV PULSED RTM

A.N.Ermakov, V.V.Khankin, N.I.Pakhomov, V.I.Shvedunov, SINP MSU, 119992 Moscow, Russia
A.I.Karev, V.G.Raevsky, P.N.Lebedev Physical Institute, RAS, 119991 Moscow, Russia

Abstract

Operational experience with 55 MeV pulsed race-track microtron (RTM) is reported. The upgrade of the accelerator after the commissioning and some results of the physical experiments with a beam of the RTM are presented.

INTRODUCTION

The 55 MeV RTM [1] was designed and manufactured in framework of the contract between Lebedev Phisical Institute (Russia) and Lawrence Livermore National Laboratory (USA). The purpose of the work consists in development of an effective photonuclear detector of hidden explosives [2].

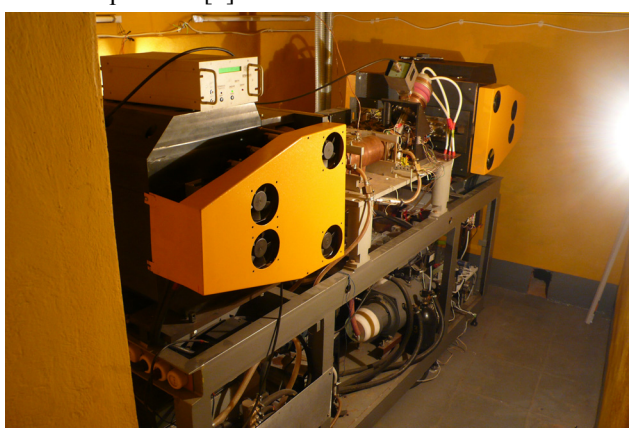

Figure 1: RTM photo.

Table 1: RTM parameters

Output energy	55 MeV
Output pulse current	Up to 10 mA
Repetition rate	6.25 – 50 Hz
Number of linac passages	11
Energy gain / turn	5 MeV
Current pulse length	6 μs
Operating frequency	2856 MHz
End magnet field	1.0 T
Maximum RF power	6 MW
Orbit circumference increase / turn	1 λ

RTM has been built following a classical scheme with two 1 T end magnets and a standing wave linac between them providing 5 MeV energy gain per pass. A 50 keV beam from an electron gun is injected into linac through a 45^0 magnet and a solenoidal lens. The 5 MeV electron beam after the first acceleration is reflected by the end magnet field back to the linac axis and is accelerated up to 10 MeV - the energy sufficient to bypass the linac at the next turn. The beam is extracted from the last orbit with a dipole of 17.5^0 deflecting angle. The RF system is based on a 6 MW multibeam klystron KIU-168 [3]. A pumping port, a vacuum window, and a circulator are installed between the linac and the klystron. Parameters of the vacuum window and the circulator during commissioning restricted the maximum RF power transported to the linac by 2.5 MW and thus restricted a maximum exit pulsed beam current. To simplify the RF system we use a auto-oscillation mode of klystron operation with accelerating structure in a feed-back loop [4]. More details about the RTM systems can be found in [1].

RTM commissioning had been conducted at temporary place at SINP MSU accelerator hall and temporary solutions had been used for some RTM systems. During commissioning the first physical experiment also had been conducted with RTM beam after which the work to install RTM at designated area with final solutions for its systems has been done. The main RTM parameters are listed in Table 1.

UPGRADE OF THE RTM SYSTEMS

Since the last report [1] part of the RTM systems have been upgraded, specifically: RF system, gas system, system of high voltage power supply, control system and beam diagnostics. The accelerator has been moved to specially built bunker in order to reduce background radiation in experimental hall. Photo of RTM in bunker is shown at Fig. 1.

RF System

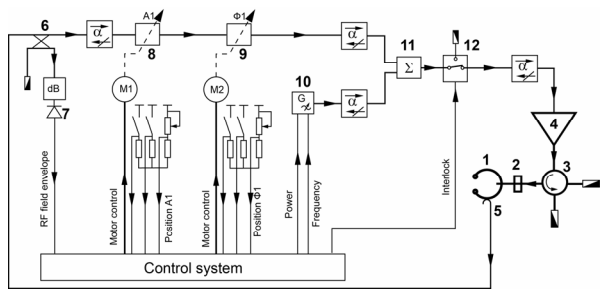

Figure 2: RTM RF system. 1 - accelerating structure, 2 - vacuum window, 3 - circulator, 4 - klystron, 5 - RF antenna, 6 - directional coupler, 7 - RF diode, 8 - attenuator, 9 – phase shifter, 10 - RF generator, 11 - RF power combiner, 12 - RF switch.

Upgraded RTM RF system is shown in Fig. 2. Klystron operation in auto-oscillation mode has several advantages as compared with traditional scheme with excitation from external generator, the most important is automatic following of the oscillations frequency to frequency of accelerating structure. However in pulsed mode the RF

field building up from the klystron noise is accompanied by essential jitter of leading edge of a RF pulse. In upgraded version of RF system we modified feedback circuit by admixing low power, ~ 10 mW, "ignition" RF signal from external generator and thus decreased the RF pulse front jitter to less than 0.1 μs. There is no need to adjust generator frequency to oscillation frequency with accuracy better than ±1 MHz.

To remove limitation in RF power which can be supplied to linac new 6 MW vacuum window and circulator were installed between linac and klystron instead of 2.5 MW units used during commissioning.

Gas System

The gas system shown in Fig. 3, provides automatic support of isolating SF_6 gas pressure at 2 bars and automatic procedure for waveguide system filling by gas and for gas replacement. Gas system consists of a gas cylinder with reducer, two solenoidal valves, pressure gauge, safety valve and diaphragm pump. Operation of system is controlled by dedicated microcontroller, integrated into RTM control system.

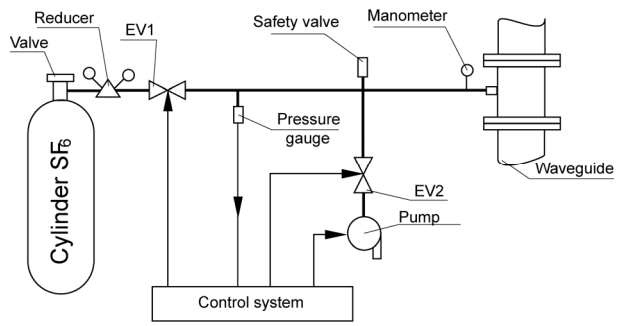

Figure 3: Gas system.

High Voltage Modulator

Figure 4: High voltage modulator.

A new high voltage modulator shown in Fig. 5 have been built by "Protom Ltd" [5] to feed RTM klystron and electron gun. Modulator principle of operation is based on a PFN charged to 20 kV by high voltage power supply and discharged by TGI1-3K/30 thyratron to 1:6 pulse transformer connected with klystron. Additional thyratron of the same type is used to cut of the trailing edge of a high voltage pulse. The modulator provides 10 μs pulses with maximal amplitude 60 kV, current 280 A at repetition rates from 6.25 Hz to 50 Hz synchronized with the mains. Pulse top flatness is within ±0.3%. High voltage pulse form is shown in Fig. 5.

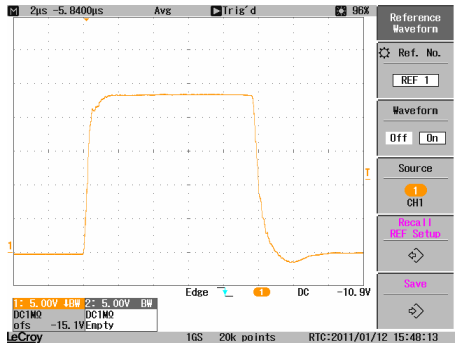

Figure 5: High voltage pulse.

Control System and Beam Diagnostic

Control system of upgraded RTM was built using standard National Instruments modules for signals control and LabView software [6]. Operator interface, providing access to control of current sources feeding steering coils and end magnets, to control of RF system, modulator and gas system is show in Fig. 6. By clicking an appropriate element at diagram the window with element parameters is opened providing possibility for their adjustment.

Beam diagnostic was improved by using multiplexer at oscilloscope input which allows to view beam current signals simultaneously from all beam current monitors, installed at RTM orbits.

To get better beam transmission through RTM orbits additional steering coils were installed at 3, 5, 7 and 9 orbits.

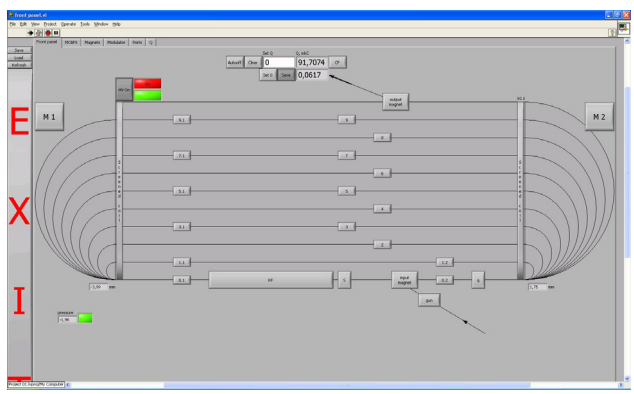

Figure 6: Screenshot of operator interface.

PHISICAL EXPERIMENTS WITH RTM BEAM

Production of the F18-Isotope With Electron Accelerator

The positron activity radionuclide F^{18} is perspective isotope for Positron Emission Tomography (PET). Now this isotope is produced by means of proton or deuteron beams from cyclotrons. But F^{18} may be obtained from $^{23}Na(\gamma,\alpha n)^{18}F$ reaction with bremsstrahlung radiation. To study the possibility F^{18} production for nuclear medicine the metal Na sample was irradiated by bremsstrahlung from 55-MeV RTM electron beam [7]. In Fig. 8. it is shown a typical spectrum of secondary γ-quanta from irradiated target, measured by high purity Ge spectrometer.

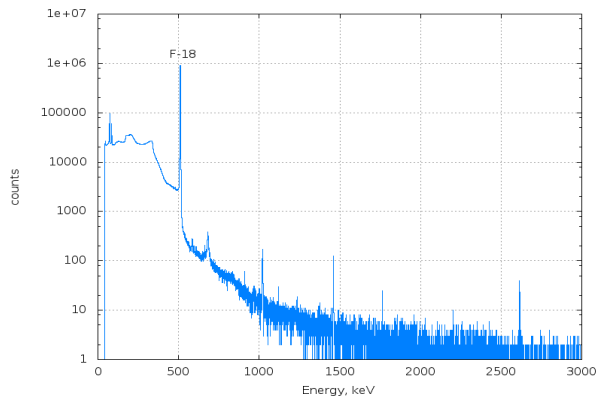

Figure 5: The γ-spectrum from the irradiated ^{23}Na sample.

This experiment shows that at the average beam current ≈40 μA, the Na target thickness ≈5 g cm^{-2}, and the irradiation time ≈5.5 h, the produced activity can be as high as ~0.1 Cu, what is about necessary level.

Besides there was studied production of ^{18}F in reaction $^{19}F(\gamma,n)$ using $(C_2F_4)_k$ – targets [8]. Results of this work for total produced activity of ^{18}F and, respectively, value of moment of cross section σ_{-1} are in reasonable agreement with known data for maximum energies of γ-quanta up to ~28 MeV.

Radiation Safety of the Photonuclear Method for Detection Explosives

The photonuclear method for detection of hidden explosives is based on registration of short-lived ^{12}N and ^{12}B radioisotopes, which are produced when a sample with carbon and nitrogen is irradiated by high-energy photons. The carbon and nitrogen are base of the modern explosives and by means of the analysis of the time-spectrum of the secondary radiation from sample the explosive may be identified. However, the irradiation of a sample with arbitrary chemical composition is able to create many different radionuclides which may be dangerous [9].

To assess the level of the radiation safety (or danger) for case when photonuclear detector will be used for inspection of airline passengers' luggage the experiments with RTM beam were done. The samples imitated the contents of the luggage were irradiated by bremsstrahlung photons as they will be irradiated in the real inspection procedure. The list of the samples included the different kinds of natural and synthetic textiles, shoes, metals (steel, copper, aluminium, gold and silver in jewelry), and gadgets (camera, radio, watch, etc). After the irradiation the dose and dose rate from the samples was measured. Besides the radioisotopes in the samples was analyzed by means of high purity Ge spectrometer. As a result of the experiments it was shown that dose from 20 kg bags is very low and the irradiated luggage is not dangerous for passengers and airport staff.

CONCLUSION

As a result of RTM upgrade higher beam stability and higher beam current are obtained with more simple tuning procedure. Radiation shielding bunker strongly reduced background radiation thus permitting to conduct more accurate experiments.

The authors would like to thank prof. B.S. Ishkhanov and Dr. L.Z. Dzhilavjan for providing by results of physical experiments.

REFERENCES

[1] A.I.Karev, A.N.Lebedev, V.G.Raevsky, et al, RuPAC-2010, p. 316-318
[2] A.I.Karev, V.G.Raevsky, J.A.Konyaev et al, Patent RF #2226686. Filed Dates: August 14, 2002, RF.
[3] I.A. Frejdovich, P.V. Nevsky, V.P. Sakharov et al, Proceedings of IVEC-IVESC 2006, Report N13.5
[4] A.N. Ermakov, D.I. Ermakov, B.S. Ishkhanov et al, Instruments and Experimental Techniques, Vol. 45, No. 4 (2002) 482–489
[5] www.protom.ru
[6] www.ni.com/labview/
[7] S.S.Belyshev, L.Z.Dzhilavyan, A.N.Ermakov, et al, Moscow University Physics Bulletin, 2012, Vol. 67, No. 3, pp. 246–250.
[8] S.S.Belyshev, L.Z.Dzhilavyan, A.N.Ermakov, et al. LXII International Conference NUCLEUS 2012, Saint-Petersburg, p. 246.
[9] L.Z.Dzhilavayan, A.I.Karev, Bulletin of the Russian Academy of Sciences. Phisics, 2011, Vol.75, No.11, pp.1557-1561.

STATUS OF 1 MEV 25 KW CW ELECTRON ACCELERATOR

D.S. Yurov, A.S. Alimov, B.S. Ishkanov, N.I. Pakhomov, V.P. Sakharov, V.I. Shvedunov, Skobeltsyn Institute of Nuclear Physics, Lomonosov Moscow State University, 119992 Moscow, Russia

Abstract

Status of 1 MeV 25 kW continuous wave (CW) linear electron accelerator for radiation technologies which is under construction at SINP MSU is described. Driven by 50 kW CW klystron on-axis coupled standing wave accelerating structure was optimized, manufactured and tuned. The results of accelerating structure measurements and tuning are presented. RF system, high voltage, vacuum and control systems of the accelerator are described.

INTRODUCTION

Industrial CW linear electron accelerator with beam energy 1.0 MeV and maximum beam power 25 kW is under construction at SINP MSU using as a prototype the two-section accelerator with 1.2 MeV energy and 50 kW maximum beam power [1]. Accelerator general view is shown in Fig. 1, main parameters are listed in Table 1.

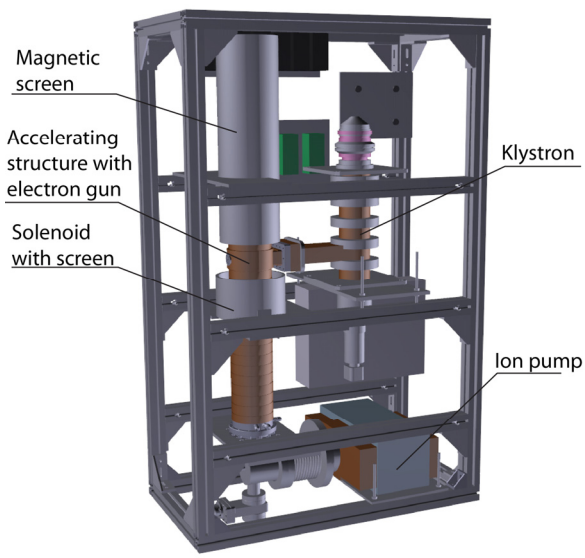

Figure 1: Accelerator general view.

Advantages of the proposed accelerator are its compactness and low weight which allows to use local radiation shielding and to incorporate the accelerator into operating material production lines which need radiation processing. The accelerator power supply system has no voltages exceeding 15 kV therefore operates without high voltage discharges.

The accelerator will be used at SINP MSU for the following purposes [2]:

- Electronics radiation stability testing.
- Solar batteries radiation degradation testing.
- Obtaining new data on variations of mechanical properties, surface structure, phase composition and microstructure of model and construction materials for nuclear reactors and nanostructure objects.
- Investigations of radiation resistance of optical materials with bremsstrahlung beam.
- Investigations of radiochemical processes.

Table 1: Project parameters of the accelerator

Beam energy	1,0 MeV
Beam current	0 - 25 mA
Maximum beam power	25 kW
Gun /Klystron high voltage	15 kV
Operating frequency	2450 MHz
Klystron power	50 kW
Electric power consumption	~75 kW
Efficiency	~33%
Dimensions	500x900x1400 mm3

ELECTRON GUN

15-keV electron gun with two intermediate anodes providing current regulation from 0 to 250 mA has been designed and manufactured (Fig. 2). The electron gun is joined directly to the input accelerating section flange without any drift space, standing alone pre-bunching cavity, and focusing elements between the gun and the accelerating section.

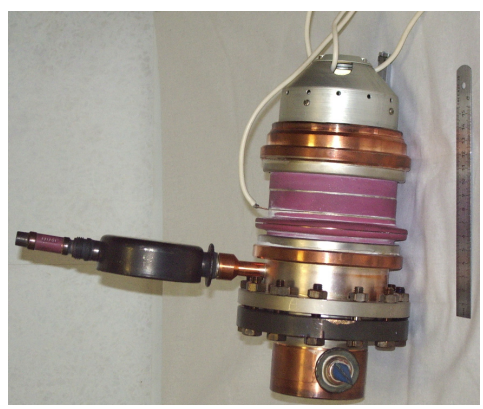

Figure 2: Electron gun after manufacturing.

ACCELERATING STRUCTURE

The accelerating structure is a standing wave bi-periodic on-axis coupled structure. As it is described in [3,4] the first accelerating cell acts as a buncher cavity while the second cell increases the beam energy to level sufficient for further acceleration in low strength field inherent to CW operation. This approach permits to get

more than 50% capture efficiency at only 15 keV injection energy.

The optimization of the accelerating structure was performed simultaneously with the computations of the beam dynamics following the iteration procedure.

Sectional view of accelerating structure is shown at Fig. 3. It includes 18 accelerating cells and 17 coupling cells. The 10th accelerating cell is used as an RF power coupler, it also carries an antenna, which provides RF signal proportional to the level of accelerating field.

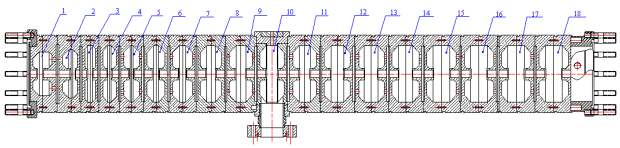

Figure 3: Sectional view of accelerating structure.

The accelerating gradient of 1 MeV/m corresponds to an RF power dissipated in the walls of the structure of ~1.07 kW per cell. The calculated distribution of accelerating field on the axis of the structure is shown at Fig 4. Fig. 5 shows calculated spectrum of accelerated beam for the RF wall losses level ~17 kW.

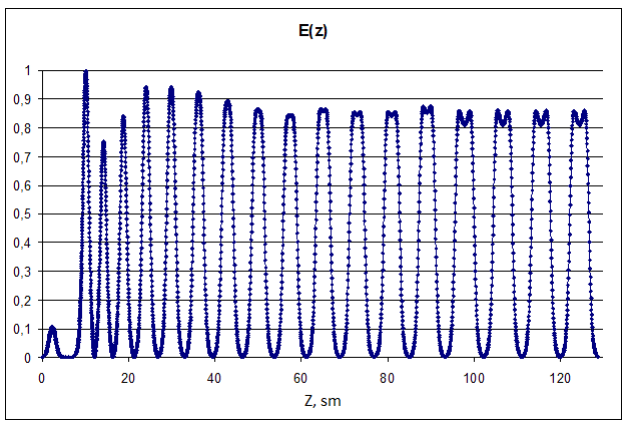

Figure 4: Calculated distribution of accelerating field on the axis of the structure.

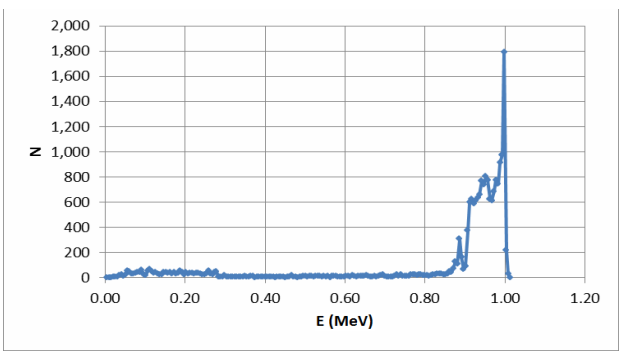

Figure 5: Calculated spectrum of accelerated beam.

On the basis of the calculations half-cells of the accelerating structure have been manufactured. The electrodynamics characteristics of the accelerating cells were measured after manufacturing, after that it was tuned [5] and brazed. The distribution of the accelerating field on the axis of the brazed structure and the photo of the structure equipped with focusing solenoid and steering coils are shown at Figs. 6 and 7, respectively.

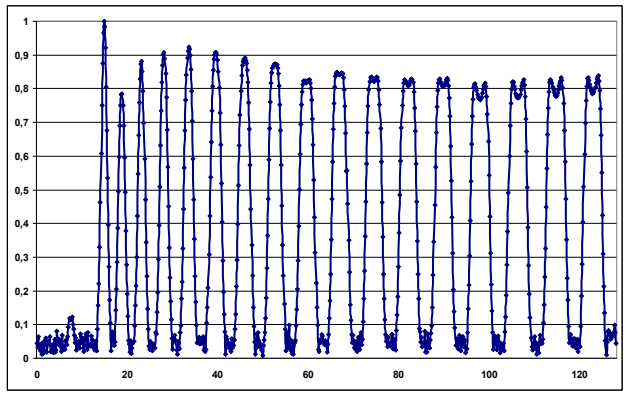

Figure 6: Distribution of the accelerating field on the axis of the structure after tuning and brazing.

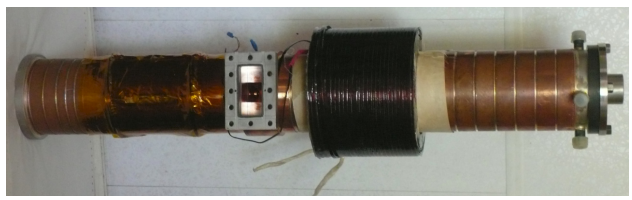

Figure 7: The photo of the accelerating structure.

RF SYSTEM

Our RF system shown in Fig. 8 uses self-excitation in a positive klystron–accelerating structure feedback loop, which makes it possible to operate accelerator without master oscillator, isolating circulator between the klystron and the accelerating structure, and without control of structure resonance frequency.

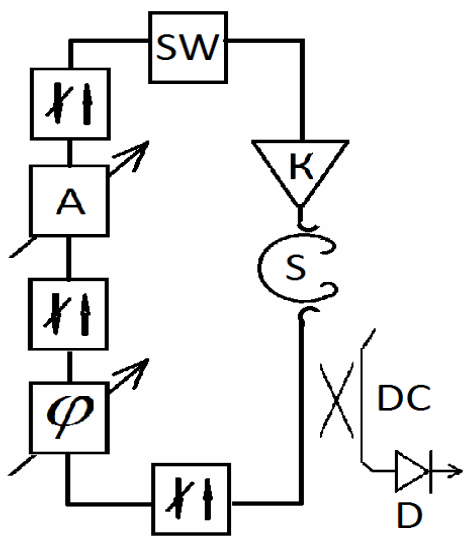

Figure 8: Block diagram of the RF system.

The phase shift and attenuation in the feedback loop, as well as monitoring of the accelerating field level, are controlled by low power RF unit. The signal from an RF

probe of the section *S* goes through a controlled attenuator *A* and a phase shifter φ to the klystron coaxial input. Due to a high loaded *Q* of the section, which is 6000–7000, self-excited oscillations are produced near the section's resonance frequency. The phase shifter and attenuator are used to select the conditions for self-excited oscillations and regulate their amplitude and frequency within given margins. The signal from the diode *D* via the directional coupler *DC* is used by control system to stabilize the accelerating field amplitude. The accelerator operation safety is provided by RF switch *SW*, which allows to cut the positive feedback loop in case of low coolant consumption, vacuum degradation, opening of the doors of acceleration chamber or switching key in the safety lock.

The operation of the RF unit is managed by the RF unit controller and interlocking controller.

To feed accelerating structure a low voltage multi-beam klystron with periodic permanent magnet focusing system KU-399A with field reverses developed at FSUE "Toriy", Moscow, Russia [6], is used. Klystron photo is shown in Fig. 9.

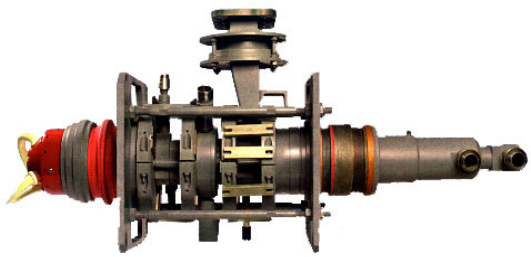

Figure 9: CW multi-beam klystron KU-399A.

VACUUM SYSTEM

Operating vacuum of the electron gun is 10^{-5} Pa, while in the accelerating structure it could be 5×10^{-4} Pa. Pumping of the acceleration structure and electron gun from atmosphere is produced by rotary vacuum pump.. High vacuum pumping is provided by 100 l/s ion pump which is installed at the exit of the accelerating structure and by separate 5 L/s ion pump, mounted at the electron gun. The accelerating structure and the klystron are separated by the klystron's vacuum window. The irradiation chamber is separated from the accelerator by the vacuum valve. Vacuum is measured by universal digital vacuum meter and the resulted value is transmitted to the control system.

HIGH VOLTAGE SYSTEM

Injection energy is chosen to be 15 keV, coinciding with the klystron high voltage, 15 kV, which allows to use common power supply for the electron gun and the klystron. To power the klystron and the electron gun, high-voltage power supply was designed. It provides high voltage to the cathode, filament voltage of the cathode heater, voltage of the control electrode, high voltage of the klystron's ion pump. It also provides 15 kV high voltage to the electron gun and allows to supply and regulate the voltages of electron gun control electrodes, as well as filament current of the gun cathode heater. The photo of the power supply is shown at Fig. 10.

Figure 10: High-voltage power supply.

CURRENT ACTIVITY PROGRESS

At the moment the accelerator is being assembled, the accelerator control system development is at the final stage

REFERENCES

[1] A. S. Alimov et al., "A Continuous-Wave Linear Accelerator with an Output Electron Energy of 600 keV, Average Beam Current of 50 mA", PTE #5 (2002) 114.

[2] A. S. Alimov, B.S. Ishkanov, V.I. Shvedunov, "Compact Linear Electron Accelerator for Radiation Technologies", MSU Herald, Series 3: Physics, Astronomy #4 (2008), p. 28-31.

[3] A.S. Alimov et al., "Method for accelerating electrons in a linear accelerator and an accelerating structure for carrying out said method". US Patent 8,148,923 B2. Apr. 3, 2012.

[4] A.S. Alimov et al., "Low-injection energy continuous linear electron accelerator". US Patent 8,169,166. May 1, 2012.

[5] A.S. Alimov, B.S. Ishkanov, V.I. Shvedunov, "Method of Measurements and Tuning of Accelerating Structures", PTE #4 (2008), p. 1-9.

[6] I.A. Frejdovich, P.V. Nevsky, V.P. Sakharov et al., "Proceedings of IVEC-IVESC 2006", Report N13.5.

PROTON CHANNEL THAT PROVIDES SIMULTANEOUS INDEPENDENT OPERATION OF A TREATMENT ROOM OF PROTON THERAPY AND NEUTRON SOURCES OF THE EXPERIMENTAL COMPLEX INR RAS

M.I. Grachev, E.V. Ponomareva, S.V. Akulinichev, L.V. Kravchuk, INR RAS, Moscow, Russia
V.N. Zapolsky, IHEP, Protvino, Russia

Abstract

During 2012 we have developed the system for beams separation, based on the splitter magnet, for simultaneous work of neutron source RADEX and a treatment room of the complex of proton therapy (CPT).

This set up also allows for an independent change of protons energy in the channel of proton therapy in a wide range from 209 MeV to 70 MeV.

The system is an extension of the main channel of the proton and H^- beams, previously described in [1]. Main channel carries out the simultaneous transportation and elevation of the beams H^- and protons in the experimental hall of INR RAS.

BEAMS SEPARATION AND UPGRADE OF THE CHANNEL TO RADEX

Figure 1 depicts the layout of the beams separation the beams line. After magnet 4MC the main beams line (protons and H^-) from Linac distributes to three beam lines as shown in Fig.1. Magnet 2MC2 [1] has been replaced by a pair of magnets 4MC and 4M.

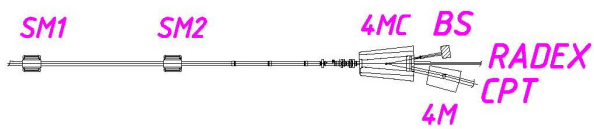

Figure 1: Layout of the beams separation: SM1, SM2 – steering magnets, 4MC – Lambertson magnet, 4M – bending magnet, BS – beam stopper, RADEX – neutron source, CPT – complex proton therapy.

A pair of magnets of this scheme provides a correction in the position of the deflected beam at its axial passage through the hole without the field of magnet 4MC.

The poles of magnet 4MC were developed by NIIEFA as part of the design Lambertson Septum Magnet for the proton storage ring. Coil of the magnet 4MC have been manufactured from the radiation-resistant water-cooled cable of PYROTENAX type.

The block of water-cooled poles is placed in the thin walled vacuum stainless steel chamber. There are the apertures in the upper and lower poles.

Wall thickness between the aperture and the gap is about 1 mm. Fig.2 and Fig.3 represent the photos of magnet 4MC (downstream and upstream respectively).

Detailed description of this magnet will be presented in the next paper.

Figure 2: 4MC magnet assembly view downstream.

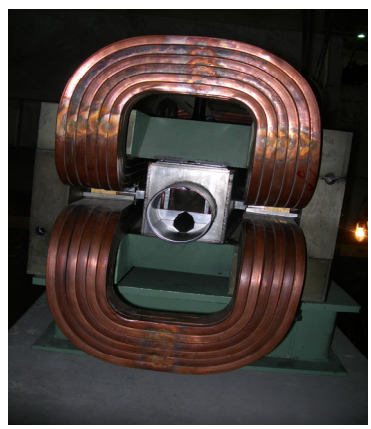

Figure 3: 4MC magnet assembly view looking upstream.

Wall thickness between the hole and the pole is about 1 mm. Detailed description of the magnet will be presented in the next paper.

In front of the magnet 4MC a thin foil is installed, with aperture of different diameters, to control the intensity of the beam H^-. The thickness of the foil is sufficient for a recharge H^- in protons. Protons from distribution tails are deflected after recharging in the BS - beam stopper.

Due to the fringe fields, especially at the exit of the magnet, the direct beam experiences a deflection on some mrad. The set of doublet lenses L31-L32 is installed in order to fix the position of the beam on the target of the neutron source RADEX. These lenses focus the centre of magnet 4MC on the target centre (Fig.4).

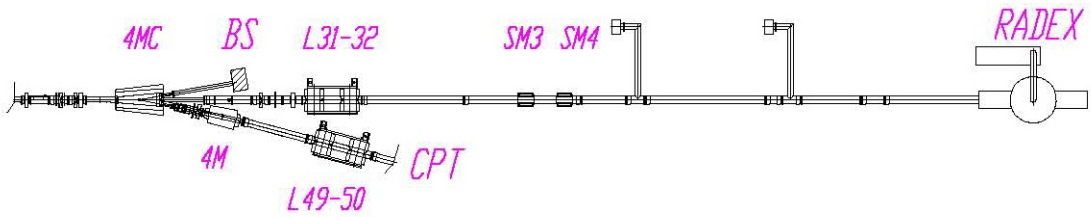

Figure 4: Part of the channel to RADEX : 4MC – Lambertson magnet, SM3,SM4 – steering magnets, doublet L31-L32, BS – beam stopper for recharged protons from H^-, RADEX – neutron source.

Calculations showed that the coefficient of magnification in x and y at the target is 3 and 7 respectively, depending on the type of focus, eliminating the beam focus to critically small size.

Beams H^- and protons are displaced vertically relative to each other by 4 cm by steering magnets SM1 and SM2 (see on Fig.1), that have opposite polarity. Further inside the magnet 4MC, one beam passes through the aperture in the pole (bottom pole on Fig.3); the other is deflected by an angle of 11.5^0.

The water-cooled magnetic screen is placed at the entrance of the magnet to reduce local fringe magnetic field, and to protect the iron plate septum from high intensive beam. Table 1 shows the results of the measurements of magnetic fields in the septum magnet.

Table 1: Septum Magnet 4MC (209 MeV).

Magnetic field in the gap	0.4 T
Integral fringing field at the beam entrance of magnet with magnetic screen	0.002 T x m
Integral fringing field at exit of magnet	0.01 T x m

CHANNEL TO COMPLEX OF PROTON THERAPY

The deflected beam is directed into the channels on the installation CPT or other neutron sources. Here we present the work of the channel for the CPT, whose optical scheme is changed for independent adjustment of the energy of the protons in the beam.

Channel functionally consists of two parts:

- Head channel, focusing the beam on a wedge-shaped absorber.
- Main medical channel, shaping of the beam for the treatment room of CPT.

One of the features of the main part optical scheme is the availability of considerable coefficient of the magnification at the end of the channel. This allows us to increase the number of protons after the wedge-shaped absorber by reducing the angular divergence of the particles in the channel and thus reduce the losses.

Compared to the previous scheme of the channel [4] the following changes have been implemented:

- Beam H^- is the basic beam of the channel.
- Control of the intensity of particles in the beam is done by recharging the beam in front of the magnet 4MC to protons, which are deflected in the opposite direction and are absorbed in a beam stopper outside the channel (Fig.1, Fig.2).
- Lenses L49-L50 and L51-L54 are included.
- Wedge-shaped beryllium degrader and tantalum collimator with diameter 4mm, have been installed;
- The tantalum aperture collimator has been installed.
- The momentum collimator has been installed.
- The second aperture collimator for halo beam absorption has been installed.

Fig.5 shows the optical scheme of the main channel onto the installation CPT and the beam envelope.

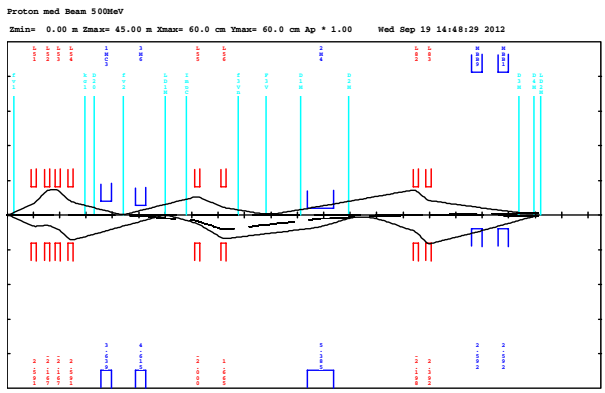

Figure 5: Optical scheme of the channel for CPT calculated by Transport [3].

Results of calculations show that a modernised channel scheme makes it possible to obtain the necessary intensity of the beam under working energies of the accelerator of 209, 160 and 127 MeV [2]. Using the movement of the degrader allows changing the beam energy continuously with acceptable losses. However any significant insertion of the degrader and a simultaneous decrease in the proton energy from 209 MeV to 70 MeV leads to the fact that beam intensity of the protons, reaching the end of the medical channel, is greatly reduced. Calculation results are given in Tables 2 and 3 (calculations are done using TURTLE program [5]). Part of number of particles at the end of the

channel (Table 2) and the main parameters of the beam in Table 3 are shown for three value of energy.

Table 2: Calculation results for the beam's intensity in the channel onto CPT, using beryllium degrader and tantalum aperture collimator with diameter 40 mm

The change in energy of the protons in the channel, MeV	**Part of number of particles that reached the end of the channel, %**
209 → 160	2.74
160 → 120	2.45
120 → 70	0.64

Table 3: Parameters of the beam (RMS half width) in the channel onto CPT, using beryllium degrader and tantalum aperture collimator with diameter 40 mm

The energy of the protons in the beam after the degrader, MeV	**X, mm**	**X′, mrad**	**Y, mm**	**Y′, mrad**	**ΔE, MeV**
160	4.83	2.70	0.72	1.62	0.717
120	4.89	2.80	0.82	1.60	0.650
70	5.03	3.22	1.20	1.61	0.569

Currently the assembly and installation of the equipment is carried out in the experimental hall at INR RAS. Testing of the new channel is expected to take place in the early 2013.

ACKNOWLEDGMENT

Authors are grateful to the fund RFFI for the support of the project.

REFERENCES

[1] M.I. Grachev, E.V. Ponomareva, "Optical Design of the Proton Beam Lines for the Neutron Complex INR RAS and Medical Application," IPAC'11, San-Sebastian, September 2011, WEPCO21, p. 2049-2051, (2011); http://www.JACoW.org

[2] S.V. Akulinichev, V.N.Vasiliev, Yu.K. Gavrilov, M.I.Grachev, E.V. Ponomareva, V.N.Zapolsky, "Tuning of the INR Therapeutic Proton Beam," RuPAC-2010, Protvino, Russia, p.396-398, (2010).

[3] U. Rohrer, Graphic Transport, downloadable code with some online documentation via the web, http://people.web.psi.ch/rohrer_u/trans.htm.

[4] M.I. Grachev, E.V. Ponomareva, L.V. Kravchuk, V.K. Gorbunov, V.M. Skorkin, INR, Moscow, Zapolsky V.N.# IHEP, Protvino, "System of preliminary formation of the beam for the channel of proton therapy", proceedings of XXI RuPAC 2008, Zvenigorod, Russia, p.352-354, (2008).

[5] U. Rohrer, Graphic TURTLE, downloadable code with some online documentation via the web, http://aea.web.psi.ch/Urs_Rohrer/MyWeb/turtle.htm

BEAM SCANNING SYSTEM OF LINEAR ACCELERATOR FOR RADIATION PROCESSING

M.I.Demsky, V.V.Krotov, D.E.Trifonov, CORAD Ltd., Saint-Petersburg, Russia

INTRODUCTION

Company CORAD Ltd. has elaborated the beam scanning system for irradiation of opposite sides of the boxes during one pass. This system will be useful for irradiation of products which are difficult to rotate on 180 degrees mechanically and as alternative instead of a mechanical rotation system.

SYSTEM DESCRIPTION

Beam scanning system is shown at Fig.1 has two windows for the irradiation of products from two opposite sides.

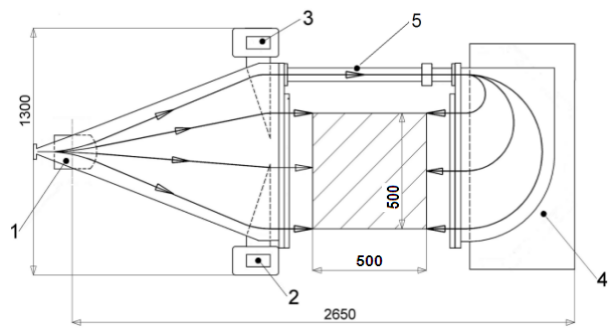

Fig.1. Beam scanning system scheme.

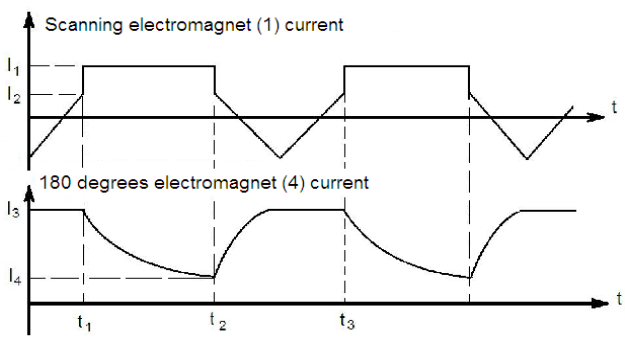

Fig.2. Electromagnets currents.

This device consists of two vacuum chambers, connected by electron beam channel (5), which is placed sideways from an irradiated product. Electron beam is scanning in vertical strip of 500 mm length by means of the scanning electromagnet (1) with the saw-tooth shape of a current in a winding as shown at Fig.2 in the time period t_2- t_3. The beam moves from the top to bottom and back along the first extraction window, and afterwards jumps up to input of bending electromagnet (3) and transits in the second 180 degrees electromagnet (4) through the electron beam channel, due to the abrupt change of a current in a scanning electromagnet (1) to the given constant value I_1. The beam moves from the top to the bottom along the second extraction window due to the changing current in the electromagnet (4) from value I_3 up to value I_4 and the product is irradiating from the opposite side. The field in a scanning electromagnet (1) jumps sharply to the value corresponding to the top position on the first window I_2 and process is repeating again. Electromagnets (2) and (3) allow improving parallelism of the beam, which comes out of the first extraction window. The computer control system produces the required hyperbolic shape of current in the time period t_1- t_2 and quite linear saw-tooth shape of current in time period t_2- t_3 in order to achieve the necessary homogeneity of dose along both scanning windows.

EXPERIMENTAL RESULTS

This system has been tested on the linear electron accelerator UELR-10-15S2 with the electron energy of 10 MeV and up to 15 kW of the beam power. This accelerator was made on the base of standing-wave accelerating structure made by NIIEFA (St.Petersburg, Russia) with use of the klystron TH2173F made by Thales Electron Devices S. A. (France). The photo of this system is shown at Fig.3.

Fig.3. Beam scanning system photo.

The beam pulse measured after the first extraction window on a beam stop has 290 mA amplitude and 19,2 microseconds of pulse width and after the second extraction window – 270 mA and 18,2 microseconds respectively. The beam losses reached ~900W in the second electromagnet for 15 kW beam power. These losses were compensated by increasing the time period t_1-t_2. The dose distribution after extraction windows measured by plastic dosimeters is shown on Fig. 4 and Fig. 5. Dose uniformity was better than +/-5 % for both sides.

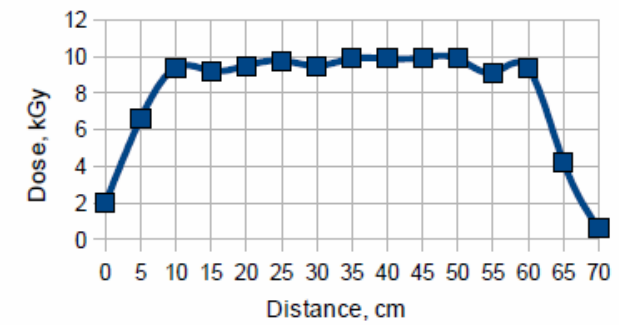

Fig. 4. Dose distribution on the distance of 300 mm from the first extraction window.

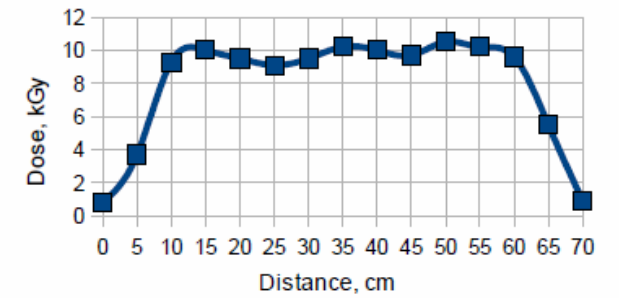

Fig.5. Dose distribution on the distance of 300 mm from the second extraction window

THE IDK-6/9MEV LINEAR ELECTRON ACCELERATOR AND ITS APPLICATION IN THE CUSTOMS INSPECTION SYSTEM

V.P. Malyshev#, A.V. Sidorov, P.O. Klinovskiy, K.V. Kotenko, B.O Bolshakov., V.S. Smekalkin, D.V. Efremov Scientific Research Institute of Electrophysical Apparatus, Saint Petersburg, Russia.

Abstract

A linear electron accelerator IDK-6/9MeV has been designed for operation as a source of ionizing radiation in a customs inspection system intended for inspection of large-scale cargos. The main operating mode of the accelerator is the X-ray mode with an energy of 6 MeV, which ensures the penetrability more than 300 mm (for steel). The operating mode of the accelerator can be quickly changed for 9 MeV, which allows the objects under study to be discriminated based on the organics/non-organics criterion using the "two energies" method.

A triode electron source with cathode and grid modulators is applied in the accelerator. A system of collimators located at the output of the accelerating device serves to form a fan-shaped X-ray beam in the vertical plane with an opening angle of 46^0 directed towards the detector line. The accelerator is equipped with a computerized system of protective interlocks and control, which makes possible its operation both in the setting mode and as a component of the whole customs inspection system.

IDK-6/9MEV LINEAR ELECTRON ACCELERATOR

Up-to-date equipment for inspection of the cargos transported abroad are nowadays a mandatory requirement to ensure a high throughput, efficiency and quality of inspection at customs checkpoints. Customs inspection of large-scale containers and trucks is the most complicated procedure as it involves labor and time – consuming handling operations. Design features of vehicles can also be used to hide smuggled goods. An X-ray customs – inspection system allows an image necessary for the identification of a large-scale container or vehicle to be obtained within several minutes. In the case of any suspicious goods observed on the obtained image or non-compliance of the actual cargo with that described in the cargo customs declaration, a manual inspection can be assigned.

The linear electron accelerator IDK-6/9MeV has been designed as a source of ionizing radiation to be used in a customs inspection system intended for inspection of large-scale cargos and vehicles (Fig. 1).

Figure 1: The IDK-6/9ÌeV accelerator in a customs inspection system.

#npkluts@niiefa.spb.su

The IDK-6/9MeV linear electron accelerator generates the X-ray radiation with energies of 6 and 9 MeV.

The main operating mode of the accelerator is the X-ray mode with an energy of 6 MeV, which ensures the penetrability more than 300 mm (for steel). If more accurate identification of objects under inspection is necessary, the operating mode of the accelerator can be quickly changed for 9 MeV. This allows the objects under inspection to be discriminated based on the organics/non-organics criterion using the "two energies" method [1].

A 950 mm - long standing-wave accelerating structure, which allows the acceleration of electrons up to 9 MeV, is applied in the IDK-6/9ÌeV accelerator. The working vacuum in the accelerating structure is provided by two ion pumps installed near the electron source and target unit. Energy is changed by changing the accelerated electron beam pulse current loading of the accelerating structure. If necessary, the energy can be adjusted by changing the level of the microwave power supplied to the accelerating structure from the MG6090 magnetron generator. A triode electron source with cathode and grid modulators applied in the accelerator ensures the accelerator change-over from one energy to the other by adjusting the amplitude of the beam current pulse. Optimization of the X-ray dose rate on the detector line is also possible by changing the beam current pulse length separately for each operating mode of the accelerator. The magnetron modulator used in the accelerator allows the pulse voltage across the magnetron cathode to be smoothly controlled in the 40-48 kV range. This makes possible the 2-3 MW pulse power to be obtained at the magnetron output with a pulse length of 5 μsec and pulse repetition rate of 200 Hz. A possibility to adjust the magnetron output power allows the operating mode of the accelerating structure to be optimized when the accelerator is set for boundary X-ray energies, and the output power decrease caused by the magnetron aging can be compensated in the process of operation. The operating frequency of the accelerating structure varies in the process of operation as the equipment is warmed-up. The magnetron frequency is tuned to the operating frequency of the accelerating structure by means of an AFT system operating on the principle of minimizing the RF power pulse reflected from the structure. The setting mode provides for the manual control of the magnetron frequency.

The accelerator is equipped with a computer-controlled system of protective interlocks and control made on the basis of the Siemens S7-300 logical controller. This system allows the accelerator operation to be controlled and its complete functionality to be ensured. The control system of the accelerator realizes protective interlocks, measures analog operating parameters of the accelerator, switches on and off necessary units and components of the accelerator in accordance with the control program and sends commands to the power supply sub-system to set up necessary parameters. Special-purpose modules are controlled by means of the RS-485 digital serial interface. The control system is designed for remote control via the Industrial Ethernet interface and is a part of the whole customs inspection system. The system provides for a log book, in which operating parameters and main events occurring during the accelerator operation are entered. When operating the accelerator in the automatic mode, an operator usually gives the four following commands: "Warm up the accelerator", "Start the inspection", "Start the inspection in the additional mode" and "Switch the accelerator off". In so doing, status messages and main parameters are sent to the operator's workstation. For fine setting of the accelerator parameters and for the setting of operating modes, a setting mode is provided for. In this mode, setting of separate parameters of the accelerator can be done, detailed control of the accelerator operating stages and obtaining of a wider range of the accelerator operating parameters.

A system of collimators located at the output of the accelerating structure serves to form a fan-shaped X-ray beam in the vertical plane with an opening angle of 46^0 directed towards the detector line.

Structurally the accelerator consists of four parts, in particular, the irradiator cabinet, water cooling and temperature control unit, control cabinet mounted on a gantry moving along an object inspected, and control panel located in the operators' room. The irradiator cabinet houses the main units of the accelerator: the accelerating device with an electron source and target unit, magnetron modulator, electron source modulator, ion pumps, waveguide line, power supply units, actuator components of the control system and a system of collimators.

Nowadays, works on the accelerator updating are underway. The main objectives are:

- to ensure the accelerator operation in the "dual energy" mode;
- to make simpler the schematic and design of the accelerator;
- to ensure higher reliability and stability of the accelerator equipment operation.

REFERENCES

[1] S.A. Ogorodnikov, V.I. Petrunin, "Radioscopic System with the Dual Energy for Customs Inspection of Large-Scale Vehicles and Containers," XVII Conference on Charged Particle Accelerators, Protvino, Russia, October 2000.

UPDATING OF THE "ELECTRON-3M2" ACCELERATOR IN THE LINE FOR RADIATION CURING OF POLYMER COATINGS

V.P. Ovchinnikov#, I.V. Druzgalckiy, V.P. Maznev, M.P. Svinin,
D.V. Efremov Scientific Research Institute of Electrophysical Apparatus, Saint Petersburg, Russia
O.V. Borisov, V.V. Koltsov, A.I. Seleznev,
JSC "Admiralty Shipyards", Saint Petersburg, Russia

Abstract

More than thirty years ago the «Electron-3M» accelerator was delivered to FSUE "Admiralty Shipyards" to be operated in the line for radiation curing of polymer coatings. In 2008-2009, works on updating the machine were performed to increase its reliability and make much easier its maintenance in the process of operation. After obtaining nominal parameters on the updated accelerator «Electron-3M2», the intensity of bremsstrahlung on the surface of the accelerator shielding was measured; the obtained data confirmed its compliance with corresponding normative documents. Measurements of parameters of the accelerator electron radiation field have demonstrated that the uniformity coefficient of the beam current linear density is 5%, and the symmetry coefficient amounts to 1%. The beam current and accelerating voltage instability during one hour of operation does not exceed 1%. After the updating, the lifetime of the accelerator will be not less than 10 years.

High voltage «Electron-3» accelerators and their modifications manufactured in NIIEFA in 1975-1985 [1, 2, 3] have been widely used in various research and industrial radiation-processing facilities. More than fifteen similar machines have been manufactured including 12 accelerators to be used in the shipbuilding industry. Inspection of these machines performed after the end of the planned 10-year operation period have demonstrated that major components, in particular, high voltage generator, electron source and accelerating structure remained in good working condition. However, a series of units and systems needed replacement because of depreciation and obsolescence.

The «Electron-3M1» accelerator was put into operation in 1977 in the JSC "Admiralty Shipyards". In 2001-2002, works on its updating were performed. In the process of the updating the following devices and systems were designed, manufactured, adjusted and put into operation:

- scanning device with a bellows branch pipe, which allowed the non-uniformity of the beam current distribution in the irradiation zone to be reduced;
- independent closed water cooling system;
- systems to control the filament current of the electron source and to stabilize the accelerator beam current by using fiber-optics lightguides;
- system for automatic control of the accelerator based on an industrial computer.

#ovchinnikov@luts.niiefa.spb.su

High-vacuum pumps were also replaced with pumps of higher pumping capacity.

To meet the requirements of the new Principal Sanitary Radiation Safety Rules (OSPORB-99), means of radiation monitoring have been replaced and thickness of the radiation shielding has been increased.

In the updated accelerator, there was used an extraction window with a supporting grid made with wedge ribs with a variable inclination angle α (see Fig. 1), which transparency coefficient for the electron beam K is higher than its optical transparency (see Table 1).

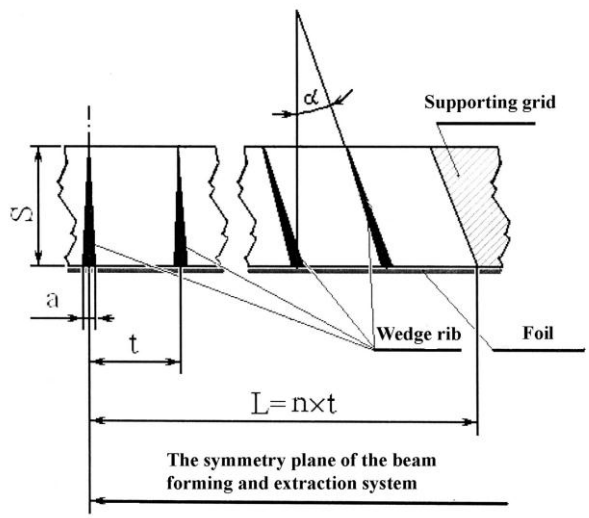

Figure 1: Fragment of the extraction window with the supporting grid (the cross-section along the window long side): "L" is the maximum beam deviation from the plane of symmetry; "S" is the thickness of the supporting grid; "t" is the distance between ribs; "a" is the rib thickness.

Table 1: Measurement of the beam current passed through the extraction window.

Distance from the beam absorber to the diaphragm, mm	Supporting grid	Current recorded by the beam absorber, mA	*K*
50	Without grid	0.80	0.95
	With grid	0.76	
105	Without grid	0.76	0.93
	With grid	0.71	

K is the transparency coefficient of the supporting grid for electrons; it is found as a ratio of current magnitudes at the beam absorber with and without supporting grid. Measurements were carried out with an accelerating tube beam current of 1 mA and accelerating voltage of 700 kV. The extraction window was covered with a titanium foil of 50 μm thickness. Optical transparency of the supporting grid was 0.86. Beam dimensions at the extraction window diaphragm were 15×940 mm.

The works carried out increased appreciably the reliability of the accelerator and made much more easy maintenance of the machine. However, the irradiator with the film-oil insulation was still used, which long ago had worked out its lifetime and was not subject to repair in the case of its failure.

Therefore, in 2008-2009 works to replace the irradiator of the «Electron-3M1» accelerator installed in the JSC "Admiralty Shipyards" with a gas-insulated irradiator shown in Fig. 2 were performed Its design is similar to that of the «Electron-10» accelerator [4], differing in larger number of turns in sections of its secondary winding. This allows the available ATO-20 electric generator to be used to supply power to the irradiator.

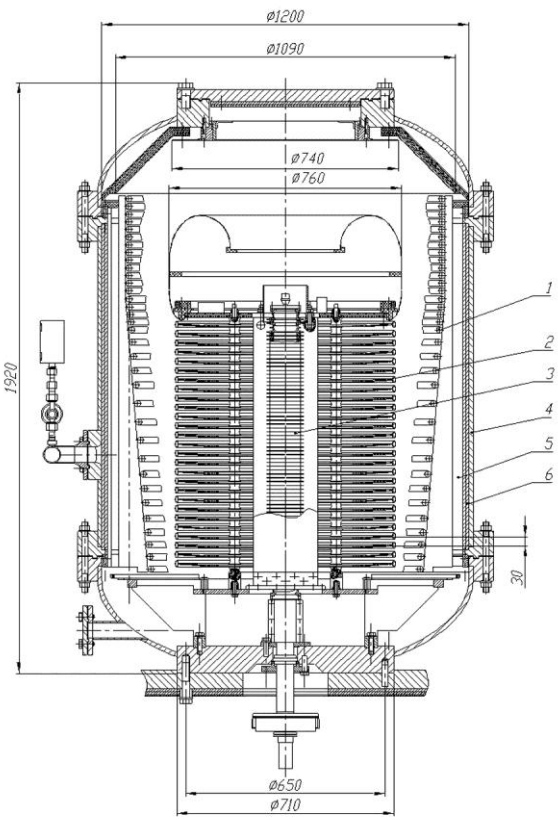

Figure 2: Irradiator with the gas insulation of the «Electron-3M2»: 1 - primary winding, 2 - section of the secondary winding, 3 - accelerating tube, 4 - high-pressure vessel, 5 - core-type magnetic circuit, 6 - lead shielding.

The single-layer primary winding of the irradiator, disk sections of the secondary winding (located coaxially with the primary winding) with connected to it rectified voltage doubling circuits and accelerating tube are placed inside a metal vessel filled with a pressurized gas. On the inner surface of the vessel, core-type magnetic circuits, which close the magnetic flux created in the primary winding of the irradiator, and the lead shielding against bremsstrahlung are installed.

The irradiator and a site for its maintenance/repair are installed on the chamber of the accelerator radiation shielding (see Fig. 3).

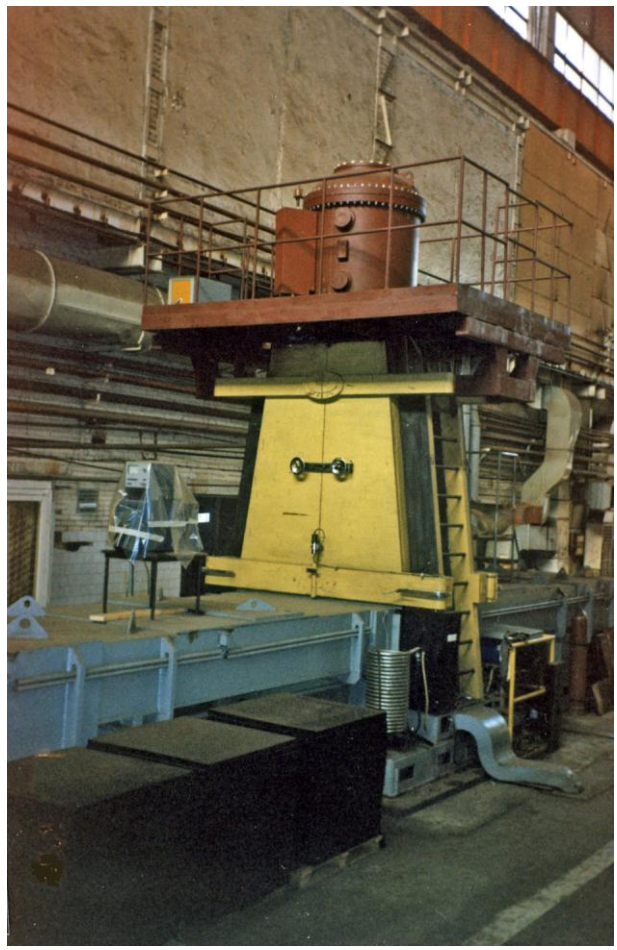

Figure 3: The «Electron-3M2» accelerator in the line for radiation curing of polymer coatings.

When the «Electron-3M2» accelerator with the updated irradiator was put into operation, the following nominal parameters of the electron beam were attained: energy of electrons of 700 keV and beam current of 10 mA. In this case the voltage of the ATO-20 generator was 220 V and the load current amounted to 65A. An increase in the accelerator beam current up to 15 mA will result in the ATO-20 generator voltage and current of 225 V and 80 A, which are also acceptable.

Radiation inspection of the accelerator has been performed and a sanitary-epidemiological certificate has been issued by Interregional Administration №122 of the Federal Medical and Biological Agency of the Russian Federation certifying the compliance of the accelerator with normative documents.

Specialists of the Department of Ionizing Radiation Measurement Department of FSUE "All-Russian D.I.

Mendeleev research Institute for Metrology" measured parameters of the accelerator electron radiation field. Figure 4 shows a graph demonstrating a current distribution at the electron beam probe (Faraday cup) along the accelerator radiation field with a total beam current of 5 mA. At the 70 mm distance between the accelerator foil and the probe and an irradiation field width of 1000 mm, the uniformity coefficient was 5%, and the symmetry coefficient amounted to 1%.

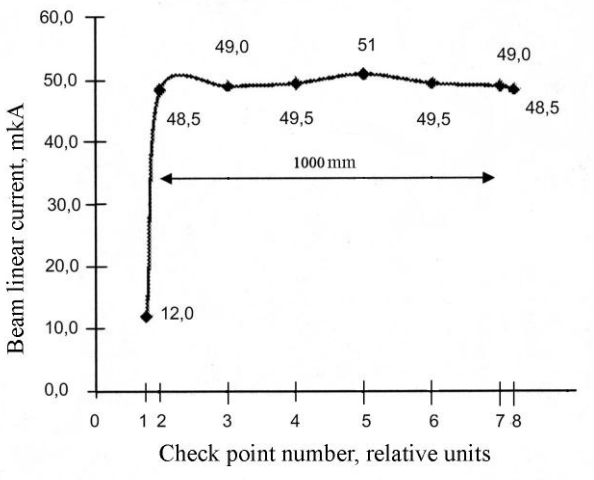

Figure 4: The «Electron-3M2» accelerator. Current distribution of the beam current probe in the irradiation zone.

Measurements carried out in the process of testing the accelerator with the updated irradiator, have also shown that the beam current and accelerating voltage instabilities during one hour did not exceed 1%.

Nowadays, the «Electron-3M2» accelerator is still operated in the line for radiation curing of polymer coatings in the JSC "Admiralty Shipyards" and ensures the fulfillment of a production program.

The results obtained allow similar updating to be recommended at other enterprises where accelerators of the «Electron-3» series are used. After the updating, the lifetime of these accelerators will be not less than ten years.

REFERENCES

[1] A.E. Kurbatov, O.B. Ovchinnikov, M.T. Fedotov et al., "Operation experience and possibilities for updating radiation chemical facilities with «Electron» accelerators for production of radiation cured articles of polyethelene", Proceed of the 3rd All-Union Conference on Applied Charged Particle Accelerators, St. Petersburg, v. 1, p. 74 (1979).

[2] V.V. Akulov, A.S. Ivanov, V.P. Ovchinnikov et al., "The «Electron-3M1» accelerator and its updating", Proceed. of the 3rd All-Union Conference on Applied Charged Particle Accelerators, v. 1, p. 81 (1979).

[3] B.I. Albertinsky, M.P. Svinin, S.G. Tsepakin, "The use of the operation experience of high voltage accelerators to increase their reliability indices", Proceed of the 4th All-Union Conference on Applied Charged Particle Accelerators. St. Petrsburg, v.1, p. 186 (1982).

[4] M.P. Svinin, "Status of high voltage accelerators development in the D.V. Efremov Institute (NIIEFA)", Proceed of the 10th International Conference on Applied Charged Particle Accelerators in Medicine and Industry (ICAA'01), St. Petersburg, p. 15 (2001).

.

HIGH EFFICIENCY [F18]FLUORIDE TARGET SYSTEM FOR THE EFREMOV INSTITUTE CC-18/9 CYCLOTRON

D. Sysoev, V. Zaytsev, M. Mostova, O. Shtukovskiy, RRCRST, Saint-Petersburg, Russia

Abstract

Positron emission tomography (PET) is a nuclear medicine imaging technique that produces a three-dimensional image or a picture of functional processes in a body. The system detects pairs of gamma rays emitted indirectly by a positron-emitting radionuclide (tracer), which is introduced into the body on a biologically active molecule.

If a biologically active molecule chosen for PET is FDG, 2-deoxy-2-[18F]fluoro-D-glucose, an analogue of glucose, concentrations of the tracer imaged then give tissue metabolic activity in terms of regional glucose uptake. Use of this tracer, to explore the possibility of cancer metastasis (i.e., spreading to other sites), results in the most common type of the PET scan in the medical care (95% of current scans).

Due to the short half-lives of the most positron-emitting radioisotopes, the radiotracers have traditionally been produced using a cyclotron in close proximity to the PET imaging facility. The half-life of fluorine-18 is long enough for manufacturing radiotracers labeled with fluorine-18 commercially at offsite locations and transporting to the imaging centers. Since radiochemistry lab in the RRCRST produces FDG for needs of our PET-center and also for two PET-centers in Saint-Petersburg (currently), it is of major importance to produce sufficient amount of fluorine-18 and to obtain FDG with a high radiochemical yield.

The aim of this work was to develop and construct a highly efficient target system for producing fluoride-18 with the Efremov CC-18/9 cyclotron, which is a negative ion system that accelerates 18 MeV ions. The maximum achievable beam current is 100 μA. The beam profile measured with a scanner indicates that approximately 95% of the beam is distributed within a 20 mm diameter circle.

The former fluoride-18 target system for this cyclotron, supplied by the cyclotron producer, the Efremov Institute, had insufficient productivity, not greater than 1 Ci of fluorine-18 during 2 hour irradiation, and didn't allow achieving high radiochemical yields in producing radiopharmaceuticals due to contamination of irradiated water with metallic impurities from target body.

TARGET CONTRUCTION

The major demerits that caused poor performance were inadequate heat transfer rate of the target body and an inadequate water layer. Since the heat input exceeded the heat removal capability of the target, excessive voiding occured in the target water. Protons of a given energy have a characteristic range in water which is inversely related to the water density. Since the water density decreases with the void fraction, the operating void fraction dictates the necessary target depth to prevent the beam from penetrating to the target rear surface. If the proton beam penetrates the water volume and deposits heat in the back wall of the target, the fluoride-18 yield will be reduced due to less proton interactions in the water. Interactions between the beam and the target surface can also release metal ions into water, which react with the ionic fluorine-18 and cause further reduction of the yield.

To prevent the proton beam from striking the back wall of the target, the target must be range thick. The target depth should exceed the range of the protons in the saturated mixture. The range of protons with incident energy between 0 and 18 MeV in water has been determined using the Stopping and Range of Ions in Matter program (SRIM), presented in fig. 1. A 5 mm depth of the target chamber was chosen to provide full functionality with 65/35 % water/vapour mixture (at 8 bar).

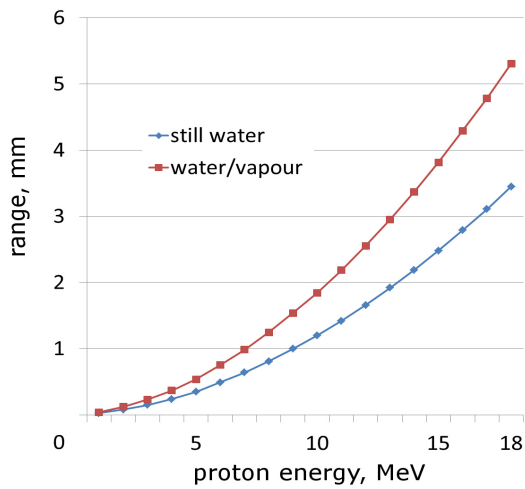

Fig.1. Proton range in water (SRIM).

Niobium has been chosen as a material for the target body, since it is a proper and well-known interface material due to its excellent chemical compatibility. Unfortunately, niobium suffers from a relatively low thermal conductivity. To overcome this problem, heat exchange mechanisms other than simple water-metal-cooling water conduction have to be considered. The new target has been designed to allow boiling in the target chamber to take advantage of the high rate of heat transfer. Heat deposition in the water causes boiling and results in formation of voids or bubbles. The buoyancy

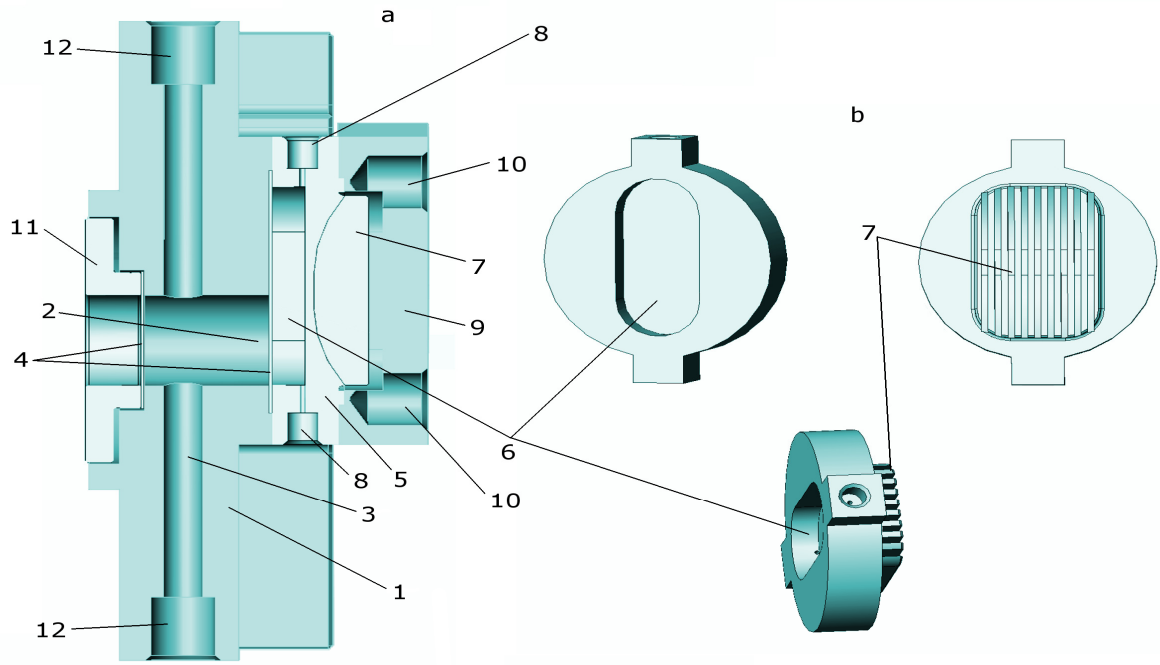

Fig.2. Target system scheme.

forces cause these bubbles to rise and condensate on the walls of the target. The condensation region mode of operation implies that bubbles, which rise to the top of the target, enter a distinct condensation region. Steam condenses on the chamber walls and flows back down the walls into the boiling pool. Aluminum has been used for the target housing due to its low cost and ease of machining. Since the target cooling system is located completely within the tantalum internals, good thermal contact between the internals and the housing is not necessary.

Target system scheme is presented in fig. 2a, target body is presented in fig. 2b, where 1– main flange, 2 – proton window, 3 – helium cooling chamber, 4 – foils, 5 – target body, 6 – irradiated volume/condensation surface, 7 – fins (grill), 8 – 1/4"-28 UNF threads for Supelco fittings, 9 – cooling water flange, 10 – cooling water inlet/outlet, 11 – vacuum-helium foil holder, 12 – G1/4 pipe threads.

COMSOL HEAT EXCHANGE MODEL

To improve heat exchange between cooling water and the target body, fins are used. The fins significantly increase the target surface area for heat transfer without significant increase of the effective conduction distance. For certain geometries, addition of fins can greatly improve heat removal capability. Effectiveness of adding fins has been investigated to gain additional heat removal margin. Additional heat transfer gained by adding fins has been calculated using a COMSOL Multiphysics heat transfer model (fig. 3). Fins of different rectangular configurations have been investigated (1, 1.5 and 2 mm thick). In all cases, calculations were carried out at the wall thickness of 1.5 mm. Boiling and cooling heat transfer coefficients have been acquired experimentally for model niobium target body with 1.5 mm fins. Mode that ensured yield at least 80% of the theoretical saturation yield for the model target has been chosen as a reference point (37 μA, 629 W). Calculated effect of fin height on total dissipated heat is represented in fig. 4. One can see that under described conditions (8 bar pressure inside target chamber and existing cooling system with known heat transfer coefficients) dissipated power as high as 860 W (50 μA) is achievable. It should be noted that operation of the target is still possible above the defined thermal limit, though 18F yields will suffer.

Since it is difficult to evaluate the exact contribution of different heat transfer mechanisms that affect chamber inner wall, simulated heat input is considered to be uniform throughout the chamber wall surface. That simplification still leaves a possibility to evaluate optimal fin configuration and improve productivity of the target system.

Target system has proven its efficiency and reliability in over 110 production runs with average productivity of 90 GBq at 40 μA (1 hour irradiation). No noticeable yield reduction is observed during routine production, which indicates that target body and seals (Tefzel) do not degrade.

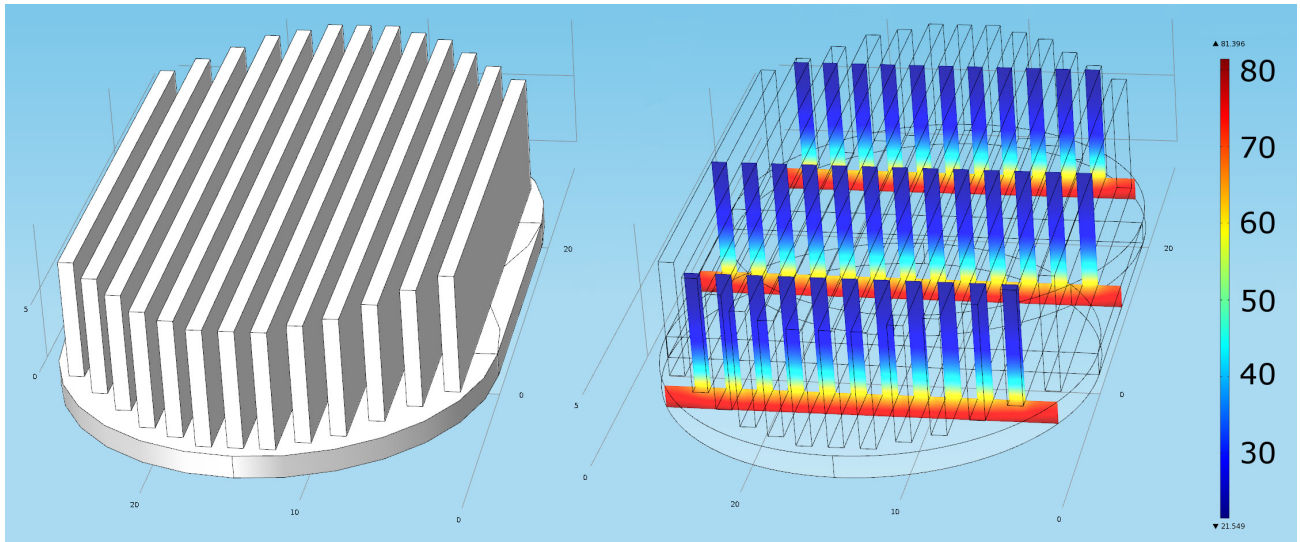

Fig. 3. COMSOL Multiphysics heat transfer model.

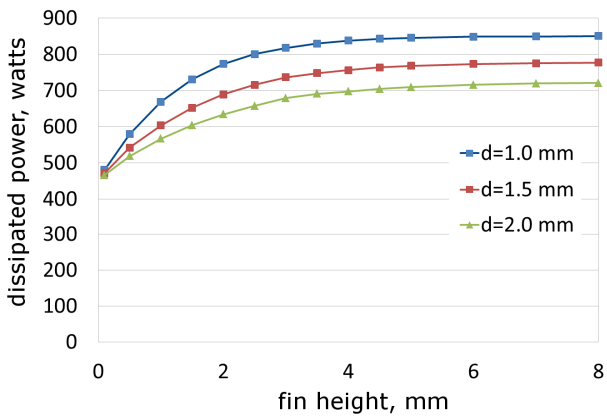

Fig. 4. Effect of fin height on total dissipated heat.

REFERENCES

[1] B. Zabrodin et al., "Radionuclide visualisation methods", Sain-Petersburg Polytechnical Univ., 2006.

[2] J. Peeples, "Design and testing of termosyphon batch targets for production of 18F", PhD diss., North Carolina State Univ., 2008.

IMPROVING OF UNIFORMITY OF THE ELECTRON-BEAM TREATMENT OF MATERIALS BY ELV ACCELERATORS

N.K. Kuksanov, S.N. Fadeev, D.A. Kogut, BINP SB RAS, Novosibirsk, Russia

Abstract

The problem of the absorbed dose distribution during the EB treatment by ELV accelerator is considered. The value of the absorbed dose is determined by the speed of scanning electron beam along the accelerator exit window (i.e. the movement across the conveyor). It is determined both by the shape of scanning current and by the geometry of scanning magnets. A simple way to improve the dose distribution near the edges of the extraction device of accelerator is suggested. It allows to provide the non-uniformity less 4%.

INTRODUCTION

ELV accelerators produced by the Budker Institute of Nuclear Physics (Novosibirsk), has the leading position among the proposed equipment for radiation processing of materials. High performance, wide range, covering almost all the needs of modern industrial technology, reliability and relative ease of use and maintenance form the strong demand for this product in tough market conditions. The technology development radiation modification increases the requirements for the parameters of industrial accelerators produced by stimulating the creation of more powerful and energy efficient models [1]. In a number of industrial applications emerge and increased demands on other characteristics ELV accelerators, such as the stability of the energy of the beam current, the uniformity of the irradiation and etc. The condition of uniform dose distribution to be no more than 4% of the length of the material is an example of such a requirement. It occurs when you use the extended length of the output window, as in the modernization of the accelerator, which took place in spring 2012.

THEORETICAL PART

The dose of radiation is determined by the current density and linear scanning speed of the beam along the axis of the output device. In Figure 1 shows the trajectory of the electron beam in the deflecting magnets in the form of unlimited axis x band width l (the using of cylindrical poles, that takes into account the effect of the edge focusing, is shown in Figure 2) and the calculated reduced velocity (V) of a beam and reduced radiation dose (D ~ 1 / V) as a function of deflecting magnets current. These formulas are obtained by taking into account that

$$\sin(\varphi) = \int_l Hdl \Big/ (H\rho)$$

where $H\rho$ – given the relativistic momentum of the electron, and the integral can be written as

$$\int_l Hdl = K \cdot I(t), K = Const.$$

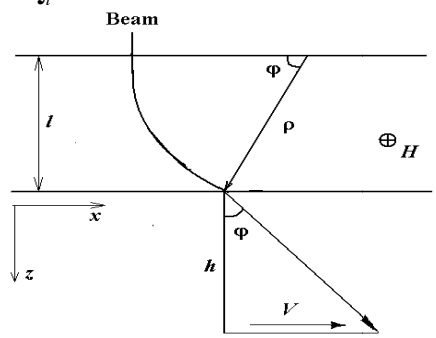

$$Y_V = \frac{V(\varphi)}{V(\varphi = 0)} = \frac{1}{\cos^3(\varphi)}; Y_D = \cos^2(\varphi)$$

Figure 1: Forms of the scanner current in case of the unlimited axis x magnetic field band.

Thus obtain the following formula for the rate and dose

$$V = h \cdot \frac{K}{(H\rho)} \cdot \frac{1}{\cos^3(\varphi)} \cdot \frac{dI}{dt}; D \sim \frac{1}{V} \cdot \frac{1}{\cos(\varphi)} = \cos^2(\varphi)$$

and similarly for Figure 2 –

$$V = h \cdot \frac{K}{(H\rho)} \cdot \frac{\cos^2(\varphi/2)}{\cos^2(\varphi)} \cdot \frac{dI}{dt}; D \sim \frac{\cos(\varphi)}{\cos^2(\varphi/2)}$$

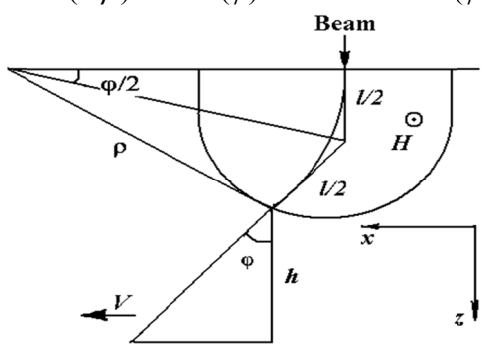

$$Y_V = \frac{V(\varphi)}{V(\varphi = 0)} = \frac{\cos^2(\varphi/2)}{\cos^2(\varphi)}; Y_D = \frac{\cos(\varphi)}{\cos^2(\varphi/2)}$$

Figure 2: The trajectory of the electron beam and the horizontal velocity and dose formula.

In Figure 3 shows graphs of the calculated dose distribution and the actual measurements made by different energies. Differences are due to the scattering of the electron beam as the output device in the foil, and in the air. Contribute to the actual shape also makes scanning electromagnets, which real view (Figure 4) differs from the above described cases and have the form closer to Figure 1.

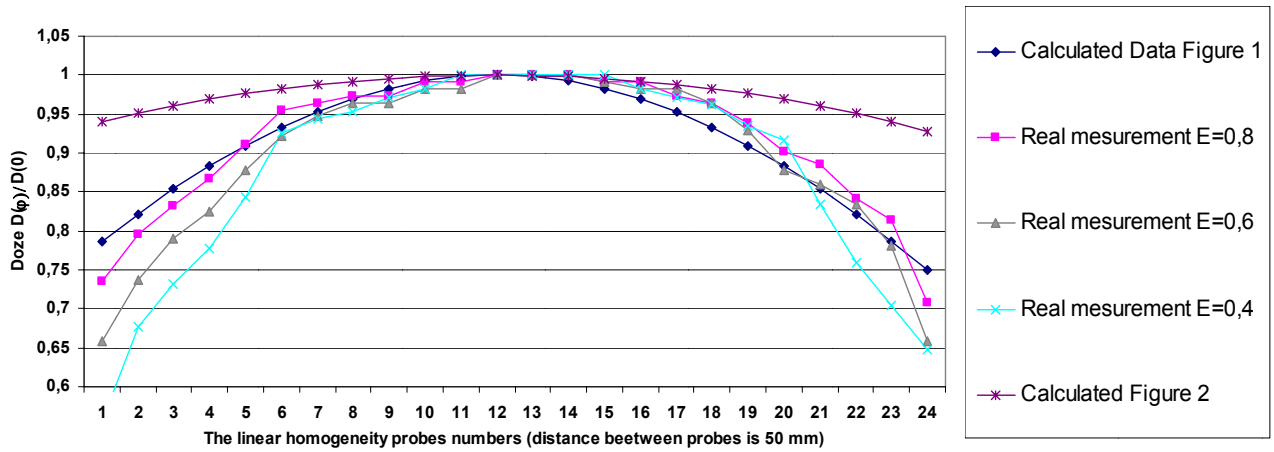

Figure 3: Comparison of calculations and actual measurements of the linear dose uniformity.

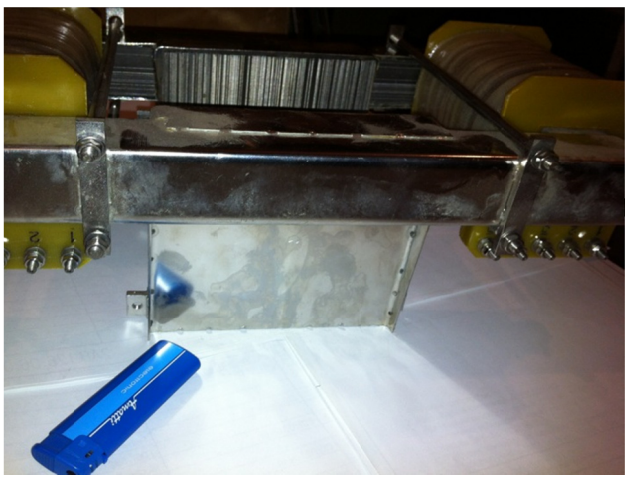

Figure 4. LF scanner coils.

The supply voltage is rectangular, and the functional dependence of the current on time can be represented as a series:

$$I(t)=\frac{4U_m}{\pi}\sum_{k=2n+1}\frac{\sin(wkt+\varphi_k)}{\sqrt{(kwL)^2+R^2}};\varphi_k=arctg\left(\frac{wkL}{R}\right)$$

where R - the total series resistance of the coil and wires, L - inductance coil scanner.

Current scanning system has a symmetrical sawtooth shape (Figure 4) due to the fact that the ratio of $wL/R \approx 35 >> 1$. With this form of current uneven dose in length 1800 mm exit window was ~ 10-12%. To increase the dose at the edges of the output device is necessary to reduce the rate of change of the current at the edges of the exit window. To do this, it was suggested to connect consistently with scanning coils capacitors. Form of the current in this case is defined as

$$I(t)=\frac{4U_m}{\pi}\cdot\sum_{k=2n+1}\frac{kw\sin(wkt+\varphi_k)}{\sqrt{(kwRC)^2+\eta^2}};$$

$$\varphi_k=-arctg\left(\frac{\eta}{kwRCR}\right);\eta=1-(kwLC),$$

where C - series capacitance is shown in Figure 5.

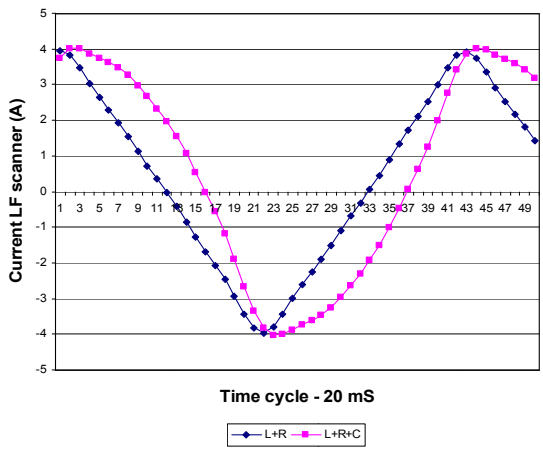

Figure 5. Forms of the scanner current.

The design capacity is in range from 240 to 300 μF.

EXPERIMENT

This technique was used to upgrade the accelerator to irradiate a wide polyethylene sheet in March 2012. When configuring in the real capacity was 250 uF. Measurement results of heterogeneity at different exposure settings, capacity and energy are shown in Figure 6. The result was achieved uneven doses of less than 4%.

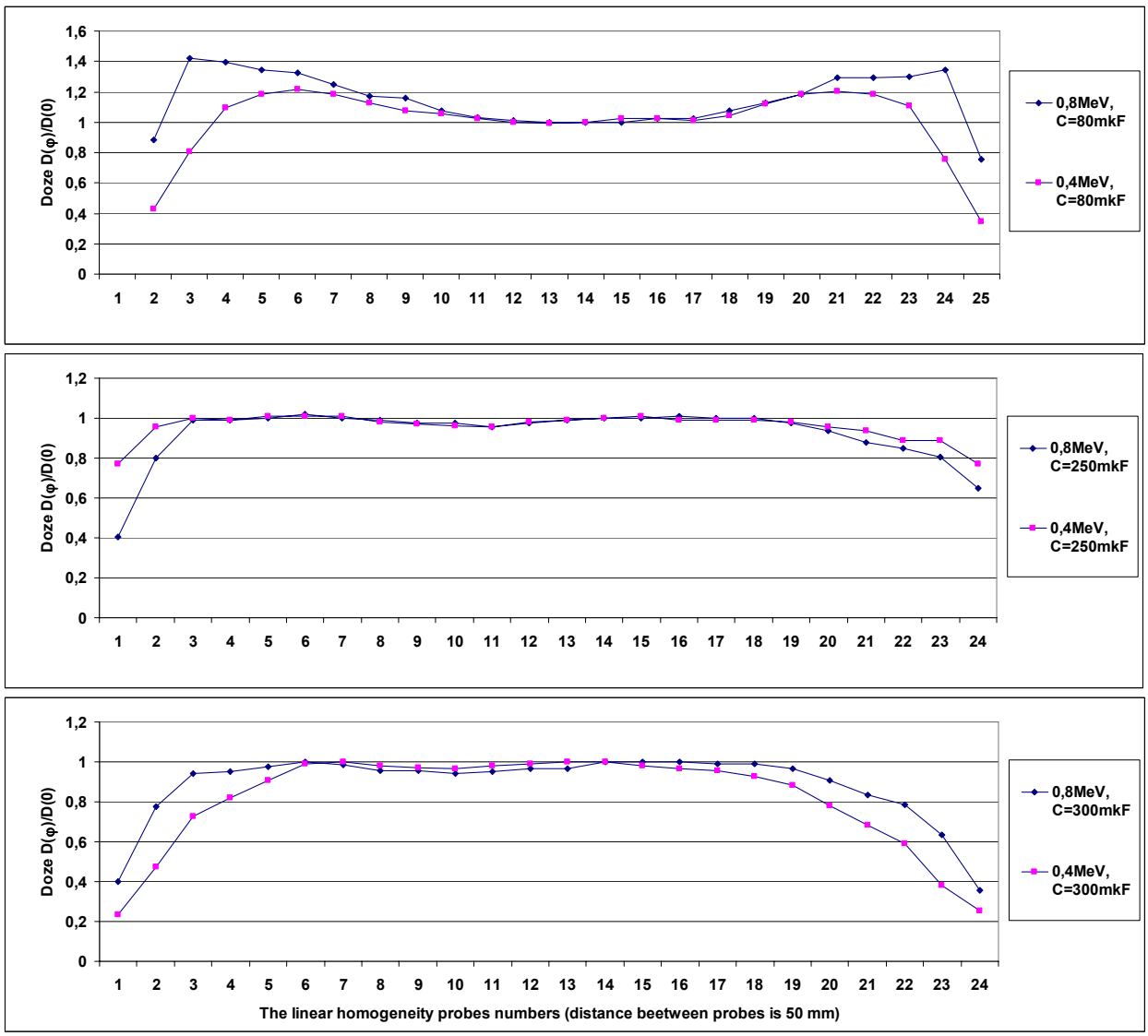

Figure 6: The dependencies of the radiation dose from the energy and capacity along the output window.

CONCLUSION

Proposed a simple method of increasing the dose at the edges of the output device of the accelerator (i.e. the reduction of inhomogeneous dose) will meet the manufacturing process by using existing hardware without a significant change of control systems by scanning the beam, which in the current small-scale manufacturing (it is now about 20 ELV accelerators produced each year and have been already successfully operated over 150 accelerator), unifies and simplifies the hardware support from the supplier.

REFERENCES

[1] N. Kuksanov, S. Fadeev, Y. Golubenko, D. Kogut et al, «High Power ELV Accelerators for Industries Application» // Proceeding of RuPAC-2010, Protvino, Russia, 2010

[2] S. Fadeev, Salimov R., et al, "Underbeam equipment to expand technological capabilities ELV accelerators", Proceedings of the X International Workshop on the Application of Charged Particle Accelerators in industry and medicine, St. Petersburg, October 1-4, 2001. 68. See also Bulletin "Radteh-Eurasia", Novosibirsk, 2002. p. 8.

[3] N. Kuksanov, S. Fadeev, et al, BINP SB RAS, Novosibirsk, “The development of the model range and the improvement of the performance accelerators”, VANT №3 March 2012, p. 15 (1996); http://vant.kipt.kharkov.ua

CALIBRATION TESTING OF THE STRIPPING TARGET OF THE VACUUM INSULATED TANDEM ACCELERATOR

A. Kuznetsov, V. Aleynik, I. Sorokin, S. Taskaev, M. Tiunov, I. Shchudlo,
BINP SB RAS, Novosibirsk, Russia

Abstract

Presented work is aimed on modernization of the gas stripping target that is used in the Vacuum Insulated Tandem Accelerator (VITA) to recharge negative hydrogen ions into protons. The target was modernized to get higher efficiency of the beam transportation and to raise the current of the accelerated proton beam. The design of the modernized stripping target, the calculated data on the gas flow rate and recharge effectiveness, also the results of experimental measurement of transported current depending on the gas flow rate are presented. The method of the target thickness determination and the procedure to adjust the regime of the gas flow rate to get the required recharging effect were suggested.

INTRODUCTION

The Vacuum Insulated Tandem Accelerator (VITA) was developed in the Budker Institute of Nuclear Physics [1] to produce epithermal neutrons for boron neutron capture therapy in the ^{7}Li(p,n)^{7}Be reaction. The parameters of the generated radiation allow us to carry out in vitro and in vivo investigations of BNCT. In present moment the modernization of the facility elements is carrying out to meet the parameters required for clinical usage.

The design of the VITA facility is shown at figure 1. The principle of the tandem accelerating scheme is accelerating of the negative hydrogen ions to the 1 MeV energy determined by the high voltage electrode potential, recharging the ions into protons in the gas stripping target and then accelerating to the 2 MeV energy by the same accelerating potential. The vacuum insulation of the electrodes, the circumstance that the feedthrough insulator is located at significantly big distance to the accelerating gaps and the gas pumping realized through the electrode shutters allows us to believe in capability of the VITA to produce a high current proton beam.

The optimal stripping target is supposed to be the argon gas target constructed as a cooled tube with the gas injection in the middle of the tube [2]. The tube length is 400 mm, inner diameter was made 10 mm, and from 2011 year the diameter was increased to 16 mm. The photo of the new target is shown at the figure 2.

The protons equilibrium yield is 99.9880%. The beam charged components and the full current in the output of the stripping target in dependence on the linear density of the argon in the target are presented at figure 3. The gas consumption for the 16 mm tube with length 400 mm and 300 K temperature is in linear dependence on the target density and described as an equation:

$$Q\ [10^{18}\ s^{-1}] = 2.63\ nl\ [10^{16}\ cm^{-2}],$$
$$\text{or } Q\ [mTorr\ l\ s^{-1}] = 75\ nl\ [10^{16}\ cm^{-2}].$$

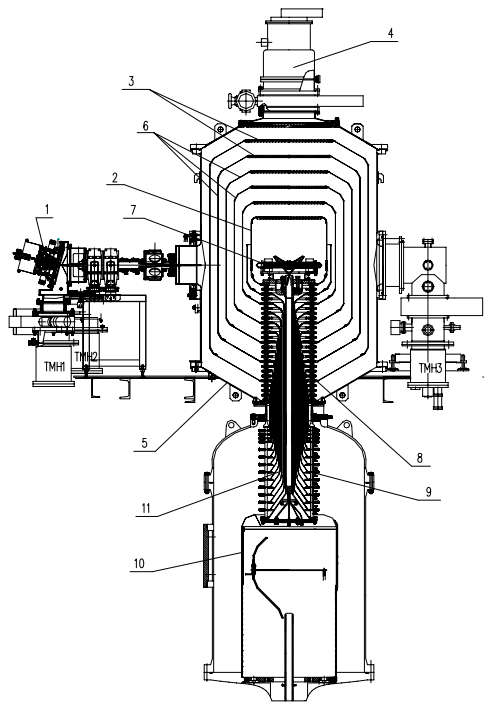

Fig. 1. Scheme of the VITA facility. 1 – ion source (H^-); 2 – high voltage electrode; 3 – electrode shutters; 4 – cryo pump; 5 – accelerator vacuum volume; 6 – intermediate electrodes; 7 – stripping target; 8 – feedthrough insulator (vacuum part); 9 – feedthrough insulator (gas part); 10 – high voltage source; 11 – coaxial feeding tubes.

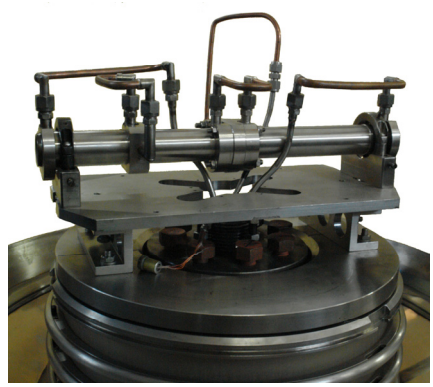

Fig. 2. New Ø16-mm stripping target placed on the feedthrough insulator.

EXPERIMENTAL LAYOUT

The gas injection system consists of the gas vessel with pressure regulator, electromechanical gas flapper, the buffer volume and high precision leak valve which are located in the high voltage source. The gas flows from the buffer to the target through the leak valve and long tube with 2 m length and 4 mm inner diameter placed inside the feedthrough insulator. The gas flow rate can be managed with help of the gas flapper by manual or automatic control. The pressure of the gas in the buffer volume is determined by the frequency of the gas flapper opening. In the experiments carried out the duration of the gas pulse was 160 ms and output pressure of the pressure regulator was 4 atm. Characteristic time of the gas extraction is 500 s.

The gas pressure in the accelerator volume was controlled by the vacuum lamp located in the output of the accelerator.

The measuring of the high voltage feeding current (accelerator current) I_{acc}, the current in the feedthrough insulator resistive divider I_{div} and the current in the output beam collector I_{out} allows us to determine the full injected current as $I_{inj} = I_{acc} - I_{div} - I_{out}$ taking into account that the dark currents become almost negligible after good accelerator training.

EXPERIMENTAL RESULTS

The measurements of the accelerator output beam current and the residual pressure in dependence on the gas flow rate was carried out. With out gas puffing the residual pressure was about 0.5 10^{-4} Pa. With the gas puffing frequency 1/40 Hz the pressure come to the stationary level 6 10^{-4} Pa, with the frequency 1/20 Hz – 11 10^{-4} Pa, with the frequency 1/10 Hz – 22 10^{-4} Pa, with the frequency 1/5 Hz – 33 10^{-4} Pa. The dependence of the residual pressure on the gas puffing frequency is almost linear up to 1/10 Hz frequency. So the gas target density can be mediately determined by the residual gas pressure.

The negative hydrogen ion beam with 21 keV energy was injected into the accelerator with 800 kV high voltage electrode potential. The injected current was 225 ± 10 mA, and the dark current was 24 ± 4 mA (Fig. 4).

With the gas target density 0.29 10^{16} cm^{-2} (the value calculated for the 800 keV ion beam) the output proton current is equal to the output negative ion current and the total registering current I_{out} equals zero. Registering of the residual gas pressure in this moment allows us to calibrate the target density and the gas flow rate in the context of pressure.

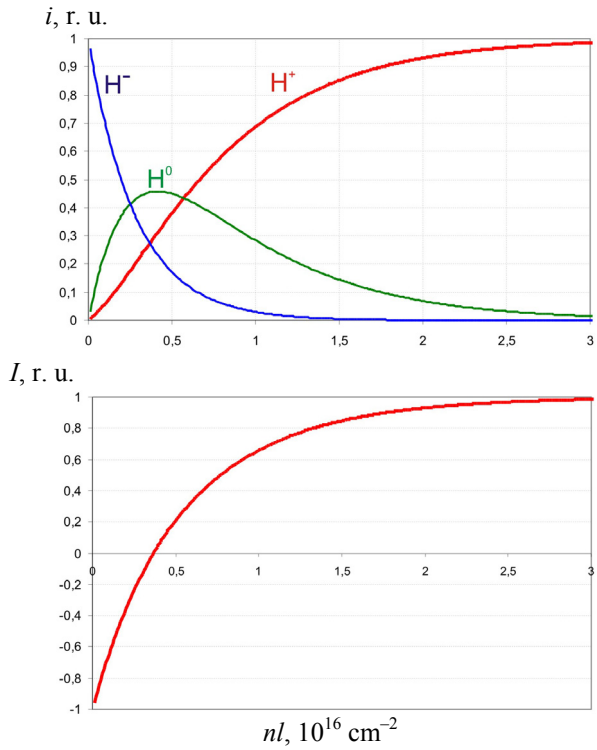

Fig. 3. The beam charged components (a) and full current in the output of the stripping target (b) in dependence on the linear density of the argon gas target..

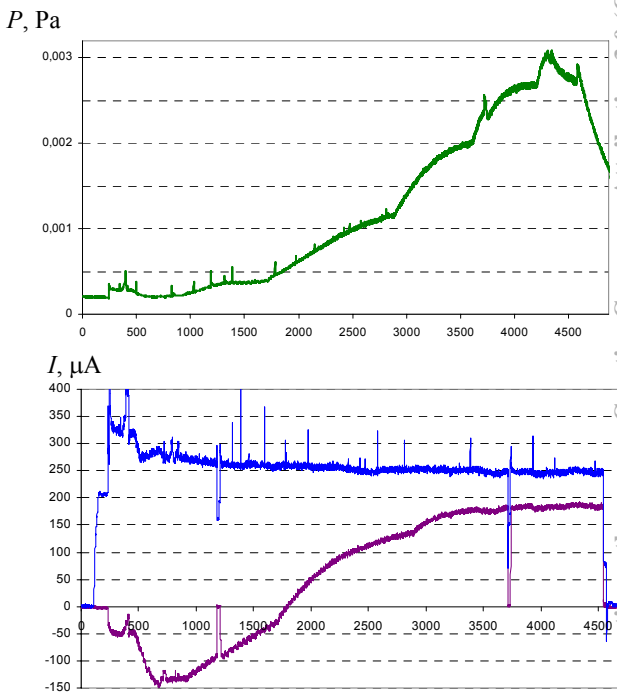

Fig. 4. Time dependence of the residual gas pressure P (a), the accelerator current I_{acc} (b, upper line) and beam collector current I_{out} (b, bottom line).

The measured and calculated dependences of the output current on the residual gas pressure is presented at figure 5. The measurement was made after the time 690 s when no any corrections were made in the magnetic focusing and beam correctors of the low energy beam line. In the calculation it was supposed that maximum output proton current equals 188 mA and 20% of accelerated particles were lost in the accelerating tract between the stripping target and accelerator output. The particle loss in the accelerator tract coming from the decelerating of negative ions by contrast to protons and the beam diameter expanding to the bigger size then accelerating apertures allows to transport. (The apertures diameters were 43, 43, 35, 30, 25 and 20 mm in the negative ions accelerating tract, and all by 20 mm in the proton accelerating tract).

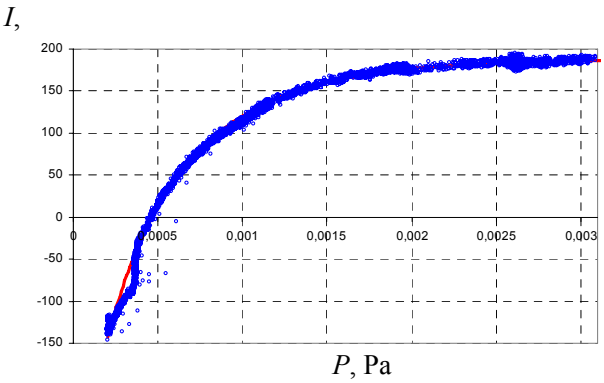

Fig. 5. Measured and calculated output current in dependence on the residual gas pressure.

Result of the ions trajectory calculations is presented at figure 6. It was calculated that the last 3 electrodes capture 20% of particles and this value is in the good agreement with 22% experimental particle loss determined as a relation of 146 mA maximal registered negative ions current to 188 mA maximal proton current in the output collector (Fig. 5).

At the figure 5 one can see the good agreement of measured and calculated dependences of the output beam current on the target density, and using the point of measured zero current the dependence can be normalized.

To guarantee recharging of the 90% of ions to protons at the energy 0.82 MeV the argon gas target with linear density 1.5 10^{16} cm^{-2} is required. The gas consumption should be 0.1 Torr l s^{-1}. With cryo pumping speed limited by the electrode shutters in the range about 3 000 l/s, the pressure in the high voltage electrode will be 4 10^{-3} Pa.

Thus, the experiments carried out allowed us to calibrate the stripping target and to test the procedure of the gas flow regulation to get the required recharging of the injected negative hydrogen ion beam.

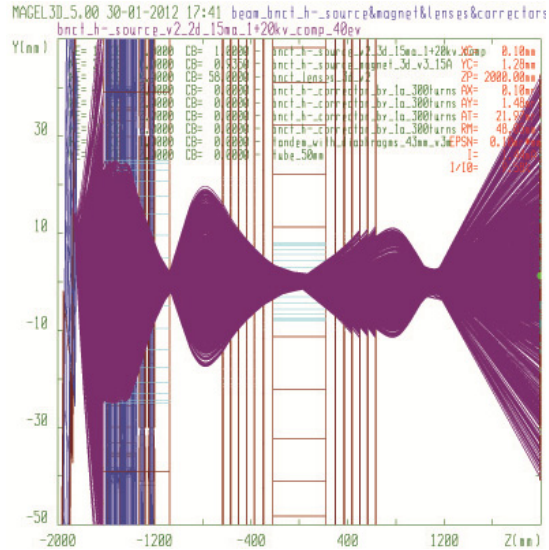

Fig. 6. Calculated trajectories of negative ions in the tandem-accelerator (ion source is located at the left side, Z=0 corresponds to the middle of the stripping target and the output beam collector is located at the right side at the point Z = 1500 mm.

SUMMARY

To provide recharging of the negative hydrogen ions to protons in the Vacuum Insulated Tandem Accelerator the stripping target is used, that is an oil-cooled tube with length 400 mm and diameter 16 mm with gas injection in the middle of the tube.

In the paper the calculated data on the beam components and current in dependence on the linear target density was presented alone with the experimental results on output current measuring in dependence on the gas flow rate. The method of regulation of the gas flow rate using the residual pressure measurements to get the required negative hydrogen ions recharging is tested. All experimental measurements are in good agreement with calculations. The residual pressure in the accelerating channel is estimated.

The work was partially supported by the Ministry of Education and Science of the Russian Federation.

REFERENCES

[1] V. Aleynik, et al., Applied Radiation and Isotopes, 69 (2011) 1635-1638.

[2] V. Davydenko, et al., AIP Conference Proceedings, v. 763, NY, 2005, p. 332-335.

ELECTRON BEAM IMAGE VISUAL MONITORING

V.N. Boriskin, V.V.Zakutin, N.G.Reshetniak, S. K. Romanovsky#, V.P.Romasko, A.Eh. Tenishev, V.J.Titov, I.A.Chertishev, V.A. Shevchenko, I.N. Shlyakhov, V.L. Uvarov,
NSC KIPT, Kharkov, 61108, Ukraine

Abstract

The system for visual monitoring of the electron beam was developed and implemented. The technique is based on registration of optical radiation, which is generated under object-beam interaction. The system comprises image transferring channel, remote-controlled digital photo-camera, connected with PC by USB-interface as well as proper software. The images obtained give information on the beam density distribution over the surface of the object being irradiated. 40 KeV and 10 MeV electron beams were researched.

VISUAL MONITORING OF ELECTRON BEAM WITH ENERGY OF 40 KEV IN VACUUM

Tubelike electron beam was formed by magnetron gun with a secondary-emission 40 mm aluminium cathode [1] providing 40 kV and 50 A pulse of 40000 nS in width. The beam hit an eight-segment Faraday cup (see Fig. 1).

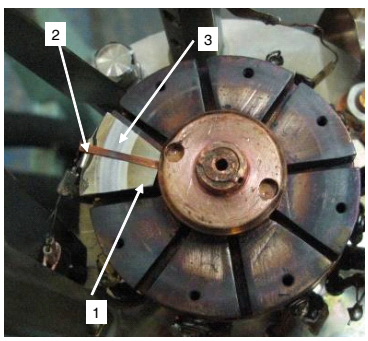

Figure 1: Faraday cup with electron beam traces. 1- target, 2- calibration strip, 3- beam image.

One of its segments has a stainless steel cover with calibration strip. For visual control, electron beam image is taken out by system of mirrors and lenses (see Fig. 2) and fixed with a digital camera controlled by PC.

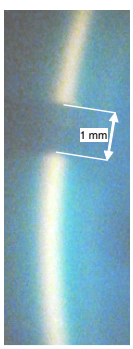

Figure 2: Electron beam image of magnetron gun with 40 keV electron energy at the target.

romanovsky@kipt.kharkov.ua

Processing of images is provided using program Origin7.5 (see Fig. 3).

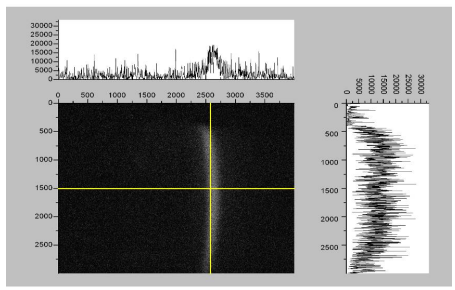

Figure 3: Image of beam profile at the target.

VISUAL MONITORING OF ELECTRON BEAM WITH ENERGY OF 10 MEV IN ATMOSPHERE

The system was created for visual monitoring of the objects being irradiated on LUE-10 LINAC (see Fig. 4) as still as fixed and moved by transfer conveyor[2].

Figure 4: LINAC LUE-10 with conveyor and supercritical water convection loop.

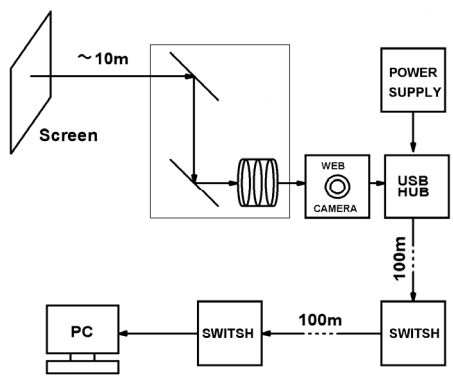

Fig. 5. Functional chart of the system for visual monitoring of electron beam at LINAC LUE-10.

Condition: average beam current – 0.8 mA; beam energy – 10 MeV; beam pulse rate – 250 Hz; beam scanning frequency – 3 Hz. Structural arrangement of electron beam visual monitoring system show at Fig. 5.

Electron beam image was observed with the use of such targets:

- carton (blue color of light, see Fig. 6),
- plastic (white color of light, see Fig. 7),
- aluminium screen coated with luminophor (yellow color of light).

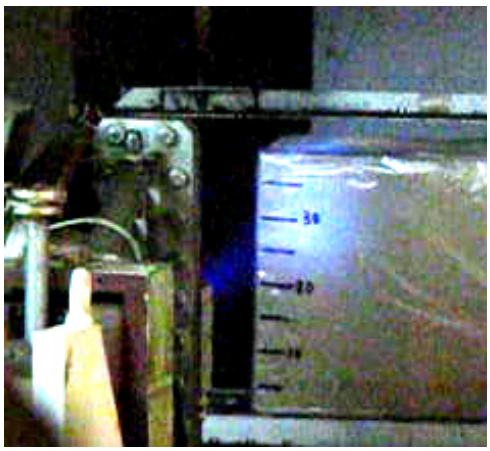

Figure 6: Electron beam image on carton (distance between lines – 50 mm).

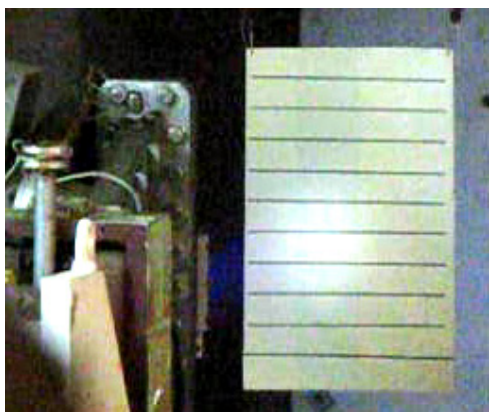

Figure 7: Electron beam image on plastic (distance between lines – 50 mm).

Recovery of the beam density distribution is able by summarizing of beam images of irradiated plastic surface (see Fig. 8).

Electron beam density profile was processed in Origin 7.5 (see Fig. 9).

The profiles obtained by proposed optical technique as well as by means of beam exposure of glass sheets and dosimetry film B3 are agreed satisfactory.

The pilot testing of the electron accelerator driven convection loop with water in supercritical state [3] was carried out during the summer 2012 (see Fig.10).

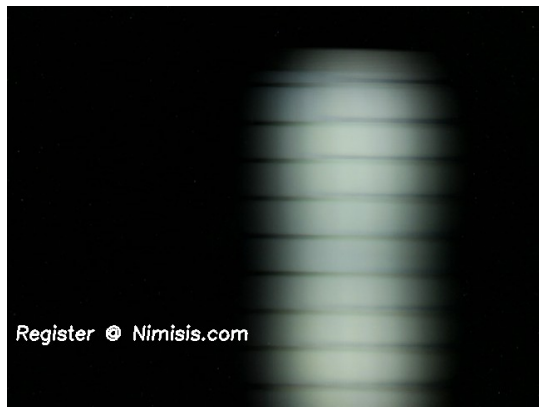

Figure 8: Picture of summarized electron beam images on plastic (distance between lines – 50 mm).

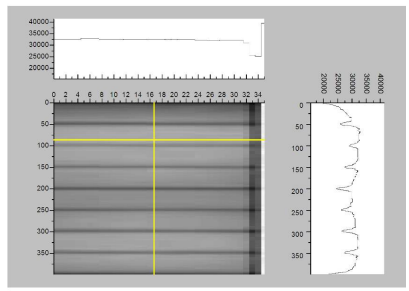

Figure 9: Electron beam density profile on plastic (distance between lines – 50 mm).

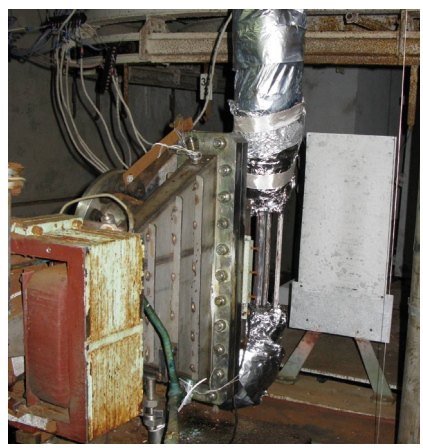

Figure 10: Irradiated chamber with the loop and screen for electron beam monitoring.

Implementation of on-line beam monitoring system was essential for its success. Patterns of constructional materials for next-generation reactors were exposed to radiation for 500 hours at pressure of 240 atm and temperature of about 400° C.

Electron beam on-line visual monitoring was enabled by aluminium screen coated with luminophor (see Fig. 11).

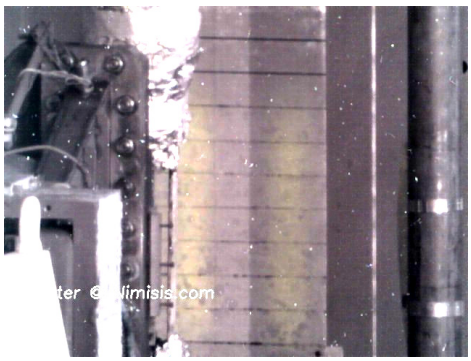

Figure 11: Summarized beam image on aluminium screen coated with luminophor (a shadow of the loop is visible).

CONCLUSION

1. The system developed enables on-line monitoring of electron beam profile.
2. The pictures of beam density profiles resulted using this procedure are similar to those, obtained by the conventional method on glass and film B3.
3. The described procedure enables to operate with electron beams of energy within the range from tens of keV up to tens of MeV.

REFERENCES

[1] N.I.Ayzatsky, A.N.Dovbnya, V.V.Zakutin, N.G.Reshetnyak, V.N.Boriskin, N.A.Dovbnya, V.P.Romas'ko, and I.A.Chertishchev. Investigations of Electron Beam Characteristics Using an Accelerator Based on a Magnetron Gun with a Secondary-Emission Cathode. // Physics of Particles and Nuclei Letters, 2008, Vol. 5, No. 7, pp. 86-89.

[2] K.I. Antipov, M.I. Ayzatsky, Yu.I. Akchurin, V.N. Boriskin, E.Z. Biller, N.V. Demidov, A.N. Dovbnya, L.S. Dovbush, V.A. Gurin, S.P. Karasyov et al. Electron Linacs in NSC KIPT: R&D and Application //PAST, 2001, №1, Ser.: NPhI (37), p.40-47

[3] A.S. Bakai, V.N. Boriskin, A.N. Dovbnya, S.V. Dyuldya and D.A. Guzonas. Supercritical water convection loop (NSC KIPT) for materials assessment for the next generation reactors /Proc. The 5th Int. Sym. SCWR (ISSCWR-5) Vancouver, Canada, March 13-16, 2011.

EXPERIMENTAL CHANNEL FOR PROTON BEAM WITH ENERGY 9 GEV

Mark Kats, ITEP, 25, B.Cheremushkinskaya, Moscow, Russia

Abstract

It was described one of possible version of experimental channel for proton beam with energy 9GeV for ITEP. It based on proton beam after quick extraction, on existing experimental hall and on existing quadrupoles.

INTRODUCTION

For investigation of inner design of different target it is possible to use proton beam which can pass through the target and specific channel for transport scattered beam between the target and equipment for measurement shape of the beam at the end of the channel. Now in ITEP there is such channel for proton beam with energy 0.8GeV. This report is devoted to one of possible version of new channel on extracted from ITEPs synchrotron proton beam with energy 9GeV. New channel will be able investigate more thick targets with more high resolution.

OPTICAL SOLUTION

It was suggested to use optical scheme of channel with minimal angular sizes of the beam at the target, and with focus of the beam by two symmetrical parts (like triplets of quadruples). The first triplet focus initial (without scattering into the target) beam in middle point. Scattered beam can be collimated in this point according angle of scattering. The second triplet focus initial beam in both planes on equipment for measurement its profile with magnification -1. So, scattered in any point of the target proton beam will be focus at the equipment with magnification -1. It was suggested to use 8 quadrupoles ML15 (L=0.9m, D=0.15m, B<0.7Tl), which are free now in ITEP. Optical properties of the channel were calculated by TRANSPORT in second order.

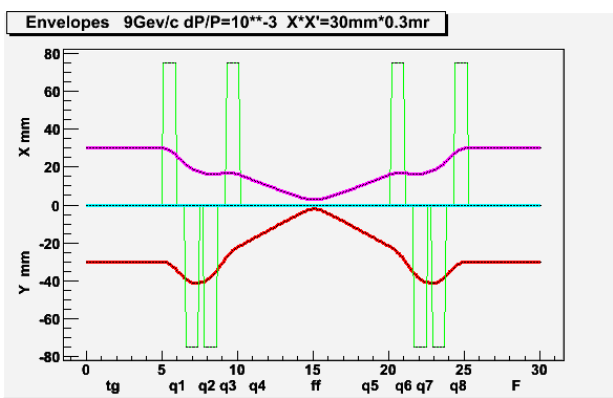

Figure 1. Scheme of proton beam envelopes into the cannel for beam without scattering in the target

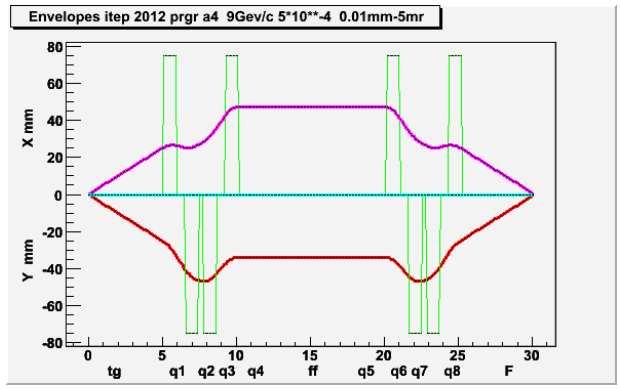

Figure 2. Scheme for beam envelopes for protons scattered in the target at angles 5mrad.

R11=R33=-1.0 magnifications are -1.0 in both planes. R116=R336=10^{-6}. Across sizes of the target have small influence on precision of measurements.

Chromatic aberration, which has strong influence on resolution, can be estimated in both planes as multiplication of those coefficients on angular sizes X' or Y' of scattered beam and on momentum spread dP/P of the scattered beam. According of calculations R126 = R346 = 30m. For dP/P=10-3 and X'=Y'≤5mrad limit of resolution according of chromatic aberration is like 0.15mm, for dP/P=10-4 and X'=Y'≤2mrad the same limit is like 0.006mm. Angular sizes of the beam in channel at measurement depend on initial angular sizes of the beam, on initial energy of protons, on properties of the target (length and material) and on collimation of the beam in middle point of the channel.

PRELIMINARY TRANSPORT OF EXTRACTED BEAM

Extracted proton beam at energy 9GeV has momentum spread in interval $10^{-3} < dP/P < 10^{-4}$, its phase volumes are less 10mmmrad. If the target can change its properties quickly (10^{-6}sec) steel window with thickness like 10mm must be installed on the beam direction in 1m after 303 magnet of accelerator. Such window scattered protons on angles like 1mrad. At this condition sizes of beam for its transport to the target can be estimated 3mm*mrad < XX' < 16mm*mrad. Input proton beam at the target must be with diameter like 60mm and with minimal angular sizes. 4 existing quadrupoles 20K100 can be used for this aim.

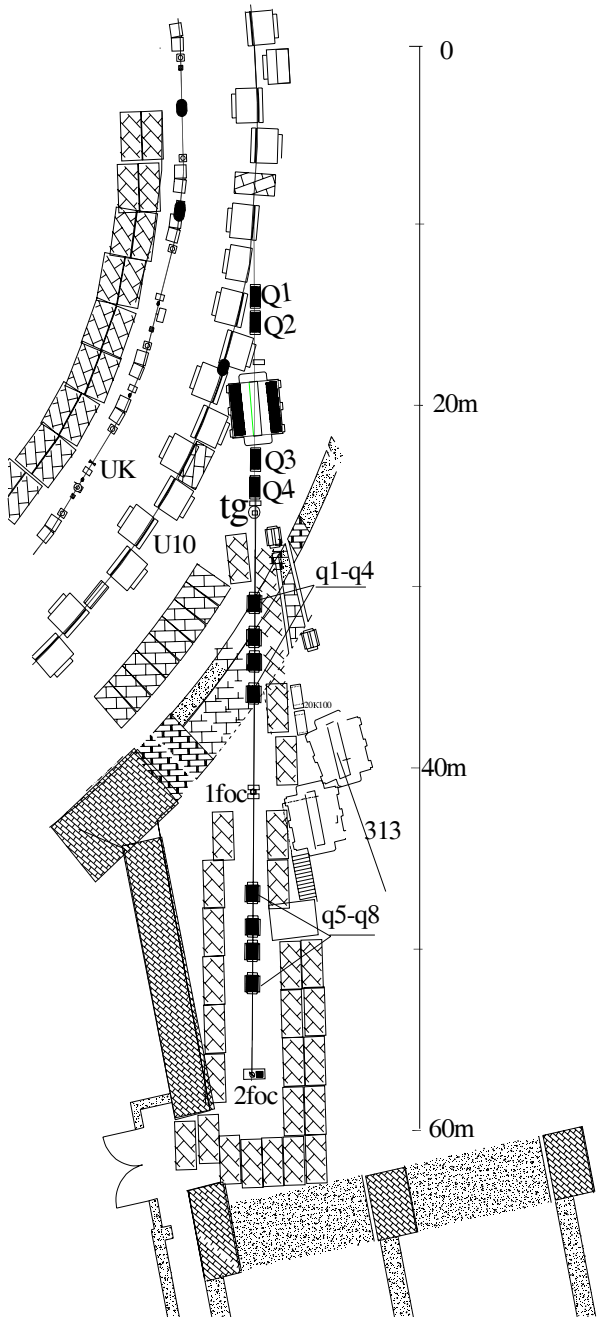

Figure.3. Layout of total channel and synchrotron ITEP.

LAYOUT OF THE CHANNEL

Initial direction of extracted proton beam is not fare from existing channel 311. New channel can be designed together with its quadrupoles, collimators, target, correctors, devices and concrete walls without destroy of existing channel 313 with its experimental equipments.

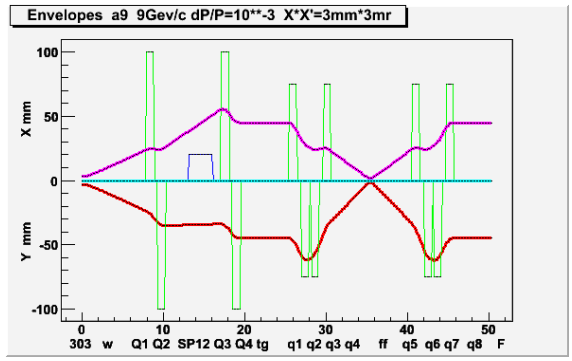

Figure.4. Scheme of proton beam envelopes into total channel for initial beam without of the target.

ESTIMATION OF REAL RESOLUTION

Resolution of the channel depends on properties of the initial beam and the target strongly. In addition to chromatic aberration it is necessary take in account scattering protons into the target and length of the target, quality of a surface between of different part of the target and bends of this surface to beam direction, on possibilities of equipment for measurement shape of the beam, on quality of magnetic fields in all quadrupoles, on un stability of currents in all quadrupoles and mistakes at choosing optimal currants in all quadrupoles.

MK REVMOC [1] program was used for estimation resolution for different ideal targets (materials C, Fe, W and with length 2mm, 10mm, 30mm, 100mm. For each condition were calculated distribution protons by its momentum and its linear distribution in final point with steps 0.01mm. A few examples of calculations are shown on Figure 5 for Fe targets with different length and with rigid boundary between Fe and vacuum. Shape of decreasing intensity in point of boundary show ideal resolution of suggested channel.

L=10mm X'=0.5mrad
Momentum distribution

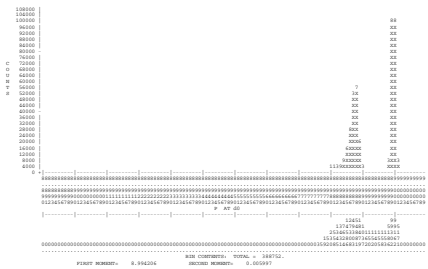

Linear distribution
step 0.01mm
resolution 0.01mm
vacuum Fe

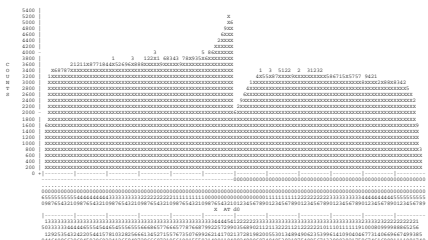

L=30mm X'=0.5mrad
Momentum distribution

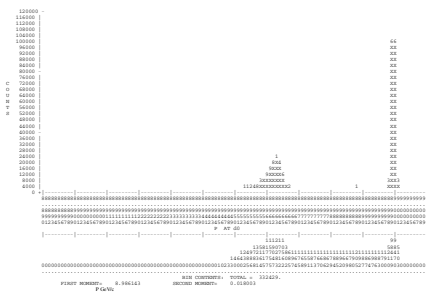

Linear distribution
step 0.01mm
resolution 0.02mm
vacuum Fe

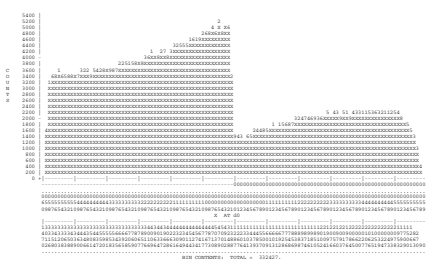

L=100mm X'=0.5mrad
Momentum distribution

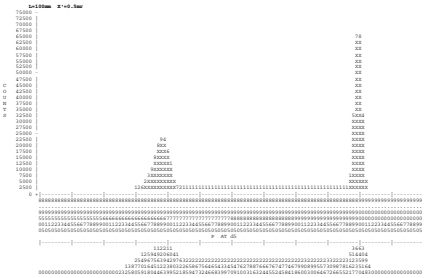

Linear distribution
step 0.01mm
resolution 0.06mm
vacuum Fe

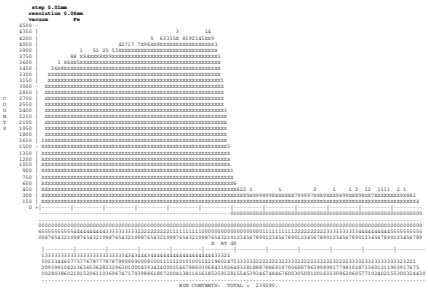

Figure 5. Calculated momentum distributions and linear distributions of the beam in point of measurement for Fe-vacuum targets with different length (10mm, 30mm, 100 mm).

CONCLUSIONS

Resolution of the channel better 0.01mm can be useful only for targets with length less 30mm.

Suggested on base of free in ITEP quadrupoles channel can be suitable for investigation targets without or with quick changes of the targets properties.

REFERENSIS

[1] C.J.Kost, P.Reeve. A MonteCarlo Beam Transport Program REVMOC TRI-DN-82-28, TRIUMF, Canada

SIMULATIONS AND DESIGN OF THZ WIGGLER FOR 15-40 MEV FEL

E.M. Syresin, N.A. Morozov, R.S. Makarov, S.A. Kostromin, D.S. Petrov
Joint Institute for Nuclear Research, Dubna, Russia

Abstract

The electromagnetic wiggler is applied for narrow-band THz radiation in the 30 μm to 9.35 mm wavelength range. This is a planar electromagnetic device with 6 regular periods, each 30 cm long. The end termination pattern structure is +1/4,-3/4,+1,…,-1,+3/4,-1/4. This structure is more appreciable for compensation of the first and second fields, especially, to provide the small value of second integral of 500 G×cm^2. The peak magnetic field is up to 0.356 T, it is defined by large wiggler gap of 102 mm and a capacity of water cooling system of 70 kW. The parameter is varied in the range K=0.5- 7.12 corresponding to a field range B=0.025- 0.356 T peak field on axis. The wiggler is used in 15-40 MeV. The bunch compression scheme allows the whole wavelength range to be covered by super-radiant emission with a sufficient form factor. The wavelength range corresponds to 217 μm-9.35 mm at electron energy of 15 MeV, it is equal to 54 μm-2.3 mm at electron energy of 30 MeV and it is 30 μm-1.33 mm at electron energy of 40 MeV. The 3D Opera simulations of THz wiggler is under discussion.

INTRODUCTION

The design of THz wiggler and technical solution at its construction are based on FIR FLASH undulator constructed in JINR [1-5].

Table 1: Summary of wiggler technical data.

Parameter of THz wiggler	value
period length, mm	300
number of full periods	7
number of poles including end-pieces	14+4
maximum wiggler parameter K_{RMS}	7.12
peak field on axis, T	0.356
height of magnetic axis above floor level, m	1.4
minimum clear gap, mm	102
position accuracy of magnetic axis, mm	0.5
angular precision of magnetic axis, mrad	0.5
field flatness at ±20 mm off-axis (horizontally), %	-0.1… +0.5
first field integral I1, G×cm	50
second field integral I2, G×cm^2	500
stability and reproducibility of magnetic axis, mm/μrad	±0.1/ ±50

The second peculiarity of wiggler is related to the trim coils. The four trim coils with individual power supply should be installed in wiggler. These trim coils permit to compensate on the full wiggler length the first and second integrals. However it does not permit to compensate integral on period length. The first integral on period length should be smaller than 50 G×cm and also very low second integral 500 G×cm^2. To provide both these requirements it is propose to install in each regular coil an additional correction coil. The individual correction coils should compensate imperfection of wiggler mechanical construction and errors in coil position. In the parallel to each individual correction coil a variable resistance divider will be installed. As a result through each individual correction coil will pass the individual optimal correction current; however for all 7 pairs of correction coils will use only 1 power supply system.

The 3D wiggler simulations at its full scale were performed by TOSCA code (Fig.1). The maximal available magnetic field corresponds to 0.356 T at number of Ampere×turns of $I_W=1.85\cdot10^3$. An increase of the number of Ampere turns up $I_W=2.1\cdot10^3$ permits to linearly increase the magnetic field up the value of 0.375 T (Fig.1, Table 1.).

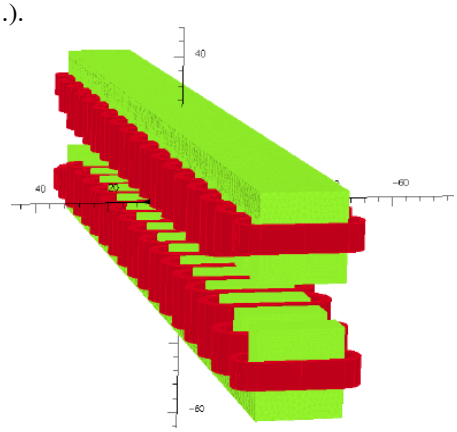

Figure 1: TOSCA 3D simulation of THz wiggler.

The 3 layer coil at the magnetic field of 0.356 T corresponds to following water cooling system parameters: dissipated power of 70 kW, water cooling flow of 2.6 l/min through one coil (about 94 l/min for 36 coils) and temperature rise of 12^0. So the maximum available magnetic field is defined by water cooling system. The increase of the magnetic field up to 0.375 T is required an increase of dissipated power up 96 kW and temperature up 16^0.

The diffraction spot size of radiation defines the diameter of vacuum chamber and wiggler gap. The diffraction angle and spot radius of wiggler radiation are equal to

$\theta_d \cong (\lambda/\pi L)^{0.5}$, $r_d \cong (\lambda L/\pi)^{0.5}$, where L = 2.1 m is the wiggler length, λ is the wave length. The diffraction parameters are equal to 3.5mrad/7mm at λ=80μm, 2mrad/2.5cm at wavelength of 1 mm and 20 mrad/4 cm at wavelength of 2.3 mm.

MAIN COILS

The parameters of main coils are given in Table 2 for 3 winding layers. The coil design with 3 winding layers provides parameters of the water cooling system of 70 kW.

Table 1. Parameters of main coils.

Number of layers	3
Bo (G)	3560
Conductor cross section, mm	8.5*8.5/D5.3
Coil cross-section with isolation (mm)	30*130
Number of turns	42 (3*14)
Number of A×turns	18500
Current, A	440
Total voltage (V)	160
Current density, A/mm^2	8.9
1 coil power (kW)	2.2
Total power (kW)	70
Water cooling l/min (1 coil)	2.6
Temperature rise, C	12
Weight (kg) 1 coil	13.7
Total copper weight (kg)	440

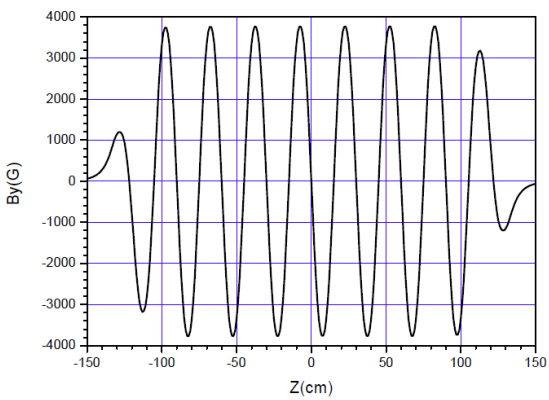

Figure 2: Wiggler magnetic field

For electron beam transport through a wiggler especially at low beam energies the transverse field profile is of great importance. Considering the wiggler amplitude at low beam energies and high wiggler parameters the good-field region must be defined to extend ±20 mm off-axis horizontally. The wiggler design discussed below with rectangular poles of 200 mm width shows a field roll-off by -0.2% at 20 mm off-axis. This can not be handled by the beam delivery for beam energies below 25 MeV. This consideration puts a limit of -0.1% at 20 mm to the off-axis field roll-off. In accordance with 3 D TOSCA simulation the transverse magnetic field variation is smaller than -0.1% at aperture of 20 mm.

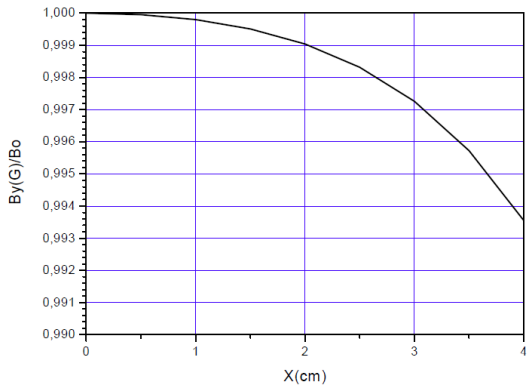

Figure 3: Dependence of normalized wiggler magnetic field at Iw=21.5 kA×turns on transverse coordinate.

TRIM AND CORRECTION COILS

Four correction coils should be able to drive 2% of the magnetic flux of a single pole from a 10 A supply. The trim coils 1 and 4 are installed on the first 3 poles and on the last 3 poles correspondingly. The trim coils 2 and 3 are placed on 4-9 poles and on 10-15 poles. The parameters of trim coils are given in Table 2 and Fig.4 and Fig.5. The currents in each corrector trim coils were optimizing to reduce the first and second integrals.

Table 2. Parameters of trim coils.

Parameter	Coil 1-4/coil 2-3
Corrected field (G)	15/10
A×turns (one coil)	105
Number of turns (one coil)	15
Current (A)	7
Conductor D(mm)/ S_{con} (mm^2)	2/3.1
J (A/mm^2)	2.2
Voltage (two coils) (V)	2/3
Power (two coils) (W)	14/21
Coil cross-section (mm)	2×30

Individual correction coils (14 pairs) on regular poles are placed overhand main regular coils and higher the corrected trim coils. The inputs from individual correction coils in to the first integrals along longitudinal axis are

given in Fig.6. The parameters of individual correction coil are presented in the Table 3.

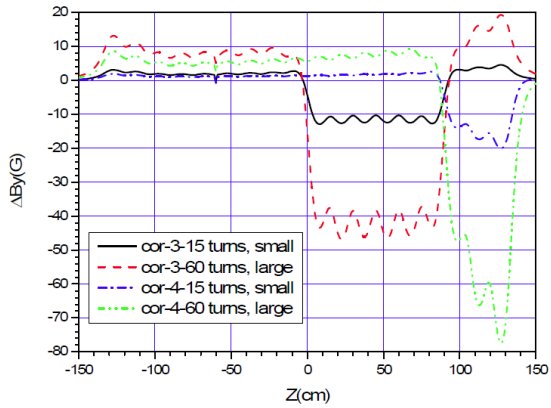

Figure 4: Magnetic field of correction trims coils.

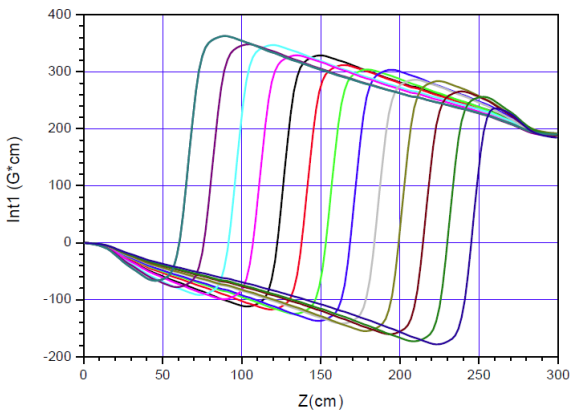

Figure 5: Second integral produced by trims coils.

Table 3. Parameters of the regular correction coils and the edge coils.

Parameter	Regular coil	Pole 1	Pole 2
Corrected field (G)	28	700	480
A×turns (one coil)	308	3696	3696
Number of turns (1 coil)	110	528	384
Current (A)	2.8	7	7
Conductor D(mm)	1.5	2	2
$S_{conductor}$ (mm^2)	1.75	3.14	3.14
J (A/mm^2)	1.6	2.2	2.2
Voltage (two coils) (V)	3.75	32	21
Power (two coils) (W)	10.5	220	150
Coil cross-section (mm)	3×85	11×96	13×116

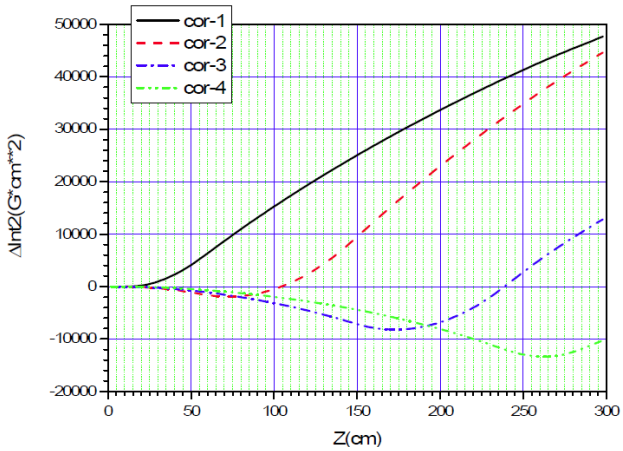

Figure 6: First integral of individual correction coils (I_w =308 A×turnes).

Correction coils of first-last poles and second – seventeen poles are placed overhand main coils and higher to the corrected trim coils. The inputs from these correction coils in to the second integrals along longitudinal axis are given in Fig.7.

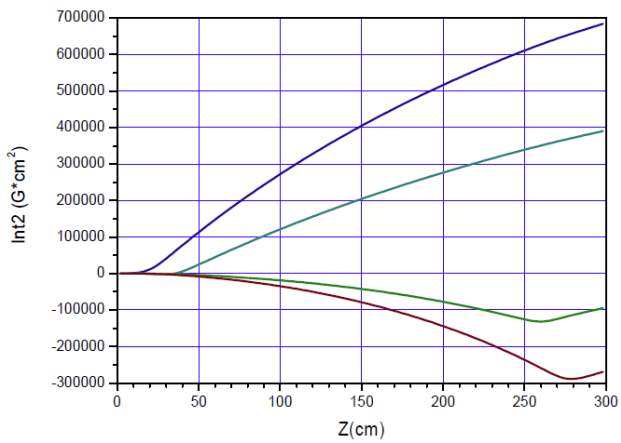

Figure 7: Second integral produced by correction trims coils.

REFERENCES

[1] O.Grimm et al, NIM A 615, is.1, (2010) 105.

[2] M.Gensh et al, Infrared physics and technology, v.51, Iss.5, (2008) 423.

[3] O.Brovko, et al, Particle and Nuclei Letters, v.7 № 1, (2010) 78.

[4] O.Brovko et al, Applied physics, №3, (2010), 46.

[5] R. Makarov et al, Particle and Nuclei Letters,, v.7 №7, (2010) 737.

DIAGNOSTIC TECHNIQUE WITH FEMNTO SECOND RESOLUTION APPLIED FOR FEL ELECTRON BUNCHES

O. Brovko, A. Grebentsov, R.Makarov, N.Morozov, A.Shabunov, E. Syresin#, M. Yurkov,
Joint Institute for Nuclear Research, Dubna, Russia

Abstract

Diagnostic technique applied for FEL ultrashort electron bunches is developed at JINR-DESY collaboration within the framework of the FLASH and XFEL projects. Photon diagnostics developed at JINR-DESY collaboration for ultrashort electron bunches are based on calorimetric measurements and detection of undulator radiation. The infrared undulator constructed at JINR and installed at FLASH is used for longitudinal bunch shape measurements and for two-color lasing provided by the FIR and VUV undulators. The pump probe experiments with VUV and FIR undulators provide the bunch profile measurements with resolution of several femtosecond. The MCP based radiation detectors are effectively used at FLASH for VUV pulse energy measurements. The new three MCP detectors operated in X-ray range are under development now in JINR for SASE1-SASE 3 XFEL.

FLASH MCP-BASED PHOTON DETECTOR

The free electron laser FLASH has been in operation at DESY since the year 2000. The maximal electron energy since 2007 up 2009 was equal 1 GeV, rms bunch length is 50 μm, the FWHM radiation pulse duration is about 30 fs, the normalized emittance is 2 π·mm·mrad, the bunch charge is 0.5 nC, the peak power is up to 1 GW, the peak brilliance is of 10^{28} ph/s/mrad^2/mm^2/(0.1%bw). In 2010 FLASH was upgraded to maximum electron energy 1.25 GeV and third harmonic RF system was installed which provides by few times longer the VUV pulse radiation comparing with the previous FLASH operation.

Successful operation of FLASH strongly depends on the quality of the radiation detectors. The key issues are: the wide wavelength range 4-100 nm, the wide dynamic range (from the spontaneous emission level to the saturation level), and the high relative accuracy of measurements which is crucial for detection of radiation amplification and characterization of statistical properties of the radiation.

The key FLASH photon detector developed by the JINR-DESY collaboration is a micro-channel plate (MCP) detector intended for pulse energy measurements [1-4]. The MCP detector is used for measurement of statistical properties of the radiation allowing determination of the pulse length. Key element of the detector is a wide dynamic MCP which detects scattered radiation from a target. With four different targets and MCPs in combination with optical attenuators, the present FLASH detector covers an operating wavelength range 4 -100 nm, and a dynamic range of the radiation intensities, from the level of spontaneous emission up to the saturation level of SASE FEL.

The gold target is perfect for the wavelength range above 10 nm, however its reflectivity falls dramatically for shorter wavelengths, and different targets and geometries of the detector are used. We added three more targets to gold mesh: two iron meshes, and one copper mesh. This helps us to operate the detector in a range below 10 nm.

For tuning SASE at very short wavelengths we use movable MCPs directly facing photon beam. Light intensity variation by a factor of 50 is controlled by a mechanical attenuator of light located in the target unit. To have full control of light intensity in a wide range we installed a side MCP which detects radiation reflected by the iron mirror. The mirror serves for two purposes. One is to deflect the photon beam off- the axis, which allows placing the MCP in better background conditions.

The FLASH bunch has non-Gaussian longitudinal distribution of electrons at operation in 2007-2009. The bunch edge or so named leading spike has a high peak current that is cable of driving the high intensity lasing process. Energy in radiation pulse and integrated spectral density fluctuate accordance with the gamma distribution with an energy width σ_w. Parameter $M=1/\sigma_w^2$ characterizes the number of modes in the radiation pulse. This parameters corresponds to a ratio of the electron bunch leading spike length σ_z to the coherence time τ_c at a saturation of the radiation in the SASE mode: $M=\sigma_z/c\tau_c$. The measurements of the integrate spectra density in radiation pulse permit to define the VUV pulse duration.

The r.m.s. VUV radiation pulse length was equal to $\tau_{VUV}= 8\pm1$ fs at the end of the regime of exponential growth for wavelength radiation of 13.7 nm and bunch charge 0.5 nC at electron energy 1 GeV [1]. After 2010 upgrade the r.m.s. VUV pulse radiation time corresponds to $\tau_{VUV}= 41\pm8$ fs at electron energy 1.25 GeV and bunch charge 0.5 nC [5].

DESIGN OF THE XFEL MCP DETECTOR

An important task of the photon beam diagnostics at the European XFEL is providing reliable tools for measurements aiming at the search for and fine tuning of the FEL creating SASE process. The problem of finding SASE amplification is crucial for the XFEL because of a large synchrotron radiation background. This requires a detector with a wide dynamic range, controllable tuning to the required wavelength range, and suppression of the unwanted radiation background. The JINR-XFEL

#syresin@nusun.jinr.ru

collaboration proposes to design, manufacture, and install MCP-based photon detectors [6] as a primary tool for the search and fine tuning of the SASE process. Three MCP devices will be installed after each SASE undulator of the European XFEL (SASE1, SASE2, and SASE3).

Three different tasks can be fulfilled with the XFEL MCP-based photon detectors [6]: study of the initial stage of the SASE regime; measurement of the photon pulse energy; and measurement of the photon beam image. The MCP detector will resolve each individual pulse at a repetition rate of 4.5 MHz. The following wavelength ranges are to be covered by three MCP stations: 0.05-0.4 nm for MCP1 and MCP2, 0.4-5 nm for MCP3.

MCP detector for SASE1&SASE2 [6] consists of three MCPs equipped with the anode as a pulse energy monitor and one MCP detector for imaging the photon beam and silicon semiconductor photo detector (Fig.1). The first MCP detector port houses silicon photo detector and two F4655 Hamamatsu MCPs 18 mm in diameter, which are used for measuring the pulse energy and for searching for initial indication of SASE regime. The second detector port houses two MCPs: F4655 Hamamatsu for measurement of the pulse energies, and beam observation system (BOS) MCP (model BOS-40-IDA-CH/P-47) of 40 mm diameter with a phosphor screen.

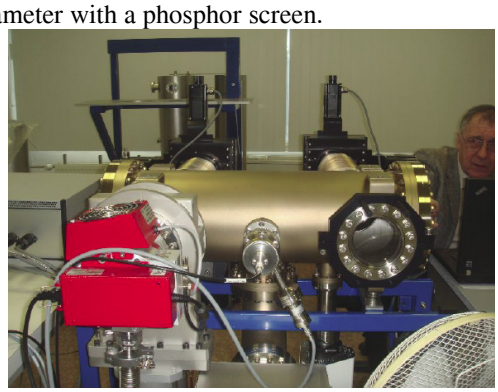

Figure 1: XFEL SASE1&SASE2 MCP detector.

MCP detector for SASE3 will have an additional port with movable semitransparent mesh and wire targets for production of scattering FEL radiation similar to those used at FLASH [1-4].

JINR FAR INFRARED UNDULATOR AT FLASH

The FLASH was equipped with an infrared electromagnetic undulator (Fig.2), tunable over a K–parameter range from 11 to 44, and producing radiation up to 200 μm at 500 MeV and up to 50 μm at 1 GeV [2-4, 6-7]. The purpose of the device is two-fold: firstly, it is used for longitudinal electron bunch measurements, secondly, it is a powerful source of intense infrared radiation naturally synchronized to the VUV FEL pulses, as both are generated by the same electron bunches and being therefore well suited for precision pump-probe experiments.

The undulator was designed and constructed by JINR to the FLASH requirements [6]. The undulator period corresponds to 40 cm, the number of periods is 9, the magnetic field is varied in range of 0.1-1.1 T. Output undulator radiation has the following parameters: wavelength 5-200 μm, peak power 4 MW, micropulse energy 1 mJ, micropulse duration 0.5-6 ps.

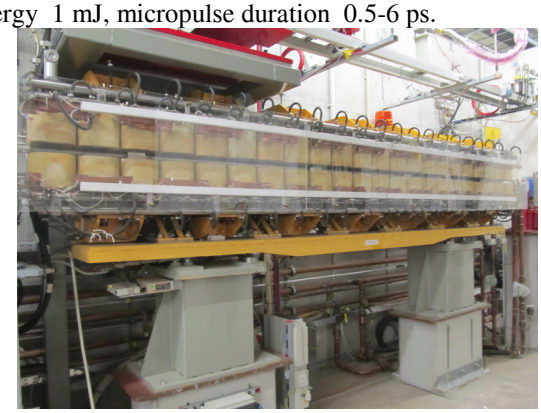

Figure 2: FLASH far infrared undulator constructed by JINR.

The energy radiated by the FIR undulator is defined by the number of electrons per bunch N and a form-factor F(λ):

$$\varepsilon_{coh} = \varepsilon_e \times \left[N + N(N-1)\left|\overline{F}(\lambda)\right|^2\right],$$

where ε_e is energy radiated by single electron. The form-factor is equal to $|F(\lambda)|^2 = \exp(-2\pi\sigma/\lambda)^2$ for Gaussian bunch with r.m.s. length σ. When the wavelength is longer than the bunch length, the coherent radiation dominates. Measuring the spectrum that regime one can extract the form-factor and thus the charge distribution and the bunch leading spike length. The Gaussian fit (Fig.3) corresponds to the r.m.s. leading spike length of σ_{ls}= 12 μm. The r.m.s duration of FIR pulse radiation is equal to $\tau_{FIR}=\sigma_{ls}/c$=40 fs, it is few times larger than r.m.s. pulse duration of the VUV pulse radiation.

After 2010 upgrade the detailed measurements of form-factor for FIR radiation were performed (Fig.4) [6]. The form-factor permits to reconstruct the time distribution of the electron current in the electron bunch (Fig.5) [6]. The reconstructed electron current pulse has complicated shape with two peaks at electron energy 1.25 GeV and bunch charge 0.5 nC.

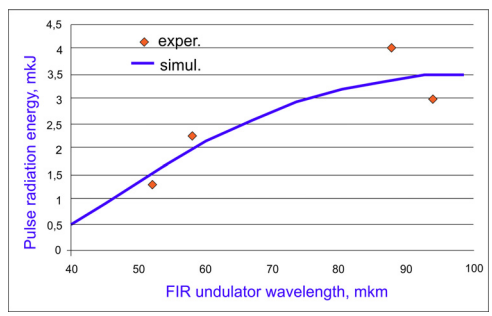

Figure 3: Dependence of the FIR undulator pulse radiation energy on the wavelength.

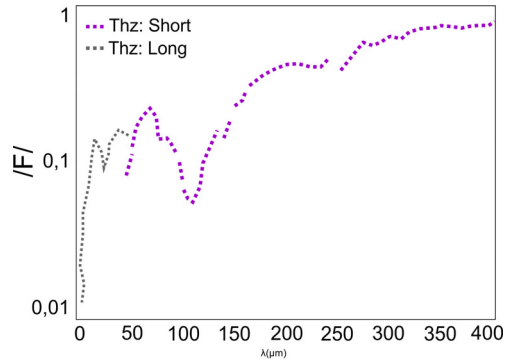

Figure 4: Dependence of form-factor on FIR radiation wave length.

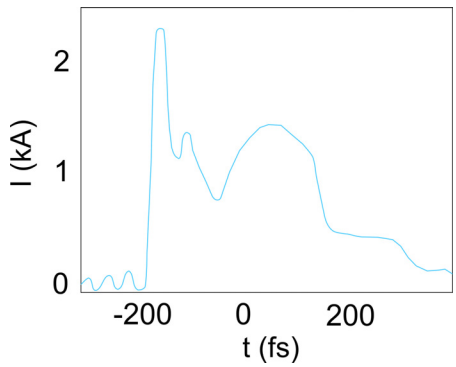

Figure 5: Reconstructed from form-factor of FIR radiation the time distribution of electron current in single short electron bunch.

PUMP PROBE EXPERIMENTS AT FLASH WITH JINR FIR UNDULATOR

The pump-probe experiments are very promising application of FLASH VUV and FIR undulators. The VUV and FIR undulator radiations are truly synchronized and tunable in a board spectral range that opens new perspective for two–color pump probe experiments at FLASH. In first pump probe experiments performed in 2009 [9] both FIR and VUV undulator radiations at wavelengths of 91 μm and 13.5 nm, correspondingly, pass through a krypton gas chamber. The 4-p krypton electrons are ionized in the gas chamber by the VUV photons generated during short pulse duration of 30 fs. The ionized electrons are accelerated during 3 ps in the electric field of IR light. The electron energy E_e is defined by VUV photon energy $h\omega$=91.8 eV, the krypton electron bind energy E_{bind}=14.1 eV and the vector potential of FIR electrical field A_{THz}: $E_e=h\omega-E_{bind}+evA_{THz}$, here v is the electron velocity. The difference of the electron energy spectrums along and across of the vector potential A_{THz} direction gives same information about the time structure of VUV radiation pulses. There is an asymmetry of the electron spectrums at small vector potentials $A_{THz}\rightarrow\pm0$ for two opposite directions of vector potential $A_{THz}\rightarrow+0$ and $A_{THz}\rightarrow-0$ (Fig. 6) .

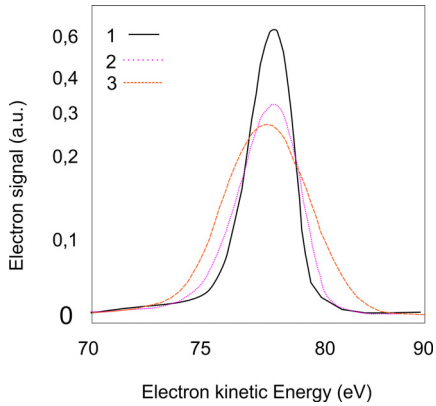

Figure 6: Dependence of electron intensity on its kinetic energy for three different vector potential of FIR radiation: 1 - v⊥A_{THz}, 2 - v// A_{THz}, $A_{THz}\rightarrow-0$, 3 - v// A_{THz}, $A_{THz}\rightarrow+0$.

The effective electron energy rate S_{eff} is defined by equation $S_{eff}^2=S^2\pm4SC$, where $S=veE_{THz}\cong100$meV/fs is the electron energy rate corresponded to FIR undulator electric field $E_{THz}=dA_{eff}/dt$, $C=hd\omega/dt\cong5\pm7$ meV/fs is the VUV photon energy chirp related to the beam electron energy chirp produced in FEL lasing spike at bunch compression. The sign ± corresponds two cases of the vector potential $A_{THz}\rightarrow\pm0$. The r.m.s. VUV radiation pulse duration is equal to $\tau_{VUV}=(\sigma^2_{E\text{-}THz}-\sigma_E^2)^{0.5}/S_{ef}$ =15±3fs for measured 1000 FLASH micro pulses, where $\sigma_{E\text{-}THz}$ and σ_E are the r.m.s. widths of the krypton electron energy spectrum with and with out FIR radiation.

The FIR undulator in this pump-probe experiment operates in regime of a streak camera with 10 femtosecond resolution. The internal envelope phase stability of infrared pulse in combination with femtosecond synchronized VUV pulse permits to investigate dynamics of atomic and molecular systems with 10 femtosecond resolution.

REFERENCES

[1] W. Ackerman et al., Nature Photonics, 1 (2007) 336.
[2] Y.Holler et al., FEL'07, p.318 (2007); http://www.JACoW.org.
[3] O.Brovko et al, Physics of elementary particles and atomic nuclei letters, 7 (2010) 78.
[4] O. Brovko et al, J. of Applied Physics, 3 (2010), 46.
[5] C. Behrens et al, TESLA-FEL 2012-01.
[6] E.Syresin et al, IPAC'10, p.1229, http://www.JACoW.org.
[7] O.Grimm et al, NIM A 615, 1 (2010),105.
[8] M.Gensh et al., Infrared physics and technology (2008) 358.
[9] U. Fruhling et al, Nature Photonics, 3 (2009) 523.

LONGITUDINAL STABILITY OF ERL WITH TWO ACCELERATING RF STRUCTURES

Ya. V. Getmanov#, O. A. Shevchenko, Budker INP, Novosibirsk, Russia
N. A. Vinokurov, Budker INP,Novosibirsk, Russia and KAERI, Daejeon, Korea

Abstract

Modern ERL projects use superconductive accelerating RF structures. Their RF quality is typically very high. Therefore, the RF voltage induced by electron beam is also high. In ERL the RF voltage induced by the accelerating beam is almost cancelled by the RF voltage induced by the decelerating beam. But, a small variation of the RF voltage may cause the deviations of the accelerating phases. These deviations then may cause further voltage variation. Thus, the system may be unstable. The stability conditions for ERL with one accelerating structure are well known [1, 2]. The ERL with split RF structure was discussed recently [3, 4]. The stability conditions for such ERLs are discussed in this paper.

INTRODUCTION

The scheme of an ERL with two accelerating structures is shown in Fig. 1.

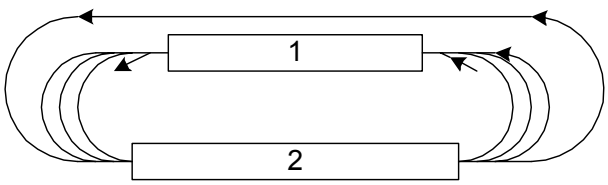

Figure 1: Scheme of ERL with two linacs.

Electrons are injected to the linac 1. After two passes through linac 1 and linac 2 they are used, for example, in undulators. After that electrons are decelerated.

There are four electron beams in each linac simultaneously. Each beam induced large voltage in the linac, but the sum is not so large. If the phases of the beams vary, the sum voltage also varies, and initially small phase deviation may increase due to the dependence of flight times through arcs on the particle energy. This longitudinal instability is considered in our paper.

THE VOLTAGE EQUATIONS

To simplify the picture, consider each linac as one RF cavity. Its equivalent circuit is shown in Fig. 2.

The gap voltage expression $U = L\,d\left(I_b + I_g - C\,dU/dt - U/R\right)/dt$, I_b and I_g are the currents of the beam and of the RF generator, leads to the standard equation

$$\frac{d^2U}{dt^2} + \frac{1}{RC}\frac{dU}{dt} + \frac{1}{LC}U = \frac{1}{C}\frac{d}{dt}\left(I_b + I_g\right) \qquad (1)$$

Taking the effective voltage on the linac with number α in the form $\mathrm{Re}(U_\alpha e^{-i\omega t})$ (ω is the frequency of the RF generator), one obtains:

$$\frac{2}{\omega}\frac{dU_\alpha}{dt} = \frac{i\xi_\alpha - 1}{Q_\alpha}U_\alpha + \rho_\alpha(I_{b\alpha} + I_{g\alpha}), \quad (2)$$

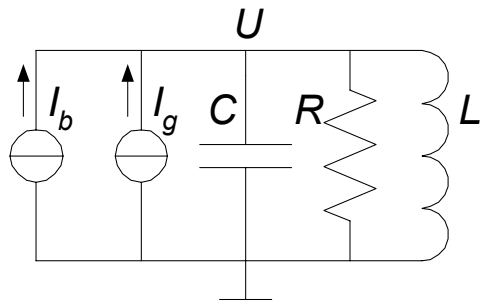

Figure 2: Equivalent circuit of the RF cavity.

where $\omega_\alpha = 1/\sqrt{L_\alpha C_\alpha} = (1 - \xi_\alpha/2Q_\alpha)\omega$ is the resonant frequency, $Q_\alpha = R_\alpha/\sqrt{L_\alpha/C_\alpha} >> 1$ is the loaded quality of the cavity, $\rho_\alpha = R_\alpha/Q_\alpha = \sqrt{L/C}$ and R_α are the characteristic and the loaded shunt impedances for the fundamental (TM_{010}) mode, and $I_{b\alpha}$ and $I_{g\alpha}$ are the complex amplitudes of the beam and (reduced to the gap) generator currents correspondingly. We are interested in the case of constant $I_{g\alpha}$. The beam currents $I_{b\alpha}$ depend on all U_α due to phase motion. Linearization of Eq. (2) near the stationary solution

$$U_{0\alpha} = \frac{R_\alpha}{1 - i\xi_\alpha}\left[I_{b\alpha}(\mathbf{U}_0) + I_{g\alpha}\right] \qquad (3)$$

gives:

$$\frac{2}{\omega}\frac{d\delta U_\alpha}{dt} = \frac{i\xi_\alpha - 1}{Q_\alpha}\delta U_\alpha + \qquad (4)$$

$$+ \rho_\alpha \sum_\beta \left(\frac{\partial I_{b\alpha}}{\partial\,\mathrm{Re}\,U_\beta}\mathrm{Re}\,\delta U_\beta + \frac{\partial I_{b\alpha}}{\partial\,\mathrm{Im}\,U_\beta}\mathrm{Im}\,\delta U_\beta \right)$$

Strictly speaking, I_b depends on the values of U at previous moments of time, so Eq. (4) is valid only if the

damping times Q_α/ω is much longer than the time of flight through the ERL.

THE STABILITY CONDITIONS

Considering the exponential solutions $\exp(\omega\lambda t/2)$ of system of linear differential equations Eq. (4), one can find the stability conditions. Indeed, the system Eq. (4) corresponds to the system of the linear homogeneous equations $\lambda\delta\mathbf{U} = \mathbf{M}\delta\mathbf{U}$ with the consistency condition $|\mathbf{M} - \lambda\mathbf{E}| = 0$. Re($\lambda$) < 0 for all roots of this equation (i. e., eigenvalues of the matrix **M**) is the stability condition.

The stability condition for ERL with one linac was derived in paper [2]. In this case

$$\mathbf{M} = \begin{pmatrix} -\frac{1}{Q} + \rho\frac{\partial \mathrm{Re}\, I_b}{\partial \mathrm{Re}U} & -\frac{\xi}{Q} + \rho\frac{\partial \mathrm{Re}\, I_b}{\partial \mathrm{Im}U} \\ \frac{\xi}{Q} + \rho\frac{\partial \mathrm{Im}\, I_b}{\partial \mathrm{Re}U} & -\frac{1}{Q} + \rho\frac{\partial \mathrm{Im}\, I_b}{\partial \mathrm{Im}U} \end{pmatrix} \quad (5)$$

and the characteristic equation is

$$\lambda^2 - \lambda Tr(\mathbf{M}) + |\mathbf{M}| = 0 \quad (6)$$

According to Eq. (5) the stability condition is

$$Tr(\mathbf{M}) = \rho\left(\frac{\partial \mathrm{Re}\, I_b}{\partial \mathrm{Re}U} + \frac{\partial \mathrm{Im}\, I_b}{\partial \mathrm{Im}U}\right) - \frac{2}{Q} < 0\,. \quad (7)$$

One can say, that the beam "active conductivity" $\left(\partial \mathrm{Re}\, I_b/\partial \mathrm{Re}U + \partial \mathrm{Im}\, I_b/\partial \mathrm{Im}U\right)/2$ has not to exceed the linac active conductivity $(\rho Q)^{-1}$.

For the ERL with two linacs

$$\mathbf{M} = \begin{pmatrix} \rho_1\frac{\partial \mathrm{Re}\, I_{b1}}{\partial \mathrm{Re}U_1} - \frac{1}{Q_1} & \rho_1\frac{\partial \mathrm{Re}\, I_{b1}}{\partial \mathrm{Im}U_1} - \frac{\xi_1}{Q_1} & \rho_1\frac{\partial \mathrm{Re}\, I_{b1}}{\partial \mathrm{Re}U_2} & \rho_1\frac{\partial \mathrm{Re}\, I_{b1}}{\partial \mathrm{Im}U_2} \\ \rho_1\frac{\partial \mathrm{Im}\, I_{b1}}{\partial \mathrm{Re}U_1} + \frac{\xi_1}{Q_1} & \rho_1\frac{\partial \mathrm{Im}\, I_{b1}}{\partial \mathrm{Im}U_1} - \frac{1}{Q_1} & \rho_1\frac{\partial \mathrm{Im}\, I_{b1}}{\partial \mathrm{Re}U_2} & \rho_1\frac{\partial \mathrm{Im}\, I_{b1}}{\partial \mathrm{Im}U_2} \\ \rho_2\frac{\partial \mathrm{Re}\, I_{b2}}{\partial \mathrm{Re}U_1} & \rho_2\frac{\partial \mathrm{Re}\, I_{b2}}{\partial \mathrm{Im}U_1} & \rho_2\frac{\partial \mathrm{Re}\, I_{b2}}{\partial \mathrm{Re}U_2} - \frac{1}{Q_2} & \rho_2\frac{\partial \mathrm{Re}\, I_{b2}}{\partial \mathrm{Im}U_2} - \frac{\xi_2}{Q_2} \\ \rho_2\frac{\partial \mathrm{Im}\, I_{b2}}{\partial \mathrm{Re}U_1} & \rho_2\frac{\partial \mathrm{Im}\, I_{b2}}{\partial \mathrm{Im}U_1} & \rho_2\frac{\partial \mathrm{Im}\, I_{b2}}{\partial \mathrm{Re}U_2} + \frac{\xi_2}{Q_2} & \rho_2\frac{\partial \mathrm{Im}\, I_{b2}}{\partial \mathrm{Im}U_2} - \frac{1}{Q_2} \end{pmatrix} \quad (8)$$

and the characteristic equation is (see, e. g., [5])

$$\lambda^4 - S_1\lambda^3 + S_2\lambda^2 - S_3\lambda + S_4 = 0\,, \quad (9)$$

where $S_1 = \sum_{1\le k\le 4} A\begin{pmatrix} k \\ k \end{pmatrix} = \sum_{1\le k\le 4} M_{kk} = Tr(\mathbf{M})$,

$$S_2 = \sum_{1\le k<l\le 4} A\begin{pmatrix} k & l \\ k & l \end{pmatrix}, S_3 = \sum_{1\le k<l<m\le 4} A\begin{pmatrix} k & l & m \\ k & l & m \end{pmatrix},$$

and $S_4 = A\begin{pmatrix} 1 & 2 & 3 & 4 \\ 1 & 2 & 3 & 4 \end{pmatrix} = |\mathbf{M}|$ are the sums of main minors of the matrix **M**. The necessary conditions for stability (Re(λ) < 0 for all four roots of Eq. (9)) is positivity of all the coefficients of the polynomial Eq. (9). In particular, the only independent on detunings ξ_1 and ξ_2 condition $S_1 < 0$ gives

$$\rho_1\left(\frac{\partial \mathrm{Re}\, I_{b1}}{\partial \mathrm{Re}U_1} + \frac{\partial \mathrm{Im}\, I_{b1}}{\partial \mathrm{Im}U_1}\right) + \rho_2\left(\frac{\partial \mathrm{Re}\, I_{b2}}{\partial \mathrm{Re}U_2} + \frac{\partial \mathrm{Im}\, I_{b2}}{\partial \mathrm{Im}U_2}\right) < \frac{2}{Q_1} + \frac{2}{Q_2} \quad (10)$$

The sufficient conditions are given by the Liénard-Chipart criterion [5]. It requires the positivity of of all the coefficients of the polynomial Eq. (9) and the third Hurwitz minor

$$S_1 < 0, S_2 > 0, S_4 > 0, \Delta_3 = S_1(S_2S_3 - S_1S_4) - S_3^2 > 0 \quad (11)$$

In the simplest case of the isochronous ERL arcs the conductivity matrix is zero. Then it is easy to proof, that all stability conditions are satisfied.

As the qualities of the superconducting cavities are very large, it is interesting to consider the opposite limiting case, neglecting small terms $1/Q_{1,2}$ in the matrix Eq. (8). Then all stability conditions do not depend on the beam current. They depend only on the ratio ρ_1/ρ_2 and the beam conductivity matrix, which is fully defined by the ERL magnetic system.

THE CONDUCTIVITY MATRIX

To proceed further, we have to specify the elements of the beam conductivity matrix in the stability conditions. The complex amplitude of the beam current I_b may be written in the form

$$I_{b\alpha} = -2I\sum_{n=0}^{N-1}\left(e^{i\varphi_{2n+\alpha-1}+i\psi_{2n+\alpha-1}} + e^{i\varphi_{4N-2n-\alpha}+i\psi_{4N-2n-\alpha}}\right) \approx$$
$$\approx I_{b\alpha}(\mathbf{U}_0) - 2iI\sum_{n=0}^{N-1}\left(e^{i\varphi_{2n+\alpha-1}}\psi_{2n+\alpha-1} + e^{i\varphi_{4N-2n-\alpha}}\psi_{4N-2n-\alpha}\right) \quad (12)$$

where I is the average beam current, $\varphi_{2n+\alpha-1}$ is the equilibrium phase for the n-th pass through the resonator with the number α (α = 1, 2), and N is the number of orbits for acceleration. The small energy and phase deviations ε_n and ψ_n obey the linear equations:

$$\varepsilon_{n+1} = \varepsilon_n + e\,\mathrm{Im}\left[U_{0\alpha(n)}e^{-i\varphi_n}\right]\psi_n + e\,\mathrm{Re}\left[\delta U_{\alpha(n)}e^{-i\varphi_n}\right], \quad (13)$$

$$\psi_{n+1} = \psi_n + \omega\left(\frac{dt}{dE}\right)_{n+1}\varepsilon_{n+1}\,, \quad (14)$$

where $\alpha(2n) = 1, \alpha(2n+1) = 2$ *for* $0 \le n \le N-1$ and $\alpha(2n) = 2, \alpha(2n+1) = 1$ *for* $N \le n \le 2N-1$. $(dt/dE)_n$ is the longitudinal dispersion of the n-th 180-degree bend. The initial conditions for the system of Eqs. (13) and (14) are, certainly, ε_0=0 and ψ_0=0, if we have no special devices to control them for the sake of the beam stabilization, or other purposes. The solution of Eq. (13) and Eq. (14) may be written using the longitudinal sine-like trajectory S_{nk} and its "derivative" S'_{nk} (elements 56 and 66 of the transport matrix). These functions are the solutions of the homogenous system

$$S'_{n+1,k} = S'_{n,k} + e\,\mathrm{Im}\left[U_{0\alpha(n)}e^{-i\varphi_n}\right]S_{n,k}\,, \quad (15)$$

$$S_{n+1,k} = S_{n,k} + \omega\left(\frac{dt}{dE}\right)_{n+1} S'_{n+1,k}, \quad (16)$$

with the initial conditions $S_{k,k} = 0$, $S'_{k,k} = 1$. Then

$$\psi_n = e\sum_{k=0}^{n-1} S_{nk}\,\mathrm{Re}\left[\delta U_{\alpha(k)} e^{-i\varphi_k}\right], \quad (17)$$

$$\varepsilon_n = e\sum_{k=0}^{n-1} S'_{nk}\,\mathrm{Re}\left[\delta U_{\alpha(k)} e^{-i\varphi_k}\right]. \quad (18)$$

Substitution of Eq. (20) to Eq. (15) gives

$$\delta I_{b\alpha} = -2ieI\sum_{n=0}^{N-1}\{e^{i\varphi_{2n+\alpha-1}}\sum_{k=0}^{2n+\alpha-2} S_{2n+\alpha-1,k}\,\mathrm{Re}\left[\delta U_{\alpha(k)} e^{-i\varphi_k}\right] + e^{i\varphi_{4N-2n-\alpha}}\sum_{k=0}^{4N-2n-\alpha-1} S_{4N-2n-\alpha,k}\,\mathrm{Re}\left[\delta U_{\alpha(k)} e^{-i\varphi_k}\right]\} \quad (19)$$

For an ERL it needs to satisfy (at least approximately) the recuperation condition

$$\mathrm{Re}\left[U_{01}\sum_{n=0}^{N-1}\left(e^{-i\varphi_{2n}} + e^{-i\varphi_{4N-2n-1}}\right)\right] = 0$$
$$\mathrm{Re}\left[U_{02}\sum_{n=0}^{N-1}\left(e^{-i\varphi_{2n+1}} + e^{-i\varphi_{4N-2n-2}}\right)\right] = 0 \quad (20)$$

For the longitudinal stability it also needs to have longitudinal focusing for most of passes through the linac (see Eq. (12, 13)):

$$e\,\mathrm{Im}\left[U_{0\alpha(n)} e^{-\varphi_n}\right] < 0 \quad (21)$$

if all $(dt/dE)_n > 0$). Conditions Eq. (20) and Eq. (21) may be satisfied simultaneously, if ($0 \le n \le 2N-1$)

$$\arg(eU_{0\alpha(n)}e^{-i\varphi_n}) + \arg(eU_{0\alpha(4N-n-1)}e^{-i\varphi_{4N-n-1}}) = -\pi, \quad (22)$$

which leads to

$$\varphi_{4N-n-1} = \pi - \varphi_n + 2\arg\left(eU_{0\alpha(n)}\right) \quad (23)$$

Conditions Eq. (26) affords equality of beam energies after n-th and ($4N$-n)-th passes through a linac.

To make the stability condition Eq. (10) more explicit, consider a simple example. Assume that equilibrium phases are equal during acceleration. In this simplest case $\varphi_{2n} - \arg(eU_{01}) = \Phi_1$, $\varphi_{2n+1} - \arg(eU_{02}) = \Phi_2$ for $0 \le n \le N-1$. Eq. (20) defines the equilibrium phases for deceleration. Then Eq. (19) gives

$$e\rho_1 I\sin(2\Phi_1)\sum_{n=0}^{N-1}\sum_{k=0}^{N-1} S_{4N-2n-1,2k} + e\rho_2 I\sin(2\Phi_2)\sum_{n=0}^{N-1}\sum_{k=0}^{N-1} S_{4N-2n-2,2k+1} < \frac{1}{Q_1} + \frac{1}{Q_2} \quad (24)$$

SIMULATIONS

Numerical calculations were made for proposed scheme of ERL with two accelerating structures (the simplest scheme is shown in Fig. 1). Parameters of accelerating structures: $Q_1 = Q_2 = 10^6$, $\rho_1 = 40\,\mathrm{M\Omega}$, $\rho_2 = 90\,\mathrm{M\Omega}$, $\omega = 2\pi\cdot 1.3\cdot 10^9\,\mathrm{Hz}$, $I = 10\,\mathrm{mA}$, $U_1 = 0.9\,\mathrm{GV}$, $U_2 = 1.9\,\mathrm{GV}$. Considering the magnetic structure with acceptable growth of the horizontal emittance [6, 7], one can check the stability conditions Eq. (11). Simulations show that there exist phase regime of the accelerating cavities with stability induced voltage and thus high threshold current. Stability condition for phase shift $\Phi_1 = \Phi_2$ between RF voltage and accelerating beam current is shown on Fig. 3 (approximately from -12 to -8 degrees) in case of equal accelerating phase gains on the magnetic structures.

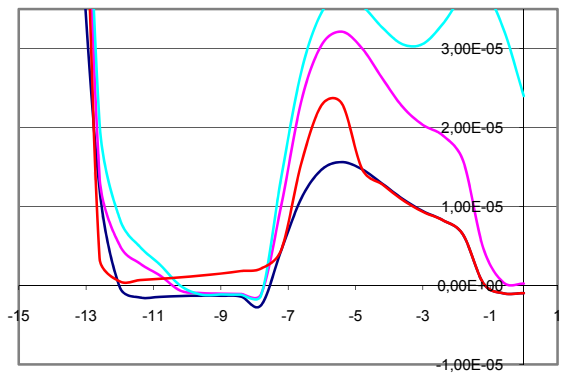

Figure 3: Dependence between the max real part of eigenvalues matrix M (vert.) and RF phases (hor.), calculated at the different detuning parameters (ξ=-1;- 0.1 ;1;1000).

CONCLUSION

In this paper we derived the criterion of the longitudinal stability for the ERL with two accelerating structures. Numerical calculations specify stability phase region with high threshold current for the accelerating cavities of accelerator with two linacs.

REFERENCES

[1] L. Merminga et al., Annu. Rev. Nucl. Part. Sci. 53(2003) 387.
[2] N.A. Vinokurov et al., Proc. SPIE 2988 (1997) 221.
[3] D. Douglas, ICFA BD-Nl 26 (2001)40.
[4] N.A. Vinokurov et al., Proc. IPAC'10.
[5] F.R. Gantmacher [F.R. Gantmakher], The theory of matrices , 1, Chelsea, reprint (1977) (Translated from Russian).
[6] G.N. Kulipanov et al., J. of synchrotron radiation v. 5, pt 3 (1998). P. 176.
[7] G.N. Kulipanov et al., Nucl. Instr. and Meth. A467/468 (2001), P. 16.

VERTICAL SIZE OF AN ELECTRON BEAM AT SIBERIA-2

A.G.Valentinov, V.N.Korchuganov, Yu.V.Krylov, Yu.L.Yupinov, NRC Kurchatov Institute, Moscow, Russia

Abstract

Brightness of the synchrotron radiation light sources is defined by electron beam sizes at radiation point. Horizontal size depends mainly from designed magnetic structure. Vertical size is defined by two processes: first, betatron coupling between vertical and horizontal motions and second, presence of vertical dispersion function at bending magnets. Vertical dispersion creates non-zero vertical emittance even without coupling.

The report is dedicated to methods of vertical beam size decreasing at SIBERIA-2 storage ring. There are two families of skew-quadrupoles on the ring, one lens of every family in each of 6 cells of the magnetic structure. After analyzing of betatron coupling coefficient equation we stayed only two lenses in each family. As a result power supplies' currents for coupling compensation became much lower.

In order to decrease vertical dispersion a special algorithm was developed and tested. Vertical dispersion on beam position monitors (BPM) azimuths was corrected by vertical displacements of chromaticity compensating sextupoles. Maximal value of the dispersion became four times lower. It leaded to prominent vertical beam size decreasing.

INTRODUCTION

The vertical size of the electron beam in storage ring SIBERIA-2 is mainly determined by two factors. Firstly, there is a vertical emittance ε_z, which is generated by the vertical dispersion function η_z in the places, where the electrons radiate energy - similar to the way that the horizontal dispersion function leads to the appearance of the horizontal emittance. Vertical dispersion occurs in the presence of any horizontal fields on the orbit, such as fields of vertical corrective magnets, fields due to deviation of the beam from the centers of quadrupoles and sextupoles, any parasitic fields. In addition, there are the inevitable errors in the position of the magnetic elements, which may lead to the distortion of vertical orbit. Secondly, there is a coupling of vertical and horizontal betatron. It appears in the presence of skew-quadrupole fields on a closed orbit. These fields can be a consequence of the rotation of quadrupole lenses along their longitudinal axis, as well as errors in the upright position of the sextupole lenses. The betatron coupling leads to the periodic transfer of energy between the horizontal and vertical betatron oscillations.

Other mechanisms to increase the vertical size of the beam, such as multiple internal scattering of electrons in the bunch (the Toushek effect), and the interaction of a beam with the currents, induced on the walls of the vacuum chamber, give negligibly small contribution to the vertical size of the beam at SIBERIA-2 at 2.5 GeV.

To decrease the vertical size of the beam it is necessary to control the vertical dispersion function, as well as the coupling of betatron oscillations.

VERTICAL DISPERSION FUNCTION CONTROL

In the case of small connection between transversal betatron oscillations an equation for the vertical dispersion is written as

$$\eta_z'' + K_1\eta_z = K_2 z_c \eta_x - K_{1s}\eta_x + K_1 z_c - \frac{1}{\rho_z} = F \qquad (1)$$

where η_x - horizontal dispersion function, K_1, K_2, K_{1s} - normalized power of quadrupoles, sextupoles and skew-quadrupoles respectively, z_c - vertical deviation of a closed orbit, ρ_z is the radius of rotation in vertical plane [1]. The solution to this equation has the same form like for a closed orbit:

$$\eta_z = \frac{\sqrt{\beta_z(s)}}{2\sin\pi\nu_z}\int_s^{s+C}\sqrt{\beta_z(y)}\cos(\phi_z(s)-\phi_z(y)+\pi\nu_z)F\,dy \qquad (2)$$

where ν_z - vertical betatron frequency, C – ring circumference, β_z - vertical β-function.

For us the important thing here is that η_z is described by exactly the same formulas as the vertical closed orbit. This means that η_z, as well as the orbit, can be corrected to obtain its acceptable view. As for correction of the closed orbit, the goal is to decrease the value of RMS η_z deviations from zero: $\sigma_{\eta z} \rightarrow 0$. Magnetic elements contributing to the function F can be used as correctors. In fact, with already adjusted closed orbit, one can affect only the second term in the expression for F, because in this case the following conditions are satisfied: z_c = const and ρ_z = const. Thus, only the magnetic elements with skew-quadrupole component in the field can influence on the vertical dispersion without the distortion of the orbit. They must be located inside achromatic bend with a non-zero η_x. It is preferable to have skew-quadrupole lenses with independent power supplies inside each achromatic bend. There are no that kind of lens at SIBERIA-2, but we can use sextupole lenses for natural chromaticity correction as correctors for η_z. We can get skew-quadrupole field K_{1s} from sextupole vertical displacement Δz: K_{1s}= -K_2·Δz. Impact on the closed orbit is small enough, because components of the field arising from sextupole moving ΔB_z and ΔB_x are proportional, respectively, to z_c·Δz and x_c·Δz, where z_c and x_c - vertical and horizontal orbit distortions at sextupoles' azimuths. Each of the z_c, x_c and Δz does not exceed 1-2 mm, and the

angular deviation of the orbit generated by the field, does not exceed $2 \cdot 10^{-6}$. This is a very small value in comparison with the typical angular deviation 10^{-4}, arising from typical 0.01 mm transverse quadrupole deviations. The maximum orbit distortion because of the shift of one sextupole will not exceed several tens of microns.

SIBERIA-2 sextupoles are not designed for this type of η_z correction, so their vertical movements are quite limited. Vacuum chamber of the storage ring is an obstacle. About one-third of the 24 sextupoles may be displaced for no more than 0.2 - 0.3 mm; others allow a more notable movement up to 1.5 mm.

The same mathematical methods can be used for the correction of η_z as for the correction of the closed orbit (LSQ, MICADO, SVD). A response matrix for ideal magnetic structure is calculated, linking the shift of the sextupoles and vertical dispersion changes at azimuths of beam position monitors (BPM). Vertical dispersion is measured through changes in the frequency of RF system (and hence the revolution frequency f_{REV}). Energy deviation $\Delta p/p$ is connected with change in revolution frequency Δf_{REV} through momentum compaction factor $\alpha = 0.0103$. So we can calculate vertical dispersion from

$$\eta_z = \frac{\Delta z}{\Delta p / p} \qquad \frac{\Delta p}{p} = -\frac{1}{\alpha}\frac{\Delta f_{REV}}{f_{REV}} \qquad (3)$$

where Δz – vertical orbit distortions from BPMs, f_{REV} = 2.4151 MHz, Δf_{REV} usually equals ± 20 Hz.

Solution of the η_z correction problem is a set of shift values for sextupoles. Next you need to select the variant of correction, which can be physically implemented, that is there would be no obstacles for sextupoles' moving, and then make it. After this the cycle of correction can be repeated. Neighboring sextupoles, located on the edges of the quadrupole doublet, affect the η_z practically by the same way (with accuracy up to the sign!), because of small betatron phase distance between them. Thus, there is 12 independent «correctors» to regulate η_z at azimuths of 24 BPMs. Of course, it is not possible to reach full compensation of dispersion function, moreover, a behavior of η_z remains unknown between BPMs.

The correction process led to a strong decrease in the $\sigma_{\eta z}$ value at BPM azimuths. Figure 1 shows the vertical dispersion function at SIBERIA-2 before and after correction. 8 sextupoles were moved, maximal shift was Δz = 1.5 mm. As a result of $\sigma_{\eta z}$ decreased from 3.4 cm down to 0.9 cm, the maximum value of η_z decreased from 6 cm down to 3 cm. Theoretically we can make the $\sigma_{\eta z}$ approximately 2 times less by using all of the 12 independent «correctors», however, sextupoles' shifts would be too big.

Reduction of dispersion led to a considerable reduction in the vertical size of the electron beam, visible even on the TV screen, which shows the profile of the beam in visible light. In the visible range there is quite a strong dispersion of light in an optical observation system, which leads to an increase in the visible vertical size. However, the effect of correction is well seen in this case (Fig. 2).

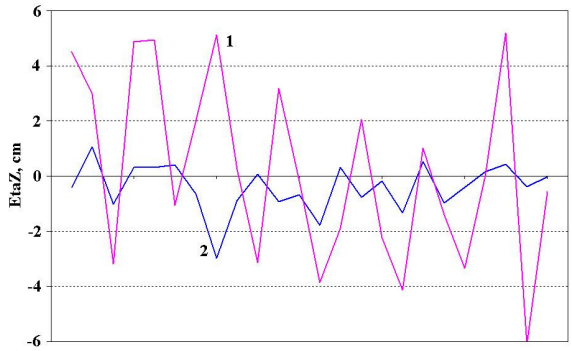

Figure 1: Vertical dispersion function at SIBERIA-2 BPMs before correction (1) and after it (2).

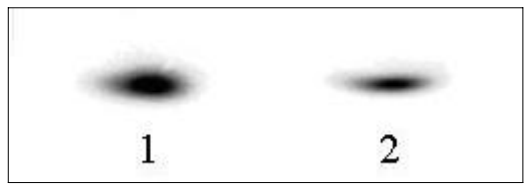

Figure 2: Electron beam image on TV screen (converted colors) before (1) and just after (2) η_z correction.

BETATRON COUPLING

The coupling coefficient can be described analytically (excluding the effect of solenoid fields) [2]:

$$C^- = \frac{1}{2\pi R}\int_0^{2\pi}\sqrt{\beta_x \beta_z}\cdot K(\theta)\cdot \exp^{i\Psi(s)}\, d\theta \qquad (4)$$

$$\Psi(s) = (\mu_x - \mu_z) - (Q_x - Q_z - p)\theta$$

Here R is the average radius of the ring, $\beta_{x,z}$ - optical functions, $\mu_{x,z}$ - betatron phase, $Q_{x,z}$ – betatron tunes, θ = s/R, p - the difference between integer parts of the betatron tunes, and K is the normalized gradient of the skew-quadrupole lenses:

$$K(\theta) = \frac{R^2}{2 \cdot B\rho}\left(\frac{\partial B_x}{\partial x} - \frac{\partial B_z}{\partial z}\right) \qquad (5)$$

C^- is a complex value, its module $|C^-|$ corresponds to minimum distance between betatron tunes, which can be reached on the approach to the resonance $Q_x - Q_z - p = 0$. The values of the imaginary and real parts of C^- depend on the starting point, while the value $|C^-|$ remains unchanged. The vertical emittance due to betatron coupling can be written as:

$$\frac{\varepsilon_z}{\varepsilon_x} = \frac{\left|C^-\right|^2}{\Delta^2 + \left|C^-\right|^2}, \qquad (6)$$

where $\varepsilon_{x,z}$ – horizontal and vertical emittances, $\Delta = Q_x - Q_z - p$, $Q_x = 7.77$, $Q_z = 6.70$ for SIBERIA-2 structure, $|C^-|$ value without skew-quadrupole lenses was equal approximately to 0.03 after compensation of closed orbit distortions.

In order to compensate betatron coupling the magnetic structure of SIBERIA-2 contains 2 skew-quadrupole families SQ1 and SQ2 - one lens of the family in each of the 6 machine superperiods. It turned out, however, that their forces are not enough to compensate the coupling: the requested currents were about 30 A with the highest possible level of 25 A. The fact is that the influence of each skew-quadrupole depends on the phase $\Psi(s)$ in the exponential factor of the expression (4). If the magnetic structure consists of N identical superperiods, the phase advance of $\psi(s)$ on one superperiod is equal to $2\pi \cdot p/N$. Therefore, the lenses of one family, located in the same manner within each superperiod, will be equally influence the imaginary and real parts of the C^- only if p is equal to zero or a multiple number of superperiods N. In our case $p = 1$ and $N = 6$, so phase advance of $\psi(s)$ for one superperiod is equal to 60 degrees. In this case, the skew-quadrupoles, belonging to one family, but located in different superperiods, will compensate the influence of each other. They affect on betatron coupling only because there are differences in the betatron functions and phases between different superperiods because of imperfections of the magnetic structure.

For more efficient use of the skew-quadrupoles we changed commutation inside the SQ1 and SQ2 families. In principle, it was possible to leave on one lens in each family. In practice two lenses was left on opposite sites of the ring (in the 2nd and 5th superperiods), and the sign of skew-quadrupole gradient in 2nd superperiod was changed to the opposite. The phase advance between lenses inside one family became equal to 180°, the phase difference between SQ1 and SQ2 lenses inside one superperiod is equal to ~60°. This allowed the halving of the required power supply current for the coupling compensation. New type of commutation allows to achieve full compensation of the coupling with the currents SQ1 = -0.1 A, SQ2 = -2.8 A.

CONCLUSIONS

As a result we have been able to reduce the vertical size of the electron beam considerably. The new commutation in the families of the skew-quadrupole lenses allowed us to reduce currents (and, hence, the field) needed to compensate the betatron coupling. Thus, vertical emittance due to coupling can be easily reduced to an amount not exceeding 0.01% from the horizontal one. The correction of the vertical dispersion function led to 3.5 times lower η_z value at BPM azimuths. All these factors provide a substantial decrease of the electron beam vertical size in radiation points of the bending magnets.

REFERENCES

[1] T.O.Raubenheimer, R.D.Ruth, "Analytic Estimates of Coupling in Damping Rings", PAC 1989, p.1435.

[2] G.Guignard, "The General Theory of All Sum and Difference Resonances in a Three-dimensional Magnetic Field in a Synchrotron", CERN 76-06 (1976).

ENERGY RAMPING AT SIBERIA-2

A.G.Valentinov, V.N.Korchuganov, Yu.V.Krylov, Yu.L.Yupinov, NRC Kurchatov Institute, Moscow, Russia

Abstract

Siberia-2 storage ring has great difference between injection energy 0.45 GeV and working energy 2.5 GeV. Beam lifetime at injection energy is equal to approximately 1 hour. In order to minimize beam losses of the stored beam it is necessary to accelerate energy ramping process. It is not very simple because power supplies of bending magnets, quadrupole lenses and sextupoles have different response time and behavior after changes in regulated current level. Magnetic elements are manufactured from non-laminated iron. It leads to slower field/gradient increasing at high current values.

Complicated algorithm with 9 intermediate regimes (collections of power supplies' settings) was developed to produce fast and efficient energy ramping. First, correction of closed orbit, betatron tunes and chromaticity is accomplished in each regime in static conditions. Special file is used to provide acceleration or deceleration of power supplies in dynamic conditions. This scheme allows to compensate betatron tune shifts during energy ramping. Power supplies are not stopped on intermediate regimes; speed of current changing is continuous function of time. This algorithm allowed decreasing ramping time down to 2 minutes 40 seconds. Beam losses are not exceeding 2 – 3%; betatron tune shifts as a rule are lower than 0.01. The algorithm can easily be modified to stop in any intermediate regime.

INTRODUCTION

Synchrotron radiation source SIBERIA-2 [1] has a big difference between injection energy (450 MeV) and working energy (2.5 GeV). Beam lifetime at energies below 1 GeV is small and does not exceed 1.5 hours. To avoid losses of electrons, immediately after the accumulation of the necessary current energy should be increased as soon as possible. The process of energy ramping consists in proportional change of magnetic field in bending magnets, field gradients in quadrupole and sextupole lenses. The difficulty lies in the fact that different magnetic elements have different curves of magnetization, that is, the dependence of the field/gradient on supply current. In addition, power supplies of the magnetic elements have different speed of reaction on change of nominal current. Magnetic elements are manufactured from nonlaminated iron, which leads to delay of the field in the working gaps of the magnets and lenses. As a result, betatron tuneshifts arise after the start of energy ramping. Too large shifts can lead to losses of the current on the closest resonances. Also chromaticity can change, resulting in additional losses due to a decrease of the dynamic aperture or the occurrence of instabilities in the beam.

To solve all these problems a unique algorithm for energy ramping was developed and implemented.

DIFFERENCIES IN MAGNETIZATION CURVES

Magnetic system of SIBERIA-2 includes one family of bending magnets, 6 families of quadrupole lenses, two families of sextupole lenses for chromaticity correction. The supply current of the bending magnets varies from 1270 A up to 7200 A, it determines the machine energy. The currents of the quadrupole power supplies vary from 80 A up to 760 A depending on the energy and number of the family, the currents of sextupole power supplies vary from 0.4 A up to 8 A. As a result saturation of iron exists at high energy, while residual magnetization manifests at low energies. The magnetization curve of the bending magnets is also influenced by busbar layout near current sensor. Thus, a simple proportional increase of the currents will lead to the betatron tuneshifts during energy ramping.

To facilitate the energy ramping process, 9 intermediate regimes were introduced at a distance of 10 - 20% in energy one from another. The regime means list of power supply settings. Magnetic measurements were conducted to determine right currents for all power supply families in each regime. Field in bending magnets was measured with an accuracy of 10^{-5} using NMR sensor. For the quadrupole lenses measurements were carried out by Hall effect sensor with an accuracy of 10^{-3}. Relative changes of the field gradients in each family in all intermediate regimes were measured. According to the results of measurements a correction of the setpoint currents was carried out so the relations of the gradients in different families in each regime remained the same as at the injection energy. Some of the results after this correction are shown in Fig. 1.

For more accurate reproduction of the results standard demagnetization cycle was introduced. After the work on the energy of 2.5 GeV currents of power supplies of the magnetic elements rise above the maximum working value, then gradually, over 80 seconds, fall below the minimum values of the injection energy, then regime of injection is restored. In every state a 30 seconds pause is maintained. The practice showed that after this demagnetization cycle betatron tunes returned to its initial values with a good accuracy of about 0.003.

TRANSIENT PROCESSES IN POWER SUPPLIES AND MAGNETIC ELEMENTS

Power supplies of the SIBERIA-2 magnetic elements have different speed of reaction to the change of current settings. In addition, magnets and lenses are manufactured

from nonlaminated iron. This leads to the fact that the magnetic field/gradients in working gaps are installed with a time delay with respect to the change in the current. This is especially noticeable at high energies, where the influence of the saturation of iron is greater. In practice it turns out that the change of the field in the bending magnets lags behind the changes in the gradient of quadrupole lenses. This lag is well seen in measurement of betatron tunes during the energy ramping.

Betatron frequencies are measured through the beam excitation with a varying frequency and finding the resonant growth of the amplitude of transverse vibrations. This method has an accuracy of better 0.002, one measurement usually takes 1.2 - 1.4 seconds, which allows us to measure the frequencies during the energy ramping.

Under proportional rise of the currents in the bending magnets and lenses both betatron tunes begin to decrease, therefore field in magnets goes behind gradients in the lenses. Thus, for the effective energy ramping it is necessary to change current settings for bending magnets in advance with respect to the current settings for quadrupole lenses.

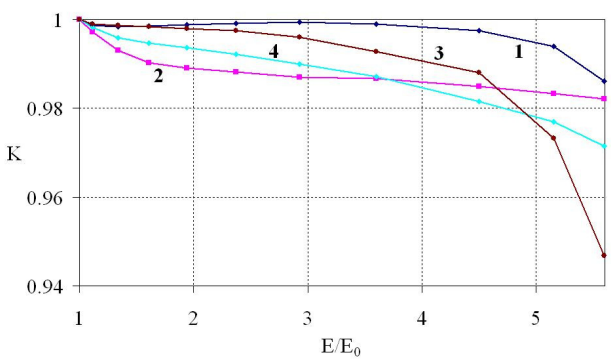

Figure 1: Magnetization curves $K = \left(\frac{H}{I}\right) / \left(\frac{H_0}{I_0}\right)$ for bending magnets (1), quadrupole family with minimum current (2), with maximum current (3), quadrupole with different yoke design (4). H – field or gradient, I – current of power supply, 0 index corresponds to injection energy. Curve (2) demonstrates the effect of residual magnetization (at the left), curve (3) shows the effect of the iron saturation (at the right). Points on the curves correspond to different regimes. Machine energy changes from E_0 = 450 MeV up to 2.5 GeV.

ENERGY RAMPING ALGORITHM

Adjustment of the energy ramping is carried out as follows:

- Adjustment of the intermediate regimes. Slow energy rising with 2 – 4 mA of electron current is carried out with a stop in each regime. Closed orbit correction, betatron frequency tuning, chromaticity correction are produced. Results are written to regime files, and then the cycle of demagnetization is performed.
- In the operating mode energy rising occurs without a stop at intermediate regimes. The algorithm is designed so that speed of current growth in the power supplies was a continuous function of time and changed linearly between neighboring regimes (Fig.3). The speed grows up to 1.6 GeV, after 2 GeV it begins to decline. At the beginning and at the end of the process the speed is equal to zero. So-called advance coefficients may be implemented into growth law. Additional change of the speed between the regimes is directly proportional to such coefficient and to a number of steps of the control program counted from previous regime.
- Several energy ramping are completed with the measurement of betatron tunes for the selection of the advance coefficients the number of control steps for each regime. Betatron tunes at the moment of regime passage must be equal to those seen at the injection energy. All values are saved in a file-descriptor of the ramping. The advance coefficients and the regimes duration are changed very rarely, only in case of significant modification of the algorithm (because of change of these parameters in one regime lead to the change of speed of current growth in rest part of the process).
  For operational adjustment of betatron tunes during the energy ramping the file-descriptor contains amendments to betatron frequencies for each regime and for possible changes in the frequencies within the regime. Correction of frequencies $\Delta Q_{x,z}$ is performed with the help of two quadrupole families F3 and D3, located in the region with zero dispersion function. regime. The same families are used for compensation of betatron tuneshifts $\Delta Q1_{x,z}$ in the middle of the regime installing. In this case, the correction of the current is concentrated within the current regime; the principle of continuity of the speed of current growth is still respected. Usually tunes amendments are modified once in 1-2 weeks (if it is necessary).
- When the last 2.5 GeV regime is installing the speed of current growth does not vary linearly with time, but like a square of time (Fig.2). This is done because one must compensate all the advance coefficients that were introduced previously. Power supply currents are strictly defined in this case and final speed for them must be equal to zero. So additional degree of freedom is needed in the law of the current changes.

Ramping file-descriptor looks as follows (Table 1). The table also contains four additional columns (not shown here): DQX,Z – amendments to betatron tunes for given regime, DQX1,Z1 – amendments in the middle of the regime recording. The process can be easily modified to stop in any intermediate regime. For this one need to delete rows from a table, following the required regime and increase the number of steps for the latter regime (for

example, to stop at the regime 2G30 one needs to specify 220 steps instead of 90, at the 2G00 - 280 instead of 107). If the advance coefficient is equal to 100, it corresponds to additional 1% of speed V = dI/dt at the end of given regime installing. For bending magnets such coefficients' distribution provides the relative growth in the rate of current increase in the range of 1 - 2%, except for the last regime, on which the advance is compensated (see Fig. 2).

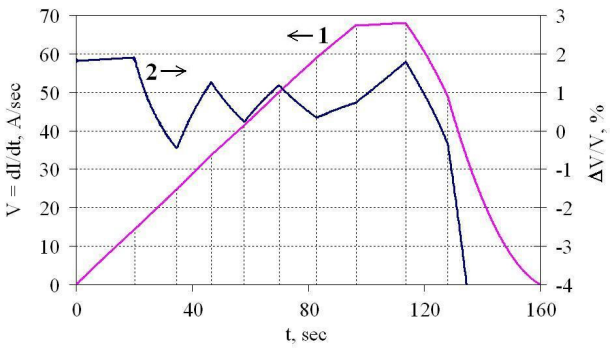

Figure 2: Speed of current growth in the power supply of the bending magnets (1) and relative increase of this speed due to advance coefficients (2). An influence of these coefficients is compensated in the last regime. Dotted lines correspond to regime borders.

Table 1: Typical view of the file-descriptor. NREG – regime's name, NSTE – number of steps for control program (160 msec each), KHS2, KD2 – advance coefficients for power supplies of bending magnets and D2 quadrupole family. Energy (in MeV) is given for reference.

NREG	NSTE	KHS2	KD2	Energy
G550	126	115	-70	499
G600	91	95	-70	598
G750	74	105	-70	719
G900	71	130	-70	868
1G00	75	160	-70	1060
1G30	81	190	-70	1307
1G60	85	210	-70	1608
2G00	107	340	-70	2012
2G30	90	520	-70	2305
2G50	200	0	0	2500

The view of energy growth and beam current changing are shown in Fig.3. Whole process takes 2 minutes 40 seconds, loss of current generally do not exceed 2 - 3%, they due to the low beam lifetime at energies below 1 GeV. Figure 4 demonstrates betatron tuneshifts around initial working point Q_x = 7.773, Q_z = 6.701 during energy ramping. Nearest resonances up to 5th order are presented. Resonances $2Q_x + 2Q_z = 29$ and $4Q_x = 31$ are the most dangerous, causing a loss of electrons. The greatest tune deviations occur when the last 2.5 GeV regime is installed.

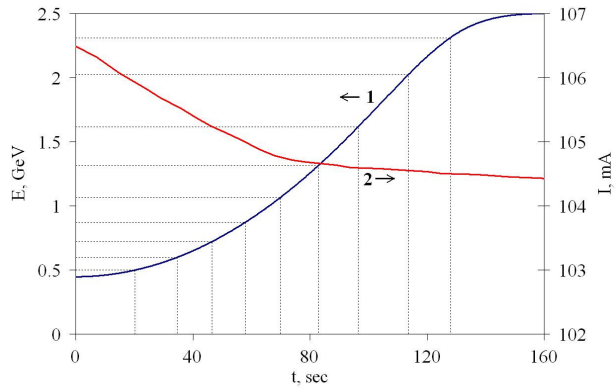

Figure 3: Energy growth (1) and electron current changing (2) during energy ramping (19/04/12). Dotted lines correspond to regime borders.

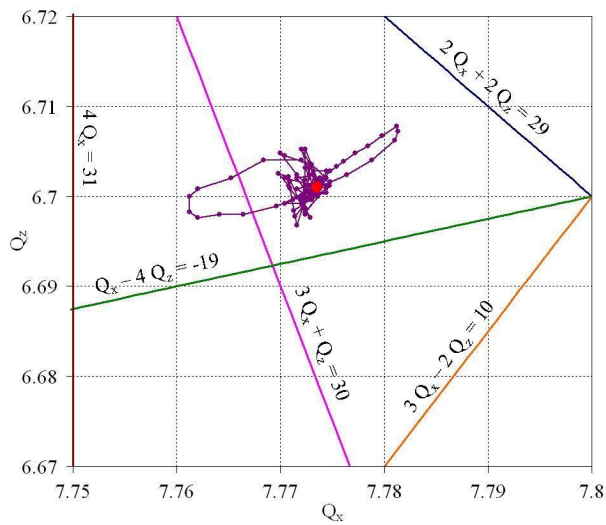

Figure 4: Betatron tuneshifts during energy ramping. Red point corresponds to initial (and final) working point. Nearest resonances up to 5th order are presented. Largest tuneshifts occurred in the last regime.

CONCLUSIONS

Fast and reliable energy ramping algorithm was developed and implemented at SIBERIA-2 storage ring. Whole process takes 2 minutes and 40 seconds, beam losses doesn't exceed 2 – 3 %, betatron tuneshifts are less than 0.015.

REFERENCES

[1] V.Korchuganov, M.Blokhov, M.Kovalchuk et al. "The status of the Kurchatov center of SR", Nuclear Instruments and Methods, A 543 (2005) pp. 14-18.

MEASUREMENT OF SPEED OF LIGHT EMITTED BY ULTRARELATIVISTIC SOURCE*

A.I. Stirin#, P.A. Aleksandrov, V.N. Korchuganov, National Research Center Kurchatov Institute, 123182 Moscow, Russia
E.B. Aleksandrov, Ioffe Physical–Technical Institute, Russian Academy of Sciences, 194021 St. Petersburg, Russia
V.S. Zapasskii, St.Petersburg State University, 198504 St. Petersburg, Russia

Abstract

The paper focuses on the results of experiments on direct measurement of speed of the light emitted by an ultrarelativistic source. The source of synchrotron radiation (SR), electron storage ring Siberia-1 at the Kurchatov Institute, was used as a pulsed source of light. Experiments were made on the visible part of the SR emitted by ultrarelativistic electron bunch moving along a curved trajectory in the magnetic field of the bending magnet.

The measured velocity is within 0.3 % of the standard speed of light in a vacuum.

INTRODUCTION

The statement that "the speed of light is independent of the velocity of the source" was put forward by Einstein as the second postulate of special relativity [1]. In the last century, many astronomical observations and experimental studies have been devoted to accrediting this postulate, see, e.g., recent review [2]. During this time, the validity of this postulate was questioned many times with regard to the insufficient accuracy of the measurements, which was usually due to the low velocity of the source v compared to the speed of light *c*. In this work, we directly measured the speed of the light emitted by a source moving with an ultrarelativistic velocity and found that this speed does not differ from the standard speed of light in a vacuum, which is in agreement with Einstein's postulate.

SETUP AND THE IDEA OF THE EXPERIMENT

The experiment was based on the use of synchrotron radiation from a bunch of relativistic electrons moving at a velocity very close to the speed of light *c* along a curved trajectory in the magnetic field of the bending magnet of the electron storage ring. Under these conditions, it is easy to measure the speed of the emitted light in a very high laboratory vacuum.

According to the Newton–Ritz corpuscular ballistic hypothesis [3–5], which is most popular among opponents of special relativity, the speed of the light emitted by an electron bunch in the forward direction at a tangent to the trajectory should be twice as high as the speed of the light emitted by a source at rest. If this very large effect existed, it could easily be detected without special tricks in view of a high intensity of the synchrotron radiation.

The general layout of the experiment is shown in Fig. 1. The magnetic system of the electron storage ring Siberia-1 forming a closed orbit of electrons consists of four 90° bending magnets M1–M4 separated by four 60-cm-long rectilinear segments and forms a closed orbit of electrons. The radius *R* of the stationary orbit of electrons in the bending magnets is 1 m.

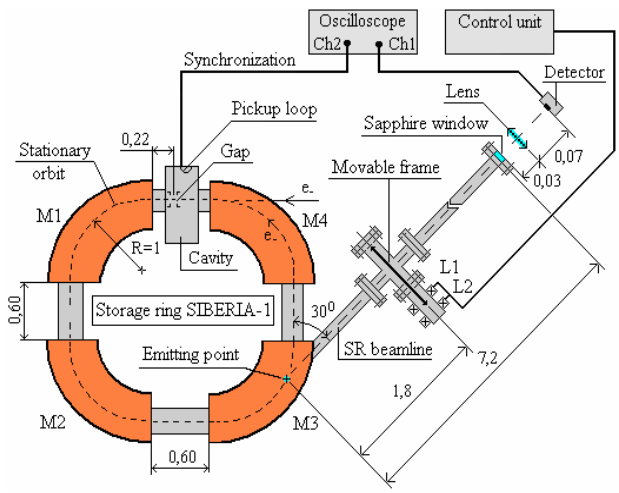

Figure 1: Layout of the experiment: L1, L2-magnetic drive coils of carriage; M1-M4 - bending magnets. Distances are given in meters.

The magnetic flux density on the stationary orbit is 1.5 T at a nominal electron energy of 450 MeV. Synchrotron radiation emitted by relativistic electrons in bending magnets covers a wide spectral range from infrared to X-ray with a characteristic wavelength of 61.3 Å. This emission leads to a 3.69 keV energy loss of each electron per round trip.

To compensate for these losses, a high-frequency cavity was placed in the first segment of the storage ring. Due to the high-frequency power supplied to the cavity, a voltage with an amplitude of 15 kV and a frequency of

*The work was supported by the Russian Foundation for Basic Research under Project No. 11-02-00538-a.
staxiv@mail.ru

34.53 MHz, which is equal to the frequency of the rotation of the electron bunch in the storage ring, is created in the accelerating gap of the cavity.

The distribution of the transverse electron density in the bunch is Gaussian with a standard size of σ = 0.30 m.

The angle between the axis of the synchrotron radiation output channel, which is tangent to the stationary orbit in magnet M3, and the axis of the fourth rectilinear segment succeeding magnet M3 was 30°. This means that the emission point (the beginning of the path of the synchrotron radiation along the channel axis) is at a distance of $\pi R/3$ from the input end of magnet M3. The length of the channel from the emission point to the output sapphire window was L = 7.2 m. The chamber of the storage ring and the synchrotron radiation output channel compose a single vacuum volume.

A collecting lens placed behind the output window focused the synchrotron radiation beam on the window of a photodetector. As the detector, we used a silicon PIN photodiode Hamamatsu S5972, which has a spectral range of (0.32–1) μm, a frequency bandwidth of 500 MHz, and an effective sensitive area of 0.5 mm^2. The voltage created by the photocurrent of the diode on the 50 Ohm load (optical signal) was fed to the first input of a two-channel oscilloscope Tektronix 3052C (bandwidth of 500 MHz). Electric circuit of the photodetector is shown in Fig. 2.

A continuous sinusoidal high-frequency synchronization signal from the pickup loop of the cavity was fed to the second input of the oscilloscope. The pickup loop is oriented in such a way that the phase of its output voltage is shifted by 180^0 with respect to that of the voltage of the accelerating gap of the cavity. To exclude the error that results from different phase shifts of signals, the signals were transmitted through identical anti-interference (with a double screen) coaxial cables of the same length.

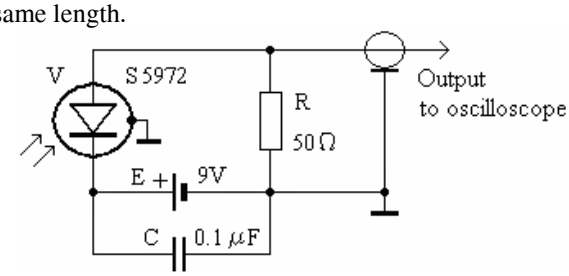

Figure 2: Schematic of the photodetector circuit.

Two Versions of the Experiment

The *first version* implied operative shutdown of the light beam in the synchrotron radiation output channel by a glass plate that was fixed in a movable frame and was introduce into the beam using a magnetic drive. In terms of the ballistic hypothesis, the refracting plate is considered as a secondary source of light at rest. For this reason, the light should pass section l of the synchrotron radiation output channel from the plate to the output window at a velocity of c (rather than $2c$, as in the absence of the plate). The length of section l is 5.4 m (Fig. 1); thus, the shutdown of the synchrotron radiation beam by the glass plate will lead to a time delay in the optical signals by 9.0 ns.

The *second version* of the experiment implied the direct measurement of the velocity of the synchrotron radiation pulse by dividing the section length $L = 7.2$ m of the output channel to the output sapphire window by the pulse passage time τ. This time can be measured by the oscilloscope using the synchronization signal and taking into account its calculated phase shift with respect to the time instant of passage of the electron bunch by the window of the synchrotron radiation-output channel.

EXPERIMENTAL RESULTS

In the *first version*, the time shift of the optical pulses was measured when the glass plate was introduced into the synchrotron radiation beam. With an accuracy of about 0.05 ns, no shift was detected (see Fig. 3 and Fig. 4).

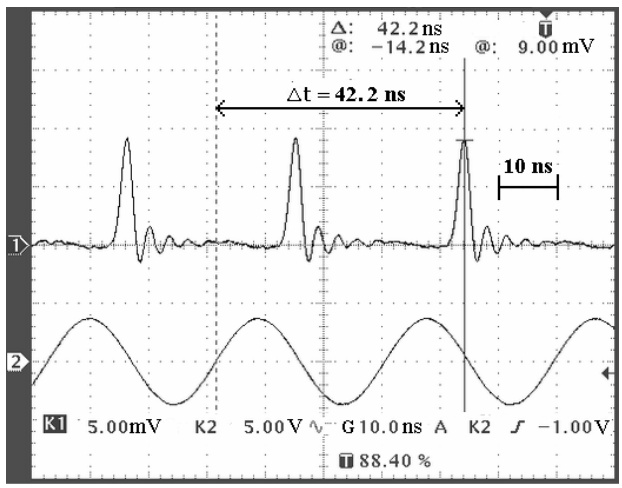

Figure 3: The optical signal (channel 1) for the light propagating through the radiation output channel in vacuum with open aperture at the entrance and the synchronization signal (channel 2).

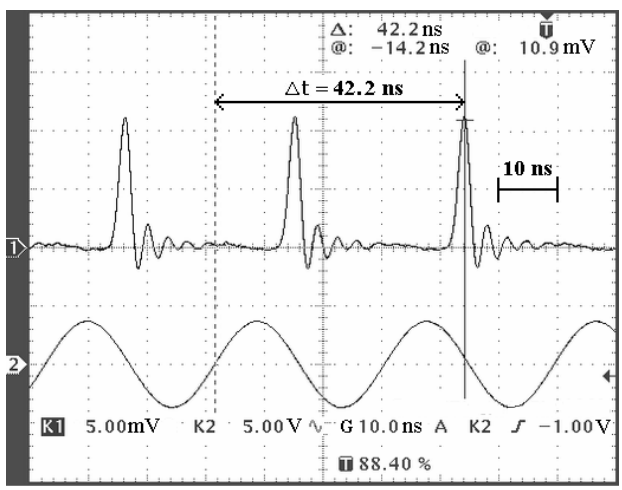

Figure 4: The optical signal (channel 1) for the light propagating through the radiation output channel in vacuum with the aperture at the entrance blocked by the glass plate and the synchronization signal (channel 2).

The delay related to the refraction of light in the thin plate is negligibly small. As can be seen, the optical signal in shape and duration is very close to the ideal expected pattern, which is a periodic sequence of Gaussian pulses with FWHM of 2.35 ns. The only difference is the ringing on the trailing edge of the photocurrent pulses due to oscillatory processes in the circuits of the photodetector. However, this distortion of the pulse shape does not prevent the solution of the formulated problem.

Note that amplitude of the optical signal in Fig. 3 is slightly smaller than that in Fig. 4, which is explained by insignificant vignetting of the transmitted light beam by side edge of the aperture with no glass.

In the *second version* of the experiment, the velocity of the synchrotron radiation pulse was measured directly Details of the calculation and measurement of τ were reported in [6].

Oscillogram of Fig. 5 shows the measured delay of the detected optical pulse with respect to the moment of passing the center of the accelerating gap by the electron bunch.

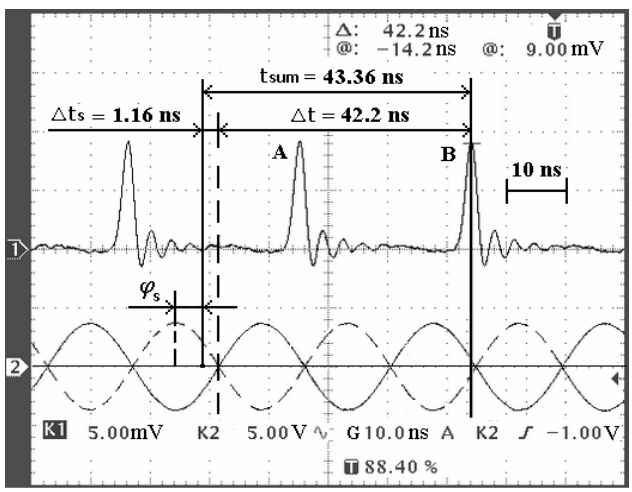

Figure 5: Measuring the light pulse delay in the photodetector with respect to phase of the synchronized particle in the accelerating gap of the cavity.

The solid and dashed lines in channel 2 show the output voltage of the pickup loop and voltage of the cavity gap, respectively. Synchronized particles of the bunch pass through the accelerating gap with a certain phase φ_S, counted from maximum of the falling part of the accelerating voltage. The value of φ_S depends on amplitude of the HF voltage on the cavity and electron energy loss per round trip. In [6], this value was calculated to be $\varphi_S = 75.61^\circ$, and, with allowance for the period of the HF oscillations (at 34.53 MHz) equal to 28.96 ns, the corresponding time interval was found to be $\Delta t_s = 1.16$ ns. As is seen from Fig. 5, time delay of the optical pulse in the photodetector with respect to phase of a synchronized particle in the accelerating gap of the cavity t_{sum} is obtained by summing up the calculated quantity Δt_s with the value of the time interval $\Delta t = 42.2$ ns measured with the oscilloscope. We analyzed here the light pulse B emitted by the electron bunch entering the accelerating gap of the cavity with the phase φ_S. The light pulse A is emitted by the electron bunch that enters the gap one round trip earlier. With allowance for geometry of the stationary orbit of the storage ring Siberia-1 (Fig. 1), the time of flight, by the electron bunch, of the distance from the center of the accelerating gap to the point of emission was found to be $t_e = 18.7$ ns (the electron bunch velocity was taken equal to standard speed of light in vacuum).

To calculate velocity of the light emitted by the electron bunch we subtracted from t_{sum} the time t_e and the times of propagation of light through the output sapphire window, 2.4 cm thick, the air gap, 10 cm in length, and glass of the collecting lens, 1.4 cm thick, obtained using refractive indices of the appropriate media (total time 0.55 ns). Thus we have found the time of propagation of the distance $L = 7.2$ m by the light pulse: $\tau = 24.1$ ns. The delay of the electric signal formation in the photodiode was here neglected. As a result, by dividing L by τ, the velocity of the synchrotron radiation pulse was found to be 2.99×10^{10} cm/s, which was only ~0.3 % lower than the standard speed of light in a vacuum.

The standard statistical error of the measurement was about 0.2 %. The systematic error was determined by the accuracy of the measurement of the electron and synchrotron radiation pathlengths and did not exceed 0.5 %.

CONCLUSIONS

In this work, the speed of the light emitted by the relativistic source is directly measured. The results are inconsistent with the Ritz ballistic hypothesis, which assumes the Galilean summation of the speed of light and the velocity of the source. It is shown that introduction of a glass plate into the light beam emitted by the ultrarelativistic source does not change the speed of light to within fractions of a percent, whereas according to the Ritz hypothesis, this speed would be halved after passing through the plate at rest. In addition, the direct measurement of the synchrotron radiation pulse velocity in a vacuum yielded a value in agreement with the standard speed of light with an accuracy of 0.3 %.

REFERENCES

[1] A. Einstein, Ann. Phys. (Berlin, Ger.) **17**, 891 (1905).
[2] G.B. Malykin, Opt. Spectrosc. **107**, 592 (2009); Opt. Spectrosc. **109**, 951 (2010).
[3] W. Ritz, Ann. Chim. Phys., Ser. 8 **13**, 145 (1908).
[4] W. Kantor, J. Opt. Soc. Am. **52**, 978 (1962).
[5] O.M. Duplishcheva and I.I. Shpirka, Results of M.I. Duplishchev Experimental Studies of Regularities of Light Emission and Propagation Phenomena in Space (ART-PRESS, Dnepropetrovsk, 2008) [in Russian].
[6] E.B. Aleksandrov, P.A. Aleksandrov, V.S. Zapasski et al., Usp. Fiz. Nauk **181** (12) (2011).

STUDY OF TWO CAVITIES ACCELERATING MODULE AT SR SOURCE SIBERIA-2

V. Korchuganov, V. Moiseev, A. Smygacheva, A. Vernov, RNC KI, Moscow, Russia.

Abstract

SR source Siberia-2 RF system includes an accelerating module consisting of two 181 MHz cavities powered by one amplifier. Some problem occurred now is the accelerating voltage instability under high beam currents conditions. The phase shift between the voltages at cavities causes the asymmetry in beam loading and detuning of cavities. To study the performances of accelerating module, the analytical description has been developed. The whole system can be characterized by seven parameters. These base parameters give the relations of voltages and currents in system. Measurements determine the real values of the base parameters. Set of non linear equations received can be reduced to the voltages and currents in system as the functions of beam current and energy. The results can be applied to injection and ramping in Siberia-2.

ANALYTICAL DESCRIPTION

Accelerating Cavity with Beam

Accelerating cavity with beam can be described by four parameters (see Fig. 1): cavity impedance Z, reflectivity Γ at any cross section of feeder and two coefficients k and m for the same cross section.

.

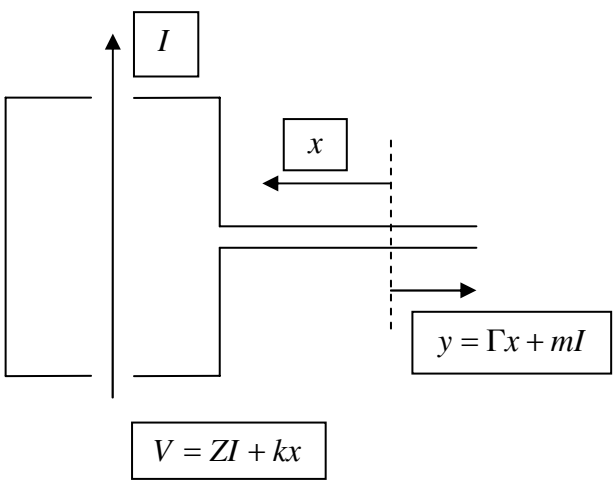

Figure 1: Accelerating cavity with beam (I - the main harmonic of the beam current, V - complex amplitude of accelerating voltage, x and y - complex amplitudes of normalized waves in feeder).

The energy conservation requirements for any beam current harmonic I and any wave x from generator give the relations:

$$4|m| = k,$$
$$-2|m|^2 = \frac{|Z|^2}{R_{sh}} + \mathrm{Re}\,Z, \quad (1)$$
$$-2m^*\Gamma = k\left(\frac{Z^*}{R_{sh}} + \frac{1}{2}\right),$$

where R_{sh} is the shunt impedance of the cavity.

For two fields exited in cavity by beam and by generator, Lorenzt lemma gives additional to (1) relation:

$$-4m = k. \quad (2)$$

The expression for impedance Z can bee written in conventional form:

$$Z = -\frac{R_{sh}}{1+g+i\eta}, \quad (3)$$

where g is the cavity coupling with feeder and η is the cavity detuning. The system (1), (2) and (3) can be reduced to expressions for coefficients k and m:

$$k = \frac{k_0}{|k_0|}\sqrt{8R_{sh}g}\,\frac{1}{1+g+i\eta},$$
$$m = \frac{m_0}{|m_0|}\sqrt{\frac{R_{sh}g}{2}}\,\frac{1}{1+g+i\eta}.$$

The phase factors

$$\frac{k_0}{|k_0|} = -\frac{m_0}{|m_0|}$$

depend on position of equivalent representation cross section in feeder.

Simpler cavity description (see Fig. 2) can be reached by using the beam loading parameter

$$M = \frac{IR_{sh}}{V}. \quad (4)$$

It can be seen that real part of this parameter

$$\mathrm{Re}\,M = \frac{\frac{\mathrm{Re}\,IV^*}{2}}{\frac{|V|^2}{2R_{sh}}} = \frac{P_{beam}}{P_{walls}}$$

and imaginary part $\mathrm{Im}\,M$ presents the cavity detuning by beam. At Fig. 2,

$$k_b = \frac{k_0}{|k_0|}\frac{1}{1+g+i\eta+M}\sqrt{8R_{sh}g}\ ,$$
$$\Gamma_b = -\frac{k_0}{|k_0|}\frac{m_0}{|m_0|}\frac{g-1-i\eta-M}{1+g+i\eta+M} \qquad (5)$$

and feeder current

$$I_f = V\sqrt{\frac{1}{4Z_0R_{sh}g}}\frac{|k_0|}{k_0}(1+g+i\eta+M)\left(1+\frac{k_0}{|k_0|}\frac{m_0}{|m_0|}\frac{g-1-i\eta-M}{1+g+i\eta+M}\right).$$

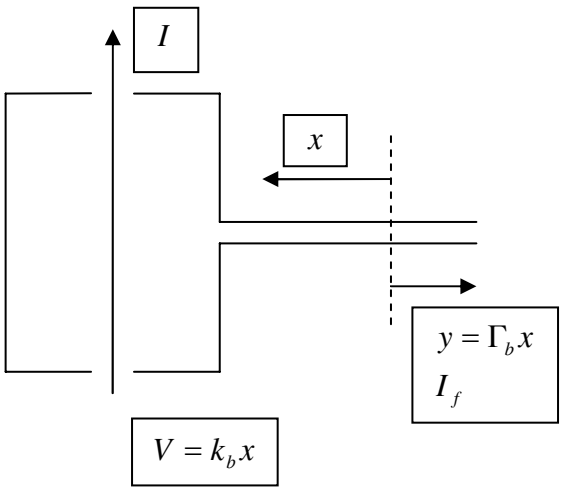

Figure 2: Accelerating cavity with beam.

To control the total cavity detuning by tuner (η) and by beam ($\mathrm{Im}\,M$), the phase Ψ' of accelerating voltage V to feeder current I_f is used. For feeder cross section with $\frac{k_0}{|k_0|} = e^{i\xi_0}$, the relation between accelerating voltage and feeder current is given by

$$I_f = V\sqrt{\frac{1}{Z_0R_{sh}g}}\cos\xi_o(1+\mathrm{Re}\,M)(1-itg\Psi'). \qquad (6)$$

Two Cavities Accelerating Module

Two cavities accelerating module consists of two cavities powered by one generator (see Fig. 3). Rectangular waveguide from generator is splitting on two coaxial feeders. Cavities are spaced along the beam orbit at RF wave length. Cavities differ by input power loops orientations – the loop in cavity number 2 is turned opposite the loop orientation in cavity 1. This difference is compensated in module construction by length of coaxial feeders. The feeder to cavity number 1 is half RF wave length longer then the feeder to the cavity 2.

For analytical system description, the formalism of normalized waves and scattering matrix can be used. At Fig. 3, the coaxial feeder cross sections 2 and 4 correspond to arrangements of loops for feeder current measurements. The cross section 3 is symmetrical to cross section 2 with respect to the rectangular waveguide. As it was mentioned above, the section 4 must be distant from section 3 half RF wave length to compensate the different input power loops orientation in cavities.

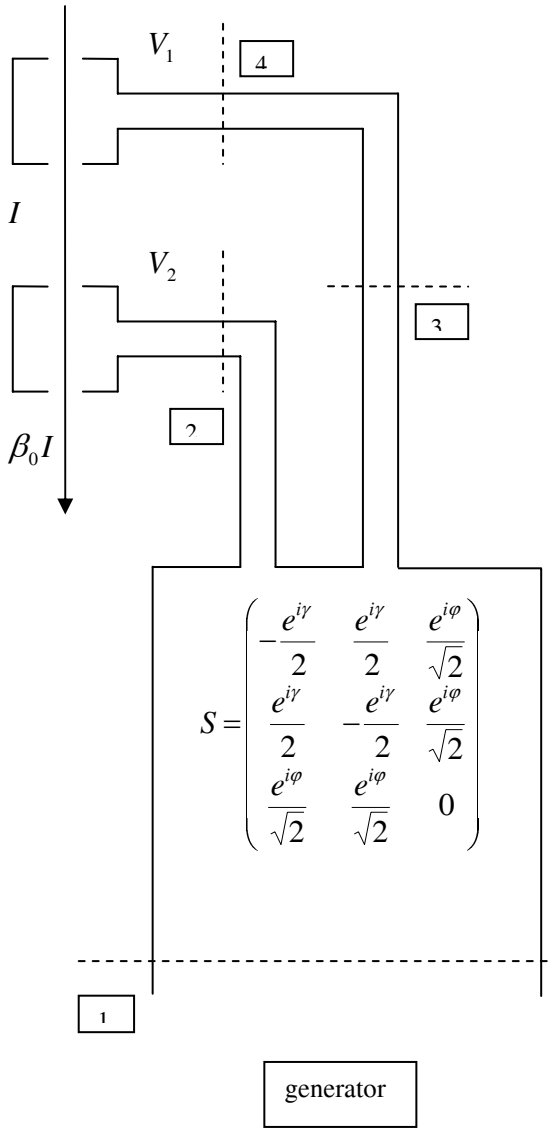

Figure 3: Two cavities accelerating module (I and $\beta_0 I$ - the main harmonic of beam current at cavities).

The cross sections 1, 2 and 3 bound the part of system that can be represented as symmetrical six-pole with scattering matrix S (see Fig. 3). The crucial parameter of two cavities module concerned is the phase factor $e^{i\gamma}$.

In system including two cavities, all expressions for one cavity must be written with index. So, the expression (6) must by written as

$$I_{f1} = V_1\sqrt{\frac{1}{Z_0R_{sh1}g_1}}\cos\xi_{o1}(1+\mathrm{Re}\,M_1)(1-itg\Psi_1'),$$

$$I_{f2} = -V_2\sqrt{\frac{1}{Z_0 R_{sh2} g_2}}\cos\xi_{o2}\left(1+\mathrm{Re}M_2\right)\left(1-itg\Psi_2'\right).$$

These expressions give the feeder currents in cross sections 4 and 2 respectively.

Within the frame of the scattering matrix formalism, the set of equations can be received for the normalized waves in the two cavities module. This set gives the ratio of the accelerating voltage complex amplitudes V_1 and V_2 at cavities:

$$\frac{V_1}{V_2} = \frac{\sqrt{R_{sh1}g_1}}{\sqrt{R_{sh2}g_2}}\cdot\frac{g_2\dfrac{\cos\frac{\gamma}{2}}{\cos\xi_{02}} - i\left(1+\mathrm{Re}M_2\right)\left(1-i\tan\Psi_2'\right)\sin\left(\xi_{02}+\frac{\gamma}{2}\right)}{g_1\dfrac{\cos\left(\frac{\gamma}{2}-h\right)}{\cos\xi_{01}} - i\left(1+\mathrm{Re}M_1\right)\left(1-i\tan\Psi_1'\right)\sin\left(\xi_{01}+\frac{\gamma}{2}-h\right)}.$$

The right side of the equality above contains the construction errors ξ_{01} and ξ_{02} of the feeder current measuring loops positions and the error h of the coaxial feeder length from section 3 to section 4 (see Fig. 3). If these errors can be assumed to be negligible the role of the dominant module parameter γ is evident. For the case $\cos(\gamma/2)=0$, the ratio of voltages at cavities is changing with beam loading and cavities detuning but the ratio of feeder currents remains constant. For the other case $\sin(\gamma/2)=0$, the ratio of the voltages at cavities remains constant but the ratio of feeder currents is changing.

MEASUREMENTS AND CALCULATIONS

Experimental Study of Module Parameters

The two cavities module can be characterized definitely by seven parameters: cavities shunt impedances R_{shi} and couplings g_i ($i=1,2$), construction errors ξ_{0i}, h and the dominant parameter of system γ. These parameters are evaluated from experimental functions without the beam

$$I_{f1} = V_1\sqrt{\frac{1}{Z_0 R_{sh1} g_1}}\cos\xi_{o1}\left(1-itg\Psi_1'\right),$$

$$I_{f2} = -V_2\sqrt{\frac{1}{Z_0 R_{sh2} g_2}}\cos\xi_{o2}\left(1-itg\Psi_2'\right),$$

$$\frac{V_1}{V_2} = \frac{\sqrt{R_{sh1}g_1}}{\sqrt{R_{sh2}g_2}}\cdot\frac{g_2\dfrac{\cos\frac{\gamma}{2}}{\cos\xi_{02}} - i\left(1-i\tan\Psi_2'\right)\sin\left(\xi_{02}+\frac{\gamma}{2}\right)}{g_1\dfrac{\cos\left(\frac{\gamma}{2}-h\right)}{\cos\xi_{01}} - i\left(1-i\tan\Psi_1'\right)\sin\left(\xi_{01}+\frac{\gamma}{2}-h\right)}.$$

The Accelerating Voltage Stabilized Mode

In this mode, the total accelerating voltage of two cavities module is stabilized to any desirable value V_o in phase and amplitude:

$$V_1 + \beta_0^* V_2 = V_0.$$

To calculate complex amplitudes V_1 and V_2, this linear equality can be considered as the first equation. As the second equation, the essential non linear equality for ratio V_1/V_2 in the two cavities module is used (see above). For example, the typical results of calculations are presented in Table1. It is seen that the ratio of voltages at cavities is changing with the beam storage.

Table 1: Injection at Siberia-2 (total voltage at two cavities module 200 kV, $\Psi_1=\Psi_2=-78^0$)

I_b, A	$\lvert V_1\rvert$, kV	$\lvert V_2\rvert$, kV	$\arg(V_1/\beta_0^* V_2)$
0.00	87	114	4.74^0
0.02	98	102	4.53^0
0.04	108	93	4.35^0
0.06	116	85	4.18^0
0.08	123	78	4.05^0
0.10	129	71	3.93^0
0.012	135	66	3.84^0
0.014	140	60	3.76^0

To compensate the disproportion of voltages at cavities, the different detuning of cavities is introduced (Tab. 2).

Table 2: Injection at Siberia-2 (total voltage at two cavities module 200 kV, $\Psi_1=-78^0$, $\Psi_2=-75^0$)

I_b, A	$\lvert V_1\rvert$, kV	$\lvert V_2\rvert$, kV	$\arg(V_1/\beta_0^* V_2)$
0.00	77	123	2.52^0
0.02	83	117	2.30^0
0.04	88	112	2.18^0
0.06	92	108	2.08^0
0.08	96	104	1.98^0
0.10	99	101	1.90^0
0.012	102	98	1.82^0
0.014	104	96	1.76^0

CONCLUSIONS

- Analytical description developed can be used efficiently for cavities based complex accelerating RF systems.
- At Siberia-2, the two cavities module is characterized definitely by seven parameters. These parameters are evaluated experimentally.
- Analytical description and calculations reveal features of two cavities module modes.
- Two cavities module is exploited successfully at Sberia-2.

STANDING WAVE RF DEFLECTORS WITH REDUCED ABERRATIONS *

V. Paramonov†, L. Kravchuk, P. Orlov, INR RAS, Moscow, Russia
K. Floettmann, DESY, Hamburg, Germany

Abstract

Deflecting structures are now widely used for bunch phase space manipulations either to rotate a bunch for diagnostics purposes or in emittance exchange concepts. Even though the field of the synchronous harmonic is aberration free, the higher spatial harmonics provide nonlinear additions to the field distribution, leading to emittance growth during phase space manipulation. For short deflectors Standing Wave (SW) operation is more efficient. The criterion to estimate the field quality is developed and applied in order to minimize aberrations in the total deflecting field. The solution for dispersion correction together with the optimization of the end cells is described too.

INTRODUCTION

Deflecting Structures (DS), originally introduced for bunch deflection and particle separation [1], are now mainly used to rotate a bunch either for short bunch longitudinal diagnostics, [2], or in emittance exchange optics or to increase the luminosity. For deflection the bunch center crosses the DS at the maximal deflecting field, i.e. $\phi = 0$, while for bunch rotation $\phi = 90^o$ is used.

Modern DS applications are transformations of particle distributions in six-dimensional phase space. A tool for a transformation should provide as minimal as possible distortions of the original distribution.

The framework for the treatment of deflecting fields has been laid in the 60's by introducing the basis of hybrid HE and HM waves, [4], [3], and some results and conclusions, with certain assumptions and approximations, have been derived.

Even the synchronous harmonic of a deflecting field is inevitably nonlinear. The nonlinearity vanishes with $\beta \to 1$ and the aberration free, ideal case is reached for $\beta = 1$ only. But in the total DS field are always higher spatial harmonics which are by their nature nonlinear. The nonlinear terms lead to emittance growth during phase space manipulations, which can become important for precise measurements of very low emittance beams, or in case of multiple DS crossing.

FIELD DISTRIBUTIONS ANALYSIS

A recipe for estimates of field aberrations can be based on the general properties of periodicity and linearity, [5].

In any periodical structure the distribution of each field component $E_j(r,z)$ in the beam aperture can be represented in the complex form

$$E_j(r,z) = \widehat{E_j(r,z)}e^{i\psi_j(z)} = \sum_n^n a_{jn}(r)e^{\frac{-i(\Theta_0+2n\pi)z}{d}}, \quad (1)$$

where $\widehat{E_j(r,z)}$ and $\psi_j(z)$ are the amplitude and phase distributions, $d = \frac{\Theta_0\beta\lambda}{2\pi}$ is the structure period, $a_{jn}(r)$ is the transverse distribution of the n-th spatial harmonics and Θ_0 is the phase advance. Spatial harmonics are essential at the aperture radius $r = a$ while higher harmonics attenuate toward the axis as

$$a_{jn}(0) \sim a_{jn}(a) \cdot exp(-\frac{4\pi^2 n}{\beta\Theta_0} \cdot \frac{a}{\lambda}), \quad |n| \gg 1, \quad (2)$$

where λ is the operating wave length. To estimate the harmonics in detail and 'in total', we use the parameters $\delta\psi_j(z)$ and Ψ_j at the axis $0 \le z \le d, r = 0$, [5]

$$\delta\psi_j(z) = \psi_j(z) + \frac{\Theta_0 z}{d}, \quad \Psi_j = max(|\delta\psi_j(z)|). \quad (3)$$

The total force on a charged particle - the Lorenz force

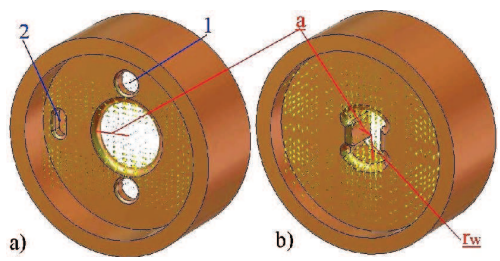

Figure 1: Structures with the minimized E_d aberrations, the optimized DLW structure (a) with holes for deflecting plane stabilization (1) and slots for dispersion correction (2) and the decoupled structure (b).

$\vec{F}^L$ - can be split in Cartesian coordinates into the longitudinal eE_z and the transverse eE_d components, assuming deflection in x direction,

$$\vec{F}^L_{z,x} = eE_z\vec{z}_0 + eE_d\vec{x}_0, E_d = E_x - \beta Z_0 H_y, Z_0 = \sqrt{\frac{\mu_0}{\epsilon_0}}. \quad (4)$$

Parameter Ψ_j can be used to estimate the level of harmonics (aberrations) both in the longitudinal eE_z, Ψ_z and in the transverse eE_d, Ψ_d force component.

The structures, obtained by optimizing aberrations, are shown in Fig. 1. Besides the well-known Disk Loaded Waveguide (DLW), Fig. 1a, a decoupled deflecting structure has been optimized. This structure follows the design idea of separated functions, see [6] for details.

* Work supported in part by RBFR N12-02-00654-a
† paramono@inr.ru

ABERRATION REDUCTION FOR DLW

The attenuation (2) works both for E_z and E_d at low values of Θ_0 in the Traveling Wave (TW) regime in any structure, even for small aperture radii, [5], [6]. For SW

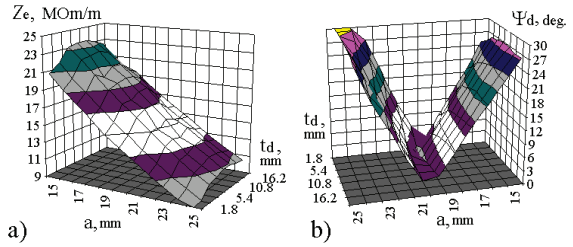

Figure 2: The surfaces $Z_e(a, t_d)$ (a) and $\Psi_d(a, t_d)$ (b) for the DLW structure, $\lambda = 10cm, \Theta_0 = 180^o$

.

operation, $\Theta_0 = 180^o, (= \pi)$, the attenuation is not effective and the field components have a higher aberration level as compared to the TW mode. The longitudinal force F_z^L is generated by a single field component E_z and an essential aberration reduction is not possible. For a precise transformation of the longitudinal distribution a TW mode is preferable.

The transverse component F_x^L is composed of two components, and the mutual phasing of E_x and H_y is crucial. For opposite phasing the synchronous harmonics components E_x^0 and $Z_0 H_y^0$ contribute in (4) together to the deflection, but the higher harmonics in E_x and H_y partially compensate, leading to an aberration reduction in E_d.

In Fig. 2 surfaces of $Z_e(a, t_d)$ and $\Psi_d(a, t_d)$ for the DLW structure are shown, where t_d is the disk thickness and Z_e is the effective shunt impedance. It can be seen that for every value of t_d a value of a exists which realizes $\Psi_{d(min)} \sim 2^o$, corresponding to $a_{dn}(0) \sim 10^{-2}$ in contrast to $a_{d1}(0) \sim 0.4, a_{d2}(0) \sim 0.1$ for other DLW cases. The optimum of $\Psi_{d(min)}$ a_{opt} slightly rises with increasing t_d: $a_{opt} = 19.41mm$ for $t_d = 5.4mm$ and $a_{opt} = 20.54mm$ for $t_d = 10.8mm$. The DLW RF efficiency, Z_e, decreases with increasing a and has a shallow maximum at $t_d \sim 9.8mm$, Fig. 2a. As compromise for a SW DLW deflector with minimized E_d aberrations we chose $t_d = 8.1mm, a = 20.17mm$. Thus for classical DLW in SW mode the aberration reduction in the transverse F_x^L component can be achieved by a selection of the aperture radius, but on the expense of a moderate shunt impedance of $Z_e \sim 17 \frac{MOm}{m}$.

DISPERSION CURVE CORRECTION

The opposite E_x and H_y phasing defines a negative dispersion of the DS. For an effective aberration reduction the amplitudes should be balanced, $|E_x^0| \sim |Z_0 H_y^0|$. But this balance can be obtained only in the vicinity of the inversion point with $\beta_g = 0, \Theta_0 < 180^o$, [5]. Cavities with minimized aberrations have therefore a narrowed operating passband with not large frequency separation near the operating mode.

To improve the frequency separation, we apply the resonant method, proposed for deflecting plane stabilization in DLWs, [7]. One resonant slot (2 in Fig. 1a) with eigenfrequency f_s much higher than the operating frequency f_0 is introduced into the disk to interact with the modes of the operating deflection direction. The intensity of the slot excitation depends on both f_s and Θ of the cavity mode. The mode frequency shift, caused by the slots, is $\delta f \sim \frac{(sin\frac{\Theta_0}{2})^2}{f_s^2 - f_0^2}$, resulting in a better frequency separation near the operating mode $\Theta_0 = \pi$. To provide a larger δf with smaller slot excitation and avoid that $E_z \neq 0$ at the deflector axis, slots in adjacent disks are rotated by 180^o. For the optimized DLW the application of the slots improves the frequency separation by 1.4 times the number of periods in the cavity $N = (4 \div 8)$.

The same approach can be applied for the correction of the dispersion curve distortions in low Θ_0, low β_g TW DLWs, [5], operating with minimal E_z and E_d aberration

END CELLS

The input/output end cells with the connected beampipes deteriorate the periodicity of the structures and cause a transverse kick of the bunch. The field penetrating into the beampipe decays away from the cavity but provides an initial transverse kick. To reduce this part of the deflection and thus simultaneously reduce the total kick the beampipe radius should be as small as reasonably possible. The end cells together with the beampipe can be tuned to the operating frequency as separate units by adjusting the cell radius r_{ce} while keeping the boundary condition $E_\tau = 0$ in the middle of the iris connecting to the periodic structure. This ensures that the frequency and the field distribution are independent of the number of regular cells.

By changing the length L_e of the end cell the distribu-

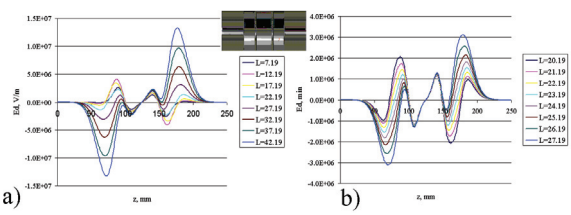

Figure 3: Distribution of E_d at $\phi = 90^o$ for various end cell length L_e in a broad range (a) and tuned around for $Int_{1t}(z) = 0$ (b).

tion of E_d can be changed in a wide range, Fig. 3. The transverse field can be reduced but does not disappear completely. The transverse kick is however proportional to the first field integral $Int_{1t}(z)$

$$Int_{1t}(z) = \int_{-\infty}^{z} E_d(z', \phi = 90^o) dz'. \qquad (5)$$

The condition $Int_{1t}(z) = 0$ results in a reduced variation of $E_d, \phi = 90^o$ in the end cell, comparable to the residual $E_d, \phi = 90^o$ variation in the regular cells, see Fig. 3, and a minimized kick in the end cells.

DECOUPLED STRUCTURE

The designer of a DLW structure has effectively only one degree of freedom - the aperture radius which defines simultaneously both the $E_x and H_y$ amplitudes and balance. Thus a high RF efficiency with minimized aberrations cannot be achieved simultaneously. The possibility to control both the E_x and H_y phasing and balance demonstrated for a TE - type deflector [6] allows to design an effective DS with a strong transverse electric field, a positive dispersion due to the same E_x and H_y phasing and decoupled control of RF efficiency and coupling. As shown in [6], the E_x and H_y amplitudes, phasing and balance depend on the combination of $a - r_w$, see Fig. 1b.

Choosing the aperture radius a as small as possible a high shunt impedance Z_e is realized due to a strong E_x component. Reducing the window radius r_w the difference in the phasing of E_x and H_y increases from the equal phasing as in the original design through the point with $H_y^0 = 0$ to the opposite phasing, where the compensation of aberrations becomes possible. Continuing to reduce the window radius the balance $|E_x^0| \sim |Z_0 H_y^0|$ with minimized E_d aberrations is obtained. During this transformation the shunt impedance Z_e reduces but still remains higher as compared to a DLW. The obtained field distribution is shown in Fig. 1b and there is indeed no reason to name the obtained structure TE - like. As a result we have a very flexible solution which allows to combine a high shunt impedance $Z_e > 30 \frac{MOm}{m}$ with minimized aberrations $\Psi_{d(min)} \sim 2^o$ and different $|E_x^0|, |Z_0 H_y^0|$ balance.

DEFLECTING CAVITIES

In Fig. 4 the field distributions for the same stored energy of different SW deflectors are shown: The optimized DLW, (Fig. 4a) with $\frac{Z_0 H_y^0}{E_x^0} = 0.8549, \Psi_d = 2.39^o$ and two options of decoupled structures with $\frac{Z_0 H_y^0}{E_x^0} = 0.7904, \Psi_d = 2.07^o$, Fig. 4b, and $\frac{Z_0 H_y^0}{E_x^0} = 1.0008, \Psi_d = 2.10^o$, Fig. 4c . Strongly reduced residual $E_d, \phi = 90^o$

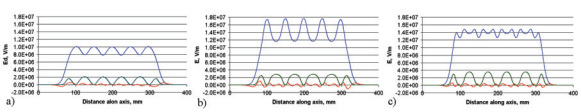

Figure 4: The field distributions along the deflector axis for the optimized DLW, (a) and two decoupled structures, (b) and (c). Blue - $E_d, \phi = 0^o$, red - $E_d, \phi = 90^o$, green - $E_z, \phi = 90^o$

oscillations inside the cavity together with a reduced input kick in the end cells can be seen. Because the quality factors for the deflectors are comparable, the decoupled structure provides a higher deflecting field. For the deflector length of $\sim 20cm$, meaning two regular cells, RF coupler cells and two end cells, the calculated total shunt impedances are $2.84MOm, 4.57MOm$ and $6.04MOm$, respectively.

The technical solutions for the SW deflectors are shown in Fig. 5

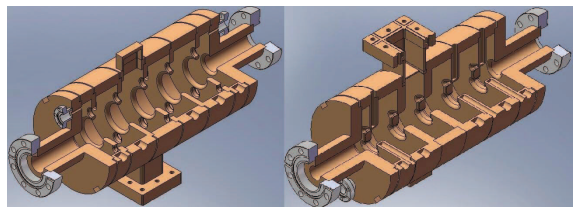

Figure 5: Deflectors with minimized E_d aberrations, the optimized DLW (left) and the decoupled structure (right).

SUMMARY

Different standing wave deflectors are considered for applications in bunch rotation with the aim to reduce distortions of the incoming particle distribution by minimizing aberrations in the effective force. For a SW operating mode aberration minimization in the longitudinal force component is not significant. For the transverse force component a strong reduction of the aberration is achieved by appropriate balancing of transverse field components. For the well-known DLW structure a reduction of aberrations is achievable at the expense of RF efficiency. A flexible solution - a decoupled deflecting structure - is described to combine high RF efficiency with minimized aberrations for different field distributions. A publication containing more detailed descriptions of field distributions and beam dynamics results including numerical simulations is in preparation.

REFERENCES

[1] T.H. Fieguth, R.A. Gearhart, RF Separators and Separated Beams at SLAC, Proc. 1975 PAC, p. 1533

[2] R. Akre et. al., RF Deflecting Structure for Bunch Length and Phase Space Diagnostic. Proc. 2001 PAC, p. 2353

[3] Y. Garault, CERN 64-43, CERN, 1964

[4] H. Hahn, Deflecting Mode in Circular Iris-Loaded Waveguides, Rev. Sci. Inst., v. 34, n. 10, p. 1094, 1963

[5] V. Paramonov, RF field distributions quality in deflecting structures. (to be published).

[6] V. Paramonov, L. Kravchuk, K. Floettmann, RF Parameters of a TE-type Deflecting Structure for the S-band frequency range, Proc. Linac 2012, 9-14 Sept. 2012, Tel-Aviv

[7] V. Paramonov, L. Kravchuk, The Resonant Method of Deflection Plane Stabilization. Proc. Linac 2010, p. 434, 2011

INVERSE COMPTON SOURCES ON THE BASIS OF ELECTRON ACCELERATORS WITH BEAM ENERGY RECOVERY

V.G.Kurakin, P.V.Kurakin, Lebedev Physical Institute, Moscow, Russia

Abstract

In inverse Compton Source, photons in Roentgen range originate from visible light laser photons scattered back on electrons with the energy of dozens MeV. Several schemes are suggested in the paper, beam energy recovery conception being the common idea of all of them. The first one is based on synchrotron with flat part of guiding magnetic field. Being accelerated, electron bunch interacts with photon bunch of free electron laser mounted on straight paths of the accelerator, then is decelerated during falling down period of magnetic field cycle, and extracted at low energy from synchrotron to absorb in beam dump. This measure decreases background that originates from bremsstrahlung of lost electrons inherent to classical schema with linear accelerator and storage ring. Two other schemes use superconducting linac that produces relativistic electron bunches which energy is recovered after use, free electron laser (FEL) driven by bunches from linac being used to produce photons bunches for source. In one scheme the same electron bunches are use to drive FEL and inverse Compton Source, while in the other one beam splitting technique is suggested. It is based on beam energy modulation with subsequent separation of successive bunches. The expected self excitation inverse Compton sources parameters are estimated followed by critical issues discussion for all schemes suggested.

INTRODUCTION

They say that back Compton scattering takes place when part of electromagnetic radiation is reflected backward by relativistic electron moving in the direction opposite to electromagnetic wave flow. In spite of low cross section of this process the devices based of this phenomenon find practical applications due to narrow spectrum of the radiation. The maximum energy of back scattered photons scales as square of electron energy thus allowing the radiation in Roentgen wave range obtaining scattering visible light on the electron bunch with the energy of several dozens of MeV. The availability of power lasers as well as charged bunch formation technique that came from accelerator based technique makes it possible Compton sources developing with intensities quite sufficient for applications.

Classical scheme of the light source based on the back Compton scattering represents optical cavity and electron storage ring arranged in such a way that these have an interaction point [1], one turn time circulations of electron bunch in storage ring and photon bunch in the cavity being synchronized to cross this point at the same moment. This arrangement is complemented by electron linac with injection system and a laser with appropriate cavity excitation system. The project based on this scheme had already realized successfully and might serve as prove of principle. It seems quite natural in further study and the development of such Roentgen source to move from oscillator scheme to self oscillator, and one of the main elements of existing equipment namely electron accelerator might be a basis for similar extension.

In this paper, we discuss the possibility to develop back Compton scattering source on the basis of free electron laser (FEL) and the energy recovery accelerator that drives this FEL. Three schemes are studied, one of these being built on the basis of electron synchrotron while two others on the basis of superconducting rf linac. In these schemes, electron bunches from an accelerator are used to drive FEL and to be a target for photons generated in the FEL. The critical issues of all schemes as well their advantages and shortcomings are discussed.

THE MAIN FEATURES OF FEL AND BACK COMPTON SCATERING

Fig.1 illustrates schematically back Compton scattering process. There is an incident electromagnetic wave of frequency ω with the energy density U_{ins} and relativistic electron with relative energy γ moving towards electromagnetic wave.

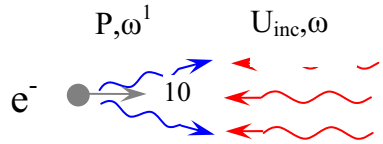

Fig.1 Back Compton scattering

The following formulae take place

$$\omega' \cong 4\omega\gamma^2,\ P \cong \frac{4}{3}\sigma_T c\gamma^2 U_{inc}. \qquad (1)$$

Here P is scattered wave power calculated per one electron, ω' is the frequency of scattered wave, c is light velocity and σ_T is so called Thomson cross section of an electron:

$$\sigma_T = \frac{8\pi}{3}\left(\frac{e^2}{m_e c^2}\right)^2 \approx 6{,}65\times10^{-25}\,см^2, \qquad (2)$$

where e, m are the electron charge and its mass.

It follows from the above formulae that inferior limit of the total number of scattered photons might be represented in the form

$$N \cong \frac{\sigma_T}{3\sigma_{ph}} N_{ph} N_e, \qquad (3)$$

where N , N_{ph} and N_e are number of scattered photons, number of photons in incident light bunch and number of electrons in electron bunch that scatters incident light bunch. It is assumed all photons in scattered bunch to have the same frequency defined by formula (1) that is quite justified for estimations. It is also assumed that target electrons covered completely by incident photon bunch.

Here we remind briefly principle of free electron laser. Schematically its arrangement is shown on fig.2.

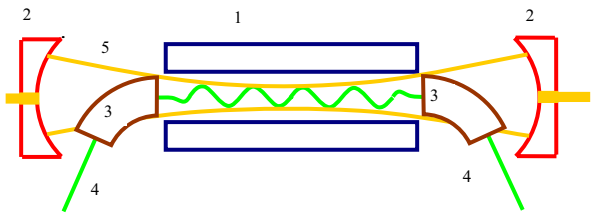

Fig.2. FEL layout. 1 – undulator, 2 – mirror, 3 – magnet, 4 – electron beam, 5 – optical mode envelope, 6 – laser radiation

Electron beam with the help of bending magnet is injected on undulator axis. Cavity optical mode interacts with moving electrons in undulator area. One path gain of electromagnetic wave might estimated from formula

$$G = 4\sqrt{2}\pi N \lambda_w^{1/2} \lambda_s^{3/2} \frac{K^2}{(1+K^2)^{3/2}} \frac{i}{si_A} \left(\frac{\Delta\omega_s}{\omega_s} \right)_t^{-2} \quad (4)$$

Here λ_w - undulator period, λ_s - generated radiation wavelength

$$\lambda_s = \frac{\lambda_w}{2\gamma^2}(1+K^2) \quad (5)$$

$$K = eH_{W0}\lambda_w / 2\pi mc^2 \quad (6)$$

H_0 - the amplitude of periodic magnetic field on undulator axis. $\Delta\omega$ is line widening, soused by undulator finite length, finite length of the radiated electron bunch and non zero value of bunch longitudinal emittance (non zero energy spread). s is bunch cross section.

$$\left(\frac{\Delta\omega_s}{\omega_s} \right)_t^2 = \left(\frac{\Delta\omega_s}{\omega_s} \right)_h^2 + \left(\frac{\Delta\omega_s}{\omega_s} \right)_i^2 \quad (7)$$

$$i_A = mc^3 / e = 17\kappa A \quad (8)$$

$$\left(\frac{\Delta\omega_s}{\omega_s} \right)_t^2 = \left(\frac{1}{N} \right)^2 + \left(\frac{\lambda_s}{2l_e} \right)^2 \quad (9)$$

$$\frac{\Delta\omega}{\omega} = 2\frac{\Delta E}{E} \quad (10)$$

To move from oscillator to self oscillator scheme of Compton light source we suggest the arrangement shown schematically on fig.3.There is a traveling wave cavity with two active arms. One of these is in FEL active part area where the beam-optical mode interaction takes place providing FEL generation process. The second one serves to provide electron bunch-optical train collisions. Depending on electron beam propagation direction an optical cavity might be of different configuration. For the case of the electron beams moving in opposite direction in two cavity arms just shown on fig.3 light lines have intersection area. If electron bunches move in the same direction in both arms optical train represents a rectangular with successive reflection from mirrors in rectangular vertexes.

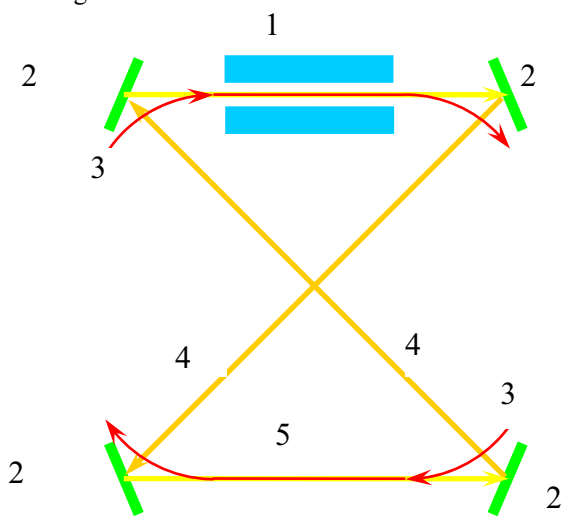

Fig.3. Possible electron beam-light optics configuration in self excitation back Compton scattering light source.
1 – FEL undulator, 2 – mirrors, 3 – electron beams trajectories, 4 – light path, 5 – electron bunch-light bunch collisions area.

BACK COMPTON SCATTERING LIGHT SOURCES

Fig. 4. represents a back Compton scattering light source on the basis of electron synchrotron. Injected from laser injector electron bunch is accelerated up to maximum energy. At this energy guiding magnetic field has a plateau that provides constant bunch energy during some time. FEL is formed by undulator installed in straight path and four mirrors cavity. All lengths are chosen to realize bunch-light collisions in opposite straight path. Electron bunch strikes moving in opposite direction light train generated in undulator area. Electron bunch decrease its energy during falling down phase of magnetic field cycle. The energy recovery phase is stopped by bunch extraction. Extracted at low energy bunch is directed to a dump.

Synchrotron scheme seems to have an advantage as compared to a linac-storage ring configuration. First, additional accelerator (that is used for electron bunch injection) is not required and second beam energy recovery process reduces background.

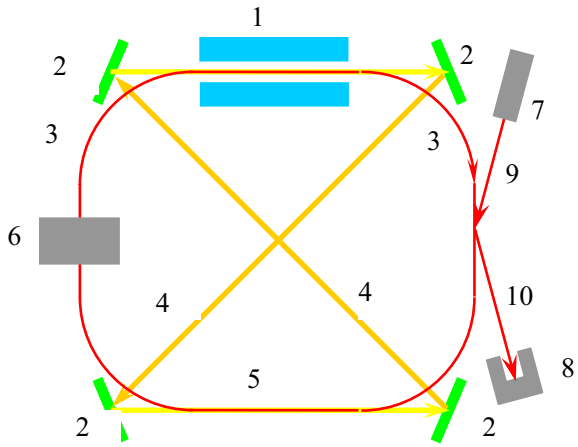

Fig.4. Back Compton light source on the synchrotron basis. 1 – FEL undulator, 2 – mirrors, 3 – electron beams trajectories, 4 – light path, 5 – electron bunch-light bunch collisions area, 6 – rf cavity, 7 – injector, 8 – dump, 9 – injected beam, 10 – extracted beam.

Shown on fig. 5 light source scheme is built on the basis of superconducting rf linac with beam energy recovery. Electron bunches from accelerator enter the active area of free electron laser consisting of undulator and optical cavity similar to that used in synchrotron based scheme. Leaving undulator area bunches are rotated by magnet arrangement (not shown) and second time traverse the cavity where interact with light trains. Then used bunches are directed to linac entrance in decelerating rf field phase thus transferring kinetic energy to rf field. Being decelerating down to injecting energy the bunches are deflected out of linac axis to be absorbed in beam dump.

A feature of the scheme represented on fig.6 consists of the use undisturbed beam in both active arms of four mirrors optical cavity. Opposite to the configurations just discussed the electron bunches move in the same direction in both arms while light trains in opposite directions. To have two beams from the same linac additional cavity is used at linac exit, the main linac and additional cavity being operated at frequencies bounded by condition

$$2n\omega_2 = (2n+1)\omega_1, \qquad (11)$$

where ω_1, ω_2 are the frequencies of linac and cavity respectively and n is the number of rf periods between two successive bunches. Thus successive bunches traverse the cavity in accelerating and decelerating phases that provides beam energy modulation and subsequent beam splitting with appropriate magnet arrangement. After interaction in optical cavity with light bunches two electron beams are combined by similar magnet arrangement to form again one line, while similar additional cavity on linac axis equalizes successive bunches energy. Then used beam enters the linac in decelerating phase and energy recovery process is ended by low energy beam absorption in beam dump.

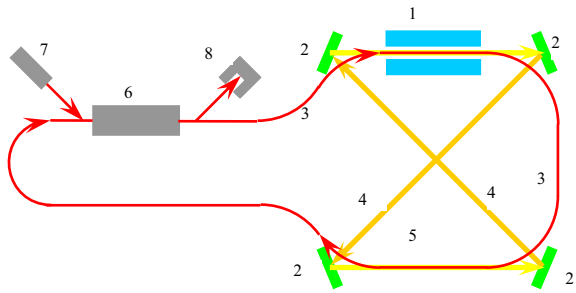

Fig.5. Back Compton light source on the basis of rf superconducting linac. 1 – FEL undulator, 2 – mirrors, 3 – electron beams trajectories, 4 – light path, 5 – electron bunch-light bunch collisions area, 6 – rf linac, 7 – injector, 8 – dump.

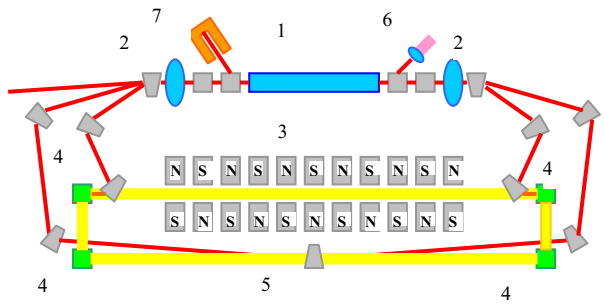

Fig.6. Back Compton light source on the basis of rf superconducting linac and beam splitting technique. 1- rf linac, 2 – rf cavity, 3- FEL undulator, 4 – traveling wave resonator mirror, 5 – beam-light interaction area, 6 – injector, 7 – beam dump.

To estimate the number of back scattered photons we assume bunch current to be 100 A ($N_e \cong 10^{10}$), bunch energy 100 MeV, bunch pulse duration 10 psec $\sigma_{ph} = 1mm^2$ and 1 percent of FEL efficiency. This corresponds to approximately 10^{18} photons in the light train moving in the cavity. According formula (3) this gives 10^5 Roentgen photons per one collision.

CONCLUSION

We have considered three schemes of Roentgen light sources based on free electron lasers, back Compton scattering and energy recovery technique. In spite of apparent complexity these schemes might be useful for small multi purposes facilities.

REFERENCES

[1] Z.Huang, R.D.Ruth. Phys. Rev. Letters, Volume 80, Number 5, 2 Feb. 1998. pp. 976-979.

HELICAL 1T×1CM PULSED INSERTION DEVICES FOR PRODUCTION OF INTENSE POLARIZED X- & GAMMA-RAYS

A.V. Smirnov, RadiaBeam Technologies Inc., Santa Monica, CA 90404, USA

Abstract

Two types of high-field, pulse undulators are revisited as non-coherent or partially coherent sources capable of undulator factor approaching unity at substantial gap-to-period ratios exceeding 0.4 not achievable with conventional technology. One type is a microwave guide, smooth-wall undulator powered by wake-fields extracted with CLIC-type scheme adapted for the two-beam undulator (TBU). Another novel ID is represented here by a bifilar transmission line energized by a high voltage, ~ns-pulse, solid-state generator. These two devices fit well future linear colliders based on high-gradient microwave linac technology and radiation facilities respectively.

INTRODUCTION

Development of electron–positron colliders requires a source of intense polarized positron beams. Polarized positrons can be produced from polarized γ-rays irradiating a thin target (a fraction of radiation length [1]). One way is using of SC helical undulator having at least hundred meters length, limited period (<1.2cm), sufficient gap (>4–5mm), and field magnitude (>0.7T). Existing helical undulator technology is not failure-free and viable enough as requires close to critical currents (for SC undulators), has too small gaps (~1mm) implying bypassing, very limited section length because of low vacuum conductivity, gas bremstrahlung and radiation-induced desorption. Normal-conducting, pulse-current option is limited by heat deposition and pulsed power supply. Unique Cornell design [2] employs sophisticated ferrofluid cooling system and operates at <30Hz rep rate (12μs pulse length), whereas a normal-conducting linear collider operates at higher rep rates (about 100Hz).

Another possibility is photon backscattering on energetic electrons. The polarization of backscattered gammas is determined entirely by the polarization of incident electromagnetic radiation and changes a little with scattering angle or gamma-photon energy. A terawatt laser produces a deflecting force equivalent to several tens of Tesla of undulating field. However, the interaction length is limited by diffraction to about a centimeter [3]. Substantial problems [4] are related to multistaging, jitter, sustainability of optical elements, synchronized timing, dramatic reduction of the polarized gamma-photons yield for off-axis electrons.

Somewhat similar problems are related to development of IDs for intense polarized synchrotron radiation sources, applied, e.g., for circular dichroism studies.

In this paper, two novel concepts of a helical undulator are proposed: a microwave undulator powered by a microsecond- range wakefield extractor (two-team undulator, TBU), and a pulse-line undulator (PLU) powered by a ns-pulse, high-voltage source.

MICROWAVE UNDULATOR AS A PULSED, POLARIZED RADIATION SOURCE

A microwave undulator is especially suitable for long radiators of spontaneous X- and γ-ray emission. Such a waveguide-based ID does not need tapering (unlike FEL), can have shorter period and much better active/physical length ratio due to shorter interruptions (if any) compared to any conventional magnetic undulator. One can also provide a larger gap that exceeds considerably the equivalent undulator period (or operating wavelength in an oversized, open mm-wave guide [5]). It may have side openings (using open type structure) or evanescent slots/holes for better pumping and insertion of wakefield BPMs. The microwave undulator is perfectly compatible with superimposed focusing/correcting elements (quadrupoles and sextupoles). For a normal-conducting linear collider active cooling of the waveguide undulator is not a challenging problem due to larger aperture and lower power deposition than pulsed electromagnetic undulator (for the same pulse rate). Fore example, the ferrofluid-cooled, 1mm aperture, 1m length undulator consumes about a half kW power at 30Hz pulse rate [2], which is comparable to that for the two-wave undulator considered here at higher rep rates and much larger $5.6\times5.6\text{mm}^2$ cross-section at about the same peak field. Bypassing can be eliminated due to enlarged aperture and enhanced vacuum conductivity, super-imposed focusing, reduced period, and absence of undulator fields in the idle mode. That also means that the undulator physical length can be reduced from ~790m [1] down to ~150m making the physical and active undulator lengths equal.

And finally a waveguide undulator to be more robust and easier in manufacturing as the smooth-wall square or elliptical pipe tolerances are determined only by minimal reflection and insertion losses (about 1 mill tolerance at 30GHz) and the bremstrahlung radiation is less dangerous for the waveguide unlike magnetic undulators subjected to quench and/or degradation of the insulation undergoing to enormously high mechanical stress at strong X-ray and gamma-radiation background (~100MRad dose) and extremely low (for SC ID) or elevated temperatures (NC ID). On the other hand, the waveguide bremstrahlung may seed high–order multipactor to be taken into account in the design (including external magnetic fields).

The microwave source framework is represented by decelerator sections extracting high power (~462MW at 30GHz, ~130ns in CLIC [6]) from the driving beam with inherently proper timing. The microwave power in a traveling wave undulator can be subsequently reused in corresponding high-power network to enhance overall efficiency. The accelerating module is replaced by counter-propagating traveling wave undulator module. One can distinguish in Figure 1 the following variants: (a) direct scheme with two decelerators feeding one undulator section (one decelerator per polarization—-horizontal or vertical); (b) one decelerator per one undulator section; and (c) continuous waveguide with partial power recuperation.

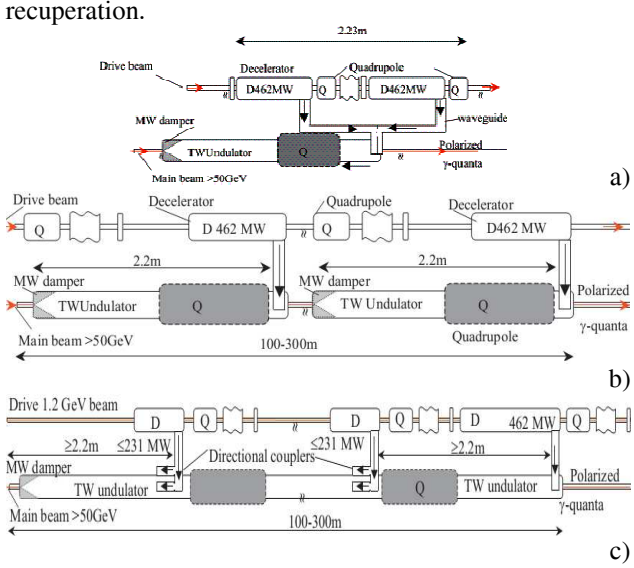

Figure 1: TBU schematic layouts: (a) one module (period) of two-beam undulator (TBU); (b) two modules of sectioned TBU and reduced field and power budget; (c) TBU with a continuous long waveguide and partial RF power recuperation.

Such a partial recuperation of the power losses is possible if the microwave pulse length exceeds at least twice the sum of filling time and beam time-of-flight of a single unit (2.2m in our example). These two amounts of power can be made equal and properly phased. It gives reduction of power required by about of factor of two and keeping about the same rms deflection force or increasing the deflecting force by ~√2 for the same power budget.

For quadratic guide operating TE_{01}+TE_{10} modes at 30GHz we estimate the optimal dimension as 5.6mm at λ_w=6.9mm.

For the CLIC PETS scheme a 2×462MW maximum power corresponds to 2.23m length (see Figure 1a.) and equivalent helical undulator field Bw=1.1T.

At least few MeV energy radiated by the polarized photons per electron per meter is required for a linear collider. For the Figure 1a scheme we obtain ~2.8 MeV/m at relatively moderate 50GeV beam energy and ~1.1dB/m attenuation (with copper waveguide) resulting to 5kW power deposition per undulator section. Another option (see Figure 1b) gives still substantial equivalent field Bw=0.76T or 1.4 MeV/m photon energy per meter. Minimum pulse length required is L(1/β+1/βgr)/c=24ns which is much less than the CLIC drive beam pulse length ~130ns making feasible the coherent recuperation of microwave energy (see Figure 1c). Thus the power consumption per unit length of TBU can be at least as twice as smaller than that in CLIC TBA [6].

Circular polarization is usually considered as two cross-polarized, 90°-shifted waves coupled to the undulator pipe. The waveguide can be square rectangular or circular. Circular waveguide pipe perfectly fits the cases of Figure 1a,b and offers maximum simplicity at higher series impedance and lower losses. Besides, a simplified coupler without splitter can be used (tapper with bend) along with a TE_{10}-TE_{11} transducer to circularly polarized wave (see Figure 2). The transducer can be placed on the decelerator output allowing transporting the circular polarized wave to the undulator via a circular pipe.

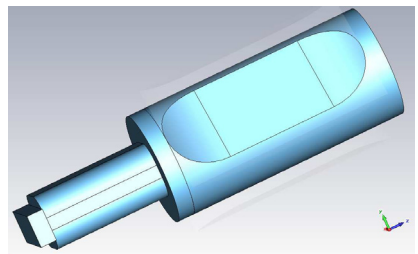

Figure 2: Transducer design that provides circular polarization in a circular waveguide. .

PULSE-LINE UNDULATOR

A microwave source capable to provide hundreds of megawatts of microwave peak power to energize the high-field, traveling wave undulator is a part of normal conducting TBA linear collider but not available on synchrotron radiation facilities. A high-voltage short pulse can be used to energize bifilar transmission line structure. A table-top solid-state pulser from FID technology produces up to 250–500kV voltage and up to 100 J energy for close to Gaussian nanosecond pulses at 50–100Ω load and rep rates up to tens kHz [7]. Both generator and terminator to be broad-band matched with the transmission line impedance. In the conceptual design we assumed 1cm period, 4mm aperture diameter, ~3.8 dielectric constant for the insulator, and 0.2×2mm^2 cross-section of the helical conductor (see Figure 3).

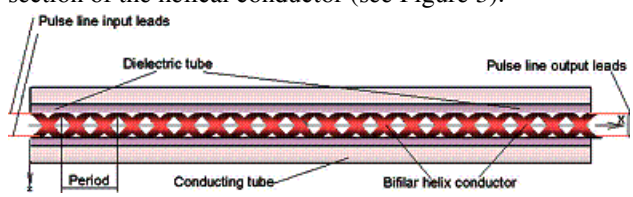

Figure 3: Schematic view of PLU based on a bifilar helical conductor made as an internal coating of an insulating tube enclosed by a conducting cylinder. The period is 1cm, length 10cm, and aperture ID is 4mm.

In the quasi-static system the characteristic wavelength related to ns-pulse duration would be much longer than the transverse dimension of the structure and hence the pulse can co-propagate with the electron beam, which would undergo periodic impact with spatial period close to the structure period.

A HV nanosecond range, Gaussian, 0.62ns rms length pulse is considered here. The transverse electric and magnetic fields along the undulator axis simulated at different longitudinal positions are given in Figure 4.

A ''snapshot'' of the periodic pattern of transverse fields on the axis is given in Figure 5 at t=3.65ns.

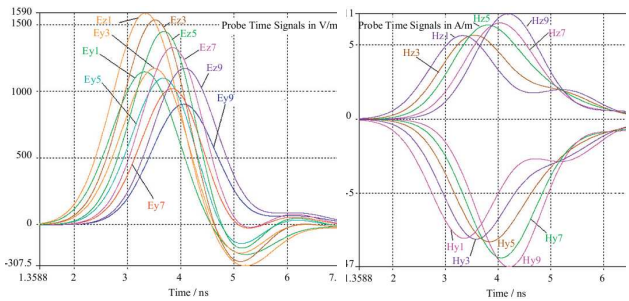

Figure 4: Transverse on-axis components of electric (on the left) and magnetic (on the right) fields at 0.8V excitation. The temporal profiles are given for the 1st through the 9th odd numbers of periods along the undulator length.

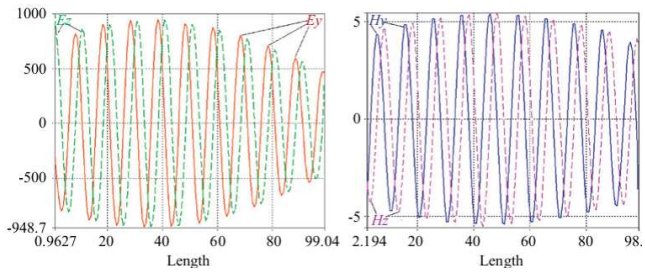

Figure 5: Horizontal and vertical transverse components for electric (V/m, on the left) and magnetic (A/m, on the right) fields along the axis (mm) at t=3.65ns and 0.8V magnitude excitation (see figure) applied to the input leads of the PLU (see figure)

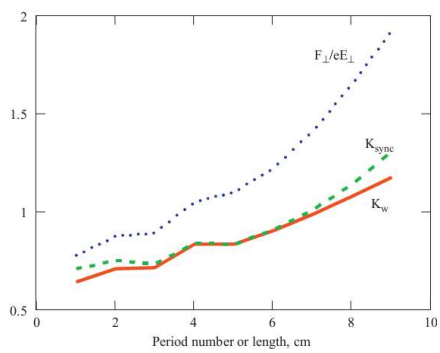

Figure 6: Longitudinal profiles for undulator factor Kw seen by relativistic beam (solid line), undulator factor Ksync seen by a synchronous β=0.32 beam (dashed), and deflecting force related to electric field (dotted) at 100kV voltage magnitude applied to the PLU input.

The undulator factor based on such a direct calculation (i.e. using peak fields only) would correspond to a synchronous motion of the particle and the pulse. In our example the pulse propagation velocity along the PLU is β=0.32. Relativistic bunch will undergo some slippage that decreases the effective force. Let us assume that the beam is synchronized with the pulse in such a way that there is no slippage in the undulator center. Resulting plots for the actual force related to the electric field and undulator factor with and without slippage are given in Figure 6 for 100kV applied peak voltage of the Gaussian incident pulse. One can see that a substantial undulator factor is produced by applying relatively moderate voltage 100kV and pulse energy (less than a few joules).

Similar to pulse DC [8] and DC-RF injectors [9,10] the key enabling feature of the PLU is that the breakdown threshold is much higher for shorter pulses and may considerably exceed a GV/m level for ns pulses.

REFERENCES

[1] V. Bharadwaj, Y. Batygin, R. Pitthan, J. Sheppard, H.G. Vincke, J. Wang, J. Gronberg, W. Stein, in Proc. of the 2005 Particle Accelerator Conference, Knoxville (2005) 3230.

[2] A. Michailichenko, in: Proc. of the 2005 Particle Accelerator Conference, Knoxville, May 16–20, 2005, p. 3676; PAC2003 Proceedings, Portland, OR, 2003, p. 2784.

[3] A. Doyuran, J. England, C. Joshi, P. Musumerci, J. Rosenzweig, S. Tochitsky, G. Travish, O. Williams, AIP Conf. Proc. 737 (2004) 750.

[4] T. Omori, in: Proc. of the 9th Int. Workshop on Linear Colliders, SLAC, Stanford (2002)

[5] R. Hiddleston, S.B. Segall, G.C. Catella, in: Physics of Quantum Electronics, V. 9, Addison-Wesley, Reading, MA

[6] J.P. Delahaye, et al., in: Proc. of the 1999 Particle Accelerator Conf., New York (1999) 250.

[7] V.M. Efanov, M.V. Efanov, A.V. Kricklenko, P.M. Yarin, A.V. Komashko, N.K. Savastianov, in: Proceedings of the 28th ICPIG, Prague, Czech Republic (2007) 1515. Also see URL:/www.fidtechnology.com

[8] K. Batchelor, J.P. Farrell, R. Conde, T. Srinivasan-Rao, J. Smedley, in:Proc. of the 23rd Advanced ICFA Beam Dynamics Workshop (2001)

[9] Q. Schengwen, Z. Kui, Z. Baocheng, H. Jiankui, W. Lifang, Z. Feng, C. Jiaer, in: Proceedings of the Second Asian Particle Accelerator Conf.(2001) 538.

[10] D. Yu, D. Newsham, Y. Luo, A. Smirnov, J. Yu, J. Lewellen, J. Smedley, T. Srinivasan-Rao, A. Zholents, in: Proc. of the 2003 Particle Accelerator Conf.(2003) 2132.

HTS WIGGLER CONCEPT FOR A DAMPING RING

A. Mikhailichenko, Cornell University Ithaca, NY 14853, USA
A.V. Smirnov, RadiaBeam Technologies Inc., Santa Monica, CA 90404, USA

Abstract

Magnetic design proposed for a damping ring (DR) is based on second generation HTS cabling technology applied to the DC windings with a yoke and mu-metal-shimmed pole to achieve ~2T high-quality field within a 86 mm gap and 32-40 cm period. Low levels of current densities (~90-100A/mm^2) provide a robust, reliable operation of the wiggler at higher heat loads, up to LN_2 temperatures with long leads, enhanced flexibility for the cryostats and infrastructure in harsh radiation environment, and reduced failure rate compared to the baseline SC ILC DR wiggler design at very competitive cost.

INTRODUCTION

Damping rings (DR) play a crucial role in producing the beams of sufficient quality and stability in achievement both peak and integrated luminosity in a Linear Collider. The baseline technology choice for the ILC damping ring [1], but based on the design developed for the CESR-c program [2,3,4]. However, the low temperature superconducting (LTS) DR wiggler is subject to failures caused by the cryogenics, power supplies, control system, and by quench. Normal-conducting alternative appears to be the most robust against long-term radiation effects. However, it would require enormously high electrical power of MW order [5]) even for small 25-mm gap TESLA DR wigglers [5,6].

Hybrid, permanent magnet ILC DR wiggler prototype having 56mm gap and ~1.7T amplitude was designed [7]. The analysis showed technical feasibility to build a prototype of such a failure-free wiggler at zero maintenance cost. Cryogenic variant of the hybrid design may sustain much higher radiation levels and also substantial heat loads, [8]. The problem is mass production: the total amount of rare-earth material required for 160-200 m wiggler (76-172 tons dependently on grade and cooling) is comparable with global year production (~130 tons in 2010 and up to 250 tons in 2015 [9]).

High Temperature Superconducting (HTS) winding made from 2nd generation wires are considered here (Figure 1). With energy cost rising and conductor cost falling, HTS magnets operating in the 20-77 K° temperature range are gaining renewed interest for the lower cost of ownership (capital and operation). Moreover, in a few low to medium field R&D applications, HTS magnets not only provided a better technical solution but also proved to be less expensive to build and test than the magnets made with conventional LTS. In addition, HTS magnets can tolerate large energy and radiation loads and can operate with a simpler cryogenic system [10].

Bismuth Strontium Calcium Copper Oxide (BSCCO) HTS wire is referred to as Generation 1 conductor [11,12]. BSCCO wire requires relatively expensive batch production process and relatively high quantities of silver (<10% of the cost). Manufacturers are transitioning to and scaling up manufacturing capacity to produce YBCO coated conductors in a semi-continuous process [13,14]. The Generation 2 technology utilizes epitaxial growth, where films deposited on a prepared structure can assume the substrate's crystal orientation. Manufacturers planning large volume price reduction in to 50% to 20% of BSCCO. That would make it competitive with copper in many large industrial applications, putting aside the cost of cooling [15].

State-of-the-art Gen.-II wire (e.g., Amperium™ [14]) presents significant leap in technological improvements to build magnets. Engineering properties exhibit good fit to the ILC damping ring wiggler needs due to high strength and stability, hermetical solder fillets at the edges, high strength, and enhanced electrical stability, sufficient robustness, mechanical strength and bend tolerance. The 1.1-1.5cm bending radius of the wire tape is perfectly small enough to be used in 32 cm-period wiggler (though too large for some other insertion devices like short-period undulators).

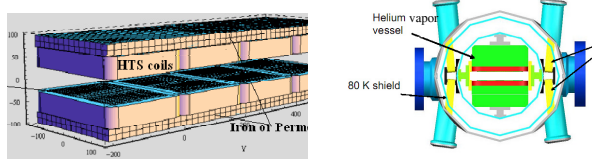

Figure 1: On the left: conceptual design of two periods of HTS wiggler. On the right: the cryostat schematics with a two phase Helium in the central chamber.

Robustness also means better sustainability to harsh radiation environment than conventional SC coils. Several HTS magnets (see, e.g., [16,17]) or insertion devices having HTS leads have been implemented [18]. Radiation-resistant dipole and quadrupole HTS magnets were developed for Rare Isotope Accelerator (RIA) [19].

MAGNETIC DESIGN

Different modifications of the Figure 1 design to accommodate both field-gap requirements (1.97T, 86mm) and HTS limits have been analyzed to achieve engineering (bulk coil) current density J in HTS wires, which is ~100A/mm^2 [20,21]. Permendur–based variant provides a viable design (see Table 1). Further

optimization of Permendur-steel pole composition allows better magnetization distribution and reduce current loading J<100A/mm^2. More advanced, Dysprosium-based variant allows reducing J down to ~90A/mm^2.

Table 1: Maximum magnetization, winding-averaged current density, and rare-earth mass for 1.97T field magnitude, 32mm period, 86mm gap, and 238mm pole width.

Pole material	Magnetization, T	Averaged J, A/mm^2	RE mass kg/m
Iron	2.11	150	0
NdFeB N52	1.63	106	132
Permendur	2.34	100.4	0

We estimated material-dominant wiggler cost using Table 1 for mass-produced ~2500 coils required for at least one damping ring. It turned out is ~50-75% of that compared to the baseline superferric design [1]. Important to note, that unlike the PM-hybrid variant, the wire production volume required for the two ILC damping rings is well within manufacturing capabilities today.

To compensate field roll-off in the good-field region (±10mm) we applied shimming. Despite the Iron is saturated, so each piece could be considered as an equivalent of permanent magnet with magnetization ~2T, it is possible to correct the field distribution [2,22]. The horizontal profile of the vertical magnetic field for the 86 mm gap design is given in Figure 2. For that well-shimmed variant we have dB/B=0.16% for Δx=3cm, and less than 0.0016% for Δx≤1cm (in the "good field" region). Thus the field flatness achieved is better than both the previous hybrid design (0.0045%, [7]) and the CESR-C design (0.0077% [23]) in the same "good field" region. Note, the Figure 2 means that focusing is provided in both planes and no roll-off in the good field region unlike that in the current superferric variant having defocusing in horizontal plane. That means Figure 2 variant demonstrates superior field quality.

Higher multipole field components control primarily the nonlinear properties of the wiggler transfer maps and eventually the dynamic aperture reduction caused by presence of the wigglers. There are a number of methods (e.g., generalized gradients and generalized surfaces [24,25,26]) developed for accurate field representation of insertion devices on the base of measurements or finite element simulation data. However, in our RADIA code model the material segmentation is relatively moderate and for the each segment the fields are calculated analytically. Therefore the numerical noise is considerably reduced (compared to standard OPERA-3D simulations). Therefore a conventional least square high-order approximation is applied to evaluate the multipole components. In Table 2 we summarize results for characterization of multipole components extracted from the 3D Radia field for ±10mm (horizontally) and ±6mm (vertically) areas along the 2 – period, three-fold symmetrical model.

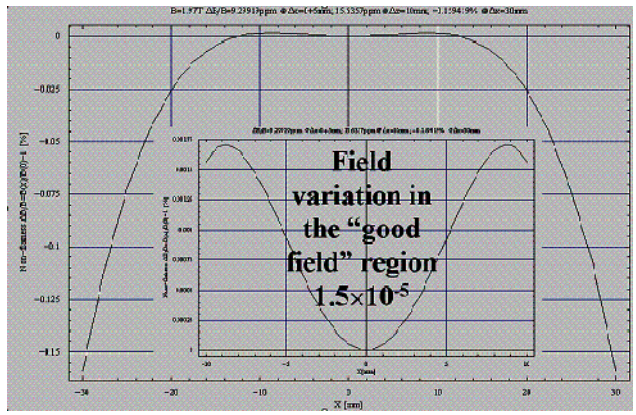

Figure 2: Field horizontal profile for 1.97T, 86mm gap wiggler having two μ-metal shims and Permendur pole. The insert: the same but for the good-field region only. The relative sextupole focusing component in the "good field" region is k_x^2=0.88/m^2.

Table 2: Multipole moments and its integrals for ±10mm (hor.) and ±6mm (vert.) areas along the 2- period short model.

	Qmax T/m	IQ, attoT	Smax T/m^2	IS, nT/m	Octmax T/m^3
Hor.	6·10-14	0.7	0.9	0.1	1·10-9
Vert	1·10-13	1.7	144	0.09	1.2·10-8

	IOct fT/m^2	Dmax T/m^4	ID, μT/m^3	Dodmax T/m^5	IDod nT/m^4
H	67	5641.	1.4	4.2·10-3	0.4
V	204.	44275.	2.8	0.019	2

These dominant dynamic aperture terms are determined by lattice unperturbed beta functions (β_x≈25 and β_y≈31m in our example) including wiggler linear focusing (periodic sextupole and, if any, periodic gradient) for the given 1.97T amplitude, 0.32m period, ~2 m wiggler length, 5GeV energy. It gives about A_{xw}≈2.2 m, A_{yw}≈0.1 m for a single wiggler section (0.058m and 0.01m for 80 sections correspondingly). Note this dominant (in terms of minimal dynamic aperture) term does not depend on higher order multipole components (beyond sextupole) and about the same for any wiggler (undulator) having the same period, similar field profile along the insertion device, and the same wiggler beta function(s).

Relative contribution of the multipole components in the dynamic aperture is estimated neglecting cross correlation with canonical perturbation theory [7,27]. The partial multipole dynamic apertures found are dominated by decapole component resulting from trapezoidal-like (or hat-like) horizontal profile of the vertical field. However, being compared to the dominant (i.e., minimum) partial dynamic apertures A_{xw}, A_{yw} found above, the higher multipole contribution turns out more than an order less (for inversed value) for horizontal and more than two orders for vertical aperture. Thus the non-linear wiggler field distortions do not perturb considerably the dynamic aperture in that design.

The tune shifts are determined by periodical (linear) focusing, which includes influence of parabolic coefficient of field profile. In our model design the corresponding coefficient is only $k_x^2 \approx 0.88 m^{-2}$ (for $|\Delta x| \leq 10$mm) and the corresponding tune shifts estimated with [27] are: 0.007 and 0.0004 for horizontal and vertical planes correspondingly (compare to 0.003 and 0.04 for the hybrid variant). The shifts are much less than the incoherent tune shift and small enough to keep the operating point apart from dangerous resonances. Simultaneously the shimming suggests a useful opportunity to reduce the vertical tune shift at the expense of the horizontal one by means of increasing k_x^2 (i.e. moderate enhancement of horizontal focusing reduces the natural vertical focusing). Conventional acceptances, defined as the largest phase space ellipse that the wiggler and its chamber could accept, are large enough (about 1 and 0.3m·rad for the beta functions above and chamber accommodating 86 mm gap. However, positron ring admittance is more meaningful than the conventional acceptance because of injection limitation $A_x+A_y<0.09$m·rad. Assuming unperturbed ring dynamical apertures $A_{x,y}=(0.06,0.05)$m·rad we get $A_x+A_y=0.058+0.01=0.068$ m·rad for 80 wigglers using the analytics [27].

Thus presence of the wiggler in terms of dynamic aperture meets the basic ILC DR requirements as dominated primarily by its linear focusing terms that can effectively be adjusted by shimming.

CONCLUSION

The HTS wiggler design is very competitive with a Low-Temperature Superconductor wiggler, while providing significant reduction in failure rate due to much simpler cryogenic system, sustainability to much higher magnetic fields and radiation, much wider range of temperatures, faster changes in current and “smoothed quench” specifics in HTS wires (slowed growth of the resistance).

Usage of HTS windings opens a possibility for *indirect cooling* by liquid Helium in a view of safety restriction for usage of liquid Nitrogen in confined spaces of ILC tunnels. In this case the Helium chamber not required, just tubings with liquid Helium thermally attached to the cold mass. So the cost of cryostat might be reduced substantionally. No doubdt, usage of HTS windings will be beneficiary for the ILC wiggler design.

ACKNOWLEDGEMENTS

The authors deeply appreciate Dr. Marc Palmer from Fermilab, Mr. R.J. Rouse of Amercan Superconductor, and Arthur P. Kazanjian of SuperPower Inc. for their enthusiastic interest for this design.

REFERENCES

[1] M. Pivi, M. Palmer, C. Celata, A. Markovic. Electron Cloud update and Overview of International Effort 46mm OCS aperture. Presented at SLAC (2006).
[2] A. Mikhailichenko, “Wiggler for CESR operation at 2 GeV, CBN 02-03, Cornell 2002; available at http://www.lns.cornell.edu/public/CBN/2004/CBN04-7/CESR_2GeV.pdf .
[3] A. Mikhailichenko, “Optimized Wiggler Magnet for CESR, PAC 2001, Chicago, Proc., pp.3648-3650
[4] Crittenden, A. Mikhailichenko, A. Temnykh, “Design Considerations for the CESR-C Wiggler Magnets”, PAC 2003, Proc., pp.1954-1956.
[5] C. Sanelli, “An Electromagnetic Damping Wiggler for TESLA”, TESLA-LNF Technical Note
[6] W. Decking. The TESLA Damping Ring, presented at Snowmass 2001.
[7] A. V. Smirnov, in Rev. Sci. Instrum. 80, 013301 (2009); http://link.aip.org/link/?RSI/80/013301
[8] T. Shioya, S.Yamamoto, S. Sasaki, M. Katoh,Y. Kamiya, H. Kitamura, Rev. Sci. Instrum. 60, 1855 (1989).
[9] D. Cramer. In Physics Today, May 2010, p. 22
[10] R. Gupta, W. Sampson. in Proc of ASC 2008 Conf.
[11] http://www.oe.energy.gov/hts_02.htm
[12] http://www.amsc.com/products/htswire/1Gwire.html
[13] http://www.amsc.com/products/htswire/index.html
[14] http://www.superpower-inc.com/content/2g-hts-wire
[15] http://www.amsc.com/products/htswire/documents/2GWhitePaper-July04.pdf
[16] K. Hatanaka, M. Fukuda, J. Nakagawa et al., in Proceedings of IPAC’10, Kyoto, Japan, p. 352
[17] R. Gupta, Ma. Anerella et al, in Proc.of 2005 Particle Accelerator Conference, Knoxville, Tennessee, p. 3016
[18] A. Mikhailichenko. In Proc. of Satellite Workshop on SC Undulators and other new ID sources, Argonne, September 21, 2010
[19] R. Gupta, et al., "Radiation Resistant HTS Quadrupole for RIA", ASC 2004
[20] http://www.amsc.com/pdf/AMP_COPPER_0910_A4.pdf
[21] http://www.magnet.fsu.edu/library/presentations/NHMFL_Presentation-4659.pdf
[22] A.Mikhailichenko, ”Improvement of SC Wiggler Performance”, PAC2003, Proceeding, vol.3, pp. 1960-1962, available at http://accelconf.web.cern.ch/AccelConf/p03/PAPERS/WPAE011.pdf .
[23] M. A. Palmer, J. A. Crittenden, J. Urban, in Proceedings of PAC07, Albuquerque, New Mexico, USA (2007) 3014
[24] R. M. G. M. Trines, S. J. L. van Eijndhoven, J. I. M. Botman, T. J. Schep, H. L. Hagedoorn, in PRSTAB V. 4, 062401 (2001)
[25] C. E. Mitchell, A. J. Dragt, in Proc. of ICAP 2006, Chamonix, France, WEPPP08 (2006) 198
[26] C Mitchell, A. Dragt. Computation of Transfer Maps from Surface Data with Applications to Damping Rings. University of Maryland, Presentation, March 2007.
[27] J. Gao, in Nucl. Instrum. and Methods, A451(3) (2000) 545

DUBNA-MINSK ACTIVITY ON THE DEVELOPMENT OF 1.3 GHZ SUPERCONDUCTING SINGLE-CELL RF-CAVITY

N.Azaryan#, J.Boudagov, D.Demin, G.Shirkov, JINR, Dubna, Russia
M.Baturitsky, V.Karpovich, N.Liubetsky, S.Maximov, V.Rodionova, BSU, Minsk, Belarus
S.Kolosov, A.Kurayev, A.Sinitsyn, BSUIR, Minsk, Belarus
V.Petrakovsky, I.Pobol, A.Pokrovsky, S.Yurevich, A.Zhuravsky, PhTI NASB, Minsk, Belarus
S.Demyanov, E.Kanyukov, SSPA SPMRC NASB, Minsk, Belarus
B.Kephart, L.Ristori, FNAL, Batavia, USA

Abstract

In 2011 Dubna-Minsk collaboration started an activity on the development and manufacture the series of superconducting niobium cavities in the enterprises in Belarus. First results of this work are presented.

Simulation code was developed to compute EM characteristics, and to calculate the shape and geometric dimensions of SC niobium RF-cavity taking into account higher order oscillations modes. The calculations of a single-cell and 9-cell cavity were made: the found ratio of the maximum electric field on the cavity axis to an average accelerating field is 2 within 1%; the found geometric factor equals 283 Ohm.

Half-cells will be made by hydraulic deep drawing and welded by electron-beam (EBW). A stamping tool for hydraulic deep drawing of the half-cells and a set of technological tools for probing of EBW of two half-cells have been designed. Mechanical properties of niobium and model material (Cu, Al) were investigated.

Cryogenic system for low temperature RF tests of the SC single-cell cavity was successfully tested at 4.2 K.

Coupling device for RF measurement of the single-cell SC niobium cavity was synthesized and manufactured – the measured standing wave ratio is about 1.01-1.07. Warm RF tests with etalon single-cell cavity were made: fundamental frequency – 1.273 GHz, quality factor (warm) – $28 \cdot 10^3$.

INTRODUCTION

Since 2007 Joint Institute for Nuclear Researches officially joined the ILC project and proposed Dubna site for ILC accelerator [1]. The key technology of the ILC is the accelerator that uses superconducting RF cavities for acceleration of electrons and positrons. R&D in superconducting radio-frequency technology is of a high priority and makes a global technical challenge for the R&D organizations worldwide.

Nowadays, in the framework of the ILC project, JINR laboratories perform several tasks. One important task is creation of series of superconducting niobium cavities in tight collaboration with the leading research centers of Republic of Belarus. First production series of 1.3 GHz superconducting niobium single-cell cavities will be manufactured in Minsk by 2015. After the tests in Minsk and Dubna these cavities will be presented to international ILC community for the expertise.

#azaryan@jinr.ru

COMPUTER SIMULATIONS

Group of specialists from Belarus State University of Informatics and Radioelectronics has developed a program package CEDR [2] for simulations and optimization of electrodynamic processes in non-regular RF systems including ohmic losses in the surface. The package allows finding all the electromagnetic characteristics of the single-cell and multi-cell RF cavity, and obtaining its optimal geometry and dimensions.

Table 1: Calculated EM characteristics of the cavity

Parameter	ILC requirements	BSUIR results
f_0	1.3 GHz	1.3 GHz
E_{peak}/E_{acc}	2	2.026
B_{peak}/E_{acc}	4.26 mT/MV·m	4.731 mT/MV·m
G	270 Ω	283 Ω
k_{sell}	1.87 %	1.94 %

RF-calculations of the main electromagnetic characteristics of a single-cell and a nine-cell cavity were made and higher order oscillation modes were investigated [3-5]. Thus, using the package, one can find the optimal shape of the cavity which provides maximum accelerating gradient on the cavity axis with minimal electric and magnetic field on the surface. The results of these computer simulations along with the ILC requirements [6] are presented in Table 1. In the Fig.1 we present the conceptual sketch of the calculated half-cell being the base detail for cavity manufacturing.

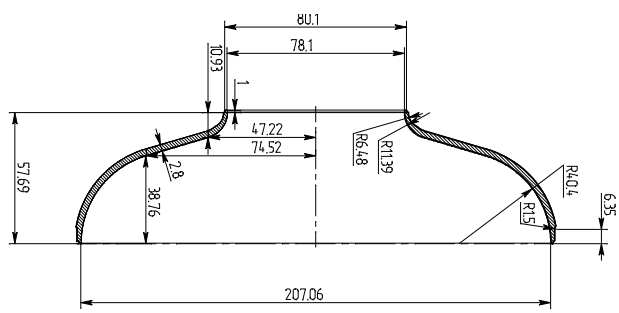

Figure 1: Conceptual draw of the half-cell.

CAVITY MANUFACTURING

Manufacturing of the half-cells will be made by the hydraulic punch-free deep drawing. Schematically, this method is shown on Fig.2. Stamping with usage of a liquid instead of some standard solid die stamping allows avoiding the possible mechanical damage of the inner cavity surface. At present, the stamping tool for hydraulic deep drawing is elaborated and placed in production.

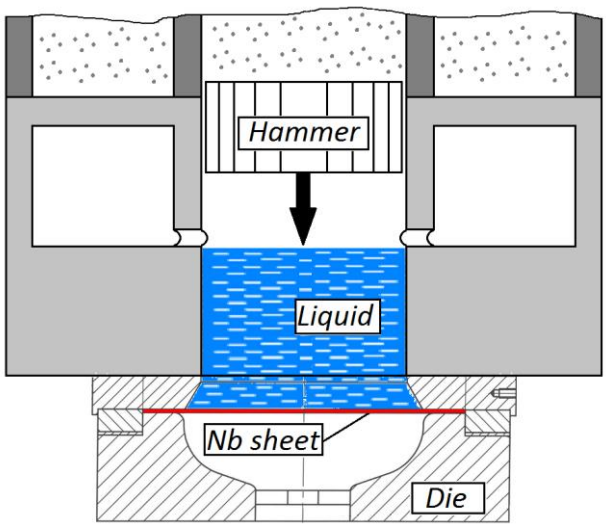

Figure 2: Scheme of hydraulic deep drawing.

In parallel, we consider the possibility of using of niobium material from Russia and Kazakhstan for the cavities manufacturing. It has been found that both materials do not meet the requirements for superconducting cavities: measured value of RRR was 40 for samples from Russia and 60 for samples from Kazakhstan. Therefore, we decide using Nb plates from an approved Nb manufacturer from China with *RRR*>300. Also we made a research of mechanical properties of Nb Cu, and Al to compare their drawability (Table 2, Fig.3).

Table 2: Mechanical properties of Nb, Cu and Al

Material	Tensile Strength, N/mm^2	Yield Strength, N/mm^2	Elongation, %
Al	119 117	40-50	38.7 33.5
Cu	219 220	70-80	55 57
Nb	168 164	70-80	55 58

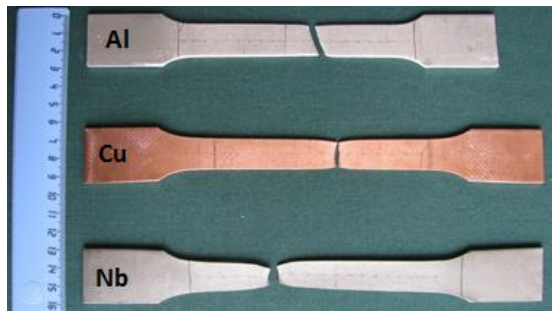

Figure 3: Nb, Cu and Al samples after tension test.

PhTI has all necessary equipment for hydraulic deep-drawing of half-cells, electron-beam welding and developed infrastructure for chemical processing of the materials, equipment for X-ray photoelectron spectroscopy and de-ionization to obtain ultrapure water for cavity rinsing on different stages of the manufacturing. EBW setup (Fig.4) consists of vacuum chamber (ø1350×2500 mm), vacuum pumps and electron gun which provide the power of 15 kW with 250 mA current and 60 keV electron energy.

Figure 4: Equipment for electron-beam welding.

Using of EBW technics allows obtaining a deep narrow weld with low impurity contamination. Technological tool for probing and perfection of modes of electron-beam welding of two half-cells (Fig.5) is in production.

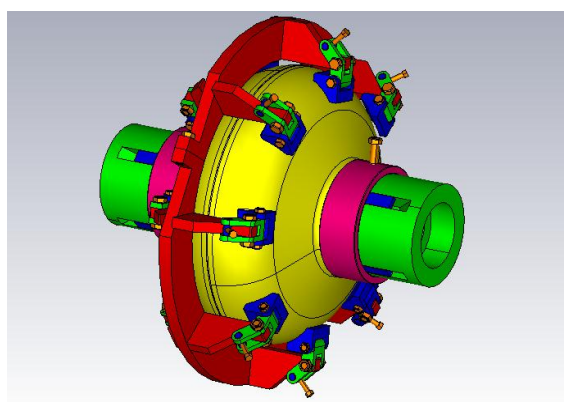

Figure 5: Design of EBW tool.

STANDS FOR RF MEASUREMENTS

RF stand for cavity room temperature characteristics measurements at 100 mW power level is elaborated in INP BSU. Coupling device with Q of about 10^6 for RF measurement is developed and manufactured – measured standing wave ratio is 1.01-1.07. The shop-draw of the coupling device is presented in Fig.6.

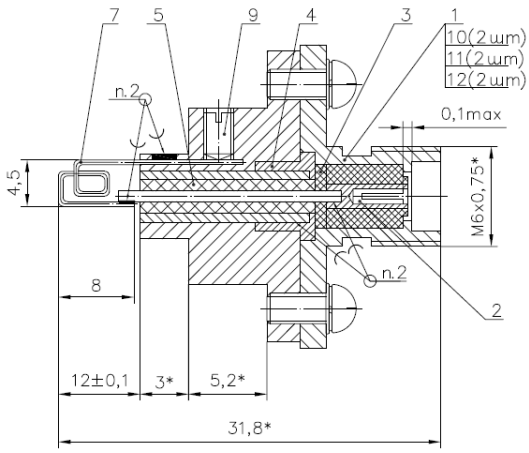

Figure 6: Shop draw of coupling device.

Warm RF tests with etalon cavity from FNAL were made by using 3 different methods and equipment sets; the results were well consistent with each other: fundamental frequency - 1.273 GHz, quality factor (warm) - 28193. The RF stand for the room-temperature RF-measurements of the FNAL niobium cavity during the tests is presented in Fig.7.

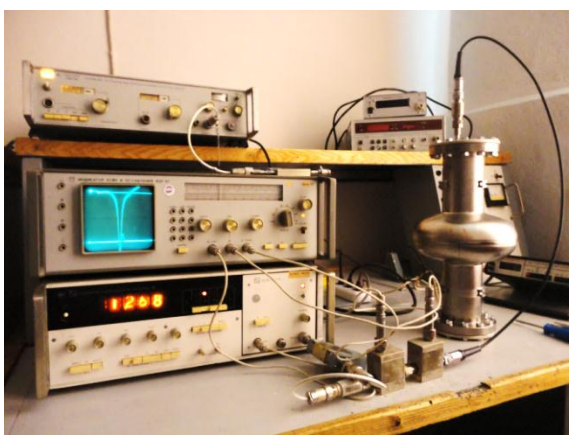

Figure 7: Room-temperature measurements of etalon cavity unit.

Equipment for RF-measurements at liquid helium temperature is elaborated and placed in production. Cryogenic setup is manufactured and successfully tested at operation temperature 4.2 K. The parameters of cryogenic setup are presented in Table 3. Scheme of the stand for RF tests of the cavity at liquid helium temperature and photo of the helium dewar are shown in Fig.8.

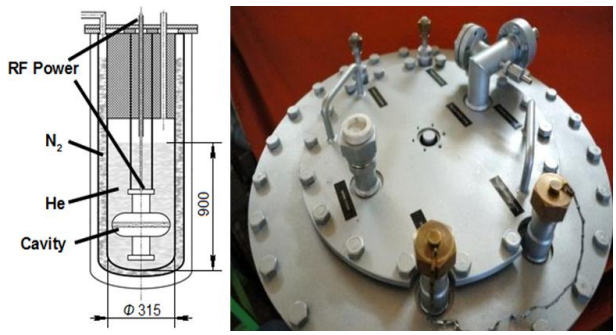

Figure 8: Scheme of the low-temperature RF stand and photo of the dewar.

Table 3: Parameters of cryogenic setup

Parameter	Value
Operating temperature	4.2 K
Helium vessel volume	70 l
Nitrogen vessel volume	25 l
Helium evaporating rate	0.65 l/h
Nitrogen evaporating rate	1.25 l/h

Low-temperature RF tests with etalon cavity will start soon.

ACKNOWLEDGMENT

We would like to thank our colleagues from FNAL who have kindly supply our research with etalon single-cell niobium cavity and our colleagues from DESY as well who provide us with valuable information on the cavity production technology. We would like to thank personally Xenia and Waldemar Singer from DESY.

REFERENCES

[1] A.Dudarev et. all, “Dubna Site Investigation - An Evaluation of a Proposed Site for the International Linear Collider near Dubna, Moscow Region, Russia”, ILC REPORT-2010-026, 2010.

[2] Kolosov S. V., Kurayev A. A., Senko A. V. “The simulation code CEDR”, IVEC-2010, USA, Monterey. P.115-116.

[3] N.S. Azaryan et al., “Computation of Single Cell Superconducting Niobium Cavity for Accelerator of Electrons and Positrons”, Physics of Particles and Nuclei Letters, vol. 9, No. 2, 2012.

[4] Kolosov S. V., Kurayev A. A., Senko A. V., “Calculation of Nine Section Resonator for Line Collider”, 21st Int. Crimean Conference “Microwave & Telecommunication Technology” (CriMiCo’2011), p.267, Sevastopol, 2011.

[5] N.S. Azaryan et al., “Superconducting Niobium Cavity for ILC Accelerator”, XVI Conference of Young Science and Specialists (AYSS`12), p.79, JINR, Dubna, 2012

[6] ILC Reference Design Report, 2007.

THE QUENCH DETECTION SYSTEM FOR SUPERCONDUCTING ELEMENTS OF NUCLOTRON ACCELERATION COMPLEX

E.Ivanov, A. Sidorin, G. Trubnikov
JINR, Dubna, Moscow Region

Abstract

New quench detection system for Nuclotron is described. The system provides highly effective detection of quenches in superconducting elements of Nuclotron. Full information about quench element is transmitted to control room. Diagram of analogue quench signal could be displayed on screen for further analysis. The system performs scheduled self-test diagnostics in real time and controls power elements of energy evacuation.

INTRODUCTION

Cryogenic magnetic system of the Nuclotron accelerator facility consists of the Nuclotron ring and measurement superperiod [1]. The last one includes four dipole and four quadrupole (two focusing and two defocusing) magnets. The Nuclotron ring includes 96 structural dipole magnets, 64 structural quadrupole magnets, two lambertson magnets and four quadrupole magnets of slow extraction system, inflector magnet of the injection system and a few tens of dipole, sextupole and oqtupole corrector magnets. Quench protection of the corrector magnets is provided by individual low current supply units. Quench protection system of all other elements is based on energy evacuation system including thyristor power switches and dump resistors. Status of the magnets is monitored by quench detectors based on a bridge scheme. For main part of the magnets the arms of the bridge are formed by inductivity of the coils of nearest identical magnets (dipole, quadrupole or lambertson), the balancing resistor is located outside the cryostat (Fig. 1).

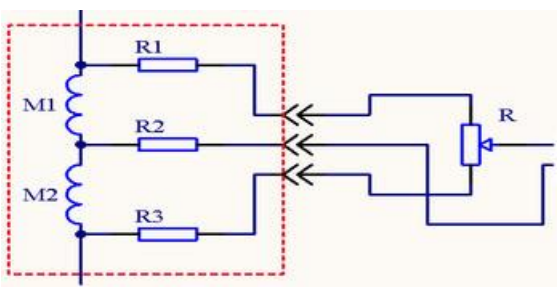

Figure 1. Scheme of the Voltage comparison: M1 and M2 – coils of nearest identical magnets, R1 – R3 – protective resistors, R – balancing resistor.

Currents of four structural dipole magnets, which are used to provide an orbit bump in the slow extraction area, are adjusted by additional suppliers. The quadrupole magnets of the slow extraction system are supplied individually also. For these magnets, and for inflector magnet of the injection system, the bridge arms are formed by two halves of the magnet coil using potential feed through.

First quench detection system at the Nuclotron was created in the end of 80-th. In reality it was full scale prototype which was in operation during about 15 years without serious modifications. The system of the quench detector monitoring and control became outdated and obsolescent. In 2007 the modernization of the accelerator facility was started in order to prepare the Nuclotron as an element of an injection chain of heavy ion collider creating in the frames of the NICA project [2]. One of the goals of the Nuclotron upgrade was to provide safe and stable operation at maximum design magnetic rigidity, that corresponds to 2 T field of the dipole magnets. New power supply and energy evacuation systems are successfully tested at this field during the Nuclotron run #42 (December 2011) [3]. Creation of new quench detection system is in the final stage now. This system based on modern technical and design solutions is described in this paper.

DESCRIPTION OF THE SYSTEM

The new quench detection system was designed on the basis of serial interfaces: all the detectors are connected to the common CAN bus used for information exchange. This solution permits to change operatively number of detectors, to work uniformly with group and individual detectors and realize total reservation of the line controlling the energy evacuation system. The system provides monitoring of current status of all its elements, signals testing of external systems and indication of malfunctions. Such a design requires more complicated electronics but sufficiently simplifies operative service and improves reliability of the operation.

General element of the system is quench detector aiming to compare two signals in order to detect a change of one of them due to appearance of active component of resistance after loss of the superconductivity.

Peculiarity of the quench detector design relates to the requirement that each detector has to be galvanically insulated from common ground circuits as well as from other detectors. Parasitic leakages in the electrical circuits of the accelerator have to be avoided as well. Accordingly the detector consists of two constructive parts: insulated from the ground, which detects and amplifies an input signal, and grounded part, at which the obtained signal is processed, analyzed and so on. Insulated and grounded parts are connected using insulated analog amplifier.

The quench detector consists of the following elements (Fig. 2):

at the insulated part:

- bridge balance resistor Rbal
- amplitude limiter of the input signal,
- preliminary scaling amplifier with function of integration,
- insulated analog amplifier;

at the grounded part:

- insulated analog amplifier,
- amplitude comparator,
- analog switch,
- microcontroller,
- bus drivers,
- insulated DC/DC converter,
- power supply.

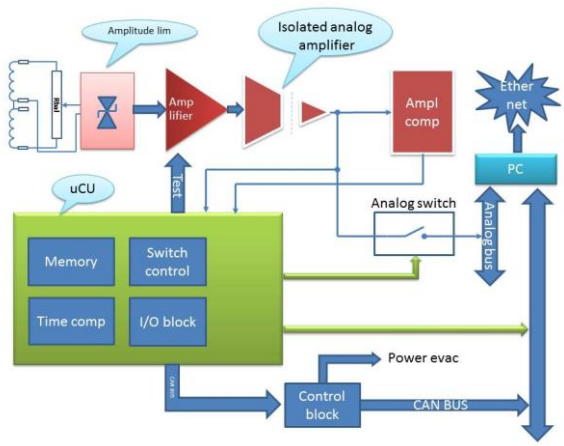

Figure 2. Schematics of the quench detector.

The bridge is a passive element and it can compare the signals in wide dynamical range: from 0 V up to maximum voltage at the magnetic elements. It is general advantage of this detection scheme. One of disadvantages – the bridge can be balanced exactly at one frequency only (for direct current in the real work) and therefore it can have parasitic disbalance at the interference frequencies or at fast variation of the power supply voltage.

The signal from the bridge is amplified by amplifier-integrator. The integration diminishes influence of short pulses of interferences. To eliminate wrong widening of short pulses with large amplitude by the integrator the amplitude limitation is applied at the entrance of the amplifier. This protects the amplifier input from an overload as well. Thereafter the amplified signal is transferred to the grounded part of the detector using the insulated analog amplifier.

Due to small amplitude of the differential signal one can use an insulated amplifier with relatively small dynamic range of the input signal (0 – 300 mV). The Nuclotron quench detectors use the amplifiers HCPL7800.

The obtained signal of the disbalance is transferred to the input of amplitude comparator and to the ADC input of the microcontroller. This signal can be commutated also to analog bus to transfer it to remote ADC for visualization with external PC.

The microcontroller analyses the disbalance signal and, if an amplitude and duration are larger than limiting values, activates the energy evacuation system.

Digital signal from ADC is recorded into internal memory of the microcontroller for further analysis and visualization if necessary.

The microcontroller provides connection of the detector with external devices and PC via CAN bus for control signals exchange.

During each pause between the magnetic field cycles the controller generates the signal “TEST” to check-out the total tract of the signal processing as well as integrity of the cable connection lines. In case of malfunction the controller generates the signal blocking the field cycle.

COMMISSIONING RESULTS

First prototype of the new quench detector was tested during the Nuclotron run #39 (June 2009). The results confirm correctness of the signal processing concept and absence of principal mistakes in the schema technical solution. The minimum frequency for the signal digitizing, required for reliable visual monitoring of the signal shape, was specified. On the basis of the test the required modification of the prototype was provided. During the Nuclotron run #41 (March 2010) the real quench process at one of the Nuclotron magnets was recorded using the new quench detector. Heater of the magnet coil was used to initiate the quench process. The heating was performed at three values of the heater power: 17, 12 and 3 W. At large heating power (Fig. 3, left) the appearance and development of the active phase requires about 20 ms thereafter the quench detector switches on the energy evacuation system. At small heating power (Fig. 3, right) the process duration is sufficiently longer.

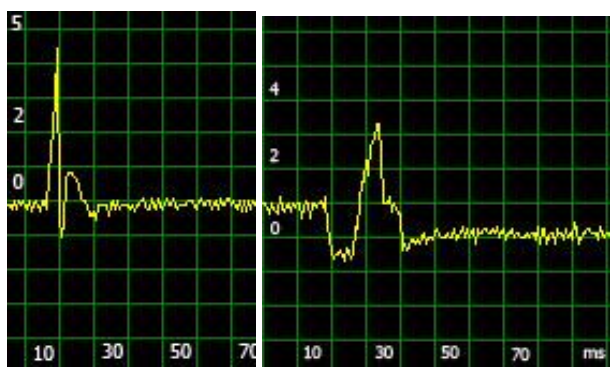

Figure 3. Signals from the quench detector at the heater power of 17 W (left) and 3 W (right). The Nuclotron run #41.

In these experiments the dynamics of the quench process in the superferric magnets during the accelerator operation was recorded for the first time. The stable and

reliable work of the quench detector was demonstrated and after the run the serial production of the detectors has been started. Total number of the detectors (including reservation and detectors for magnet clusters) is 200. The equipment is mounted in the Euromechanics U3 crates using standard elements (power suppliers, buffers and so on). To the beginning of the Nuclotron run #44 (December 2011) 20 quench detectors were constructed and prepared for operation (Fig. 4). During the runs #44 and #45 (March 2012) the test operation of the fragment of the new quench detection system was provided.

Figure 4. Quench detector and crate containing 20 detectors and power supply.

During operation dynamical misbalances (does not related to quench) at two magnetic elements were detected at the initial phase of the magnetic field cycle. At the initial stage of the field cycle the field is changed in time in accordance with parabolic law and then the field increases in time linearly. Correspondingly the voltage at the magnet coil increases linearly in time during the parabolic phase and is constant during the linear phase of the field. Unexpected misbalances appear during linear increase of the voltage when the voltage derivative was sufficiently increased. At the duration of the voltage increase below 10 ms the dynamical misbalances provoked false actuation of the energy evacuation system. The signal shape after ADC is shown in Fig. 5. A small artificial disbalance between the arms of the bridge was introduced to see all phases of the field cycle.

Analysis of this unwanted effect was performed by numerical simulation of the processes in the bridge using PSPICE simulator in the OrCad CADENCE package. This simulation shows that the dynamic disbalance is driven by parasitic capacities between midpoint of the bridge and the ground in the cable feed through into the cryostat. During the phase of voltage fast increase the capacitive leak current creates voltage on the protective resistors located at the edges of the magnetic elements (see Fig. 1).

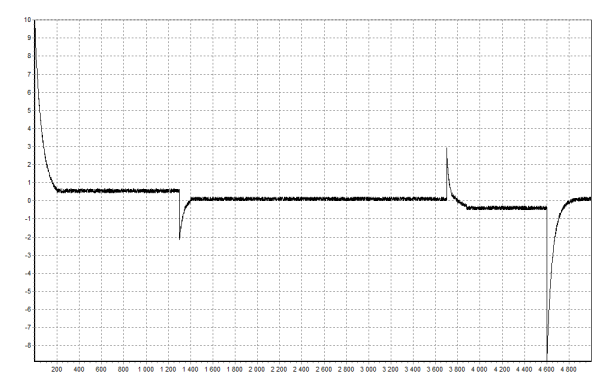

Figure 5. Misbalance signal during magnetic field cycle. The Nuclotron run #45.

The dynamical misbalance takes a place when actual values of the protective resistors are not equal to each other (usually the resistance value is at the level of ±10%). To the nearest Nuclotron run the protective resistors at all magnets will be checked and replaced by new ones if necessary.

CONCLUSIONS

In the frame of the Nuclotron upgrade program a new quench detection system was designed. Prototypes of the quench detector were consequently tested during two runs of the accelerator. On the basis of the test results the serial production of the quench detectors was started in 2010. During two runs of the accelerator the fragment of the new quench detection system including 20 quench detectors was operated during more than 1500 hours. Stable and reliable work of all elements was demonstrated. The system performs scheduled self-test diagnostics in real time and controls power elements of energy evacuation. Full scale implementation of the new quench detection system is scheduled for nearest Nuclotron run (at the fall of 2012). The expertise obtained during construction of the Nuclotron quench protection system is used to design the quench protection systems for new accelerators of the NICA facility – the Nuclotron booster and heavy ion collider.

REFERENCES

[1] A.A.Smirnov, A.D.Kovalenko, “Nuclotron-superconducting accelerator of nuclei at LHE JINR (Creation, Operation, Development)” Particles and Nuclei, Letters, 2004, v.1, №6 (123), p.11-40

[2] G.Trubnikov, N.Agapov, V.Alexandrov et. al., Project of the Nuclotron based ion collider facility (NICA) at JINR, proceedings of RuPAC2010, http://accelconf.web.cern.ch/AccelConf/r10/papers/tuchb02.pdf

[3] A.Sidorin, A.Kovalenko, G.Trubnikov et. al., Status of the Nuclotron, these proceedings.

BEAM POSITION MONITOR SYSTEM FOR 2 MEV ELECTRON COOLER FOR COSY

E.A. Bekhtenev, V.P.Cherepanov, G.V. Karpov, V.B. Reva, E.I.Shubin, D.N. Skorobogatov
Budker Institute of Nuclear Physics, Novosibirsk, Russia

Abstract

The 2 MEV electron cooler for COSY storage ring FZJ is assembling in BINP. Beam position monitor (BPM) system for orbit measurements has been developed and fabricated at BINP. The system contains 2 BPMs inside the cooling section and 10 BPMs in transport channels. Continuous electron beam is modulated with a 3 MHz signal for capability to get signals from pickup electrodes. The beam current modulation can be varied in the range of 0.3-1.5 mA. The BPMs inside the cooling section can measure both electron and proton beams. It is achieved by means of switching the reference signals inside the BPM electronics. The BPM electronics provides highly precise beam position measurements. Position measurement error doesn't exceed 1 micron. Design features of the BPM system, its parameters and testing results are presented in this paper.

INTRODUCTION

The 2 MEV electron cooler for COSY storage ring FZJ has been designed and assembled in BINP [1, 2]. Beam position monitor (BPM) system consists of 12 BPMs and electronics. 2 BPMs are located inside the cooling section. 10 BPMs are located in transport channels. Continuous electron beam current is modulated with a ~3 MHz signal for capability to get signals from BPM electrodes. Some parameters of cooler and main BPM system requirements are presented in Table 1.

Table 1: Main requirements to BPM system

Electron current	0.1-3 A
Modulation amplitude of electron current	0.3-1.5 mA
Proton current	0.1-2 mA
COSY RF frequency	~0.5-1.5 MHz
Position measurement error	less than 100 μm
Measurement rate	0.1-1 sec

To achieve the best cooling effectiveness electron and proton beams must be aligned inside the cooling section with accuracy better than 100 μm. This condition requires simultaneous measurements of electron and proton beams position by 2 BPMs located inside the cooling section. 10 BPMs in the transport channels measure only electron beam position. A new feature of the gun four-sector control electrode allows measuring not only electron beam position but the beam shape and rotation [2].

SYSTEM STUCTURE

The structure chart of the BPM system is presented in Fig. 1.

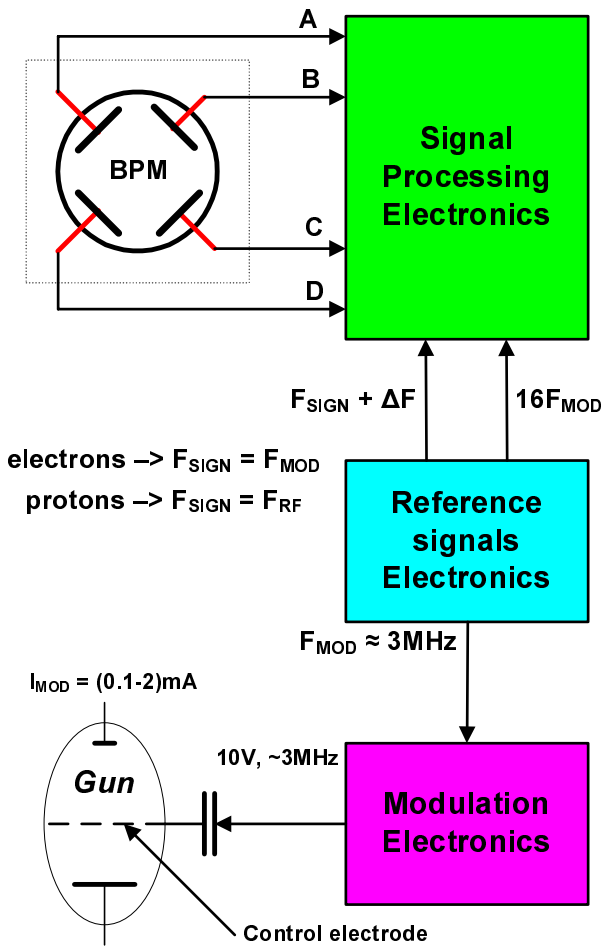

Fig.1. The structure of the BPM system.

The system consists of 12 BPMs, Signal Processing Electronics, Modulation Electronics and Reference signals Electronics. The four-electrode electrostatic BPM for transport channels is represented in Fig.2.

Modulation Electronics provides electron beam current modulation with frequency F_{MOD} ~3 MHz. Signal Processing Electronics measures the beam signals amplitude at each of four BPM electrodes. The measurement is based on synchronous detecting of the BPM signal with frequency F_{SIGN}, which equals F_{MOD} for electron beam and F_{RF} for proton beam. The sinusoidal

signal with frequency $F_{SIGN} + \Delta F$ generated by Reference signals Electronics is used as reference signal.

Fig.2. A piece of vacuum chamber with BPM.

The simultaneous measurements of electron and proton beams position is achieved by means of switching the reference signal between $F_{MOD} + \Delta F$ and $F_{RF} + \Delta F$.

ELECTRONICS

Modulation Electronics

A functional diagram of the Modulation Electronics is presented in Fig.3.

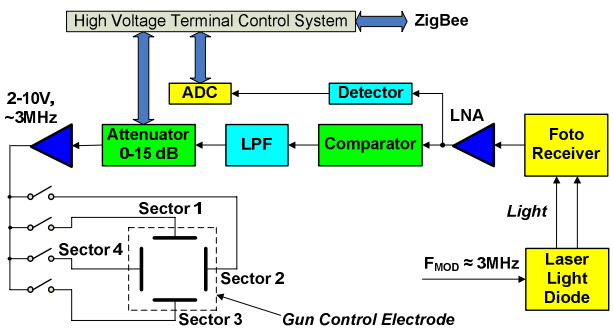

Fig.3. Functional diagram of the Modulation electronics.

Gun Control electrode consists of four sectors. Modulation voltage can be applied both to all sectors and to one of them. In the last case only a part of electron beam in transverse cross-section will be modulated. By switching on different sectors in turn one can get information about the beam shape and beam precession due to longitudinal field in different BPM locations [2].

Main part of Modulation electronics is located inside the High Voltage (HV) tank at potential of up to 2 MV. Modulation signal ~3 MHz is transmitted to high voltage part by means of light. Laser diode ADL-66505TL mounted on HV tank flange is used as optical transmitter. Its optical output power is stabilized at the level of 20 mW. Silicon PIN photodiode BPW34 located at ~0.3 m distance from laser diode is used as optical receiver. Combination of low noise amplifier (LNA) and comparator allows us to have a stable modulation voltage at the control electrode even for sufficient deviation of optical transmitter angle from optimal – up to 10 degrees. Measuring the modulation voltage at the LNA output by means of detector and ADC allows optical transmitter angle adjustment for maximization of optical power coming to optical receiver.

Signal Processing Electronics

Functional diagram of the Signal Processing Electronics is presented in Fig. 4.

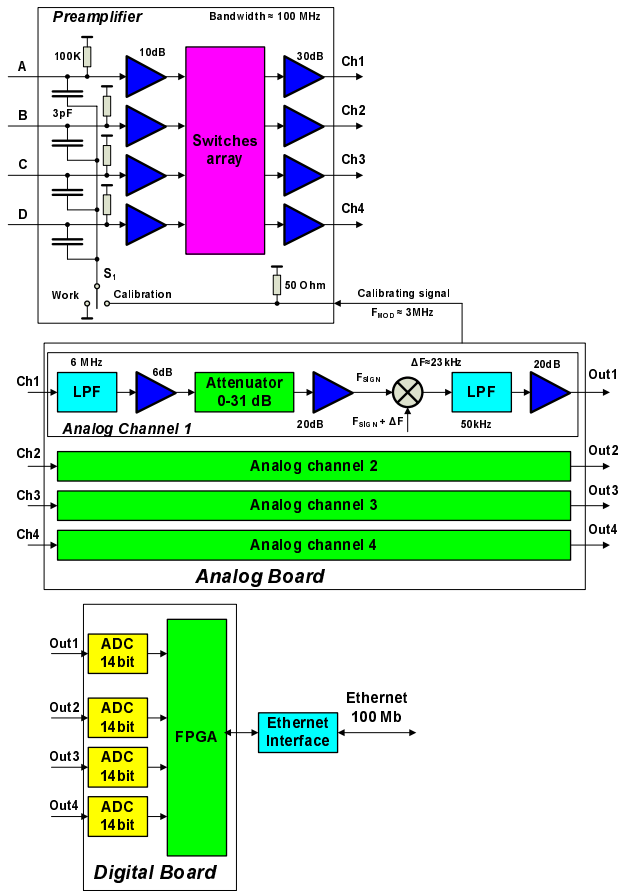

Fig.4. Functional diagram of the Signal Processing Electronics.

Signal Processing Electronics for each BPM consists of Preamplifier with high input impedance located near BPM and BPM Processor which has two boards: Analog board and Digital board. Preamplifier is connected with BPM via four 75 Ohm cables with length 1.2 m. Switches array used in Preamplifier provides 4 connection combinations between 4 BPM electrodes and 4 signal processing channels. Use of the Switches array allows to eliminate measurement error caused by inequality of the channels transmission coefficients.

After amplification the BPM signals with frequency F_{SIGN} are mixed with reference frequency $F_{SIGN} + \Delta F$. Then the signals with frequency $\Delta F \approx 23$ kHz after low pass filtering and amplification are sampled by 14 bit ADC. The signals in digital form come to FPGA where digital processing is performed. This digital signal processing includes synchronous detecting and accumulation.

In calibration mode special calibrating signal with frequency ~3 MHz comes through the switch S_1 and capacitances to each Preamplifier input.

BPM Processor occupies one 1U 19" chassis. Each BPM Processor can serve two BPMs.

EXPERIMENTAL RESULTS

BPM system has been fabricated and tested. Since November 2011 the system works in the cooler with electron beam at the BINP test stand.

To define the measurements accuracy a sinusoidal test signal with frequency ~3 MHz was used. It was applied via four-way splitter to four Preamplifier inputs. Signal amplitude was changed in the range 0.2-1 mV which corresponds to beam current modulation range 0.3-1.5 mA. Three measured main parameters of accuracy (for $K_X \approx K_Y \approx 43$ mm) are presented in Table 1.

Table 1: Main accuracy parameters of the BPM system.

Dependence of the result on beam modulation current (I_{MOD} = 0.3-1.5 mA)	~4 μm
Resolution (I_{MOD} = 0.3-1.5 mA)	< 1 μm
Dependence of the result on the temperature	~2 μm/°C

In Fig.5 results of continuous beam position measurements with one of the BPM (№5) with modulation current $I_{MOD} \approx 1$ mA are represented.

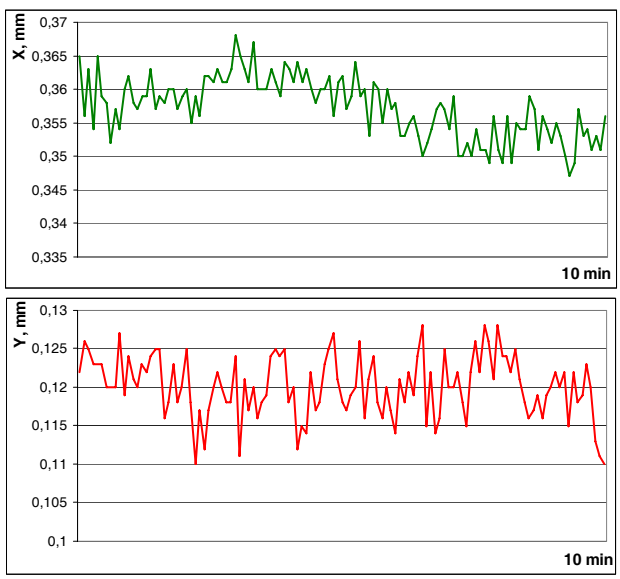

Fig.5. Results of horizontal (upper figure) and vertical (lower figure) beam position measurements for BPM №5.

Root-mean-square deviation of measured beam position for most BPMs is at the level of 4-6 μm. It is more then system measurement resolution and can be caused by real instability of the beam position in the cooler.

Applying of the modulating voltage to separate Gun Control electrode sectors gives possibility to get information about beam shape. In Fig.6 beam positions for three different BPMs are represented.

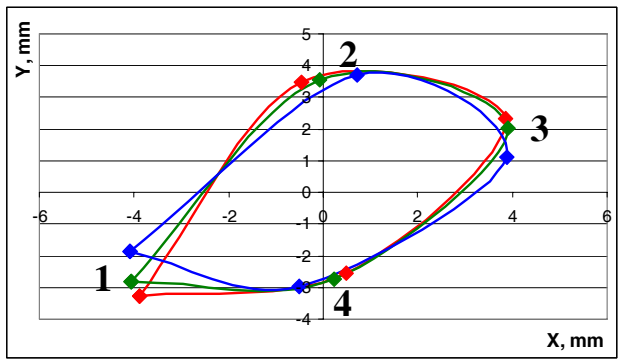

Fig.6. Measured beam positions for three different BPMs:
- red colour – BPM №2
- green colour – BPM №4
- blue colour – BPM №10.

Points "1" correspond to the case when modulating voltage was applied only to sector 1, points "2" correspond to the case when modulating voltage was applied only to sector 2 and so on. One can see approximate beam shape and its rotation.

SUMMARY

Developed and fabricated at BINP BPM System satisfies all cooler requirements. Since November 2011 BPM system is successfully working with beam at the BINP test stand. Regular work at COSY storage ring is planned before the end 2012.

REFERENCES

[1] J. Dietrich at al/ "Status of 2 MeV electron cooler for COSY-Julich/HESR" // PAC'11 New York, NY, USA, WEP229, p.1918-1920.

[2] V. Reva at al/ "The first commission results of the high voltage magnetized cooler for COSY" // COOL'11 Alushta, Ukraine, THIOA02, p.37-42.

FAST TUNE MEASUREMENT SYSTEM

E.A. Bekhtenev, V.P.Cherepanov, G.V. Karpov, A.S.Styuf
Budker Institute of Nuclear Physics, Novosibirsk, Russia

Abstract

Tune measurement system developed in Budker Institute of Nuclear Physics provides fast and accurate measurements of fractional part of betatron tunes in electron-positron storage rings and accelerators.

The tune measurements rate can achieve 1 kHz. It is especially important for electron-positron accelerators to have tunes measurement data for each phase of accelerating cycle.

The developed system is planned to be installed at the NSLS-II Booster Synchrotron. The system can perform up to 330 measurements during 300ms time interval of Booster energy ramping. The kicking technique is used as measurement method. The kicks are carried out by a radio frequency (RF) pulses. Each RF pulse contains two frequencies and thus can simultaneously excite the horizontal and vertical betatron oscillations.

All signal processing including FFT is performed inside FPGA. The tune measurement accuracy is better than 0.0005.

The developed system was put into operation at the February 2011 in VEPP-3 electron-positron storage ring at BINP.

INTRODUCTION

Booster synchrotron for third generation synchrotron light source NSLS II is presently under construction in BNL, USA [1]. The Booster main parameters are given in Table 1.

Table 1: Main parameters of the NSLS II Booster

Beam energy injection/extraction	200 MeV/3 GeV
Repetition rate	1 Hz (2 Hz)
Revolution frequency F_0	1.894 MHz
RF frequency	499.68 MHz
Betatron tunes: ν_x/ν_y	9.6455 / 3.4105
Beam current	1-30 mA
Energy ramping time	300 (150) ms

Requirements to Tune measurement system (TMS) for the Booster synchrotron are:

- Tune measurements rate has to be up to 1 kHz
- Tune measurements accuracy has to be better than 0.5×10^{-3}.

TMS satisfied to these requirements has been designed and fabricated at BINP. The system includes two identical sets of of four 50-Ω striplines and TMS electronics. One set is a Kicker for beam excitation; another one is a Pickup for measurement of a beam response signal.

The system uses the kicking method for tunes measurement. The beam is excited by radio frequency (RF) pulse with the frequency f_e close to $f_B = (1 - \nu_{x,y})f_0$, where f_0 is the revolution frequency, $\nu_{x,y}$ – is the fractional part of the horizontal (vertical) tune. Duration of the RF pulse is 100-200 μs. The measurements are possible when the difference between frequency f_e and betatron frequency $(1 - \nu_{x,y})f_0$ does not exceed $(0.01\text{-}0.02)f_0$. In this case, the signal of the beam betatron oscillations is received by the stripline pickup after the end of the exciting RF pulse. Then the signal is transferred to the signal processing electronics, where it is sampled by ADC and is processed by a Field Programmable Gate Array (FPGA) circuit. The result of signal processing is the values of $\nu_{x,y}$.

SYSTEM STUCTURE

The structure chart of the Tune measurement system is presented in Fig. 1.

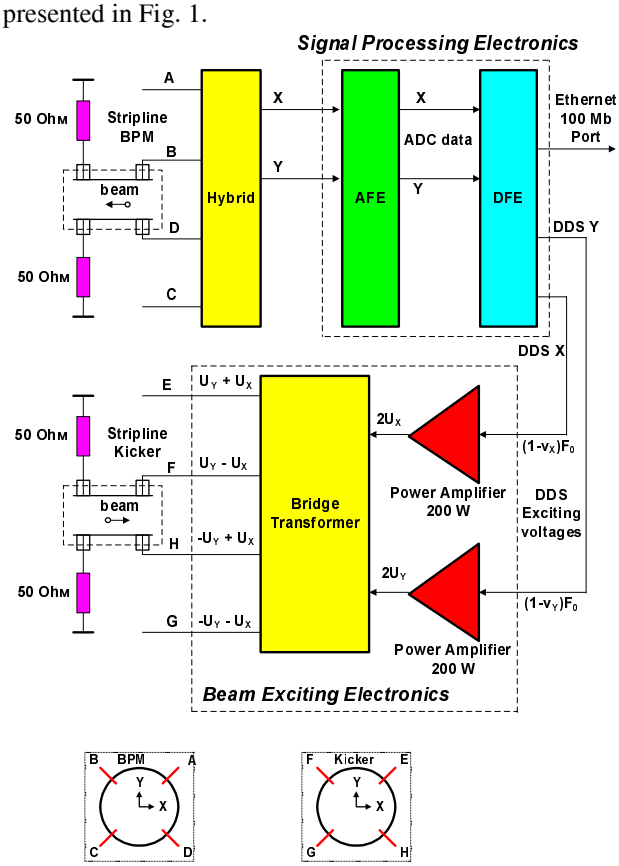

Fig.1. The structure of the Tune measurement system.

The system consists of Pickup, Kicker, Hybrid, Signal Processing Electronics and Beam Exciting Electronics. The Pickup and Kicker stripline electrodes are mounted at

the angle of 45° relative to the horizontal plane using a BINP-made 50 Ω/450°C vacuum-tight feedthrough for SMA plug with bearing capacity. The length of stripline is 450 mm, which is about 3λ/4 (λ is the wavelength) at RF frequency of 499.68 MHz.The printed circuit Hybrid is placed near the Pickup. The signals proportional to horizontal (X) and vertical (Y) beam oscillations come from Hybrid to Signal Processing electronics which consists of Analog Front End (AFE) Electronics and Digital Front End (DFE) Electronics.

Beam Exciting Electronics consists of two 200 W Power Amplifiers, Bridge transformer and 50 Ω loads. Two RF pulses from DDS synthesizers located in Signal Processing electronics come to the Power Amplifiers (PA) inputs. From PA outputs RF pulses with amplitude up to 140 V are distributed to four kicker striplines by Bridge transformer. Such scheme provides selective or simultaneous excitation of both horizontal and vertical betatron oscillations. Sum power of 400 W allows excite beam oscillations up to 1 mm amplitude in all beam energy range.

SIGNAL PROCESSING ELECTRONICS

Analog Front End (AFE)

A functional diagram of the AFE electronics is presented in Fig.2.

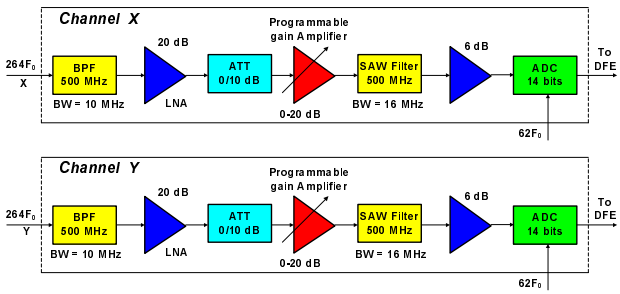

Fig.2. Functional diagram of the AFE electronics.

The Analog Front End consists of two identical processing channels (*X* and *Y*). The first harmonics of RF frequency ($264F_0$) is extracted from the signal spectrum. Input printed-circuit Band Pass Filter has the following parameters:

- central frequency – 500 MHz
- bandwidth – 10 MHz
- insertion loss – 3 dB

After amplification by the Low Noise Amplifier (LNA) HMC616LP3 the signal passes through programmable Attenuator 0/10 dB (HMC541LP3) and programmable Gain Amplifier (PGA). The PGA provides 3 fixed gain values: 0 dB, 10 dB and 20 dB. The second Band Pass Filter (SAW filter TA0979A of Goledge) with bandwidth of 16 MHz minimizes noise and distortions and provides additional suppression of mirror components, thereby providing insensitivity to signal phase. The signals are sampled by 14-bit ADC (AD9246 of Analog Devices) with sampling frequency $f_{ADC} = 62f_0 \approx 117$ MHz. The digitized signals come to the Digital Front End, where they are processed by the FPGA.

Digital Front End (DFE)

Functional diagram of the Digital Front End (DFE) is presented in Fig. 3.

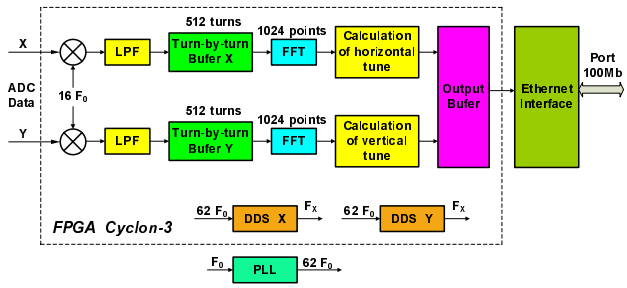

Fig.3. Functional diagram of the DFE.

The core of the DFE is FPGA Cyclon-3 EP3C40 produced by Altera. Due to frequency folding the signal frequency at the FPGA input is $16f_0$. Digital processing performed by the FPGA includes synchronous detecting, filtering and Fast Fourier Transformation (FFT) of the turn-by-turn data array. Before FFT two additional procedures are performed:

1) the average value (signal of orbit displacement) is subtracted from the turn-by-turn data array;
2) the array is multiplied by Hann window.

After 1024-points FFT the spectrum centre of gravity is calculated. This centre of gravity corresponds to the desired betatron tune. The time required for digital signal processing of two signals (X and Y) is about 0.5 ms.

The FPGA also contains two Direct Digital Synthesizers (DDS). Each DDS generate a sinusoidal signal. These 10-bit digital signals come to DACs and then to Power Amplifiers of the Beam Exciting Electronics.

A clock signal for ADCs and FPGA with frequency of $62f_0 \approx 117$ MHz is generated by the low jitter PLL AD9516-4. Measured jitter of this PLL is 0.4-0.5 ps.

Signal Processing electronics occupy two 1U 19" chassis.

MEASUREMENT CYCLE

Time diagram of the measurement cycle is represented in Fig.4.

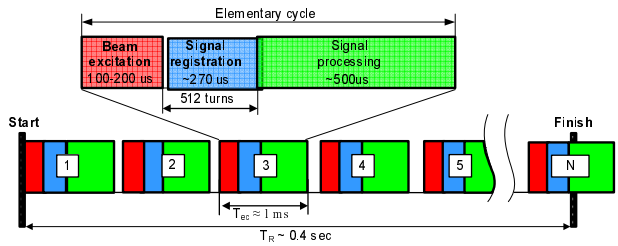

Fig. 4. Time diagram of the whole measurement cycle.

The whole measurement cycle starts from beginning of the Booster energy ramping and consists of N elementary cycles. Each elementary cycle includes 3 stages: beam excitation, signal registration and signal processing. The total time of one elementary cycle T_{ec} is less than 1 ms. The tune measurement is possible when the difference between DDS frequency and frequency $(1 - \nu_{x,y})f_0$ does not exceed $(0.01\text{-}0.02)f_0$. In this case, the signal of the beam betatron oscillations appears at the end of the exciting RF pulse. If the betatron frequency is not known with accuracy $(0.01\text{-}0.02)f_0$, the search mode is required. In the search mode DDS frequency for elementary cycle n+1 differs from DDS frequency for elementary cycle n in fixed value Δf. So, during the whole measurement cycle DDS frequency is scanning in specified range. For elementary cycle n_0 where DDS frequency is more close to $(1 - \nu_{x,y})f_0$ the signal of betatron oscillations is maximal and betatron frequency is found. Then the measurement mode can be started. In the measurement mode, the DDS frequency tracks to the betatron frequency. DDS frequency for elementary cycle n+1 is set equal to betatron frequency measured during elementary cycle n. The search mode can be used in fixed energy, for example in injection energy. Then before energy ramping DDS frequency is set to $(1 - \nu_{xi,yi})f_0$, where $\nu_{xi,yi}$ is the measured tune at injection energy.

EXPERIMENTAL TESTS RESULTS

Made at BINP TMS electronics had been tested at Lab test stand. Scheme of Lab test is presented in Fig.5.

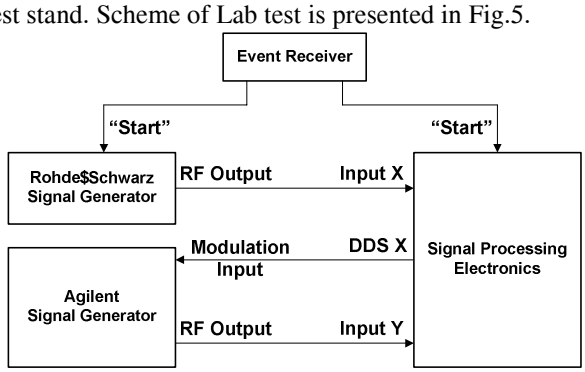

Fig.5. Scheme of Lab test of TMS electronics.

Two RF signal generators are used in this test. The first one (Rohde&Schwarz SMB 100A signal generator) generates sinusoidal signal ~500 MHz, 1mV with amplitude modulation. Amplitude modulation frequency F_{MOD1} is changing linearly in the range $(0.1\text{-}0.2)\ f_0$ during the time 300 ms after "Start" pulse coming from Event Receiver (EVR). The same pulse comes to Signal Processing electronics starting the measurement cycle. Signal Processing electronics measure modulation frequency F_{MOD1}. DDS X frequency F_{DDSX} is tracking to the measured frequency F_{MOD1}. Output of DDS X is connected to the external modulation input of the second RF signal generator (Agilent). So, at the Agilent output we have ~500 MHz, 1mV sinusoidal signal with F_{DDSX} amplitude modulation. This signal comes to the Input Y of the Signal Processing electronics. Difference between two measured frequencies F_X and F_Y gives the measurement error. This test gives tune measurement error does not exceed 10^{-4}.

Analogues TMS electronics has been installed at BINP storage ring VEPP-3. The difference between the systems is tied mainly with another VEPP-3 RF frequency – 72.54 MHz. The second harmonics of RF frequency is used in the Signal Processing Electronics. Results of tune measurements with beam at VEPP-3 (beam energy is ~1.8 GeV) are represented in Fig.6.

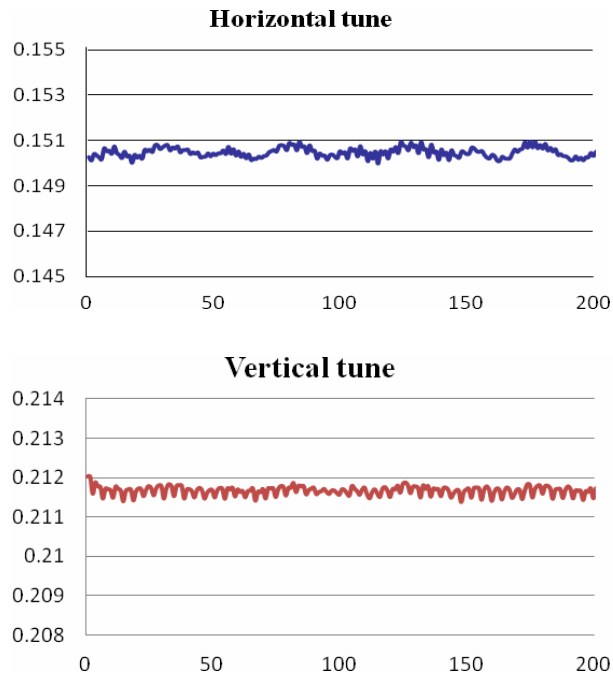

Fig.6. Results of horizontal (upper) and vertical (lower) tune measurements with beam at VEPP-3 at ~1.8 GeV.

Beam oscillation amplitude was about 200 microns. Root-mean-square deviation of measured betatron frequencies σ is 3×10^{-4} for horizontal plane and 2×10^{-4} for vertical plane. Such relatively large σ can be caused by real instability of the betatron frequencies at VEPP-3.

SUMMARY

Developed at BINP Tune Measurement System satisfies all requirements of NSLS-II Booster. At present all TMS components have been manufactured and tested. It is planned at the beginning of 2013 the system will be commissioned at BNL. Analogues TMS successfully works in VEPP-3 storage ring at BINP since February 2011.

REFERENCES

[1] S. Gurov at al/ STATUS OF NSLS-II BOOSTER // PAC'11 New York, NY, USA, WEP201, p1864.

NEW BEAM POSITION MONITOR ELECTRONICS FOR VEPP-5 PREINJECTOR

G.V. Karpov, A.S.Styuf, Budker Institute of Nuclear Physics, Novosibirsk, Russia

Abstract

A new beam position monitor (BPM) electronics has been designed, manufactured and tested in VEPP-5 preinjector. Preinjector BPM system measures position of single electron and positron bunches for each injection cycle. New BPM electronics provides more high sensitivity with respect to existing one developed in 2004. The system can measure the position of bunches with 10^8 - 10^{10} particles per bunch. The resolution of measurements of single bunch is better than 10 μm for 10^{10} particles per bunch. The features of BPM electronics design, the main parameters and results obtained in VEPP-5 preinjector are presented.

INTRODUCTION

It is planned to put VEPP-5 preinjector [1] into regular operation in 2012. The preinjector produces electron and positron bunches with main parameters given in Table 1.

Table 1: Main parameters of the preinjector

Number of electrons in a bunch	$(2\text{-}3)\times10^{10}$
Number of positrons in a bunch	$(2\text{-}3)\times10^{8}$
Longitudinal bunch size	4 mm
Repetition rate for electrons for positrons	 1 Hz 50 Hz

The preinjector includes 300 MeV electron linac, conversion system and 510 MeV positron linac [1]. Existing Beam position monitor (BPM) system developed and fabricated in 2004 consists of 14 stripline BPMs and electronics [2]. The main problem with this system operation is insufficient position measurement accuracy of the positron bunches due to low signal-to noise ratio caused with interferences on the cables connecting BPMs with electronics. New BPM electronics developed in 2012 has signal-to noise ratio at least in one order better than old one. This improvement is achieved with help of two main changings:

- increasing of processing electronics bandwidth;
- decreasing of the timing circuit jitter.

Signal processing used in both new and old systems is low pass filtering. Signal amplitude at the Low Pass Filter (LPF) output U_{LPF} strongly depends on the LPF cut-off frequency F_{LPF}. In Fig.1 calculated dependence of the U_{LPF} value on the F_{LPF} for our sripline BPM signal is represented. In low frequency domain the signal amplitude grows with increasing of F_{LPF} almost as square of F_{LPF} value whereas the noise r.m.s. amplitude grows as square root of F_{LPF}.

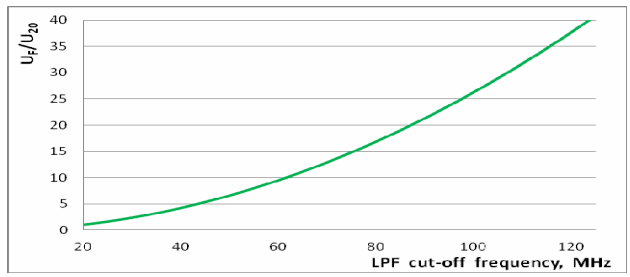

Fig.1. Calculated dependence of the relative signal amplitude in the LPF output U_F / U_{20} on the F_{LPF}.

In new electronics we have chosen F_{LPF} = 120 MHz. It is in 6 times more compare with old electronics. It gives a gain in signal-to-noise (S/N) ratio approximately in 15 times. Taking into account that main part of interference power is located in frequency domain 1-20 MHz total increasing of S/N ratio is more considerable. But increasing of the signal processing bandwidth imposes more hard requirements to jitter of the ADC clock signal. Therefore main efforts were applied to this aspect.

BPM ELECTRONICS STRUCTURE

A functional diagram of the new BPM electronics is presented in Fig. 2.

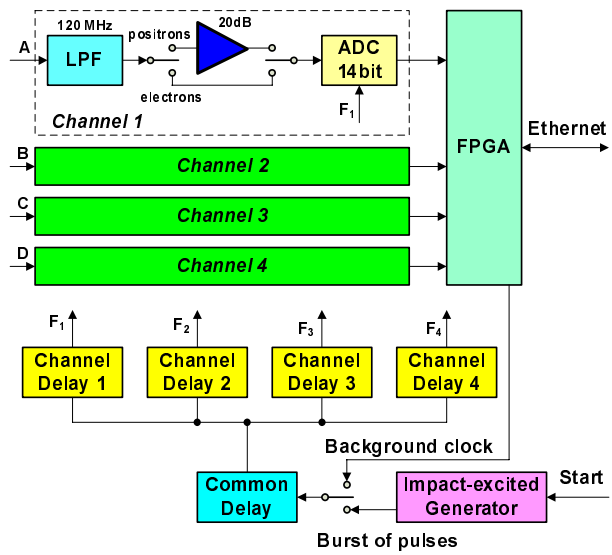

Fig.2. A functional diagram of the new BPM electronics.

The Electronics consists of four identical signal processing channels, timing circuit and FPGA. Signal processing channel contains LPF, switched amplifier and 14-bit ADC. The BPM signals are amplified by fixed gain

(~20 dB) amplifier if number of particles per bunch is less than 10^9 (for positron bunches). For electron bunches with number of particles more than 10^9 the signals bypass the amplifier.

A key part of the electronics is timing circuit which produces ADC clock signal. Pulse "Start" tied with gun shot causes generation by impact-excited generator a burst of 32 pulses with period of ~17 ns (Fig.3).

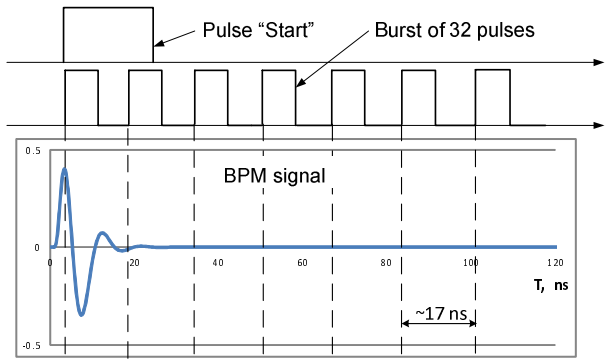

Fig.3. A time diagram of the timing circuit.

The burst of pulses passes through two-level fine delay. The first level delay on base of MC100EP195B is common for all four channels. It has delay range ~10 ns and delay step ~10 ps. The second level delay on base of the same chip MC100EP195B is individual for each channel. Ability of individual delay adjustment for each BPM electrode allows us to eliminate the problem of different cables lengths. The total fine delay range is about 20 ns. It overlaps the period between burst pulses. After gun shot we have for each BPM electrode a digital array of 32 ADC samples. We use only one sample which is more close to the top of the BPM signal. Adjusting the fine delay we set the rising edge of the clock pulse corresponding to this sample exactly on the signal top. The measured jitter of the timing circuit is about 13 ps. It caused mainly by the fine delay.

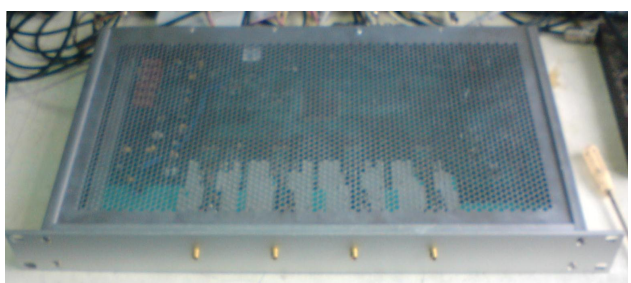

Fig.4. Prototype of BPM electronics.

Pipeline-type ADC requires continuous clock signal for correct work. So the large time intervals between the bursts of pulses are filled with background clock with frequency ~58 MHz from FPGA. Besides of the BPM signal amplitude zero levels for all ADCs are measured after every shot.

BPM electronics for one BPM occupies one 1U 19" chassis (Fig.4).

EXPERIMENTAL RESULTS

Prototype of new BPM electronics has been fabricated and tested with beam at VEPP-5 Preinjector.

For defining of single bunch position measurement resolution the special test had been made. The signal from one of BPM striplines was applied via four-way splitter to four inputs (Fig.5).

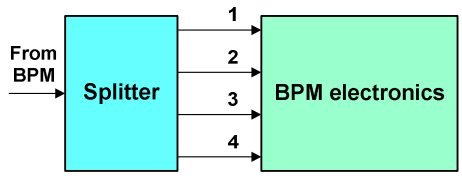

Fig.5. The test scheme.

Resolution was measured with two different numbers of electrons per bunch. The results are represented in Fig.6.

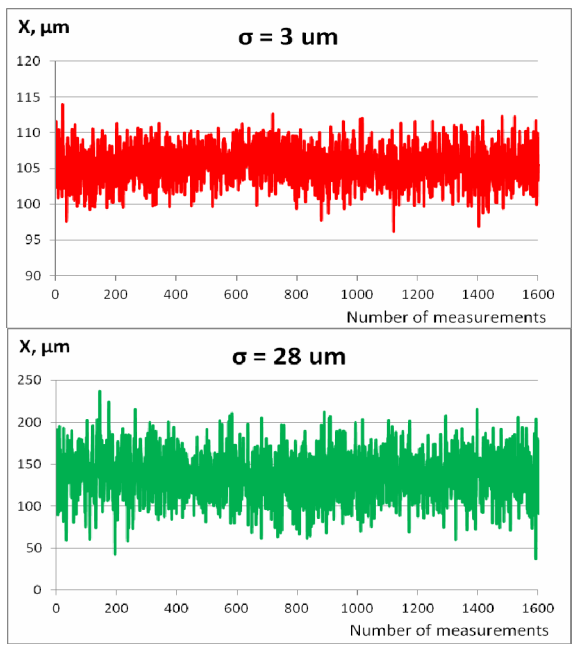

Fig.6. Results of the test with electron beam with number of particles per bunch ~0.5×10^{10} (upper picture) and ~2×10^8 (lower picture).

Resolution of measurements for number of particles per bunch ~0.5×10^{10} is about 3 μm. For number of particles per bunch ~2×10^8, which equals to nominal number of positrons per bunch, resolution is about 30 μm. Note that accumulation of data during the time 1 sec for positrons improves the resolution in 5-7 times.

Connecting each BPM electrode to its own input we had got the results represented in Fig.7. In this case root-mean-square deviation of measured beam position for number of particles per bunch ~0.5×10^{10} was ~18 μm. It is in six times more then electronics measurement

resolution for such bunch charge and caused by real instability of the beam position in the linac. However it less then electronics resolution for small numbers of particles per bunch (~2×10^8) corresponding to positrons.

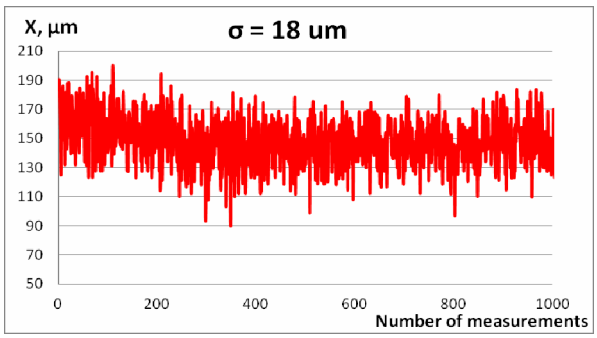

Fig.7. Results of horizontal beam position measurements for number of particles per bunch ~0.5×10^{10}.

Measured main accuracy parameters for $K_X \approx K_Y \approx 6$ mm are presented in Table 2.

Table 2: Accuracy parameters of the BPM electronics.

Dependence of the result on number of particles per bunch ($N = 10^9$-10^{10})	< 4 μm
Resolution for single bunch $N = 2\times10^8$ $N = 10^{10}$	 < 30 μm < 3 μm
Resolution for measurement time 1 sec $N = 2\times10^8$	 < 5 μm
Dependence of the result on the temperature	< 0.2 μm/°C

SUMMARY

Developed at BINP new BPM electronics for VEPP-5 preinjector has better accuracy parameters in comparison with old one. Tests with beam had shown ability of the electronics to measure positrons beam position with sufficient accuracy. Accumulating the data during the time 1-2 sec allows achieving almost the same measurement resolution for positrons as for electrons. It is planned to produce all electronics and to install it in preinjector before the end 2012.

REFERENCES

[1] A.V. Akimov at al/ “Status of VEPP-5 injection complex” // RuPAC’06, Novosibirsk, Russia, MOAO10, p.19-21.

[2] E.A. Bekhtenev at al/ “Beam position measurement system of the VEPP-5 preinjector” // RuPAC’06, Novosibirsk, Russia, MODP21, p.250-252.

MULTIMODE DIGITAL INTEGRATORS FOR PRECISE MAGNETIC MEASUREMENTS

A. Batrakov, A. Pavlenko, D. Shickov, BINP, Novosibirsk, Russia
P. Vagin, DESY, Hamburg, Germany

Abstract

Increasing demands of the accelerator techniques and modern electronics capabilities stimulate the creation of more accurate and fast instrumentation, based on the induction method. This report describes multimode integrators VsDC2 and VsDC3 (**V**olt-**s**econds to **D**igital **C**onverter), intended for precise measurements of the magnetic fields, both pulsed and constant. These integrators utilize new, digital integration method, which allows reaching accuracy close to the 10^{-5}.

INTRODUCTION

The induction method of magnetic measurements is the most important, widely used and oldest measurement method for particle accelerator magnets. This method generally requires integration of an input signal. In recent years, two types of the integrators have been developed in Budker INP (Russia). These devices are based on the digital integration method. Integrators provide high accuracy both for the constant magnetic field measurements using movable coils and for the pulsed measurements also. It is possible to achieve relative accuracy better than the 10^{-4} and even better than the 10^{-5} in special cases.

DIGITAL INTEGRATION METHOD

The digital integration method is shown in Figure 1.

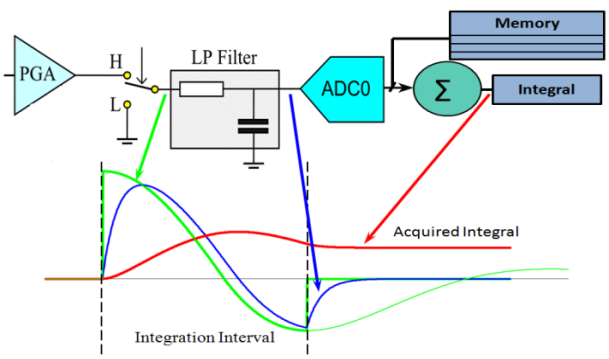

Figure 1: Digital integrator stricter and signal passing.

An input signal is converted to appropriate scale by preliminary amplifier with programmable gain (PGA). The integration interval is determined by the fast analog switch. During integration interval the scaled input signal passes through the switch to the low pass (LP) filter input. Remaining time LP filter is connected to ground. The required integral equals to volt-second square of the signal shaped by the analog switch. After LP filtering the signal is converted to the digital form by the ADC.

Let's mention, that similar structure one may found out in the device FDI2056 [1], but the last one doesn't contain the fast switch and LP filter, which are principal elements in the described integrators.

It should be noted that LP filter does not change integral of the incoming signal. Let's show it. Suppose that input signal *f(t)* is non-zero only in the interval from 0 to τ. This signal spectrum equals to:

$$S_{in}(\omega) = \int_{-\infty}^{\infty} f(t)\cdot e^{-j\omega t}dt = \int_{0}^{\tau} f(t)\cdot e^{-j\omega t}dt\ .$$

Note that spectral component at zero frequency equals to required integral. It is known that the LP filter output is given by:

$$S_{out}(\omega) = K(\omega)\cdot S_{in}(\omega)\ .$$

Where $K(\omega)$ is the filter transfer function. So the output integral equals to the required one if the LP filter has unity transfer function value at zero frequency:

$$\int_{0}^{\infty} f_{out}(t)dt = S_{out}(0) = S_{in}(0) = \int_{0}^{\tau} f(t)dt\ .$$

Digital integration method implies that the signal integral is calculated by summing ADC samples multiplied by the ADC time quant. Consider now the accuracy of continuous integral interpolation by the sum of discrete samples. Suppose that the LP filter limits the incoming signal spectrum to half the ADC sampling frequency. Therefore, according the Kotelnikov theorem [2], the continuous input can be precisely interpolated by a digital string as:

$$f(t) = \sum_{n=-\infty}^{n=+\infty} f(nT_s)\,\mathrm{sinc}\left(\pi\frac{(t-nT_s)}{T_s}\right).$$

Hence, for input signal integral we can write:

$$\int_{-\infty}^{+\infty} f(t)dt = \int_{-\infty}^{+\infty} dt \sum_{n=-\infty}^{n=+\infty} f(nT_s)\,\mathrm{sinc}\left(\pi\frac{(t-nT_s)}{T_s}\right).$$

Changing summing and integration order and integrating we obtain:

$$\sum_{n=-\infty}^{n=+\infty} f(nT_s)\int_{-\infty}^{+\infty}\mathrm{sinc}\left(\pi\frac{(t-nT_s)}{T_s}\right)dt = \sum_{n=-\infty}^{n=+\infty} f(nT_s)\cdot T_s$$

i.e. in the case of the ideal filter and infinite discrete sequence the required integral exactly equals to the digital sum.

It is impossible to satisfy these conditions strictly in the real device. Therefore, high theoretical accuracy of digital

integration method is achieved by choosing appropriate relation between LP filter parameters and the ADC sampling rate. Moreover, LP filter spreads incoming signal in time, so it allows the middle speed but precision and low noise ADC to be used.

INTEGRATORS VsDC2 AND VsDC3

The cited above integration method has been implemented in integrators VsDC2 and VsDC3. Integrator VsDC2 is a 3U and 4HP Eurocard module equipped with two identical channels and CAN bus communication interface. VsDC3 is a subsequent development. It has slightly improved performance and is designed as a 6U 4HP module with VME64 interface, Figure 2.

Figure 2: VsDC3 board.

The magnetic fields stability is well-known and often solved task for pulsed measurements. Thus the relative noise ratio of the output integral versus integration time is one of the most important parameter of the measuring device. Plot in Figure 3 shows this relation.

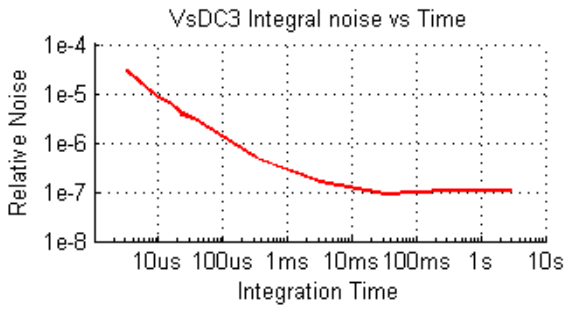

Figure 3: VsDC3 SNR of integrals versus time.

At integration time larger than few milliseconds noise decreases enough to become less important and the influence of other error sources rises. For constant field measurements, one of the most important parameter is nonlinearity of the device. Figure 4 demonstrates relative to scale non-linearity of the VsDC2.

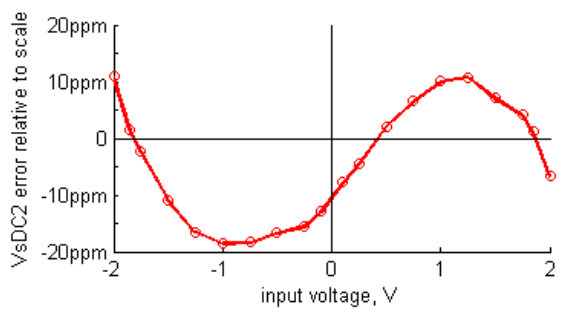

Figure 4: VsDC2 non-linearity versus input voltage.

Rigid timing to reach precise and stable integration interval is a significant condition for accurate measurement. Both devices have complex synchronization logic and can be triggered from a number of external events with uncertainty less than the 2 ns. Integrators stores digital plot of signal and can be used as waveform recorder with 110 dB SNR at 150 kHz bandwidth. Oscilloscope mode of operation is very useful especially during system tuning. Table 1 lists VsDC2 and VsDC3 main features.

Table 1: Parameters of the integrators

	VsDC2 (CAN version)	**VsDC3** (VME version)
# chanles	2	2
Input ranges	±0.2V; ±0.5V; ±1V; ±2V; ±5V; ±10V	±0.2V; ±2V program selectable
SNR at 10 μs at 1 ms at 1 s	 $5{\cdot}10^{-5}$ 10^{-6} $5{\cdot}10^{-7}$	 10^{-5} $5{\cdot}10^{-7}$ $\sim10^{-7}$
Absolute error at 10 μs at 100 μs > 1 ms	 10^{-3} $<10^{-4}$ $\sim10^{-5}$	 10^{-3} $<10^{-4}$ $\sim10^{-5}$
Non-linearity	±20 ppm max	±20 ppm max
From factor	3U 4HP Eurocard	6U 4HP Eurocard

PULSED FIELD MEASUREMENTS

As the example of the digital integrators implementation for pulsed measurements, consider the system for measurement of pulsed magnets of NSLS-II 3GeV-booster. The next magnet parameters were measured:

- Transverse distribution of the first field integral.
- Influence of vacuum chamber on it.
- Field stability.

The system was equipped with 4 VsDC2 integrators, timing and power control electronics. Two ways of transverse distribution measurement has been used: some magnets we processed with long coil, the rest were worked on with PCB coil matrixes. Figure 5 shows BUMP with measuring coil installed on positioning system.

Figure 5: BUMP with coil sensor.

Figure 6 presents first integral distribution for BUMP magnet.

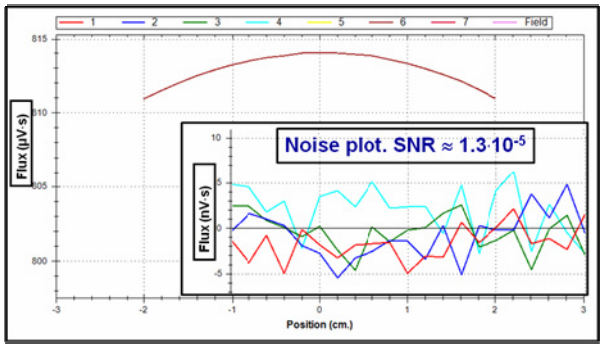

Figure 6: BUMP first field distribution and VsDC2 noise plot.

The whole measuring process was automated. The VsDC2 self noise lead to achieve measurements accuracy close to 10^{-5}.

The induction coil signal and capacitor bank discharge recorded by the VsDC2 are shown on Figure 7.

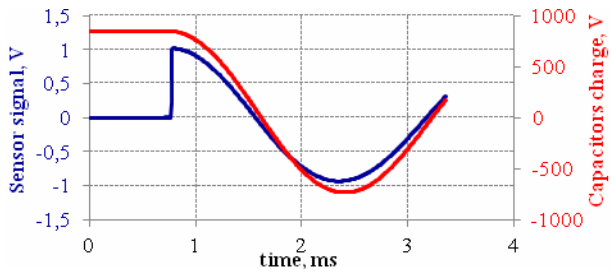

Figure 7: Waveforms of sensor signal.

Oscilloscope mode of operation allows one to tune start/stop integration time, and to study effects of phase delay between the pulsed magnetic field inside and outside the vacuum chamber.

CONSTANT FIELD MEASUREMENTS

To demonstrate constant field measurements application of VsDC's, consider the rotating coils system which was used to adjust and certify quadruples for the NSLS-II main ring. More detailed description of this system is presented in [3]. Two VsDC3 channels are combined together so as the end of the integration in one VsDC3 channel of each module coincide with the start in another. Such combination gives a non-stop measurement of the magnetic flux while coils rotate. The angular position of the coil is sampled every integration start/stop moment. Resulting dependence of the magnetic flux from the angle is used to calculate lens parameters.

Harmonics are calculated from compensated signals, resulting in cancellation of mechanical vibration and power supply noise sources. Figure 8 shows comparison between compensated and original channels.

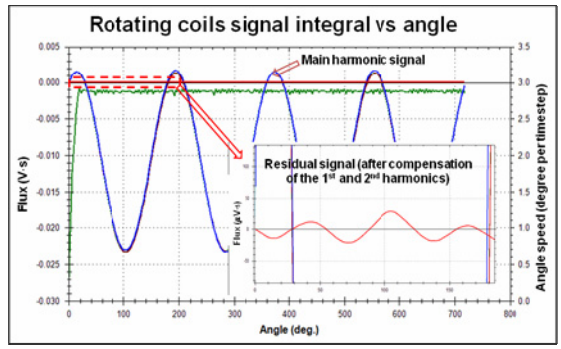

Figure 8: Layout of papers.

The 1st and the 2nd harmonics are compensated more than 100 times. It is possible to see harmonic with the naked eye. This features and outstanding VsDC3 noise performance result in extremely low harmonics noise (repeatability of results). Relative noise is better than 10^{-6} for the typical lens current, figure 9.

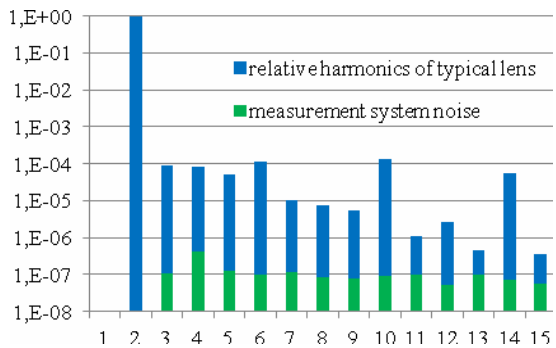

Figure 9: Relative harmonics of lens #9807-0029.

SUMMERY

Digital integrators possess unachievable before combination of high speed and precision. These devices can successfully solve a plenty of task in the sphere of magnetic measurements both constant and pulsed fields. Measurements accuracy better than 10^{-5} could be achieved.

REFERENCES

[1] http://www.metrolab.com/index.php?id=24
[2] V.A Kotelnikov, "On the carrying capacity of the "ether" and wire in telecommunications", Material for the First All-Union Conference on Questions of Communications, Izd. Rep. Upr. Svyazi RKKA, Moscow, 1933.
[3] A.Batrakov et al,. "Stand for precise measurements of magnetic lenses for synchrotron light sources NSLS-II", these proceedings

THE SYSTEM FOR CONTROL OF AN ELECTRON BEAM WELDING MACHINES

V.V. Repkov, E.A. Kuper, A.U. Protopopov, A.A. Zharikov,
Budker Institute of Nuclear Physics, Novosibirask, Russia

INTRODUCTION

A cathode unit of electron beam welding is a device that generates beams of electrons of required intensity.The report examines the main issues, that had to be overcome in developing this unit.

-the electronics of the unit is under cathodic potential of the accelerating voltage (60kV), therefore it required solving the problem of power transmission and control signals.

- the volume of the device had to be minimized as the room to put the electronics was limited.

- the electronics must be resistant to high voltage breakdowns as when breakdowns there may be a voltage pulse of 60 kV with energy to 20 J in any electrode of the cathode unit.

- to control the current of the electron beam (welding current), a linear amplifier, which produces the voltage on the control electrode in the range 0 – 4kV, was developed. The amplifier bandwidth is 1 kHz.

- to control the current beam, current intensity, and to control the parameters of the gun, a specialized controller was developed. The connection of the controller with a computer is carried out with the help of optical links.

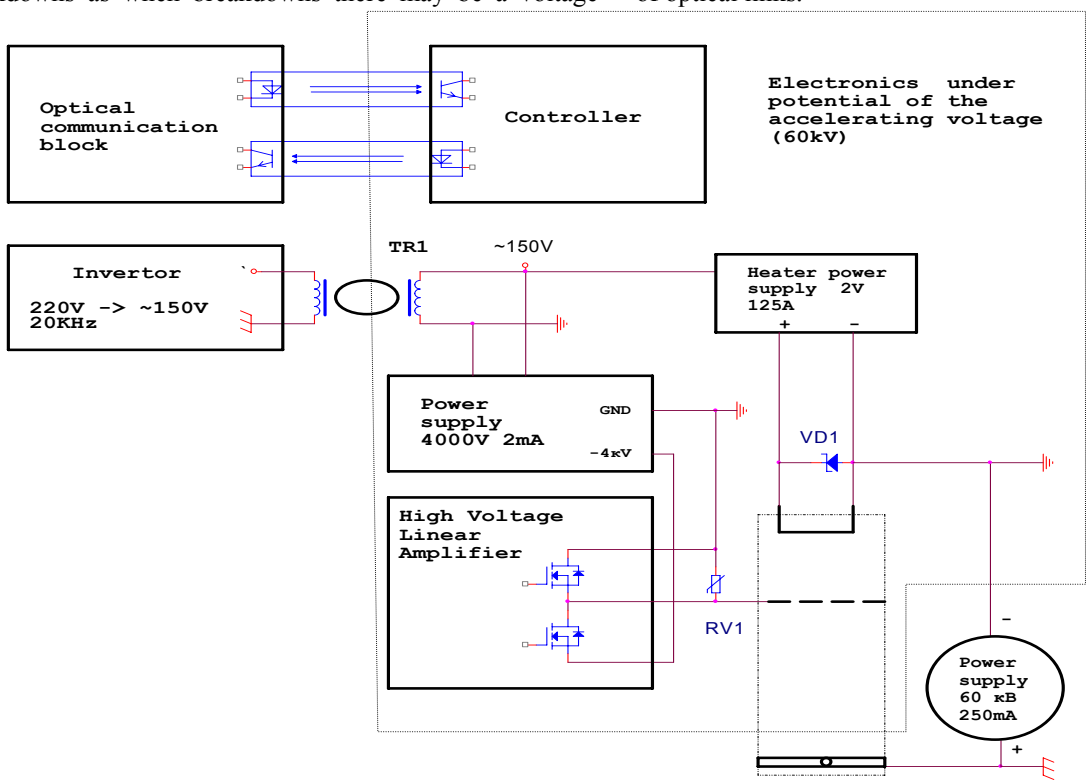

Figure 1: Block diagram of the electronics of the cathode unit.

TRANSFORMER

Power required to operate the power supply is passed through a special isolation transformer TR1. Voltage of isolation between the primary and secondary windings of the transformer is 100kV.

Transmission capacity is up to 300W. The transformation ratio is 1:1. It should be noted that the voltage between the primary and secondary windings is 60 kV, so structurally transformer consists of two cores. The primary winding was wound on one core, the secondary winding is on the other one. Coupling between cores is carried out by the volume coil. It is easier to provide high-voltage isolation.

CONTROLLER

Management of all parts of the unit is carried out by a specialized controller made with a microprocessor ADUC 842.

The controller sets the following parameters:

- The current gun (welding current), is set during the welding process in the range of 0 - 250 mA. The

voltage on the control electrode varies from -4kV to zero. During setting and testing the voltage can be set directly on the control electrode.

- Filament current is regulated from 0 - 125A. Operating filament current is usually in the range of 50 - 100 A, it may depend on the type of cathode, and even the degree of deterioration of the cathode

During the welding process, the controller measures the following parameters: welding current, the voltage on the control electrode, heater voltage, control electrode current, and the stability of power supply.

The permanent control of the welding current is required in order to make sure that the session of welding is for a given scenario. The cathode may lose the emission as a result of "poisoning" or deterioration, in this case the gun will not be able to produce set current.

Current control of control electrode is necessary for the early detection of pollution of gun insulators by welding products. The fact is that, when the pollution, the resistance of the insulators falls and there comes a moment when the power supply (4kV) is not able to maintain the blocking voltage on the electrode. Thus there is an uncontrolled gun current (welding). Obviously, this is an emergency, which is inadmissible to allow.

Control of the heater voltage gives the information concerning the degree of wear of the cathode and thus predicts its remaining life time.

Communication with the controller is carried out by fiber-optic cables. Electric-to-optical conversion and back is exercised by the block of optical communications – OCB.

All in all between the unit of optical communication and the controller of the gun there are following fiber-optic cables:

- Two cables for CAN interface through which information is exchanged.
- Two cables for RS232 – are used to set-up and test the equipment.
- Cable lock current gun on an external signal, bypassing the processor
- Reserve cable.

THE HEATING POWER SUPPLY

As a regulatory element in the power supply a magnetic amplifier is used. There are several reasons for this decision:

- the magnetic amplifier controls the amplitude of the high frequency voltage, which is supplied by an isolating transformer, so there is no need of additional converters.
- the scheme operates as a current generator, and is protected against overload and short circuit
- the scheme is resistant to high voltage breakdown.

THE HIGH-VOLTAGE MODULATOR

To adjust the welding current in the specified range (0 - 250 mA), the voltage on the control electrode should vary in the range 0 - 4 kV. Frequency band can reach 1kHz. To solve this problem a high-voltage linear amplifier was developed.

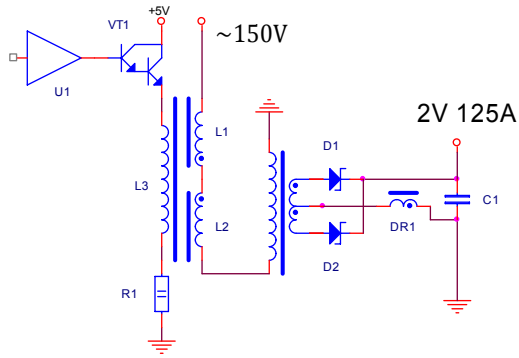

Figure 2: The heating power supply.

The output voltage of the amplifier must be changed from 0 to 4kV

Since the industry does not produce low-power transistors and of voltage higher than 1500 volts, it is necessary to set these transistors in series. It causes 2 problems. First, we must make sure that the voltage at each transistor does not exceed its certified value, and second, we need the scheme of transistor to control in the chain.

The basis of the scheme consists of two identical parts, each of which consists of four series-connected field-effect transistors. Varistors RV1-RV8 protect transistors from overvoltage. Resistors R11 - R18, and capacitors C1 - C8 provide DC and AC mode of transistors.

Due to the fact that the voltage of power supply is negative, we have to manage both stages through optocouplers U4, U5. To power the output transistor of optocouplers, DC-DC converters with isolation 6 kV (U2, U3) are used.

IC U1 - error amplifier. The control signal goes through resistor R1 to the input of this chip, and the feedback is taken either from the amplifier through resistor R2, or with a current sensor through resistor R3. Thus, the amplifier can operate in the constant current mode of welding machine or in the constant voltage mode on the control electrode.

This amplifier allows to stabilize the current of the welding machine in the band up to 1kHz. In the mode of constant voltage on the control electrode pulses 200mks and amplitude of up to 4 kV can be produced.

REFERENCES

[1] A. Bryazgin, B. Factorovich, E. Kuper, V. Repkov, Modulator for the electron injector of the industrial Accelerator ILU-10, RuPAC 2006 proceedings.

[2] Yu.I.Semenov, et al., 60 keV 30 kW electron beam facility for electron beam technology. Proc. Of EPAC08, Genoa, Italy

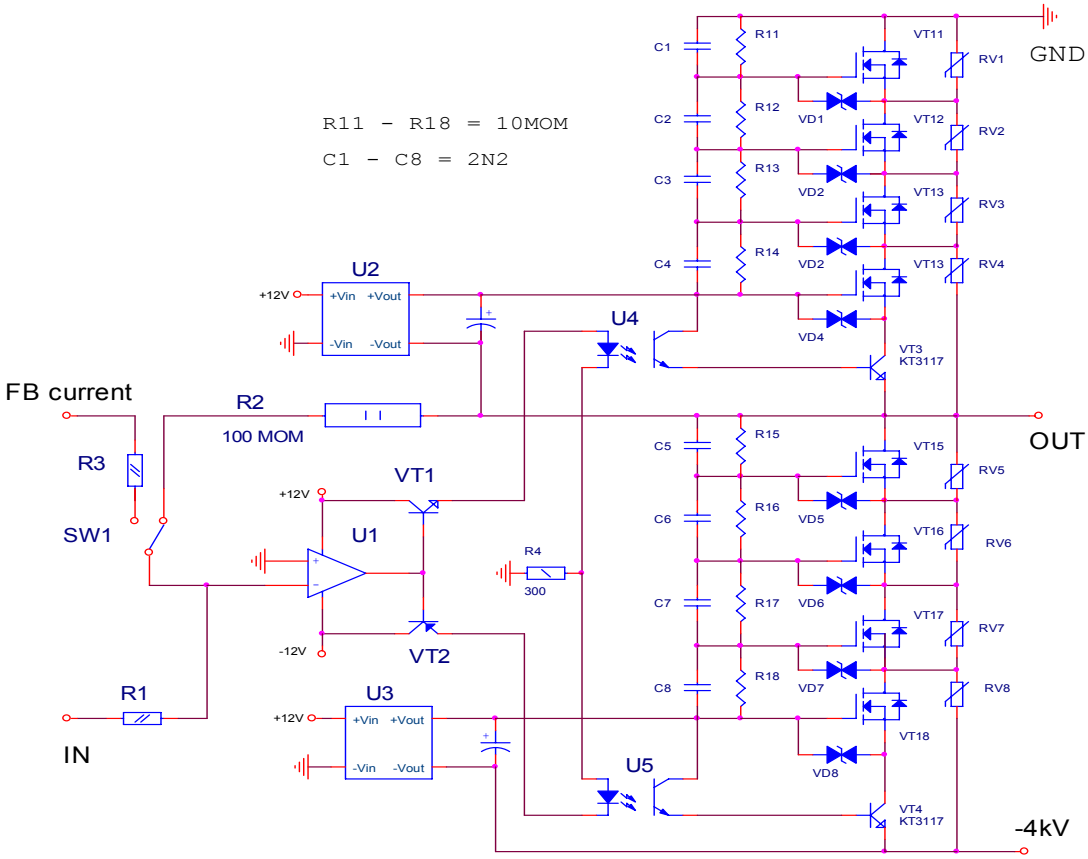

Figure 3: High voltage amplifier.

OPTIMIZATION OF THE NEGATIVE HYDROGEN ION BEAM INJECTION INTO THE TANDEM ACCELERATOR WITH VACUUM INSULATION

A. Makarov#, V. Aleynik, A. Kuznetsov, I. Sorokin, S. Taskaev, M. Tiunov,
BINP SB RAS, Novosibirsk, Russia,
Bashkirtsev, I. Shchudlo, Novosibirsk State Tehnical University, Russia

Abstract

The beam of negative hydrogen ions is injected into the tandem accelerator with vacuum insulation in order to obtain high-current proton beam. To accurately direct the beam into the accelerator the magnetic focusing lenses are used. In this paper it is described the design of the special beam detector mounted in front of the first accelerating electrode and intended to measure beam profile and the current density. The results of measurements of the dependence of the current density on the power of the magnetic focusing lenses are shown. The parameters of the beam resulting in the best agreement of calculation and experiment are specified. The optimum focusing mode to inject the negative hydrogen ions into the accelerator is determined.

INTRODUCTION

Negative hydrogen ions are injected into the accelerator and accelerated up to 1 MeV by potential applied to the electrodes, then H^- turn into protons in the charge-exchange target and at last the protons are accelerated up to 2 MeV by the same potential [1].

Although the accelerator is designed to obtain a 5 mA proton beam, but in the experiments carried out in 2008-2010 we usually got the proton beam currents of hundreds of microamperes, and occasionally for a short time - a few milliamps. Such a current was enough to demonstrate the generation of neutrons [2] and monochromatic gamma-quanta [3], but it is clearly not sufficient for the thorough BNCT research and other applications.

To clarify current-limiting reasons, a detailed study of the transportation of negative hydrogen ions have been carried out using multichannel detector mounted in front of the first accelerating electrode of the accelerator.

EXPERIMENTAL SETUP

The scheme of the experiment is shown on Fig.1. Negative ion beam with energy of 21 keV, current up to 5 mA and angle distribution of 100 mrad is created by surface-plasma source with Penning discharge and hollow cathode. After turning at an angle of 15 degrees the peripheral part of the beam is cut off by 28mm cone diaphragm and the rest center of the beam enters into the transport channel.

Next, the expanding beam is focused by two magnetic lenses. Each of the magnetic lenses is powered by an independent power supply and currents of lenses may be different, but in our experiments they were set the same and opposite. For a typical current of 50 A maximum magnetic field on the axis of the lens has a value of 2.1 kG. Following the lenses it is installed magnetic corrector. Each of the two elements of the corrector consists of two pairs of coils, powered by independent power sources. The angular displacement of the beam from each pair of coils is characterized by 10 mrad/A.

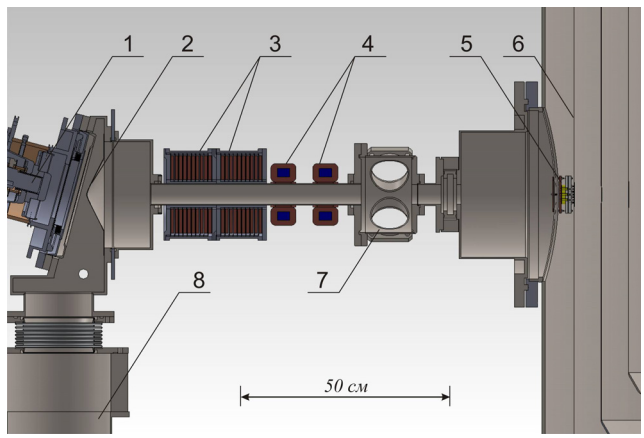

Fig. 1. Experimental setup: 1 - the source of negative hydrogen ions, 2 - cone aperture, 3 - magnetic focusing lenses, 4 - corrector, 5 - beam detector, 6 - the first electrode of the accelerator, 7 - diagnostic chamber, 8 - TM pump.

Focused and corrected the beam then strikes the detector mounted in front of the accelerator so the surface of the beam receiver is 47 mm in front of the surface of the first electrode. The detector is centered along the transporting channel using a laser (Fig. 2).

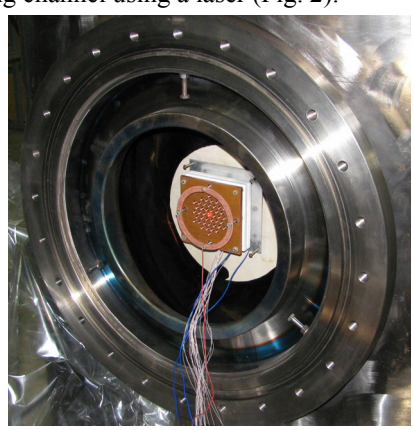

Fig. 2. Photo of the beam detector.

Tandem accelerator with vacuum insulation is characterized by rapid acceleration and strong input electrostatic lens. Entering of the beam into the accelerator assumes it refocuses in front of the input lens, i.e. prior to the first electrode. The desire to measure experimentally beam parameters in this area has determined the choice of the detector location. Also it should be kept in mind that during the experiment the voltage on the accelerator and, accordingly, on the first electrode was not supplied.

THE DESIGN OF THE BEAM DETECTOR AND SOFTWARE

The main element of the detector is a copper plate having size 10x10 cm, 6 mm thick, serving as the receiver of the beam (Fig. 3a). To prevent the secondary electron emission and to measure the ion current properly the grid is mounted under suppressing potential. In the copper plate 43 holes of 5 mm diameter are made. The distance between the centers of adjacent holes is 7.5 mm. Behind each hole it is installed a copper Faraday cup, 10 mm high with an internal diameter of 5 mm. All cups are mechanically fixed between two square insulating plates and centered to the holes of the copper beam receiver. Peripheral Faraday cups are combined into 3 groups of 8 cups in each, as shown on Fig. 3b.

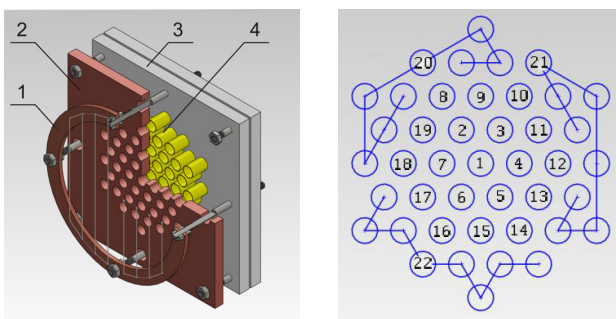

a b

Fig. 3. a) Beam detector: 1 - suppressing grid, 2 - copper plate, 3 - insulating plates, 4 - Faraday cups. b) Numbering of detector channels.

Currents taken from the copper beam receiver, from 19 central Faraday cups and 3 groups of peripheral cylinders through the 24-pin vacuum socket were supplied to the inputs of 32-channel ADC PCI-1713 (Advantech, Taiwan). Shunt resistance at the input of the ADC had a value of 1 kOhm.

ADC is installed into a PCI slot in the computer placed near the accelerator. The computer is connected to the network and using the server transmits an array of digitized voltage values to the client interface in the control room. Client interface software recovers the current density distribution of the beam by voltages of ADC channels. Also in real time it is constructed a normal distribution approximation of the discrete current distribution using a Levenberg-Markvadt algorithm [4]. Application of the algorithm for the two-dimensional distribution and necessity for assuming the presence of a maximum in the center of the beam limits the reliability of this approximation. However, the use of this approximation, as it turned, became a convenient operational tool for estimation of the beam size and its position in real time. Example of the user interface of the beam registration program is shown on Fig. 4.

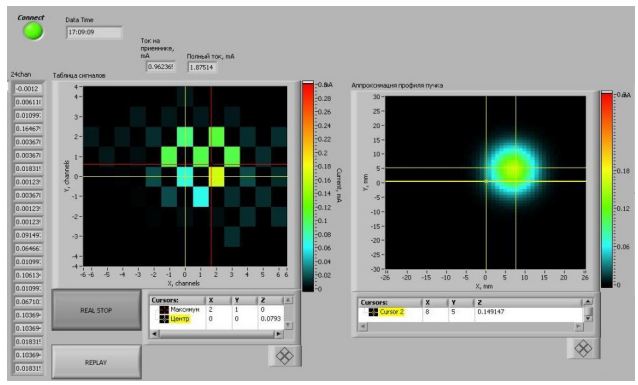

Fig. 4. User interface of the beam registration program.

RESULTS AND DISCUSSION

In Fig. 5 shows the current-voltage characteristics of the detector, measured at focusing lenses current of 46 A.

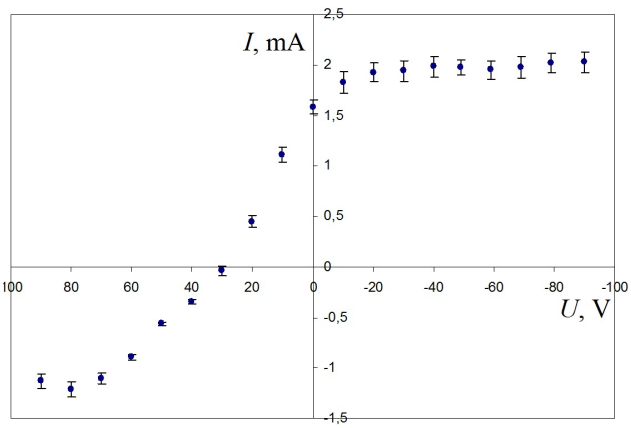

Fig. 5. Dependence of the total current recorded by the detector on the grid voltage.

It is determined that the coefficient of secondary electron emission is 1.6±0.2 and the suppressing grid voltage must be at least -20 V for accurate measuring of the beam current.

All currents in Faraday cups were normalized to the total current, and then maximum values were taken and analyzed for reliability. These measurements were taken at different currents in magnetic lenses - from 40 to 62 A. It is found that the maximum focusing is achieved with a lens current of 50 A. In this case, single 5 mm hole of the detector gets 57% of the beam.

Fig. 6 shows the experimentally measured maximum current (normalized to the total), recorded by one Faraday cup with a diameter of 5 mm, with different currents of magnetic focusing lenses. Also Fig. 6 shows the calculated dependences of the percentage of the current in the axial region of 5 mm in diameter, assuming the "cold"

and "hot" beam, when the transverse temperature on the plasma boundary of the ion source is set to either 0 eV, or 10 eV respectively. The calculations assumed full compensation of the space charge of the beam from the output of the ion source to the Faraday cup. It can be seen that the calculation of "cold" beam corresponds much better to the measured values.

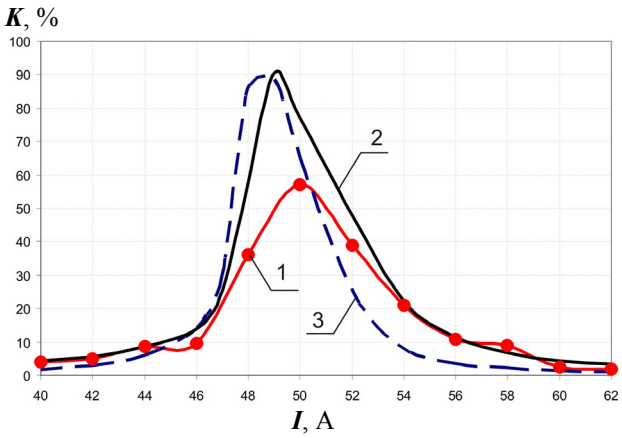

Fig. 6. The dependence of the percentage ***K*** of beam current in the axial region with a diameter of 5 mm on the current of magnetic focusing lenses ***I***: 1 - measured, 2 - calculated at T = 0 eV, 3 - calculated at T = 10 eV.

Thus, we can conclude that the study has helped to clarify the parameters required for the proper calculation, and to improve the transportation of negative hydrogen ions.

REFERENCES

[1] B. Bayanov, et al., NIM A 413 (1998) 397.
[2] A. Kuznetsov, et al., Tech. Phys. Lett. 35 (2009) 346.
[3] A. Kuznetsov, et al., NIM A 606 (2009) 238.
[4] P. Gill, et al., Practical Optimization, (London: Academic Press, 1981), 134.

DEVELOPMENT OF THE NEW CONTROL SYSTEMS FOR JINR e- LINAC ACCELERATOR TEST-BENCH

M.A. Nozdrin#, N.I. Balalykin, V.F. Minashkin, V.Yu. Schegolev, G.D. Shirkov, G.V. Trubnikov,
JINR, Dubna, Russia

Abstract

Linear accelerator test-bench in the Joint Institute for Nuclear Research is based on the part of the accelerator complex which was transferred to the possession of JINR by The National Institute for Subatomic Physics (NIKHEF, Amsterdam). Analysis of the transferred accelerator equipment has shown that full re-engineering is required for its control systems; all other systems are in good condition and have considerable endurance. Results of development and creation of the Electron Gun Control System (EGCS), Video and Analog Signals Control System (VASCS) and Automatic System of Radiation Safety Control (ASRSC) are presented. These systems allowed achieving a commissioning of the first accelerator section of the bench with current of 3 mA in 1 μs pulse and at beam energy of 23-25 MeV.

INTRODUCTION

JINR linear accelerator test-bench is based on the so-called Medium Energy Accelerator (MEA) equipment. MEA [1] was developed by Haimson Research Corporation (USA) in 1969-1974, built in 1975-1978 and put into operation in 1978. In the end of 1990s the accelerator complex was transferred to JINR.

A set of projects for realization of the base of the test-bench is proposed:

- Free electron lasers (FEL) complex. Test-bench construction allows beam extraction with energy of 15 to 200 MeV. Beam with such energy can be used for infrared to ultraviolet FEL radiation generation with wavelength of 300 μm to 200 nm. First undulator of the IR range (transferred to JINR by NPO of automatic systems, Samara; E = 25 MeV, λ = 18.7 μm) is going to be installed.
- Testing of the accelerating structures and diagnostics, e.g. intensity monitors for short-pulse facilities like ILC [2]. This issue may require replacement of the current gun by the photocathode gun.
- Volume FEL with centimetric to infrared energy range creation [3].
- Experiments with RF gas discharge in quasi-optical cavity to confirm nuclear fusion in resonant streamer. [4]

At the present time the injector (composed of electron gun, chopper, prebuncher and buncher) and the first accelerating section are assembled and put into operation. Schematic view of this setup is presented in Fig. 1.

Most of the transferred control systems were obsolete and complete renewal of control equipment was needed. Results of the development of the new control systems are described in this paper.

ELECTRON GUN CONTROL SYSTEM

Triode type DC electron gun [5, 6] with an impregnated thermionic cathode (W with 20% Ba, Ca and Al oxides) is being used at the test-bench. Gun focusing system consists of extractor electrode and 15 anodes with forced resistive (R = 200 MΩ) potential distribution (about 30 kV per interval). The voltage of the first focusing electrode can vary from 12 to 30 kV. Electron gun control system (Fig. 2) consists of following components:

- ICT (Insulating Core Transformer) power supply unit provides cathode voltage of -400 kV with stability of $10^{-4} – 10^{-5}$.
- Cathode electronics unit allows remote control of the gun.
- Computer with the GunCtrl program provides interface with the cathode electronics.
- Communication line consists of protocol converters and fibre-optic cables.

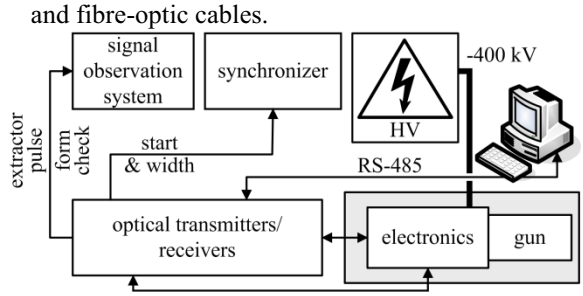

Figure 2: Scheme of the Electron Gun Control System.

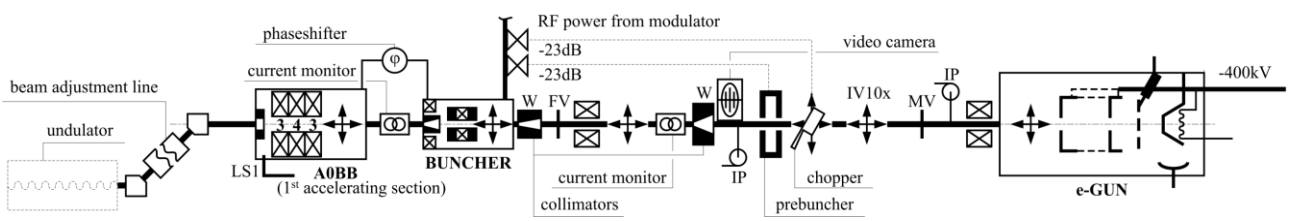

Figure 1: Schematic view of the injector and 1st accelerating section.

#nozdrin@jinr.ru

Cathode Electronics

Cathode electronics comprises:

- Gun controller board designed for connection with control computer, reference voltages assignment and main parameters of the gun control.
- 50 kHz supply board converts input AC voltage of 187 V (50 Hz) to AC voltage of 2x65 V (50 kHz). This board provides required supply voltages to all cathode electronics elements.
- Filament supply board controls cathode filament heating current.
- Extractor pulser module provides required gun unlocking pulse (from -400 V to +5 kV).
- Focusing electrodes board controls gun first focusing electrode voltage.

GunCtrl Software

GunCtrl (Fig. 3) is the software developed to provide a user with friendly interface between the gun controller and system operator. It is programmed in Object Pascal using Turbo Delphi software and runs on Windows XP operating system.

This software allows to set the reference voltages for filament heating, first focusing electrode and extractor.

Operator can also watch real voltage and current of filament heating, first focusing electrode voltage, pressure and temperature of the SF_6 insulating gas, cathode electronics board voltage and cooling system status.

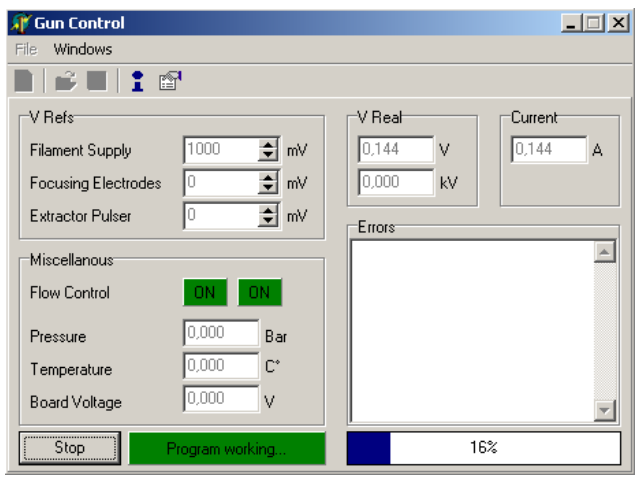

Fig. 3: Main window of GunCtrl software.

VIDEO AND ANALOG SIGNALS CONTOL SYSTEM

Video control system consists of four cameras:

- IP-camera Aviosys 9060 A is used for accelerator room general surveillance.
- IP-camera Aviosys 9000 is installed next to the prebuncher to observe initial beam profile. The screen position in the beamline can be controlled remotely from the control room. IP-cameras are connected to the video control system computer by LAN. Aviosys Surf16Ch software is used for imaging.
- Sun Kwang SK-2005 PH analog camera is installed next to the first bending magnet.
- Q-cam QM-68PAT analog camera is installed next to the second bending magnet, just before the position where the undulator is going to be installed. Both analog cameras are connected to the video control system computer using BeholdTV 409 FM TV-tuner (with manual switching so far).

The video and analog signals control system also includes several current monitors, faraday cup and two oscilloscopes (200 MHz Tektronix and PC-scope Velleman PCS500) for their signals representation.

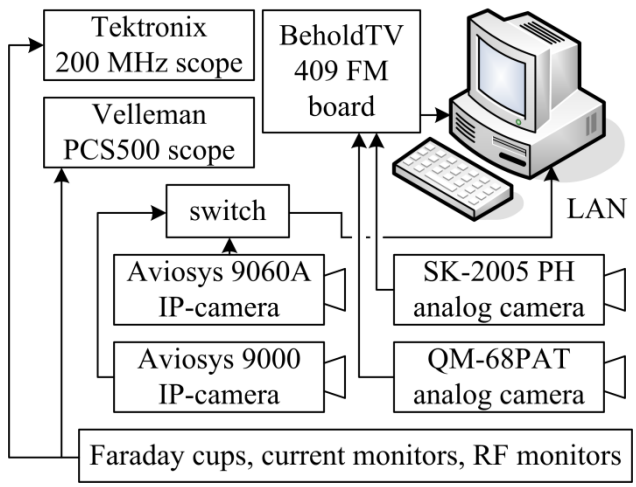

Fig. 4: Scheme of the Video and Analog Control System.

AUTOMATIC SYSTEM OF RADIATION SAFETY CONTROL

This system is designed to ensure radiation safety for test-bench personnel during regular operations and in emergency cases. The radiation control devices of the MEA accelerator were not transferred to JINR since that equipment had not been certified for use in Russia. More detailed information on system requirements and setup can be found in [6].

The main source of radiation during bench operation is background and emergency losses of an electron beam, which generate the bremsstrahlung with a wide energy spectrum. In addition, if the photon energy is higher than the reaction threshold (12-14 MeV), secondary neutrons (photoneutrons) appear. Beyond the biological shielding of the accelerator room, the radiation environment will be determined by long-range radiation: high energy photons and photoneutrons.

During accelerator shutdown the radiation environment for the personnel will be determined by the induced gamma and beta activity of the equipment exposed to high-energy photons and neutrons. The formation of loose contamination on the equipment and of radioactive aerosols in the air is also probable.

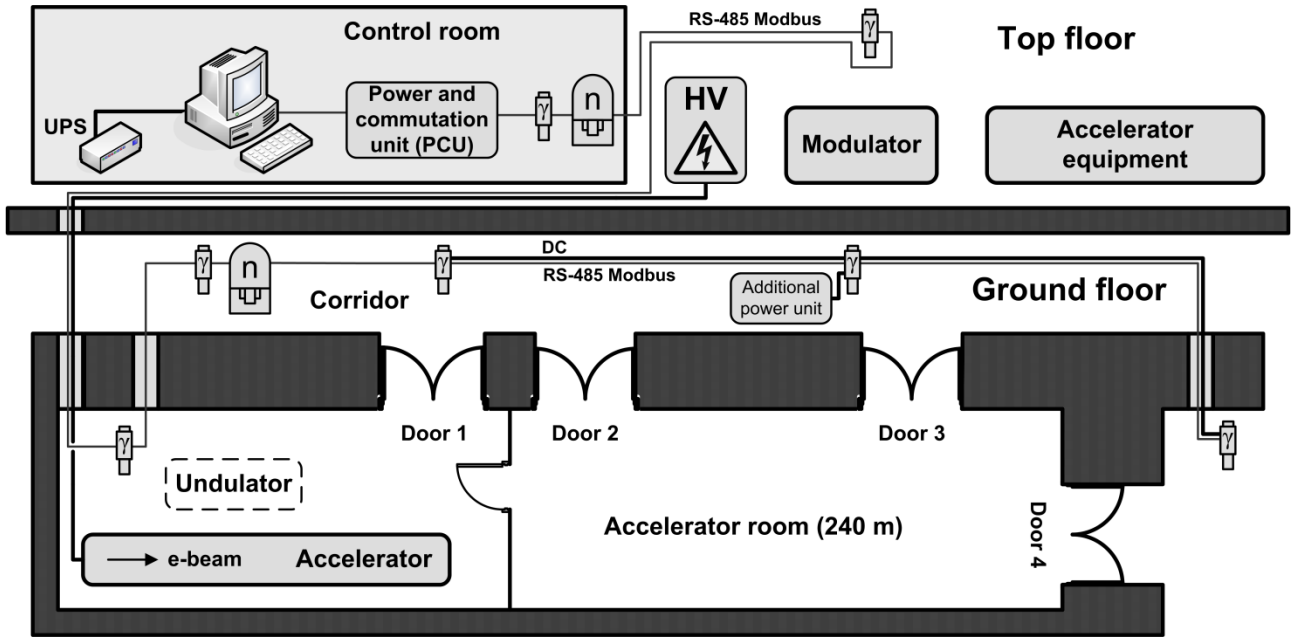

Fig. 5: Scheme of the Radiation Control System.

Radiation Control System Hardware

Main devices of the Radiation Control System are 7 scintillation detector units and 2 neutron radiation detectors. Scheme of the detectors layout is presented in Fig. 5. All this detectors are connected among themselves and with the Power and Commutation Unit (PCU) by the serial RS-485 communication link supporting the Modbus RTU communication protocol. PCU is connected to the control computer by the serial RS-232 communication link.

Owing to the pulse character of the accelerator operation (a relative pulse duration of $1 \times 10^4 - 3 \times 10^5$ at a pulse duration of 1 – 10 μs) it will be necessary to correct the indications of the gamma-detectors on the basis of the readout of the DKS-AT1123 portable X-ray and gamma-radiation dosimeter, which is capable of adequately measuring the dose rate of pulse radiation with a minimal pulse duration of 10 ns.

RadCtrl Software

This software (Fig. 6) is programmed in Object Pascal using Turbo Delphi software, runs on Windows XP operating system and performs the following functions:

- Displaying the current readout of all radiation detectors in both numeric and graphic representation.
- Signalization when one of the two threshold values ("yellow" and "red") is crossed.
- Signalisation when a detector is disconnected.
- Displaying the object's scheme as appropriate.
- Displaying the measurements archive for a chosen detector as appropriate (archive date can be saved in MS Excel format).
- Changing of the threshold values and the chart representation (linear/logarithmic).

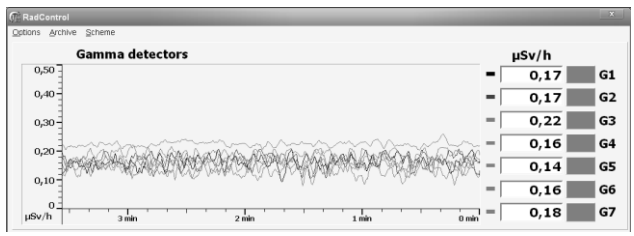

Fig. 6: Part of the main window of RadCtrl software with gamma-detectors readout (background radiation).

CONCLUSION AND OUTLOOK

At the end of 2011 test launch of the accelerator was performed. The pulse current was 3 mA (with the pulse length of 1 μs) with the energy of 23-25 MeV. All control systems worked in normal mode.

At the present time the IR undulator is going to be installed. It will provide first bench capabilities for users. All described control systems are mature and ready for the operation in regime of the FEL radiation generation.

REFERENCES

[1] Kroes F.B., Electron linac MEA, Compendium of scientific linacs, LINAC'96, 1996, p. 151.
[2] N.I. Lebedev, A.A. Fateev, Physics of Particles and Nuclei Letters, Volume 5, Number 7 (2008), 609-611.
[3] V.G. Baryshevsky et al., Nuclear Instruments and Methods in Physics Research B 252 (2006) 86-91.
[4] V.S. Barashenkov et al., Technical Physics, Volume 45, Number 11 (2000), 1406-1410.
[5] Kroes F.B. et al., Improvement of the 400 kV linac electron source of AmPS, Proc. of EPAC'92, p. 1032.
[6] N.I. Balalykin et al. Physics of Particles and Nuclei Letters. Volume 7, Number 7 (2010), 525-528.
[7] N.I. Balalykin et al. Physics of Particles and Nuclei Letters, Volume 9, Number 4-5 (2012), 452-455.

PRECISION THERMOSTATIC CONTROL FOR LUE-200 ACCELERATOR SECTION

V.N. Zamriy, A.P. Sumbaev, JINR, Dubna, Russia

Abstract

A two-loop thermostating system for the accelerating section of the S-band electron linac has been developed. To provide the required heatsink path and an opportunity of re-changing the section while altering the acceleration mode, the temperature in the system of the thermostat and the cooling water channel in the external contour are regulated. To achieve the required precision and stabilization time of the temperature of the thermostat having extended waterways (~70 m), the method of proportional-integral-derivative (PID) control has been applied. The programmed controller allows one to adapt the system for several operating modes: the fast warming up, operated establishment of temperature and thermostabilization, change of the preset temperature of the thermostat. It provides the reduction of setting time of the thermostatting regime, and also of minimization of errors and power consumption of the thermostat.

INTRODUCTION

The LUE-200 linac based on the traveling wave (2856 MHz) is used in IREN installation as the driver of a pulse photoneutron source [1]. For the LUE-200 thermal energy losses on RF-warming up of walls of the accelerating structure are about 30% of RF-power reached from the klystron, and in dependence on the repetition rate of cycles the losses can reach 10÷12 kW. The change of a of the accelerating structure temperature mode leads to displacement of its resonant frequency that results in the following: decreasing the mean energy of the accelerated electron beam, increasing the beam energy spread out and, eventually, decreasing the intensity of the neutron flux of the source. Influence of fluctuations of the temperature on the electron beam and, as a result, on the intensity of neutron flux is illustrated in Figs. 1 and 2, that was observed while adjustment of the accelerating section. Fluctuations of intensity of the neutron flux (Fig. 2) correlate on time with temperature deviations ±0.3°C (Fig. 1), repeating with a period of time of ~10 minutes.

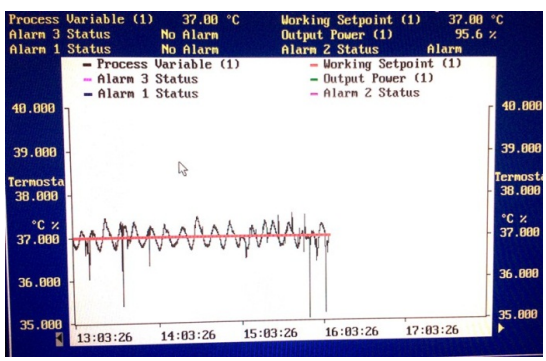

Figure 1: Fluctuation of the thermostat temperature.

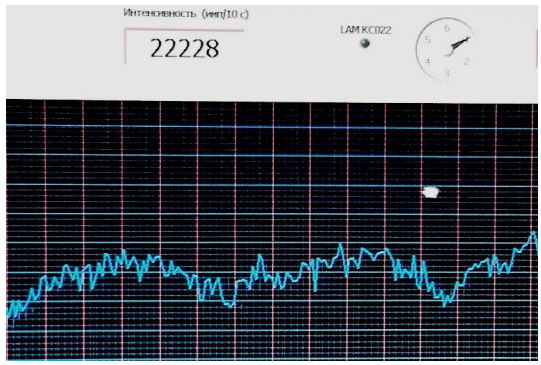

Figure 2: Fluctuations of neutron intensity.

THERMOSTATIC CONTROL SYSTEM

The Structure Chart of the Thermostatic Control

The structure of system of the thermostabilized cooling for the accelerating section is presented in Fig. 3.

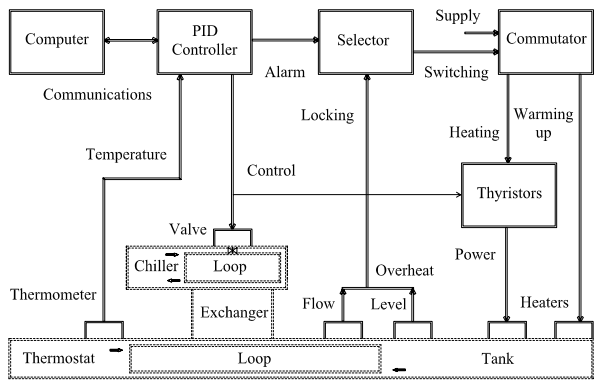

Figure 3: The system of thermostatic control.

The thermostat loop connects a tank of water heating, the thermostat, the heat exchanger, and also the built-in detector showing the lack of the water flow. The thermometer is installed at the exit of the pumped water from the thermostat. In the tank there are heaters and sensor controls of emergency overheating and the water level. The cooling loop joins a linac chiller and the heat exchanger, and, also, the built-in valve and the electric drive. Besides, the equipment for water mains has casual valves, pumps, etc.

The PID-controller (type 906S Eurotherm Controls) has measurement lines with the Pt-resistance thermometer and a control line. At the length of lines (~ 70 m) under the conditions of high-intensity noises the raised interference protection of the control unit is provided. The

relays of the alarm system supervising the temperature conditions manage the mode choice.

Thyristor units (type 425A Eurotherm Automation) and the electric driven valve motor (type VBA-90 Clorius Controls) control the output power and the water flow.

The mode selector has been developed for diagnostics of the alarm state and also of the possible interlocks from thermostat warning devices. The unit provides turning on, checking out, heating interlock, and also mode switching. The commutator was built for switching the three-phase supply for thyristor units and heaters. The solid-state relays commutate the heating supply and warming up.

The computer and the adapted program [2] supplement the controller while adjustment of the system configuration and parameters. The program supports data accumulation and graphic representation [3] of thermostatic control processes (Fig. 4).

Figure 4: The monitor of the thermostatic control.

The process variable is shown while warming up, temperature settling and stabilising on the working setpoint. Change of the status of the alarm leads to switching off the warming up. Then the temperature goes to the preset level.

Basic Control Modes and Processes

The system controls not only heating of the distilled water, submitted to the thermostat, but also water flowing in the cooling system. To reduce the time of temperature setting in addition to PID-control, the fast warming up is carried out. The checking of temperature conditions and the choice of modes of the preliminary warming up, operated heating and thermostabilization, are performed for this purpose (see Table 1).

Table 1: Basic Control Modes and Processes

Mode	Temperature	Process
Warming up	Below Threshold	Sped Growth
Operated Heating	Up to a Setpoint	Settling
Thermostabilization	Near the Setpoint	Maintenance
Warming up Selection	Threshold 1	Mode Choice
Heating Selection	Threshold 2	Mode Choice
Heating Protection	Alarm	Locking

An impotent condition of mode selection is the predetermined level of temperature, a temperature threshold or an alarming state. Warming up or heating switch-off happens at the excess of the threshold temperature. Their reclosure is possible when the temperature is below the threshold on a hysteresis specified value. The programmed switch-off of heating protects the microwave section against excessive heating. Protection of turning on of the heating is possible at the diagnostic of conditions of emergency signalling and interlocking. At the chosen process conditions there is a speeded up rising of the temperature, warming up switch-off, smooth settling and temperature maintenance at the preset level, or interlocking of the thermostat heating.

Operating Sequence

The water temperature at the thermostat exit is measured with a sampling rate of 10 Hz. The controller analyzes the temperature change (concerning the predetermined level) and appoints the necessary PID regulation. By a warming up mode (at the beginning) all electric heaters of the thermostat are completely powered up, and the cooling valve is closed, therefore there is the fastest growth of temperature of the thermostat. At the subsequent settling and temperature stabilising the power of controlled heating decreases and the valve of cooling of the heat exchanger (used for the water temperature drop after the thermostat) is slightly opened. The settling time and the errors depending on inertia of the thermostat are minimised by adjustment of parameters of PID regulation. While heat-setting the steady-state level of temperature (and balance of heating power and compensating cooling) is maintained. Increase of RF heating-up level is compensated by the thermostabilized cooling system.

Figure 5 presents processes of establishing the temperature level and thermostabilization of LUE-200 accelerating section.

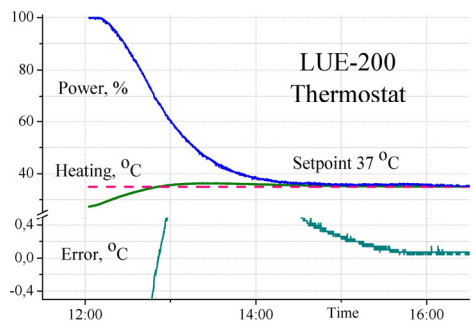

Figure 5: Processes of precise thermostabilization.

Changes of the controlled power and heating temperature (concerning the setpoint of 37°C) provide temperature error reducing up to 0.1°C.

Main Parameters of Thermostatic Control

The main system parameters, their typical values and some predetermined conditions of thermostatic control for

the first LUE-200 section are given in Table 2. Variations of the temperature settling time and the bound errors depend on the regime variations of the accelerating section and cooling conditions.

Table 2: Parameters of Thermostatic Control

Parameter	Value	Condition
Thermostat Temperature	37°C	Working setpoint
Warming up Threshold	36.6°C	Below Setpoint
Settling Time	50÷200 min	Related Error
Error of Settling	0.1÷1°C	Time of Settling
Error of Stabilizing	Less 0.1°C	Integral time
Heating Threshold	40°C	Above Setpoint
Power of heating	0÷9 kVA	3 Heaters
Power of Warming up	6÷15 kVA	5 Heaters
Controlled Cooling	0÷3 kG/cm^2	Pressure

PID-regulating allows one to minimize the period of time and errors of temperature settling, and as the Table 2 shows, - to multifold improve the quality of regulating.

THE CONCLUSION

The precision system of a thermostatic control based on methods of PID regulation allows one to reduce errors of temperature setting and stabilization at the level below 0.1%.

The controlled heating and switching of warming up allow one to increase the range of the thermostat power from 0 to 15 kVA and in the result - to reduce the influence of instability factors. The power stock makes it possible to reduce the warming up of the period of time by 1.5÷2 times. Application of warming up and two loops for heating and cooling enable one to reduce the settling time of temperature and also the thermostat power consumption.

The system of thermostatting of the section is used in regular operating modes of the linac, both at short-term setting cycles, and at the long periods of operation.

The further development of the systems for the first and then - second accelerating sections of linac is related with step-by-step escalating of the beam power and frequency of start-up of the accelerator. The growth of the RF warming up accompanying the above mentioned, requires to extend the power regulation range and its adapted algorithms.

REFERENCES

[1] A.V. Belozerov et al., Physical Startup of IREN Facility. Physics of Elementary Particles and Atomic Nuclei, Letters, **7**, №7. JINR, Dubna, 2010, p. 923.

[2] V.A. Belkovets et al., System of Thermostabilization for Section of Accelerator. XVII International Symposium on Nuclear Electronics (Varna, 1997), Proceedings. JINR, D13-98-66, Dubna, 1998, p.233;

[3] V.N. Zamrij, Data Acquisition Electronics with Timing for Control of the IREN Test Facility. XVIII International Symposium on Nuclear Electronics & Computing (Varna, 2001), Proceedings. JINR, D10,11-2002-28, Dubna, 2002, p. 235.

ACCELERATION OF LOW-CHARGE KRYPTON IONS IN THE CYTRACK CYCLOTRON

Yu. N. Denisov, G. A. Karamysheva, O. V. Karamyshev
Joint Institute for Nuclear Research, Dubna, Russia

Abstract

The basic results of numeric simulations of krypton ion motion with decreased charge in the CYTRACK cyclotron are presented. CYTRACK is the world's first industrial cyclotron dedicated to the production of track membranes. Computer modeling confirms the possibility of ion acceleration in the magnetic field with an increase in the level of the magnetic field by 1.6% on the 6 harmonic of the accelerating system. The beam energy will be sufficient for the exposure of a film with a thickness of 10 μm.

INTRODUCTION

The CYTRACK cyclotron [1], designed to irradiate polymer films used in the production of separating and filter elements for medical, industrial, and domestic purposes, was devised and manufactured at the Joint Institute for Nuclear Research. This cyclotron is intended for the acceleration of heavy ions with $A/Z \approx 5$ up to the energy 2.4 MeV/nucleon.

CYTRACK was commissioned in August 2002: a beam of Ar_{40}^{+8} ions was accelerated and ejected [2,3]. The world's first industrial cyclotron for track membrane production has become the basic facility of NPK ALFA, which manufactures medical equipment for membrane plasmapheresis. Nowadays NPK ALFA is a unique research and production complex that stock produces track membranes (with a pore diameter of 400 nm) as well as medical apparatus for plasmapheresis. The track membrane is a polymer film made of lavsan (polyethylene terephthalate) or polycarbonate 10 to 25 μm thick in which there is a system of through pores.

To improve the quality of the membranes to extend the field of application, it is necessary to irradiate a film with heavier ions, especially with accelerated krypton ions. The currently operating ECR source does not produce krypton of the needed charge size. In this paper we analyze the possibility of accelerating krypton ions with a charge below the design one, namely 11+ and 12+.

CYTRACK PARAMETERS

The CYTRACK accelerator is an isochronous cyclotron with an azimuthal variation of magnetic field (a four sector structure), an axial ion injection, a high frequency accelerating system, and an electrostatic ejection system. The main specifications of the CYTRACK cyclotron are presented in Table 1. The general view of the accelerator is shown in Fig. 1.

Table 1: Cyclotron parameters

Accelerated ions	Ar_{40}^{+8}
Initial energy, MeV/nucleon	0.003
Final energy, MeV/nucleon	2.4
Final acceleration radius, mm	730
Operating vacuum, Torr	3×10^{-7}
Magnet overall dimension, m^3	$3.7 \times 2 \times 1.65$
Magnetic field level, T	1.48
Dees voltage, kV	40
Resonant frequency, MHz	18.25
Acceleration ratio	4

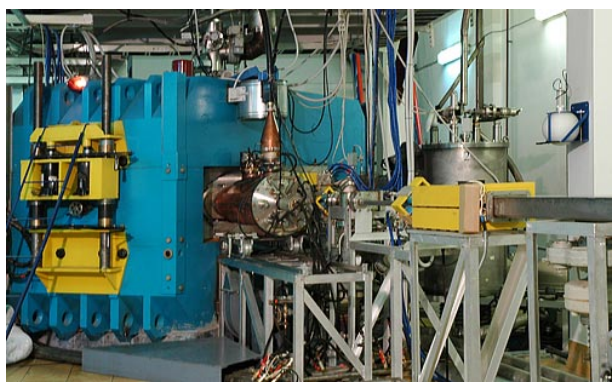

Figure 1: General view of the accelerator.

The ECR type ion source produces 3 keV/nucleon ions; the intensity of an argon beam on the Faraday cup placed in the diagnostic unit at the beginning of the injection line is on the order of 10 μA. The injection system incorporates a buncher. It also includes an ion guide, an analyzing and a turning two section magnet, and beam focusing and adjustment elements.

A spiral electrostatic inflector is used to turn the ion beam from the vertical to the horizontal plane of the CYTRACK cyclotron. A device is designed that allows the inflector to rotate around its axis (±8°) to adjust the ion trajectory to the starting radius and starting angle in order to optimize the initial conditions for ion acceleration in the cyclotron. The ions are injected into the cyclotron's chamber at a radius of 5.3 cm.

A radio-frequency accelerating system tuned to a fixed frequency is used to accelerate ions in the cyclotron's magnetic field. The RF system consists of two quarter wave resonators with accelerating electrodes in the form of dees. The RF resonators assure a frequency range from 18.250 to 18.600 MHz. The two dees of the accelerating system have an azimuthal extent of 45° and are located in the opposite valleys of the magnetic system.

KRYPTON ION ACCELERATION IN THE CYTRACK CYCLOTRON

Our aim is to accelerate krypton ions of lower charge at a generator frequency identical to that for the acceleration of argon ions with A/Z = 5, namely at 18.25 MHz. Without changing the RF system frequency, the lower charge ions will be accelerated at a higher harmonic of the RF system. Recall that the design ions are accelerated at the fourth harmonic. Let us first decide on the charge of the accelerated ion and hence on the corresponding acceleration multiplicity. Of practical use will be krypton ions of energy no less than 1 MeV/nucleon. Upon the acceleration of ions of krypton 8+ or 9+ on the 8 harmonic of the RF system, the final energy will be around 0.6MeV/nucleon, which is obviously inadequate. Therefore, we have restricted ourselves to an analysis of the possibility of accelerating krypton ions on an accelerating field harmonic that is not over 6. For such an acceleration regime, the krypton ions with charge 11+ and 12+ will have the closest revolution frequency in the produced magnetic field of the cyclotron, so they were chosen for the calculations presented below.

The acceleration of ions with a charge distinct from the design one involves a number of problems. First, ions with nondesigned A/Z are injected onto a different starting position; therefore, for the beam to be positioned onto the equilibrium accelerated orbit, it is necessary first and foremost to decrease the ion injection energy.

Second, in our case it is impossible to accelerate ions only at the expense of a multiple change in frequency; the level of the magnetic field should be changed in addition. A strong change in the magnetic field level may lead to a disruption of the formed isochronous increase of the average field.

Third, the dependence of the average magnetic field along the cyclotron radius is formed to match the ion with specified A/Z, i.e., the change in the dependence of the average field along the radius must correspond to the change in the ion charge. The missing correcting magnetic coils in the CYTRACK cyclotron constrain the acceleration of ions with nondesigned A/Z values.

An exact model of the cyclotron center (including the inflector, the inflector's housing, and the accelerating electrodes (see Fig. 2)) was made to analyze the possibility of accelerating krypton ions of lower charge.

The starting coordinates of the beam can be changed over a certain range by turning the inflector; in doing so their incomplete correspondence with the starting coordinates of the equilibrium accelerated orbit may be compensated for by changing the amplitude of the accelerating voltage on the dees. In Fig. 3 the solid and dashed and dotted lines correspond to the ion trajectories for two positions of the inflector; the accelerating voltage amplitude is chosen so that the orbit is centered as well as possible. The solid line corresponds to the trajectory of a particle at an accelerating voltage of 41 kV; the dashed–dotted line corresponds to the particle trajectory at an accelerating voltage of 60 kV.

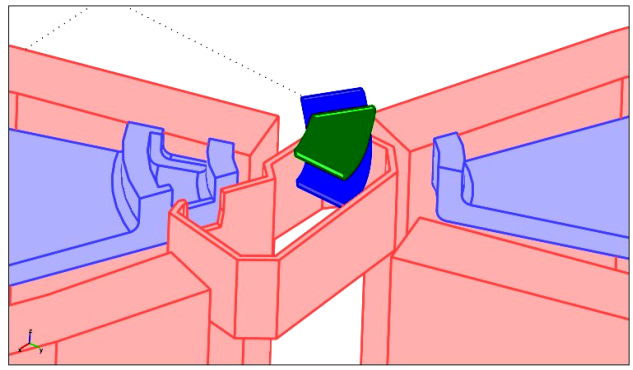

Figure 2: The CYTRACK cyclotron center model.

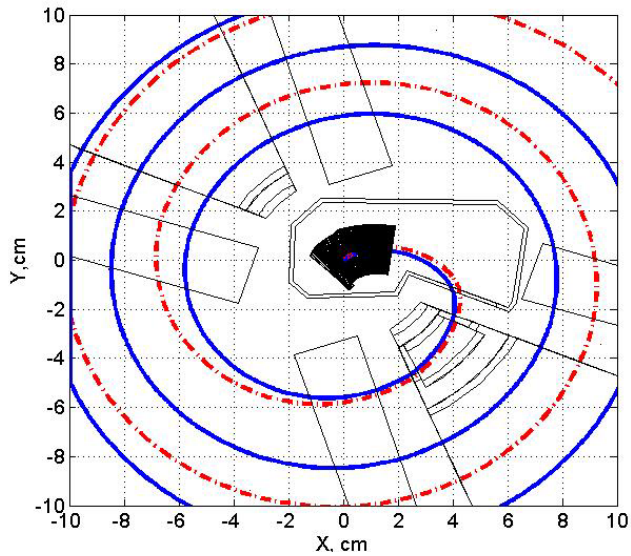

Figure 3: Trajectories of the central particle in the CYTRACK cyclotron center for different positions of the inflector.

The calculations of the cyclotron center showed that it is necessary to decrease the beam injection energy and then accurately position the beam onto the equilibrium well centered accelerated orbit by turning the inflector and changing the amplitude of accelerating voltage.

Acceleration of Kr_{84}^{+11} Ions

The acceleration of Kr_{84}^{+11} on the 6 harmonic of the accelerating field will require a minimum change in the level of the magnetic field; the beam energy in this case will be the 1.04 MeV/nucleon.

The motion of krypton ions in the magnetic field formed in the cyclotron from injection to extraction was simulated. Calculations showed that the average magnetic field should be increased by a factor of 1.016 to accelerate ions in the cyclotron field with no change of frequency. On the left of Fig. 4, the dashed line shows the energy of the central krypton ion as a function of the number of turns in the cyclotron.

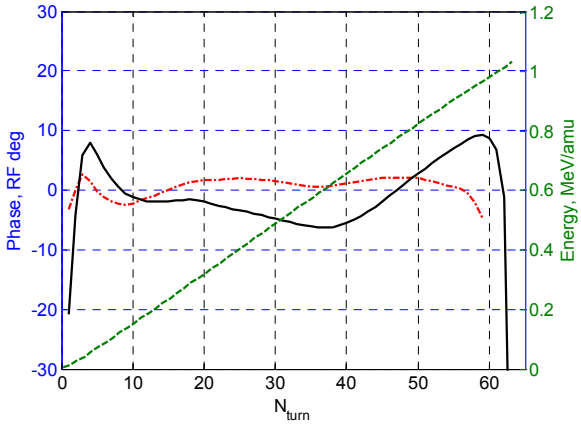

Figure 4: On the right, the phase motion of the equilibrium Kr_{84}^{+11} ion is show as a solid line; Ar_{40}^{+8} is a dashed–dotted line. The dependence of the equilibrium Kr_{84}^{+11} ion energy on the number of turn (dashed line) is shown on the left.

The phase ion drift (the change in the difference value of the ion phase and the phase of the RF system averaged over four accelerating gaps) may be taken as a criterion of correspondence between the formed cyclotron field and the isochronous one. From the right part of Fig. 4, it is seen that the phase drift of the equilibrium ion during acceleration is less than ±10° RF (solid curve), which is allowed. For comparison, the dashed and dotted line shows the phase motion of the central argon ion with A/Z = 5 during acceleration. It is clear that the drift of the argon ion phase is below ±5° RF.

Thus, the field formed in the CYTRACK cyclotron ensures a fixed equilibrium phase of the particle during the acceleration of ions with drift less than ±10° RF; i.e., the isochronism of the formed field is adequate for the acceleration of ions.

The accurate parameters of this and other modes of krypton ion acceleration are listed in Table 2.

Table 2: Acceleration parameters

Accelerated ion	Kr_{84}^{+12}	Kr_{84}^{+12}	Kr_{84}^{+11}
Injection energy, keV*Z	11	11	10
Final energy, MeV/nucleon	1.04	1.26	1.04
Inflector electrodes voltage, kV	5.5	5.5	5
RF_generator frequency, MHz	18.25	18.25	18.25
Acceleration ratio	6	5	6
Voltage amplitude of accelerating field, kV	41	40	45
Average field level	B0 * 0.9315	B0 * 1.118	B0 * 1.016

Acceleration of Kr_{84}^{+12} Ions

Calculations showed that, in accelerating Kr_{84}^{+12} ions on the 6 harmonic, one has to change the magnetic field level by a factor of 0.9315. The decrease in the current in the magnet winding will lead not only to a 7% reduction in the average field level, but also to some decrease in the growth of the isochronous field along the radius, which will serve to decrease the beam phase drift in the extraction area.

To accelerate Kr_{84}^{+12} on the 5 harmonic with no change in the working frequency of the generator, the average field should be increased by a factor of 1.118.

Such an acceleration mode will require a phase shift between the dees of 180°. The increased level of the magnetic field will increase the growth of the average field along the radius, worsening the beam phase motion, which in its turn calls into question the feasibility of this version. The advantage of this mode over the preceding one is the slightly larger final beam energy, 1.26 MeV/nucleon versus 1.04 MeV/nucleon.

CONCLUSION

A computer model of the CYTRACK cyclotron center has been made. The possibility of accelerating krypton ions of lower charge has been studied in the proposed model. Based on the results of an analysis of the krypton ion dynamics in the CYTRACK cyclotron, the acceleration of ions may be recommended owing to a minimum change in the magnetic field level (a 1.6% increase). It is also possible to accelerate ions on the 6 harmonic of the accelerating field with the average magnetic field decreased by 6.8%. In both cases the final energy will be 1.04 MeV/nucleon, which is sufficient for the exposure of the film with a thickness of 10 μm.

REFERENCES

[1] Yu. G. Alenitskii et al.,"Development and Construction of "Al'fa" Radiation Complex for the Production of Track Membranes," At. Energ. **97**, 474–480 (2004).

[2] Yu. N. Denisov, S. N. Dolya, V. V. Kalinichenko, G. A. Karamysheva, and S. B. Fedorenko, "Regime of Irradiation of Film by Accelerated Argon Ions for the Production of Track Membranes," Prikl. Fiz., No. 4, 100 (2004).

[3] Yu. N. Denisov, S. N. Dolya, V. V. Kalinichenko, G. A. Karamysheva, C. A. Kostromin, and S. B. Fedorenko, "First Criticality of CYTRACK Cyclotron," Phys. Part. Nucl. Lett. **2**, 144 (2005).

VACUUM AUTOMATIC CONTROL SYSTEM (ACS) FOR NICA PROJECT

A.Bazanov, A.Butenko, A.Galimov, H.Khodzhibagiyan, A.Nesterov,
R.Pivin#, A.Smirnov, G.Trubnikov, JINR, Dubna, Russia
P.Hedbavny, Vacuum Praha, Praha, Czech Republic
J.Moravec, FOTON, Nova Paka, Czech Republic

Abstract

Upgrade of the Nuclotron [1] is the first step in the Nuclotron-based Ion Collider fAcility [2] project. A modernization of the Nuclotron vacuum system leads to decreasing of the heavy ion losses due to scattering on the rest gas. The successful realization of the modernization takes possibility to use Nuclotron as a part of NICA project. It's impossible to image the modern vacuum system without the automation control system (ACS). The goal of ACS at Nuclotron is to manage about 70 units of the vacuum system and the data acquisition.

VACUUM SYSTEM MODERNIZATION

Modernization of the Nuclotron high vacuum system had the aim to increase the beam lifetime which is the necessary condition for the using of Nuclotron for the NICA project. For this work it was chosen non-oil pumps such as ion pump, turbo pump and forvacuum pump "Pfeiffer Vacuum" company (Figure 1). It allowed to reach the pressure about 10^{-10} Torr. Mass-spectrometer PrismaPlus were installed to rest gas composition definition.

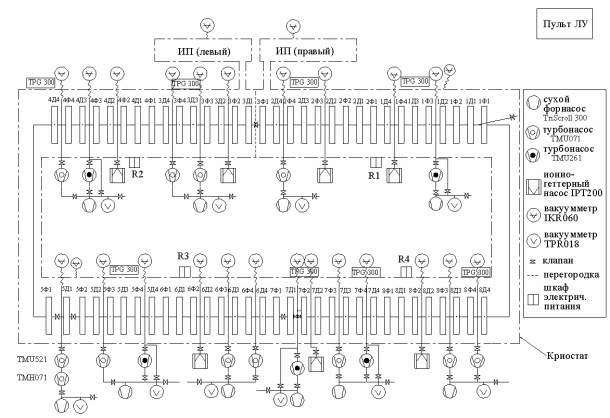

Figure 1. The scheme of the Nuclotron high vacuum system.

First step of the modernization includes the mounting of new turbo pumps. It permits to decrease a vacuum pressure about ten times. Problem vacuum parts also were reconstructed, measurement units were added.

Second step includes the installation of the tandem with two turbo pumps at each parts of the ring (22 points) and scrappers which are used for the lost ions absorption.

#pivin@jinr.ru

THE CONTROL SYSTEM FOR THE VACUUM OPERATION

Structure

ACS system consists of two main parts:

- Master controller (PLC), touch-panel and PC in the control room;
- Four Racks in the center of Nuclotron and units at the experimental hall.

PLC (Figure 2) works at the main controller and defines system logic. RS485 protocol is used for communication between units.

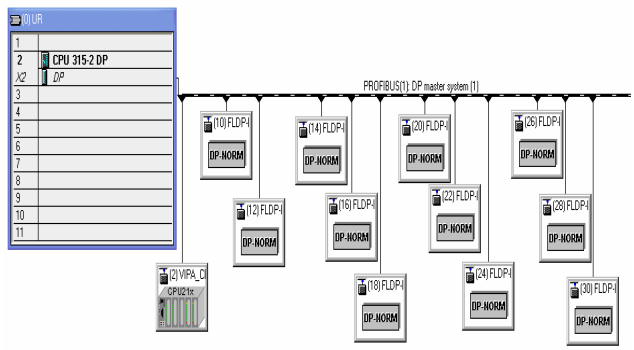

Figure 2. PLC controller with Profibus protocol.

The touch-panel (Figure 3) is placed on the central rack, creates visual interface for vacuum system components and hand mode provides.

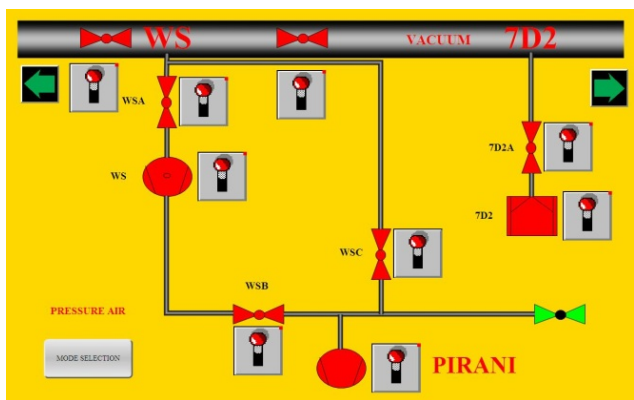

Figure 3. Touch-panel of control system.

PC allows to display vacuum units parameters like speed, current and vacuum values (Figure 4). The program creates graphics and collects information in the database.

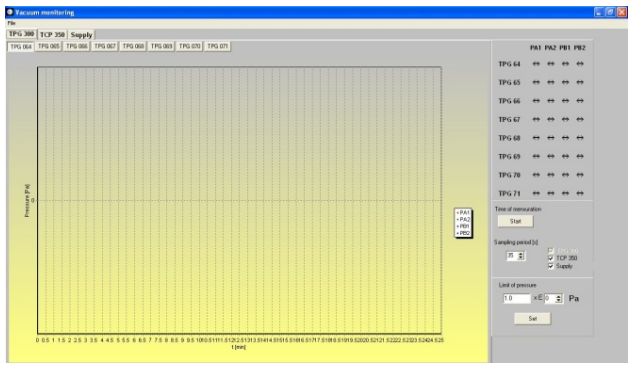

Figure 4. Window of the vacuum monitoring program.

Control and Operation

ACS has 3 modes:

Ad 1 –this mode is for the manual control of all elements;

Ad 2 – this mode correspond to the required automatic mode. If the current running operation is indicated then the local position of this operation is indicated too (e.g. forvacuum pumping in the section 2D4);

Ad 3 – this mode of the operation defines the hardware components (stages) which are used (it enables/disables several posts identified by their position).

The parameters of TPG300 (Pfeiffer Vacuum company) are monitored by means of the RS485 interface. All TPG300 devices are equipped with the Data convertor (FOTON company). This data convertor has a form of a small-case electronic device which converts not only the electric level of IO signals, but it also establishes the Pfeiffer Vacuum Protocol. Thus, in spite of the original RS232 interface of TPG300 (point-to-point communication only), these convertors make the TPG 300 Pfeiffer Vacuum Protocol compatible. The alarm signals are connected directly to IO modules inside the racks. The data are monitored via RS485 interface.

The PC handles the line of TCP350 and power supplies for ion pumps and the line of TPG300. Each device is identified by its address. The data are presented in the graphs (max and actual rotation and the pump current for the turbo pumps, the pressure of gauges for the TPG300. Moreover, the progress of the pressure is simply summarized and presented in the table form (see right part of the screen). The colours indicate the pressure trends: green = the pressure becomes lower, yellow = the pressure becomes higher, red = the pressure is higher than the preset threshold. These limits are simply preset; the scan period is also modifiable (sampling period).

The measurement starts after <START> button is pressed. The data are stored in the separated files; the filenames contain the data and time of starting measurement. Each file has the same structure: 1st row is the head, following lines represent the measured data. All the information is in ASCII-character forms and separated by <;> sign. Thus, the work with datafile outside the ACS is simple (Excel etc.).

Blocking and Protection

Summary of blocking events :

- All gate valves are closing in case of emergency signal coming from any IKR gauges; also malfunction or switch-off of TPG300 instrument causes closing of all gate valves;
- Each gate valve cannot be opened if the corresponding turbo pump is not running;
- The gate valve can be opened in the case of the running of the corresponding turbo pump (for ESS – higher pump) and
  - the good high vacuum inside chamber, or
  - the key-operated switch on ASU is in the Pos I, i.e. left (=High Vacuum Disabled Mode);
- The gate valves B1WS and B2WS are not blocked through the turbo pumps;
- Turbo pump can start if the forvacuum valve is opened;
- The forvacuum valve can be opened if the corresponding forvacuum pressure is good (Pirani signal);
- All gate valves are closing in case of decreasing of air pressure in pneumatic system;
- Low forvacuum (higher pressure) implies closing of corresponding gate valve;
- Key –operated switch on ASU = selection of protection mode (Table 1).

Table 1: Protection modes of ASC

Pos 0 (central) *Standard Mode*	*Pos I (left)* *High Vacuum Disabled Mode*	*Pos II (right)* *No Protection Mode*
All protection is applied, including high vacuum check	The protection through the high vacuum detection inside the chamber is blocked. This mode is needed if the manual control of chamber-valves is required, it must be operated with qualified persons only. The risk of damages!	No protection is implemented. This mode is useful for extraordinary situation and must be operated with qualified persons only. The risk of damages!

Indications

- The state of the high vacuum is indicated on the touch panel by means of the colour of the word VACUUM located in the picture of chamber tube (usually top-left position on the screens):
  - green VACUUM ..... low pressure = good high vacuum inside the chamber;
  - red VACUUM ..... higher pressure = bad high vacuum inside the chamber; alarm signal from any gauges IKR implies this red stage;
- The state of the vacuum inside the chamber (see above) is forwarded to the main control room through DWDT relay contacts:
  - Closed contacts ..... good high vacuum;
  - Open contacts ..... bad high vacuum;
- The event of the bad high vacuum signal is latched and indicated by means of the yellow indicator on the front panel on ASU; this alarm signal can be reset only manually by pushing the black button on the front panel of ASU (if the vacuum is good inside the chamber);
- The state of the forvacuum (primary vacuum) is indicated by means of the colour of PIRANI word located in the picture near the forvacuum pump (bottom position):
  - green PIRANI ..... low pressure = good forvacuum;
  - red PIRANI ..... higher pressure = bad forvacuum.

Software

The system is under the control of three software packages :

- PLC software. This is the standard PLC program written in STL form of Siemens STEP7 language;
- Touch panel software. This is the application build up in the ZenOn Editor 6.21 (COPA-DATA GmbH);
- PC program. This is the Delphi based PC application.

REFERENCES

[1] A.Sidorin, G.Trubnikov, V.Kekelidze, et.al. Status of the Nuclotron. These proceedings.

[2] I.Meshkov. NICA Project at JINR. These proceedings.

CONCEPT OF THE SOFTWARE FOR ITEP-TWAC CONTROL SYSTEM

P. Alekseev, F. Sizov, ITEP, Moscow, Russia

Abstract

The work is in progress on development of new control system for ITEP accelerators complex. All software for the system should be developed from very beginning. Core element of new software is PostgreSQL object-relational database management system. All interactions between programs on device side and on operator side are made utilizing the database functionality. The database is also provides storage space for all configuration data, operational modes, logs and so on.

INTRODUCTION

ITEP accelerators complex is located in several buildings in the area of the institute. Control functions should be available for staff located at main control room and at local control panels of subsystems. In addition, diagnostic signals and some control parameters should be accessible from outside the complex. Therefore, the control system will be distributed and multiuser.

Common architecture of the control system is shown on Fig. 1. Offered structure allows connecting to the system almost any equipment with any known control interface. Supposed that the equipment may be industry manufactured or self designed.

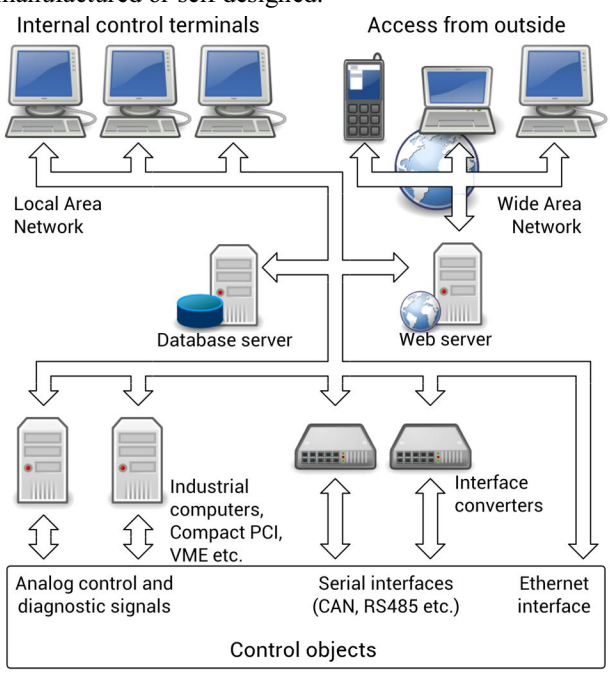

Figure 1: Common control system structure.

Front-end programs that user interacts with, may be called from the LAN or even from internet using the web server. Back-end software that interacts with control objects, executes on industrial PCs or on the database server.

The investigation of capabilities of various software products was made relative to our problem. The results coupled with existing resources and expertise allows to offer configuration of software described below.

Control of data flows between front-end and back-end software is implemented by PostgreSQL database. In addition, the database is used to store all the information related to the control system. Main functions of the database are illustrated in Fig. 2.

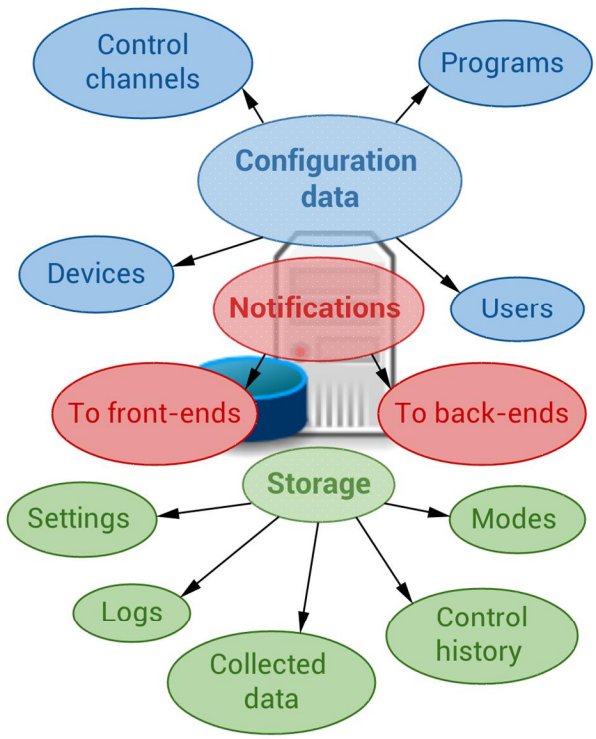

Figure 2: Database functions.

DATABASE STRUCTURE

There are three types of objects are used to describe the control system structure. These are daemons, devices and channels. Database table DAEMONS contains data about all back-end programs of the control system. Equipment of the control system should be described in the DEVICES data table. Each device such as communication port, dac board, peripheral module etc. has its own database record.

All the physical parameters of the control system are presented as channels. Database table CHS contains an information that used by front-end programs to configure control elements. Each channel should be linked to device that operates with it.

A set of tables that are used in the database to describe all the objects of the control system are shown in Fig. 3.

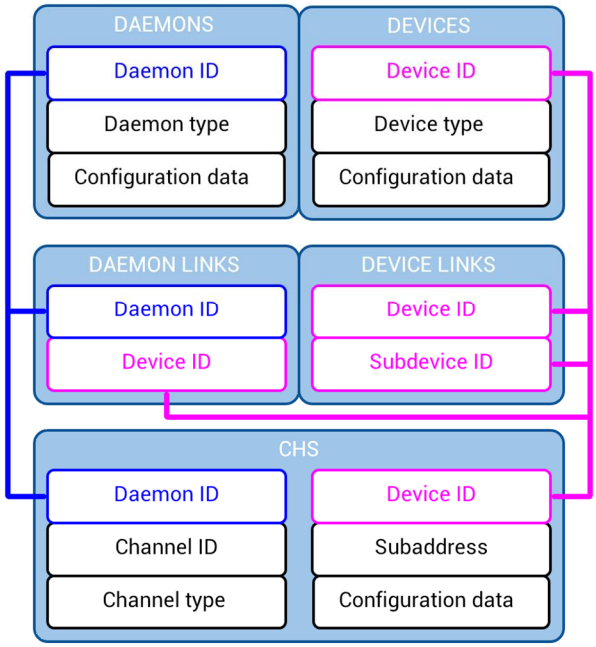

Figure 3: Configuration data.

Tables DAEMON_LINKS and DEVICE_LINKS allows to define what software should service the device and how the devices linked to one another. This way is possible to describe any hierarchy of devices.

The channels could be combined into groups, database tables GROUPS and GROUP_LINKS provides this. Groups of channels may be used to create modes of operations, to handle sets of values etc.

Other database tables are used to store information about the users, front-end programs, schedule, access logs etc.

DATA MANIPULATIONS

The core element of the control system software is an algorithm for requests processing and transfer of responses. This algorithm could be implemented using native PosgreSQL asynchronous notification commands. PostgreSQL offers asynchronous notification via the LISTEN and NOTIFY commands [1]. A client session registers its interest in a particular notification condition with the LISTEN command. All sessions listening on a particular condition will be notified asynchronously when a NOTIFY command with that name is executed by any session.

We could not find similar functionality in the other database management systems. Sometimes it may be implemented by using server and client programming. In our case, application of PostgreSQL allows to minimize programming time because all the functions are present already.

Changing Parameters Values

Actually we should consider two types of notifications for each of two types of requests. First type of requests is the request to change setting of a channel. Data flow diagram for that request is shown on Fig. 4.

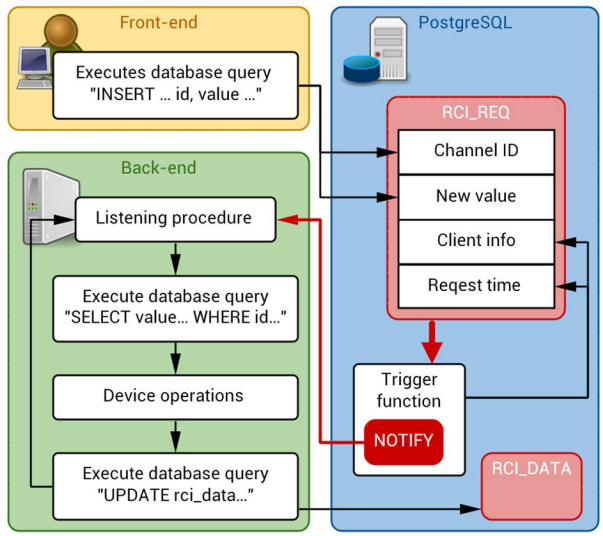

Figure 4: Data flow of control request.

Database table RCI_REQ is responsible for processing of request for parameter changing. Client should insert its request into this table with only channel id and new value. This operation will trigger database function that finds id of the back-end program, sends the notification to it and writes some additional information about the request into the database. Whenever the notification will be delivered to the back-end it selects new tasks from RCI_REQ and process them. If at one time more then one request will be found in RCI_REQ only the recent one will be handled, but all the clients that listen should be notified about the changes. Data flow of daemon's response is illustrated on Fig. 5.

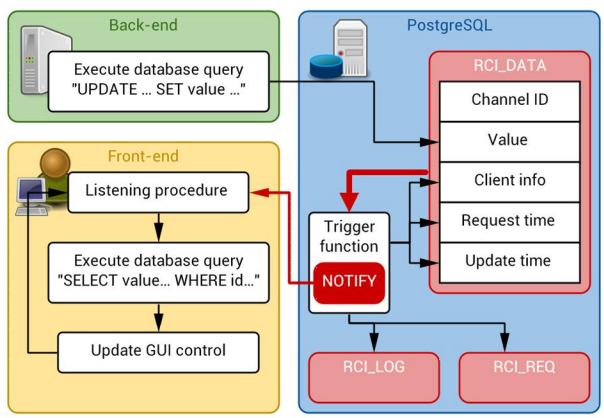

Figure 5: Data flow of daemon response.

Database table RCI_DATA keeps actual values of all the control system parameters. When any of the parameters changed by request or by the other reason the daemon, servicing the channel, should update RCI_DATA. Such update will trigger database function that notifies the clients, clears requests and may even

store the operation details into the log. The only thing that client shall do, receiving the notification, is to select new value from RCI_DATA.

Data Acquisition

The other type of requests is request to get measured values or collected data. The main difference from control requests is that measurement requests from different clients to the same channel should be serviced simultaneously.

All the data collected from measuring channels are stored in DAQ_DATA table. This table has field named REQ that should be positive in case of any client is waiting for new value of a channel. When REQ is set to zero corresponding back-end program may stop the cycle of measurements. Thus, the only thing that client should do to start measurement is ensure that REQ is more than zero by updating it with positive value. On the other hand, REQ should be decreased by one each time the daemon updates data.

To distinguish front and back-end commands on DAQ_DATA, virtual table, so called "view", named DAQ_REQ is used. DAQ_REQ should be updated only by client programs while DAQ_DATA by daemons.

When client writes positive value into REQ field of table DAQ_REQ triggered function that copies this value into DAQ_DATA and sends notification to back-end program. If at that moment the program is inactive it will wake up and continue data acquisition procedure until any of the channels linked to it has non zero REQ field. This process is illustrated in Fig. 6.

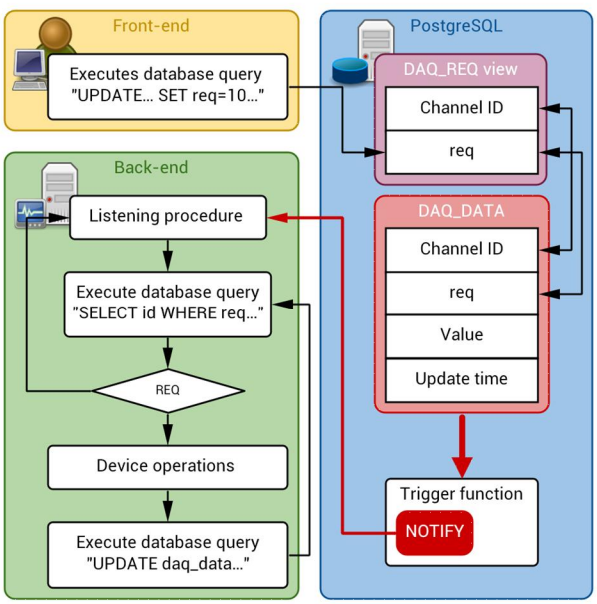

Figure 6: Request for measurement

The second part of the data acquisition algorithm is illustrated in Fig. 7.

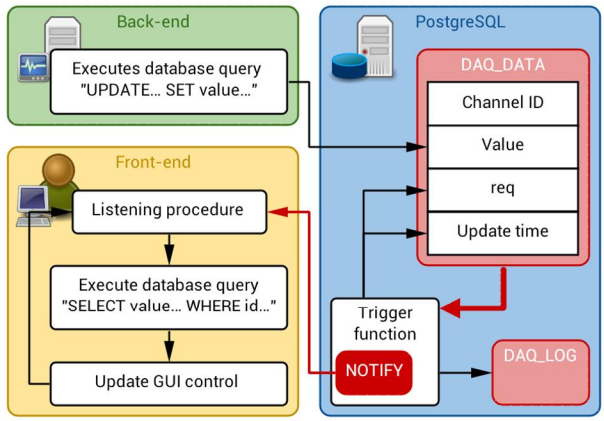

Figure 7: Data ready notification

The same way as in control algorithm measured data is placed into DAQ_DATA table. This operation triggers the function that notifies clients and automatically decreases the value of REQ or copies new value into log table if needed.

CONCLUSION

All the algorithms and methods described was implemented and tested on subsystems of old control system. They were used to control master oscillators, current sources for beam lines magnets, to broadcast of diagnostics signals of U-10 proton synchrotron. It allows to expect successful application of these methods in the new control system.

It should be noted that the algorithms described may be implemented rather simple inside the database with minimal programming. The clients are utilize standard database control functions to perform queries. Thus, almost any programming language may be used to interact with the system. It gives an opportunity to involve wide range of specialist to development of the control system software.

REFERENCES

[1] The PostgreSQL Global Development Group, “PostgreSQL 8.3.20 Documentation”, 1996-2012, http://www.postgresql.org

DEVELOPING OF THE SYNCHRONIZATION SYSTEM FOR ACCELERATION-STORAGE FACILITY ITEP-TWAC

A. Orlov, P. Alexeev, S. Barabin, D. Liakin, SSC RF ITEP Moscow, Russia

Abstract

The renovation of the ITEP-TWAC synchronization system is a complex and challenging matter. This system must provide a full-scale timing signal set for all existing and foreseeing modes of operation of the two-ring accelerator facility. The workflow of the complete design covers all levels of a design management hierarchy like decision concerning, the new system architecture or basic electronic modules development. In this article we present a description of most critical elements of the synchronization system.

INTRODUCTION

Two general rules were formulated before starting the design of the novel synchronization system. Those rules are following:

- New elements must be compatible with existing system. Partly they are replacing obsolete components giving them where it is necessary a new functionality. A principle of organization of the synchronization system in ITEP-TWAC accelerating complex could be illustrated by Fig.1.

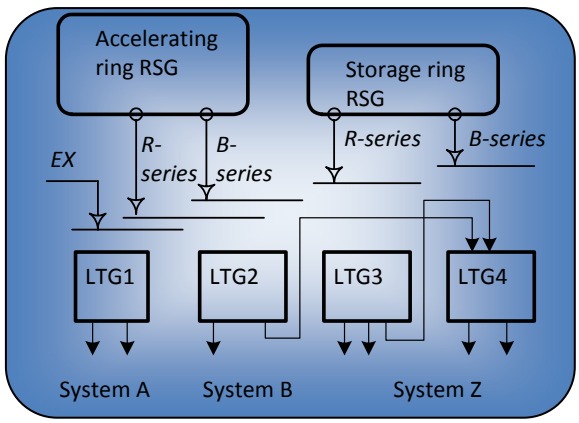

Figure 1.A structure of the synchronization system of the ITEP-TWAC accelerating complex.

- Reference signal generators (RSG) issue so called B- and R- sequences of control pulses which are synchronized with magnetic field strength (B) and RF oscillations(R). The system also accepts external synchronization signals (EX) from independent or adjusted installations like injector and target systems. A general module of the local timing generator LTG is an assembly of logical modules, programmable time-delay modules and signal duplication modules.
- New elements provide possibility to upgrade to the new principles of organization of the synchronization system, namely using serial timing bus (STB) for building synchronization system. A principle of organization of the synchronization system based on STB shown on Fig.2.

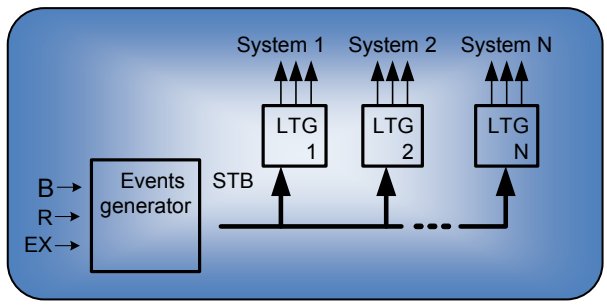

Figure 2. A principle of organization of the synchronization system based on serial timing bus architecture - STB.

STRUCTURE OF THE DEVICES

There are two families of devices, which require for building of the synchronization system with serial timing bus. The first type is a master or event generator shown in Fig.3. The master analyses incoming events of different format on B,R and EX lines and generates unified data frames on the serial bus. The second type is a service module shown on Fig.4.

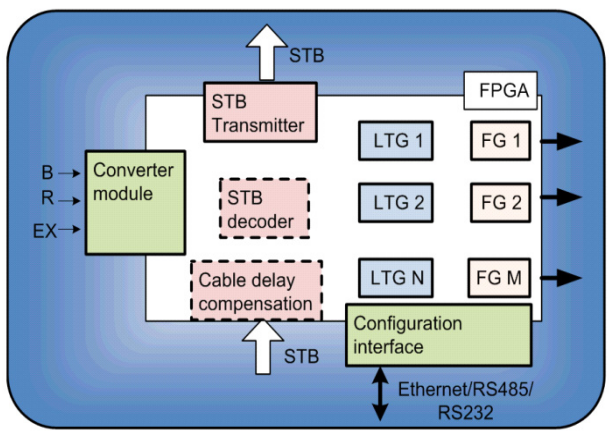

Figure 3. The block scheme of the events generator.

The differences between those two types of devices are nominal because the logical structure of the STB transmitter(master) can be completely realized inside FPGA, except the physical interface of the STB. A service module also can be logically implemented inside FPGA, except the schematic of the input signal converter. Both modules can be realized in the same hardware, therefore

the module behavior depends only from the micro program loaded into the device.

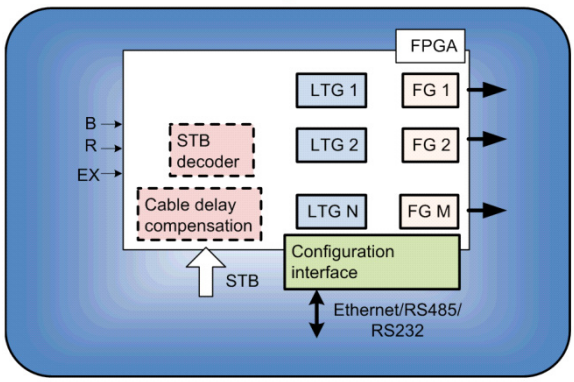

Figure 4. The block scheme of the service module.

The complexity of the contemporary programmed logic makes it possible to place several functional blocks in the single universal module. Functional modules FG give a possibility to generate comprehensive sequences of pulses at the outputs of the device. A serial timing bus decoder's standard component is including into firmware when it is necessary to operate with STB. As a standard option, it is also possible to compensate a cable delay.

DEVELOPMENT OF THE DEVICES

Presently several devices are developed to be used in synchronization system, they are presented below in chronological order. All of the following devices are designed to work with STB which based on RS485 or GSI standard (MIL-STD bus variation) physical interface.

The first of the developed devices is the synchronization module with "Configurable interface" based on single-board Linux computer TS 7800 equipped with extension cards built in PC104 standard. Such module and two extension cards are shown on Fig. 5.

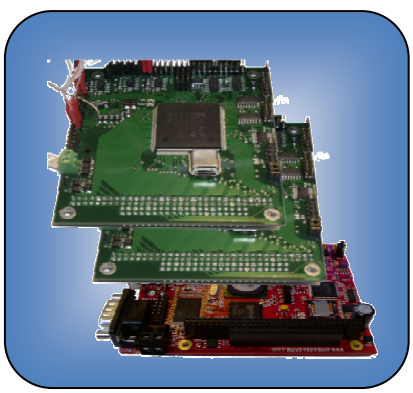

Figure 5. Synchronization module based on single board computer TS 7800.

This solution has several advantages:

- A wide range of physical interfaces RS485, MIL-STD Bus, RS232, USB2.0 and Ethernet 10/100 provide wide opportunities for construction and configuration of the synchronization system. PC104 bus is an easy way to add extension cards, which in their turn provides good scalability and functionality of the module as a whole.
- High computation power of the single-board computer together with possibility of using specialized extension cards for example ADC cards or specific interface cards provides the possibility to use this module as events generator module for synchronization system.

The synchronization system of the linear heavy ion accelerator I4, which is a latest linac built in ITEP, has been designed with use of this module. One module, shown on Fig.5. includes 20 LTG and FG and provides the synchronization of all subsystems of the accelerator.

The next module, which was developed for the synchronization system, is a single board computer based on ARM 7 core processor. This module shown on Fig. 6.

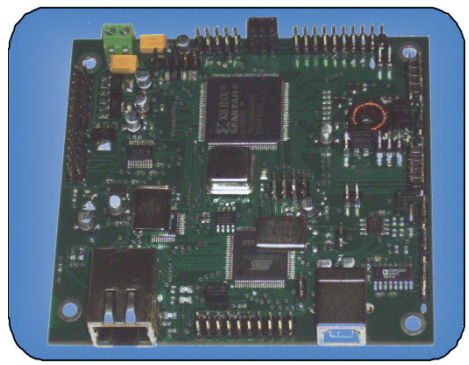

Figure 6. Synchronization module based on single board computer with ARM7 core processor.

In comparison with commercial SBCs this module uses a light weighted RTOS with minimal latency time and effective use of processor's peripherals. This single board computer has the same set of the serial I/O interfaces as extension modules from fig.5, which provides the same opportunities for communication and remote configuration of the synchronization system. For compactness and lowering the price this module does not support any parallel bus for extension modules. This module will be used for emulations of various signals and for testing of the synchronization system. Processor-FPGA combination allows using this module as a multipurpose component in different systems. For instance this module is used as a timing signal decoder and simulator in some beam diagnostic subsystems in GSI.

The latest device developed for synchronization system is the module based on the 8-bit microprocessor. This module is shown on Fig. 7. The module is equipped by two RS485 and RS 232 interfaces for configuration and one RS485(GSI MIL_STD Bus) interface for STB input. This module is used only for service modules for the synchronization system. At the moment four similar modules are made.

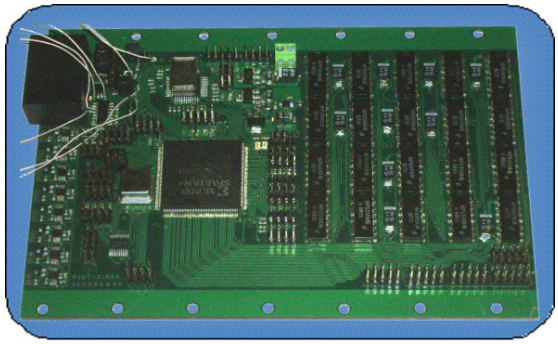

Figure 7. Synchronization module based on Mega microcontroller.

The software developed for this module allows using it as the a service module of the synchronization system. The microprogram loaded into FPGA provides:

- Periodical generation of starting impulses with programmable period from 20mks to 85sec.
- Four inputs for external starting impulses.
- Four inputs for external frequency.
- Twenty 32bit LTG
- Forty FG with programmable pulse duration of the output impulse and light indication.

CONCLUSION

For the moment, a several different modules are designed for synchronization system of TWAC ITEP. These modules allow replacing the existing synchronization system and are ready to be used in future system with new principles of synchronization. Using a single board computer with FPGA allows fast and reliable dynamic reconfiguration of a particular module and the whole synchronization system.

REFERENCES

[1] N.N.Alexeev et al. ITEP_TWAC status report**.** Proc. RuPAC 2008, Zvenigorod, Russia, pp134.136. http://cern.ch/AccelConf/r08/papers/TUBAU02.pdf

[2] A. Orlov et al. Universal timer module for the timing system of the accelerating storage complex ITEP-TWAC. RuPAC 2010, Protvino, Russia.

[3] IEEE 1588 Standard for a precision clock synchronization protocol for networked measurement and control systems. http://ieee1588.nist.gov/

OPTIMIZATION OF THE DETECTOR GEOMETRY AND DATA PROCESSING ALGORITHMS FOR FAIR CR BPMs

A.Orlov, S.Barabin, D.Liakin, SSC RF ITEP, Moscow, Russia
F.Becker, GSI, Germany

Abstract

A beam diagnostic is an important part of all FAIR accelerators and storage rings. A small flux of antiprotons in the collector ring CR (10^8 particles in a store ring) as well as dominated at first turns p-meson component of a beam require careful design for all elements of the beam position monitoring system. To increase a BPM resolution and sensitivity we propose a compact multi-electrode design of the position detector, matched low-noise electronics in connection with dedicated enhanced digital data processing algorithms. Here we present a comprehensive set of aspects of a preliminary design of the BPM system for FAIR CR.

SYSTEM OVERVIEW

The antiproton and rare isotopes collector ring (CR) is a specific component of FAIR. It is designed for conditioning of crude assemblies of particles with large initial transversal emittance and wide energy spectra. The estimated beam intensity for antiprotons is 10^8 particles in the ring. For rare isotopes only the highest intensity is specified as 10^{10} stripped ions in the ring. Geometrical constrains of the beam position monitor chamber are shown on 0. This figure shows the possible beam profiles and their envelope. Due to the limited space BPM chambers must be installed inside of quadrupole magnet so the chamber's outline must follow the inner shape of the yoke.

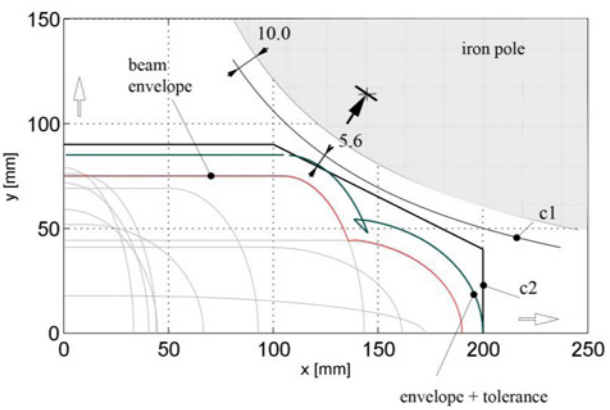

Figure 1. Geometrical constrains for the BPM chamber and electrodes design. c1 – the inner surface of the vacuum chamber, c2 – electrodes.

NUMERICAL MODEL OF THE BPM CHAMBER

A detailed investigation of the BPM antenna has been performed by numerical simulation. An electrostatic and low frequency AC approaches had been chosen according to operating frequencies and characteristic length of the system. A general 3D CAD model used for simulation of the BPM chamber is shown on 0. In this model electrodes are presented as a conducting surfaces connected to the circuit with defined impedance. A high-Z preamplifier, impedance transformer and direct 50-ohm cable connection were investigated.

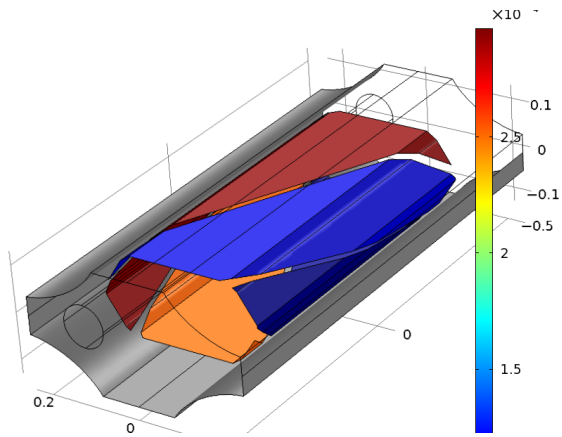

Figure 2. A 3D simulation model of the BPM chamber.

The beam of charged particles was simulated by space charge distribution. Generally the distribution is uniform in longitudinal direction and limited by volume of the circular or elliptical cylinder as it is shown on 0. Practically the charge density used in simulation was given by formula

$$Q = A(1-r)^2;\ r^2 = \left(\frac{x}{a}\right)^2 + \left(\frac{y}{b}\right)^2;$$

where a and b are semi axes of the cylinder crossection, A is a normalisation coefficient.

THE TOPOLOGY OF ELECTRODES

The signal strength and therefore signal to noise ratio important for low current measurements directly depend on effective length of pick-up electrodes. 0 on bottom schematically shows a classical design with separate electrodes for vertical and horizontal measurements. Such two modules are placed in space allotted for the BPM. The length of each section is about 40% of full dedicated length taking into account the gap required for decoupling of the vertical and horizontal sections. To obtain a higher sensitivity for CR BPM we consider a combined topology of the BPM. Because of digital signal processing it is possible to use more comprehensive algorithms for beam position detection. Particularly it allows dynamic 'reconfiguration' system consisting of four or even more

electrodes like in the system shown on top of 0. There pairs of double length electrodes 1-2 and 3-4 are used for position detection in horizontal direction, and in same time the combination 1-3 and 2-4 gives a vertical position of the beam.

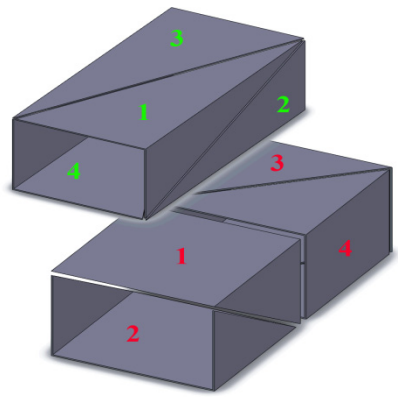

Figure 3. Combined (on top) and classical(bottom) configuration of electrodes.

GOALS AND PARAMETERS OF SIMULATION

Important functional properties of the BPM are position sensitivity, sensitivity to beam current, conversion linearity, beam shape tolerance, direction decoupling, accepted signal frequency bandwidth.

Various models of different level of abstraction using corresponding constrains were used to get an optimal result for beam position monitor system. Fig. 4 shows tools and models interconnection during entire BPM system design and optimization. Most comprehensive and time and computation power consuming 3D simulation is used for accurate simulation of electromagnetic parameters of the BPM elements. 3D model is only suitable model for quantitative analysis of the system linearity sensitivity and estimation of coupling between horizontal and vertical measurements. Results of simulation are used then for estimation of parameters of equivalent schematic. A proper schematic model is effective for analog chain design – selection of the amplification model, amplifier design, noise analysis. PSpice models of electrodes coupled to proper loads are used also for behavioural simulation of the system.

SIGNALS AND MODES OF OPERATION

Beam position monitoring distinguishes four stages – injection, debunching, stochastic cooling, extraction. For debunching stage Collector Ring has two fixed revolution frequencies for antiprotons and rare isotopes. This means that for bunched beam the frequency domain and narrow-band operation are well suited for the beam position monitoring.

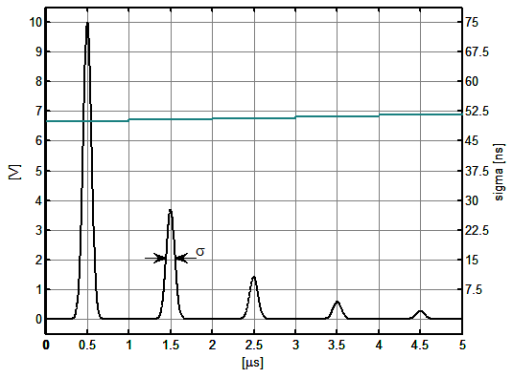

Figure 5. The signal at the beginning of antiproton cycle.

During injection the BPM system could be an important part of first-turn non-destructive diagnostics. The signal in this case is a short pulses fast decaying (see Fig.5.) due to pi-meson decay in the case of antiproton cycle. Because of the spectra of short pulse the BPM system must support a wideband operation which is achieved by using fast ADCs and data buffers of sufficient size.

The main goal of CR is a conditioning of the charged particle beam. Most of the time in the ring the beam is non-bunched and the revolution frequency signal strength is pretty low. Nevertheless the beam position still could be detected using the Schottky noise of beam current.

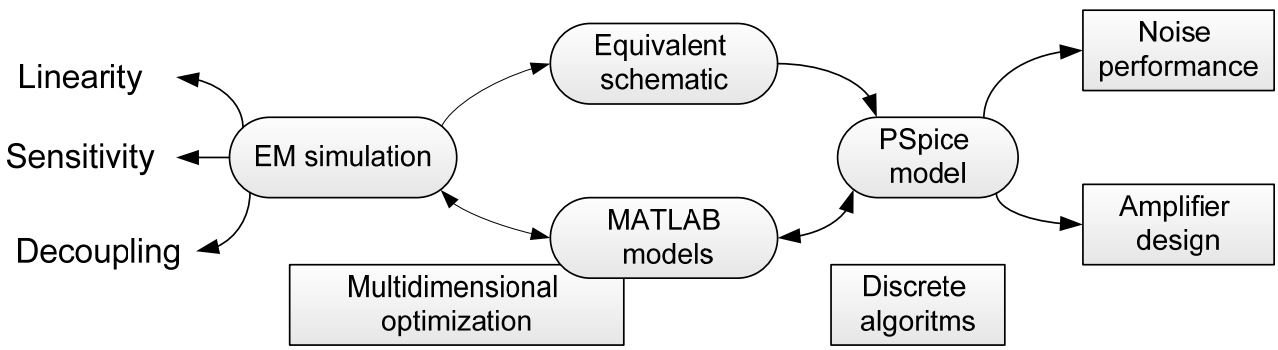

Figure 4. Design flow and models interconnection.

SIGNAL PROCESSING

The structure of the CR BPM data processing in FPGA based processing module is shown on Fig.6. This meet to requirements of reliable evaluation of BPM data for all modes of operation. The input stage is a data deserializer from input serial ADC data stream to parallel 12-bit word. A synchronization module with adaptive phase locked loop mechanism allows compensating of all thermal and temporal instabilities of the high throughput serial receiver implemented in the FPGA. A most critical data then stored as a raw stream in the data buffer for further investigation.

The first stage is a digital down converter equipped with numerically controlled oscillator NCO. By setting the NCO frequency one can investigate different phenomena, like closed orbit position, betatron oscillation etc. The next module is a data rate decimator which is a multirate low pass CIC filter and which reduce the sampling rate down to 1MSPS per channel. 1024-point FFT module generates a new spectrum with millisecond period. The conversion time is less than 100 microsecond and same FFT module is used for all four channels by multiplexing the input data. This data is useful for low-level application, when full spectrum containing also noise data is a subject of interest. With relatively clear spectrum the data pass to the second decimator and reduced down to several samples per millisecond for real-time position data analysis.

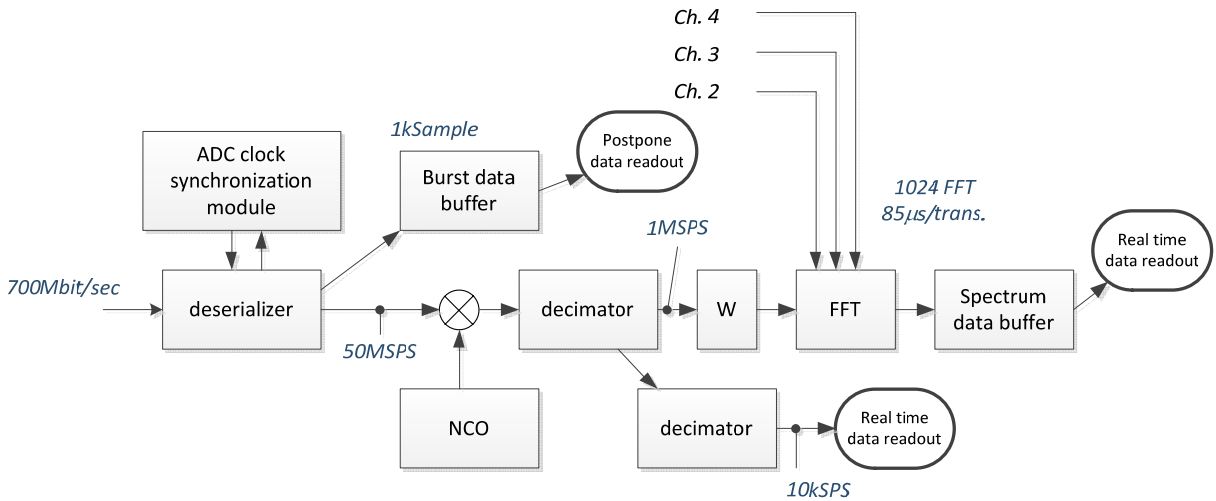

Figure 6. Data processing elements.

CONCLUSION

A large amount of simulation work has been done to optimize every component of BPM system of the FAIR collector ring. It was proved that performance of the whole system is sufficient for operation under nominal eam parameters condition. Further work will be an optimization of mechanical design, estimation of design tolerances, prototyping of the antenna and signal chains.
b

REFERENCES

[1] D. Liakin et al., Advanced digital signal processing for effective beam position monitoring. Proc. Of DIPAC2011, Hamburg, Germany.

[2] K. Lang et al., Performance test digital signal processing for GSI synchrotron BPMS. Proc. Of PCaPAC08, Ljubljana, Slovenia.

[3] A. Galatis et al., Digital beam position measurement at GSI-SIS and CERN-PS. Proc. Of DIPAC 2005, Lyon France.

[4] S. Stergiopoulos (Editor), Advanced signal processing handbook, CRC Press LCC, 2001.

DIGITAL DELAY-LINE PERIODIC FIR FILTER LAYOUT OF TRANSVERSE FEEDBACK IN THE U70

O. Lebedev, N. Ignashin, S. Ivanov, and S. Sytov
Institute for High Energy Physics (IHEP), Protvino, Moscow Region, 142281, Russia

Abstract

A novel architecture of the wide-band transverse feedback system was successfully beam-tested in the U70 proton synchrotron of IHEP-Protvino. It employs a finite-time impulse response (FIR) non-recursive filter layout based on 3 (or 4, optionally) variable (–10%) multi-turn digital delay lines. Apart of using these natural-to-DSP components, the configuration involved has, at least, two operational advantages: (1) A single beam-pickup layout plus acceptability of an arbitrary betatron phase advance between pickup and kicker. (2) A straightforward rejection of hampering DC and higher rotation frequency harmonic signals from beam position raw readouts. The latter occurs due to a periodic notch nature inherent in the amplitude-frequency in-out open-loop feedback transfer function. The paper reports on technical solutions implemented, problem-oriented R&D, and beam observations.

PREHISTORY

The inventory of transverse beam feedbacks available in the U70 is outlined in Ref. [1].

Layout of the existing wide-band feedback is plotted in Fig. 1. Its two pickups (PU) are located in straight sections (SS) #107 and #111. In the U70, azimuth Θ of SS#*n* is $2\pi n/120$. A properly weighted sum of beam position readouts produces a virtual pickup located 33 (an odd number) quarter betatron wavelengths upstream of the fast EM kicker (deflector) K in SS#90. A variable (–10% ca) delay line matches open-loop delay rime τ to beam time-of-flight between pickups and kicker.

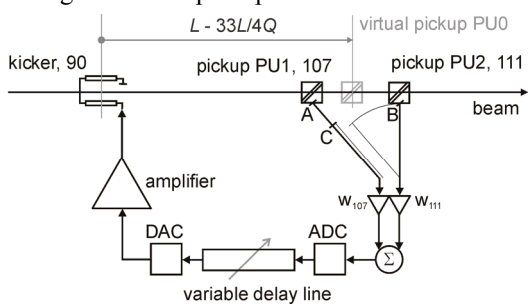

Figure 1: Layout of the existing wide-band feedback.

Suppression of closed-orbit offset signal at $\omega = k\omega_0$, with DC ($k = 0$) included, is accomplished via a variable electrical center of a pickup biased with balance amplifiers. Here, ω_0 is circular beam rotation frequency, integer $k = 0, \pm1, \pm2, \ldots$ is rotation harmonic number.

A single-delay-line layout of Fig. 1 is inherited from the earlier, all-analog implementation of the circuit. Indeed, in the analog world, a 5–20 μs variable delay line is by itself a sufficiently intricate device to preclude any use of a multiple number of them.

To be on the safe side in running the U70 and get experience with the DSP techniques, we have first converted the proven layout of Fig. 1 to a fraction-of-turn digital 1-delay-line version. The outcome is reported in Ref. [1].

In an attempt to better suppress (reject) the persisting closed-orbit offset signal at $\omega = k\omega_0$, a supplementary option using a one-tap periodical (with a period ω_0) digital notch FIR filter in the feedback path was also tested.

Thus, de facto, the U70 has got a digital transverse feedback employing the key techniques of (1) weighted summation of beam signals, (2) two digital delay lines (delays $\tau < 2\pi/\omega_0$ and $\tau + 2\pi/\omega_0$).

Next self-suggesting step was to arrange a more straightforward and promising single-pickup option with 3 (or 4, optionally) variable delay lines shown in Fig. 2.

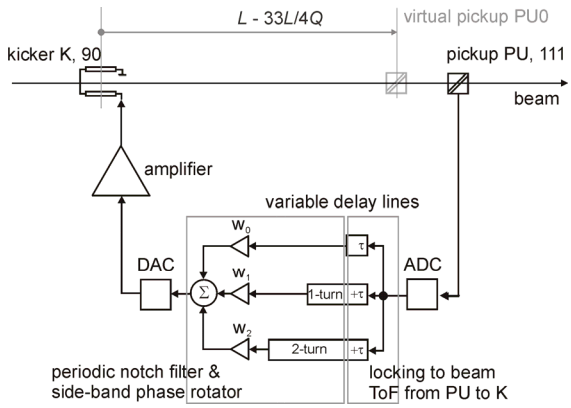

Figure 2: Layout of the new wide-band digital feedback (here, with 3 delay lines).

FIR FILTER LAYOUT

This topology was put forward in Refs. [2, 3]. Its attractive features are:

1. Use of natural-to-DSP circuits, esp., variable delay lines realized, say, as FIFO shift registers clocked by the higher (16^{th}) harmonic of (the U70) acceleration frequency ($\omega_{RF}/2\pi$ = 5.516–6.062 MHz).
2. A single beam-pickup layout that saves a room on the orbit.
3. An arbitrary betatron phase advance between pickup and kicker.
4. A natural built-in rejection of (unwanted) steady-state DC and higher rotation frequency harmonic signals present in raw beam position monitor readouts.

The latter occurs due to in-out open-loop feedback transfer function that is synthesized as a periodic notch filter.

Following the approach of Refs. [1–3], effect of the feedback on beam is treated in terms of a transverse coupling impedance $Z_k^{(FB)}(\omega)$ imposed by the circuit,

$$Z_k^{(FB)}(\omega) = -iG(\omega)\exp(-ik\Delta\Theta_{K-PU}) \qquad (1)$$

where $G(\omega)$ is in-out transfer function of electronics in the open feedback loop, reduced to units of Ohm/m; distance between PU and K (both are short) is $\Delta\Theta_{K-PU} = \Theta_K - \Theta_{PU}$.

On putting aside finite bandwidths of PU, power amplifier and K sections, one gets for the layout of Fig. 2

$$G(\omega) = G_0 \exp(i\omega\tau)\sum_{h=0}^{H} w_h \exp(i\omega 2\pi h/\omega_0) \qquad (2)$$

where a purely real $G_0 > 0$ is feedback gain, τ is delay time of signal processing, w_h are real summation weights, $H+1$ is the number of delay lines employed (3 or 4). Time τ is set equal to beam time-of-flight from PU to K,

$$\tau = \Delta\Theta_{K-PU}/\omega_0 < 2\pi/\omega_0 , \qquad (3)$$

that is the minimal (fraction-of-turn) delay in the system.

The $\exp(-i\omega t)$ and upper betatron side-band conventions are adopted with frequency line series $\omega \cong (k+Q)\omega_0$ where Q is betatron tune (about 9.8–9.9 in the U70).

Then, to impose a purely imaginary (damping) coherent tune shift one has to adjust the feedback to obtain

$$Z_k^{(FB)}(\omega) = G_0 + i0 \quad \text{at} \quad \omega = (k+Q)\omega_0 . \qquad (4)$$

Still more, to get the 1st order periodic notches, one sets

$$G(\omega) = 0 \quad \text{at} \quad \omega = k\omega_0 \qquad (5)$$

that requires $H = 2$, or 3 delay lines (FIR-3 filter, Fig. 2).

To widen the rejection stop bands, the 2nd order notches might be foreseen by putting an additional constraint

$$dG(\omega)/d\omega = 0 \quad \text{at} \quad \omega = k\omega_0 \qquad (6)$$

that now requires $H = 3$, or 4 delay lines (FIR-4 filter).

Equations 4, 5 are solved for a 3-delay-line option with

$$w_0 = -\frac{\sin((3\pi + \Delta\Theta_{K-PU})Q)}{2\sin\pi Q \sin 2\pi Q}, \qquad (7)$$

$$w_1 = +\frac{\sin((2\pi + \Delta\Theta_{K-PU})Q)}{2\sin^2 \pi Q}, \qquad (8)$$

$$w_2 = -\frac{\sin((\pi + \Delta\Theta_{K-PU})Q)}{2\sin\pi Q \sin 2\pi Q}. \qquad (9)$$

Weights for a 4-delay-line option are given in Ref. [3].

In the U70, $\Delta\Theta_{K-PU} = 2\pi\cdot 99/120$. Consider, for definiteness, a base-line (central) betatron tune $Q_0 = 9¾$. The resultant weight coefficients $w_h(Q_0)$ are listed in Table 1.

Table 1: Summation weights for FIR filters

FIR-	w_0	w_1	w_2	w_3	Σw_h
3	0.617	–0.963	0.346	0	0
4	0.481	–0.827	0.210	0.136	0

Re and Im parts of $Z_k^{(FB)}(\omega)$ are plotted in Fig. 3. Plots are odd (Re) or even (Im) about the abscissa zero due to reflection symmetry $Z_{-k}(-\omega) = -Z_k(\omega)^*$ of any transverse coupling impedance. Notches in amplitude transfer are 0.10 or $0.13\omega_0$ wide (FW@G_0/10) for 3 or 4 delays, resp.

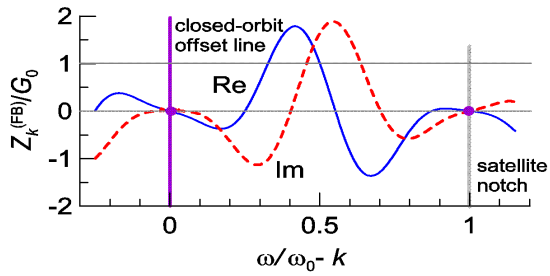

Vicinity of the fundamental notch at $\omega = k\omega_0$, Eq. 5.

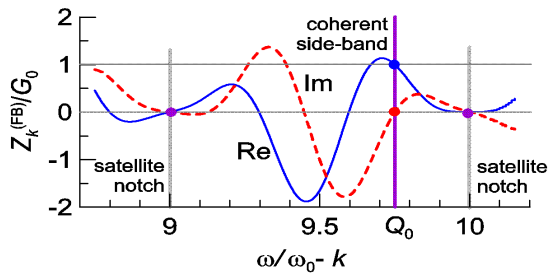

Vicinity of line $\omega = k\omega_0 + Q$ due to coherent motion, Eq. 4.

Figure 3: Transverse coupling impedance imposed by feedback, a 3-dealay-line option. For a given k, beam probes impedance only in 2 frequency domains shown.

Given fixed weights $w_h(Q_0)$, the feedback will keep on damping in a certain range of tunes Q around the base-line value Q_0. Safety margins are listed in Table 2, where phase $\varphi = 0$ is ascribed to perfect damping (purely imaginary coherent tune shift) at $Q = Q_0$; $\varphi = \pm\pi/2$ stand for a loss of damping, while range $|\varphi| \le \pi/4$ corresponds to the operational data set. Even the unattended system that is not resetting $w_h = w_h(Q)$ in response to $Q \neq Q_0$ is well robust with respect to a variation of the working point.

Table 2: Phase safety margins in Q near Q_0

FIR-	$-\pi/2$	$-\pi/4$	0	$+\pi/4$	$+\pi/2$
3	9.60	9.67	9.75	9.83	10.0
4	9.61	9.68	9.75	9.82	9.88

We have tried but found no practical reasons to employ a 4-delay-line option in the **digital** feedback in question.

Indeed, on the one hand, the last row of Table 2 shows that due to a widened satellite 2nd order notch, the FIR-4 feedback gets a narrower safety margin in the tune offset from Q_0 towards the closest integer $Q = 10$.

On the other hand, the 3 digital delays clocked by a higher harmonic of the RF produce a periodic 1st order notch FIR-3 filter whose stop band zeros by default perfectly follow the rotation harmonics $k\omega_0$ to be rejected. In the final analysis, the same source (the master oscillator and RF) governs the notches and interferences they reject. There is no need to widen the stop bands altogether.

HARDWARE

Analog part of the system is specified in Ref. [1].

Digital part employs COTS digital processing board XDSP-3PCM [http://www.setdsp.ru/] equipped with the

Xilinx FPGA matrix, 2 ADC (12 bit), 2 DAC (14 bit) and plugged into a PCI slot of an industrial PC iROBO-2000.

Sampling is performed at the 16th harmonic of RF frequency (use of the 8th harmonic invokes under-sampling). Since RF harmonic number in the U70 is 30, the one-turn record length $N = 30 \cdot 16 = 480$ samples. Sampling period Δt is around 10 ns. The delay lines are FIFO shift registers. The fraction-of-turn delay τ is factored out of parallel branches shown in Fig. 2 and is a common variable-length register, while all the multi-turn delays (2 or 3) being the fixed-length devices. The latter constitute a "periodic notch filter and side band phase rotator" network whose optimized topology adopted is shown in Fig. 4.

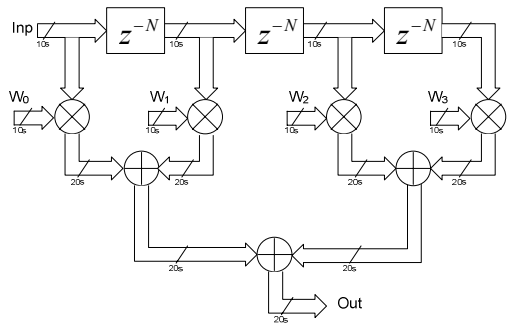

Figure 4: Periodic notch filter and side band phase rotator. z^{-N} is a one-turn delay in the z-transform notation.

Mathematics of the digital processing is executed with truncated 10-bit variables to save resources. Intrinsic in-out delay over the entire DSP section is $10\Delta t$ (100 ns ca).

BEAM OBSERVATIONS

Figures 5 show results of setting variable-length register to lock signal-processing delay τ to beam time-of-flight from pickup PU#111 to kicker K#90, Eq. 3. Top trace is a control signal from the K#90 caused by the earlier bunch traversal through PU#111. Central trace is the same bunch seen with a half of the service PU#90 close to K#90. The correction is applied to the measured beam sample with a time mismatch of about $\pm\Delta t/2$ (± 5 ns).

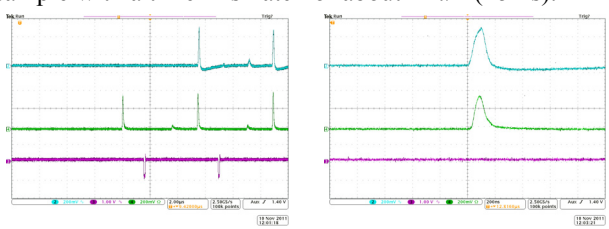

Figure 5: Tuning a fraction-of-turn delay τ.

Operation of the notch filter and side band phase rotator is illustrated by Figs. 6. Raw beam readouts from PU#111 have an unsuppressed DC offset. It is safely eliminated with filtering. In Fig. 6 (left) phase of residual slow coherent signal is rotated by π, intentionally. In Fig. 6 (right) the phase rotation is reduced to $\pi/2$ which allows to convert beam displacement AC signal acquired by PU#111 into beam trace slope correction forced by K#90.

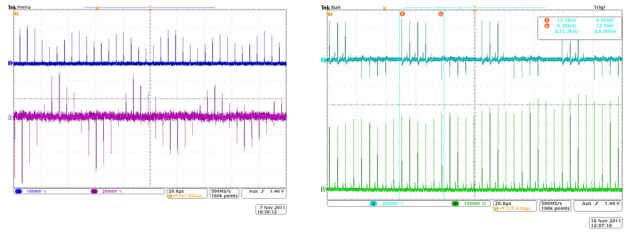

Figure 6: Operation of the notch filter and side band phase rotator with beam signals.

Figure 7 shows effect of closing the 3-delay-line beam feedback at flat-bottom in a linear (proportional) mode. Zoom scan width is 4 ms. Damping time is about 2 ms.

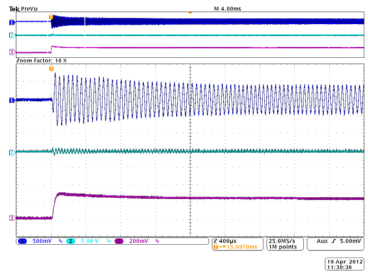

Feedback OFF, a natural decay due to phase-plane mixing

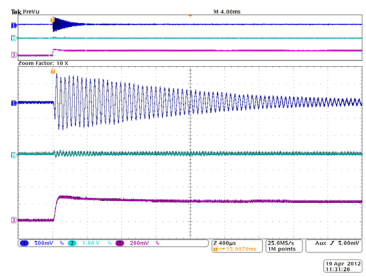

Feedback ON, a forced decay

Figure 7: Damping of radial oscillations at injection (upper trace). Lower trace is beam intensity (DCCT).

CONCLUSION

The novel digital wide-band transverse (horizontal and vertical) beam feedback system was successfully beam-tested in the U70 proton synchrotron during machine runs 2011-2, 2012-1. It was found transparent for tuning and effective in managing the beam.

The most attractive features of the system are (1) an integrated all-in-one handling of steady-state (rejection) and coherent (damping) beam signals, and (2) a single-pickup configuration with an arbitrary betatron phase advance between pickup and kicker allowed.

REFERENCES

[1] O. Lebedev et al., Proc. of RUPAC-2010, Protvino, 2010, p. 239–241.
[2] S. Ivanov, Preprint IHEP 97–64, Protvino, 1997.
[3] S. Ivanov, Proc. of the 17-th Int. Conf. on High Energy Accel., HEACC-98, Dubna, Report 50, 1998.

THE OPTIMIZATION OF RF DEFLECTOR INPUT POWER COUPLER

A. Smirnov, O. Adonev, N. Sobenin,
NRNU MEPhI, Moscow, 115409, Kashirskoe sh., 31, Russia
A. Zavadtsev, NanoInvest, Moscow, Russia

Abstract

This paper concerns the investigation of different types of input power cell for S-band RF electron deflector. This device serving for slice emittance diagnostics is a disc-loaded waveguide which operates with TE_{11}-like wave in travelling wave regime with 120 deg phase shift per cell. Since this deflector meets the restriction on its length and has to provide high enough deflecting potential to a particle during its flight time it is significant to increase the transversal field strength in coupling cell or to shorten it so that the deflecting potential remains constant. The total structure consists of 14 regular cells and two couplers. As it is now all cells have the same length equal to D=33.34 mm and the field in couplers is lower than that of regular cells. In this paper different lengths are considered and numerically simulated in order to choose the best one.

INTRODUCTION

A deflecting voltage seen by a particle travelling along the axis of a disc-loaded waveguide driven with dipole TE_{11} (Fig. 1) mode can be calculated using transversal values of on-axis electric and magnetic fields or using longitudinal value of the electric field at some offset from the axis (Panofsky-Wenzel theorem) [1].

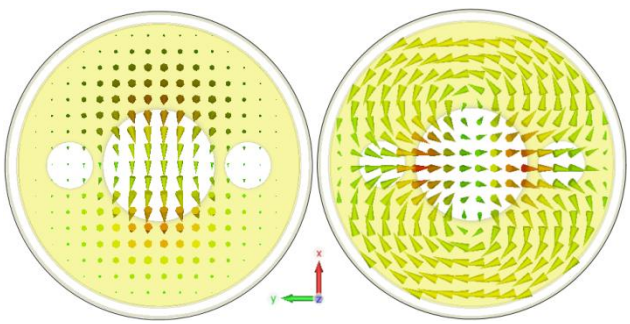

Figure 1: Electric (left) and magnetic (right) fields of TE11 mode

In the first method, we can use x-component (vertical) of E-field and y-component (horizontal) of H-field distributions along the axis z, since the particle experiences actions from both fields. Electric and magnetic fields are orthogonal to each other. The equivalent transversal deflecting field can be derived from the expression of Lorentz force $F_L=eE_d=e(E_x\pm vB_y)$:

$$\dot{E}_d(z)=\dot{E}_x(z)\pm\mu_0\beta c\dot{H}_y(z)\,, \qquad (1)$$

where (and further on) the sign '±' refers to the interplay of the particle and the wave propagation directions. According to time dependence of field components as $\exp(i[\omega t+\theta])$, this gives the equation for the transversal potential that is gathered by electron on a path from z=0 to z=L (structure length):

$$V_d(\theta)=\int_0^L\Re\left(\dot{E}_d(z)\right)dz=$$

$$=\int_0^L\left|\dot{E}_d(z)\right|\cos\left(\varphi_{E_d}(z)\pm\frac{2\pi}{\lambda}z+\theta\right)dz\,, \qquad (2)$$

where λ=c/f is the wavelength and θ is the initial phase of the deflecting voltage with respect to particle. Now by varying θ through the range from 0 to 2π one can find the maximal value of the deflecting voltage V_{dmax}.

An approach through Panofsky-Wenzel theorem requires longitudinal component of the electric field only, which is taken at some small enough vertical offset from the structure axis a – $E_z(z, x=a)$. The transverse deflecting field in this case is

$$\frac{\lambda}{2\pi}\left.\frac{\partial\dot{E}_z(z)}{\partial x}\right|_{x=0}\approx\frac{\lambda\dot{E}_z(z,x=a)}{2\pi a} \qquad (3)$$

due to the fact that longitudinal on-axis field $E_z(x=0)$ is nil for hybrid waves. And the corresponding potential V_{dmax} can be found from the following expression by varying θ from 0 to 2π:

$$V_d(\theta)=\frac{\lambda}{2\pi a}\times$$

$$\times\int_0^L\left|\dot{E}_z(z,x=a)\right|\cos\left(\varphi_{E_z}(z,x=a)\pm\frac{2\pi}{\lambda}z+\theta\right)dz. \qquad (4)$$

Both dependencies (2) and (4) are sin-shaped and shifted with 90^0, which is result of Maxwell equations.

TRANSVERSE DEFLECTING STRUCTURE

The structure layout [2] is presented on Fig.2. Cell irises have two additional holes used both for coupling between the cells and for stabilization of the mode polarization plane. The deflector consists of 14 regular cells with length of D=33.34mm (required for a phase shift of 120^0 per cell) and two power couplers, therefore

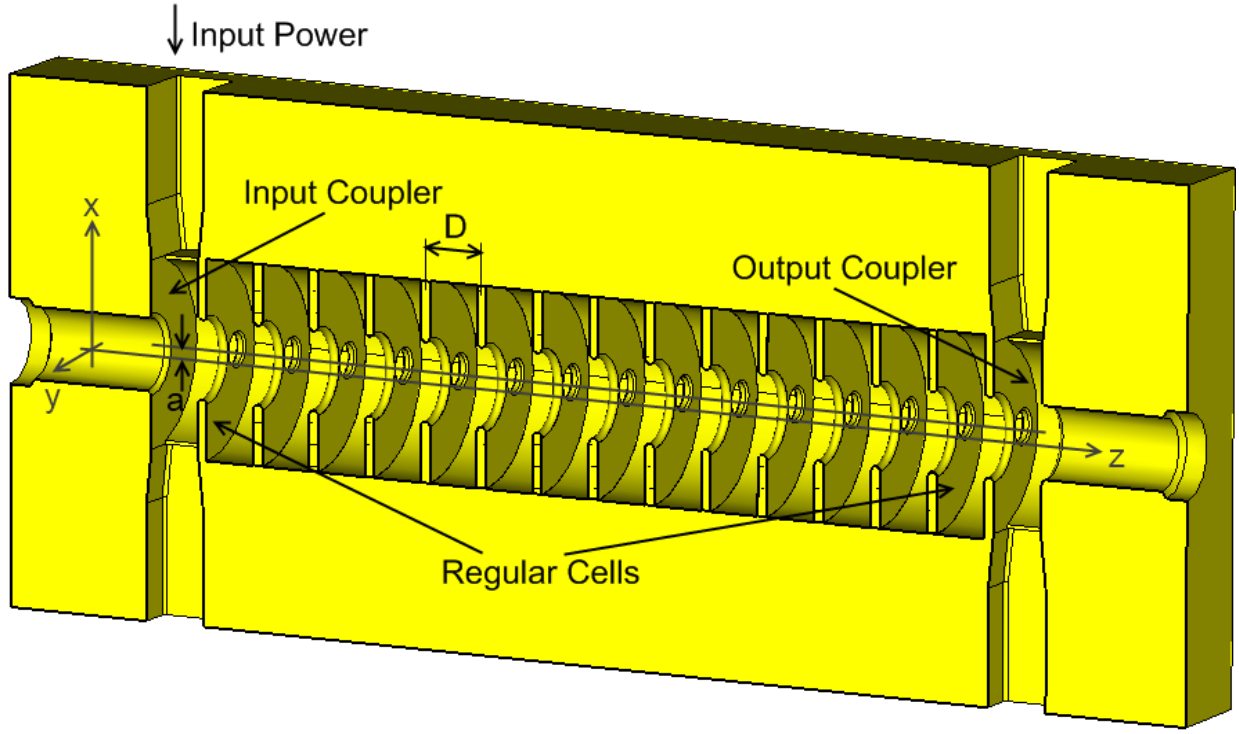

Figure 2: Transverse deflecting structure (longitudinal section)

total length is 16*D*=533.44mm. It operates at frequency of 2.9972 GHz. The input power is 2.5 MW, which provides total deflecting voltage of 1.8 MV. Both couplers are equal and are tuned to provide matching with feeding rectangular waveguides at the operating frequency, which results in travelling wave regime inside the structure.

COUPLERS COMPARISON

In this section we will describe the investigation of three couplers with different lengths – *D*, 3*D*/4 and *D*/2 (the latter one is shown on Fig. 3) – in terms of deflecting efficiency.

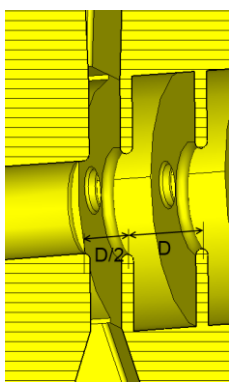

Figure 3: Input power coupler with length of D/2

In order to calculate the transversal voltage we first tune all couplers by adjusting its radius and the width of coupling window to have good matching at 2997.2 MHz (as shown on Fig.4) and travelling wave with phase shift of $120^0 \pm 1^0$ per cell.

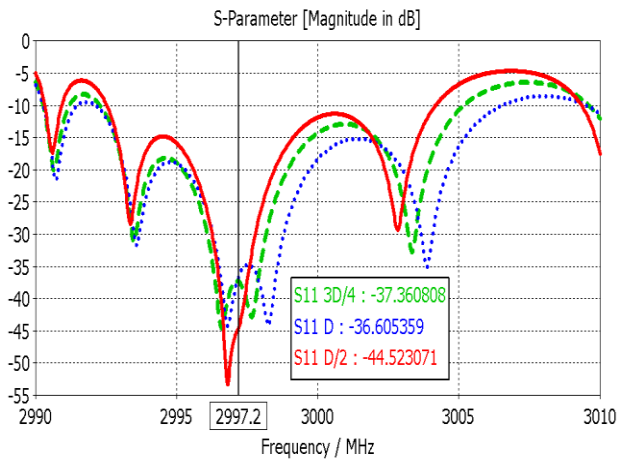

Figure 4: S11 vs. frequency for different coupler lengths: *D* (blue, dotted), 3*D*/4(green, dashed), *D*/2 (red, solid).

Second, we extract required field distributions along the specified lines from numerical simulations and then we renormalize these values for input power of 2.5 MW in order to calculate deflecting fields with (1) and (3). The corresponding curves are plotted on Fig.5 and Fig.6 respectively.

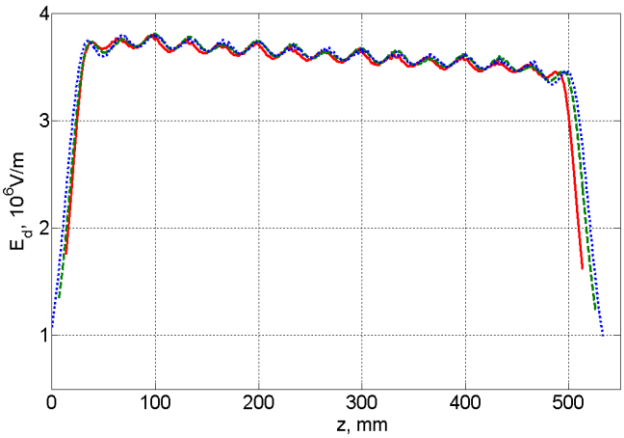

Figure 5: E_d (z) for different coupler lengths: D (blue, dotted), 3D/4(green, dashed), D/2 (red, solid).

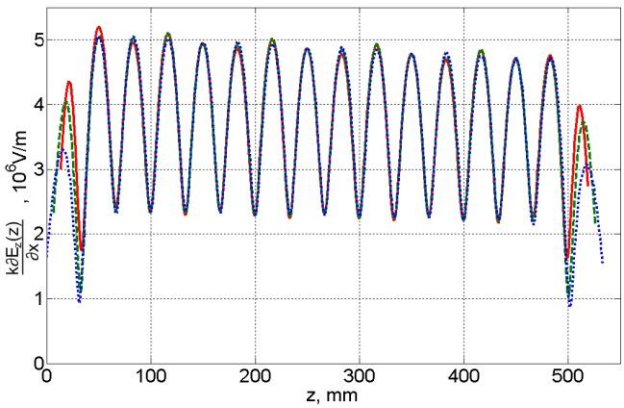

Figure 6: $k\partial E_z(z)/\partial x$ (z,x=a=4mm) for different coupler lengths: D (blue, dotted), 3D/4(green, dashed), D/2 (red, solid).

The plots on Fig.5 and Fig.6 are snapped over the range from D to 15D (33.34..500.10 mm) to indicate that the deflecting fields corresponding to the regular cells are equal and do not depend on the coupler geometry. The only difference appears in couplers. The slope along z-axis is due to the RF power dissipation in copper walls.

Third, using (2) and (4) we calculate the deflecting voltages inside two regions: the full structure including all cells and in regular cells only. The field penetration inside the beampipes is not considered. The difference between potentials of these two regions is sum of both couplers potentials. The results of the calculations are listed in Table 1.

Table 1: Deflecting voltages with different couplers

Coupler Length	Method	V_{dmax}, MV		
		Full Structure	Regular Cells	Couplers
D	On-axis	1.8356	1.6858	0.1498
	P-W	1.8138	1.6782	0.1356
3D/4	On-axis	1.8164	1.6864	0.130
	P-W	1.8012	1.6791	0.1221
D/2	On-axis	1.7982	1.6924	0.1058
	P-W	1.7863	1.6832	0.1031

It is shown that the two methods coincide well. The average value of potential contribution from each regular cell is 0.1202 MV. The renormalization of the deflecting potentials to the same coupler length gives the following relation between the coupler efficiencies with respect to a regular cell:

D : 3D/4 : D/2
62.5% : 72.1% : 83.2%

If the deflector is being used for bunch rotation instead of deflection, the field seen by the centre of the bunch is presented on Fig.7. Total deflecting voltage is zero in this case.

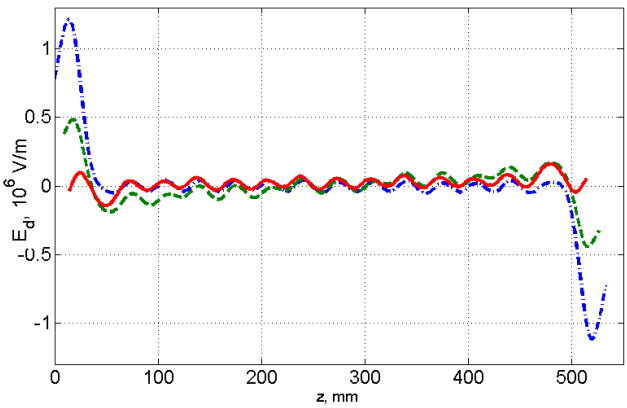

Figure 7: The transversal field at bunch centre along structure axis for different coupler lengths:
D (blue, dotted), 3D/4(green, dashed), D/2 (red, solid).

It is shown that coupler with D/2 provides much lower perturbing kick to a bunch.

CONCLUSIONS

In this work the three types of power coupler for RF deflector were considered. The total deflecting voltage seen by a particle was calculated with direct approach using on-axis fields and with Panofsky-Wenzel theorem. It was shown that twice as shorter coupler provides 1.33 times better deflecting efficiency. This fact can be used when it is preferable to increase the total deflecting potential of the deflector but also to keep its length the same by adding one regular cell. Also short coupler benefits in lower field perturbing kick when the deflector is being used for beam rotation.

REFERENCES

[1] W.K.H. Panofsky, W.A. Wenzel, Rev. Sci. Instrum. 27, 967, 1956

[2] L.V. Kravchuk et al., "Layout of the PITZ Transverse Deflecting System for Longitudinal Phase Space and Slice Emittance Measurements", Proc. of LINAC10, Tsukuba, Japan, 2010

SOFTWARE FOR VIRTUAL ACCELERATOR ENVIRONMENT

N. Kulabukhova*, St.Peterburg State University

Abstract

The article discusses appropriate technologies for software implementation of the Virtual Accelerator. The Virtual Accelerator is considered as a set of services and tools enabling transparent execution of computational software for modeling beam dynamics in accelerators on distributed computing resources. Control system toolkits EPICS (Experimental Physics and Industrial Control System), realization of the Graphical User Interface(GUI) with existing frameworks and visualization of the data are discussed in the paper. The presented research consists of software analysis for realization of interaction between all levels of the Virtual Accelerator.

INTODUCTION

In order to control large-scale accelerators efficiently, a control system with a virtual accelerator model was constructed by many facilities [1, 2]. In many papers by the words Virtual Accelerator an on-line beam simulator provided with a beam monitor scheme is mean. It works parallel with real machine. The machine operator can access the parameters of the real accelerator through the client and then feed them to the virtual accelerator, and vice versa. Such a virtual machine scheme facilitates developments of the commissioning tools; enable feasible study of the proposed accelerator parameters and examination of the measured accelerator data. That is the common scheme of virtual accelerators used in different laboratories [3]. Until now there is no virtual accelerator working without real machine. Our goal is to construct virtual accelerator application can be used independently from any machine.

CONCEPT OF THE VIRTUAL ACCELERATOR

The model of Virtual Accelerator like any other model is standard. As it is shown on the figure 1 first comes the approximation model where all necessary options are determined. Further, the theoretical models are constructed. On them computational models are build. After that the time for testing and verifying comes.

The key idea of Virtual Accelerator (VA) concept is beam dynamic modeling by the set of several packages, such as COSY Infinity, MAD, etc., based on distributed computational resources, organized on Grid- and Cloud-technologies. Simulation beam dynamics by different packages with the opportunity to match the results (in case of using different resources for the same task) and the possibility to create the set of tasks when the results of using

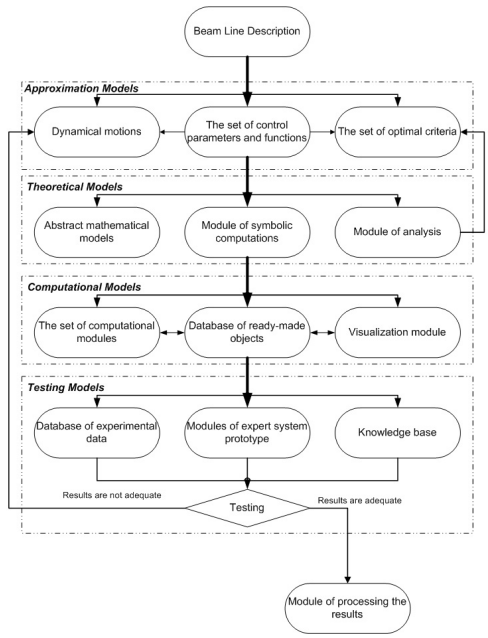

Figure 1: The total circle of computational experiment

one package can be sent to the input of another is the main use of VA [6]. Users will get the access to VA resources by unified interface including GUI on different platforms. Figure 2 shows the scheme of VA

The natural parallel and distributed structures of beam physics problems allow the use of parallel and distributed computer systems. But the usual approaches based on traditional numerical methods demand using the resources of supercomputers. This leads to the impossibility of using such multiprocessing systems as computational clusters. There are two classes of problems in beam physics which demand very extensive computer resources. The first class includes long-time evolution problems, the second is concerned with the computer realization of optimization procedures for beam lines. Examples of the first type of problem include multi-turn injection and extraction of the beam in circular accelerators. Usually, these problems do not consider space charge effects. For advanced applications it is essential to study beam dynamics in high-intensity accelerators. Such machines are characterized by large beam currents and by very stringent uncontrolled beam loss requirements. An additional difficulty of numerical simulation is connected with long-time beam evolution that requires the computation of hundreds of thousands or millions of turns. It requires the use of high-performance computers for beam evolution study. The problems of similar multi-turn evolution such as transverse stability with

* kulabukhova.nv@gmail.com

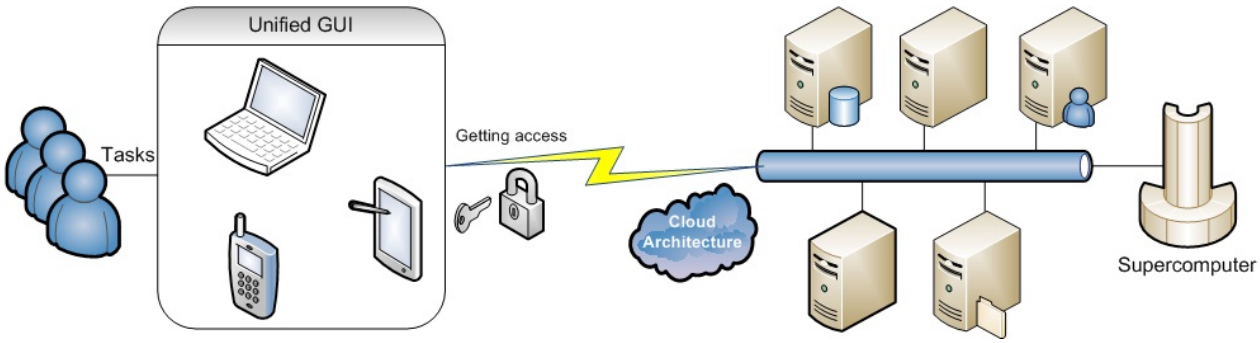

Figure 2: VA scheme

nonlinear space charge, uncontrolled beam losses due to space-charge-induced halo generation, etc. can also be mentioned. These problems are peculiar to modern high-intensity machines and require careful investigations of long-time evolution effects. From the computational point of view there are some problems related to the choice of models for beams with space charge, the presentation form of the beam propagator, and so on.

Construction of VA

The common scheme of VA as a computational resource can be presented as following:

- Access to the VA resources by the authorization and authentication of users (symbolic password, graphical password, etc.)
- Specify initial data and settings for calculation. Interaction between user (unified GUI interface) and different packages (COSY Infinity, MAD, OptiM)
- Choice of the packages and simulation algorithms (more deeply in section Methods realisation will be discussed)
- Monitoring of the task states, data visualization and representation. Access to a logging system with error tracking.
- Access to the storage of user data that can be represented as simple remote file system with users directories and files.

Grid environment allows coordinated resource sharing and problem solving among groups of trusted users within Virtual Organizations. Such environments enable global distributed collaborations involving large numbers of people and large scale resources, and make data and computing intensive scientific experiments feasible. One of the important research topics in e-Science is to develop effective Grid enabled Problem Solving Environments (PSE), also called Virtual laboratories, for different scientific domains. Organizing software utilities (e.g. simulators, visualization and data analysis tools) as a meta experimental environment, a PSE allows a scientist to plan and conduct experiments at high level of abstraction [4].

Methods realisation

It has already been said that Virtual Accelerator in itself can use different packages to calculate. Note that user can define the structure on one language (for example, on COSY Infinity notation) and select another program for calculation (e.g. OptiM). In this case conservation of system description will be made by the VA infrastructure invisible for user. And give the instructions to start the simulation. How it will be is shown on Figure 3.

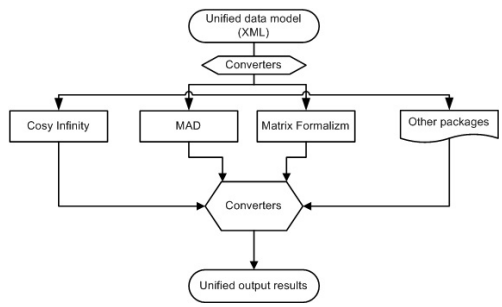

Figure 3: Scheme of unified access to different packages

SOFTWARE FOR VA

Client Application

As we mentioned above VA can provide unified access to it services both for web and desktop application. Not all services are required in each case. For example, for EDM-search project[1] it is necessary to include only electrostatic elements, optimization modules and related components. Other modules are enabled but available for the research purposes.

Task Monitoring

For the calculation complex problems it is important to provide monitoring tools. Researchers at any time can have an opportunity to see progress of the task, restart or cancel it, save obtaining result and etc. This requirements provide

[1] St. Petersburg State University collaborates with Institute for Nuclear Research of Forschungszentrum Julich, Germany.

a complete integrated computing environment for composing, running, controlling and visualizing applications (see figure 4).

Figure 4: VA tools

Connection to Physical Equipment

From our point of view model of Virtual Accelerator should consist of a simulation engine that reads in all relevant lattice settings from the accelerator control system and computes data corresponding to the real diagnostic data output from the real accelerator. Or, if it is no accelerator exist at that time, mathematical model will be given to compare the results. Here would ideally be a one-to-one map between all relevant control parameters and output data from the machine and its simulated counterpart. This model inherently assumes that the simulated lattice updates automatically any time the physical lattice settings are modified. If we speak about mathematical model, it means that at any time we can change settings and continue the computations This model should represent an extremely valuable tool to the beam physicist by providing a useful way to benchmark the simulation engine as well as providing a detailed description of the dynamics in the accelerator in real time. By saying real time, it means the time the system needs to get the problem, to analyze it and to give the message about it on the screen. It does not allow the beam physicist to directly use the simulation engine to guide beam operation because the virtual lattice settings are limited to those read in from the physical machine. This is the problem that led us to identify the three key requirements used in the design and implementation of our application (having mathematical model it is not a problem):

- The ability to simultaneously and independently operate two accelerators in real time: one real and one virtual.
- The ability to synchronize the lattice settings in both machines.
- The ability to control and display relevant data from both machines in one integrated graphical user interface.

To fulfill these requirements we use Experimental Physics and Industrial Control System (EPICS)[5]because it has followed a threetiered approach common to many high-level accelerator control and simulation systems. Figure 5 shows the basic layout of implementation. The three tiers in this scheme include the distributed Input/Output Controllers (IOCs) serving data from the physical accelerator (bottom), the EPICS-DDS middle layer (middle), and the Machine Client application (top). That is exactly we need to our system.

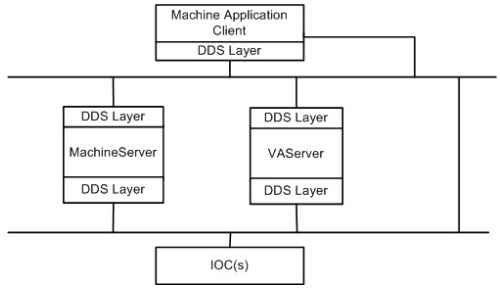

Figure 5: The Virtual Accelerator layout

CONCLUSION

The future development of the research can be based on writing software using different parallel techniques and complete implementation of the described approaches.

ACKNOWLEDGMENTS

Author thanks prof. Serge Andrianov and Andrey Ivanov for many useful discussions about Virtual Accelerator development.

REFERENCES

[1] P.C. Chiu, C.H.Kuo, Jenny Chen, Y.S. Cheng, C.Y.Wu, Y.K.Chen, K.T. Hsu, "Virtual Accelerator Development For The TPS,IPAC'10, Kyoto, Japan 2010, WEPEB019, p. 2728, http://www.JACoW.org.

[2] H. Harada, K. ShigakiF, Noda, H. Hotchi, H. Sako, H. Suzuki, K. Furukawa, S. Machida, "VIRTUAL ACCELERATOR AS AN OPERATION TOOL AT J-PARC 3 GEV RAPID CYCLING SYNCHROTRON (RCS), EPAC'06, Edinburgh, Scotland, 2006, WEPCH128, p. 2224, http://www.JACoW.org.

[3] A.Shishlo, P. Chu, J. Galambos, T. Pelaia, "THE EPICS BASED VIRTUAL ACCELERATOR CONCEPT AND IMPLEMENTATION, Proceedings of the 2003 Particle Accelerator Conference, pp. 2366-2368.

[4] V. Korkhov, D. Vasyunin, A. Belloum, S. Andrianov, A. Bogdanov, "Virtual Laboratory and ScientificWorkflow Management on the Grid for Nuclear Physics Applications, Distributed Computing and Grid-Technologies in Science and Education: Proc. of the 4th Intern, Dubna, Russia 2010, p. 153,http://www.JACoW.org.

[5] C. Gulliford, I. Bazarov, J. Dobbins, R. Talman, N. Malitsky,"The NTMAT EPICS-DDS Virtual Accelerator for the Cornell ERL Injector, IPAC'10, Kyoto, Japan 2010, WEPEB022, p. 2734, http://www.JACoW.org

[6] N. Kulabukhova, A. Ivanov, V. Korkhov, A. Lazarev, "Software for Virtual Accelerator Designing, ICALEPCS'11, Grenoble, France,2011, WEPKS016, p. 816, http://www.JACoW.org.

APPROXIMATE METHOD FOR CALCULATION OF FIELD OF CHARGED PARTICLE MOVING THROUGH DIELECTRIC OBJECT*

Ekaterina S. Belonogaya#, Sergey N. Galyamin, Andrey V. Tyukhtin,
Saint Petersburg State University, Saint Petersburg, Russia

Abstract

Cherenkov radiation is widely used for particle detection. As well, it is prospective for particle bunch diagnostics. Therefore, it is actual to elaborate methods for calculation of the fields of bunches moving in the presence of different dielectric objects. We offer the approximate method based on calculation of the field in unbounded medium and accounting of boundary influence with help of geometrical optics. First, we consider the problem concerning the field of charge crossing a dielectric plate. This problem has an exact solution. It is used as a "test" problem for estimation of precision of the approximate method. Computation of the field is performed using both methods and the results have a good agreement. Further, we analyze the cases of more complex objects, in particular, a dielectric cone. Note that the offered method allows to obtain wave fields using neither complex analytical transformations nor laborious numerical calculations.

INTRODUCTION

Problems of radiation of charged particles in the presence of dielectric objects are of interests for some important applications in the accelerator and beam physics. It can be mentioned for example a new method of bunch diagnostics offered recently [1]. For realization of this method, it is necessary to calculate the field of radiation outside a dielectric object. As a rule the form of object in such problems does not allow obtaining an exact analytical solution. Computer simulation of electromagnetic field is also very cumbersome. Therefore development of approximate analytical methods for analyses of radiation in such problems is an actual task. One of such methods will be offered and developed in this paper.

BASIS OF THE METHOD

The method offered here concerns problems which are characterized by some large geometric parameters. Let a charged particle bunch move in some dielectric or magnetic object. It is possible as well that the charge moves in a vacuum channel in the object, and radius of the channel can be arbitrary. In addition, the case of charge moving along one of borders of object can be considered, and in such case the distance from this border to the charge trajectory can be arbitrary. Anyway we assume that the sizes of the object are much more than wave lengths under consideration. Therefore, the Cherenkov radiation (CR) excited by the bunch runs inside the object some distance which is much more than wave lengths.

Under such conditions we can apply the following approach. At first, we calculate analytically the field of the charge in the infinite medium without "external" border. It is important that we can take into account such peculiarities of the problem as a vacuum channel (if the charge moves into the object) or finite distance from trajectory to the object's border (if the charge moves along the object). We underline that a lot of such problems have been solved in the literature.

The second step is approximate calculation of radiation going out of the object (sometimes it is named "Cherenkov-transition radiation" (CTR) [2]). The idea of this calculation is related to Fok's method of analysis of reflection of waves from arbitrary surfaces [3] but we deal with transmission instead of reflection. The incident field is multiplied by the Fresnel transmission coefficient, and then we should take into account decrease of the radiation because of spreading of a ray tube in the external medium. Thus we obtain the first of refracted rays of CTR. Probably, this will be enough for the majority of applied problems. If it will be necessary, multiple reflections and refractions on the object borders can be taken into account.

TESTING OF THE TECHNUQUE FOR DIELECTRIC LAYER

For testing the method, we use the problem about the field of point charge flying through the dielectric layer with permittivity ε placed at $0 < z < d$. The charge density is set in the form $\rho = q\delta(x, y, z - Vt)$. Such a problem has exact solution [4] which has been proved by us independently. We compare computations performed with use of exact formulae and approximate ones. Some results concerning the magnetic strength Fourier component $H_{\phi\omega}$ are given in Fig. 1. Note that approximate curves have a break on the boundary of "the light bar". Naturally, the exact solution is continuous everywhere (excepting the layer boundaries).

One can see that some agreement takes place even for $d \sim \lambda_2 = 2\pi c / \left(\omega\sqrt{\varepsilon}\right)$ if the distance from the plate is $\sim \lambda_2$ as well. In the case when $d \sim 10\lambda_2$ we have very good agreement for the most part of "the light bar". This result is very encouraging, and it stimulates applying the

*Work was supported by Saint Petersburg State University, the Dmitry Zimin "Dynasty" Foundation and Russian Foundation for Basic Research (Grant No. 12-02-31258)
ekaterinabelonogaya@yandex.ru

method under consideration for more complex object where the exact solution cannot be obtained.

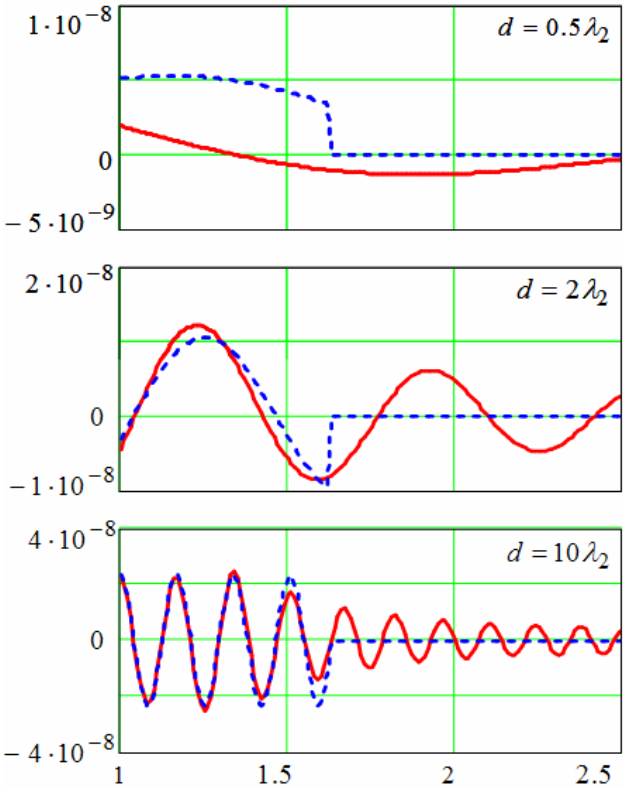

Figure 1: The magnetic strength Fourier component $H_{\phi\omega}(\mathrm{A\cdot s/m})$ depending on distance $z(\mathrm{cm})$ for charged particle crossing the plate: computations using exact (red solid curve) and approximate (blue dashed curve) formulae; $q = -1\mathrm{nC}$, $\varepsilon = 1.5$, $\rho = 0.6\,\mathrm{cm}$, $\beta = 0.99$

THE CASE OF CONE WITH CHANNEL

We apply the method under consideration to the case of a dielectric cone with a cylindrical vacuum channel (Fig. 2). The external boundary of the cone is determined by the equation $\rho = (z_0 - z)\tan\alpha$ where $0 < \alpha < \pi/2$. The channel radius a can be both less and more than the typical wave lengths. A point charge moves along the channel axis (z-axis). It is assumed that the wave of CR in the dielectric passes a distance much more than wave lengths.

The first step of our consideration is solving the problem with infinite medium with vacuum channel (the solution of this problem is known [5]). At the second step, we firstly determine the point M_* of incidence of wave of CR on the cone boundary. The coordinates ρ_*, z_* of this point is a function of the coordinates of the observation point. Further, one can show that spreading of the ray tube outside the cone is the same as inside it. As result we obtain the expression for field outside the cone in the form

$$H_{\phi\omega} \approx H^*_{\phi\omega}\sqrt{\frac{\rho_*}{\rho}}\,T\exp\left(i\,\omega L/c\right),$$

where $H^*_{\phi\omega}$ is an incident field at M_*, T is Fresnel transmission coefficient, L is a ray path in vacuum.

Figures 3 - 6 illustrate some properties of the solution obtained by the method under consideration. All graphics

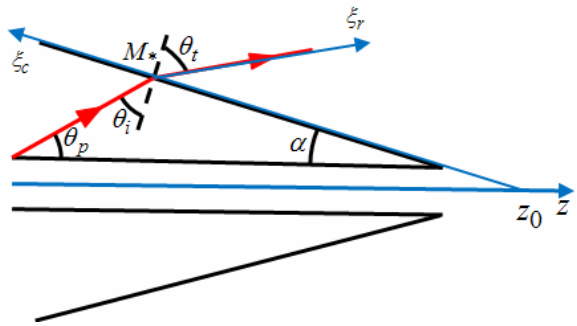

Figure 2: Cross-section of the cone.

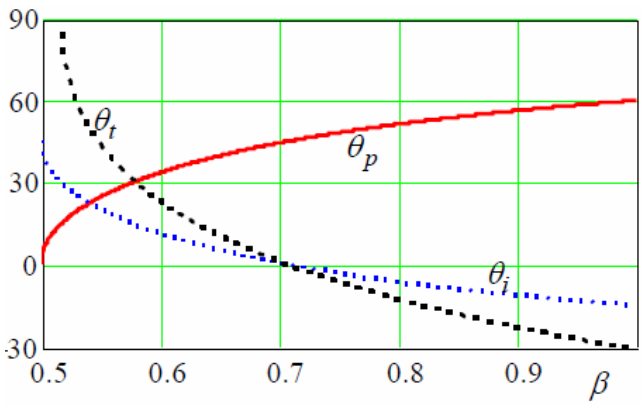

Figure 3: Angle of CR, angle of incidence and angle of refraction (in degrees) depending on the charge velocity for $\varepsilon = 4$.

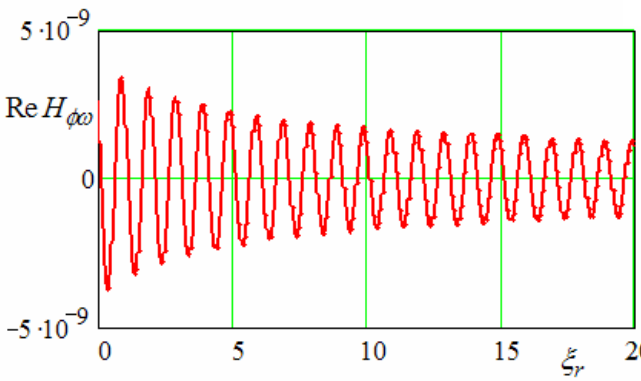

Figure 4: The magnetic field Fourier transformation $(\mathrm{A\cdot s/m})$ depending on distance $\xi_r(\mathrm{cm})$ from the cone surface along the transmitted ray; $q = -1\mathrm{nC}$, $\omega = 2\pi\cdot3\cdot10^{10}\,\mathrm{s}^{-1}$, $\varepsilon = 4$, $a = 2\mathrm{mm}$, $\alpha = 45^{\circ}$, $\beta = 0.99$

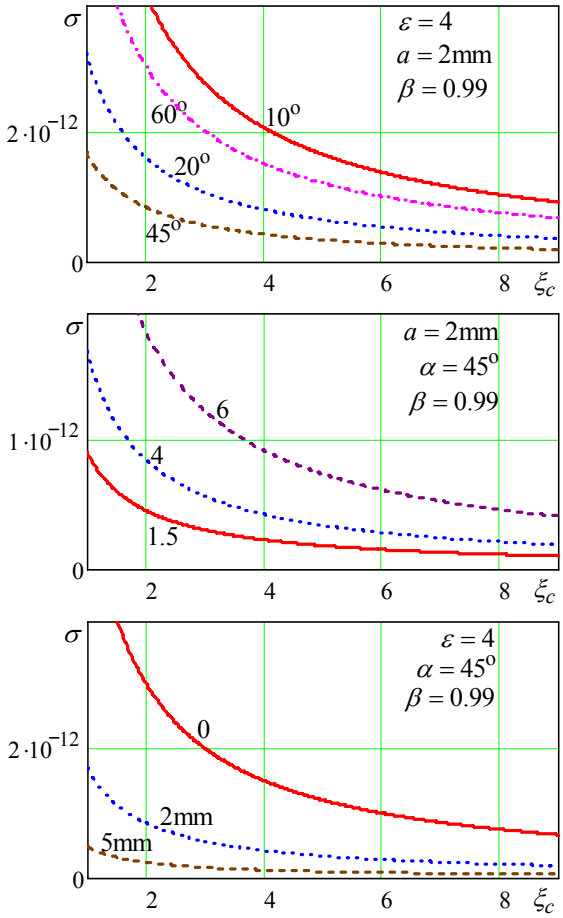

Figure 5: Dependency of the spectral density of the radiation energy $\sigma\left(\mathrm{J}\cdot\mathrm{s}/\mathrm{m}^2\right)$ on the distance ξ_c(cm) along the cone surface for different angles α (top), different permittivity values ε (middle), and different channel radii a (bottom).

All graphics have been obtained for $q=-1\mathrm{nC}$ and $\omega = 2\pi\cdot 3\cdot 10^{10}\,\mathrm{s}^{-1}$. Figure 3 shows the angle of CR, the incidence angle and the refraction one (see Fig. 2) depending on the charge velocity. Note that positive values of θ_i and θ_t correspond to the case shown in Fig. 2, these angles are negative at other positional relationship of the rays and the normal to the cone boundary.

Figure 4 illustrates typical dependency of the magnetic field Fourier transformation on the distance ξ_r from the cone surface along the direction of the transmitted wave propagation. Naturally, decrease of amplitude is explained by cylindrical divergence of radiation.

Figure 5 shows the spectral density of the radiation energy $\sigma\sim\left|H_{\phi\omega}\right|^2$ depending on the distance ξ_c along the cone surface (see Fig. 2). This value determines the total energy Σ passing through a unit square: $\Sigma=\int_0^\infty \sigma d\omega=\int_{-\infty}^{\infty} S dt$, where S is a Pointing vector.

Dependencies of σ on the charge velocity and the cone angle at some fixed point on the cone surface are shown in Fig. 6. It is interesting, for example, that dependence of σ on the cone angle is not monotonous. Note that for some value of α this magnitude tends to infinity that is connected with approach of θ_i to the limit angles of total reflection.

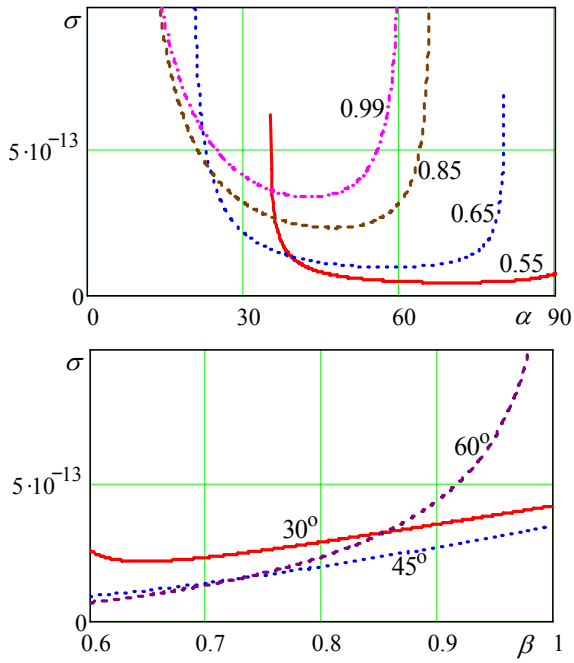

Figure 6: The spectral density of the radiation energy $\sigma\left(\mathrm{J}\cdot\mathrm{s}/\mathrm{m}^2\right)$ on the cone surface at ξ_c=5cm depending on α for different β (top) and on β for different α (bottom); $\varepsilon=4$, $a=2\mathrm{mm}$.

REFERENCES

[1] A. P. Potylitsyn, Yu. A. Popov, L. G. Sukhikh, G. A. Naumenko, M. V. Shevelev, Journal of Physics: Conference Series 236 (2010) 012025.
[2] S. N. Galyamin, A. V. Tyukhtin, Phys. Rev. B 81 (2010) 235134.
[3] V. A. Fok, Electromagnetic diffraction and propagation problems (Oxford, New York: Pergamon Press, 1965).
[4] V. L. Ginzburg, The propagation of electromagnetic waves in plasma (London: Pergamon, 1964).
[5] B. M. Bolotovskii, Sov. Phys. Usp. 4 (1962) 781.

MODERNIZATION OF THE AUTOMATED CONTROL SYSTEM IN THE KURCHATOV SYNCHROTRON RADIATION SOURCE

E. Kaportsev, A. Valentinov, V. Dombrovsky, V. Korchuganov, Yu. Krylov, K. Moseev, N. Moseiko, Yu. Yupinov, RRC Kurchatov Institute, Moscow, Russia
Yu. Efimof, CJSC RTSoft, Moscow, Russia

Abstract

The running cycle of Kurchatov Synchrotron Radiation Source (KSRS) includes the injection of electrons with energy 80 MeV from the linear accelerator in the booster storage ring Siberia-1, the accumulation of a electron current up to 400 mA and, then, electron energy ramping up to 450 MeV with the subsequent extraction of electrons in the main ring, storage ring Siberia-2, and accumulation there up to 300 mA, and at last the energy ramping up to 2.5 GeV. [1]

The current automated control system (ACS) of KSRS «SIberia» – synchrotron radiation source and the center of communities, NRC Kurchatov institute, was founded over 20 years ago on the basis of control equipment in the CAMAC standard. It is physically and morally outdated and does not meet modern requirements for speed, accuracy and data transmission.

This paper presents some options for replacing the old control system of KSRS with modern components, high-speed CPUs, standard VME, and high-speed industrial network CAN.

OPERATIONAL MANAGEMENT OF THE COMPLEX

The network consists of a machine operator workstations running Windows, connected with the local network Ethernet. [2] Applications obtain the diagnostic information from the database server based on MS SQL Server, where it comes from the application server. The database server and application server are located within one computer. The ADC and DAC integrated into CAN-network. The application server executes the control program and collecting data from sensors and diagnostics. We have three servers: Canserver, CAMAC messaging server и Vacuum server. [3]

Canserver, used to control the DAC and ADC via CAN network. The application server runs specialized programs that support communication with the CAN-network actuators, K167 controllers, RF generators and power systems. [4]

Messaging Server CAMAC organizes communication with controllers that have not adapted to the standard CAN. [5]

The management server of the vacuum system is located directly in the vacuum console. It has its own database, which stores the archive of the currents of vacuum pumps. [6]

The most important disadvantage of the control system is outdated equipment, made on a hardware platform CAMAC. Currently, developed in BINP (Novosibirsk), controllers and control modules are Non-Repair, due to obsolete element base and removed from the production of most parts, which have no analogue in the free distribution. Due to the failure of most modules of the control system, there was an urgent need to replace outdated equipment with modern, easily upgradeable and scalable.

Canserver server used to control the DAC and ADC via the CAN network. On the application server run specialized programs, which support communication on CAN-network with executive devices, such as high-frequency generators and power of magnetic systems. [3]

Messaging Server CAMAC [4] organizes the exchange of data with CAMAC crate controller with CAN interface type of K167 [5].Through it passed all the information from the controllers and modules that have not yet adapted to the standard CAN.

Management server of vacuum system is directly in the vacuum control room. It has its own database that stores the archive currents of vacuum pumps. [6]

UPGRADED ACS

Upgraded ACS of KSRS (further - UACS) will be a multi-level structure, conventionally divided into upper and lower level, server level and peripherals (fig.1). UACS structurally divided into five branches of management: control of the injection part of the complex (linear accelerator and small storage ring “Siberia-1”), management of large storage ring (“Siberia-2”), diagnostic of beam in accelerators, vacuum control and temperature control.

Lower Level of UACS

Lower level of UACS must be made on the basis of bus-modular equipment in the standard VME and control equipment with embedded processors, running under operating systems like Lynxos. At this level should be gathered diagnostic information and perform control algorithm of the complex systems. This equipment is connected to a server level with Ethernet or CAN.

Server Level of UACS

Server level of UACS includes application servers and a database management system (DBMS). At this level, to be implemented:

- general algorithm for management and monitoring of the KSRS;
- communication with the VME standard CPUs;
- communication with the CAN-controller;

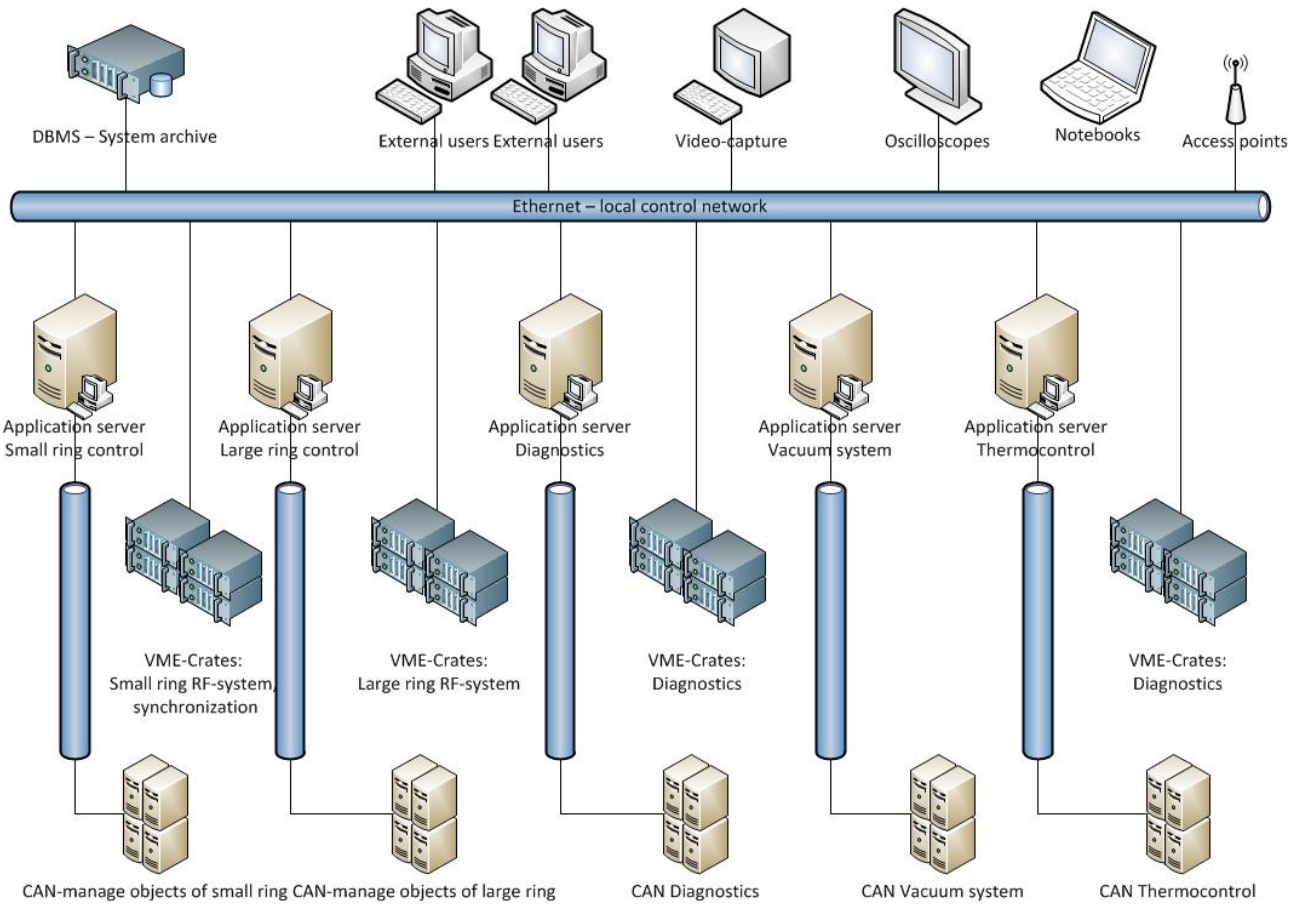

Fig.1. Structure of UACS.

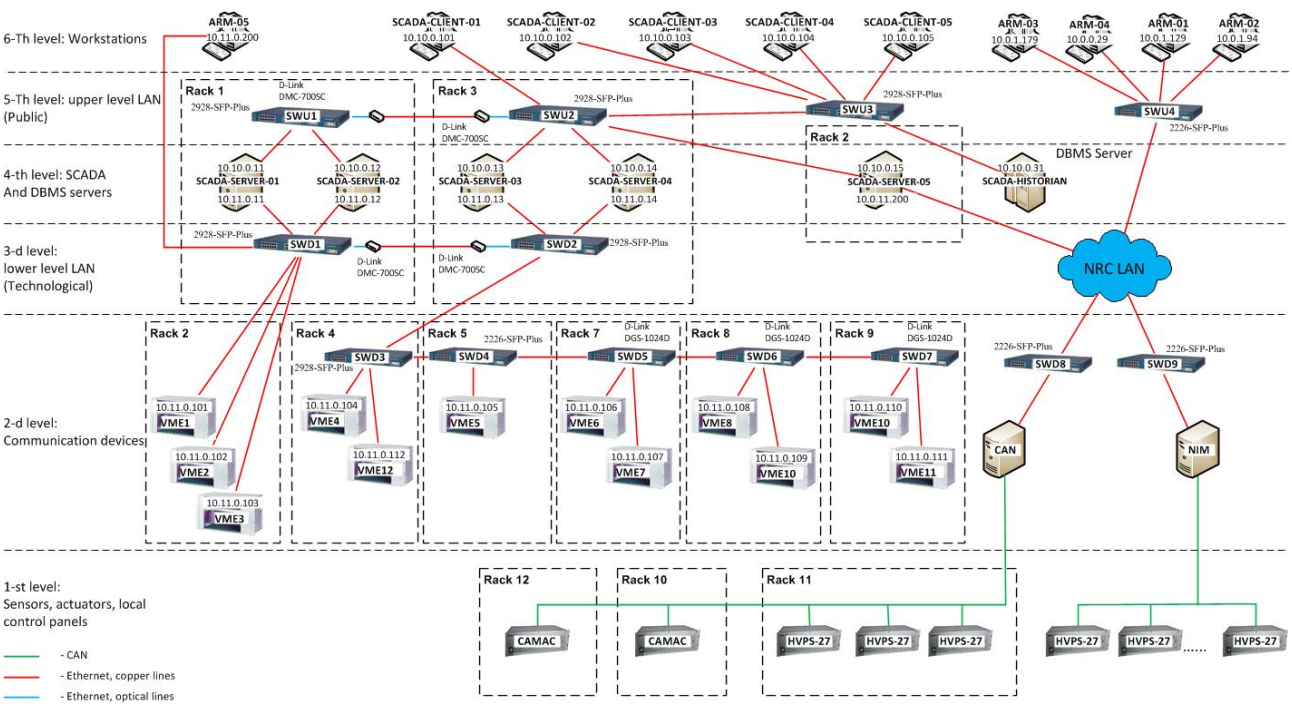

Fig.2. Block diagram of the TS.

- communication with the operator's workstations;
- operator's sessions logging;
- storage of information in the database;
- selection and provision of information to users' queries;
- diagnosis of software and hardware complex of UACS of KSRS (self-diagnostics).

Upper Level of UACS

The upper level includes the workstations of operators and other users of KSRSAt the top level must work full-featured system for monitoring and control - CitectSCADA.

CitectSCADA software enables: process visualization in graphic mode, management of workstations, tracking systems in real time in a graphical form and access to archived data, preparation of detailed reports, executing of subprogrammes, developed with CitectVBA and CiCode.

In the first phase of modernization was created test stand (TS), which is designed to develop and debug software for local UACS systems of KSRS. Block diagram of TS is shown in Fig. 2.

Functional structure of the TS is shown on Fig. 3. The functional structure of the TS has three levels of hierarchy:

On the 3rd level of the hierarchy are the operator's workstation (upper level);

At the 2nd level of the hierarchy are SCADA servers and database server (server level);

On the 1st level of the hierarchy are VME processor assembly and CAN-servers (lower level).

In conclusion, the new modernized system of automatic control of the complex will be run on modern hardware, provide operators and users with the necessary information in real time, provide the scientific community with sufficient historical data to allow further study of the physical processes.

REFERENCES

[1] V.Korchuganov et al., Kurchatov Synchrotron Radiation Source Facities Modernization. Proceedings of RuPAC XXII, Protvino, Russia, 2010.

[2] Yu.Krylov et al., Archiving and Monitoring of Status for KSRS. Proceedings of ICALEPCS 2005, Geneva, 2005.

[3] E.Kaportsev et al., The Expanded Program Tools for KSRS Operation with Archivation of Data. Proceedings of RuPAC XXII, Protvino, Russia, 2010.

[4] N.Moseiko et al., Intellectual Crate-controller K167. Proceedings of RuPAC XXI, Zvenigorod, Russia, 2008.

[5] E.Kaportsev et al., The Program Tools for KSRS Operation. Proceedings of RuPAC XXI, Zvenigorod, Russia, 2008.

[6] N.Moseiko et al., Modernization of the Vacuum System of Synchrotron Radiation Sources at the National Research Centre Kurchatov Institute. Physics of Particles and Nuclei Letters, 2012, vol.9, No.4-5, pp.456-460.

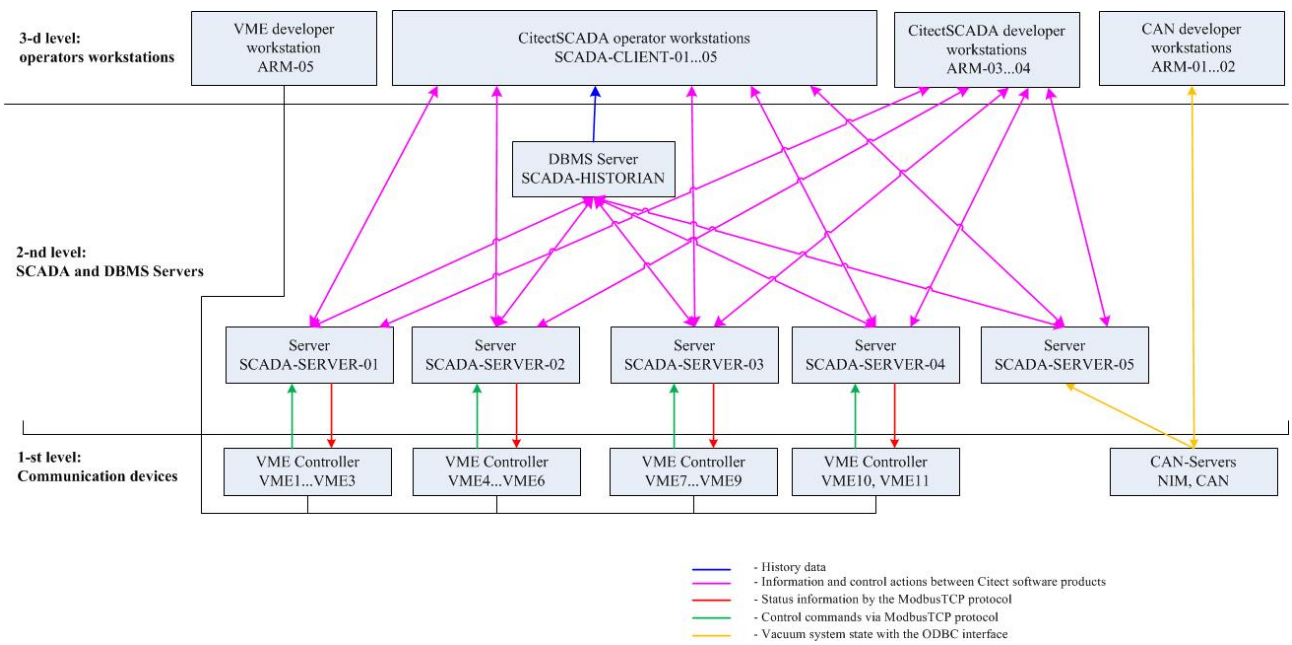

Fig.3. Functional structure of the TS.

NEW ELECTRON BEAM REFERENCE ORBIT MEASUREMENT SYSTEM AT DEDICATED SYNCHROTRON RADIATION LIGHT SOURCE SIBERIA-2

Ye. Fomin, V. Korchuganov, N. Moseiko, A. Valentinov, NRC Kurchatov Institute, Moscow, Russia
R. Hrovatin, P. Leban, Instrumentation Technologies, Solkan, Slovenia

Abstract

The paper focuses on the project of the electron beam closed orbit measurement system at SR source SIBERIA-2 realizing at present time at Kurchatov Institute.

The main purpose of new closed orbit measurement system creation is an improvement of the electron beam diagnostic system at storage ring. In addition, it will be a part of fast feedback system which will damp the distortions of the closed orbit at SIBERIA-2. This system provides continuous measurements of the electron beam closed orbit during storing, ramping and operation for users. Besides, with the help of the system it is possible to carry out turn-by-turn measurements of the electron beam trajectory during injection process.

The paper describes the new orbit measurement system, the principle of operation and its technical characteristics.

INTRODUCTION

The electron beam reference orbit measurement system which is currently operating at SIBERIA-2 is obsolete and outdated. The initial part of the orbit measurement system consists of 24 beam position monitors (4 pickups at one superperiod) and the preliminary signal processing electronic device located near each beam position monitor (BPM). The main purpose of this electronic devices are preliminary signal processing to transmit its to main control room for final processing and calculating electron beam horizontal and vertical positions (X and Z). Into the main control room all 96 signals from each button of BPM consecutively are digitized with the help the switch and one ADC made into the CAMAC standard bus. Control of the switch and the ADC as well as the beam center of gravity position calculation and results display are performed by micro controller Odrenok. As a result, the process of the electron beam reference orbit measurement takes a lot of time – 5 s.

Due to very slowly orbit measurement process it is possible to measure the electron beam orbit only in stationary accelerator operation mode. It is not possible to perform correct measurement of the beam trajectory during electron beam injection or acceleration process. It would also like to note the electron beam reference orbit correction process takes a lot of time - up 1 hour.

Now the synchrotron radiation light source SIBERIA-2 is being upgraded and the synchrotron radiation beam quality is being improved. New synchrotron radiation sources (superconductive and normal conductive wigglers), new synchrotron radiation beam lines and experimental stations are constructed. So both the synchrotron radiation and electron beam requirements will be only become stronger. Some electron beam parameters at storage ring SIBERIA-2 are presented at Table 1.

Table 1: Electron beam parameters at SIBERIA-2

Beam current, mA	1 - 200
Revolution frequency, MHz	2.4152
Beam emittance, nm·rad	98
Lifetime at 160 mA current, h	~ 20
Number of bunches	1 - 75
Bunch sizes, mm: σ_x, σ_z, σ_s	0.34, 0.059, 20.0

In the nearest future the existing electron beam reference orbit measurement system and the global orbit feedback system will be not able to provide required photon beam quality for all synchrotron radiation users.

NEW ELECTRON BEAM ORBIT MEASUREMENT SYSTEM

New electron beam reference orbit measurement system at dedicated synchrotron radiation source SIBERIA-2 is being created based on the electron beam position processor Libera Brilliance units developed by Instrumentation Technologies company, Slovenia. In all respects the new system is better the old one.

The architecture of the new orbit measurement system is looking like the old one. 24 Libera Brilliance processors are used to process the signals from BPMs. These processors are combined into 4 groups with the help of 4 Clock Splitter units and 4 ethernet switches. Each device group (6 Libera Brilliance units, 1 Clock Splitter and 1 Ethernet switch) is installed into one rack. The all 4 racks are mounted at the equal distance (one quarter of the accelerator circumference) from each other on the inner side of the shielding wall of the storage ring at a 1.5 m height from accelerator median plane. Such arrangement of racks with the equipment is allowed to reduce radiation background to the equipment. Measured radiation background at the place of racks location does not exceed the maximum radiation level for normal equipment operation.

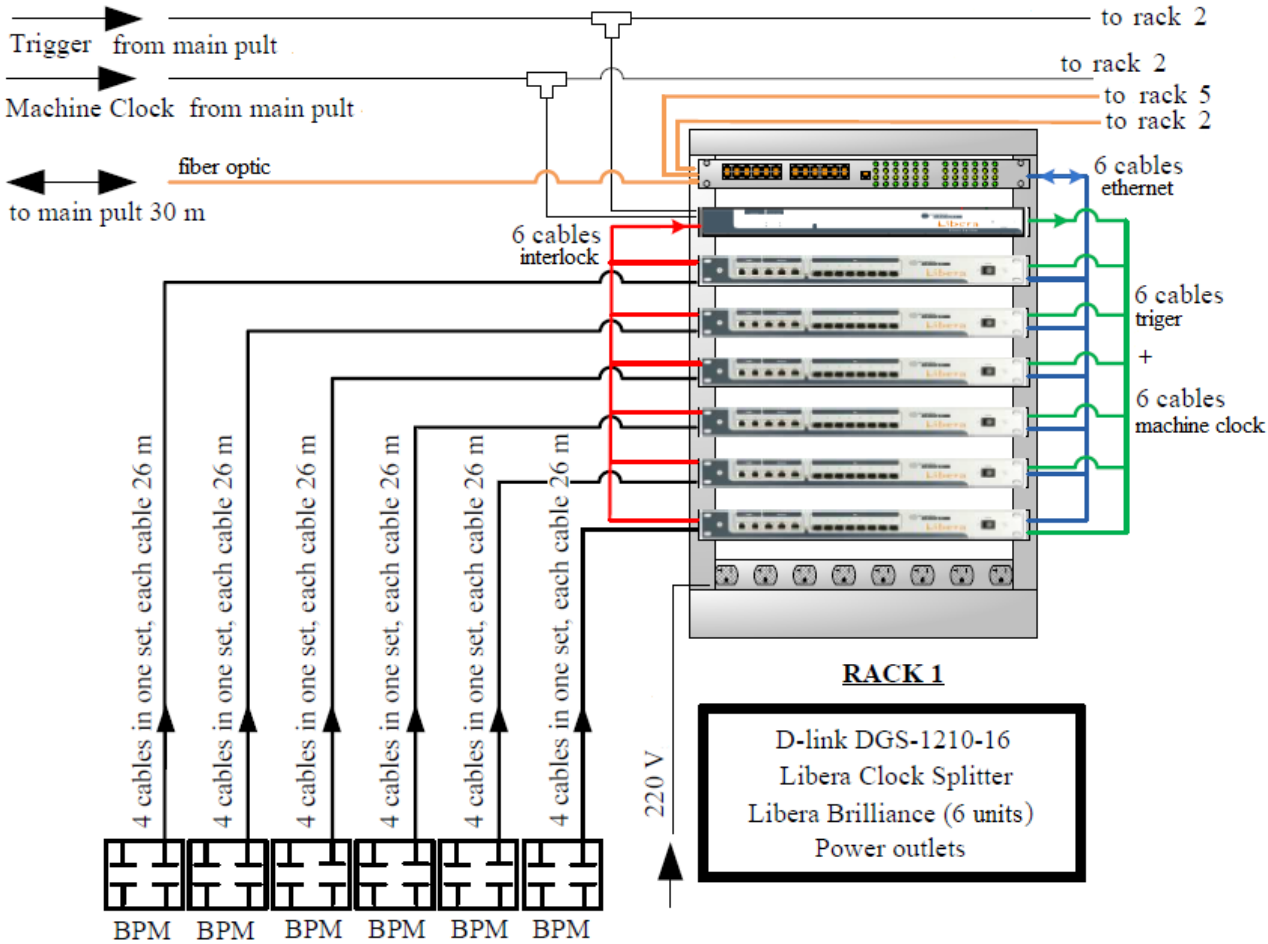

Figure 1: One rack with electron beam reference orbit measurement system equipment inside and all connections general layout.

Such choice of the equipment location is caused by the fact that one Clock Splitter can-not operate with more than 10 Libera Brilliance processors. At the same time, such distribution optimizes the RF cable lengths from BPM buttons to the Libera Brilliance units thus reducing the cost of cabling.

At the Fig.1 the general layout of one rack with electron beam reference orbit measurement system equipment inside and all connections is presented. All 4 racks with the orbit measurement system equipment are connected to a ring circuit type with the help a optic fiber cable and connected into the join accelerator local network. This type of connection is used to exchange the data between accelerator control system and Libera Brilliance processors.

The Clock Splitter installed into each rack is used to distribute clock signals to the Libera Brilliance instruments and combine Interlock signals. Synchronous events' arrival (Machine Clock, Trigger, Post-mortem) is essential for performing synchronized measurements using multiple Libera Brilliance processors. To synchronize the measurements two type of signals are necessary: Machine Clock and Trigger. Optionally it is possible to use System Clock and Post-mortem signals. All signals are LVTTL type.

The Machine Clock signal is used to specify zero separatrix. This signal is a continuous series of pulses with electron beam revolution frequency (in our case - 2.415 MHz).

The Trigger signal is a single pulse. This signal is used to start a single measurement of beam trajectory (for example, measurement a beam trajectory during injection process). The maximum repetition rate of this signal pulses is 20 Hz.

The Post-mortem signal is similar to the Trigger signal, but this signal is used to get and save a beam trajectory before the Post-mortem signal arrival. For example, when the electron beam is lost the accelerator control system sends the Post-mortem signal to Libera Brilliance processors. The control system then requests the so called "Post-mortem" data, which contains the electron beam trajectory data before a beam loss. This feature is very useful for an electron beam loss analysis.

Electron beam position processor Libera Brilliance is a main component of the new electron beam reference orbit measurement system. Libera Brilliance processors feature the high precision position measurement of the electron beam in the booster or storage ring. Digital signal processing inside the Libera units support programmable bandwidth and can facilitate all the position

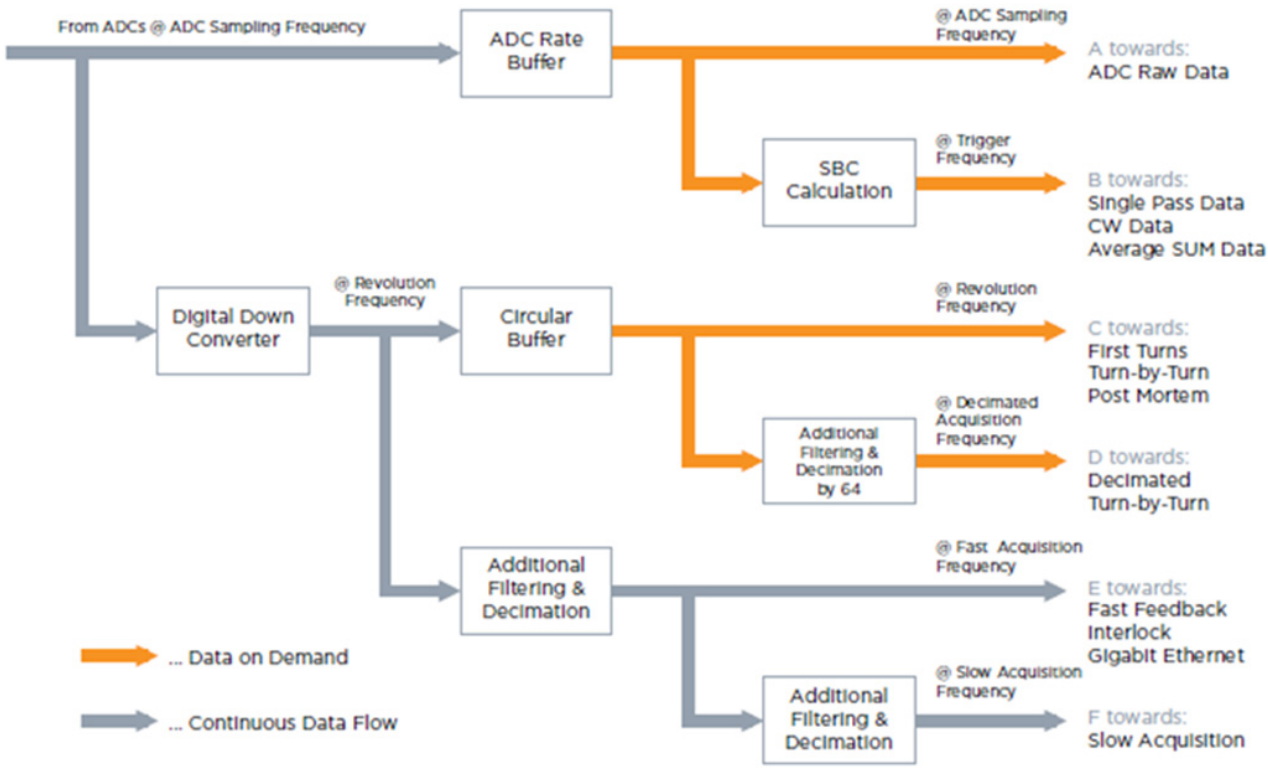

Figure 2: Data paths inside electron beam position processor Libera Brilliance.

measurements required: pulsed, first turns, turn-by-turn (measurement accuracy up to 0.35 μm) and regular closed orbit (measurement accuracy up to 0.07 μm).

The Libera electron beam position processors are fully customizable and can also be programmed to control the control units for corrector magnets. This can be carried out by the users with the FPGA development kit. So, there is a possibility to create the fast global orbit feedback system based on this new electron beam orbit measurement system. The maximum frequency update of electron beam orbit data is 10 kHz.

The Libera electron beam position processors are optimized to work with input signals from button BPMs. Variable attenuators on four parallel analog chains are used to adapt the input signal to the proper level. The signal processing chain on the units are composed of analog signal processing, digitalization for fast ADCs and digital signal processing. Each channel consists of a digital down-converter (DDC), which is followed by parallel processing in wideband and narrowband paths. Beam position is calculated using the standard equation.

There are several types of output data of the Libera Brilliance processor: pickup amplitudes (A, B, C, D), calculated beam position (X and Z) and the sum signal from 4 BPM buttons (this signal is proportional to the beam current). Also information about current operation mode of the equipment is available.

The Libera electron beam position processors provide several data paths at different sampling rates with different bandwidth and resolution (see Fig. 2) thus allowing detail machine studies and stable user operation. Acquisitions can be done simultaneously on all four major data paths (ADC raw data, turn-by-turn data, fast acquisition and slow acquisition data). The injection studies (efficiency, ramp-up) are supported by first-turns acquisition with turn-by-turn data as well as with rich raw ADC-data based single pass acquisition which returns the raw button signals, SUM value and position at every injection trigger. Fast acquisition data is provided through deterministic fast ports (SFP) at a 10 kHz data rate and serves as the input data for fast global orbit feedback.

Special software for Electron beam reference orbit measurement system will allow for automated monitoring and control of electron beam reference orbit and trajectory during injection process. Graphical user interface will enable the operator to set and control system operation modes, to control electron beam orbit at the current time. Special software will be developed by using the SCADA system and integrated into accelerator control system.

CONCLUSION

New electron beam reference orbit measurement system will lead the diagnostic system to a new level and allow improvement of both the electron and the photon beam quality. Farther new electron beam global orbit feedback system will be created based on this electron orbit measurement system.

SOME ASPECTS OF THE CAVITY RESONANT FREQUENCY CONTROL SYSTEM HEATER OPERATING POINT CHOICE

V.V. Grechko, G.I. Yamshikov, INR RAS, Moscow, Russia

Abstract

To adjust and to stabilize a resonant frequency of the accelerating cavities INR Linac comprises a Cavity Resonant Frequency Control System (CRFCS). The main final control element of the system is an electric heater (EH). Operating point of EH determines power consumption of the system and rf power feed in duration. Electromagnetic noise originated from thyristor regulators of the heaters and influencing linac electronics also depends on the operating point. One of the most sensitive systems is Fast Beam Interlock System (FBIS) intended for prevention of excessive activation and damage of linac components. To exclude false responses of FBIS and to decrease power consumption of CRFCS operating point of the heater has been shifted to a range of smaller power. This approach has been tested during several beam runs with the following results: no false responses of FRIB were observed; the quality of frequency stabilization during beam runs remained at the same level; relatively rare restarts of RF channels did not increase a downtime to beam time ratio; CRFCS power consumption was decreased twice. The rf power feed in duration increased insignificantly.

INTRODUCTION

The cavity resonant frequency control system (CRFCS) is intended for:

- warming up of cavity to the resonant temperature and its stabilizing before to begin rf power feed in (rf feeding) both at primary rf channel switching on and at the unauthorized switching off rf generator or system on the whole;
- providing of attenuating transient process in the system at rf power feed in (according to principle of Ljapunov - the stability "in large");
- stabilizing of cavity resonant frequency during beam run (stability "in small").

All these tasks are solved by the change of temperature of desalted water circulating in closed contour. A heat-exchanger with the regulated efficiency of heat exchange and power regulated electric heater (EH) with a corresponding measuring and regulating equipment allow to support the required thermal balance in any mode of CRFCS operation.

The circuit of EH power (current) control contains sensors measuring the regulated coordinate (cavity temperature or cavity phase off-tuning), corresponding threshold sensors, null device, PID-regulator, block of the signal transformation and fixing of EH operation point (OP) and also the thyristor regulator with the changeable angle β of thyristor switching on. Here under a concept "EH OP" the following is implied: bipolar signal of CRFCS unbalance from the PID – regulator should be transformed in unipolar ones before signal giving in the control unit RNTO-250 or ROT-250 type of thyristor regulator. Electric heater OP is point on the regulation curve, corresponding to CRFCS off-tuning $\xi = 0$.

Fronts of thyristor switching on have duration about tens of microseconds and cause appearance of noise affecting near-by located electronic equipment, and choice of angle $\beta = \pi/2$ leads to the increasing of noise amplitude to the maximally possible value. (Angle $\beta = \pi/2$ at unbalance in CRFCS $\xi = 0$ was chosen at tuning of CRFCS as providing the best condition of rf power feed in).

It should be noted the high intensity of noise: firstly, EHs are energized from the network of 220V 50Hz, that at antiparallel on of thyristors gives 100Hz frequency noise, secondly, at the present state of accelerator up to 20 channels can be involved in operation.

AFFECT OF NOISE ON FBIS AND OTHER ELECTRONIC EQUIPMENT OF LINAC

Fast beam interlock system (FBIS) is intended for prevention of the excessive activation and thermal damages of linac components. In the system there are 74 detectors of the secondary radiations located on length of linac tunnel and electronics racks behind of shield in control rooms and PS gallery. Constructively detectors are executed as plastic scintillator connected by light guides with photomultipliers. On the area of beam turn with energy of 160 MeV PM is used as a detector directly. Synchronized with linac operation electronic part of FBIS is a threshold device reacting on external signals only during the beam acceleration. FBI system produces a signal "Prohibition of FBIS" and injection of beam in linac is terminated if permissible beam losses and corresponding threshold level (~10 ÷ 20 mV) are exceeded. The reset of "Prohibition of FBIS" is performed by either an operator or automatically. During this a beam in linac is absent ~ 0.5 sec.

FBIS forms a false response "Prohibition of FBIS" and stops the acceleration of beam if attending linac work noise is coming at time gate of beam loss registration and threshold level is exceed. The losses of beam run time may reach a few percents, and on occasion - to block the work of accelerator fully.

To find the source of noise during working linac and at the regular mode and complete volume of FBIS equipment different parts of linac were independently switched on: injector, rf channels, equipment of CRFCS, pulse magnet, equipment of accelerator control system, etc. As a result the high degree of correlation between false responses of FBIS and value of EH current of CRFCS was revealed.

Further researches allowed:

- to eliminate the FBIS feed in circuits from a number of noise conductors;
- to localize CRFCSs which produce noise and false responses of FBIS: in one or another degree these are channels of main part of linac (cavities with disks and washers). Placing on the same cable shelves of EH power cables and FBIS control cables makes possible noise in ones during fast changes of EH current because of electromagnetic induction;
- to fix cross influence of CRFCS and initiation of autooscillations in the circuit of EH control (including the channels of DTL).

Many other devices and systems of accelerator are exposed to negative influence of the noise massively generated by the apparatus of CRECS: beam observation system; systems of remote-control and adjusting; systems having in the composition computers etc.

It is necessary to improve noise immunity of every specific system and at the same time it is urgent problem to reduce deeply of noise level produced CRFCS.

A few attempts to decrease the size of noise to the acceptable level (selection of points of grounding, LC - filtering etc.) were undertaken, but without success. It was therefore suggested to shift the operation point of EH from initial position (on the Fig.1 it is point on the interrupted curve P_{EH}=24 kW at regulation current of regulator I_{reg}=100 mA) to a range of smaller currents, some lowering rf power feed in duration.

INFLUENCE OF EH OPERATION POINT POSITION ON THE CRFCS FAST-ACTING

Supposition about increasing of rf power feed in time at shifting of OP from regular position (on the Fig.1 it is point on the interrupted curve P_{EH}=24 kW at regulation current of regulator I_{reg}=100 mA) in the range of smaller EH power is based on decreasing of degree of CRFCS stability "in large" and, as a result, the damping is increased at approaching to the dog leg of adjusting curve (switched off of EH).

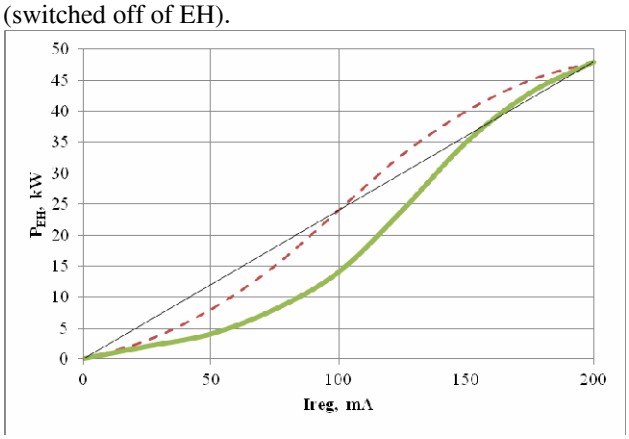

Fig.1. EH regulation curve

RF feed in, as a rule, produced for a few steps the number of that depends on the great number of factors: of value of cavity phase unbalance, admissible value of the reflected wave, condition of vacuum, pre-history of cavity and waveguides breakdowns etc. All this does correct comparison of the different settings of CRFCS concerning of operation speed very laborious without deciding practical application. Therefore an analysis on the digital model of CRFCS is more reasonable. On Fig.3 results are presented as a dependence of $Y = \theta(x)/\theta(0.5)$, where θ is duration of transitional process at a corresponding value $X=P_{op}/P_{EHmax}$. An analysis of CRFCS behavior was realized on the model of CRFCS in MATLAB, described in details in [1] and [2]. The model of CRFCS was modified according to a Fig. 2 for the linearized regulation curve (Fig.1) at rf power feed in of P_{rf} = 20 kW in the cavity.

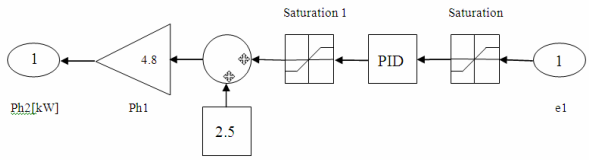

Fig..2. Model of EH regulation circuit with a possibility to change an operation point

For a situation on a Fig.2: operation point is X =0.25 if in the block of Saturation 1 upper (7.5) or lower (-2.5) limits are set; P_{EHmax} = 48 kW.

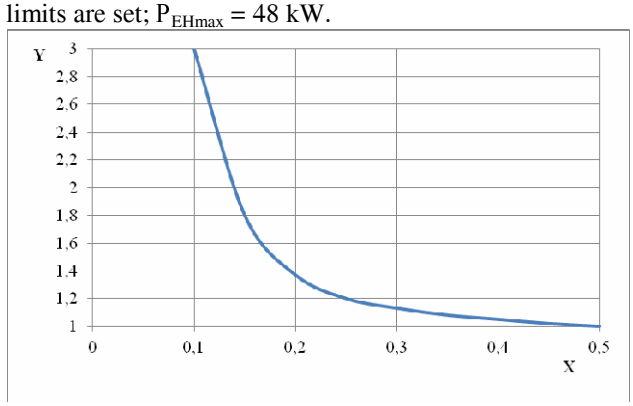

Fig.3. Relative change of transient duration

It is necessary to expect the double reduction of rf feed in duration at shifting of OP to the level with X = 0.14. It is true and at step by step rf power feed in because every next step is executed after completion of previous transition process.

CHOICE OF EH OPERATION POINT FROM THE CONDITION OF RF FEED IN DURATION

For definiteness the double reduction of rf feed in duration was accepted. From the Fig.3 X=0.14, that corresponds of P_{op} = 6.7 kW. But practically placing of OP at this level was not succeeded, because in an existent apparatus there is no possibility to set I_{reg} < 70 mA at ξ = 0. By the readjust of thyristor regulators for all channels (of three - during work of linac on an isotopic complex) single regulation characteristic was got and presented on Fig.1 as continuous curve.

At the test of this variant during three beam runs it is not fixated false responses of the FBIS because of noise generated by the CRFCS thyristor regulators, that confirms the successful choice of EH operation point position. For channels, having advanced reliability (1 ÷ 2 unauthorized switching-off in a week), deeper shifting of operation point is possible. For the individual adjusting of every channel it is possible to recommend the choice of X coefficient from a range 0.1 ÷ 0.15. For example, channel 3 of main part of INR linac worked at X = 0.11 successfully.

INFLUENCE OF EH OPERATION POINT SHIFTING ON THE QUALITY OF CAVITY FREQUENCY CTABILIZING DURING BEAM ACCELERATION

In loaded with beam high-Q cavities having disks and washers with D~15*10³ even small variations of frequency within of frequency strip lead to the considerable changes of rf power for compensation of that with the purpose of stabilizing of cavity frequency equal power of EH is required at least. In this situation, shifting of OP from a linear area in nonlinear one (Fig.1) will lead to the lowering of CRFCS stability "in small". However, during beam run the system of cavity rf field amplitude automatic control compensates part of rf power intended for acceleration of beam. Oscillations of rf power losses do not exceed of units of percents, that allows not to take into account curvature of characteristic on Fig.1 in the viciniity of any OP, except a border one.

INFLUENCE OF EH OPERATION POINT SHIFTING ON THE ENERGY CONSUMPTION OF CRFCS DURING BEAM ACCELERATION

Full power of CRFCS energy consumption during beam acceleration is $P = 2(P_{op} + P_{p}) + P_{ra}$, where coefficient "2" takes into account work of refrigeration machine in a warm season; P_p = 14 kW - power of pump, providing a circulation of desalted water; $P_{ra} \approx$ 2 kW - total power of rack apparatus feed in sources. For the given example the energy consumption of the system is decreased in 1,8 time. Coefficient 2.5 (2.6 - in summer) is achieved in theory at $P_{op} \rightarrow 0$, but such regime practically could not be realized because of appearance of undamped transient during rf feed in (Fig.3).

Note. Power of EH was determined on the formula $P_{EH} = U^2$, because R_{EH} = 0.97 Ohm at the temperature T_{EH} = 16ºC. Voltage on EH was measured by digital multimeter of type DT9203. Authors understand that such method gives a considerable irregular error at $0 < \beta < \pi$. However, this fact did not prevent to make correct conclusions out of the performed researches and achieve the put aim.

SUMMARY

1. Accurate shifting of EH operation point of all working channels of main part of linac will allow to solve a compromise the problem of excluding of FBIS false responses due to the noise generated by the thiristor regulators of CRFCS at the acceptable decreasing in practice of rf feed in duration in a cavity.
2. At the same time, maximally possible an actual question of CRFCS energy-saving is solved.

ACKNOWLEDGMENT

The authors express their gratitude to all collaborators from INR for the help at these researches, especially A.Feschenko, A.Kvasha, V.Silnichenko, V.Kopin.

REFERENCES

[1] Yu.Kiselev., A.Kovalishin, A.Kvasha, D.Hlustin. Simulation of the INR DTL frequency stabilization system, Proceedings of RUPAC 2006, Novosibirsk, Russia, p.258-260.

[2] A.I.Kvasha, Yu.V.Kiselev., A.S.Kovalishin, V.S.Kopin. Analisis and Modernization of the INR DTL Frequency Control System. Problems of Atomic Sciene and Technology. Series “Nuclear Physics Investigations” (49), 2008, N3, p.46-50

EMITTANCE MEASUREMENTS AT THE EXIT OF INR LINAC

P. Reinhardt-Nickoulin, S. Bragin, A. Mirzojan, I. Vasilyev, O. Volodkevich, Institute for Nuclear Research of RAS, Moscow, Russia
A. Feschenko, S. Gavrilov, Institute for Nuclear Research of RAS, Moscow, Russia and Moscow Institute of Physics and Technology, Moscow, Russia

Abstract

Emittance measurements at the exit of INR linac are of importance for proper beam matching with the beam line of the downstream experimental facility. Emittance ellipses are reconstructed from beam profile data obtained with three wire scanners and one ionization beam cross section monitor (BCSM). A possibility of quadrupole gradients adjustment not only increases the reconstruction accuracy but also enables to find emittances with BCSM data only. The latter provides completely transparent measurements and can be done within a wide range of beam currents. The results of measurements by wire scanners and BCSM are presented and compared, the reconstruction procedure features are discussed.

INTRODUCTION

Accelerated proton beam of INR linac is used on the experimental facility of Neutron Studies Laboratory, proton therapy complex of Medical Physics Laboratory, facility for dibaryon resonances study and on other experimental targets.

Neutron Studies Laboratory experiments are carried out on the beams of 0.3 to 200 μs duration at repetition rate of 1 to 50 Hz with a pulse current up to 15mA, i.e., the average current can be as high as 150 μA, while for the proton therapy complex one should apply an average current of about 10 nA. The beam energy can be varied from 70 to 209 MeV. So each experiment requires specific values of beam energy, intensity, duration, and matching of these parameters with the characteristics of beam channels at INR experimental complex.

For INR proton linac operation in wide dynamic range of beam parameters one has to carry out proper retuning and matching procedures according to the features of the experiments. This in turn requires more attention to the dynamic range of the beam measuring system to ensure reliable diagnostic abilities for different beams.

Last years the linac diagnostics has been supplemented and upgraded. In particular, the system of wire scanners (WS) was developed. Besides the ionization beam cross section monitor was installed [1], which allows to measure transverse beam profiles at the linac exit.

Beam cross section monitor (BCSM) of accelerated protons provides possibility to observe the following beam parameters during adjustment and operation of the linac: protons distribution in beam cross section (BCS), beam centre position and its displacement relative to linac axis. The transverse beam profiles can be obtained from the beam cross section distribution too.

In process of linac tuning various interactive procedures are used [2]. They give the possibility to carry out transverse matching of the beam, centre correction and minimization of beam losses. Description of the equipment at the linac exit is presented. The emittance measurement procedures, as well as a comparison of the results obtained by different methods are discussed.

BEAM INSTRUMENTS AT LINAC EXIT

The measuring area at the linac exit for transverse beam matching and centre correction is shown in Fig.1a. The following equipment is installed at this area:

- 8 quadrupole magnetic doublets D106 ÷ D113. Their windings are supplied from a common current source;
- beam current transformer;
- 4 quadrupole magnetic doublets D114 ÷ D117. Their windings are supplied from different current sources;
- 3 wire scanners. They are installed downstream the doublets D113, D114, D115. Each scanner consists of two mutually perpendicular wires of 0.1 mm, which are parallel to horizontal and vertical axes.
- BCSM is installed upstream the doublet D114.

Procedures of transverse beam matching and correction are realized using the profiles obtained by WS at the same time with BCSM.

High sensitivity of BCSM allows to extract profiles from beam cross-sections measurements in very wide dynamic range of beam intensities for high- and low-current beams, while WS measurements are effective only in limited range of beam pulse currents due to noises induced on electronics and cables.

PROFILE AND EMITTANCE MEASUREMENTS

Linac tuning is performed strictly with 1 Hz pulse frequency to avoid excessive equipment activation and damage due to overheating of linac equipment in the point of significant beam losses.

Profile measurement with BCSM during linac tuning is also executed with 1 Hz beam frequency. Single pulse of 100 μA÷10 mA with 100 μs duration is sufficient to obtain profile. However, it is possible to measure beam profiles with pulse current lower than 100 μA using higher beam frequency e.g. 10÷50 Hz. In former case average proton beam current would be smaller than 10 mA of 100 μs pulse current with 1 Hz repetition rate. Low current beam Profiles are generally measured by BCSM using averaging over multiple pulses.

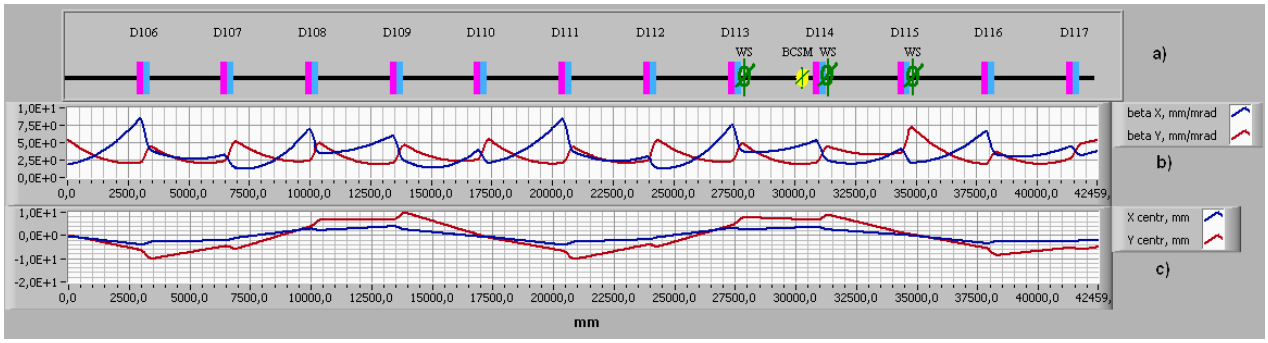

a)

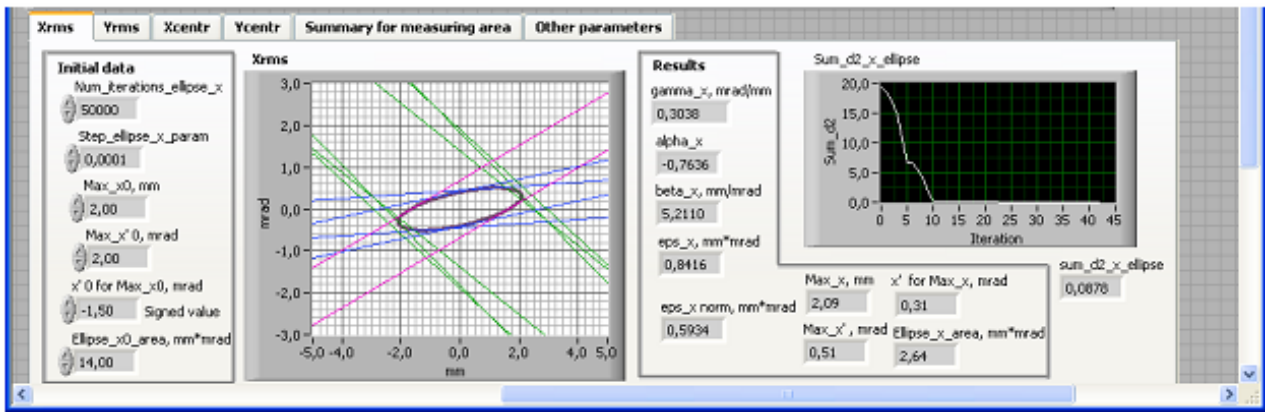

b)

Fig. 1. BCSM and Wire Scanners locations on beam line; beam envelope and beam centre at the linac exit (a), example of beam emittance measurement by WS(b).

Linac tuning procedure [2] is used to define the coincidence of beam parameters obtained by WS and BCSM. The results of beam center position and RMS size measurements at WS location are represented with lines for each transverse phase plane. These lines can be transformed to any location along beam line with magnetic optics transmission matrices.

There are several methods for emittance measurement at exit of the linac:

- Three WS located along beam transport line after three quadrupoles with constant magnetic field gradient. Measurements are processed with above mentioned matrix method. It takes 3 minutes to make a scan with 3 WS simultaneously.

Wire scanners (WS) are driven with stepper motors. The scan of single profile with WS takes 3 minutes. Actuators of WS's can be driven either individually or simultaneously.

- One WS measurement where multiple profiles are obtained by varying fileds of 8 quadrupoles. The scan takes 10 minutes.

- Multiple profile measurement with BCSM by varying fields of 8 quadrupoles. Scan time is determined by settling time of fields in the quadrupoles. Typical time necessary for BCSM to measure single profile is 140 ms for high intensity beam, and 1 s for low intensity beam average profile.

EXPERIMENTAL RESULTS

Procedure to define the coincidence of beam parameters obtained by WS and BCSM is carried out after linac preliminary tuning to minimize beam losses at the linac exit.

Beam of 209 and 127 MeV with 1 Hz repetition rate, 170 μs pulse width and 10 mA pulse current is used for measurement and comparison.

Comparison measurements are carried out by varying fields of 8 quadrupoles in the range of ±20 A with 5 A steps around the optimal current value. These variations provide enough slope changing of the lines bounding the beam profiles to calculate the inscribed ellipse of the emittance. The results of emittance measurement (Fig. 2) for 209 MeV beam are shown in green for BCSM and in red for WS. Bottom figure shows overall picture with overlapped ellipses.

Measurements for 127 MeV beam are shown on Fig. 3. Currents in quadrupoles were varied with the same varying and comparison results are also carried out.

Measured RMS beam size non-coincidence between WS and BCSM is within few percent.

The comparative results of emittance measurements by WS and BCSM shown on Fig. 2 and Fig. 3 are satisfactory too.

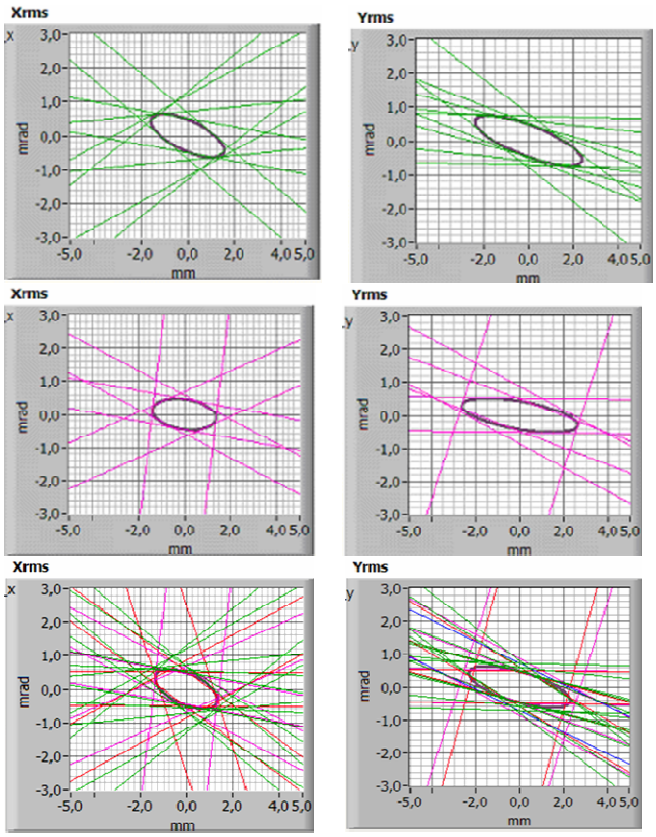

Fig. 2. Emittance comparison for WS (red line) and BCSM (green line) of 209 MeV beam.

CONCLUSION

There are two possibilities to measure the proton beam tranverse parameters at the exit of INR linac using either wire scanners or BCSM. These procedures includes emittance and beam position measurement, the optimization of beam size and correction of beam position to minimize beam losses at the linac exit and to match these parameters with the experimental complex beam channels. The result of emittance measurements by these two methods shows satisfactory coincidence. But transverse beam measurement procedure carried out by BCSM has two advantages over wire scanners: this method does not violate the beam and can be used for low intensity beams. This method expands beam monitoring and control for wide range of beam intensities. That is particularly very important for medical physics beam formation.

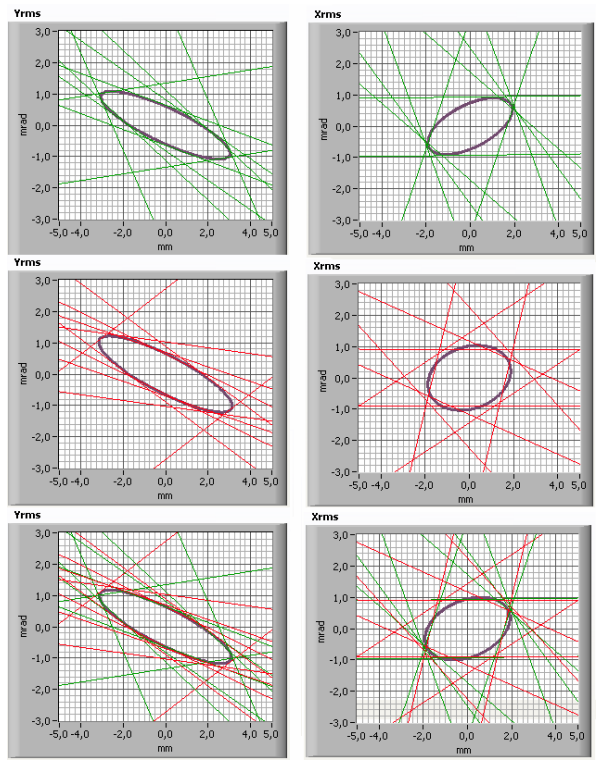

Fig. 3. Emittance comparison for WS (red line) and BCSM (green line) of 127 MeV beam.

REFERENCES

[1] P. Reinhardt-Nickoulin et al., Beam Parameters Measurements by Ionization Cross Section Monitor on Proton Linac of INR RAS. Proceedings of DIPAC-2011 conference, 16-18 May, 2011, Hamburg, Germany, p. 161-163.

[2] S. Bragin et al., Transverse Beam Matching and Correction Procedures in INR Linac. Proceedings of LINAC-2006 conference, August 21-25, Knoxville, Tennessee USA, p. 435-437.

DEVELOPMENT OF INR LINAC BCT SYSTEM

P. Reinhardt-Nickoulin, S. Bragin, V. Gaidash, O. Grekhov, Yu. Kiselev, N. Lebedeva,
A. Mirzojan, A. Naboka, I. Vasilyev, O. Volodkevich.
Institute for Nuclear Research of RAS, Moscow, Russia

Abstract

New electronics of automatic BCTs system was developed to improve beam parameters measurements along INR Linac. BCT electronics details are described. The available results of beam pulse measurements are given.

INTRODUCTION

At proton beam acceleration process in initial part of INR linac from 750 keV to 100 MeV high level of interference and hum are produced in measuring channels on beam current transformers (BCT), preamplifiers (Preamp); cables between Preamps and Main modules of amplification (AMP) and calibration (CLB), that are installed in control room of initial part.

These low frequency (LF) and high frequency (HF) interference distort the BCT measurement results with single channel Preamp [1].

Besides that at time of proton acceleration in initial part, when beam from RFQ is accelerated from 750 keV to 20 MeV in first drift tube linac (DTL) tank, the amplitude of beam pulse is decreased from 23÷18 to 12÷10 mA approximately in process of the accelerating beam formation. But significant level of interference and hum don't permit to estimate with sufficient accuracy the rate of beam losses in first DTL tank and in another DTL tanks of linac initial part. Therefore, efforts were made to improve of resolution ability of BCT measuring system in initial part.

In the past two years system has been expanded with a new BCT on ferrite core and two differential Preamp circuits of two types, that enable to reduce interference and hum from high-power devices of linac.

Upgraded BCT system provides reliable and stable beam parameters representation along the linac in high level of activation of the equipment also.

THE STRUCTURE OF INITIAL PART BCT SYSTEM

Block-scheme of automated BCT system [2] for initial part of linac is shown on Fig. 1. The beam is injected from the RFQ in the initial part, which consists of five tanks (R1÷R5) of DTL type. After acceleration to 100 MeV, beam is injected into the main part of the linac, consisting of 27 accelerating sections of disk and washers (DAW) types.

BCT's and Preamps are installed on the exits of each DTL tanks excluding R2. Preamps are located in linac tunnel 1.5 m away from corresponding BCT. Analog pulse signals from Preamps are fed inputs of amplifiers (AMP) by RF cables. Generator of calibration pulses CLB is combined with appropriate AMP in common module MAC. All MAC's are installed in control room of linac initial part. CLB signals are fed to corresponding BCT. AMP output signals are fed on ADC inputs of corresponding servers (PC1÷PC5), installed in each of 5 sectors of linac. All ADC's are built into server computers of corresponding sectors of linac (PC1÷PC5). Servers are built into control system of linac (CSL).

The programs for data acquisition and processing are on the servers and remove the remnant distortions due to hum and interference. Processed data are transmitted into CSL. The final results of treatment are represented on computers of linac central control room.

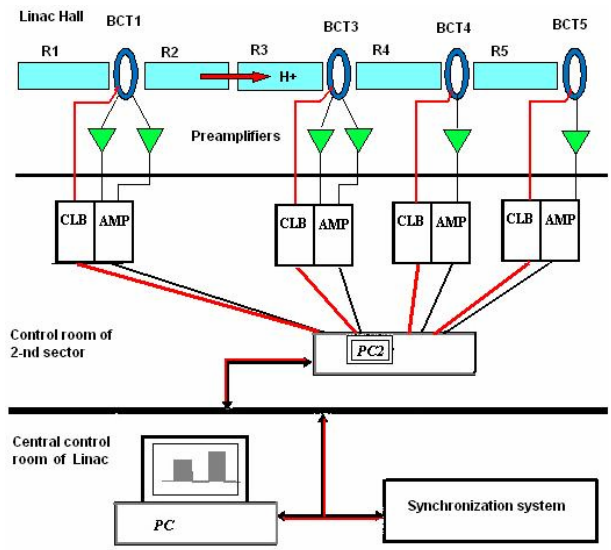

Fig. 1. Block diagram of automated BCT system of linac initial part.

BEAM LOSSES AND RADIATION CONDITIONS ON INITIAL PART OF INR LINAC

Currently, INR linac proton pulses have the 10÷12 mA pulse amplitudes, up to 200 μs pulse duration and 1÷50 Hz pulse repetition frequency. The beam amplitude formation is produced into first DTL tank.

RFQ, operating on the frequency of initial part 198.2 MHz, injects in R1 the beam of ions with 200 μs duration, consisting from $4*10^4$ bunches of 0.8 ns duration. The number of particles in bunches is decreased in R1 in process of formation of more short bunches at acceleration.

Ions, lost during acceleration, produce in metal walls of ion guide neutrons and γ-quanta. Quantity of these background particles increased very rapidly with growing of energy of lost particles. Increasing of lost proton energy from 1 MeV to 20 Mev gives increasing of output of neutrons from ~10^{-7} to ~10^{-3} on single proton [3]. It is known from INR linac operating experience, that at standard adjustment of phases and amplitude of accelerating fields in next DTL tanks and DAW cavities, the losses of accelerated beam is decreased to average level less than 0.1 nA/m for 100 μA average proton current, but neutron background gradually increases at approximately constant beam losses along linac, due to growing of energy of lost protons from 20 to 209 MeV. The output of neutrons on single lost proton is increased from 10^{-3} to 1. And so, if in second half of R1 at growing energy from 10 to 20 MeV is lost ~10^{12} protons in 200 μs pulse then, in this case, will be produced ~10^{9} neutrons in single pulse or ~10^{5} neutrons/(1 cm^{2}s) on 1 m distance in 50 Hz repetition frequency. So radiation background on R1 output is comparable with this one on main part of linac [1], and it is need take into account for new preamplifiers constructions.

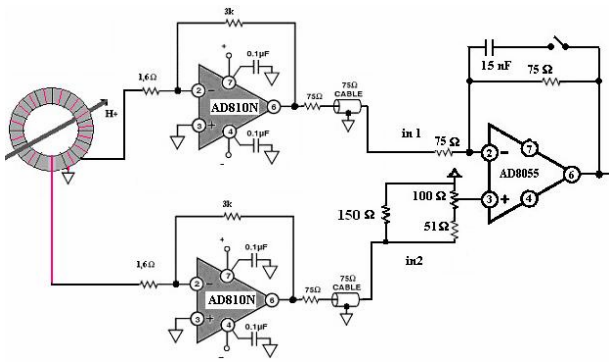

Fig. 2. Differential preamplifier for BCT1 with interference-hum suppression scheme.

FERRITE-CORE BCT AND PREAMPLIFIER DESIGN

The project of installation of isotope production facility on 20 MeV proton beam requires to develop a compact BCT that doesn't take the extra space between R1 and R2 and decreases the interference-hum level. This goal was achieved using new differential BCT1 located after R1 (fig. 2). The symmetric winding is wrapped around 65x40x9 mm M2500HMC ferrite toroidal core and tapped at the center. First type differential Preamp circuit is based on AD810N opamps. These chips are used in single channel Preamps and confirm operational reliability in more severe radiation background in INR isotope facility for the last 8 years [1].

The influence of ferrite core on the vacuum in the beamline was tested beforehand. It was determined that the core doesn't effect on vacuum. It also turned up that the induced activity remained at the same level after year and a half operation.

Inside diameters of the core and the beamline are 40 and 30mm correspondingly. BCT1 has additional screen protecting both particles and interference. Both halves of the winding consist of 100 turns of copper wire that is winded in the same direction. Center-tapping point and preamplifier common rail are interconnected. Opposite ends of the winding are connected to Preamp inputs. Signal currents on the inputs flow in the opposite directions. The resulting pulses on the outputs of two «current-to-voltage» converters have the opposite sign. The LF interference present in the ground wire and the interference on the output cables are of the same sign. Signals from the beam are summed in the main amplifier whereas LF interference is suppressed by subtraction. The less severe problem of HF interference elimination, however, remains in this construction. This interference is much smaller than LF hum but it considerably (by several times) increases the overall noise level. It is possible to suppress this interference by adjusting the balance of the main amplifier though, but it breaks the LF interference balance. Also we observed an interference of 5 kHz frequency that couldn't be suppressed due to lack of balance range. To overcome these problems more complicated second new circuit of differential Preamp (Fig.3) was designed and tested.

Either BCT or interconnection cables are subject to electrostatic noise pickup. The amplitude of LF hum on BCT1, BCT3 and BCT4 channels is comparable with the signal. It is possible to take advantage of differential connection scheme, as is shown on Fig.2, since BCT1, BCT3 and BCT4 have center-tapped symmetric winding. This method with second Preamp allows to suppress common-mode noise over than 20 dB (Fig.4).

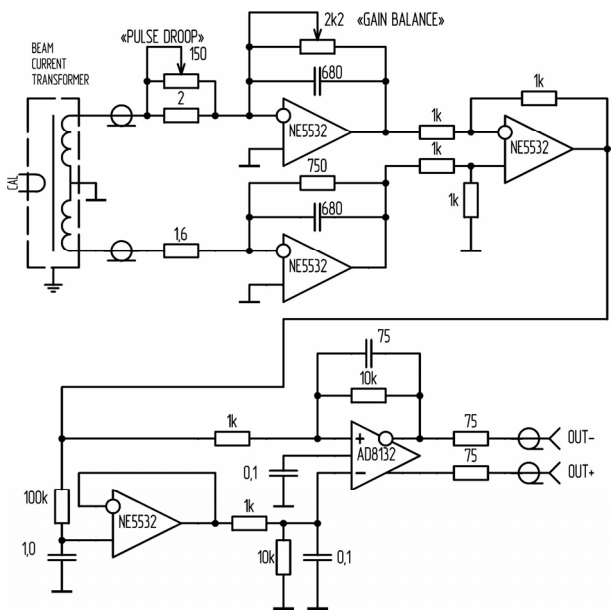

Fig. 3 Differential preamplifier circuit with pulse droop and gain adjustment capability.

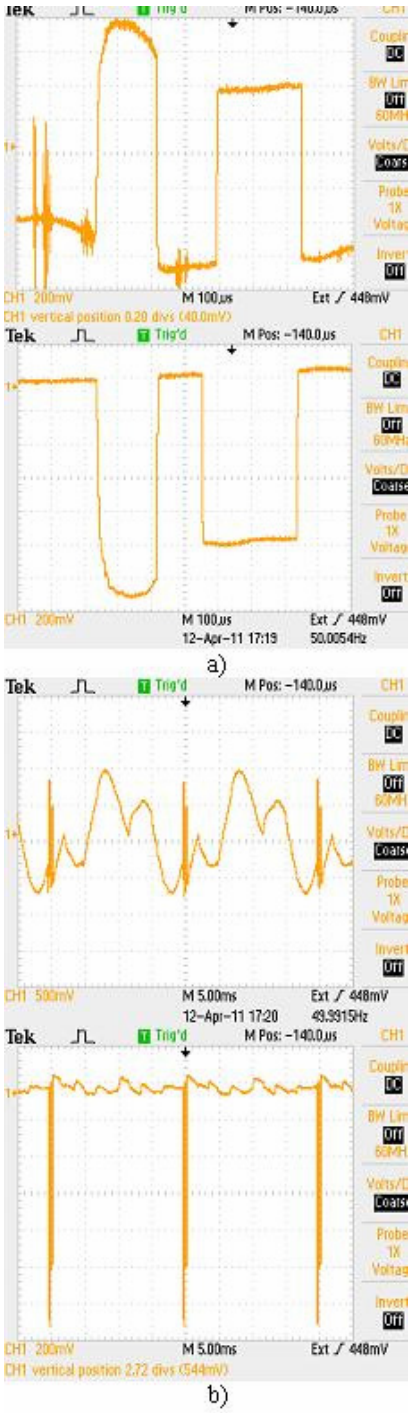

Fig.4. BCT oscillograms with single channel and differential preamplifiers.

BCT3 is connected to the new type of Preamp in the same manner as BCT1 is connected to Preamp shown on fig. 2. One of the input stages has variable input resistance which allows to set the pulse droop time constant of two channels close together. Furthermore it is possible to tune the feedback resistance if channel gain is mismatched for some reason. Pass band is limited to 350 kHz by the capacitor in the feedback in order to prevent self-oscillation of preamplifier and to cut off RF interference. The influence of balance mismatch in the main amplifier on LF hum suppression is eliminated by subtracting the interference in the second stage of this Preamp.

The resulting signal is fed to the output differential amplifier that drives two output coax cables symmetrically. The inverting input of the output stage is connected to biasing potential of integrating circuit with 100 ms time constant. Thus temperature and LF drifts of input stages are compensated. HF interference is additionally decreased by narrowing pass band to 100 kHz with capacitor in feedback.

Cables are connected to the main amplifier which further suppresses the interference induced on cables using the differential balance circuit as is shown on fig. 2.

RESULTS

Beam and calibration current source (CLB) pulses for single and differential preamplifiers of BCT3 are shown on Fig.4. The upper trace corresponds to single channel Preamp [1] and the lower trace corresponds to differential interconnection of BCT3 to the new Preamp circuit (Fig.3). This differential Preamp is less prone to LF and HF interference. It also produces a few times lower noise level because of decreased pass band.

The suppression of LF interference is shown on Fig.4b. The hum is decreased from 2 V to 50 mV by differential interconnection of the BCT. This residual hum is successfully eliminated in signal processing software [2].

CONCLUSIONS

New BCT1 and differential preamplifiers are suitable for the radiation environment of the initial part of INR linac.

BCT3 channel electronics allows to observe beam pulses without LF and HF distortions. The pulse droop and gain adjustment capability of BCT3 preamplifier allows for precise matching between input signals resulting in efficient interference suppression. The balancing circuit of main amplifier is now used for eliminating interference induced on the interconnection cables only. It doesn't impair the LF and HF interference suppression efficiency of BCT3 preamplifier anymore.

REFERENCES

[1] Modernization of BCT for INR linac, P. Reinhardt-Nickoulin, A. Feschenko, A. Mirzojan, RuPAC-2008, Zvenigorod, September 28 - October 3, 2008. Proceedings RuPAC 2008, p. 261-263.

[2] Automatic BCT system for INR linac proton beam. P. Reinhardt-Nickoulin, S. Bragin, O. Grekhov, A. Feschenko, Yu. Kiselev, A. Mirzojan, I. Vasilyev, O. Volodkevich. Problems of Atomic Science and Technology. 2010. № 3.Series: Nuclear Physics Investigations (54) p. 35-39.

[3] N. Sobolevskiy, INR RAS. Private communication 2008.

COMMISSIONING OF NEW DIAGNOSTIC DEVICES AT PITZ

D. Malyutin, M. Krasilnikov, J. Meissner, F. Stephan, G. Vashchenko, DESY, 15738 Zeuthen, Germany
K. Kusoljariyakul, S. Rimjaem, Department of Physics and Materials Science, Faculty of Science, Chiang Mai University, Chiang Mai, 50200, Thailand

Abstract

The Photo Injector Test facility at DESY, Zeuthen site (PITZ) is the test stand of the electron source for the European X-ray Free Electron Laser (XFEL). The main goal of the facility is the detailed characterization of the electron bunch parameters produced by the RF photo-cathode gun. Characterization of the bunch longitudinal properties such as bunch length or longitudinal phase space earlier was done using a streak camera, which measures the Cherenkov light produced by electron bunches passing through aerogel radiators. Recently, a Transverse Deflecting Structure (TDS) and a Second High Energy Dispersive Arm (HEDA2) were installed in the PITZ beamline. They will enable time resolved measurements of the electron bunch with much better time resolution than the streak camera system.

The first results of the commissioning of the HEDA2 section at PITZ are presented in this contribution.

INTRODUCTION

PITZ develops and optimizes electron sources for Free-Electron Lasers (FELs) like FLASH and the European XFEL in Hamburg (Germany). The main goal is to produce high brightness electron bunches whose quality fulfills the stringent requirements of these FELs [1].

A schematic layout of the current PITZ beamline is shown in Fig. 1. The main components are: the RF photo gun as electron source, an accelerating cavity Cut Disk Structure – CDS booster, three dipole spectrometers, three Emittance Measurement SYstems (EMSYs), a transverse deflecting structure (TDS) and a phase-space tomography module (PST). The three dipole spectrometers are located in the low energy section downstream the gun (Low Energy Dispersive Arm – LEDA), in the high energy section downstream the booster cavity (First High Energy Dispersive Arm – HEDA1) and at the end of the PITZ beam line (Second High Energy Dispersive Arm – HEDA2). A slit scan [2] is the standard technique for the projected emittance measurement at PITZ. The longitudinal phase space of the electron bunch is measured at PITZ with Cherenkov radiators in dispersive sections [3] up to now. The most recent upgrade of the PITZ facility included the installation of the TDS and the HEDA2. The TDS cavity is a multipurpose device, which is expected to provide a significant improvement in time resolved measurements. Beside measurements of the bunch length, the TDS is planned to be used in combination with HEDA2 for measurements of the longitudinal phase space. The main goals and working principles of the TDS and the HEDA2 are described in this paper. First results of the HEDA2 commissioning at PITZ are presented.

TRANSVERSE DEFLECTING STRUCTURE

The TDS cavity was designed and manufactured by the Institute for Nuclear Research (INR, Troitsk, Russia) as a prototype for the European XFEL [4]. The basic operation principle of the TDS is illustrated in Fig. 2.

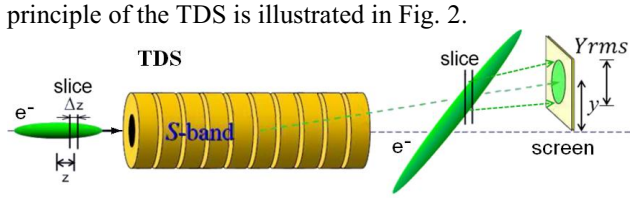

Figure 2: TDS working principle.

The structure deflects electrons vertically in linear dependence on their longitudinal coordinates within the bunch, which as a result enables measurements of the longitudinal bunch properties. An electron bunch propagates from left to right, passing through the deflecting structure. After a drift space, it is imaged on a screen. In case the bunch length is much shorter than the RF wavelength and if the bunch center propagates through the structure in the "zero" RF phase, then the

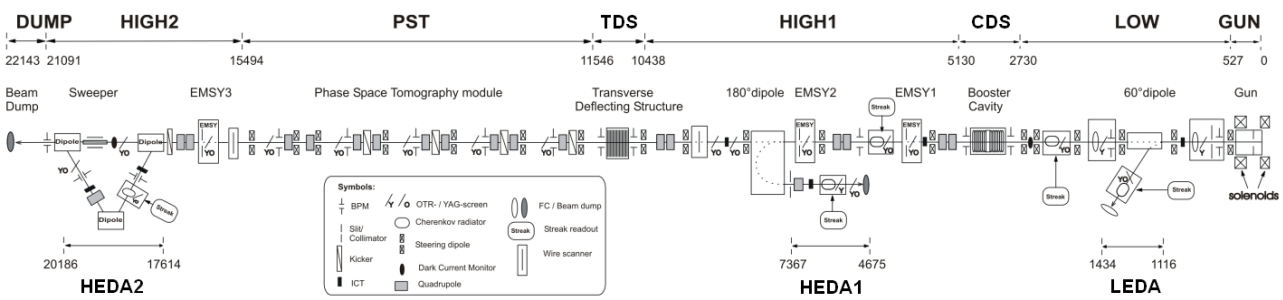

Figure 1: Current PITZ beamline layout.

deflection angle of each electron depends linearly on its longitudinal coordinate inside the bunch. As a result the mean vertical position y of the bunch longitudinal slice on the screen can be obtained from the following equation [5]:

$$y = \theta \cdot l = \frac{eV_0 k}{pc} z \cdot l = S \cdot z, \quad (1)$$

where θ is the deflection angle, l is the distance between the TDS and the screen, V_0 is the amplitude of the deflecting voltage, k is the wave number ($2\pi f_{RF}/c$), p is the bunch mean momentum, e is the electron charge, c is the speed of light, z is the slice longitudinal coordinate within the bunch and S is the TDS shear parameter.

The vertical size Y_{rms} of the bunch slice on the screen (see Fig. 2) can be calculated as [5]:

$$Y_{rms}^2 = \beta_y \varepsilon_y + (S \cdot \Delta z)^2, \quad (2)$$

where ε_y is the bunch vertical geometrical emittance at the screen position, β_y is the vertical beta function and Δz is the slice length.

Two slices of the electron bunch can be resolved on the screen if the vertical distance between their images is bigger than the vertical size of each of them. As a result, the minimum resolution length can be estimated for an infinitesimally small slice length as follows:

$$\delta z_{\min} = \frac{\sqrt{\beta_y \varepsilon_y}}{S}. \quad (3)$$

For typical PITZ operation conditions with β_y equals 5 m, ε_y equals $2 \cdot 10^{-8}$ mm·mrad and a TDS shear parameter S of 4 the resolution length δz_{min} is expected to be about 0.1 mm (0.3 ps).

SECOND HIGH ENERGY DISPERSIVE ARM

The HEDA2 is designed and manufactured in a collaboration between LAL (Orsay, France) and DESY (Germany). The main goals of this section are [6]:

1. High resolution beam momentum measurements up to 40 MeV/c.
2. Longitudinal phase-space measurements with a slice momentum spread resolution down to 1 keV/c (screen imaging system resolution).
3. Transverse slice emittance measurements.
4. Long pulse train monitoring.

A sketch of the HEDA2 section is shown in Fig. 3. It consists of three dipole magnets – Disp3.D1, Disp3.D2 and Disp3.D3, two screen stations – Disp3.Scr1 and Disp3.Scr2, a quadrupole magnet – Disp3.Q1, three beam position monitors (BPMs) and two Integrating Current Transformers (ICTs) for bunch charge measurements.

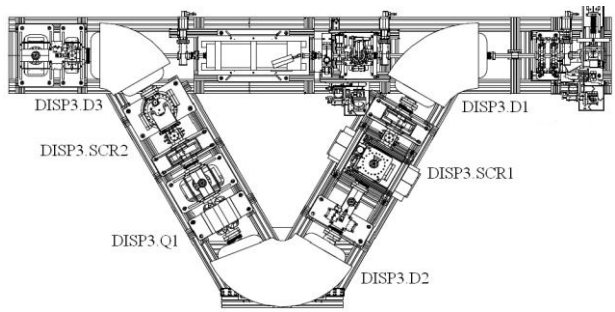

Figure 3: Sketch of the HEDA2 section, the electron bunch propagates from right to left.

Each screen station has two types of screens – a YAG (Ce-doped Yttrium Aluminum Garnet powder coated screen) and an OTR (Optical Transition Radiation screen). The screens are fixed on movable actuators. In addition, the first screen station has an aerogel radiator for streak measurements and a horizontal slit to select a longitudinal slice for vertical slice emittance measurements.

Momentum Measurements

For measurements of the electron beam momentum the first dipole Disp3.D1 and the screen Disp3.Scr1 are used (Fig. 3). The entrance of the dipole is 17.14 m downstream the gun, the bending angle α and radius ρ are 60° and 0.6 m, respectively. The distance L between the dipole exit and the screen is 0.7 m.

The horizontal size of the electron bunch on the Disp3.Scr1 screen is defined by the bunch transverse phase space at this position and momentum spread [7]:

$$X_{rms}^2 = \beta_x \varepsilon_x + (D \cdot \delta p)^2, \quad (4)$$

where X_{rms} is the rms bunch size on the screen, β_x is the horizontal beta function, ε_x is the horizontal geometrical emittance, D is the dispersion as $D = \rho(1-\cos(\alpha))+L\sin(\alpha)$ and $\delta p = \Delta p/p$ is the relative rms momentum spread of the electrons in the bunch. For the parameters mentioned above D = 0.905 m.

The horizontal bunch size corresponds to the momentum spread when the contribution of the last term on the right part of Eq. (4) is dominating. This means, the minimum achievable momentum resolution is defined as the momentum spread when the contributions from both terms on the right side of Eq. (4) are equal. Therefore, one gets the following limitation for the relative momentum resolution [7]:

$$\delta p_{\min} = \frac{\sqrt{\beta_x \varepsilon_x}}{D}. \quad (5)$$

For typical PITZ operation conditions with β_x equals 5 m, ε_x equals $2 \cdot 10^{-8}$ mm·mrad the minimum relative momentum resolution δp_{min} is about $3.5 \cdot 10^{-4}$ or 8 keV/c for 25 MeV/c beam.

Longitudinal Phase Space Measurements

The longitudinal phase space can be measured on the Disp3.Scr1 screen using the TDS cavity (see Fig. 1). The cavity center is located at 10.985 m downstream the gun, its length from flange to flange is 0.7 m, the distance between the cavity and the entrance of the dipole Disp3.D1 is 6.155 m. The beam image measured on the screen corresponds to the longitudinal phase space, where the image along the horizontal and vertical axes corresponds to the momentum and the longitudinal coordinate inside the bunch [8], respectively.

Slice Emittance Measurement

Vertical slice emittance measurements can be performed with a quadrupole scan technique using the quadrupole magnet Disp3.Q1 and the second screen Disp3.Scr2. A horizontal slit at the Disp3.Scr1 screen station will be used to select a longitudinal slice of the energy chirped beam. The energy chirped beam will be realized with off-crest acceleration using the CDS booster. The horizontal slice emittance is measured with the same technique in the HEDA1 section upstream [9].

The third dipole Disp3.D3 is used to bend the beam back to the common beam dump at the end of the beamline of the straight section.

RESULTS OF MOMENTUM MEASUREMENTS AT HEDA2

The first HEDA2 commissioning was done at PITZ in May 2012 with the following electron beam and PITZ parameters:

- Electron bunch charge – 0.8 nC (1 bunch in train).
- Beam momentum after the gun – 6.7 MeV/c.
- CDS Booster RF power – 4.5 MW.

As a test measurement, momentum measurements as a function of the booster RF phase were performed and results are shown in Fig.4.

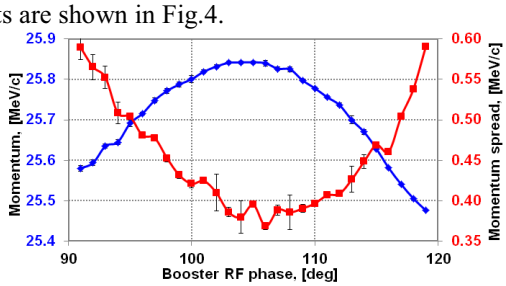

Figure 4: Beam momentum and momentum spread measurements performed at HEDA2.

The blue curve shows the mean beam momentum and the red curve shows the rms beam momentum spread as a function of the RF phase of the booster. The error bars show the standard deviation of 10 measurements for each RF phase.

An example of a beam image on the Disp3.Scr1 screen is shown in Fig. 5 together with the corresponding beam momentum distribution. The color code corresponds to the light intensity measured at the screen. The horizontal axis corresponds to the longitudinal beam momentum.

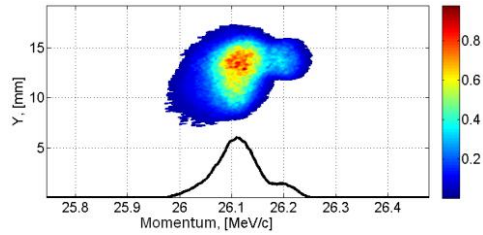

Figure 5: Beam image at the Disp3.Scr1 YAG screen and its corresponding momentum distribution.

CONCLUSION AND OUTLOOK

The installed HEDA2 section enables momentum measurements of the electron beam up to 40 MeV/c. A beam momentum of up to 26 MeV/c was measured during the first commissioning in summer 2012. With the booster off-crest operation, it will be possible to perform vertical slice emittance measurements at the second screen station using a quadrupole scan technique. The TDS cavity will enable longitudinal phase space measurements with a minimum slice momentum spread resolution down to 1 keV/c. The TDS cavity was installed at PITZ in winter 2011. The klystron and high voltage modulator of the TDS were installed this summer. First tests with the cavity are planned for autumn 2012.

REFERENCES

[1] F. Stephan, C. H. Boulware, M. Krasilnikov, J. Bähr et al., "Detailed characterization of electron sources yielding first demonstration of European X-ray Free-Electron Laser beam quality." Phys. Rev. ST Accel. Beams 13, 020704 (2010).

[2] L. Staykov et al., "Measurement of the projected normalized transverse emittance at PITZ", FEL2007, MOPPH055.

[3] M. Mahgoub et al., "Longitudinal Phase Space Studies at the PITZ Facility," IPAC2012, MOPPP032.

[4] L. Kravchuk et al., "Layout of the PITZ transverse deflecting system for longitudinal phase space and slice emittance measurements," LINAC2010, TUP011.

[5] P. Emma et al., "A Transverse RF deflecting structure for bunch length and phase space diagnostics," LCLS-TN-00-12, The LCLS Technical Notes 2000.

[6] S. Rimjaem et al., "Physics and technical design for the second high energy dispersive section at PITZ", DIPAC2009, MOPD26.

[7] H. Wiedemann, *Particle accelerator physics I, second edition.* (Springer, 1999), 176.

[8] D. Malyutin et al., "Simulation of the longitudinal phase space measurements with the transverse deflecting structure at PITZ", IPAC2012, MOPPP034.

[9] Y. Ivanisenko et al., "Slice Emittance Measurements for Different Bunch Charges at PITZ", IPAC2011, THPC113.

AIRIX MEASUREMENT CHAIN OPTIMIZATION FOR ELECTRON BEAM DYNAMIC AND DIMENSIONAL CHARACTERISTICS ANALYSIS

F. Poulet, V. Bernigaud, C. Chollet, H. Dzitko, J. Kranzmann, C. Noel, O. Pierret
CEA, DAM, DIF, Bruyères le Châtel, F-91297 Arpajon, France

Abstract

AIRIX is a linear accelerator dedicated to X-ray flash radiography at CEA's hydrotest facility. It has been designed to generate an intense X-ray pulse using a 2 kA, 19 MeV and 60 ns electron beam.

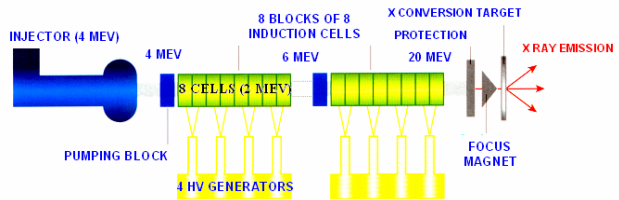

Figure 1: AIRIX accelerator

The electron beam transport in the accelerator is insured by the knowledge of the dynamic and dimensional characteristics of the beam created downstream the injector. These characteristics are assessed from a measurement chain, established by adapted optics and an intensified camera, aiming at observing the Cerenkov radiation produced during the interaction of electrons with a mylar target placed in the beam. This paper deals with the characterization, and comparison with the previous model, of a new intensified camera which was experimentally tested on AIRIX during an injector characterization campaign. This allowed to define profile and emittance beam characteristics. The obtained results are promising and revealed very interesting properties in particular in term of dynamic, temporal resolution, linearity and signal-to-noise ratio.

INTENSIFIED CAMERAS THEORETICAL CHARACTERIZATION

This characterization was achieved in laboratory, both on the intensified camera PROXITRONIC (NANOCAM HF4-S-5N model) currently set up on AIRIX, and on the new PRINCETON camera (PIMAX3 model).

Table 1: General characteristics

Parameters	PROXITRONIC	PRINCETON
Type	Analog	Numeric
CCD captor cooling	No	Down to -25°C air cooled
CCD format	512 x 512	1024 x 1024
Digital conversion	8 bits	16 bits
Gate width	5 ns to 65 ms	2 ns to 20 s
CCD pixel size	11.2 x 11.6 µm²	12.8 x 12.8 µm²
Image area	8.7 x 6.5 mm²	13.1 x 13.1 mm²
MCP-captor coupling	O.F – reducing cone – O.F	O.F – O.F
Usual configuration	Black level : 30% Video Gain : 90% MCP Gain : 90%	

Signal Base Line Adjustment

For PROXITRONIC camera, a "Black Level" parameter allows the adjustment of the signal base line. With a homogeneous pulsed DEL source, we estimate the signal base line mean level relatively to the "Black Level" variation, and we note that decreasing Black Level of 10% reduces the pixel level of 20 ADU. Finally, in the PROXITRONIC camera usual configuration, pixels which are lower than 48 ADU are reduced to 0 (threshold effect). For new PRINCETON camera, the signal base line and video gain can not be changed.

Linearity

The tests are achieved with a 532 nm nanosecond LASER and an integral sphere of 40 mm diameter. By convention, we reach camera sensitivity saturation when linearity defects are higher than ±5%. For the PROXITRONIC camera (figure 2), we note a beginning of sensitivity saturation around 130 ADU/pixel. In linear mode, the ±10% dispersion is representative of the weak signal to noise ratio.

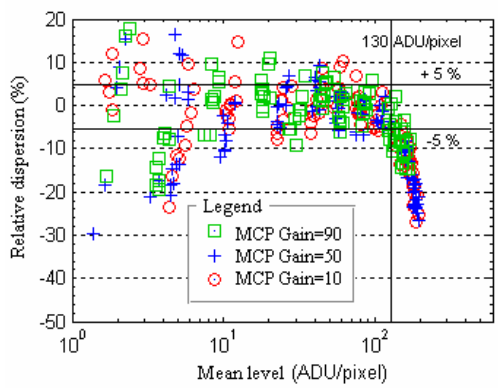

Figure 2: PROXITRONIC camera linearity defects

As for the new PRINCETON intensified camera (figure 3), sensitivity saturation defects are observed around 8000 ADU/pixel. We remark a weak dispersion level in linear

mode with CCD captor cooling. Furthermore, captor dimensions allow the possibility to increase the analysis dynamic and signal to noise ratio by binning 2x2 operations.

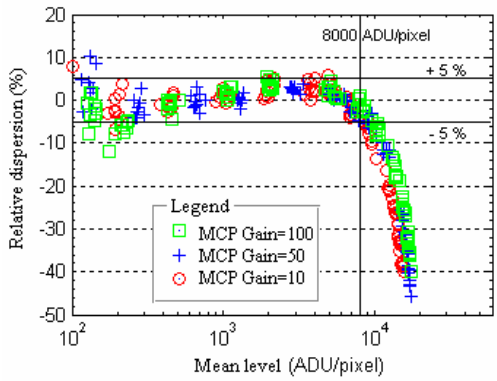

Figure 3: PRINCETON camera linearity defects

Absolute Gain Transfer Function

For this measurement, we use a 525 nm homogeneous pulsed DEL source. A calibrated CCD camera allows to measure the incident energy density. At the end of the experiment, we note that the sensitivity range covered by the PROXITRONIC camera when changing MCP gain from 10% to 100%, is the same as the one covered by the PRINCETON camera when changing MCP gain only from 50% to 100%.

Sensitivity Uniformity

This experiment is driven by a 525 nm pulsed DEL and an integral sphere of 40 mm diameter. For PROXITRONIC camera (figure 4), the response can be explained by the presence of the reducing cone. This study reveals that 95% of pixels are homogeneous in sensitivity at ±17%.

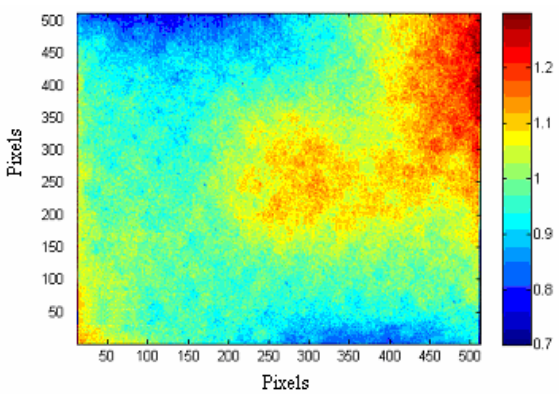

Figure 4: PROXITRONIC camera sensitivity defects

Concerning the new PRINCETON camera (figure 5), this is an unexpected profile. This behaviour reveals a bad O.F–O.F coupling between the CCD captor and the intensifier. 95% of pixels are homogeneous at only ±22%. In this point, the PRINCETON performances are disappointing in comparison with the PROXITRONIC camera which however includes a reducing cone.

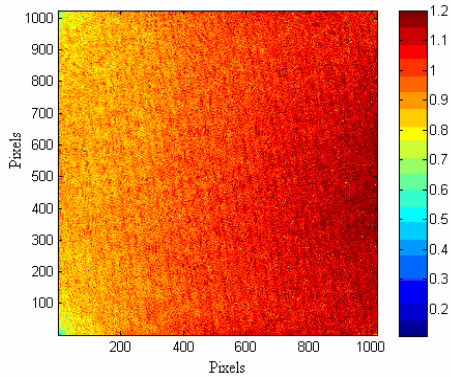

Figure 5: PRINCETON camera sensitivity defects

Signal to Noise Ratio

This characteristic is essential for a rigorous beam dimension measurement. By working with a 90% PROXITRONIC camera MCP gain (figure 6), signal to noise ratio is very low (≤ 5) even in the dynamic high part. Only 10% and 50% MCP gain values allows to reach a 10 signal to noise ratio nearly the saturation boundary (130ADU/pixel).

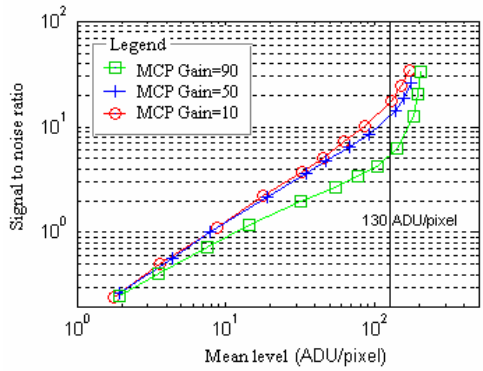

Figure 6: PROXITRONIC camera signal to noise ratio

With a 10% PRINCETON MCP Gain (figure 7), we can reach a 10 signal to noise ratio on a decade. This performance is made possible by the 16 bits CCD image resumption and the CCD captor cooling.

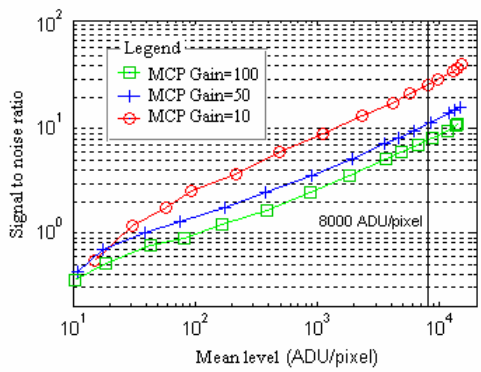

Figure 7: PRINCETON camera signal to noise ratio

Finally, by setting MCP gain to 50% for the PROXITRONIC camera, and to 10% for the PRINCETON camera, we obtain the same energetic sensitivity and we can establish an absolute comparison which reveals that the PRINCETON signal to noise ratio is 2.5 time better than the PROXITRONIC one.

Pixel Dynamic

$$D_{S/B\geq K} = \frac{A_{pixel}^{SAT}}{A_{pixel}^{Min}(S/B = K)} \quad (1)$$

K corresponds to the minimum signal to noise ratio criterion to check on the $[A_{pixel}^{Min}, A_{pixel}^{SAT}]$ range. From K=4, we considerate that is possible to quantify a localised information. Unfortunately, for K=4 and in usual configuration, the best PROXITRONIC pixel dynamic value is equal to 1.3 (against 33 with the PRINCETON camera and a 10% MCP Gain). This means that contrary to the PRINCETON camera, the PROXITRONIC camera does not allow to observe an important incident ray fluctuation except when adapted optical densities are used. Figure 8 is obtained from a 5 mm diameter circular homogeneous central lighting, after pixel level normalization.

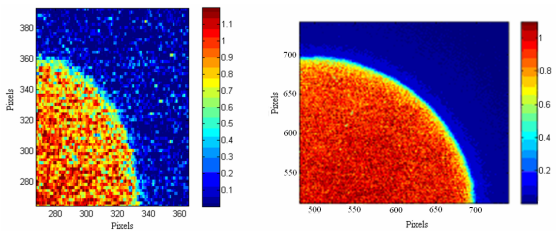

Figure 8: PROXITRONIC and PRINCETON acquisitions

INTENSIFIED CAMERAS EXPERIMENTAL CHARACTERIZATION

Injector Characterization Campaign

2 or 3 times a year, this campaign consists in validating the AIRIX injector working and determinating the beam characteristics to transport up to the X-ray conversion target. By varying the intensity inside the extraction magnet situated downstream the injector, and by studying the beam RMS dimension variations with the Cerenkov imaging diagnostic (3 gradient method), we deduce the beam emittance.

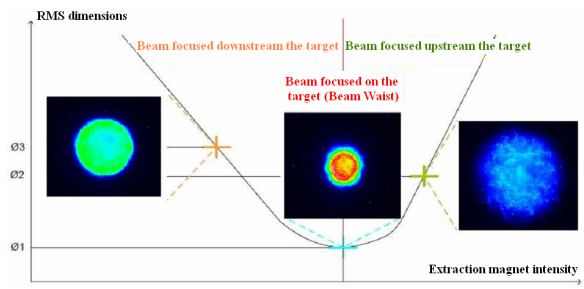

Figure 9: AIRIX emittance measurement

This measurement precision strongly depends on the image quality. This is why we chose this campaign to characterize experimentally and compare with the PROXITRONIC previous model our new PRINCETON intensified camera.

Results

The experimental points (figure 10) are extracted from a single treatment software. The aim consists in discarding all mistakes potentially introduced by different algorithms.

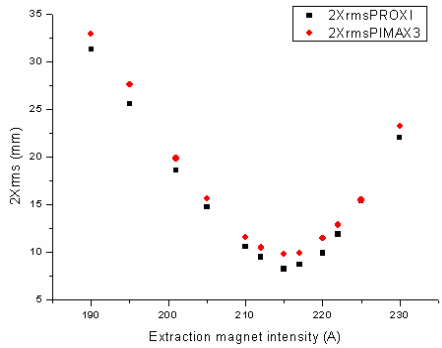

Figure 10: PROXITRONIC and PRINCETON results comparison (Xrms dimension only)

The AIRIX injector characterization campaign achieved with PROXITRONIC and PRINCETON cameras shows a similar variation of the beam RMS dimensions. In both case, the beam waist is obtained for a same intensity inside the extraction magnet. The light offset recorded between the curves can however be perceived as the possibility to optimize the electron beam transport and so the X-ray conversion efficiency.

CONCLUSION

In a first time, we have noted that the PRINCETON camera performances in term of linearity, signal to noise ratio and pixel dynamic was better (up to a 2.5 factor for signal to noise ratio and 25 for the pixel dynamic) than the PROXITRONIC camera ones. Furthermore, by setting up this new intensified camera during the injector characterization campaign, we obtained results witch confirmed our reference experimental points with a better information quality than with our previous camera model. Thus, the PRINCETON camera allows us to optimize the measurement chains currently deployed on AIRIX. The next step is to compare with the PROXITRONIC camera the other PRINCETON camera characteristics (in particular its capacity in term of exposure time), in order to develop new time resolved diagnostics, which could allow to acquire several images during a same pulse.

DISTRIBUTED CONTROL SYSTEM FOR AN INDUSTRIAL ELECTRON BEAM ACCELERATOR

Vijay Sharma*, S. Acharya, & K.C. Mittal
Electron Beam Centre, BARC, Mumbai-400085, India

Abstract

A PCVM type 3MeV DC Electron beam accelerator has been developed at Electron Beam Centre, BARC, Mumbai, India. A PLC based distributed control system has been incorporated for the control of the accelerator. A touch screen user interface (HMI) has been provides for single point control of the entire accelerator. The accelerator operation/fault related data is stored in the memory Flash card of the HMI. The Accelerator has many subsystems such as scan magnet supply to scan the electron beam, Chiller unit to supply the chilled water to the accelerator for cooling, vacuum system to maintain the vacuum inside the beam tube, high voltage unit to generate the EHV for electron acceleration and other support system. All the above subsystems have to be controlled from the central location in order to operate the accelerator safely. Each of the subsystem has been controlled by an independent PLC controller with all the safety features and control flow controlled by the program logic algorithm written into the PLC. After each of the subsystem has been tested separately all the PLCs are connected to the central PLC on Modbus TCP-IP. The main central PLC has been programmed to fetch the processed data from the individual subsystems PLCs and provides control and monitoring of the accelerator. In auto mode of operation setting the accelerator parameters operates all the subsystems automatically.

INTRODUCTION

The electron beam accelerator has various subsystems. All the subsystems have to work together in a defined sequence to generate the desired accelerated electron beam from the accelerator. All the subsystem such as vacuum system, sweep scan magnet unit, high voltage unit, chiller water unit, air circulation unit, search-secure, safety, interlock unit, steering/focussing magnet unit has to be controlled. Each group of similar units has been provided with a PLC controller in order to perform the fully automatic operation of that its subsystem. Finally all the PLCs are connected together on Modbus TCP-IP network to achieve a single point control of the accelerator. A touch screen panel has been provided at the control panel as an institutive user interface.

SYSTEM OPERATION

The 3 MeV electron beam accelerator is an industrial accelerator developed for the various industrial electron beam processing applications. The accelerator control system has been designed using industrial PLC in such a way that an operator with short duration training can operate the accelerator. The control system has been equipped with the self diagnostic features for quick finding of faults in the failed subsystem. This feature reduces the down time of the accelerator by giving type and location of fault hence helps in quick recovery of the accelerator.

All the PLCs of the various subsystems are connected to the main PLC. All the subsystem PLCs, operate their subsystems in the desired sequence in the pre-defined control flow. All the operate/control trip limits are set by the operator. Each of the subsystem PLC reports about the current state of operation to the main PLC. The main Master PLC initiates the inter-PLC operation based on its program to start the next subsystem operation when the previous stage operation gets over. For example after the desired vacuum has been achieved in the system the electron gun can be started. All these operations are performed automatically by the control system. The failure of any subsystem is reported on the control panel for the notice of the operator.

The control panel has three levels of control privileges as 'Engineer', 'Supervisor' and 'Operator' in their decreasing order of privileges. There are three login password based on the type of privileges. Log-in as an 'Engineers' allows the user to access/modify all the information related to each of the subsystem. Engineer also has the freedom to operate all the subsystem in manual mode instead of predefined sequence. This operator (Engineer) also has the privilege to bypass certain soft interlocks. This helps him in modifying the process or debugs the system fault. Login as supervisor allows him to access all the information related to accelerator operation, fault timings, system fault locations etc but he cannot modify the process or bypass any interlock. Operator login has only one mode of operation 'AUTO MODE'. The Auto mode is also called as 'operator mode' of operation. This is the simplest mode of operation designed for the regular operation of the accelerator. In auto mode operation, the operator has to set the desired accelerating voltage and current and press start button. The control system starts the mains stabilizer to energize all the power supplies. Switches ON the electron gun filament then waits for it to heat up. Starts the HVDC supply and set the accelerating voltage to the set value by making incremental changes in the HVDC. When the set accelerating voltage is reached, the 'Accelerator Ready' is displayed' on the HMI. During the automatic operation when any type of severe fault occurs say high voltage arc fault or over heating fault occurs, the accelerator high voltage is tripped automatically besides displaying and

* vijay9819420563@gmail.com

logging the type and time of fault. The operator has to restore the fault and press the reset button to acknowledge the fault.

CONCLUSION

The control system has been commissioned and it is working satisfactorily. Operation of the accelerator has been done on trial basis. In radiation environment, high-cost paper insulated Lead sheathed (PILCA) cables make the control wiring an expensive item, but the use of this distributed control has reduced the wiring length and its maintenance cost besides increasing the reliability of the accelerator.

ACKNOWLEDGMENT

We gratefully acknowledge the technical support offered by the vacuum, high Voltage and other auxiliary system groups in making their process understand. This has helped us a lot in the development, commissioning and operation of the control system.

DESIGN AND SIMULATION OF A NEW FARADAY CUP FOR ES-200 ELECTROSTATIC ACCELERATOR

E. Ebrahimibasabi, S.A.H. Feghhi, M. Khorsandi, Department of Radiation Application, Shahid Beheshti University, Tehran, Iran

Abstract

Faraday Cups have been used as diagnostic tools to measure the charged particle beam current directly. Up to now, different designs have been introduced for this purpose. In this work, a new design of Faraday Cup has been performed for ES-200 accelerator, a proton electrostatic accelerator which is installed at SBU. FC's dimensions and desirable material have been considered Based on the ES-200 beam characteristics (maximum energy of 200 keV and maximum current of 500 μA). Thickness and dimensions of FC has been calculated by SRIM and MCNPX codes according to the range of proton and induced electrons. The Appropriate FC geometry specifications have been simulated by using CST Studio package. In addition, the heat power generated by proton collision with FC material has been calculated analytically and then required cooling system has been designed by ANSYS. The results showed that the new designed Faraday Cup has a good performance to measure the proton beam current in ES-200 ion accelerator.

INTRODUCTION

An electrostatic accelerator is a type of accelerator that uses static electric field to accelerate charged particles. ES-200 is a 200 keV electrostatic proton accelerator at Shahid Beheshti University (SBU), which has four main components as shown in Fig (1). In this accelerator; RF ion source is positioned inside the high voltage terminal and injects protons into the accelerating tube. A variable high voltage is used to create a 200 kV potential difference between the ion source and the high voltage terminal. Within the accelerating tube is a strong uniform electric field which accelerates protons toward the target. The vacuum system lowers the pressure of the accelerating tube down to at least 10^{-5} Torr to ensure that the accelerated protons have no interaction with air molecules and energy loss [1]. This machine will require ultra-sensitive instrumentation for its proper operation. So a new design of Faraday Cup (FC) will be considered to do more precise measurement of accelerator beam current.

DESIGN CONCEPTS

FCs are used as a destructive instrument, which can provide accurate information on the beam current in a very straightforward manner [2]. Designing proper cooling system, determining the optimal dimensions of a FC and backscatter loss reduction techniques (including: Geometry-based techniques, Electromagnetic techniques, and using of a low-Z material) are a number of issues that need to be considered for designing a FC [3].

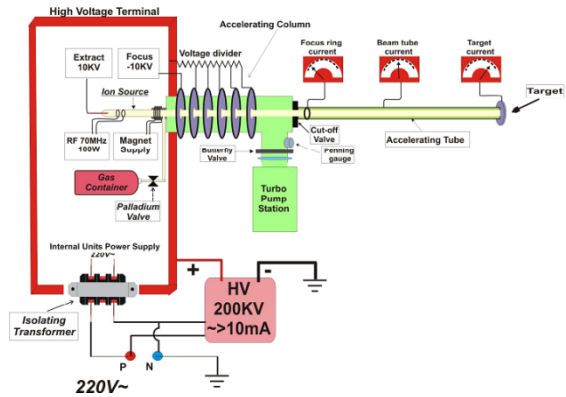

Figure 1: Electrical Schematic of 200keV Electrostatic System [1].

As is shown in Fig (2) heavy charged particles such as proton interact with matter primarily through coulomb forces between their positive and negative charge of the orbital electrons within the absorber atoms [4]. Although nuclear interaction of the charged particle with material (as in Rutherford scattering) is also possible at high energies, but because of the low energy of proton beam in ES-200, forward and backward distribution of electrons due to nuclear interactions could not be possible. The energy spectrum of the secondary electrons, has a peak at a few eV with a spread at half height of the same order of magnitude, thus about 80-95% of emitted particles are below 100 eV [5]. This behaviour may indicate that the emission of low-energy electron is indeed due to the cascade process. High-energy part of the spectrum reflects the direct energy transfer process from the impinging ion to an electron within the matter.

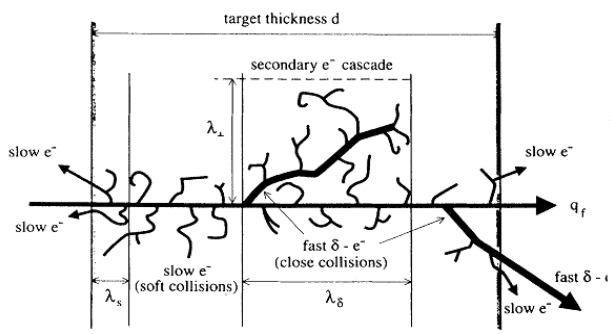

Figure 2: Ionization of the mater by ions and process of electron emission [6].

The first step in the FC design process involves determination of material, so that the thickness of the beam stopper should be much larger than the penetration depth of 200 keV protons. In this paper, Copper was chosen because of its good electrical conductivity and its excellent heat conductivity [7]. The maximum energy of ejected electrons is given by

$$E_{\max} = 4\frac{m_e m_p}{(m_e + m_p)^2} E_{\max} Cos^2\theta \qquad (1)$$

Where E_{Proton} is the incident proton energy and Θ is the angle between the direction of the incident beam and the trajectory of secondary electrons. m_p and m_e are the proton and electron mass respectively[8]. So for 200 keV protons, the maximum energy transfer to the orbital electrons of copper atoms, as a FC material, is about 459 eV.

It should be mentioned that the target thickness not only depends on the range of protons but also on forward and backward-electron yield [6]. Range of 200 keV protons in copper has been calculated to be 0.99 μm using SRIM code. The same result has been confirmed using MCNPX simulations [9]. According to MCNPX results range of the electron with maximum energy of 459 eV (in forward direction) is 0.5 mm. It seems that a 1mm thickness of neck wall in FC will be enough for our purpose. But to ensure the preservation of the vacuum, the thickness of 3mm has been chosen.

MECHANICAL DESIGN OF FC

Although the angular distribution of high energy electrons has a strongly forwarded peak [6], but by optimization in structure and using a high voltage in cup entrance, the backscattered electrons eject towards the neck wall or the beam stop region.

Using a suitable cone shaped aperture and a proper suppressing voltage; we can reduce the backscatter electrons. Since secondary electrons emission follows a cosine distribution about the normal to the surface, a cone shaped aperture increases the geometrical path length of the impinging particles within the escape region and the total electron yield decrease by a factor of $\cos^{-1}\Theta$ (Θ is The angle of incidence of the beam respect to the surface normal) [2]. In order to redirect the secondary electrons back into the FC, The FC angel of 45^0 leads to radius of 22 mm, and length of 53 mm for a cone shaped aperture. Schematic of the FC, simulated by CST Studio package, has been shown in Fig.3 [10]. Suppressor material close to the entrance of the cup was considered of stainless steel to prevent the secondary electrons leaving the FC. The position and dimension of this segment is very important to reduce the necessary suppressing voltage. For electric isolation of the cup components, ceramic was used. According to selected angle, suppressing voltage -230 V is sufficient to capture all of charges in the FC.

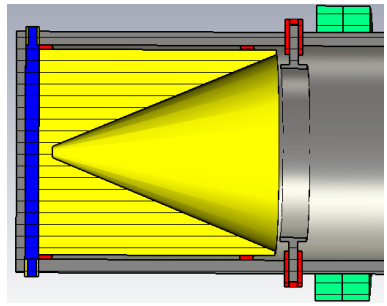

Figure 3: final design of the FC simulated with CST.

Fig (4) and Fig (5) shows Simulations of the field distribution and the secondary electron emission modelled with the CST Studio package respectively.

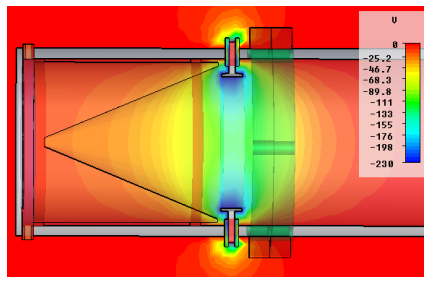

Figure 4: Simulation of the field distribution.

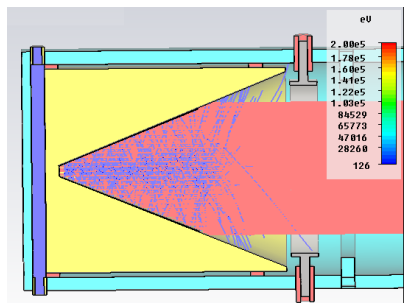

Figure 5: Simulation of secondary electrons emission.

HEAT TRANSFER

According to the simulations using ANSYS, produced thermal power in the desired FC, by considering the proton energy of 200 keV and continues beam current of 500 μA, will not exceed 100 W. A cooling system has been designed so that a pipe with diameter of 0.3 cm, that covers whole backward side of FC, extracts the produced heat. The used cooling water system has been depicted in Fig. 6. Simulation of cooling water system was done by ANSYS [11]. In this system, temperatures of inlet and outlet water of the coolant tube are about 295 K and 300 K respectively. The simulation results show that, if the water flows with a volumetric flux of 1×10^{-4} m^3s^{-1}, the maximum temperature of FC would be 300 K.

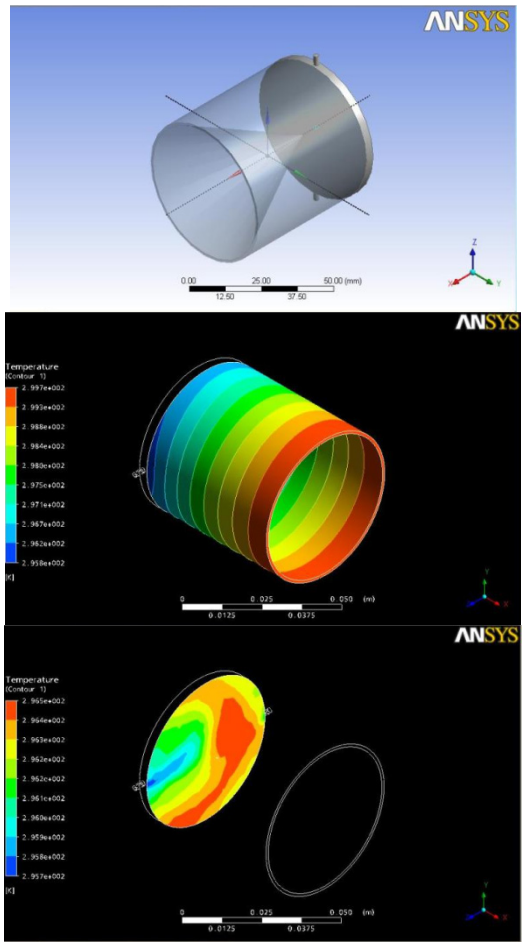

Figure 6: Distribution of heat on cooling system with ANSYS.

RESULTS & CONCLUSION

By choosing copper as proper material for our FC, range of 200 keV protons was calculated by SRIM and MXNPX. Choosing a cone shaped aperture with the angel of 45^0 leads to total electron yield decrease by a factor of 1.4. So that suppressing voltage -230 V can capture all of charges in the FC. In following water cooling system for our FC designed and simulated by ANSYS. Results showed that with a flow of 1×10^{-4} m^3s^{-1}, the maximum temperature of FC could be 300 K.

Based on the results from this work we plane to construct the FC and compare its practical performance with the previous one in our accelerator.

ACKNOWLEDGMENTS

It is our pleasure to thank Mr M. Aghayee and Mr H. Sayyar for their collaborative help in this study.

REFERENCES

[1] J. Rahighi, M. Jafarzadeh Khatibani, M. Lamehi Rachti, P. Taherparvar, H. Ghods, , A. Vakili, F. Zonobi and H. Azizi, “Construction of the first Electrostatic Accelerator in Iran with a maximum energy of 200 keV”, Nucl. Science and Technology, 2010

[2] J. Harasimowicz, C. P. Welsch, “Faraday cup for low-energy, low-intensity beam measurement at the USR” Cockcroft Institute, Warrington WA4 4AD, UK, and Department of Physics, University of Liverpool, Liverpool L69 7ZE, UK.

[3] Patrick McChesney, Thesis “Faraday Cup Design and Geant4 Simulation for the ALPHA Project at IUCF Patrick Mc Chesney”, department of physics, Indiana University, December 10, 2009

[4] John David Jackson, Classical electro dynamics, Third edition, John,Wiley and Sons,Inc. (1999).

[5] D. Hasselkamp et al., “Particle Induced Electron Emission 2”, Springer-Verlag (1992).

[6] Hermann Rothard, Christophe Caraby, Amine Cassimi, Benoit Gervais, Jean-Pierre Grandin, Pascal Jardin, and Matthias Jung, Annick Billebaud and Michel Chevallier, Karl-Ontjes Groeneveld and Robert Maier “Target-thickness-dependent electron emission from carbon foils bombarded with swift highly charged heavy ions” PHYSICAL REVIEW A VOLUME 51, NUMBER 4 APRIL 1995.

[7] A.F.D. Morgan, Diamond Light Source, UK. “DESIGN OF THE FARADAY CUPS IN DIAMOND” Proceedings of DIPAC 2005, Lyon, France

[8] Cambriay R, H’eraultz J, Brassartz N, Silarixk M, Chauvelz P. Phys Med Biol 1997;42:1185.

[9] Denise B. Pelowitz, MCNPX User's Manual, Version 2.6.0, Los Alamos National Laboratory, April 2008.

[10] CST Studio 2010, http://www.cst.com.

[11] ANSYS, Inc., 2010. http://www. ANSYS.com.

List of Authors

Bold papercodes indicate primary authors

— L —

Institutes List

Allrussian Electrotechnical Institute
Moskow, Russia
- Chikhachev, A.S.
- Kovalenko, Y.A.

AN Krylov SRI
St. Petersburg, Russia
- Bogdanov, A.A.
- Kudinovich, I.V.
- Struev, V.P.

ANL
Argonne, USA
- Gai, W.

BARC-EBC
Mumbai, India
- Sharma, V.

Belarus State University of Informatics and Radioelectronics (BSUIR)
Minsk, Belarus
- Kolosov, S.V.
- Kurayev, A.A.
- Sinitsyn, A.K.

Belarussian State University, Scientific Research Institute of Nuclear Problems
Minsk, Belarus
- Maximov, S.I.
- Rodionova, V.N.
- Sytov, A.I.
- Tikhomirov, V.V.

BINP SB RAS
Novosibirsk, Russia
- Aleynik, V.I.
- Alinovskiy, N.
- Arbuzov, V.S.
- Astrelina, K.V.
- Barnyakov, A.M.
- Bashkirtsev, A.G.
- Batrakov, A.M.
- Bayanov, B.F.
- Bekhtenev, E.A.
- Belikov, O.V.
- Berkaev, D.E.
- Bezuglov, V.V.
- Borisov, A.A.
- Bragin, A.V.
- Bryazgin, A.A.
- Bryzgunov, M.I.
- Bubley, A.V.
- Bulatov, A.V.
- Burdin, P.N.
- Cheblakov, P.B.
- Chekavinskiy, V.A.
- Cherepanov, V.P.
- Chernousov, Y.D.
- Chernov, K.N.
- Chudaev, V.Ya.
- Dementyev, E.N.
- Devyataikina, T.A.
- Domarov, E.V.
- Dovzhenko, B.A.
- Dudnikov, A.V.
- Emanov, F.A.
- Erokhin, A.I.
- Fadeev, S.
- Faktorovich, B.L.
- Fatkin, G.A.
- Fedotov, M.G.
- Gambaryan, V.V.
- Getmanov, Ya.V.
- Golubenko, Yu.I.
- Goncharov, A.D.
- Gorniker, E.I.
- Gusev, I.A.
- Ilyin, I.V.
- Ivanov, A.A.
- Kadyrov, R.A.
- Kamkin, M.V.
- Karnaev, S.E.
- Karpov, G.V.
- Kasatov, D.A.
- Kazantseva, E.S.
- Kenzhbulatov, E.
- Khrushchev, S.V.
- Kirpotin, A.N.
- Knyazev, B.A.
- Kogut, D.A.
- Kokin, E.N.
- Kolmogorov, V.V.
- Kolobanov, E.I.
- Kondakov, A.A.
- Kondaurov, M.N.
- Koop, I.
- Korchagin, A.I.
- Korobeynikov, M.V.
- Kozak, V.R.
- Kozyrev, E.V.
- Krutikhin, S.A.
- Kubarev, V.V.
- Kuksanov, N.K.
- Kulipanov, G.N.
- Kuper, E.A.
- Kuptsov, I.V.
- Kurkin, G.Y.
- Kuznetsov, A.S.
- Lavrukhin, A.
- Lev, V.K.
- Levichev, A.E.
- Levichev, E.B.

- Lysenko, A.P.
- Makarov, A.N.
- Makarov, I.
- Maltseva, Y.
- Mamkin, V.R.
- Medvedev, L.E.
- Medvedko, A.S.
- Mezentsev, N.A.
- Miginsky, E.G.
- Mironenko, L.A.
- Nekhaev, V.E.
- Nemytov, P.I.
- Osipov, V.N.
- Ovchar, V.K.
- Panasyuk, V.M.
- Panfilov, A.D.
- Parkhomchuk, V.V.
- Pavlenko, A.V.
- Pavlov, V.M.
- Perevedentsev, E.
- Persov, B.Z.
- Petrenko, A.V.
- Petrov, V.M.
- Pilan, A.M.
- Podobaev, V.S.
- Popik, V.M.
- Potapov, S.I.
- Prisekin, V.G.
- Protopopov, A.Yu.
- Pureskin, D.N.
- Putmakov, A.A.
- Radchenko, V.M.
- Repkov, V.V.
- Reva, V.B.
- Rogovsky, Yu. A.
- Romanov, A.L.
- Rybitskaya, T.V.
- Salikova, T.V.
- Salimov, R.A.
- Sazansky, V.Ya.
- Scheglov, M.A.
- Schudlo, I.M.
- Sedlyarov, I.K.
- Semenov, A.V.
- Senchenko, A.I.
- Senkov, D.V.
- Serdobintsev, G.V.
- Serednyakov, S.S.
- Shatunov, P.Yu.
- Shatunov, Y.M.
- Shchudlo, I.M.
- Shevchenko, O.A.
- Shichkov, D.
- Shkaruba, V.A.
- Shtarklev, E.A.
- Shubin, E.
- Shwartz, D.B.
- Sidorov, A.V.
- Singatulin, S.R.
- Skarbo, B.A.
- Skorobogatov, D.N.
- Skrinsky, A.N.
- Sorokin, I.N.
- Starostenko, A.A.
- Styuf, A.S.
- Syrovatin, V.M.
- Tararyshkin, S.V.
- Tarnetsky, V.V.
- Taskaev, S.Yu.
- Tcheskidov, V.G.
- Tiunov, M.A.
- Tkachenko, V.O.
- Tsukanov, V.M.
- Tsyganov, A.S.
- Veremeenko, V.F.
- Vinokurov, N.
- Vlasenko, M.G.
- Vlasov, A. YU.
- Vobly, P.
- Volkov, A.A.
- Volkov, V.
- Voronin, L.A.
- Yaminov, K.R.
- Zemlyansky, I.
- Zharikov, A.A.
- Zharinov, Yu.M.
- Zolotarev, K.
- Zorin, A.V.
- Zverev, D.A.

BINP
Novosibirsk, Russia
- Bubley, A.V.

BNL
Upton, Long Island, New York, USA
- Smaluk, V.V.
- Yakimenko, V.

BSU
Minsk, Belarus
- Karpovich, V.A.
- Liubetsky, N.V.

CAEP/IAE
Mianyang, Sichuan, People's Republic of China
- Li, M.
- Wang, H.B.
- Yang, X.

CEA/DAM/DIF
Arpajon, France
- Chollet, C.

CEA/DSM/IRFU
France
- Chauvin, N.
- Desmons, M.

- France, A.
- Piquet, O.

CEA
Arpajon, France
- Bernigaud, V.
- Dzitko, H.
- Kranzmann, J.K.
- Noël, C.
- Pierret, O.
- Poulet, F.

CELLS-ALBA Synchrotron
Cerdanyola del Vallès, Spain
- Einfeld, D.

CERN
Geneva, Switzerland
- Maury, S.
- Rossi, C.
- Schmickler, H.

Chiang Mai University
Chiang Mai, Thailand
- Kusoljariyakul, K.
- Rimjaem, S.

CLASSE
Ithaca, New York, USA
- Mikhailichenko, A.A.

CORAD Ltd.
St. Petersburg, Russia
- Demsky, M.I.
- Krotov, V.V.
- Trifonov, D.E.

DAE/VECC
Calcutta, India
- Banerjee, A.S.

DELTA
Dortmund, Germany
- Dietrich, J.

DESY Zeuthen
Zeuthen, Germany
- Krasilnikov, M.
- Malyutin, D.
- Meissner, J.
- Stephan, F.
- Vashchenko, G.

DESY
Hamburg, Germany
- Brinkmann, A.
- Delsim-Hashemi, H.
- Ermakov, A.
- Flöttmann, K.
- Grebenyuk, J.
- Iversen, J.
- Matheisen, A.
- Singer, W.
- Singer, X.
- Vagin, P.V.

EB TECH Co. Ltd.
Daejeon, Republic of Korea
- Han, B.S.
- Kang, W.G.
- Kim, S.M.

Elamt-PM
Kaluga, Russia
- Chernov, I.V.
- Zacharov, V.V.

Euclid TechLabs, LLC
Solon, Ohio, USA
- Antipov, S.P.
- Jing, C.-J.
- Kanareykin, A.

European XFEL GmbH
Hamburg, Germany
- Geloni, G.
- Pflüger, J.

Fermilab
Batavia, USA
- Kephart, R.D.
- Nagaitsev, S.
- Ristori, L.

FZJ
Jülich, Germany
- Dietrich, J.
- Kamerdzhiev, V.
- Mao, L.J.
- Stassen, R.

GSI
Darmstadt, Germany
- Adonin, A.
- Barth, W.A.
- Chetvertkova, V.
- Dimopoulou, C.
- Dolinskii, A.
- Fischer, E.S.
- Gorda, O.E.
- Hollinger, R.

- Katayama, T.
- Kester, O.K.
- Litvinov, S.A.
- Meier, J.P.
- Mierau, A.
- Mustafin, E.
- Nolden, F.
- Pfister, J.
- Schnizer, P.
- Spiller, P.J.
- Steck, M.
- Strašík, I.
- Sugita, K.
- Tinschert, K.
- Weick, H.

HU/AdSM
Higashi-Hiroshima, Japan
- Okamoto, H.
- Osaki, K.

I-Tech
Solkan, Slovenia
- Hrovatin, R.
- Leban, P.

IAP
Frankfurt am Main, Germany
- Chetvertkova, V.
- Jameson, R.A.

IBA
Louvain-la-Neuve, Belgium
- Cahay, P.
- Jongen, Y.
- Paradis, Y.

ICKC SB RAS
Novosibirsk, Russia
- Ivannikov, V.
- Shebolaev, I.V.

ICKC
Novosibirsk, Russia
- Chernousov, Y.D.

ICM&MG SB RAS
Novosibirsk, Russia
- Gorpinchenko, D.

ICT SB RAS
Novosibirsk, Russia
- Dudnikova, G.

IHEP
Moscow Region, Russia
- Afonin, A.G.
- Ageev, A.I.
- Bakay, A.
- Baranov, V.I.
- Bogdanov, I.
- Chesnokov, Y.A.
- Ignashin, N.A.
- Ivanov, S.V.
- Kashtanov, E.
- Kozub, S.
- Lebedev, O.P.
- Maisheev, V.A.
- Orlov, A.P.
- Pokrovsky, V.A.
- Shcherbakov, P.A.
- Shirshov, L.S.
- Slabodchikov, I.
- Smirnov, V.
- Stolyarov, M.N.
- Sytnik, V.
- Sytov, S.E.
- Terekhov, V.
- Tkachenko, L.
- Yazynin, I.A.
- Zapolsky, V.N.
- Zinchenko, S.

ILSF
Tehran, Iran
- Ahmadi, E.
- Ghasem, H.
- Saeidi, F.
- Sarhadi, Kh.S.

IMP
Lanzhou, People's Republic of China
- Li, G.H.
- Li, J.
- Li, P.
- Ma, X.M.
- Mao, R.S.
- Yan, T.L.
- Yang, J.C.
- Yang, X.D.
- Yuan, Y.J.
- Zhao, T.C.

INFLPR
Bucharest - Magurele, Romania
- Scarisoreanu, A.M.
- Scarlat, F.

INFN/LASA
Segrate (MI), Italy
- Michelato, P.

INFN/LNL
Legnaro (PD), Italy
- Poggi, M.

Institute of Nuclear Chemistry and Technology
Warsaw, Poland
- Zimek, Z.

IOFFE
St. Petersburg, Russia
- Aleksandrov, E.B.

IPM
Tehran, Iran
- Ghasem, H.
- Rahighi, J.
- Salimi, E.

IPPE
Obninsk, Russia
- Bazhal, S.V.
- Romanov, V.

ITEP
Moscow, Russia
- Alekseev, P.N.
- Alexeev, N.N.
- Andreev, V.
- Balabaev, A.
- Balabin, A.I.
- Balanutsa, V.N.
- Barabin, S.V.
- Barminova, H.Y.
- Bolshakov, A.
- Drozdovsky, A.A.
- Drozdovsky, S.A.
- Golubev, A.
- Kats, M.M.
- Kolomiets, A.
- Koshelev, V.A.
- Kulevoy, T.
- Liakin, D.A.
- Minaev, S.
- Nikolaev, V.I.
- Novozhilov, Yu.B.
- Orlov, A.Y.
- Rodionova, M.E.
- Ryabtsev, A.S.
- Sasorov, P.V.
- Satov, Yu.A.
- Savin, S.M.
- Schegolev, V.A.
- Sharkov, B.Y.
- Shumshurov, A.
- Sitnikov, A.
- Sizov, F.A.
- Stolbunov, V.
- Tretyakova, T.
- Yanenko, V.V.
- Zavodov, V.P.
- Zenkevich, P.R.

iThemba LABS
Somerset West, South Africa
- Bark, R.A.
- Botha, A.H.
- Conradie, J.L.
- Cornell, J.C.
- Crombie, M.A.
- De Villiers, J.G.
- Delsink, J.L.G.
- Du Plessis, H.
- Du Toit, J.S.
- Duckitt, W.
- Fourie, D.T.
- Hogan, M.E.
- Kohler, I.H.
- McAlister, R.H.
- Mostert, H.W.
- Pilcher, J.V.
- Rohwer, P.F.
- Sakildien, M.
- Slabbert, J.P.
- Stodart, N.
- Thomae, R.W.
- Van Niekerk, M.J.
- van Schalkwyk, P.A.

JAEA/TARRI
Gunma-ken, Japan
- Yuri, Y.

JAI
Oxford, United Kingdom
- Seryi, A.

JIHT RAS
Moscow, Russia
- Kuznetsov, S.V.

JINR/DLNP
Dubna, Moscow region, Russia
- Horodek, P.
- Meshkov, I.N.
- Onischenko, L.M.
- Smirnov, V.L.

JINR/VBLHEP
Dubna, Moscow region, Russia
- Bazanov, A.M.
- Brovko, O.I.
- Butenko, A.V.
- Donets, D.E.
- Kozlov, O.S.
- Kuznetsov, A.B.
- Nesterov, A.

- Philippov, A.V.
- Shabratov, V.
- Shabunov, A.V.
- Sidorin, A.O.
- Trubnikov, G.V.
- Tuzikov, A.

JINR
Dubna, Moscow Region, Russia

- Agapov, N.N.
- Ahmanova, E.V.
- Akishin, P.G.
- Aleksandrov, V.
- Alenitsky, Yu.G.
- Alfeev, A.V.
- Andreev, V.
- Azaryan, N.S.
- Balalykin, N.
- Batin, V.
- Bekhterev, V.B.
- Bogomolov, S.L.
- Boudagov, Ju.
- Butenko, A.V.
- Bychkov, A.V.
- Chesnov, A.
- Demin, D.L.
- Denisov, Yu.N.
- Dolbilov, G.
- Donets, D.E.
- Donets, E.D.
- Donets, E.E.
- Donyagin, A.
- Efremov, A.A.
- Eliseev, A.V.
- Fateev, A.A.
- Filatov, G.A.
- Fimushkin, V.V.
- Galimov, A.R.
- Gikal, B.
- Gorbachev, E.V.
- Govorov, A.
- Grebentsov, A.Yu.
- Gudkov, S.V.
- Gulbekyan, G.G.
- Gurskiy, S.
- Ivanov, A.
- Ivanov, E.V.
- Karamyshev, O.
- Karamysheva, G.A.
- Karpinsky, V.
- Kazarinov, M.Y.
- Kekelidze, V.D.
- Khodzhibagiyan, H.G.
- Kirichenko, A.
- Kobets, A.G.
- Kobets, V.
- Korovkin, S.A.
- Kostromin, S.A.
- Kostyukhov, Yu.K.
- Kovalenko, A.D.
- Kozlov, O.S.
- Kuznetsov, G.L.
- Lebedev, N.I.
- Lebedev, N.
- Lepkina, O.
- Loginov, V.N.
- Lokhmatov, V.I.
- Makarov, R.S.
- Meshkov, I.N.
- Mikhailov, V.A.
- Mikhaylov, V.A.
- Minashkin, V.
- Mokrenko, S.P.
- Monchinsky, V.
- Morozov, N.A.
- Muravieva, E.V.
- Nikitaev, P.I.
- Nozdrin, M.A.
- Olshevsky, A.G.
- Paraipan, M.
- Pavlov, V.
- Perelstein, E.A.
- Petrov, D.
- Pivin, R.V.
- Ramsdorf, A.Yu.
- Romanov, S.
- Romanov, V.M.
- Rudakov, A.Yu.
- Rukoyatkina, T.V.
- Salnikov, V.V.
- Samsonov, E.
- Schegolev, V.Y.
- Sedych, I.M.
- Seleznev, V.V.
- Shabunov, A.V.
- Shakun, N.G.
- Shirkov, G.
- Shirkov, S.G.
- Shurkhno, N.
- Shutov, V.B.
- Shvetsov, V.N.
- Sidorin, A.A.
- Sidorin, A.O.
- Slepnev, I.
- Slepnev, V.
- Smirnov, A.V.
- Smirnov, V.L.
- Sorin, A.
- Starikov, A.Y.
- Sumbaev, A.P.
- Syresin, E.
- Taratin, A.M.
- Teryaev, O.V.
- Timoshenko, G.N.
- Topilin, N.D.
- Trubnikov, G.V.
- Tuzikov, A.
- Tyutyunnikov, S.I.
- Valkovich, A.S.
- Vasilishin, B.
- Volkov, V.
- Vorozhtsov, S.B.

- Yakovenko, S.
- Yazvitsky, Yu.
- Yudin, I.P.
- Yurkov, M.V.
- Zamriy, V.N.
- Zhabitsky, V.

KAERI
Daejon, Republic of Korea
- Vinokurov, N.

KIT
Eggenstein-Leopoldshafen, Germany
- Bornschein, L.

Kyoto ICR
Uji, Kyoto, Japan
- Nakao, M.
- Noda, A.
- Souda, H.
- Tongu, H.

Kyoto University, Institute for Advanced Energy
Kyoto, Japan
- Jimbo, K.

LBNL
Berkeley, California, USA
- Sessler, A.

LETI
Saint-Petersburg, Russia
- Altmark, A.
- Baturin, S.
- Sheynman, I.L.

LPI
Moscow, Russia
- Bashmakov, Y.A.
- Karev, A.I.
- Kurakin, P.V.
- Kurakin, V.G.
- Raevsky, V.G.

MEPhI
Moscow, Russia
- Adonev, O.A.
- Aliev, K.A.
- Belyaev, V.N.
- Blinnikov, A.A.
- Bogdanovich, B.Y.
- Bondarenko, T.V.
- Dyubkov, V.S.
- Fadeev, A.M.
- Gusarova, M.
- Ilyinsky, A.V.
- Kalashnikova, A.A.
- Khasaya, D.R.
- Kulago, A.
- Lalayan, M.V.
- Nesterovich, A.
- Petrushina, I.I.
- Plastun, A.S.
- Polozov, S.M.
- Proskin, S.
- Samoshin, A.V.
- Savin, E.A.
- Shikanov, A.E.
- Shikanov, E.A.
- Smirnov, A.Yu.
- Sobenin, N.P.
- Suleymenov, E.
- Tatsyuk, O.A.
- Tikhonov, D.B.
- Toporkov, S.E.
- Vorontsov, V.A.

MIPT
Dolgoprudniy, Moscow Region, Russia
- Ekhmenina, I.V.
- Raufov, A.
- Sheshin, E.P.
- Shornikova, A.

MPI-K
Heidelberg, Germany
- Grieser, M.
- Wolf, A.

MRRC
Obninsk, Russia
- Beketov, E.E.
- Isaeva, E.V.
- Koryakin, S.N.
- Lychagin, A.A.
- Ulyanenko, S.E.

MRTI RAS
Moscow, Russia
- Alekseev, M.A.
- Bystrov, P.A.
- Durkin, A.P.
- Rozanov, N.E.

MSIU
Moscow, Russia
- Shishanin, O.E.

MSU SINP
Moscow, Russia
- Sayapin, V.G.
- Vladimirov, I.
- Yurov, D.S.

MSU
Moscow, Russia
- Alimov, A.S.
- Ermakov, A.N.
- Ishkanov, B.S.
- Kamanin, A.N.
- Khankin, V.V.
- Pakhomov, N.I.
- Rudanov, G.S.
- Sakharov, V.P.
- Shurkhno, N.
- Shvedunov, V.I.

Muons, Inc
Batavia, USA
- Dudnikov, V.G.
- Johnson, R.P.

NAFU
Arkhangelsk, Russia
- Eseev, M.K.
- Vititnev, A.N.

Nano
Moscow, Russia
- Zavadtsev, A.A.

NC PHEP BSU
Minsk, Belarus
- Baturitsky, M.A.

NIIEFA
St. Petersburg, Russia
- Bagrievich, V.P.
- Bogdanov, P.V.
- Bolshakov, B.O.
- Borisov, O.V.
- Budtov, A.A.
- Druzgalckiy, I.V.
- Efremov, A.V.
- Filatov, O.G.
- Galchuck, A.V.
- Gavrish, Yu.N.
- Grigorenko, S.V.
- Grigoriev, V.I.
- Kalinichenko, M.A.
- Klinovskiy, P.O.
- Koltsov, V.V.
- Korolev, L.E.
- Kotenko, K.V.
- Kozienko, M.T.
- Kuzhlev, A.N.
- Machecha, A.I.
- Malyshev, V.P.
- Maznev, V.P.
- Menshov, Yu.D.
- Mikulinas, N.P.
- Morozov, A.V.
- Mudrolyubov, V.G.
- Ovchinnikov, V.P.
- Pavlukhov, D.E.
- Ponomarenko, V.I.
- Popov, A.V.
- Pozhensky, A.V.
- Seleznev, A.I.
- Shiltsev, V.D.
- Shishov, V.A.
- Sidorov, A.V.
- Smekalkin, V.
- Solnyshkov, D.A.
- Stepanov, A.V.
- Stogov, Yu.I.
- Strokach, A.P.
- Svinin, M.P.
- Svistunov, Y.A.
- Terentiev, V.V.
- Tolstun, N.G.
- Tsygankov, S.S.
- Vasilchenko, I.N.
- Vorogushin, M.F.
- Voronin, G.G.
- Zuev, Yu.

NIRS
Chiba-shi, Japan
- Noda, K.
- Shirai, T.

NRC
Moscow, Russia
- Aleksandrov, P.
- Belkov, A.
- Dombrovsky, V.
- Efimov, Y.V.
- Fomin, Y.A.
- Gorev, V.V.
- Kaportsev, E.V.
- Korchuganov, V.
- Kovachev, G.A.
- Kovalchuk, M.V.
- Krylov, Y.V.
- Kuznetsov, K.
- Kvardakov, V.V.
- Leonov, V.V.
- Moiseev, V.I.
- Moryakov, V.P.
- Moseev, K.
- Moseiko, N.I.
- Odintsov, D.G.
- Pesterev, S.G.
- Smolyakov, N.V.
- Smygacheva, A.S.
- Stirin, A.
- Tarasov, Yu.F.
- Tomin, S.I.
- Ushkov, V.
- Valentinov, A.G.

- Vernov, A.
- Yupinov, Y.L.
- Zabelin, A.V.

NSC/KIPT
Kharkov, Ukraine
- Bomko, V.A.
- Boriskin, V.N.
- Chertishchev, I.A.
- Dovbnya, A.N.
- Galaydych, K.V.
- Guk, I.S.
- Ivanov, B.I.
- Khoruzhiy, V.M.
- Kniaziev, R.R.
- Kobets, A.P.
- Kononenko, S.G.
- Mytrochenko, V.V.
- Nikiforov, V.I.
- Panov, V.V.
- Pavlij, K.V.
- Peev, F.A.
- Perezhogin, S.A.
- Reshetnyak, N.G.
- Rogov, Yu.V.
- Romanovsky, K.
- Shevchenko, V.A.
- Shlyakhov, I.N.
- Shramenko, B.I.
- Sotnikov, G.V.
- Tarasenko, A.S.
- Tenishev, A.Eh.
- Torgovkin, A.V.
- Tur, Y.D.
- Uvarov, V.L.
- Zajtsev, B.V.
- Zakutin, V.

NSU
Novosibirsk, Russia
- Fedotov, M.G.
- Serbo, V.G.

Omega-P, Inc.
New Haven, USA
- Marshall, T.C.
- Sotnikov, G.V.

ORNL
Oak Ridge, Tennessee, USA
- Murray, S.N.
- Nesterenko, I.
- Pennisi, T.R.
- Piller, M.F.
- Santana, M.
- Stockli, M.P.
- Welton, R.F.

PAVAC
Richmond, B.C., Canada
- Edinger, R.

Pfeiffer Vacuum GmbH
Asslar, Germany
- Hedbavny, P.

Physical-Technical Institute of the National Academy of Sciences of Belarus
Minsk, Belarus
- Petrakovsky, V.S.
- Pobol, I.L.
- Pokrovsky, A.I.
- Yurevich, S.V.
- Zhuravsky, A.Yu.

PNPI
Gatchina, Leningrad District, Russia
- Artamonov, S.A.
- Barzakh, A.E.
- Batist, L.Kh.
- Chernov, A.N.
- Fedorov, D.V.
- Filatova, A.M.
- Ivanov, E.M.
- Mezilev, K.A.
- Mikheev, G.F.
- Mironov, Yu.T.
- Molkanov, P.L.
- Moroz, F.V.
- Panteleev, V.N.
- Riabov, G.A.
- Samsonov, V.M.
- Tokarev, B.B.
- Volkov, Yu.M.

PPRC
Tehran, Iran
- Pazirandeh, A.
- Taheri, A.
- Torkamani, A.

RadiaBeam
Santa Monica, USA
- Smirnov, A.V.

RAS/INR
Moscow, Russia
- Akulinichev, S.V.
- Belov, A.
- Bragin, S.
- Brusova, N.I.
- Drugakov, A.N.
- Feschenko, A.
- Frolov, O.T.
- Gaidash, V.
- Gavrilov, S.A.

- Gorbunov, V.K.
- Grachev, M.I.
- Grechko, V.V.
- Grekhov, O.V.
- Kalinin, Y.Z.
- Kiselev, Yu.V.
- Kravchuk, L.V.
- Kvasha, A.I.
- Lebedeva, N.F.
- Mikhailov, V.N.
- Mirzojan, A.N.
- Naboka, A.N.
- Nikulin, E.S.
- Orlov, P.
- Paramonov, V.V.
- Ponomareva, E.V.
- Reinhardt-Nickoulin, P.I.
- Serov, V.L.
- Stepanov, A.A.
- Vasilyev, I.V.
- Volodkevich, O.
- Yabzhanov, V.V.
- Yakushev, V.P.
- Yamshikov, G.I.
- Zubets, V.

RRC KI
Moscow, Russia
- Semenov, B.I.

RRCAT
Indore (M.P.), India
- Ahlawat, M.
- Shinde, R.S.

RRCRST
Pesochniy, Russia
- Sysoev, D.

RRC
Moscow, Russia
- Korchuganov, V.
- Krylov, Y.V.
- Moseiko, L.A.
- Moseiko, N.I.
- Shirokov, A.V.
- Vernov, A.

Saint-Petersburg State University
Saint-Petersburg, Russia
- Belonogaya, E.S.
- Egorov, N.V.
- Fomenko, M.G.
- Galyamin, S.N.
- Kapshtan, D.Y.
- Makarova, M.A.
- Tyukhtin, A.V.
- Vinogradova, E.M.
- Zapasskii, V.S.

sbu
Tehran, Iran
- Asgarpour, M.
- Ebrahimibasabi, E.E.
- Feghhi, S.A.H.
- Khorsandi, M.

Scientific-Practical Materials Research Centre of the National Academy of Sciences of Belarus
Minsk, Belarus
- Demyanov, S.E.
- Kaniukov, E.Yu.

Siemens AG
Erlangen, Germany
- Heid, O.
- Hughes, T.J.S.

Siemens LLC
Moscow, Russia
- Bondarenko, T.V.
- Sharkov, G.B.

Siemens Research Center
Moscow„ Russia
- Ivanov, E.V.
- Nikolskiy, K.I.
- Polikhov, S.A.
- Smirnov, A.Yu.
- Tikhomirova, N.V.

SLAC
Menlo Park, California, USA
- Stupakov, G.V.

Soreq NRC
Yavne, Israel
- Ben Aliz, Y.
- Berkovits, D.
- Dudovich, O.
- Eliyahu, I.
- Fishman, I.
- Gertz, I.G.
- Grin, A.
- Kreisler, A.
- Lempert, G.
- Mardor, I.
- Perry, A.
- Reinfeld, E.
- Rodnizki, J.
- Weissman, L.

SSU
Sumy, Ukraine
- Baturin, V.A.
- Ignatev, I.G.
- Karpenko, A.Yu.
- Litvinov, P.A.
- Pustovoitov, S.A.

St. Petersburg State University
St. Petersburg, Russia
- Altsybeyev, V.V.
- Andrianov, S.N.
- Antonov, A.Yu.
- Antonova, L.I.
- Drivotin, O.I.
- Egorov, N.V.
- Golovkina, A.G.
- Gordeev, D.F.
- Ivanov, A.N.
- Kotina, E.D.
- Kozynchenko, S.A.
- Kozynchenko, V.A.
- Kulabukhova, N.V.
- Maximov, C.M.
- Nikiforov, K.A.
- Ovsyannikov, A.D.
- Ovsyannikov, D.A.
- Ploskikh, V.A.
- Rubtsova, I.D.
- Shirokolobov, A.Yu.
- Suddenko, E.N.
- Televnyi, D.S.
- Trofimov, V.V.
- Varajun, M.I.
- Yelaev, Y.V.

TPU
Tomsk, Russia
- Gogolev, A.S.
- Uglov, S.R.

TRIUMF, Canada's National Laboratory for Particle and Nuclear Physics
Vancouver, Canada
- Amini, B.
- Fong, K.
- Harmer, P.R.
- Kishi, D.
- Kolb, P.
- Koveshnikov, A.
- Lang, D.
- Laxdal, R.E.
- Mitra, A.K.
- Muller, N.
- Schaub, C.
- Shanks, R.W.
- Waraich, B.S.
- Zheng, Q.
- Zvyagintsev, V.

TUB
Beijing, People's Republic of China
- He, Z.Q.

UBC
Vancouver, B.C., Canada
- Vrielink, A.

UMD
College Park, Maryland, USA
- Liu, C.-S.
- Liu, T.-C.
- Sagdeev, R.Z.
- Shao, X.
- Su, J.J.

Uni HH
Hamburg, Germany
- Mehrling, T.
- Osterhoff, J.

University of Minnesota
Minneapolis, Minnesota, USA
- Kriske, R.M.

University of Toronto
Toronto, Ontario, Canada
- Abidi, S.H.
- Orr, R.S.

UPC
Barcelona, Spain
- Kubyshin, Yu.A.
- Rigla, J.P.

Uzbekistan Academy of Sciences, The Institute of Nuclear Physics
Tashkent, Uzbekistan
- Gulamov, I.R.
- Shukurov, Z.V.
- Umerov, R.A.
- Uzakov, Ya.M.

VINCA
Belgrade, Serbia
- Beličev, P.
- Dobrosavljević, A.
- Nešković, N.
- Vujović, V.

VNIIEF
Sarov (Nizhnii Gorod), Russia
- Basmanov, V.F.
- Devyatkin, A.A.
- Gordeev, V.S.

- Gornostay-Polsky, S.A.
- Grishin, A.V.
- Grunin, A.V.
- Kolesov, V.F.
- Myskov, G.A.
- Nazarenko, S.T.
- Punin, V.T.
- Savchenko, V.A.
- Telnov, A.V.
- Vorintsov, S.
- Zavyalov, N.V.

Yale University, Beam Physics Laboratory
New Haven, Connecticut, USA
- Shchelkunov, S.V.

Yale University, Physics Department
New Haven, CT, USA
- Hirshfield, J.L.

YSU
Yerevan, Armenia
- Kotanjyan, A.
- Saharian, A.A.

Zanjan University
Zanjan, Iran
- Khosravi, N.

Participants List

Last Name	First Name(s)	Affiliation	E-mail
Afonin	Alexander	IHEP, Protvino	afonin <at> ihep.ru
Akhmanova	Ekaterina	JINR	ahmanova <at> jinr.ru
Alekseev	Petr	ITEP	palex <at> itep.ru
Alexandrov	Vladimir	JINR	aleks <at> jinr.ru
Alexeev	Nikolay	ITEP	nalex <at> itep.ru
Aleynik	Vladimir	BINP SB RAS	v.i.aleynik <at> inp.nsk.su
Aliev	Kara-Ali	NRNU MEPhI	alien-box <at> yandex.ru
Altmark	Alexander	Saint-Petersburg Electrotechnical University	aaltmark <at> mail.ru
Altsybeyev	Vladislav	SPbSU	altsybeyev <at> gmail.com
Andreev	Vladimir	ITEP	andreev <at> itep.ru
Andrianov	Serge	SPbSU	sandrianov <at> yandex.ru
Antonov	Andrew	SPbSU	antonov_emsm <at> hotmail.com
Artamonov	Stanislav	Petersburg Nuclear Physics Institute (PNPI)	start <at> pnpi.spb.ru
Asgarpour	Mehdi	Shahid Beheshti University	mehdi.ap77 <at> gmail.com
Astrelina	Kseniya	BINP SB RAS	ks.astrelina <at> gmail.com
Azaryan	Nikolay	JINR	azaryan <at> jinr.ru
Banerjee	Ajoy	Variable Energy Cyclotron Centre	ajoybanerjee2011 <at> gmail.com
Barminova	Helen	ITEP	barminova <at> bk.ru
Barnyakov	Aleksey	BINP SB RAS	skalpel <at> inbox.ru
Bashmakov	Yuriy	P.N.Lebedev Physical Institute RAS	bashm <at> x4u.lebedev.ru
Baturin	Stanislav	SPbETU (LETI)	s.s.baturin <at> gmail.com
Baturin	Volodymyr	Institute of Applied Physics NAS of Ukraine	baturin49 <at> gmail.com
Bekhtenev	Evgeniy	BINP SB RAS	e.a.bekhtenev <at> inp.nsk.su
Belonogaya	Ekaterina	SPbSU, LETI	ekaterinabelonogaya <at> yandex.ru
Bezuglov	Vadim	BINP SB RAS	bezuglow <at> rambler.ru
Bogdanov	Aleksey	Krylov Shipbuilding Research Institute	KSRI42422 <at> gmail.com
Bogomolov	Sergei	JINR	bogomol <at> nrmail.jinr.ru

Bolshakov	Boris	NIIEFA	Bolshakov.BO <at> luts.niiefa.spb.su
Bondarenko	Taras	NRNU MEPhI	tvbondarenko <at> mephi.ru
Borgulev	Miron	Rosnano	
Boriskin	Viktor	NSC KIPT	boriskin <at> kipt.kharkov.ua
Bornschein	Lutz	Karlsruhe Institute of Technology, Institute for Nuclear Physics	lutz.bornschein <at> kit.edu
Bryazgin	Alexander	BINP SB RAS	A.A.Bryazgin <at> inp.nsk.su
Bubley	Alexander	BINP SB RAS	bubley <at> inp.nsk.su
Bystrov	Peter	MRTI RAS	bpeter <at> mail.ru
Chepurnov	Alexander	Марафон	
Chernousov	Yuriy	ICKC SB RAS	chern <at> catalysis.ru
Chikhachev	Alexander	All-Russian Electrotechnical Institute	churchev <at> mail.ru
Conradie	Lowry	iThemba LABS	lowry <at> tlabs.ac.za
Cousin	Richard	CST	
Demsky	Mikhail	CORAD Ltd	corad.pro <at> gmail.com
Dietrich	Juergen	TU Dortmund and Helmholtz Institute Mainz	juergen.dietrich <at> tu-dortmund.de
Doll	Jochen	GLYNVED RUSSIA	
Donets	Evgeny	JINR	ddonets <at> sunhe.jinr.ru
Dovbnya	Anatoliy	NSC KIPT	dovbnya <at> kipt.kharkov.ua
Drivotin	Oleg	SPbSU	drivotin <at> yandex.ru
Drozdovskiy	Alexander	ITEP	drozdovsky <at> itep.ru
Dudnikov	Andrei	BINP SB RAS	andreidud <at> gmail.com
Dudnikova	Galina	ICT SB RAS	gdudnikova <at> gmail.com
Durkin	Alexander	MRTI RAS	durkinap <at> mail.ru
Dydnikov	Vadim	Muons, Inc.	dvg43 <at> yahoo.com
Ebrahimibasabi	Ehsan	Shahid Beheshti University	ehsan.eb.64 <at> gmail.com
Edamenko	Nikolay	SPbSU	nse47 <at> yandex.ru
Egorov	Nicolaj	SPbSU	robby7 <at> mail.ru
Eliseev	Alexey	JINR	aeliseev <at> jinr.ru

Eseev	Marat	Northern (Arctic) Federal University named after M. V.	m_eseev <at> mail.ru
Fadeev	Alexey	NRNU MEPhI	amfadeev <at> gmail.com
Fateev	Anatoly	JINR	fateev <at> sunse.jinr.ru
Feschenko	Alexander	Institute for Nuclear Research of the Russian Academy of Sciences	feschenk <at> inr.ru
Filatov	Georgiy	JINR	filatov.jinr <at> mail.ru
Filatov	Oleg	NIIEFA	filatov <at> niiefa.spb.su
Filippov	Dmitriy	Intech	sevryukova <at> ihep.ru
Fischer	Egbert	GSI Darmstadt	e.fischer <at> gsi.de
Fomin	Yevgeniy	NRC Kurchatov Institute	yafomin <at> gmail.com
France	Alain	CEA/DSM/IRFU,	afrance <at> cea.fr
Frolov	Oleg	Institute for Nuclear Research of RAS	f45ot <at> mail.ru
Galaydych	Konstantin	KIPT	kgalaydych <at> gmail.com
Galyamin	Sergey	SPbSU, Phisical fac	galiaminsn <at> yandex.ru
Gambaryan	Vaagn	BINP SB RAS	gambaryanv <at> gmail.com
Gavrilov	Sergei	INR RAS	s.gavrilov <at> gmail.com
Gavrish	Yuriy	NIIEFA	npkluts <at> luts.niiefa.spb.su
Getmanov	Yaroslav	BINP SB RAS	y_getmanov <at> mail.ru
Ghasem	Hossein	IPM, Tehran	ghasem <at> ipm.ir
Gikal	Boris	JINR	gikal <at> nrmail.jinr.ru
Glukhikh	Vasiliy	NIIEFA	vag <at> niiefa.spb.su
Gogolev	Aleksey	Tomsk Polytechnic University	gogolev <at> tpu.ru
Golovkina	Anna	SPbSU	golovkina.a <at> gmail.com
Gonchar	Olga	NSC KIPT	ogonchar <at> kipt.kharkov.ua
Goncharova	Anastasia	SPbSU	
Gordeev	Dmitry	SPbSU	dima31415 <at> gmail.com
Grekov	Oleg	INR RAS	
Gribov	Igor	Maraphon	
Guchkin	Alexander	NIITFA	

Guk	Ivan	NSC KIPT	guk <at> kipt.kharkov.ua
Gulbekyan	Georgy	JINR	georgy <at> nrmail.jinr.ru
Gusarova	Mariya	NRNU MEPhI	MAGusarova <at> mephi.ru
Gusev	Igor	BINP SB RAS	i.a.gusev <at> inp.nsk.su
HAN	BUMSOO	EB TECH CO., LTD	bshan <at> eb-tech.com
Hollinger	Ralph	GSI	r.hollinger <at> gsi.de
Horodek	Pawel	JINR	Pawel.Horodek <at> ifj.edu.pl
Hrovatin	Rok	Instrumentation Technologies, d. d.	tanja.hladnik <at> i-tech.si
Ignat'ev	Igor	Istitute of Applied Physics, Academy of Sciences of Ukraine	iignatew <at> yandex.ru
Ivanov	Andrei	SPbSU	05x.andrey <at> gmail.com
Ivanov	Eugeny	Petersburg Nuclear Physics Institute (PNPI)	vanovem <at> pnpi.shd.ru
Ivanov	Sergey	IHEP Protvino	sergey.ivanov <at> ihep.ru
Jameson	Robert	Inst. Applied Physics	jameson <at> riken.jp
Kalikov	Boris	INR RAS	kalikhov <at> inr.ru
Kamerdzhiev	Vsevolod	Forschungszentrum Juelich	v.kamerdzhiev <at> fz-juelich.de
Kanareykin	Alexei	Euclid TechLabs	alexkan <at> euclidconcepts.com
Kaportsev	Eugene	NRC Kurchatov Institute	kaporcev <at> gmail.com
Karamysheva	Galina	JINR	galina.karamysheva <at> gmail.com
Katayama	Takeshi	GSI	tkatayama.vc <at> nifty.com
Kats	Mark	ITEP	markmkats <at> gmail.com
Khankin	Vadim	Skobeltsyn Institute of Nuclear Physics , Lomonosov Moscow	v-k32 <at> yandex.ru
Khodzhibagiyan	Hamlet	JINR	hamlet <at> jinr.ru
Kniaziev	Roman	Kharkov national university of the name V.N.Karazin	titannatit <at> yandex.ru
Kobets	Andriy	JINR	kobets <at> jinr.ru
Kobets	Valeriy	JINR	vkobets <at> jinr.ru
Kogut	Dmitrij	BINP SB RAS	dkogut <at> mail.ru
Konyashin	Alexander	National Instruments	evgenia.kurguzova <at> ni.com
Korchuganov	Vladimir	NRC Kurchatov Institute	vnkorchuganov <at> mail.ru

Kostromin	Sergey	JINR	kostromin <at> jinr.ru
Kotina	Elena	SPbSU	ekotina123 <at> mail.ru
Kozub	Sergey	Institute for High Energy Physics	kozub <at> ihep.ru
Kozynchenko	Sergey	SPbSU	Sergey_Kozyntchenko <at> hotmail.com
Kozynchenko	Vladimir	SPbSU	vladkoz <at> mail.ru
Krylov	Yury	All-Russian Electrotechnical Institute	krylov_yv <at> nrcki.ru
Kudinovich	Igor	Krylov Shipbuilding Research Institute	igor_kudinovich <at> mail.ru
Kuksanov	Nikolay	BINP SB RAS	kuksanov47 <at> mail.ru
Kulabukhova	Natalia	SPbSU	kulabukhova.nv <at> gmail.com
Kulago	Alexander	MEPhI	kulago_ne <at> mail.ru
Kurakin	Vyacheslav	Lebedev Physical Institute	postmaster <at> lebedev.ru
Kuzin	Maxim	BINP SB RAS	kuzin <at> inp.nsk.su
Kuznetsov	Sergey	JINR	shenau <at> rambler.ru
Kuznetsov	Alexander	BINP SB RAS	a.s.kuznetsov <at> inp.nsk.su
Kvasha	Adolf	Institute for nuclear research RAS	kvasha <at> inr.ru
Kwiatkowski	Slawomir	LBNL	skwiatkowski <at> lbl.gov
Lalayan	Mikhail	NRNU MEPhI	mvlalayan <at> mephi.ru
Lampe Rupnik	Mateja	Instrumentation Technologies, d. d.	tanja.hladnik <at> i-tech.si
Lancelot	Jean-luc	SIGMAPHI	contact <at> sigmaphi.fr
lazarev	Vitalii	Siemens LLC	vitali.lazarev <at> siemens.com
Lebedev	Oleg	Institute for High Energy Physics (IHEP)	Oleg.Lebedev <at> ihep.ru
Levichev	Eugene	BINP SB RAS	levichev <at> inp.nsk.su
Litvinov	Sergey	GSI Darmstadt	S.Litvinov <at> gsi.de
Makarov	Alexandr	BINP SB RAS	alexxmak314 <at> gmail.com
Makarova	Margarita	SPbSU	vincat2008 <at> yandex.ru
Malyshev	viktor	NIIEFA	vm <at> eltech.ru
Malyutin	Dmitriy	DESY	dm.malyutin <at> gmail.com
Meshkov	Igor	JINR	meshkov <at> jinr.ru

Mizintseva	Maria	SPbSU	lqi87 <at> yandex.ru
Moseiko	Nikolai	NRC	nmoseiko <at> mail.ru
Moseyev	Kirill	NRC Kurchatov Institute	kirit <at> yandex.ru
Mudrolyubov	Victor	NIIEFA	Mudrolubov_VG <at> luts.niiefa.spb.su
Mustafin	Edil	GSI Darmstadt	e.mustafin <at> gsi.de
Nagaitsev	Sergei	FNAL	nsergei <at> fnal.gov
Nikiforov	Konstantin	SPbSU	nikiforov_k <at> mail.ru
Nikolaev	Alexey	Марафон	
Noda	Akira	Institute for Chemical Ressearch, Kyoto University	noda <at> kyticr.kuicr.kyoto-u.ac.jp
Nozdrin	Mikhail	JINR	nozdrin <at> jinr.ru
O'HARA	Patrick	Intech	
Orlov	Andrey	SSC RF ITEP	Andrey.Orlov <at> itep.ru
Ovchinnikov	Valeriy	NIIEFA	ovchinnikov <at> luts.niiefa.spb.su
Ovsyannikov	Alexander	SPbSU	ovs74 <at> mail.ru
Ovsyannikov	Dmitri	SPbSU	dovs45 <at> mail.ru
Panteleev	Vladimir	Petersburg Nuclear Physics Institute (PNPI)	vnp <at> pnpi.spb.ru
Pfister	Jochen	GSI	j.pfister <at> gsi.de
Ploskikh	Victor	SPbSU	manac2000 <at> mail.ru
Polozov	Sergey	NRNU MEPhI	SMPolozov <at> mephi.ru
Ponomareva	Elena	INR RAS	ponomlen <at> inr.ru
POULET	Frederic	CEA DAM	frederic.poulet <at> cea.fr
Proskin	Stanislav	NRNU MEPhI	qstpss <at> gmail.com
Reinhardt-Nickoulin	Petr	Institute for Nuclear Research of RAS	petrrein <at> inr.ru
Repikhov	Oleg	NSC KIPT	repikhov <at> kipt.kharkov.ua
Repkov	Vladimir	Institute of Nuclear Physics	v.v.repkov <at> inp.nsk.su
Reshetnyak	Nikolay	NSC KIPT	reshetnyak <at> kipt.kharkov.ua
Riabov	German	Petersburg Nuclear Physics Institute (PNPI)	riabov <at> pnpi.spb.ru
Rubtsova	Irina	SPbSU	rubtsova05 <at> mail.ru

Rudanov	Grigory	National Instruments	evgenia.kurguzova <at> ni.com
Ryabtsev	Alexander	ITEP	aleksandr.ryabtsev <at> itep.ru
Rybitskaya	Tatyana	BINP SB RAS	tanij-r <at> mail.ru
Savchenko	Igor	SPbSU	mail.nsdolphin <at> gmail.com
Scarlat	Florea	INFLPR	scarlat.f <at> gmail.com
Schmickler	Hermann	CERN	hermann.schmickler <at> cern.ch
Schnizer	Pierre	GSI Darmstadt	p.schnizer <at> gsi.de
SERBO	Valeriy	Novosibirsk State University	serbo <at> math.nsc.ru
Serov	Valeriy	Institute for Nuclear Research of the Russian Academy of Sciences	serov <at> inr.ru
Seryi	Andrei	John Adams Institute	andrei.seryi <at> adams-institute.ac.uk
Sessler	Andrew	Lawrence Berkeley National Laboratory, MS 71B-287	AMSessler <at> lbl.gov
Shamarin	Alexander	Марафон	
Sharkov	Boris	ITEP	boris.sharkov <at> itep.ru
Sharkov	Georgiy	Siemens LLC	georgy.sharkov <at> siemens.com
Sharlay	Artem	SPbSU	sharlayar <at> mail.ru
Sharma	Vijay	Bhabha Atomic Research Centre	vijay9819420563 <at> gmail.com
Shatunov	Yury	BINP SB RAS	shatunov <at> inp.nsk.su
Shcherbakov	Alexander	NSC KIPT	shcherbakov <at> kipt.kharkov.ua
Shebolaev	Igor	ICKC SB RAS	lacgroup <at> catalysis.ru
Shestakova	Valentina	NSC KIPT	
Shevchenko	Oleg	BINP SB RAS	O.A.Shevchenko <at> inp.nsk.su
Sheynman	Ilya	SPbETU (LETI)	isheinman <at> yandex.ru
Shirkov	Grigory	JINR	shirkov <at> jinr.ru
Shirokolobov	Alexander	SPbSU	aleksandr.shir <at> gmail.com
Shishanin	Oleg	Moscow State Industrial University	shisha-n <at> msiu.ru
Shmyrov	Vasiliy	SPbSU	vasilyshmyrov <at> yandex.ru
Shtarklev	Evgeny	BINP SB RAS	shtarklev <at> gmail.com
Shurkhno	Nikolay	MSU	shurkhno <at> physics.msu.ru

Sidorin	Aleksey	JINR	aleksei_sidorin <at> mail.ru
Sidorin	Anatoly	JINR	sidorin <at> jinr.ru
Silkin	Alexander	GLYNVED RUSSIA	silkin_mike <at> pht.univer.kharkov.ua
Singer	Waldemar	DESY	waldemar.singer <at> desy.de
Singer	Xenia	DESY	xenia.singer <at> desy.de
Skorobogatov	Dmitry	BINP SB RAS	d.n.skorobogatov <at> inp.nsk.su
Skrinsky	Alexander	BINP SB RAS	skrinsky <at> inp.nsk.su
Smirnov	Alexander	NRNU MEPhI	smirnov.alexander <at> siemens.com
Smirnov	Alexander	JINR	smirnov <at> jinr.ru
Smirnov	Victor	JINR	vsmirnov <at> jinr.ru
Smirnov	Alexei	RadiaBeam Technologies	asmirnov <at> radiabeam.com
Smygacheva	Antonina	NRC Kurchatov Institute	sasmyga <at> mail.ru
Sokol	Vratislav	CST	
Solnyshkov	Dmitriy	NIIEFA	d-soln <at> luts.niiefa.spb.su
sorokin	Igor	BINP SB RAS	astar <at> inp.nsk.su
Sotnikov	Gennadij	NSC KIPT	sotnikov <at> kipt.kharkov.ua
Spiller	Peter	GSI Darmstadt	p.spiller <at> gsi.de
Starostenko	Alexander	BINP SB RAS	staxiv <at> mail.ru
Steck	Markus	GSI Darmstadt	M.Steck <at> gsi.de
Stirin	Alexander	nrc kurchatov institute	staxiv <at> mail.ru
Strokach	Andrey	NIIEFA	directorluts <at> luts.niiefa.spb.su
Stupakov	Gennady	SLAC	stupakov <at> slac.stanford.edu
Styuf	Aleksey	BINP SB RAS	a-styuf <at> yandex.ru
Sukhov	Vyacheslav	VMA	
Sumbaev	Anatoly	JINR	sumbaev <at> nf.jinr.ru
Svistunov	Yuri	NIIEFA	svistunov <at> luts.niiefa.spb.su
Syresin	Evgeny	JINR	syresin <at> nu.jinr.ru
Sysoev	Dmitry	RRCRST	dssysoev <at> mail.ru

Sytov	Alexei	Belarusian State University, Research Institute for Nuclear	alex_sytov <at> mail.ru
Taskaev	Sergey	BINP SB RAS	taskaev <at> inp.nsk.su
Tatsyuk	Oleg	Mephi	oleg-mephi <at> mail.ru
Televnyi	Denys	SPbSU	vincat2008 <at> yandex.ru
Tolstun	Nikolay	NIIEFA	ngtolstun <at> yahoo.com
Trofimov	Vasiliy	SPbSU	vavtr <at> mail.ru
Trubnikov	Grigory	JINR	trubnikov <at> jinr.ru
Tsymbal	Vladimir	NSC KIPT	wind <at> kipt.kharkov.ua
Tur	Yuriy	NSC KIPT	tur <at> kipt.kharkov.ua
Tyukhtin	Andrey	SPbSU, Phisical fac	tyukhtin <at> bk.ru
Usanova	Marina	NiEFA	
Uvarov	Vyacheslav	NSC KIPT	uvarov <at> kipt.kharkov.ua
Valentinov	Alexander	NRC Kurchatov Institute	a.g.valentinov <at> mail.ru
Varajun'	Marina	SPbSU	antonov_emsm <at> hotmail.com
Vasiliev	Ivan	INR RAS	vasilyev <at> inr.ru
Vinogradova	Ekaterina	SPbSU	vincat2008 <at> yandex.ru
Vinokurov	Nicolay	BINP SB RAS	nikolay.vinokurov <at> gmail.com
Vladimirov	Ivan	Skobeltsyn Institute of Nuclear Physics , Lomonosov Moscow	timerke <at> mail.ru
Vorobjov	Viktor	SPbSU	
Vorogushin	Mikhail	NIIEFA	vorogushin <at> luts.niiefa.spb.su
Wang	Hanbin	CAEP/IAE	plzuhbw <at> hotmail.com
Weissman	Leonid	Soreq NRC	leo.weissman <at> gmail.com
Wolf	Andreas	Max Planck Institute for Nuclear Physics	A.Wolf <at> mpi-hd.mpg.de
Yakovenko	Sergey	JINR	yakoven <at> jinr.ru
Yaminov	Kamil	BINP SB RAS	yaminov <at> inp.nsk.su
Yamshikov	Gennadiy	Russian Academy of Sciences/Institute for Nuclear	yamshikov.gen <at> yandex.ru
Yelaev	Yevgeny	SPbSU	yelaevevgen <at> gmail.com
Yurov	Dmitry	Skobeltsyn Institute of Nuclear Physics, Lomonosov Moscow	d_yurov88 <at> mail.ru

Zakutin	Valeriy	NSC KIPT	zakutin <at> kipt.kharkov.ua
Zamriy	Victor	JINR	zamrij <at> nf.jinr.ru
Zavyalov	Nikolay	RFNC-VNIIEF	zavyalov <at> expd.vniief.ru
Zbigniew	Zimek	Institute of Nuclear Chemistry and Technology	z.zimek <at> ichtj.waw.pl
Zdorovenko	Vera	NSC KIPT	
Zenkevich	Pavel	ITEP	zenkevich <at> itep.ru
Zhabitsky	Vyacheslav	JINR	V.Zhabitsky <at> jinr.ru
Zhabko	Aleksey	SPbSU	
Zolotarev	Konstantin	BINP SB RAS	zolotarev <at> inp.nsk.su
Zuev	Yurii	NIIEFA	Yuri_Zuev <at> mail.ru
Zvyagintsev	Vladimir	TRIUMF	zvyagint <at> triumf.ca